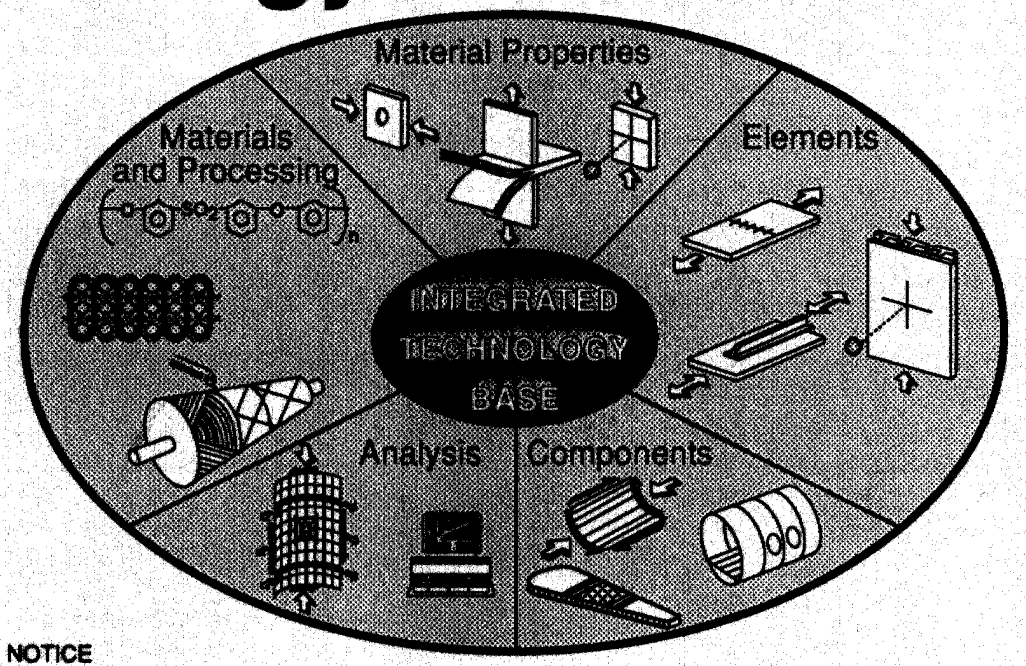
19960628 132

NASA Conference Publication 3104
Part 2

First NASA Advanced Composites Technology Conference



NOTICE

FOR EARLY DOMESTIC DISSEMINATION

Because of its significant early commercial potential, this information, which has been developed under a U.S. Government program, is being disseminated within the United States in advance of general publication. This information may be duplicated and used by the recipient with the express limitation that it not be published. Release of this information to other domestic parties by the recipient shall be made subject to these limitations.

Foreign release may be made only with prior NASA approval and appropriate export licenses. This legend shall be marked on any reproduction of this information in whole or in part.

Review for general release January 31, 1993

DISTRIBUTION STATEMENT A
Approved for public release
Distribution Unlimited

Proceedings of a conference held in
Seattle, Washington
October 29–November 1, 1990

PLASTEC 05470
Cpc-05470-pc-05470

DEPARTMENT OF DEFENSE
PLASTICS TECHNICAL EVALUATION CENTER
ARDEC PICATINNY ARSENAL, N.J. 07806

NASA

DTIC QUALITY INSPECTED 1

NASA Conference Publication 3104
Part 2

First NASA Advanced Composites Technology Conference

Compiled by
John G. Davis, Jr.
NASA Langley Research Center
Hampton, Virginia

Herman L. Bohon
Lockheed Engineering & Sciences Company
Hampton, Virginia

Proceedings of a conference sponsored by the National Aeronautics and Space Administration, Washington, D.C., and held in Seattle, Washington
October 29–November 1, 1990

NASA
National Aeronautics and Space Administration
Office of Management
Scientific and Technical Information Division
1991

PREFACE

The First NASA Advanced Composites Technology Conference was sponsored by the NASA Langley Research Center to review recent advances in research and development of advanced composites technology for applications to military and commercial aircraft. The NASA Advanced Composites Technology (ACT) Program is a major new multiyear research initiative to achieve a national goal of technology readiness before the end of the decade. This initiative is carried out through a cooperative program between industry, universities, and the Government conducting research in materials processing, analysis development, innovative designs and manufacturing methodology.

The First NASA Advanced Composites Technology Conference was held in Seattle, Washington, October 29 through November 1, 1990. The conference provided a forum for the composites community to exchange information and an opportunity to observe recent progress in advanced composites technology. Fifty-two papers were organized into sessions that emphasized composite transport technology development, advances in design and manufacturing, and research in materials and structural mechanics. In addition, a session sponsored by the Department of Defense emphasized lessons learned from current applications programs. This conference publication is a compilation which contains the papers presented in these sessions.

The use of trademarks or manufacturers' names in this publication does not constitute endorsement, either expressed or implied, by the National Aeronautics and Space Administration.

John G. Davis, Jr.
Herman L. Bohon

CONFERENCE ORGANIZATION

Sponsor: Structures Technology Program Office
Structures Directorate
NASA Langley Research Center
Hampton, VA

General Chairman	Technical Chairman	Administrative Assistant
John G. Davis, Jr.	Herman L. Bohon	Stuart E. Pendleton
NASA Langley	Lockheed Engineering & Sciences Company	Lockheed Engineering & Sciences Company

SESSION ORGANIZERS

John G. Davis, Jr.	NASA Langley Research Center
James H. Starnes, Jr.	NASA Langley Research Center
Norman J. Johnston	NASA Langley Research Center
David Beeler	Wright Research and Development Center

SESSION OUTLINE

FIRST NASA ADVANCED COMPOSITES TECHNOLOGY CONFERENCE

Session I

Composite Transport Technology
Chairman: **Michael F. Card**, Chief, Structural Mechanics Division
NASA Langley Research Center

Session II

Advances in Design and Manufacturing
Chairman: **Darrel Tenney**, Chief, Materials Division
NASA Langley Research Center

Session III

DoD Composites Applications
Chairman: **David Beeler**, Head, Nonmetals Branch
Wright Research and Development Center

Session IV

Materials Research
Chairman: **Norman J. Johnston**, Chief Scientist, Materials Division
NASA Langley Research Center

Session V

Work in Progress - Materials and Structures
Chairman: **W. Tom Freeman**, ACT Structures Technology Program Office
NASA Langley Research Center

Session VI

Structural Mechanics Research
Chairman: **James H. Starnes Jr.**, Head, Aircraft Structures Branch
Structural Mechanics Division, NASA Langley Research Center

CONTENTS

PREFACE iii

Conference Organization iv

Session Outline v

Part 1*

Luncheon Address: Composites: A Viable Option 3
John E. McCarty

Session I

Advanced Composite Structural Concepts and Material Technologies for Primary Aircraft Structures 39
Anthony Jackson

Composites Technology for Transport Primary Structure 71
Victor Chen, Arthur Hawley, Max Klotzsche, Alan Markus, and Ray Palmer

Advanced Technology Commercial Fuselage Structure 127
L. B. Ilcewicz, P. J. Smith, T. H. Walker, and R. W. Johnson

Session II

Design, Analysis and Fabrication of the Technology Integration Box Beam 157
C. F. Griffin and L. E. Meade

Design and Manufacturing Concepts for Thermoplastic Structures 179
Michael P. Renieri, Steven J. Burpo, and Lance M. Roundy

Structural Evaluation of Curved Stiffened Composite Panels Fabricated Using a Therm-X^{sm} Process 207
Christos Kassapoglou, Albert J. DiNicola, Jack C. Chou, and Jerry W. Deaton

Noise Transmission Properties and Control Strategies for Composite Structures 233
Richard J. Silcox, Todd B. Beyer, and Harold C. Lester

Long Discontinuous Fiber Composite Structure—Forming and Structural Mechanics 247
R. B. Pipes, M. H. Santare, B. J. O'Toole, A. J. Beaussart, D. C. DeHeer, and R. K. Okine

*These papers are presented in NASA CP-3104, Part 1.

Resin Transfer Molding for Advanced Composite Primary Aircraft Structures 271
Alan Markus and Ray Palmer

Consolidation of Graphite/Thermoplastic Textile Preforms for Primary Aircraft Structure 293
J. Suarez and J. Mahon

Cost Studies for Commercial Fuselage Crown Designs 339
T. H. Walker, P. J. Smith, G. Truslove, K. S. Willden, S. L. Metschan, and C. L. Pfahl

A Unified Approach for Composite Cost Reporting and Prediction in the ACT Program 357
W. Tom Freeman, Louis F. Vosteen, and Shahid Siddiqi

Session III

F-15 Composite Engine Access Door 371
Ramaswamy L. Ramkumar and James C. Watson

Fabrication of the V-22 Composite Aft Fuselage Using Automated Fiber Placement 385
Robert L. Pinckney

Lessons Learned for Composite Structures 399
R. S. Whitehead

Part 2

Session IV

Preliminary Properties of a Resin From Ethynyl Terminated Materials PL-054687 (419) 01
Paul M. Hergenrother and John W. Connell

Infiltration/Cure Modeling of Resin Transfer Molded Composite Materials Using Advanced Fiber Architectures 425
Alfred C. Loos, Mark H. Weideman, Edward R. Long, Jr., David E. Kranbuehl, Philip J. Kinsley, and Sean M. Hart

Powder Towpreg Process Development 443
Robert M. Baucom and Joseph M. Marchello

Effects of Intra- and Inter-Laminar Resin Content on the Mechanical Properties of Toughened Composite Materials PL-054688 (455) 02
Dodd H. Grande, Larry B. Ilcewicz, William B. Avery, and Willard D. Bascom

Studies of Fiber-Matrix Adhesion on Compression Strength PL-054689 (477) 03
W. D. Bascom, J. A Nairn, and D. J. Boll

The Initiation, Propagation, and Effect of Matrix Microcracks in Cross-Ply and Related Laminates PL-054690. 497 04
John A. Nairn, Shoufeng Hu, Siulie Liu, and Jong Bark

Comparison of Impact Results for Several Polymeric Composites Over a Wide Range of Low Impact Velocities PL-054691. 513 05
C. C. Poe, Jr., M. A. Portanova, J. E. Masters, B. V. Sankar, and Wade C. Jackson

Delaminations in Composite Plates Under Impact Loads PL-054692. 549 06
Scott R. Finn and George S. Springer

Micromechanics of Fatigue in Woven and Stitched Composites . PL-054693 579 07
B. N. Cox, M. S. Dadkhah, R. V. Inman, M. R. Mitchell, W. L. Morris, and S. Schroeder

Characterization of Multiaxial Warp Knit Composites PL-054694. 589 08
H. Benson Dexter, Gregory H. Hasko, and Roberto J. Cano

Development of Stitching Reinforcement for Transport Wing Panels PL-054695. 621 09
Raymond J. Palmer, Marvin B. Dow, and Donald L. Smith

Session V

Development of Resins for Composites by Resin Transfer Molding 647
Edmund P. Woo, Paul M. Puckett, and Shawn J. Maynard

Advanced Fiber/Matrix Material Systems PL-054696. 659 10
J. Timothy Hartness

Mechanical and Analytical Screening of Braided Composites for Transport Fuselage Applications PL-054697. 677 11
Mark J. Fedro, Christian Gunther, and Frank K. Ko

Ultrasonic Detection and Identification of Fabrication Defects in Composites PL-054698. 705 12
Edward R. Long, Jr., Susan M. Kullerd, Patrick H. Johnston, and Eric I. Madaras

Developments in Impact Damage Modeling for Laminated Composite Structures 721
Ernest F. Dost, William B. Avery, Gary D. Swanson, and Kuen Y. Lin

Multi-Parameter Optimization Tool for Low-Cost Commercial Fuselage Crown Designs 737
Zelda Zabinsky, Mark Tuttle, Douglas Graesser, Gun-In Kim, Darrin Hatcher, Gary Swanson, and Larry Ilcewicz

Comparison of Hand Laid-Up Tape and Filament Wound Composite Cylinders and Panels With and Without Impact Damage 749
Dawn C. Jegley and Osvaldo F. Lopez

Effects of Scale in Predicting Global Structural Response 761
R. B. Deo and H. P. Kan

Design and Analysis of Grid Stiffened Concepts for Aircraft Composite Primary Structural Applications PL-054699 779 (13)
Damodar R. Ambur

Optimization of Composite Sandwich Cover Panels Subjected to Compressive Loadings PL-054700. 791 (14)
Juan R. Cruz

A Comparison of Classical Mechanics Models and Finite Element Simulation of Elastically Tailored Wing Boxes 809
Lawrence W. Rehfield, Richard D. Pickings, Stephen Chang, and Michael Holl

Advanced Fiber Placement of Composite Fuselage Structures 817
Robert L. Anderson and Carroll G. Grant

Process and Assembly Plans for Low Cost Commercial Fuselage Structure 831
Kurtis Willden, Stephen Metschan, and Val Starkey

Session VI

Progressive Failure Methodologies for Predicting Residual Strength and Life of Laminated Composites PL-054701. 843 (15)
Charles E. Harris, David H. Allen, and T. Kevin O'Brien

Multiple Methods Integration for Structural Mechanics Analysis and Design 875
J. M. Housner and M. A. Aminpour

Probabilistic Composite Analysis 891
C. C. Chamis and P. L. N. Murthy

A Rayleigh-Ritz Analysis Methodology for Cutouts in Composite Structures 901
Steven G. Russell

Effects of Bolt-Hole Contact on Bearing-Bypass Damage-Onset Strength 921
John H. Crews, Jr. and Rajiv A. Naik

Prediction of Stiffener-Skin Separation in Composite Panels 939
Han-Pin Kan, Mary A. Mahler, and Ravi B. Deo

Experimental Behavior of Graphite-Epoxy Y-Stiffened Specimens Loaded in Compression 953
P. D. Sydow and M. J. Shuart

Structural Response of Bead-Stiffened Thermoplastic Shear Webs . PL-054702 969 (16)
Marshall Rouse

Evaluation of Some Scale Effects in the Response and Failure of Composite Beams 979
Karen E. Jackson and John Morton

An Overview of the Crash Dynamics Failure Behavior of Metal and Composite Aircraft Structures 1005
Huey D. Carden, Richard L. Boitnott, Edwin L. Fasanella, and Lisa E. Jones

Tailored Composite Wings With Elastically Produced Chordwise Camber 1037
Lawrence W. Rehfield, Stephen Chang, Peter J. Zischka, Richard D. Pickings, and Michael W. Holl

Part 2

PRELIMINARY PROPERTIES OF A RESIN FROM ETHYNYL TERMINATED MATERIALS

Paul M. Hergenrother and John W. Connell
Materials Division
NASA Langley Research Center
Hampton, VA

SUMMARY

A blend composed of an ethynyl terminated aspartimide (brittle component) and an ethynyl terminated arylene ether oligomer (tough component) was thermally cured to yield a resin which underwent preliminary evaluation to determine the potential for use in structural applications on aerospace vehicles. The blend exhibited good compression moldability, allowing for the fabrication of neat resin moldings, adhesive specimens and composites at temperatures of 250°C under a pressure of [1.4 MPa (200 psi)]. Neat resin moldings and adhesive specimens provided relatively high mechanical properties. Composite specimens provided promising results in spite of fiber misalignment, fiber washout and a small amount of panel warpage.

INTRODUCTION

As part of a NASA program to develop technology on high performance/high temperature structural resins, particularly composite matrices, the chemistry and properties of blends of ethynyl (acetylenic) terminated materials are under investigation (ref. 1-6). Specifically, low molecular weight diethynyl compounds such as ethynyl terminated aspartimides (ETA), are mixed with ethynyl terminated arylene ether oligomers (ETAE) of different molecular weights. The number average molecular weights (M_n) ranged from 3000 to 12,000 g/mole. The ETA served as the brittle thermosetting component while the ETAE was the tough linear component.

Various blends have been prepared and subsequently thermally cured under different conditions to determine the effect of composition and crosslink density on final resin properties. The objective was to obtain materials with good compression moldability and cured neat resins and composites with a favorable combination of mechanical properties at temperatures as high as 177°C. The work reported herein concerns the chemistry and the mechanical and physical properties of one of these blends.

EXPERIMENTAL

Ethynyl Terminated Aspartimide

The ethynyl terminated aspartimide was prepared from the reaction of N,N-bismaleimido-4,4,'-diphenylmethane and 3-ethynylaniline as previously reported (ref. 1). The aspartimide was obtained in the form of a tan solid as a mixture of d, l and meso stereoisomers, mp 104-110°C.

Ethynyl Terminated Arylene Ether Oligomer

The ethynyl terminated arylene ether oligomers was prepared following a known procedure (ref. 2) by reacting 4,4'-dichlorobenzophenone with a calculated excess of 9,9-bis(4-hydroxyphenyl)fluorene to afford a hydroxy terminated oligomer with M_n of ~ 8000 g/mole. The hydroxy terminated oligomer was subsequently end-capped with 4-ethynylbenzoyl chloride. The ETAE oligomer had an inherent viscosity of 0.29 dL/g and initial glass transition (T_g) of 238°C. The 300°C cured resin exhibited a T_g of 248°C.

Blend

The blend was prepared by dissolving an equal weight of each component in 1,4-dioxane to yield clear solutions. To isolate the blend, the solution was added to water in a high speed blender. The solid was collected, washed with water and stage-dried to 100°C under vacuum. These powders were used to prepare moldings and films. The blend had an initial T_g of 140°C and the cured resin exhibited a T_g of 245°C, fracture toughness (K_{Ic}) of [1.57 MPa $m^{1/2}$ (1425 psi $in^{1/2}$)] and a coefficient of thermal expansion (23 to 200°C) of 36.8 ppm/°C.

Films

Thin films [approximately 0.127 mm (5 mils thick)] of the blend were prepared by melt pressing powders of the blend at [6.7 to 10.3 MPa (1 to 1.5 Ksi)] for 0.5 h at 250°C. The film specimens [5.1 cm x 0.63 cm x 0.013 cm (2 in x 0.25 in x 0.005 in)] were bent back upon themselves to place the rounded portion under stress and immersed in hydraulic fluid (Chevron Hyjet IV) for 24 h and in chloroform for 1 h to determine sensitivity towards these solvents.

Molded Specimens

Powdered blend was compression-molded by heating to 200° and then 250°C, each for 0.5 h under [1.4 MPa (200 psi)] in a stainless steel mold. Miniature compact tension specimens [1.6 cm x 1.6 cm x 0.95 cm thick (0.62 in x 0.62 in x 0.375 in thick)] were machined from the moldings and subsequently tested to determine fracture toughness (K_{Ic}, critical stress intensity factor) according to ASTM E399 using four specimens per test.

Flat moldings [7.6 cm x 7.6 cm x 0.18 cm (3.0 in x 3.0 in x 0.070 in)] were prepared by compression-molding the powdered blend using the conditions described above. Dogbone specimens [6.35 cm x 0.92 cm x 0.18 cm (2.5 in x 0.375 x 0.070 in)] were machined from the moldings and subsequently tested to determine neat resin tensile properties according to ASTM D638 using four specimens per test.

Adhesive Specimens

Adhesive tape was prepared by multiple coating of 112-E glass (A-1100 finish) with a 1,4-dioxane solution (~ 30% solids content) of the blend and subsequently stage dried to 100°C for 1 h after each coat. The final volatile contents of the tapes were less than 1%. Standard adhesive specimens [bond area 2.54 cm (1.00 in) wide x 1.27 cm (0.5 in) overlap)] using titanium (Ti, 6Al-4V) adherends with a Pasa Jell 107 (Products Research and Chemical Corp., Semco Div.) surface treatment were fabricated using conditions similar to those described for the molded specimens. The Ti adherends were initially primed with a dilute 1,4-dioxane solution (~ 5% solid content) of the blend and subsequently dried at 100°C for 1 h. Tensile shear specimens were tested according to ASTM D1002 using four specimens per test condition.

Composite Specimens

Prepreg was prepared by using a 25% solid solution of the blend in 1,4-dioxane to coat unsized AS-4 (12K tow) carbon/graphite fiber on a drum winding machine. The solutions had Brookfield viscosities of ~ 400 centipoise at 23°C. After drying the prepreg to a final temperature of 100°C for 1 hour, the volatile content was ~ 1% (determined by heating a weighed piece of prepreg for 1 hour at 300°C). Unidirectional and cross-ply laminates were fabricated in a stainless steel mold by heating to 200°C and then 250°C for 0.5 hour each under [1.4 MPa (200 psi)]. In some cases the panels were postcured by heating at 250°C for 2 hours under [1.4 MPa (200 psi)]. After ultrasonic scanning to detect voids, the panels were cut into specimens and tested for various properties according to ASTM procedures. Fracture energy was determined by testing double cantilever beam specimens according to a previously reported method (ref. 7). Tensile, flexural and short beam shear properties were determined according to ASTM D-3518, D-790, and D-2344 respectively.

Radiation Exposure

Electron beam radiation exposure was performed on composite and neat resin test specimens. The specimens were exposed to 1 MeV electrons using a Radiation Dynamics, Inc., Dynamitron Model 1000/10 accelerator. The samples were mounted side by side on a temperature-controlled aluminum plate positioned in the uniform area of the electron beam. The absorbed dose and dose rate were calculated from current flux levels monitored with a Faraday cup mounted in the exposure area of the aluminum plate. The Faraday cup was calibrated through the use of National Bureau of Standards calibrated polymeric dosimeter films. The exposure chamber operated at a pressure of 2×10^{-7} torr and the temperature of the specimens did not exceed 40°C. The materials received doses of 5.5×10^{8} rads and 1.0×10^{9} rads at a dose rate of 5×10^{7} rads/h without interruption. After exposure the specimens were stored in a desiccator until tested.

Other Characterization

Differential Scanning Calorimetry (DSC) was performed at a heating rate of 20°C/min with the T_g taken at the inflection point of the ΔT versus temperature curve after heating the sample to 300°C and quenching. Coefficient of thermal expansion (CTE) measurements were performed on a DuPont 9900 Computer/Thermal Analyzer at a heating rate of 5°C/min over the temperature range of 25-200°C using an expansion probe.

RESULTS AND DISCUSSION

Although a number of different ETAs have been reported (ref. 1), the ETA in figure 1 was selected for this study because of the following factors. It is easy to synthesize and it exhibited a favorable combination of highly desirable processing properties such as low and broad melting range, low melt viscosity, and a wide range between the melting and curing temperatures. In addition, it cures to provide a material with relatively high solvent resistance and tensile modulus.

The ETAE was selected from a variety of candidates on the basis of compatibility with the ETA and providing a cured material with a relatively high T_g. The blend was readily prepared by dissolving an equal quantity of each component in 1,4-dioxane. A portion of the solution was poured into water to precipitate a solid for characterization and neat resin molding studies. The remaining solution was used to prepare adhesive tape and prepreg.

The initial neat resin properties of the cured blend and those after exposure to various conditions are presented in table 1. The initial properties after a 0.5 hr cure at 250°C under [1.4 MPa (200 psi)] are respectable and suggest that this material should perform well as a composite matrix. The room temperature tensile properties were essentially unchanged after processing for 2 hr at 250°C. The tensile modulus of 3.6 GPa should be adequate to support the composite reinforcement filaments under compressive loading, thereby inhibiting microbuckling of the fibers. Upon exposure, the T_g and tensile modulus increased with a decrease in the elongation. This is due to further cure that resulted in higher crosslink density.

The Ti to Ti tensile shear strengths are given in table 2. The initial strengths at 23 and 150°C are relatively good whereas the initial 177°C value was low, presumably due to inadequate cure. After aging specimens for 650 hr at 200°C in air, further cure occurred that is reflected in a lower 23°C strength and a significantly higher 177°C value. In essence, after exposure for 650 hr at 200°C in air, the 23, 150 and 177°C values are essentially the same (within the scatter normally obtained for tensile shear specimens).

Small flat composites were fabricated from solution-coated drum-wound prepreg using unsized AS-4 fiber. No work was conducted to optimize prepreg preparation or composite processing conditions. The initial laminates exhibited problems frequently associated with the use of drum-wound prepreg. These include fiber misalignment, non-uniform resin content and areas of poor fiber wetting. In addition, the cured composites exhibited fiber washout and a small amount of warpage. Further work will be performed in an attempt to correct these problems. The preliminary laminate properties are presented in table 3. In

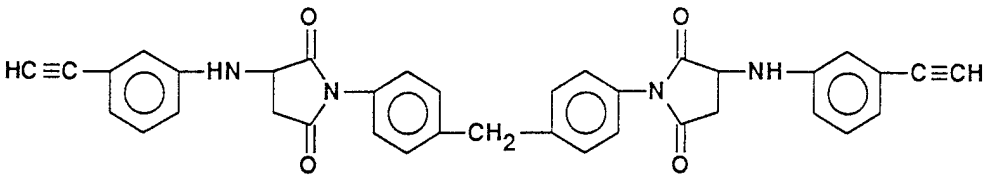
spite of the quality of the laminates, promising mechanical properties were obtained. The retention of flexural strength and modulus at 150 and 177°C after a cure for 2 hr at 250°C under [1.4 MPa (200 psi)] is particularly noteworthy. It appears that a 2 hr cure at 250°C is necessary to develop useable properties at 177°C. In addition, fracture energy of [438 J/m^2 (2.5 in lb/in^2)] is an acceptable value.

CONCLUSIONS

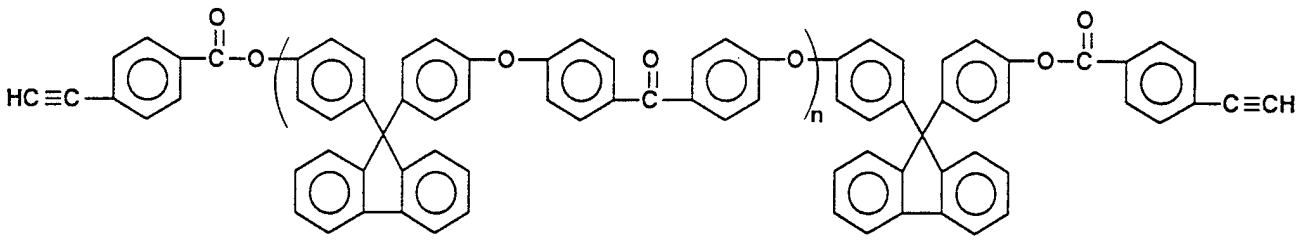
A blend of an ethynyl containing aspartimide and an ethynyl terminated arylene ether oligomer (M_n ~ 8000 g/mol) was prepared, characterized and evaluated as a composite matrix. The material performed well despite problems associated with prepreg quality. Further efforts will be expended to overcome these shortcomings.

REFERENCES

1. P. M. Hergenrother, S. J. Havens and J. W. Connell, Polym. Prepr. 27(2), 408 (1986)
2. J. W. Connell, R. G. Bass and P. M. Hergenrother, Sci. Adv. Matl. Proc. Eng. Series 33, 251 (1988)
3. J. W. Connell and P. M. Hergenrother, Intl. SAMPE Tech. Conf. Series 21, 1029 (1989)
4. J. W. Connell, P. M. Hergenrother and S. J. Havens High Perf. Polym. J. 1(2), 119 (1989)
5. P. M. Hergenrother, J. W. Connell and S. J. Havens U.S. Pat. 4,889,912 (1989) to NASA
6. J. W. Connell, R. G. Bass and P. M. Hergenrother U.S. Pat. 4,861,882 (1989) to NASA
7. J. M. Whitney, C. E. Browning and W. J. Hoogsteden, Reinf. Plast. Composites, 1, 297 (1982)



Ethynyl Terminated Aspartimide (ETA)



Ethynyl Terminated Arylene Ether Oligomer (ETAE $\bar{M}_n$~ 8000 g/mol, n = ~15)

Figure 1. Chemical structure of blend components.

Table 1 - Neat Resin Properties

Property	Cure and/or Exposure Conditions: 0.5 hr @ 250°C/200 psi	0.5 hr @ 250°C/200 psi 650 hr @ 200°C, air	0.5 hr @ 250°C/200 psi 1 X 10^9 Rads (electron beam exposure)	2 hr @ 250°C/200 psi
Tg, °C	245	254	254	249
Tensile St., MPa (Ksi)	93.1 (13.5)	95.8 (13.9)	76.5 (11.1)	89.0 (12.9)
Tensile Mod., GPa (Ksi)	3.6 (525)	3.9 (569)	3.9 (571)	3.55 (515.5)
Elong. (break), %	2.6	2.4	2.0	2.6
K_{Ic}, MPa $m^{1/2}$ (psi $in^{1/2}$)	1.57 (1425)	—	—	—
G_{Ic}, J/m^2 (in lb/in^2)	675 (3.8)	—	—	—
Coef. Therm. Expansion, ppm/°C	36.8	34.7	—	—

Table 2 - Ti to Ti Tensile Shear Strengths

Test Condition	Strength, MPa (psi) [failure mode]
23°C	22.8 (3300) (cohesive)
23°C after 650 hr @ 200°C, air	17.9 (2600) (mixed)
150°C	17.2 (2500) (cohesive)
150°C after 650 hr @ 200°C, air	20.5 (2975) (mixed)
177°C	8.3 (1200) (thermoplastic)
177°C after 650 hr @ 200°C, air	18.6 (2700) (mixed)

Table 3 - Preliminary Unidirectional Laminate Properties

Property	Cure and Exposure Conditions	Resin Content, %	Test Temperature, °C 23	150	177
Tensile St., MPa (Ksi)	2 hr @ 250°C/1.4 MPa	35	1917 (278)	1737 (252)	—
Tensile Mod., GPa (Msi)			121 (17.6)	139 (20.2)	—
Tensile Strain, %			1.33	1.21	—
Flexural St., MPa (Ksi)	0.5 hr @ 250°C/1.4 MPa	36	1613 (234)	683 (99)	—
Flexural Mod., GPa (Msi)			106 (15.4)	60.0 (8.7)	—
Flexural St., MPa (Ksi)	0.5 hr @ 250°C/1.4 MPa	36	1530 (222)	1323 (192)	1214 (176)
Flexural Mod., GPa (Msi)	650 hr @ 200°C, air		99.3 (14.4)	104 (15.1)	89.6 (13.0)
Flexural St., MPa (Ksi)	0.5 hr @ 250°C/1.4 MPa	36	1661 (241)	1131 (164)	—
Flexural Mod., GPa (Msi)	1 X 10^9 rads		108 (15.6)	90.3 (13.1)	—
Flexural St., MPa (Ksi)	2 hr @ 250°C/1.4 MPa	33	1517 (220)	1462 (212)	1359 (197)
Flexural Mod., GPa (Msi)			104 (15.1)	100 (14.5)	97.2 (14.1)
Flexural St., MPa (Ksi)	2 hr @ 250°C/1.4 MPa 500 hr @ 200°C, air	33	1483 (215)	1290 (187)	1124 (163)
Flexural Mod., GPa (Msi)			102.7 (14.9)	97.2 (14.1)	90.3 (13.1)
Short Beam Shear St., MPa (Ksi)	0.5 hr @ 250°C/1.4 MPa	38	74.5 (10.8)	32.4 (4.7)	29.0 (4.2)
Fracture Energy (G_{Ic}), J/m^2 (in lb/in^2)	2 hr @ 250°C/1.4 MPa	36	438 (2.5)	—	—

INFILTRATION/CURE MODELING OF RESIN TRANSFER MOLDED COMPOSITE MATERIALS USING ADVANCED FIBER ARCHITECTURES[1]

Alfred C. Loos and Mark H. Weideman
Virginia Polytechnic Institute and State University

Edward R. Long, Jr.
Langley Research Center

David E. Kranbuehl, Philip J. Kinsley and Sean M. Hart
College of William and Mary

SUMMARY

A model was developed which can be used to simulate infiltration and cure of textile composites by resin transfer molding. Fabric preforms were resin infiltrated and cured using model generated optimized one–step infiltration/cure protocols. Frequency–dependent electromagnetic sensing (FDEMS) was used to monitor in situ resin infiltration and cure during processing. FDEMS measurements of infiltration time, resin viscosity, and resin degree of cure agreed well with values predicted by the simulation model. Textile composites fabricated using a one–step infiltration/cure procedure were uniformly resin impregnated and void free. Fiber volume fraction measurements by the resin digestion method compared well with values predicted using the model.

INTRODUCTION

Resin transfer molding (RTM) has been identified as a cost–effective manufacturing technique for fabricating damage tolerant composite structures with geometrically complex reinforcements. Dry textile preforms are infiltrated with resin and cured in a single step process thus eliminating separate prepreg manufacture and ply–by–ply layup. The number of parameters which must be controlled during infiltration and cure make trial and error methods of process cycle optimization extremely inefficient. Analytical processing models combined with in situ monitoring sensors are a superior alternative for the determination of optimum processing cycles.

In this paper a finite element model is presented which can be used to simulate one–dimensional, through–the–thickness, nonisothermal infiltration and cure of resin into a fabric preform. Compaction and permeability characteristics of the fabric preform along with the kinetic and viscosity characteristics of the thermosetting resin are incorporated into the model to predict, as a function of applied temperature and pressure boundary conditions, the following parameters: a) initial resin mass; b) resin front position and time required for preform infiltration; c) resin viscosity and degree of cure; and d) final part thickness and fiber volume fraction.

Textile composites were fabricated by RTM using model generated processing cycles. During fabrication, frequency dependent electromagnetic sensors (FDEMS) were used to monitor in situ infiltration time, resin viscosity, and resin degree of cure. The fabricated panels were C–scanned and cut into specimens for photomicrographs, fiber volume fraction measurements and mechanical testing. Measured values of infiltration time, resin viscosity and degree of cure, and fiber volume fraction, were compared with model predictions.

---

[1]This work was made possible through the support of the National Aeronautics and Space Administration–Langley Research Center grant no. NAG1–343 with Virginia Tech and grant no. NAG1–237 with the College of William and Mary.

PREFORM CHARACTERIZATION

Infiltration is the process by which a fluid permeates a porous material. Infiltration is dependent on the applied pressure, the viscosity of the fluid, and the geometry of the solid micro–structure.

Infiltration into a simple rectangular preform can be accomplished either through the thickness or in–plane. With more complex three–dimensional materials, infiltration could occur in many directions at once. This study has been limited to one–dimensional, through–the–thickness infiltration of a rigid porous material.

Application of the pressure causes the preform to deform. The deformation is due to a combination of tow deformation, nesting of the plies, and flattening of individual layers. The changes in size and geometry of the interstitial spaces affect the rate of infiltration.

The internal structure of a porous material can be described by the porosity and permeability of the material. The porosity is the maximum volume of resin that a porous material can contain divided by the total volume and can be related to the solid volume fraction ν_f by the following expression,

$$\phi = 1 - \nu_f \tag{1}$$

As the compaction pressure is increased, the porosity will decrease. Relationships between applied pressure and porosity and porosity and permeability are required to completely characterize a fabric preform and as input into the simulation model. Only a brief summary of the techniques used to determine these relationships will be presented. A detailed documentation of the experimental procedures is given in reference 1.

Pressure–Porosity Relationship

Following the approach of Guavin, Chibani and LaFontaine (ref. 2) the fabric areal weight ξ, can be defined as the mass of fabric per unit surface area. The porosity can then be written as,

$$\phi = 1 - \frac{n\xi}{t\rho_{solid}} \tag{2}$$

where t/n is the thickness of one ply, and ρ_{solid} represents the density of the fibers. The values of ξ and ρ_{solid} are typically supplied by the fabric manufacturer.

One–dimensional compression tests were performed to characterize the deflection of various fabric preforms. Specimens were placed in a fixture, and then loaded in compression. The load was applied by an Instron multiaxial testing machine and the deflection of the preform was measured by a LVDT attached to the lower actuator. Data was recorded via an IBM PC during the loading and unloading cycles.

The measured data was described by a polynomial of the form,

$$d = a_1 + a_2 \ln P + a_3(\ln P)^2 + a_4(\ln P)^3 + a_5(\ln P)^4 \tag{3}$$

where d is the deflection of the fiber bed and P is the compaction pressure. A nonlinear least squares procedure was used to determine the coefficients a_1, a_2, a_3, a_4 and a_5. Substituting equation (3) into equation (2) the relationship between pressure and porosity is obtained. Figure 1 represents the pressure–porosity relationship for an eight harness satin fabric woven from Hercules IM7 fibers (IM7/8HS). As expected the porosity decreases with increasing compaction pressure.

Permeability–Porosity Relationship

The permeability of a porous material can be experimentally determined using D'Arcy's law. The one–dimensional form of D'Arcy's law can be written as

$$q = K \frac{A}{\mu} \frac{\Delta P}{t} \tag{4}$$

where q is the volumetric flow rate, K is the permeability, A is the area normal to the flow direction, μ is the fluid viscosity, and ΔP is the pressure differential across the material.

An experimental program was implemented to determine the through–the–thickness permeability of fabric preforms. The fixture used to measure the permeability of a fabric preform is shown schematically in figure 2. The fixture allows constant compaction pressures to be applied independent of the pressure gradient.

To measure the permeability of the preform, the fabric was compressed to a known thickness and constant flow conditions were established. The flow through the preform was measured with a bubble–type flow meter, and the pressure drop was measured. Tap water was used in all tests.

Flow results from twelve plies of IM7/8HS are shown in figure 3. The flow rate behaves in a linear fashion with respect to the pressure gradient indicating D'Arcy's law is applicable to flow through fabric preforms. From the slope of the experimental curves, the permeability of the porous material can be determined as follows,

$$\text{Slope} = \frac{q}{\frac{\Delta P}{t}} = K \frac{A}{\mu} \tag{5}$$

The effect of the compaction pressure is clearly evident from the changing slope of the data. As the pressure on the material increases, the interstitial spaces become smaller, which increases the resistance to flow and decreases the permeability.

For fibrous materials the Kozeny–Carman relation has been used to relate permeability to porosity, and can be written as follows:

$$K = \frac{d_f^2}{\kappa} \frac{\phi^3}{(1 - \phi)^2} \tag{6}$$

where d_f is the fiber diameter and κ is the Kozeny–Carman coefficient which must be determined experimentally.

The measured permeability versus porosity for the first loading cycle of an IM7/8HS fabric is shown in figure 4. From the figure it can be seen that as the compaction pressure increases, the porosity decreases with a corresponding decrease in permeability. The solid line plotted on figure 4 was obtained from the Kozeny–Carman equation when $\kappa = 38.8$.

INFILTRATION/CURE SIMULATION MODEL

The compaction characteristics, pressure–porosity relationship, and Kozeny–Carman equation were combined with D'Arcy's law and an unsteady heat transfer analysis to produce a comprehensive model of the infiltration and cure of a viscous resin into a fabric preform. Also included in the model formulation are cure kinetics and viscosity models to calculate the advancement of the resin and the changes in viscosity with resin advancement during infiltration and cure. The model was developed to simulate one–dimensional, through–the–thickness infiltration. Solution of the governing equations was obtained using the finite element technique. The infiltration/cure model is shown diagrammatically in figure 5. A detailed description of the model formulation and numerical procedures is given in reference 1.

For a specified compaction pressure and temperature cure cycle, the model can be used to predict the following parameters during infiltration and cure: a) initial resin mass; b) resin front position and preform infiltration time; c) preform temperature distribution; d) resin viscosity and degree of cure; and e) final part thickness and fiber volume fraction.

FREQUENCY DEPENDENT ELECTROMAGNETIC SENSING (FDEMS)

In studies of epoxies, polyimides, phenolics and unsaturated polyesters, frequency dependent electromagnetic sensing (FDEMS) has been shown to be a convenient automated instrumental technique for monitoring in situ the processing properties of these thermoset resins continuously throughout the cure process. FDEMS is able to monitor the progress of cure including reaction onset, point of and magnitude of maximum flow, fluidity, solvent evolution, buildup in modulus, approach to Tg, reaction completion and degradation (refs. 3–9). FDEMS measurements are particularly useful as they can be conveniently made both in a laboratory and in situ in the tool during processing in the fabrication environment. Measurements are made continuously throughout the entire fabrication cycle. Further, FDEMS provides a convenient computerized method for recording, storing, and comparing resin processing properties throughout cure. As such FDEMS can be used to evaluate and control resin properties prior to use, to provide a signature verifying the cure process during fabrication, and to provide in situ sensor feedback for intelligent closed loop control of fabrication.

Theory

Measurements of the capacitance, C, and conductance, G, were made using a Dek Dyne FDEMS sensor. The complex permittivity $\epsilon^* = \epsilon' - i\epsilon''$ was calculated from

$$\epsilon' = \frac{C_{material}}{C_o} \tag{7}$$

and

$$\epsilon'' = \frac{G_{material}}{C_o 2\pi f} \tag{8}$$

at each of 10 frequencies between 50 Hz and 1 MHz. This calculation is possible when using the

Dek Dyne sensor whose geometry independent capacitance, C_0, is invariant over all measurement conditions.

Both the real and the imaginary parts of ϵ^* have an ionic and dipolar component. The dipolar component arises from diffusion of bound charge or molecular dipole moments. The dipolar term is generally the major component of the dielectric signal at high frequencies and in highly viscous media. The ionic component often dominates ϵ^* at low frequencies, low viscosities and/or higher temperatures.

Simultaneous measurement of the frequency dependence of both ϵ' and ϵ'' or C and G in the Hz to MHz range is, in general, optimum for determining both the ionic mobility or conductivity, σ, and a mean dipolar relaxation time, τ. These two parameters are directly related on a molecular level to the rate of ionic translational diffusion and dipolar rotational mobility and thereby to changes in the molecular structure of the resin which reflect the reaction rate, changes in viscosity – modulus, and the degree of cure.

Instrumentation

The Dek Dyne FDEMS sensor was developed as an inert, disposable, planar, geometry–independent microsensor system. The sensor consists of only a fine array of two interdigitated comb electrodes. Further, the sensor is constructed from noble metals and high temperature ceramics and does not contain solid state circuitry, which is vulnerable to the harsh processing environment. The sensor is designed to withstand the curing/tool temperature, pressure, and oxidative conditions during processing for temperatures exceeding 400° C and pressures of 1 MPa. This single disposable sensor is capable of monitoring simultaneously the entire range in magnitude (usually $10^{-2} - 10^{8}$) of both the real ϵ' and imaginary ϵ'' components of the permittivity continuously without interruption throughout the cure cycle. The sensor and the accompanying software are designed for modular use with commerically available advanced impedance and conductivity bridges.

EXPERIMENTAL

Composite Fabrication

Textile composites for this program were fabricated from Textile Technologies, Inc. eight harness satin fabric woven from Hercules IM7 graphite fibers (TTI 8HS/IM7) and Hercules 3501–6 epoxy resin. Sixteen ply, 15.2 cm x 15.2 cm fabric preforms were resin infiltrated and cured using the mold assembly shown in figure 6. The advantage of this technique is that fabric preforms can be infiltrated and cured in a one step process using a heated platen press. A 15.2 cm x 15.2 cm resin panel is made in a separate step prior to fabrication of the composite. The amount of resin required to produce a composite with a specified fiber volume fraction can be calculated using the infiltration/cure model. For hot melt resin systems, the resin panel must be completely degassed prior to fabrication of the composite. This is a key step and will ensure production of a void free laminate.

During layup, two FDEMS sensors and two type J thermocouples were placed inside the mold. A sensor and thermocouple were each placed on the bottom of the mold between the release film and the resin panel as shown in figure 6. A second sensor and thermocouple were each placed on top of the graphite fiber preform. Thus the bottom sensor was able to make continuous measurements of the state of the resin at the bottom of the mold below the fabric. The top sensor was able to monitor the time it takes for the resin to infiltrate to the top of the fabric and the state of the infiltrated resin at the top of the mold.

The mold assembly was vacuum bagged and placed between the upper and lower platens of the press. A full vacuum of 760 mm Hg and the platen compaction pressure were applied to the mold at the beginning of the process and held constant for the duration of the infiltration and cure cycle. The platens were then heated according to the prescribed temperature cure cycle. Thermocouples were mounted on the upper and lower platens to monitor the temperature.

During processing, the thermocouple temperatures and the multiple frequency FDEMS capacitances and conductances were measured and recorded using a computer controlled data acquisition system. The deflection of the plunger as a function of time was recorded with a dial gauge utilized to estimate the position of the resin infiltration front.

Upon completion of cure, the textile composite was C–scanned and the final weight and dimensions were recorded. The composites were cut into specimens for photomicrographs, fiber volume fraction measurements and mechanical testing. Fiber volume fraction measurements were made in accordance with the ASTM Test Method for Fiber Content of Resin–Matrix Composites by Matrix Digestion (D3171–76). Compression strength measurements were made using the short–block compression specimen configuration described in reference 10. A minimum of five specimens from each panel were tested.

RESULTS AND DISCUSSION

Infiltration/Cure Processing Cycles

For the investigation, four textile composite panels were fabricated using the one–step infiltration and cure technique described in the preceding section. Two panels were manufactured using the recommended cure cycle for Hercules 3501–6 resin prepregs (see temperature cure cycle, figure 11). The remaining two panels were manufactured using a "rapid" cure cycle developed using the infiltration/cure model. In the rapid cure cycle, the composite is heated at 3.0° C/min from room temperature to the final hold temperature of 177° C. The intermediate hold has been eliminated and the final hold time has been reduced by 20 minutes. Two compaction pressures were used to produce composites with fiber volume fractions of 60% or 65%. The infiltration/cure model was used to calculate the compaction pressure required to fabricate a composite with the desired fiber volume fraction. For the TTI IM7/8H fabric, compaction pressures of 276 kPa and 551.5 kPa are required to fabricate composites with fiber volume fractions of 60% and 65%, respectively.

FDEMS Measurements

Figure 7 is a plot of the loss factor ϵ'' multiplied by the frequency ω measured by the bottom sensor (sensor 1, figure 6) during infiltration and cure using the manufacturer's recommended cure cycle. Figure 8 is a similar plot for the sensor placed at the top of the fabric preform (sensor 2, figure 6) during RTM using the model generated rapid cure cycle. Plots of ϵ'' multiplied by frequency ($\epsilon'' \cdot \omega$) are recommended because they conveniently display the frequencies and times where ϵ'' is dominated by ionic diffusion. That is, overlapping lines of ϵ'' multiplied by frequency indicate the frequencies and time periods when ϵ'' is dominated by ionic diffusion. At these frequencies, the ionic mobility can be tracked through the specific conductivity σ. The specific conductivity is calculated from the ionic component of ϵ'' (ϵ_i'') and the frequency (f) using the following relationship:

$$\sigma = 8.854 \times 10^{-14} \cdot 2\pi \cdot f \cdot \epsilon_i'' \tag{9}$$

The relationship of ϵ_i'' or σ to viscosity and degree of cure was determined through a previous series of isothermal resin characterization runs in the laboratory using FDEMS sensors, differential scanning calorimetry, and dynamic mechanical measurements of viscosity. These runs were used to construct a look–up table which related the ionic mobility as tracked by σ for a particular temperature to the viscosity. A second independent look–up table was constructed relating σ for a given temperature to the degree of cure. These characterization matrices were used to determine the changing magnitude of the viscosity and the buildup in degree of cure at a particular position in the mold from the FDEMS sensor output.

The beginning of resin flow at the bottom of the mold (figure 7) and the time of resin infiltration to the top of the fabric preform (figure 8) are readily seen as the time at which the magnitude of ϵ'' jumps up several decades indicating resin wet out of the sensor.

Infiltration/Cure Model Simulations

A comparison between the measured and calculated infiltration front position for the IM7/8HS preform infiltrated and cured using the manufacturer's cure cycle and the low compaction pressure is shown in figure 9. The infiltration front position was estimated by measuring the deflection of the mold plunger during infiltration. At early times there is some difference between the calculated and measured infiltration front position. This could be due to the fact that there are slight differences between the data used to develop the resin viscosity and fabric permeability models and the actual values used in the experiment. It is also possible that there are errors in the infiltration front measurement due to the small initial changes in mold plunger deflection. The bottom FDEMS sensor indicates that wet out and the beginning of infiltration occurs at about 26 minutes into the process (figure 7). If plunger deflection measurements are used, infiltration begins at 17 minutes into the process which is earlier than indicated by the FDEMS sensor measurements.

Comparisons between the calculated and measured infiltration times for the four composite panels manufactured are shown in figure 10. As can be seen from the figure there is very good agreement between the calculated and measured values. In all cases, the measured infiltration times are within 8% of the model predicted infiltration times.

For the composite panel fabricated using the rapid cure cycle and the high compaction pressure, the FDEMS sensor mounted at the top of the preform indicated wet out at 36 minutes (figure 8) which agrees well with the calculated and plunger deflection measured infiltration time.

The resin viscosity and degree of cure are shown in figures 11 and 12 for the manufacturer's cure cycle and in figure 13 and 14 for the rapid cure cycle. Agreement between the model predicted and the FDEMS sensor measured viscosity and degree of cure at the bottom of the preform (sensor 1, figure 6) is very good. With the rapid cure cycle, complete infiltration of the preform is easily achieved without the use of the intermediate hold period. Total cure time is reduced by almost 80 minutes.

Comparisons between the calculated and measured fiber volume fractions for the four textile composites are shown in figure 15. As can be seen from the figure the measured values of fiber volume fraction are within 5% of the model calculated values.

Mechanical Tests Results

Results of the short block compression tests are shown in figure 16. The measured fiber volume fraction (ν_f) of each composite is denoted in the figure. The results show that the maximum compression stress at failure is slightly higher for the composites fabricated using the

rapid cure than for the composites fabricated using the manufacturer's cure cycle. It is interesting to note that the compressive strengths of the high volume fraction specimens are lower than the compressive strengths of the low volume fraction specimens. Photomicrographs of the high volume fraction specimens showed a fully infiltrated and well consolidated structure. However, high magnification photomicrographs did reveal a low percentage of micro–voids (void diameter on the order of filament diameter) which may have caused the slight reduction in compressive strength.

CONCLUDING REMARKS

A process simulation model was developed for one–dimensional, through–the–thickness infiltration and cure of textile composites by resin transfer modeling. For a specified temperature cure cycle, the model was shown to accurately predict the required compaction pressure, initial resin mass, and time required to infiltrate a fabric preform to the desired fiber volume fraction. Frequency dependent electromagnetic sensing (FDEMS) was shown to be a convenient and accurate technique for in situ monitoring of resin infiltration and cure of a fabric preform. FDEMS sensors can be placed at different positions inside the fabric preform and used to monitor the resin fluidity and position of the resin front during infiltration and resin advancement during cure. With the proper calibrations, output of the FDEMS sensors can be directly related to resin viscosity and degree of cure for comparison with the predictions of the simulation model.

Textile composites for this investigation were manufactured using a newly developed one–step infiltration and cure technique. The non–autoclave process can be used to fabricate high quality textile composites to the desired fiber volume fraction.

REFERENCES

1. Claus, S. J. and Loos, A. C.: A Cure Process Model for Resin Transfer Molding of Advanced Composites. Virginia Tech Center for Composite Materials and Structures., Report no. CCMS–89–07, Virginia Tech, Blacksburg, VA, April 1989.

2. Gauvin, R.; Chibani, M.; and Lafontaine, P.: The Modeling of Pressure Distribution in Resin Transfer Molding. Journal of Reinforced Plastics and Composites, vol. 6, Oct. 1987, pp. 367–377.

3. Kranbuehl, D.; Eichinger, D.; Loos, A.; and Long, E. R.: Sensor–Model Control of the Resin Transfer Molding Process. Proceedings of the 48th SPE ANTEC Conference, May 7–11, 1990, Society of Plastics Engineers, pp. 912–914.

4. Kranbuehl, D.: Cure Monitoring. Encyclopedia of Composites, S. M. Lee, ed., VCH Publishers, 1989, pp. 531–543.

5. Kranbuehl, D.; Delos, S.; Hoff, M.; and Haverty, P.: Use of Frequency Dependence of the Impedance to Monitor Viscosity During Cure. Polymer Eng. & Sci., vol. 29, no. 5, May 1989, pp. 285–289.

6. Kranbuehl, D.; Hoff, M.; Haverty, P.; Loos, A.; and Freeman, T.: In–situ Measurement and Control of Processing Properties of Composite Resins in a Production Tool. 33rd International SAMPE Symposium, vol. 33, 1988, pp. 1276–1284.

7. Kranbuehl, D.; Delos, S.; Hoff, M.; Weller, L.; Haverty, P.; and Seeley, J.: Dynamic Dielectric Analysis: Monitoring the Chemistry and Rheology During Cure of Thermosets. ACS Division of Polymeric Materials: Science and Engineering, vol. 56, 1987, pp. 163–168.

8. Kranbuehl, D.; Delos, S.; Hoff, M.; Weller, L.: Dynamic Dielectric Analysis: A Means for Process Control. 31th International SAMPE Symposium, vol. 31, 1986, pp. 1087–1094.

9. Kranbuehl, D. E.; Delos, S. E.; Yi, E. C.; Mayer, J. T.; Hou, T.; and Winfree, W.: Correlation of Dynamic Dielectric Measurements with Viscosity in Polymeric Resin Systems. 30th International SAMPE Symposium, vol. 30, 1985, pp. 638.

10. Dow, M. B. and Smith, D. L.: Properties of Two Composite Materials Made of Toughened Epoxy Resin and High–Strain Graphite Fiber. NASA Technical Paper 2826, July, 1988.

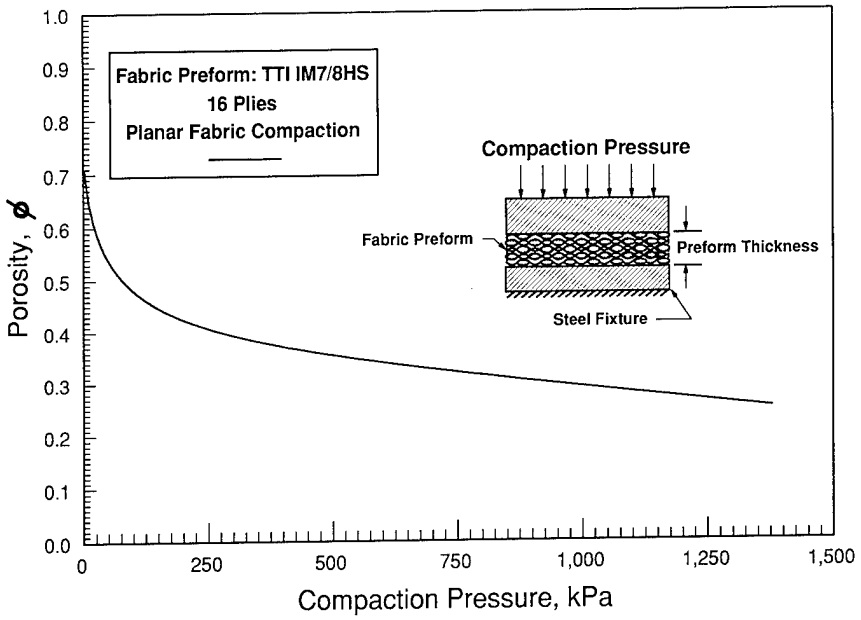


Figure 1. Relationship between porosity and compaction pressure for IM7/8HS woven fabric.

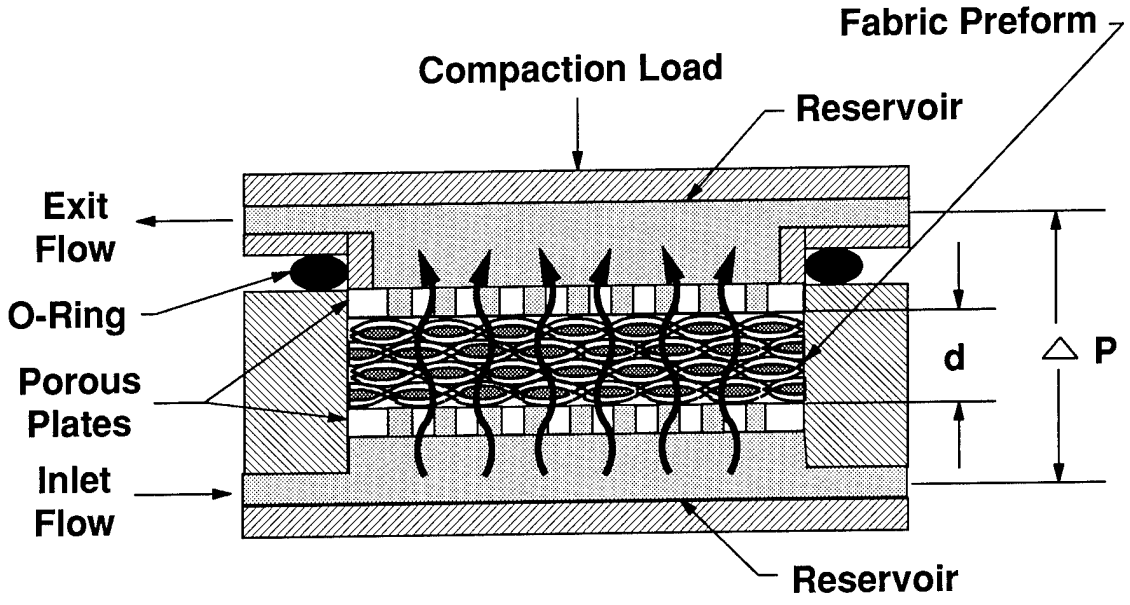


Figure 2. Schematic of the permeability test fixture.

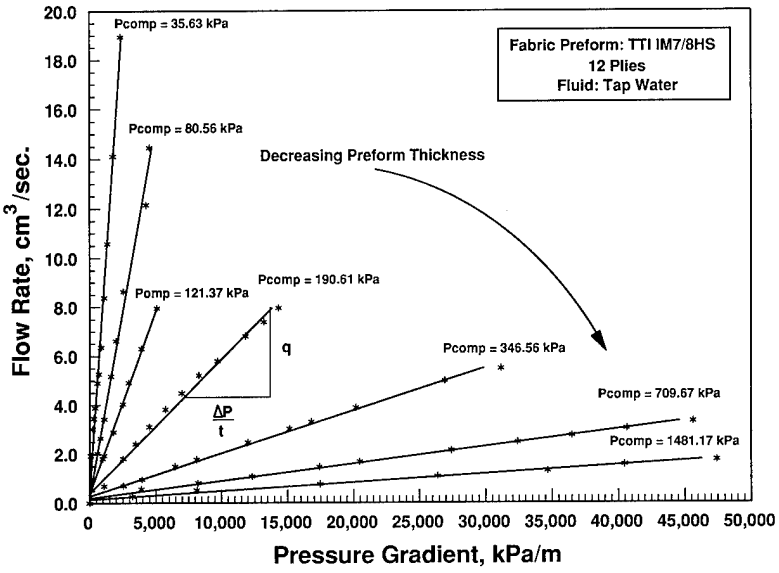


Figure 3. Flow rate–pressure gradient data for through–the–thickness flow of IM7/8HS woven fabric.

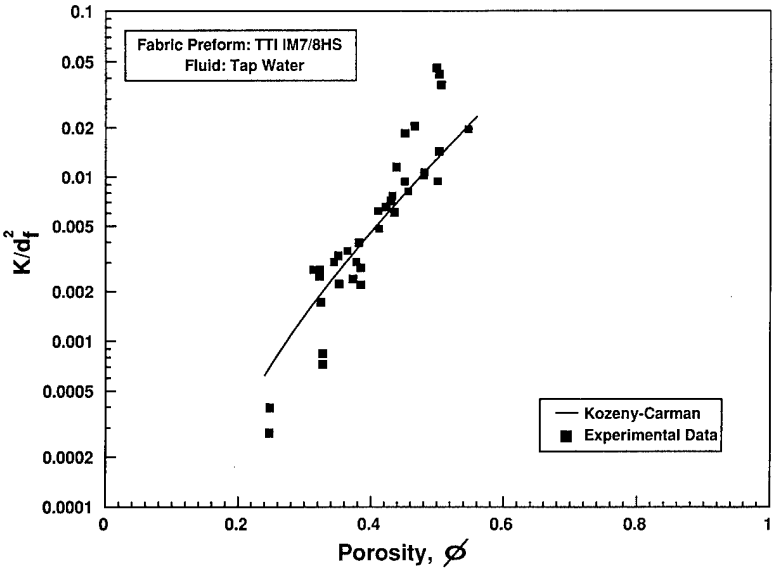


Figure 4. Normalized through–the–thickness permeability versus porosity for IM7/8HS woven fabric.

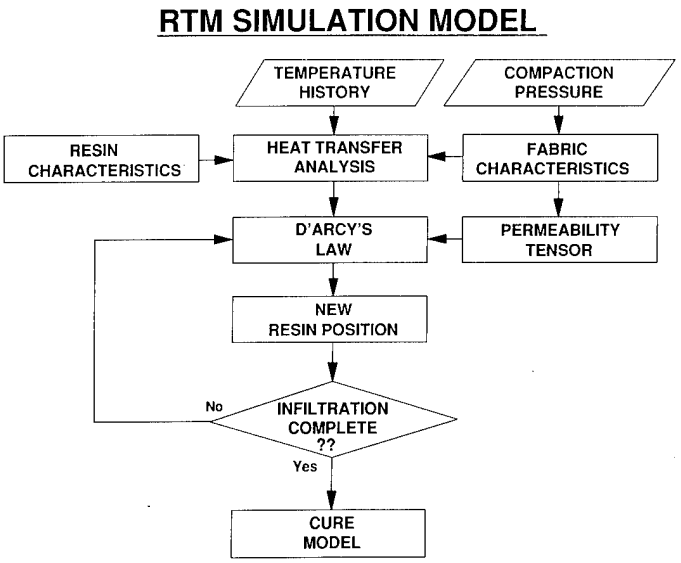


Figure 5. RTM simulation model.

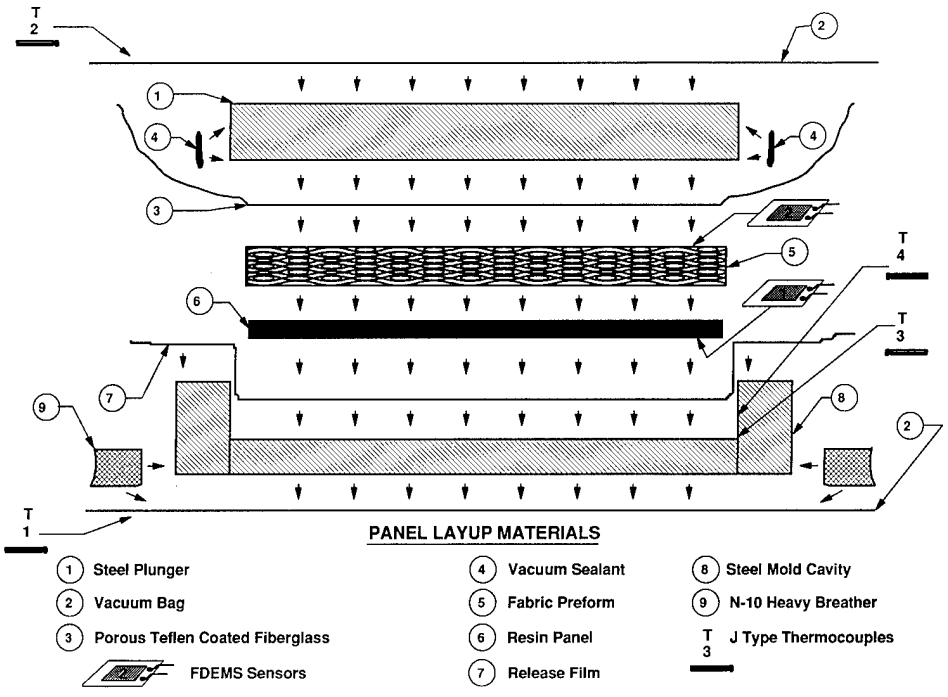


Figure 6. Schematic of the lay–up and mold assembly.

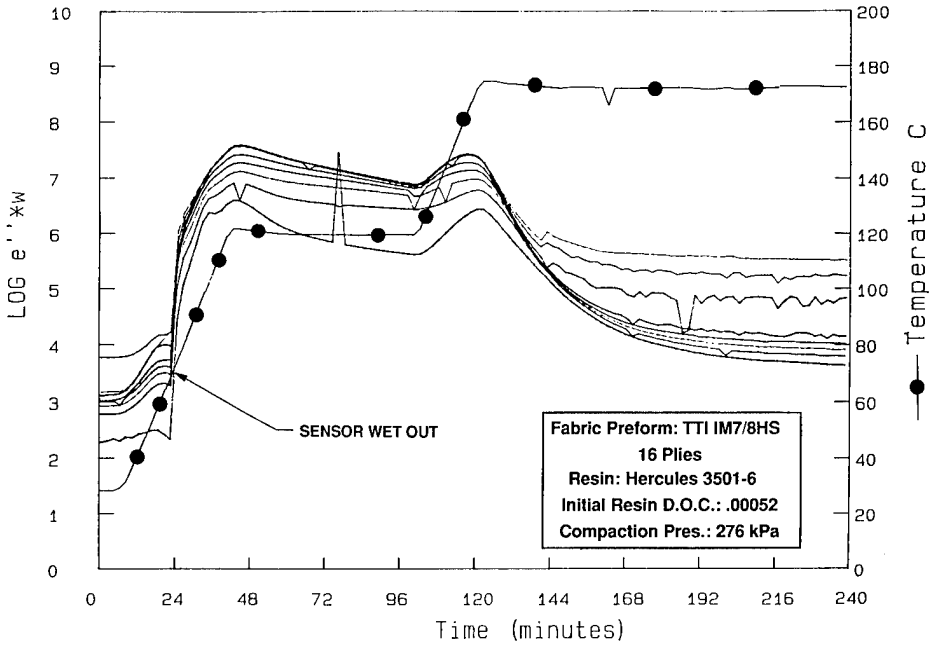


Figure 7. Values of ϵ'' multiplied by frequency ($\epsilon'' \cdot \omega$) for the bottom sensor. Constant frequency lines plotted from bottom to top are 50 Hz, 125 Hz, 250 Hz, 500 Hz, 5 kHz, 25 kHz, 50 kHz, 0.25 MHz, and 0.50 MHz. Wet out of sensor occurs at 26 minutes.

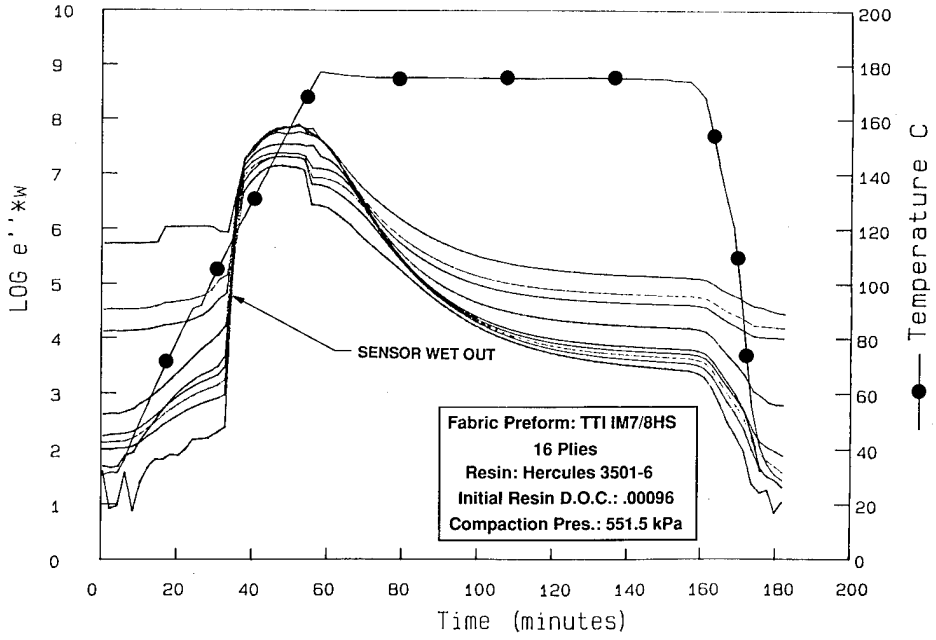


Figure 8. Values of ϵ'' multiplied by frequency ($\epsilon'' \cdot \omega$) for the top sensor. Constant frequency lines plotted from bottom to top are 50 Hz, 125 Hz, 250 Hz, 500 Hz, 5 kHz, 25 kHz, 50 kHz, 0.25 MHz, and 0.50 MHz. Wet out of sensor occurs at 36 minutes.

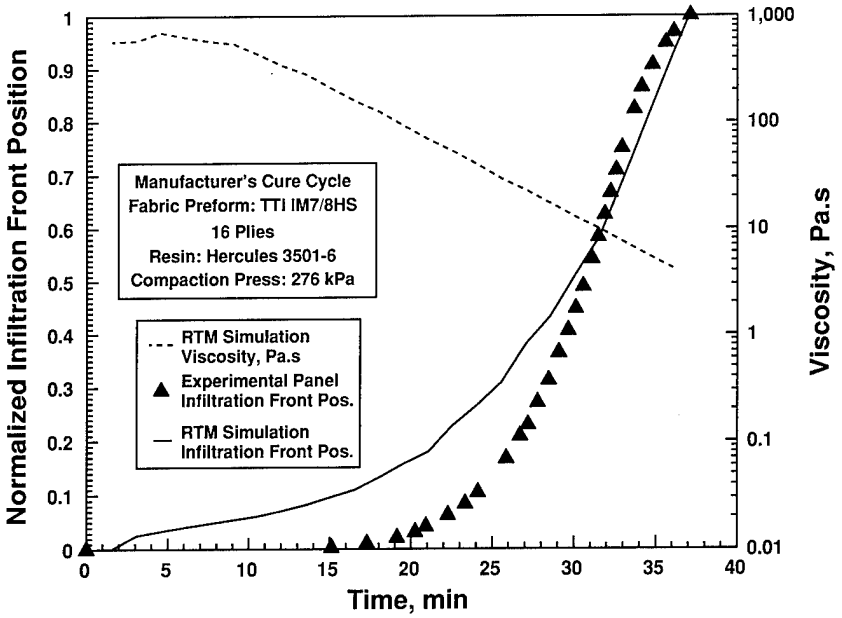


Figure 9. Normalized infiltration front as a function of time.

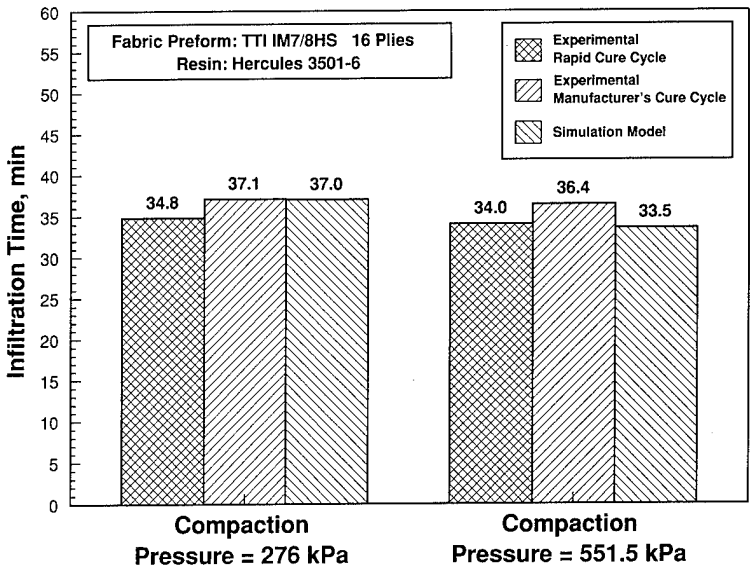


Figure 10. Comparison between measured and model calculated infiltration times.

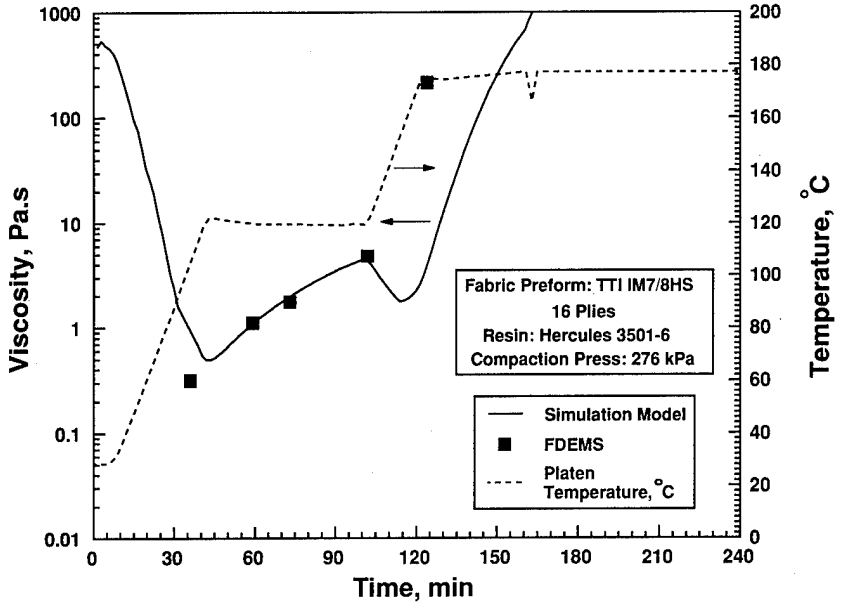


Figure 11. Resin viscosity as a function of time at the bottom of the fabric preform. Comparison between FDEMS measured and model calculated values of resin viscosity.

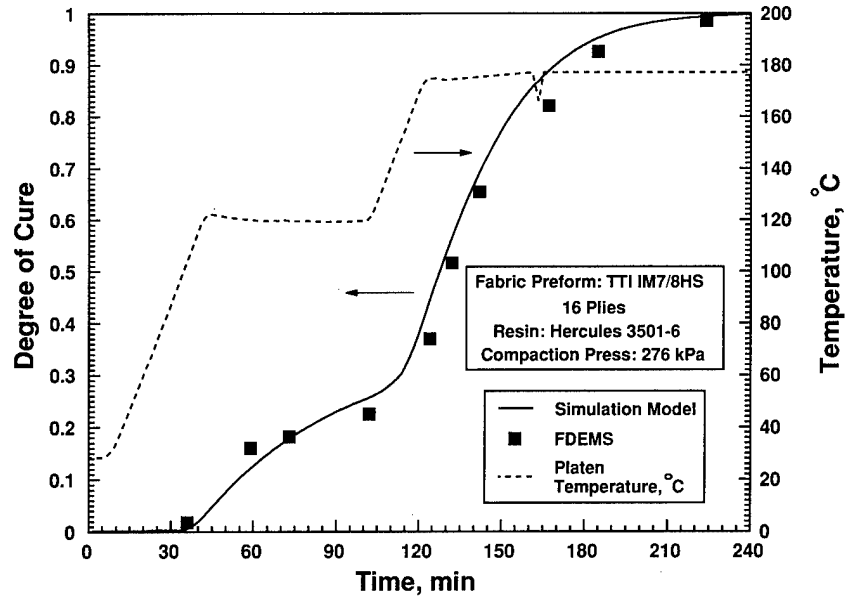


Figure 12. Resin degree of cure as a function of time at the bottom of the fabric preform. Comparison between FDEMS measured and model calculated values of resin degree of cure.

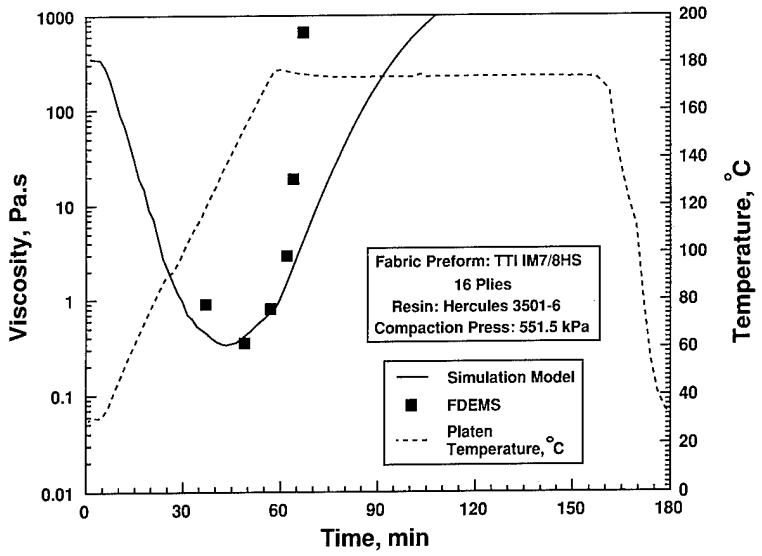


Figure 13. Resin viscosity as a function of time at the bottom of the fabric preform. Comparison between FDEMS measured and model calculated values of resin viscosity.

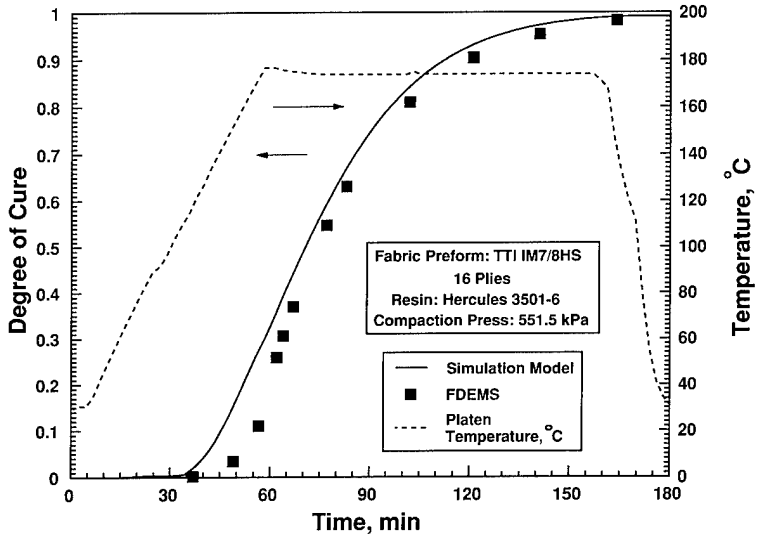


Figure 14. Resin degree of cure as a function of time at the bottom of the fabric preform. Comparison between FDEMS measured and model calculated values of resin degree of cure.

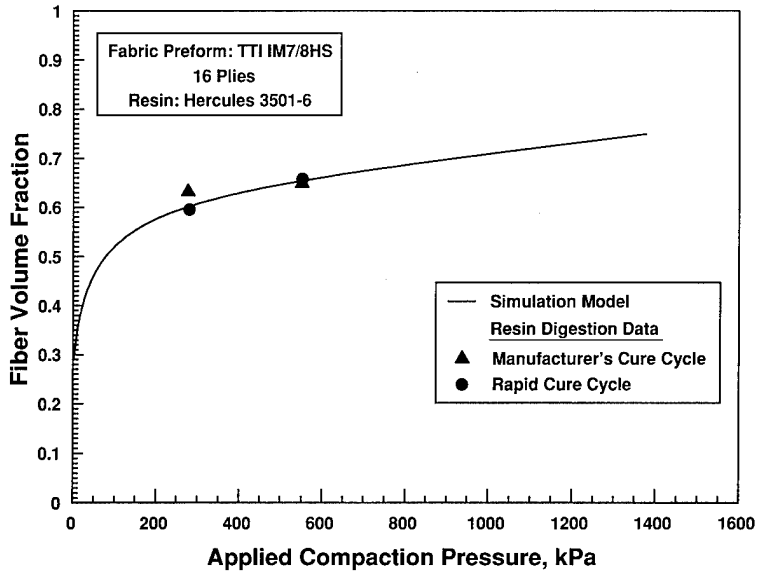


Figure 15. Fiber volume fraction as a function of compaction pressure.

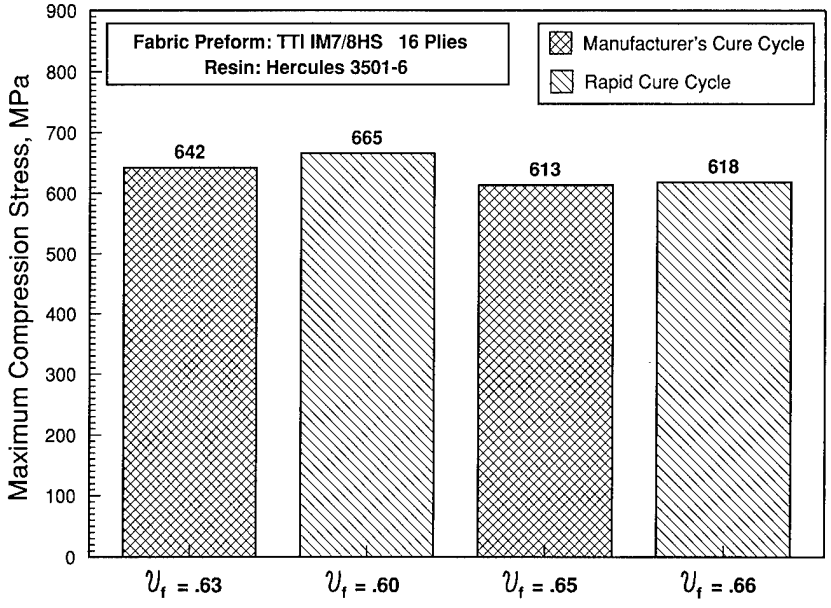


Figure 16. Maximum compression stress for IM7/8HS fabric preforms infiltrated and cured using different compaction pressures and thermal cure cycles.

POWDER TOWPREG PROCESS DEVELOPMENT

Robert M. Baucom
Langley Research Center

Joseph M. Marchello
Old Dominion University

SUMMARY

The process for dry powder impregnation of carbon fiber tows being developed at LaRC overcomes many of the difficulties associated with melt, solution, and slurry prepregging. In the process, fluidized powder is deposited on spread tow bundles and fused to the fibers by radiant heating. Impregnated tows have been produced for preform, weaving and composite materials applications.

Design and operating data correlations have been developed for scale up of the process to commercial operation. Bench scale single tow experiments at tow speeds up to 50 cm/sec, have demonstrated that the process can be controlled to produce weavable towpreg. Samples have been woven and molded into preform material of good quality.

INTRODUCTION

Because of the high melt viscosities of thermoplastics and toxicity and handling problems with solvents, several years ago NASA Langley Research Center (LaRC) began investigating ways to powder coat carbon fiber using fluidized bed, slurry, and electrostatic technology (1). It was felt that powder coated prepreg would have good drape and perhaps some tack. Powder coated tow was thought to have the potential to be woven into cloths and preforms and to be filament wound and pultruded. Powder based composites offered the potential of being cost-effective to produce and fabricate.

Experiments at LaRC and elsewhere have confirmed many of the expectations for powder prepregging (2). Some of the important features of the powder coating process are these:

- Versatile: Thermoplastics and thermosets
- Operates at room temperature
- Involves no solvents
- Has manageable exposure to toxic materials
- Requires no significant refrigeration: reduces waste/spoilage
- Can be woven, pultruded and thermoformed
- Offers a viable alternative to RTM processing of textile preform composites

The dry powder process under development at LaRC overcomes many of the difficulties associated with melt, solution and slurry prepregging. In the process, fluidized powder is deposited on spread tow bundles and fused to the fibers by radiant heating. This paper reports the results of bench scale experiments that have provided test materials and design and scale up information needed for process development.

EXPERIMENTAL

The experimental system was composed in sequence of the tow feed spool with tow tension brake; the fluidization chamber with powder feeder; the electric oven; the quality control monitor; the take-up spool with tow speed control, Figures 1 and 2. Unsized Hercules AS-4 carbon fibers in 3K and 12K tows were used with six matrix polymer powders, Table I.

DESIGN RELATIONS

The experimental equipment and operating procedures have been described in detail in previous reports (2,3). The bench scale dry towpreg system was operated over a wide range of conditions to confirm design theory and operating correlations for each component and thereby provide the basis for scale up to produce commercial quantities of towpreg.

Tow Spreader

The tow bundle enters the spreader at the throat of a flat expansion section, air enters at the tow outlet and is drawn through holes in the sidewalls of the expansion section into a vacuum manifold. The angle of fiber spread in the pneumatic tow spreader is the result of the force balance between the tow tension applied by the brake and the air drag on the tow fibers due to flow toward the spreader walls. Tow spread is controlled and maintained by adjusting the tension and vacuum pressure.

Powder Deposition

In the powder deposition chamber, the expanded fiber tow behaves like a fibrous filter. Particle collection is by momentum impaction, inception owing to van der Waals forces, Brownian diffusion and in some cases electrostatic force. Theoretical analysis (2) provides the following design relationship for the level of powder deposition on the tow as it passes through the chamber where the tow residence time is

$$(P/[1-P]) = \{\eta_i U[D_p + D_f]\ (N/W_t)\}\ (Ln/U_t) \qquad (3.1)$$

$\theta_c = L/U_t$, P is the weight percent resin in the towpreg, W_t, the clean tow weight per unit length, U_t, the linear tow rate, D_p the particle diameter, U, the gas velocity, ρ_p, the particle density, D_f, the fiber diameter length, N the number of fibers in the tow, L the chamber, n the particle cloud density, and the average fiber collection efficiency $\eta_i = 0.00465$ over a wide range of chamber flow recirculation conditions. The appropriateness of this design relationship for the powder deposition rate was demonstrated for the powders over a wide range of operating conditions, Figure 3, during experiments at LaRC (2,3).

Powder Recirculation

The fluidized bed unit is comprised of two different particle fluidization systems - upflow and downflow. In the external return tube gas flows up through the fluidized powder and conveys it to the top of the fluidized deposition chamber. The powder and gas flow into the chamber, pass through and around the spread tow with some powder being deposited on it, and flow down to the fan inlet at the bottom. The fan accelerates the particles and gas into the external tube to complete the flow cycle.

Beginning at the fan outlet the pressure losses for each section of the powder recirculation system are as follows (4).

Acceleration:

$$\Delta P_1 = (\eta_t + \rho_g)U^2/2g_c \qquad (3.2)$$

where ΔP_1 is the pressure drop on acceleration to velocity U and n_t is the dispersed particle density in the external tube.

The suspension flows from the fan outlet into the tube with a reduction of the flow cross-sectional area. The pressure drop for flow contraction is

$$\Delta P_2 = K(n_t + \rho_g)U^2/2gc \quad (3.3)$$

where $K = 0.4(1.25 - S_2/S_1)$, S_2 is the tube area and S_1 is the fan outlet area.

Vertical flow:

For solids-to-gas weight rate ratios over 50 the sum of the pressure drops due to friction can be estimated using the correlation for vertical flow.

$$\Delta P_3 = 2.5L_e n_t U_s^{0.45} (D_p/D_t)^{0.25} \quad (3.4)$$

The correlation is not dimensionless (4): L_e is the equivalent length of pipe, ft; n_t is the dispersed solids density, lb/ft^3; D_p is the particle diameter, ft; and, D_t is the tube diameter, ft. The solids flow slower than the gas. Solids flow slippage correlations for high particle loadings level off at the limit of one half the gas velocity,

$$U_s = U/2 \quad (3.5)$$

Flow resistance due to smooth 90° bends may be expressed as $26D_t$ of equivalent pipe length (4) so that for the two bends

$$L_e = L + (2)\ (26)D_t = L + 52D_t \quad (3.6)$$

combining equations gives

$$\Delta P_3 = 2.5(L + 52D_t)\ (n_t + \rho_g)\ (U/2)^{0.45}(D_p/D_t)^{0.25} \quad (3.7)$$

Column pressure:

The vertical column pressure difference between that of the tube and the chamber is

$$\Delta P4 = (n_t - n)h \quad (3.8)$$

where n_t is the particle cloud density in the vertical tube and n the particle cloud density in the deposition chamber.

Chamber flow:

The suspension flows from the tube into the chamber with an expansion of the flow cross-sectional area. The pressure drop for flow area expansion is

$$\Delta P_5 = (n_t + \rho_g)(U^2/2g_c)(1 - S_1/S_2) \quad (3.9)$$

Friction resistance for flow downward in the deposition chamber is assumed to be negligible compared to the other flow resistances.

Total pressure loss:

The sum of the above pressure losses represents the system resistance to flow and is provided by the fan recirculation. Consideration of the magnitudes of the various terms indicates that flow friction in the pipe and support of the suspended column of solid particles make up over 90% of the pressure drop or work required of the fan.

Cloud Density

The fan horsepower, system total pressure losses, and powder material balance may be used to calculate the cloud density achievable for a specific design at a given set of operating conditions (2). As indicated in equation 3.1, the cloud density is an important factor in establishing the rate of powder deposition on the tow.

The stalling condition of the recirculation system is reached when the air flow in the tube, U, equals the maximum carrying velocity, $U_{g,m}$, at which point powder accumulates in the vertical tube stopping the fan. Operation just below the stalling point provides the maximum particle cloud density.

For upflow of gases and solids in a vertical pipe, the maximum carrying velocity can be estimated using the correlation (4)

$$U_{g,m} = 910\ (\rho_p/[\rho_p + 62.3])D_p^{0.60} \qquad (3.10)$$

The correlation is not dimensionless (4): $U_{g,m}$ is in ft/sec, ρ_p is the density of the solid particles in lb/ft^3, and D_p is the particle diameter in ft.

Powder-Tow Fusion

Towpreg flexibility and powder-fiber fusion are important for weaving and molding applications. These properties of the towpreg depend upon the temperature of the oven and the time that the powder laden tow takes to travel through the oven. Flexural rigidity data were obtained for towpreg having a range of resin content and fused at several different oven temperatures and residences times. The standardized cantilever test, ASTM D 1388-64, for fabrics, was used to determine the flexural rigidity of towpreg samples (5).

Quality Control

An instrument for on-line continuous detection of the towpreg resin content was developed in conjunction with Analytical Services and Materials, Inc. of Hampton, VA. Towpreg is composed of electrically conducting carbon fibers and dielectric polymer resin. The resin level monitor measures the electric capacitance of the towpreg, which is a function of its resin content.

Once the system design has been selected, the operating variables are used to achieve towpreg quality control during production. The process outputs to be maintained, within certain setpoints, by the control system are towpreg resin content, powder fusion, and flexibility. During continuous operation, regulatory control over output variances is accomplished by adjusting the tow speed, powder feed rate, and oven temperature.

COST ESTIMATION

A preliminary estimate of the cost to make towpreg by the dry powder process was made based on the cost of the bench scale equipment, Table II. There are no multi-tow dry powder units upon which to base cost projections for commercial operation. Assuming that the process can be scaled up to the 25 tow level in 5-tow units, projections of the cost of such a system were made and are presented in Tables II and III.

The impact of tow and resin costs are reflected in Table III and Figure 4. The powder impregnation process alone costs approximately $9.30 per pound of towpreg. Grinding solid resin to powder costs about $3.00 per pound. The cost of towpreg is the cost of the resin and tow plus the cost of milling the resin into powder and impregnating the fiber tow.

Towpreg may be stitched into uniweave tape/sheet or woven and braided into broadgoods and preforms. The cost to weave towpreg yarn in an 8 harness satin, 40 inches wide, is approximately $10.00 per pound. These estimates suggest that the costs incurred in producing powder coated towpreg should be comparable to, and perhaps even less than, those incurred for producing conventional hot melt prepreg.

RESULTS AND DISCUSSION

Extensive testing of the bench scale dry towpreg system over a range of conditions has confirmed design theory and operating correlations for each component and provides the basis for scale up to produce commercial quantities of towpreg. The unit operated reliably with the various powders, using both 3K and 12K tows, for periods as long as eight hours, at tow speeds as high as 50 cm/sec (2).

Test specimens of both unidirectional fiber towpreg and woven towpreg were prepared and molded for testing, Table IV. Weaving experiments indicate that the towpreg used as fill material must have a flexural rigidity below 10,000 mg-cm so that it bends and follows the shuttle action without breaking. Towpreg used as beam material must have a flexural rigidity below 100,000 mg-cm so that it does not break during heddle and comb action, and it must bind together the fibers so that they do not come loose, resulting in material thinning and comb clogging. This last condition requires using resin fusion to bind the unidirectional tow fibers in the beam material.

CONCLUDING REMARKS

Significant progress has been made on the development of the LaRC dry powder towpreg system. Polymer powders can be deposited on a moving carbon fiber tow in a recirculating fluidized bed and then fused to the tow using radiant heating. The flexibility of the resulting towpreg may be controlled by adjusting the temperature and time of the oven fusion process such that weavable towpreg can be obtained. Unidirectional and woven test samples, using both thermoplastics and thermosets, produced by the process have been of good quality.

Design information and operating data correlations have been developed for scale up to commercial operation. Cost estimates suggest that processing cost are comparable to those of conventional hot melt prepreg. In the future, from a part fabrication point of view, powder coated prepreg tape, woven broad goods and woven and braided preforms may be considered as options to similar materials made by other methods.

ACKNOWLEDGMENT

The authors gratefully acknowledge the assistance of Mr. John Snoha in constructing and operating the fluidized bed system. They also greatly appreciate the advice and suggestions of Dr. Terry St. Clair and Dr. Norman Johnston.

REFERENCES

1. Terry L. St. Clair, Norman J. Johnston and Robert M. Baucom, "High Performance Composites Research at NASA Langley," SAE/SP-88/748, paper 880110, pp. 1-19, SAE Intl. Congress, Feb. 1988.

2. Robert M. Baucom and Joseph M. Marchello, "LaRC Dry Powder Towpreg System," NASA TM 102648, April 1990.

3. R. M. Baucom and J. M. Marchello, "LaRC Powder Prepreg System," 35th Intl. SAMPE Symposium, pp. 175-188, April 1990.

4. J. H. Perry, Ed. Chemical Engineer's Handbook, 5th Edition, pp. 8-27, 5-46, 6-20, McGraw Co. 1981.

5. J. Muzzy, B. Varnghese, V. Thammougkol and W. Tincher, "Electrostatic Prepregging of Thermoplastic Matrices," SAMPE J., 25, 15, 1989.

TABLE I.- POWDER PREPREG PRECURSOR DATA*

Polymer Description	Particle Size, μ	Supply Source
LARC-TPI 2000	7.0	Mitsui Toatsu Chemical, Inc.
LARC-TPI 1500	19.0	Mitsui Toatsu Chemical, Inc.
PEEK 150	17.0	ICI Fiberite
PMR-15 PI	1.5	Dexter-Hysol Aerospace
PR500 Epoxy	19.0	3M Company
Fluorene Epoxy	3.0 (12.0)**	3M Company

*All prepreg utilized unsized Hercules AS-4 graphite fibers in 3K and 12K tows

**The fluorene epoxy was supplied in two different particle sizes

TABLE II.- TOWPREG COST ESTIMATION

Laboratory Single Tow System Equipment Cost	Dollars
Feed Spool Holder and Tow Tension Brake	1,500
Pneumatic Spreader and Vacuum System	2,000
Powder Screw Feeder	6,000
Powder Deposition Chamber and Recirculation Fan	2,000
Electric Oven	1,500
Resin Level Sensor and Controller	5,000
Traversing Takeup Spool and Tow Speed Control	6,000
Subtotal	24,000
Installation @ 25% of equipment cost	6,000
Total Cost	30,000
25 Tow System Equipment Cost Estimate*	
Feed Spool Creel and Tension Brakes	7,500
Pneumatic Spreaders and Vacuum Systems	10,000
Powder Screw Feeders	30,000
Powder Deposition Chambers and Recirculation Fans	10,000
Electric Ovens	7,500
Resin Level Sensors and Controllers	25,000
Takeup Spools and Speed Controls**	60,000
Subtotal	150,000
Installation @ 25% of equipment cost	37,500
Total Cost	187,500

*No multi-tow information is available. The above estimate assumes that the 25 tow system is made up of 5 deposition chambers, each handling 5 tows, complete with a pneumatic tow spreader and feeder. There are 5 resin level sensors, one for each chamber. The creel, ovens, and takeup system may be single units or multiple units.

**Estimate is for 25 spools with traversing mechanisms and speed control.

TABLE III.- PROJECTED ANNUAL COSTS*

	Dollars/Year	
	Epoxy	LARC-TPI
Direct Costs		
Equipment (3 year life)	62,500	62,500
Space (1,000 sq ft @ 10$/yr sq ft)	10,000	10,000
Utilities (20,000 KWH/yr @ $.15/KWH)	3,000	3,000
Personnel (1 FTE + benefits)	40,000	40,000
Tow (13,300 lb @ 20$/lb)	266,000	266,000
Resin (7,200 lb; Epoxy @ 20$/lb;	144,000	
LARC-TPI @ 150 $/lb		1,080,000
Subtotal	525,500	1,461,500
Indirect Costs @ 50%	262,750	750,750
Total Annual Cost	788,250	2,192,250

Estimated Towpreg Production Costs

The annual production rate is 8,500 kg or 18,600 pounds. With the above annual costs the cost to produce towpreg is estimated to be:

Epoxy/carbon fiber	42.38 $/lb
LARC-TPI/carbon fiber	117.86 $/lb

*Assumptions

The 25 tow system operates at 25 cm/sec or (50 ft/min) tow speed Standard 1.0 kg (2.2 lb) spools of 3K tow are used. The spool tow is 15,600 ft long giving a running time of 5.2 hours.

Allowing for loading, unloading, and maintenance it was felt that this level of operation would require one full-time technician.

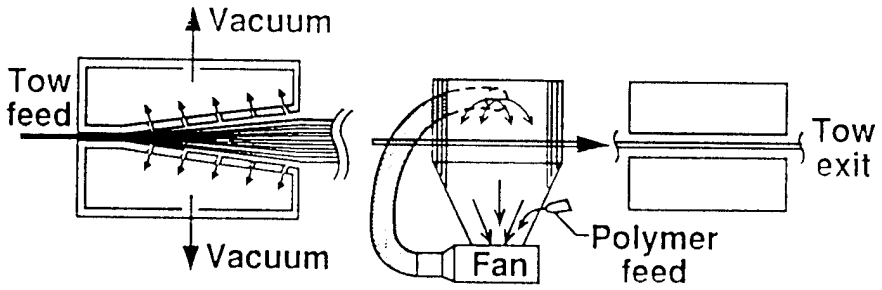
At this production rate 26 million meters (85 million feet) of 3K towpreg would be produced per year. For 35 wt % resin this amounts to 8,500 kg per year of towpreg (18,600 lb). Materials consumption, assuming 10% waste, would be 6,000 kg of tow per year (13,300 lb/yr) and 3,300 kg of resin per year (7,200 lb/yr).

Equipment life is taken to be 3 years using linear depreciation and no scrap value. With storage and handling access the system would occupy 1,000 sq ft. The major utility required is electricity for the motors and ovens estimated at 20,000 KWH/yr.

TABLE IV.- MECHANICAL PROPERTIES OF DRY POWDER COATED COMPOSITES

Composite- AS-4 Carbon Fiber-	Short Beam Shear strength ksi (MPa)	Flexure Strength ksi (MPa)	Flexure Modulus msi (GPa)
12K Unidirectional LARC-TPI 2000*	12.3 ± 1.3 (848 ± 8.9)	323 ± 14.1 (2227 ± 97)	19.4 (134)
3K 0/90 4-Harness woven, LARC-TPI 1500**, Specimen:			
0° Beam		134 ± 3.5 (924 ± 24)	8.1 (56)
0° Fill		83 ± 4.0 (572 ± 28)	5.7 (39)
3K Unidirectional PR 500***	14.5 ± 0.4 (100 ± 2.8)	206 ± 11.1 (1419 ± 76)	16.4 (113)
3K Unidirectional fluorene-based epoxy****	11.8 ± 0.6 (81.3 ± 4.1)	240 ± 15.8 (1654 ± 109)	15.4 (106)

	molding conditions	resin content
*	1 hr/660°F/800 psi	33.5 wt %
**	1 hr/700°F/300 psi	29 wt %
***	4 hr/350°F/85 psi	32.5 wt %
****	4 hr/350°F/85 psi	35 wt %



Prepreg Processing Modules

Tow spreader chamber

- Adjustable tow spread
- Minimum fiber damage
- Fast line speed

Powder coater

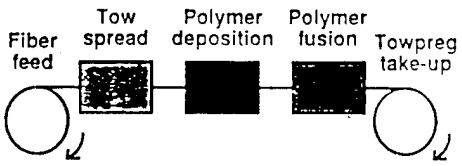
- Recirculating chamber
- Uniform coating
- Precise resin control

Powder fusion

- Convection furnace
- Individual fiber coating

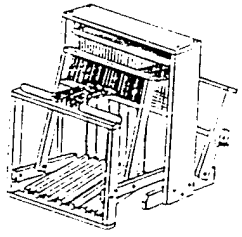
FIGURE 1. DRY POWDER PREPREGGING

Dry powder prepreg



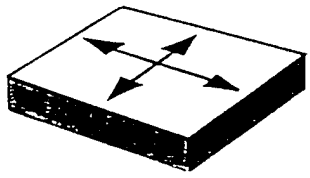
- Stable, adjustable tow spread
- Uniform polymer application/ distribution
- Continuous polymer mass fraction monitor/control
- Rapid towpreg production speeds

Powder prepreg weaving



- Towpreg weavibility established
- Towpreg drape limits determined
- 1,3 twill fabric preform woven

Composite evaluation



- 8-ply woven cloth laminated fabricated
- Excellent C-scan results
- Excellent flexural strength

FIGURE 2. INNOVATIVE PREPREG RESEARCH

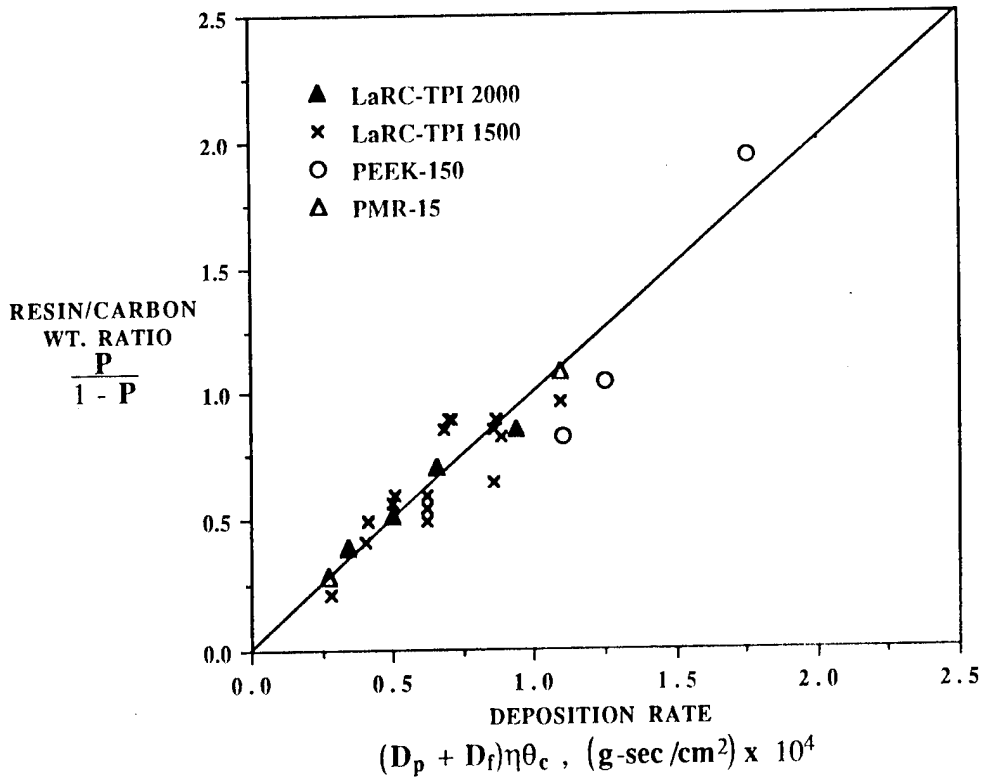


FIGURE 3. POWDER DEPOSITION DATA CORRELATION

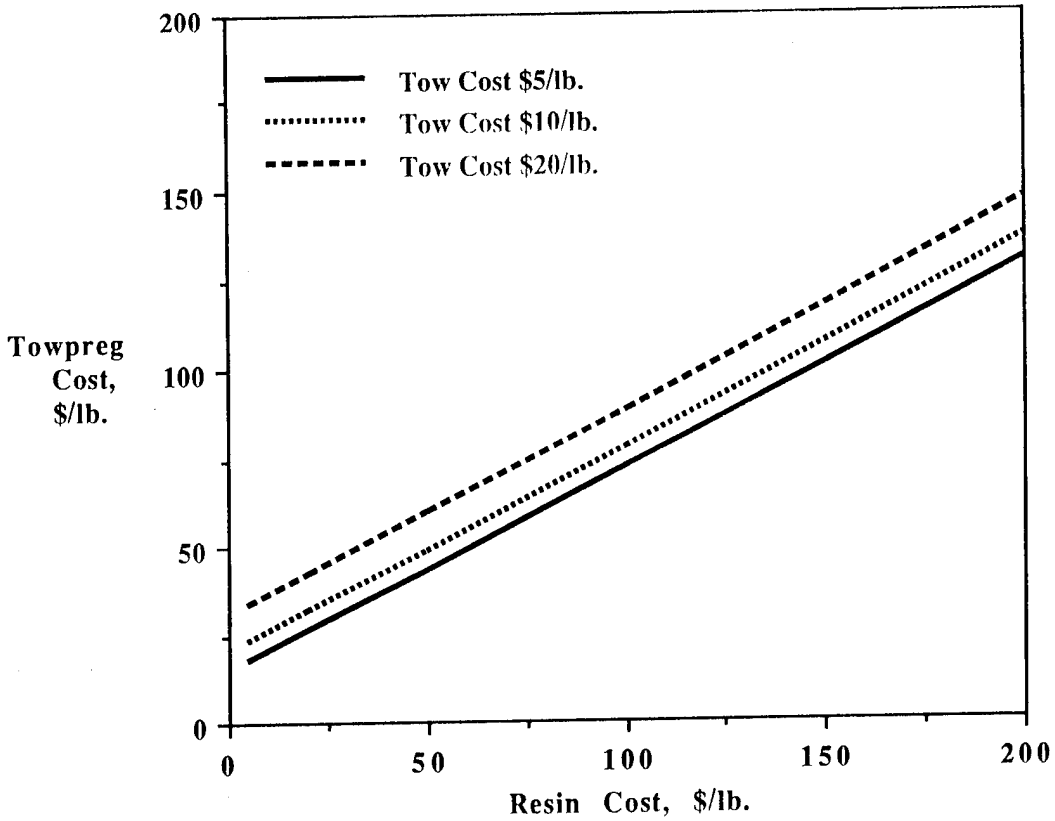


FIGURE 4. TOWPREG COST ESTIMATION

EFFECTS OF INTRA- AND INTER-LAMINAR RESIN CONTENT ON THE MECHANICAL PROPERTIES OF TOUGHENED COMPOSITE MATERIALS[1]

Dodd H. Grande and Larry B. Ilcewicz
Boeing Commercial Airplane Group

William B. Avery
Boeing Defense and Space Group

Willard D. Bascom
University of Utah

ABSTRACT

Composite materials having multiphase toughened matrix systems and laminate architectures characterized by resin rich interlaminar layers (RIL) have been the subject of much recent attention. Such materials are likely to find applications in thick compressively loaded structure such as the keel area of commercial aircraft fuselages. The effects of resin content and its interlaminar and intralaminar distribution on mechanical properties were investigated with test and analysis for two such carbon/epoxy systems. The RIL was found to reduce the in situ strengthening effect for matrix cracking in laminates. Mode II fracture toughness was found to increase with increasing RIL thickness over the range investigated, and mode I interlaminar toughness was negligibly affected. Compressive failure strains were found to increase with increasing resin content for specimens having no damage, holes, and impact damage. Analytical tools for predicting matrix cracking of off-axis plies and damage tolerance in compression after impact (CAI) were successfully applied to materials with RIL.

INTRODUCTION*

Historically, there has been a general trend towards increased fiber volume fraction in composite materials. For example, some applications favor higher fiber content to maximize fiber dominated properties such as stiffness. Little has been done to investigate optimum resin contents for properties dominated by the matrix (e.g., toughness and compression strength). The keel area in an aircraft fuselage may favor a somewhat higher resin content due to the need for enhanced interlaminar shear load transfer. Important issues for keel applications include (a) impact damage resistance and tolerance, (b) the effect of stress concentrations such as holes and ply drops, and (c) response to compressive loadings.

Control of lamina scale architecture is one route which has been employed in recent years to influence matrix-dominated composite properties. This approach has been used to produce composite laminates having resin rich zones in the interlaminar region. One advantage of such architecture is high damage resistance to shear dominated impact events.

The purpose of this work was to investigate the effects of resin content, and its inter- and intra-laminar distribution on the mechanical performance of toughened epoxy matrix composites. In particular, the effects of resin-rich interlaminar layers (RIL) were examined. A range of mechanical properties were studied. Experimental and analytical studies were performed to determine the effects of an RIL on in situ strengthening and matrix cracking in off-axis plies. The effects of inter- and intra-laminar resin

[1] This work was funded by Contract NAS1-18889, under the direction of J.G. Davis and W.T. Freeman of NASA Langley Research Center.

* [This paper cites references 1--19.]

content on mode I and mode II interlaminar toughness, compressive strength, and impact damage resistance and tolerance were studied experimentally for four batches of materials which were produced with varying inter and intra-laminar resin contents. Analytical models were used to predict the damage tolerance for these materials.

BACKGROUND

It is important to examine the available analytical tools for their applicability to emerging composite forms and architectures. In some cases, such as for matrix cracking in RIL materials, modifications to existing approaches are necessary to adequately predict behavior. Other cases such as damage tolerance of CAI panels may be adequately addressed using current approaches as long as the damage zone is dominated by delaminations or other well understood mechanisms.

Examples of materials which tend to have RIL architectures are American Cyanamid interleaf materials, Hercules IM7/8551-7, and Toray T800/3900-2. The presence of RIL has been shown to influence mode II interlaminar toughness, CAI behavior and matrix cracking in off-axis plies (Refs. 1,2,3). Other cases in which this type of architecture may be important include behavior in the vicinity of ply drops for tape structures and the cured matrix distributions in resin transfer molded parts.

Previous studies have indicated a relationship between compression strength after impact (CAI) and mode II interlaminar toughness test results (Refs. 1,4,5). Increased mode II interlaminar toughness restricts the size of delaminations which form a damage zone comprised of sublaminates (increases damage resistance). The smaller sublaminate areas lead to higher residual compression strengths. This trend is indicated in Figure 1 showing results for several batches of Hercules IM7/8551-7 studied in earlier work (Ref. 4). It was noted during this work that the batches displaying higher values of CAI also tended to have thicker RIL. Similar observations of the influences of polymeric interlaminar layers on CAI performance have been reported in the literature (Refs. 1,2). Studies using aluminum adherends and controlled adhesive bondlines have shown the effects of adhesive thickness on mode I and mode II toughness (Ref. 6). The mode II toughness was found to increase with increasing adhesive thickness. Similar Results have been reported for studies on composites (Refs. 7,8).

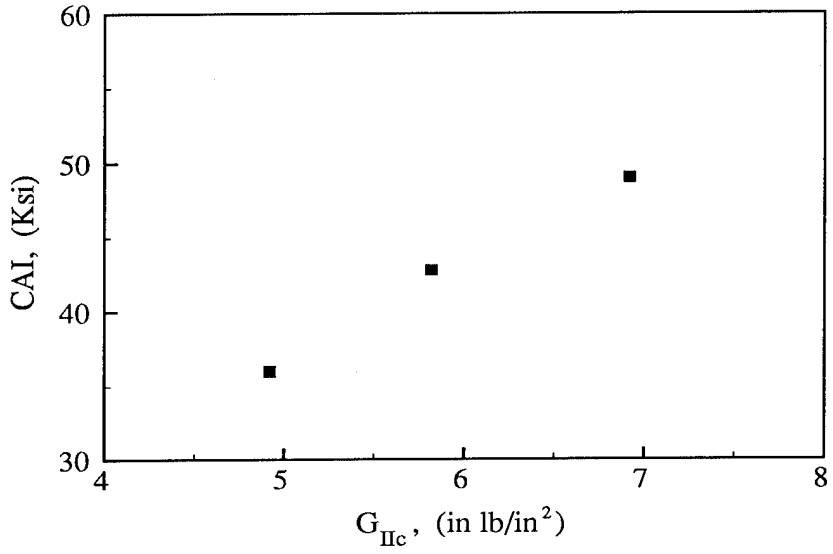


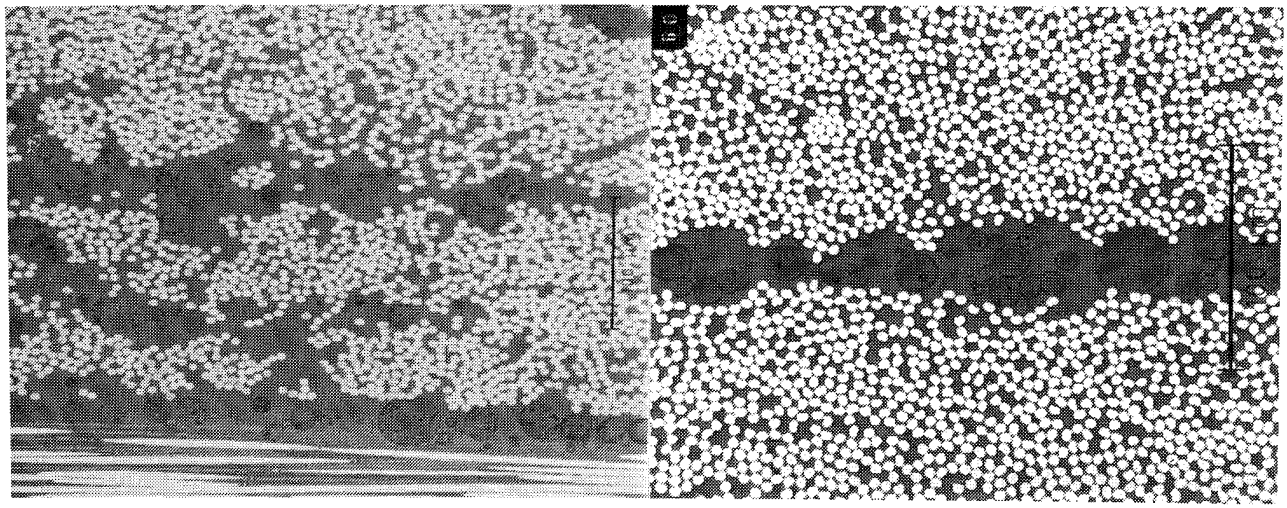
Figure 1. Relationship Between Interlaminar G_{IIc} and CAI.

The residual strength of impact damaged structure is influenced by undamaged compressive strength as well as by the damage which is present (Ref. 9). Analytical studies reported in the literature suggest that ultimate compressive strains may be improved by increased resin content (Refs. 10,11). Verification of such behavior has not been widely reported in the literature.

While the presence of an RIL appears to suppress delamination caused by impact, it has also been found to influence the resistance to matrix cracking in off-axis plies. The presence of relatively compliant RIL reduces the in-situ transverse strengthening provided to off-axis plies by neighboring plies. This can result in lower resistance to matrix cracking than would be expected for such toughened materials when neglecting the RIL effect (Ref. 3).

MATERIALS

Materials studied in this work were Hercules IM7/8551-7 and Toray T800/3900-2. Both systems consist of intermediate modulus fibers in toughened multi-phase epoxy matrices, and both systems tend to display RIL architectures. Photomicrographs showing the interlaminar regions of these two materials are given in Figure 2.



(A) (B)

Figure 2. Cross Sections of RIL Microstructure in a.) IM7/8551-7 and b.) T800/3900-2.

A summary of materials used in this study is given in Table 1. Hercules IM7/8551-7 was used as a model RIL material to study matrix cracking in 90 degree plies of multiaxial tensile specimens. Toray T800/3900-2 was used to study the effects of RIL architecture as inter- and intra-laminar resin content were varied. Four batches of Toray materials were obtained in which the inter- and intra-laminar resin contents were systematically varied as given in Table 1. The carbon fiber areal weight was held constant in these studies, so increased resin content also led to increased ply thickness as shown in the Table. The carbon fiber areal weights and resin contents given in Table 1 are the nominal or target

values. Actual experimentally determined values of areal weight and resin content did not vary greatly from these targets. The per ply thicknesses given are typical experimental values from the range of panels fabricated.

MATERIAL	FIBER AREAL WEIGHT (g/m^2)	RESIN CONTENT (% WT) INTER	INTRA	TOTAL	PLY THICK. (10^{-3} in)	FIBER VOLUME (%)
IM7/8551-7	190	---	---	35	7.5	0.575
T800/3900-2						
Batch B1	145	Low	Low	35	5.8	0.573
Batch B2	145	Low	High	39	6.3	0.530
Batch B3	145	High	Low	39	6.3	0.530
Batch B4	145	High	High	43	6.9	0.489

Table 1. Material Descriptions

TEST METHODS

Mechanical tests used in this work are listed in Table 2. Specimen stacking sequences and dimensions are given in Table 3. Loadings for all mechanical tests were performed using a servo-hydraulic testing machine. The displacement rate for all tests was 0.05 in/min except as noted below. Displacement rates for interlaminar fracture tests were 1.0 in/min for double cantilever beam and 0.10 in/min for end notch flexure. Impacting was performed on a Dynatup instrumented impact tower. Impact damage area was measured using through transmission ultrasonic inspection (TTU).

PROPERTY	TEST TYPE
Unidirectional Compression Strength	IITRI
Unidirectional Compressive Modulus	Face Supported - Untabbed
Unidirectional Tensile Strength	Tabbed
Mode I Interlaminar Fracture	Double Cantilever Beam
Mode II Interlaminar Fracture	End Notch Flexure
Open Hole Compression	Face Supported
Quasi-isotropic Compression Strength	Face Supported
Compression After Impact	4" X 6" Coupon, 5/8" Dia. Tup
Matrix Cracking	Straight Sided Tabbed Tension
Mode I Intralaminar Fracture	Double Edge Notch

Table 2. Test Methods And Specimen Types

PROPERTY	STACKING SEQUENCE	SPECIMEN DIMENSIONS
Compression Strength	$(0)_{16}$	5.5 in. x 0.5 in.
Compressive Modulus	$(0)_8$	3.18 in. x 0.5 in.
Tensile Strength	$(0)_8$	9 in. x 0.5 in.
Mode I Interlaminar Fracture	$(0)_{26}$	13 in. x 0.5 in.
Mode II Interlaminar Fracture	$(0)_{26}$	13 in. x 0.5 in.
Open Hole Compression[1]	$(+45/0/-45/90)_{2S}$	12 in. x 1.5 in.
Open Hole Compression[2]	$(+45/0/-45/90)_{2S}$	12 in. x 2.5 in.
Compression After Impact	$(+45/0/-45/90)_{4S}$	4 in. x 6 in.
Matrix Cracking	$(+45/90_2/-45/0_4/90_2)_S$	6 in. x 1 in.
Mode I Intralaminar Fracture	$(90)_{12}$	12 in. x 1 in.

Notes: [1] For no hole, 1/8", and 1/4 " diameter holes, face supported.
[2] For 1/2" diameter hole, face supported.

Table 3. Specimen Dimensions And Stacking Sequences Used For Mechanical Tests

RESULTS AND DISCUSSIONS

Matrix Cracking Studies

Transverse matrix cracks can occur in composite laminates due to the combined effects of mechanical loading and environment. The transverse strength of a composite ply is not, strictly speaking, a material property as it is strongly influenced by laminate stacking sequence. The influence of neighboring plies on the transverse ply strength is referred to as in situ strengthening. Stiff neighboring plies tend to increase the strains at which matrix cracks develop in off-axis plies due to the crack opening restraint that they provide. The strains for matrix cracking in traditional untoughened materials have been found to decrease with increasing numbers of off-axis plies which are stacked together.

The RIL provides a compliant layer between plies which reduces the constraint provided by neighboring plies. Thus, one of the expected effects of the RIL would be a decrease in the in situ strengthening effect and reduced strains for onset of matrix cracking in off-axis plies for certain stacking sequences. Another influence of the isolation provided by the RIL is to reduce the effect of grouping multiple plies of the same orientation.

Matrix cracking experiments were performed using the IM7/8551-7 material. The lamina architecture of this material tends to exhibit a resin rich zone between adjacent laminae. A photomicrograph showing the RIL in IM7/8551-7 is shown in Figure 2a. The RIL layer was observed to exhibit local variations in thickness, and contains second phase material.

Specimen geometry and stacking sequences were as given in Table 3. Experimental determinations were made of the strain at onset of cracking in the 90° plies at a number of temperatures and humidity conditions. A finite element approach was used to predict the onset of off-axis cracking (Ref. 3). This approach utilizes a crack closure technique to determine the strain energy release rate for cracks in the

90° plies. Mode I intralaminar G_{IC} values were determined using the double edge notch test (Ref. 12). Composite, neat resin and fracture properties used for the analysis were all obtained at the environmental conditions being modelled. Neat resin data were obtained from reference (Ref. 13).

Three different finite element models were constructed to predict onset of matrix cracking in laminates with RIL. The first model ignored RIL architecture and used average ply properties. The second model discretely simulated RIL architecture by concentrating fibers in the central 80% of a ply, with a correspondingly higher local fiber volume fraction. The outer 10% on either side of the ply was modelled as a neat resin layer. Properties of fiber rich regions were scaled to account for increased fiber volume fraction, and RIL were assigned neat resin properties. The third model had the same geometry as the second, with RIL moduli reduced to 25% of the neat resin modulus. The reduced moduli were intended to reflect reductions from bulk stiffness that would be expected due to preferential additions of elastomeric or other modifiers to the RIL layer.

Predicted results from the three models are shown in Figure 3 along with experimental data for the 70°F/dry condition. The figure shows that RIL must be discretely modeled to obtain a good prediction of the onset of matrix cracking. Similar plots for conditions of -75°F/dry and 180°F/wet are shown in Figures 4 and 5. Comparison of these results show that the experimental data fall close to the RIL model using neat resin moduli for the -75°F/dry and 70°F/dry conditions and closest to that using the reduced RIL moduli for the 180°F/wet condition. Reference 3 gives additional experimental and analytical results for matrix cracking in IM7/8551-7.

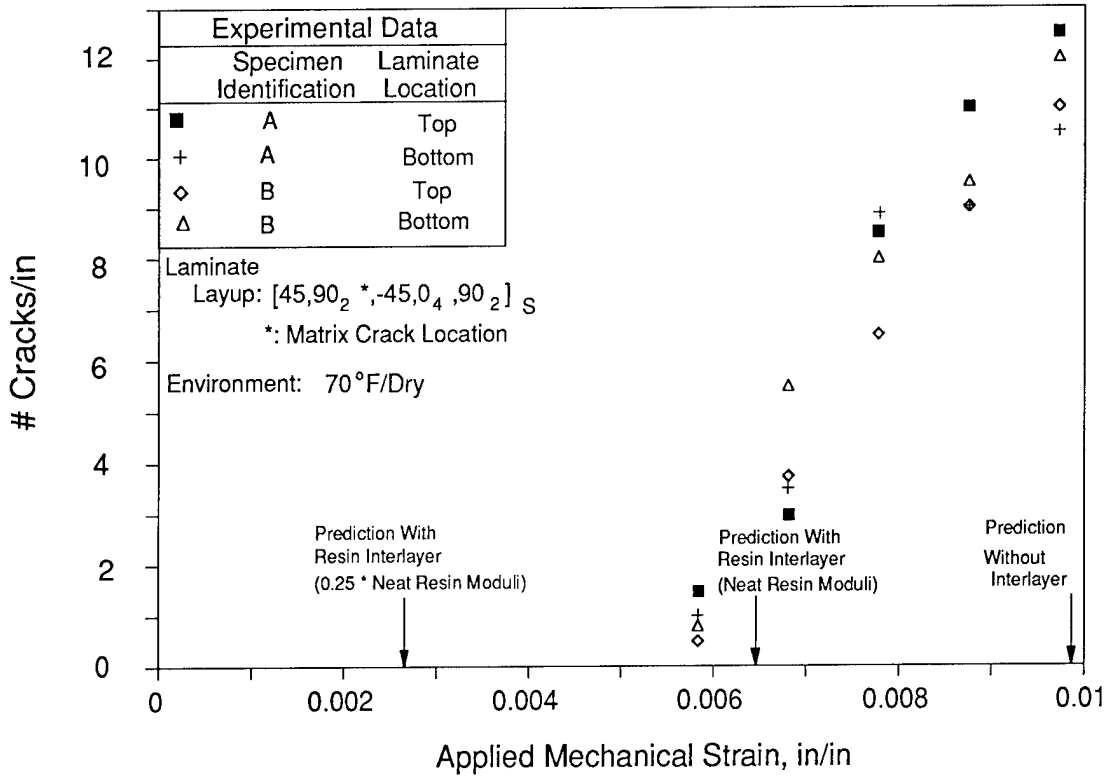


Figure 3. Matrix Crack Onset Predictions and Test Data for a Laminate Exposed to 70°F/Dry.

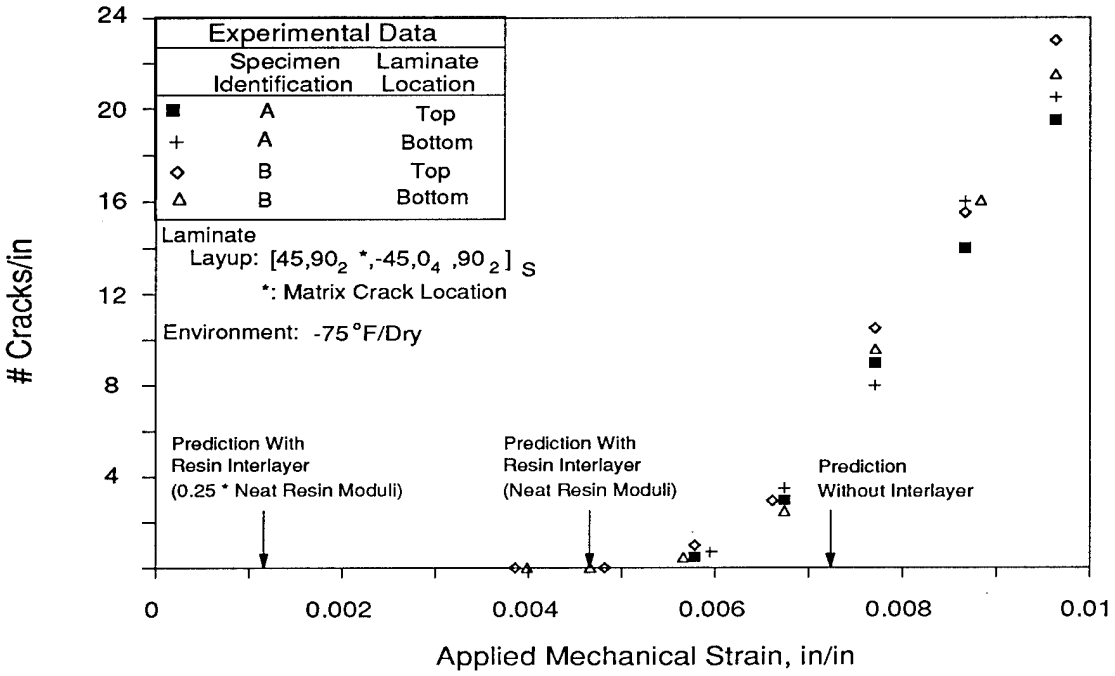


Figure 4. Matrix Crack Onset Predictions and Test Data for a Laminate Exposed to -75°F/Dry.

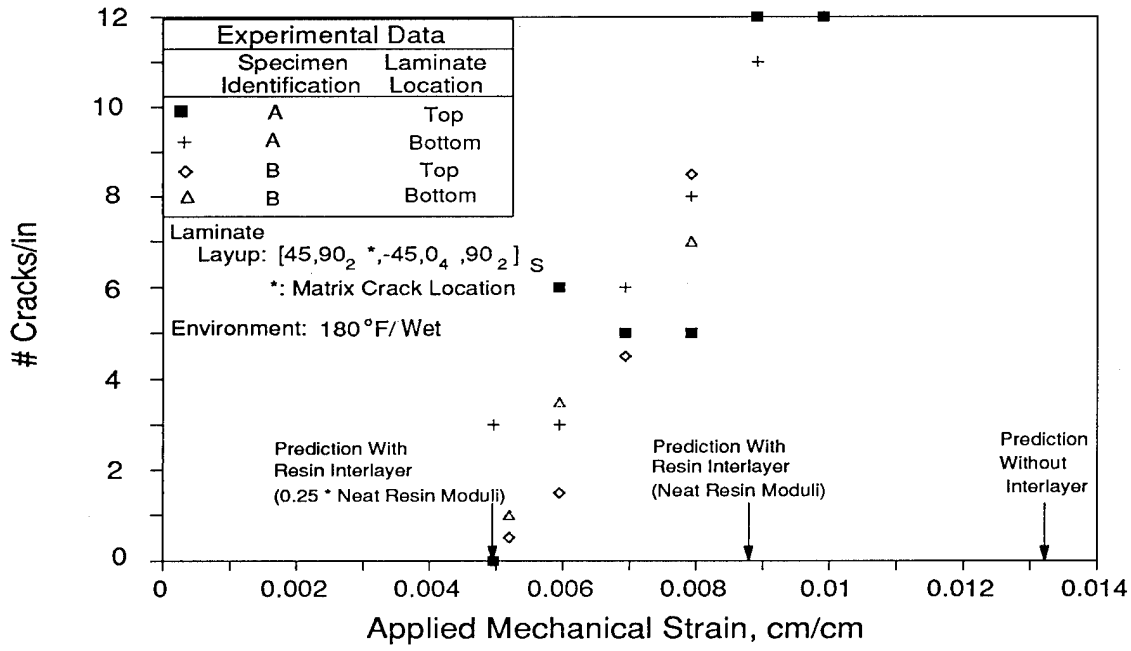


Figure 5. Matrix Crack Onset Predictions and Test Data for a Laminate Exposed to 180°F/Wet.

As mentioned above, the RIL properties used were obtained from measurements of neat resin material. It is likely that the RIL contains preferential amounts of elastomer and other modifiers. Therefore, it is reasonable that environmental conditions will affect the stiffness of the RIL differently than that of the bulk matrix materials in which these agents are interspersed uniformly throughout. Realizing that the assignment of reduced RIL moduli values equal to 25% of the bulk resin was rather arbitrary, the relation between experimental and predicted results indicate that the stiffness of the RIL is probably affected more by environment than was indicated from the neat resin data.

Effects Of Inter- And Intra-laminar Resin Content

A range of mechanical properties were investigated to study the effects of inter- and intra-laminar resin content. Properties of primary interest due to the intended applications of these materials (i.e., fuselage keel panels) were impact damage resistance and tolerance, interlaminar fracture toughness and compressive strength.

Unidirectional Strength and Stiffness: Increasing resin content tends to decrease fiber dominated properties such as unidirectional tensile behavior and compressive stiffness. This was confirmed by experimental results from this study that included different resin distributions (see Table 4). Moduli reported in Table 4 were calculated using the secant between strains of 0.001 in/in and 0.006 in/in. Micromechanics methods (Ref. 18) were used to predict the effect of increasing resin content on lamina axial moduli. Axial tension and compression fiber properties used for these predictions were back-calculated by matching predicted and measured moduli of the baseline material (batch B1). Table 4 shows that micromechanics accurately predicted the effect of decreasing resin content for batches B2, B3, and B4. The experimental tensile failure strains were unaffected by resin content. Since areal weights were held constant in this study, ultimate tensile loads were also unaffected and failure stresses were inversely proportional to specimen thickness.

Material Batch	Tensile Modulus Measured (Msi)	Tensile Modulus Predicted (Msi)	Ultimate Tensile Strength (Ksi)	Ultimate Tensile Strain (in/in)	Compressive Modulus Measured (Msi)	Compressive Modulus Predicted (Msi)
B1	21.6	21.6	384	0.0163	18.3	18.3
B2	19.9	20.0	350	0.0164	16.8	17.0
B3	19.9	20.0	351	0.0163	17.0	17.0
B4	18.5	18.5	318	0.0159	15.5	15.7

Table 4 - Fiber Dominated Properties For Resin Content Study (Average of Five Specimens)

Flexural stiffnesses (determined while performing end notch flexure tests for fracture toughness) for unidirectional specimens with equal numbers of plies increased as a squared function of per ply thickness. This resulted from the moment of inertia increasing as a cubed function of thickness while the modulus decreased approximately as the inverse of per ply thickness. Changes in flexural stiffness were found to be important in this work for cases involving impact response and sublaminate stability. This will be discussed later.

Ultimate compressive strength properties were observed to be influenced by resin content. Materials displayed higher ultimate compressive loads and failure strains with increasing resin contents. Table 5

shows results that are the average of five specimens per batch. Failure strains were calculated by dividing the measured ultimate strength by measured compression moduli listed in Table 4.

Material Batch	Failure Load, lb (Stand. Dev.)	Ultimate Strength, Ksi (Stand. Dev.)	Failure Strain (in/in)	Specific Strength, in. σ_{ult}/ρ
B1	9400 (227)	207.4 (5.8)	0.0113	3.62×10^6
B2	9876 (765)	200.8 (16.3)	0.0119	3.55×10^6
B3	9904 (626)	200.5 (14.5)	0.0118	3.54×10^6
B4	10,538 (350)	195.5 (7.2)	0.0126	3.50×10^6

Table 5. Ultimate Compressive Properties From Resin Content Study: Unidirectional IITRI Specimens

Unlike the tensile case, increased compressive failure strains were measured for samples with increased resin content. One unidirectional compression specimen (IITRI) from each batch was strain gaged and the load-strain curves from these specimens are given in Figure 6. The observed trends of increasing ultimate compressive strain with increased resin content agree qualitatively with the analysis of Reference 10. To date, experimental results in Table 5 have not been quantitatively compared to predictions based on this analysis.

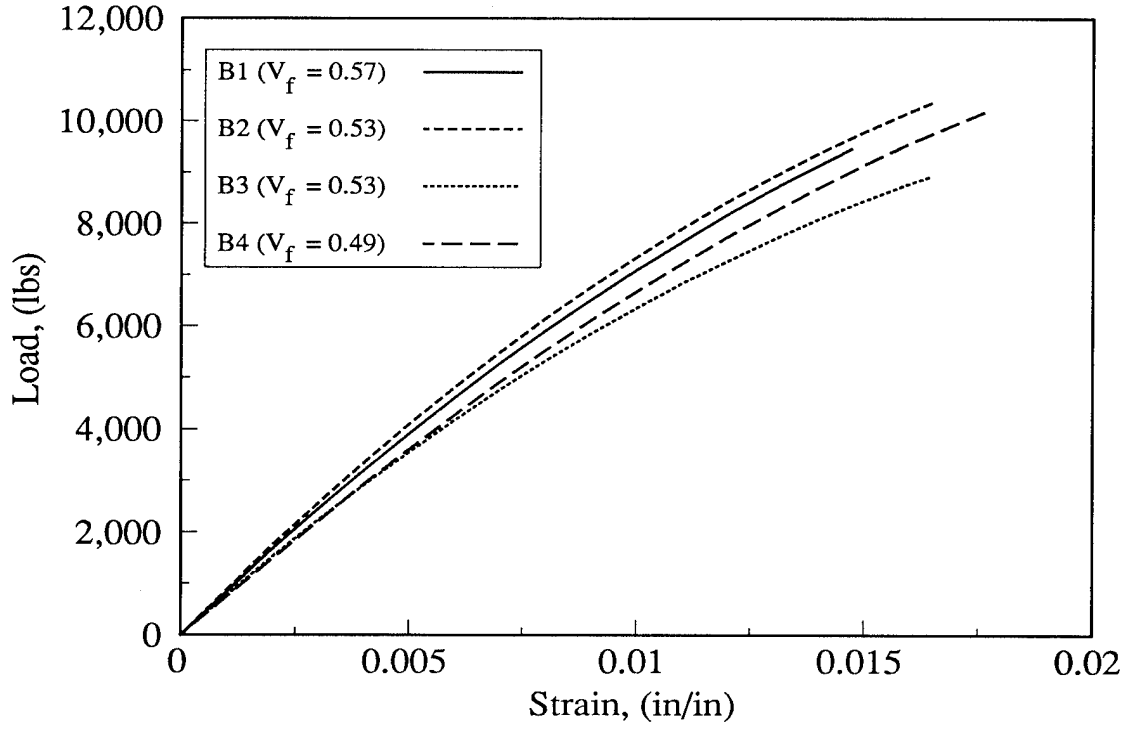


Figure 6. Compressive Load Versus Strain Curves for Samples From Each Batch in the Resin Content Study

Improvements in compression performance are also noted by other columns in Table 5. Increases in compressive failure loads with increasing resin content reported in Table 5 are greater than would be expected due to the added specimen thickness (i.e., load carrying capability of the additional resin). For instance, the additional resin for specimens from batch B4 (highest resin content) carry approximately 60 lb more than batch B1 (lowest resin content) at a failure strain of 0.013 in/in. A far greater incremental increase in ultimate load was observed for these tests. In order to compare the results on a per weight basis, specific compressive strengths (ultimate strength/density) were calculated for each batch. As shown in Table 5, the decreasing density due to increased resin content nearly counteracted the increased thickness (and hence specimen weight) in the specific strength calculation.

Open Hole Compression Strength: A similar influence of resin content was found in results from open hole compression tests. These results are shown below in Table 6. These results were obtained from face supported open hole specimens. The relative increases in failure loads with increasing resin content were approximately the same as for the unidirectional results. Results from face supported quasi-isotropic compression specimens without holes are also included in Table 6. Results from the specimens with no holes did not show the same ordering of the batches as did the specimens with holes. The results from specimens without holes also showed greater scatter than those with holes.

	BATCH							
Hole Diameter (in)	B1		B2		B3		B4	
	Load (Kips)	Strength (Ksi)	Load (Kips)	Strength (Ksi)	Load (Kips)	Strength (Ksi)	Load (Kips)	Strength (Ksi)
No Hole	11.6	84.0	11.0	72.7	11.0	72.4	12.2	74.7
1/8"	7.1	51.2	7.5	49.6	7.4	48.4	7.8	48.0
1/4"	5.9	42.7	6.4	42.2	6.3	41.4	6.6	40.5
1/2"[1]	4.9	35.5	5.3	34.5	5.3	34.3	5.5	33.9

Notes:[1] 1/2 in. diameter OHC specimens were 2.5" wide compared to 1.5" width with other hole sizes. Failure loads reported were adjusted by the ratio of the widths for comparison purposes.

Table 6. Open Hole Compression Results For Resin Content Study

Interlaminar Fracture Toughness: Table 7 lists the critical mode I (G_{IC}) and mode II (G_{IIC}) interlaminar strain energy release rates that were obtained for the four batches of Toray material. Mode I fracture specimens were given a mode I precrack from an FEP insert prior to testing, and mode II specimens were given a mode II precrack. Mode I results were calculated using the area method. Mode II values were calculated using the beam theory solution corrected for shear (Ref. 14). Shear corrections were between 4 and 6% for the specimens tested. Note that comparisons between G_{IIC} values given in Figure 1 for IM7/8551-7 and those listed for T800/3900-2 in Table 7 should be made with caution, as the former were obtained using mode I precracks. In many cases, G_{IIC} values obtained using mode I precracks are significantly lower than those obtained with mode II precracks.

Values of average RIL thickness were measured experimentally from photomicrographs of polished cross sections. Both unidirectional and quasi-isotropic specimens were used for RIL thickness measurements. The values reported in Table 7 are the average of approximately 45 measurements of RIL thickness for each batch.

Experimental results in Table 7 show that G_{IIC} increases with interlaminar resin content and RIL thickness. Values of G_{IC} were only minimally affected by resin content and distribution. Figure 7 shows a plot of G_{IIC} versus RIL thickness for the four batches. Also shown on Figure 7 are trend lines for similar experiments conducted in Reference (6) with adhesive layers between aluminum adherends. Data from the current work falls in a similar range to results from the cited reference.

Material Batch	G_{IC} (in-lb/in^2)	G_{IIC} (in-lb/in^2)	RIL THICKNESS (10^{-3} in)
B1	1.43	10.7	0.6
B2	1.48	12.1	0.7
B3	1.39	12.8	0.7
B4	1.41	13.2	0.9

Table 7. Interlaminar Fracture Toughness For Resin Content Study

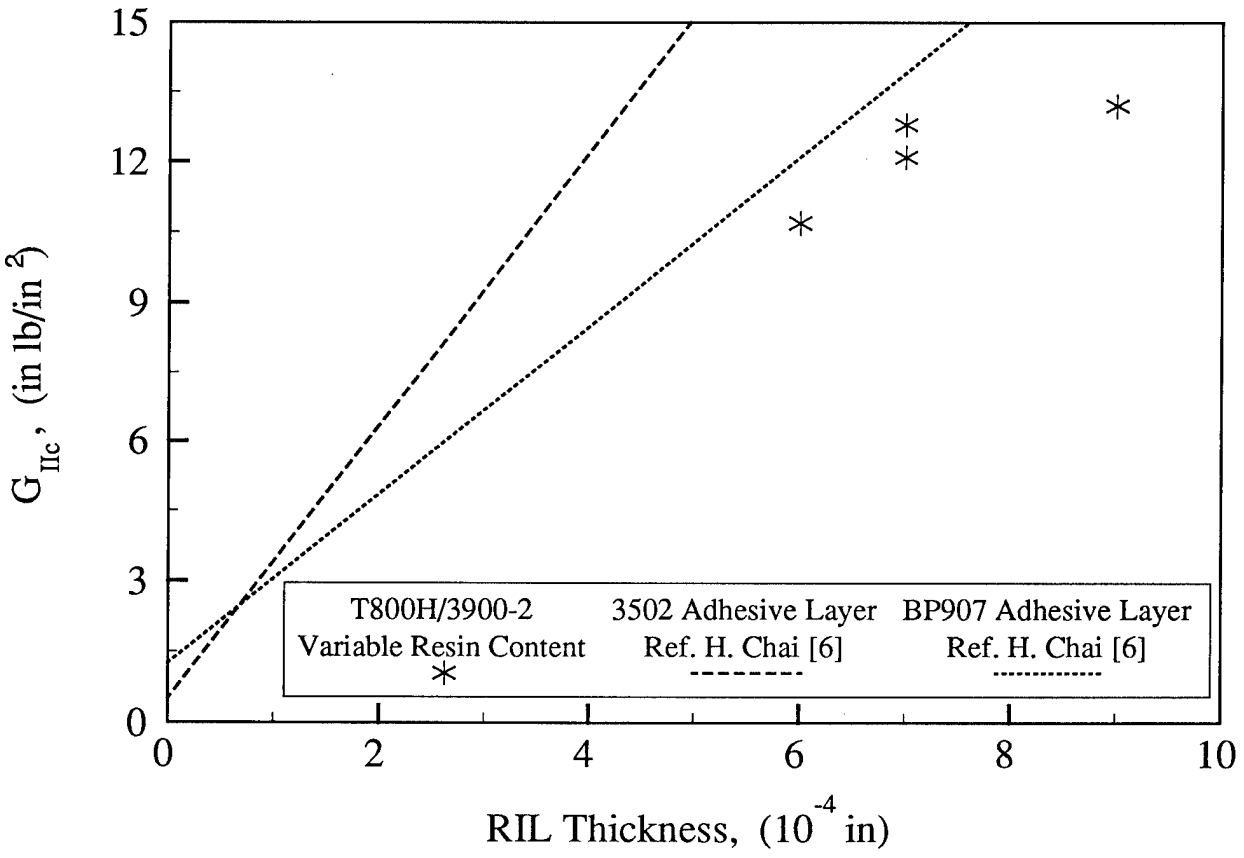


Figure 7. Average RIL Thickness Effects on G_{IIc} for Various Matrices.

It is interesting to note that although the target interlaminar resin contents were different for Batches B2 and B3, the experimental measurements of RIL thickness did not detect differences between these batches. This may indicate that some redistribution of the constituents occurs during cure, and may indicate a limit to the precision with which the RIL lamina architecture may be achieved.

Impact Damage Resistance: The study of composite impact damage resistance is complex due to interactions of materials properties, competing failure mechanisms, structural variables and impact geometry. General analysis tools to predict the formation of impact damage currently do not exist. In some instances, when groups of specimens display behavior that is sufficiently self-similar, relationships can be developed between materials properties and damage resistance. One example of such a case is given in Figure 8 for IM7/8551-7 showing the relationship between mode II interlaminar toughness and damage area for CAI specimens impacted at energies of 270 in.-lb. The corresponding plot of CAI strength versus mode II toughness was given in Figure 1.

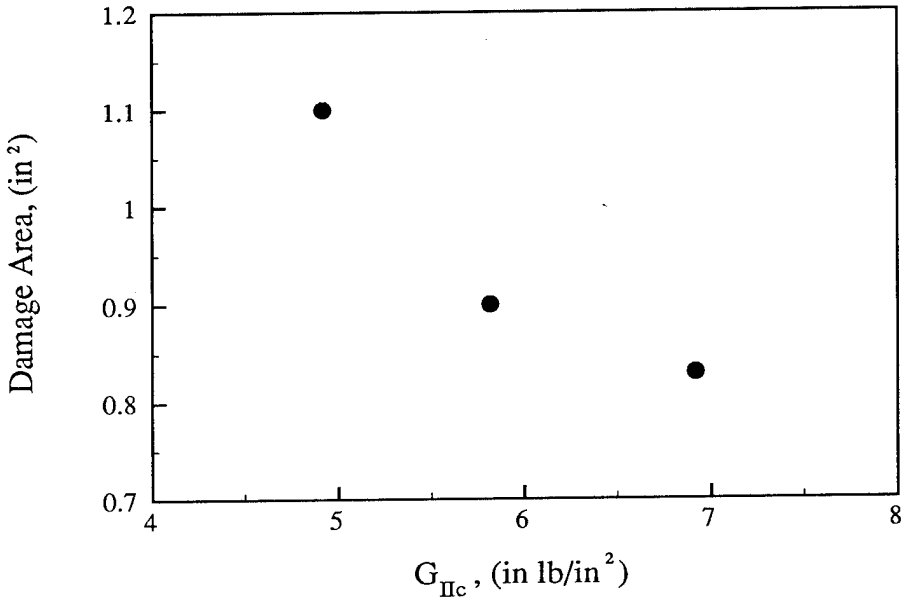


Figure 8. Relationship Between Impact Damage Area and G_{IIc} for IM7/8551-7

The relationships shown in these figures are dependent upon obtaining a degree of similarity in the damage for each case. For the data shown in Figures 1 and 8 the damage zones were dominated by sublaminates formed by impact induced delaminations (Ref. 9). Such relationships in damage resistance and tolerance may break down if a change in the dominant damage mechanism occurs. For instance, different material parameters influence the formation of competing failure mechanisms such as delaminations and fiber breaks. In addition, the post impact response (damage tolerance) is different for delamination and fiber failure dominated damage zones (Ref. 15). Simple relationships may also break down due to differences in the dynamics of the impact event. For example, changes in structural variables such as panel thickness can affect the stress fields that occur during impact.

Past work has indicated that higher values of G_{IIc} tend to increase impact damage resistance and CAI in standard CAI coupon tests. As discussed earlier, experimental values of G_{IIc} increased with increasing resin content in the current study. The higher resin contents also led to greater panel thickness, and hence increased flexural stiffness. The net effect of increased resin content on impact damage resistance is shown in Figure 9 for the four batches tested. As can be seen from these results, damage area tended to be greater for the higher resin content batches. This seems to indicate that the increased specimen thickness associated with higher resin contents more than offsets the increased toughness. Methods to scale results from impact events with varying panel sizes have been reported in the literature (e.g., Ref. 16); however, the simultaneous changes in important material and structural variables for specimens in the current work complicates such an approach.

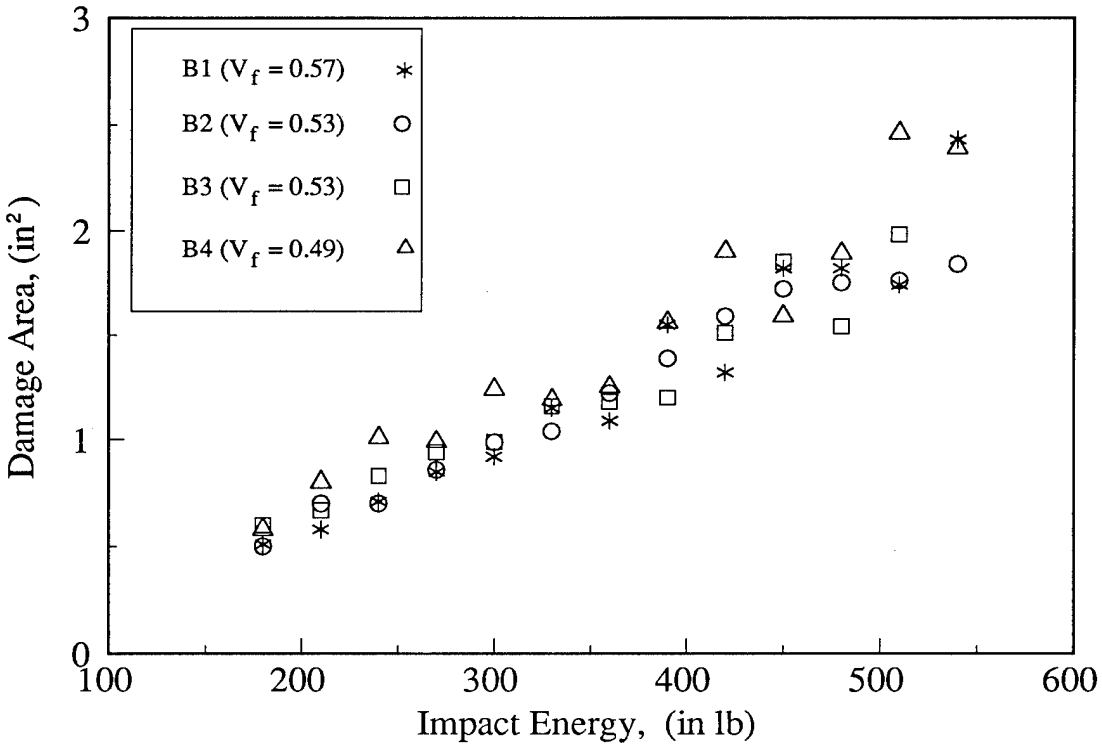


Figure 9. Damage Resistance Results for Resin Content Study

Impact response of the CAI panels was studied experimentally and analytically in order to develop further understanding of this behavior. Impacting was performed using an instrumented impact tower which recorded force-time data at the rate of 40 data points per millisecond for the first 24 milliseconds of the impact events. Force-time, force-displacement and energy-time curves were reduced from these data. Predictions of the elastic impact response of test coupons used a series solution for a laminated composite plate subjected to low velocity impact (Ref. 17). Transverse shear is included in this analysis. The analysis provides force-time and displacement-time predictions for the impact event, as well as stress and strain distributions. The required lamina properties which were not measured experimentally (e.g., E_{22}, G_{12}) were determined from a combination of results from existing databases for the baseline material and calculations using micromechanics (Ref. 18).

Figure 10 shows experimental force-time curves for batches B1, B2 and B4 subjected to a 180 in-lb impact. Results are not presented for B3 since B2 and B3 displayed very similar impact response. The overall resin contents were identical for batches B2 and B3 and thus the panel thicknesses and flexural stiffnesses were essentially the same. As shown in Figure 10, higher peak loads and faster load response were obtained from the batches with increased resin content. This reflects increases in flexural stiffness due to greater specimen thickness. Maximum loads measured experimentally during the impact event varied by 7.5% between batches with the highest and lowest resin content. Elastic analysis predicted a 12% difference indicating the greater driving force for damage formation due to increased specimen thickness.

Figure 11 shows analytical and experimental results for a specimen from batch B4 impacted at 180 in-lb. The 180 in-lb impact was the lowest impact energy studied in this work. As mentioned above, the analysis is for elastic behavior and does not include local loss of stiffness due to damage accumulation. The model corresponds well with the experimental results for times of less than

approximately 1 millisecond. The deviation of curves at times greater than 1 millisecond is hypothetically due to the development of damage in the panel. Thus, the analytical model was used as a benchmark from which to judge the onset of damage. Damage onset loads determined by comparison of the experimental and analytical data as outlined above were 1929 lb, 2094 lb, and 2400 lb for batches B1, B2, and B4, respectively (24% difference between B1 and B4). This appears to relate to increases in G_{IIc}. Any additional correlations would require the formulation of an analytical model to predict the net effect of the competing material and structural variables.

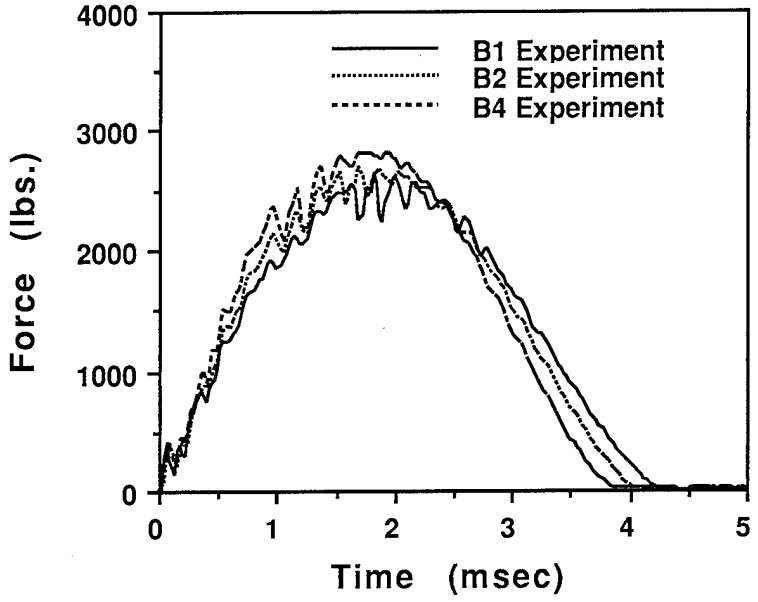


Figure 10. Instrumented Impact Results for the Resin Content Study

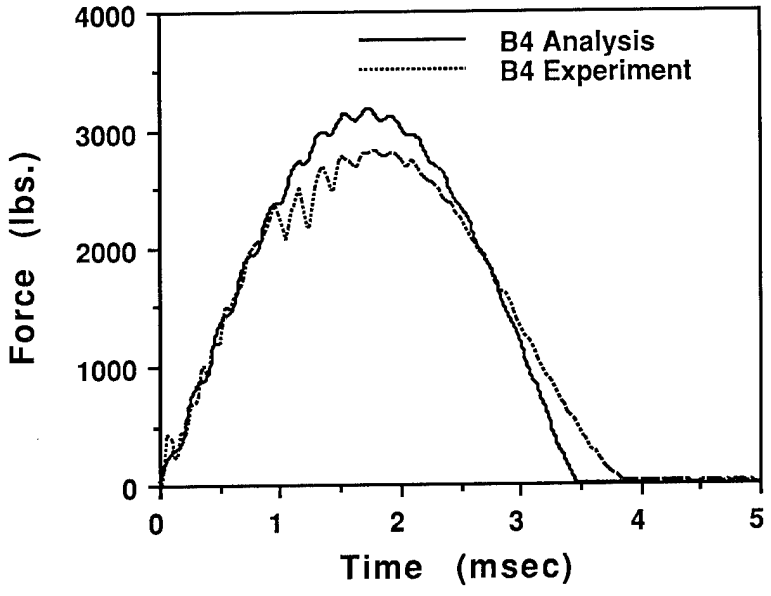


Figure 11. Predicted and Experimental Results for a Specimen from Batch B4, Impacted at an Energy of 180 in-lb.

Competing Failure Mechanisms: Damage mechanisms which are operative during the impact event include delamination, intraply matrix cracking and fiber failure. The relative occurrence of these mechanisms varies with structural configuration, material properties, impact energy, and impactor geometry. Complex interactions between various damage mechanisms contribute to the challenges involved in modeling impact damage resistance of composite materials.

The intraply matrix cracking and delamination which contribute to the formation of a characteristic damage state for the quasi-isotropic CAI specimen has been well documented (e.g., Ref. 9). Delaminations are connected by intralaminar cracks to form a spiral staircase configuration of sublaminates. The relative ratio with which these two mechanisms occur can vary depending on the balance of material properties (Ref. 4). Matrix cracking and interlaminar fracture studies discussed earlier indicated differing relationships with the RIL. The increase in interlaminar G_{IIc} and decrease in in situ strengthening with greater RIL thickness would be expected to favor intralaminar matrix cracking over delamination as a mode for dissipating impact energy. Further work will be performed to study the relative contributions of delamination and matrix cracks to the impact damage state. Clearly, the latter is expected to have less of an effect on CAI.

The TTU method was used to obtain a measurement of the damage area as viewed in the plane of the panel. This has proved to be a useful measure that quantifies the size of known characteristic damage states for CAI analysis. Visible indications of impact damage are also important, both for in-service detection of damage and to identify failure mechanisms. The visible damage documented in this work included dent depth measurements and surface damage descriptions (front and back).

Dent depth measurements are shown in Figure 12 as a function of impact energy for the lowest (B1) and highest (B4) resin content batches. Dent depths were greater for a given impact level in the lower resin content materials. Other visible indications of damage, such as fiber breakage on the front and back surfaces of impacted panels, were also observed to occur at lower energy levels for the lower resin content materials. Local damage mechanisms under the point of impact which lead to visible damage indications are thought to be dominated by fiber failure. It is likely that changes in sublaminate thickness between different material batches affect the ratio of local fiber failure and delamination that occurs.

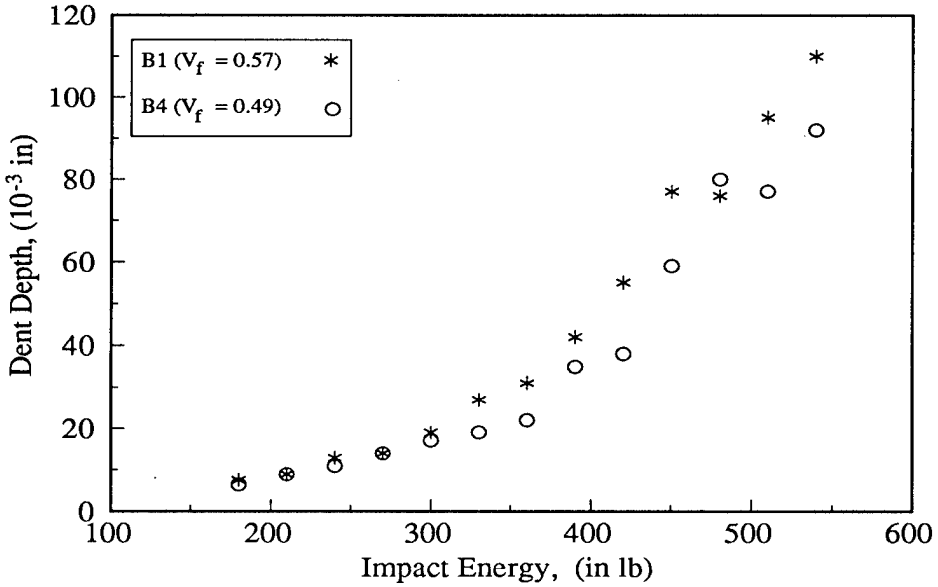


Figure 12. Experimental Measurements of Impacted Surface Damage

Figure 13 shows TTU measurements of damage area plotted versus dent depth for batches B1 and B4. The higher resin content materials, which also had the greatest sublaminate thickness, had larger delamination for a given dent depth. Measurements of the elastic rebound of the impactor indicated that a greater amount of energy was absorbed in tests involving lower resin content materials. This is consistent with increased fiber breakage in these materials. More work is needed to clarify the role of fiber failure in impact damage development.

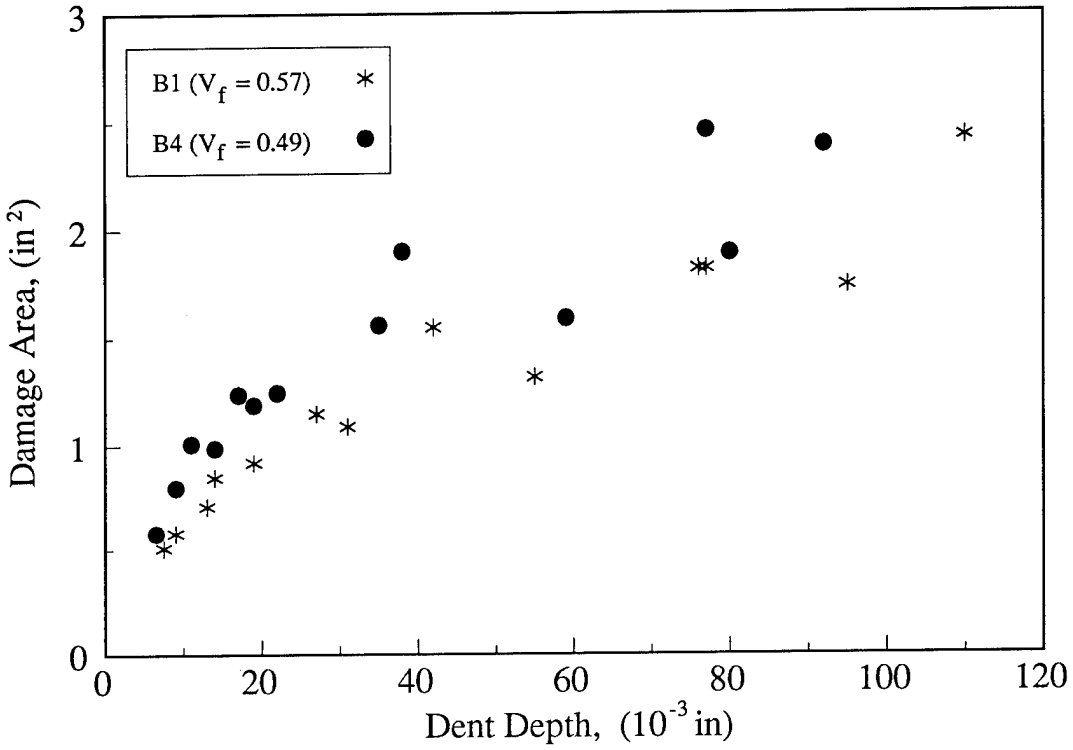


Figure 13. Measurements Relating Delamination Area and Surface Damage

Damage Tolerance: Damage tolerance was investigated using the 4 in. by 6 in. CAI coupon test. Figure 14 shows experimental failure strains versus damage area for the four batches of Toray material. The higher resin content materials exhibit greater failure strains for a given damage size. Since the moduli are lower for higher resin contents, the CAI results for the four batches of material very nearly superposed when plotting failure stress versus damage area.

Results of the CAI tests were compared with predictions obtained using a sublaminate stability analysis described in Reference 9 with good success. This approach has shown good agreement with past experimental data for damage sizes in the range of 1 inch diameter and greater. The model redistributes load in the neighborhood of buckled sublaminates, and then predicts failure due to the effect of this discontinuity. The load carried by sublaminates is assumed to be constant following buckling. Final failure is predicted due to compressive failure at the boundary of damaged and undamaged material. Experimental measurements of compression moduli (Table 4) and compressive failure strains (Table 5) were used in CAI analysis. Per ply thicknesses used in the model were also experimentally determined for the four batches. Other lamina properties required for the analysis were calculated using existing data for batch B1 and micromechanics (Ref. 18) for the three different resin contents.

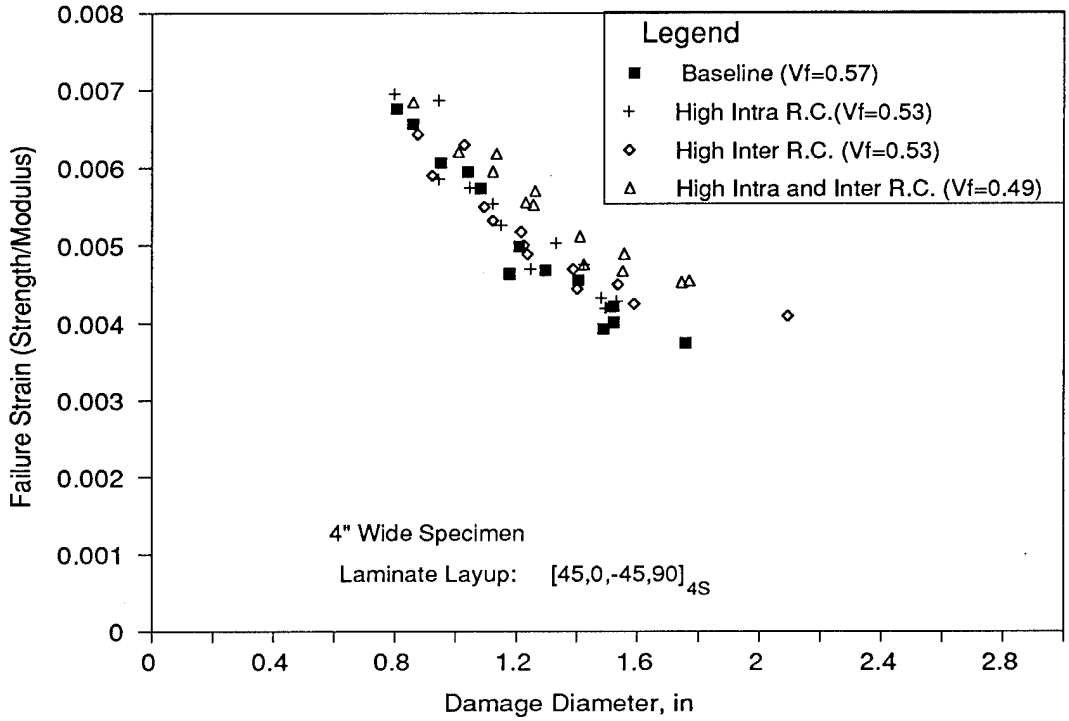


Figure 14. Damage Tolerance Results for the Resin Content Study

Plots of predicted and experimentally determined CAI strengths are shown in Figures 15, 16, and 17. Results for batches B2 and B3 are superposed in Figure 16 because analysis results were equivalent for materials having the same overall resin content. The comparison between theory and experiment is excellent for each case.

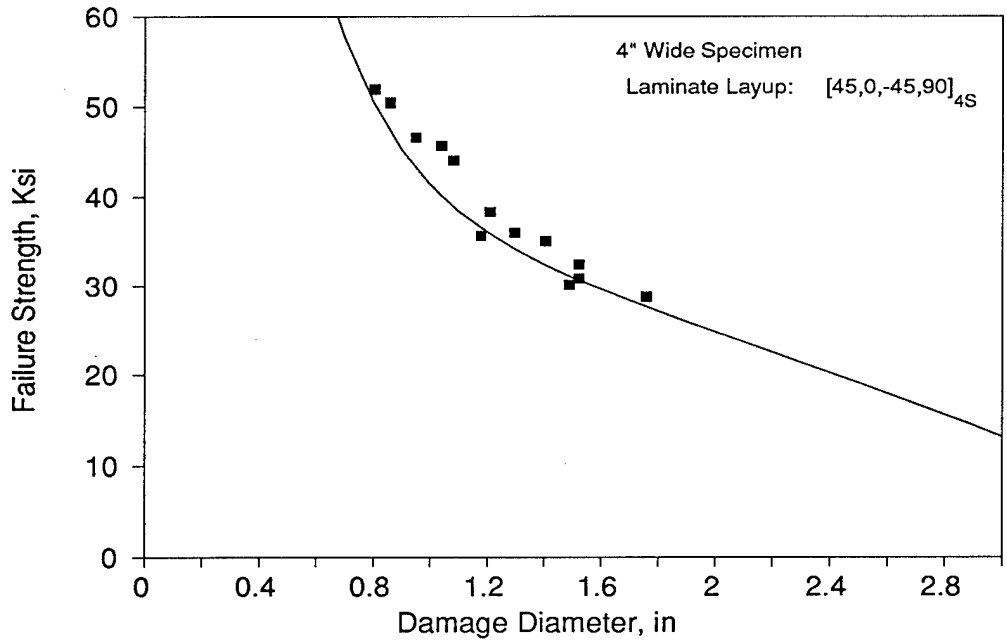


Figure 15. Damage Tolerance Analysis and Test for Batch B1.

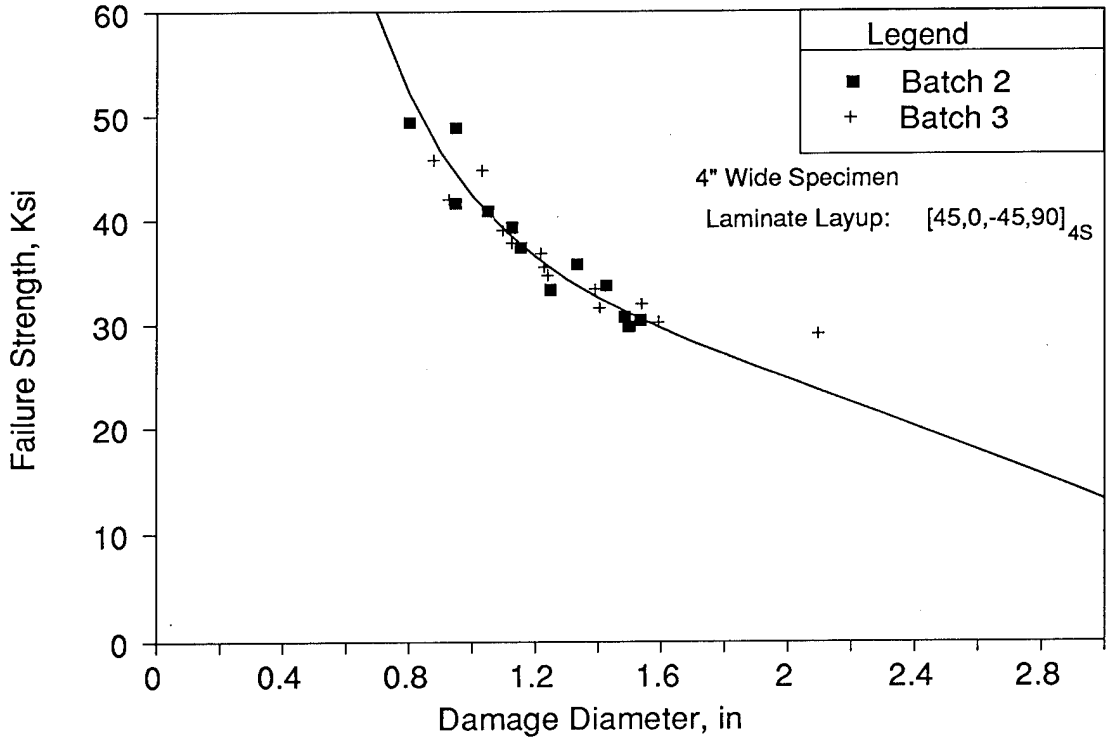


Figure 16. Damage Tolerance Analysis and Test for Batches B2 and B3.

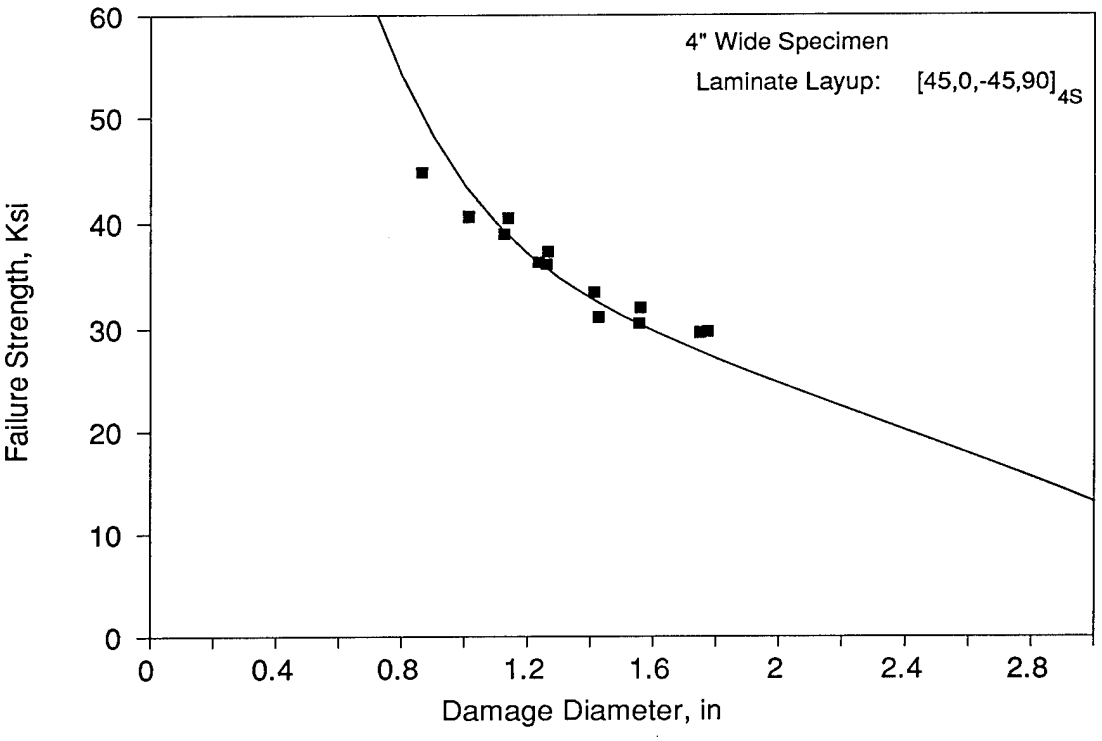


Figure 17. Damage Tolerance Analysis and Test for Batch B4.

A slight deviation was observed between theory and experiment from the highest resin content batch (see Figure 17) for small damage sizes. This is believed to be due to the greater stability of the thicker sublaminates. At small damage sizes, the thicker sublaminates have a greater relative stability and the effect of other impact damage such as fiber failure increases. This deviation of the experimental data from the predicted trend has been noted in past work for materials with per ply thicknesses of greater than 0.007 in. (Ref. 19). The lower resin content materials which have thinner sublaminates comprising their damage zone reflect trends dominated by stability for smaller damage diameters.

ECONOMIC CONSIDERATIONS

Cost and weight trades need to be considered when evaluating the merits of increased resin content. Resin can cost as much as an order of magnitude less than fiber. As a result, the performance value associated with lower material costs may offset marginal increases in weight. Increased resin content may also yield a more robust material for processing (e.g., minimize the void content of complex laminate geometries). If increased resin content results in thicker plies, as in the current study, additional benefits are possible by attaining the required structural thickness with reduced ply layup labor costs. Since flexural stiffness is enhanced with increasing ply thickness, stability performance trades would likely favor increased resin content. The current study provides an example in which damage tolerance is also favorably influenced by increased ply thickness and greater compressive failure strains associated with higher resin contents.

Additionally, approaches have been proposed in which discrete layers of adhesive are selectively placed between plies in areas requiring enhanced interlaminar shear properties. If the performance penalty for uniformly increasing the RIL thickness is small, the economics may favor a uniform RIL rather than adding additional process steps for selectively inserting the adhesive layers. A need for additional interlaminar resin may be required in applications involving considerable amounts of interlaminar load redistribution. Several examples exist for a transport fuselage; including, (1) doubler plies near door and window cutouts, (2) laminate thickness tailoring in keel panels near the keel beam for the redistribution of large compressive loads. The effects of increased resin content on compressive load redistribution in the neighborhood of ply drop-offs will be the subject of additional studies under Contract NAS1-18889.

CONCLUSIONS

Several mechanical properties were evaluated for toughened materials having resin-rich interlaminar layers (RIL). The studies included variations in intra- and inter-laminar resin content. Results indicate that materials with RIL may be favored for applications dominated by compressive loads and interlaminar shear. The keel area of a transport fuselage (i.e., lower portion of the fuselage near the wing-to-body intersection) is one such application. Economic benefits were identified for increased resin content materials. In addition to lower raw material cost, high resin content materials may be more robust for manufacturing. The use of thicker plies in coordination with higher resin content could also reduce layup costs.

The influence of RIL architecture on matrix cracking was investigated with the help of experiments and analysis. The RIL decreased the in-situ transverse strengthening effect noted in past composite studies. Comparisons of analytical and experimental results indicate that matrix crack predictions could be off by more than a factor of two if the effects of RIL and environmental are not adequately simulated.

Increased resin content in RIL materials had little or no benefit for fiber dominated properties such as axial moduli. Changes in axial tension and compression moduli with increasing resin content were accurately predicted by micromechanics methods. The flexural stiffness of high resin content samples increased, despite lower moduli, due to the increased ply thickness.

Compressive failure strains increased with increasing resin content. For example, an 8% by weight addition of resin increased the compressive failure strains of unidirectional specimens by 12%. Similar increases in open-hole compression failure strains were also observed. These results agree qualitatively with the compressive behavior predicted by the model of (Ref. 10).

The increased resin content in the form of an RIL was found to increase mode II interlaminar toughness. The critical mode II interlaminar strain energy release rate was observed to increase 23% due to the addition of 8% by weight of resin. Mode I interlaminar toughness was not affected by resin content in this study.

Higher mode II toughness did not translate to increased impact damage resistance in standard coupon tests. This was due to interactions with structural variables (e.g., increased panel thickness and flexural stiffness) which increased the severity of the impact event for high resin content samples. In the absence of such effects, the increased mode II toughness would be expected to confer improved damage resistance to impact stresses dominated by interlaminar shear.

Visible damage (dent depth and surface fiber breakage) at a given impact energy was greatest for the thinnest specimens (i.e., lower resin content materials). This, combined with the larger delamination areas for the thickest specimens (i.e., high resin content materials), led to a larger ratio of visible to invisible damage for the relatively thin specimens. This reflects differing contributions from the various damage mechanisms which depend on structural variables as well as material properties.

Compression failure strains for a given damage diameter were improved for CAI coupons with higher resin contents. Analytical predictions based on a sublaminate stability approach agreed well with the experimental CAI data for all resin contents. Model variables identified as playing a key role in increasing CAI for higher resin content materials were sublaminate stability and undamaged failure strains. The influence of increased sublaminate stability is apparent in CAI failure strain curves for small damage sizes, while the influence of increased undamaged compressive failure strain is reflected at the larger damage sizes.

ACKNOWLEDGMENTS

The authors would like to acknowledge Toray Industries, Inc. and M. Katsumoto for providing the special resin content materials used in this study. We would also like to thank J. McCool for experimental support.

REFERENCES

1. Masters, J.E., "Characterization of Impact Damage Development in Graphite/Epoxy Laminates," Fractography of Modern Engineering Materials, ASTM STP 984, ASTM, Philadelphia, 1987, pp. 238-258.
2. Evans, R.E., and Masters, J.E., A New Generation of Epoxy Composites for Primary Structural Applications: Materials and Mechanics," Toughened Composites, ASTM STP 937, ASTM, Philadelphia, 1987, pp. 413-435.

3. Ilcewicz, L.B., Dost, E.F., McCool, J.W., and Grande, D.H., "Matrix Cracking in Composite Laminates with Resin Rich Interlaminar Layers, Presented at 3rd Symposium on Composite Materials: Fatigue and Fracture, Nov. 6-7, Buena Vista, Fla., ASTM, 1989.
4. Grande, D.H., and Schaffnit, R.S., "Materials Parameters and Mechanisms Associated with Toughening and Compression After Impact Behavior of Composite Materials," Presented at 2nd Topical Conference on Emerging Technologies in Materials, Nov. 6-9, 1989, San Francisco, American Institute of Chemical Engineers.
5. Recker, H.G., et. al., "Toughened Thermosets for Damage Tolerant Carbon Fiber Reinforced Composites," SAMPE Journal, Vol. 26, No. 2, March/April 1990, pp. 73-78.
6. Chai, H., "Shear Fracture", International Journal of Fracture, Vol. 37, 1988, pp. 137-159.
7. Sela, N., Ishai, O., and Bank-Sills, L., "The Effect of Adhesive Thickness on Interlaminar Fracture Toughness of Interleaved CFRP Specimens," Composites, Vol. 20, No. 3, May 1989, pp. 257-264.
8. Chai, H., "Interlaminar Shear Fracture of Composites," International Journal of Fracture, Vol. 43, 1990, pp. 117-131.
9. Ilcewicz, L.B., Dost, E.F., and Coggeshall, R.L., "A Model for Compression After Impact Strength Evaluation," Proc. 21st International SAMPE Technical Conf., 1989, pp. 130-140.
10. Shuart, M.J., "Short-Wavelength Buckling and Shear Failures for Compression-Loaded Composite Laminates," NASA Technical Memorandum 87640, National Aeronautics and Space Administration, Nov. 1985.
11. Shuart, M.J., "Failure of Compression-Loaded Multi-Directional Composite Laminates," AIAA Paper No. 88-2293, Presented at the AIAA/ASME/ASCE/AHS 29th Structures, Structural Dynamics and Materials Conference, Williamsburg, VA, April, 1988.
12. Coxon. B.R., Walker, T.H., Ilcewicz, L.B., and Seferis, J.C., Proc. of Spring SEM Conf., Society for Experimental Mechanics, 1987.
13. Coquill, S.L., and Adams, D.F., "Mechanical Properties of Several Neat Polymer Matrix Materials and Unidirectional Carbon Fiber Reinforced Composites," NASA CR-181805, National Aeronautics and Space Administration, April, 1989.
14. Carlsson, L.A., Gillespie, J.W. Jr., and Pipes, R.B., "On the Analysis and Design of the End Notched Flexure (ENF) Specimen for Mode II Testing," J. Comp. Mat., Vol. 20, 1986, p. 594.
15. Cairns, D.S., "Impact and Post-Impact Response of Graphite/Epoxy and Kevlar/Epoxy Structures," PhD Dissertation, Massachusetts Institute of Technology, 1987, (TELAC Report #87-15).
16. Quian, Y., Swanson, S.R., Nuismer R.J., and Bucinell, R.B., "An Experimental Study of Scaling Rules for Impact Damage in Fiber Composites," Journal of Composite Materials, Vol. 24, May 1990, pp. 559-570.
17. Dobyns, A.L., and Porter, T.R., "A Study of the Structural Integrity of Graphite Composite Structures Subjected to Low Velocity Impact," Polymer Science and Technology, Vol. 21, No. 8, 1981, pp. 493-498.
18. Chamis, C.C., "Simplified Composite Micromechanics Equations for Hygral, Thermal and Mechanical Properties," NASA TM-83320, National Aeronautics and Space Administration, Feb. 1983.
19.) Dost, E.F., et al, "The Effects of Stacking Sequence On Impact Damage Resistance and Residual Strength for Quasi-Isotropic Laminates," Presented at 3rd Symposium on Composite Materials: Fatigue and Fracture, Nov. 6-7, Buena Vista, Fla., ASTM, 1989.

STUDIES OF FIBER -MATRIX ADHESION ON COMPRESSION STRENGTH[a]

W. D. BASCOM and J. A. NAIRN

University of Utah, Salt Lake City, Ut

D. J. BOLL

Hercules Aerospace, Inc., Magna, Ut

SUMMARY

A study has been initiated on the effect of the matrix polymer and the fiber-matrix bond strength on the compression strength of carbon fiber-polymer matrix composites. The work includes tests with micro-composites, single ply composites, laminates and multi-axial loaded cylinders. The results obtained thus far indicate that weak fiber-matrix adhesion dramatically reduces 0° compression strength. Evidence is also presented that the flaws in the carbon fiber that govern compression strength differ from those that determine fiber tensile strength. Examination of post-failure damage in the single ply tests indicates kink banding at the crack tip.

INTRODUCTION

In the development of advanced carbon fibers over the past decade, improvements in the compressive strength of carbon fiber reinforced polymer (CFRP) laminates has not kept pace with improvements in tensile strength. In Fig. 1, for example, there has been an increase of 40% in the tensile strength of Type II fibers with essentially no improvement in compression strength.

The increase in tensile strength has come about by decreasing the number and perhaps the type of flaws in the fiber through processing changes in the production of the polyacrylonitrile precursor and in the production of the carbon fiber itself. Obviously, these changes in the fiber microstructure have had no effect on compressive strength. In fact, the micromechanics of the compressive failure of CFRP is poorly understood. It is generally believed that failure occurs by a buckling of the fiber based on the observation of kink banding in post-failure examination (1,2). However, there is some evidence that the fibers fail in shear (3-5). Most of the theoretical work assumes fiber microbuckling (6,7) but the agreement between predicted and measured compressive strength is generally poor.

---

[a] NASA Contract NAS1-18883

In the work reported here an effort is being made to identify the micromechanics of compressive failure with emphasis on the effect of the polymer matrix and the bond strength between matrix and fiber. The experimental approach is to examine compressive failure at several levels of test specimen complexity; microcomposites of 1 to 5 fibers embedded in matrix polymers, embedded single ply specimens, unidirectional laminates and finally multiaxially loaded cylinders. Work with the cylinders is not scheduled to begin until April 1991.

MATERIALS

Batches of carbon fiber taken from specific production lots were procured from Hercules (Hercules Aerospace, Magna UT) and set aside for all of the tests in this study. The fibers include sized and G-sized AS4, IM7, and HMS4. The G-sizing is a commercial epoxy compatible sizing. In addition, AS4 and IM7 fibers were coated with a release agent (Frecote 700) and given the designation AS4F and IM7F.

Samples of these fibers were analyzed for surface chemical composition using x-ray photoelectron spectroscopy. The results are listed in Tables I and II. The percent elemental composition for the unsized and G-sized fibers are consistent with published data (8,9). Note the high silicon content on the AS4F and IM7F fibers (Table I) and that the silicon is present as an organo-silicon moiety, i.e., -Si-O-C- (Table II). These results indicate that the release coating is a polysiloxane. Depth profiling of the F-coating using Auger spectroscopy indicated that the coating is approximately 25nm thick and uniformly distributed.

The embedding resins used in the microcomposite and single ply experiments were two diglycidylether Bisphenol A epoxides (DGEBA, Dow DER 332 and Shell Epon 828) cured with either m-phenylene diamine (m-PDA), a polyamine (Texaco D230) or a proprietary amine (Dow DEH 24). An accelerator (AC399) was used with the polyamine curative.

MICROCOMPOSITES

Test Methods

In these experiments the test specimen consists of a single filament embedded lengthwise through the center of a block of transparent epoxy (DGEBA + m-PDA) measuring 3cm x .95cm x .35cm (1.19in. x 0.375in. x 0.125in). The specimen is placed in a compression test fixture fitted with a piezoelectric stress transducer. The specimen is held by side supporting key ways with a clearance of about 1.2×10^{-2}mm (0.005in.). The load is applied hydraulically through an actuator which transmits the force through the load cell and then to a steel bar in contact with the specimen. The space between the side supports permits viewing the fiber using transmitted light with crossed polarizing filters.

The test fixture was mounted on an optical bench as shown in Fig. 2.

Further details of this test procedure can be found in reference 5.

Tensile tests were also done on embedded single filament specimens to determine the fiber-matrix bond strength. Details of this technique can be found in reference 10. Briefly, the specimen, in the form of a miniature dogbone, is placed in a tensile test fixture on the stage of a transmitted light microscope. The test fixture is fitted with an LVDT to measure strain. As the specimen is loaded, the filament fragments until reaching a critical fragment length, l_c, which can be related to the fiber-matrix boundary strength. Ancillary information about the interphase or interfacial strength is obtained from the stress birefringence patterns at fiber breaks when the specimen is viewed between crossed polarizing filters.

Results: Single Filament Compression Tests

In an effort to determine the onset load for fiber fragmentation, the load was applied incrementally at 100 lb. increments. Initial tests indicated that there is a short delay in the development of fiber breaks at a given load so the load was held constant for 3min before counting the number of breaks. Tests were conducted on AS4, AS4G, IM7G and AS4F and the results are presented in Fig. 3.

For the AS4, AS4G and IM7G fibers the majority of fragmentation occurs between 15-20 ksi (103-138 MPa) beyond which the number of breaks increases by only 10 -20% up to the maximum load of 30 to 35ksi (210-240 MPa). Some of the breakage at the higher loads may be due to yielding of the matrix. We are presently determining the load at which yielding (permanent deformation of the specimen) begins. Each datum point in Fig. 3 is an average from 3-4 specimens.

The fact that the onset of extensive fragmentation occurs over the same load range for all three fibers, suggests that they have essentially the same compression strength. As discussed later the 0° laminate strengths for these fibers are reported to be essentially the same. It is instructive to compute the stress in the fiber at the fragmentation loads in Fig. 3 which can be obtained by multiplying the fragmentation stress by the ratio of the fiber modulus to the matrix modulus; $E_f/E_m = 90$. The majority of the fragmentation took place between 12-20ksi (827-138MPa) so the failure strains of the fibers are of the order of 1080-3150ksi (74.4-283 GPa). These values are more than 4x the compression strength of a 0° laminate. However, it is doubtful that the full compressive strength of the fiber is realized in laminate testing. On the other hand, whether the fiber failure strains calculated here are realistic is highly problematical.

It is not obvious why the IM7G fiber developed 3X the number of breaks than the AS4 or AS4G. This result would suggest a higher population of flaws in the IM7 fiber compared to AS4. However, we cannot rule out some mechanical aberration of the test condition. For example, stress transfer may be more efficient into the higher modulus IM7 fiber. Also, the tensile modulus of IM7 is about 20% greater than AS4 so that for a given load on the specimen the strain in the IM7 fiber is approximately 20% greater.

The results for the AS4F fiber are also presented in Fig. 3. This fiber had been sized with a release agent in order to reduce fiber-matrix adhesion. Results are presented below that the coating did essentially eliminate adhesion. The embedded AS4F exhibited a very low level of fragmentation that increased more or less linearly with increasing load. It would appear that the low adhesion significantly reduced the transfer of compression stress from the matrix into the fiber.

Results: Single Filament Tensile Tests

The fiber-matrix adhesion strength can be determined using the single embedded filament tensile test. When the fiber fragment length reaches the critical length, i.e., the fragment is too short for stress transfer to reach the fiber tensile strength, σ_c. The boundary shear strength, τ, is given by

$$\tau = \frac{\sigma_c d_f}{2 l_c} \qquad [1]$$

where d_f is the fiber diameter and l_c is the critical length. A number of assumptions are needed to transform the experimental critical length data into boundary shear strengths, the most difficult being how to express the statistical distribution of the fiber tensile strength. Some of this uncertainty can be avoided by simply taking the critical aspect ratio, l_c/d_f as a *relative* measure of interfacial strength. This approach requires that comparisons be made for fibers that have similar tensile strengths and strength distribution. This assumption is not entirely valid for the fibers tested here. None the less, for present purposes the comparison of critical aspect ratios is a useful approximation.

The critical aspect ratios for the AS4 and IM7 fibers are listed in Table III. The matrix was DGEBA (Epon 828) cured with m-PDA. Each datum point is the average of 10-12 specimens. The observed values are comparable to values published elsewhere (10). They are in the range expected for strong adhesion and this conclusion was supported by the stress birefringence observations.

No fiber breaks were observed for the AS4F fiber in the same epoxy up to a nominal strain level of over 4.6%. Evidently, the critical length is greater than the length of the embedded filament, 2.5cm, and so the critical aspect ratio is greater than 3751! Clearly, the release coating on this fiber has essentially eliminated any adhesion both frictional as well as chemical.

In these tests the fragmentation "rate" was measured and plotted as breaks/mm *vs* applied strain. The results are presented in Figs. 4-7. There was a more or less linear increase in the fragmentation up to the critical length. Note that this initial slope is lower for the AS4G compared to the unsized AS4 and dramatically reduced in the case of IM7G compared to IM7. The lower slopes for the sized fibers indicate fewer weak flaws. Evidently, the sizing does protect the fiber from damage during spooling and packaging. Flaws produced during processing are usually severe surface flaws.

SINGLE PLY COMPRESSION TESTS

Test Methods

Our goal in single ply compression experiments is to develop a test procedure by which we can directly measure the compression strength of single plies and can also observe the initiation and propagation of compression damage during the experiments. The testing jig is shown in Fig. 8. In brief, the sample is sandwiched between two constraining plates. The plates are coated with grease or a similar non-stick substance to minimize the loads transferred into the sample sides through friction. The compressive load is applied uniaxially using shim stock whose thickness is matched to the single-ply specimen. The front constraining plate is made of transparent Lucite to allow observation of the samples during testing.

Our first experiments were with rectangular shaped single ply graphite/polysulfone composites. These failed at the sample ends by a crushing mechanism. To minimize end-effects we adopted the mini-dogbone geometry shown in Fig. 8. Single-ply mini-dogbone specimens failed by longitudinal splitting or by out-of plane buckling. These types of failures are not representative of uniaxial compression failure. To get uniaxial compression failures we added extra constraint to the single-ply specimens by embedding them in an epoxy. By using the lateral side supports shown in Fig. 8 in addition to an embedding epoxy, we were able to minimize the amount of embedding epoxy required to get compressive failures. The less embedding epoxy used, the less we need to correct our measurements to determine composite compression strength.

To determine the amount of embedding epoxy required, we measured the load at failure as a function of total specimen thickness. In each sample, the single-ply was 5 mils thick and located approximately at the center of the specimen and the amount of embedding epoxy was varied to vary the total sample thickness. The measured load at failure was converted to the compression of the composite using a simple rule-of mixtures formula:

$$\sigma_c = \frac{P_{total} E_c}{(E_c A_c + E_e A_e)}$$

where E_c and E_e are the moduli of the composite single ply and of the embedding epoxy and A_c and A_e are the cross-sectional areas of the composite single ply and of the embedding epoxy at the location of the compression failure.

Experimental results for a graphite/polysulfone matrix single-ply composite are presented in Fig. 9. The 5 mil samples are for unembedded single plies and they fail at a very low loads. As the thickness of the embedding epoxy is increased, the failure load increases and appears to reach a plateau value for samples with thicknesses above 24 mils. Observation of the failures also suggests that the thicker samples fail by an in-plane axial compression failure mode while the thinner samples exhibit significant out-of plane buckling. The average compressive stress of the 24 mil and thicker

specimens was 810 MPa. This result is close to 0° compression strength literature values for graphite/polysulfone laminates (800-1000 GPa).

Similar tests of AS4/3501 single-ply composites gave similar results. The compression strength increased and reached a plateau for specimens thicker than 19 mils. The average compression strength for the samples thicker than 19 mils was 1470 MPa. This result is close to the literature value of 1600 to 1700 MPa for 0° compression strength.

The amount of embedding epoxy required to achieve in-plane compression failure is about 3-4 times the thickness of the single ply. By measuring the compression properties of neat embedding epoxy, it was determined that in these specimens, about 80% of the load is carried by the composite and therefore the amount of correction required to extract the composite compression strength is small. We also note that the compression failure, which is always at the middle of the sample, begins at one edge and propagates towards the middle. The crack propagates across the sample in about 1 second.

A specimen preparation procedure has been developed that addresses two critical problems: minimizing bubble formation in the embedding resin and alignment of the ply so that it is centered and parallel to the loading direction. Sample misalignment within the embedding epoxy will introduce scatter in the experimental results. The single-ply specimens are cured in a mold under pressure in a hot press. If pressure is applied too soon after start of cure, the embedding epoxy viscosity is too low and the pressure causes movement of the single ply resulting in poor alignment. To avoid this problem, pressure is not applied until 10 to 15 minutes after the start of cure. During this waiting time the viscosity of the epoxy increases (as observed by a parallel batch of neat epoxy). When pressure is applied to the higher viscosity curing epoxy there is much less movement of the ply. Alignment can easily be checked visually by observing the specimen edge-on which is routinely done for all specimens.

The number of entrapped bubbles was minimized by out-gassing the epoxy before specimen preparation.

Results

Single-ply compression tests have been done on the following fiber types — AS4, AS4G, IM7, IM7G and HMS4. Each of these fibers was prepregged with Hercules 3501-6 epoxy. The embedding epoxy consisted of a DGEBA epoxide (DER332) a curative (D230) and an accelerator (AC399). The results are presented in Table IV. Each reported number is an average of at least 20 measurements.

There is some dependence of the compression strength on the fiber type with the AS4 fibers giving the highest compression strength, IM7 fibers giving a slightly lower compression strength, and HMS4 fibers giving a significantly lower compression strength. The difference between the AS4 and IM7 results may not be statistically significant. In addition to the observed strength differences there were differences in the mode of failure. The AS4

and the IM7 plies fail suddenly; in other words, immediately after crack initiation, the damage propagates through the entire cross section of the specimen. In contrast, the HMS4 plies fail by slow crack growth. With HMS4 plies, it is possible to stop the test and arrest the damage process.

There was no significant effect of the G sizing. The AS4 fibers showed no effect and the result for the IM7G fiber was 7% lower than for the unsized fiber. This 7% difference is probably within experimental error.

An anticipated advantage of the single ply tests is the ability to observe failures as they occur. Samples of AS4/3501-6 and IM7/3501-6 tested at relatively high cross-head rates (0.1 mm/sec) exhibited two types of failure - rapid unstable failure across the entire composite cross section and slow stable compression failure propagation. The stable crack growth was nearly always associated with flaws in the embedding epoxy, notably trapped air bubbles.

Post-failure analyses have been done on the single-ply compression samples where the crack had arrested within the ply. The samples were potted in a clear epoxy, sectioned through the compression damage as shown in Fig. 2, polished, and examined using light microscopy. Two types of damage were observed as shown in Fig. 10. The side of the section cut near the crack tip revealed a distinct kink band (Fig. 10A). The other side of the section which was about 2.5cm (0.1in.) back from the crack tip revealed a complex damage pattern that included kink banding, longitudinal splitting and planes of shear failure (Fig. 10B). Presumably, some of this damage was the result of post-failure crushing.

An obvious concern is that the embedding epoxy should only provide support and not influence the compression strengths measured for the single plies. To test for this effect we tested specimens that were identical except for the embedding epoxy. The most important property of the epoxy is probably its modulus and we therefore varied the embedding epoxy modulus.

We used two different epoxys; Epoxy 1 (DER332 + D230 + AC399) which has a compression modulus of 2.85 GPa and Epoxy 2 (DER 332 + DEH24) which has a compression modulus of 2.25 GPa. Thus, Epoxy 2 has a compression modulus that is 21% lower than that of Epoxy 1. The compression moduli of these two epoxies were measured on specimens prepared identically to the single-ply compression specimens except lacking the single ply. We used these epoxies to embed IM7/3501-6 and HMS4/3501-6 single plies. The specimens were tested in compression and the results are presented in Table V; each reported number is an average of at least 20 specimens.

The compression strengths in Epoxy 2 are 2% to 8% lower than those in Epoxy 1. These differences are small and within experimental uncertainty. We suggest that for embedding epoxys with compression moduli greater or equal to those used here ($\geq$2.25 GPa) that the observed compression strengths and compression properties of embedded single plies are independent of the properties of the embedding epoxy. It is possible that much lower moduli embedding epoxies would not provide sufficient support and therefore might affect the results.

LAMINATE TESTING

0° Compression Tests

Tests have been completed for AS4, AS4G, AS4F, IM7, IM7G, IM7F, HMS4, HMS4G and HMS4F fibers in 3501-6. The results are presented in Table VI. The AS4 and the IM7 laminates have essentially the same compression strength for both unsized and G-sized fiber. The HMS4 laminates, unsized and G-sized, had compression strengths of one-half of that obtained for the AS4 and IM7.

Sizing the fiber with a release coating reduced the compression strength of the AS4 and IM7 laminates by nearly a factor of three. The effect of the release coating on the HMS4 compression strength was less than 25%.

Clearly, a reduction in the fiber-matrix adhesion significantly reduces the 0° compression strength. The fact that the compression strength of the HMS4 laminates was significantly less than for the AS4 and IM7 laminates and that applying a release coating to the HMS4 fiber had less of an effect than for the AS4 or IM7 suggests that the adhesion between the HMS4 and the 3501-6 matrix is inherently low. This conclusion is supported by adhesion measurements using the single embedded filament test (11,12) and from short beam shear tests (13). The low adhesion of the HMS4 has been attributed to a cohesively weak skin of highly oriented graphite basal planes that have low resistance to interfacial shear stresses. Application of the release coating to the HMS4 fiber reduces the adhesion even further and probably shifts the interfacial failure from the fiber skin to the fiber-matrix interface.

GENERAL DISCUSSION

The results of the single filament microcomposite compression tests indicate that failure occurs as a sudden avalanche of fiber breaks over a relatively narrow stress range. This behavior is distinctly different than the fragmentation of single filament microcomposites tested in tension where fragmentation is progressive with increasing load. This difference in behavior indicates different types of fiber flaws are involved in compression failure compared to tensile failure.

Application of a polysiloxane release coating to the AS4 and IM7 fibers essentially eliminated any bonding between fibers and matrix. In microcomposite compression testing of the IM7F fiber, the rate of fragmentation was significantly reduced indicating that, because of the loss in adhesion, there was little capability for stress transfer from the matrix into the fiber.

A single ply compression test technique has been developed. When failure is confined to in-plane crack propagation across the ply, the measured compression strengths were comparable to the 0° laminate compression strengths.

In the single ply tests and the 0° laminate tests of the HMS4/3501-6, the

compression strengths were significantly lower compared to the compression strengths of AS4/3501-6 and IM7/3501-6. The low strengths of this high modulus fiber is attributed to low fiber-matrix adhesion (12,13).

The G-size had no discernable effect on compression strength in the single ply and 0° laminate tests. However, the application of a release coating on the AS4 and IM7 fibers reduced the 0° laminate compression strength by a factor of three. The effect of the release coating on the HMS4 fiber resulted in only a 25% reduction in compression strength which suggests that the release coating made an inherently weak interface only slightly worse.

CONCLUSIONS

Single filament microcomposite tests indicated that the fiber flaws responsible for compression failure are different from the fiber flaws that control tensile failure.

The single filament microcomposite tests, the single ply composite tests and the 0° laminate tests all indicate that the compression strength of AS4 and IM7 are essentially identical. The HMS4 single ply and laminate tests resulted in a much lower compression strength than the other fibers due to low fiber-matrix adhesion.

Applying a polysiloxane release coating to the AS4 and IM7 fibers effectively eliminated any adhesion between fiber and matrix. As a result, there was very little stress transfer from the matrix into the fiber and the laminate compression strengths were reduced by a factor of three compared to the unsized and G-sized fibers.

It should be kept in mind that this paper represents "work in progress". The results and conclusions presented here should be viewed as tentative and subject to revision as the study progresses.

REFERENCES

1. Parry, T. V. and Wronski, A. S., "Kinking and Tensile Compression and Interlaminar Shear Failure Mechanisms in CFRP Beams Tested in Flexure," J. Mat. Sci., 16 439 (1981)

2. Hahn, H. T. and Williams, J. G., Mechanics of Composites Review, Dayton OH, Oct. 1984, p.121

3. Ewins, P. D., and Potter, R. T., Phil. Trans. Roy. Soc., A295 507 (1980)

4. Hawthorne, H. M. and Teghtsoonian, E., J. Mat Sci., 1041 (1975)

5. Boll, D. J., Jensen, R. M., Cordner, L. and Bascom, W.D., "Compression Behavior of Single Carbon Filaments Embedded in an Epoxy Polymer," J. Comp. Mat., 24 209 (1990)

6. Rosen, V. M., "Mechanics of Composite Stengthening in Fiber Composite Materials", ASM, 1965, p37

7. Hahn, H. T. and Williams, J. G., "Composite Failure Mechanisms in Unidirectional Composites, NASA Tech. Memo, 85835, Aug, 1984

8. Procter, A. and Sherwood, P. M. A., "X-ray Photoelectron Spectroscopic Studies of Carbon Fibre Surfaces. I. Carbon Fibre Spectra and the Effects of Heat Treatment," J. Electron Spectroscopy and Related Phenomena, 27 39 (1982)

9.Takahagi, T. and Ishitani, A., "XPS Studies by use of the Digital Difference Spectrum Technique of Functional Groups on the Surface of Carbon Fiber," Carbon 22 43 (1984)

10.W. D. Bascom and R. M. Jensen,"Stress Transfer in Single Fiber/Resin Tensile Tests," J. Adhesion, 19 219 (1986)

11. Drzal, L. T.; Rich, M.J.; and Lloyd, P.F.; "Adhesion of Graphite Fibers to Epoxy Matrices; I, The Role of Fiber Surface Treatment, "J. Adhesion, 161 (1983)

12. Dilandro, L. DiBenedetto, A. T. and Groeger, J., "The Effect of Fiber-Matrix Stress Transfer on the Strength of Fiber-Reinforced Composite Materials," Polymer Composites 9 209 (1988)

13. Hercules Carbon Fiber Product Data Sheets, Hercules Inc. Hercules Plaza, Wilmington DE 19895

TABLE I

ELEMENTAL SURFACE ANALYSIS CARBON FIBERS

(Atomic Elemental %)

Fiber Type	C	O	N	Si	Na	Cl	F	Ca
AS4/12K	84	9.1	4.8	0.4	1.0	0.0	0.0	0.0
AS4G/12K	82	14	2.5	0.7	0.6	0.3	0.0	0.0
AS4F/12K	52	26	1.1	21	0.0	0.0	0.0	0.0
IM7/12K	82	13	4.3	0.4	0.1	0.0	0.0	0.0
IM7G/12K	84	13	3.1	0.0	0.1	0.0	0.0	0.2
IM7F/12K	56	26	2.3	17	0.0	0.0	0.0	0.0
HMS4/12K	93	5.1	0.0	0.3	1.4	0.1	0.0	0.0
HMS4G/12K	88	10	0.0	0.0	1.6	0.0	0.0	0.0
HMS4F/12k	59	22	0.0	18	0.0	0.0	0.0	0.0

G in the fiber type is for "G" sizing
F in the fiber type is for FreKote size

TABLE II

HIGH RESOLUTION ESCA FOR CARBON AND SILICON

Atomic Elemental %*

Fiber Type	C_1	C2	C_3	S_1	S_2
AS4/12K	64	14	6.3	0.2	0.2
AS4G/12K	61	21	0.0	0.2	0.5
AS4F/12K	50	2.9	0.0	21	0.0
IM7/12K	62	13	6.4	0.4	0.0
IM7F/12K	49	5.6	0.9	17	0.0
HMS4/12K	80	13	0.0	0.3	0.0
HMS4F/12K	58	1.0	0.0	18	0.0

*Where C_1 = C-R or R-CH
C_2 = C-OR
C_3 = O-C-OR
S_1 = Organic silicone
S_2 = SiO_2

Table III
Critical Aspect Ratios for the AS4 and IM7 Fibers

Fiber	Critical Aspect Ratio	Standard Deviation
AS4	46	6
AS4G	52	8
IM7	66	9
IM7G	66	4

Table IV
Single-ply Compression Strengths

Fiber Type	Compression Strength (GPa)
AS4	1.42
AS4G	1.43
IM7	1.39
IM7G	1.29
HMS4	0.73

Table V
The Compressions Strengths of IM7G/3501-6 and HMS4/3501-6 Single Plies Embedded in Epoxys having Different Moduli.

Fiber Type	σ_c in Epoxy 1 (GPa)	σ_c in Epoxy 2 (GPa)	$\frac{\sigma_c \text{ in Epoxy 2}}{\sigma_c \text{ in Epoxy 1}}$
IM7G	1.31	1.29	0.98
HMS4	0.73	0.67	0.92

Table VI
0° Compression Strengths

	Unsized		G sized		Release coat sized	
Fiber Type	Mean GPa/ksi	Std. Dev. GPa/ksi	Mean GPa/ksi	Std. Dev. GPa/ksi	Mean GPa/ksi	Std. Dev. GPa/ksi
AS4	1.97/285	.149/21.6	1.92/279	.108/15.6	.724/105	.08/11.8
IM7	2.05/296	.095/13.8	2.08/302	.103/14.9	.869/126	.10/14.9
HMS4	1.03/149	.058/8.4	1.00/145	.038/5.5	.786/115	.08/11.9

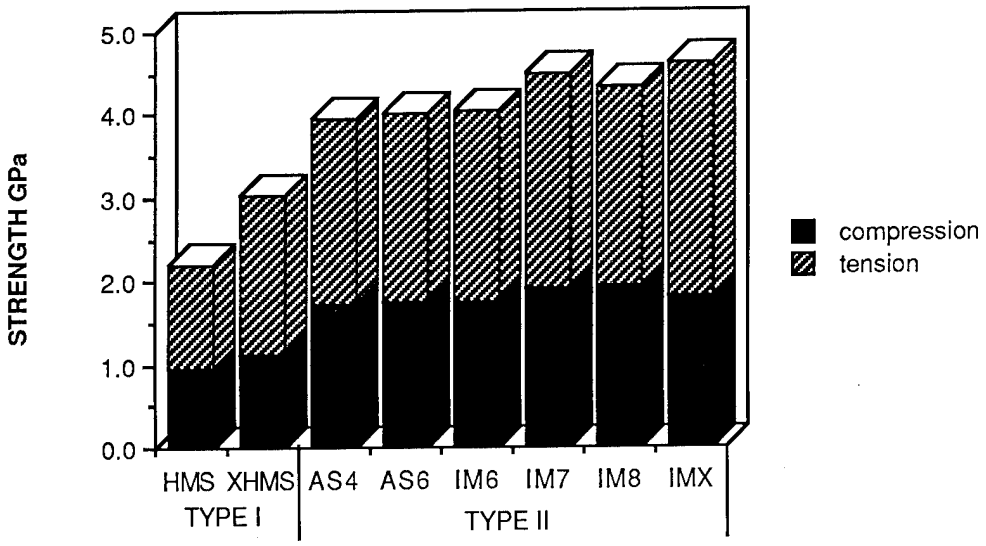


Figure 1 - Uniaxial laminate compression strength *vs* tensile strength (Hercules 3501-6 matrix)

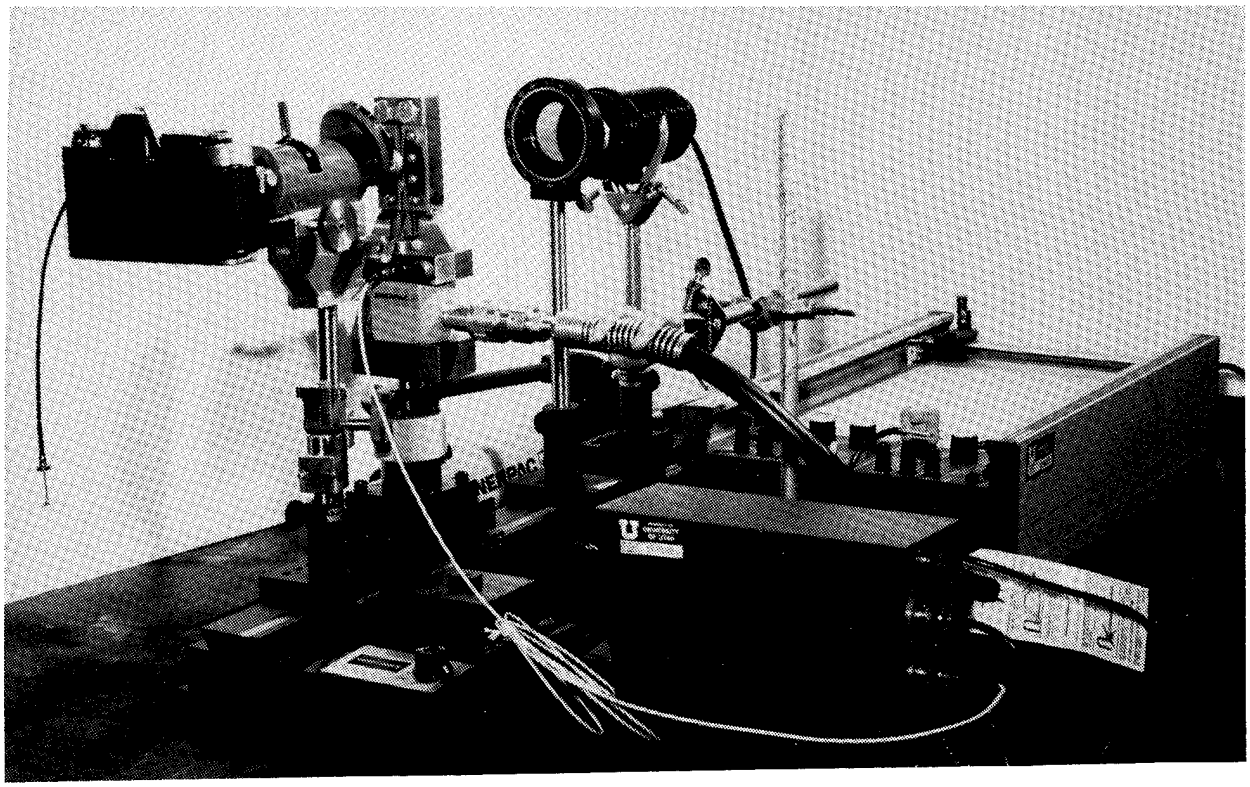


Figure 2 - Optical bench with test fixture for microcomposite compression studies

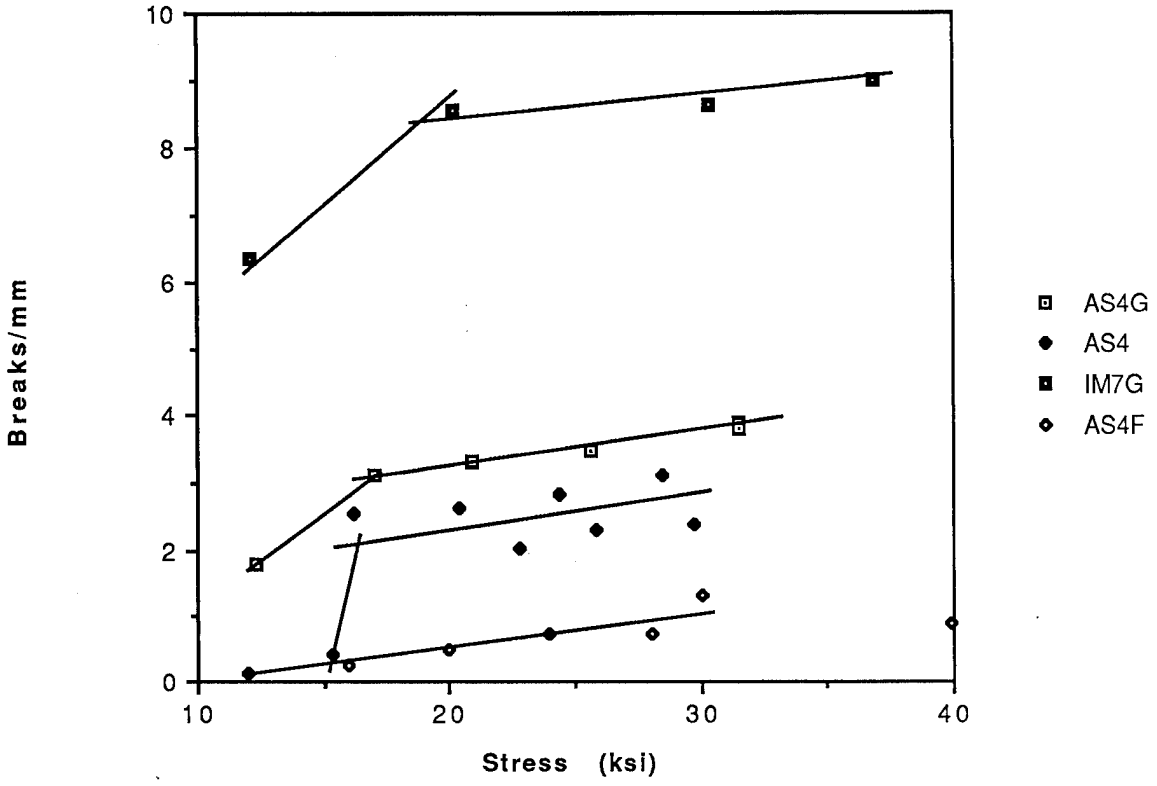


Figure 3 - Fiber fragmentation with increasing stress for single embedded filament compression tests.

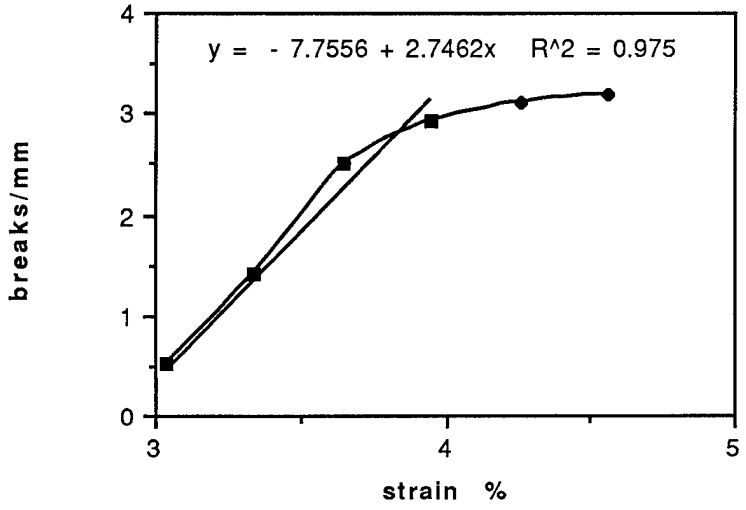


Figure 4 - Fragmentation of AS4 fiber in tension

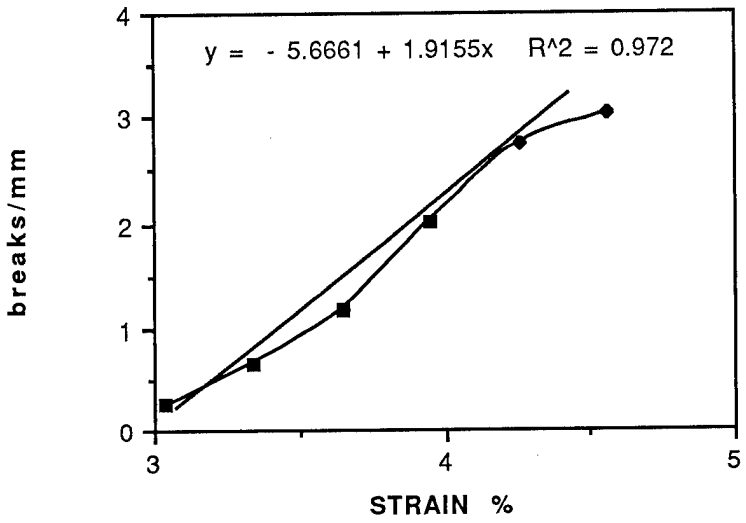


Figure 5 - Fragmentation of the AS4G fiberin tension.

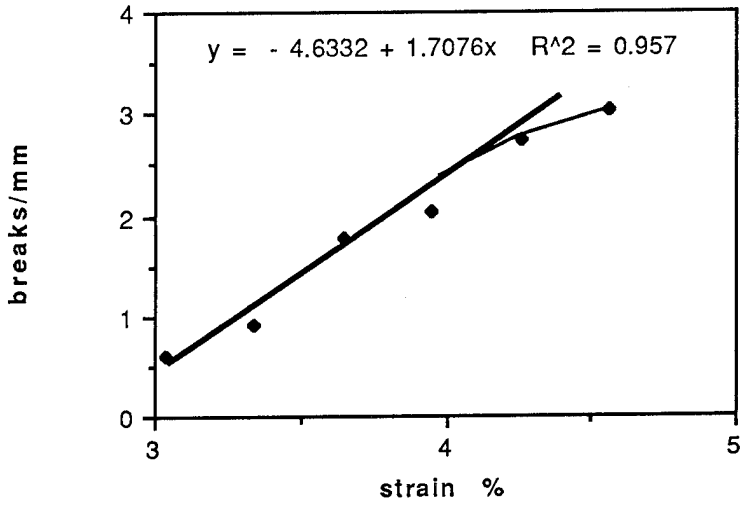


Figure 6 - Fragmentation of the IM7 fiber in tension.

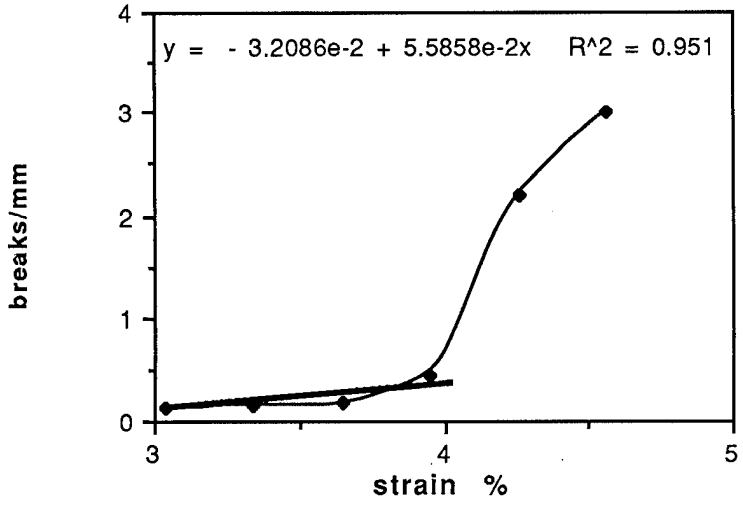


Figure 7 - Fragmentation of the IM7G fiber.

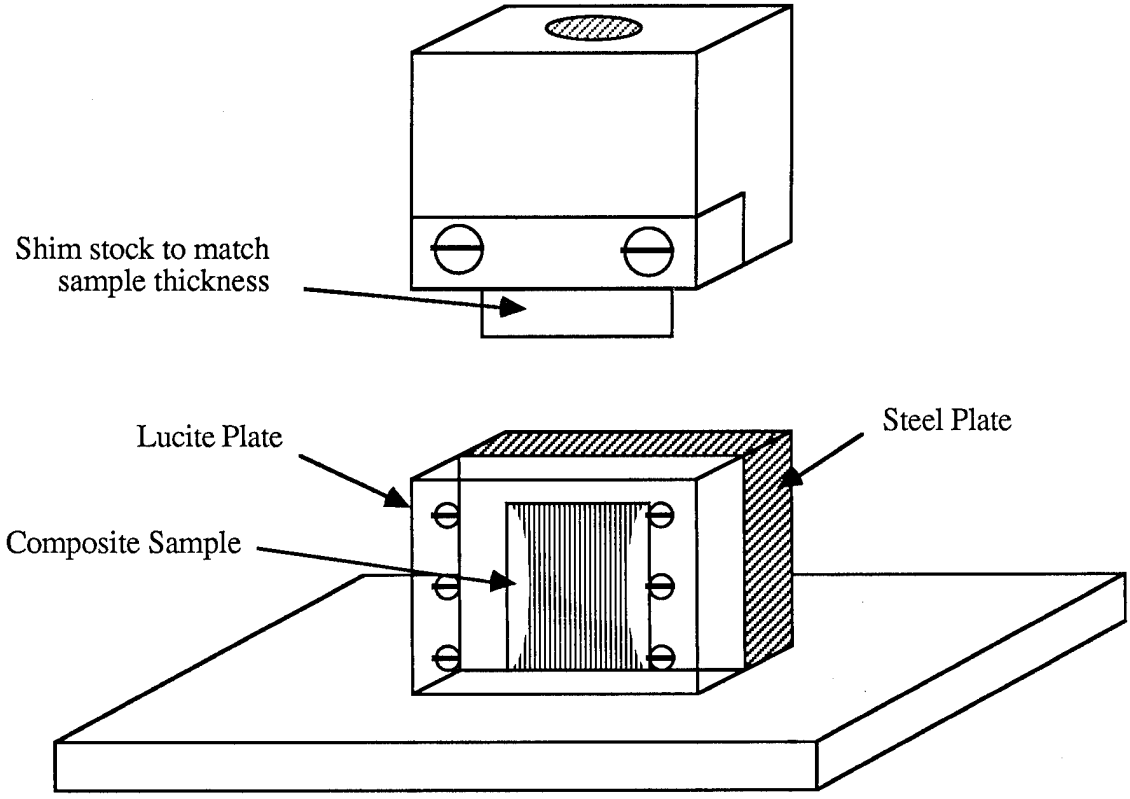


Figure 8 - Test configuration used to obtain compression failures of single-ply composites.

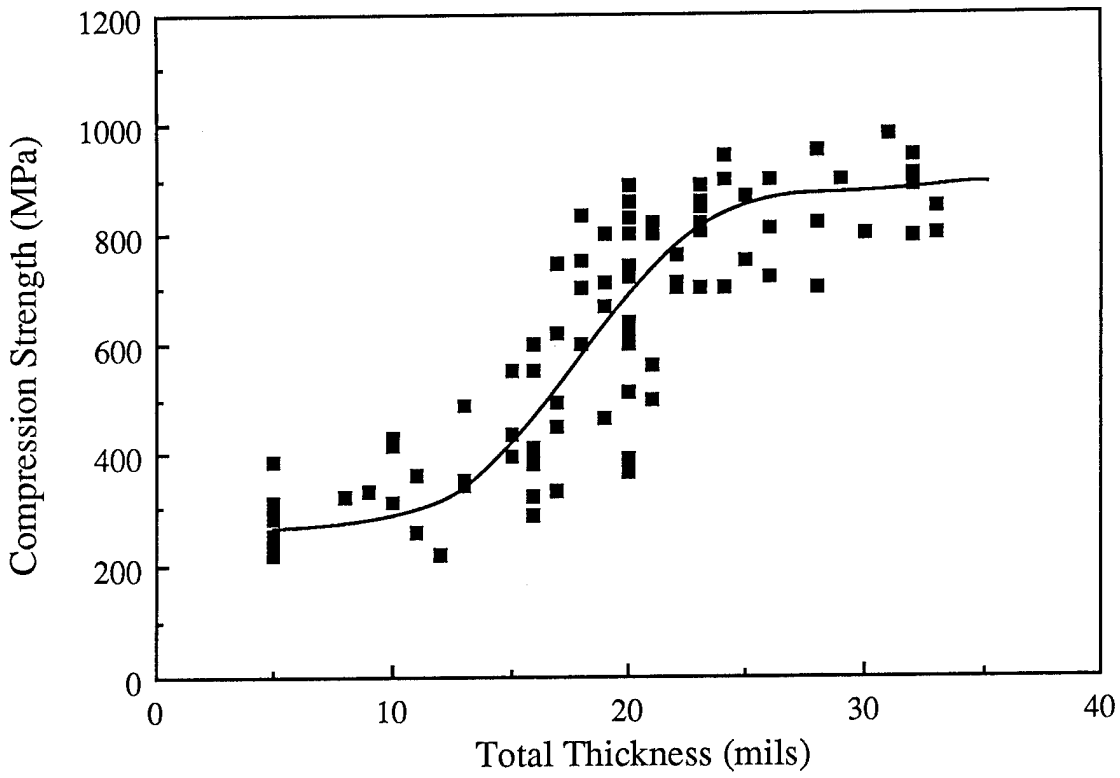


Figure 9 - The compression strength of single-ply graphite/polysulfone composites as a function of total sample thickness.

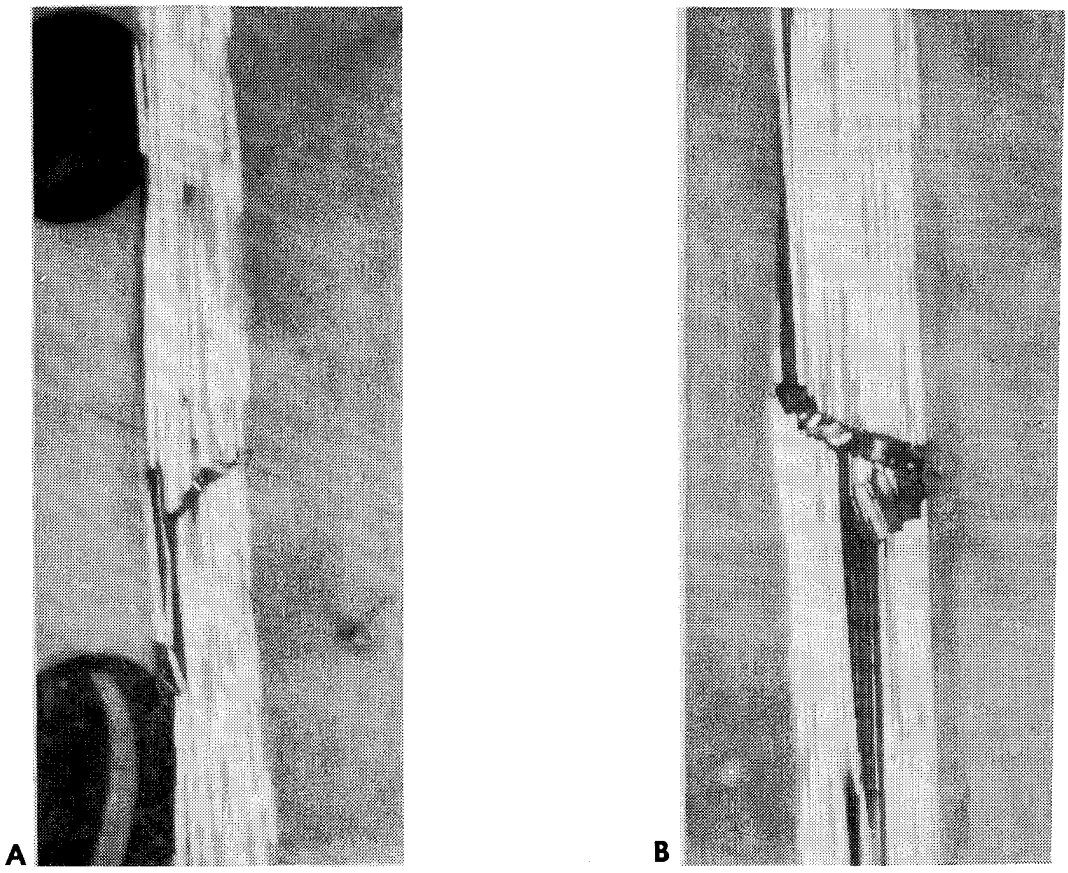


Figure 10 - Damage observed at a crack tip (A) and 2.5cm behind the crack tip(B) for a single ply compression crack.

The Initiation, Propagation, and Effect of Matrix Microcracks in Cross-Ply and Related Laminates †

John A. Nairn, Shoufeng Hu, Siulie Liu, Jong Bark
Material Science and Engineering Department
University of Utah, Salt Lake City, Utah 84112

ABSTRACT

Recently, a variational mechanics approach has been used to determine the thermoelastic stress state in cracked, $[0_n/90_m]_s$ laminates (J. A. Nairn, *J. Comp. Mat.*, **23**, 1106 (1989)). This paper describes a generalization of the variational mechanics techniques to handle other cross-ply laminates ($[90_n/0_m]_s$), related laminates ($[\pm\theta/90_m]_s$, $[90_m/\pm\theta]_s$, *etc.*), and to account for delaminations emanating from microcrack tips. Microcracking experiments on Hercules 3501-6/AS4 carbon fiber/epoxy $[90_n/0_m]_s$ laminates show a staggered cracking pattern. These results can be explained by the variational mechanics analysis. The analysis of delaminations emanating from microcrack tips has resulted in predictions about the structural and material variables controlling competition between microcracking and delamination failure modes.

INTRODUCTION

Many observations have confirmed that the initiation of damage in multidirectional laminates is often by microcracks in the off-axis plies that run parallel to the fibers in those plies [1–8]. These microcracks have typically been studied in cross-ply laminates in which the cracks form in the 90° plies [1–8]. Microcracks form during static testing [1–8], during fatigue testing [3,9,10], and during thermal cycling [11]. Because microcracks cause a reduction in stiffness [3], a change in the thermal expansion coefficient [12,13], and provide sites for the initiation of delaminations, it is important to gain a quantitative understanding of the formation and propagation of microcracks. Two important factors that must be understood are

1. The formation of microcracks in 90° plies is dependent on laminate structure. That is, the cracking process depends on the thickness of the 90° layers, the support provided to the 90° layers by other plies, and whether the 90° plies are on the inside or are adjacent to a free edge.
2. The residual thermal stresses in the 90° plies of cross-ply laminates are typically tensile and of sufficient magnitude to influence the microcracking process.

STRESS ANALYSIS TECHNIQUES

Several attempts have been made at the stress analysis of cross-ply laminates using simplistic analyses (e.g. shear-lag analyses [2,4,6,7,14,15]). While these simplistic models often yield qualitatively reasonable results, they are unsuitable for a thorough understanding of microcracking. Hashin [16,17] was the first to apply variational mechanics techniques. He solved for the modulus [16,17] and the thermal expansion coefficient [18] of $[0_n/90_m]_s$ laminates as a function of microcrack density. Nairn *et al.* [19,20] have extended Hashin's analysis to include residual thermal stresses and to the fracture mechanics analysis of microcracking in $[0_n/90_m]_s$ laminates. This paper describes the variational mechanics approach, how it can be extended to more difficult problems involving $[90_n/0_m]_s$, $[\pm\theta/90_n]_s$, and $[90_n/\pm\theta]_s$ laminates, and how it can analyze delaminations emanating from microcrack tips. In this section, we outline the variational mechanics stress analysis techniques.

Consider a laminate plate with the x axis parallel to the zero degree fibers, the y axis parallel to the 90° fibers, and the z axis normal to the plane of the plate. When the 90° plies have through-the-width microcracks (as is invariably observed in static testing), a two-dimensional analysis of the x-z plane suffices. The x-z plane, or laminate edge, can conveniently be divided into multiple layers (n layers). The layers may

† NASA Contract NAS1-18833

be assigned to individual plies, ply groups, or portions of a ply, depending on the nature of the problem being solved and on the desired accuracy. For the stress state within any layer, we make one and only one assumption — that the x-axis tensile stresses depend only on x and are independent of z. A general stress state for the ith layer that fulfills this assumption and equilibrium is [19,20]

$$\sigma_{xx}^{(i)} = \sigma_{x0}^{(i)} - \psi_i(\xi) \tag{1}$$

$$\sigma_{xz}^{(i)} = \lambda_i f_i(\xi, \zeta) \tag{2}$$

$$\sigma_{zz}^{(i)} = -\lambda_i^2 g_i(\xi, \zeta) \tag{3}$$

where superscript (i) denotes stress in the ith layer, $\sigma_{x0}^{(i)}$ is the x axis tensile in the uncracked laminate, $\lambda_i = t_i/t_*$, $\psi_i(\xi)$ is a function of the dimensionless x direction coordinate $\left(\xi = x/t_*\right)$, f_i and g_i are functions of ξ and of the dimensionless z direction coordinate $\left(\zeta = (z - z_0^{(i)})/t_i\right)$, and $z_0^{(i)}$ is the z coordinate at the start of the ith layer. In these equations, t_i is the thickness of the ith layer and t_* is the thickness of any arbitrarily chosen normalization thickness. The functions f_i, g_i, and ψ_i are interrelated by

$$\frac{\partial f_i}{\partial \xi} = \frac{\partial g_i}{\partial \zeta} \tag{4}$$

$$\psi_i' = \frac{\partial \psi_i}{\partial \xi} = \frac{\partial f_i}{\partial \zeta} \tag{5}$$

We consider a unit cell of damage of a multilayered sample that extends from $x = a$ to $x = -a$ or from $\xi = \rho = a/t_*$ to $\xi = -\rho$. We further consider each layer to be orthotropic with at least one symmetry axis aligned with either the x or z axes. Generalizing the two-layer results from Ref. [19] to n layers, the total complementary energy in the unit cell of damage per unit depth (y direction dimension) can be written as

$$\Gamma = \Gamma_0 + t_*^2 \sum_{i=1}^{n} \int_{-\rho}^{\rho} \left[\frac{\lambda_i \psi_i^2}{2E_{xi}} - \frac{\nu_i \lambda_i^3 \psi_i}{E_{xi}} \int_0^1 g_i d\zeta + \frac{\lambda_i^5}{2E_{zi}} \int_0^1 g_i^2 d\zeta + \frac{\lambda_i^3}{2G_i} \int_0^1 f_i^2 d\zeta \right.$$
$$\left. + \lambda_i^3 \left(\frac{\sigma_{x0}^{(i)} \nu_i}{E_{xi}} - \alpha_{zi} \Delta T \right) \int_0^1 g_i d\zeta - \alpha_{xi} \lambda_i \Delta T \psi_i \right] d\xi \tag{6}$$

where E_{xi}, E_{zi}, G_i, ν_i, α_{xi}, and α_{zi} are the mechanical properties of the ith layer, being, respectively, x and z direction tensile moduli (E_{xx} and E_{zz}), in-plane shear modulus (G_{xz}), in-plane Poisson's ratio (ν_{xz}), and x and z direction thermal expansion coefficients. The term $\Delta T = T_0 - T_s$ is the temperature differential between the stress-free temperature (T_0) and the specimen temperature (T_s). The term Γ_0 is a constant energy term that does not enter energy minimization procedures.

The analysis procedure for a large variety of problems are similar:

1. From observation of experimental results, model microcracking damage by a unit cell of damage extending from $x = -a$ to $x = a$.
2. Divide the laminate into n layers where the divisions are chosen for sufficient accuracy.
3. Using boundary conditions and stress continuity conditions, express the f_i and $g_i$functions in terms of the ψ_i functions and explicit functions of ζ (this step is always possible).
4. Rewrite the total complementary energy in integral form involving only the ψ_i functions.
5. Using the calculus of variations, minimize the complementary energy to solve for the ψ_i functions. The principals of variational mechanics state that these functions will provide the best approximation to the true stress state.
6. With knowledge of the ψ_i functions, it is possible to find the sample modulus [16,17,19], the thermal expansion coefficient [18,19], the total strain energy [19,20], and the energy release rate due to the propagation of damage [19,20].

When n is large, solving for all the ψ_i functions will necessarily involve numerical calculations. The solution of such problems can be viewed as a complementary energy based finite element (or layer) analysis. When n is small ($n \leq 4$), however, it is often possible to eliminate all but one or two of the ψ_i functions. In such situations, the resulting calculus of variations problem can be solved in closed form. Fortunately, many interesting and relevant cross-ply laminate problems can be expressed with four or fewer layers. The remainder of this paper outlines the solutions to some of these problems.

MICROCRACKING IN $[0_n/90_m]_s$ LAMINATES

When loaded in tension, $[0_n/90_m]_s$ laminates fail in a nearly periodic array of through-the-width microcracks in the 90° plies. The unit cell of damage is shown in Fig. 1A. Because the problem is symmetric about the midplane, the laminate can be divided into two layers of thicknesses t_1 and t_2 (see Fig. 1A). Layer 1 is half the 90° ply group and layer 2 is one of the 0° ply groups. We need to solve for ψ_1 and ψ_2, one of which can be eliminated by force balance. As shown in Ref. [19], the total complementary energy in the unit cell of damage per unit depth can be written in terms of ψ_1 as

$$\Gamma = \Gamma_0 + t_1^2 \int_{-\rho}^{\rho} \left[C_1\psi_1^2 + C_2\psi_1\psi_1'' + C_3\psi_1''^2 + C_4\psi_1'^2 - 2\Delta\alpha\Delta T\psi_1\right] d\xi \tag{7}$$

where $\Delta\alpha = \alpha_T - \alpha_A$, and

$$\begin{aligned} C_1 &= \frac{1}{E_T} + \frac{1}{\lambda E_A} & C_2 &= \frac{\nu_T}{E_T}\left(\lambda + \frac{2}{3}\right) - \frac{\lambda\nu_A}{3E_A} \\ C_3 &= \frac{1}{60E_T}\left(15\lambda^2 + 20\lambda + 8\right) + \frac{\lambda^3}{20E_T} & C_4 &= \frac{1}{3G_T} + \frac{\lambda}{3G_A} \end{aligned} \tag{8}$$

Here, E, G, ν and α denote tensile and shear moduli, Poisson's ratio, and thermal expansion coefficient, subscripts A and T denote axial and transverse properties of the ply material, and $\lambda = t_2/t_1$.

Minimization of the complementary energy in Eq. (7) has been accomplished in Ref. [19]. We quote some useful results. Consider a sample with N unit cells of damage characterized by crack spacings $\rho_1, \rho_2, \ldots, \rho_N$. The sample compliance is [16,19]

$$C = C_0 + \frac{2t_1C_3LE_T^2}{B^2WE_c^2}\frac{\sum_{i=1}^{N}\chi(\rho_i)}{\sum_{i=1}^{N}\rho_i} \tag{9}$$

where W is the sample width (y-direction dimension), L is the sample length (x-direction dimension), E_c is the modulus of the uncracked sample, and $C_0 = L/BE_cW$ is the compliance of the uncracked sample. The new function $\chi(\rho)$ has a physical interpretation as being proportional to the excess strain energy caused by the presence of the microcracks. Defining $p = (C_2 - C_4)/C_3$, $q = C_1/C_3$,

$$\chi(\rho) = 2\alpha\beta\left(\alpha^2 + \beta^2\right)\frac{\cosh 2\alpha\rho - \cos 2\beta\rho}{\beta\cosh 2\alpha\rho + \alpha\sin 2\beta\rho} \qquad \text{for } \frac{4q}{p^2} > 1 \tag{10}$$

$$\chi(\rho) = \alpha\beta(\beta^2 - \alpha^2)\frac{\tanh\beta\rho\tanh\alpha\rho}{\beta\tanh\beta\rho - \alpha\tanh\alpha\rho} \qquad \text{for } \frac{4q}{p^2} < 1 \tag{11}$$

where for $4q/p^2 > 1$

$$\alpha = \frac{1}{2}\sqrt{2\sqrt{q} - p} \quad \text{and} \quad \beta = \frac{1}{2}\sqrt{2\sqrt{q} + p} \tag{12}$$

and for $4q/p^2 < 1$

$$\alpha = \sqrt{-\frac{p}{2} + \sqrt{\frac{p^2}{4} - q}} \quad \text{and} \quad \beta = \sqrt{-\frac{p}{2} - \sqrt{\frac{p^2}{4} - q}} \tag{13}$$

We note that the expression for sample compliance (Eq. (9)) has no adjustable parameters and is applicable to any distribution of crack spacings (not just periodic arrays of cracks). Hashin [16] has shown that this expression is in excellent agreement with experimental data.

Table I: The critical microcracking fracture toughness, G_{mc}, for five different carbon fiber composite material systems. Details of experiments given in Ref. [20].

Prepreg Material	G_{mc} (J/m^2)
Hercules 3501-6/AS4	240
Fiberite 934/T300	690
DuPont Avimid® K Polymer/IM6	960
Fiberite 977-2/T300	1800–2400
ICI PEEK/AS4	3000

The total strain energy in the N crack intervals can be written as [19]

$$U = \left(\frac{\sigma_0^2}{2E_c} + \frac{t_1\Delta\alpha^2\Delta T^2}{BC_1}\right) BWL + (C - C_0)\frac{B^2W^2E_c^2}{2E_T^2}\left(\frac{E_T^2}{E_c^2}\sigma_0^2 - \frac{\Delta\alpha^2\Delta T^2}{C_1^2}\right) \tag{14}$$

where σ_0 is the total stress applied to the laminate. The longitudinal thermal expansion coefficient of the cracked sample is [19,20]

$$\alpha_L = \alpha_L^0 - \frac{C - C_0}{C_0}\frac{\Delta\alpha}{C_1E_T} \tag{15}$$

where α_L^0 is the longitudinal thermal expansion coefficient of the uncracked sample. Finally, combining all expressions, we can derive an expression for the energy release rate due to the formation of additional microcracks [19,20]

$$G_m = \left(\frac{E_T}{E_c}\sigma_0 - \frac{\Delta\alpha\Delta T}{C_1}\right)^2 C_3t_1\frac{d}{dD}(D\langle\chi(\rho)\rangle) \tag{16}$$

where $\langle\chi(\rho)\rangle$ is the average value of $\chi(\rho)$ over the N crack spacings and $D = \frac{N}{L}$ is the crack density. We note that Eq. (16) is slightly different than the result from Ref. [19] and corrects an error in that paper. The correct result is derived in Ref. [20].

If we assume that the formation of microcracks is governed by a critical energy release rate or a microcracking fracture toughness, G_{mc}, we can use Eq. (16) to predict the initiation and the increase in crack density in $[0_n/90_m]_s$ laminates. To use Eq. (16), we must evaluate the density derivative of $D\langle\chi(\rho)\rangle$. The formation of a new microcrack between two existing microcracks is shown in Fig. 1B; the crack is shown to form in the middle because that is the location of the maximum stress and because of the tendency of these laminates towards periodic crack spacings. By a discrete evaluation of the required derivative

$$G_m = \left(\frac{E_T}{E_c}\sigma_0 - \frac{\Delta\alpha\Delta T}{C_1}\right)^2 C_3t_1(2\chi(\rho/2) - \chi(\rho)) \tag{17}$$

Given a value of the fracture toughness of a material system, G_{mc}, we can solve Eq. (17) for applied stress, σ_0, and predict the crack density as a function of applied stress. This approach was applied in Ref. [20] to five material systems; for each material system, two to five cross-ply laminates were used. Some typical results for Hercules 3501-6/AS4 carbon fiber/epoxy laminates are given in Fig. 2. For this material, G_{mc} was found to be 240 J/m^2. An important result for this and other materials systems is that a single value of G_{mc} for a given material system suffices to predict the results from all cross-ply laminates tested. Some measured values of G_{mc} are given in Table I.

The variational mechanics analysis of microcracked $[0_n/90_m]_s$ laminates has been useful. Without any adjustable parameters it gives an excellent prediction of the sample modulus as a function of crack density [16]. When implemented into a fracture mechanics analysis of microcracking, it can predict the crack density as a function of applied load [19,20]. Combining experimental results and the energy release rate expression in Eq. (17), it is possible to measure G_{mc}. G_{mc} appears to be a useful material parameter characterizing microcracking or *intralaminar* fracture toughness of composite materials.

MICROCRACKING IN $[90_n/0_m]_s$ LAMINATES

The damage process in $[90_n/0_m]_s$ laminates is more complicated than in $[0_n/90_m]_s$ laminates. When $[90_n/0_m]_s$ laminates are loaded in tension, the 90° plies on either side develop nearly periodic arrays of through-the-width microcracks. Comparing the crack patterns on either side, however, we observe that the cracks on one side are shifted by half a crack spacing from the cracks on the opposite side. Thus, any given microcrack is located approximately midway between two microcracks on the opposing surface. The unit cell of damage for such "staggered" microcracks is shown in Fig. 3A. Because the problem is no longer symmetric about the midplane, we must analyze the entire laminate; we thus divide the laminate into four layers according the ply groups (see Fig. 3A). Layers 1 and 4 are 90° ply groups and layers 2 and 3 divide the 0° ply group into two layers. We need to solve for ψ_1 to ψ_4, two of which can be eliminated by force balance and transverse stress free-edge effects. Finding the complementary energy for this system is a much more difficult than for the $[0_n/90_m]_s$ laminates. The details will be described in a future publication. In this paper we give the key results. The total complementary energy in the unit cell of damage per unit depth in terms of ψ_1 and ψ_4 is

$$\Gamma = \Gamma_0 + t_1^2 \int_0^{\frac{\rho}{2}} \Big(C_1 X^2 + C_{2a} X X'' + C_{3a} X''^2 + C_4 X'^2 - 4\Delta\alpha\Delta T X + C_1^* Y^2 + C_2^* Y Y'' + C_3^* Y''^2 + C_4^* Y'^2 \Big) d\xi \tag{18}$$

where $X = \psi_1 + \psi_4$, $Y = \psi_1 - \psi_4$, C_1 and C_4 are given in Eq. (8), and the new constants are

$$\begin{aligned} C_{2a} &= -\frac{\nu_T}{3E_T} + \frac{\nu_A}{E_A}\left(1 + \frac{2\lambda}{3}\right) & C_{3a} &= \frac{1}{20E_T} + \frac{\lambda}{60E_T}\left(8\lambda^2 + 20\lambda + 15\right) \\ C_1^* &= \frac{1}{E_T} + \frac{(1+2\lambda)^2}{\lambda^3 E_A} & C_2^* &= -\frac{\nu_T}{3E_T} + \frac{\nu_A}{E_A}\left[\frac{(1+2\lambda)(2+\lambda)}{3\lambda}\right] \\ C_3^* &= \frac{1}{20E_T} + \frac{\lambda}{60E_T}\left(2\lambda^2 + 7\lambda + 8\right) & C_4^* &= \frac{1}{3G_T} + \frac{1+\lambda+\lambda^2}{3\lambda G_A} \end{aligned} \tag{19}$$

Minimizing the complementary energy in Eq. (18) would be an intractable problem if it were not for the following symmetry relation between ψ_1 and ψ_4:

$$\psi_4(\xi) = \begin{cases} \psi_1(\xi - \rho) & \text{for } \xi > 0 \\ \psi_1(\xi + \rho) & \text{for } \xi < 0 \end{cases} \tag{20}$$

With this relation, it is possible to minimize the complementary energy in closed form. The details (which are more complicated than the $[0_n/90_m]_s$ problem) will be described in a future publication.

Because the stress analysis of $[90_n/0_m]_s$ laminates is a new solution, we begin with a brief discussion of the resulting stresses. The tensile stress $\sigma_{xx}^{(1)}$, or the tensile stress in the 90° ply on the left of Fig. 3A is plotted in Fig. 4; the plot is for a Hercules 3501-6/AS4 carbon fiber/epoxy $[90_2/0]_s$ laminate with a crack spacing characterized by $\rho = 3$. At the two crack faces $\sigma_{xx}^{(1)} = 0$ as required by boundary conditions. Midway between the two microcracks and directly opposite the crack in the 90° ply on the opposing surface (see Fig. 3A) there is a local minimum in tensile stress. This local minimum is caused by a bending effect that results from the asymmetric arrangement of microcracks. Two local maxima in stresses are located near $\rho = \pm 1$ or at positions roughly $\frac{1}{3}$ and $\frac{2}{3}$ of the way from the bottom microcrack to the top microcrack. The form of the stresses in Fig. 4 can be used to explain the tendency towards staggered microcracks. In Fig. 3B, we show new microcracks formed at all local stress maxima. It is observed that the new microcrack pattern is equivalent to three unit cells of damage and thus the distribution of the stresses naturally leads to the propagation of staggered microcracks.

We next quote some useful results of the new $[90_n/0_m]_s$ laminate analysis. It is possible the cast these results in a form that is reminiscent of the $[0_n/90_m]_s$ laminate results. Consider a sample with N unit cells of damage characterized by crack spacings $\rho_1, \rho_2, \ldots, \rho_N$. The sample compliance is

$$C = C_0 + \frac{2t_1 C_{3a} L E_T^2}{B^2 W E_c^2} \frac{\sum_{i=1}^N \chi_a(\rho_i)}{\sum_{i=1}^N \rho_i} \tag{21}$$

where the new function $\chi_a(\rho)$ has a physical interpretation as being proportional to the excess strain energy caused by the presence of the microcracks; it is defined by

$$\chi_a(\rho) = \frac{2\chi\left(\frac{\rho}{2}\right)}{1 + \frac{C_{3a}\chi\left(\frac{\rho}{2}\right)}{C_3^*\chi^*\left(\frac{\rho}{2}\right)}} \tag{22}$$

In Eq. (22), $\chi(\rho)$ is defined by Eq. (11), except that C_{2a} and C_{3a} replace C_2 and C_3, and $\chi^*(\rho)$ is a new function. Defining $p^* = (C_2^* - C_4^*)/C_3^*$, $q^* = C_1^*/C_3^*$,

$$\chi^*(\rho) = 2\alpha^*\beta^*\left(\alpha^{*2} + \beta^{*2}\right)\frac{\cosh 2\alpha^*\rho + \cos 2\beta^*\rho}{\beta^*\sinh 2\alpha^*\rho - \alpha^*\sin 2\beta^*\rho} \qquad \text{for } \frac{4q^*}{p^{*2}} > 1 \tag{23}$$

$$\chi^*(\rho) = \alpha^*\beta^*\left(\beta^{*2} - \alpha^{*2}\right)\frac{1}{\beta^*\tanh\alpha^*\rho - \alpha^*\tanh\beta^*\rho} \qquad \text{for } \frac{4q^*}{p^{*2}} < 1 \tag{24}$$

where for $4q^*/p^{*2} > 1$

$$\alpha^* = \frac{1}{2}\sqrt{2\sqrt{q^*} - p^*} \qquad \text{and} \qquad \beta^* = \frac{1}{2}\sqrt{2\sqrt{q^*} + p^*} \tag{25}$$

and for $4q^*/p^{*2} < 1$

$$\alpha^* = \sqrt{-\frac{p^*}{2} + \sqrt{\frac{p^{*2}}{4} - q^*}} \qquad \text{and} \qquad \beta^* = \sqrt{-\frac{p^*}{2} - \sqrt{\frac{p^{*2}}{4} - q^*}} \tag{26}$$

As with $[0_n/90_m]_s$ laminates, the expression for the compliance of $[90_n/0_m]_s$ laminates (Eq. (21)) has no adjustable parameters and is applicable to any distribution of crack spacings (not just periodic arrays of cracks). We do not yet have experimental data that can be used to compare predictions to observations.

The total strain energy in the N crack intervals and the longitudinal thermal expansion coefficients are given by expressions identical to the $[0_n/90_m]_s$ laminates (see Eqs. (14) and (15)). A difference between $[90_n/0_m]_s$ and $[0_n/90_m]_s$ laminates occurs because the expressions for compliance, C, that must be used with Eqs. (14) and (15), differ. Finally, combining all expressions, we can derive an expression for the energy release rate due to the formation of additional microcracks

$$G_m = \left(\frac{E_T}{E_c}\sigma_0 - \frac{\Delta\alpha\Delta T}{C_1}\right)^2 C_{3a}t_1\frac{d}{dD}\left(D\langle\chi_a(\rho)\rangle\right) \tag{27}$$

where $\langle\chi_a(\rho)\rangle$ is the average value of $\chi_a(\rho)$ over the N unit cells of damage.

If we assume that the formation of microcracks is governed by a critical energy release rate or microcracking fracture toughness, G_{mc}, we can use Eq. (27) to predict the initiation and the increase in crack density in $[90_n/0_m]_s$ laminates. To use Eq. (27), we must evaluate the density derivative of $D\langle\chi_a(\rho)\rangle$. If we consider the cracking process in Fig. 3B, which perpetuates the staggered arrangement of microcracks, we can evaluate the derivative by the methods used for $[0_n/90_m]_s$ laminates [19,20]. The result is

$$G_m = \frac{1}{2}\left(\frac{E_T}{E_c}\sigma_0 - \frac{\Delta\alpha\Delta T}{C_1}\right)^2 C_{3a}t_1\left(3\chi_a(\rho/3) - \chi_a(\rho)\right) \tag{28}$$

Given a value of the fracture toughness of a material system, G_{mc}, we can solve Eq. (28) for applied stress, σ_0, and predict the crack density as a function of applied stress. Our first experiments have been with Hercules 3501-6/AS4 carbon fiber/epoxy laminates; the results for a $[90_2/0/90_2]_T$ laminate are given in Fig. 5. To be useful, G_{mc} should be a material constant that is independent of stacking sequence. We thus fit the $[90_2/0/90_2]_T$ laminate results using the G_{mc} of 240 J/m^2 found during experiments on $[0_n/90_m]_s$ laminates [20]. The results in Fig. 5 show that Eq. (28) fits the experimental results at high crack density and at zero crack density (microcrack initiation) but shows some deviations at crack densities between 0.0 and 0.4 cracks/mm. The cause of the deviations will require more analysis. We speculate, however, that it is related to the discrete evaluation of the density derivative of $D\langle\chi_a(\rho)\rangle$ inherent in Eq. (28). When the crack

density is low and the microcracks are far apart, the local stress maxima located at $\pm\rho/3$ become diffuse and move away from $\pm\rho/3$ towards $\pm\rho/2$. In other words, it is only at high crack densities that the distribution of the stresses causes cracks to form at $\pm\rho/3$, that damage is driven towards a staggered cracking pattern, and that Eq. (28) gives the true energy release rate. At low crack densities, the cracks will be more random and the expression for energy release rate needs to be modified. Experiments which measure the crack patterns at low crack densities can be used to confirm this speculation and to suggest ways to modify Eq. (28).

Although much more difficult than previous analyses, a closed-form variational mechanics analysis of $[90_n/0_m]_s$ laminates has been obtained. Literature results concentrate of $[0_n/90_m]_s$ laminates to the near exclusion of $[90_n/0_m]_s$ laminates. Clearly more experimental results for $[90_n/0_m]_s$ are desirable. It is our expectation that the variational mechanics analysis will provide the tools necessary for a quantitative understanding of those results.

MICROCRACKING IN $[\pm\theta/90_m]_s$ AND IN $[90_n/\pm\theta]_s$ LAMINATES

The results in the previous two sections can readily be adapted to handle problems of microcracking in 90° plies supported by any orthotropic sublaminate. One simple example is microcracking in $[\pm\theta/90_m]_s$ and in $[90_n/\pm\theta]_s$. In these laminates, θ should be relatively small (*e.g.* $\theta \leq 45$) or else microcracking of the 90° plies may not be the dominant failure mode. The adaptation of the variational mechanics analysis consists merely of adjusting the constants C_1 to C_4, C_{2a}, C_{3a}, and C_1^* to C_4^*. We note that each of these constants, defined in Eqs. (8) and (19), is the sum of two terms. In all cases, the first term results from the 90° plies and the second term results from the 0° plies. To construct a solution for laminates in which the 0° plies are replaced by a $[\pm\theta]$ sublaminate, we merely replace the mechanical properties of the 0° plies in each second term with those of the $[\pm\theta]$ sublaminate.

DELAMINATIONS EMANATING FROM THE TIPS OF MICROCRACKS

All variational mechanics analyses of cross-ply and related laminates can be extended to account for delaminations emanating from the tips of existing microcracks. We illustrate the delamination analysis using $[0_n/90_m]_s$ laminates. Figure 6 shows the region between two microcracks separated by a distance $2a$ having delaminations of length d_1 and d_2 emanating from the top and bottom microcracks and propagating into the region between the two microcracks.

We consider the right half of the symmetric laminate in Fig. 6. We split the area between the two existing microcracks into three regions. Region I is the region within the top delamination or the region from $x = a - d_1$ to $x = a$. Region II is the region between the tips of the delaminations or the region from $x = -a + d_2$ to $x = a - d_1$. Region III is the region within the bottom delamination or the region from $x = -a$ to $x = -a + d_2$. Within each region we divide the right half of the laminate into two layers. Layer 1 is the 90° ply group and layer 2 in the 0° ply group.

We begin with the stresses in the 90° plies in regions I and III. By symmetry, the shear stress at the sample middle must be zero ($\sigma_{xz}^{(1)}(0) = 0$). Because of the requirement for stress free surfaces on the delamination crack face, the shear stress and the normal stress at the right edge of the 90° plies must also be zero ($\sigma_{xz}^{(1)}(1) = 0$ and $\sigma_{zz}^{(1)}(1) = 0$). From these boundary conditions and the form of the stresses in Eqs. (1)–(3) which assume that the normal stress $\sigma_{xx}^{(i)}$ is a function of x only, the stresses in regions I and III are uniquely determined to be

$$\begin{aligned} \sigma_{xx}^{(1)} &= 0 & \sigma_{xx}^{(2)} &= \frac{1+\lambda}{\lambda}\sigma_0 \\ \sigma_{xz}^{(1)} &= \sigma_{zz}^{(1)} = 0 & \sigma_{xz}^{(2)} &= \sigma_{zz}^{(2)} = 0 \end{aligned} \tag{29}$$

The boundary conditions in region II are unaffected by the length or even the presence of the delaminations. With or without the delaminations, the x direction tensile stress and the shear stress are both zero at the top and bottom of region II. The stresses in region II are therefore identical to the stresses calculated in Ref. [19] except that the crack spacing needs to be adjusted. We introduce the dimensionless quantity

$$\delta = \frac{d_1 + d_2}{2t_1} \tag{30}$$

The stresses in region II are identical to the stresses calculated in Ref. [19] for two microcracks whose spacing is characterized by $\rho - \delta$.

With the stresses completely determined, we can follow procedures similar to those in Ref. [19] and evaluate properties of microcracked and delaminated cross-ply laminates. Consider a sample with N unit cells of damage characterized by crack spacings $\rho_1, \rho_2, \ldots, \rho_N$ and by extents of delamination within each crack interval of $\delta_1, \delta_2, \ldots, \delta_N$. The sample compliance is

$$C = \frac{L-d}{L}\left(C_0 + \frac{2t_1 C_3 L E_T^2}{B^2 W E_c^2}\frac{\sum \chi(\rho_i - \delta_i)}{\sum(\rho_i - \delta_i)}\right) + \frac{d}{L}\left(\frac{1+\lambda}{\lambda}\frac{L}{BE_A W}\right) \tag{31}$$

where $d = \sum_{i=1}^{N} 2t_1\delta_i$ is the total sample delamination length. Although we have no experimental evidence to verify Eq. (31), its limiting values are appropriate. In the limit of no delaminations, or $d = 0$, Eq. (31) reduces to Eq. (9). In the limit of complete delamination, or $d = L$, the sample compliance reduces to

$$C_\infty = \frac{1+\lambda}{\lambda}\frac{L}{BE_A W} \tag{32}$$

This is the compliance for a sample in which the 90° plies carry no load. In terms of compliance, the total strain energy is found to be

$$\begin{aligned} U = &\left(\frac{\sigma_0^2}{2E_c} + \frac{t_1 \Delta\alpha^2 \Delta T^2}{C_1 B}\right)(L-d)BW + \frac{\sigma_0^2}{2E_A}\frac{1+\lambda}{\lambda}dBW \\ &+ \left(C - C_0 - \frac{d}{L}(C_\infty - C_0)\right)\frac{B^2W^2E_c^2}{2E_T^2}\left(\frac{E_T^2}{E_c^2}\sigma_0^2 - \frac{\Delta\alpha^2\Delta T^2}{C_1^2}\right) \end{aligned} \tag{33}$$

and the thermal expansion coefficient is found to be

$$\alpha_L = \alpha_L^0 - \frac{d}{L}\frac{\Delta\alpha}{\lambda E_A C_1} - \frac{\Delta\alpha}{C_1 C_0 E_T}\left(C - C_0 - \frac{d}{L}(C_\infty - C_0)\right) \tag{34}$$

The above two-dimensional analysis can immediately be used to find the energy release rate for the growth of a through-the-thickness delamination — G_d. The energy release rate is

$$G_d = -\left.\frac{\partial U}{\partial A}\right|_{const.disp.} = -\frac{1}{2W}\left.\frac{\partial U}{\partial d}\right|_{const.disp.} \tag{35}$$

where A is total delamination area which is equal to $2dW$. We differentiate Eq. (33) realizing that σ_0 and C will depend on d. The result after much simplification (details can be found in Ref. [20]) is

$$G_d = \left(\frac{E_T}{E_c}\sigma_0 - \frac{\Delta\alpha\Delta T}{C_1}\right)^2 C_3 t_1 Y_D(\vec{\rho}, \vec{\delta}) \tag{36}$$

where the function $Y_D(\vec{\rho}, \vec{\delta})$ depends on $\vec{\rho} = (\rho_1, \rho_2, \ldots, \rho_N)$ and on $\vec{\delta} = (\delta_1, \delta_2, \ldots, \delta_N)$. It is given explicitly by

$$Y_D(\vec{\rho}, \vec{\delta}) = \frac{B^2 W E_c^2}{4E_T^2 C_3 t_1}\left(\frac{C_\infty - C}{L-d}\right) + \left(\frac{L-d}{2}\right)\frac{\partial}{\partial d}\frac{\sum\chi(\rho_i - \delta_i)}{\sum(\rho_i - \delta_i)} \tag{37}$$

Imagine a sample with N crack intervals characterized by dimensionless crack spacings and delamination lengths defined by the vectors $\vec{\rho}$ and $\vec{\delta}$. Imagine further some delamination growth confined to the kth crack interval. The $Y_D(\vec{\rho}, \vec{\delta})$ function for this delamination growth simplifies to [20]

$$Y_D(\vec{\rho}, \vec{\delta}) = \frac{1}{2}(\chi'(0) - \chi'(\rho_k - \delta_k)) \tag{38}$$

The differentiation of $\chi(\rho)$ is with respect to the variable ρ.

If we assume that delamination will propagate when $G_d > G_{dc}$ where G_{dc} is a critical energy release rate or *interlaminar* fracture toughness, we can use Eq. (36) to predict the initiation and growth of microcrack induced through-the-width delaminations. One possible problem of this approach is that it uses total energy release rate instead of partitioning it into the various modes — mode I, mode II, and mode III. We suggests that the assumed x-direction propagation of a through-the-width delamination will be mostly mode II deformation. The distinction between using total energy release rate and the mode II part of the energy release rate will therefore be minor. Experimental results are required to determine the adequacy of using total energy release rate as a failure criterion. For the purpose of this discussion, we assume that the total energy release rate failure criterion is valid.

We can use the delamination analysis to discuss competition between microcracking and delamination. The first form of damage in cross-ply laminates is always microcracking. Once the first microcrack has formed, we can ask if a delamination will initiate at that microcrack or if instead another microcrack will form. Comparing the energy release rate for microcracking (Eq. (17)) to the energy release rate for delamination (Eq. (36)), the predicted failure mode will depend on the values of G_{mc} and G_{dc} and on the relative magnitudes of $2\chi(\rho/2) - \chi(\rho)$ and $\frac{1}{2}(\chi'(0) - \chi'(\rho))$. Assuming G_{mc} and G_{dc} are the same (they both represent crack growth through the matrix, albeit possibly by different fracture modes — mode I *vs.* mode II), the predicted failure mode can be determined by plotting the latter two quantities. Figure 7 plots $2\chi(\rho/2) - \chi(\rho)$ and $\frac{1}{2}(\chi'(0) - \chi'(\rho))$ for a typical $[0/90_2]_s$ laminate. The conclusions that can be drawn from this and other similar plots are as follows:

1. At low crack densities, microcracking is preferred. At some critical density, the energy release rate for delamination will surpass the energy release rate for microcracking and delaminations will be expected to initiate at the tips of the microcracks. Once delaminations begin, microcracking will cease and the delaminations will grow.

2. The critical density depends on the laminate structure. For a fixed number of 0° plies, the more 90° plies there are, the lower will be the crack density required to get delamination. For a fixed ratio of 0° to 90° plies, the more plies there are, the lower will be the crack density required to get delamination.

3. If the relative toughnesses for microcracking and delamination are different because of material properties of because of different deformation modes, the critical density for initiation delamination will change. For example, as the delamination fracture toughness gets lower than the microcracking fracture toughness, the critical crack density to initiate delamination will get lower. In the limit of relatively low delamination fracture toughness, delamination will begin after the first microcrack.

When delamination is not through-the-thickness, the problem is no longer two-dimensional and requires a three-dimensional analysis. Although a complete three-dimensional variational mechanics analysis seems intractable, it appears possible to construct a quasi-three-dimensional analysis based on the two-dimensional analysis and a lumped spring model of a laminate containing an arbitrary profile of delamination growth. This problem will be considered in a future publication.

ACKNOWLEDGMENTS

This work was supported in part by a contract from NASA Langley Research Center (NAS1-18833) monitored by Dr. John Crews, in part by a gift from the Fibers Department of E. I. duPont deNemours & Company monitored by Dr. Alan R. Wedgewood, and in part by a gift from ICI Advanced Materials monitored by Dr. John A. Barnes.

REFERENCES

1. H. T. Hahn and S. W. Tsai, *J. Comp. Mat.*, **8**, 288 (1974).
2. K. W. Garret and J. E. Bailey, *J. Comp. Mat.*, **12**, 157 (1977).
3. A. L. Highsmith and K. L. Reifsnider, *ASTM STP*, **775**, 103 (1982).
4. A. Parvizi, K. W. Garrett, and J. E. Bailey, *J. Mat. Sci.*, **12**, 195 (1978).
5. D. L. Flaggs and M. H. Kural, *J. Comp. Mat.*, **16**, 103 (1982).
6. M. G. Bader, J. E. Bailey, P. T. Curtis, and A. Parvizi , *Proc. 3rd Int'l Conf. on Mech. Behavior of Materials*, **3**, 227 (1979).
7. J. E. Bailey, P. T. Curtis, and A. Parvizi, *Proc. Roy. Soc. London*, **A366**, 599 (1979).

8. S. E. Groves, C. E. Harris, A. L. Highsmith, and R. G. Norwell, *Exp. Mech.*, 73 (March, 1987).
9. L. Boniface, P. A. Smith, S. L. Ogin, and M. G. Bader, *Proc. 6th Int'l Conf. on Composite Materials*, **3**, 156 (1987).
10. L. Boniface and S. L. Ogin, *J. Comp. Mat.*, **23**, 735 (1989).
11. C. T. Herakovich and M. W. Hyer, *Eng. Fract. Mech.*, **25**, 779 (1986).
12. D. S. Adams and C. T. Herakovich, *J. Thermal Stresses*, **7**, 91 (1984).
13. D. E. Bowles, *J. Comp. Mat.*, **17**, 173 (1984).
14. P. W. Manders, T. W. Chou, F. R. Jones, and J. W. Rock, *J. Mat. Sci.*, **18**, 2876 (1983).
15. D. L. Flaggs, *J. Comp. Mat*, **19**, 29 (1985).
16. Z. Hashin, *Mechanics of Materials*, **4**, 121 (1985).
17. Z. Hashin, *Eng. Fract. Mech.*, **25**, 771 (1986).
18. Z. Hashin, *Comp. Sci. & Tech.*, **31**, 247 (1988).
19. J. A. Nairn, *J. Comp.Mat.*, **23**, 1106 (1989).
20. J. A. Nairn, Quarterly Report for NASA Contract NAS1-18833, June 1, 1990 (Note: report contains preprint of S. Liu and J. A. Nairn, *J. Comp. Mat.*, submitted, a paper that describes the $[0_n/90_m]_s$ experiments).

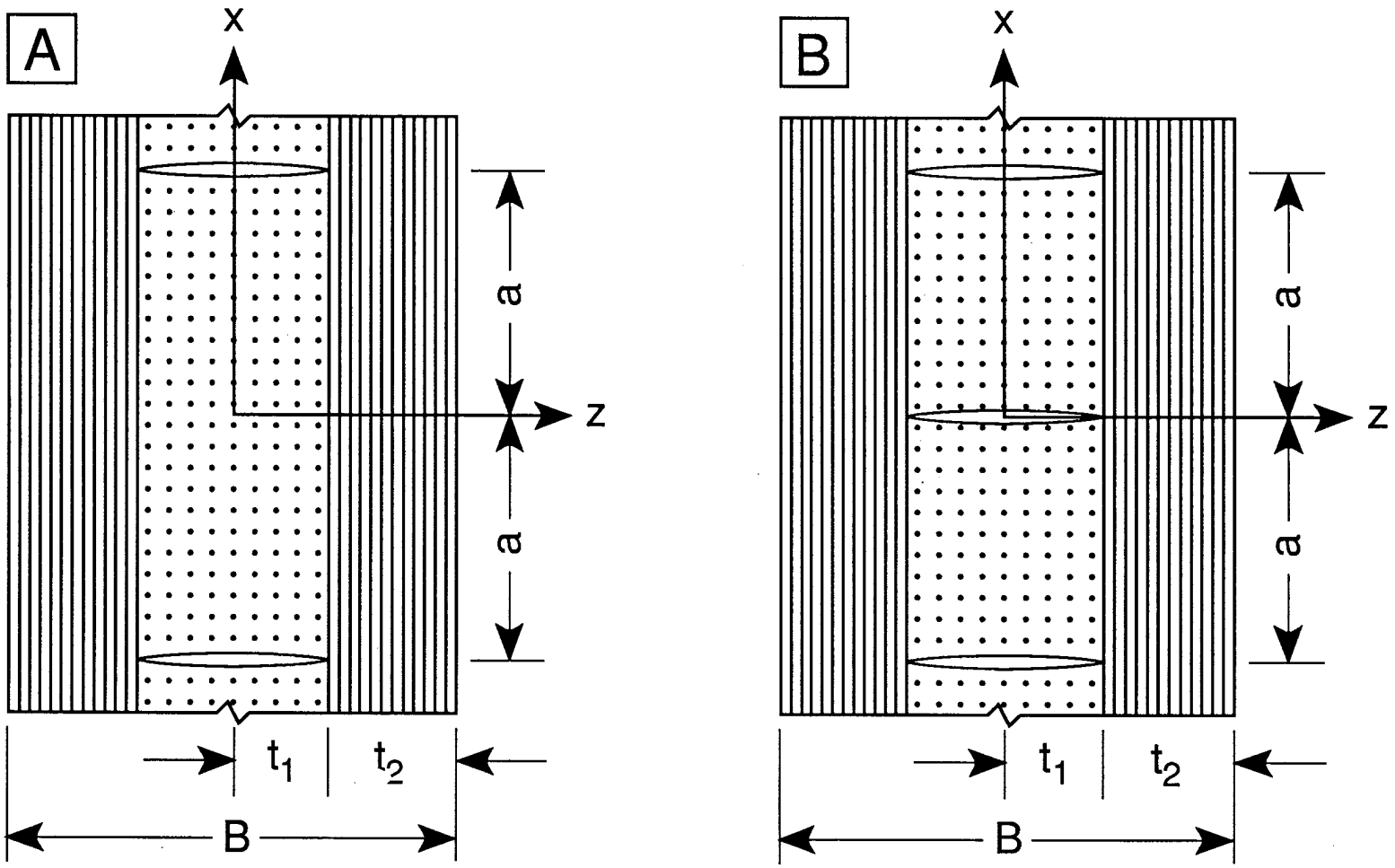


Figure 1: Edge view of a $[0_n/90_m]_s$ cross-ply laminate with microcracks. A: Two microcracks in the 90° plies. B: The formation of a new microcrack midway between to two existing microcracks.

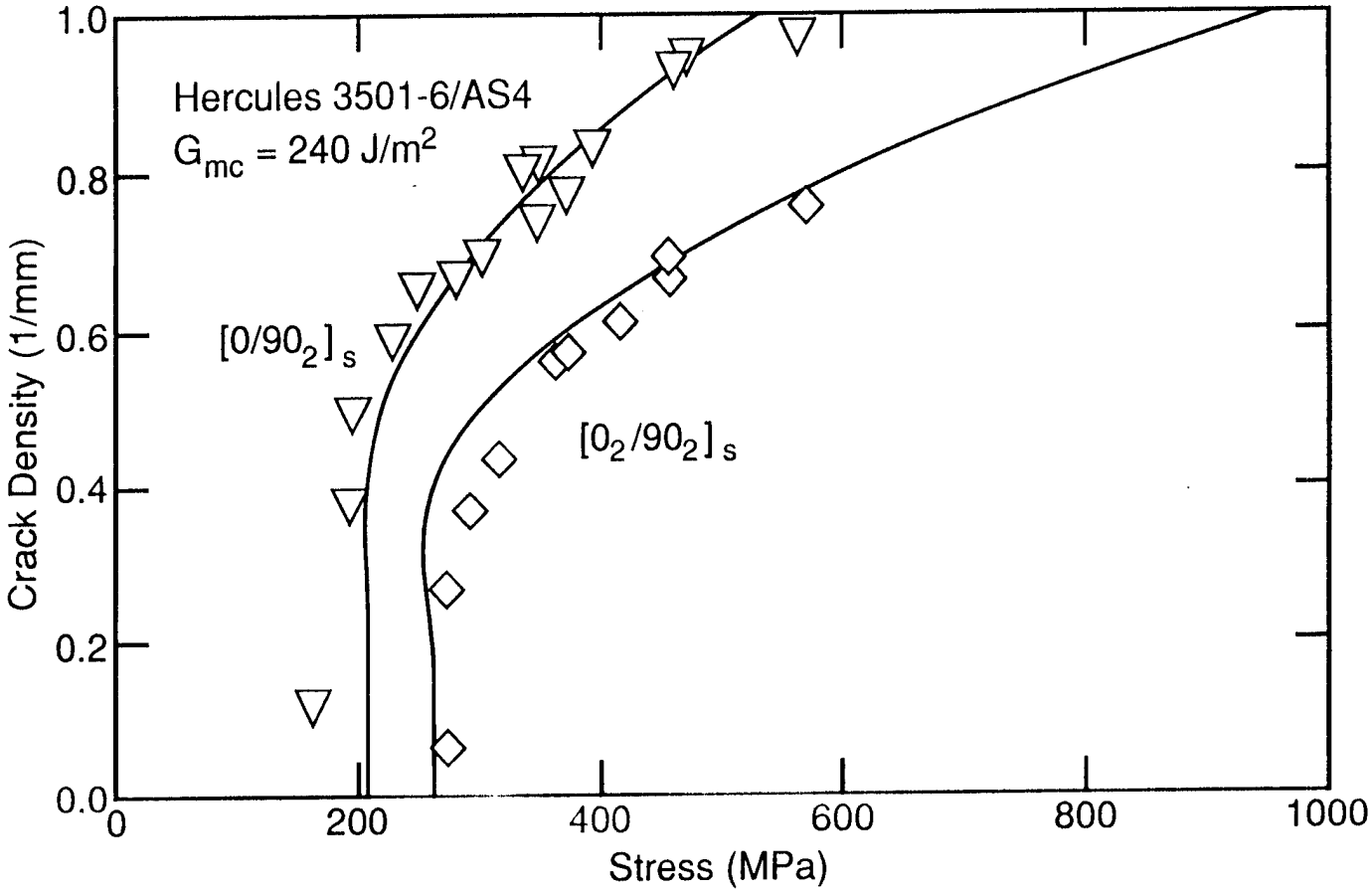


Figure 2: The microcrack density as a function of applied load in Hercules 3501-6/AS4 carbon fiber/epoxy cross-ply laminates. The symbols are experimental data points and the smooth lines are best fits using G_{mc} of 240 J/m^2.

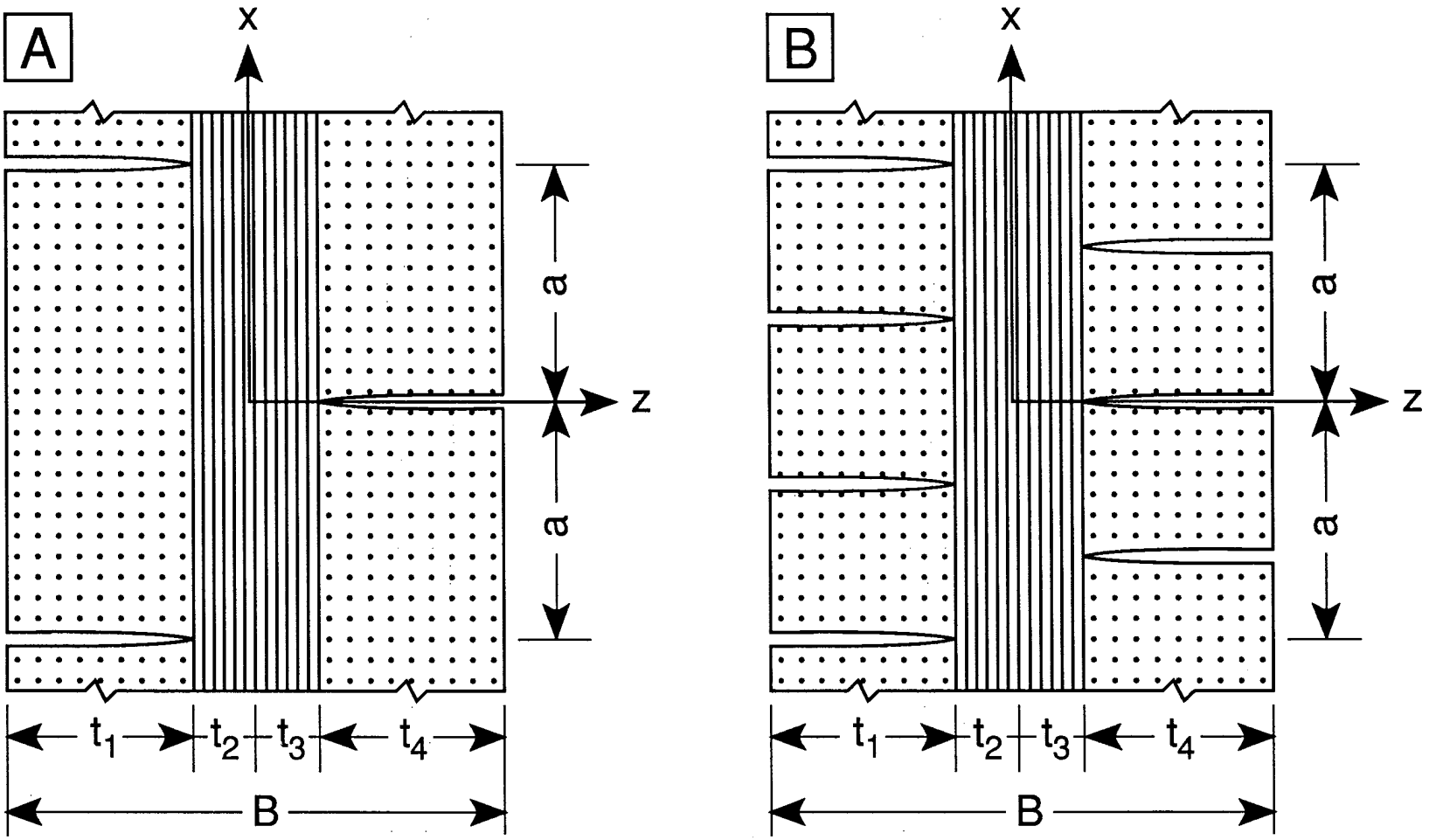


Figure 3: Edge view of a $[90_n/0_m]_s$ cross-ply laminate with microcracks. A: Staggered microcracks in the 90° plies. B: The formation of a new microcracks $\frac{1}{3}$ and $\frac{2}{3}$ of the way between existing microcracks.

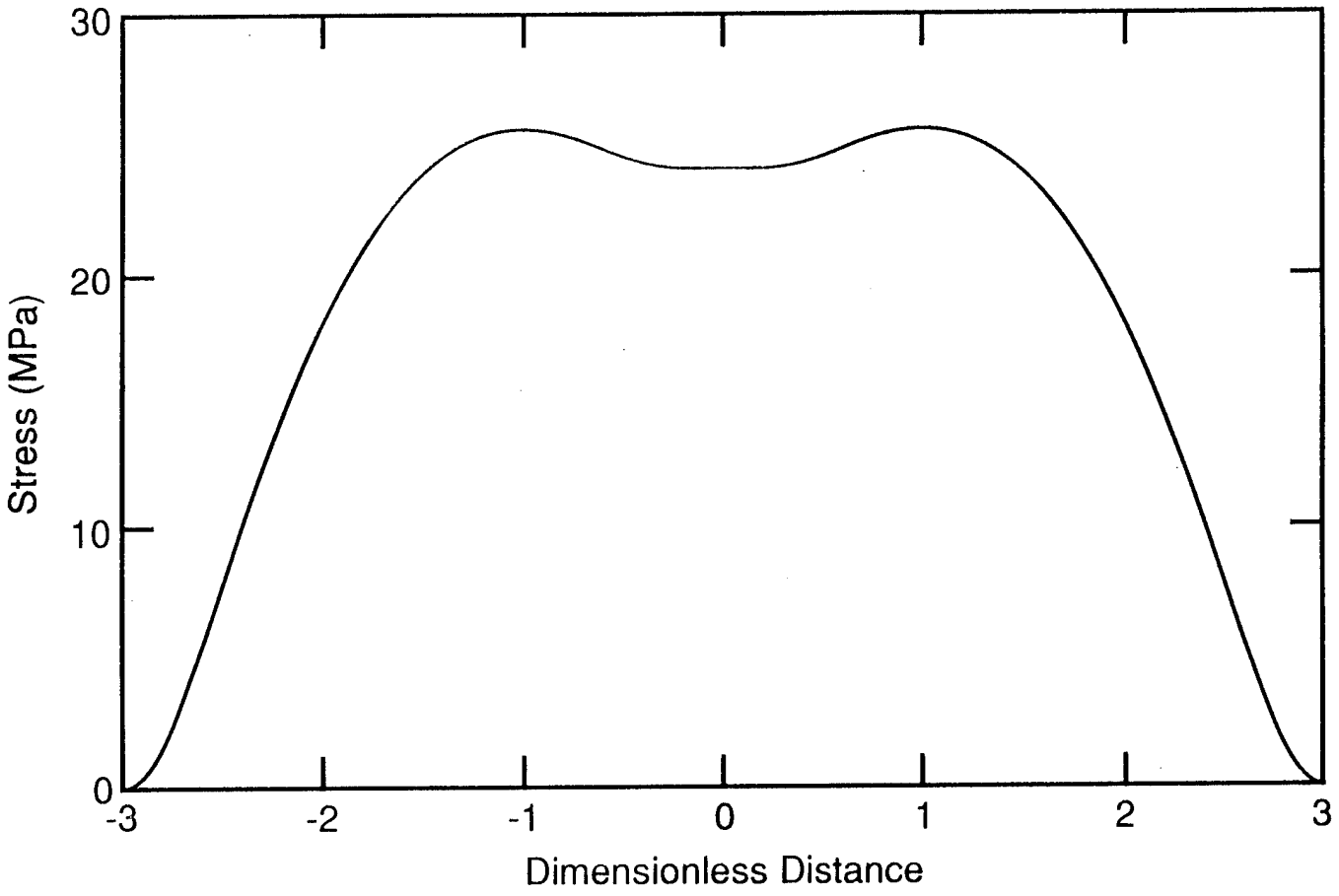


Figure 4: The x direction tensile stress in the 90° ply in a $[90_2/0]_s$ carbon fiber/epoxy laminate ($\sigma_{xx}^{(1)}$). This ply has microcracks located at $\rho = \pm 3$.

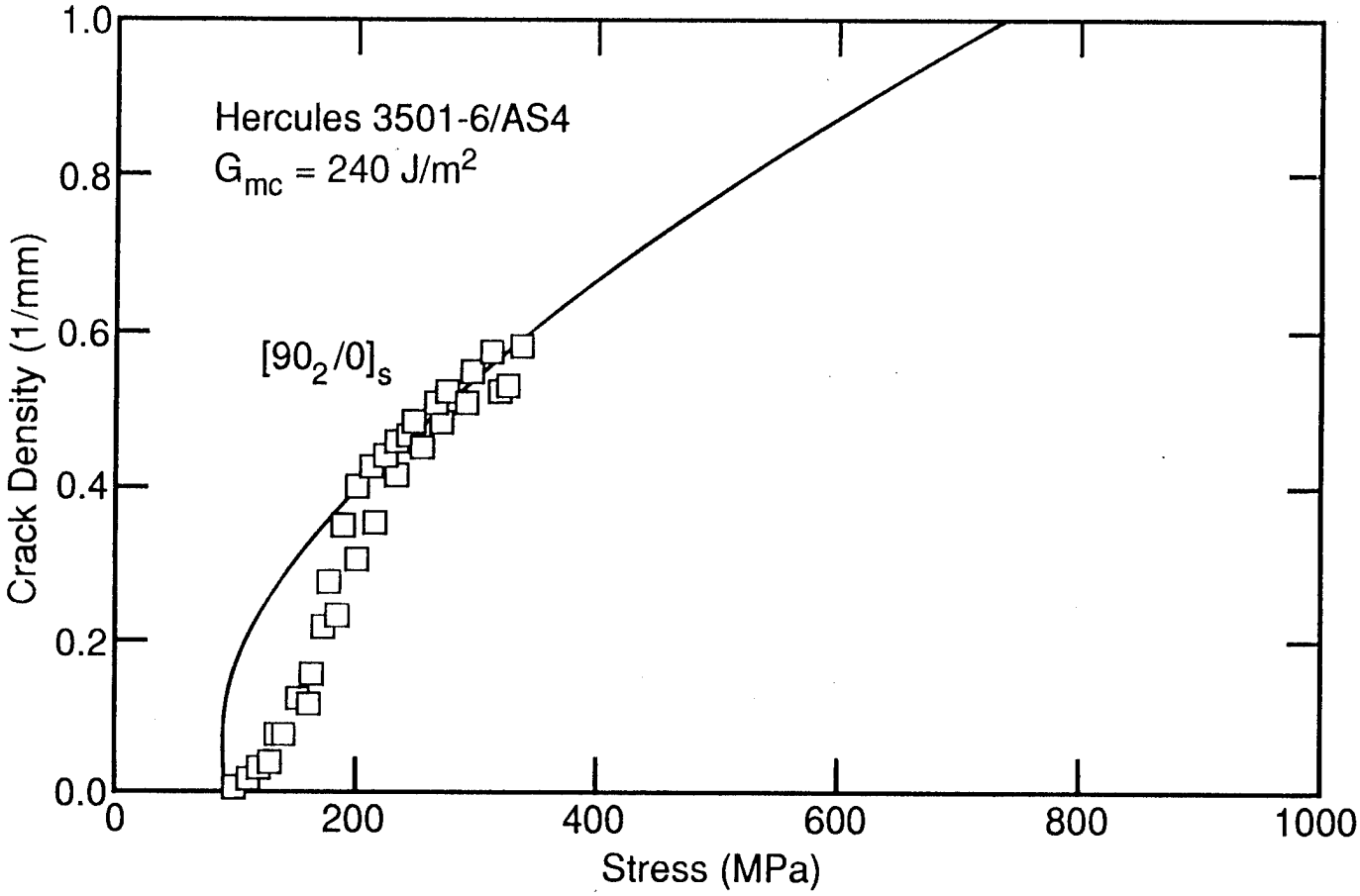


Figure 5: The microcrack density as a function of applied load in a Hercules 3501-6/AS4 carbon fiber/epoxy $[90_2/0]_s$ laminate. The symbols are experimental data points and the smooth line is calculated using G_{mc} of 240 J/m^2.

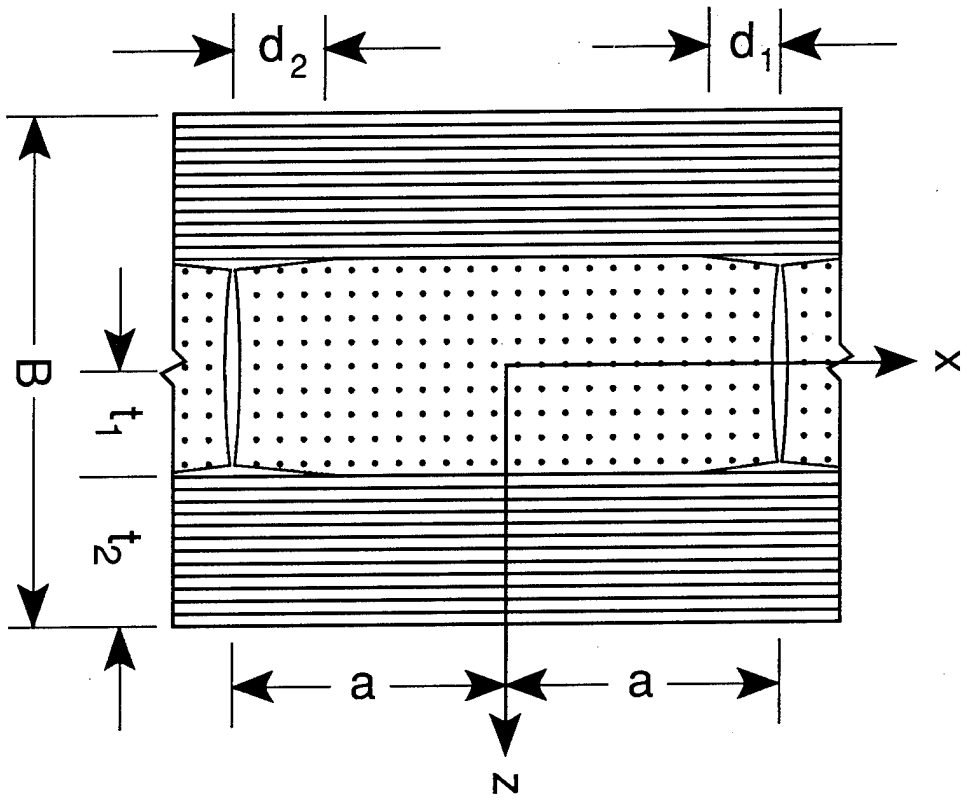


Figure 6: Edge view of a $[0_n/90_m]_s$ cross-ply laminate with microcracks and delaminations emanating from the tips of those microcracks.

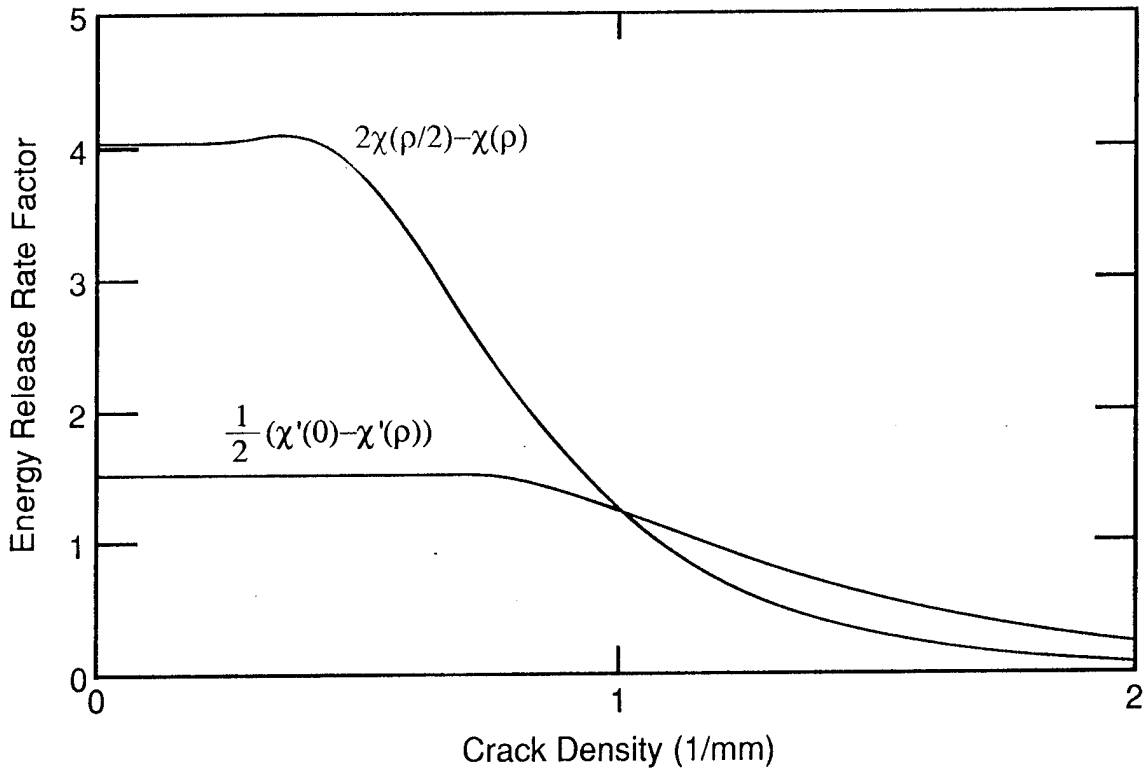


Figure 7: The energy release rate factor for microcracking $[\,2\chi(\rho/2)-\chi(\rho)]$ and for delamination $[\frac{1}{2}(\chi'(0)-\chi'(\rho))]$ as a function of crack density.

COMPARISON OF IMPACT RESULTS FOR SEVERAL POLYMERIC COMPOSITES OVER A WIDE RANGE OF LOW IMPACT VELOCITIES

C. C. Poe, Jr.
NASA Langley Research Center
Hampton, VA

M. A. Portanova
and
J. E. Masters
Lockheed Engineering and Sciences Co.
Hampton, VA

B. V. Sankar
University of Florida
Gainesville, FL

Wade C. Jackson
U.S. Army Aerostructures Directorate, USAARTA-AVSCOM
Hampton, VA

SUMMARY

Static indentation, falling weight, and ballistic impact tests were conducted on clamped plates made of AS4/3501-6 and IM7/8551-7 prepreg tape. The transversely isotropic plates were nominally 7-mm thick. Pendulum and ballistic tests were also conducted on simply supported plates braided with Celion 12000 fibers and 3501-6 epoxy. The 20^0 braided plates were about 5-mm thick. The impacters had spherical or hemispherical shapes with a 12.7 mm diameter. Residual compression strength and damage size were measured. Except for the ballistic tests, impact force was measured. An impact analysis was conducted using plate equations to aid in understanding the experimental results.

For a given kinetic energy, damage size was least for IM7/8551-7 and greatest for the braided material. Strengths varied inversely with damage size. For a given damage size, strength loss as a fraction of original strength was least for the braided material and greatest for AS4/3501-6 and IM7/8551-7. Strength loss for IM7/8551-7 and AS4/3501-6 was nearly equal. No significant differences were noticed between damage sizes and residual compression strengths for the static indentation, falling weight, and ballistic tests of AS4/3501-6 and IM7/8551-7. For the braided material, on the other hand, sizes of damage were significantly less and compression strengths were significantly more for the falling weight tests than for the ballistic tests. The impact analysis revealed that the response to static indentation and falling weight tests should

be essentially the same for the same boundary conditions, but that ballistic tests are more severe than static indentation and falling weight tests when plates are simply supported but not necessarily when plates are clamped.

INTRODUCTION

Low-velocity impacts from dropped tools, falling equipment, runway debris and hail can cause damage to conventional carbon-reinforced-plastics that reduce tension and compression strength by as much as two-thirds. (See for example [1-7].) Strength can even be reduced significantly without the impact damage being visible on the surface. In a very thick AS4 laminate wet-wound with a conventional epoxy, the impact damage from hemispherical indenters initiated at a contact pressure of 500 MPa, but the damage was not in evidence on the surface until the pressure exceeded 700 MPa [5]. The damage, which consisted of translaminar matrix cracks and broken fibers, initiated just below the contact site and did not spread much beyond the contact region. In thin epoxy laminates, the damage can initiate at a lower pressure, and delaminations can also develop and extend far beyond the contact region. Compression strengths are also reduced by delaminations, which cause sublaminates to buckle and overload the remainder of the laminate. In most structural metals, a 500 MPa contact pressure would only cause local yielding and no strength loss.

The impact damage was also successfully predicted in [5]. An energy balance model was used to predict impact force and a quasi-static stress analysis, and maximum shear stress criterion was used to predict damage for the contact problem. Impact damage was predicted to be independent of impacter mass and velocity as long as the kinetic energy was a constant and the impacter mass was small relative to that of the target.

For thin laminates, Elber proposed that static indentation tests, which are simple to conduct, can be equivalent to falling weight or pendulum impact tests [8]. In a static indentation test, the impact is simulated by a quasi-static application of a transverse load through an indenter or tup of desired shape.

In addition to falling weight and static indentation tests, impact tests have also been conducted using swinging pendulums and gas guns. The velocity and mass for the pendulum and falling weight tests are similar because both rely upon gravity. On the other hand, velocities for the gas gun tests, hereafter called ballistic tests, can be more than an order of magnitude times those of falling weight tests. Yet falling weight and ballistic tests are both called "low velocity" impact tests.

Comparisons between ballistic and falling weight tests of tape laminates in [2] indicate that residual compression strengths were less for ballistic tests than for falling weight tests for a given kinetic energy. Ballistic tests were also shown to be more severe than falling weight tests in [6,7]. For a given kinetic energy, delamination area was larger and residual tension strengths were smaller for ballistic tests than for falling weight tests. Also, the energy threshold for penetration was smaller for ballistic tests than for falling weight tests.

During impact, the specimens in [2] were simply supported on the long sides and clamped on the short sides, and those in [6,7] were free on the long sides and clamped on the short sides. However, circular plates clamped on the edges were also tested in [7]. For 8-ply tape laminates, the residual tension strengths for ballistic tests were less than those for falling weight tests. For 16-ply laminates, on the other hand, tension strengths were about equal for ballistic and falling weight tests. Thus, thickness and boundary conditions appear to have a significant effect on the outcome of impact tests.

Thus, published results indicate that, even when kinetic energy is fixed, impact response can differ between falling weight and ballistic tests. Energy balance models and quasi-static stress analyses such as those in [5] may be accurate for falling weight tests where impacter velocities are relatively low but may not be accurate for ballistic tests where velocities are relatively large. Accordingly, experiments were conducted to quantify differences between impact damage and residual compression strength for static indentation, falling weight, pendulum, and ballistic impact tests. A braided material and two tape laminates (one made with a brittle epoxy and one made with a toughened epoxy) were tested. The 48 ply, transversely isotropic tape laminates have been used as a standard by NASA for determining damage tolerance allowables for toughened and untoughened composites. Analyses were also conducted to develop an understanding of the impact response for varying impacter mass and velocity. The analyses were conducted for a simply supported anisotropic plate using plate theory with local indentation represented by Hertzian contact [9]. The plate theory takes into account the higher mode shapes that are important for high velocity impacts like those in the ballistic tests.

SYMBOLS

Values are given in SI Units. Measurements were made in U.S. Customary Units.

A_{11}, A_{22}, A_{12}	constants in Hertz's equation, Pa
E_1	Young's modulus of isotropic impacter, Pa
E_r, E_z	Young's moduli of transversely, isotropic plate, Pa
F_{max}	impact force, N
G_{zr}	shear modulus of transversely, isotropic plate, Pa
k_1, k_2	constants in Hertz's equation, Pa
k_b	spring constant for plate, N/m
KE_{eff}	effective kinetic energy, J
M	effective mass, kg
m_1, m_2	mass of impacter and plate, respectively, kg
n_o	constant in Hertz's equation, Pa
r_c	contact radius, m
R_i	radius of spherical impacter, m

v_1	velocity of impacter, m/s
α	αm_2 is the effective mass of the plate
ν_1	Poisson's ratio of isotropic impacter
ν_r, ν_{rz}	Poisson's ratio of transversely, isotropic plate
Subscripts:	
r,z	cylindrical coordinates (The z-direction is normal to the plate.)

EXPERIMENTS

Materials

The stacking sequence of the 48-ply IM7/8551-7 and AS4/3501-6 tape laminates was $[45/0/-45/90]_{6S}$. The fracture toughness (mode I strain energy release rate) of 8551-7 epoxy is significantly greater than that of 3501-6 epoxy [10]. The thickness of the tape laminates was 7.0 mm, and the fiber volume fractions were 0.547 and 0.567 for the IM7/8551-7 and AS4/3501-6 laminates, respectively. The undamaged compression strength of IM7/8551-7 laminates with the same layup was reported to be 620 MPa in [4,11], and the undamaged compression strength of an AS4/3501-6 laminate with the same layup but made with uniweave fabric and resin transfer molding was 586 MPa [12].

The Celion 12000 braided material was impregnated with 3501-6 epoxy. The epoxy was introduced into the braided fiber using a resin transfer molding process. The braid pattern was 1x1x1, the braid angle was about 20^0, and the thickness of the cured plates varied from 5.8 mm on the edges to 4.8 mm in the center. The fiber volume fraction was 0.60 with 2 percent void. The undamaged compression strength was 156 MPa, which is less than one-half that of similar braided materials [13]. The reason for the lower strengths was not evident.

Test Procedures

Tape Laminates.- Static indentation, falling weight, and ballistic impact tests were conducted at NASA Langley Research Center on the plates made with AS4/3501-6 and IM7/8551-7 prepreg tape. Contact diameters were measured by placing a sheet of white bond paper on the front surface of the plate and a sheet of carbon paper on top of the white bond paper. Contact by the impacter caused carbon to transfer to the white paper. The diameter of carbon on the white paper was assumed to equal the contact diameter. Following impact, an ultrasonic C-scan map was made of each plate, and the size of the damaged area was measured. Then the plates were loaded to failure in uniaxial compression in a fixture that simply supported the free edges to prevent global buckling. The loading direction was parallel to the long dimension of the plates.

For the static indentation tests, 12.7- by 12.7-cm square composite plates were clamped to a metal plate containing a circular hole with a diameter of 10.2 cm. A servo-controlled testing machine was used to apply the monotonically increasing contact force at the center of the opening. A steel hemisphere with 12.7-mm diameter was used for an indenter or tup. See figure 1.

For the falling weight and ballistic impact tests, rectangular composite plates 17.8 by 25.4 cm were clamped to a metal plate containing a 12.7- by 12.7-cm square opening [4]. The impacts were centered on the opening. The width of the plates was trimmed from 17.8 to 12.7 cm before the plates were loaded to failure. See figure 2.

The falling weight impacter had a mass of 4.63 kg and was instrumented to measure impact force. A steel hemisphere with 12.7-mm diameter was attached to the end of the impacter for an indenter. The velocities ranged from 1.71 to 5.14 m/s, and the kinetic energies ranged from 6.78 to 61.0 J.

A gas gun was used for the ballistic impact tests. A 3.00-g, 12.7-mm-dia. aluminum sphere was used for the impacter. The velocities ranged from 67.8 to 160 m/s, and the kinetic energies ranged from 6.78 to 37.7 J.

One AS4/3501-6 specimen (D05A) and one IM7/8551-7 specimen (D05IR) impacted with the falling weight and one AS4/3501-6 specimen (D15A) impacted with the gas gun were sectioned through the impact site. The sections were polished and edge replicas were made of the polished sections using a cellulose acetate film. The edge replicas were examined to reveal the pattern of damage. The portions of plates that were not polished were pyrolized to reveal broken fibers in the individual plies. The kinetic energy for all three specimens was 27.1 J.

Braided material.- Pendulum and ballistic impact tests were conducted at the University of Florida on plates made with the braided material. The square plates were 10.2 by 10.2 cm and simply supported on all sides. Following impact, the plates were radiographed and damage sizes were measured. Then the plates were trimmed to a size of 7.62 by 7.62 cm and loaded uniaxially in compression in a fixture that simply supported the free edges to prevent global buckling. See figure 3.

For the pendulum tests, a steel hemisphere with 12.7-mm diameter was attached to the end of the impacter for an indenter. The mass of the pendulum was 13.84 kg, the velocities ranged from 1.42 to 2.68 m/s, and the values of kinetic energy ranged from 14.0 to 49.9 J. The pendulum was instrumented to measure impact force.

A gas gun was used for the ballistic tests. A steel rod with a diameter of 12.7 mm, a length of 15.9 mm, and a hemispherical end was used for the impacter. The mass of the impacter was 0.0145 kg, the velocities ranged from 43.2 to 86.3 m/s, and the values of kinetic energy ranged from 13.5 to 54.0 J.

Results

Impact parameters, impact force, damage size (area), and compression strength for each test are given in Tables I and II for the AS4/3501-6 and IM7/8551-7 laminates, respectively, and in Table III for the braided material. Contact diameters, descriptions of the damage visible on front and back faces, and the maximum depth of broken fibers in the deplied specimens (D05A, D15A, and D05IR) are also given in Tables I and II.

The approach used in presenting the results is to first compare static indentation and falling weight test results for a given impact force, then to

compare falling weight (or pendulum) and ballistic impact test results for a given kinetic energy, and finally to compare residual strengths for a given damage size determined from nondestructive examinations. No static indentation results are available for the braided material.

Impact damage.- The damage size is plotted against impact force for the static indentation and falling weight impact tests in figure 4(a) for AS4/3501-6 and figure 4(b) for IM7/8551-7. As in subsequent figures of experimental results, lines were drawn through the data to show trends. The area of damage increases with increasing impact force and is much smaller for IM7/8551-7 than AS4/3501-6 for a given impact force. The damage sizes for the static and falling weight impact tests agree quite well for both AS4/3501-6 and IM7/8551-7. Both materials exhibit an impact force threshold for initiating damage. The threshold is larger for IM7/8551-7 than for AS4/3501-6.

The damage size is plotted against kinetic energy for the ballistic and falling weight impact tests in figure 5(a) for AS4/3501-6 and figure 5(b) for IM7/8551-7. The vertical lines correspond to an industry standard of 6.67 J/mm thickness (1500 in-lbf/in thickness) [14]. Damage size increases with increasing kinetic energy. For AS4/3501-6 in figure 5(a), the damage sizes were somewhat larger for the falling weight tests than for the ballistic tests for a given kinetic energy; and, for IM7/8551-7 in figure 5(b), the damage sizes for the falling weight and ballistic tests were equal. For a given kinetic energy, damage sizes were much less for IM7/8551-7 than for AS4/3501-6. Much as the impact force threshold in Figs. 4(a) and 4(b), the kinetic energy threshold for initiating damage in Figs. 5(a) and 5(b) is larger for IM7/8551-7 than for AS4/3501-6. The aluminum spheres that were used as impacters in the ballistic tests permanently deformed for kinetic energies of 20.3 to 27.1 J and greater.

The undulations in the data in figure 5(a) give an appearance of large scatter. However, the difference between duplicate tests for kinetic energies of 13.6 and 27.1 J is relatively small. (Each symbol represents one test.)

The values of impact force and kinetic energy at which damage became visible on the front and back faces are also shown in Figs. 4 and 5. Damage becomes visible on the front face at a lower impact force and kinetic energy than on the back face. On the front face, damage is visible first as a dent. The dent increases in size and depth with increasing impact force and kinetic energy, and eventually fibers are broken in the dent. Except for the static indentation tests, damage is visible on the back face first as a bump. The bump is opposite the dent on the front face, indicating through-the-thickness damage. Like the dent on the front face, the bump on the back face increases in size and height with increasing kinetic energy and impact force, and eventually fibers are broken on the bump. There was no significant difference between the values of kinetic energy for damage to become visible on the front and back faces for the falling weight and ballistic tests. For the static indentation test, however, no broken fibers were observed on the front face and no damage was observed on the back face before the indenter penetrated the laminate. With regard to material effect, somewhat larger values of impact force and kinetic energy were required for damage to become visible on the faces of IM7/8551-7 than on those of AS4/3501-6. Thresholds for visible damage in the C-scans were also larger for IM7/8551-7 than for AS4/3501-6.

Photographs of an edge replica for specimen D05A (falling weight test) and for specimen D15A (ballistic test) is shown in figure 6(a) and 6(b), respectively. Both specimens are AS4/3501-6 and were impacted with a kinetic energy of 27.1 J. Large delaminations were observed at each of the eleven -45/0 ply interfaces in each specimen and transverse matrix cracks were observed in most of the plies within this region. However, the patterns of damage differed as follows: 1. The delaminations were larger for the falling weight test than for the ballistic test, as evidenced in the C-scans. See figure 5(a). 2. For the ballistic test, a damage free zone extends from the front face to the laminate midplane. But, for the falling weight test, delaminations and transverse matrix cracks are present in this same zone. 3. The distribution of translaminar cracking is conical for the falling weight test and more cylindrical for the ballistic test.

Examination of the deplied sections of specimen D05A in figure 6(a) for the falling weight test revealed that only the top nine plies of the front face contained broken fibers. On the other hand, no broken fibers were found in the deplied sections of specimen D15A in figure 6(b) for the ballistic test.

A photograph of an edge replica for the IM7/8551-7 specimen impacted with a kinetic energy of 27.1 J is shown in figure 7 for the falling weight test. Delaminations were observed at each of the eleven -45/0 ply interfaces similar to the AS4/3501-6 specimens in Figs. 6(a) and 6(b). However, the delaminations were much smaller for the IM7/8551-7 specimen than the AS4/3501-6 specimens, as evidenced by the C-scan areas in figure 5(b). Also, the number of translaminar cracks is much less in the IM7/8551-7 specimen than in the AS4/3501-6 specimens. The pattern of cracks is similar to that of AS4/3501-6 in figure 6(a). Examination of the deplied section revealed that broken fibers were limited to the top three plies of the front face compared to the top nine plies of the AS4/3501-6 specimen in figure 6(a).

The damage size is plotted against kinetic energy for the ballistic and pendulum impact tests of the braided material in figure 8. The vertical line corresponds to an industry standard of 6.67 J/mm thickness (1500 in-lbf/in thickness) [14]. Damage size increases with increasing kinetic energy and, in contrast to AS4/3501-6, was less for the pendulum tests than for the ballistic tests. Damage sizes for the ballistic tests of the braided material were larger than those for the tape materials for a given kinetic energy. Notice that the damage size scale for the braided material is two times that for the tape laminates. The damage sizes for the braided material were associated with disbonded yarns. However, the disbonds did not form a continuous plane as in the case of laminates made from tape.

Residual strength.- The residual compression strengths for the static indentation and falling weight tests are plotted against impact force in figure 9(a) for AS4/3501-6 and in figure 9(b) for IM7/8551-7. For both materials, the strengths are in good agreement for a given value of impact force. The strength of AS4/3501-6 drops precipitously at the threshold for damage initiation, about 6 J in figure 4(a), whereas the strength of IM7/8551-7 in figure 9(b) decreases more gradually. The undamaged compression strengths, which are also plotted in Figs. 9(a) and 9(b), appear to be somewhat larger than those indicated by extrapolating the test data.

The residual compression strength is plotted against kinetic energy for the falling weight and ballistic tests in figure 10(a) for AS4/3501-6 and in figure 10(b) for IM7/8551-7. For AS4/3501-6, the compression strengths for a given kinetic energy were equal except for the lowest energies where the strengths were somewhat less for the falling weight tests than the ballistic tests. For IM7/8551-7, strengths for the falling weight and ballistic tests agree quite well. For the kinetic energies that correspond to the industry standard, the impacts reduced compression strength of AS4/3501-6 by about 70 percent and that of IM7/8551-7 by about 60 percent. The corresponding strength of IM7/8551-7 was about 2 times that of AS4/3501-6. Much as in Figs. 9(a) and 9(b), the undamaged compression strengths for the tape laminates in Figs. 10(a) and 10(b), appear to be somewhat larger than those indicated by extrapolating the test data.

The residual compression strength is plotted against kinetic energy in figure 11 for the pendulum and ballistic tests of the braided material. For a given value of kinetic energy, strengths are lower for the ballistic tests than the pendulum tests. For the kinetic energy that corresponds to the industry standard, the impacts reduced the compression strength by about 20 or 30 percent, depending on type of test. The corresponding strengths are about equal to that of AS4/3501-6 in figure 10(a) and about half that of IM7/8551-7 in figure 10(b).

The residual compression strength is plotted against damage size in Figs. 12(a) and 12(b) for AS4/3501-6 and IM7/8551-7, respectively. Results are shown for the static indentation, falling weight, and ballistic impact tests. The strengths decrease with increasing damage size, and all three types of tests are in reasonable agreement for a given damage size, somewhat better for IM7/8551-7 than AS4/3501-6. For a given damage size, the strengths for both tape laminates are nearly equal.

The residual compression strength is plotted against damage size in figure 13 for the pendulum and ballistic impact tests of the braided material. The strengths decrease with increasing damage size but not as precipitously as those of the tape laminates in Figs. 12(a) and 12(b). The strengths were lower for the pendulum tests than for the ballistic tests for a given damage size.

Back-face strain.- The back-face tension strain is plotted against contact force in figure 14 for a static indentation test (ST01IR) and a falling weight test (D01IR) of IM7/8551-7 specimens. The data for the falling weight test is somewhat erratic because of noise in the impact force signal. These two tests were selected because the maximum values of contact force are essentially equal. The area between the loading and unloading curves (hysteresis) is larger for the static indentation test than the falling weight test, indicating more damage in the static indentation test than in the falling weight test. Indeed, the C-scan maps indicated damage in specimen ST01IR but not in specimen D01IR. See Table II. The strains during loading of specimens D01IR and ST01IR agree below a force of 6 kN. Above a force of 6 kN, the strains for specimen ST01IR are greater than those for specimen D01IR. The initiation of delaminations at a force of 6 kN in specimen ST01IR would cause the response in figure 14.

The back-face strain is plotted against time in figure 15 for a falling weight test (D01IR) and a ballistic test (D19IP) of IM7/8551-7 specimens. The kinetic energy for both tests was 6.78 J. The maximum back-face strain, which is tension, is larger for the falling weight test than the ballistic test.

Also, the duration of the impact for the falling weight test is much larger than that for the ballistic test. For kinetic energies greater than 27.1 J, the output of strain gages was affected by back-face damage; and, for ballistic tests with kinetic energies greater than 13.6 J, strain gages separated from the specimens.

Contact diameter.- Contact diameter is plotted against impact force in figure 16 for static indentation and falling weight tests of AS4/3501-6 and IM7/8551-7 laminates. For the tests with penetration, the indenter diameter was plotted for the contact diameter. Contact diameters are in agreement except for the highest impact forces near penetration. The contact force to penetrate IM7/8551-7 was about 33 percent greater than that to penetrate AS4/3501-6. In the falling weight tests, the impact forces were not quite large enough to penetrate either laminate. Extrapolation of the falling weight test data indicate that the impact force associated with penetration for the static indentation and falling weight tests are similar.

Contact diameter is plotted against kinetic energy in figure 17 for the falling weight and ballistic tests of AS4/3501-6 and IM7/8551-7. Penetration did not occur for any of these tests. The contact diameters for the ballistic tests are significantly greater than those for the falling weight tests.

ANALYSIS

From energy balance considerations [5], the impact force F_{max} for a transversely isotropic plate is given by

$$0.4\ R_1^{-1/3}\ n_0^{-2/3}\ F_{max}^{5/3} + 0.5\ k_b^{-1}\ F_{max}^2 - KE_{eff} = 0 \tag{1}$$

where k_b is the spring constant for plate type displacements.

The term KE_{eff} is the effective kinetic energy defined by

$$KE_{eff} = 0.5\ M\ v_1^2 \tag{2}$$

where M is the effective mass defined by

$$M = [m_1^{-1} + (\alpha m_2)^{-1}]^{-1} \tag{3}$$

and v_1 and m_1 are the velocity and mass of the impacter, respectively, and m_2 and αm_2 are the mass and effective mass of the target, respectively. For a ring, $\alpha = 0.25$ was determined experimentally [5]. For a simply supported or clamped plate, α is probably greater than 0.25.

The term n_0, which is associated with Hertzian indentation, is given by

$$n_0 = 4\ (k_1 + k_2)^{-1}/3 \tag{4}$$

where

$$k_1 = (1 - \nu_1^2)\ E_1^{-1} \tag{5}$$

$$k_2 = 0.5\ (A_{22}/G_{zr})^{1/2}\ (A_{11}A_{22} - A_{12}^2)^{-1}\ \{[(A_{11}A_{22})^{1/2} + G_{zr}]^2 - [A_{12} + G_{zr}]^2\}^{1/2} \tag{6}$$

$$A_{11} = E_z\ \{1 - 2\ \nu_{rz}^2\ E_z\ [E_r\ (1 - \nu_r)]^{-1}\}^{-1} \tag{7}$$

$$A_{22} = A_{11}\ (E_r\ E_z^{-1} - \nu_{rz}^2)(1 - \nu_r^2)^{-1} \tag{8}$$

and

$$A_{12} = A_{11}\ \nu_{rz}(1 - \nu_r)^{-1} \tag{9}$$

The E_1 and ν_1 are the elastic constants of the isotropic, spherical impacter. The E_r, E_z, G_{zr}, ν_r, and ν_{rz} are the elastic constants of the transversely isotropic plate in polar coordinates.

The parameters α, k_b, and n_0 will vary with plate configuration and material. If the plate configuration and material are fixed, the impact force calculated with equations (1)-(9) will be constant for a given value of KE_{eff}. Otherwise, the impact force will increase with KE_{eff} to a power between 0.5 and 0.6, depending on whether or not Hertzian indentation is large or small compared to the plate deflection.

Sankar, et al solved the governing equations for impact of a simply supported anisotropic plate assuming classical plate theory [15] and, more recently, assuming plate theory with shear deformation [9]. The local indentation of the contact region was represented by Hertzian contact. In order to develop an understanding of the effects of impacter velocity and mass, the equations in [9] for a simply supported plate were solved. Contact force, back-face strain, and displacements were calculated. The displacements were calculated at the center of the plate, and the back-face strain was calculated at the center of the plate and midway between the edge and center. The plate was assumed to be 12.7- by 12.7-mm and made of AS4/3501-6 carbon/epoxy with a $[45/0/-45/90]_{6S}$ layup. See figure 18. The impacter had a diameter of 12.7 mm. The mechanical properties of IM7/8551-7 and AS4/3501-6 are very similar, and the results should be applicable to either.

Contact force is plotted against time in figure 19 for impacter velocities of 7.73, 16.5, and 52.1 m/s. For a given value of kinetic energy, impacter mass

varies inversely with impacter velocity squared. Thus, increasing velocity is equivalent to decreasing mass. The duration of the impacts increase with decreasing velocity (increasing mass). For velocities of 7.73 and 16.5 m/s, the contact force history consists of small amplitude plate vibrations superimposed on the forced response associated with momentum exchange. For the 52.1 m/s velocity, the forced response is too short for the vibrations to be apparent.

The values of contact force for the first peak of the force-time history, the second peak, the third peak, and so forth are plotted against impacter velocity in figure 20 as solid and dashed lines for a kinetic energy of 13.6 J. The upper envelope or maximum values of the peaks are represented by the solid line. The maximum contact force will be referred to as the impact force. For this reason, the relationship between impact force (or any other measure of plate response) and impacter velocity (or mass) will not be smooth but will contain cusps because of the vibratory response of the plate. On the whole, impact force in figure 20 increases with increasing velocity (and decreasing mass). The velocities are divided into two regions: falling weight and pendulum (1-10 m/s) and ballistic tests (10-200 m/s). For velocities below 10 m/s, impact force is relatively constant as indicated by equation (1); but, for velocities greater than 10 m/s, impact force increases significantly with velocity. Results are not shown for velocities below 1 m/s because of convergence problems in making calculations. It is expected that the impact force curve (solid curve) would approach an asymptote not too much below that for the lowest velocity shown.

The impact force is also plotted against impacter velocity in figure 20 for a kinetic energy of 20.3 J. For low velocities, the impact force for 20.3 J is approximately 1.23 times that for 13.6 J. From equation (1), the impact force for 20.3 J is 1.22 to 1.27 times that for 13.6 J, $(20.3/13.6)^{0.5}$ to $(20.3/13.6)^{0.6}$. Thus, equation (1) and the impact analysis are in agreement for small velocities. Moreover, this ratio holds approximately for the entire range of velocities.

Deflection of the plate and impacter are plotted against impacter velocity in figure 21. For low and high velocities, the impacter deflects more than the plate indicating contact. The difference is the indentation of the plate, which was represented by Hertzian contact. Between velocities of 2 and 4 m/s, the plate and impacter are not in contact, indicating multiple impacts. For velocities less than 10 m/s, the deflection of the plate and impacter are approximately independent of velocity. For velocities greater than 10 m/s, the deflection of the plate and impacter decrease dramatically with increasing velocity.

The maximum values of back-face tension strains at the center of the plate and midway between the center and edge is plotted against impacter velocity in figure 22. The x and y components of strain are equal at the center where they are also greatest. The strain at the center is a minimum at the cusp near 23 m/s. Except near this cusp, the strain at the center increases less than 20 percent with increasing velocity.

DISCUSSION

Static Indentation Versus Falling Weight Tests

For the static indentation and falling weight tests of the AS4/3501-6 and IM7/8551-7 tape materials, the sizes of damage in the C-scan maps and the residual compression strengths were in agreement for a given contact or impact force. Near the contact region, damage consisted of matrix cracking, delaminations, and broken fibers. Away from the contact region, damage consisted principally of delaminations. Thus, the size of damage measured in the C-scans are associated with delamination size. Delaminations developed at each of the -45/0 ply interfaces, making failure by sublaminate buckling probable. Residual compression strengths decreased with increasing damage size, consistent with failure by sublaminate buckling [16].

For impacter velocities less than 20 m/s, plate analysis revealed that impact force and back-face strain varied little with velocity for a given kinetic energy. Delamination size is associated with impact force. Since impacter velocities were less than 6 m/s for the static indentation and falling weight tests, the analysis confirms that damage size should have been the same for static indentation and falling weight tests for a given kinetic energy.

For the static indentation and falling weight tests, damage became visible on the front face at a lower impact force than on the back face. The threshold for visible damage and for penetration was greater for IM7/8551-7 than for AS4/3501-6. However, the impact forces at which damage became visible on the front and back faces were somewhat different for the two types of tests. On the front face, the impact force at which damage became visible was smaller for the static indentation test than for the falling weight test, more so for IM7/8551-7 than for AS4/3501-6. On the back face, damage became visible before penetration for the falling weight test, but penetration occurred before damage became visible for the static indentation test.

Falling Weight Versus Ballistic Tests

For AS4/3501-6, the damage sizes for a given kinetic energy were somewhat larger for the falling weight tests than for the ballistic tests, and the compression strengths were equal except for the lowest energies where the strengths were somewhat less for the falling weight tests than the ballistic tests. For IM7/8551-7, the damage sizes and compression strengths were equal for the two types of tests. Apparently, the high interlaminar toughness ameliorated differences between the falling weight and ballistic tests. For a given kinetic energy, damage sizes for IM7/8551-7 were less than half those for AS4/3501-6, and the energy threshold for causing damage was less for AS4/3501-6 than for IM7/8551-7. Thus, the IM7/8551-7 was more resistant to matrix damage than AS4/3501-6, which is consistent with the greater interlaminar toughness of IM7/8551-7.

Opposite to the AS4/3501-6 and IM7/8551-7 tape materials, damage sizes for the braided material were significantly smaller and compression strengths were larger for the falling weight tests than for the ballistic tests. Near the contact site, damage consisted of broken fibers, matrix cracks, and disbonded

yarns. Away from the contact site, damage consisted primarily of disbonded yarns. Thus, damage size in the radiographs is associated with disbonded yarns. Strengths varied inversely with damage size as they did with the tape materials.

One possible cause for the opposite response of the tape and braided materials is the difference between boundary conditions during impact. The plates were clamped for the tape materials and simply supported for the braided material. To determine the significance of boundary conditions, impact force is plotted against impacter velocity in figure 23 for simply supported and clamped plates. Recall that impacter velocities were between 1 and 6 m/s for the falling weight tests and between 41 and 160 m/s for the ballistic tests. The plates were assumed to be 12.7- by 12.7-mm and made of AS4/3501-6 carbon/epoxy with a $[45/0/-45/90]_{6S}$ layup. The impacter diameter was 12.7 mm, and the kinetic energy is constant, 13.6 J. The simply supported curve was taken from figure 20. The equations in [9] and [15] can only be used to analyze the impact of a simply supported plate. The response of the clamped plate was estimated using that of the simply supported plate. At the lowest velocity, the impact force was assumed to increase in proportion to the square root of plate stiffness (equation (1) with relatively large n_0). The ratio of displacements for the clamped and simply supported plates was calculated for static loading. The impact force for the simply supported plate at the lowest velocity was then multiplied by the square root of that ratio. The curve for the simply supported plate was then rotated upward about the right-hand end because boundary conditions do not affect impact force for large velocities (small masses) [7]. The overall effect of clamping the plate is to reduce or eliminate the increase in impact force with increasing impacter velocity. In other words, the differences between impact force for low and high velocities should be less for a clamped plate than for a simply supported plate. The effect of simply supported and clamped boundaries on back-face strain should be similar to that on impact force.

Since damage size is expected to increase with increasing impact force, the results in figure 23 indicate that damage size should increase with increasing velocity for simply supported plates but not necessarily for clamped plates. Thus, the curves in figure 23 are consistent with the experiments. That is, for the simply supported plates made of the braided material, damage size should be greater for the ballistic tests than for the falling weight tests but not necessarily for the clamped plates made of the tape materials.

Another contribution to the opposite response of the tape and braided materials is the difference between impacter materials. For the braided material, the impacters for the pendulum and ballistic tests were made of steel. For the AS4/3501-6 and IM7/8551-7 tape materials, the impacter for the falling weight tests was also made of steel, whereas the impacter for the ballistic tests was an aluminum sphere. For the highest velocities, the aluminum spheres flattened significantly, indicating that the aluminum yielded. Thus, some of the kinetic energy was converted to nonreversible strain energy when the aluminum yielded, perhaps as much as 1 to 10 J. This absorbed energy would have the effect of reducing the kinetic energy of the impacter. If the highest values of kinetic energy for the ballistic tests in figures 5(a), 5(b), 10(a), and 10(b) are reduced by 10 J, the ballistic tests are as severe as the falling weight tests for AS4/3501-6 and more severe than the falling weight tests for IM7/8551-7.

For the AS4/3501-6 and IM7/8551-7 tape materials, the states of internal damage were similar for a given type of test but somewhat different for the falling weight and ballistic tests. For the falling weight tests, the damage extended uniformly from the contact surface to the back face; whereas, for the ballistic tests, the damage was mostly absent in a small zone from the contact surface to the midplane.

Damage tolerance actually has two distinct facets: the resistance to damage and the tolerance to damage. The resistance to damage is measured by the extent or size of damage for a given impact energy or impact force; whereas, the tolerance to damage is measured by the strength loss for a given size of damage. Of the three materials tested, the resistance to damage was greatest for the IM7/8551-7 tape material and least for the braided material. Compare figures 5(a), 5(b), and 8. On the other hand, damage tolerance was greatest for the braided material and least for the AS4/3501-6 and IM7/8551-7 tape materials. Compare figures 12(a), 12(b), and 13. The damage tolerance of the IM7/8551-7 and AS4/3501-6 tape materials was nearly equal, indicating that both materials probably fail by sublaminate buckling. The failure mode of the braided material was obviously not sublaminate buckling because the disbonded yarns did not form large planes of delamination. Probably failure was precipitated by buckling of the disbonded yarns.

Analysis of the falling weight and ballistic test results in terms of impact force would have been of great assistance in understanding the impact response. The original intent of measuring contact diameters for the tape laminates was to estimate impact forces for the ballistic tests. The impact force [5] is given by

$$F_{max} = r_c^3 \, n_0 / R_i \tag{10}$$

where r_c is the contact radius, R_i is the radius of the spherical impacter and n_0 is the Hertzian spring constant in equation (1). Thus, for a given material and impacter radius, impact force is uniquely related to contact radius. Instead of equation (10), the actual contact diameter versus impact force data for the static indentation and falling weight tests were going to be used for a calibration curve. For the static indentation and falling weight tests, contact diameters were in good agreement with one another for a given impact force. The contact diameters for AS4/3501-6 and IM7/8551-7 were also in good agreement except near penetration. See figure 16. However, the contact diameters for the ballistic tests were 1.2 to 1.4 times those for the falling weight tests for a given kinetic energy. See figure 17. Because the impact force is proportional to contact radius to the third power, the contact diameters indicate that impact forces for the ballistic tests were 1.8 to 2.8 times those for the falling weight tests, which is inconsistent with the smaller damage sizes and larger residual compression strengths for the ballistic tests. Thus, the plan for calculating impact forces for the ballistic tests using contact diameters was abandoned.

The carbon and white papers were not bonded to the composite. Possibly, the papers, which were highly accelerated in the ballistic tests, wrapped around the sphere and inflated the contact diameters. The sensitivity of impact force to variations in contact diameter may render calculations of impact force by

this method qualitative at best. Thus, efforts should be made to develop some other method to measure ballistic impact forces.

Also, the curves in figure 23 indicate that boundary conditions for static indentation and falling weight tests (low velocities) significantly affect impact force for a given kinetic energy. However, it is expected that impact response would be essentially the same for simply supported and clamped boundaries for a given impact force.

CONCLUDING REMARKS

Static indentation, falling weight, and ballistic tests were conducted on laminates made of AS4/3501-6 and IM7/8551-7 prepreg tape. The $[45/0/-45/90]_{6S}$ laminates were 7 mm thick. Pendulum and ballistic tests were also conducted on a 20^{0} braided material made of Celion 12000 fibers and 3501-6 epoxy, which was about 5-mm thick. The AS4/3501-6 and IM7/8551-7 plates were clamped and the braided plates were simply supported on all sides during impact. The impacters had spherical or hemispherical shapes with a 12.7 mm diameter. Kinetic energies ranged from 5-50 J. Masses for the falling weight and pendulum tests were 4.63 and 13.84 kg, respectively, and velocities ranged from 1-5 m/s. Masses for the ballistic tests were 3.0 and 14.5 g and the velocities ranged from 40-160 m/s. Residual compression strengths, back-face strains, and damage sizes were measured for the static indentation, falling weight, and pendulum tests. Impact forces were measured for all but the ballistic tests. Contact areas were measured for all tests of the AS4/3501-6 and IM7/8551-7 material. An impact analysis was conducted using plate equations to aid in understanding the experimental results.

No significant differences were noticed between the static indentation and falling weight tests of AS4/3501-6 and IM7/8551-7. Sizes of damage and residual compression strengths were in agreement for a given contact or impact force. Damage size was associated principally with delamination size. The impact analysis confirmed that damage size should be relatively independent of velocity for velocities less than 20 m/s for a given kinetic energy.

Also, no significant differences were noticed between the falling weight and ballistic tests of AS4/3501-6 and IM7/8551-7. Residual compression strengths were in agreement for a given kinetic energy. Sizes of damage for IM7/8551-7 were in agreement, but sizes of damage for AS4/3501-6 were a little larger for the falling weight tests than the ballistic tests. Some of this difference can be attributed to inelastic deformation of the aluminum spheres that were used in these ballistic tests. The impact analysis also indicated that, for clamped boundaries, damage size may be relatively independent of velocity for velocities between 20 and 160 m/s for a given kinetic energy. For static indentation, falling weight, and ballistic tests, strengths varied inversely with damage size consistent with failure by sublaminate buckling.

On the other hand, significant differences were noticed between the pendulum and ballistic tests of the braided material. Sizes of damage were significantly less and compression strengths were significantly more for the falling weight tests than for the ballistic tests. Strengths varied inversely

with damage size. The impact analysis also indicated that, for simply supported boundaries, damage size should increase significantly with increasing velocity for velocities between 20 and 160 m/s for a given kinetic energy. Thus, ballistic tests are more severe than falling weight tests when plates are simply supported but not necessarily when plates are clamped.

Of the three materials tested, the sizes of damage were least for the IM7/8551-7 tape material and greatest for the braided material for a given kinetic energy. On the other hand, the strength loss as a fraction of original strength was least for the braided material and greatest for the AS4/3501-6 and IM7/8551-7 tape materials for a given size of damage. The strength loss for the IM7/8551-7 and AS4/3501-6 tape materials was nearly equal, which is consistent with both tape materials failing by sublaminate buckling. The failure mode of the braided material was obviously not sublaminate buckling because the disbonded yarns do not form large planes of delamination. Failure was probably precipitated by buckling of the disbonded yarns.

REFERENCES

1. Rhodes, Marvin D.: Impact Tests on Fibrous Composite Sandwich Structures. NASA TM 78719, October 1978.

2. Williams, Jerry G.: Comparison of Toughened Composite Laminates using NASA Standard Damage Tolerance Tests. NASA CP 2321, August 1984.

3. Williams, Jerry G.: Effect of Impact Damage and Open Holes on the Compression Strength of Tough Resin/High Strain Fiber Laminates. NASA TM 85756, February 1984.

4. Portanova, M. A.; Poe, Jr. C. C.; and Whitcomb, John D.: Open Hole and Post-Impact Compression Fatigue of Stitched and Unstitched Carbon/Epoxy Composites. NASA TM 102676, June 1990.

5. Poe, Jr. C. C.: Summary of a Study to Determine Low-Velocity Impact Damage and Residual Tension Strength for a Thick Graphite/Epoxy Motor Case. NASA TM 102678, June 1990.

6. Cantwell, W. J. and Morton J.: The Influence of Varying Projectile Mass on the Impact Response of CFRP. Composite Structures, 13, 1989, pp. 101-114.

7. Cantwell, W. J. and Morton J.: Comparison of the Low and High Velocity Impact Response of CFRP. Composites, Vol. 20, No. 6, November 1989, pp. 545-551.

8. Elber, Wolf: Failure Mechanics in Low-Velocity Impacts on Thin Composite Plates. NASA TP 2152, May 1983.

9. Sankar, Bhavani V.: A Modified Green's Function for Computing Structural Response due to Low-Velocity Impact. Department of Aerospace Engineering, Mechanics & Engineering Science, University of Florida, Gainesville, Florida 32611, Technical Report No. AeMES-TR-1-36, October 1990.

10. Johnston, N. J. and Hergenrother, P. M.: High Performance Thermoplastics: A Review of Neat Resin and Composite Properties. 32nd International SAMPE Symposium & Exhibition, Anaheim, April 6-9, 1987, Also NASA TM 89104.

11. Dow, Marvin B. and Smith, Donald L.: Properties of Two Composite Materials Made of Toughened Epoxy Resin and High Strain Graphite Fiber. NASA TP 2826, July 1988.

12. Palmer, R.; Dow, Marvin B.; and Smith, Donald L.: Development of Stitching Reinforcement for Transport Wing Panels. First NASA Advanced Composites Technology (ACT) Conference, NASA CP-3104, Part 2, 1991, pp. 621-646.

13. Simonds, Robert A.; Stinchcomb, Wayne; and Jones, Robert M.: Mechanical Behavior of Braided Composite Materials. Composite Materials: Testing and Design (Eighth Conference), ASTM STP 972, J. D. Whitcomb, Ed., American Society for Testing and Materials, Philadelphia, 1988, pp. 438-453.

14. SACMA SRM 2-88 (Suppliers of Advanced Composite Materials Association): Recommended Test Method for Compression after Impact Properties of Oriented Fiber-Resin Composites.

15. Sankar, B. V.; Ku, C.; and Nguyen, P. T.: Nondimensional Impact Models for Composite Laminates. Fifth Technical Conference of the American Society for Composites, June, 1990.

16. Ilcewicz, Larry B.; Dost, Ernest F.; and Coggeshall, Randy L.: A Model for Compression after Impact Strength Evaluation. 21st International SAMPE Technical Conference, Volume 21, Advanced Materials: The Big Payoff, Atlantic City, N.J. Sept. 25-28, 1989, pp, 130-140.

TABLE I.- Impact test data for [45/0/-45/90]6S AS4/3501-6 tape laminate.

Test no.	Kinetic energy, J	Mass, g	Velocity, m/s	Impact force, kN	Damage size in C-scan, cm^2	Contact dia., mm	Compression strength, MPa	Front face damage (a)	Back face damage (a)
ST11A	-	-	0	2.33	0	2.8	530.	NV	NV
ST13A	-	-	0	7.12	0	4.1	527.	NV	NV
ST04A	-	-	0	7.52	2.84	4.3	531.	NV	NV
ST03A	-	-	0	8.14	11.3	5.0	223.	NV	NV
ST01A	-	-	0	9.05	12.5	5.2	209.	D	NV
ST14A	-	-	0	10.3	14.7	5.4	209.	D	NV
ST12A	-	-	0	13.3	26.7	6.0	176.	D	NV
ST02A	-	-	0	15.2	87.1	-	97.9	P	P
D01A	6.78	4630	1.71	6.45	8.06	4.7	260.	NV	NV
D02A	13.6		2.42	10.0	11.3	5.1	186.	D	NV
D03A	20.3		2.97	11.6	24.6	5.4	171.	D	B,MC
D04A	27.1		3.43	12.0	22.7	5.6	166.	D,BF	B,MC
D05A	27.1		3.43	-	18.4	5.6	(b)	D,BF	B,MC
D06A	37.7		4.04	13.3	33.5	7.7	144.	D,BF	B,BF
D07A	47.5		4.53	13.8	22.1	9.0	131.	D,BF	B,BF
D08A	61.0		5.14	-	35.5	11.6	128.	D,BF	B,BF
D11A	6.78	3.00	67.8	-	3.16	5.5	485.	NV	NV
D12A	13.6		95.3	-	10.0	6.1	202.	D	NV
D17A	13.6		96.0	-	13.7	6.4	220.	NV	NV
D13A	20.3		114.	-	9.74	6.7	175.	D	NV
D14A	27.1		135.	-	12.2	7.0	153.	BF	NV
D15A	27.1		135.	-	13.9	7.5	(c)	BF	MC
D16A	37.7		160.	-	21.4	7.2	126.	BF	BF

a - Code for damage on surface.
NV - No damage was visible.
D - Dent.
P - Penetration.
B - Bump or protuberance.
MC - Matrix crack.
BF - Broken fibers.

b - Specimen was sectioned and deplied. Fibers were broken in first 9 plies of the outer face.

c - Specimen was sectioned and deplied. No fibers were broken.

TABLE II.- Impact test data for [45/0/-45/90]6S IM7/8551-7 tape laminate.

Test no.	Kinetic energy, J	Mass, g	Velocity, m/s	Impact force, kN	Damage size in C-scan, cm^2	Contact dia., mm	Compression strength, MPa	Front face damage (a)	Back face damage (a)
ST06IR	-	-	0	2.22	0	3.0	489.	NV	NV
ST13IP	-	-	0	3.18	0	3.3	500.	NV	NV
ST03IR	-	-	0	4.49	0	3.9	481.	NV	NV
ST12IP	-	-	0	5.81	0	3.9	517.	NV	NV
ST07IR	-	-	0	7.16	0	4.3	448.	NV	NV
ST01IR	-	-	0	8.86	.19	4.8	498.	D	NV
ST04IR	-	-	0	10.6	.26	5.3	465.	D	NV
ST02IR	-	-	0	13.3	4.06	5.7	332.	D	NV
ST11IP	-	-	0	15.9	8.97	6.1	309.	D	NV
ST05IR	-	-	0	19.9	45.0	-	164.	P	P
D01IR	6.78	4630	1.71	8.98	0	4.7	510.	NV	NV
D02IR	13.6		2.42	10.2	3.48	5.4	380.	NV	NV
D03IR	20.3		2.97	12.7	4.58	-	364.	NV	NV
D04IR	27.1		3.43	14.5	6.64	5.7	321.	D	NV
D05IR	27.1		3.43	14.7	5.68	5.6	(b)	D	NV
D11IP	37.7		4.04	17.1	8.77	6.0	270.	D,BF	D,BF
D12IP	47.5		4.53	18.3	11.2	8.2	228.	D,BF	B,BF
D13IP	54.2		4.84	18.7	12.8	9.0	225.	D,BF	B,BF
D14IP	61.0		5.14	18.7	14.1	9.0	216.	D,BF	B,BF
D07IR	6.78	3.00	68.4	-	0	6.0	493.	NV	NV
D19IP	6.78		66.0	-	0	5.5	479.	NV	NV
D18IP	13.6		94.5	-	2.84	6.6	439.	D	NV
D08IR	13.6		95.2	-	2.97	6.7	433.	D	NV
D09IR	20.3		117.	-	4.77	7.8	341.	D	NV
D16IP	27.1		135.	-	5.61	7.5	297.	D	NV
D10IR	27.1		134.	-	5.81	8.2	312.	D	NV
D17IP	37.7		159.	-	8.97	7.6	251.	D,BF	MC

a - Code for damage on surface.
NV - No damage was visible.
D - Dent.
P - Penetration.
B - Bump or protuberance.
MC - Matrix crack.
BF - Broken fibers.

b - Specimen was sectioned and deplied. Fibers were broken in first 3 plies of the outer face.

TABLE III.- Impact test data for CE12000/3501-6 20^{0} braided material.

Test no.	Kinetic energy, J	Mass, g	Velocity, m/s	Impact force, kN	Damage size in radio-graph, cm^2	Compression strength, MPa
B42	14.0	13840	1.42	7.8	1.5	138.5
B46	23.7		1.85	8.7	4.9	144.1
B44	34.2		2.22	8.2	10.3	131.2
B43	49.9		2.68	8.6	20.6	113.4
B36	13.5	14.5	43.2	-	11.0	146.8
B35	30.6		65.0	-	33.5	116.5
B31	54.0		86.3	-	63.2	70.5

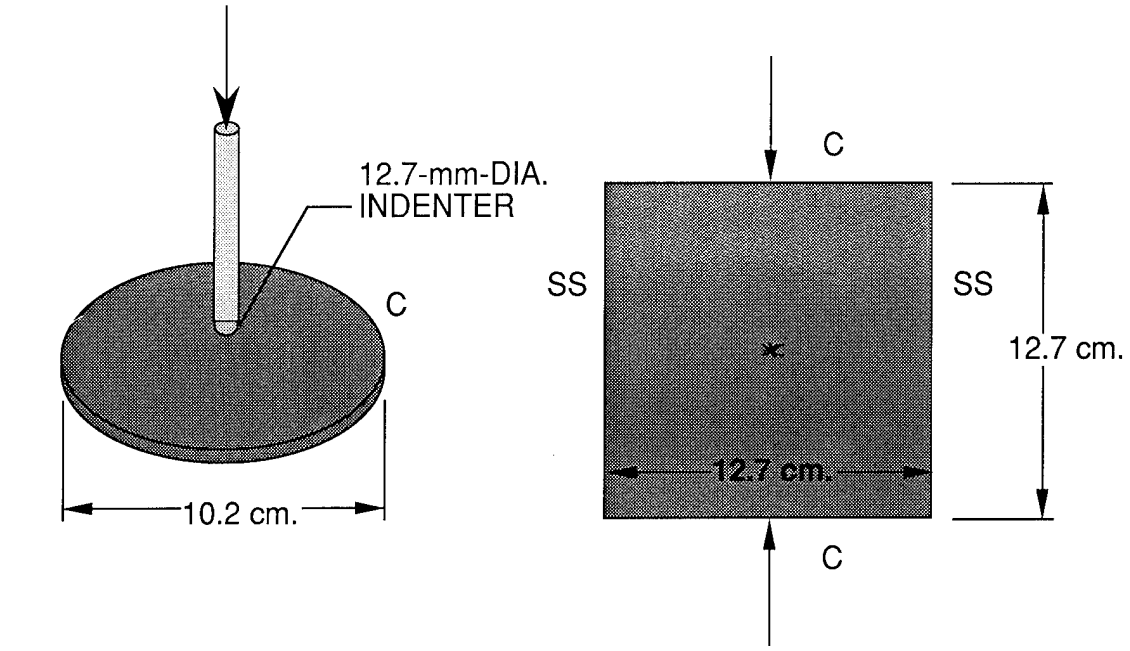
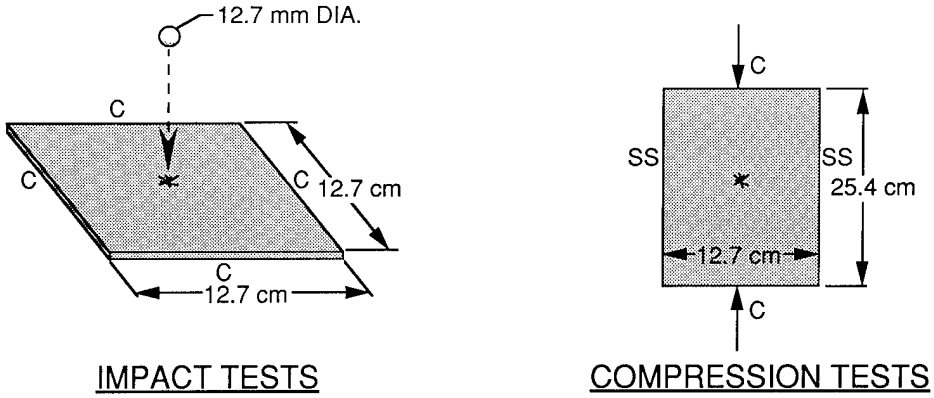


Figure 1. - Static indentation and compression tests.

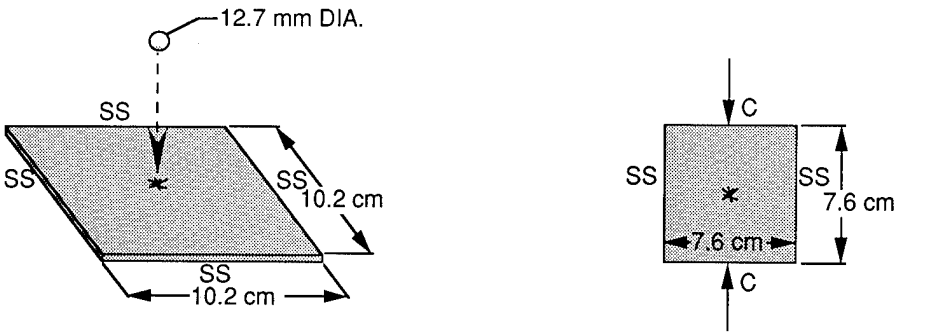


	FALLING WT.	BALLISTIC	INDUSTRY STD.
MASS	4.63 kg	0.003 kg	4.54 kg
v_1	2 - 5 m/s	68 - 160 m/s	4.54 m/s
KE	7 - 61 J	7 - 38 J	* 46.7 J

SS -- SIMPLY SUPPORTED
C -- CLAMPED

* 1500 $\frac{\text{in lbs}}{\text{in}}$

Figure 2. - Specimens and impact parameters for $[45/0/-45/90]_{6s}$ AS4/3501-6 and IM7/8551-7 tape laminates



IMPACT TESTS

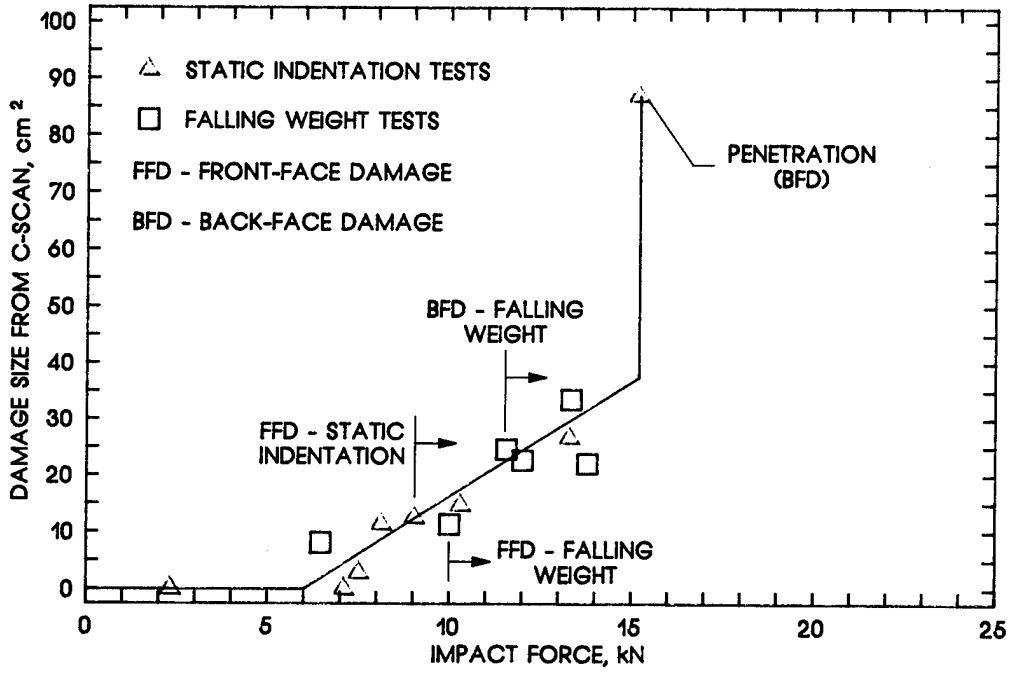
COMPRESSION TESTS

	PENDULUM	BALLISTIC	INDUSTRY STD.
MASS	13.84 kg	0.0145 kg	4.54 kg
v_1	1 - 3 m/s	43 - 86 m/s	3.95 m/s
KE	14 - 50 J	13 - 54 J	* 35.4 J

* 1500 $\frac{\text{in lbs}}{\text{in}}$

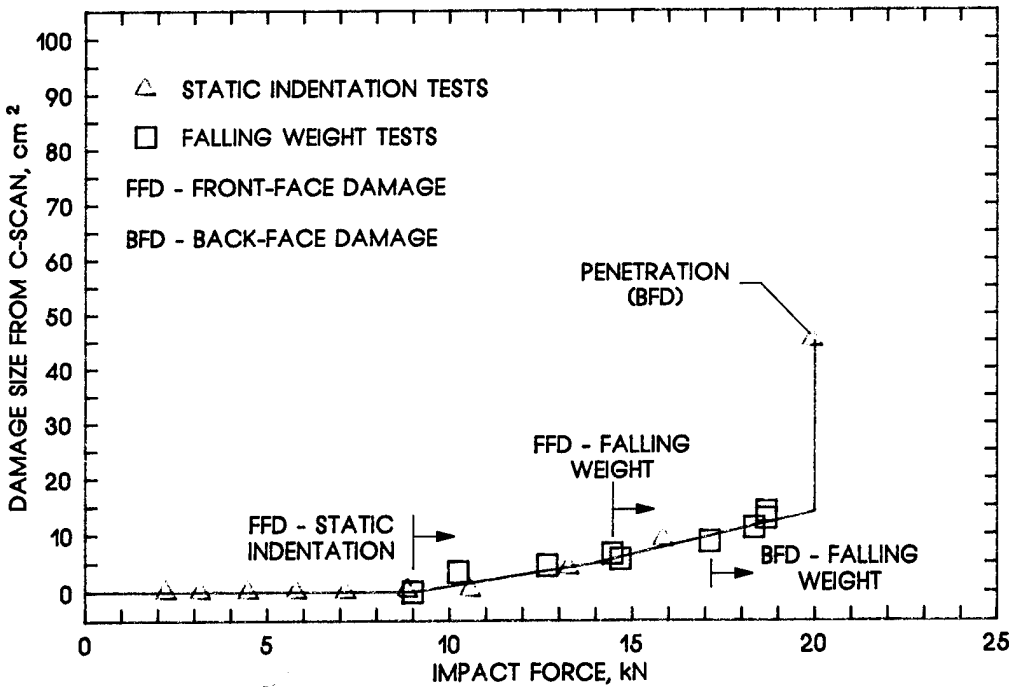
SS -- SIMPLY SUPPORTED
C -- CLAMPED

Figure 3. - Specimens and impact parameters for CE12000 3501-6 20° Braided material.



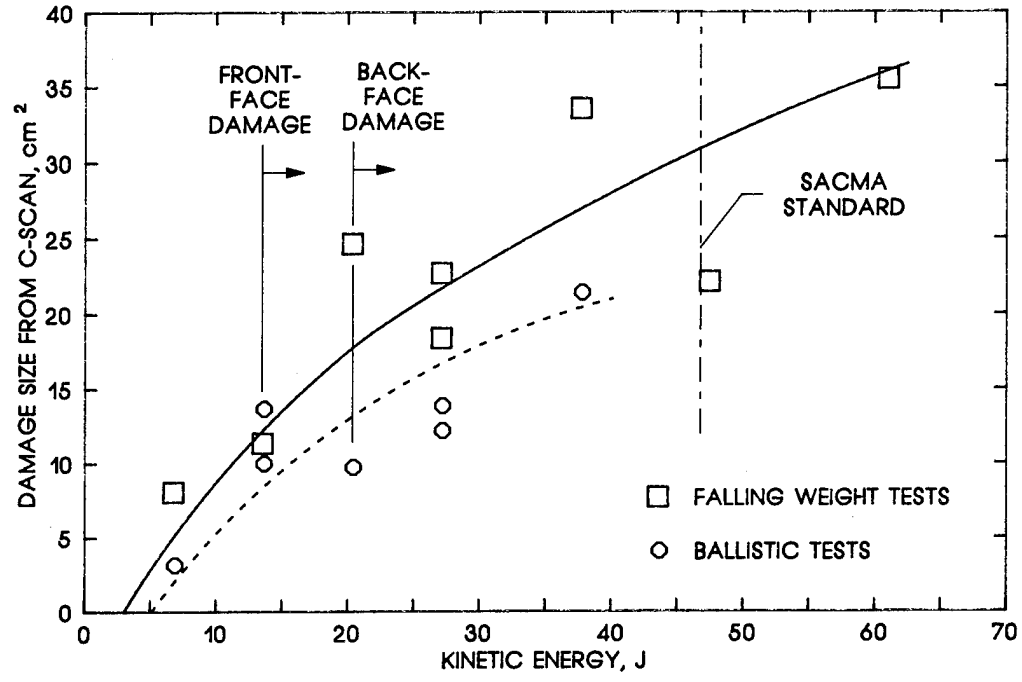
(a) $[45/0/-45/90]_{6s}$ AS4/3501-6 laminate.

Figure 4.- Damage area versus impact force.



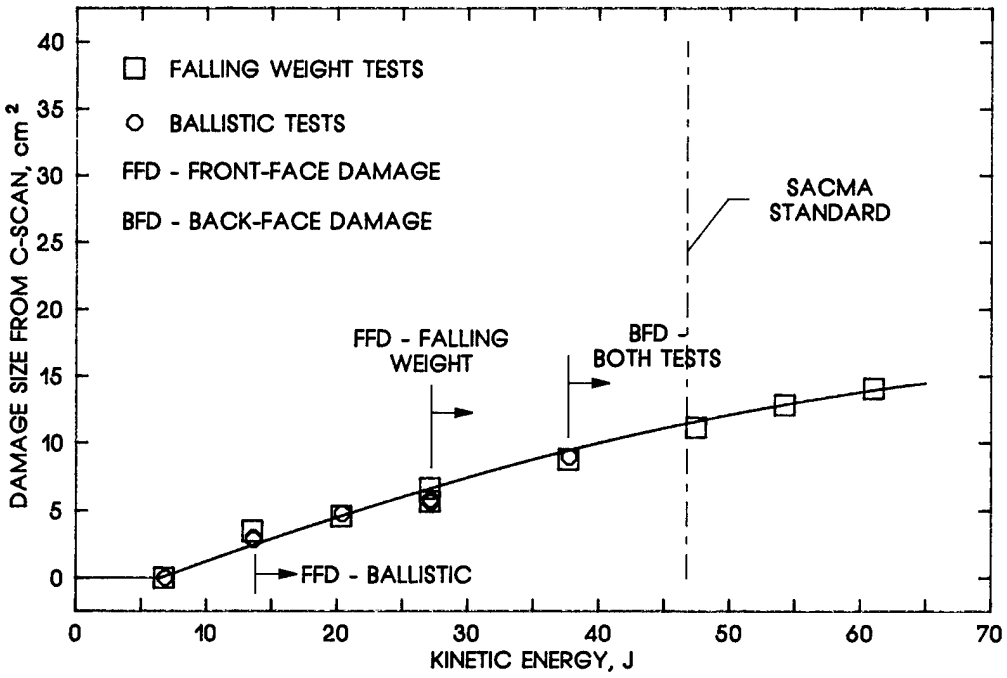
(b) $[45/0/-45/90]_{6S}$ IM7/8551-7 laminate.

Figure 4.- Concluded.



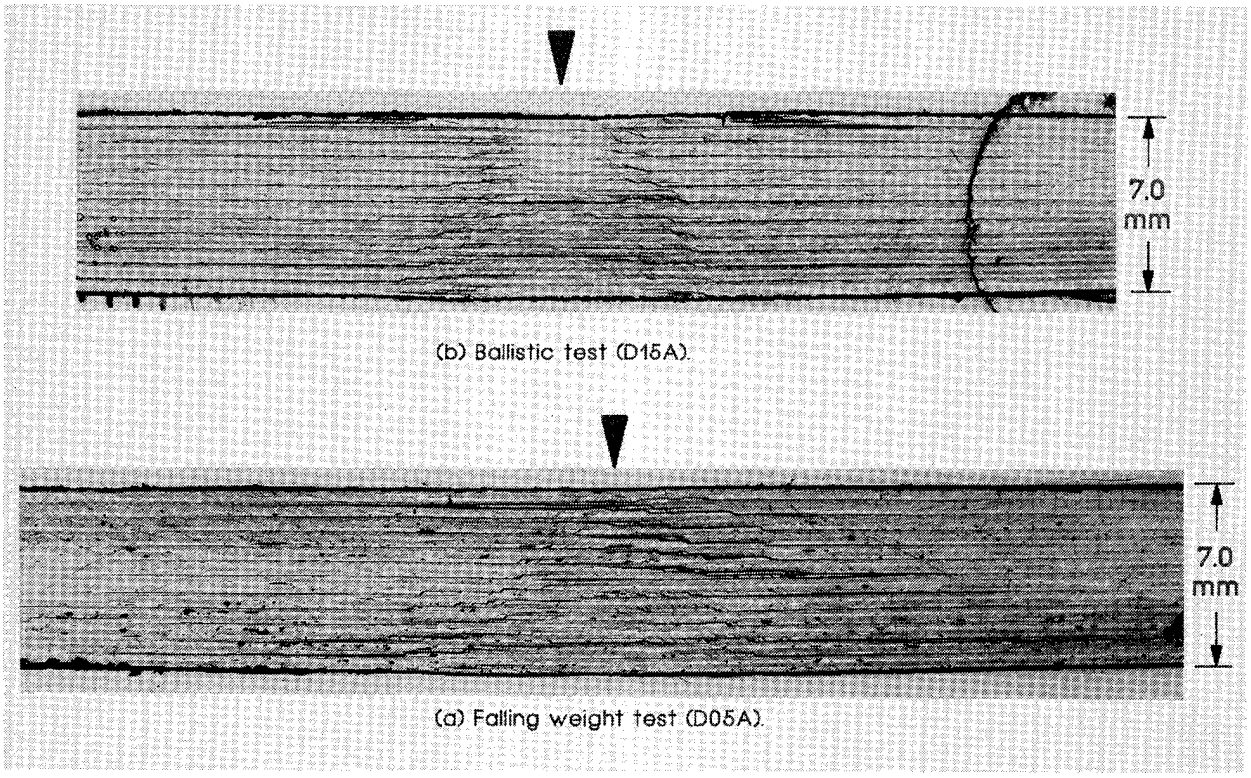
(a) $[45/0/-45/90]_{6S}$ AS4/3501-6 laminate.

Figure 5.- Damage area versus kinetic energy.



(b) $[45/0/-45/90]_{6S}$ IM7/8551-7 laminate.

Figure 5.- Concluded.



(b) Ballistic test (D15A).

(a) Falling weight test (D05A).

Figure 6.- Photographs of edge replicas of AS4/3501-6 tape laminate impacted with kinetic energy of 27.1 J.

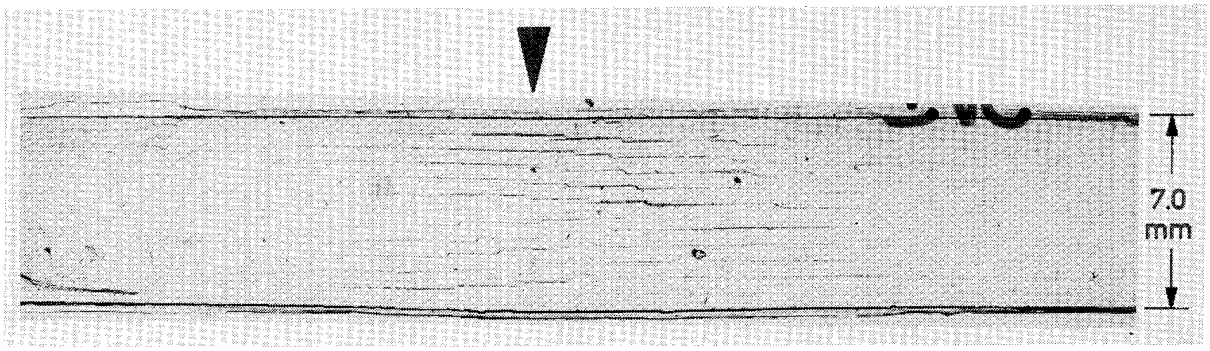


Figure 7.- Photograph of edge replica of IM7/8551-7 specimen (D05IR) impacted by falling weight with kinetic energy of 27.1 J.

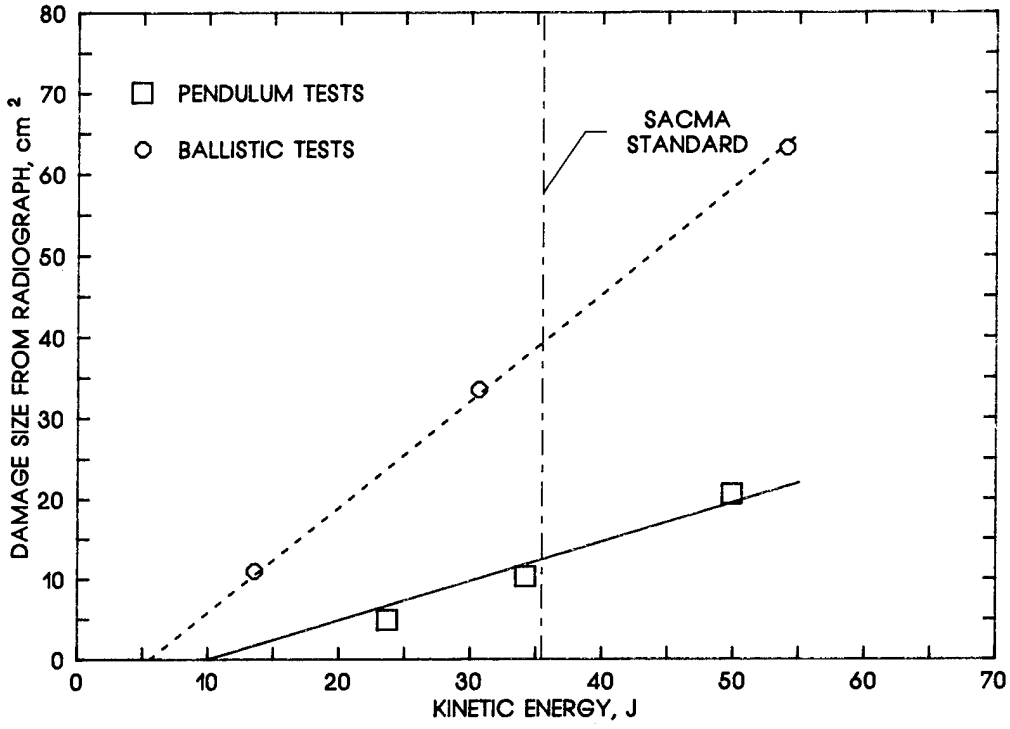
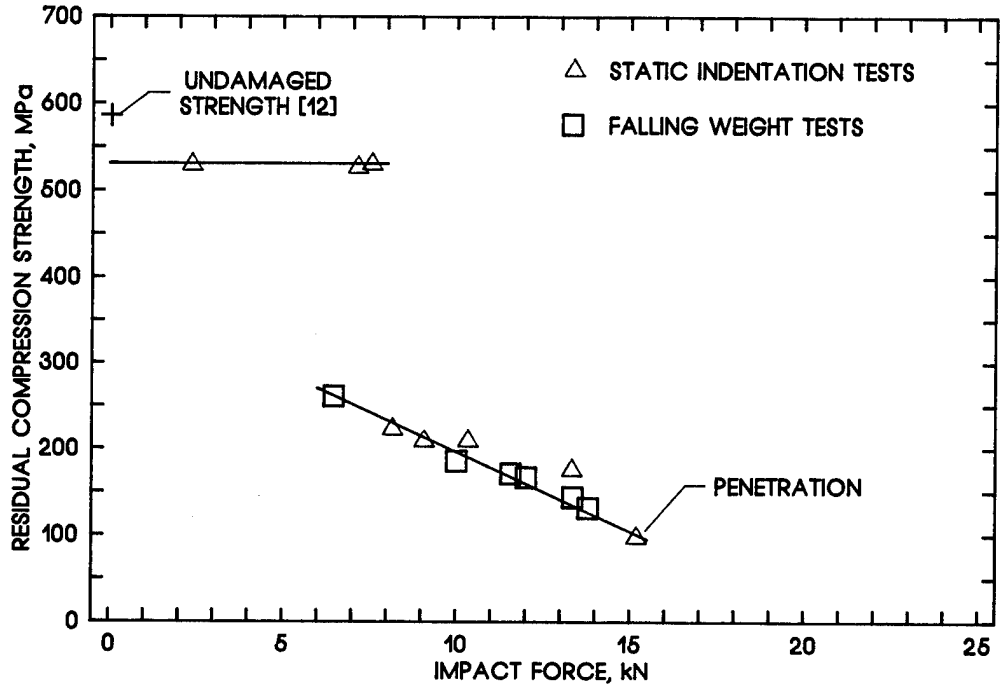
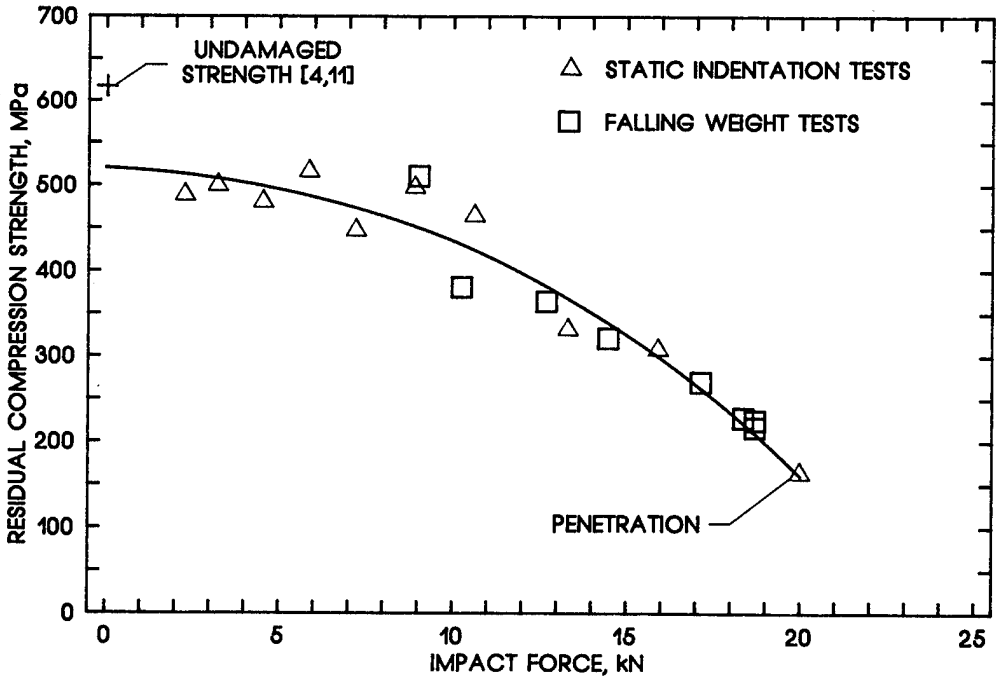


Figure 8.- Damage area versus kinetic energy for CE12000/3501-6 braided material.



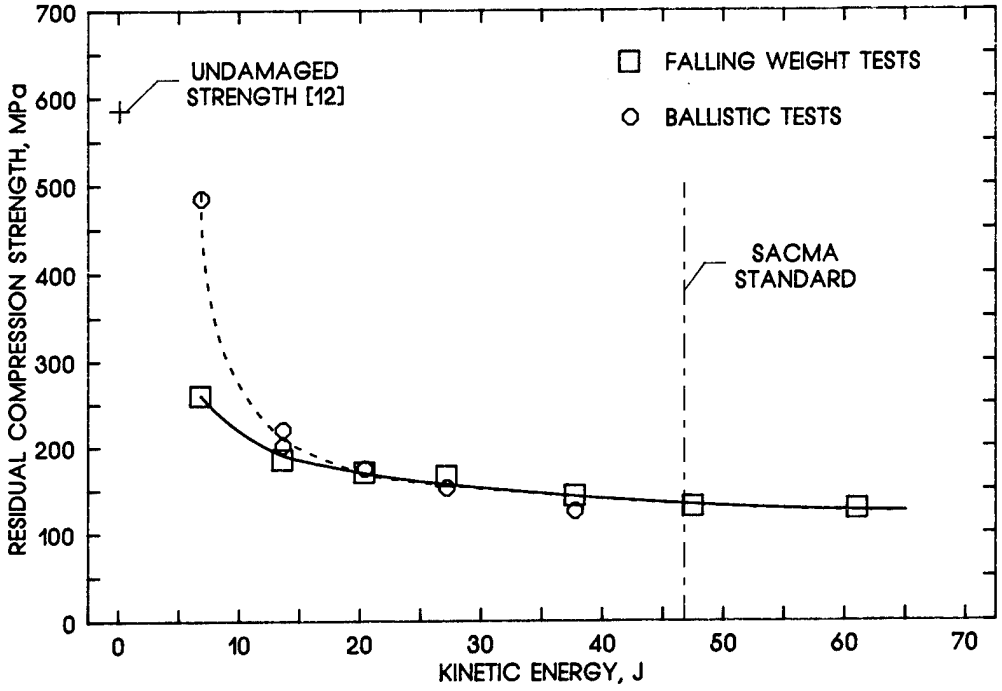
(a) $[45/0/-45/90]_{6S}$ AS4/3501-6 laminate.

Figure 9.- Residual compression strength versus impact force.



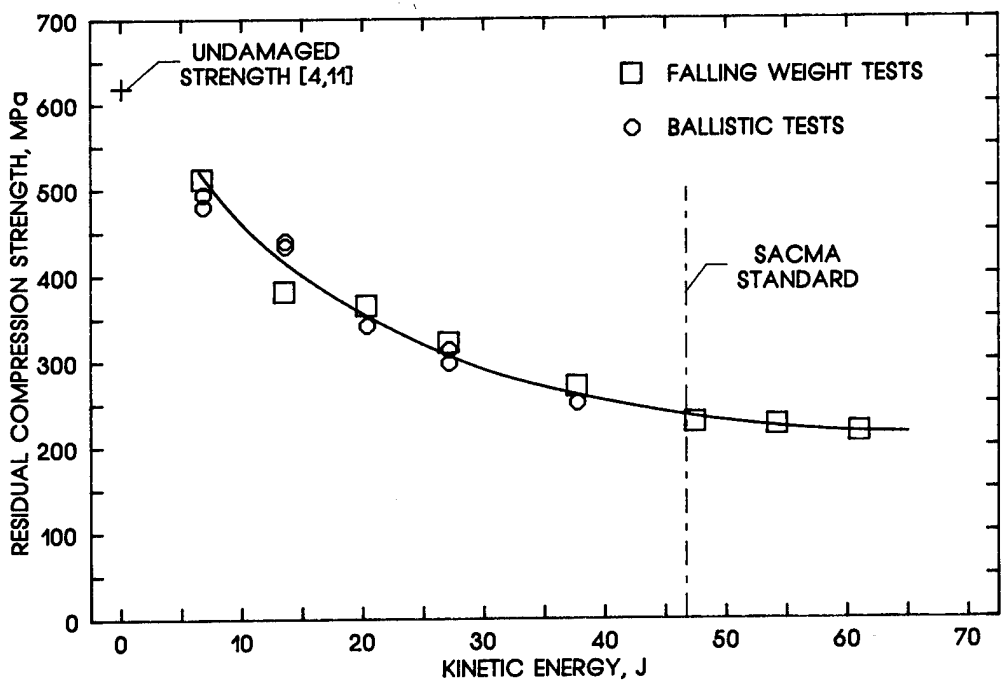
(b) $[45/0/-45/90]_{6S}$ IM7/8551-7 laminate.

Figure 9.- Concluded.



(a) $[45/0/-45/90]_{6S}$ AS4/3501-6 laminate.

Figure 10.- Residual compression strength verses kinetic energy.



(b) $[45/0/-45/90]_{6S}$ IM7/8551-7 laminate.

Figure 10.- Concluded.

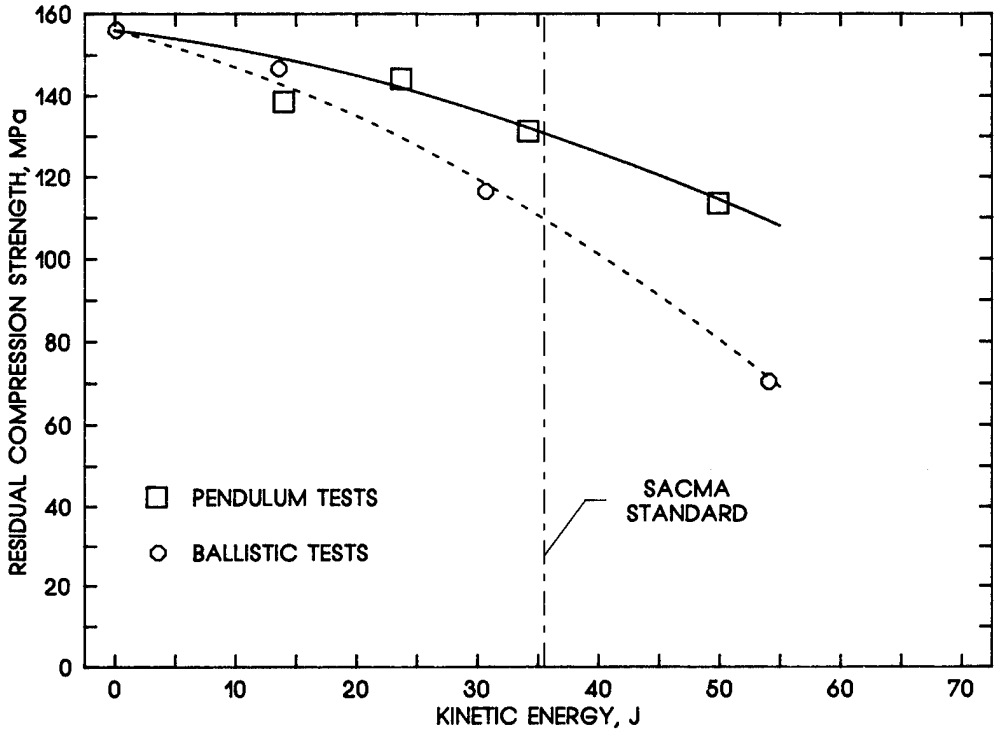
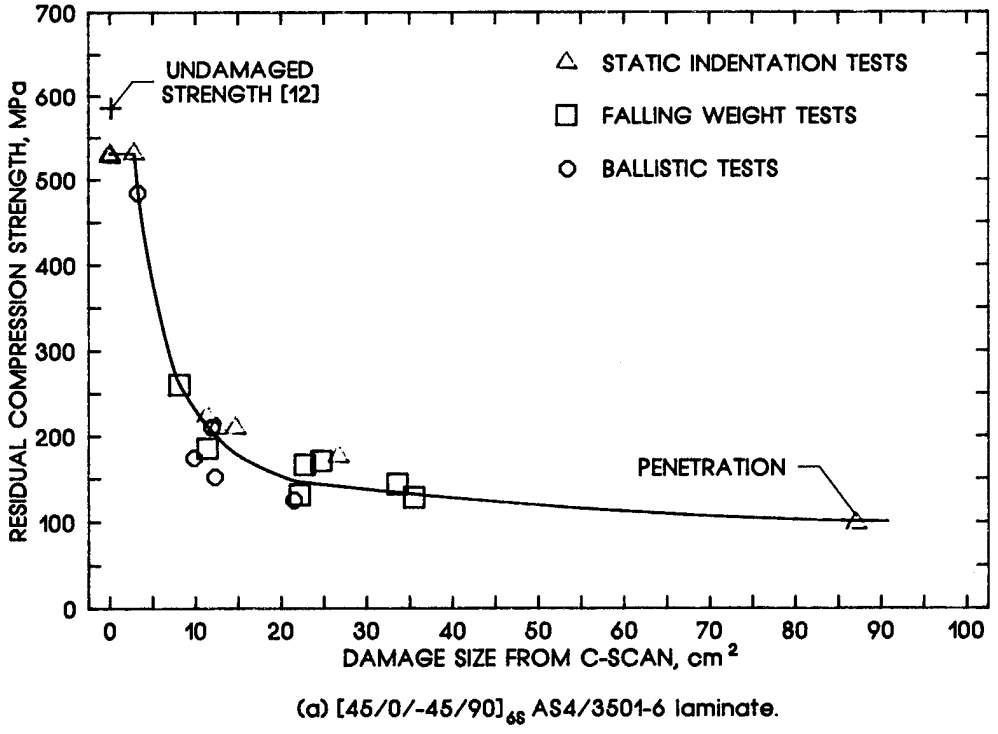
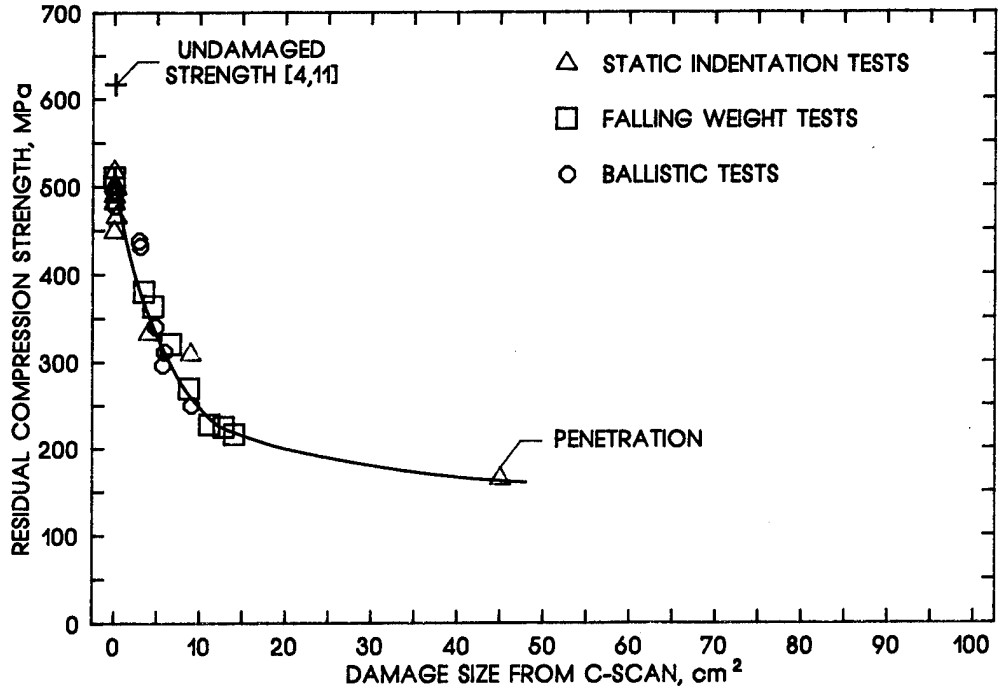


Figure 11.- Residual compression strength versus kinetic energy for CE12000/3501-6 braided material.



(a) $[45/0/-45/90]_{6S}$ AS4/3501-6 laminate.

Figure 12.- Residual compression strength versus damage area.



(b) $[45/0/-45/90]_{6S}$ IM7/8551-7 laminate.

Figure 12.- Concluded.

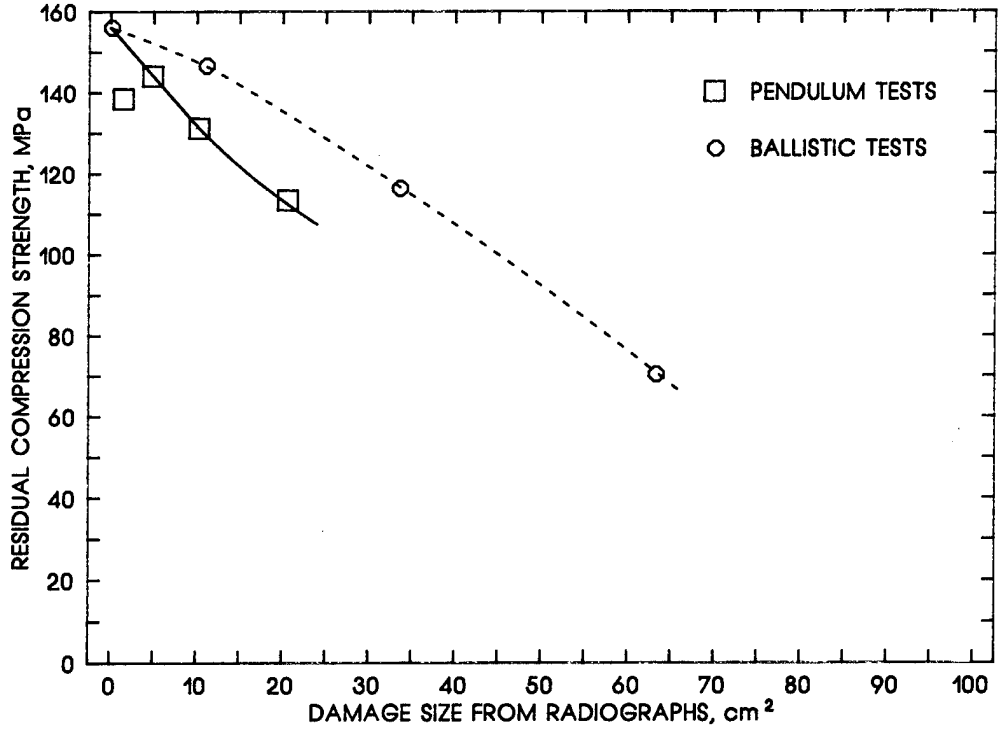


Figure 13.- Residual compression strength versus damage are for CE12000/3501-6 braided material.

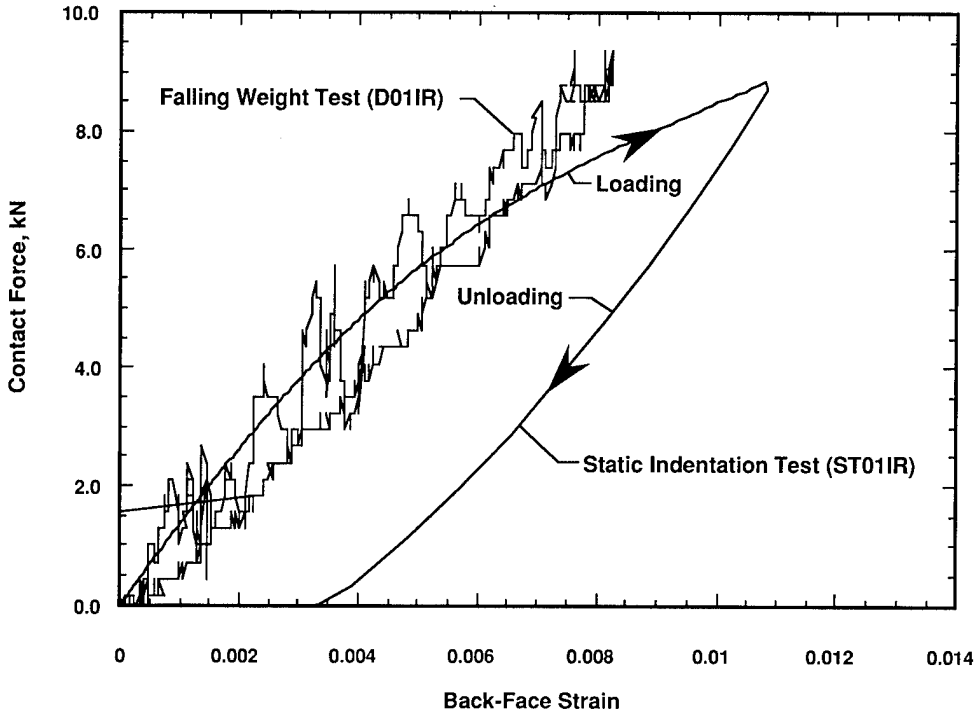


Figure 14.- Back-face strain versus contact force for static indentation and falling weight impact tests of IM7/8551-7 tape laminate

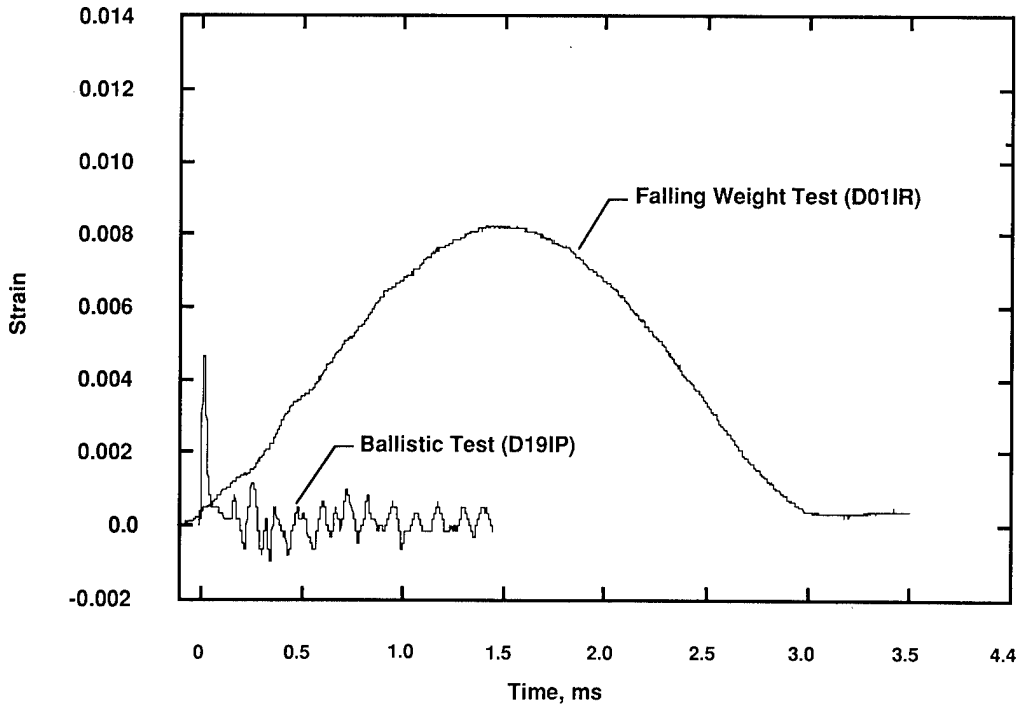


Figure 15.- Back-face strain versus time for ballistic and falling weight impact tests of IM7/8551-7 tape laminate

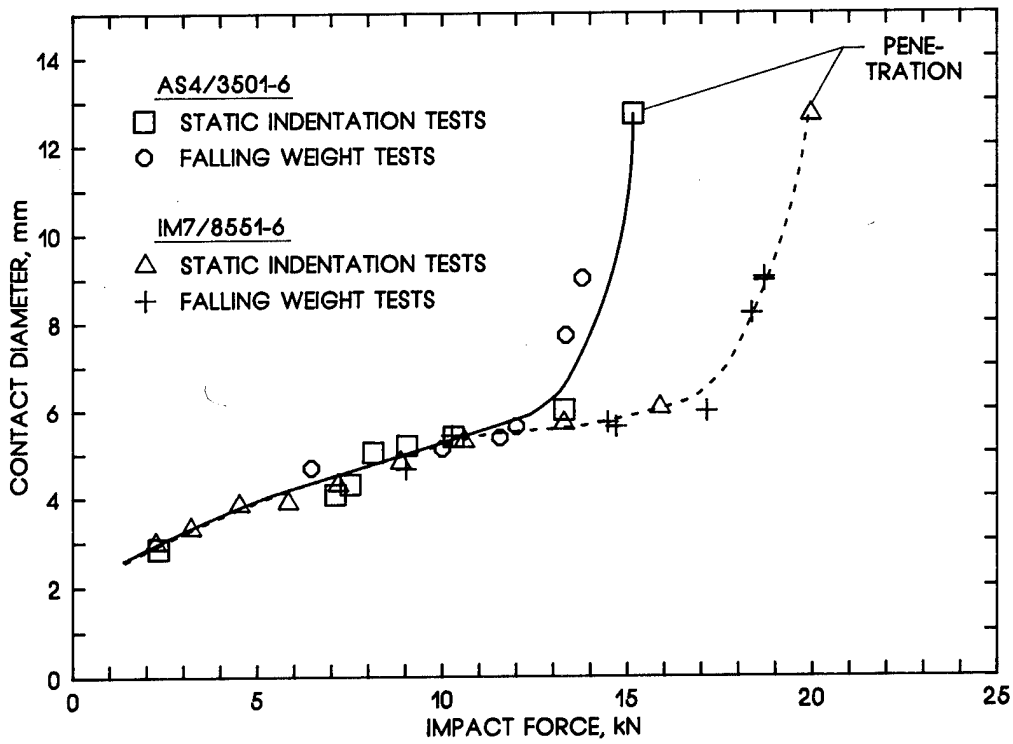


Figure 16.- Contact diameter versus impact force for $[45/0/-45/0/90]_{6s}$ tape laminates.

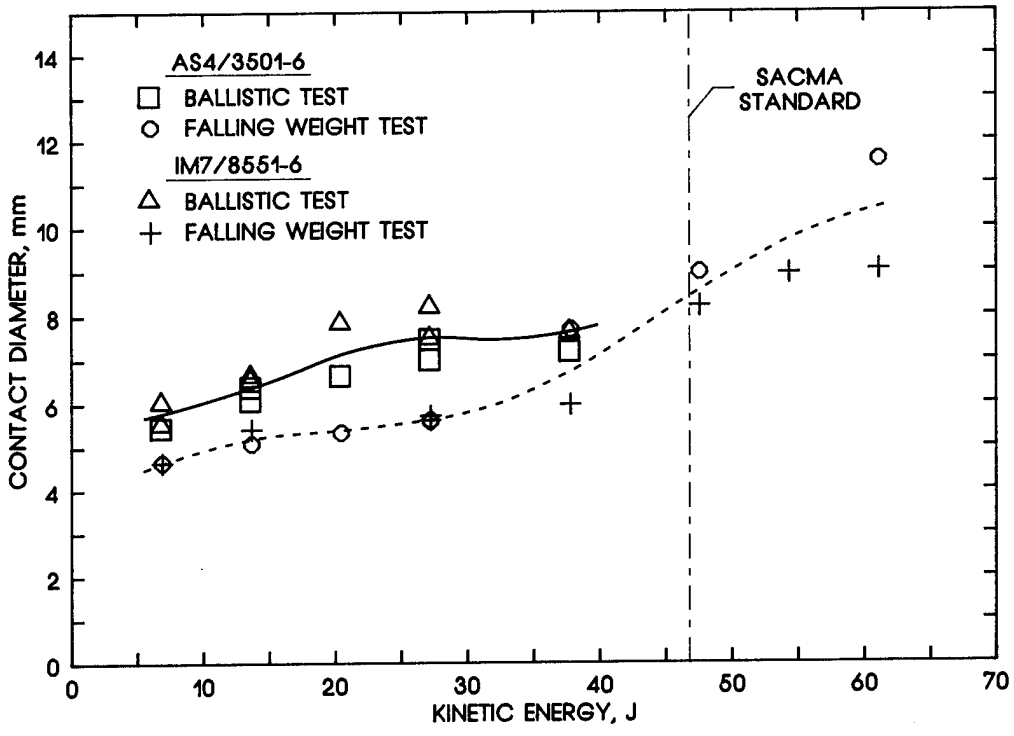
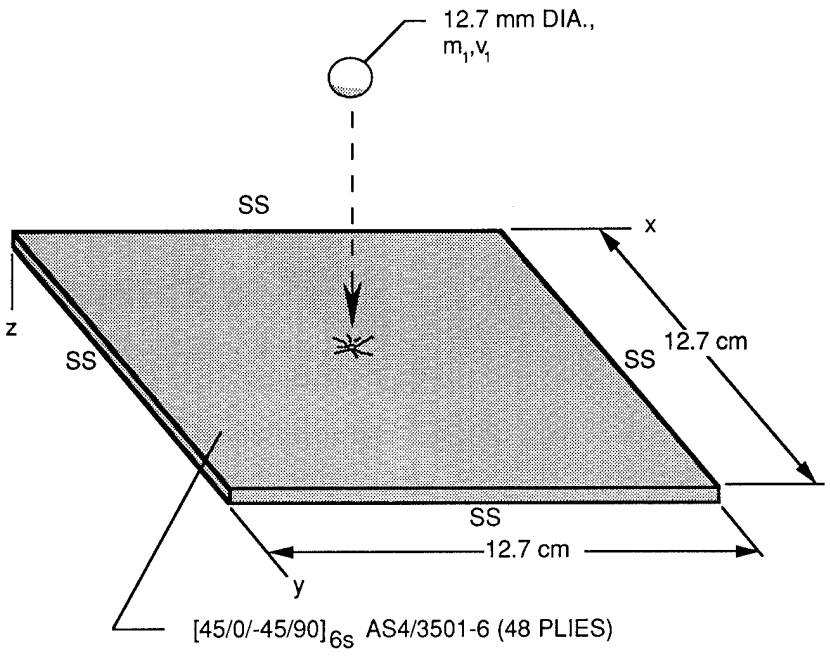


Figure 17.- Contact diameter versus kinetic energy for $[45/0/-45/0/90]_{6s}$ tape laminates.



SS -- SIMPLY SUPPORTED

Figure 18. - Plate for impact analysis

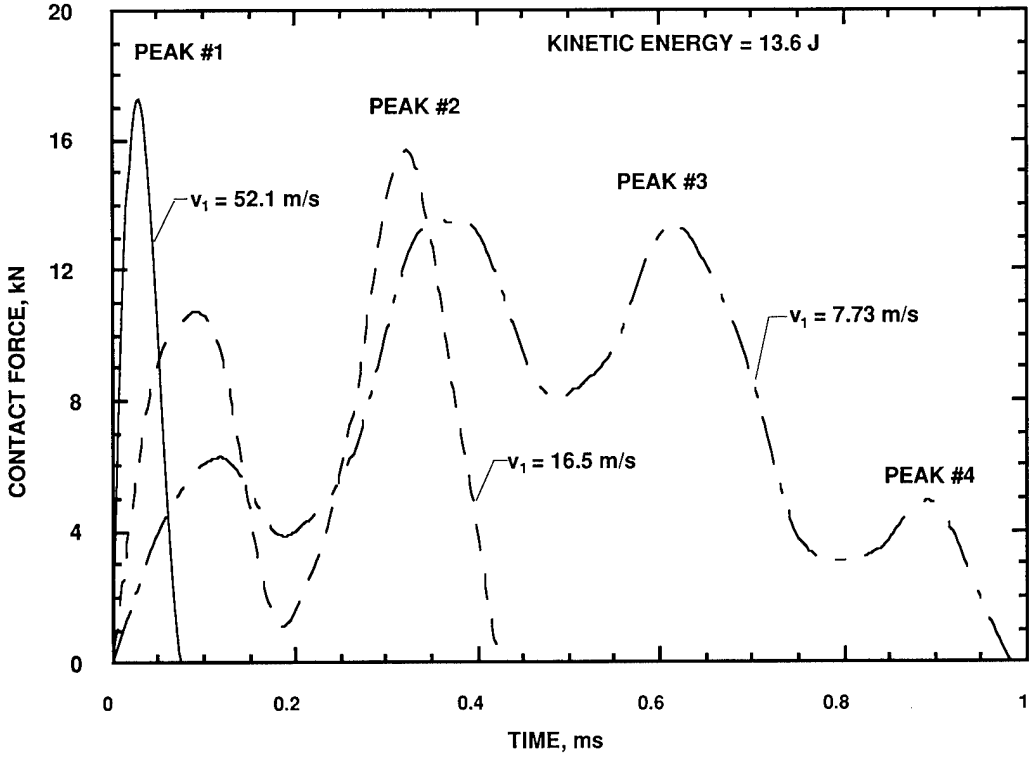


Figure 19.- Predicted effect of velocity on contact force history.

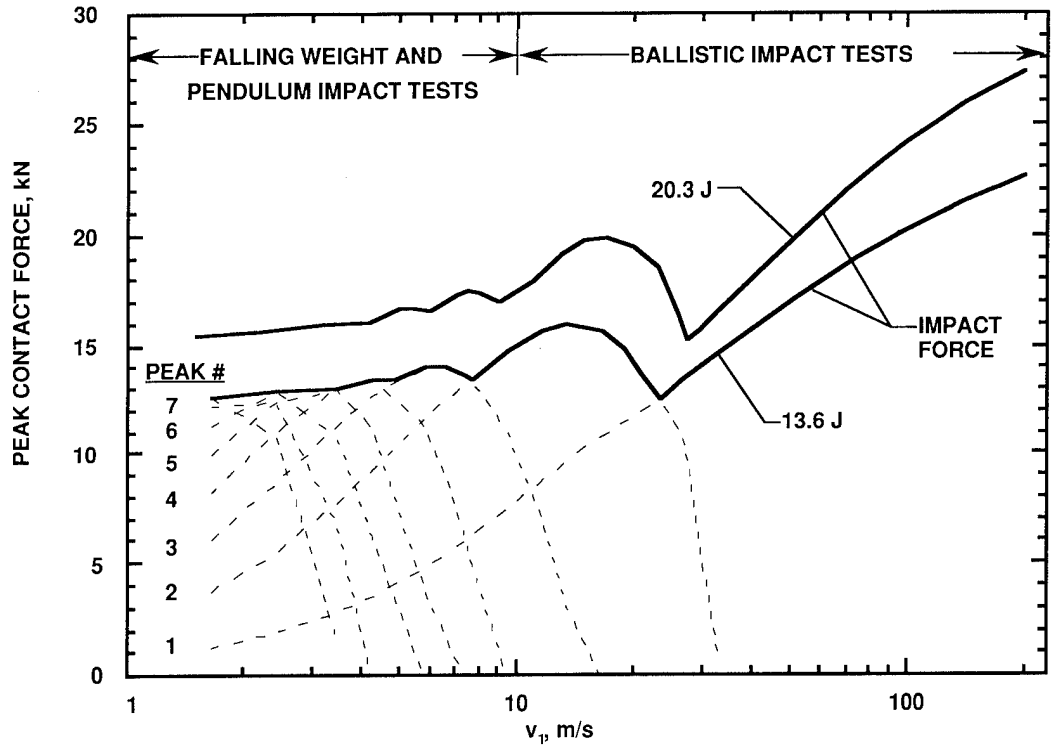


Figure 20.- Predicted peak force versus impacter velocity.

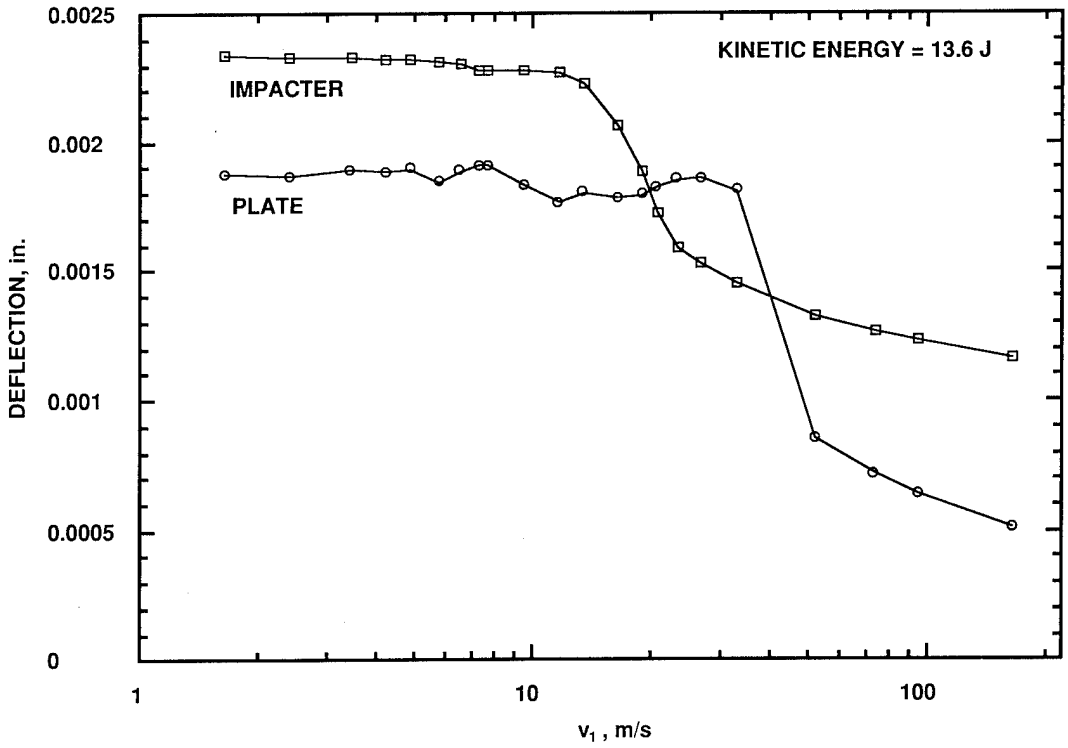


Figure 21. Predicted maximum deflection at center of plate versus impacter velocity.

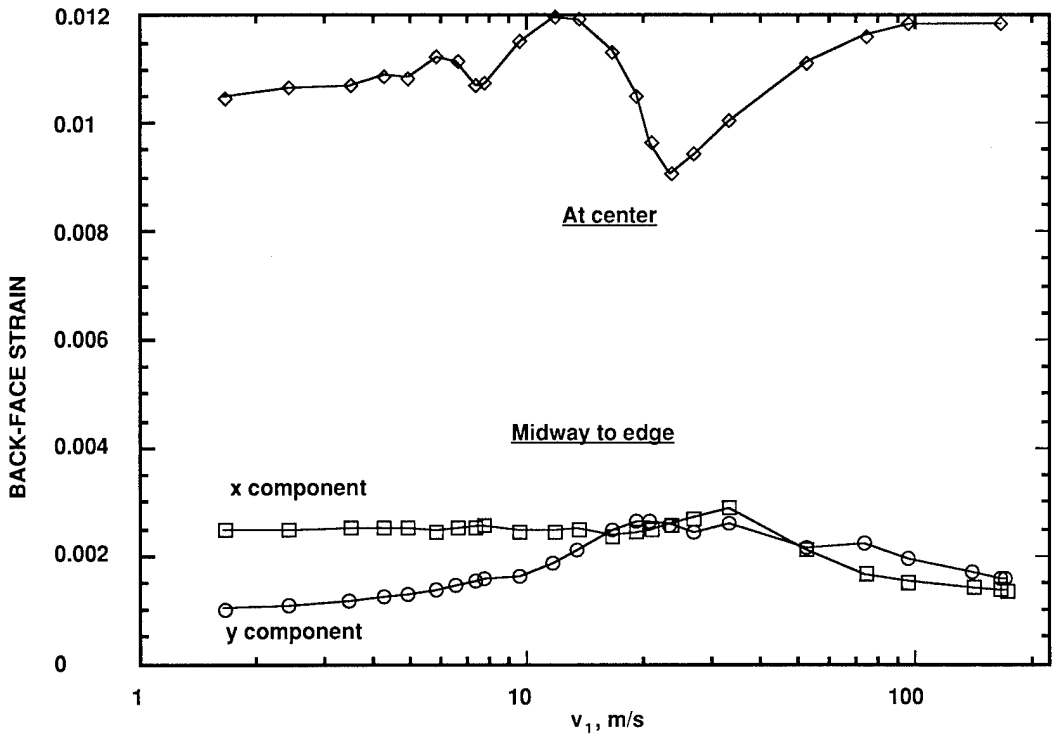


Figure 22.- Back-face strain versus velocity for a kinetic energy of 13.6 J.

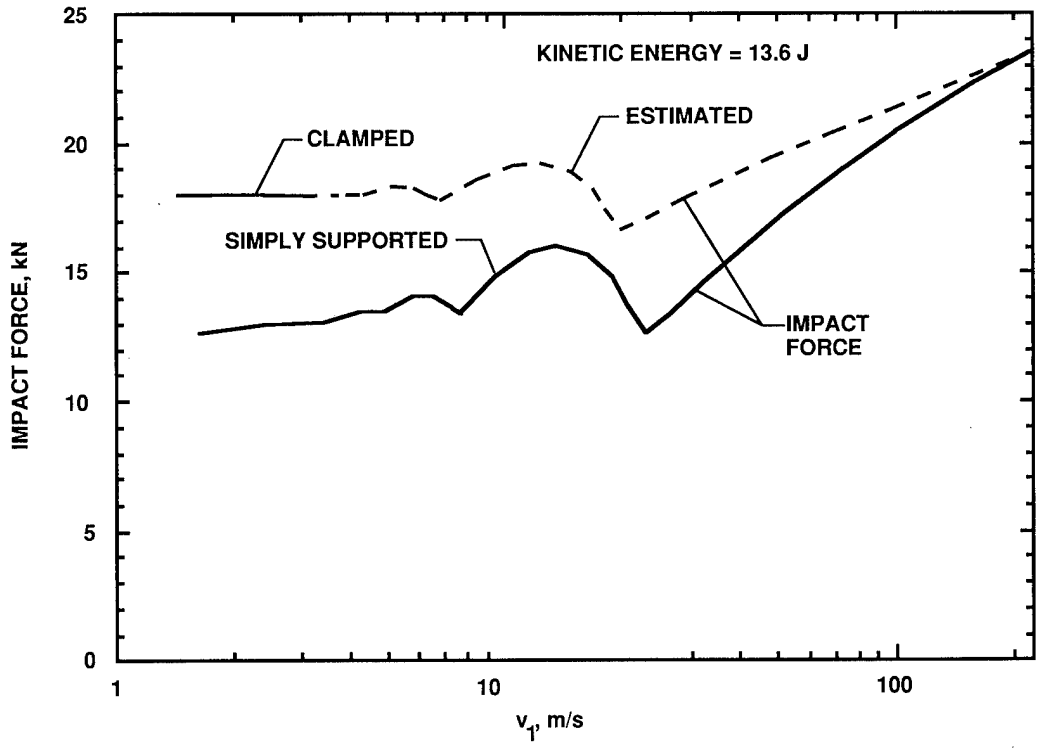


Figure 23.- Predicted impact force versus impacter velocity.

DELAMINATIONS IN COMPOSITE PLATES UNDER IMPACT LOADS*

Scott R. Finn and George S. Springer
Stanford University

SUMMARY

A method is presented for calculating the locations, shapes, and sizes of delaminations which occur in a fiber reinforced composite plate subjected to non-penetrating ("low velocity") impact of a solid object. The plate may be simply supported, clamped, or free along its edges. A failure model of the delamination formation was developed. This model was then coupled with a finite element analysis. The model and the finite element analysis were then implemented by a computer code ("IMPACT-ST") which can be used to estimate the damage initiation load and the locations, shapes, and sizes of the delaminations. Tests were performed measuring the geometries of delaminations in graphite-epoxy, graphite-toughened epoxy, and graphite-PEEK plates impacted by a projectile with a spherical tip having masses ranging from 0.355 lbm to 0.963 lbm and velocities from 50 in/sec to 225 in/sec. The data were compared to the results of the model, and good agreements were found between the measured and calculated delamination lengths and widths.

INTRODUCTION

Structures made of fiber reinforced organic matrix composites may become damaged when subjected to impact loads. The damage may manifest itself in the form of fiber breakage, matrix cracking, and delamination. Here, our main focus is on delamination. The reason for this is twofold. First, our interest is damage caused by impact where, in general, delamination is of primary concern. Second, while there are reasonable models for predicting fiber breakage and matrix cracking, there is no accurate method for predicting the locations, shapes, and sizes of delaminations in dynamically loaded composite laminates.

The formation and growth of delaminations in panels subjected to transverse static or dynamic loads have been studied by several investigators. However, the existing methods for predicting the locations, shapes, and sizes of delaminations possess certain limitations. The model of Clark [1] provides only qualitative predictions of the delamination sizes. The models of Bostaph and Elber [2] and Grady, et al [3,4] provide an estimate of the delamination growth but require a priori knowledge of the number and locations of delaminations. In addition, Bostaph and Elber assume that, in cases of

*This work is supported by NASA Langley Research Center under contract number NAS1-18778.

multiple delaminations, all delaminations grow to the same size, while Grady's model applies only to relatively large delaminations. Liu's model [5,6] shows the effect of bending stiffness mismatch between adjacent plies on delamination sizes. The models of Wu and Springer [7] and Gosse, et al [8,9] provide the locations, shapes, and sizes of delaminations. Wu and Springer's model was based on limited experimental data and has since been found not to apply to a broad range of impact conditions. The model of Gosse, still in the development stage, requires a strength parameter for which there is no known test.

It appears that no model exists which would provide with sufficient accuracy the locations, magnitudes, and shapes of delaminations inside composite laminates subjected to the impact of a solid object. Therefore, the first objective of this investigation was to develop a model which can be used to estimate the locations, shapes, and sizes of delaminations inside fiber reinforced composite laminates subjected to transverse non-penetrating ("low velocity") impact. A second objective was to generate data to evaluate the accuracy of the present model as well as any other models which may be forthcoming.

DELAMINATION MODEL

We consider a composite plate made of plies of unidirectional fibers embedded in an organic matrix. The plies may be arranged in groups of neighboring plies which all have the same fiber orientation. Initially, the plies are perfectly bonded. Each edge of the plate may be either clamped, simply supported, or free.

The plate is subjected to transverse impact loading (Figure 1). The objective is to find the "initiation load" (i.e., the load at which delamination first occurs), and the locations, shapes and sizes of the delaminations caused by loads higher than the "initiation load."

Damage Initiation

It has been observed previously [1, 8-17] that delamination is often preceded by transverse matrix cracking. This observation has further been borne out by tests performed during the course of this study. On the basis of this evidence, we postulate that transverse matrix cracking is a necessary precursor to delamination. The load at which transverse matrix cracking first occurs is designated as the "initiation load." This load is estimated by the formula [8, 9]

$$\frac{1}{2}\left(\sigma_{yy} + \sigma_{zz}\right) + \sqrt{\frac{1}{4}\left(\sigma_{yy} - \sigma_{zz}\right)^2 + \sigma_{yz}^2} \quad \begin{matrix} \geq Y & \text{damage} \\ < Y & \text{no damage} \end{matrix} \qquad (1)$$

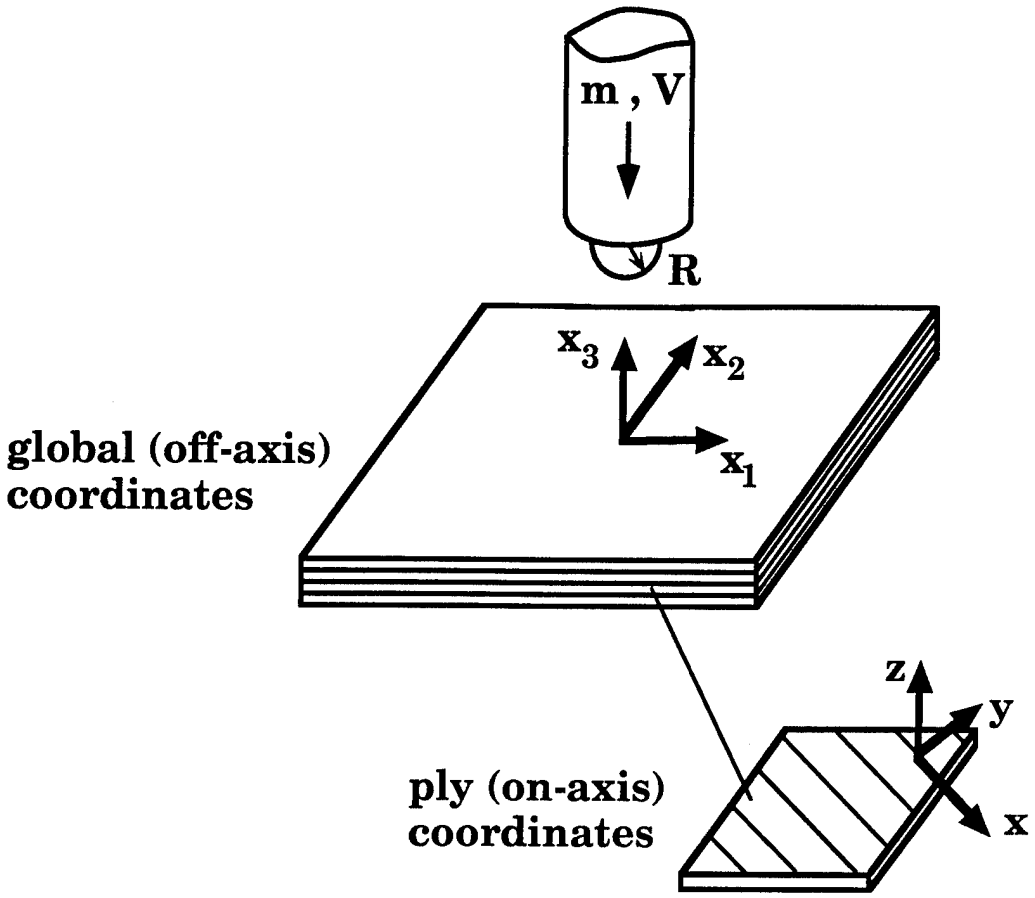


Figure 1 Description of the problem and coordinate systems

where σ denotes stress, and y and z are on-axis coordinates transverse to the fiber direction (Figure 1). Under a given load, matrix cracking occurs when in any given ply group the combination of stresses on the left hand side of this equation equals the ply group's transverse tensile strength Y. This strength is given by [18]

$$Y = Y_o\left(1 + C\frac{\sin(\Delta\theta)}{N^B}\right) \qquad (2)$$

Y_o is the transverse tensile strength of a $[90]_n$ laminate ($n \geq 12$). $\Delta\theta$ is the smaller of the two differences in fiber orientation between the given ply group and the ply groups above and below it. N is the number of individual plies within the ply group. B and C are constants which depend on the material.

Delamination Model

Delamination over a small area dA on an interface occurs when the strain energy available to form the delamination exceeds the energy required to cause delamination [19]. In general terms, this condition can be expressed as

$$\hat{S} \geq G_c dA \tag{3}$$

where $\hat{S}$ is the strain energy available to delaminate dA and G_c is the critical strain energy release rate. The available strain energy is only a portion of the total strain energy inside the plate. The total strain energy is [20]

$$\hat{S}_{total} = \frac{1}{2}\int_V (\sigma_{xx}\varepsilon_{xx} + \sigma_{yy}\varepsilon_{yy} + \sigma_{zz}\varepsilon_{zz} + \sigma_{xy}\gamma_{xy} + \sigma_{xz}\gamma_{xz} + \sigma_{yz}\gamma_{yz})\, dV \tag{4}$$

where ε and γ denote normal and engineering shear strains, respectively. x,y,z are the on-axis (ply) coordinates (Figure 1). V is the volume of the plate.

In order to apply Eq. 3, the relationship between the available and the total strain energies must be known, and the critical strain energy release rate must be specified. There are different avenues by which the available strain energy and the critical strain energy release rate can be established. Here, we propose a model which is built on two basic tenets.

1) Delaminations occur only at interfaces which are adjacent to a ply group in which longitudinal matrix cracking occurs (i.e. the crack is parallel to the fibers [8-10].

2) The matrix crack must open up for a delamination to be produced.

To describe this model we focus our attention on a ply group containing a matrix crack and the two adjacent interfaces (Figure 2). An interface is denoted as either "upper" or "lower", depending on whether it is closer to or further from the load. Each interface may be unrestrained or restrained. An interface is unrestrained either if it coincides with the front or back surface of the plate or if it is delaminated (Figure 3). An interface is restrained when perfect bonding is maintained between the cracked ply group and the adjacent laminate.

Below, the stresses and mechanisms are discussed which, according to our model, cause delaminations in the interfaces adjacent to the cracked ply group. Since our interest is in ply groups with longitudinal matrix cracks, we examine the on-axis stress field in a cracked ply group (Figure 4).

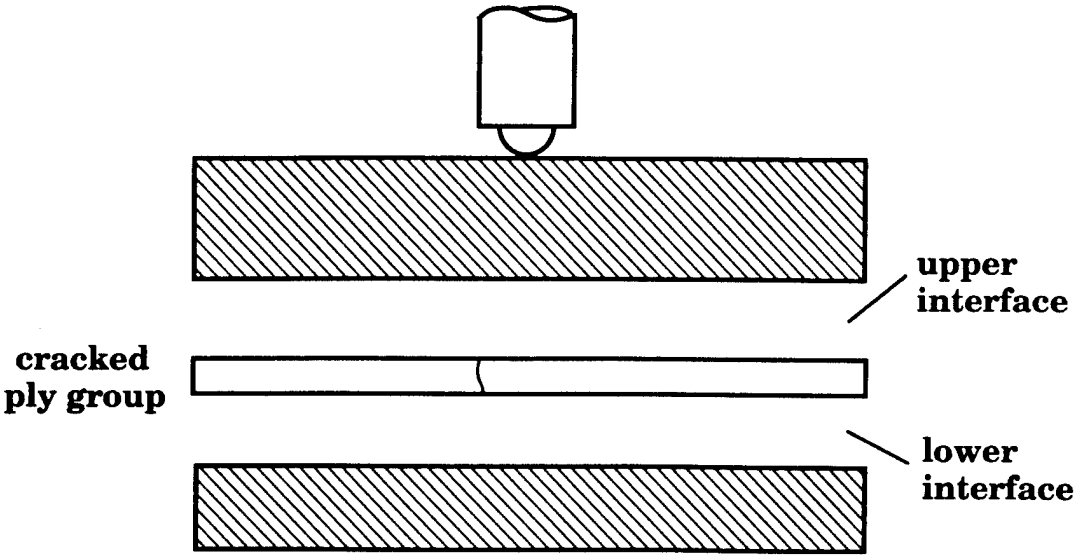


Figure 2 Cracked ply group and corresponding upper and lower interfaces

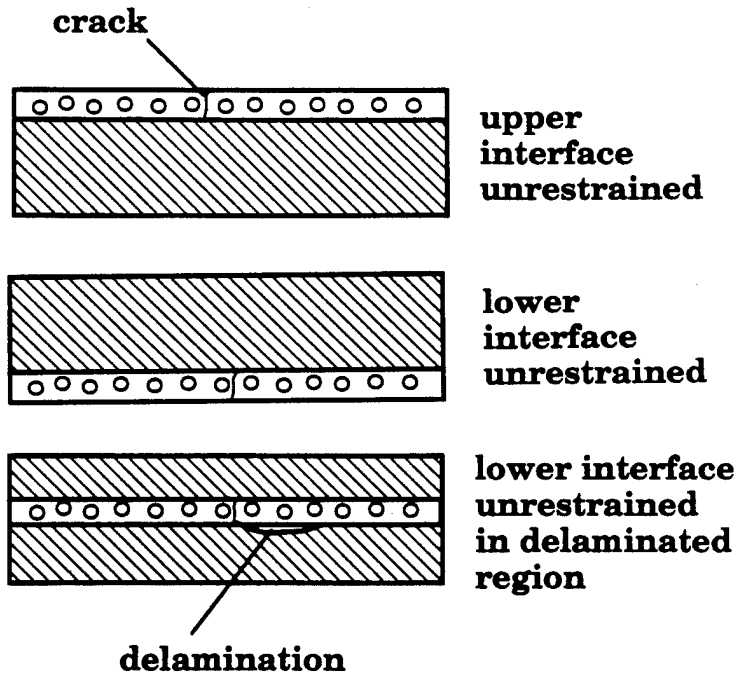


Figure 3 Illustration of an unrestrained interface

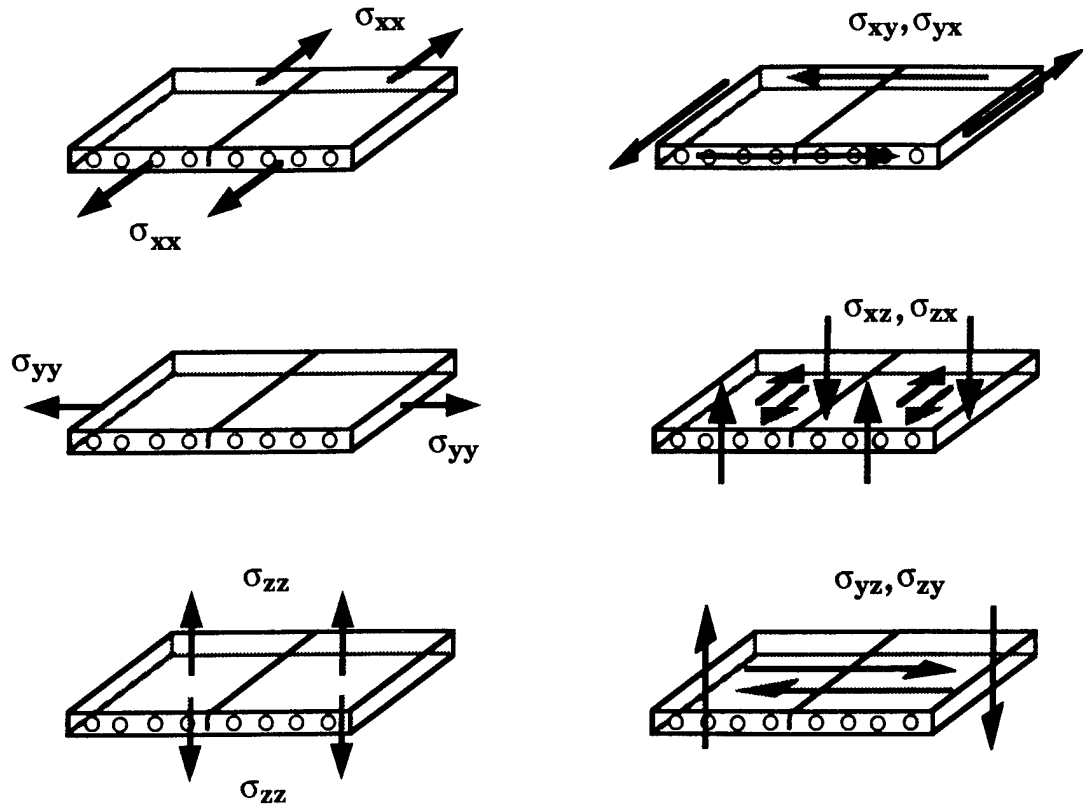


Figure 4 Stress field in a cracked ply group

Bending and Twisting. The applied transverse load may result in bending and twisting of the plate. When a ply group contains a transverse crack (and this ply group is unrestrained) the curvature of the cracked ply group will be different than that of the adjacent laminate. This difference of curvature causes a separation (delamination) between the cracked ply group and its neighboring ply groups.

First, we consider the case when the plate has a concave bend with respect to the applied load, and the lower interface of the cracked ply group is unrestrained (Figure 5). This bending introduces curvatures in the directions normal and parallel to the fibers. In the former case, the crack may open resulting in a difference in curvature between the cracked ply group and the laminate. As a consequence of this, delamination occurs along the upper interface, as depicted in Figure 5 (left). The stress in the cracked ply group associated with the bending just described is the in-plane normal tensile stress σ_{yy}^{+}. This stress must be included when calculating the strain energy available to delaminate the upper interface. Note that if the lower interface is restrained, the crack is not free to open and no delamination is produced.

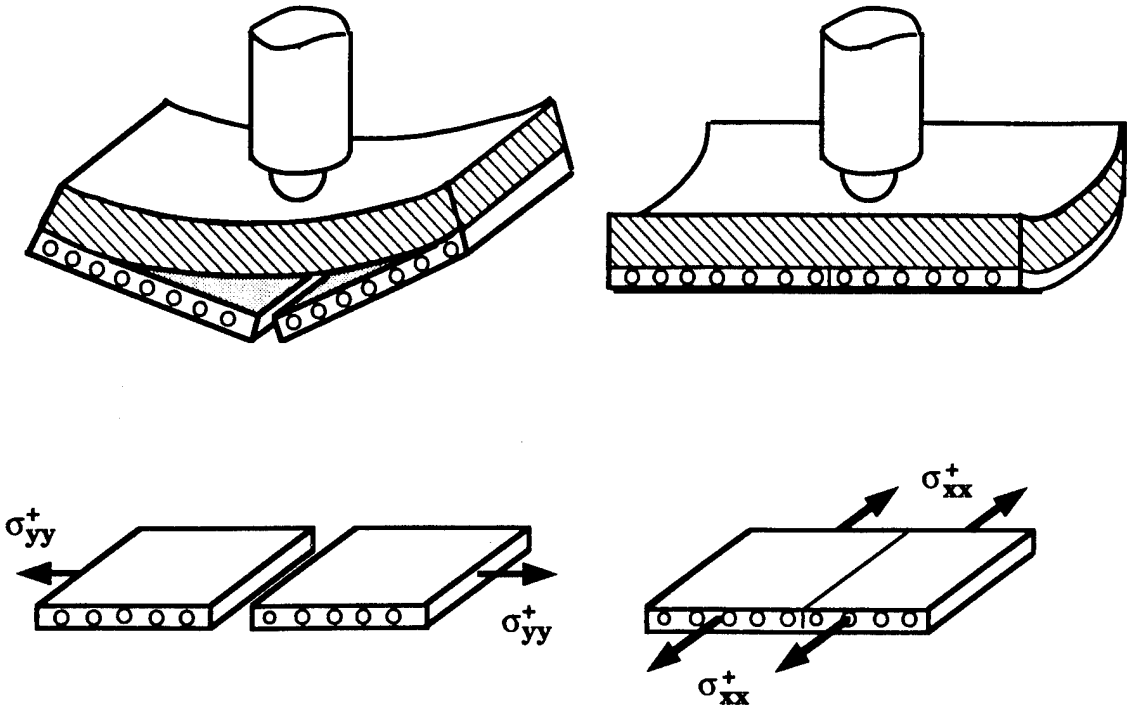


Figure 5 Bending of a plate containing a cracked ply group with its lower interface unrestrained; left: curvature in the direction normal to the fibers of the cracked ply group, right: curvature in the direction parallel to the fibers of the cracked ply group

The above scenario applies when the curvature is concave with respect to the applied load. There might be a slight convex curvature when the plate rebounds. Delamination growth resulting from this condition is neglected.

Bending may also cause a change in curvature along the fiber direction of the cracked ply group (Figure 5, right). Neglecting Poisson effects, this bending does not tend to open the matrix crack and thus, according to our model, does not contribute to delamination. In the cracked ply group, this type of bending is associated with a normal tensile stress in the fiber direction σ^+_{xx}. Since bending in the fiber direction does not play a role in delamination, σ^+_{xx} is not included in the expression for the available strain energy.

The aforementioned discussion applies when the lower interface of the cracked ply group is unrestrained. When the upper interface of the cracked ply group is unrestrained (Figure 6), the cracked ply group is in compression, the crack does not open and no delamination occurs. Hence, the associated transverse compressive stresses σ^-_{yy} and σ^-_{xx} need not be considered when calculating the available strain energy.

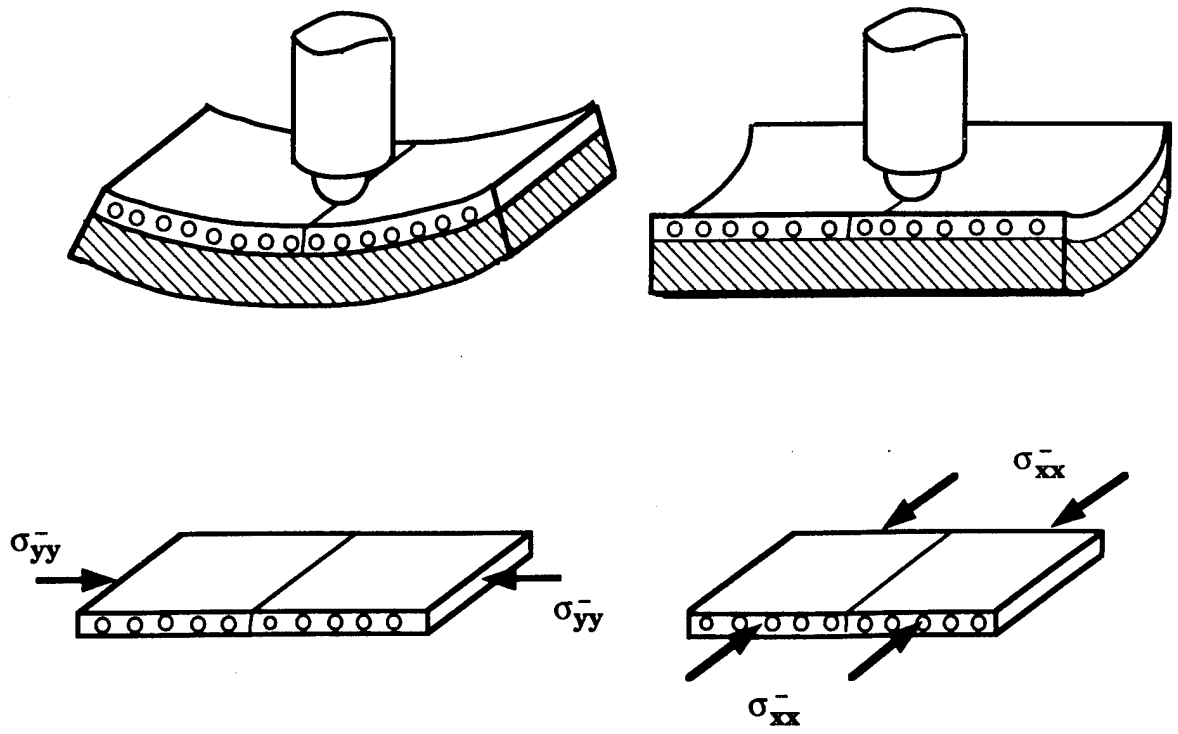


Figure 6 Bending of a plate containing a cracked ply group with its upper interface unrestrained; left: curvature in the direction normal to the fibers of the cracked ply group, right: curvature in the direction parallel to the fibers of the cracked ply group

The transverse load may also cause a twisting of the plate (Figure 7). If the lower interface is unrestrained, the crack may open, resulting in a mismatch in curvature between the cracked ply group and the laminate above it. This mismatch in curvature causes a delamination to form along the upper interface. The converse situation exists if the upper interface is unrestrained. The twisting motion just described is associated with an in-plane shear stress σ_{xy} in the cracked ply group. This stress must be considered when calculating the strain energy available to create a delamination at either the upper or lower interface. If both interfaces are restrained, the crack is not free to open and no delamination is formed.

Transverse Shear. The applied transverse load causes shearing of the plate. Shear may cause two adjacent ply groups to slide relative to one another (Figure 8). This motion does not affect the matrix crack which means that, according to our model, it does not contribute to delamination. The deformation shown in Figure 8 is associated with either or both of the transverse shear stresses σ_{zx} and σ_{zy}. Since the crack does not open, this mechanism would not require that σ_{zx} and σ_{zy} be included in the calculation of the available strain energy.

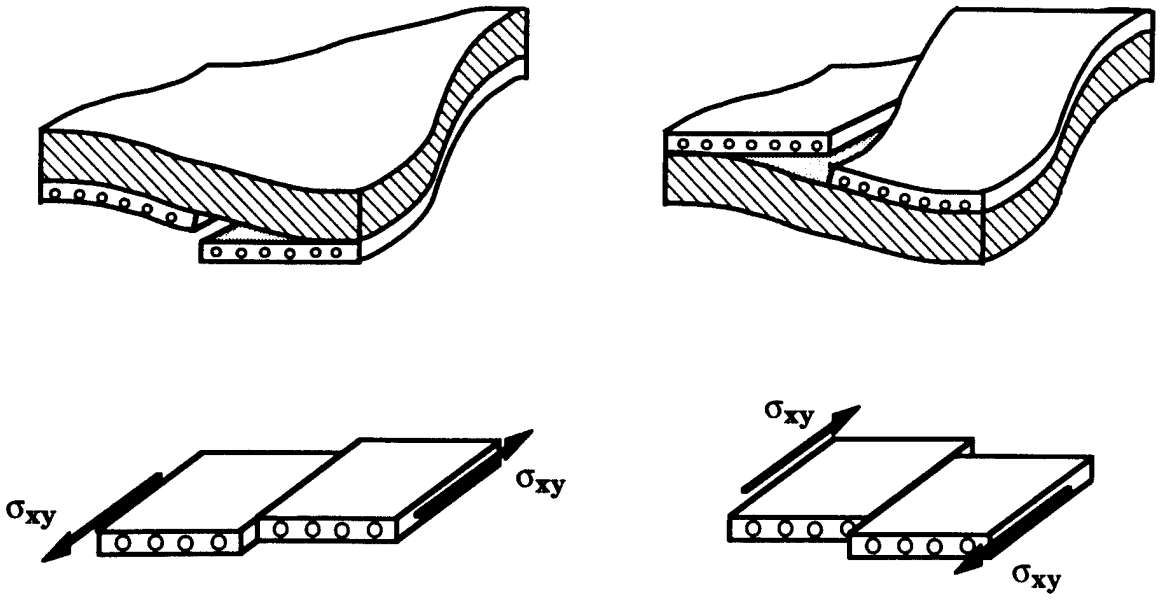


Figure 7 Twisting of a plate containing a cracked ply group; left: with lower interface unrestrained, right: with upper interface unrestrained

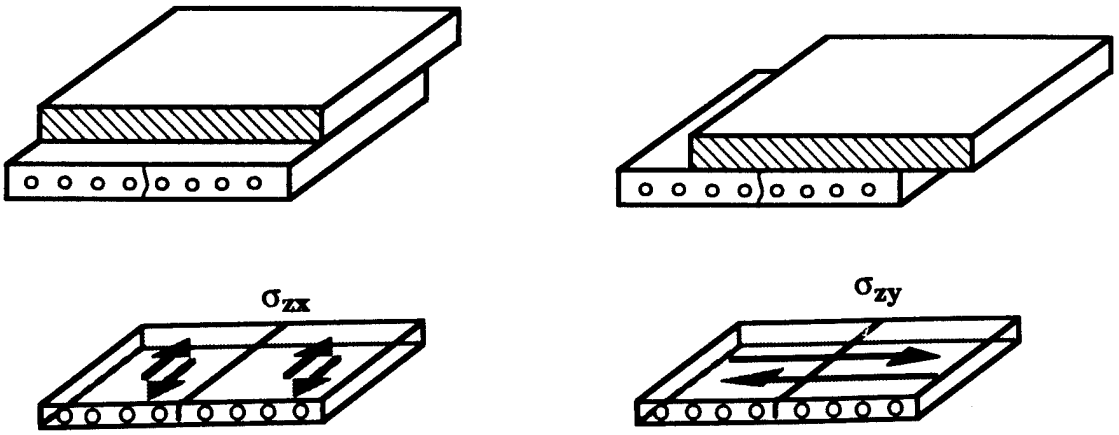


Figure 8 Interlaminar shearing of a cracked ply group; left: parallel to the fiber direction of the cracked ply group, right: normal to the fiber direction of the cracked ply group

The transverse shear introduced by the applied load also introduces local curving in the directions normal and parallel to the fibers of the cracked ply group (Figure 9). In the presence of a cracked ply group the shear introducing a curvature in the direction normal to the fibers creates a local mismatch in curvature between the cracked ply group and the adjacent ply groups (Figure 9, left). This local mismatch in curvature results in delaminations along both the upper and lower interfaces. The delamination starts at the crack and grows in the direction away from the load at the lower interface and towards the load at the upper interface. Since the inital cracks are generally located near the load, the delamination at the upper interface is smaller than that at the lower interface and is neglected in our model. This type of shearing is associated with the transverse shear stress σ_{yz} in the cracked ply, which therefore must be included in the calculation of the strain energy available to delaminate the lower interface.

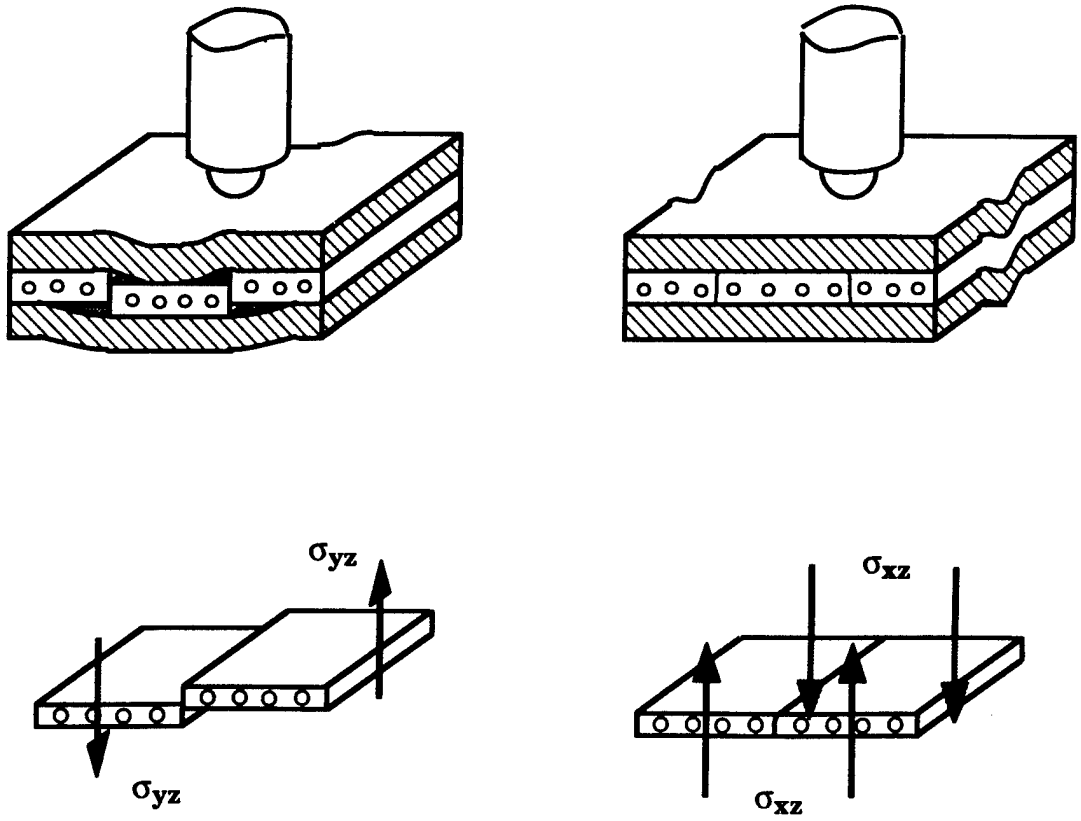


Figure 9 Shearing of a ply containing a cracked ply group; left: shear-induced local curvature normal to the fibers of the cracked ply group, right: shear-induced local curvature parallel to the fibers of the cracked ply group

Shearing may also cause a local curvature along the fiber direction of the cracked ply (Figure 9, right). This deformation does not open the matrix crack, and thus does not lead to delamination. Hence, the transverse shear stress σ_{xz}, which is associated with this type of deformation, need not be included in the calculation of the available strain energy.

Thickness Changes. Inside the plate, forces (with corresponding stresses σ_{zz}) may stretch or compress the ply groups in the thickness direction (Figure 10). Neglecting Poisson effects, this deformation does not open the matrix crack and, thus, has no affect on delamination. Since delamination does not occur, σ_{zz} is not considered when calculating the available strain energy.

Available Strain Energy. According to our model, delamination is mostly caused by differences in curvature between a cracked ply group and the adjacent laminate. Hence, when calculating the available strain energy, we include only those terms in the strain energy which are directly related to the change in curvature. Referring to the previous discussion, we note that these terms are the in-plane stresses σ^{+}_{yy} and σ_{xy} and the transverse shear stress σ_{yz}. Further, we only take into account the available strain energy of the cracked ply group. Thus, to establish the expression for the strain energy available to form a delamination, we need to consider only an interface bounded by a "top" and "bottom" ply group. The terms "top" and "bottom" refer to the ply groups which are closer to and further from the load, respectively.

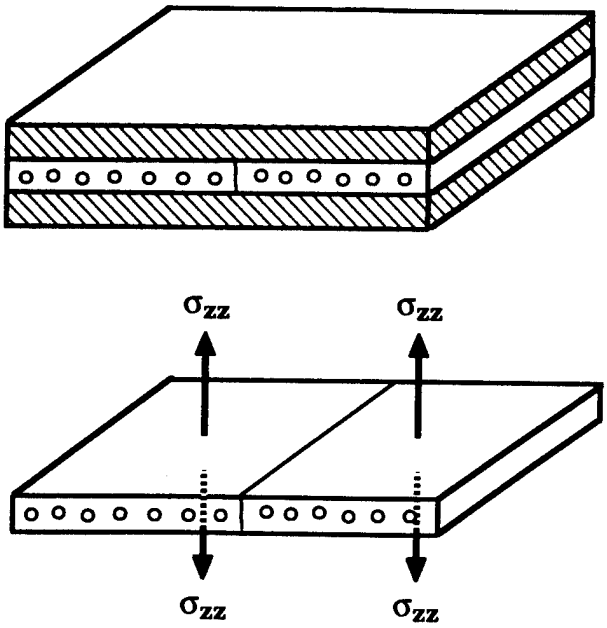


Figure 10 Normal stresses causing changes in the thickness of a cracked ply group

Then, the energy available for delamination of the interface may be supplied by both the top and bottom ply groups

$$\hat{S} = \hat{S}_t + \hat{S}_b \qquad (5)$$

where $\hat{S}_t$ and $\hat{S}_b$ are the strain energies contributing to the delamination from the top and bottom cracked ply group, respectively.

We now summarize our previous discussion on the formation of delaminations.

a) A ply group must be cracked to cause delamination along an adjacent interface.

b) A top ply group (i.e., the cracked ply group above the interface) contributes to the strain energy available to create delamination only through the stresses σ_{xy} and σ_{yz} (Figure 11). In order for the stress σ_{xy} to contribute to the delamination, the ply group's upper interface must be unrestrained.

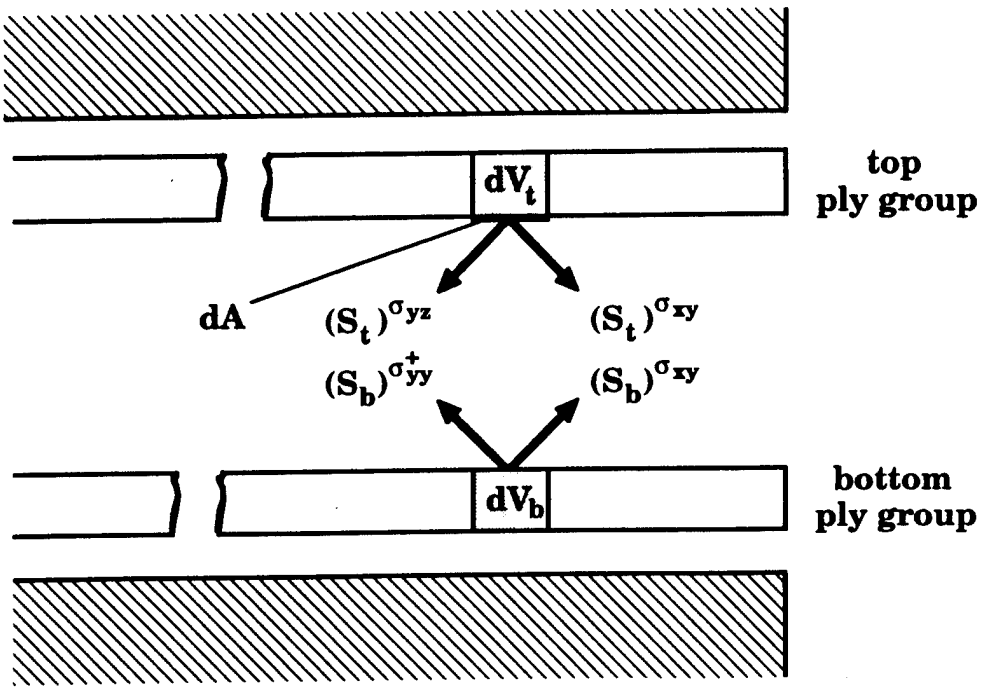


Figure 11 Stresses from the top and bottom cracked ply groups contributing to the strain energy available to form a delamination

c) A bottom ply group (i.e., the cracked ply group below the interface) contributes to the available strain energy only through the stresses σ_{yy}^{+} and σ_{xy} (Figure 11). For either of these stresses to contribute to the delamination, the ply group's lower interface must be unrestrained.

In terms of the strain energy density S, the condition for delamination is

$$S_t dV_t + S_b dV_b \geq G_c dA \qquad (6)$$

where dV_t and dV_b are volume elements in the top and bottom ply groups corresponding to the surface area dA (Figure 11). The available strain energy densities (energy per unit volume) are

$$S_t = \frac{1}{2}\left(\sigma_{yz}\gamma_{yz} + \Omega\sigma_{xy}\gamma_{xy}\right) \qquad (7)$$

$$S_b = \frac{1}{2}\Omega\left(\sigma_{yy}^{+}\varepsilon_{yy} + \sigma_{xy}\gamma_{xy}\right) \qquad (8)$$

Ω equals 1 if the ply group's "other" interface is unrestrained and 0 if it is restrained. Recall that x, y, and z are ply coordinates (Figure 1) and are different for the top and bottom ply groups.

In our model, delaminations are primarily caused by curvature changes in the cracked ply. These curvature changes result in a separation of the plies in the direction normal to the interface rather than in sliding between the plies. The critical strain energy release rate G_c corresponding to this type of separation is the mode I critical strain energy release rate G_{Ic}. Thus, the expression for predicting delamination at a point on an interface (Eq. 3) is written as

$$S_t dV_t + S_b dV_b \geq G_{Ic} dA \qquad (9)$$

where S_t and S_b are given by Eqs (7) and (8). It is emphasized that S_t and S_b are taken into account only when the corresponding top or bottom ply group is cracked.

Delamination Locations, Shapes, and Sizes

The delamination model described above is implemented in the following manner. First, the strain energy available per unit area S_a is calculated at every point of the interface by the expression

$$S_a = \int_{h_t} S_t dz + \int_{h_b} S_b dz \qquad (10)$$

where h_t and h_b are the thicknesses of the top and bottom cracked ply groups, respectively. The point is identified where this available strain energy is the highest (Figure 12a). At this point, a small rectangular element of area A_1 is considered (Figure 12b), and the available strain energy is compared to the critical strain energy necessary to delaminate the area. If the available strain energy is greater than the necessary strain energy, it is assumed that the interface delaminates over this area. Mathematically, this condition is expressed as

$$\int_{A_1}\left[\int_{h_t} S_t dz + \int_{h_b} S_b dz\right]dA \quad \begin{cases} \geq G_{Ic}A_1 & \text{delamination} \\ < G_{Ic}A_1 & \text{no delamination} \end{cases} \qquad (11)$$

Once the elemental area A_1 is found to be delaminated, the available strain energy per unit area S_a is calculated on the interface outside the delaminated area A_1 and again the point is identified where S_a is highest (Figure 12c). Then, a small rectangular element A_2 about this point is added to the area previously found to be delaminated (Figure 12d). In practice, area A_2 always adjoins area A_1. The delamination is taken to extend into area A_2 if the available strain energy is greater than the strain energy necessary for delamination

$$\int_{A_1+A_2}\left[\int_{h_t} S_t dz + \int_{h_b} S_b dz\right]dA \quad \begin{cases} \geq G_{Ic}(A_1 + A_2) & \text{delamination} \\ < G_{Ic}(A_1 + A_2) & \text{no delamination} \end{cases} \qquad (12)$$

The above procedure is then repeated. For the nth repetition (Figures 12e,f), we have

$$\int_{A_{tot}}\left[\int_{h_t} S_t dz + \int_{h_b} S_b dz\right]dA \quad \begin{cases} \geq G_{Ic}A_{tot} & \text{delamination} \\ < G_{Ic}A_{tot} & \text{no delamination} \end{cases} \qquad (13)$$

where A_{tot} is

$$A_{tot} = (A_1 + A_2 + \ldots + A_n) \qquad (14)$$

At each time step, this procedure is repeated until no further delamination is predicted on the interface under consideration. Every

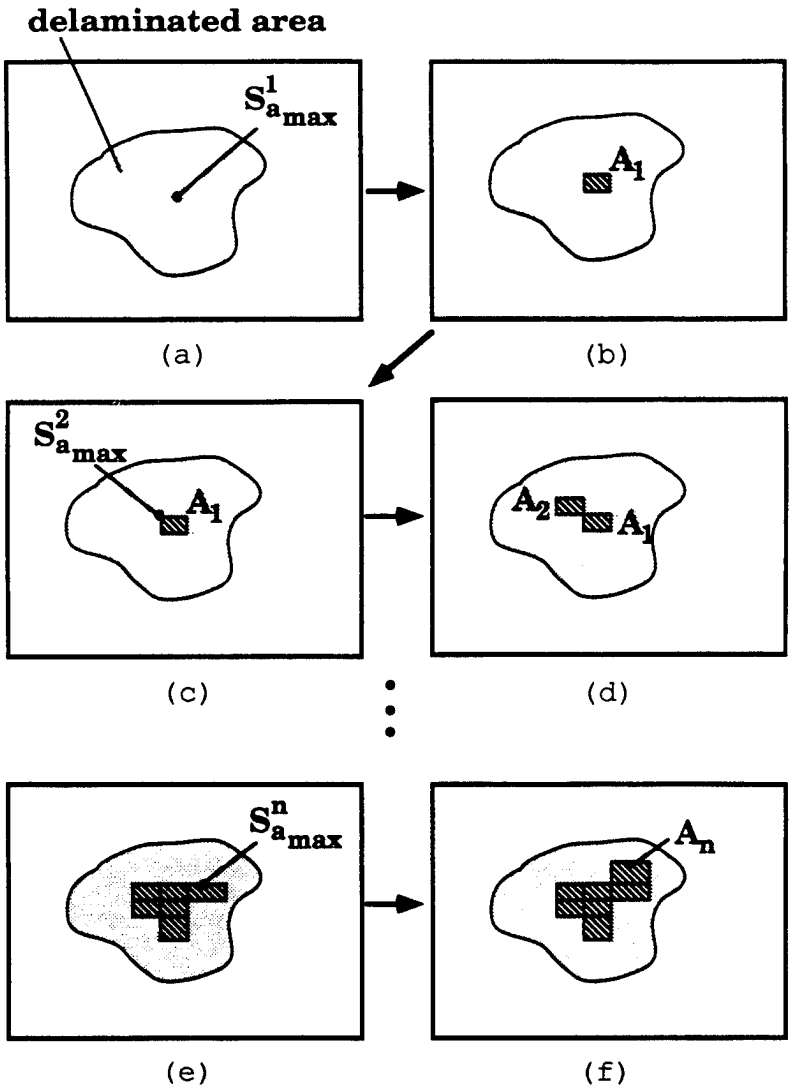


Figure 12 Steps in calculating the delamination shapes and sizes

interface inside the plate is inspected in this manner, resulting in the shapes and sizes of the delaminations along every interface. These calculations require, of course, a knowledge of the stress and strain distributions in the plate. Procedures for calculating these parameters as well as the characteristics of the delaminations are presented in the next two sections.

METHOD OF SOLUTION

Contact Force

To perform the analysis, the contact force between the plate and the impactor must also be specified. The impactor is taken to be an elastic solid with a hemispherical contact surface. To determine the contact force between the impactor and the plate during loading, the Hertzian contact model [20] is used. According to this model, the contact force F during loading is related to the indentation depth α by the equation

$$F = \kappa\alpha^{1.5} \tag{15}$$

where κ is a constant that depends on the nose radius R, the material of the impactor, and the material of the plate. For layered composite materials a suitable expression for κ is [21]

$$\kappa = \frac{4}{3}\sqrt{R}\,\frac{1}{\left[\left(1-\nu_s^2\right)/E_s + 1/E_{yy}\right]} \tag{16}$$

where ν_s and E_s are the Poisson's ratio and Young's modulus of the impactor, and E_{yy} is the Young's modulus of the top ply in the direction normal to the fibers.

Permanent deformation often occurs below the contact area during loading, and, therefore, different relations are needed for unloading and loading. For unloading, the following expression was proposed by Yang and Sun [21]

$$F = F_m\left[\frac{\alpha - \alpha_o}{\alpha_m - \alpha_o}\right]^{2.5} \tag{17}$$

where F_m is the maximum contact force and α_m is the maximum indentation during loading. α_o is the permanent deformation given by

$$\alpha_o = 0 \qquad \alpha_m < \alpha_{cr} \tag{18}$$

$$\alpha_o = \alpha_m \left[1 - \left(\frac{\alpha_{cr}}{\alpha_m} \right)^{0.4} \right] \qquad \alpha_m \geq \alpha_{cr} \qquad (19)$$

In these equations, α_{cr} is a material constant, which for graphite/epoxy materials has been found to be 0.00316 inch [21].

Because neither the impactor nor the plate are rigid, the load is distributed over a small area around a central point, this point being directly beneath the center of the impactor. According to the Hertzian model, the pressure distribution about this central point can be approximated by [20]

$$p(r) = \frac{3F}{2\pi a^3} \sqrt{a^2 - r^2} \qquad (20)$$

where r is the distance from the central point, and a is the radius of the contact region given by

$$a = \sqrt[3]{\frac{(F)(R)^{1.5}}{\kappa}} \qquad (21)$$

Stress Analysis

The stress analysis can best be effected by finite element methods. Different finite element approaches have been proposed in the past which can be applied to the present problem. In this study, for convenience, we adopt the method of Wu and Springer [7], since the IMPACT computer code based on this method has proven to be useful in calculating transient stresses in composite plates subjected to impact loading. Details of the finite element formulation is described in detail elsewhere [7, 22] and is not repeated here . The two main features of the formulation are the use of three-dimensional brick elements and incompatible modes. The brick elements may contain more than one ply group per element so that plies with different fiber orientations can be inside the same element. Incompatible modes were included in the element shape functions to improve the bending response of the elements [23, 24]. The analysis provides all six components of the stresses in plates whose edges amy be clamped, simply supported, or free.

Generally, the calculations are performed with an element containing more than one ply group. The element stiffness is obtained by averaging or "smearing" the stiffnesses of the individual ply groups. This is accomplished for an element with n ply groups by calculating the element's elasticity tensor in terms of the elasticity tensors of the individual ply groups

$$\left(E_{ijkl}\right)_{el} = \frac{1}{h_{el}}\left[h_1\left(E_{ijkl}\right)_1 + h_2\left(E_{ijkl}\right)_2 + \ldots + h_n\left(E_{ijkl}\right)_n\right] \quad (22)$$

where h_{el} is the thickness of the element containing n ply groups of thickness h_m (m=1,2,...,n). The displacements and corresponding strains in each element are calculated with the average stiffness of the element. However, the stresses in a ply group are calculated from the strains using the elasticity matrix of the individual ply group.

The finite element calculations result in the displacements in the plate as functions of position and time. From these, the stresses and strains are calculated as functions of time at every point inside each element. The numerical calculations can readily be performed by the IMPACT code. However, in its original form, the code was only for dynamic (impact) loads applied to plates supported along all four edges. To extend the applicability of the code, it was modified to include a) statically applied loads, and b) plates with up to three free edges. The resulting code is designated as IMPACT-ST. In addition to the displacements, stresses, and strains this code also includes an algorithm to calculate the delamination locations, shapes, and sizes (see below). Furthermore, in the original IMPACT code, calculations are always performed for the entire plate. In the IMPACT-ST code calculations may be performed only for a quarter of the plate, if proper symmetry exists. This increases the calculation speed by a factor of 15 to 20.

Delamination

The locations, shapes and sizes of delaminations are determined by the use of Eqs. 7-9, 13, and 14. These equations can be written in the form

$$\frac{1}{2}\left[\int_{h_t}\int_{A_1+A_2+\ldots+A_n}\left(\sigma_{yz}\gamma_{yz} + \Omega\sigma_{xy}\gamma_{xy}\right)dAdz + \right.$$

$$\left.\int_{h_b}\int_{A_1+A_2+\ldots+A_n}\Omega\left(\sigma^{+}_{yy}\varepsilon_{yy} + \sigma_{xy}\gamma_{xy}\right)dAdz\right. \quad (23)$$

$$\gtrless \quad G_{Ic}\left(A_1 + A_2 + \ldots + A_n\right)$$

When integrating over dA, the areas A_1, A_2, ..., A_n are taken to coincide with the area of an element in the x_1-x_2 plane of the plate. The stresses and strains in this area are assumed to be constant with a value corresponding to that in the center of the area. When integrating across the thickness (z direction) of the ply group, the stresses and strains are taken to be constant across each ply inside the ply group. The stress and strain values used in the calculations are those which

correspond to the stresses and strains at the center of the ply.

Once the stresses and strains are known, Eq. 23 can be applied to establish the locations, shapes, and sizes of the delaminations in the plate. In using this equation, the strain energies in a cracked ply group must be apportioned to its upper and lower adjacent interfaces. To perform the calculations, a post-processor DELAM-TRL was written. For specified stress and strain distributions in the plate, this post-processor provides the geometry (shape and size) of the delamination at every interface in the plate.

The DELAM-TRL code can be incorporated into any appropriate stress analysis code. However, in the calculations care must be exercised to account for the changes in plate response as delaminations develop and grow inside the plate. We combined the DELAM-TRL code with the IMPACT-ST code, accounting for the effects of the delaminations as described below.

As delaminations develop and grow inside a plate, the stress field and hence the available strain energy change under a given applied load. Delaminations reduce the overall stiffness of the plate, generally resulting in deflections which are higher than those which would occur in an undamaged plate. However, during impact loading, delamination is accompanied by a decrease in the applied load [25]. This decrease in the applied load may offset the change in the strain energy caused by the increased displacement due to delamination. Utilizing this observation for impact loading, the available strain energies in the cracked ply groups are taken to be the same as in the corresponding uncracked ply groups.

EXPERIMENTS

Tests were performed measuring the locations, shapes, and sizes of delaminations formed in composite plates subjected to transverse impact loads. The plates were made of unidirectional tape of graphite/epoxy (ICI Fiberite T300/976), graphite/toughened epoxy (ICI Fiberite IM7/977-2), or graphite/PEEK (ICI Fiberite APC-2). The plates were manufactured according to the procedures described in reference 26. After manufacture, each plate was inspected by an ultrasonic technique (C-scan) to establish that they were undamaged.

The plates were three inches wide and six inches long. The plates were inserted in specially built aluminum fixtures which clamped the two opposite, narrow edges of the plate (Figure 13). The two longitudinal edges of the plate were unsupported (free edges).

The force was provided by a projectile (impactor) propelled by pressurized air from a gun (Figure 14). The impactor consisted of a 3 inch tall, 2 1/2 inch wide, and 2 1/2 inch long teflon block with a steel hemisphere attached to the center of one of the ends. The mass of the impactor could be changed by attaching weights to the teflon block.

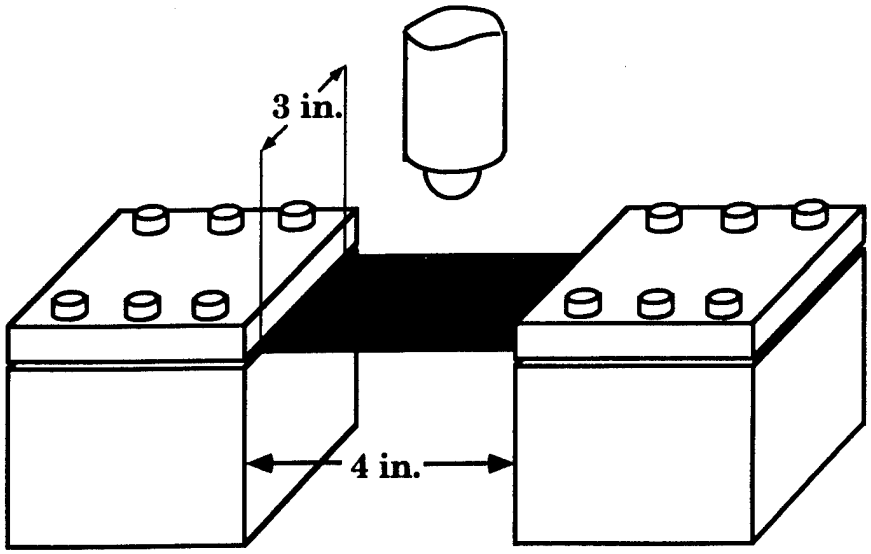


Figure 13 Test fixture used in impact tests

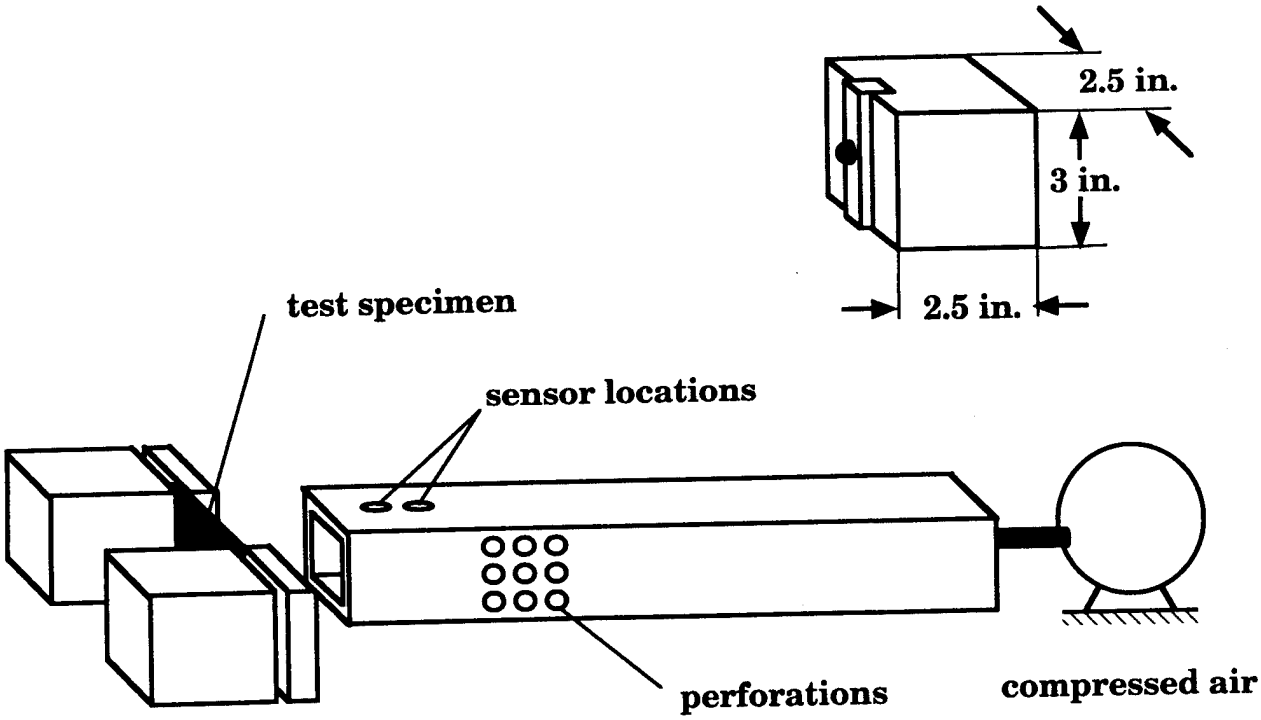


Figure 14 Impact test apparatus and the impactor

The fixture containing the plate was mounted at the exit of the gun so that the impactor hit the center of the plate. The impact velocity could be adjusted by changing the pressure of the air in the gun and the mass of the impactor. The impact velocity was measured by optical sensors placed near the exit of the gun. The barrel was perforated near the exit providing a quick release of the pressure. This facilitated rebounding of the impactor and prevented the impactor from hitting the plate more than once. After impact, each plate was inspected by C-scan and by X-ray. To make the damaged areas visible by X-ray, a dye penetrant (di-iodobutane) was applied to the edges of the plate as well as to any cracks on the surface of the plate. The pulse-echo C-scan technique provided the shape and dimensions of the delamination shape and dimensions at each ply group interface. The X-ray technique yielded the outermost periphery of all the delaminations inside the plate as well as the locations of the matrix cracks.

RESULTS

In this section the test results obtained by impacting Fiberite T300/976 graphite-epoxy, Fiberite IM7/977-2 graphite-toughened epoxy, and ICI APC-2 graphite-PEEK plates are presented. The plates were impacted by an impactor with a nose radius of R = 0.25 or 0.125 in. The impact velocity ranged from 50 in/sec to 225 in/sec, and the mass of the impactor from 0.355 lbm to 0.963 lbm. These velocities and masses resulted im impact energies from 1.15 lbf-in to 63.1 lbf-in. The test conditions are summarized in Table 1.

After impact each plate was inspected by X-ray and by C-scan. The sizes and shapes of the delaminations were deduced by these techniques. The data for all 106 plates tested are not given here but can be found in reference 26. Only a representative set of data is presented in Figure 15. In this figure the calculated delamination lengths and widths are shown as solid lines. Although all the data are not included in this paper in such detail, a summary of the data is presented in Figure 16. In this figure the measured delamination lengths and widths are plotted against the delamination lengths and widths calculated by the present model.

The results in Figures 15 and 16 show that the measured and calculated delamination lengths and widths agree well. In fact, the model not only provides the overall dimensions of the delaminations but also describes reasonably well the shapes of the delaminations. To illustrate this, three typical results are shown here (Figure 17). Similar agreements were found between the measured and calculated delamination shapes for the other plates tested.

The aforementioned comparisons (Figures 15-17) between the data and the results of the model lend confidence to the model.

Table 1. Summary of conditions of impact tests

Fiberite T300/976 (impactor nose radius R = 0.25 in)

Layup	Impactor mass, m (lbm)	Impactor Velocity, V (in/sec)
$[0_2/90_6]_S$	0.355	110, 123, 133, 135, 166, 167, 167, 167, 170, 178
$[0_3/90_5]_S$	0.355	133, 173, 191
$[0_4/90_4]_S$	0.355	46, 54, 89, 92, 105, 108, 109, 110, 111, 111, 112, 119, 121, 128, 135, 141, 141, 142, 152, 156, 161, 162
	0.395	129
	0.432	121
	0.472	122
	0.511	116
	0.704	148, 148, 158
	0.894	169, 208
$[0_5/90_3]_S$	0.355	97, 100, 107, 138
$[0_6/90_2]_S$	0.355	68, 71, 85, 101, 102, 109
$[0_4/20_4]_S$	0.355	92, 98, 128, 135, 147, 154, 164
$[0_4/40_4]_S$	0.355	129, 157
$[0_4/60_4]_S$	0.355	163
$[0_4/80_4]_S$	0.355	162
$[0_2/90_2]_S$	0.355	147, 163
$[0_3/90_3]_S$	0.355	147
$[0_5/90_5]_S$	0.355	133

Table 1. Summary of conditions of impact tests (cont.)

Fiberite IM7/977-2 (impactor nose radius R = 0.25 in)

Layup	Impactor mass, m (lbm)	Impactor Velocity, V (in/sec)
$[0_4/90_4]_S$	0.355	129, 136, 158, 179
	0.511	156
	0.704	151, 207
	0.963	155, 162, 178

ICI APC-2 (impactor nose radius R = 0.25 in)

Layup	Impactor mass, m (lbm)	Impactor Velocity, V (in/sec)
$[0_4/90_4]_S$	0.355	125, 129, 142, 154, 158, 172, 182
	0.704	155
	0.963	203, 228

ICI APC-2 (impactor nose radius R = 0.125 in)

Layup	Impactor mass, m (lbm)	Impactor Velocity, V (in/sec)
$[0_4/90_4]_S$	0.355	141, 146, 150, 161, 169, 170, 170, 171, 171, 172, 173, 176, 177, 183
	0.432	178, 179
	0.511	183

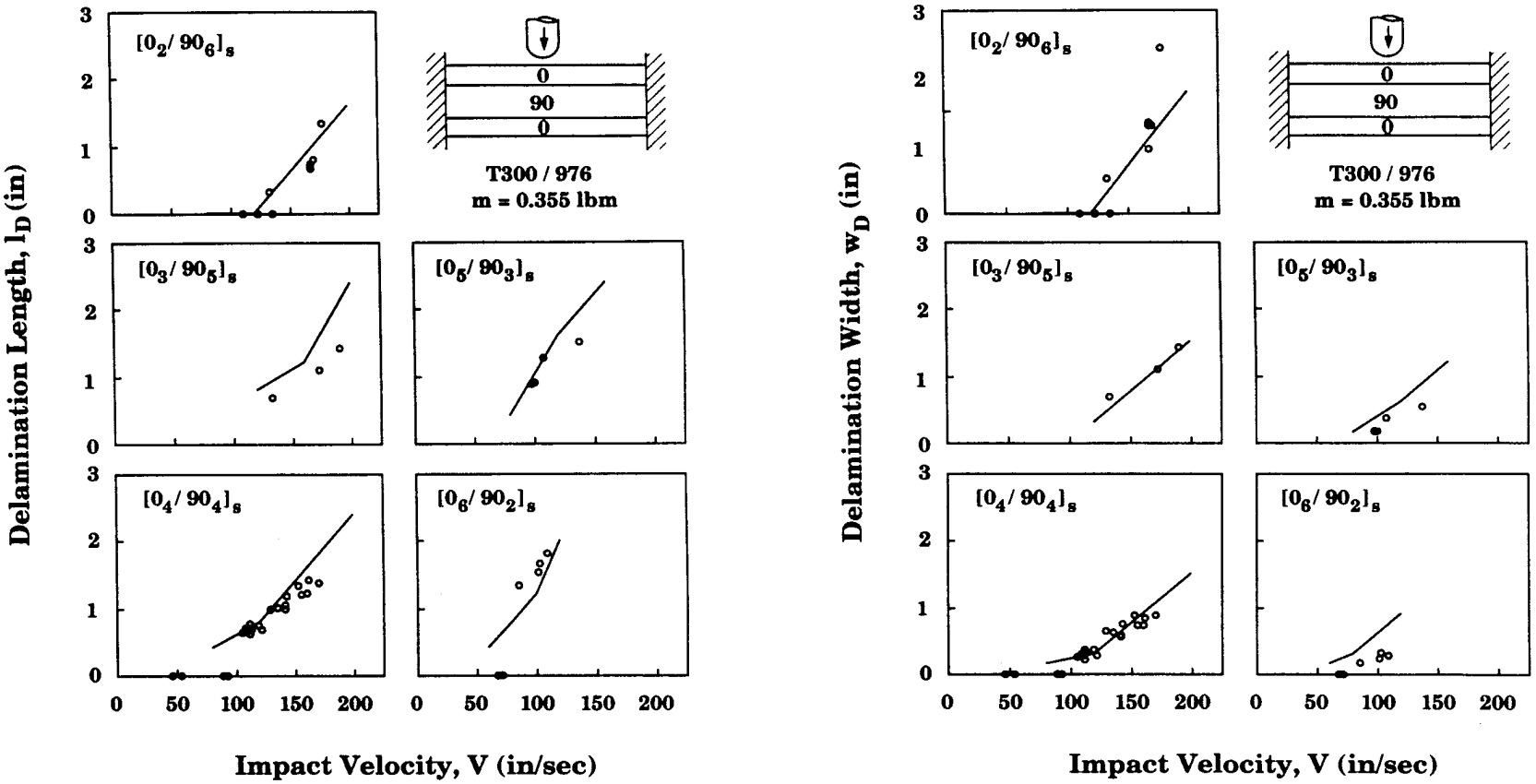


Figure 15 Delamination lengths and widths versus impact velocity for one test set

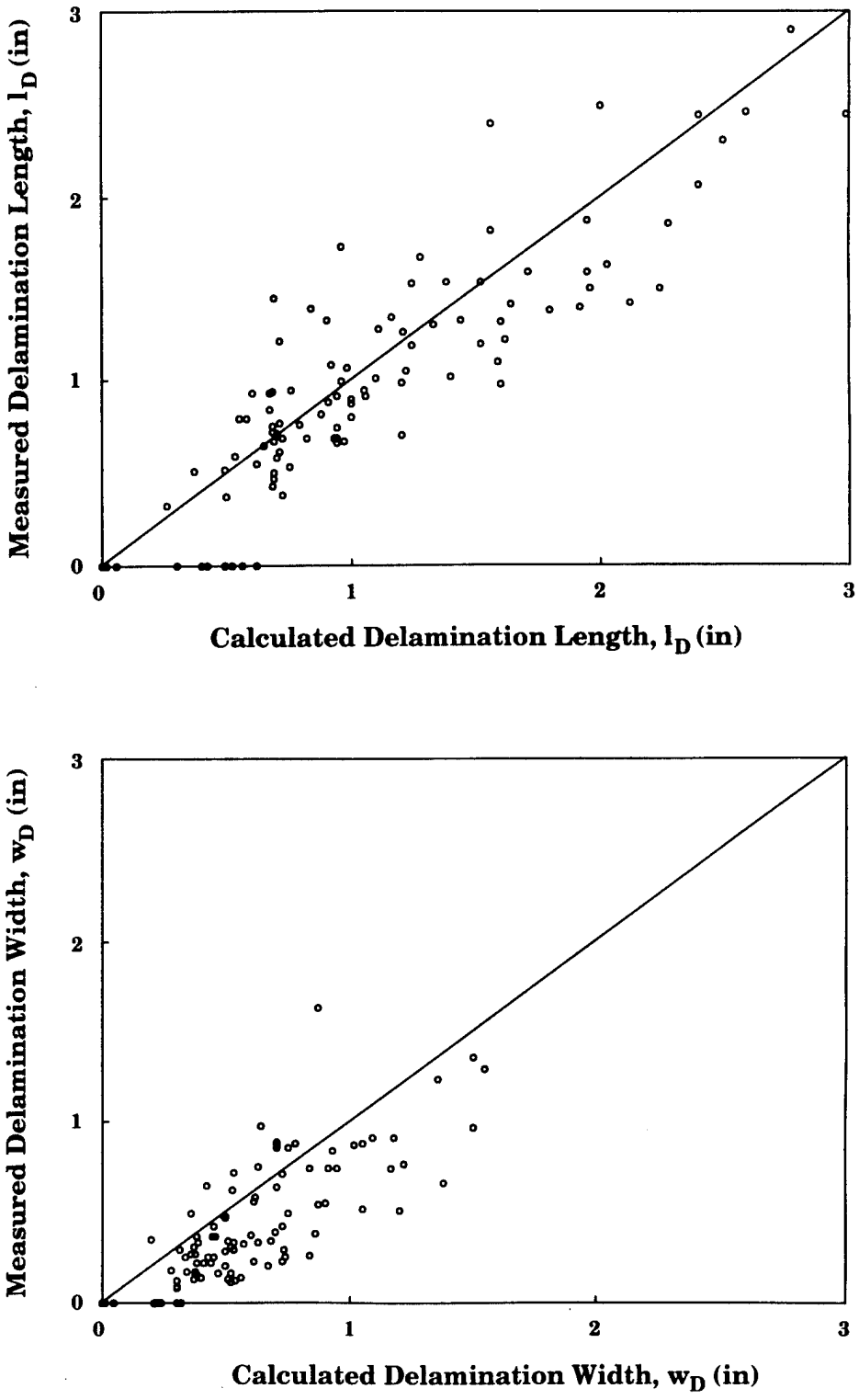


Figure 16 Comparison of measured and calculated delamination lengths and widths (see Table 1)

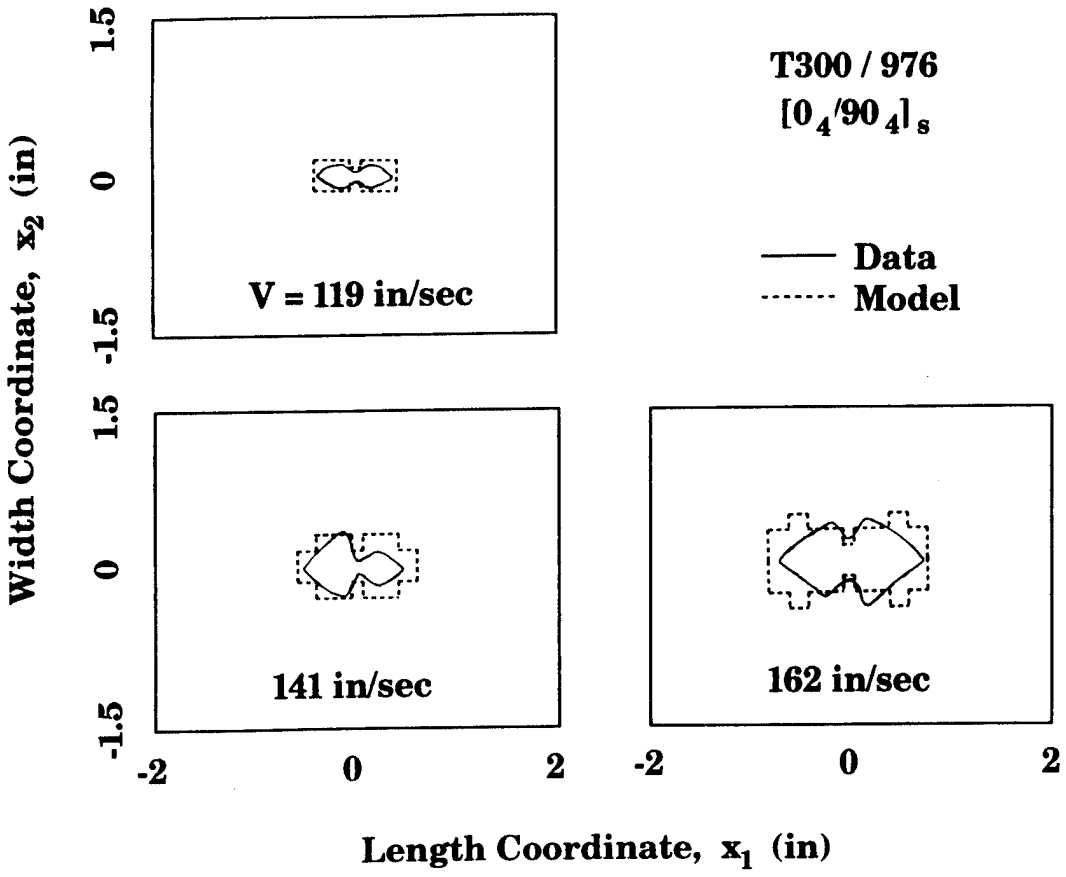


Figure 17 Comparison of measured and calculated delamination shapes at three different velocities (impactor mass m = 0.355 lbm)

CONCLUDING REMARKS

The results presented in this paper show that the model and the corresponding computer code IMPACT-ST can be used to calculate the sizes, shapes, and locations of delaminations in plates subjected to transverse, non-penetrating impact of a solid object. Hence, the computer code should be useful as an engineering design tool.

REFERENCES

1. Clark, G. "Modelling of Impact Damage in Composite Laminates," Composites, Vol. 20 (1989), pp. 209-214.

2. Bostaph, G.M. and W. Elber. "A Fracture Mechanics Analysis for Delamination Growth During Impact on Composite Plates," *Advances in Aerospace Structures, Materials, and Dynamics*, American Society of Mechanical Engineers, New York, 1983, pp. 133-138.

3. Grady, J.E. and C.T. Sun. "Dynamic Delamination Crack Propagation in a Graphite/Epoxy Laminate," *Composite Materials: Fatigue and Fracture*, ASTM STP 907, H. T. Hahn (ed.), American Society for Testing and Materials, Philadelphia, PA, 1986, pp. 5-31.

4. Grady, J.E. and K.J. DePaola. "Measurement of Impact-Induced Delamination Buckling in Composite Laminates," *Dynamic Failure; Proceedings of the 1987 SEM Fall Conference*, Society for Experimental Mechanics, 1987, pp. 160-168.

5. Liu, D. "Delamination in Stitched and Nonstitched Composite Plates Subjected to Low-Velocity Impact," *Proceedings of the American Society for Composites, Second Technical Conference*, American Society for Composites, 1987, pp 147-155.

6. Liu, D. "Impact Induced Delamination - A View of Bending Stiffness Mismatching," Journal of Composite Materials, Vol. 22 (1988), pp. 674-692.

7. Wu, H.T. and G.S. Springer. "Impact Induced Stresses, Strains, and Delaminations in Composite Plates," Journal of Composite Materials, Vol. 22 (1988), pp. 533-560.

8. Gosse, J.H. and P.B.Y. Mori. "Impact Damage Characterization of Graphite/Epoxy Laminates," *Proceedings of the American Society for Composites, 3rd Technical Conference on Composite Materials*, American Society for Composites, 1988, pp. 187-193.

9. Gosse, J.H., P.B.Y. Mori and W.B. Avery. "The Relationship Between Impact-Induced Stress States and Damage Initiation and Growth in Composite Plates," *Materials - Processes: The Intercept Point*,Society for the Advancement of Materials and Process Engineering, 1988, pp. 187-193.

10. Chang, F.K., H.Y. Choi and S.T. Jeng. "Characterization of Impact Damage in Laminated Composites," *Tomorrow's Materials: Today, 34th International SAMPE Symposium and Exhibition*, Zakrzewski, et al (ed.), Society for the Advancement of Materials and Process Engineering, 1989, pp. 702-713.

11. Joshi, S.P. and C.T. Sun. "Impact Induced Fracture in a Laminated Composite," Journal of Composite Materials, Vol. 19 (1985), pp. 51-

66.

12. Guynn, E.G. and T.K. O'Brien. "The Influence of Layup and Thickness on Composite Impact Damage and Compression Strength," *26th AIAA/ASME/ASCE/AHS Structures, Structural Dynamics and Materials Conference*, 1985, pp. 187-196.

13. Sun, C.T. and M.G. Manoharan. "Growth of Delamination Cracks Due to Bending in a $[90_5/0_5/90_5]$ Laminate," Composites Science and Technology, Vol. 34 (1989), pp.365-377.

14. Salpekar, S.A. and T.K. O'Brien. "Combined Effects of Matrix Cracking and Stress-Free Edges on Delamination," NASA TM-102591, 1990.

15. O'Brien, T.K. "Analysis of Local Delaminations and Their Influence on Composite Laminate Behavior," *Delamination and Debonding of Materials*, ASTM STP 876, W. S. Johnson (ed.), American Society for Testing and Materials, Philadelphia, PA, 1985, pp. 282-297.

16. O'Brien, T.K. "Towards a Damage Tolerance Philosophy for Composite Materials and Structures," *Composite Materials: Testing and Design*, ASTM STP 1059, P. A. Lagace (ed.), American Society for Testing and Materials, Philadelphia, PA, 1990.

17. Crossman, F.W. and A.S.D. Wang. "The Dependence of Transverse Cracking and Delamination on Ply Thickness in Graphite/Epoxy Laminates," *Damage in Composite Materials*, ASTM STP 775, K. L. Reifsnider (ed.), American Society for Testing and Materials, Philadelphia, PA, 1982, pp. 118-139.

18. Lessard, L. "Compression Failure in Laminated Composites Containing an Open Hole," Ph.D. Dissertation, Stanford University, Department of Aeronautics and Astronautics, 1989.

19. Broek, D. *Elementary Engineering Fracture Mechanics*, Martinus Nijhoff , The Hague, 1982.

20. Timoshenko, S.P. and J.N. Goodier. *Theory of Elasticity*, McGraw-Hill, New York, 1970.

21. Yang, S.H. and C.T. Sun. "Indentation Law for Composite Laminates," NASA CR-165460, 1981.

22. Wu, H.T. and F.K. Chang. "Transient Dynamic Analysis of Laminated Composite Plates Subjected to Transverse Impact," Computers and Structures, Vol. 31 (1989), pp. 453-466.

23. Wilson, E.L., R.L. Taylor, W.P. Doherty and J. Ghaboussi. "Incompatible Displacement Modes"," *Numerical and Computer Methods in Structural Mechanics*, S.J. Fenves, et al (ed.), Academic Press, New York, 1973, pp. 43-57.

24. Taylor, R.L., P.J. Beresford and E.L. Wilson. "A Non-Conforming Element for Stress Analysis," International Journal for Numerical Methods in Engineering, Vol. 10 (1976), pp. 1211-1219.

25. Sjoblom, P.O., J.T. Hartness and T.M. Cordell. "On Low-Velocity Impact Testing of Composite Laminates," Journal of Composite Materials, Vol. 22 (1988), pp. 30-52.

26. Finn, S.R. "Delaminations in Composite Plates Under Transverse Static or Impact Loads," Ph.D. Dissertation, Stanford University, Department of Aeronautics and Astronautics, 1990.

MICROMECHANICS OF FATIGUE IN WOVEN AND STITCHED COMPOSITES

B.N. Cox, M.S. Dadkhah, R.V. Inman,
M.R. Mitchell, W.L. Morris, and S. Schroeder

Rockwell International Science Center
1049 Camino Dos Rios
Thousand Oaks, CA

Summary

The goal of this basic research program is to determine how microstructural factors, especially the architecture of reinforcing fibers, control fatigue damage in 3D reinforced polymer composites.

Test materials are being fabricated from various preforms, including stitched quasi-isotropic laminates; and through-the-thickness angle interlock, layer-to-layer angle interlock, and through-the-thickness stitching effect weaves. Preforms are impregnated with a tough resin by a special vacuum infiltration method. Careful control of this process and the cure cycle is necessary to obtain specimens free of bubbles and cracks.

Most tests are being performed in uniaxial compression/compression loading. In all cases to date, failure has occurred not by delamination (as in a 2D composite) but by shear failure, which occurs suddenly rather than by gradual macroscopic crack growth.

Special apparatus has been set up to enable optical images of the gauge section to be captured, digitized, and stored at various epochs in the fatigue life. These images are subsequently analyzed by our unique high accuracy strain mapping instrument, HASMAP, to reveal the evolution of strain fields during fatigue. The strain fields are measured with sufficient resolution to illuminate micromechanical events on the scale of individual fiber tows. They reveal the subtle damage that foreshadows eventual failure.

Some theoretical aspects of bridging effects have also been examined, especially the role of the bridging length scale, which is the increment of crack growth over which bridging by 3D tows becomes effective. Among other things, these considerations reveal why impact damage can be such a strong function of specimen size and shape.

MATERIAL MATRIX

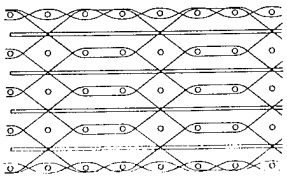
Preforms

Most preforms in the material matrix are either woven fiber mats supplied by Textile Technologies Inc. (TTI - Hatboro, Pennsylvania) or stitched quasi-isotropic laminates supplied by HiTech/Hexcel Inc. (Reno, Nevada). They are described in the following table. The TTI preforms vary in thickness from 0.35" to 0.5", while each Hexcel panel is approximately 5/16" thick.

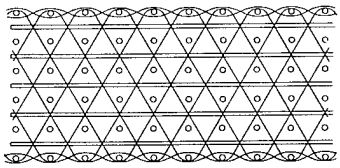
Table 1
Preform Matrix

Woven preforms from TTI:

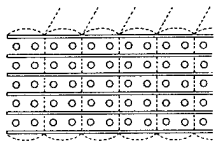
Panel	Weave Pattern	Warp and Weft	Stitching Fiber	Approximate Dimensions
A	layer-to-layer angle interlock	AS4	AS4	38" x 4"
B	layer-to-layer angle interlock	AS4	S-glass	30" x 4"
C	through-the-thickness angle interlock	AS4	S-glass	38" x 4"
D	through-the-thickness angle interlock	AS4	AS4	38" x 4"
E	through-the-thickness stitching effect	AS4	AS4	12" x 9"
F	through-the-thickness stitching effect	AS4	E-glass	12" x 9"



LAYER-TO-LAYER ANGLE INTERLOCK



THROUGH-THE-THICKNESS ANGLE INTERLOCK



"STITCHING" EFFECT

Stitched preforms from Hexcel:

Panel	Stitching Pattern	Warp and Weft	Stitching Fiber	Approximate Dimensions
G	6 rows/in.	T300	S-glass	12" x 12"
H	12 rows/in.	T300	S-glass	12" x 12"
I	Two half-thickness panels each stitched at 6 rows/in.; then joined at 6 rows/in.	T300	S-glass	12" x 12"

Resin

Most composites have been filled with Tactix 138 resin and H41 hardener, supplied by Dow Chemical (Freeport, Texas). A few specimens were filled early in the program with Epon 828 (Shell Chemical Co.). Since the Tactix 138 is tougher, it gives a much superior product (see "Specimen Fabrication" below).

Odd Specimens

The basic material matrix is supplemented from time to time by small specimens received from other research groups.

SPECIMEN FABRICATION

All the preforms in Table 1 are being processed in-house into composite specimens within this program. The processing route is as follows.

Impregnation and cure using Tactix 138 resin and H41 hardener (Dow Chemical) are effected in a reusable aluminum mold. The preform is placed in the mold, heated to 65°C, and degassed in a vacuum of ~1 Torr. The resin is then mixed with the hardener and also heated to 65°C and degassed. The resin mixture is then poured over the preform (still at 65°C) and the whole assembly is degassed twice again. The first degassing results in bubbling out of some volatiles followed by apparent boiling of the resin mixture as the pressure falls further. The second degassing pass produces very little emission of volatiles down to the pressure at which boiling began on the first degassing, where the degassing is now stopped. The mold is then closed and the specimen cured, the curing cycle (which is chosen to maximize resin toughness) comprising 2 hrs at 120°C and 2 hrs at 177°C. All fabrication runs to date have produced 10"×4" panels, from which 12-16 rectangular fatigue specimens can be machined.

In contrast to specimens cured with the more brittle resin Epon 828, in which extensive microcracking was found emanating from interior sites where glass interlock tows abutted AS4 warp or weft tows, the specimens cured with Tactix 138 are almost entirely free of microcracks. The only microcracks found are in surface resin layers. If excess resin is allowed to cure outside the preform, large, regularly spaced cracks will form in it. If care is taken to avoid excess resin (which is not especially easy for the TTI preforms, whose thickness varies), microcracks are still occasionally found in surface pockets of resin between tows (Fig. 1). Such microcracks extend into the composite until they encounter the internal microstructure. Thus their average size is about the diameter of one fiber tow. The large openings of these cracks attest to the substantial residual stresses in the epoxy that evidently drive the microcracking.

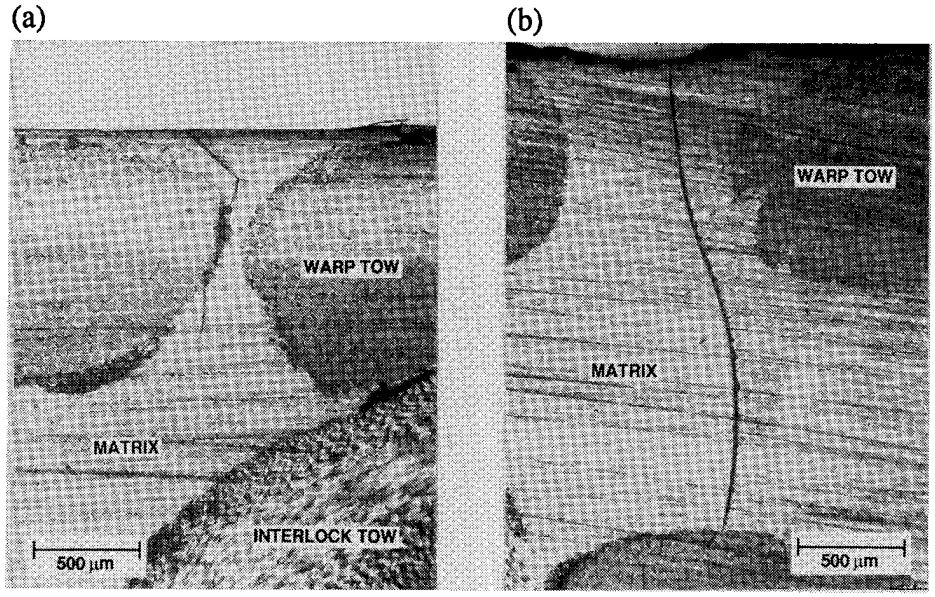


Fig. 1 Two surface microcracks found in a composite of Tactix 138/H41 and preform from panel D of Table 1.

ASSESSMENT OF PREFORM INFILTRATION

Fabricated composites have been sectioned and polished perpendicular and parallel to the warp fibers to allow porosity and fiber volume fractions to be estimated. Figure 2(a) shows an optical micrograph of a typical section through a through-the-thickness angle interlock composite (panel D of Table 1). There is no visible porosity. Figure 2(b) shows an SEM micrograph of a section of a single tow, in which it is clear that complete wetting of each individual fiber has occurred.

From Fig. 2(a), the volume fraction constituted by warp, weft, and interlock tows can be estimated at ~ 0.7; while from Fig. 2(b), the volume fraction of fibers within each tow is also ~ 0.7. Consequently, the net fiber volume fraction of the composite is ~ 0.5. More accurate values will be obtained from resin extraction measurements.

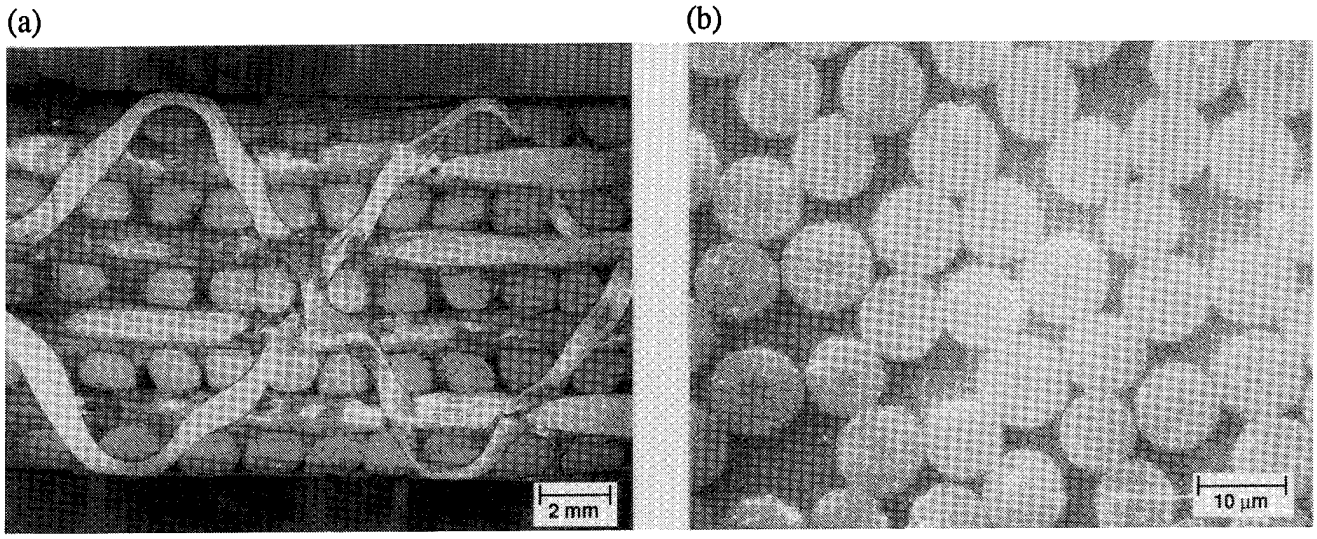


Fig. 2 (a) Optical micrograph of section parallel to warp fibers through composite of panel D of Table 1 with Tactix 138/H41 matrix. (b) SEM micrograph of section through an individual warp tow in (a).

TEST MATRIX

Macroscopic Tests

The basic test matrix consists of tests on specimens made from the preforms of Table 1. Panels fabricated as described in "Specimen Fabrication" are cut into rectangular specimens of dimensions 4" × 1/2" × panel thickness. These are being subjected to fully reversed (R = -1), tension-tension (R = 0), and compression-compression (R = -∞) uniaxial fatigue loading. For each R ratio, five load amplitudes are being covered, making a matrix of 15 tests for each material in the material matrix.

The material matrix includes the six weave types supplied by TTI and the three stitching patterns in the Hexcel panels (Table 1). Because of weave or stitching asymmetry, neither the TTI nor the Hexcel specimens possess in-plane isotropy, being instead orthotropic. Specimens are being tested with the load axis lying along both in-plane directions of reflective symmetry. The material matrix therefore comprises 18 cases.

The total number of tests in the basic matrix is accordingly 270 (15 loads × 18 materials).

Micromechanical Tests

When test results look especially significant or interesting, the micromechanics of the failure are investigated using either the actual specimens in the matrix or nominally identical ones in repeat tests. The micromechanical investigations are based primarily on HASMAP, as described on the following pages.

IN SITU DIGITAL IMAGE COLLECTION FOR HASMAP

HASMAP (for high accuracy strain field mapper) determines fields of differential surface deformation by comparing digital images of deformed and undeformed material. In its usual mode, HASMAP achieves very high spatial resolution by analyzing optical or SEM micrographs. The micrograph images are digitized by a CCD camera, which provides the maximum possible spatial stability. The pixel density in the digitization is increased by digitizing small areas on each micrograph at a time so that the entire micrograph is represented by arrays of between 1000 × 1000 and 4000 × 4000 pixels.

In this program, we have developed special apparatus to streamline this process by obviating the use of micrographs, opening the way to substantial decreases in labor costs and increasing the volume of data that can be analyzed. The CCD camera is placed in situ in the test apparatus (Fig. 3). It is mounted on a precise x-y-z stage, which can be scanned to obtain an array of overlapping (typically by 10%) digital images directly from the specimen surface. At 60X, the entire specimen gauge section can be covered by a 2 × 2 array of digitized images, each of which is represented by a 480 × 512 array of pixels (the intrinsic array size of the CCD camera).

While the rigid structure of the x-y-z stage ensures the absence of relative rotations between digitized images in the 2 × 2 array, relative translations are known only to within a few microns. These translational errors are computed and eliminated by calculating cross-correlations within the overlapping strip between each pair of images and adjusting their assigned positions within the computer accordingly.

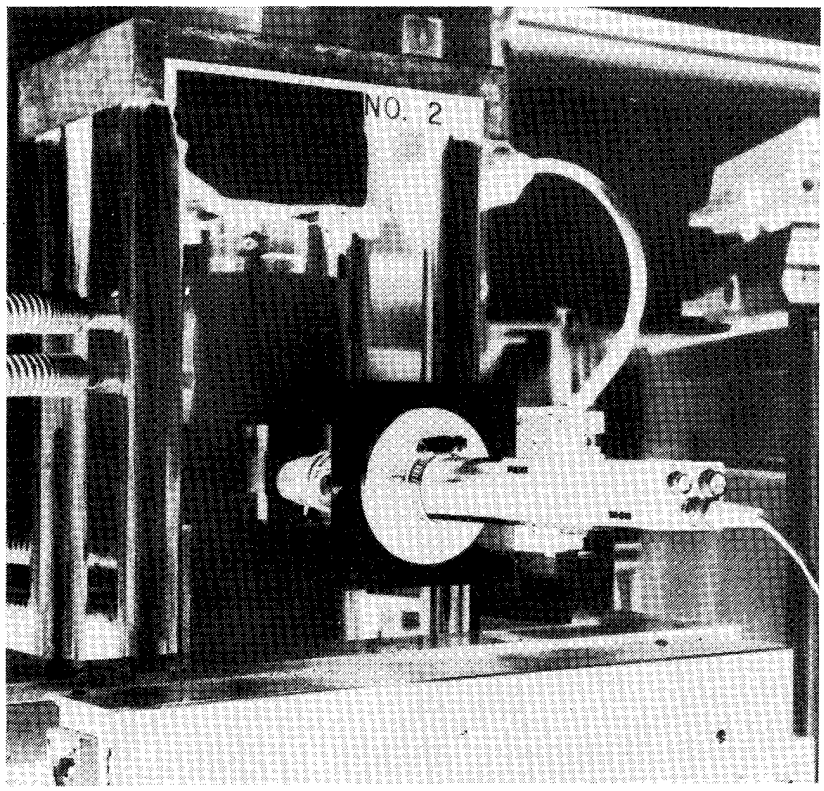


Fig. 3 Loading frame and CCD camera mounted on x-y-z stage.

DISPLACEMENT VECTORS CALCULATED BY HASMAP

The net result of the procedure described on the previous page is a digitized 1000 × 1000 pixel image of the entire specimen width over a good portion of the gauge length. Relative displacements between pairs of such images (usually recorded at constant load before and after the application of fatigue cycles) are found by high speed cross-correlation calculations. The calculations are performed over a 16 × 16 array of points, with the analysis for each point carried out over a 32 × 32 pixel image segment. The displacement accuracy of this analysis is ± 0.2 pixels, corresponding to ~ ± 0.2 μm on the specimen. (While HASMAP can achieve displacement accuracy of ± 100Å when high magnification optical micrographs are used,[1] such precision would be superfluous here. Furthermore, data must be recorded over as much of the gauge section as possible when testing smooth specimens because deformation and eventual failure can be found anywhere on it. Limitations of data storage capacity dictate that this be done at moderate magnification.)

A typical array of displacement vectors is shown in Fig. 4.

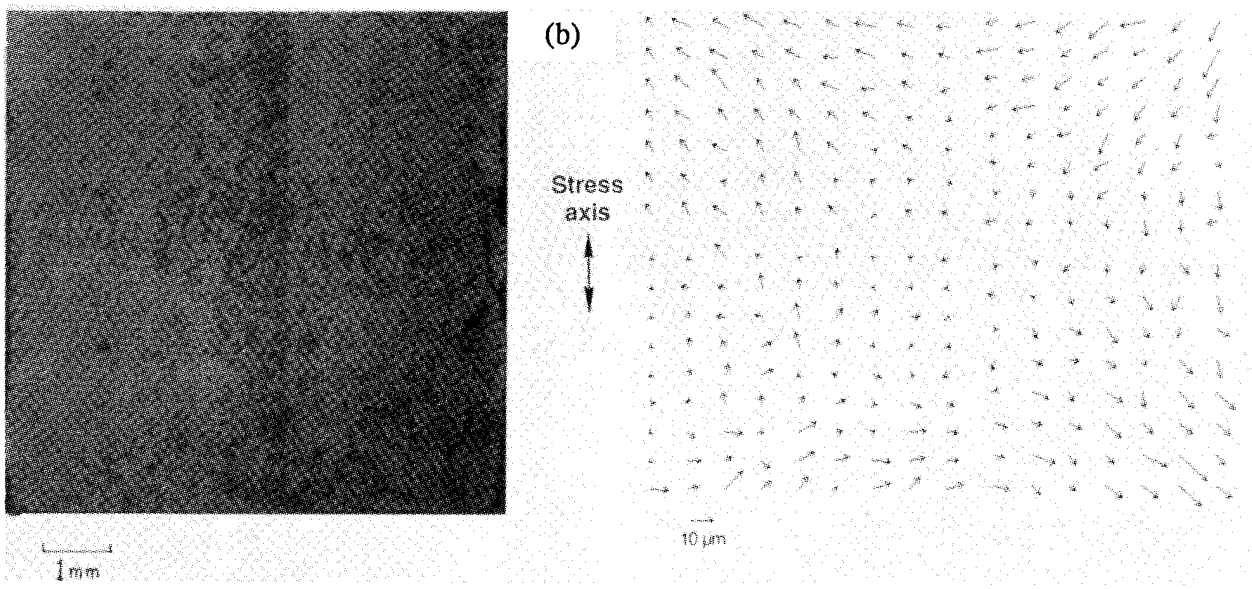


Fig. 4 Deformation in a stitched composite (supplied by B. Dexter, NASA Langley; not listed in Table 1) resulting from 8000 compression-compression fatigue cycles to a peak load of -260 MPa. Images were recorded at -130 MPa. (a) Digitized image of gauge section, which has been decorated with SiC particles to enhance contrast. (b) Differential displacement vector field computed for the area of (a) showing the irreversible displacements associated with fatigue damage.

[1]M.R. James, W.L. Morris, and B.N. Cox, "A High Accuracy Automated Strain Field Mapper," Exptl. Mech. 30, 60-67 (1990).

DISPLACEMENT AND STRAIN FIELDS FROM HASMAP

Continuous full field deformation maps are deduced from vectors such as those of Fig. 4 as follows. Contours of constant u and v (the displacements perpendicular and parallel to the sample axis) are formed by linear interpolation between values of the appropriate component of the vector array. These are then smoothed by an algorithm which dilates and then erodes each contour level, removing a prescribed amount of high frequency noise. There results a set of contours (Fig. 5(a)) which, for the present application, have a resolution comparable to high resolution moiré fringes, with the advantage over the moiré method that the absolute sense of the local deformation (i.e., whether it is compressive or tensile) is always known. The derivatives of these displacements are then taken to generate a complete set of strain fields relative either to the specimen or to the local principal stress axes as desired. Figure 5(b) shows the strain component ε_{yy} derived from Fig. 5(a), where the y-axis is the stress axis.

The zone of heavy deformation (strains ~ 10^{-2}) striking across Fig. 5(b) from center-left to center coincides with a single stitching tow, the only one falling in the field of view. Longer range deformation shows that the gauge section has also sheared during fatigue. This is clearest in Fig. 4(b): the directions of the displacement vectors at the top left and bottom right indicate tensile strain normal to the diagonal that runs from bottom left to top right. The specimen ultimately failed along this diagonal.

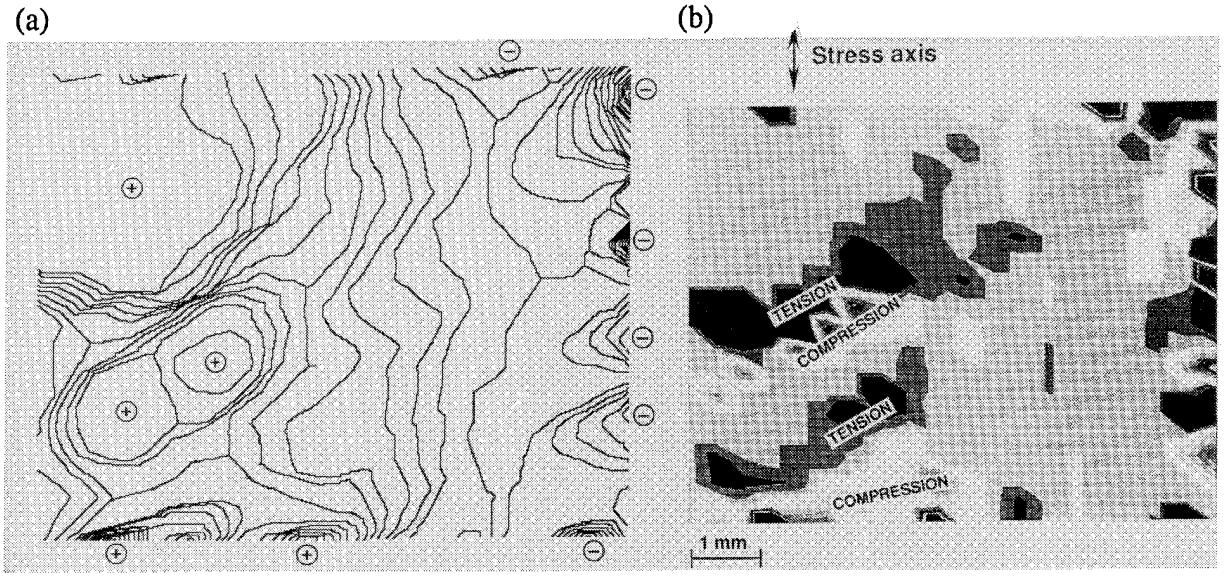


Fig. 5 (a) Contours of the displacement v (parallel to the stress axis) derived from the vectors of Fig. 4. Symbols + and - show local maxima and minima. Contours are separated by 0.6 μm in displacement. (b) The strain field ε_{yy} derived from (a). In this black and white rendition of a color image, important zones of maximum tension and compression have been labeled. Each gray level indicates a strain increment of 1.1×10^{-3}.

EXTRINSIC FACTORS IN CRACK BRIDGING

Crack bridging by 3D fiber tows is the primary source of macroscopic crack resistance following delamination in impact tests, and it is probably one of the key factors in preventing microscopic cracks from propagating into macroscopic cracks during fatigue of pristine material. Extensive theoretical studies of bridged cracks have recently been conducted, mainly under other funding.[2,3] This work has shown very clearly that the mechanics of bridged cracks depend strongly on extrinsic factors. In particular, the stress required to propagate a matrix crack and the transition from intact bridging ligaments (ductile failure) to ruptured ligaments (brittle failure) depend strongly on load distribution and the size of the specimen and any notch.

Within this program, the significance of these results for impact testing in 3D composites, and possibly for fatigue resistance too, has also been considered. A central role is played by the "bridging length scale," the characteristic length of initial crack growth over which the bridging zone matures.[3] This is a critical engineering property of any material containing bridged cracks. It can vary from the order of the fiber diameter to several meters, depending on the nature of the bridging ligaments. The length to which a microcrack might propagate before arresting is determined by the bridging length scale; the size of a delamination crack caused by impact will depend on how large the stressed area is relative to the bridging length scale; and whether such a bridged delamination will subsequently propagate to failure will depend on the specimen size in terms of the bridging length scale.

While no predictive theory for bridged cracks that is accurate for all load configurations and specimen sizes has yet been demonstrated, it is clear from simulations[3] that the critical information is the relation between the opening displacement u of a bridged crack and the tractions p imposed by the bridging ligaments. If p(u) is not known and conventional engineering methods of fracture mechanics are applied, severely nonconservative predictions are possible. The effects discussed in Ref. 3 may account for many of the discrepancies reported for different kinds of impact tests involving specimens of different sizes and shapes.[4]

ACKNOWLEDGMENTS

Work supported by NASA Contract No. NAS1-18840 under the technical monitoring of Dr. Charles Harris. Dr. Mac Puckett of Dow Chemical kindly supplied the Tactix 138 resin and H41 hardener, along with greatly appreciated advice on their use. Dr. Benson Dexter of NASA Langley supplied several specimens of stitched composites. Dr. Gary Farley of NASA Langley provided valuable assistance in procuring woven preforms.

---

[2]B.N. Cox and D.B. Marshall, "Stable and Unstable Solutions for Bridged Cracks in Various Specimens," Acta Metall., in press.

[3]B.N. Cox, "Extrinsic Factors in the Mechanics of Bridged Cracks," submitted to Acta Metall.

[4]P.E. Reed, "Impact Testing of Plastics for Design," in ATA-MAT 89, Turin, Italy, June 1989 (Associazione Tecnica Dell'automobile, Italy, 1989).

CHARACTERIZATION OF MULTIAXIAL WARP KNIT COMPOSITES

H. Benson Dexter
NASA Langley Research Center
Hampton, Virginia

Gregory H. Hasko
Lockheed Engineering and Science Company
Hampton, Virginia

Roberto J. Cano
NASA Langley Research Center
Hampton, Virginia

INTRODUCTION

Textile reinforced composites with through-the-thickness reinforcement have demonstrated excellent damage tolerance compared to state-of-the-art laminated tape composites, references 1, 2, and 3. The potential for significant cost savings for textile reinforced composites through automated preform fabrication and low-cost, out-of-autoclave resin transfer molding has increased aerospace interest in these materials. Woven fabrics are used extensively in the fabrication of composite aircraft structures. Individual plies of fabric are generally laminated together to produce various combinations of 0/90 and $\pm$45-degree layups. Recently, a relatively new class of fabrics designated as multiaxial warp knits has been developed to minimize some of the drawbacks to woven fabrics. The drawbacks include fiber crimp, limited fiber orientations, and labor intensive layup procedures. The multiaxial warp knit fabrics have minimal fiber crimp, precise fiber orientations (0, 90, $\pm\theta$), and multi-ply stacks can be knitted together to reduce labor costs.

The objectives of this investigation were to characterize the mechanical behavior and damage tolerance of two multiaxial warp knit fabrics and to determine the acceptability of these fabrics for high performance composite applications. The multiaxial warp knit fabrics were produced by Hexcel Hi-Tech and Milliken. The tests performed included compression, tension, open hole compression, open hole tension, compression after impact and compression-compression fatigue. Tests were performed on as-fabricated fabrics and on multilayer fabrics that were stitched together with either carbon or Kevlar stitching yarn. Results of processing studies for vacuum impregnation with Hercules 3501-6 epoxy resin and pressure impregnation with both Dow Tactix 138/H41 epoxy resin and British Petroleum BP E905L epoxy resin are presented.

POTENTIAL AEROSPACE APPLICATIONS OF MULTIAXIAL WARP KNIT FABRICS

The potential aerospace applications of multiaxial warp knit fabrics include broadgoods replacement for biaxial woven fabric, postformed structural shapes, and dimensionally stable sheet stock for pultrusion. The broadgoods that can be produced with multiaxial knitting machines include [0, 90], $[\pm\theta]$, $[0 \pm \theta]$, $[90 \pm \theta]$, and [0, 90, $\pm\theta$] orientations. An example of a postformed structural shape is shown in figure 1. The knitted sine wave beam was formed over forming blocks and the knitted plies were tacked together with a powdered epoxy tackifier.

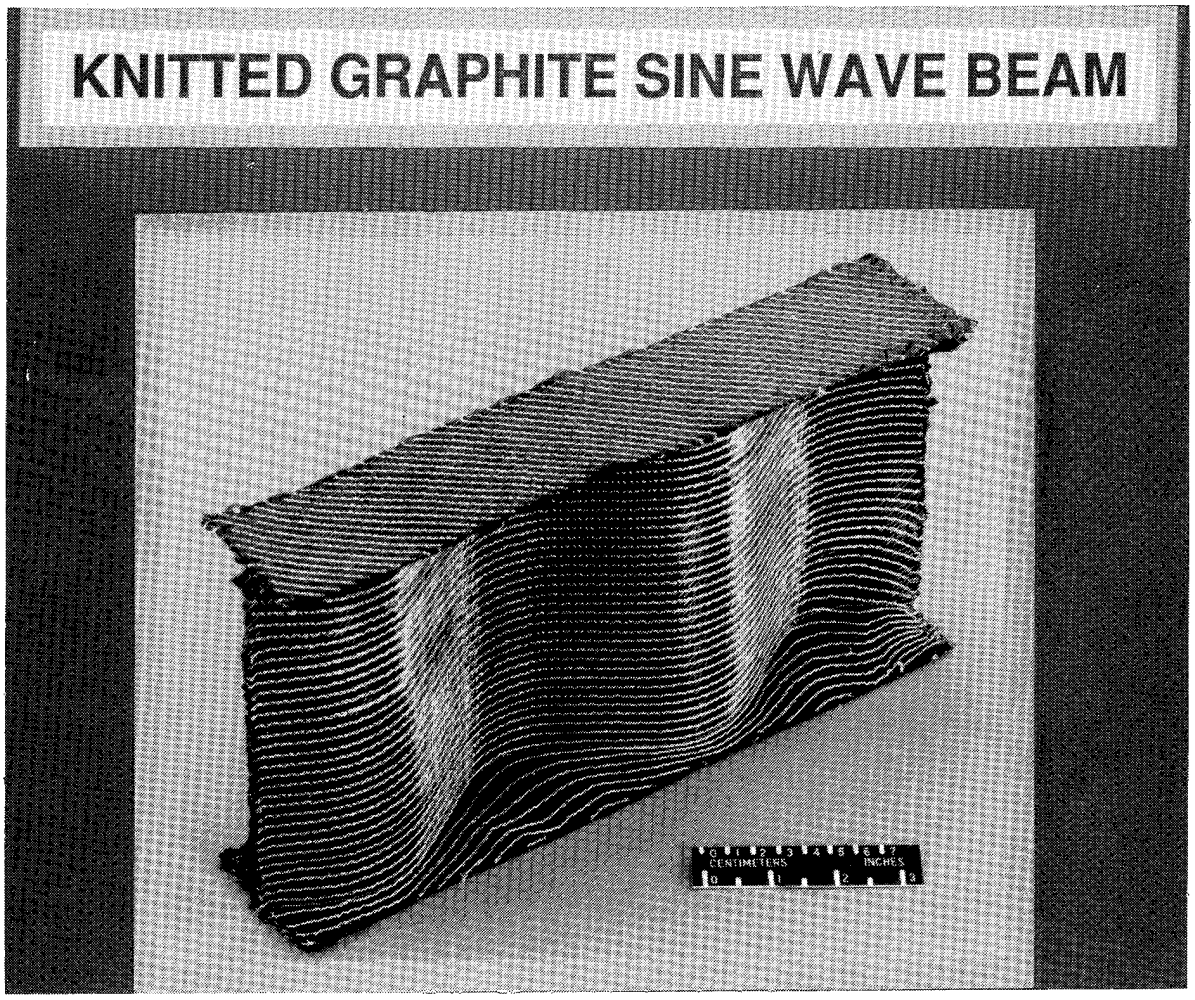


Figure 1

HEXCEL HI-TECH MULTIAXIAL WARP KNITTING MACHINE

The multiaxial warp knit fabric obtained from Hexcel Hi-Tech was fabricated on a machine that was developed by Hexcel Hi-Tech, figure 2. The Hexcel Hi-Tech machine can produce up to an 8-ply fabric with ply orientations of (0, 90, $\pm\theta$), with θ ranging from 30 to 90 degrees. The machine can produce fabrics up to 100-inches wide at a rate of 50 lineal yards/hour. The fabric for this investigation was produced by laying down bands of 6K carbon tows. The 0- and 90-degree plies had 38 tows per band and the $\pm$45-degree plies had 27 tows per band to provide a balanced areal weight. The fabric produced had an average areal weight per ply of 430 g/m^2. The sketch in figure 2 shows that the 90- and $\pm$45-degree tows are laid down by yarn carriers moving along fixed guides. The 0-degree tows are laid down off a beam just prior to the 4-ply stack being knitted together. A chain stitch was used to knit the fabric plies together.

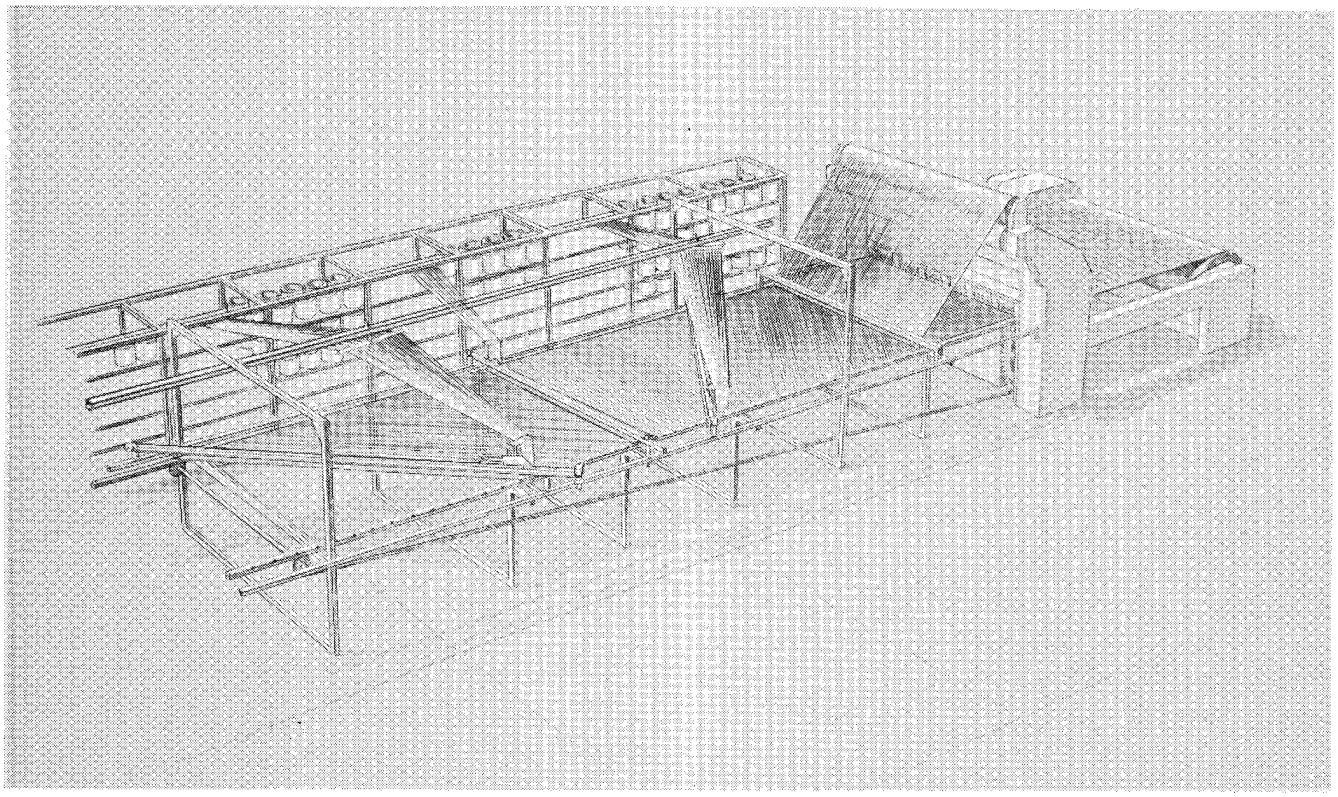


Figure 2

DESCRIPTION OF HEXCEL HI-TECH MULTIAXIAL WARP KNIT FABRIC

Hercules AS-4, 6K epoxy-sized carbon tows were used to produce the fabric. A 16-ply quasi-isotropic $(+45,\ 0,\ -45,\ 90)_{2s}$ fabric preform stack was fabricated by Hexcel Hi-Tech as shown in figure 3. Three knitted ply subgroup patterns were used to build up the required thickness as indicated in the figure. The 3-ply and single-ply subgroups were produced by knitting the carbon tows together with a 70 denier polyester yarn. Eight subgroups were stacked to form the full 16-ply laminate. Some of the 16-ply stacks were stitched together with T-900-1000-50A carbon stitching yarn using a modified lockstitch.

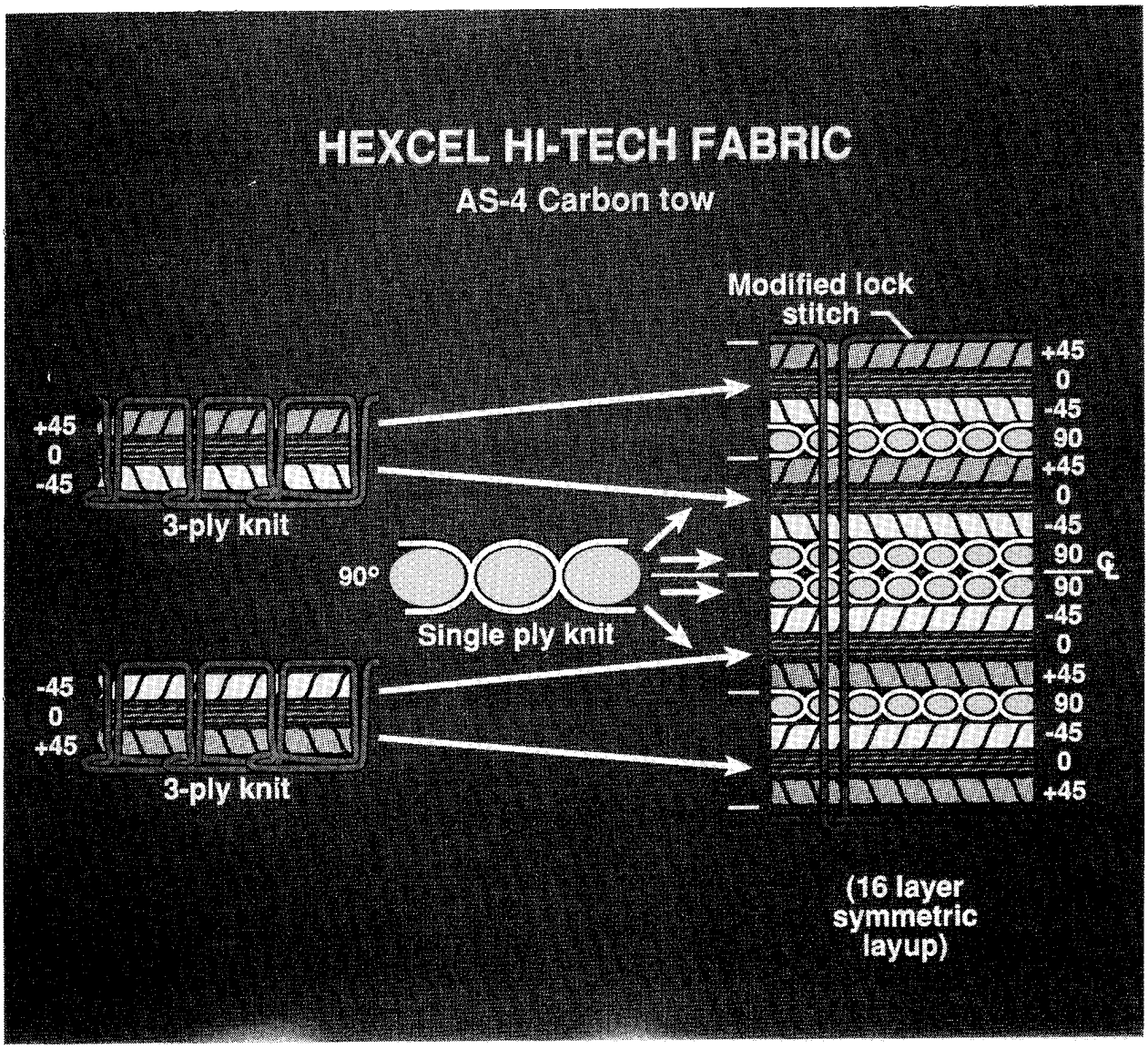


Figure 3

HEXCEL HI-TECH KNITTED AND STITCHED FABRICS

The Hexcel Hi-Tech knitted and knitted/stitched fabrics are shown in figure 4. A 70 denier polyester yarn was used to knit the carbon tows together. A chain stitch was used to knit the individual tows together and a modified lockstitch was used to stitch the 16-ply stack together. The polyester knitting yarns were spaced in rows 1/6-inch apart with a pitch of 9 stitches/inch. The carbon stitching yarns were spaced in rows and columns 1/4-inch apart with a pitch of approximately 8 stitches/inch. The polyester knit yarns pierced the carbon tows and imparted limited damage to some of the tows. The photographs shown in figure 4 indicate only minimal inplane distortion of the carbon tows due to penetration of the polyester knitting yarns. The Toray T-900-1000-50A carbon stitching yarn was much larger in diameter than the polyester knitting yarn, which resulted in additional fiber distortion and damage.

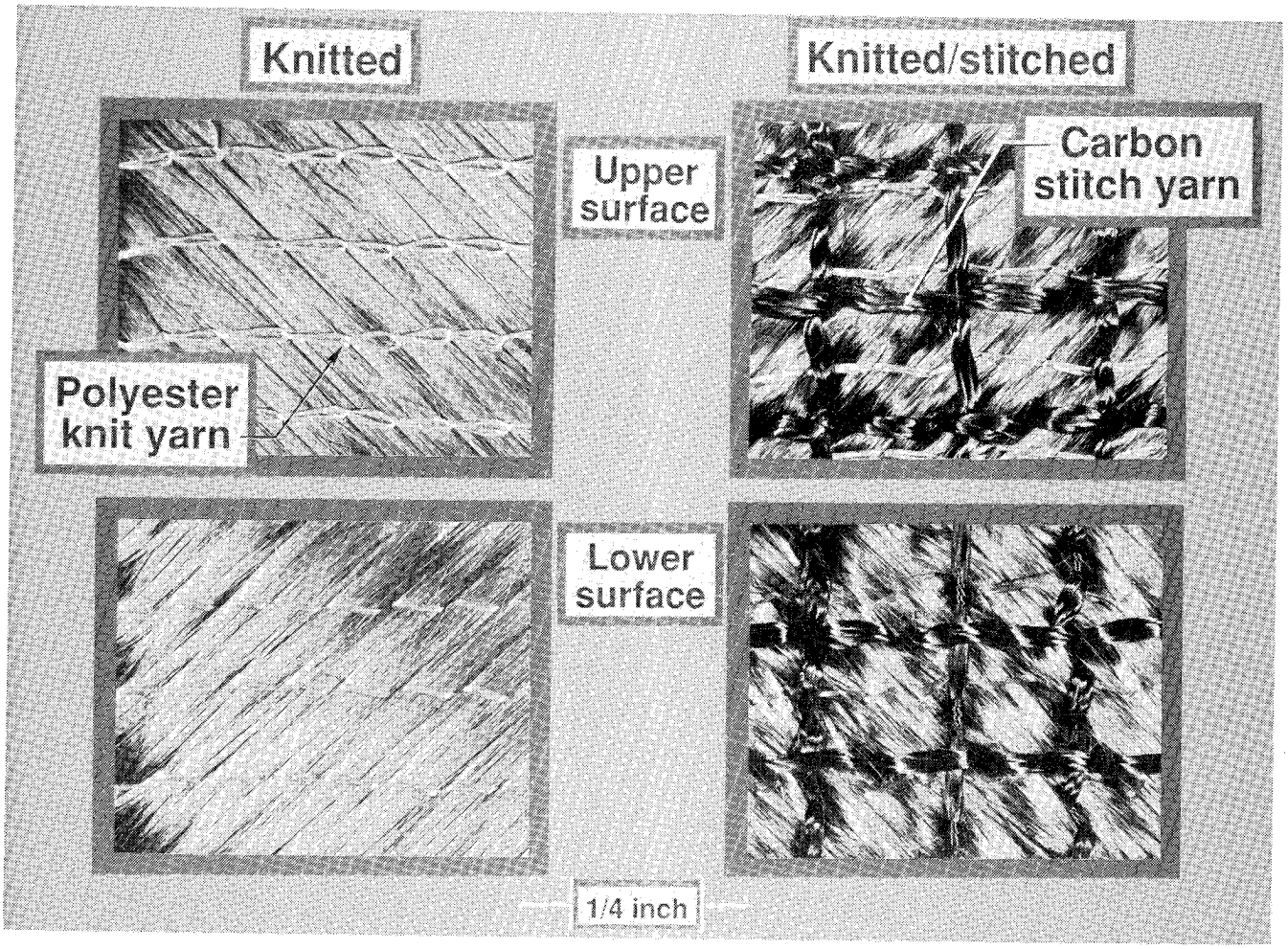


Figure 4

MILLIKEN MULTIAXIAL WARP KNITTING MACHINE

The multiaxial warp knit fabric obtained from Milliken was fabricated on a machine that was manufactured by the Mayer Textile Machine Corporation, figure 5. The Milliken machine can produce a 4-ply fabric with ply orientations of (0, 90, $\pm\theta$), with θ ranging from 30 to 60 degrees. Fabrics with (0, 90), (0$\pm\theta$), (90$\pm\theta$), ($\pm\theta$) and (0, 90, $\pm\theta$) fiber orientations can also be produced with the Milliken machine. In addition, an auxiliary backing material can be included in the knitted fabric. The machine can produce fabrics up to 62 inches wide at a rate of 50 lineal yards/hour. The machine was operated at approximately 30 lineal yards/hour to minimize damage to the carbon tows. The tow count for the fabric produced for this investigation was 12 tows/inch in the warp and fill directions and 17 tows/inch in the $\pm$45-degree directions of the fabric. A chain stitch was used to knit the (-45, $+45$, 0, 90) plies together. The fabric produced had an average areal weight per ply of 430 g/m^2.

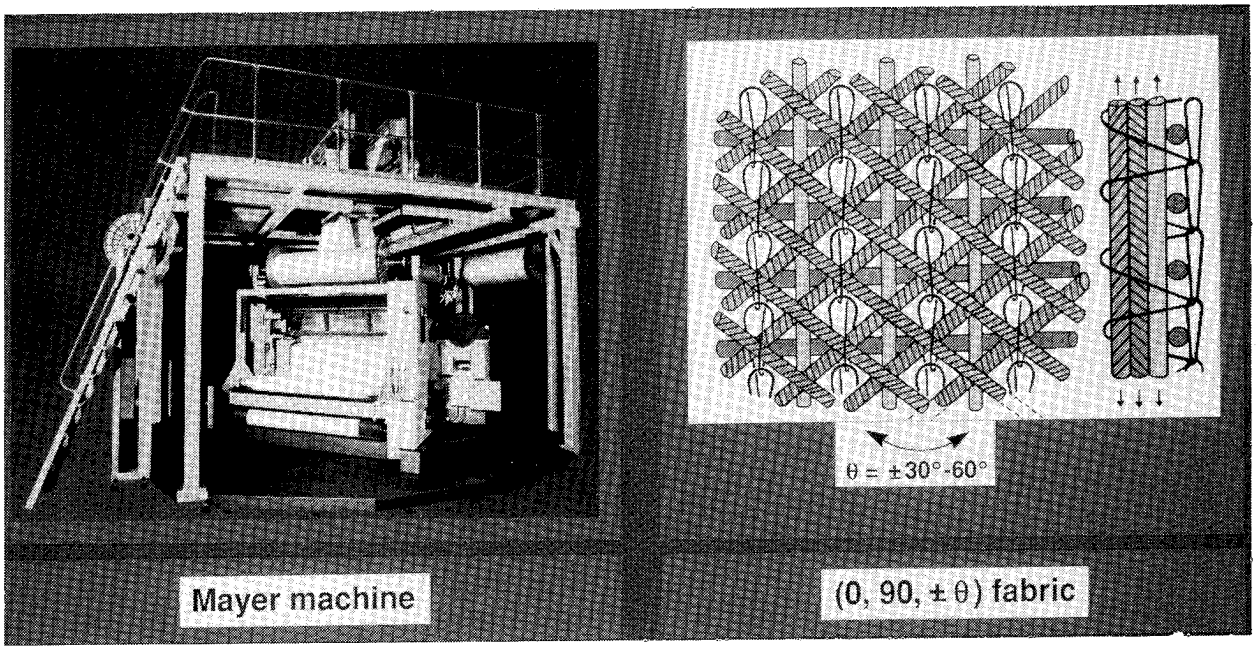


Figure 5

DESCRIPTION OF MILLIKEN MULTIAXIAL WARP KNIT FABRIC

The Milliken fabric was made on the knitting machine discussed in figure 5. The fabric design shown in figure 6 was produced with Hercules AS-4 epoxy-sized carbon tows. The 0- and 90-degree plies were produced with 12K tows, whereas 9K tows were used for the ±45-degree plies. This tow distribution was required to achieve similar ply areal weights because of the different tow count for the off-axis plies. Only the 4-ply subgroup (−45, +45, 0, 90) shown in figure 6 was produced for this investigation. An additional 4-ply subgroup (+45, −45, 0, 90) would be required to produce a symmetric quasi-isotropic fabric preform. Four 4-ply subgroups were stacked to form the full 16-ply laminate. Note that the 16-ply stack shown in figure 6 is unsymmetric. The 4-ply subgroup was produced by knitting the carbon tows together with a polyester yarn. Some of the 16-ply stacks were stitched together with Kevlar 29 1500 denier stitching yarn using a chain stitch.

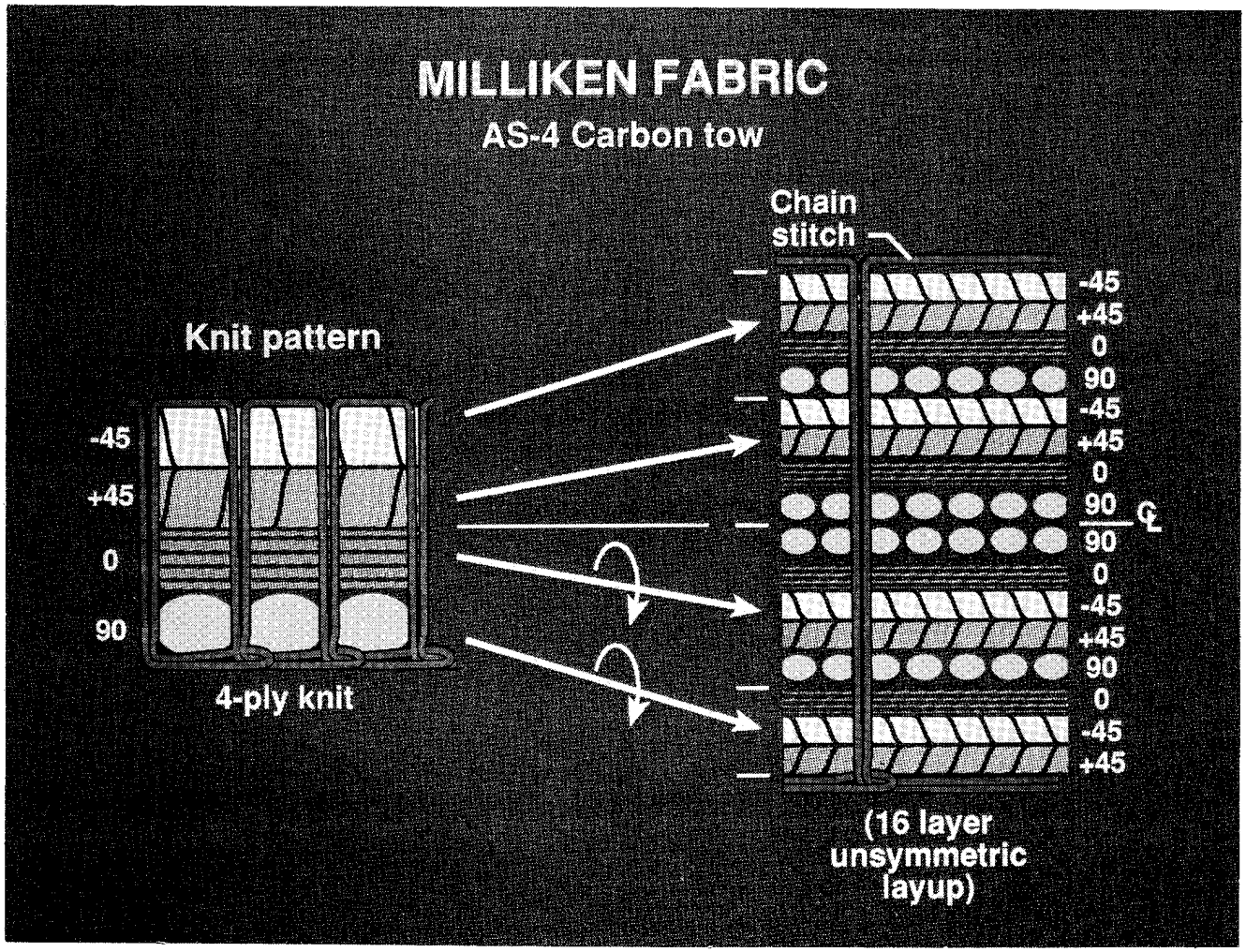


Figure 6

MILLIKEN KNITTED AND STITCHED FABRICS

The Milliken knitted and stitched fabrics are shown in figure 7. A 150 denier polyester yarn was used to knit the carbon tows together. A chain stitch was used to knit the individual tows together and a Kevlar chain stitch was also used to stitch the 16-ply stacks together. The polyester knitting yarns were spaced in rows 1/12-inch apart with a pitch of 12 stitches/in. The Kevlar 29 stitching yarns were spaced in rows and columns 1/4-inch apart with a pitch of approximately 8 stitches/inch. The polyester knit yarns surrounded the individual carbon tows which resulted in a gap of approximately 0.01-inch between the carbon tows. Since the knitting needles did not pierce the carbon tows, minimal damage was imparted to the fabric as a result of the knitting operation. The photographs in figure 7 indicate a high degree of uniformity and yarn straightness in the knitted fabric. The Kevlar 29 1500 denier stitching yarns caused some distortion in the carbon tows, especially at the intersection of the rows and columns.

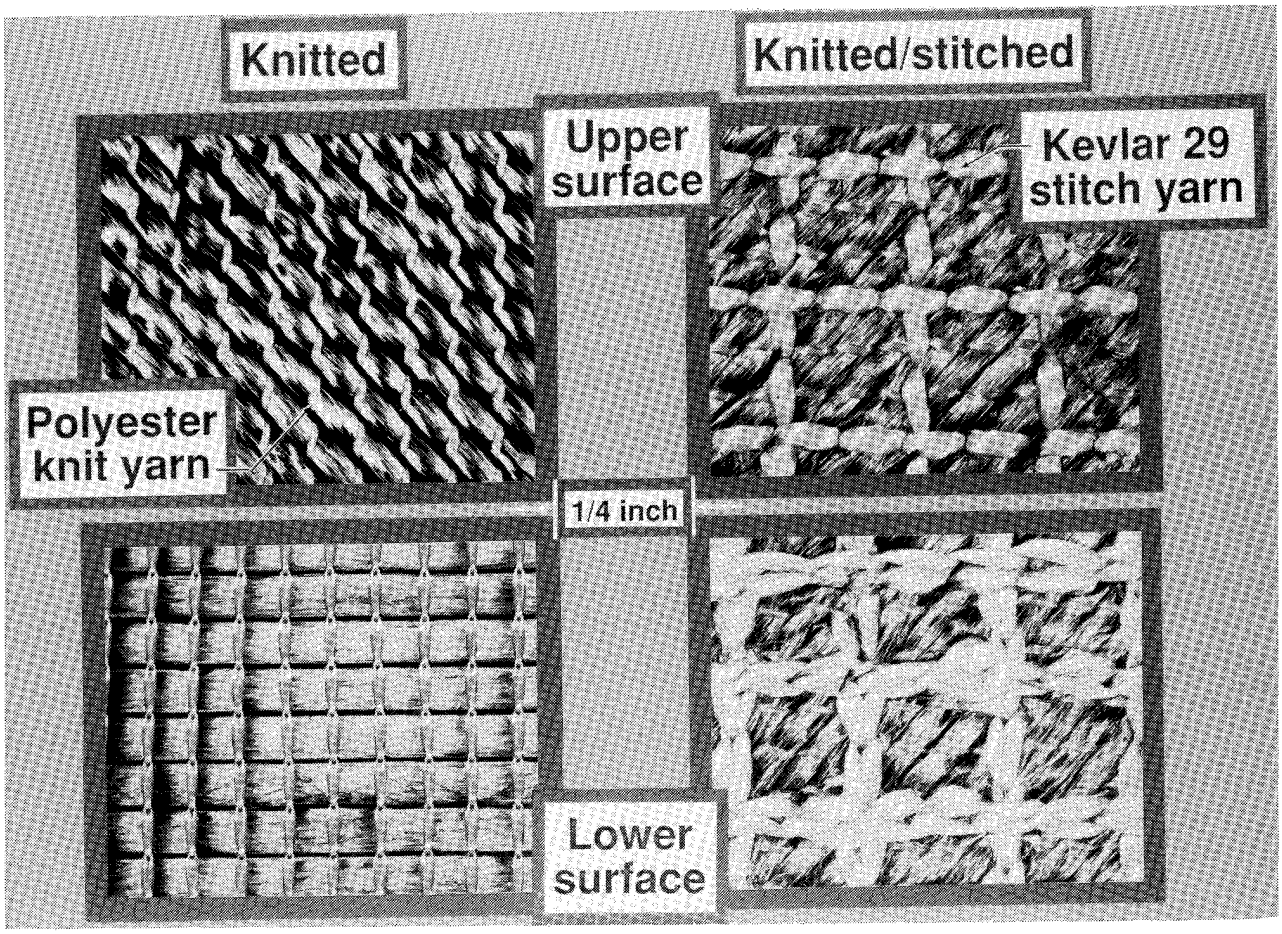


Figure 7

COMPACTION AND PERMEABILITY CHARACTERISTICS OF HEXCEL HI-TECH AS-4 KNITTED/STITCHED FABRIC

The compaction and permeability characteristics of a fabric can be used as an aid in the development of infiltration and cure cycles. As part of a NASA Langley grant, Virginia Polytechnic Institute and State University (VPI & SU) developed experimental techniques to measure fabric compaction and permeability. As shown in figure 8, the fiber volume fraction and fabric thickness is a nonlinear function of compaction pressure. The Hexcel Hi-Tech knitted/stitched fabric had a nominal uncompacted fiber volume fraction of approximately 51 percent and a thickness of approximately 0.310-inch. To achieve a fiber volume fraction of over 62 percent and a final thickness of 0.250-inch, a compaction pressure of approximately 90 psig is required.

Also shown in figure 8 is the effect of fiber volume fraction or permeability. Permeability is a function of fabric architecture, compaction, porosity, and flow direction. Permeability along a fiber bundle can be an order of magnitude greater than transverse to the fiber bundle. Through-the-thickness stitching may increase fabric permeability by providing additional flow paths through the thickness of the fabric. Tightly woven or high fiber volume fraction fabrics would have less porosity and thus be more difficult to infiltrate with resin. The compaction and permeability data generated under the VPI & SU grant were used to generate infiltration and cure cycles for the Hexcel Hi-Tech knitted/stitched fabric and the Milliken knitted fabric.

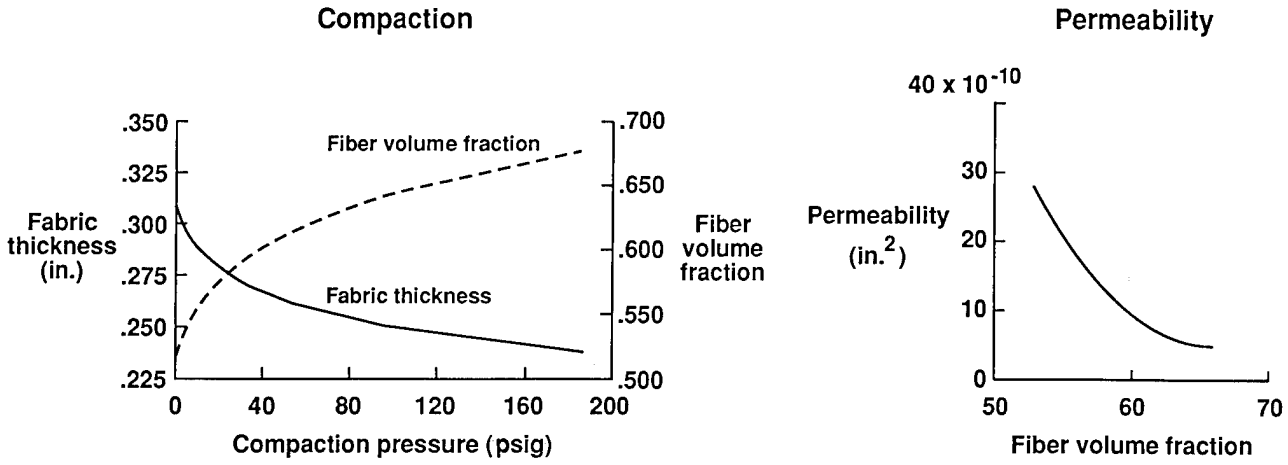


Figure 8

RESIN CHARACTERISTICS FOR IMPREGNATION AND CURE

Three types of resins and associated impregnation processes were used in this investigation. Viscosity profiles and cure cycles used for two of the resins, Hercules 3501-6 and Dow Tactix 138/H41, are shown in figure 9. The 3501-6 resin is a solid at room temperature and was used in a vacuum/pressure process where a resin film was melted and infiltrated through-the-thickness of the fabric. The 3501-6 resin melts during a ramp up to 245°F at which time a minimum viscosity of approximately 500 cps is achieved. The fabric is fully impregnated during the low viscosity window. Full vacuum plus 2 psi of platen pressure is used to impregnate the fabric. Total impregnation is completed within 40 minutes and the platen pressure is increased to 90 psi to insure proper compaction. After a 1-hour hold at 245°F, the temperature is ramped to 350°F and the cure cycle is completed after a 2-hour hold.

The Tactix 138/H41 epoxy resin mixture has a room temperature viscosity of over 1000 cps. To reduce the viscosity, the resin is heated to 150°F for impregnation. The viscosity drops below 200 cps for approximately 1 hour at which time full impregnation occurs. Resin is injected into the mold cavity and fabric under 25 psi pressure and full vacuum to remove entrapped air. The resin exit valve in the RTM tool is closed and the cure cycle is initiated. Temperature is raised to 250°F and held for 1 hour while the resin gels. A mold clamping pressure of 200 psi is applied to close the mold and to achieve the desired laminate thickness. The final cure is completed after a 2-hour hold at 350°F.

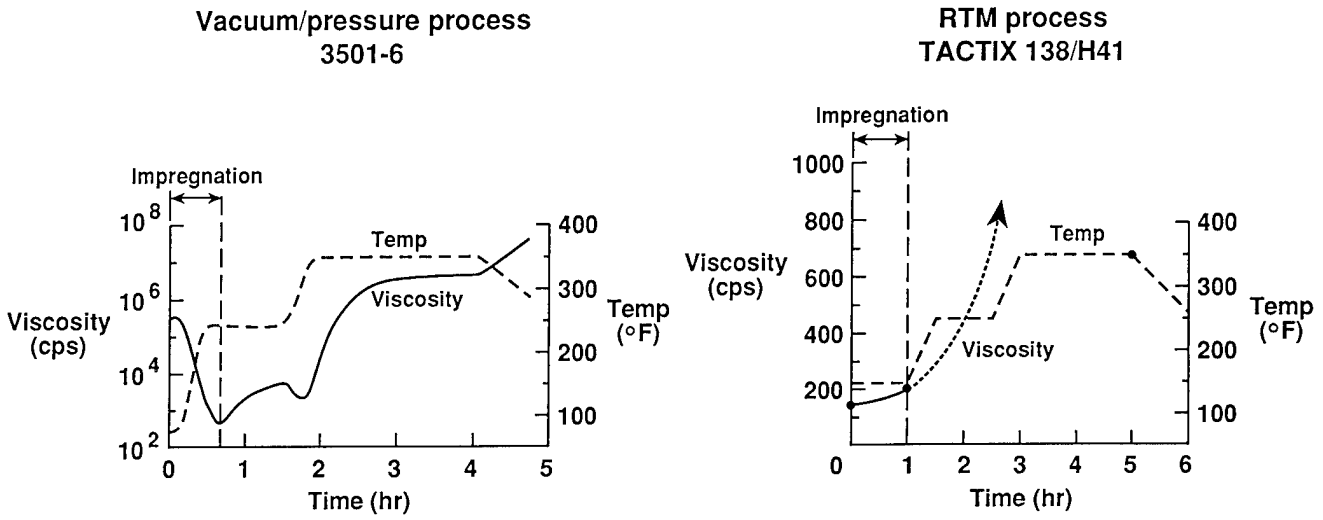


Figure 9

VACUUM/PRESSURE IMPREGNATION PROCESS

The vacuum/pressure impregnation process was used to mold panels with Hercules 3501-6 resin. As shown in figure 10, a resin film is placed in the bottom of the mold and resin flow is in one direction, up through the thickness of the fabric. A vacuum press is used to apply heat and pressure and to evacuate entrapped air. The resin is weighed to give the desired volume fraction, melted, degassed under vacuum, and poured into the mold cavity where it solidifies. The fabric is carefully trimmed to fit the 12-inch by 12-inch cavity size and placed in the mold so that all edges have a slight press fit. This insures that there are no gaps to allow resin to escape around the fabric. A breather layer of porous Teflon-coated fiberglass is placed over the fabric to allow air to escape, but to prevent excessive resin bleed. The caul plate is placed in the mold cavity to apply pressure to the fabric. Pressure must be close to that required to achieve the desired thickness and fiber volume; too much pressure results in a thin panel and too little pressure leads to voids. The caul plate is sized to allow only enough gap for the breather fabric to extend out of the mold. This tight fit allows excess resin to bleed out and provides a path for air venting. The entire mold assembly is placed between heated platens in a vacuum press for the prescribed cure cycle. Since the fabric is not pressed to thickness stops, slight variations in final part thickness may result.

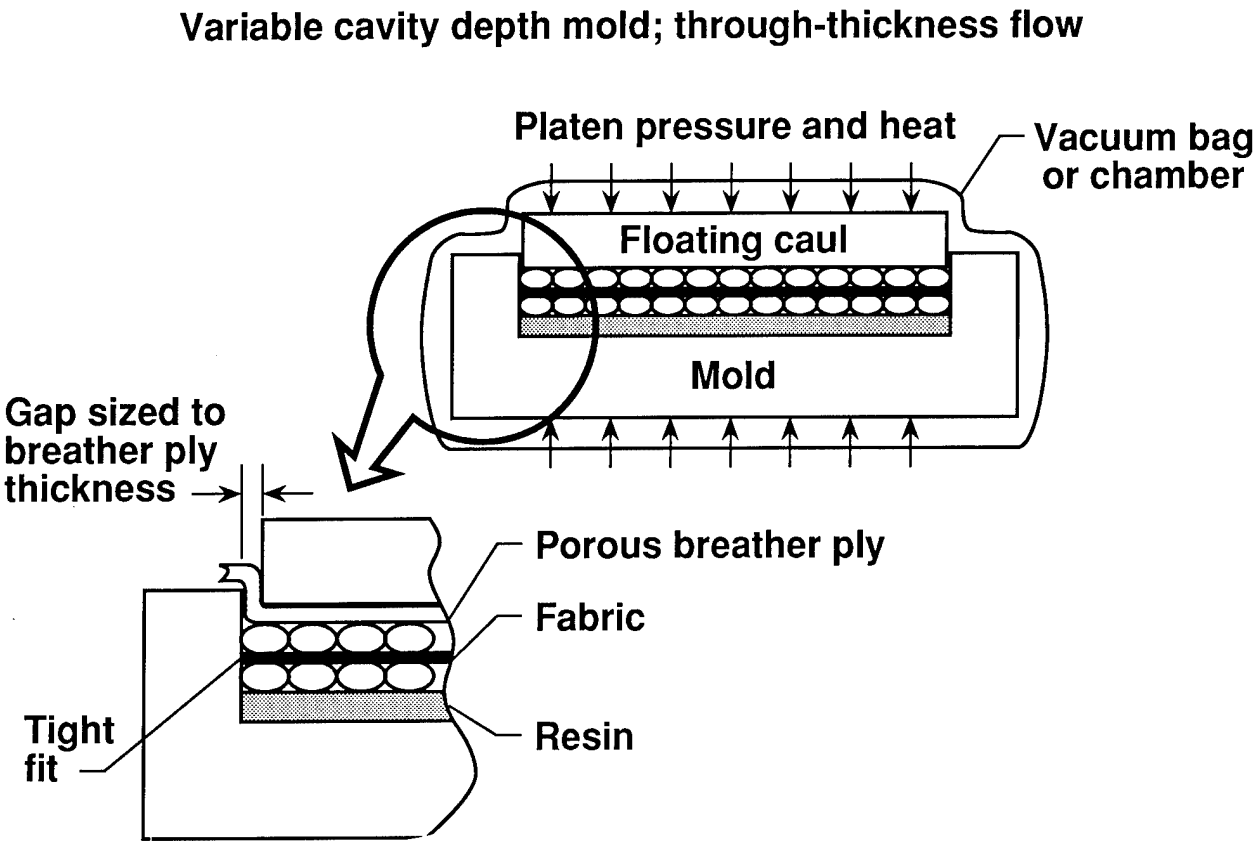


Figure 10

RESIN TRANSFER MOLDING PROCESS

The resin transfer molding (RTM) process shown in figure 11 was developed by Boeing Aerospace under contract to NASA Langley. Panels 11.5-inch by 11.5-inch by 0.250-inch were molded and shipped to NASA Langley for testing. The RTM method is used to mold panels with resins having stable, low viscosities at room or slightly elevated temperature, such as Dow Tactix 138/H41. Resin flow is two-dimensional in the plane of the fabric. As indicated in the figure, an O-ring is used to seal the mold to prevent resin leakage and air entrainment. The mold assembly is placed between two platens in a hydraulic press to close the mold and apply sufficient pressure to debulk the fabric and seat the O-ring. The mold cavity depth is sized to achieve a prescribed fabric thickness and fiber volume fraction.

Resin enters the mold from a pressurized tank and fills a channel around the perimeter of the fabric. Resin flows radially inward through the fabric to an exit port in the center of the mold. A vacuum pump is attached to the exit port to remove excess air. Once the fabric preform is fully infiltrated and air is evacuated, the exit valve is closed and the prescribed cure cycle is followed. Cured panels may have minor thickness variations due to machining tolerances of the mold.

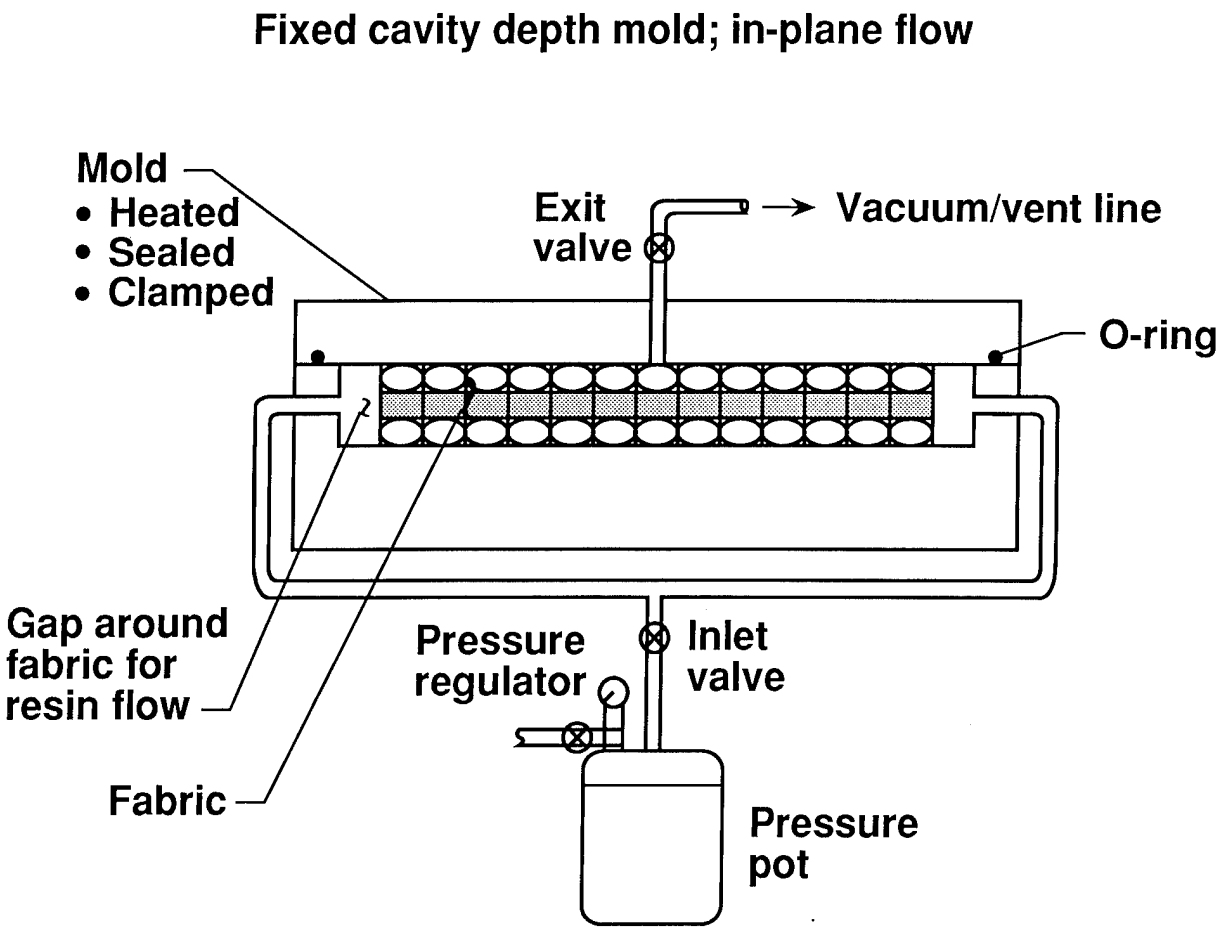


Figure 11

PHOTOMICROGRAPHS OF HEXCEL HI-TECH LAMINATES

Photomicrographs of Hexcel Hi-Tech laminates are shown in figure 12. Good compaction of the plies was achieved as evidenced by the nesting of the 90-degree plies. The well-defined shape of the 90-degree plies at the mid-plane of the knitted laminate is a result of constraint provided by the polyester knitting yarn. As a result, resin-rich areas are evident between the tow bundles. There are two significant characteristics evident in the knitted-stitched laminate shown in figure 12. Large resin-rich areas are evident around the carbon fiber stitching yarns and microcracking is evident throughout the laminate. The microcracking is caused by residual thermal stresses that occur during cool-down of the laminate after the resin is cured. As indicated in figure 12, void-free laminates were produced.

During the course of this investigation several laminates were fabricated by the vacuum/ pressure impregnation method with various levels of compaction pressure. The higher pressures resulted in laminates with higher fiber volume fractions. Fiber volume fractions, determined by acid digestion, ranged from 56 to 63 percent with an average of 59 percent.

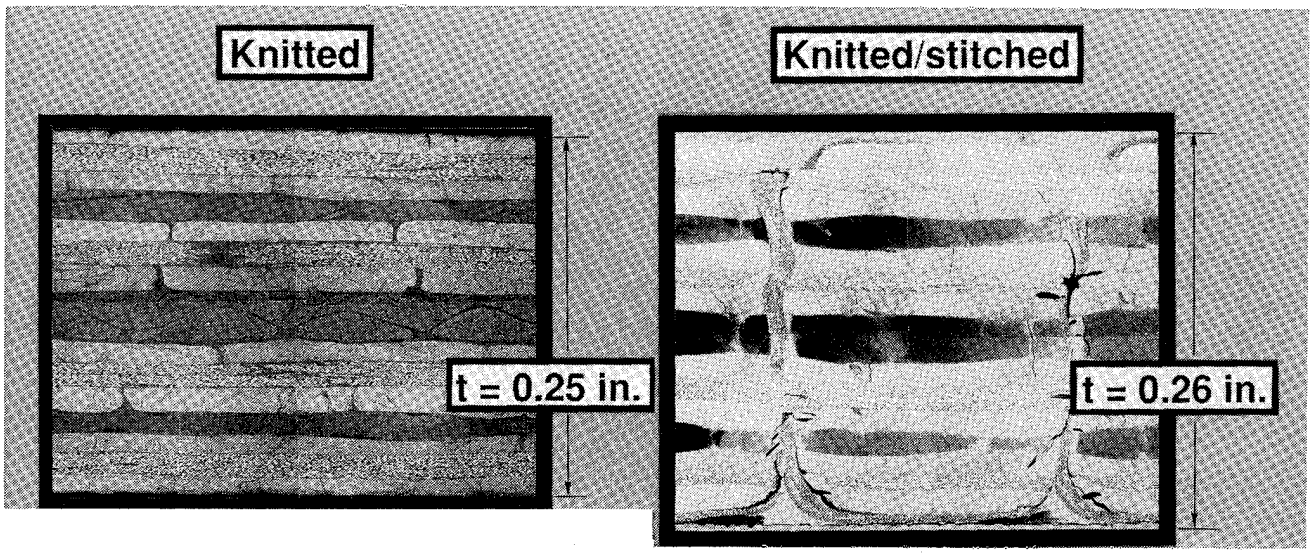


Figure 12

PHOTOMICROGRAPHS OF MILLIKEN LAMINATES

Photomicrographs of Milliken laminates are shown in figure 13. The 150 denier polyester knit yarns used in fabricating the (−45, +45, 0, 90) 4-ply fabric provided excellent stability to the fabric. A high degree of uniformity in carbon tow spacing was achieved. The individual carbon tows could not spread to fill the inherent gaps between the tows. As a result, uniform resin-rich pockets are evident throughout the laminates. The volume fraction of the resin pockets was reduced during the course of this investigation by using less resin and applying higher pressure during the compaction portion of the cure cycle. The first laminate fabricated with a pressure of 45 psi had a thickness of 0.270-inch, whereas the laminates produced with 90 psi pressure had thicknesses ranging from 0.240-inch to 0.250-inch.

Due to limited material availability, only one Kevlar-stitched laminate was fabricated by the vacuum/pressure impregnation process for this investigation. Significant resin-starved areas on the surface and internal porosity were evident for this laminate. Additional fabrication trials are required to optimize the resin impregnation and cure process. The photomicrograph of the Kevlar-stitched laminate shown in figure 13 indicates less microcracking than the Hexcel Hi-Tech carbon-stitched laminate shown in figure 12.

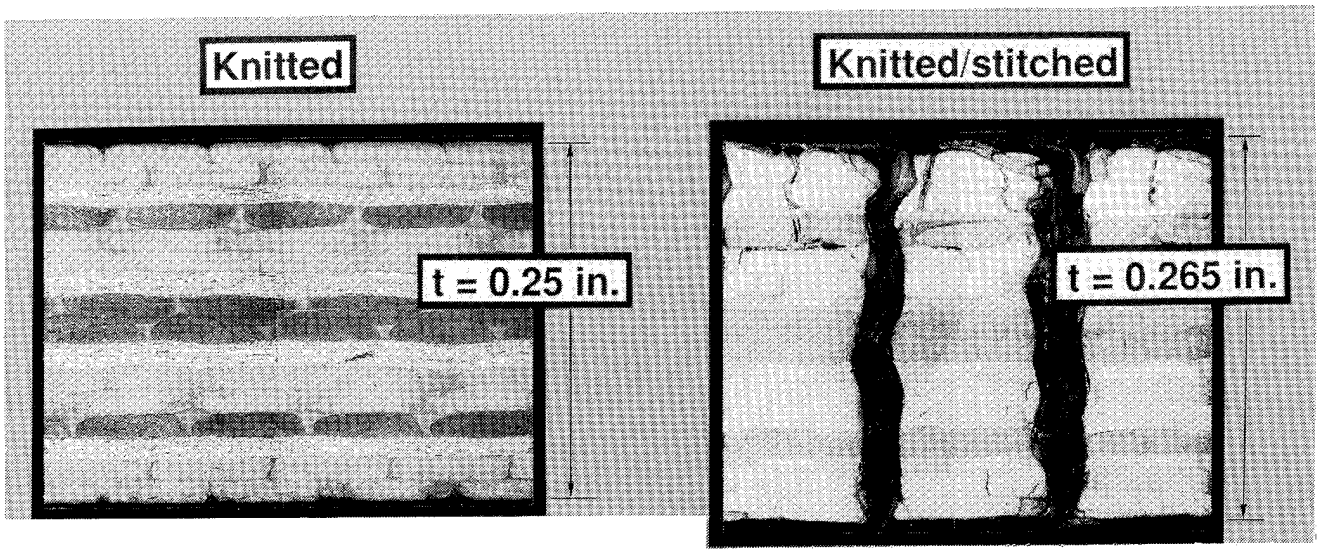


Figure 13

TEST SPECIMENS

The test specimens used in this investigation are shown in figure 14. All the test specimens had a nominal thickness of 0.250-inch and a nominal fiber volume fraction of 60 percent. The short block compression specimens were 1.50 inches wide by 1.75 inches long, and the compression-compression fatigue specimens were 1.5 inches wide by 4.0 inches long. The tension specimens were 1.0 inch wide by 10.0 inches long. The tension and compression specimens had 1/8-inch long (0/90) stacked strain gages bonded back-to-back at mid-length of the specimens. The compression-after-impact specimens were 5.0 inches wide by 10.0 inches long and had 1/4-inch long strain gages bonded back-to-back as shown in the figure. The compression after impact specimens were impacted at approximately 30 ft-lb of energy with 0.500-inch diameter aluminum balls that were fired from an air gun. The target impact energy was 1500 in-lb per inch of laminate thickness. However, due to velocity limitations of the air gun, some of the thicker laminates were subjected to energies slightly lower than the desired level of 1500 in-lb per inch of laminate thickness.

Open hole tension and compression specimens were both 10.0 inches long and had 1/4-inch holes drilled through their centers. Tension specimens were 1.5 inches wide and compression specimens were 3.0 inches wide. Open hole specimens had 1/4-inch long strain gages bonded back-to-back as shown in the figure.

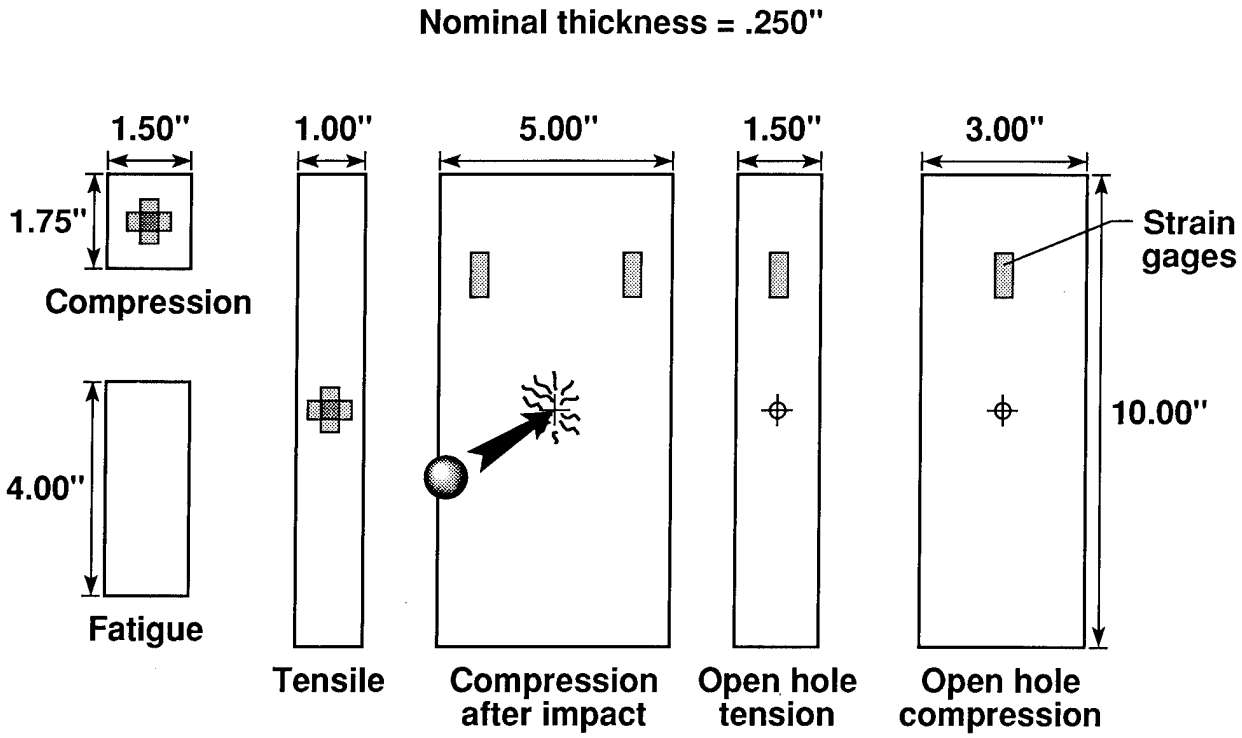


Figure 14

TEST APPARATUS AND PROCEDURES

Sketches of the test fixtures used in this investigation are shown in figure 15. Tension and compression tests were performed to measure elastic properties and strength. Compression after impact tests were performed to determine the effect of low-velocity impact on the compression strength of the knitted fabrics. Open hole tension and open hole compression tests were performed to determine the effect of stress concentrations on residual strength. Constant amplitude compression-compression fatigue ($R = 10$) tests were conducted to assess the effect of cyclic loading on residual compression strength.

The compression specimens were tested in a short block compression fixture. This fixture was used to apply uniform end-loading and to apply lateral clamping forces to the specimen ends to prevent end-brooming type failures. The specimens were tested in a 120-Kip hydraulic test machine at a load rate of 10 Kips/min until failure. Selected compression specimens were moisture conditioned and tested at 180°F. Moisture absorption was achieved by immersion of the specimens in water for 45 days at 160°F. The compression after impact and open hole compression specimens were tested in a fixture that clamps the ends and provides knife-edge supports on the sides to prevent overall panel instability. The compression after impact specimens were loaded at 20 Kips/min and the open hole compression specimens were loaded at 15 Kips/min. The tension and open hole tension specimens were tested in a 50-Kip servo-hydraulic test machine. End tabs were not used but lexan and a grit-coated wire screen were used to prevent slippage and specimen damage due to hydraulic actuated grip pressure. The tension specimens were loaded at a displacement rate of 0.05 in/min until failure.

The fatigue tests were conducted in a closed-loop servo-hydraulic test machine at a frequency of 10 Hz. The maximum number of cycles applied to the specimens was approximately 3 million cycles. The fatigue test fixture has four alignment rods that slide on linear bearings. The gripping surfaces were serrated to prevent slippage and to transmit load. In addition, end stops were used to apply end loads and to prevent slippage of the specimens.

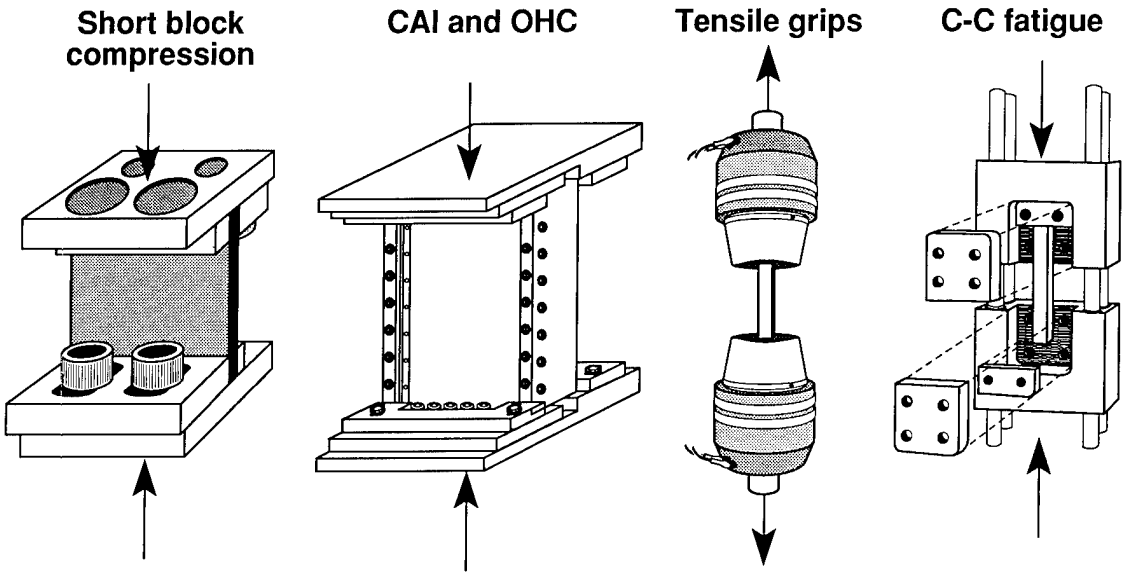


Figure 15

TENSILE STRENGTH OF HEXCEL HI-TECH FABRIC

Average tensile strengths for the Hexcel Hi-Tech knitted and knitted-stitched fabrics are shown in figure 16. Test results are shown for laminates fabricated with Hercules 3501-6 resin and Dow Tactix 138/H41 resin. The fabric results are compared with those for AS4/3501-6 prepreg tape. The prepreg laminates were fabricated with a $(+45_3, 0_3, -45_3, 90_3)_{2s}$ 48-ply layup which approximates the ply thicknesses for the 16-ply fabric layup. The test results indicate that the knitted-stitched laminates are stronger than the knitted laminates. These results are in contrast to results for Xerkon knitted-stitched laminates reported in reference 1, where it was found that stitching degrades the laminate tensile strength. The strength of the knitted laminates is approximately 22 percent lower than the strength of prepreg tape. The strength of the knitted-stitched laminates is only about 10 percent lower than the strength of the prepreg tape. Most of the tensile failures were in the test section; however, a few specimens failed at the edge of the grips. All specimens were tested without tabs in hydraulic pressure grips. It is possible that fiberglass tabs would improve load transfer and increase strength for all the laminates.

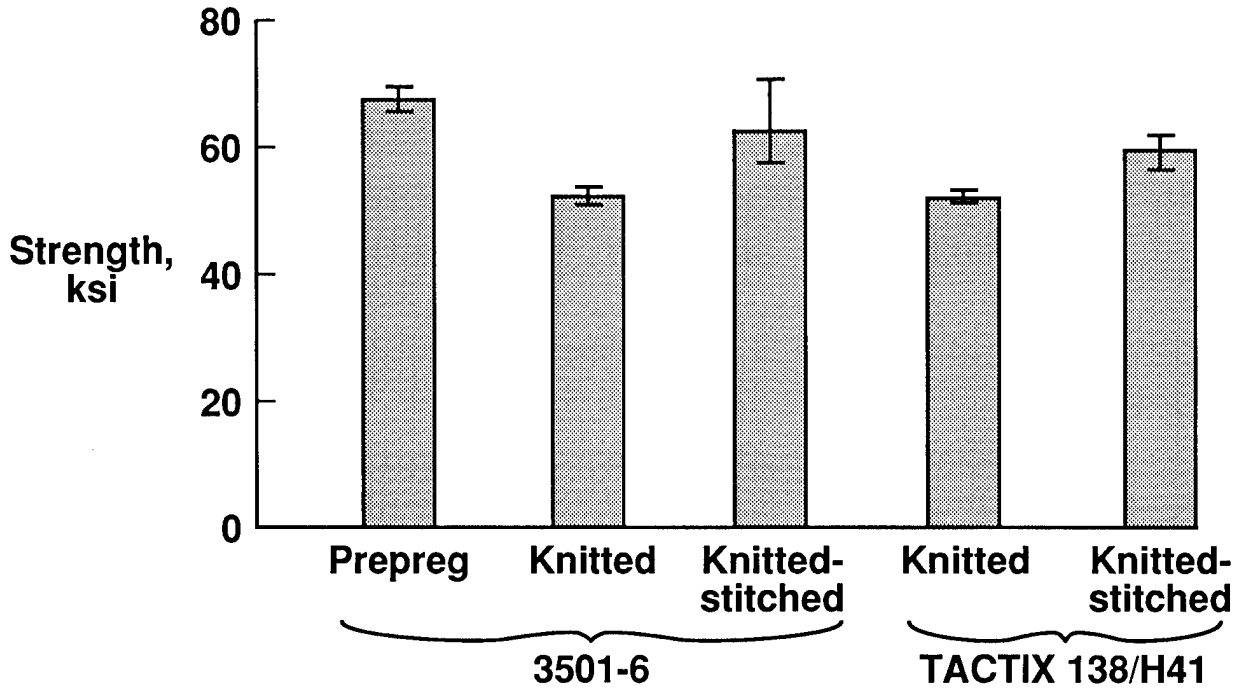


Figure 16

TENSILE STRENGTH OF MILLIKEN KNITTED FABRIC

Average tensile strengths for the Milliken knitted fabrics that were fabricated with 3501-6 resin and BP E905L resin are shown in figure 17. The strength of the 3501-6 knitted Milliken fabric is similar to the strength of the Hexcel Hi-Tech knitted fabric discussed in figure 16. The laminates with the E905L resin were about 17 percent stronger than the 3501-6 laminates. The Milliken prepreg laminate consisted of 48 plies of AS4/3501-6 prepreg tape which were stacked unsymmetrically to simulate the 16-ply Milliken knitted laminate discussed in figure 6. The average strength of the Milliken knitted laminates is approximately 26 percent lower than the strength of the prepreg tape. Due to a limited supply of Milliken fabric, knitted-stitched tensile specimens were not fabricated.

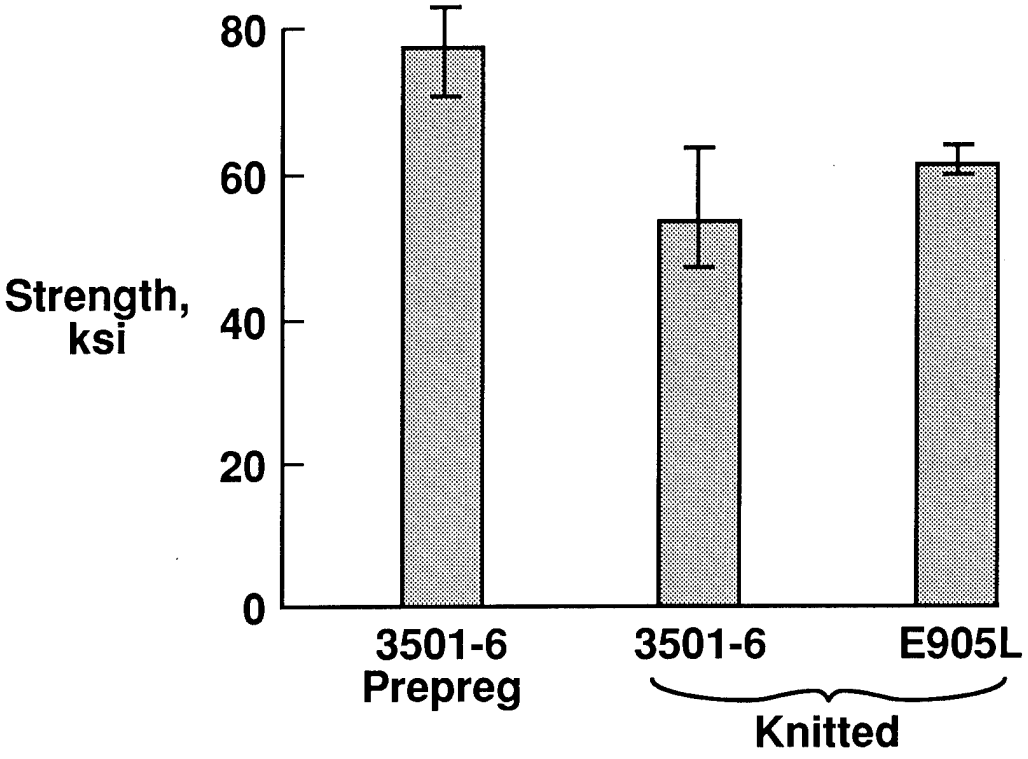


Figure 17

COMPRESSION STRENGTH OF HEXCEL HI-TECH FABRIC

Average compression strengths for the Hexcel Hi-Tech knitted and knitted-stitched fabrics are shown in figure 18. The average strength of the knitted and knitted-stitched fabrics is approximately 32 percent lower than the strength of the prepreg tape laminates. The failure mode for the tape and knitted laminates consisted of extensive ply delaminations, whereas the failure mode of the knitted-stitched laminates was primarily a transverse shear mode. Although the failure mode was significantly different between the knitted and knitted-stitched laminates, the stitching did not improve the strength. In fact, the strength of the knitted-stitched laminates with Tactix 138/H41 resin was lower than the strength of the knitted laminates. Since the modulus of the Tactix 138/H41 resin is lower than the modulus of the 3501-6 resin, it is expected that the compression strength of the laminates with Tactix 138/H41 resin would be lower.

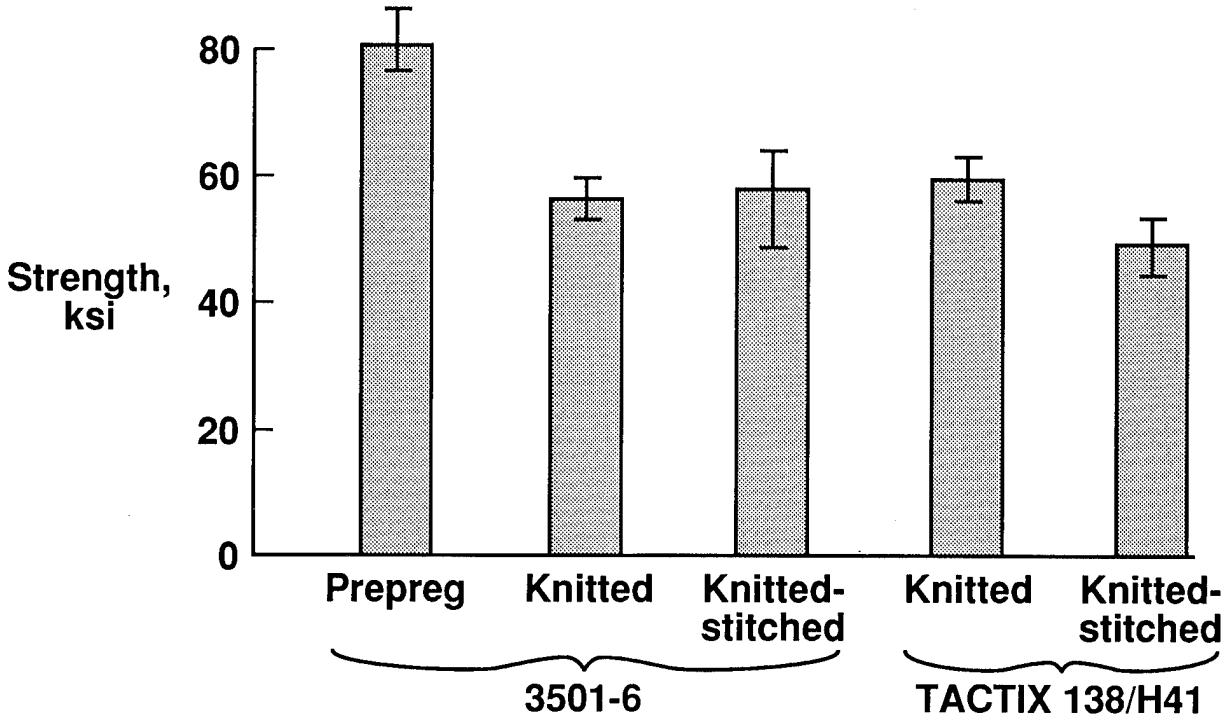


Figure 18

COMPRESSION STRENGTH OF MILLIKEN FABRIC

Average compression strengths for the Milliken knitted and knitted-stitched fabrics are shown in figure 19. The knitted fabrics with 3501-6 and E905L resins had compression strengths that were only about 10 percent lower than the strength of the prepreg tape laminates. There was only one Kevlar 29 stitched laminate available for testing; due to processing problems, this laminate had considerable porosity and its compression strength was lower than it should have been. Additional Milliken laminates will be fabricated and tested to assess the performance of Kevlar 29 stitching and E905L resin. The Milliken knitted fabric had better compression strength than the Hexcel Hi-Tech knitted fabric.

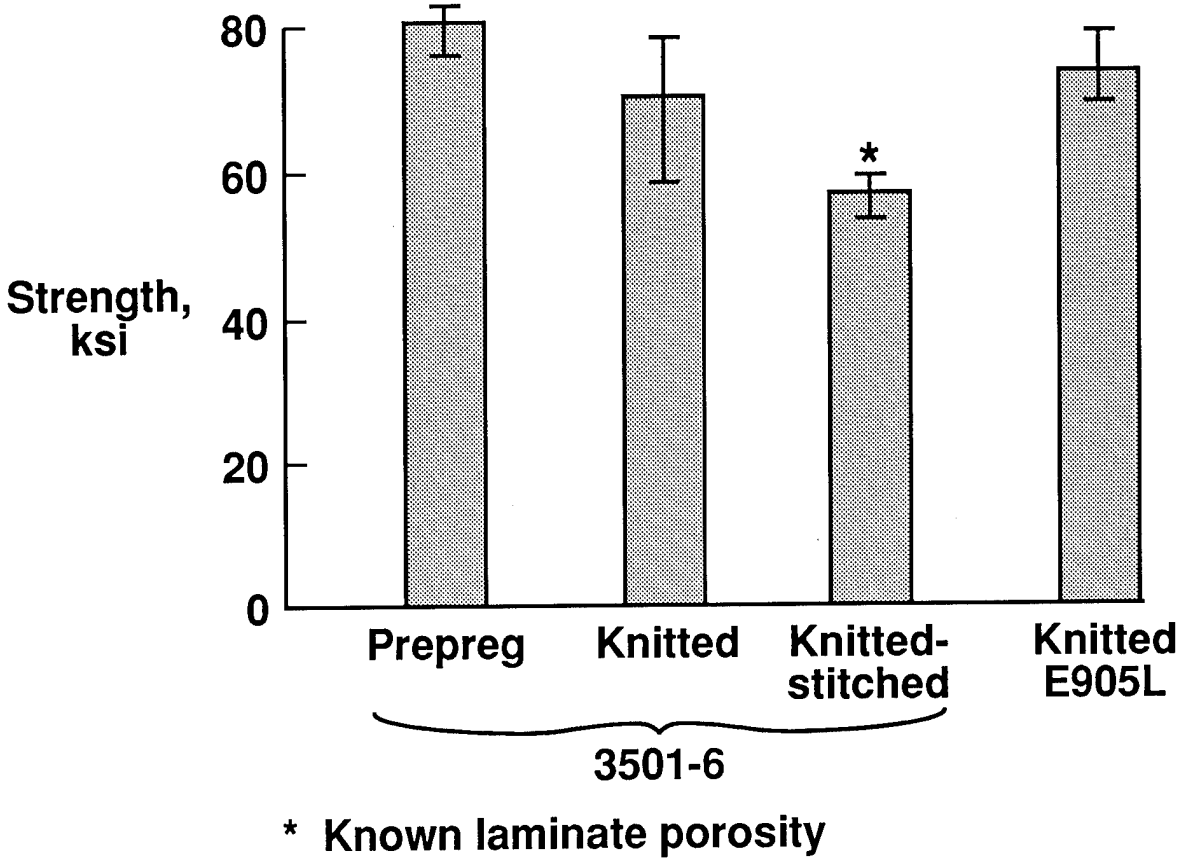


Figure 19

MODULUS OF HEXCEL HI-TECH FABRIC

Tensile and compression modulus data are presented in figure 20 for the Hexcel Hi-Tech fabric. The tensile modulus is slightly higher than the compression modulus for all the materials indicated in the figure. The moduli for the knitted and knitted-stitched fabrics are slightly lower than the corresponding moduli for the prepreg tape laminates. These results are expected since the through-the-thickness knitting and stitching yarns do not contribute to the in-plane material properties. In-plane fiber crimp could also lead to reduced in-plane moduli for the knitted and knitted-stitched composites.

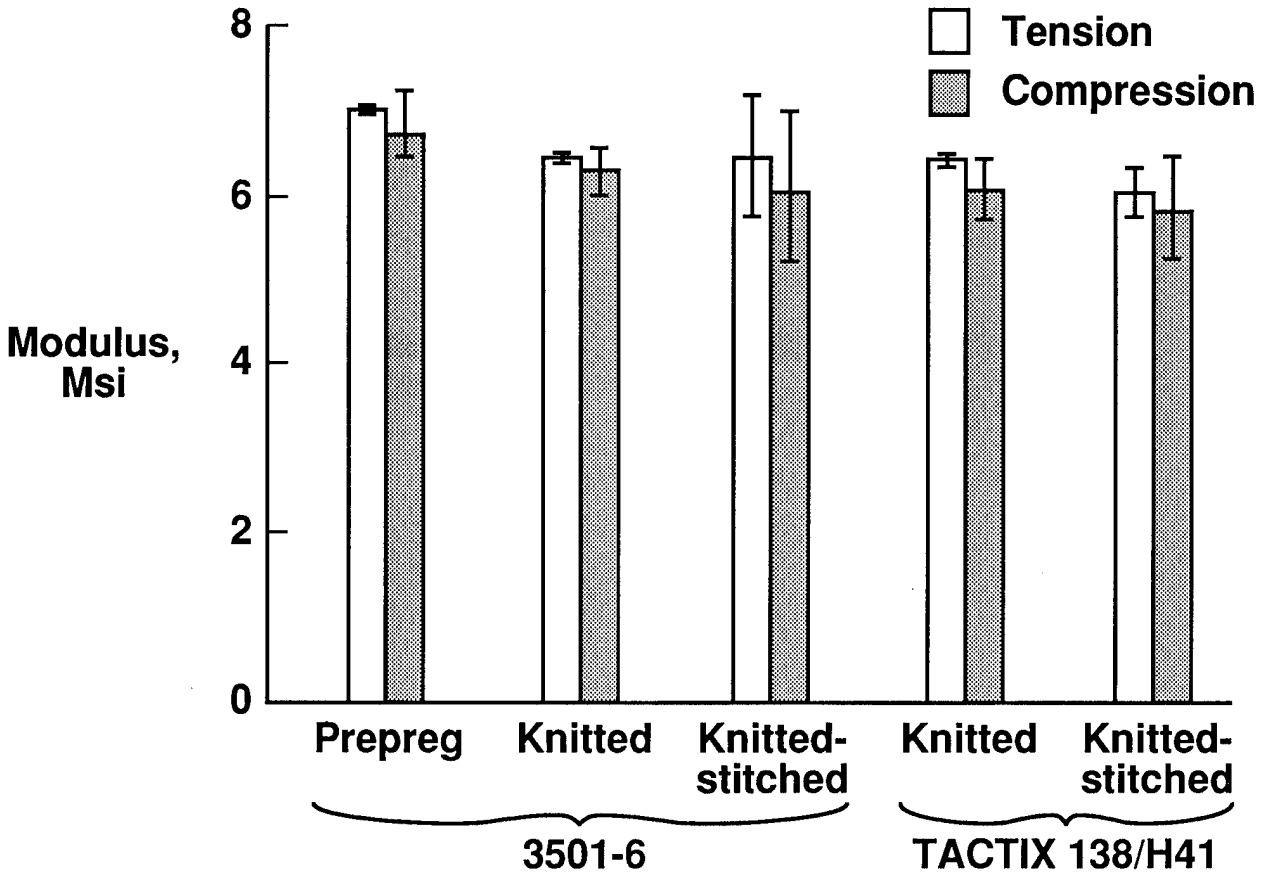


Figure 20

MODULUS OF MILLIKEN FABRIC

Tensile and compression modulus data are presented in figure 21 for the Milliken fabric. The tensile modulus is slightly higher than the compression modulus for all the materials indicated in the figure. The moduli for the 3501-6 knitted and knitted-stitched fabrics are slightly lower than the corresponding moduli for the prepreg tape laminates. The moduli for the E905L knitted fabric are equivalent to the prepreg tape moduli.

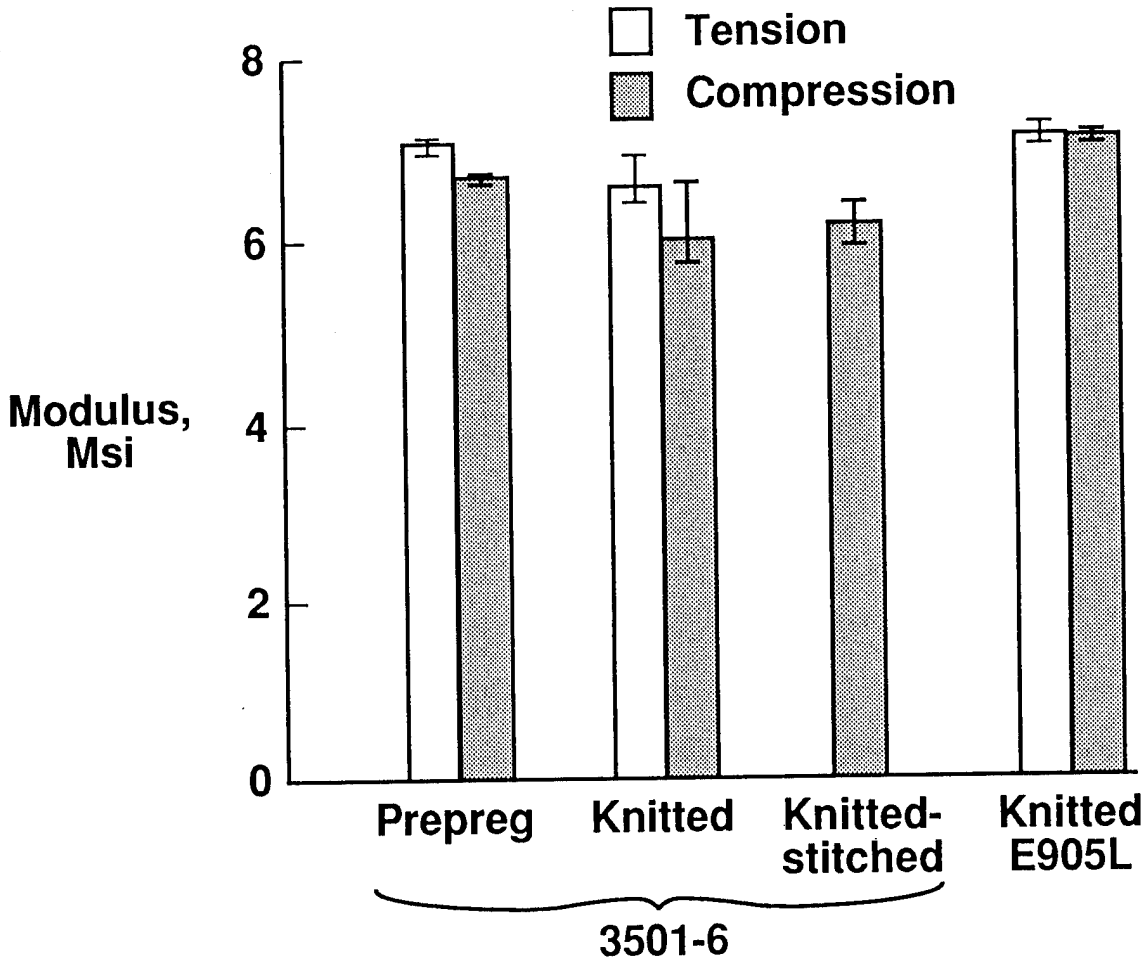


Figure 21

EFFECT OF MOISTURE AND TEMPERATURE ON COMPRESSION STRENGTH OF HEXCEL HI-TECH KNITTED-STITCHED FABRIC

The effect of moisture and temperature on the compression strength of the Hexcel Hi-Tech knitted-stitched fabric is shown in figure 22 for the 3501-6 and Tactix 138/H41 resin systems. Ten coupons were taken from panels made with each resin. Five of each were tested at ambient conditions, and another five of each were conditioned and tested at elevated temperature. The compression coupons were soaked in a water bath at 160°F for 45 days to moisture condition the coupons. The 3501-6 coupons absorbed 1.1 percent moisture whereas the Tactix 138/H41 coupons absorbed only 0.6 percent moisture. After moisture conditioning, the coupons were tested at 180°F in an environmental chamber. The test results indicate that the compression strength of the 3501-6 material was reduced by 28 percent compared to the ambient compression strength. The compression strength of the Tactix 138/H41 material was reduced by 24 percent compared to ambient compression strength. As expected, the lower moisture absorption for the Tactix 138/H41 resin system resulted in a somewhat lower percentage reduction in compression strength. As shown in figure 22, the ambient compression strength of the Tactix 138/H41 resin system was about 20 percent lower than the ambient compression strength of the 3501-6 resin system.

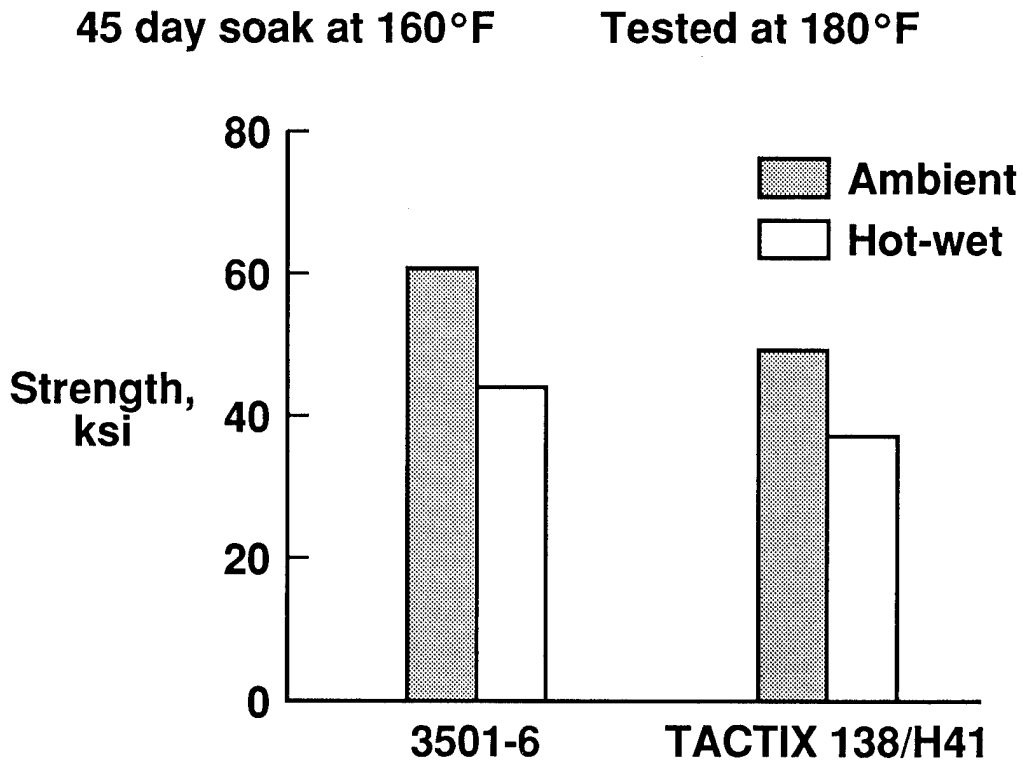


Figure 22

EFFECT OF IMPACT ON COMPRESSION STRENGTH OF HEXCEL HI-TECH FABRIC

The effect of impact on the compression strength of the Hexcel Hi-Tech fabric is shown in figure 23. The knitted and knitted-stitched fabrics are compared to prepreg tape laminates with similar ply orientations. A 30 ft-lb impact reduced the compression strength of the 3501-6 prepreg laminate from 80 ksi to less than 20 ksi. Although the baseline strengths of the 3501-6 and Tactix 138/H41 knitted laminates were 20 ksi lower than the strength of the prepreg tape laminates, compression after impact strengths were slightly higher. Stitching the knitted fabrics resulted in over 100 percent increase in compression after impact strength compared to the prepreg tape laminates. Although the baseline compression strength of the Tactix 138/H41 knitted-stitched laminates was somewhat lower than the strength of the 3501-6 knitted-stitched laminate, the strength after impact was similar for the two resin systems.

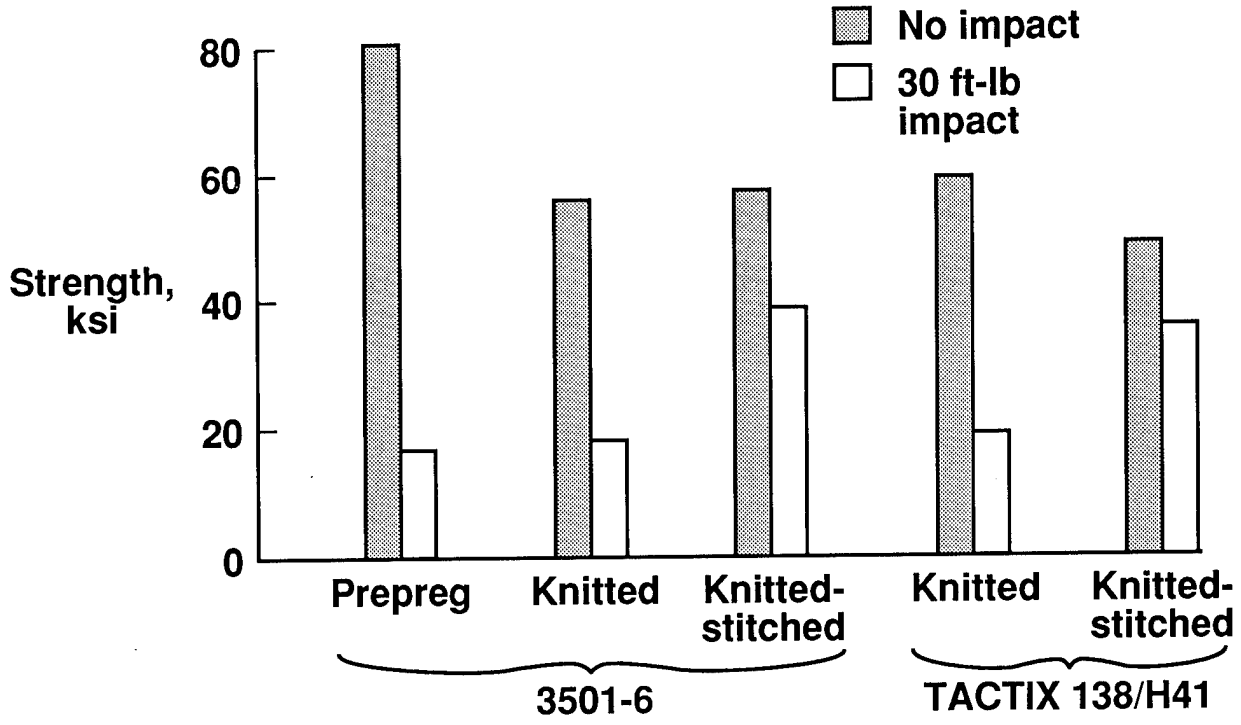


Figure 23

EFFECT OF IMPACT ON COMPRESSION STRENGTH OF MILLIKEN FABRIC

The effect of impact on the compression strength of Milliken fabric is shown in figure 24. As for the Hexcel prepreg tape laminates, a 30 ft-lb impact reduced the strength of the Milliken prepreg tape laminates from 80 ksi to less than 20 ksi. The knitted fabrics with the 3501-6 and E905L resin systems had a compression after impact strength of about 25 ksi. Only one Kevlar 29 stitched panel was fabricated and it had significant surface porosity and internal porosity. Even with the porosity, the knitted-stitched laminate had a compression after impact strength of almost 40 ksi. This result indicates the significant role that through-the-thickness reinforcement plays in improving the damage tolerance of composite materials.

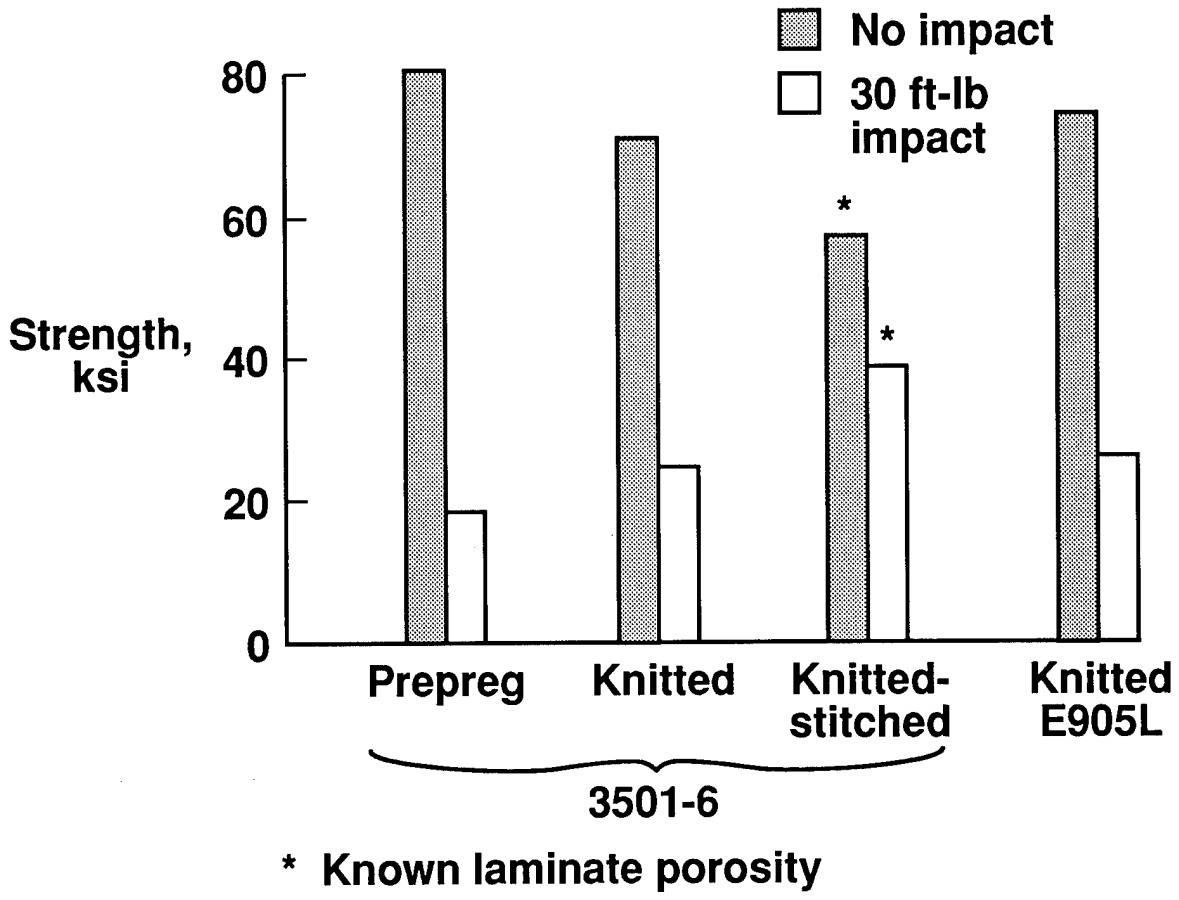


Figure 24

EFFECT OF IMPACT DAMAGE AREA ON COMPRESSION STRENGTH OF HEXCEL HI-TECH AND MILLIKEN FABRICS

The effect of damage area on the compression strength of the Hexcel Hi-Tech and Milliken fabrics is shown in figure 25. The damage areas plotted are a result of a 30 ft-lb impact and were detected by ultransonics and were calculated by computer image analysis. The prepreg tape laminates and the knitted Hexcel Hi-Tech laminates had the most damage and the lowest strength. The least amount of damage, approximately 5 in^2, was sustained by the Hexcel Hi-Tech and Milliken knitted-stitched fabrics. The Milliken knitted-stitched fabric achieved the highest strength, about 40 ksi. The somewhat higher strength and lower damage area of knitted, unstitched Milliken material compared to the knitted, unstitched Hexcel material may be due to three parameters: higher weight knitting yarn, tighter knit spacing and more knitted plies per subgroup.

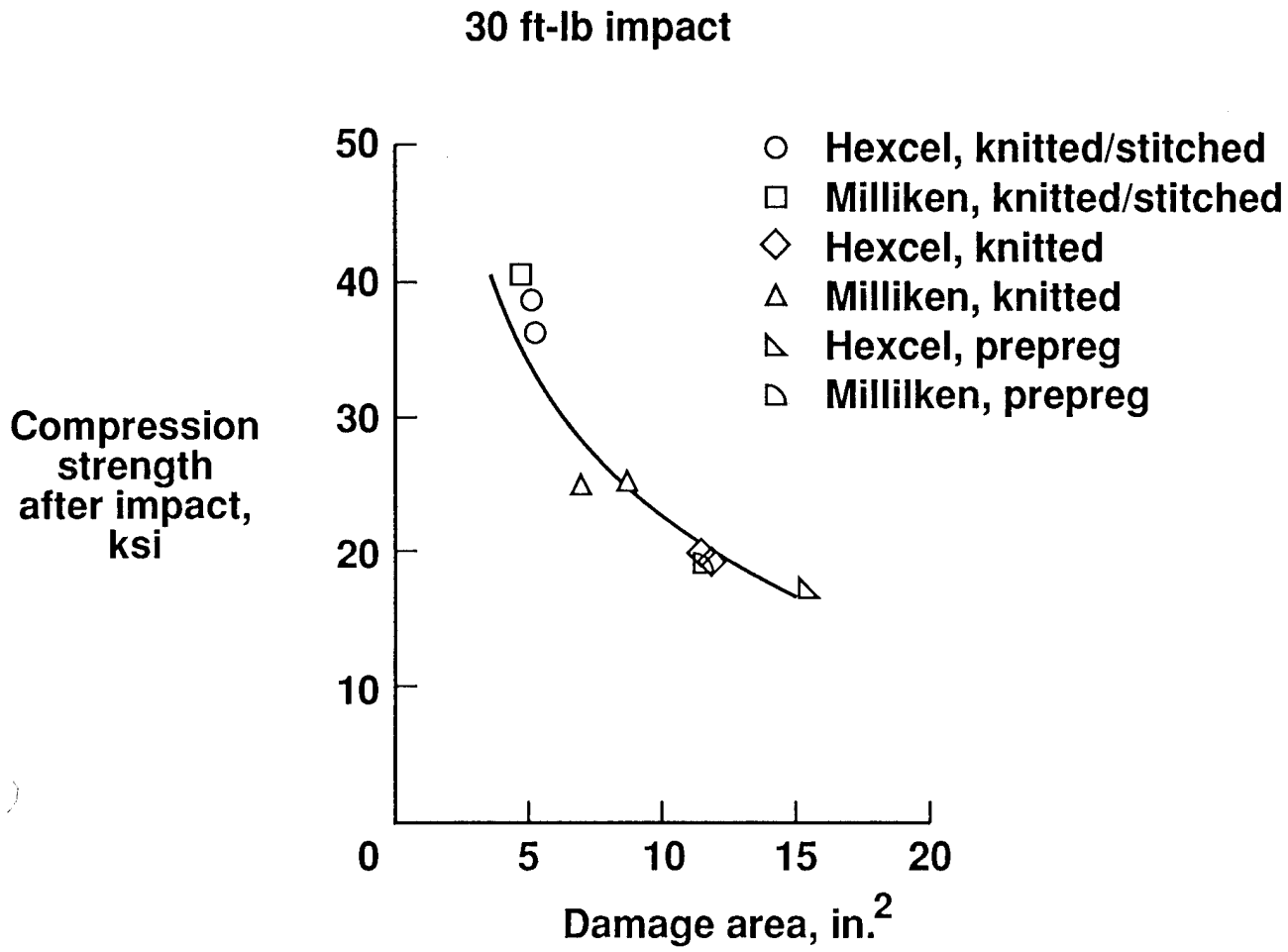


Figure 25

OPEN HOLE TENSILE STRENGTH OF HEXCEL HI-TECH FABRIC

The effect of a 1/4-inch diameter hole on the tensile strength of the Hexcel Hi-Tech fabric is shown in figure 26. The reduction in tensile strength due to the hole is less than would be expected based on loss in cross-sectional area. This result may indicate grip effects on the unnotched tensile strength. The open hole tensile strengths for the 3501-6 and Tactix 138/H41 resin systems are similar to the strengths reported in reference 4 for three AS-4/epoxy laminated tape composite material systems.

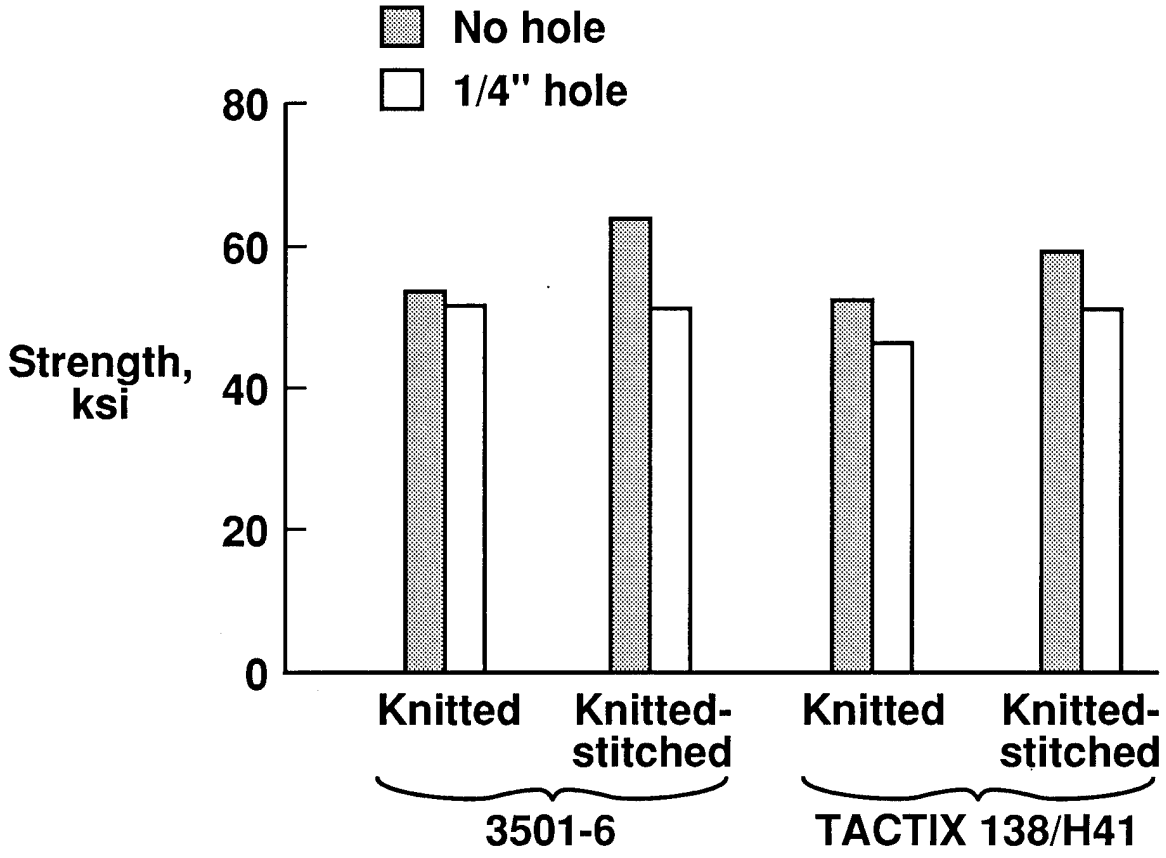


Figure 26

OPEN HOLE COMPRESSION STRENGTH OF HEXCEL HI-TECH AND MILLIKEN FABRICS

The effect of a 1/4-inch diameter hole on the compression strength of the Hexcel Hi-Tech and Milliken fabrics is shown in figure 27. Although the open hole compression specimens are twice as wide as the open hole tension specimens, the strength reduction in compression was significantly more. The open hole compression strengths for the fabrics indicated in figure 27 ranged from 40 to 50 ksi. These results are in agreement with laminated tape data presented in reference 4 for three AS-4/epoxy composite material systems. The Milliken fabric performed slightly better than the Hexcel Hi-Tech fabric.

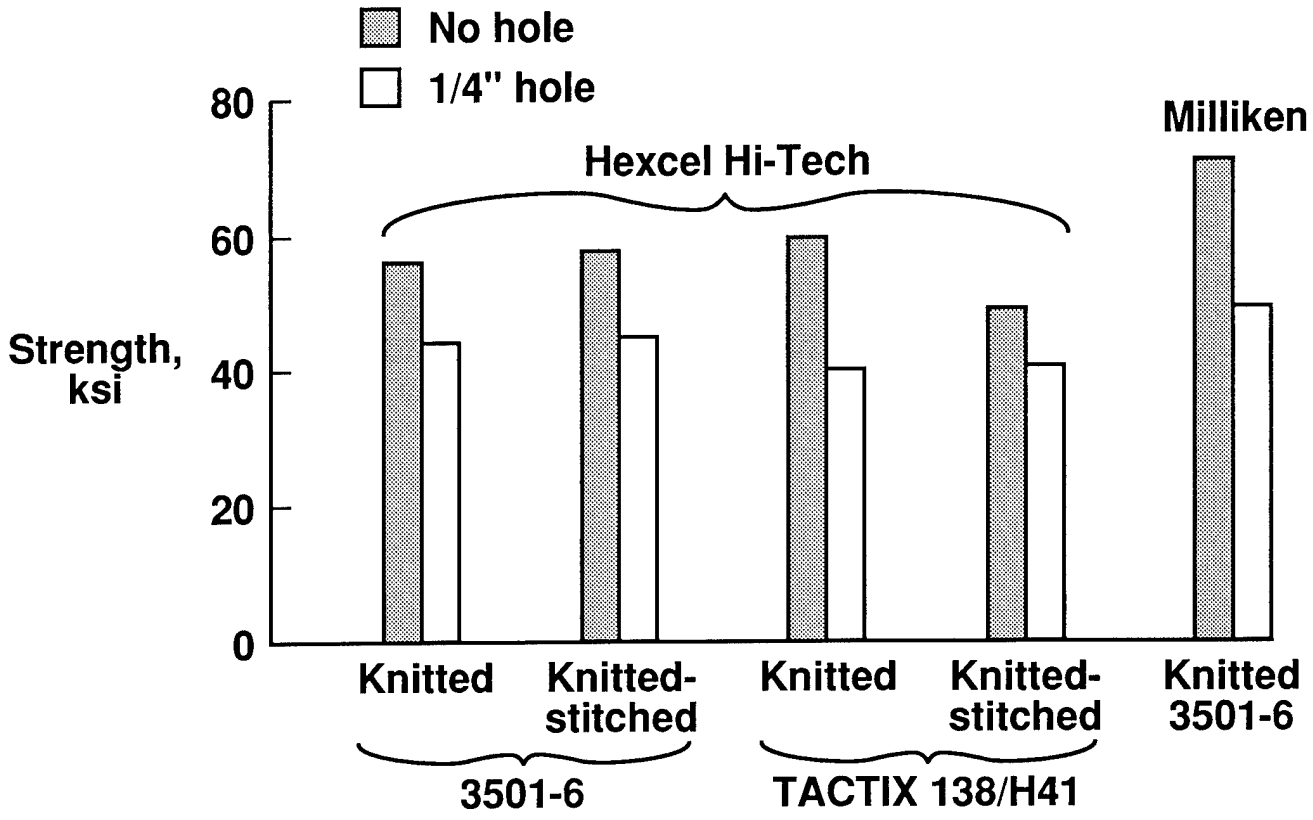


Figure 27

FATIGUE BEHAVIOR OF HEXCEL HI-TECH KNITTED-STITCHED FABRIC

Constant amplitude compression-compression fatigue tests were conducted on the Hexcel Hi-Tech knitted-stitched fabric and the results are shown in figure 28. Hercules AS-4 fiber with both Hercules 3501-6 and Dow Tactix 138/H41 resins were used to fabricate laminates. The test specimens were 1.5 inches wide by 4.0 inches long with a nominal thickness of 0.25-inch. The fatigue tests were run at room temperature in a closed-loop servo-hydraulic test machine at a frequency of 10 Hz. All specimens were tested with an R-ratio (minimum load/maximum load) of 10.

The tests were conducted by subjecting the test specimens to selected stress levels and cycling the specimens until failure. The static compression strength (one cycle to failure) of the 3501-6 specimens was approximately 28-percent higher than the static strength of the Tactix 138/H41 specimens. After the initial knockdown in strength in the Tactix 138/H41 material, the two materials had similar S-N curves. Due to the initial strength knockdown, the 3501-6 specimens had longer fatigue lives for a given stress level. Observation of selected specimens during testing indicated that damage initiated earlier in the 3501-6 specimens; however, the damage did not grow as fast compared to the Tactix 138/H41 specimens. Tactix 138/H41 is a softer (lower modulus) resin, which may account for this behavior.

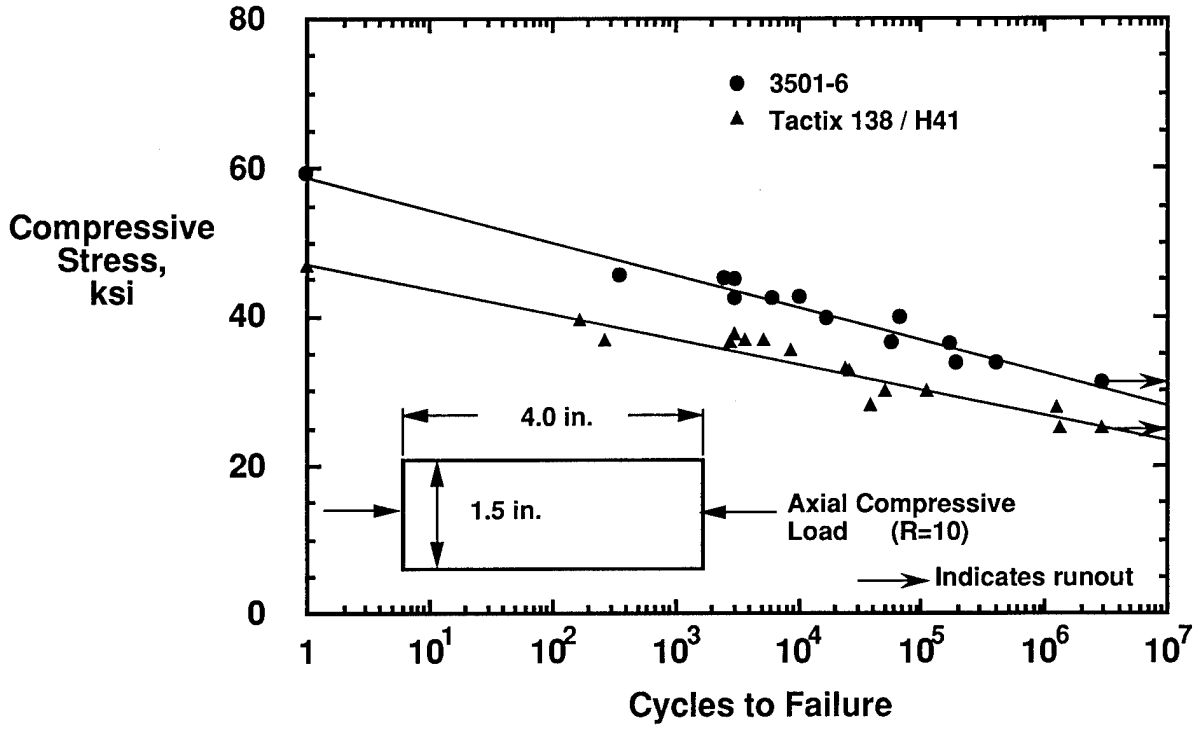


Figure 28

CONCLUDING REMARKS

Two relatively new multiaxial warp knitting processes were evaluated to establish their potential to produce aerospace quality fabrics for composite structural applications. Quasi-isotropic knitted fabrics were procured from Hexcel Hi-Tech and Milliken and composite laminates were fabricated with three different resin systems. Some of the laminates were stitched prior to resin impregnation to assess improvements in damage tolerance that may be achievable. Compaction and permeability studies were conducted on the dry fabric preforms to aid in development of infiltration and cure cycles. Viscosity profiles and cure cycles for each resin were developed to insure high quality composite laminates. Low void content composite laminates were fabricated with vacuum infiltration and pressure resin transfer molding processes.

Prepreg laminated tape composites simulating the multiaxial knitted fabrics were fabricated for property comparisons. The knitted fabric composites had tension and compression strengths that were lower than the tape composite strengths by as much as 32 percent. The knitted-stitched composites exhibited compression after impact strengths that were over 100 percent better than the strength of prepreg tape laminates. Good open hole tension and compression strengths were exhibited by the Hexcel Hi-Tech fabric. In general, the Dow Tactix 138/H41 resin did not perform as well as the Hercules 3501-6 and BP E905L resins.

Only a small quantity of the Milliken fabric was available for evaluation. The preliminary results look promising and additional material will be fabricated for a more thorough investigation. The results of this research investigation indicate that the Hexcel Hi-Tech and Milliken multiaxial warp knit machines can produce high quality broadgoods suitable for many aerospace composite applications. New resin systems that have been formulated for resin transfer molding look promising and significant cost savings may be possible through the use of dry textile preforms and resin transfer molding.

REFERENCES

1. Dexter, H. Benson, and Funk, Joan G.: Impact Resistance and Interlaminar Fracture Toughness of Through-The-Thickness Reinforced Graphite/Epoxy, *AIAA 27th Structures, Structural Dynamics and Materials Conference*, San Antonio, TX, May 19–21, 1986. AIAA Paper 86-1020-CP.
2. Smith, Donald L., and Dexter, H. Benson: Woven Fabric Composites with Improved Fracture Toughness and Damage Tolerance, *Fiber-Tex '88 Conference*, Greenville, SC, Sept. 13–15, 1988, NASA Conference Publication 3038, pp. 75–89.
3. Dow, Marvin B., and Smith, Donald L.: Damage-Tolerant Composite Materials Produced by Stitching Carbon Fabrics, *21st International SAMPE Technical Conference*, Atlantic City, NJ, Sept. 25–28, 1989, pp. 595–605.
4. Williams, Jerry G.; O'Brien, T. Kevin; and Chapman III, A. J.: Comparison of Toughened Composite Laminates Using NASA Standard Damage Tolerance Tests, *ACEE Composite Structures Technology Conference*, Seattle, WA, August 13–16, 1984, NASA Conference Publication 2321, pp. 51–73.

DEVELOPMENT OF STITCHING REINFORCEMENT FOR TRANSPORT WING PANELS

Raymond J. Palmer
Douglas Aircraft Company

Marvin B. Dow
NASA Langley Research Center

Donald L. Smith
Lockheed Engineering and Sciences Company

INTRODUCTION

The NASA Advanced Composites Technology (ACT) Program has the objective of providing the technology required to obtain the full benefit of weight savings and performance improvements offered by composite primary aircraft structures. Achieving the objective is dependent upon developing composite materials and structures which are damage tolerant and economical to manufacture. Researchers at Douglas Aircraft Company and NASA Langley Research Center are investigating stitching reinforcement combined with resin transfer molding to produce materials meeting the ACT Program objective. The Douglas work is being done under a contract entitled Innovative Composites Aircraft Primary Structures (ICAPS).

The Douglas research is aimed at materials, processes and structural concepts for application in both transport wings and fuselages, but the emphasis to date has been on wing panels. Empirical guidelines are being established for stitching reinforcement in structures designed for heavy loads. Results are presented from evaluation tests investigating stitching types, threads and density (penetrations per square inch). Tension strength, compression strength and compression strength after impact data are reported.

EVALUATION OF STITCHING REINFORCED COMPOSITES

New composite material and manufacturing concepts are required to overcome the cost and performance barriers that now limit the application of composites in aircraft primary structures. As shown in figure 1, the approach adopted by Douglas Aircraft Company for achieving affordable and durable composites involves three steps: first, stacking layers of dry carbon fabric in the desired structural orientation, second, stitching the layers of carbon fabric for through-the-thickness reinforcement, and third, resin vacuum impregnation molding of the woven/stitched preform and curing to complete the fabrication. Douglas has developed a patented method for stitching reinforcement and a patented resin transfer molding (RTM) process they call vacuum impregnation molding (VIM). The process uses low viscosity thermosetting resins to fabricate composite laminates.

Breakthrough technology for transport composites using this approach is an important objective of the NASA ACT Program. Certain toughened matrix resins and thermoplastic materials provide the required damage tolerance and structural efficiency. However, these materials cost $100/pound or more and are considered too expensive at this time for widespread application in transport aircraft. Automated manufacturing processes are being explored, but costly, labor intensive manufacturing processes still predominate.

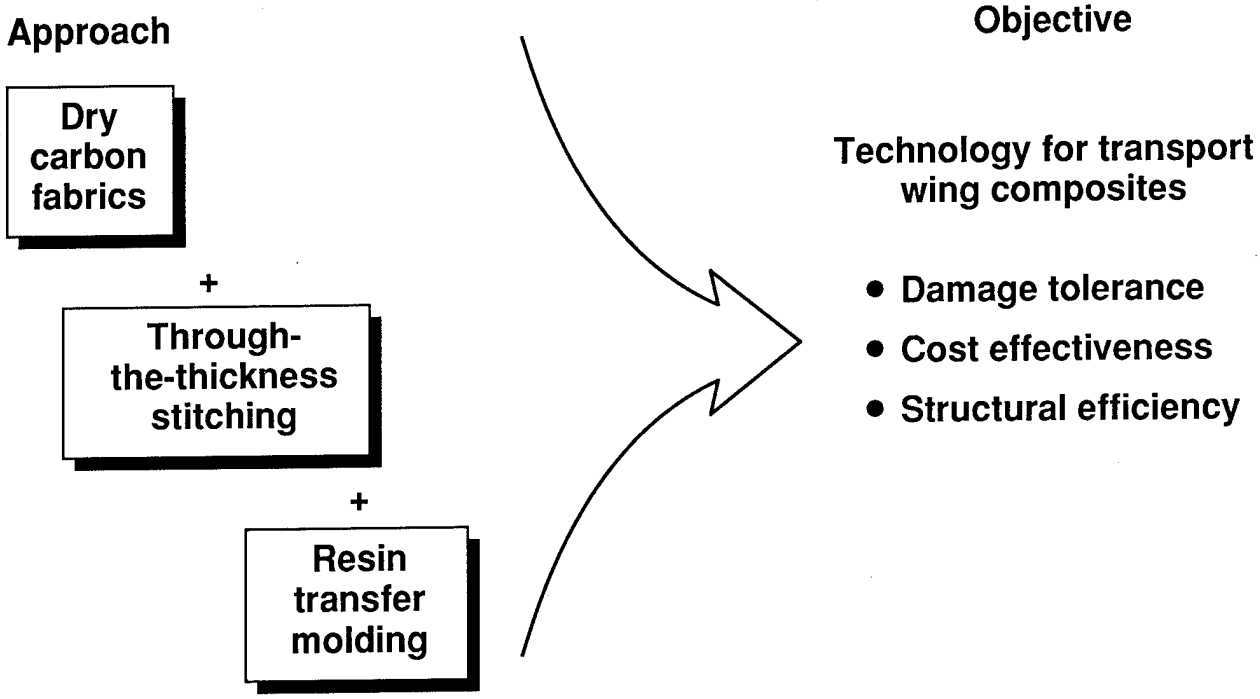


Figure 1

LOCK STITCHING REINFORCEMENT

The first step in making stitched laminates is to stack layers of dry carbon fabric in desired orientations. All the laminates discussed in this paper were stacked with $[45°/0°/-45°/90°]_{6s}$ orientation to produce a symmetric quasi-isotropic layup 48-plies thick. Next, the layers of dry fabric are stitched in the thickness direction as shown in figure 2. Figure 2 depicts an array of lock stitching, but chain stitching is an alternate method; these stitch types are described later in the paper. The stitching is done at a specified stitch pitch (penetrations per inch) and stitching rows are spaced at specified distances. Stitching density, a term used later in the paper, is defined as the number of stitching penetrations per square inch. Finally, the stitched dry preform is filled with epoxy resin by vacuum impregnation molding, a type of resin transfer molding (RTM) described in reference 1.

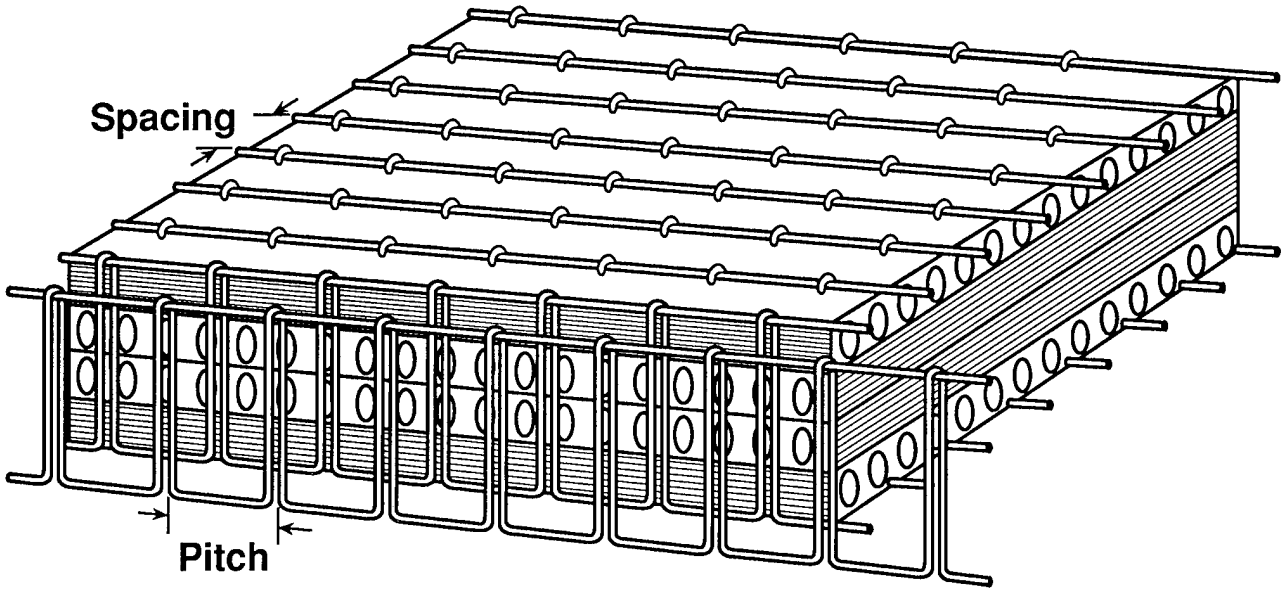
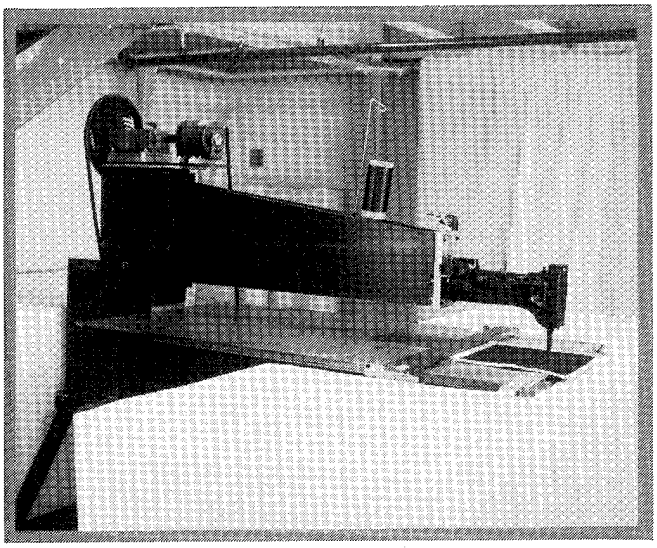


Figure 2

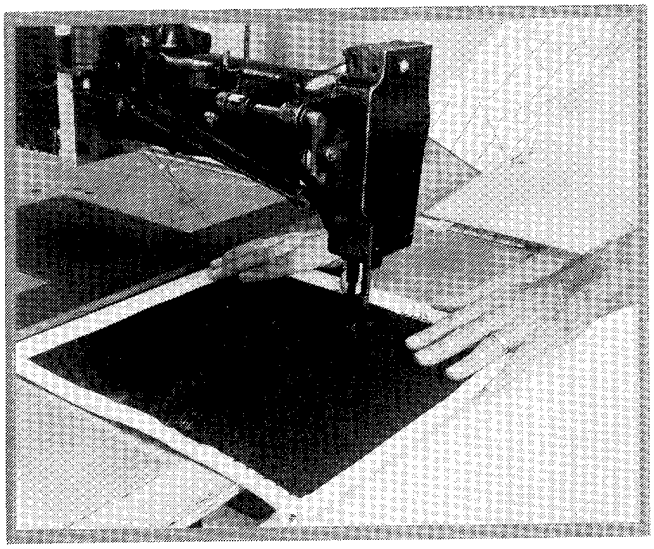
SINGLE NEEDLE LOCK STITCHING MACHINE

Figure 3a shows a single needle lock stitching machine which was used to stitch laminates for the present development. The manually controlled machine has an arm length of five feet and it can stitch through a 0.5 in. thick stack of dry carbon fabric. The stitching speed is variable but the usual speed is 120 penetrations per minute. Figure 3b shows a closeup of the machine stitching with carbon thread into layers of carbon fabric. In this instance, the lock stitches are spaced 1/8 in. apart in parallel rows. A simple guide, which is reset after each pass, is used to maintain the desired spacing.

Single needle machines of the type depicted are satisfactory for the stitching involved in concept evaluations. Obviously, such machines lack the speed and size required in the practical application of stitched aircraft structures. Under the ICAPS contract, Douglas will use stitching machines with considerably greater output to stitch preforms for large wing panels. These machines are described in reference 2.



(a)



(b)

Figure 3

COMPRESSION AFTER IMPACT STRENGTH

Previous studies (ref. 3) of the compression after impact (CAI) strengths of quasi-isotropic laminates of AS4/3501-6, with and without stitching are shown in figure 4. The left-hand figure shows data obtained on laminates without stitching (solid symbols) and laminates stitched in various patterns with 200 denier Kevlar 29 thread. Denier (d), a textile measure, is defined as weight in grams for a 9000 meter length of thread. The figure shows the dramatic loss in compression strength resulting from impact damage on unstitched laminates. Stitching improved the CAI strength, but the values were considerably below the 50 ksi target value.

The right-hand figure shows data from tests of laminates stitched with 1500 denier Kevlar 29 thread. Laminates stitched with closely spaced rows at 8 penetrations per inch showed outstanding CAI strength. In these initial evaluations, the stitching with heavy thread produced considerable fiber damage as evidenced by the drop in compression strength from over 80 ksi to about 65 ksi in tests without impact damage. Nonetheless, these data showed the potential of stitching and RTM to produce damage tolerant and cost effective structures.

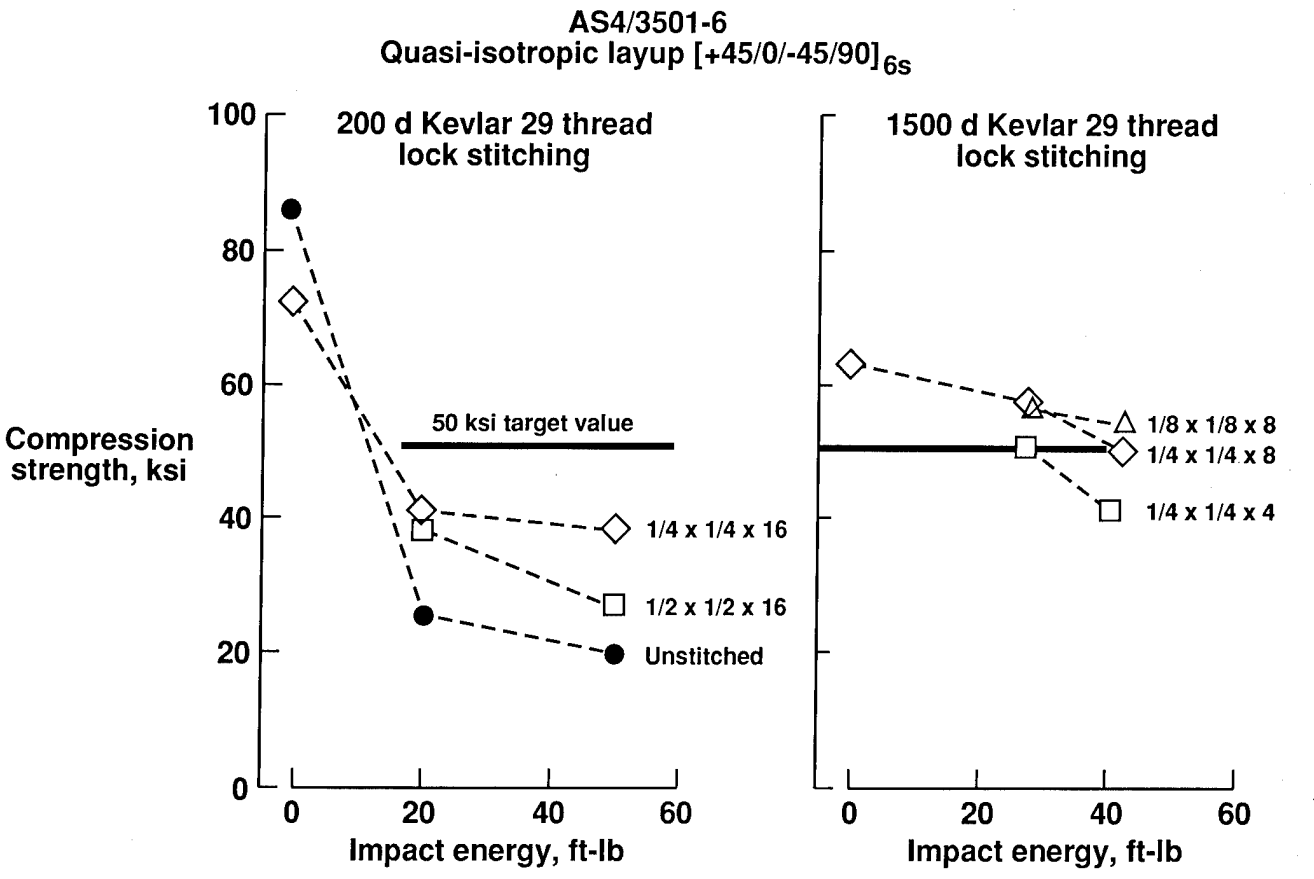


Figure 4

KEY FINDINGS FROM PREVIOUS STITCHING TESTS

During the period from 1986–88, Douglas Aircraft Company, working under a small NASA contract, made a series of stitched/VIM laminates which were tested by NASA Langley. Test results are reported in reference 4. The key findings are summarized in figure 5.

Based on these findings, the following guidelines were set for the present stitching development:

1. AS4 carbon fabric and 3501-6 resin would be the baseline materials.
2. Evaluation tests would be performed using 48-ply laminates in a quasi-isotropic layup.
3. For stitching reinforcement, closely spaced stitches with strong thread would be used, predominately with glass threads.
4. Dry carbon fabric preforms would be stitched in one direction only, parallel to the 0° carbon tows.

- **Strong threads and dense stitching produce good damage tolerance in otherwise brittle composites.**
- **Kevlar, fiberglass and carbon stitching threads are effective for damage tolerance.**
- **Stitching laminates in one direction (parallel to major load path) provides adequate damage tolerance.**
- **Stitching dry fiber preforms followed by RTM processing, holds attractive potential for transport wing structure.**

Figure 5

ACT STITCHING EVALUATION PROGRAM

The scope of the present stitching evaluation study is summarized in figure 6. Data are presented in this paper from the stitching parameter tests and from hot, wet compression tests of stitched laminates with and without impact damage. Results are shown from reference 5 for compression fatigue tests of stitched laminates with impact damage. Elements and panels will be tested to investigate the structural performance of stitched composites. Evaluation tests will be made on laminates incorporating alternate matrix resins selected for their potential to simplify the RTM process or to reduce material costs. Under a separate NASA contract, these matrix resins will be tested following exposure to typical aircraft fluids and fuel. New equipment, capable of rapidly stitching structural preforms, will be acquired and used to make the carbon fabric preforms for the 4 ft by 6 ft panels.

Data available:

- Stitching parameter tests
  - Lock vs chain stitching
  - Stitching thread weight
  - Stitching density
- Hot, wet compression tests with and without damage
- Fatigue tests after impact damage

Fabrication and testing in progress:

- Stiffener pull-off tests
- Performance tests of alternate matrix resins
- Compression tests of blade-stiffened panels (2 ft x 2 ft)
- Installation and checkout of new stitching equipment

Fabrication pending:

- Large stiffened panels (4 ft x 6 ft)

Figure 6

ELEMENTS AND SUBCOMPONENTS

Figure 7 shows the various elements and subcomponents that have been or will be fabricated and tested in the development of stitched/RTM transport wing structures. To evaluate various stitching parameters, small specimens have been tested and the results are presented in this paper. The configurations of these specimens, which were machined from flat laminates, are shown in the top part of figure 7. The 1.75 in. by 1.5 in. (short block) compression specimen is a NASA Langley configuration suitable for tests of angle ply laminates. For tension tests, the 9 in. by 1 in. specimen was used; for compression after impact tests, the 10 in. by 5 in. specimen was used, as recommended in reference 6.

Other elements and subcomponents are in various stages of completion. The stiffener pull off tests are intended to investigate the effectiveness of stitching in maintaining the structural integrity of stiffened panels. The small (2 ft by 2 ft) three-stiffener element panels and the large (4 ft by 6 ft) six-stiffener subcomponent panels will be tested in compression with and without induced damage.

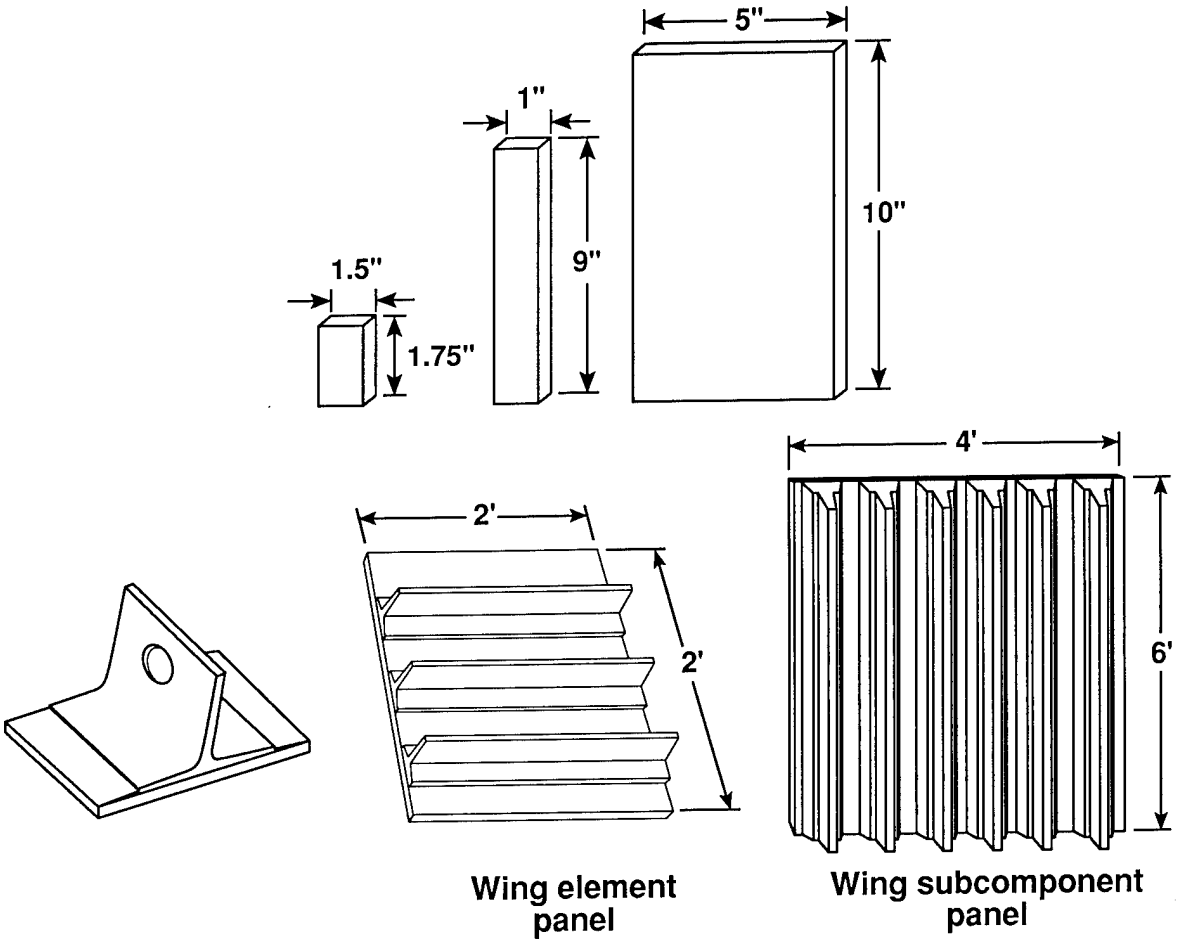


Figure 7

MATERIALS IN STITCHING EVALUATION

The carbon fiber, epoxy resin and stitching threads used in test laminates are listed in figure 8. Vacuum impregnation molding and curing of the test laminates were performed by Douglas Aircraft Company. Specimen testing was done by the NASA Langley Research Center. The AS4 fibers and 3501-6 epoxy resin were the baseline materials used in every evaluation specimen. From a cost standpoint, AS4/3501-6 at about $40/pound (tape prepreg) is an attractive choice. To facilitate stitching, the dry carbon fibers in 3K tows were woven with fiberglass fill tows to form a fabric called uniweave. Initial laminates were made with a fabric containing 95 percent 0° warp carbon and 5 percent 90° fill fiberglass by weight. To reduce crimp in the carbon tows and thereby increase stiffness properties, a second uniweave fabric with 97.5 percent carbon and 2.5 percent glass was obtained and used. Individual layers of 0° fabric were cut and stacked in a $[45°/0°/-45°/90°]_{6s}$ sequence as the preform for a quasi-isotropic laminate. These dry fabric preforms were mostly lock stitched with glass threads of various strengths and weights. A few specimens were lock stitched with Kevlar threads, and one series of specimens was chain stitched with glass thread. To reduce material scrappage, Douglas has recently started using 0°, 45° and 90° fabrics.

Carbon fibers

- 3 K AS4

Epoxy matrix resin

- 3501-6

Dry fabric No. 1

- AS4 uni-weave fabric with fiberglass fill yarn
- 95% carbon-5% glass by weight
- Areal weight carbon: 145 gm/sq m

Dry fabric No. 2

- AS4 uni-weave fabric with fiberglass fill yarn
- 97.5% carbon-2.5% glass by weight
- Areal weight carbon: 145 gm/sq m

Stitching thread materials

- Kevlar 29
- S-2 glass

Stitching

- Lock stitching
- Chain stitching

Stitching thread specifications

	Yd/lb	Breaking strength, lb
S-2 glass-CG-150 8/0	1875	39
S-2 glass-CG-150 10/0	1500	49
S-2 glass-449-1250 untwisted	1250	59
S-2 glass-449-750 untwisted	750	98
Kevlar 29 200d 2 end twisted	11162	12
Kevlar 29 1000d untwisted	4470	36

Figure 8

DRY FABRIC STITCH TYPES

Figure 9 shows the prominent features of the lock and chain stitching used to sew reinforcing threads perpendicular to the layers of dry carbon fabric. Lock stitching employs a bobbin and needle thread and requires access to both surfaces of the layers being sewed. In standard lock stitching, the knots formed by the needle and bobbin threads are located within the layers. However, in the present study, to minimize carbon fiber damage, thread tensions were adjusted to provide a modified lock stitch which positioned the knots on the outer surface of the stacked fabrics. Also, in this instance, the bobbin threads were considerably heavier and stronger than the 200 denier Kevlar needle thread. Chain stitching uses a single thread and requires access to only one surface. Because this feature might provide significant cost savings in production applications, a limited evaluation was performed. Unfortunately, however, most chain stitching machines use a needle motion to move the material being stitched, and current machines cannot be used to stitch fabric preforms of the size required for aircraft structures.

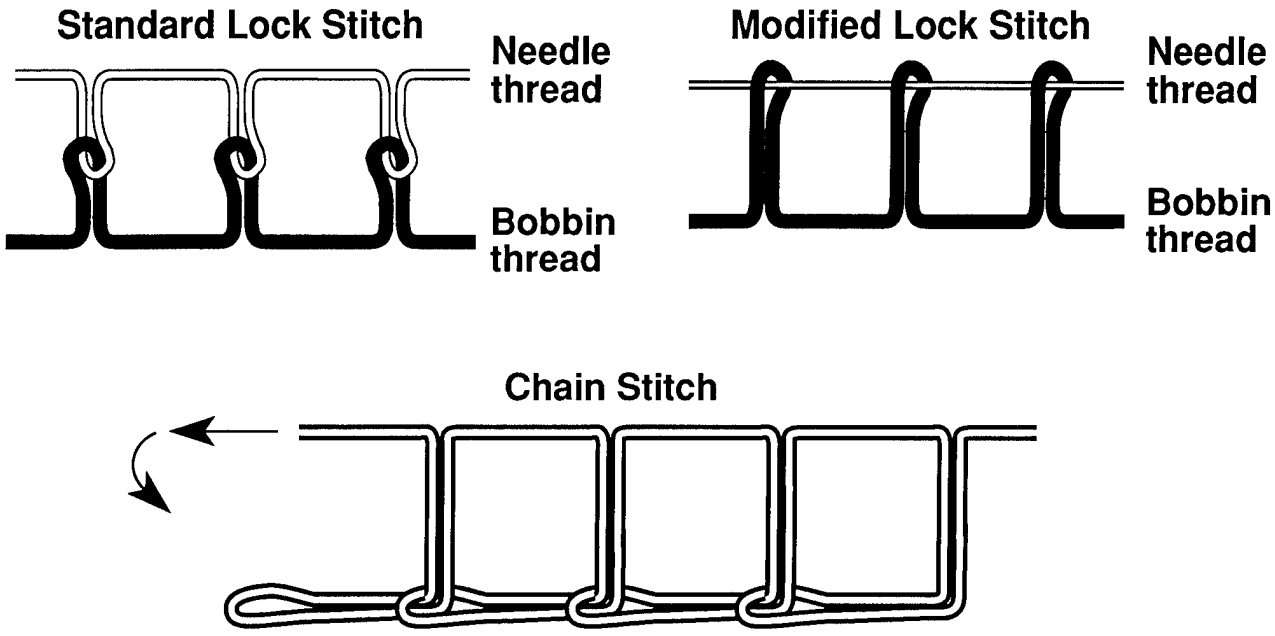


Figure 9

DROP WEIGHT IMPACT APPARATUS

Impact damage was induced in the various test laminates with a drop weight apparatus, which is shown in figure 10. The free-fall distance of the drop weight was adjusted to produce the desired impact energy. The 48-ply laminates were impacted at impact energies up to 70 ft-lb using a 0.5 in. hemispherical steel tip attached to a 10-pound drop weight. Impacts at 100 ft-lb were performed with a 1 in. hemispherical steel tip attached to a 20-pound weight. Post impact testing was performed using a NASA fixture (ref. 6) to support the specimen.

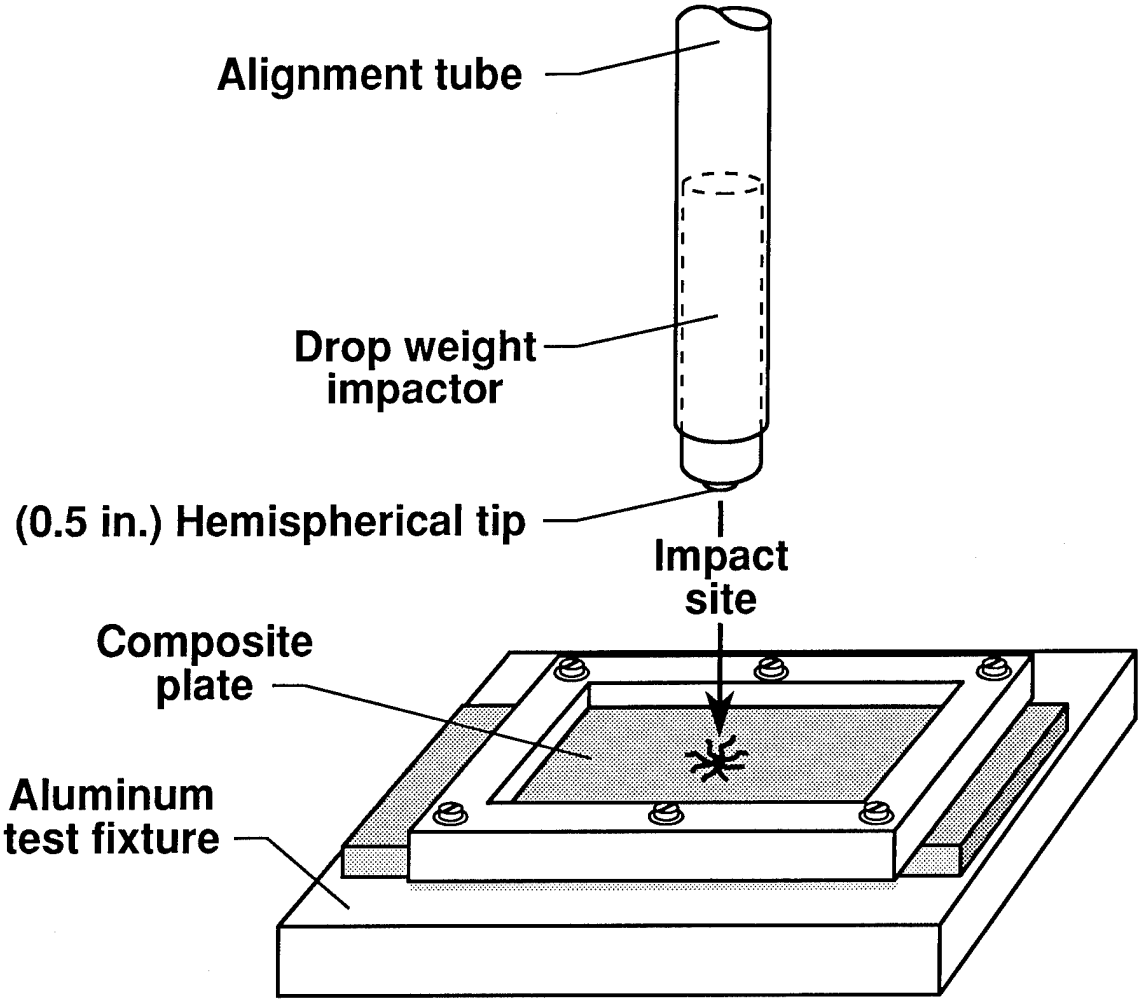


Figure 10

IMPACT PENETRATION OF A STITCHED PLATE

An example of the ability of stitched laminates to limit impact damage is shown in figure 11. In this instance, the panel (lock stitched with glass thread at 1250 yd/lb) was impacted with a 0.5 in. hemispherical impactor at an energy of 100 ft-lb. As shown, the impactor punched through the 48-ply laminate (see back view) and stopped embedded in a tangled mass of laminate fragments and stitching threads (see side view). The panel was subsequently C-scanned (damage area 3.2 sq in.) and tested in compression to failure at 33 ksi. To eliminate penetration, a 1 inch hemispherical impactor was used thereafter for 100 ft-lb impacts.

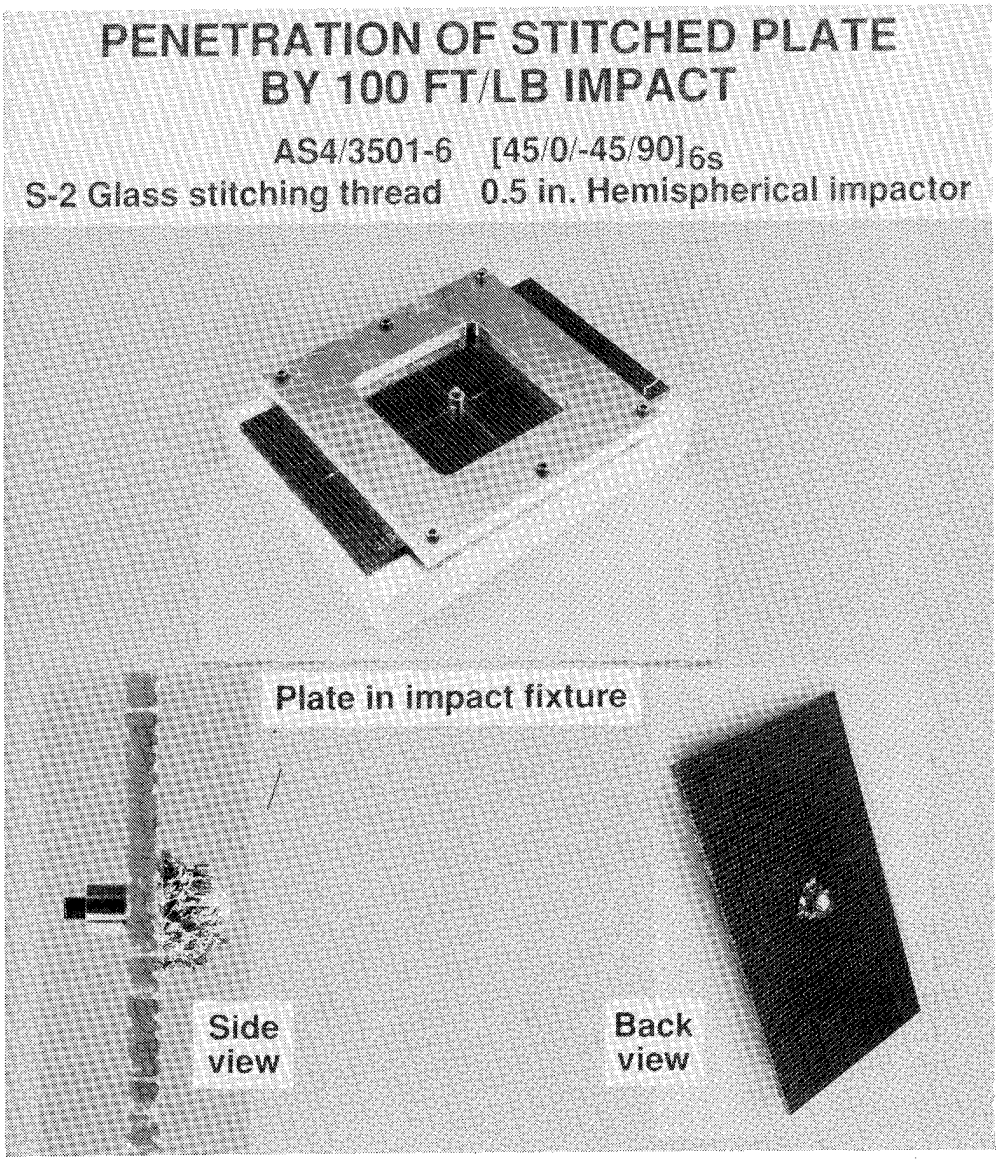


Figure 11

IMPACT-INDUCED DAMAGE OF STITCHED AND UNSTITCHED COMPOSITE PANELS

The capability of through-the-thickness stitching to limit impact damage is shown in figure 12, which presents C-scan images of specimens with and without stitching. Both panels contained 48 plies of AS4 fabric and were resin transfer molded using 3501-6 resin. Prior to the molding, the panel on the left was chain stitched with glass thread (1250 yd/lb) at a density of 64 stitches per square inch. Both panels were impacted at 100 ft-lb in the drop weight apparatus. The damaged area in the unstitched panel (19.6 sq in.) was three times greater than that in the stitched panel (6.4 sq in.). Because of the extensive damage, the unstitched panel was not tested. The stitched panel was tested in compression to failure at 44 ksi.

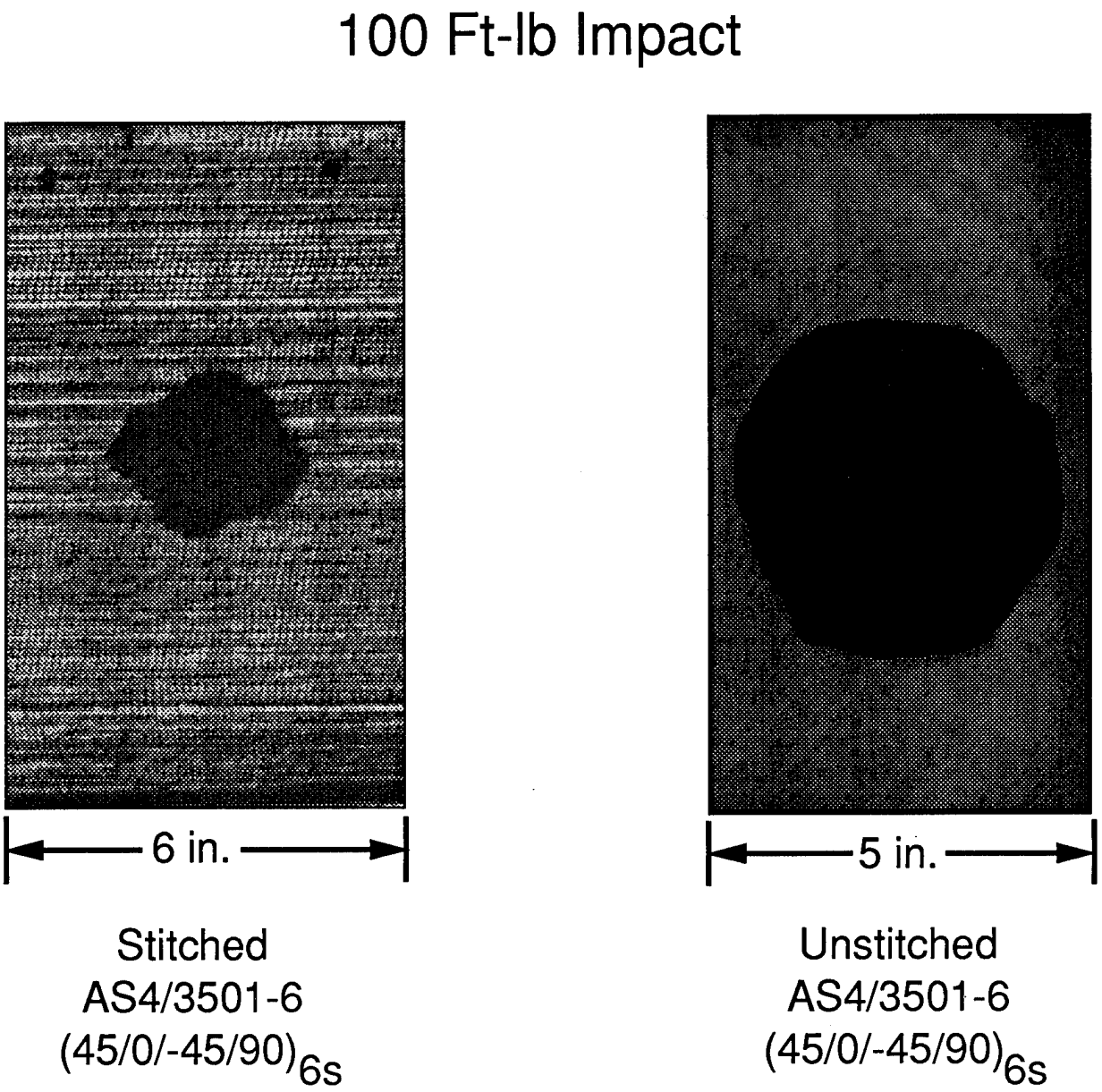


Figure 12

EFFECTS OF STITCH TYPES ON COMPOSITE PROPERTIES

Tension, compression, and compression after impact (CAI) tests were made on 48-ply laminates made using chain stitched and lock stitched fabric preforms. In each instance, identical layers of uniweave fabric no. 1 were stacked in quasi-isotropic layups which were stitched with identical S-2 glass stitching thread at 8 stitches per inch in rows spaced at 1/8 in. Chain stitching was done by Puritan, Inc., while Ketema performed the lock stitching. Vacuum impregnation molding with 3501-6 resin and autoclave curing were performed by Douglas. Test results are shown in figure 13. Neither type of stitching showed a marked advantage in strength or damage tolerance but the best values were obtained with chain stitching. Under severe impact conditions of 40 and 70 ft-lb, both types of stitched laminates demonstrated excellent damage tolerance.

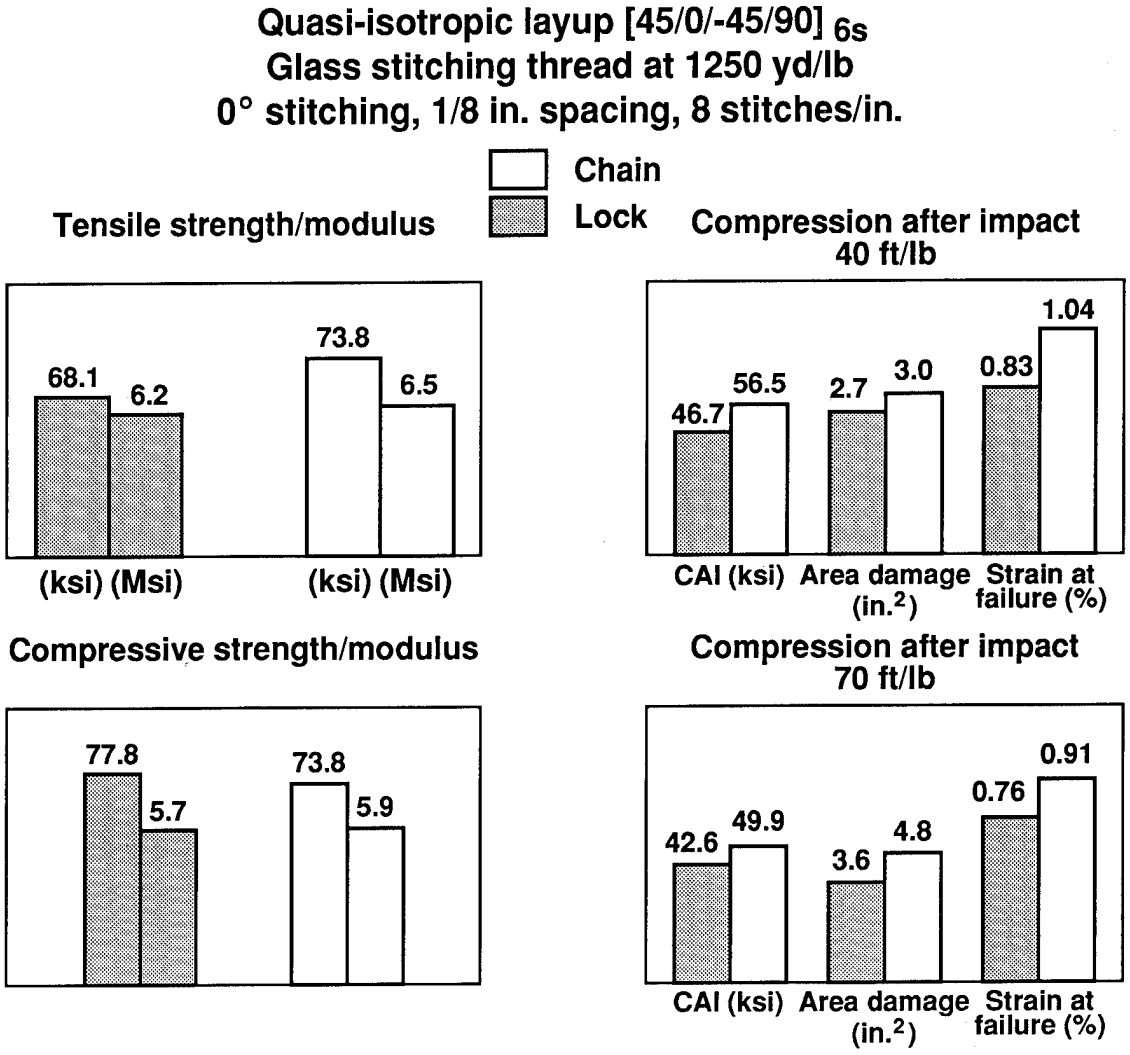
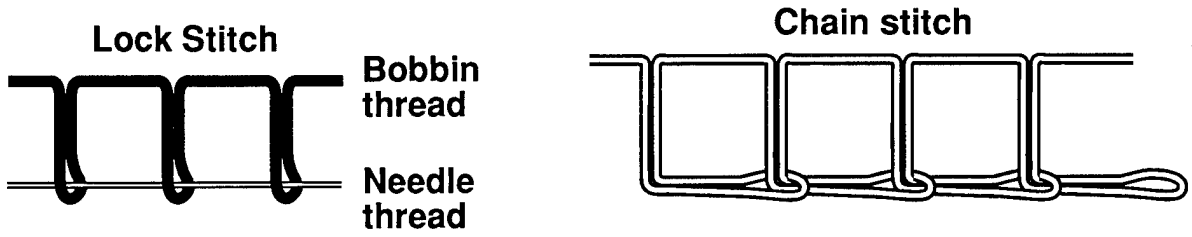


Figure 13

DRY FABRIC STITCH TYPES

In the various tests to compare stitch types, specimens with chain stitching performed as well as those with lock stitching. Nonetheless, lock stitching was selected for subsequent developments for the reasons listed in figure 14. Although lock stitching machines employ bobbins requiring frequent replacement, these machines have the ability to sew in any direction (straight lines, curves, circles, etc). The use of stitched preforms in actual wing structure was the major consideration in the selection. Actual wing preforms will require numerous cutouts, access openings, padup areas, etc. Lock stitching machines were judged to have the best capability to meet the varied stitching requirements. Lock stitching uses less heavy thread than chain stitching and, thus for a given stitching density, would provide a weight savings. Lock stitching machines provide the capability to stitch identification codes into the laminates during the manufacturing process. Stitching in this manner is useful for parts records and traceability.



Lock stitching selected for future fabrication:

- **Accomodates multidirectional stitching-cutouts, padups, etc.**
- **Uses less heavy stitching thread.**
- **Potential for stitching part identification codes-permanent records and traceability.**

Figure 14

EFFECT OF STITCHING THREAD ON STRENGTH PROPERTIES

For this investigation, the 48-ply quasi-isotropic laminates were all lock stitched in rows spaced 1/8 in. apart with eight penetrations per inch, a stitching density of 64 penetrations per square inch. Also, the preforms were made using the dry fabric no. 2, containing 2.5 percent fiberglass fill yarns. The variables were the four stitching threads used: Kevlar-29 at 4470 yd/lb (1000d) and three weights of S-2 glass at 1875, 1500 and 750 yd/lb.

Strength and stiffness data from the tension and compression tests are shown in figure 15. The values are the average from three test specimens. The best results were obtained from laminates stitched with Kevlar thread. In laminates stitched with glass threads, the strength values decreased with increased thread weight. Strength and modulus values obtained with the three lightest stitching threads (Kevlar-29, 1875 glass and 1500 glass) show considerable improvement over the values obtained with carbon fabric no. 1, figure 13. Part of the property improvement is attributed to lighter stitching threads, which cause less kinking and breaking of the carbon fibers; the remainder is contributed by the carbon fabric itself, which has fewer fiberglass fill yarns and less carbon tow crimping.

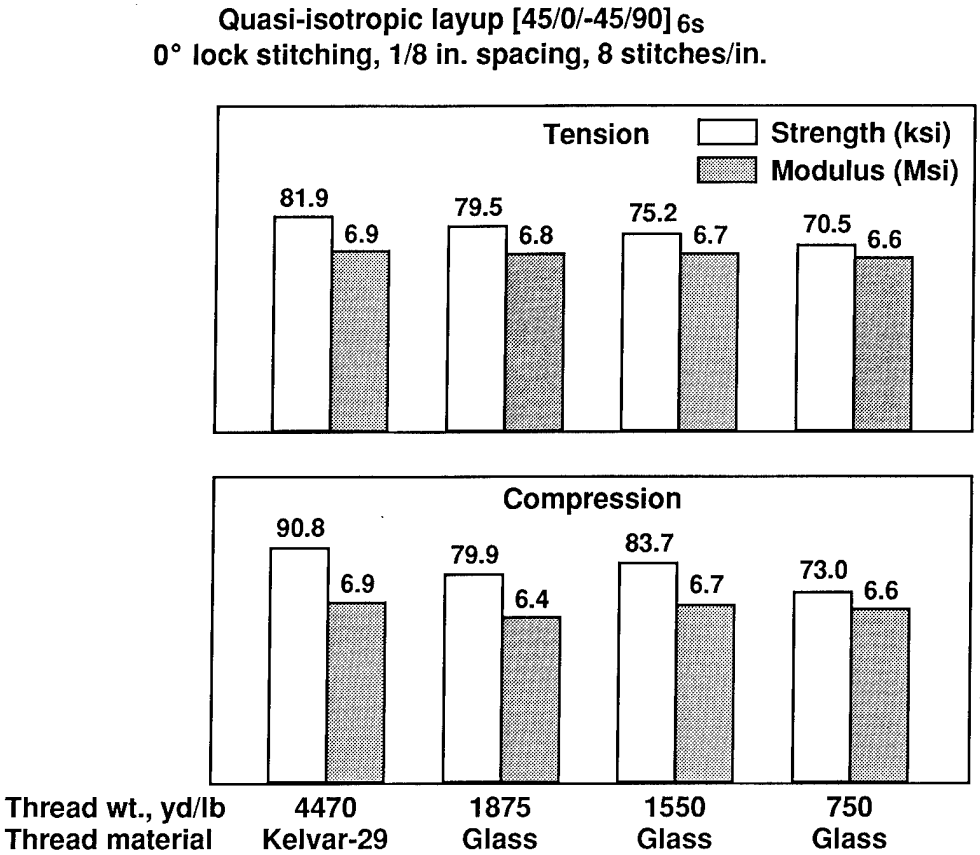


Figure 15

EFFECT OF STITCHING THREAD ON COMPRESSION AFTER IMPACT STRENGTH

Figure 16 shows the results of compression after impact (CAI) tests on 48-ply laminates fabricated as described in the narrative for figure 15. To repeat, the variables were stitching thread material and stitching thread weight. The specimens were impacted by drop weight at energy levels of 40, 70 and 100 ft-lb. These energy levels were chosen to investigate the damage tolerance of stitched laminates under severe conditions. The data show that CAI strength increases with the use of stronger threads. However, only small increases in CAI strength were obtained for large increases in thread strength and weight. For example, CAI strengths with 750 glass are only slightly better than those obtained with 1500 glass, which is half as strong and half as heavy. The laminate stitched with Kevlar thread did not perform as well as those stitched with glass threads but it has a weight advantage over glass thread. These results and those shown in figure 15 indicate that the lighter weight glass threads provided the best combination of strength and damage tolerance.

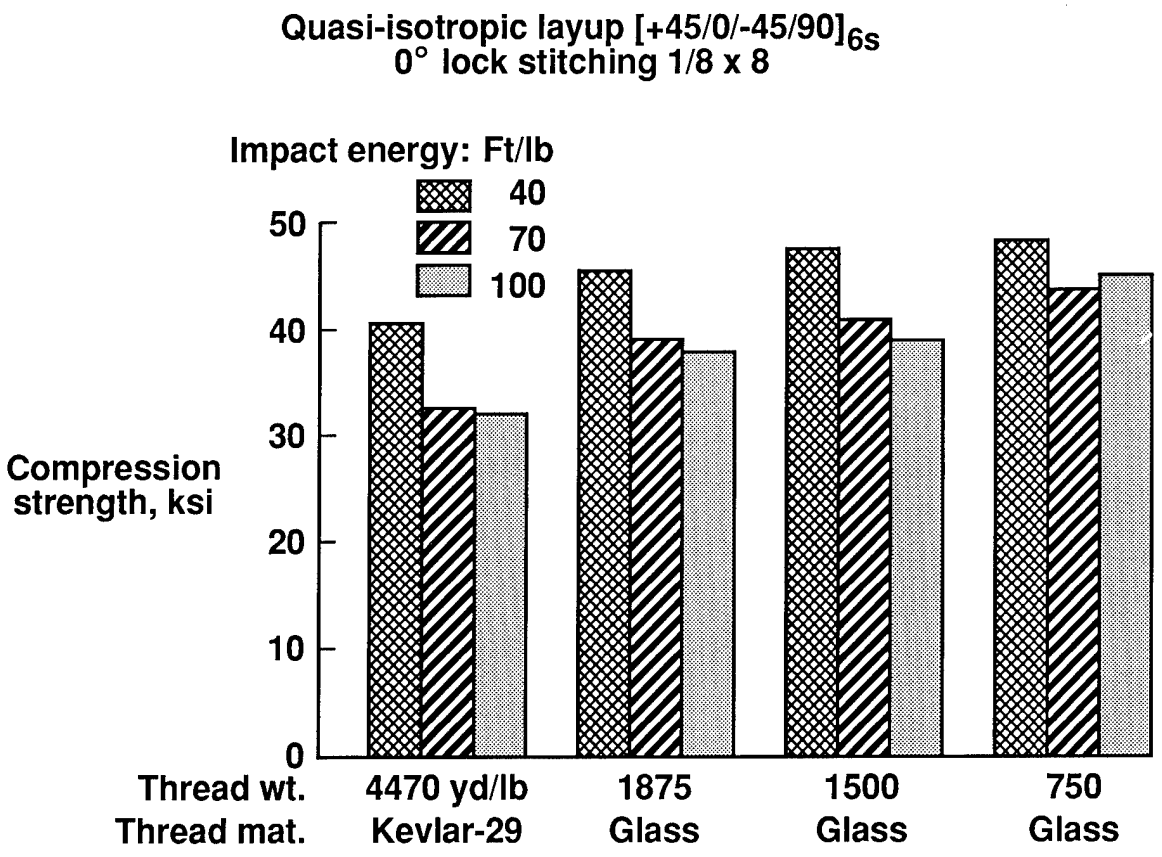


Figure 16

EFFECT OF STITCHING DENSITY ON COMPRESSION AFTER IMPACT STRENGTH

For this evaluation, the stitching density (penetrations per square inch) was the variable with each laminate lock stitched with glass thread at 1250 yd/lb. Stitching density was varied by changing the spacing between rows and by changing the pitch (number of penetrations per inch). The results of CAI tests on these laminates are shown in figure 17. Clearly, increasing the stitching density with a constant thread strength produces an increase in strength. At the highest stitching density, the CAI strength was an impressive 55 ksi at an impact energy of 70 ft-lb. However, the laminate thickness and thus its weight, also increases with increases in stitching density. The Douglas stitching/VIM process for flat plates does not employ fixed volume tooling. Thus, the compaction is limited to that achieved during preform stitching and final autoclave curing. As the amount of stitching thread increases, a thicker preform results and more resin is required to fill the preform during impregnation.

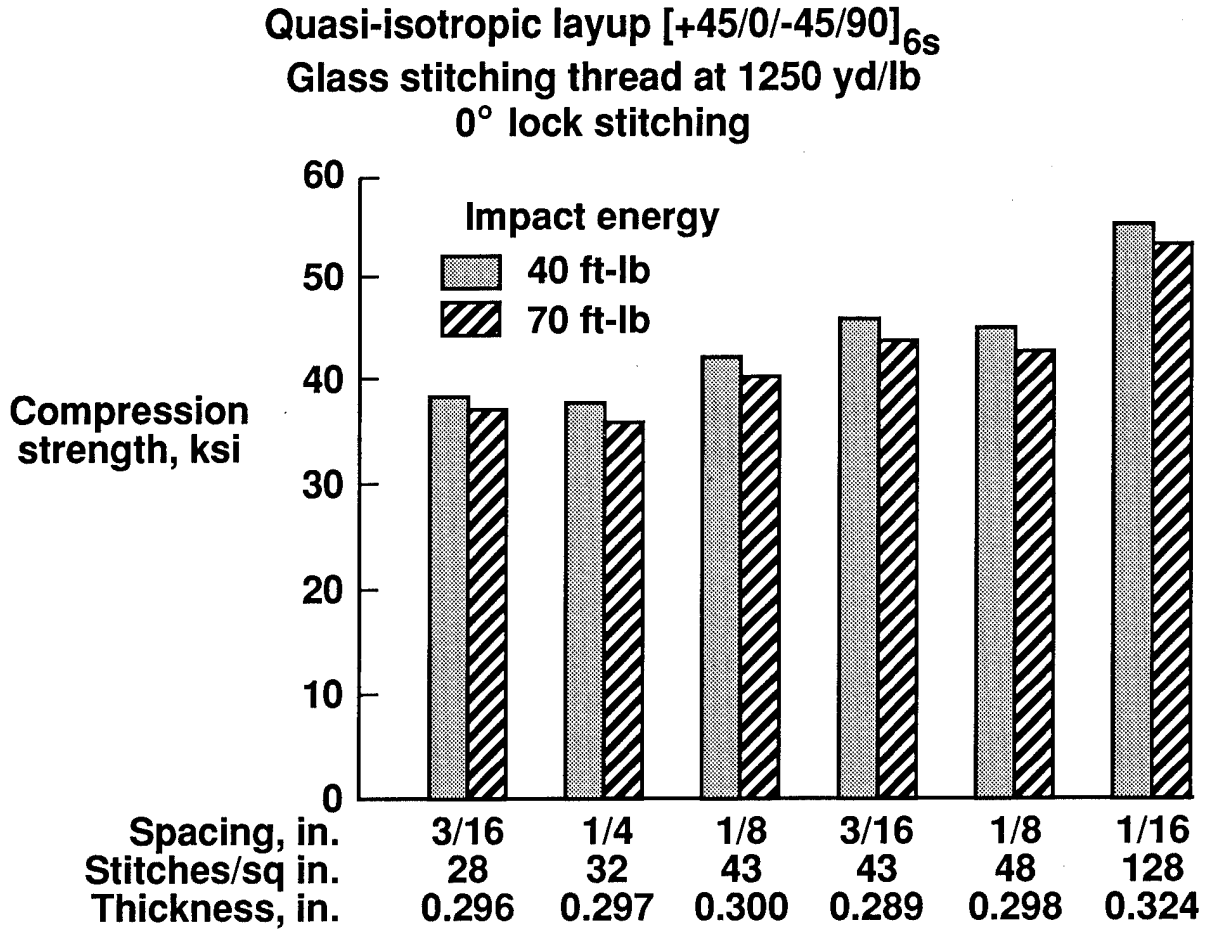


Figure 17

STITCHING DENSITY COMPARISON

A series of specimens was tested to measure strength and stiffness as a function of stitching density. Results are shown in figure 18. The laminates were identical to those discussed in figure 17. Each value is an average of three tests. At the highest stitching density of 128 stitches per square inch, there is a significant reduction in tension and compression properties. Interesting results were obtained in tests of laminates with 43 stitches per square inch. Better strength values were obtained with a 3/16 in. row spacing and 8 stitches per inch than with 1/8 in. row spacing and a stitch every 3/16 in. The results at a density of 28 stitches per square inch indicate also that 3/16 in. is a good spacing for mechanical properties and damage tolerance.

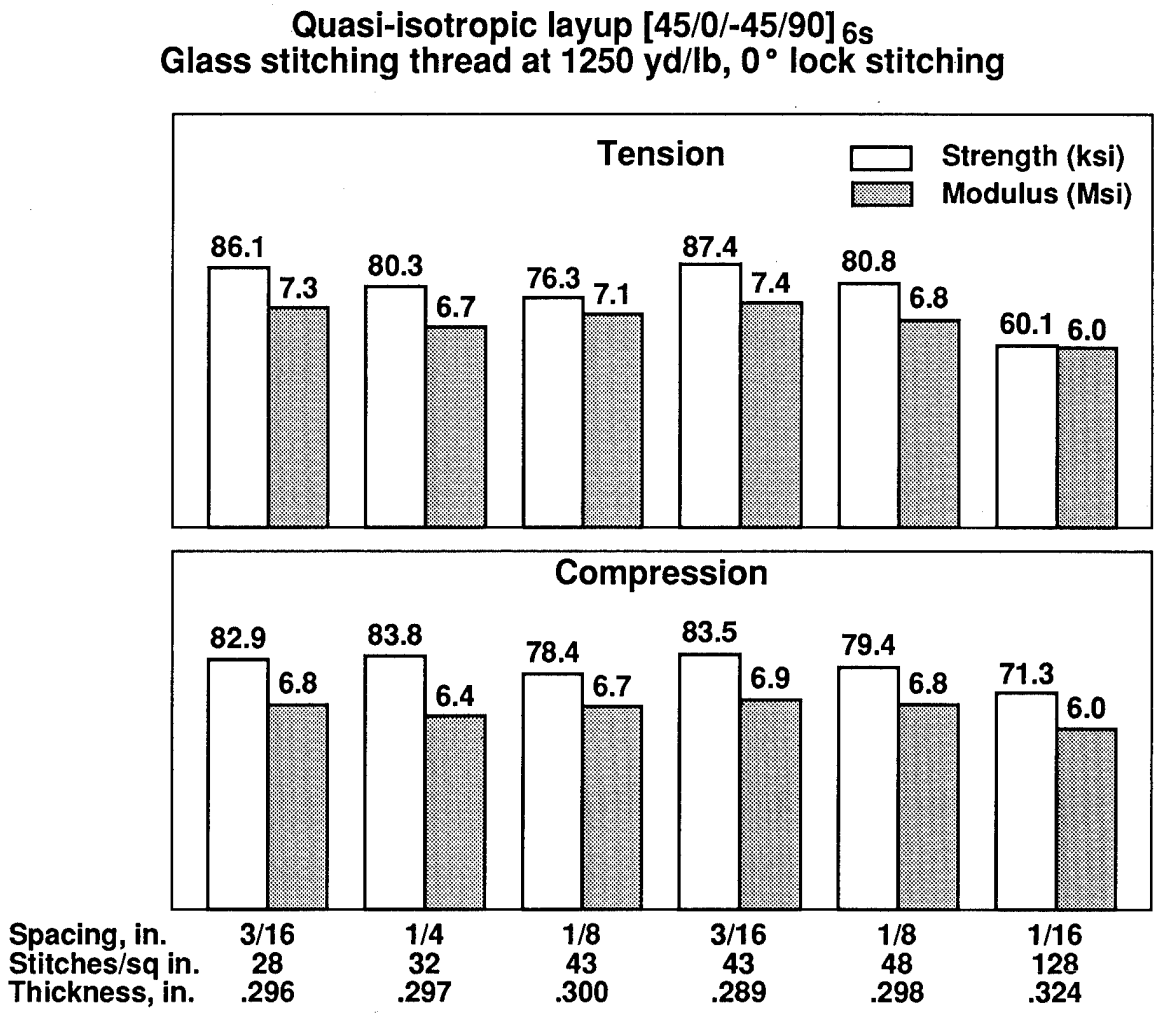


Figure 18

LAMINATE THICKNESS AS A PENALTY IN STRENGTH COMPARISON

The same amount of load carrying carbon fibers was contained in each laminate tested to investigate the effect of stitching density on strength properties. However, a preferred stitching density was not evident from the CAI data (fig. 17) and the strength values (fig. 18). Therefore, the following arbitrary guidelines were used: (1) the stitched laminate must demonstrate a CAI strength equal to or greater than 40 ksi following impact at an energy level of 40 ft-lb, and (2) the laminate must provide the best tension and compression properties for the least weight. For the second guideline, it was assumed that laminate weight varied directly with the thickness. Accordingly, laminate thickness could be considered a penalty in the strength comparison.

In figure 19, the tension and compression strength values from figure 18 are divided by the laminate thickness. This procedure shows that 3/16 in. is a preferred spacing. When the CAI guideline is applied, the stitching density of 43 penetrations per square inch at a spacing of 3/16 in. provides the best combination of properties.

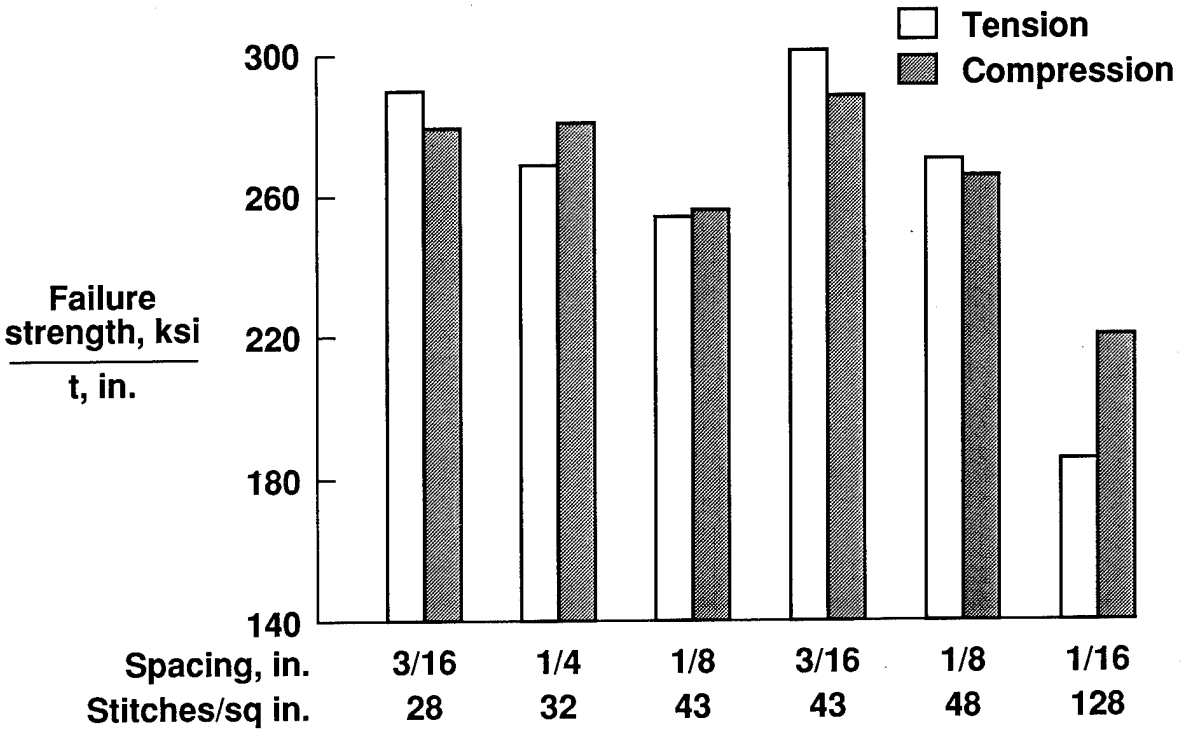


Figure 19

EFFECT OF HOT WATER SOAK ON COMPRESSION AFTER IMPACT STRENGTH

Stitched laminates identical to those discussed with figure 17 were tested at 180°F in a wet condition. The CAI results are shown in figure 20 which also shows the room temperature, dry (RTD) values from figure 17. The RTD condition means the specimens were at room temperature and contained moisture acquired only during exposure to shop and laboratory environments. Hot, wet test specimens were impacted, machined to the required 5 in. by 10 in. size, and immersed for 45 days in water at 160°F. Small follower specimens weighed before and after immersion indicated that moisture gains ranged from 0.9 percent to 1.1 percent, with the lowest weight gain in the laminate stitched with Kevlar-29 thread. Wet specimens were strain gauged after removal from the water and were tested in an expeditious manner (usually in 1 hr). The specimens were heated to 180°F in a heating chamber attached to the test machine.

The hot, wet test results show a substantial reduction in CAI strengths compared to RTD values. The specimens stitched with Kevlar-29 thread experienced the least strength reduction (11 to 16 percent) whereas the greatest strength reduction (20 to 32 percent) occurred in the specimens stitched with the heaviest glass thread, 750 yd/lb. However, these strength reductions are comparable to those measured in similar tests on toughened matrix composite materials, reference 7.

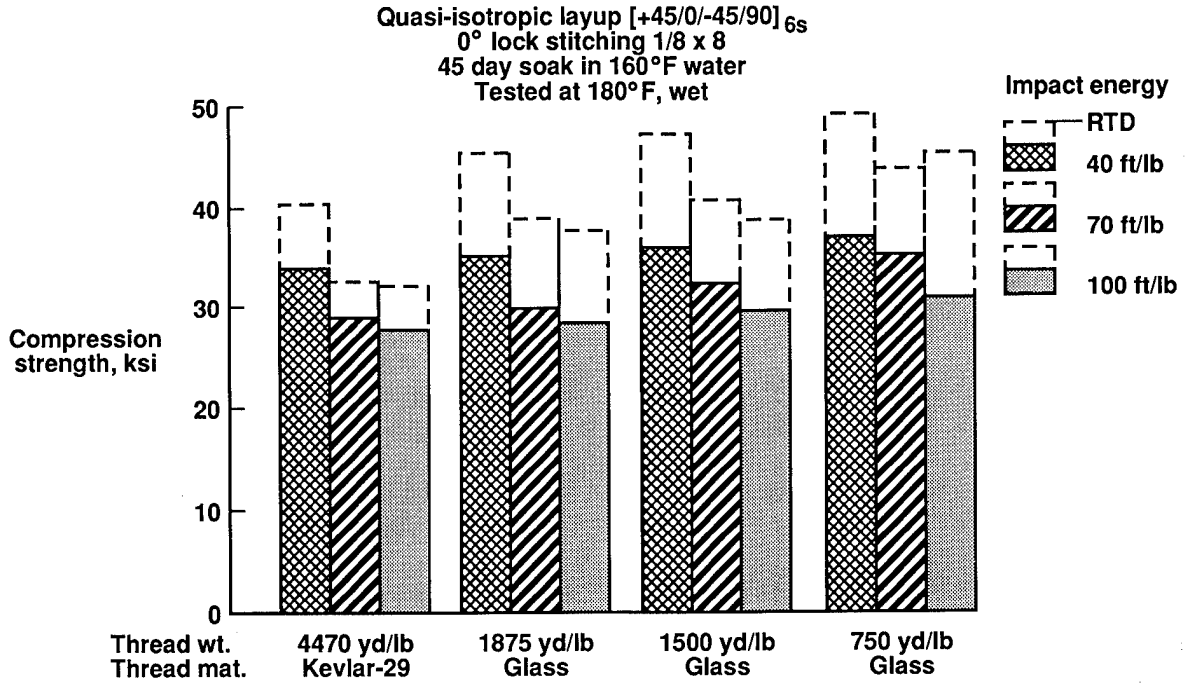


Figure 20

EFFECT OF MOISTURE AND HEAT ON COMPRESSION STRENGTH OF UNSTITCHED AND STITCHED LAMINATES

Tests were performed to determine if the CAI strength reductions measured on stitched specimens in a hot, wet condition (fig. 20) were characteristic of AS4/3501-6 composite material itself or related to the stitching. Quasi-isotropic laminates 48-plies thick were fabricated using the carbon fabric no. 2 with and without stitching. Small 1.75 in. by 1.5 in. compression specimens were machined from the laminates, conditioned variously and tested. The results are shown in figure 21. The water soak was 45 days in water at 160°F; the humidity chamber exposure was 30 days at a relative humidity of 95 percent and a temperature of 140°F. Again, the dry condition means the specimens contained moisture acquired only during exposure to shop and laboratory environments. The test results support the following observations:

1. The unstitched AS4/3501-6 composite material by itself experienced a significant reduction (over 30 percent) in compression strength under hot, wet conditions.

2. In the hot, wet condition the stitched specimen performed as well as the unstitched specimen; therefore, the through-the-thickness stitching appears to have had little harmful effect on the laminate compression strength.

3. The hot, wet strength of unstitched specimens following water soak was only marginally less than that measured following humidity chamber conditioning.

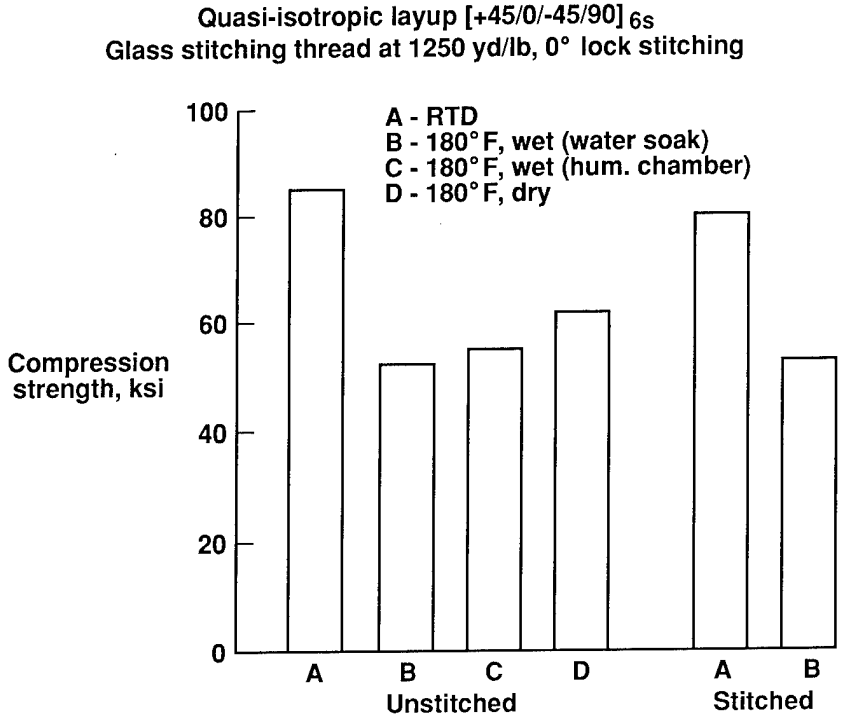


Figure 21

POST IMPACT COMPRESSION FATIGUE OF STITCHED AND UNSTITCHED LAMINATES

Figure 22 shows data from reference 5 on the post impact compression fatigue behavior of 48-ply laminates of a toughened system, IM7/8551-7 (tape prepreg), and AS4/3501-6 stitched with S-2 threads (1250 yards per pound) at a density of 64 penetrations per square inch. In accordance with reference 6, the laminate specimens were impacted by the drop weight and tested in a compression fixture. The fatigue tests were conducted at room temperature in a closed-loop servo-hydraulic test machine at a frequency of 5 Hz. Except for the initial static test (10^0 cycles) all specimens were loaded in compression-compression fatigue with an R-ratio (minimum/maximum) of 10.

Figure 22 shows that both the stitched material and the toughened tape system experienced a reduction in compression strength with constant amplitude compressive fatigue of about 33 percent at a million cycles. Static compression and fatigue strengths of the stitched and unstitched laminates were about equal. The significant finding (ref. 5) was that the crimp and puncture type damage from the stitching had no net effect on the compression fatigue strength.

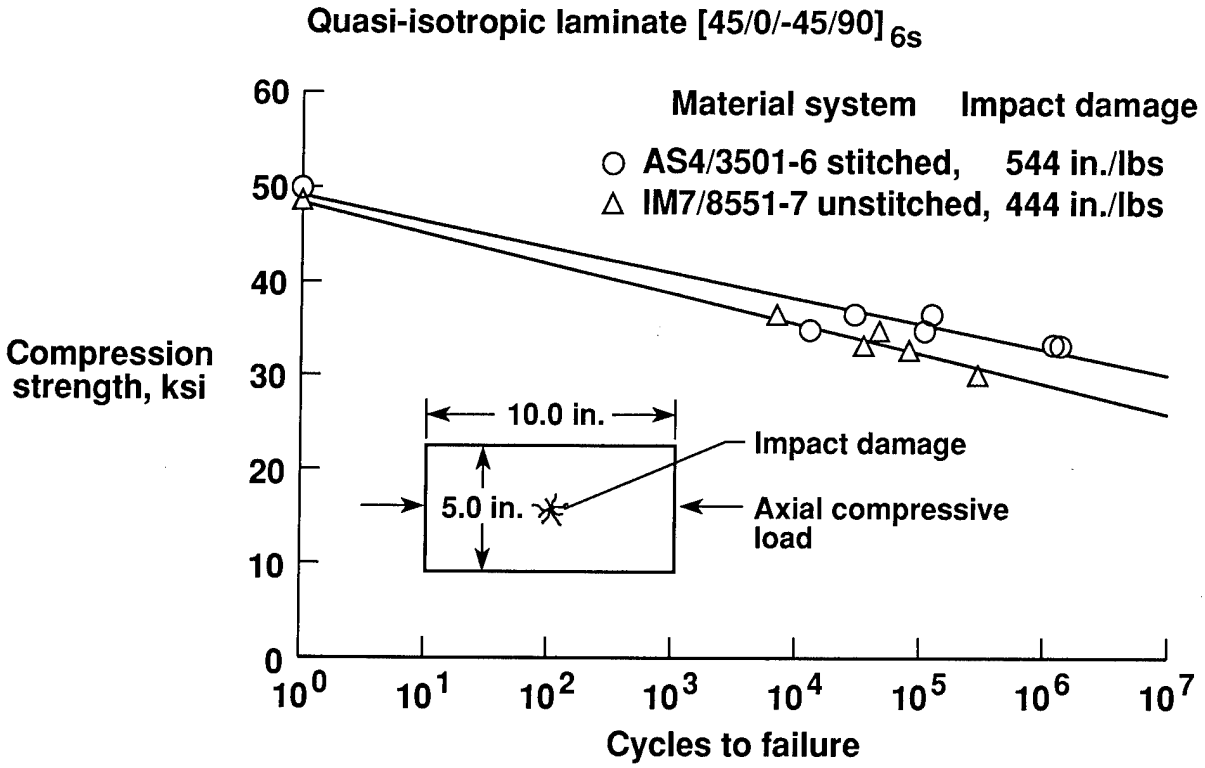


Figure 22

STITCHING CAN SIGNIFICANTLY IMPROVE DAMAGE TOLERANCE OF COMPOSITES

The findings of the ICAPS stitching development are summarized in figure 23. The results obtained clearly show that major improvements in damage tolerance are produced by stitching. Figure 23 shows the compression after impact (CAI) strength of unstitched AS4/3501-6 (curve A) and indicates the drastic loss of strength typical for brittle resin composites. The shaded region B shows the CAI strengths developed by state-of-the-art toughened matrix composites. These materials provide a considerable improvement in CAI strength over the brittle system, but the toughened materials are 2 to 3 times more expensive. Curve C shows the dramatic increase in CAI values obtained with stitched AS4/3501-6 using glass stitching threads at 1250, 1500 and 1875 yards per pound and a stitching density of 64 penetrations per square inch. Data obtained in this study show that stitching reinforcement can produce a 100 percent increase in the CAI strength of a brittle composite such as 3501-6 while incurring a weight increase of only 5–10 percent.

Composite materials are judged to hold great promise when they have a CAI strength of 50 ksi after being impacted at an energy level of 30 ft-lb (1500 in-lb per inch of plate thickness). The stitched materials exceeded the target value. The results to date indicate that stitching combined with RTM processing holds attractive potential for fabricating damage tolerant aircraft structures.

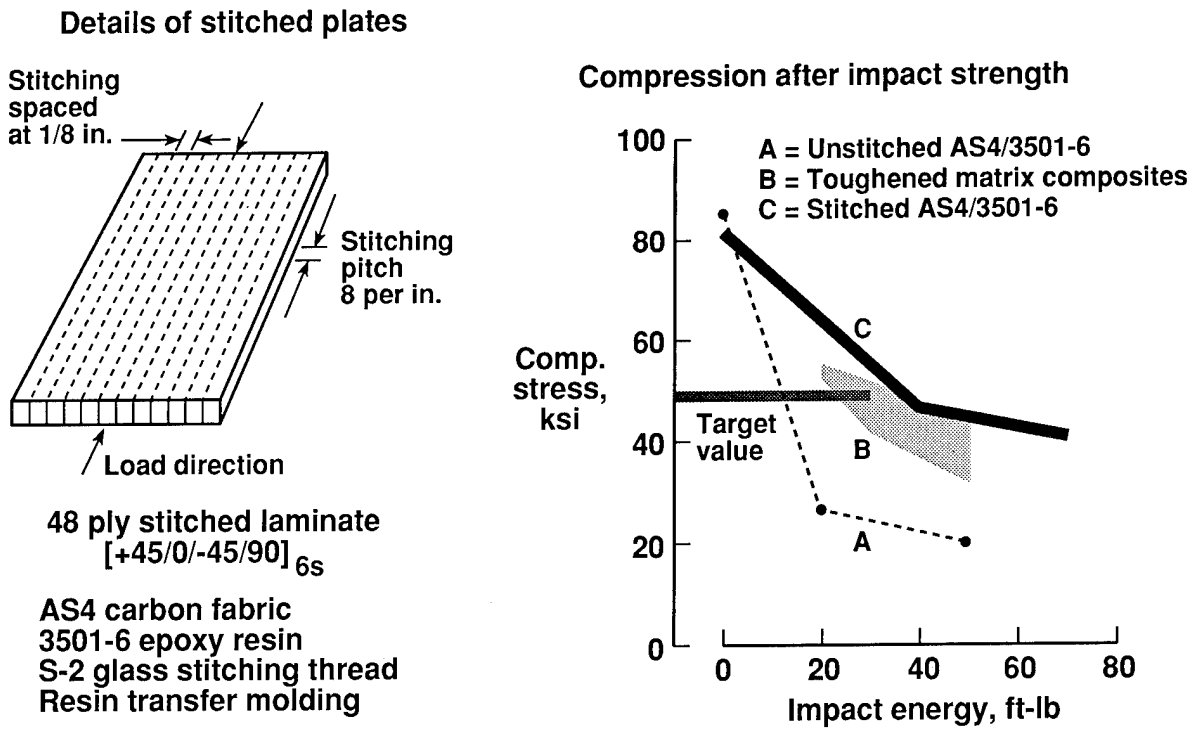


Figure 23

CONCLUDING REMARKS

The findings to date on stitched composites and planned evaluations are summarized in figure 24. To establish the full potential of stitching and vacuum impregnation molding will require an expanded testing effort. Structural integrity and efficiency of wing structures need to be explored. Another important area to explore is the use of low-cost resin matrix materials which can be oven cured. Composite fabrication of the type discussed in this paper are believed to offer exciting possibilities for cost-effective, damage tolerant structures.

- **Completed tests on stitched flat laminates showed:**
  - **Outstanding damage tolerance**
  - **Acceptable fatigue behavior**
  - **Acceptable hot-wet performance**
- **Lock stitching selected for reinforcement.**
- **Guidelines data obtained for strength vs damage tolerance.**
- **Increased laminate thickness (greater weight) is the price for improved damage tolerance.**
- **Planned evaluations:**
  - **Stiffener pull off**
  - **Candidate RTM resins**
  - **Thin (16 plies) and thick (96 plies) laminates**
  - **Stiffened panels with and without damage**

Figure 24

REFERENCES

1. Palmer, R. and Curzio, F.: Cost-Effective Composites Using Multi-Needle Stitching and RTM/VIM, presented at Fiber-Tex 1988 Conference held in Greenville, South Carolina, September 13–15, 1988. NASA CP-3038, June 1989.

2. Klotzsche, et al.: Composites Technology for Transport Primary Structure, Presented at First NASA Advanced Composites Technology Conference held in Seattle, Washington, October 29–November 1, 1990. NASA CP-3104, Part 1, pp. 71-126, January 1991.

3. Dow, M. B., Smith, D. L. and Lubowinski, S. J.: An Evaluation of Stitching Concepts for Damage Tolerant Composites, Presented at Fiber-Tex 1988 Conference held in Greenville, South Carolina, September 13–15, 1988. NASA CP-3038, June 1989.

4. Dow, M. and Smith, D.: Damage-Tolerant Composite Materials Produced By Stitching Caron Fabrics, International SAMPE Technical Conference Series, Volume 21, pages 595–605.

5. Portanova, M.; Poe, C., Jr. and Whitcomb, J.: Open Hole and Post-Impact Compression Fatigue of Stitched and Unstitched Carbon/Epoxy Composites. NASA TM 102676, June 1990.

6. Standard Tests for Toughened Resin Composites—Revised Edition. NASA RP-1092, July 1983.

7. Dow, M. and Smith, D: Properties of Two Composite Materials Made of Toughened Epoxy Resin and High-Strain Graphite Fiber. NASA TP 2826, July 1988.

DEVELOPMENT OF RESINS FOR COMPOSITES BY RESIN TRANSFER MOLDING

Edmund P. Woo, Paul M. Puckett, and Shawn J. Maynard
The Dow Chemical Company

The Dow Chemical Company was awarded a contract (NAS1-18841) by NASA Langley Research Center for the development of "Novel Matrix Resins with Improved Processability and Properties for Primary Aircraft Structures". The TRCO is Dr. Paul Hergenrother.

Designed to cover a wide range of resin technology and to meet the near-term and long-term needs of the aircraft industry, the Dow contract has three objectives as shown below.

Objectives

- RTM resins with improved processability and properties.
- Prepreg systems with high toughness and service temperature.
- New matrix resin concepts.

The contract awarded to Dow Chemical as a part of the ACT Program is divided into three distinct areas. At the facility in Freeport, TX work is being conducted on the development and evaluation of resin systems for use in resin transfer molding (RTM). The work in RTM involves formulating a number of commercial or near-commercial thermoset resins to reach the objectives of processability, service temperature, and toughness. At the facility in Midland, MI work is being conducted on the development of high temperature, highly damage tolerant prepreg composite systems. Also conducted in Midland is the development of new resin concepts which should lead to low viscosity resins that are thermally convertable to high T_g and tough polymers. Promising new resins will be studied for composite applications.

Overall Program

RTM Composite Technology

Task 1. RTM resins for 200°-300°F/wet service.

Prepreg Composite Technology

Task 2. Cyanate-based composite, 400°F/wet, CAI ≥40 ksi.

Task 3. Acetylene-based composite, 450°F/wet, CAI≥40 ksi.

New Resin Concepts

Task 4. BCB-based resins capable of linear polymerization.

Task 5. Arylene ether cyclic monomers.

The RTM task involves development of resin systems from commerical and near-commercial thermoset resins. There is no one perfect material that will be usefull in all processes and for all applications. The goal is to produce several materials which will meet the various needs in the aersopace industry including processing flexiblity, toughness and use in hot/wet service environments.

Objectives

Task 1. RTM Composite Systems

Develop a series of RTM resins for production of advanced composites that will

(a) be useful in "real-world" manufacturing and

(b) meet the needs for toughness and high temperature performance.

The RTM task will evaluate four classes of materials for their applicability to this process. The cyanate resins are a class of high T_g (≥250°C) thermosets that possess a true catalytic cure. These materials have demonstrated process flexibility, good toughenability, excellent composite properties, and retention of properties at elevated service temperatures. The vinyl esters are a well known class of materials that have demonstrated excellent potential for composite applications. New vinyl esters will be developed with higher T_g and toughness than currently available resins. Two classes of epoxy materials will be evaluated: epoxy resin formulations that are tough without the use of rubber for 200°F service environments; high T_g epoxy resin formulations that are rubber toughenable for 300°F service environments.

RTM Systems

Task 1.1. Cyanate-based composite systems

Improved toughness and processability,
Up to 300°F use temperature.

Task 1.2. Vinyl ester of hydrocarbon epoxy novolac

Excellent RT processability and fast cure,
Epoxy-like properties with improved toughness.

Task 1.3. Crosslinkable epoxy thermoplastics

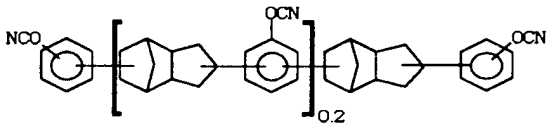
One-phase system with marked toughness improvement.

Task 1.4. High temperature epoxy resins

Up to 300°F use temperature,
Improved toughness and processability,
Based on readily available materials.

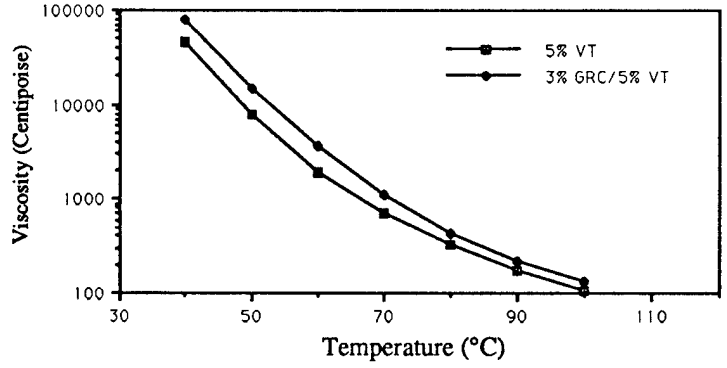
Two cyanate resin formulations have passed the screen established for RTM systems. Both formulations are one-pot systems which contain a latent catalyst. These resin systems are processable at 180-200°F (82-93°C) and provide pot-life of greater than 8 hours. Their room temperature storage stability is greater than 2 months. In addition, these formulations achieve RTM processability without losing the positive attributes of cyanate resin XU71787.02 -- high T_g, high modulus, low moisture absorption, and processing flexibility.

Cyanate RTM Resins



XU71787.02

Viscosity Profiles of Modified Cyanate Resin

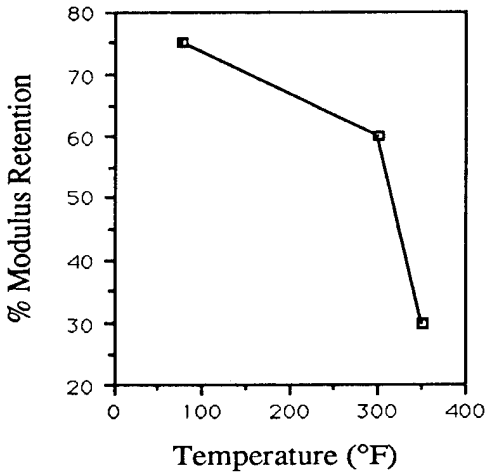


Two cyanate resin systems are being evaluated in composite form. The use of a latent catalyst in the RTM formulation provides a stable viscosity below 500 cps at 180°F (82°C) for molding. Increasing the temperature to 250°-350°F (121°-177°C) cures the resin within a few hours. A freestanding post cure of at least 475°F (246°C) is required for optimum properties. The cyanate with 5% vinyltoluene is the base resin. The same material with 3% GRC, a proprietary core-shell rubber, is being evaluated as a toughened RTM system for 300°F/wet applications. This toughened polymer system has demonstrated good fracture toughness, high modulus, high T_g and low moisture absorption.

Cyanate RTM Resins

5% VT/3% GRC

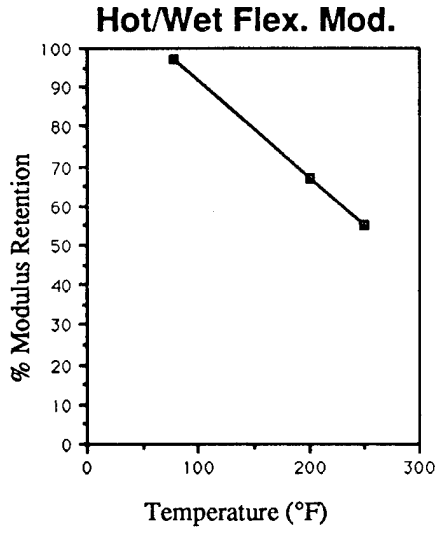
Hot/Wet Flex. Mod.



Tensile Strength	10.9 ksi
Tensile Modulus	434 ksi
Tensile Elongation	3.3%
Flexural Strength	18.2 ksi
Flexural Modulus	441 ksi
G(1c)	245 J/mm
Water Absorption	1.1%
Tg	255°C

Vinyl ester resins, because they are cured via a free radical mechanism, offer a flexibility in RTM processing not obtainble from most thermoset systems. This processing versatility, excellent thermal and mechanical properties, and corrosion resistance of these materials make them excellent candidates for composite fabrication. After screening a large number of vinyl esters, the system chosen for additional evaluation in composite applications is a 5% rubber modified material. This vinyl ester resin has demonstrated good modulus values, high T_g, and low water absorption. The material retains 55% of its room temperature modulus when tested at 250°F (121°C) following moisture saturation.

Vinyl Ester RTM Resin

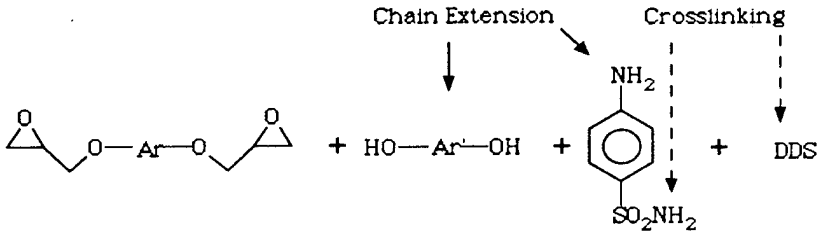


Tensile Strength	8.6 ksi
Tensile Modulus	405 ksi
Tensile Elongation	2.8%
Flexural Strength	18.3 ksi
Flexural Modulus	447 ksi
G(1c)	105 J/mm
Water Absorption	1.2%
Tg	171°C

Epoxy resins are the most widely used materials in advanced composites. A new class of epoxy materials has been developed that overcomes many of the deficiencies found in other "high performance" RTM systems. CET chemistry was originally formulated as a tough, homogeneous, prepreggable resin. The control of chain extension and crosslinking reaction rates provides the unique properties observed for this material. The combination of high polymer modulus, high ductility, and low moisture absorption produces a composite with excellent CAI and hot/wet compressive strength. The reactivity of this amine cured system makes it suitable for resin infusion molding but not, however, for liquid molding.

CET RTM Resins

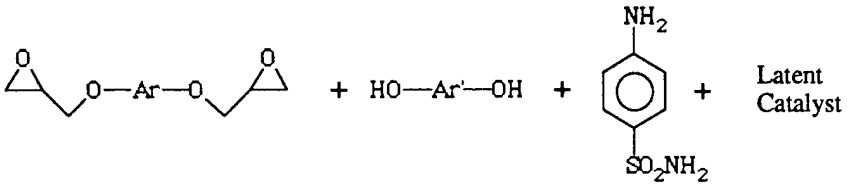
Tactix® 695

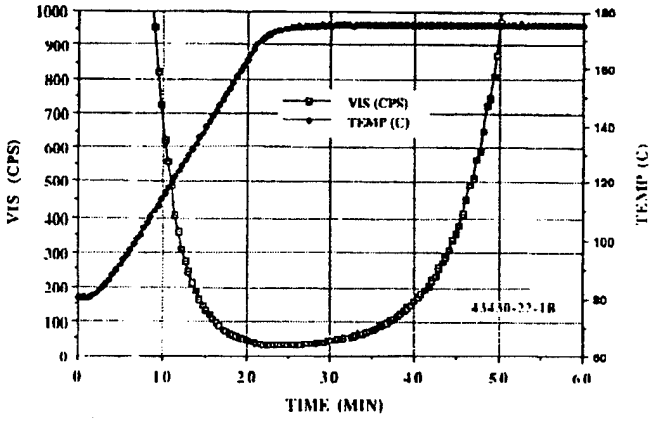


Resin Properties		Composite Properties	
Flexural strength	22 ksi	0° Comp. strength	
Flexural modulus	520	RTD	210 ksi
Water absorption	1.3%	180°F/wet	170 ksi
Tg	170°C	CAI (1500 in-lb/in)	40 ksi

A new CET formulation has now been developed. This material is a one-pot system which contains resin, hardener, and latent catalyst. Control of chain extension and crosslinking reaction rates is also provided in this material. This formulation allows production of a ductile polymer with high modulus and improved resin viscosity stability at elevated temperatures (6% per hour increase at 80°C). Therefore, this material has potential for use in either resin infusion molding or in liquid molding. Molding viscosities of less than 500 cps are obtained at 250°F (121°C).

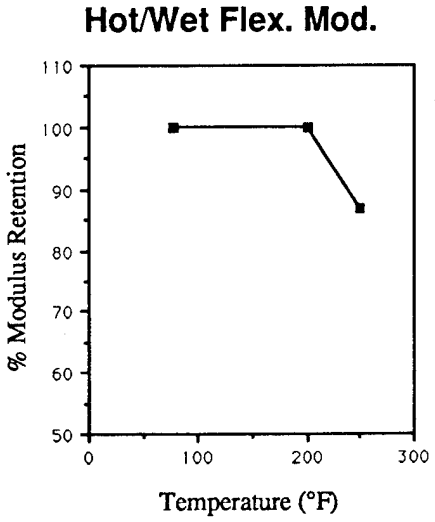
New CET Formulation





A one-pot curable resin composition has been developed that can be molded via resin infusion or liquid injection molding at temperatures greater than 250°F (121°C). It is cured at 350°F (177°C). Freestanding post cure at 400°F (204°C) is recommended for optimum properties. The polymer formed is ductile with a high tensile elongation and toughness which should provide excellent microcracking resistance and damage tolerance in the composite. The high modulus of the polymer should also produce good compressive strength. The very low moisture absorption of the polymer allows a high retention of properties (e.g. modulus) even at 250°F/wet.

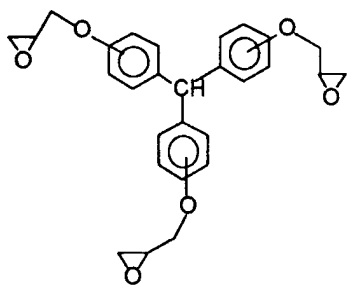
New CET Formulation



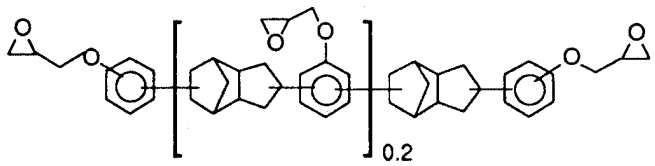
Tensile Strength	13.1 ksi
Tensile Modulus	472 ksi
Tensile Elongation	7.1%
Flexural Strength	20.7 ksi
Flexural Modulus	512 ksi
G(1c)	200 J/mm
Water Absorption	0.7%
Tg	154°C

Liquid epoxy resin systems are now commonly used for RTM applications. The processing advantages provided by low viscosity difunctional epoxies (e.g. bisphenol A and bisphenol F) are sometimes compromised by lower polymer modulus and T_g values. By use of selected higher functional materials that resist water uptake we believe we can produce improved RTMable formulations. These systems when toughened with rubber should generate high modulus, high T_g polymers which in turn should provide durable composites with good retention of properties at elevated service temperatures.

High Temperature RTM Epoxy Resins



Tactix® 742



Tactix® 556

Summary of Accomplishments

- Program balanced between near and longer term.
- Resin development phase for RTM near completion. Preferred resin identified in 3 of the 4 sub-tasks. Composite studies in progress.
- Results of RTM work shared with other ACT contractors and samples sent for evaluation.
- Close to meeting target performance of Task 2.
- Task 3 has led to a ≥450°F/wet, low viscosity resin.
- Discovered low viscosity, high Tg, high toughness BCB-based resins in Task 4.

Advanced Fiber/Matrix Material Systems*

J. Timothy Hartness
BASF Structural Materials, Inc.

Summary

Work completed in Phase I of the NASA-Advanced Composite Technology program is discussed. Two unique towpreg forms (commingled yarns and fused powder towpregs) are being characterized under the program. These towpregs will be used to evaluate textile fabrication technologies for advanced aircraft composite structures. The unique characteristic of both of these material forms is that both fiber and matrix resin are handled in a single operation such as weaving, braiding or fiber placement. The evaluation of both commingled and fused powder towpreg is described. A candidate matrix list has been proposed and is discussed. Various polymer materials were considered for both subsonic and supersonic applications. Polymers initially being evaluated include thermoplastic polyimides such as Larc-TPI and New-TPI, thermoplastics such as PEEK and PEKEKK as well as some toughened crosslinked polyimides. Preliminary mechanical properties as well as tow handling are evaluated.

Introduction

As part of the NASA Advanced Composite Technology (ACT) effort, whose primary effort is to bring about more affordable and damage tolerant composites for the aerospace industry, an effort was undertaken to explore the use of two unique composite prepreg concepts. The two concepts developed by BASF Structural Materials, Inc. address primary objectives of the ACT program. The concept of using these material forms to fabricate composite structures with through the thickness reinforcements results in improved damage tolerance and more cost effectiveness due to the reduction of the labor intensive traditional approach of laying down plies of prepreg. Of course, thermoplastics bring to the table simpler as well as faster manufacturing approaches versus thermoset materials. The range of polymers explored on the program address the current needs of subsonic and supersonic aircraft as well as the flexibility to explore materials for the future that may operate at temperatures as high as 700°F.

---

* Work accomplished under NASA Contract NASI-18834 "Advanced Composite Structural Concepts and Material Technologies for Primary Aircraft Structures"

Material Concepts

Commingled and Fused Powder Tow

In the commingled approach, thermoplastic yarns after being spun are commingled with an appropriate reinforcement. In this work carbon fiber is used exclusively but reinforcements such as glass and ceramic fiber have been evaluated. The ability to use the prescribed amount of filaments thus resulting in a net resin content can be easily achieved. The resulting tow which is very drapable is usually woven into numerous fabrics such as satin weaves, non-crimp style uni or bidirection styles for composite fabrication. Shown in Fig. 1 is a schematic of the commingled yarn. Typical polymer yarn size averages around 20 micron versus 5-7 micron for the carbon fibers.

The fused powder tow expands the technology to those polymers in which spinning is not practical due to technical or economic reasons. Thermosets, for example, are not capable of being spun. Additional benefits of fused powder eliminate the need for binders to contain the powder on the fiber. One of the primary objectives was to produce a towpreg with good powder distribution as well as good handling, such as drapability. This has been achieved with the BASF technology. Shown in Fig. 2 is a schematic of fused powder towpreg. Powder size requirements are a function of each individual polymer.

Fig. 1
Commingled Yarn Technology

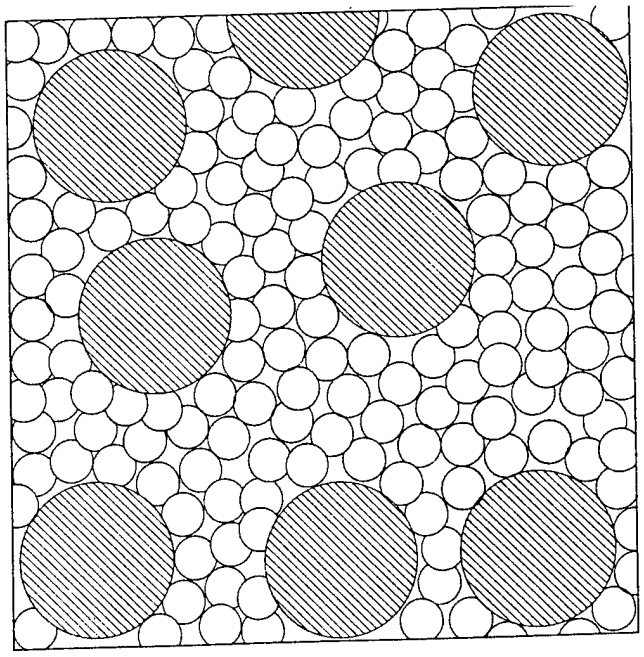
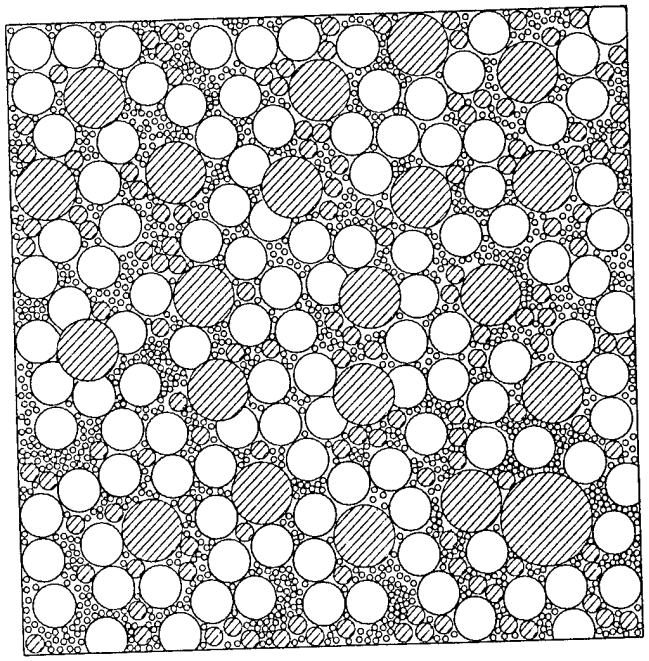


Fig. 2
Fused Powder Technology



Candidate Matrix List

Shown below in Table I is a list of polymers being explored in the program. The objective was to evaluate the commingled as well as the fused powder approach and also to address polymer systems that would have applications for subsonic and supersonic aircraft. Polymers such as PEEK and PEKEKK offer opportunities in the subsonic area. Both are semicrystalline in nature and offer exceptional toughness as well as moisture and solvent resistance. An established data base exists with PEEK. The PEKEKK offers a higher use temperature and somewhat greater toughness over PEEK based on CAI data.

New-TPI is a thermoplastic polyimide that has a use temperature in excess of 400°F. The commingled form is limited to the lower mol. wt. range. Initial mechanical properties indicate excellent potential for this system. Processing temperatures are high due to the high melt point of the polymer. Very little crystallinity remains after processing, and despite this the polymer has excellent solvent resistance.

Larc-TPI-1500 is also a thermoplastic polyimide. Recent modifications such as endcapping the polymer make it very melt stable. The medium molecular weight version has been chosen due to improved neat resin strain and toughness. As can be seen, a considerably lower melt point exists with this polymer, resulting in successful composite processing at 700°F versus 760°F for the New-TPI polyimide. NBI stands for norboreneimide and NBI #1 represents a toughened version of the fully imidized prepolymer. Only neat resin initial characterization has been accomplished.

Table I

Candidate Matrix List

Trade Name	Polymer	Tg°c	Tm°c	Comments
Victrix (ICI)	PEEK 450	143	343	Task 2 Powder
Ultrapek (BASF)	PEKEKK	175	380	Task 2 Commingle
New TPI-X	Polyimide	250	380	Task 1 Commingle
Larc-TPI-1500 (Mitsui Toatsu)	Polyimide	250	325*	Task 1 Powder
Toughened NBI #1	TP mod. Polyimide	350	- -	Task 1 Powder

*No crystallinity in processed composite

Fused Towpreg

Initial Mechanical Properties

Two thermoplastic powders, PEEK 150 and Larc-TPI-1500, were fused onto AS-4 (3K) unsized carbon fiber. Both towpregs were frame wrapped in a unidirectional pattern prior to molding with graphite tooling in a conventional press. The objective was to generate fiber and resin dominated properties as an initial attempt to evaluate the process. Shown below in Table II are initial mechanical properties on both materials as well as developed process cycles. Other than the low 90° tensile properties from the Larc-TPI, the properties are very good with a high percent translation. In both cases void free laminates were fabricated. Fracture toughness as measured by DCB specimens has been measured. The PEEK data is representative of literature values. The Larc-TPI medium mol. wt. is considerably better than the low mol. wt. data (1) reference.

Table II
FUSED TOWPREG
INITIAL MECHANICAL PROPERTIES

Property	PEEK-150 AS-4	LARC-TPI-150 AS-4
0° - Flexural Strength* (Ksi)	350	296.6
- Flexural Modulus (Msi)	16.2	17.7
90° - Tensile Strength (Ksi)	11.96	4.82
- Tensile Modulus (Msi)	1.32	1.17
Mode I - DCB In.Lbs./In.^{2}	10.8	8.75
Fiber Volume %	57	61
Void Content	0	0

*Mod. ASTM D-790

Processing Cycle:

1. Rt. ---> 600°F, 10°F/min. contract pressure
2. 600°F apply 200 psi
3. 600°F ---> 700°F (750°F for PEEK) @ 10°F/min.
4. Hold 45 min.
5. Cool 10-20°F/min. under pressure
6. Remove when under 200°F

Fiber/Resin Distribution

Fused Towpreg

For both fused towpreg systems photomicrographs were taken. The pictures indicate excellent fiber/resin distribution with little or no voids present. What is somewhat unusual is the lack of discrete ply lines normally present with conventional prepreg. Fiber bundles can be made out but they seem to be unoriented. This would probably not affect composite properties except Modes I and II where crack propagation normally would run between discrete plies. Shown below in Figs. 3 and 4 are the respective photomicrographs from both systems.

Photomicrograph
Larc-TPI-1500/AS-4
100X

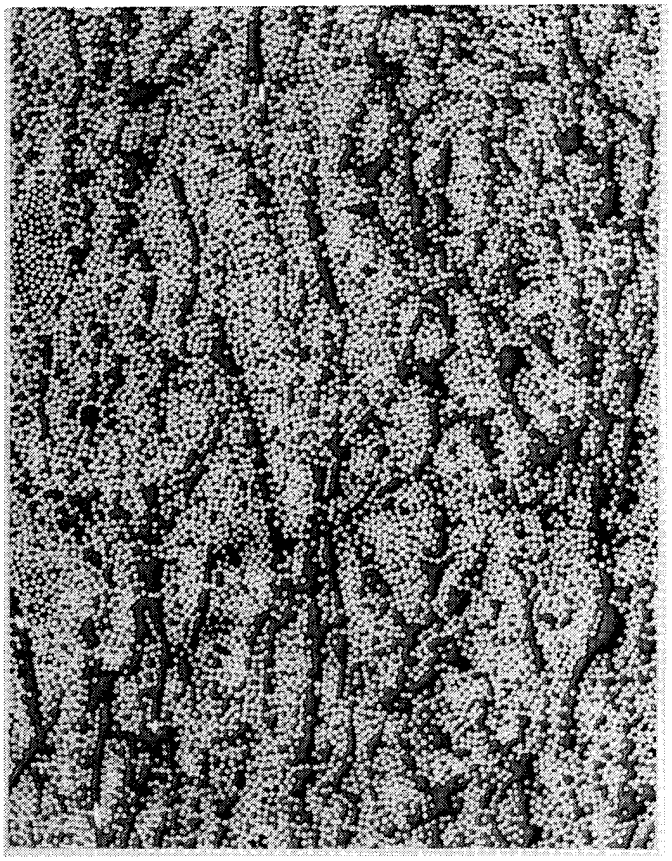


figure 3

Photomicrograph
PEEK-150/AS-4
100X



figure 4

Fracture Morphology

Observation of the fracture surface of composite specimens indicates good matrix resin adhesion. This can be observed with both PEEK and Larc-TPI-1500. Shown below in Figs. 5 and 6 are SEM's of both PEEK and Larc-TPI-1500 carbon fiber composite specimens. Little or no exposed carbon fiber can be seen for either system. Stress whiting can be observed on both systems which is indicative of a tough system. At this stage of development only simple process cycles have been explored. How changes in the process cycle, such as cooling rates, affect mechanical properties and thus fracture morphology has yet to be extensively explored.

SEM Fracture Surface
PEEK/AS-4



figure 5

SEM Fracture Surface
Larc-TPI/AS-4

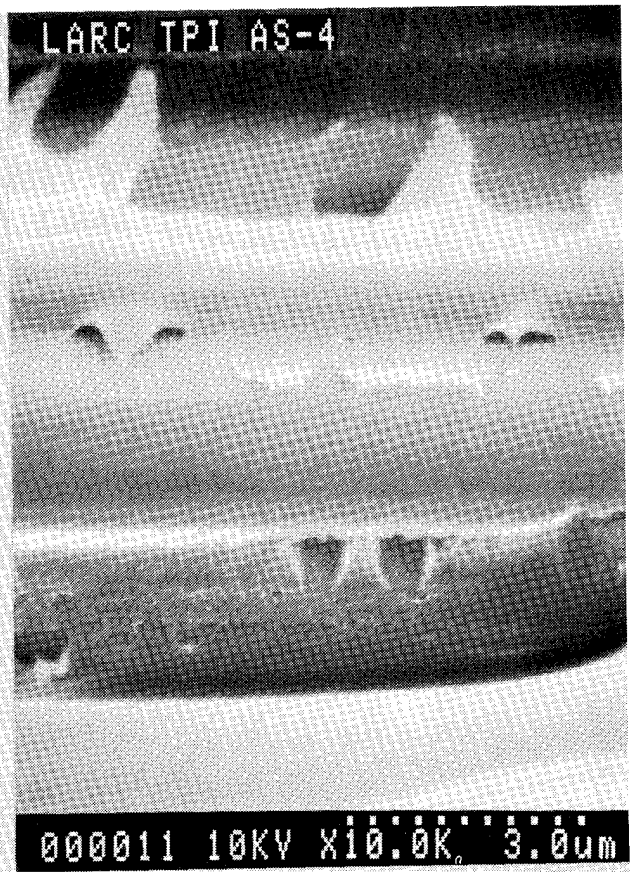


figure 6

PEKEKK Neat Resin Properties

Shown below in Table III are neat resin mechanical properties. The overall properties are excellent for a thermoplastic polymer that is being used for an aerospace composite application. The tensile modulus is most noteworthy and helps translate into good compression and CAI properties.This polymeric resin system is semi-crystalline in nature. The crystallinity helps promote excellent chemical resistance, low moisture absorption and a high level of mechanical properties over a wide range of temperatures. It possesses very good adhesion properties which promote excellent carbon fiber interface development.

Table III

Ultrapec PEKEKK
Mechanical Properties

Property	Unit	Method	
Tensile Strength at Yield	Ksi	Din 53455	15.9
Tensile Modulus	Ksi	Din 53457	625
Elongation at Yield	%	Din 53455	5.3
Elongation at Break	%	Din 53455	40

Shown in figure 7 is a press molding cycle for PEKEKK composites. There is little or no restriction in heat up or cool down rate and there is an obvious advantage in shortening the cycle as much as possible. This is probably not an optimized cycle but represents the cycle which has generated the best mechanical properties to date. It is obvious that lowering the upper process temperature to 750°F would greatly benefit autoclave processing. The pressure has been established with the autoclave in mind. Compression molding above 200 psi may allow the upper process temperature to be reduced. Additional process studies to evaluate percent crystallinity and effect of mechanical properties after annealing will be accomplished as a part of the overall effort.

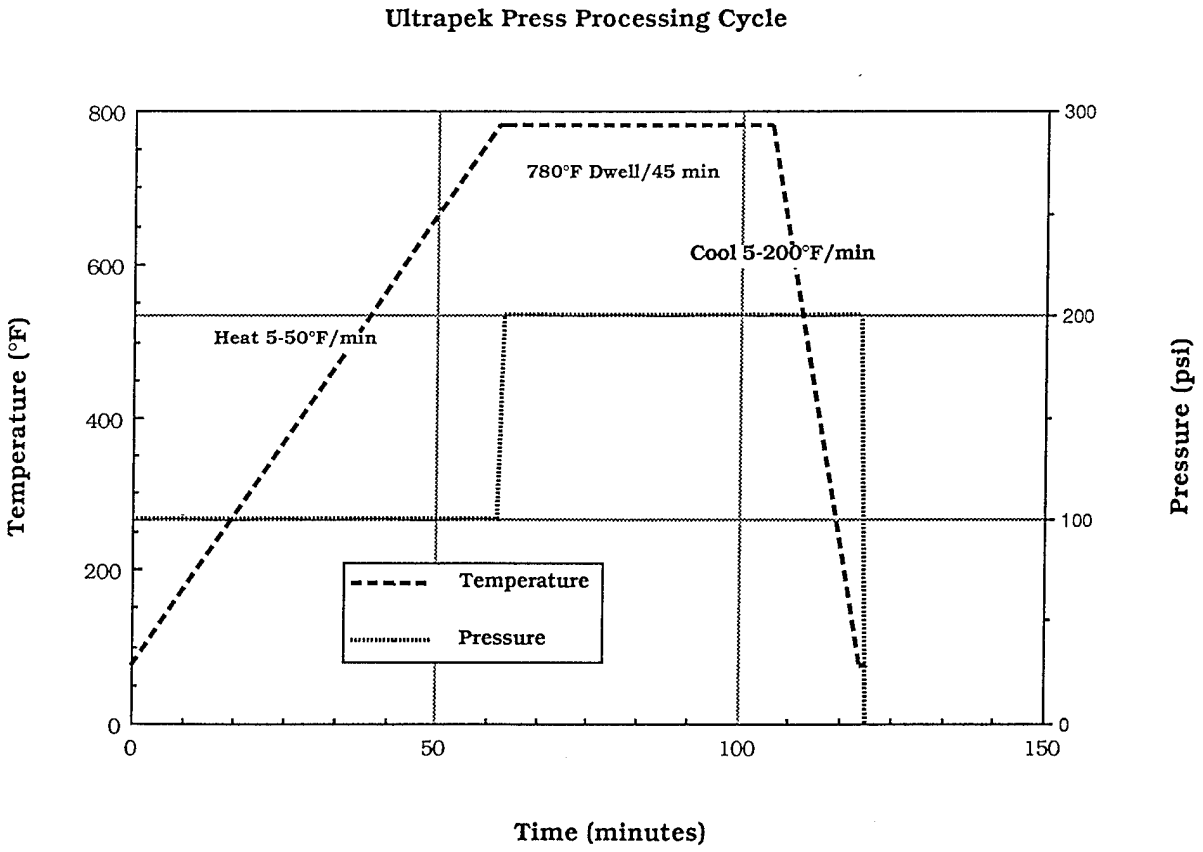


figure 7

PEKEKK Composite Properties

Shown in Table IV below are preliminary composite properties. Overall properties shown have excellent fiber translation. This is best understood by the good interface development between fiber and matrix as well as the neat resin toughness and high modulus. The CAI strength and strain values are some of the best for a thermoplastic matrix composite. A more extensive mechanical characterization will be completed in phase II of the program. Dynamic properties such as long-term fatigue as well as open-hole data are some of the additional information needed to be generated on this composite system.

Table IV

3K AS4/PEKEKK(ULTRAPEK) NCS 2381 UNIDIRECTIONAL NON CRIMP FABRIC (English Units)

TYPICAL FABRIC DATA

Carbon Fiber Volume	60.2 %	Areal Weight	334 g/m^2
Fiber Weight	67.5 %	Yield	1.40 yds/lb

TYPICAL COMPOSITE PROPERTIES

0° Properties	RT Dry	250°F Dry	325°F Wet	Unit	Test Method
Compression Strength	200			Ksi	ASTM
Compression Modulus	17.5			Msi	D695
Flexural Strength	255	219	133	Ksi	ASTM
Flexural Modulus	16.2	16.9	15.1	Msi	D790
Tensile Strength	250			Ksi	ASTM
Tensile Modulus	18.8			Msi	D3039

90° Properties	RT Dry	Unit	Test Method
Tensile Strength	13.0	Ksi	ASTM
Tensile Modulus	1.5	Msi	D3039
% Elongation	0.9	%	

+/- 45° Properties	RT Dry	Unit	Test Method
In Plane Shear Stress	17.0	Ksi	ASTM
In Plane Shear Modulus	0.87	Msi	D3518

Compression After Impact	RT Dry	Unit	Test Method
Ultimate Stress	49.9	Ksi	SACMA
Modulus	8.1	Msi	SRM
Strain To Failure	8300	µin/in	2-88
Impact Energy	1500	in lb/in	

Fracture Energy	RT Dry	Unit	Test Method
G_{IC}	12.9	in lb/in^2	NASA/DCB
G_{IIC}	13.9	in lb/in^2	PUB1092

Larc-TPI-1500 Neat Resin Mechanical Properties

Shown below in Table V are neat resin mechanical properties generated by BASF and Mitsui Toatsu. As can be observed the early testing of Larc-TPI differs from the later repeat testing.

Neat resin evaluation of two different mol. wts. of Larc-TPI-1500 indicates that the medium mol. wt. polymer possesses significantly higher properties than the lower mol. wt. This is most evident when toughness properties are compared. Strain-to-failure as well as Mode I fracture toughness indicate that the medium mol. wt. should be the resin of choice. Mechanical properties were generated from injection molded tensile dogbones and resin plaques. This technique results in high quality void free specimens. All specimens tested by BASF used an extensometer to measure tensile strain-to-failure and modulus values. Mode I fracture specimens were of the compact tension type as described in ASTM-E-399.

Table V

Larc-TPI-1500 Neat Resin Mechanical Properties

Property	Unit	Med. Flow Grade			High Flow Grade		
		Early BASF	Later BASF	Mitsui	Early BASF	Later BASF	Mitsui
Tensile Strength	Ksi	18.1	18.8	18.7	11.6	11.6	10.1
Tensile Modulus	Msi	0.310	0.650	0.625	0.330	0.680	0.625
Elongation	%	8.8	8.6	3.8	13.7	3.6	1.7
Mode I*, G_{1c}	in.lbs./in.^{2}	---	11.1	---	---	<3.0	---

*ASTM E-399

Larc-TPI-1500

Rheology

Characterization work on the apparent viscosity of the medium mol. wt. Larc-TPI indicates that the polymer is very stable at 370°C in air. As received material was run on the parallel plate Rheometrics in air. The choice of 370°C was chosen as a processing condition based on earlier viscosity studies as well as DSC work. Shown in figure 8 are two lots of material. It is understood that endcapping of the polymer has resulted in improved melt stability. Both were run at 370°C for 1 hr. as a worse case condition. For the most part, little or no air is present during consolidation. It is believed also that time for complete fiber wetout is considerably less than 1 hr. but consideration must be given to thick laminates where a thermal gradient through the thickness must be taken into consideration during molding.

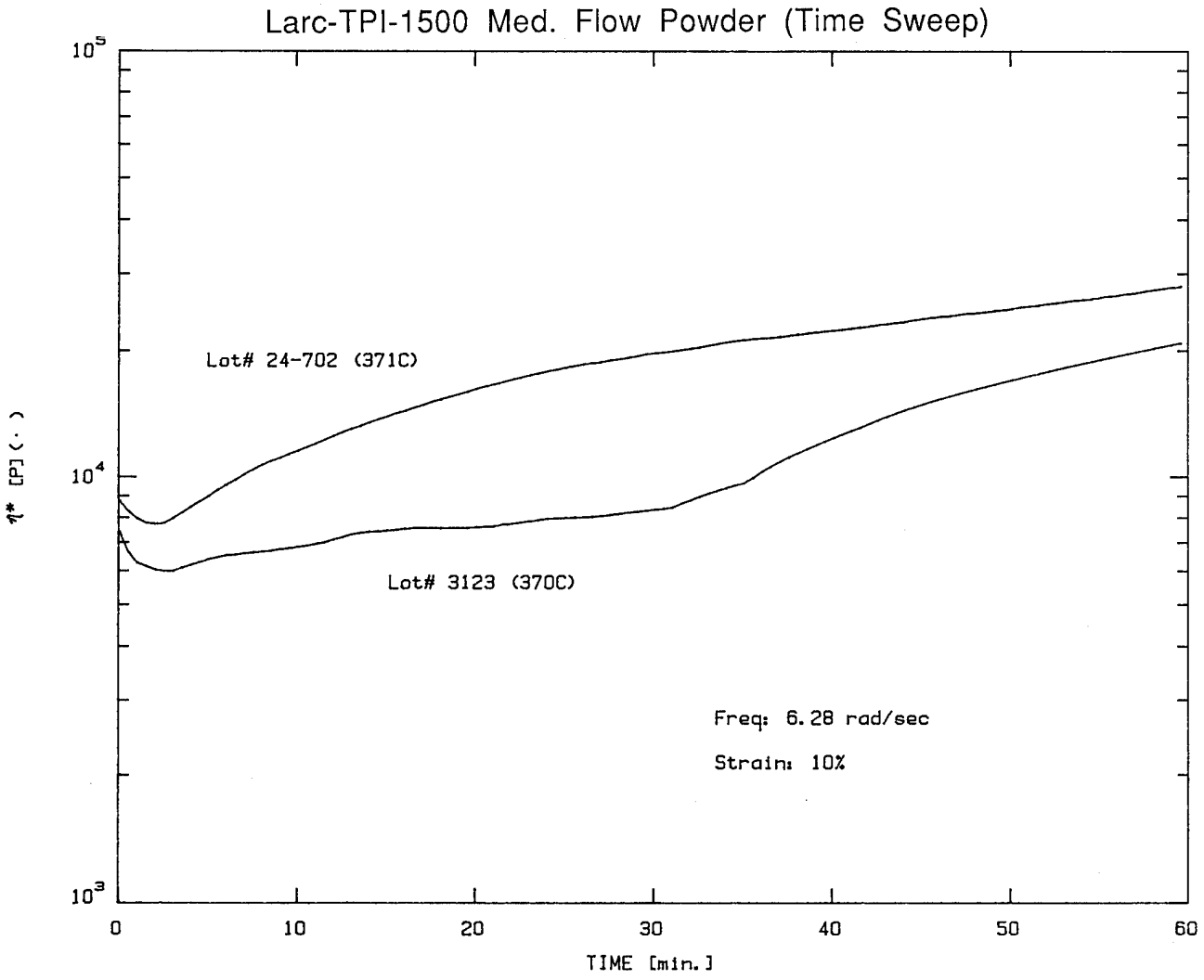


figure 8

Larc-TPI-1500

Differential Scanning Calorimetry (DSC)

A thermal analysis profile on the medium mol. wt. using DSC is shown in figure 9 below. The material was run twice as shown and exhibits a thermal profile as has been demonstrated before. A transient crystallinity is observed in the first run and disappears when the polymer is rerun. A slight shift in Tg is also noticed when one compares the first run to the second. This has also been reported in the literature.(1-2) No annealing studies have been completed on this polymer in the program to determine if Tg can be maximized. This study will be initiated.

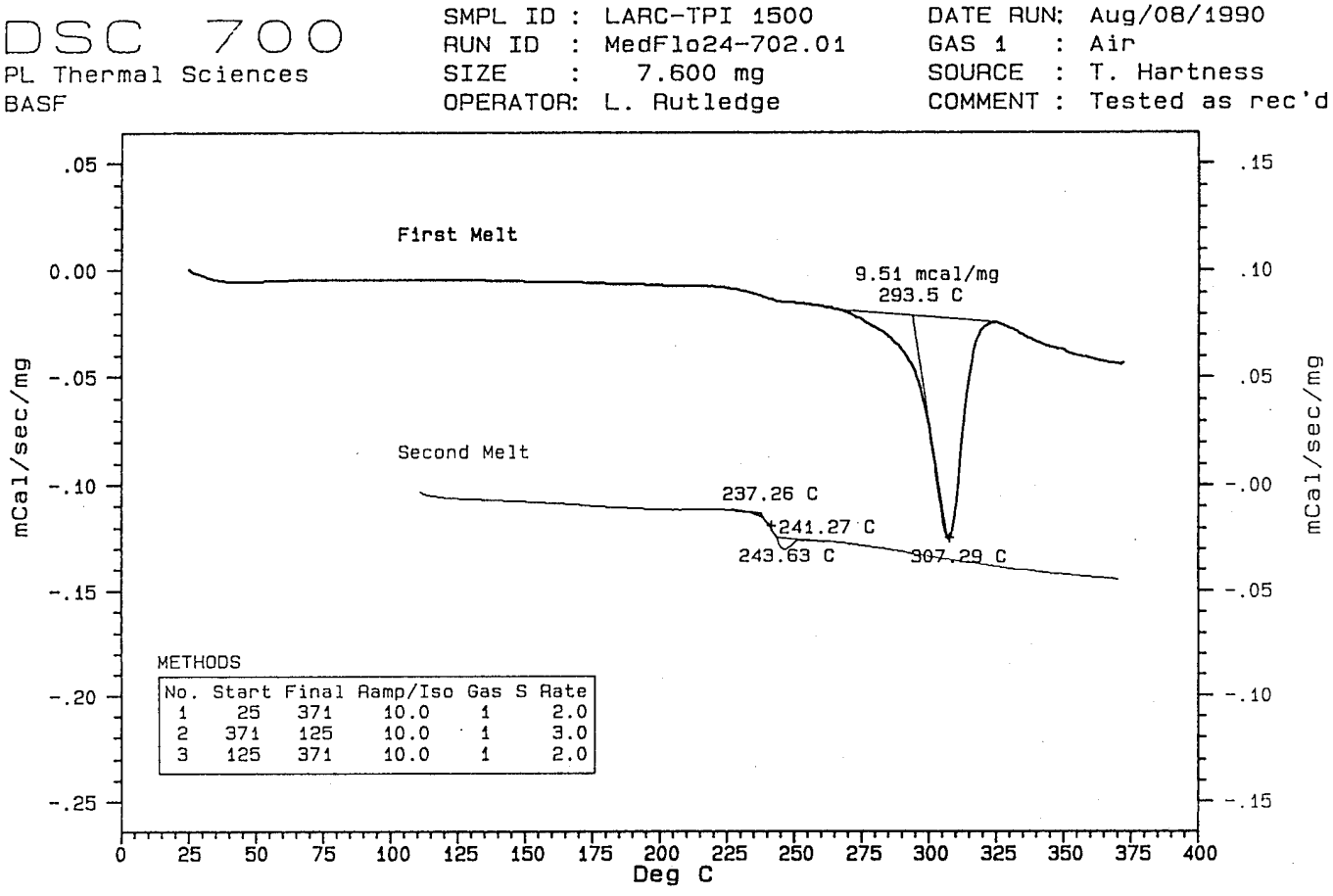


figure 9

Fused Towpreg

Consistency Study

A study was completed to evaluate the resin consistency of a 30 lbs. Larc-TPI-1500/G30-500 (6K) fiber run. Shown in figure 10 are the percent resin by weight measurements for each bobbin, 45 total, and the average. As can be observed a very consistent and tight control was achieved.

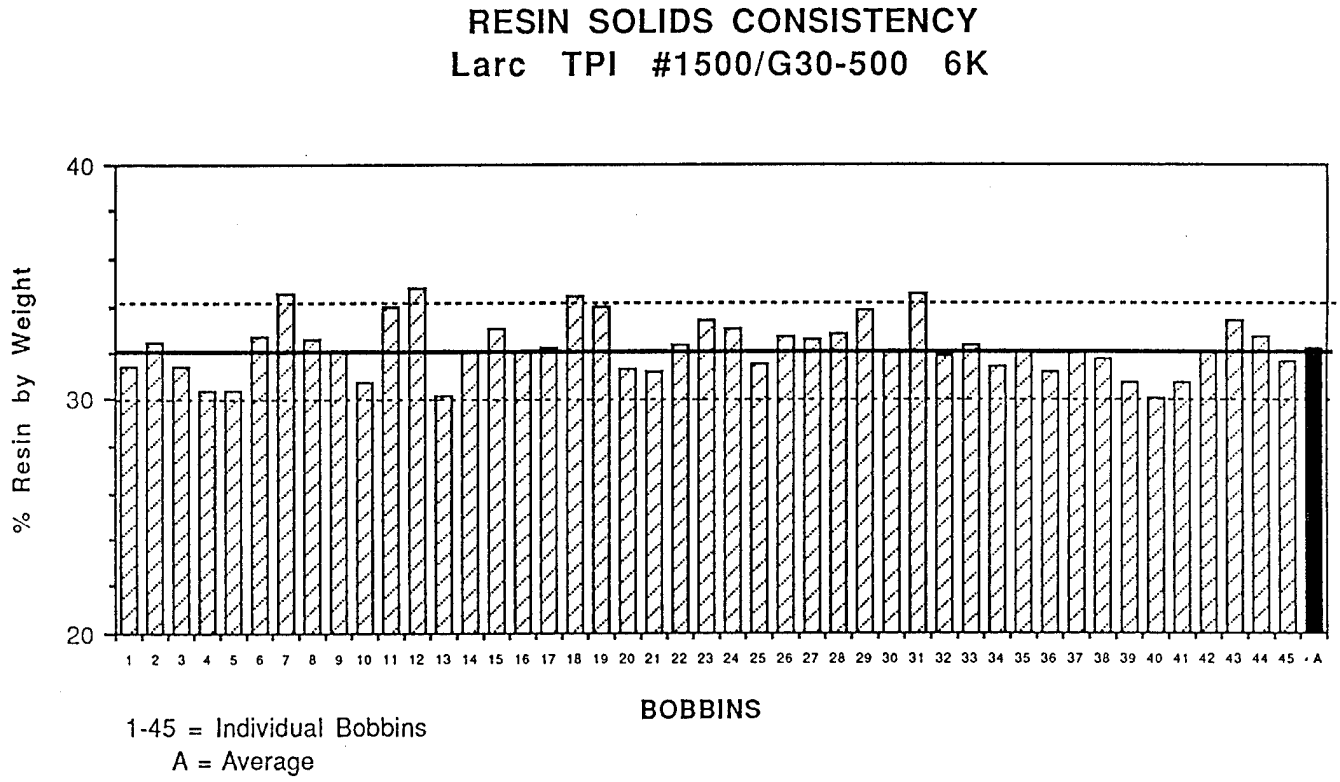


figure 10

Toughened Polyimide

Characterization was initiated on a toughened version of a fully imidized polyimide prepolymer. The objective was to develop a level of toughness in the composite where little or no microcracking occurs after thermal cycling. A neat resin target of fracture toughness was established based on work accomplished and reported on by Dr. Ruth Pater at NASA Langley Research Center[3] In this work a neat resin fracture toughness of 2 in. lbs./in.^{2} resulted in no microcracking in the composite. Shown below in Table VI are initial toughness values versus a 10% thermoplastic toughened polymer. Specimens were compression molded and then cut into compact tension specimens and tested following ASTM E-399.

Table VI

Neat Resin Fracture Toughness

	G_{ic} in.lbs./in.^{2}	E- Modulus x10^5	Test Procedure ASTM
Standard PI	1.20	5.67×10^5	E-399
10% TP Toughened PI	1.74	5.66×10^5	E-399

Note: All samples postcured 24 hrs. @ 600°F cir. air oven

Thermoplastic Toughener
Thermal Characterization

Shown in figures 11 and 12 are the thermal profiles of the TP used to toughen the polyimide. Torson rectangular samples were run on the molded neat resin as received and after a 24 hr. postcure at 600°F. The 24 hr. postcure was done as this may represent the required postcure for the polyimide. As can be observed, there was approximately an 11°C increase in Tg based on G' data. This is apparently due to some cross-linking in the polymer.

Thermoplastic No Postcure

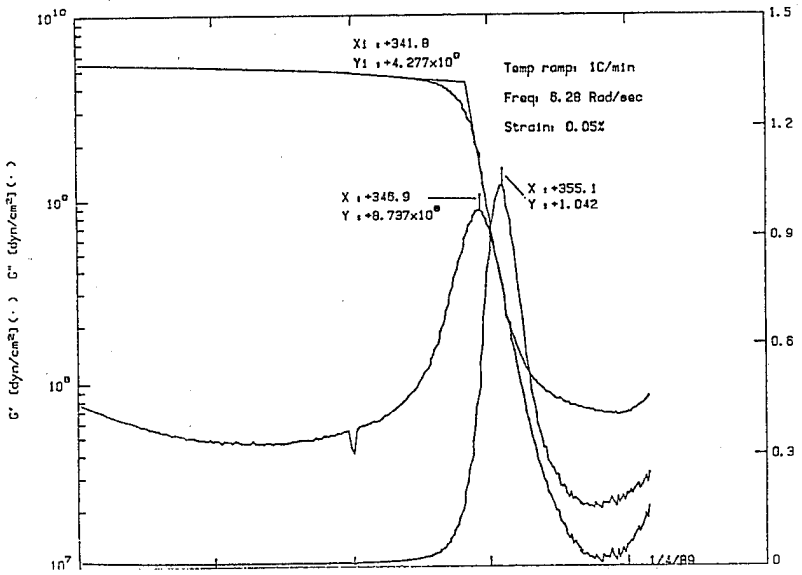


figure 11

Thermoplastic After 24 Hr. Postcure

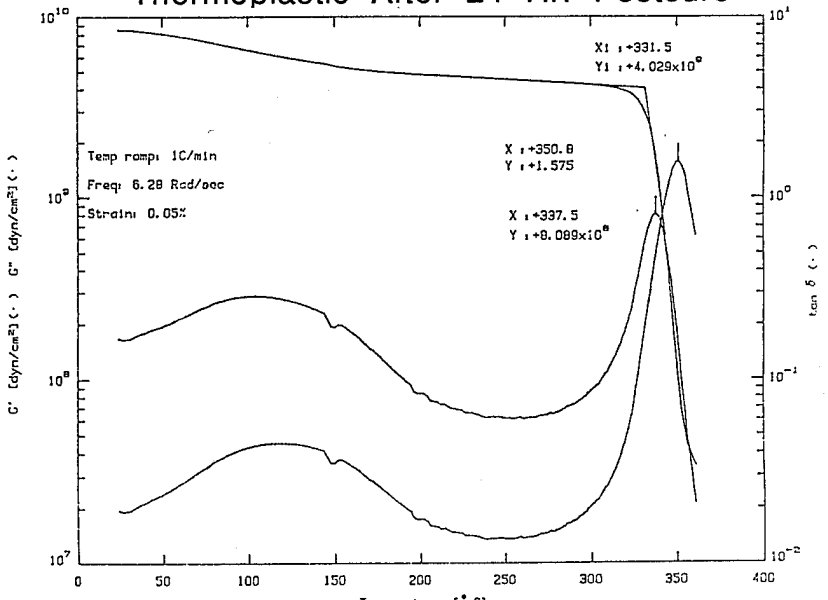


figure 12

Toughened Polyimide

Rheology

Shown in figure 13 is the apparent viscosity of the untoughened and toughened polyimide prepolymer. Obviously, some sacrifice is made in the process viscosity. It is hoped that an untoughened minimum viscosity less than 1,000 poise can be made available. This would possibly allow an increase in TP to 15%. It is believed that this level of TP would result in G_{1c} levels greater than 2 in.lbs./in.^{2}. Data WAS generated on a Rheometrics (RDA) using the parallel plate mode.

Apparent Viscosity Untoughened
vs. Toughened PI

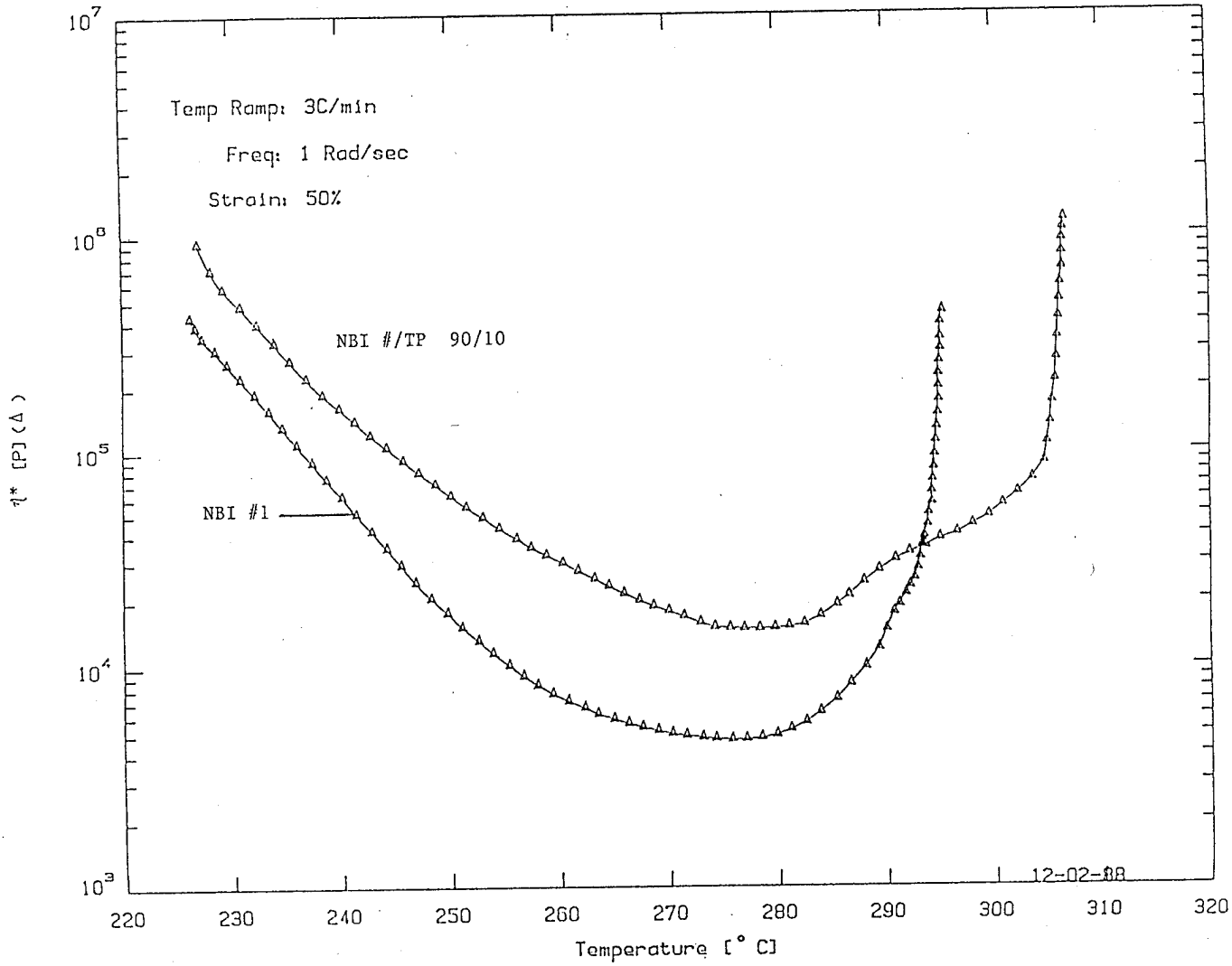


figure 13

Toughened Polyimide

Thermal Characteristics

Shown in figure 14 are Rheometric runs of the untoughened and toughened polyimide both after a postcure for 24 hrs. at 600°F. This was accomplished free standing in a circulating air oven. Specimens were rectangular torsion. Run parameters are shown on the thermal profile sheets. As can be observed there is a reduction in Tg based on G' of approx. 13°C. This is still considered an excellent Tg. There were no other apparent differences observed on the Rheometric runs. Plans in the future will evaluate a prepolymer with a lower melt viscosity. This will allow the exploration of higher TP loadings. The objective is to develop improved toughness and still maintain good processibility.

Thermal Profile of Untoughened vs.
Toughened PI after 24 Hr. 600°F Post Cure

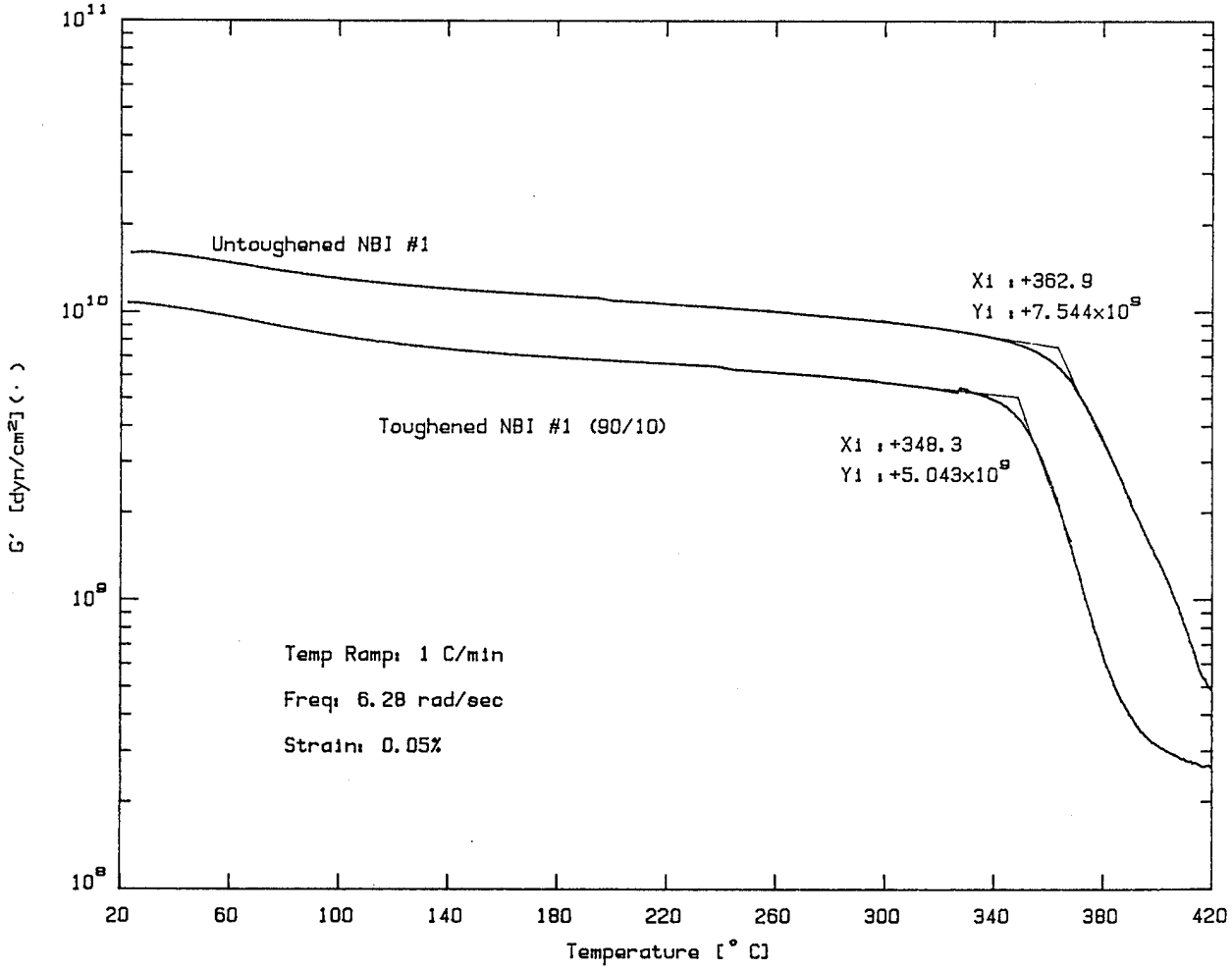


figure 14

Future Work

- Weaving trial of Larc-TPI-1500 8-harness satin bidir cloth
  - Complete mechanical characterization
- 3-D weaving trial PEKEKK/AS-4 (3K)
  - Three weave variations
  - Mechanical properties generation
- Toughened Epoxy fused towpreg characterization

References

(1) T. Towell, N. Johnston, T. St. Clair, Ohta, Tamai, 35th International SAMPE Symposium (April, 1990)

(2) J. T. Hartness, "An Evaluation of a High Temperature Thermoplastic Polyimide Composite", 32nd International SAMPE Symposium & Exhibition, Proceedings (April, 1987)

(3) R. Pater and C. Morgan, SAMPE Journal, Vol. 24, No. 5, Sept./Oct., 1988

Mechanical and Analytical Screening of Braided Composites for Transport Fuselage Applications

Mark J. Fedro
& Christian Gunther
Boeing Defense & Space Group
Philadelphia, PA

Frank K. Ko
Drexel University
Philadelphia, PA

INTRODUCTION*

Techniques developed for the textile industry are now being applied to the manufacture of composite structural parts with advanced fibers. Textile technology provides a process for introducing through-the-thickness fiber reinforcement in a single step. Furthermore, structural textile preforms can be formed near to the final shape of the desired composite component. Consequently, there is a great deal of interest in the manufacture, design, and analysis of composites with new fibrous reinforcements. Braided composite materials are one of the advanced material forms which are under investigation in Boeing's Advanced Technology Composite Aircraft Structures (ATCAS) program. The overall objective of this work is to evaluate braided composite technology for applications to a commercial transport fuselage. The ATCAS braided composite studies are being performed at Boeing Helicopters in conjunction with the Fibrous Materials Research Center at Drexel University.

Studies on the effects of process variables and fiber architecture on the mechanical performance of textile composites aid in determining suitable applications. The application to structural components, such as attachment fittings and frames, requires that the material form exhibit sufficient through-the-thickness strength, damage resistance, and the ability to be formed in a near net shape manufacturing process. The fiber architecture of braided composites is known to increase damage resistance and out-of-plane strength, although the precise amount of through-the-thickness fiber reinforcement required to improve these properties, without excessively degrading in-plane properties, is not known.

The first objective of the ATCAS braiding study is to show the feasibility of braiding near net shape structural components. The second objective, which is also manufacturing related, is to show the feasibility of fabricating these near net shape preforms into composite components using both thermoplastic and thermosetting resins. In addition, the critical processing parameters inherent to both processes will be identified and optimized in order to determine the best possible processing conditions. The third objective is to evaluate the structural performance of braided composites through a series of mechanical tests. The fourth objective is to develop an analytical model which accurately predicts the behavior of braided structures. The fifth and final objective is to identify potential structural applications for braided composites.

This paper summarizes the mechanics of materials progress in support of a goal of understanding the application of braided composites in a transport fuselage. Composites consisting of both 2-D and 3-D braid patterns are investigated. Both consolidation of commingled graphite/PEEK and resin transfer molding of graphite/epoxy braided composite processes are also studied. Mechanical tests examine the following composite properties: unnotched tension, open hole tension, compression, compression after impact, in-plane shear, transverse shear, out-of-plane tension, bearing, and crippling. Analytical methods are also developed and applied to predict the stiffnesses and strengths of test specimens. A preliminary study using the test data and analytical results is performed to assess the applicability of braided composites to a commercial transport fuselage.

The four main areas of focus in the ATCAS braiding study to be discussed here are: 1) Design and Formation of 2-D and 3-D Braided Fabrics for Advanced Composites, 2) Manufacturing Braided Composite Parts, 3) Mechanical Testing of Braided Composites, and 4) Analysis of Braided Composite Structures.

* This work was funded by contract NAS1-18889 under the direction of J.G. Davis and W.T. Freeman of NASA Langley Research Center.

DESIGN AND FORMATION OF BRAIDED FABRICS FOR ADVANCED COMPOSITES

Textile preforming plays an important role in the development of cost effective, high damage tolerant structures. With a broad supply base and a wealth of well-established mechanisms for fiber orientation, pre-shaping and pre-placement of matrices, textile preforming gives composite design engineers an additional degree of freedom in the optimization of structural composites. As shown in Figure 1, there is a large family of fiber architectures created by different preform fabrication techniques.

	Basic direction of yarn introduction	Basic formation technique
Weaving	Two (0°/90°) (warp and fill)	Interlacing (by selective insertion of 90° yarns into 0° yarn system)
Braiding	One (machine direction)	Intertwining (position displacement)
Knitting	One (0° or 90°) (warp or fill)	Interlooping (by drawing loops of yarn over previous loops)
Nonwoven	Three or more (orthogonal)	Mutual fiber placement

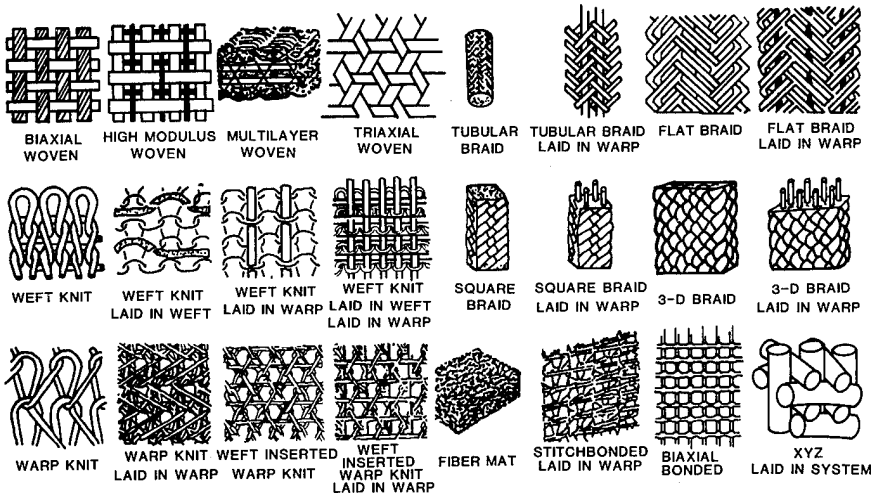


FIGURE 1.

CLASSIFICATION OF BRAIDED STRUCTURES

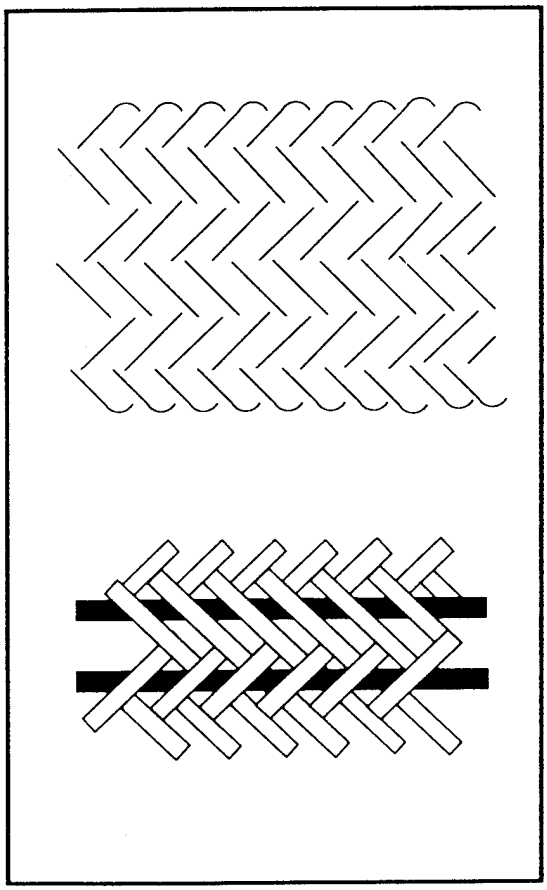
Braided structures can be generally classified into 2-D and 3-D braids. 2-D braided structures consist of two (or three, in the case of triaxial braids) yarns in the through thickness direction, whereas 3-D braids have three or more yarns in the through thickness direction. Both 2-D and 3-D braids can be fabricated into generic tubular and rectangular forms as well as many other complex structural shapes as shown in Figure 2.

PARAMETER	LEVELS	
DIMENSION OF BRAID	2-D	3-D
YARN AXES	BIAXIAL, TRIAXIAL	MULTIAXIAL
SHAPING	FORMED SHAPES	NET SHAPE
DIRECTION OF BRAID	HORIZONTAL	VERTICAL, INVERTED VERTICAL
CONTROL MECHANISM FOR CARRIER MOTION	POSITIVE	JACQUARD
BRAIDING TYPE	CIRCULAR	FLAT, JACQUARD/SPECIAL

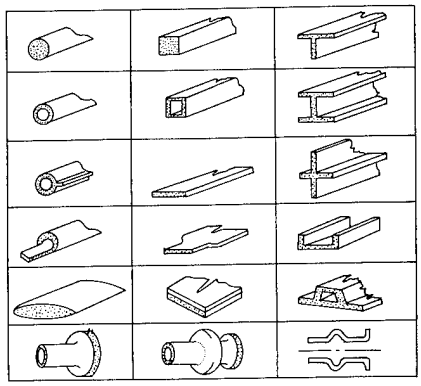
FIGURE 2.

UNIQUENESS OF BRAIDED STRUCTURE

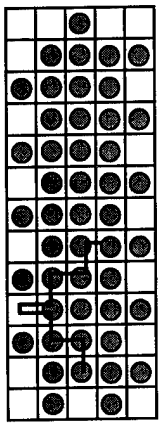
Braided preforms were selected for this study because of their unique combination of damage resistant capability and ability for near net shape and net shape manufacturing. These interesting combinations of formability and toughness are a result of the intertwining nature of the yarns in a braided structure. As shown in Figure 3, the bias yarns contribute to a high level of resistance to shear and torsional deformation. The ability to introduce 0° lay-in yarns further enhances the design flexibility of braided preforms.

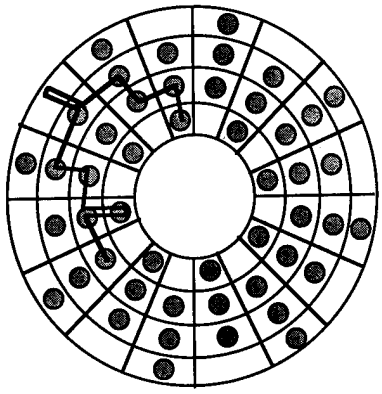


2-D Braid



Net-shape structures produced by the Fibrous Material Research Laboratory.





3-D Braid

FIGURE 3.

INTEGRATED DESIGN AND MANUFACTURING

In order to provide a solid foundation for the engineering design and large scale manufacturing of braided components, an integrated approach was employed [1]. This integrated approach is supported by three levels of modelling including processing (topological), fiber architecture (geometrical), and performance (mechanical) modelling. The flow chart of the engineering design framework is shown in Figure 4.

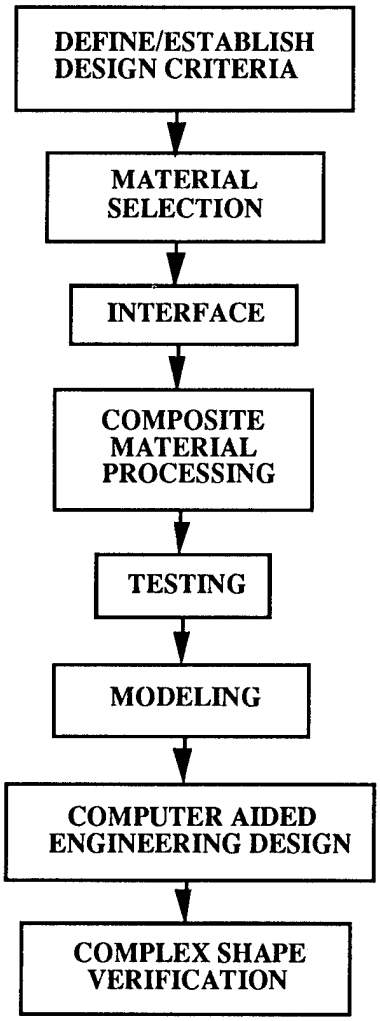


FIGURE 4.

DESIGN OF BRAIDED PREFORMS

The design of the braided preforms was based on the governing equations for braiding, which relate fiber volume fraction to yarn geometry and braiding parameters as shown below in Figure 5.

2-D Braid:

$$d_o = \frac{Mn_{ply}\, A_y}{(\pi\, T\, V_f \cos\theta) + T}$$

$$d_i = \frac{Mn_{ply}\, A_y}{(\pi\, T\, V_f \cos\theta) - T}$$

where

d_o = outer diameter; d_i = inner diameter

T = fabric thickness; M = # of carriers

A_y = yarn cross-sectional area; q = braiding angle

N_{ply} = # of plies per bobbin; V_f = fiber volume fraction.

3-D Braid:

$$V_f = \frac{N_y\, D_y}{9 \times 10^5\, \rho\, A_c \cos\theta'}$$

where

V_f = fiber volume fraction; N_y = total # of yarns in the fabric

D_y = linear density;

q = interior yarn angle

$$= \tan^{-1}\left(\frac{(1+K^2)^{1/2} \tan(\theta')}{K}\right)$$

where $K = \dfrac{\text{track movement}}{\text{column movement}}$

θ' = surface braiding angle.

FIGURE 5.

MANUFACTURING BRAIDED COMPOSITE PARTS

The overall manufacturing goal of the ATCAS braiding study in Phase A was to develop a consolidation process and resin transfer molding process that consistently produced high quality braided composite parts. The schematic of the approach followed to achieve this goal is shown below in Figure 6. This approach was used for both thermoplastic consolidation and resin transfer molding.

The first step was to design and manufacture the necessary tooling for the fabrication process. Once this was accomplished, a set of processing conditions were chosen and an optimization cycle began. A trial run was made with the chosen processing conditions, and the quality of the fabricated composite part was then determined by a number of quality assessment tests. After evaluation of the test results, necessary changes to the critical processing parameters were made. Following the optimization of the processing parameters (i.e. when the quality of the part could no longer be improved), fabrication of the braided composite specimens began.

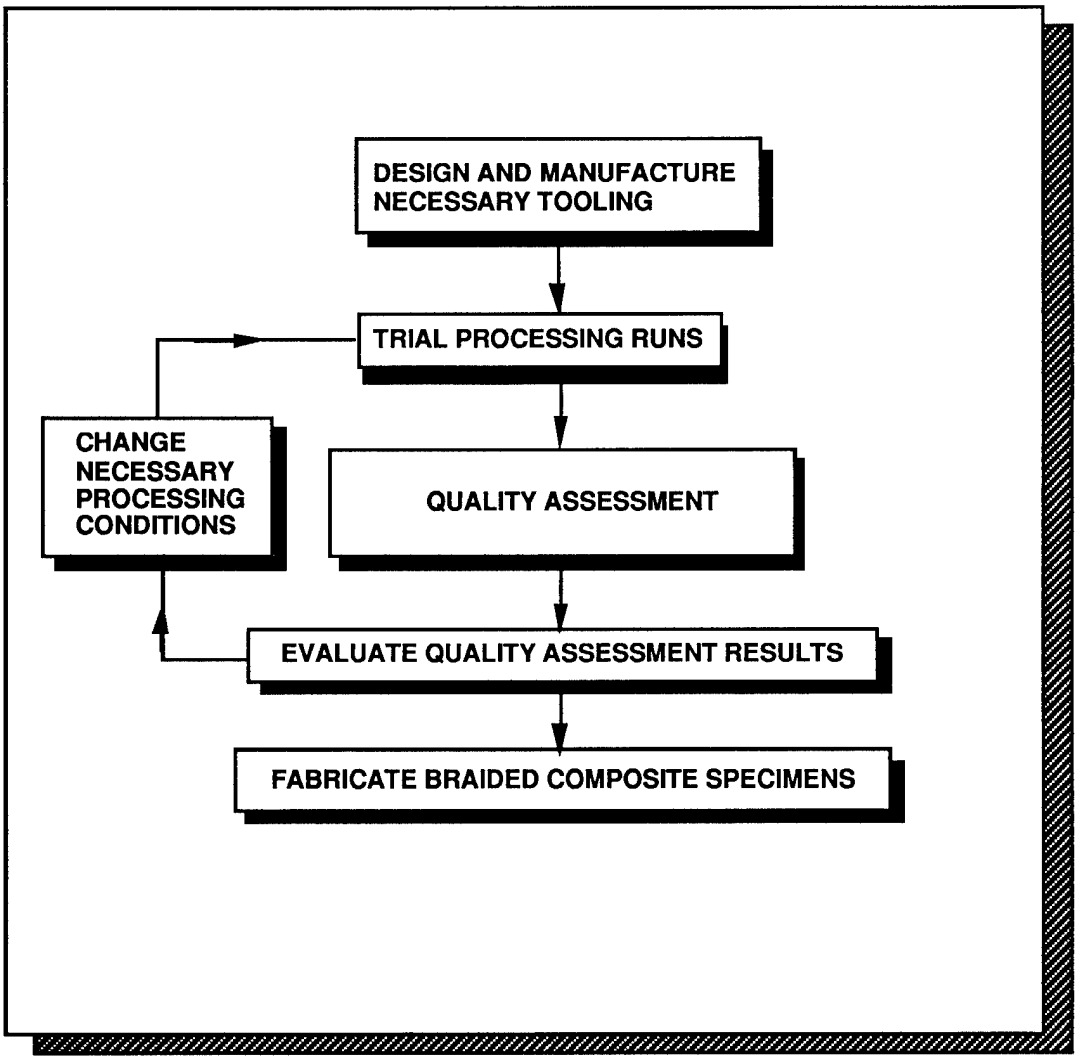


FIGURE 6.

FABRICATION OF BRAIDED PREFORMS CONTAINING A THERMOPLASTIC RESIN

Consolidation of thermoplastics is one of the two fabrication techniques used in this study. The material system used in this fabrication process was AS4 graphite/PEEK commingled hybrid yarn. The processing challenge that needed to be overcome using this material system was to achieve complete uniform wet-out of a composite preform.

Commingled yarns were chosen to be one of the material systems investigated in this study for a number of reasons. First of all, commingled yarns are currently the only way of braiding thermoplastic composites, and an evaluation of a braided thermoplastic system was desired in this study. Secondly, commingled yarns are inherently flexible and drapable which makes them easy to braid. Finally, high quality composite parts can consistently be fabricated using commingled yarns.

The design of the tooling for the high pressure/high temperature environment of thermoplastic consolidation must be done properly in order to prevent warpage and achieve dimensional accuracy of the fabricated composite. A universal tool consisting of a base plate, rails, and caul plates was designed for the flat specimens. Individual tools were designed for the more complex-shaped specimens. The universal and complex-shaped tool assemblies are shown with the autoclave in Figure 7.

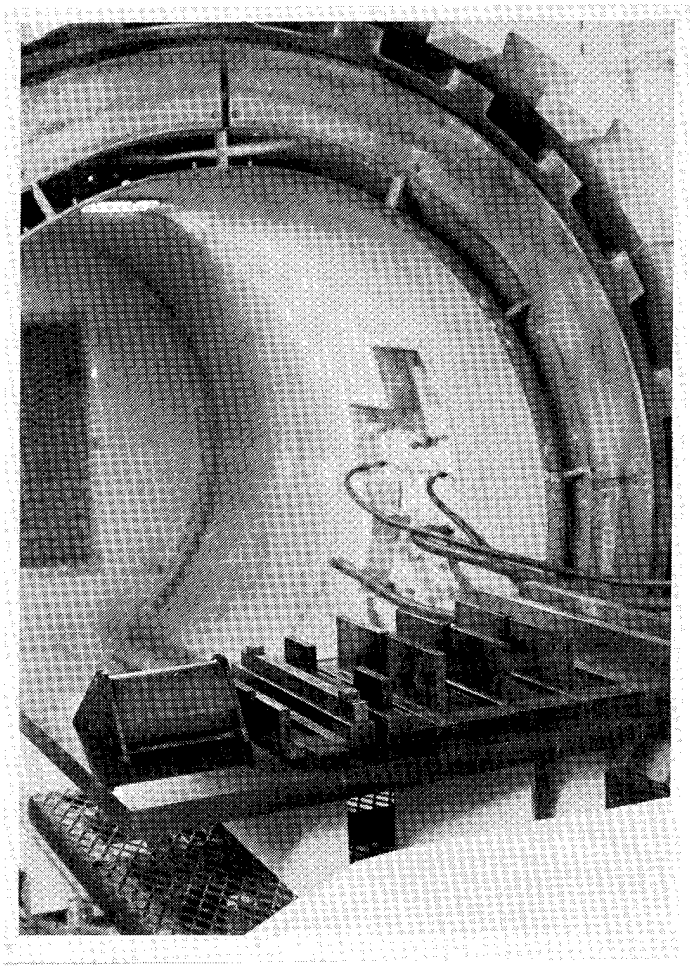


FIGURE 7.

PROCESSING GRAPHITE/PEEK HYBRID YARN BRAIDED PREFORMS

The critical parameters involved in the thermoplastic consolidation process had to be identified and optimized in order to determine the best possible processing conditions. The critical processing parameters for thermoplastic consolidation were identified as follows: part temperature, heat-up rate, cool-down rate, dwell time, pressure, and ramp-up pressure rate. The optimized consolidation cycle is shown in Figure 8a.

In determining the optimized consolidation cycle, many trial runs were made using different combinations of processing parameters. The quality of the fabricated composite parts was evaluated after each trial process. The techniques used to determine part quality included fractography studies, void content testing via resin digestion and digitized micrograph analysis, C-scans and X-rays. A photomicrograph of the cross-section of a part fabricated with the optimized consolidation cycle is shown in Figure 8b.

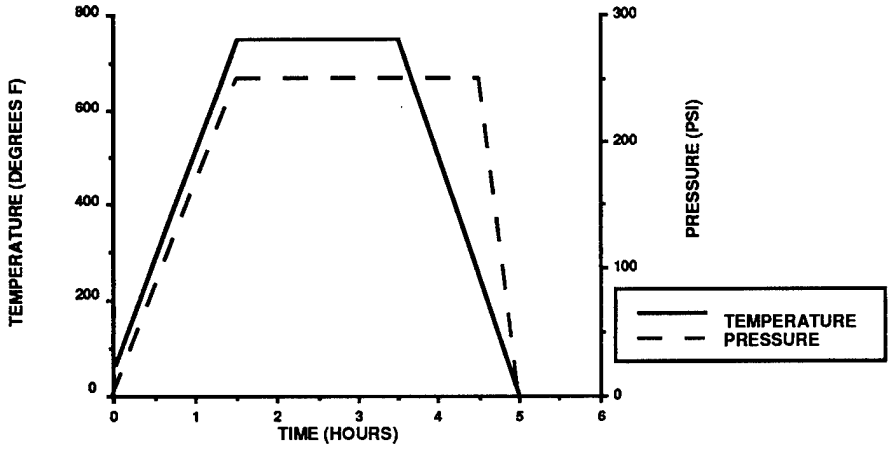


FIGURE 8a.

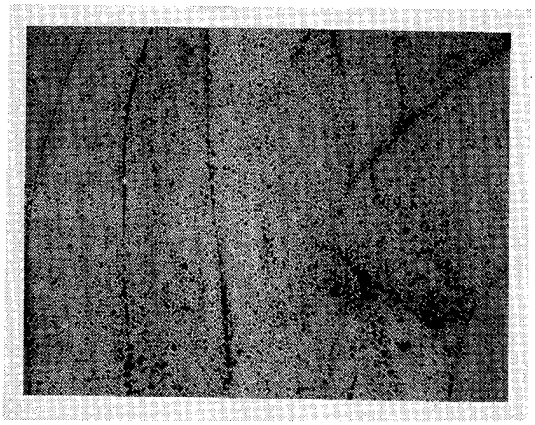
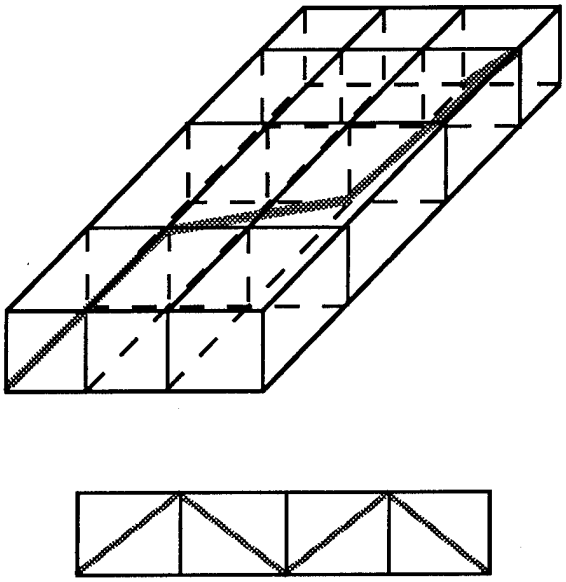


FIGURE 8b.

MANUFACTURING ISSUES OF THERMOPLASTIC BRAIDED PREFORMS

The effect of the thermoplastic consolidation process on the internal fiber architecture of the preforms was an area of concern that was addressed. The effect of consolidation on the fiber architecture was observable by braiding a copper-coated graphite tracer fiber tow into the preform. The preforms containing the tracers were X-rayed before and after consolidation in order to detect any changes in fiber architecture that might have occurred.

The first effect observed was the variability in part thicknesses of the composite parts. The final part thickness is difficult to control when preforms are not made by automated machines (i.e. the bulk factor cannot be accurately controlled when manual steps are involved in the braiding process). The X-rays also showed that there was a significant reduction (30%) in through-the-thickness angle in the 3-D preforms. Although this is a drawback, the reduction in through-the-thickness angle can be calculated if the initial preform thickness and final composite part thickness are known. Another observation made from the X-rays was the presence of fiber kinking and fiber waviness. When the preform was compressed during fabrication, the fibers kinked around the areas of fiber interlocking. A schematic of an X-ray illustrating the effects mentioned above is shown in Figure 9.



BEFORE CONSOLIDATION

AFTER CONSOLIDATION

FIGURE 9.

FABRICATION OF BRAIDED COMPOSITES BY RESIN TRANSFER MOLDING

Resin transfer molding was the other fabrication technique used in this study. The preform material used in this fabrication technique was AS4 dry graphite fibers. The resin system chosen for the process was DPL-862, which is a new resin system developed by Shell. This resin system was chosen for the following five reasons: excellent structural properties, retention of structural properties in a hot-wet environment, low viscosity, lack of a styrene, and reasonable cost. The processing challenge of this fabrication technique was to move resin uniformly through a highly interlaced structure with a high fiber volume fraction (61%).

Resin transfer molding was chosen for this study for the following reasons: RTM uses materials in their lowest cost form, the finished product of RTM is dimensionally accurate in all directions, and RTM is a low cost, high rate process that is versatile and repeatable. A schematic of the RTM process used in this study is shown in Figure 10.

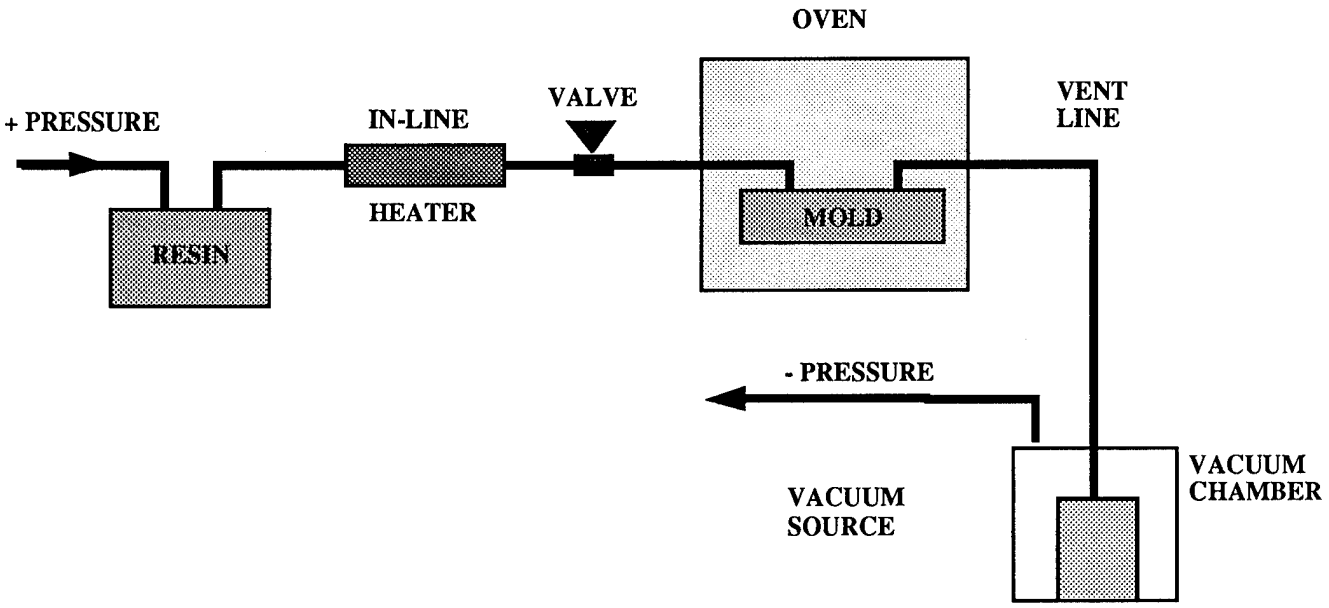


FIGURE 10.

PROCESSING BRAIDED PREFORMS BY RESIN TRANSFER MOLDING

In order to determine the best possible resin transfer molding conditions, the critical parameters of the process were identified and optimized as follows: a resin temperature of 200°F, an inlet line temperature of 225°F, a mold temperature of 250°F, and a vent/exit line temperature of 250°F. The details of the molding process are given below in Figure 11.

In determining these processing conditions an optimization cycle similar to the one used for the consolidation of the graphite/PEEK preforms was used. Many of the same manufacturing issues addressed in the thermoplastic consolidation technique are currently being investigated.

1.) Loaded preform in mold and verified vacuum integrity.

2.) Attached inlet and exit lines.

3.) Preheated mold and preform to 250°F. Mold cavity was held under vacuum to dry preform for 2 hours.

4.) Preheated resin and curing agent were mixed and desired under vacuum. (NOTE: At 250°F under approximately 30 in. Hg, the resin system boils. A slight decrease in vacuum solved this problem.

5.) Resin was then loaded into preheated pressure pot at 200°F.

6.) While maintaining full vacuum (30 in. Hg), inlet valve was opened to allow resin to flow to inlet port of mold. Vacuum was then decreased to approximately 10 in. Hg and positive pressure was applied to the resin (approximately 5 psi initially).

7.) When resin was witnessed at exit port, vacuum was reduced to zero and the pressure was increased to 20 psi.

8.) When an air bubble was observed in the free stream of resin contained in the exit line, the exit line was clamped and the resin pressure was increased to 40 psi.

9.) The mold was then blocked under 40 psi and the mold temperature was increased to 300°F to gel and cure resin.

10.) CURE CYCLE
Three hours at 300°F with slow cool down to room temperature.

FIGURE 11.

MECHANICAL TESTING OF BRAIDED COMPOSITES

The primary goal of the experimental mechanical characterization of braided composites in Phase A of the Boeing ATCAS Program is to obtain a preliminary data base for 2-D and 3-D braided composites. The schematic of the approach followed to achieve this goal is shown below in Figure 12.

The first step of the approach was to set-up a test matrix that would allow the investigation of a variety of structural mechanical properties of both 2-D and 3-D braided composites. Selection of the material systems and internal fiber architecture configurations was also an important part of the effort The next steps were the design of the test specimens and definition of the test methodology that would properly determine the desired mechanical properties. The following two steps were manufacturing oriented. The processes which were used to manufacture the braided composite parts were optimized in order to consistently produce excellent quality parts for mechanical testing. After process optimization, the test specimens were fabricated. Following fabrication, the specimens were prepared and tested. The final step to this approach was the correlation between experimental data and predicted analytical results.

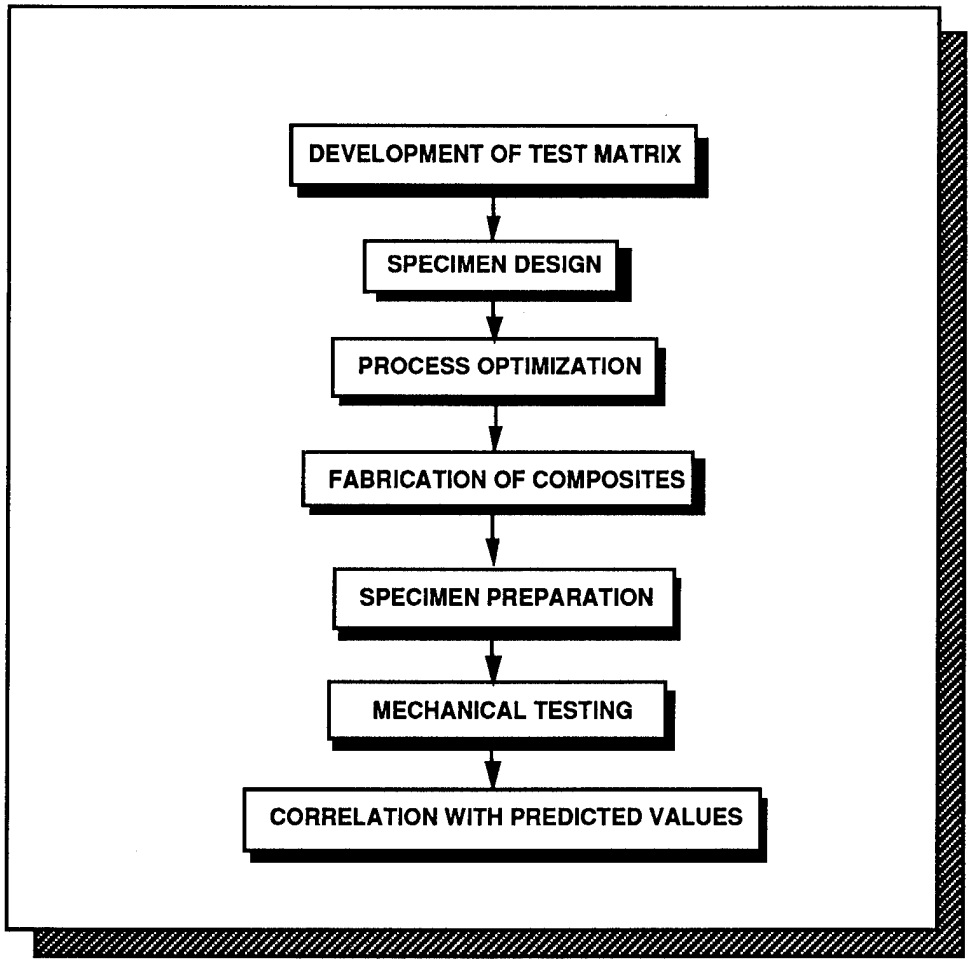


FIGURE 12.

BRAIDED COMPOSITES TEST MATRIX

The test matrix for braided composites was developed to fulfil five objectives. The first objective is to examine the response of braided composites to different types of loading conditions since collection of braided composite mechanical properties is needed to build a much needed data base. The second objective is to compare the mechanical response between 2-D and 3-D braided composites because the effect of through-the-thickness reinforcements on in-plane and out-of-plane properties must be examined. The third objective is to compare the mechanical response between braided composites containing different polymer resin systems. The fourth objective is to observe the effect of different fiber architectures on the mechanical response of braided composites. This objective will bring some insight to the dilemma of determining the precise amount of through-the-thickness fiber required to improve out-of-plane properties and damage resistance without excessively degrading in-plane properties. The fifth and final objective of the test matrix is to compare the mechanical properties of the braided composite systems with traditional laminated composite systems.

Figure 13 illustrates the braided composite test matrix which lists the nine different types of mechanical tests used in this study. The test matrix consisted of 123 test specimens, 57 two dimensional braided specimens and 66 three dimensional braided specimens. Two different internal fiber architectures were investigated. Fiber architecture "A" consisted of 60% braided yarns at a braiding angle of 20° and 40% in-laid longitudinal yarns; fiber architecture "B" consisted of 100% braided yarns at a braiding angle of 35°. The test specimens in the matrix consisted of two different material systems: an AS4 fiber/PEEK thermoplastic system, and an AS4 fiber/epoxy RTM resin. All test specimens were designed to contain a 61% fiber volume fraction.

	2-D BRAIDED SPECIMENS				3-D BRAIDED SPECIMENS			
	A		B		A		B	
TYPE OF TEST	PEEK	RTM	PEEK	RTM	PEEK	RTM	PEEK	RTM
UNNOTCHED TENSION	3	3	3		3	3	3	3
OPEN HOLE TENSION	3	3	3		3	3	3	3
UNNOTCHED COMPRESSION	3	3	3		3	3	3	3
COMPRESSION AFTER IMPACT	3				3			
IN-PLANE SHEAR			3				3	
TRANSVERSE SHEAR			3	3			3	3
TRANSVERSE TENSION			3	3			3	3
BEARING	3	3	3		3	3	3	3
CRIPPLING	3							
TOTALS	18	12	21	6	15	12	21	18

NOTES:

A - BRAIDING GEOMETRY OPTIMIZED FOR END LOAD [60% BRAIDED AT 20 DEGREES, 40% 0 DEGREES]

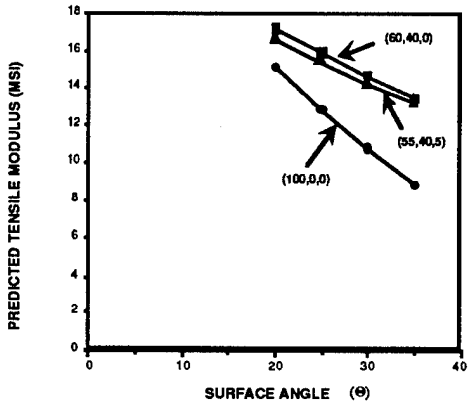
B - BRAIDING GEOMETRY OPTIMIZED FOR SHEAR [100% BRAIDED AT 35 DEGREES]

FIGURE 13.

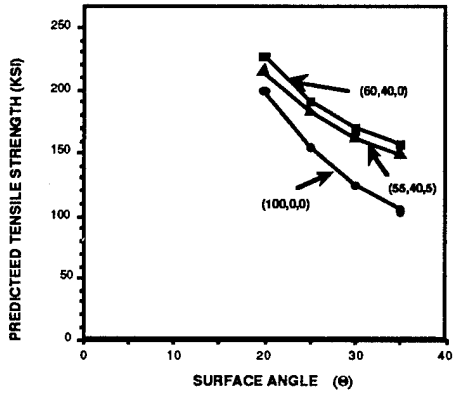
OPTIMIZED FIBER ARCHITECTURE FOR END LOADS AND SHEAR LOADS

The two fiber architectures contained in the test matrix were determined via a parametric study and the consideration of preform manufacturing constraints at the FMRC at Drexel University. The objective of the parametric study was to find the optimum configuration for two different loading conditions: end loading and shear loading. The parametric study yielded the following configuration for the optimization for end loading: 60% braided yarns at a braiding surface angle of 20° and 40% in-laid longitudinal yarns. The fiber architecture optimized for shear loading was 100% braided yarns at a braiding angle of 35°.

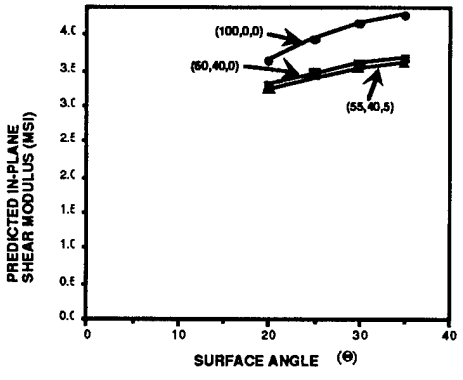
The parametric study was performed using an early version of the analytical model developed during this study. Some results from this parametric study are graphically illustrated in Figure 14 below.



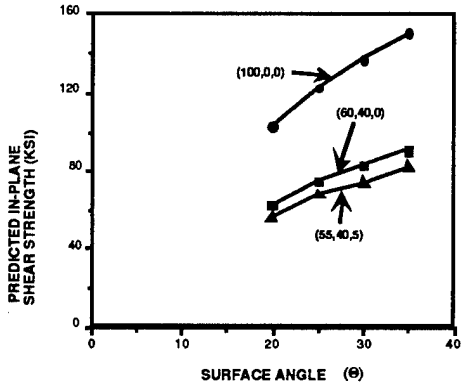
NOTE: NUMBERS IN PARENTHESIS REFER TO: [% BRAIDED, % LONGITUDINAL, % TRANSVERSE]



NOTE: NUMBERS IN PARENTHESIS REFER TO: [% BRAIDED, % LONGITUDINAL, % TRANSVERSE]



NOTE: NUMBERS IN PARENTHESIS REFER TO: [% BRAIDED, % LONGITUDINAL, % TRANSVERSE]



NOTE: NUMBERS IN PARENTHESIS REFER TO: [% BRAIDED, % LONGITUDINAL, % TRANSVERSE]

FIGURE 14.

the basic tension and compression tests are being conducted using standard specimens. However, specimens had to be designed for the out-of-plane shear test, the out-of-plane tension test, the crippling test, and the bearing test. The out-of-plane shear properties will be obtained using the Iosipescu test [2]. This test method dictated the specimen configuration which is shown in Figure 15a. The out-of-plane tension properties will be determined via a flange bending test; the specimen configuration is shown in Figure 15b. This specimen was designed to produce significant out-of-plane tension stresses (~ 20 ksi) at the bending strength of the material. The specimen designed for the crippling test was a C-section channel, Figure 15c, which was designed for the flanges to buckle first, followed by the web. The final specimen design was the bearing specimen. This configuration, shown in Figure 15d, was chosen because of the two possible failure areas, and the restriction of bending in the test specimen.

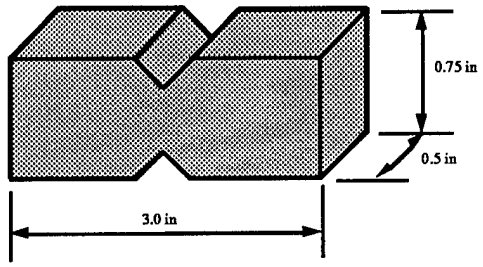


FIGURE 15a

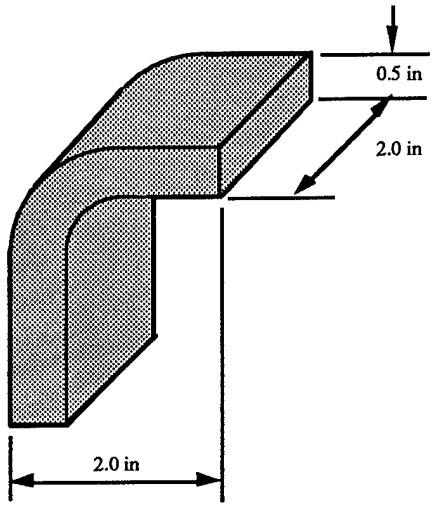


FIGURE 15b

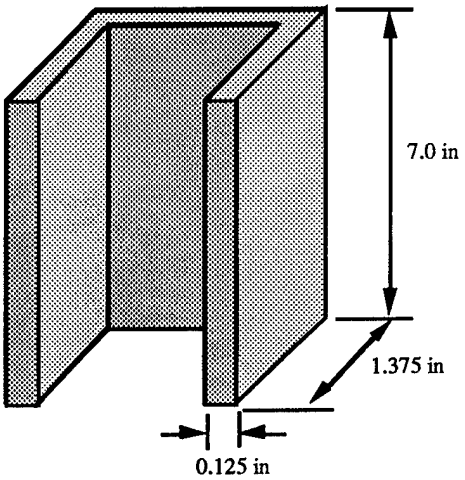


FIGURE 15c

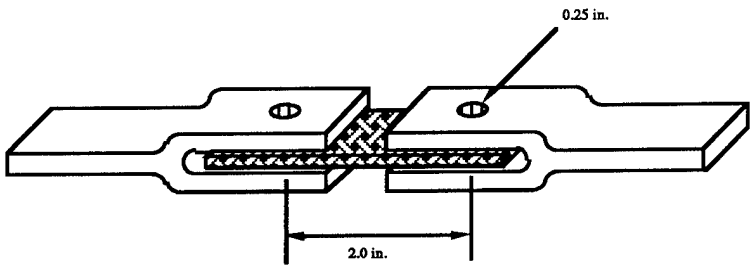


FIGURE 15d

ANALYSIS OF BRAIDED COMPOSITE STRUCTURES

The overall analysis goal of the braiding ATCAS study is to develop analytical models which accurately predict the mechanical behavior of braided composite structures. The schematic of the approach followed to achieve this goal is shown in Figure 16.

The first step to the approach was to acquire an understanding of the existing analytical models that predict the stiffnessses and strengths of braided composites. After reviewing existing models, a simple 3-D stress analysis model was developed to act as a base model which would be expanded. The next step was to expand the base model to improve physical representation of the unit cell and to add hygrothermal effects, stiffness modifications, and an advanced failure criterion in order to improve predicted results. With the aid of experimental test results, the analysis will be refined in order to produce a model which accurately predicts the behavior of braided structures under any loading condition.

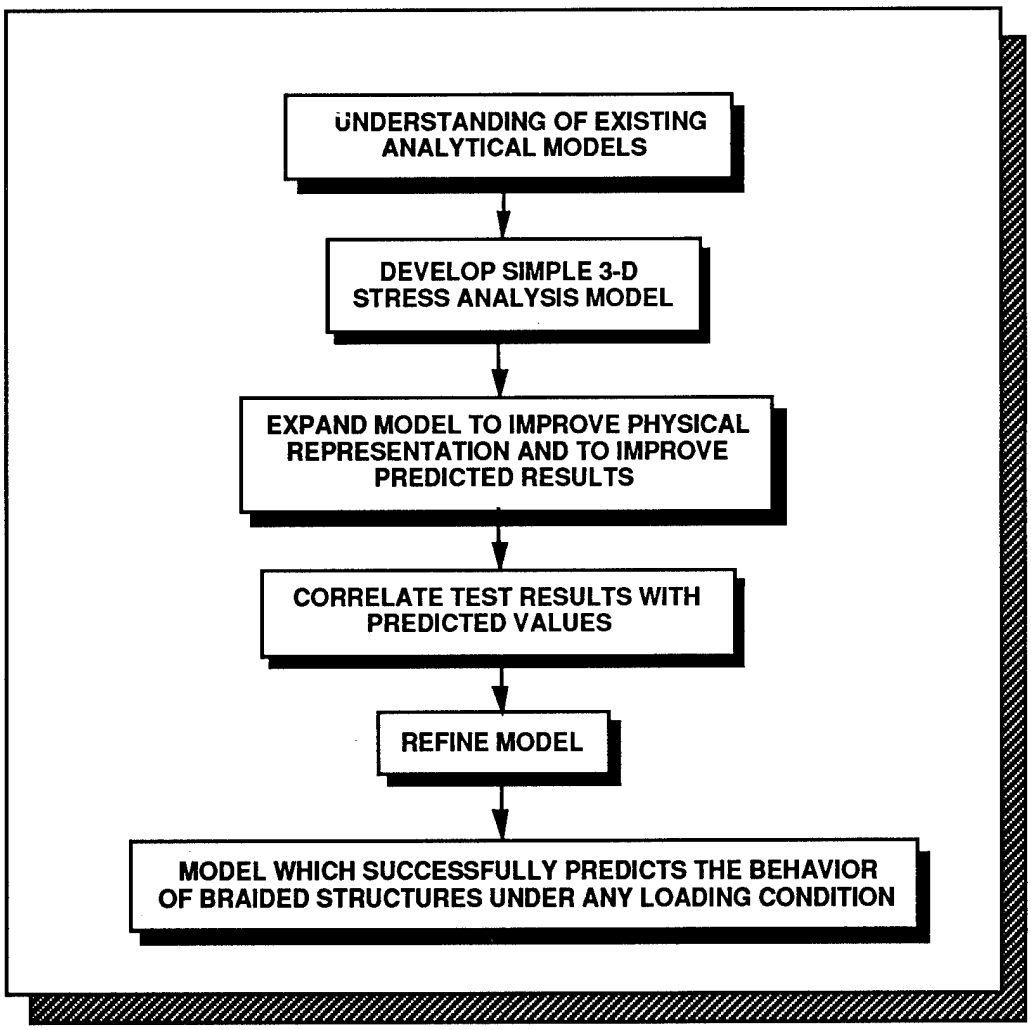
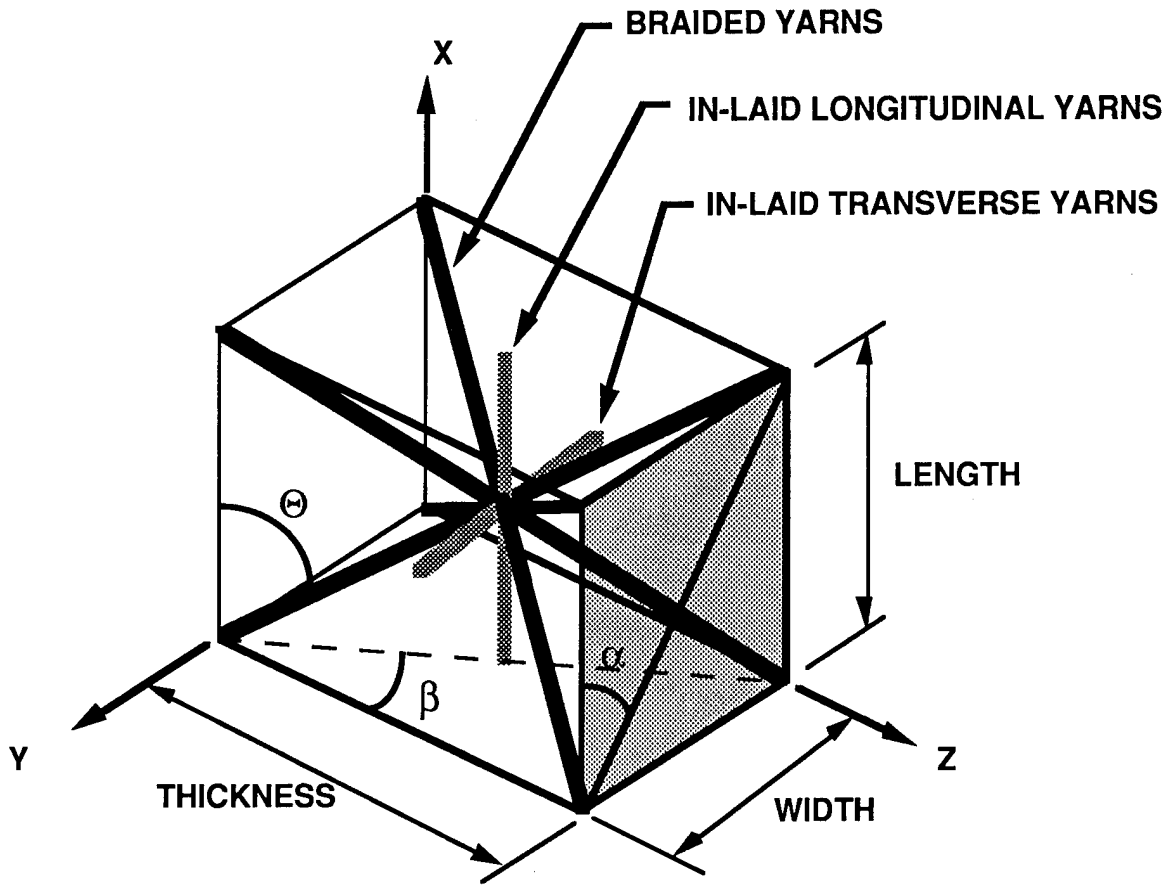


FIGURE 16.

UNIT CELL METHODOLOGY

The analysis of a 3-D textile composite structure requires the knowledge of the internal fiber architecture of the structure. The main concept presented here is that one can assume that the fiber architecture can be represented by a series of repeating building blocks called unit cells [3]. The unit cell, shown in Figure 17, is composed of six elemental component tows: four braided components which are the diagonals of the cell, a longitudinal component, and a transverse component. The orientation of the braided components are represented by the through-the-thickness angle Θ. Each component is assumed to be continuous throughout the structure, have a circular cross-section, and be embedded in a matrix. The geometry of the unit cell (length, width, height, and interior angles) is dependent on the braiding ratio (ratio of track to column movement) and braiding surface angle α shown below on the surface of the unit cell.



α = BRAIDED SURFACE ANGLE

FIGURE 17.

APPLICATION OF UNIT CELL METHODOLOGY TO PLATE THEORY

The first phase of development of the model was to incorporate 3-D stress analysis on the unit cell . The maximum stress failure criterion was applied to predict the strength of the unit cell under an applied loading condition. The second phase incorporated the unit cell methodology to shear deformable plate theory. The application to plate theory relates the unit cell to a structure with finite dimensions and provides the stiffness and strength properties for the analysis of plates with a wide variety of loading conditions including hygrothermal effects. The flow chart for the model described above is shown in Figure 18.

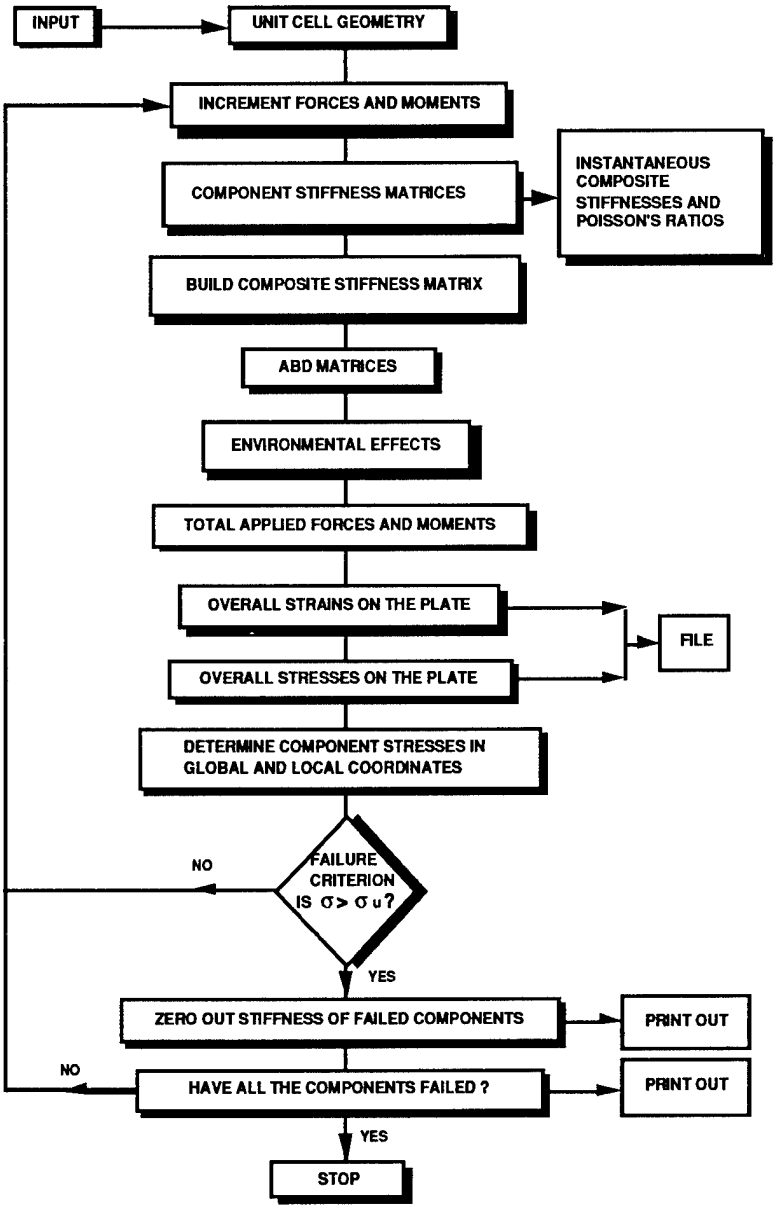
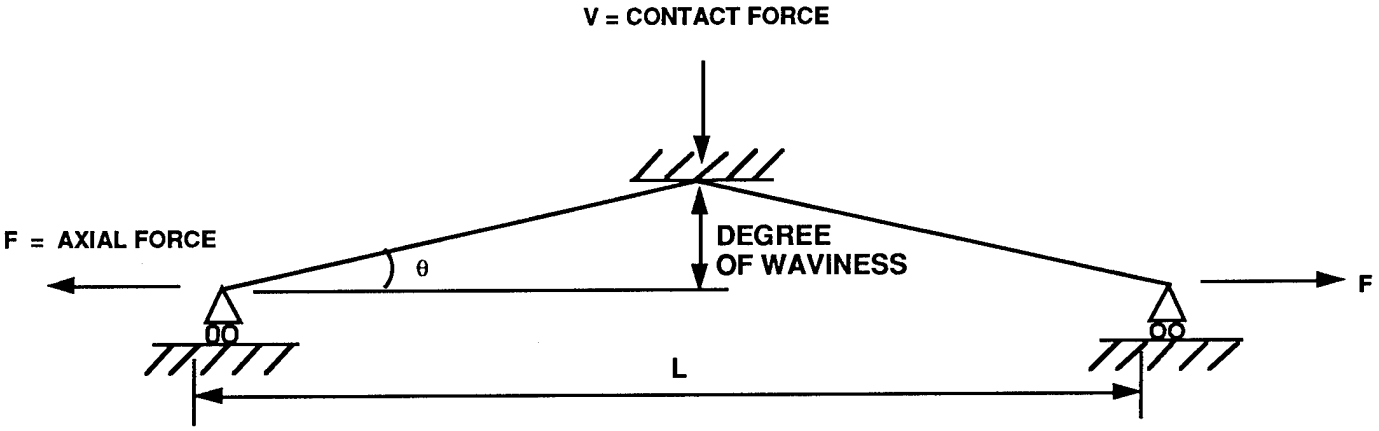


FIGURE 18.

INTRODUCTION OF STIFFNESS MODIFICATIONS

Stiffness modifications were introduced into the model to account for fiber bending because the unit cell assumes that the elemental tow components are continuous and remain straight throughout the preform. Stiffness modifications are needed to reduce the component stiffnesses since a tow experiences waviness around areas of interlacing and turn-around points as it transverses through a preform. The stiffnesses were modified by an elastic strain-energy approach [4]. This approach, which uses beam elements to represent the bending behavior of a braided tow, is shown in Figure 19. The stiffnesses of the beam element assembly are determined via the total strain energy of the system. The total strain energy includes the strain energy due to bending, extension, and compression in the matrix over the region of contact and is dependent on the length of the fiber in the unit cell "L", the material properties of the tow, and the degree of waviness of the fiber, which itself depends on the fiber architecture and the braiding ratio of the preform.



U_B = STRAIN ENERGY DUE TO BENDING

U_E = STRAIN ENERGY DUE TO EXTENSION

U_C = STRAIN ENERGY DUE TO COMPRESSION OVER THE REGION OF CONTACT

$$U_B = \frac{M^2}{2B} \qquad U_E = \frac{T^2}{2\lambda} \qquad U_C = \frac{V^2 D}{2\mu}$$

$$U_{TOTAL} = U_B + U_E + U_C$$

FIGURE 19.

AVERAGE STRESS FAILURE CRITERION

The next phase in the development of the analytical model involved the incorporation of a more advanced failure criterion. An average stress failure criterion was substituted for the maximum stress failure criterion, allowing the strength predictions to be formulated on a constituent fiber and matrix level. The yarn bundle stresses were broken down into constituent fiber and matrix stresses using an average stress procedure. The allowables for the fiber and matrix strengths were used to compute failure ratios for the fiber and matrix for tensile, compressive and shear failure modes. The strength approach was then extended into a sequential failure analysis mode wherein matrix dominated failures were not considered catastrophic. If the first failure was a matrix failure, the matrix properties for the appropriate yarn bundle were reduced and the analysis was continued until fiber failure occurred. Ultimate strength was characterized by fiber axial failure or sudden increases in strain levels due to stiffness reductions as a result of large numbers of transverse and shear failures. The average stress failure criterion was also used to observe the effects of residual and hygrothermal stresses on composite failure. A flow chart which illustrates how this failure criterion fits into the overall analytical model is shown in Figure 20.

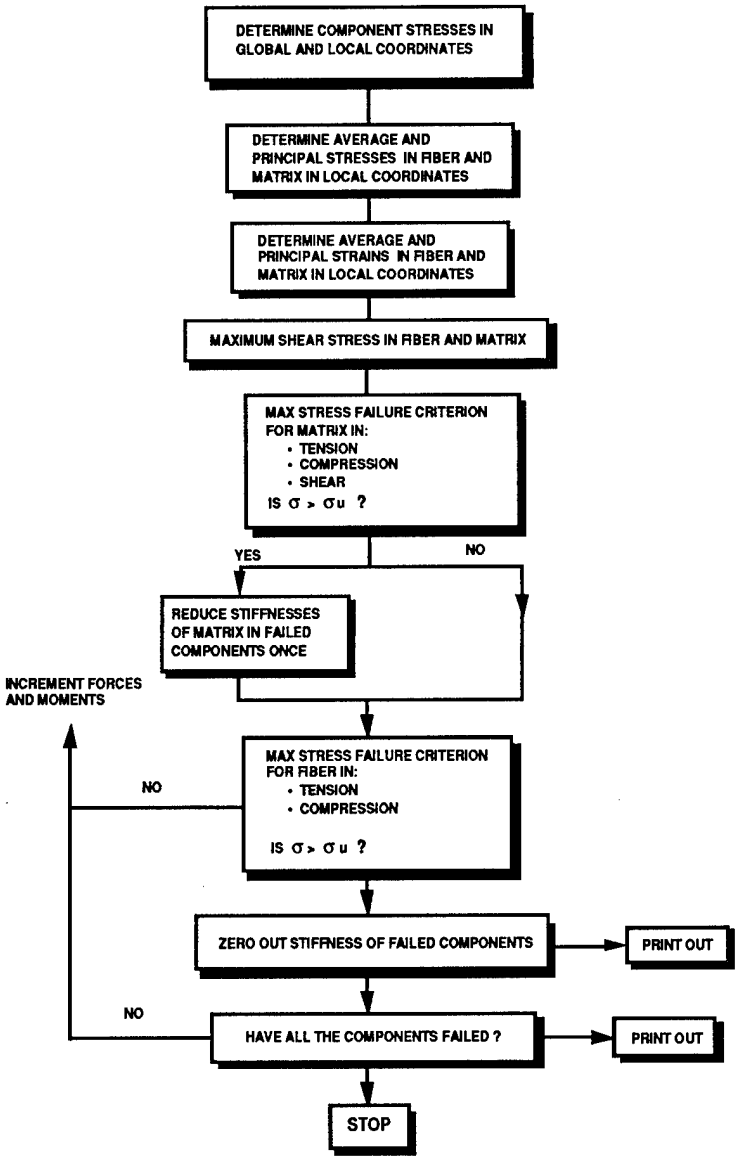


FIGURE 20.

INCORPORATING A COMBINATION OF FAILURE CRITERIA

A problem with the average stress failure criterion used in the model was unveiled after the completion of a preliminary parametric study. It was observed that the values of the predicted failure stresses and strains were too high because the average stress failure criterion only tested the fiber for tension and compression failure. Since any off-axis fiber fails in shear (before tension and compression), the correct failure mode of the fibers was not being checked. To correct this shortcoming, the failure criterion was modified to operate in the following manner: the average stress failure criterion is first used to detect matrix cracking in a component, the matrix stiffness is then reduced proportionally in the failed component, finally a maximum stress failure criterion is then used to check the component strength in each of the possible failure modes including shear. It was concluded that the average stress failure criterion cannot alone predict the strength of braided composites as first thought. The flow chart of this combined failure criterion is illustrated in Figure 21.

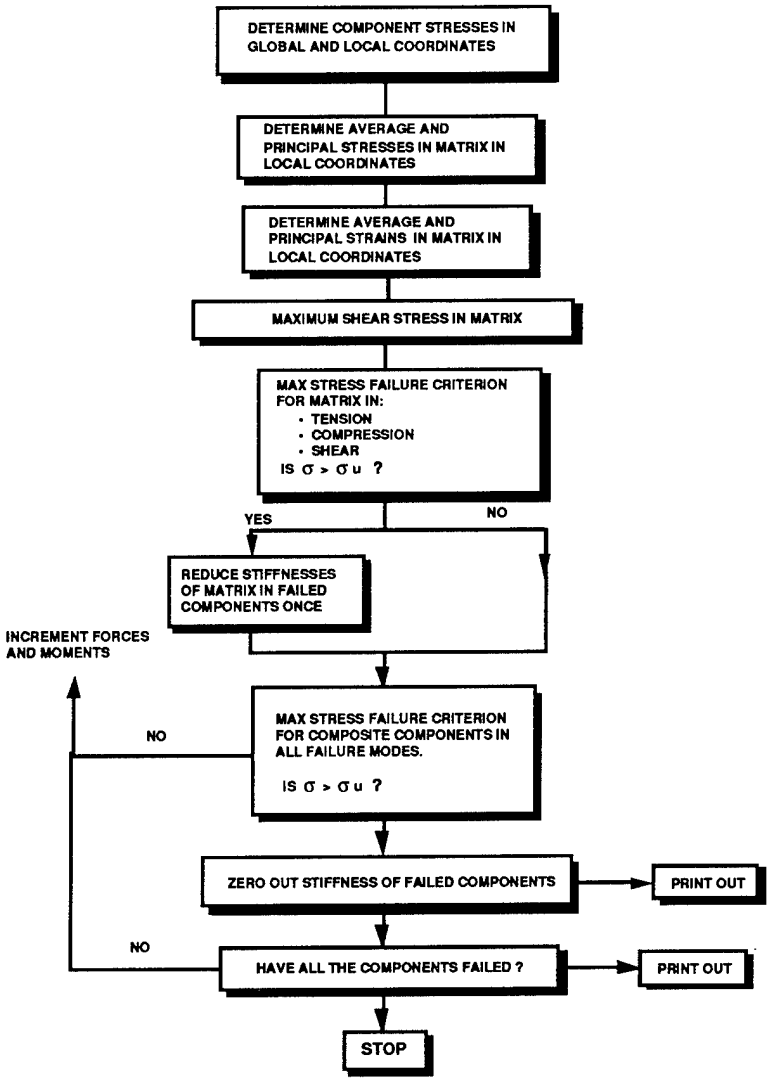


FIGURE 21.

PARAMETRIC STUDY

A preliminary parametric study investigating the mechanical behavior of 3-D braided composite plates was initiated following the addition of the combined failure criterion to the model. The purpose of this study was to provide some insight to the problem of determining the precise amount of through-the-thickness fiber reinforcement required in a preform to improve such properties as damage resistance and out-of-plane strength without excessively degrading in-plane properties.

The preliminary parametric study examined the effect of various fiber architectures on composite stiffnesses and strengths. Figure 22a through Figure 22c illustrates the relationships between fiber architecture and braided composite stiffnesses . Figure 22d illustrates the effect of braiding ratio on the preform fiber angles. Figure 22e shows the relationship between longitudinal strength and surface braiding angle, and finally, Figure 22f shows the longitudinal strength and out-of-plane shear strength for different braiding surface angles. These figures demonstrate the capabilities and the variety of studies that can be performed using the developed model.

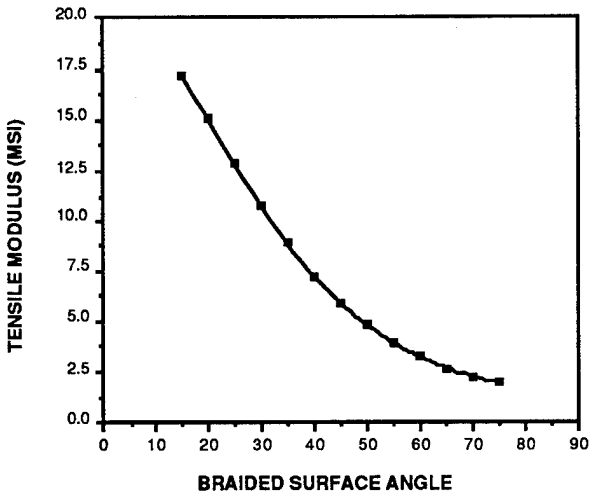


FIGURE 22a.

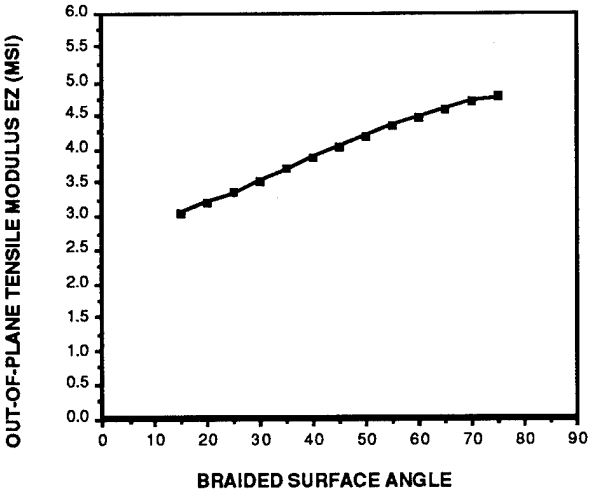


FIGURE 22b.

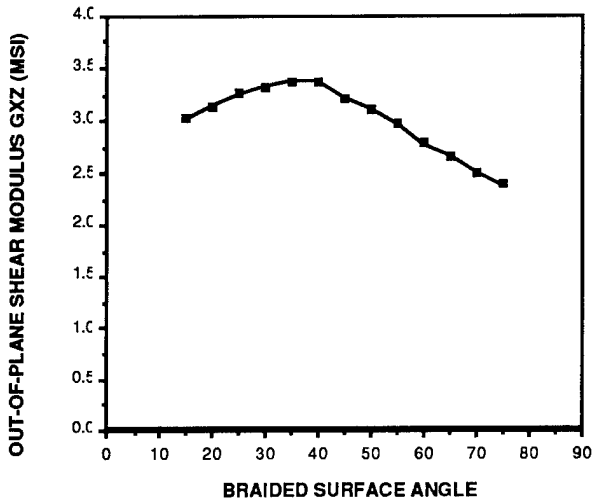


FIGURE 22c.

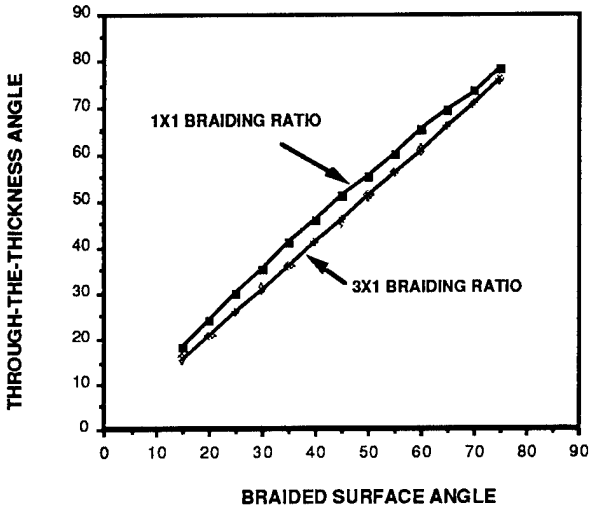


FIGURE 22d.

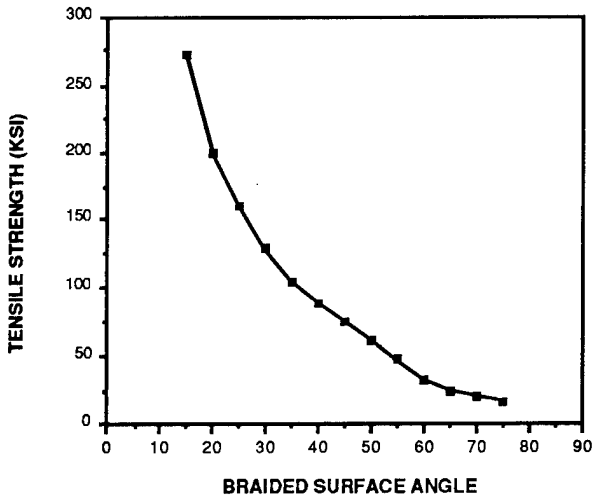


FIGURE 22e.

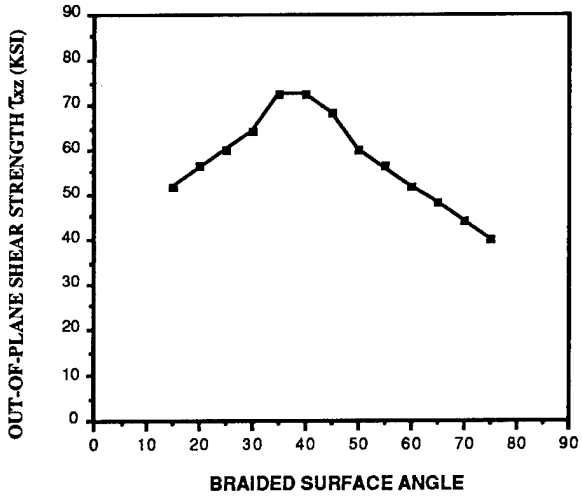


FIGURE 22f.

FINITE ELEMENT MODELLING OF BRAIDED COMPOSITE STRUCTURES

The analytical model developed in this study can be used as a tool for creating material cards for finite element models of braided structures. One example of this application is the modelling of the Iosipescu test specimen, illustrated in Figure 23, which will be used to determine the out-of-plane shear properties of braided composites in this study. This capability of the model will be used in the future to produce material cards for complicated braided structures such as full circumferential braided frames.

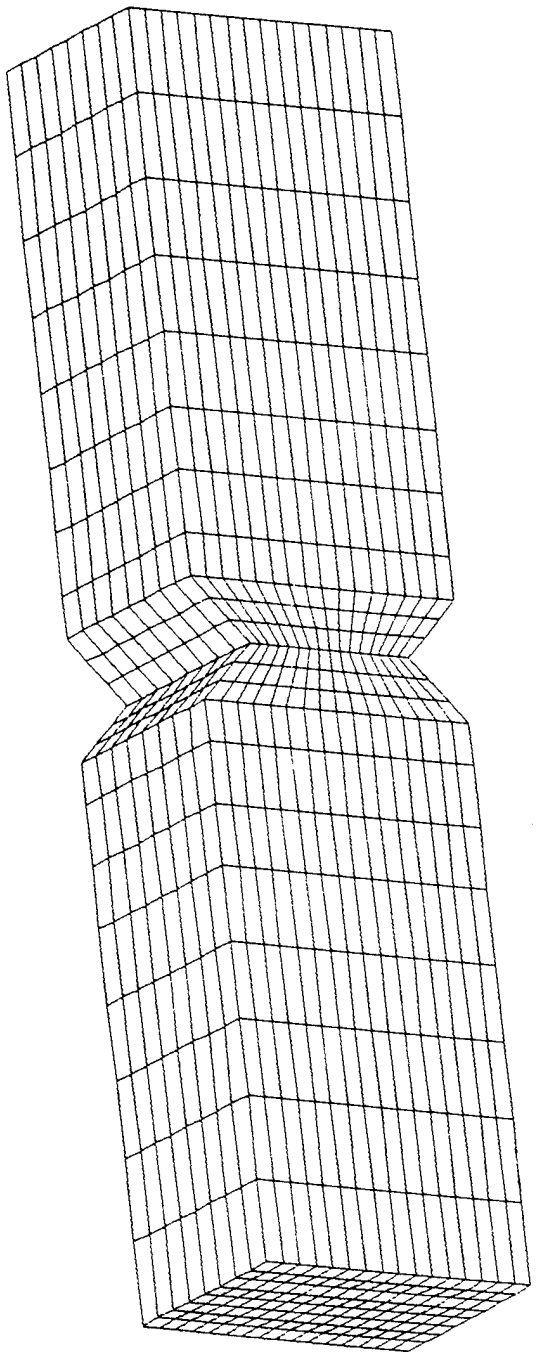


FIGURE 23.

SUMMARY OF ANALYTICAL MODEL CAPABILITIES

The analytical model developed in the ATCAS braiding program predicts stiffnesses and strengths for both 2-D and 3-D braided composite plates under a variety of loading conditions. Features of the model capabilities are summarized in Figure 24 below.

- UNIT CELL GEOMETRY (APPLICABLE TO 3-D ONLY)
  - dimensions of unit cell
  - interior fiber angles of unit cell
  - fiber lengths within unit cell
  - number of unit cells in a composite plate
- WIDE VARIETY OF LOADING CONDITIONS
  - in-plane tension and compression
  - in-plane shear
  - transverse shear
  - bending
  - twisting
  - hygrothermal loading
- PREDICTION OF COMPOSITE MODULI AND POISSON'S RATIOS
  - E, G, υ
  - stiffness modifications to account for fiber bending
- PRODUCE MATERIAL CARDS FOR FINITE ELEMENT MODELS
- STRENGTH PREDICTION
  - predicts stress state when matrix cracks in each component
  - predicts stress and strain state when a component fails
  - predicts stress and strain state at subsequent composite failure

FIGURE 24.

CONCLUSIONS AND FUTURE WORK

The primary objective of this study was to evaluate braided composite technology for applications to a commercial transport fuselage. This objective was accomplished through the investigation of four areas: 1) Design and Forming of 2-D and 3-D Braided Fabrics with Advanced Composites, 2) Manufacturing Braided Composite Parts, 3) Mechanical Testing of Braided Composites, and 4) Analysis of Braided Composite Structures.

The feasibility of braiding near net shape structural components was demonstrated by the fabrication of the simple and complex shaped preforms required by the ATCAS braiding program test matrix. The fabrication of both 2-D and 3-D braided preforms consisting of several fiber architectures and two different material tows was demonstrated.

The successful manufacturing of these preforms into composite components was demonstrated using both thermoplastic and thermosetting resins. The critical parameters inherent to the processing techniques (thermoplastic consolidation and resin transfer molding) used to manufacture the composite test specimens were identified and optimized through quality assessment testing.

A test matrix was developed to evaluate the structural performance of braided composites. The test methods that will be performed to achieve this goal include: tension, notched tension, compression, CAI, rail shear, Iosipescu shear, flange bending, bearing, and C-channel crippling.

An analytical model was developed to predict the behavior of 2-D and 3-D braided composites. The model is based on the concept of a fundamental unit cell to represent the fiber architecture. It is then expanded to provide stiffness and strength properties for analyzing structures based on shear deformable plate theory. Hygrothermal effects, stiffness modifications, and an advanced failure criterion are also incorporated to improve predicted results. The results obtained from this model will be correlated with experimental test data when it becomes available. Future work in this area will build upon the existing model by including the effects of nonlinear material properties and a progressive failure model of the matrix which will more closely represent the physical behavior of the matrix.

The study discussed in this paper will be completed by the end of 1990, at which time the ATCAS braiding program will progress from an evaluation stage to a practical application stage for commercial transport fuselage.

REFERENCES

1. Tan, T.M., Pastor, C.M., and Ko, F.K.: Engineering of Tough Ceramic Matrix Composites for Turbine Components. Transactions of the ASME, 1989.

2. Adams, D.F., Walrath, D.E.: Iosipescu Shear Properties of SMC Composite Materials. Composite Materials: Testing Aid Design (Sixth Conference). ASTM STP 787, American Society for Testing and Materials, 1982, pp.19-33.

3. Whyte, D.W.: On the Structure and Properties of 3-D Braid Reinforced Composites. PhD Thesis, Drexel University, June 1986.

4. Chou, T.W., Ishikawa, T.: Analysis and Modeling of 2-D Fabric Composites. Textile Structural Composites, Chapter 7, 1989, pp. 209 - 264.

ULTRASONIC DETECTION AND IDENTIFICATION OF FABRICATION DEFECTS IN COMPOSITES

Edward R. Long, Jr.
NASA Langley Research Center

Susan M. Kullerd
Lockheed Engineering and Sciences Company

Patrick H. Johnston
NASA Langley Research Center

and

Eric I. Madaras
NASA Langley Research Center

SUMMARY

Methods for deliberate fabrication of porosity into carbon/epoxy composite panels and the influence of three-dimensional stitching on the detection of porosity have been investigated. Two methods of introducing porosity were studied. Porosity was simulated by inclusion of glass microspheres and a more realistic form of porosity was introduced by using low pressure during consolidation. The panels were ultrasonically scanned and the frequency slope of the ultrasonic attenuation coefficient was used to evaluate the two forms of porosity. The influence of stitching on detection of porosity was studied using panels which were resin transfer molded from stitched plies of knitted carbon fabric and epoxy resin.

INTRODUCTION

Porosity in carbon fiber reinforced polymeric composites (CFRPC) caused by improper processing during fabrication has been shown to degrade the materials' mechanical performances (ref. 1-2). Therefore, methods of nondestructive evaluation (NDE) for the detection and identification of porosity are important. Ultrasonic signal attenuation is a popular NDE method for imaging and identifying porosity in CFRPC and it has been the subject of a number of recent NDE studies (ref. 3-8).

Porosity is caused by air or volatile chemical species which are not adequately released from the part during fabrication because vacuum and/or pressure is insufficient at critical points during the

cure cycle. For composites fabricated from prepreg, voids typically occur at ply interfaces and they tend to aggregate, more or less, along the direction of the fibers depending on ply orientations. Therefore, the extent to which mechanical properties are affected is dependent on a combination of the degree of improper fabrication and the orientations of the reinforcing fibers.

NDE studies of porosity in CFRPC are typically conducted with specimens in which the amount of porosity is controlled either by lowering the applied pressure or vacuum during fabrication or by using solid or hollow glass microspheres between plies to represent the porosity (ref. 1-8). Both methods provide individual spherical or aggregate cylindrical sites which cause similar characteristic scattering of ultrasonic energy. For that reason, both representations of voids provide similar frequency-dependent effects on the attenuation of ultrasonic energy and can be studied using an analysis of the slope of attenuation (ref. 3 and 7), which will be described below.

While the inclusion of microspheres allows control of the volume concentration of scatterers, this method may not provide a quantitative basis for establishing standards for production NDE. Solid inclusions have very different acoustic impedances from those for actual voids and it is not clear that a standard based on the solid-solid interface scattering will provide appropriate calibration values from which naturally occurring gas-solid interface scattering can be inferred. Inclusions of hollow microspheres does not adequately address this problem because it is not possible to prevent some unknown fraction of the hollow spheres from being crushed during the cure of the composite, making the amount of simulated porosity effectively unknown without subsequent destructive testing. In addition, both solid and hollow microspheres can act as nucleation points for naturally occurring porosity and microcracking. Lastly, for composites fabricated from three-dimensional fiber architectures consisting of woven, knitted, or stitched assemblies, there is no convenient method for introducing a uniform internal distribution of microspheres.

The use of three-dimensional fiber architectures presents a more fundamental problem for identifying porosity. For stitched, woven, knitted, or similar geometrical intertwining of fiber tows, the tows tend to stay bundled and to form concave- or convex-shaped points of intersection which provide the same spherical or cylindrical scattering surfaces as caused by voids. Consequently, the scattering from a bundled tow or of a stitch will be similar to that from a void. Therefore, the architecture of the fibers may well provide false evidence for the existence of a defect. If this would be the case, then "physics-based" methods for defect identification, such as slope-of-attenuation for porosity, may have to be modified or supplemented by more sophisticated measurement techniques when three-dimensional fiber architectures are involved.

This paper discusses recent results from ongoing research at NASA Langley Research Center to study methods for controlled representations of fabrication defects and to study the effects of three-dimensional fiber architectures on defect detection. Porosity is currently under investigation, with low-pressure and microspherical void representation being comparatively studied. The architecture of the fiber reinforcement under current study is a stitched, knitted carbon fabric and its effects on the detection of porosity are reviewed.

SPECIMEN PREPARATION

Both solid glass microspheres and low-pressure cure were used to introduce voids into the composite. The method for using low pressure is depicted in figure 1. Composite panels of AS4/3501-6* were laid up $[-45,+45]_{2S}$ using prepreg from Hercules Inc., vacuum bagged according to conventional procedures, and cured in an autoclave, using the prepreg manufacturer's recommended cure protocol, to a maintained final cure temperature of 177 ^{o}C (350 ^{o}F). A range of porosities was obtained by choosing a different curing pressure for each panel, from a low of 6.9×10^{4} Pa (10 psi) to the recommended pressure of 6.9×10^{5} Pa (100 psi). As may be seen from the photomicrographs in figure 1, the porosity varied from individual spherical voids at high pressure to larger elliptical or cylindrical voids at low pressure. Only the 6.9×10^{4} Pa (10-psi) specimen has been studied to date.

The method for using 25.4-micron (0.001-in) diameter glass microspheres is depicted in figure 2. A 15.2-cm x 15.2-cm (6.0-in x 6.0-in) composite panel was fabricated with 8 plies of AS4/3501-6 symmetrically oriented at +45 and -45 degrees. The microspheres were located at the top right between plies 1 and 2, at the middle between plies 4 and 5, and at the lower left between plies 7 and 8. During the assembly of the prepreg plies, the microspheres were deposited in a 2.5-cm x 2.5-cm (1.0-in x 1.0-in) area by holding a template containing a square hole over the lower ply for each location and distributing microspheres from a shaker. The stack was consolidated in a press mold at 6.9×10^{5} Pa (100 psi) and 177 ^{o}C (350 ^{o}F).

A stitched, knitted 15.2-cm x 15.2-cm (6.0-in x 6.0-in) panel was fabricated using a resin transfer molding technique depicted in figure 3. A 16-ply AS4/3501-6 panel, was made of knitted layers of unidirectional tows in a quasi-isotropic layup. The layers were then stitched together on 6.0-mm (0.25-in) centers in both the 0- and 90-degree directions. The 3501-6 resin was obtained from Hercules Inc. and the stitched fiber preform from Hexcel Corporation.

The details for the resin transfer process are described in another presentation at this conference (ref. 9). The panel used in this study was processed to deliberately form porosity by using a combination of 2.8×10^5-Pa (40-psi) instead of the required 5.6×10^5-Pa (80-psi) pressure and a nonheated upper platen.

EXPERIMENTAL PROCEDURE

The ultrasonic data acquisition system is depicted schematically in figure 4. Measurements were made in a water-filled tank with a motorized X-Y bridge for positioning an ultrasonic transducer pointing in the Z direction over the specimen. The panels were mounted above a sheet of flat glass, with the glass and panel lying parallel to the X-Y plane. The pulser emitted short-duration spikes, driving the transducer to launch pulses of ultrasonic energy toward the specimen along the Z-axis. Reflections of the ultrasound from the specimen and the glass behind the specimen were received by the same transducer, amplified by the receiver, and recorded by a digital oscilloscope. The digitized signals were transferred to computer and stored for subsequent display and analysis.

The set of ultrasonic reflections resulting in this system is called an A-scan. An A-scan is depicted schematically in figure 4. As shown with reference to the sketch above the A-scan, the A-scan consists of reflections from the front and rear surfaces of the specimen, any defects within the specimen, and the glass. There are also lower level scattered reflections from the internal structure of the composite, particularly the fibers. The time separation between echoes in the A-scan represent the acoustical path lengths between structures along the Z-axis and are determined by the physical distance and the ultrasonic velocity in the intervening medium.

The ultrasonic A-scan represents information in the time domain. This information can be broken into components representing different frequencies of vibration using the Fourier transformation. The squared magnitude of the resulting frequency domain function is the power spectral density, or simply the power spectrum of the signal. The power spectrum of an ultrasonic signal indicates how the ultrasonic energy is distributed among different frequency components and can be employed to investigate ultrasonic propagation phenomena, such as attenuation, which are, in general, frequency-dependent functions.

The X-Y array of the time-based peak amplitudes of the reflection from any one surface for some spatial interval between sampling points is a C-scan. For this study, C-scans were made using the amplitude of the reflection from the glass. For each sampling point, the signal passes twice through the specimen, including any flaws present at that site. C-scans were made for each panel to determine, based on the total apparent signal attenuation, the X-Y regions of the specimen for which A-scans were to be recorded. Then the A-scans were made for

specific points within those regions. Finally, Fourier transforms (FT) of the reflections from the glass were made to determine the power spectrum for each of the specific points.

SLOPE OF ATTENUATION

The analysis method based on the slope of attenuation is illustrated in figure 5. A curve representing the logarithm of a power spectrum of a glass reflection without a composite specimen in the path of the ultrasonic signal is shown as a solid line. The dot-dash curve represents the log of a power spectrum of a glass reflection for a composite specimen placed in front of the glass. Note that the amplitudes are different due to the attenuation of the sound in the sample and note also that the difference between the two power spectra varies as a function of frequency. The frequency-dependent attenuation coefficient is found from the difference between the logged power spectra which is plotted as the dotted line in figure 5.

A band width for analysis is chosen to provide sufficient signal-to-noise ratio. The vertical lines indicate the band width over which the amplitude of the reference signal power spectrum, over glass alone, is within 10 dB of its peak value. This is referred to as the 10-dB band width of the signal. In this useful band width, the attenuation curve is examined and is noted to increase approximately linearly with frequency. A linear curve fit provides a good estimation for the slope of this curve. Because porosity scatters ultrasound out of the beam by a mechanism which increases with frequency, the value of the slope of the attenuation coefficient will increase in proportion to the amount of porosity present.

RESULTS AND DISCUSSION

Microsphere and Low-Pressure Cure Representations of Porosity

Figure 6a is a C-scan for normal incidence of ultrasonic energy on the 8-ply $(+45/-45)_{2S}$ composite panel containing microspheres. The two fiber directions and, with careful inspection, the square areas in the upper right, the middle, and lower left which contain microspheres are visible. The four dark spots are images of posts which supported the panel above the glass plate.

The image in figure 6a provides one reason for concern with using glass microspheres to represent porosity. The fiber directions are visible, probably due to actual porosity which formed along the fibers during the fabrication. The squares containing microspheres are only faintly visible probably due to porosity at their boundaries, but there is nothing within the boundaries which is visibly different than in the region outside the squares. That is to say, the microspheres do not provide the same defect image as does actual porosity.

It should be noted that in order to image the microspheres the panel must be scanned at an angle of incidence less than 90 degrees with respect to the surface in a direction which also bisects the two fiber directions. In figure 6b, the angle is approximately 45 degrees. The method of scanning at an angle is discussed in reference 8. But, as can be seen from figure 6a, scanning at an angle less than 90 degrees with respect to the fiber direction is not required for imaging actual porosity. Therefore, the different scanning geometry required to image the glass beads demonstrates why glass beads are not a good representation of porosity.

One reason which is often cited in favor of using microspheres is that they provide a controlled representation of porosity (ref. 3). As may be seen in figure 7a this is not the case. Figure 7a is a photomicrograph of a cross section of the panel containing microspheres at the midplane of the panel, the center square in figure 6b. There are also concentrations of neat resin and voids in the plane containing the microspheres. This complex presence of microspheres, resin, and actual pores represents more porosity than the microspheres alone and looks more like a poor quality adhesive bond line than a region of porosity.

Figure 7b is a photomicrograph of a cross section of the panel fabricated at 10 psi. The porosity is distributed more evenly through the thickness than in figure 7a. There are regions for which there is unequal fiber/resin distribution but not to the extreme as in figure 7a in which there is almost a band of neat resin. The low-pressure configuration of porosity is more like that which actually occurs in composites due to fabrication errors.

The attenuation curves from a site over the microsphere-loaded panel and the low-pressure panel are presented in figures 8a and 8b respectively, along with the power spectra from which they were derived. Results from both types of "porosity" can be analyzed using a linear curve fit to obtain the slope of attenuation. However, as noted in the preceding discussion for figure 7, use of the microspheres also introduced voids and resin richness. This complex presence of microspheres, resin, and natural pores presents a much different loss mechanism than that provided by natural porosity. Therefore, the same concentrations of microspheres and natural porosity would not yield the same values for slopes of attenuation.

Stitched Fiber Architectures

The effects of stitching may be seen in C-scans shown in figure 9 which were made using a 0.102-cm (0.040-in) sampling interval. Figure 9a is a quasi-isotropic panel which was autoclaved from prepreg and which has no defects which could be imaged. Figure 9b is the stitched quasi-isotropic, resin transfer molded panel described earlier. For both scans, four 0.063-in diameter lead shot were placed on the upper surface in a square array to determine how well the shot could be

imaged. The four lead shot can be seen as black spots in figure 9a, but four lead shot in a similar arrray, plus two additional shot within that array, cannot be distinguished in figure 9b. (For these two scans, reflections from the front surface and the interior of panel, not including the rear surface, were used instead of reflections from the glass. Therefore, the supports holding the panel above the glass reflector plate were not imaged.) The difference in visibility of the shot points out the difficulties which will be encountered if today's current ultrasonic C-scan techniques are used to interpret the quality of composite panels fabricated from three-dimensional fiber architectures.

Figure 10 is a set of photomicrographs, at 50X, through the panel thickness for each of three areas of the stitched panel. One area is a "good area" between stitches, another is a "bad area" between stitches, and the third is the area of a through-the-thickness stitch itself.

Figure 10a shows a "good area". The fiber orientations are visible as well as regions of nonuniform distribution of fiber and resin and a small amount of microcracking.

The "bad area" is shown in figure 10b. Visible are voids as well as resin richness and microcracks. Also visible at approximately one-quarter intervals through the thickness is the thread used for knitting. The difference between the "good area" and the "bad area" would appear to be the extent of porosity. If microcracking and resin richness are included in the list of fabrication defects then there are no good areas. Thus it should be clear that the issues surrounding fabrication defects are far more complicated than just porosity.

An area containing a stitch is shown in figure 10c. There are two orientations of stitching. One orientation of the stitching is parallel to the surface of the panel and can be seen at the top of the photograph as a bundle, or tow, coming towards the viewer. The second orientation is vertical through the thickness. Also visible are microcracks around the stitch and again it is evident that fabrication defects are more complicated than just porosity.

The stitching through the thickness contributes to the complexity of the ultrasonic measurement because its sound velocity is greater than the surrounding medium. The part of the wavefront propagating through the stitch travels faster than in the surrounding material, resulting in a phase-distorted wavefront at the receiving transducer. Since the transducer sums across its face with respect to phase as well as with respect to amplitude there is a phase-cancellation effect which reduces the perceived amplitude of the signal. This explains why the parts of the C-scan in figure 9b corresponding to the intersection of stitch lines, which is where the stitching passes through the thickness, is particularly dark. The stitch running parallel to the plane of the panel distorts the local fiber geometry,

potentially causing phase-cancellation effects, as well as providing a scattering cross section which is similar to that of the voids.

Figure 11 presents the attenuation coefficients, the slopes, and the void volume fractions measured for the "good area", the "bad area", and the stitching. The void volume fractions were determined using optical analysis. The slope is slightly increased in the "bad area" relative to the "good area", in concert with its larger amount of porosity. The attenuation measured over the stitch, however, exhibits a slope that is more than double that of the "bad area", despite having less porosity.

The distortions and scatterings of ultrasonic signals caused by the stitching appear to suggest that current methods of ultrasonic characterization of porosity, such as slope of attenuation, may not be useable for three-dimensional fiber architectures unless additional advanced ultrasonic scanning techniques are developed. One advanced technique currently under investigation at Langley Research Center for use with three-dimensional fiber architectures is phase-insensitive detection (ref. 10). This technique uses an array of detectors. Each detector's sensing area is so small that the phase distortion within that area caused by the fibers oriented in the direction of the wave propagation is negligible. Therefore, the phase-cancellation effect caused by through-the-thickness oriented fibers may be eliminated.

ACKNOWLEDGMENT

The authors wish to recognize the positive support and participation of Edward C. Taylor and Carolyn J. James for this research. Both have played a significant role in the work at Langley Research Center towards establishing state-of-the-art ultrasonic capabilities for NDE of materials and structural components.

SUMMARY

A study is in progress to evaluate two methods for representing porosity in composite materials and to investigate the effects of three-dimensional fiber architectures on detection of porosity. Porosity representations were accomplished by introduction of glass microspheres between layers of fibers before fabrication and by use of reduced pressure during fabrication. Ultrasonic C-scans, Fourier transforms of the reflected ultrasonic signal, and photomicrographs of the regions of interest show that microspheres are not a good choice for representation of porosity. The same forms of data also showed that the methods which are currently in use for characterization of porosity in conventional composite laminates will not be satisfactory for characterizing porosity in composites containing three-dimensional arrays of fiber.

REFERENCES

1.- Judd, N. C.; and Wright, W. W.: Voids and Their Effects on The Mechanical Properties of Composites - - An Appraisal. SAMPE Journal, Jan/Feb 1978, pp. 10-14.

2.- Lenoe, E. M.: Effects of Voids on Mechanical Properties of Graphite Fiber Composites. U.S. Air Systems Command AD727236, 1970.

3.- Handley, S. M.; Hughes, M. S.; Miller, J. G.; and Madaras, E. I.: Characterization of Porosity in Graphite/Epoxy Composite Laminates With Polar Backscatter and Frequency Dependent Attenuation. 1987 Ultrasonic Symposium, vol. 2, 1987, pp. 827-830.

4.- Hsu, D. K.: Quantitative Evaluation of CFRP Void Contents Using Ultrasonic Attenuation and Velocity. Proceedings of the Fourth Japan-U.S. Conference on Composite Materials, Washington, DC., June 27-29, 1988, pp. 1015-1024.

5.- Fuller, M. D.; and Gammell, P. M.: Ultrasonic Characterization of Porosity in Composite Materials by Time Delay Spectroscopy. Review of Progress in Quantitative Nondestructive Evaluation, vol. 6B, 1986, pp. 1157-1163.

6.- Tittmann, B. R.; Hosten, B.; and Abel-Gawad, M.: Ultrasonic Attenuation in Carbon-Carbon Composites and the Determination of Porosity. Proceedings of the IEEE 1986 Ultrasonics Symposium, vol. 2, 1986, pp. 1047-1050.

7.- Hsu, D. K.; and Nair, S. M.: Evaluation of Porosity in Graphite-Epoxy Composite by Frequency Dependence of Ultrasonic Attenuation. Review of Progress in Quantitative Nondestructive Evaluation, vol. 6B, 1986, pp. 1185-1193.

8.- Handley, S. M.; Hughes, M. S.; Miller, J. G.; and Madaras, E. I.: An Investigation of the Relationship Between Contrast and Azimuthal Angle for Imaging Porosity in Graphite/Epoxy Composites With Ultrasonic Polar Backscatter. Proceedings of the IEEE 1988 Ultrasonics Symposium, vol. 2, 1988, pp. 1031-1034.

9.- Loos, Alfred C.; and Weideman, Mark H., et al.: Infiltration/Cure Modeling of Resin Transfer Molded Composite Materials Using Advanced Fiber Architectures. NASA CP-3104, Part 2, 1991, pp. 425-442.

10.- Johnston, Patrick H.: Phase-Insensitive Detection and the Method of Moments for Ultrasonic Tissue Characterization, Ph.D. Dissertation, Washington U., St. Louis, MO, 1985.

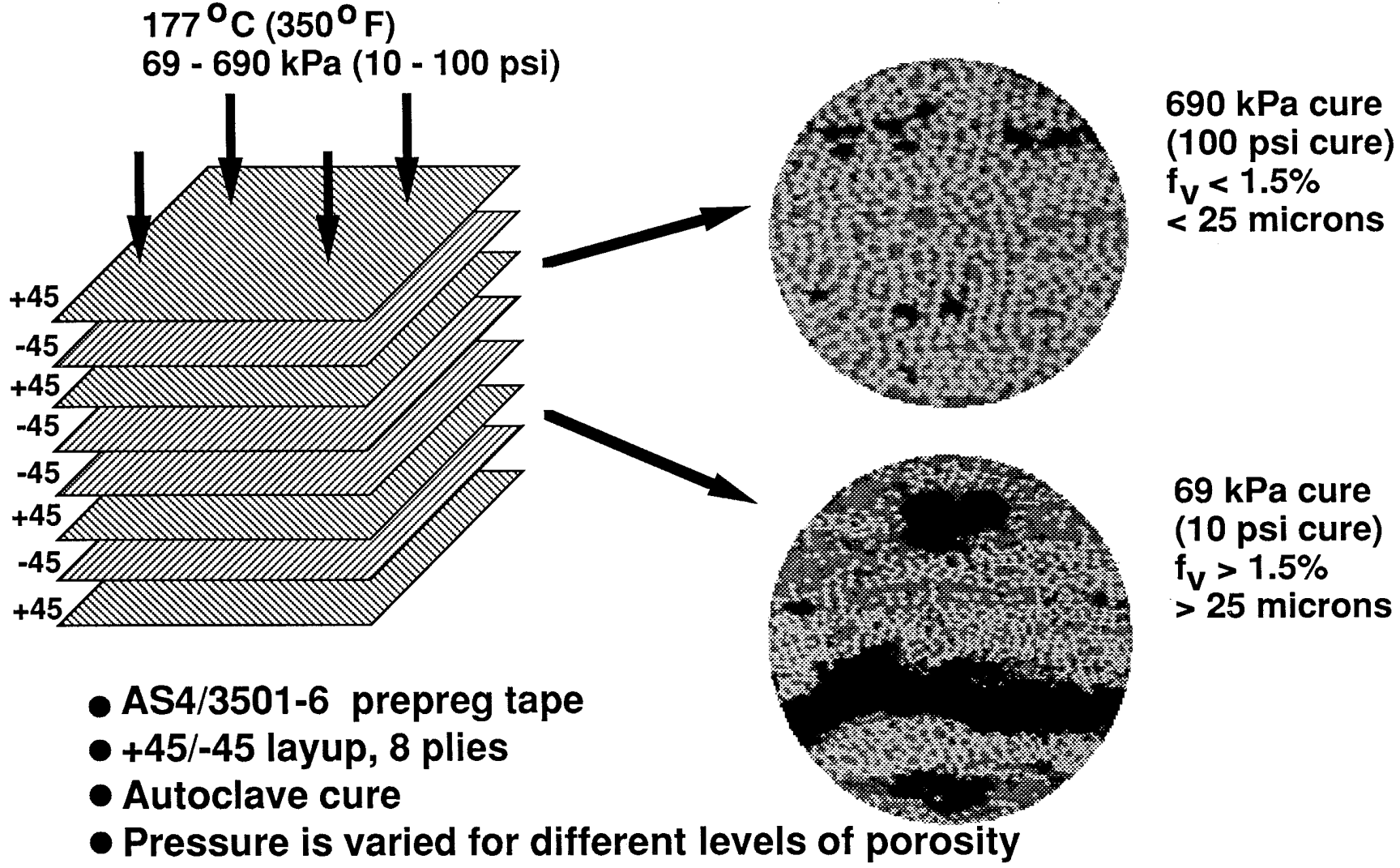


Figure 1 - Low-pressure fabrication of composite panels containing porosity.

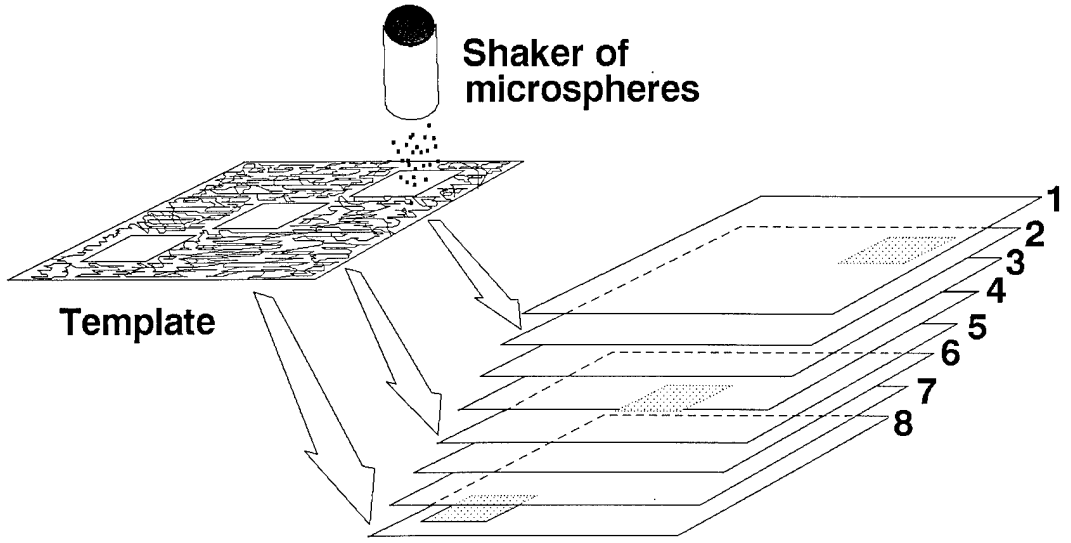


Figure 2 - Use of glass microspheres to represent localized areas containing porosity.

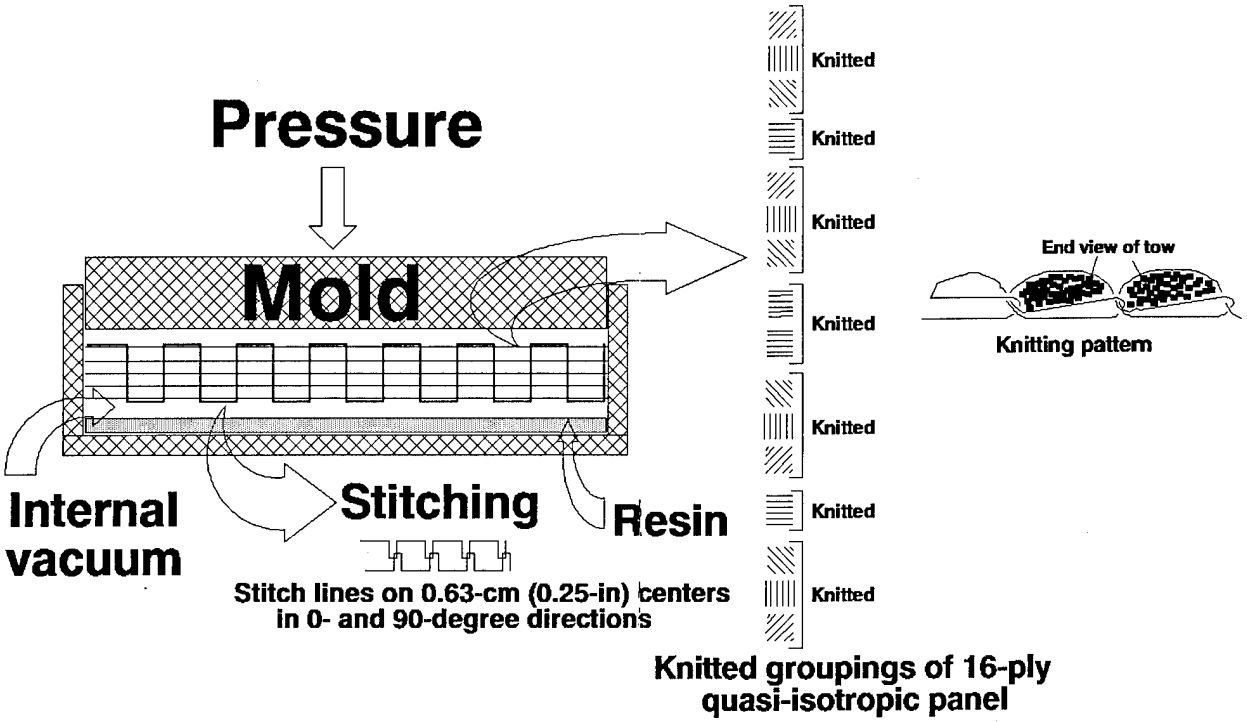


Figure 3 - Resin transfer mold fabrication of a stitched, knitted panel.

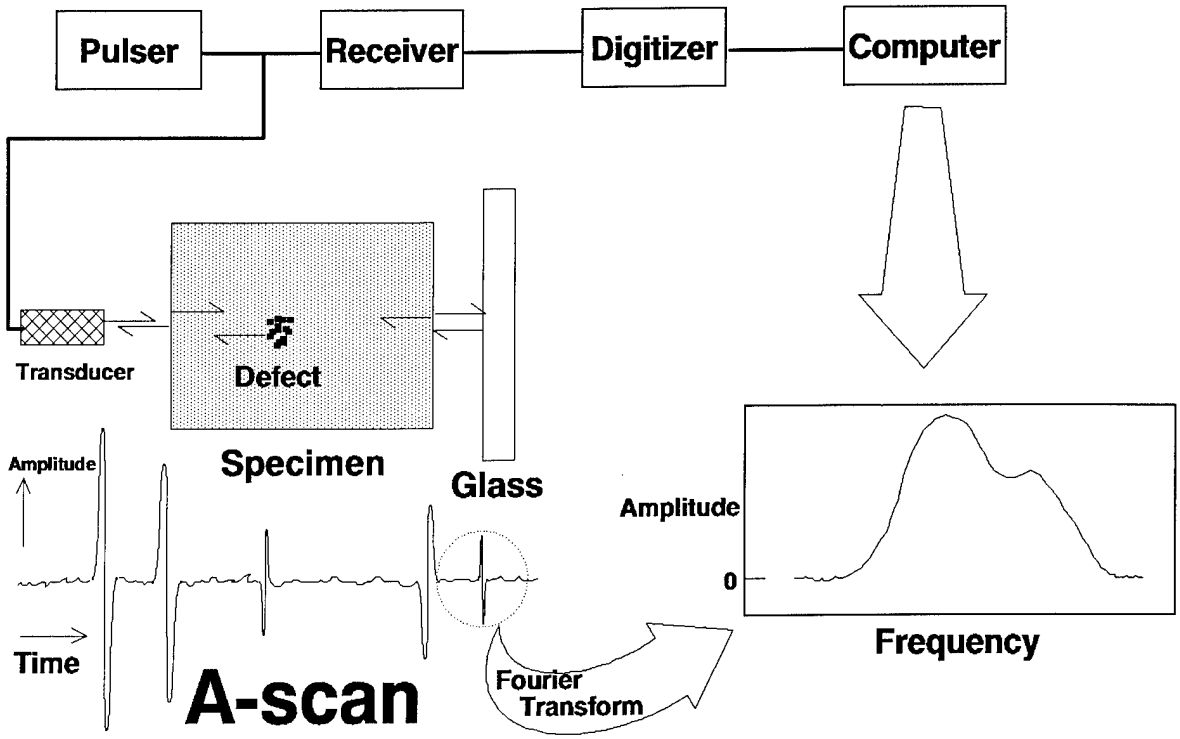


Figure 4 - Diagram of ultrasonic data acquisition system.

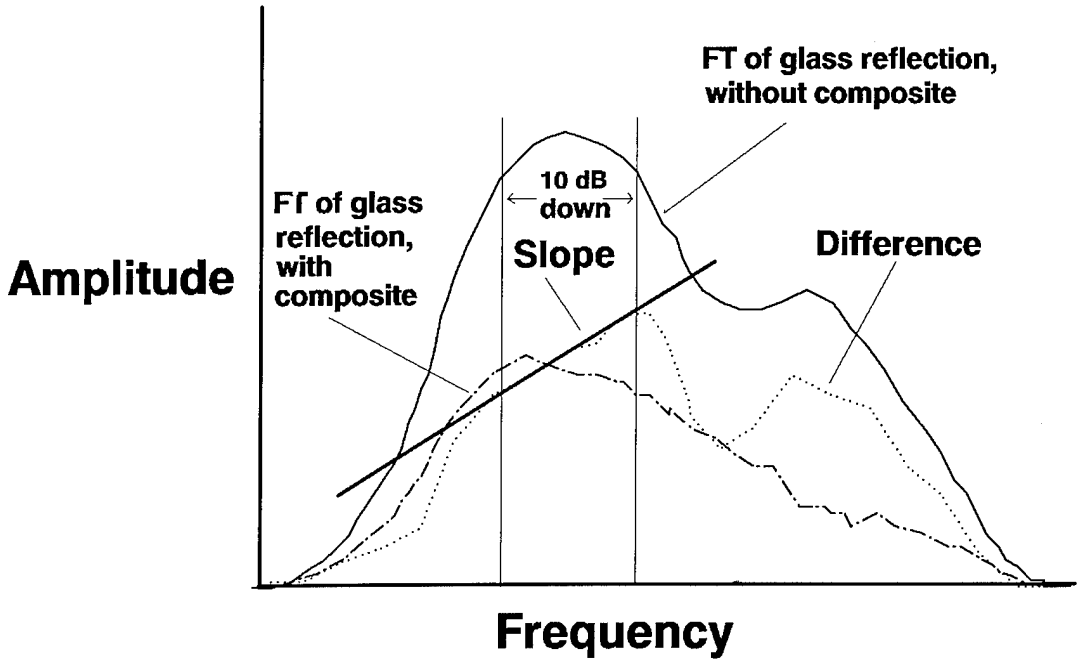
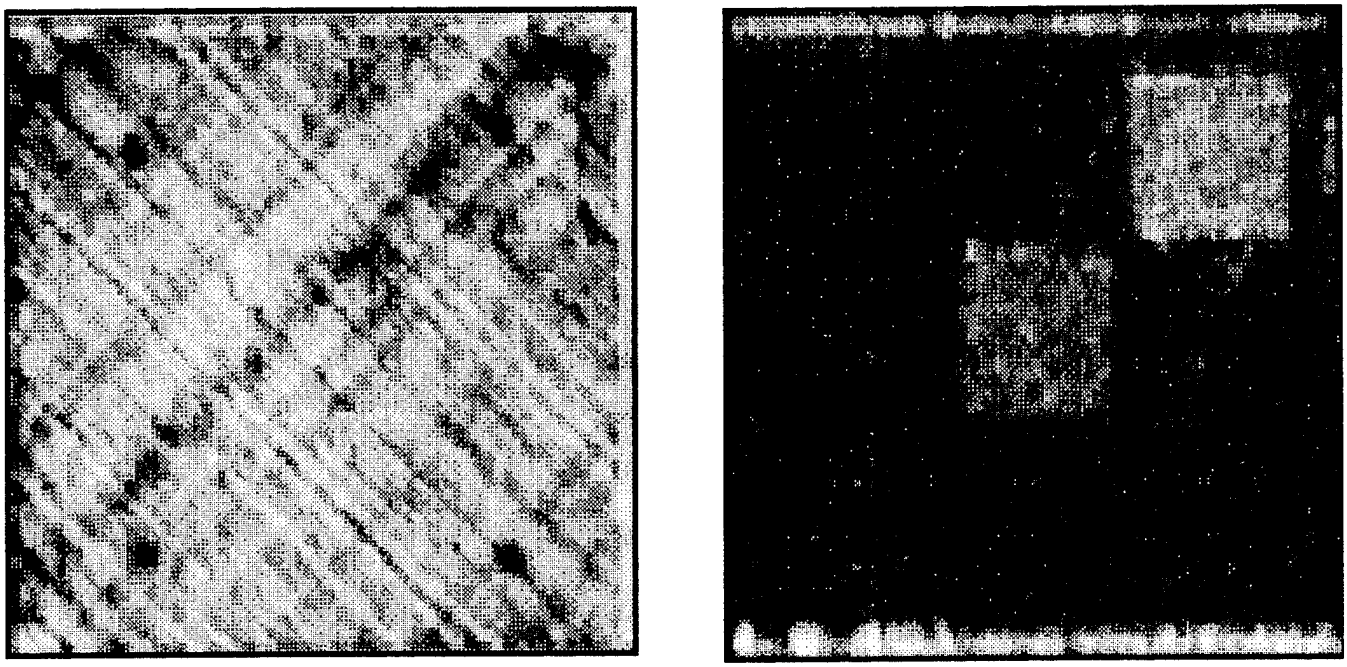


Figure 5 - Determination of slope of attenuation caused by panel defects from differences of Fourier transforms (power spectra) of reflections from the glass reflector plate with and without a composite panel in the beam path.



(a) Normal incidence

(b) 45-degree incident angle

Figure 6 - C-scan image of a 15.2-cm X 15.2-cm (6.0-in x 6.0-in), 8-ply, $(+45/-45)_{2s}$ panel containing 2.5-cm X 2.5-cm (1.0-in x 1.0-in) patches of glass microspheres.



(a) Microspheres imbedded at the midplane.



(b) Porosity induced by 69 kPa (10 psi) cure. Void volume fraction: 3.5% by resin digestion (ASTM D-3171) and 4.7% by optical analysis.

Figure 7 - Photomicrographs of sections through an 8-ply, $(+45/-45)_{2s}$ graphite/epoxy composite.

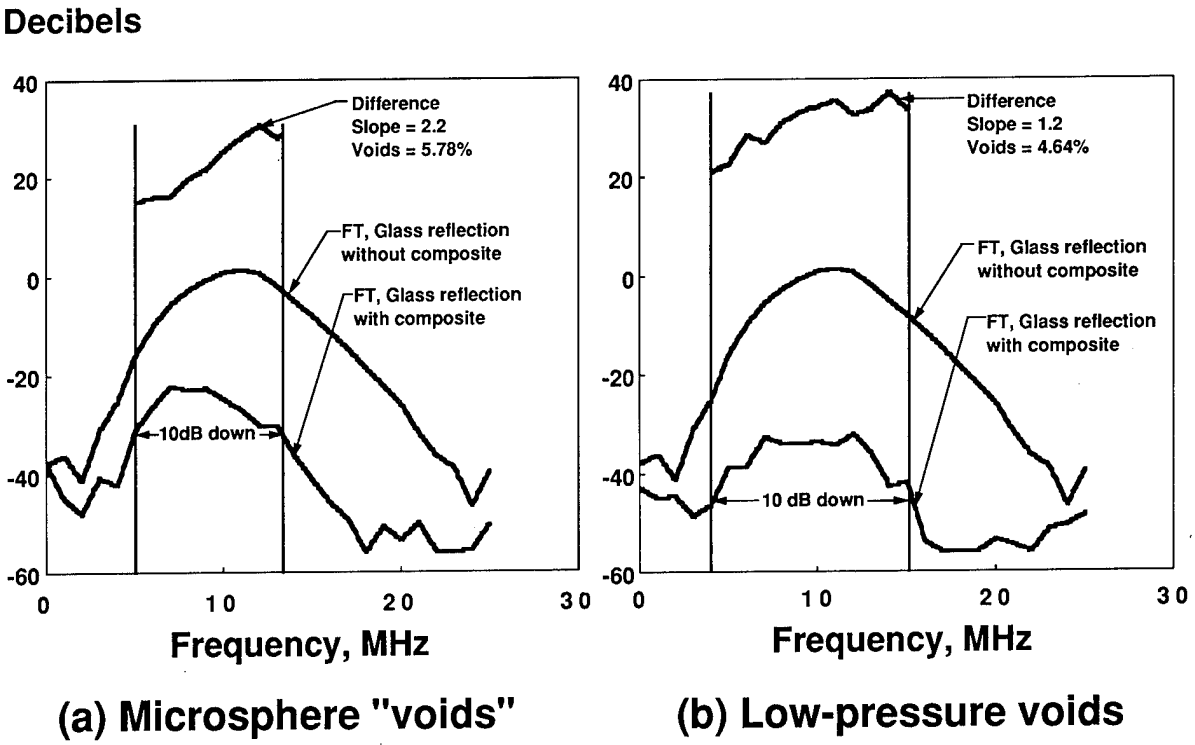
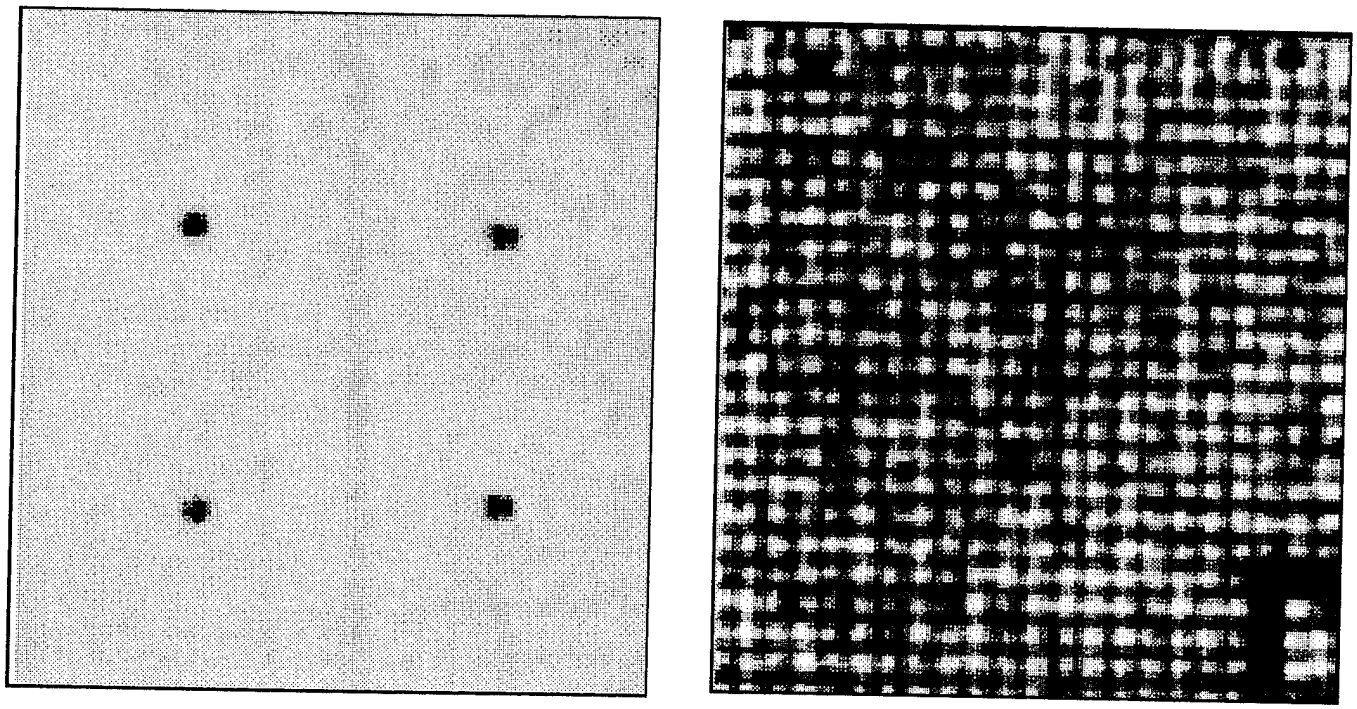


Figure 8 - Differences of Fourier transforms for glass microsphere (a) and for low-pressure (b) representations of porosity. Void content determined from optical analysis.



(a) Non-stitched

(b) Stitched

Figure 9 - C-scans of nonstitched and stitched panels, both having lead shot on their upper surface, using reflections from the panel's front surface and volume.

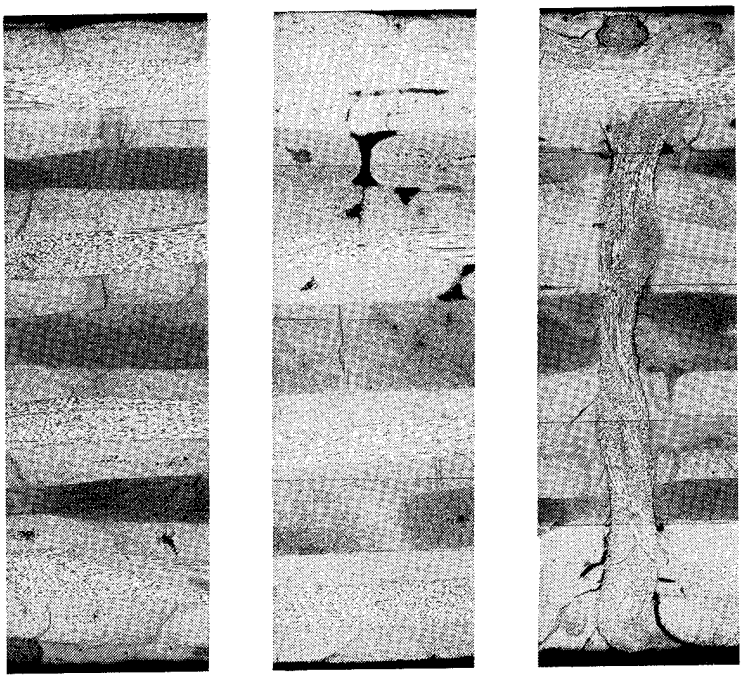


Figure 10 - Photomicrographs through three areas of the stitched panel.

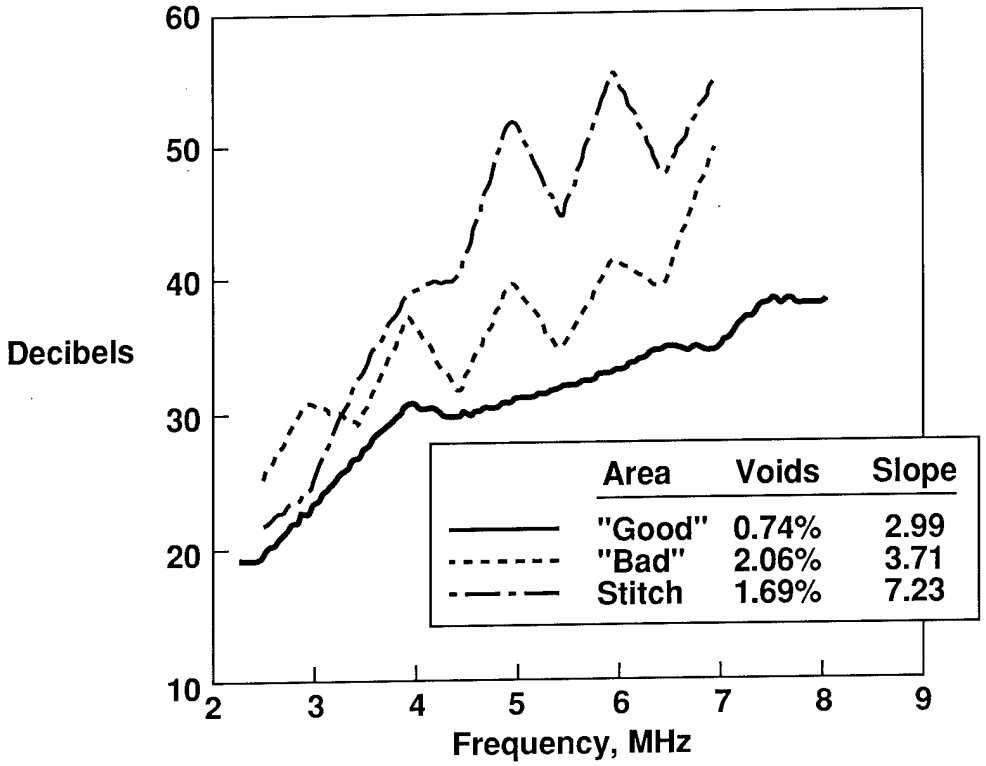


Figure 11 - Differences of Fourier transforms for good, bad, and stitch areas in figure 10. Void content determined from optical analysis.

DEVELOPMENTS IN IMPACT DAMAGE MODELING FOR LAMINATED COMPOSITE STRUCTURES[1]

Ernest F. Dost, William B. Avery, and Gary D. Swanson

The Boeing Company, Seattle, Washington

and

Kuen Y. Lin

University of Washington, Seattle, Washington

Introduction

Damage tolerance is the most critical technical issue for composite fuselage structures studied in ATCAS. The ATCAS program goals in damage tolerance include the characterization of impact damage, models for impact damage simulation, and understanding the behavior of notches and delaminations.

The characterization of potential impact damage states in fuselage is being accomplished through test. Configured structure will be impacted in different locations with a number of different impactor variables. The damage states will be assessed both nondestructively and destructively.

An approach for predicting the post-impact compressive behavior of laminated composites has been developed at Boeing over the past several years. Dr. K.Y. Lin and Dr. Z.Q. Chen at the University of Washington will be enhancing and generalizing this approach to account for the different potential damage states and failure modes found in the test program described above.

Tension damage tolerance is currently being addressed through a test program and analysis development by Dr. F.K. Chang at Stanford University. Future work with Dr. P.A. Lagace and Dr. M.J. Graves at Massachusetts Institute of Technology will address dynamic fracture including pressure effects.

Objectives

The objective of the work being presented is to understand both the impact damage resistance and residual strength of laminated composite fuselage structure. An understanding of the different damage mechanisms which occur during an impact event will (a) support the selection of materials and structural configurations used in different fuselage quadrants and (b) guide the development of analysis tools for predicting the residual strength of impacted laminates. Prediction of the damage state along with a knowledge of post-impact response to applied loads will allow for "engineered" stacking sequences and structural configurations; intelligent decisions on repair requirements will also result.

---

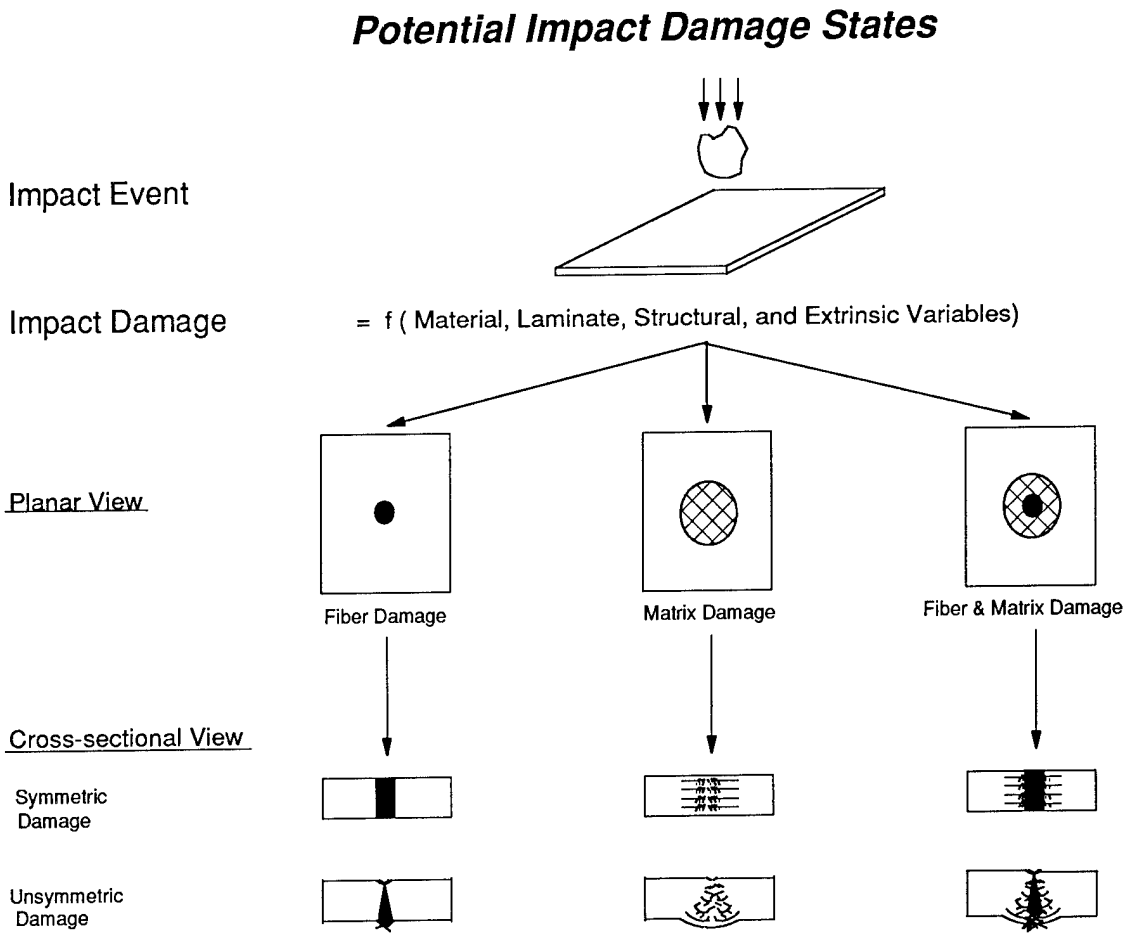
[1] This work is being funded by Contract NAS1-18889, under the direction of J.G. Davis and W.T. Freeman of NASA Langley Research Center.

Potential Impact Damage States

A schematic diagram classifying characteristic damage states (CDS) that have been observed in flat laminates following low-velocity impact by spherical objects is shown. Planar and cross-sectional views of CDS are given in the figure. Three classes of CDS consisting of symmetric damage through the laminate cross section are shown in this figure. Damage size and type (fiber, matrix, or combined) depend on variables such as delamination resistance and impact energy. The most common damage observed in experiments with a stacking sequence used for material screening tests (i.e., $[45,0,-45,90,]_{nS}$) was matrix damage [1, 2].

Plate boundary conditions, laminate thickness, and material form are among the variables which may suppress delamination, causing damage dominated by fiber failure. Fiber damage, when present, tends to concentrate at the impact site. Matrix damage is also centered at the impact site, but tends to radiate away from this point to a size dependent on delamination resistance. The most general classification of symmetric damage involves both fiber and matrix failure.

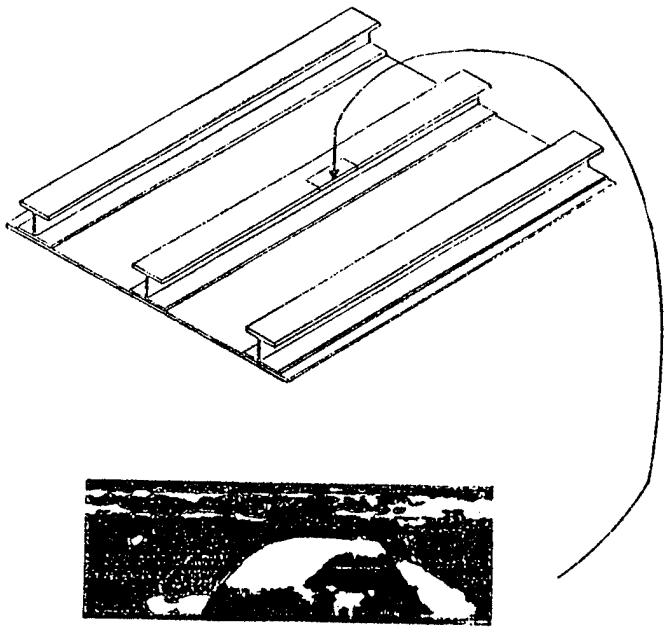
Many factors can affect the CDS symmetry. Test observations have indicated thin laminates and heterogeneous stacking sequences tend to have unsymmetric CDS with damage concentrated opposite the impacted surface. Very thick laminates are also expected to have unsymmetric damage, but with damage concentrating closer to the impacted surface. Work by the current authors has indicated that delamination resistant materials have a stronger tendency for unsymmetric CDS than brittle materials tested with the same impact variables [3].



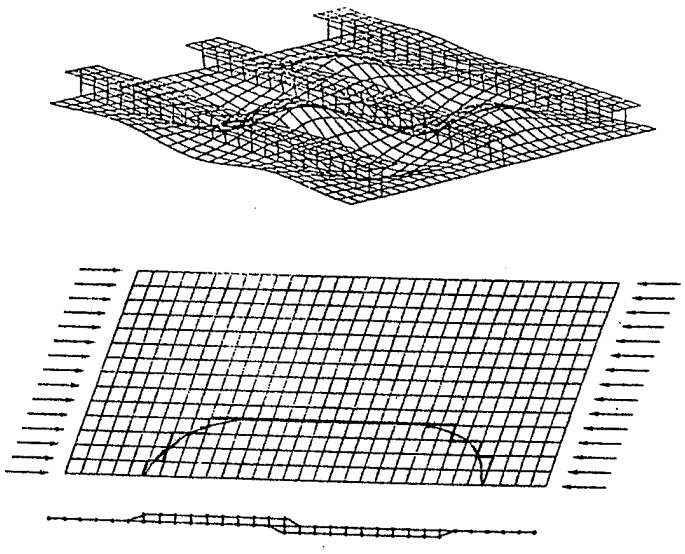
Damage Modeling Applications

The panel shown below is a carbon fiber reinforced plastic (CFRP) wing gauge panel impacted on the stiffener cap. The impact damage located on this stiffener cap was nonvisible. An identical panel had been impacted on the stiffener attachment flange edge. Both panels had significant reductions in strength from their undamaged strength. Analytical tools developed to predict the post-impact response of CFRP structure must have enough generality to account for different failure modes which occur during impact. The approaches presented take into account both stress redistribution and changes in panel postbuckling response due to sublaminate buckling [1-3]. The prediction of post-impact response due to local fiber failures was presented by Cairns [4].

Impact Damage Discrete Modeling



Wing Structure with Integral Stiffeners
Impacted on Free Flange

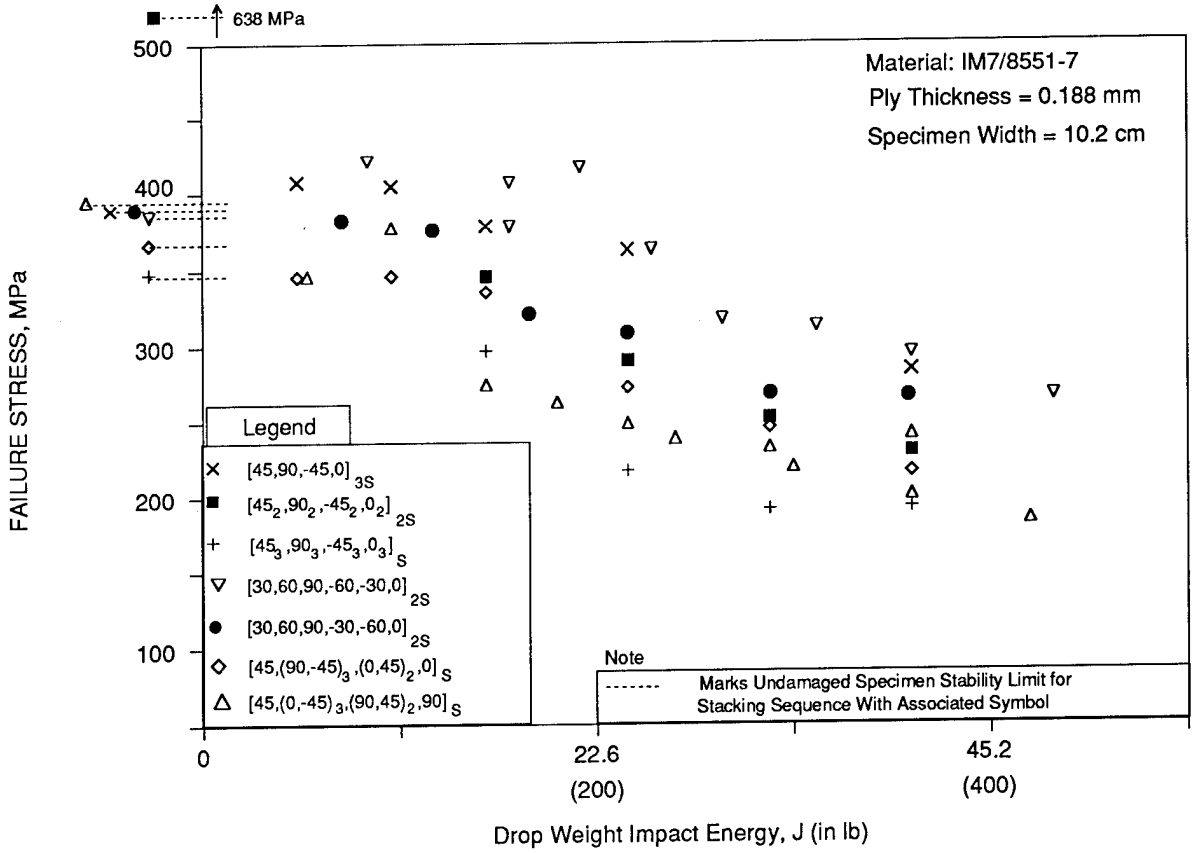


Global/Local Nonlinear Post-Buckling Analysis

Experimental Data Showing Post-impact Compression Performance as a Function of Laminate Stacking Sequence

Compression after impact (CAI) data are shown as a function of the drop weight impact energy (i.e., drop height x drop weight). Data scatter for each type of laminate layup was small compared to the total range of results. This indicated that laminate stacking sequence is critical to CAI. Note that all other material, laminate, structural, and extrinsic variables were held constant for the tests. The one exception was for the $[45_2,90_2,-45_2,0_2]_{2S}$ laminate which had 32 plies instead of 24 plies. Despite the additional thickness, this laminate did not have the highest CAI for a given impact energy, again indicating the importance of stacking sequence. These data illustrate that models to predict residual strength of impacted laminates must include stacking sequence dependent CDS details [3].

Experimental Data Showing Post-Impact Compression Performance as a Function of Laminate Stacking Sequence



SUBLAMINATE STABILITY/REDUCED STIFFNESS CAI MODELING

The CDS for a set of impact variables used in material screening tests was described in earlier work [1,2,5]. These tests use a $[45,0,-45,90]_{nS}$ laminate stacking sequence. As discussed earlier, any fiber damage caused by impact tends to concentrate at the core of the CDS. A network of matrix cracks and delaminations comprise the remainder of the CDS. Delaminations at each ply interface are connected to those at neighboring ply interfaces by transverse matrix cracks. In a planar view, double-lobed delaminations formed at each interface. These delaminations are wedge shaped due to the $\pi/4$ difference in orientation of neighboring plies, breaking the CDS into octants. The ply orientation angles increase in $\pi/4$ increments from the impacted surface to the center. The stacking sequence and CDS is reflected at the center. Ply orientations decrease by $\pi/4$ with each ply from the center to the back side. This pattern causes a CDS with interconnected delaminations spiraling toward the center, reversing direction, and proceeding out toward the back side.

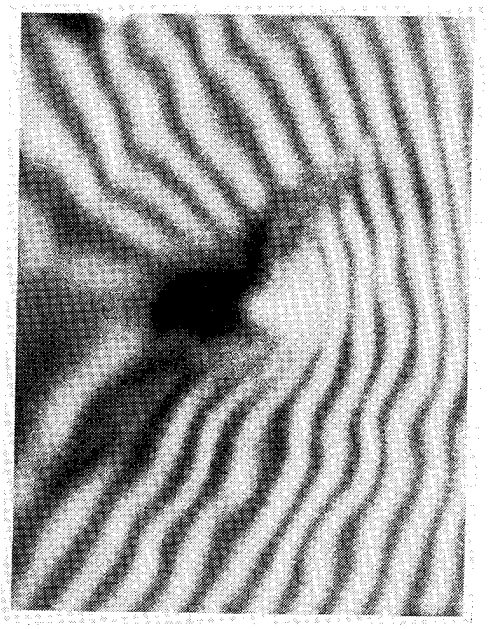
The CDS described above splits the laminate into separate sublaminates. These sublaminates are connected in a fashion similar to a spiral staircase, but are conceptualized as circular disks to simplify the analysis. The sublaminates near the outer surfaces vary in thickness from 2 to 5 plies. The next set of sublaminates are 4 plies in thickness with stacking sequence varying stepwise around the damage. This type of sublaminate can repeat several times, depending on the number of plies in the stacking sequence. Damage that occurs approaching both sides of the laminate midplane results in two discontinuous sublaminates and a symmetric core sublaminate that varies in thickness from 2 to 8 plies. The total number of sublaminates for a $[45,0,-45,90]_{nS}$ laminate stacking sequence is $(2n+1)$. This can be generalized for other repeating stacking sequences which increment by either decreasing or increasing ply angles if a sum of the difference between adjacent angles in the repeat element equals zero (i.e., $[\alpha,\beta,\phi,...,\theta]_{nS}$ where $\{\beta-\alpha\}+\{\phi-\beta\}+ ... +\{\alpha-\theta\} = 0.0$). Absolute values of each difference should also not exceed 90°.

The analysis method used for comparison with experiments is documented in [1,2]. In summary, five basic steps are followed in applying the method. First, the CDS is identified and simulated as a sublaminate with ply stacking sequence and thickness representing an average of those appearing in the real CDS. Second, a sublaminate stability analysis is performed using damage diameter as an independent variable characterizing the planar size of the CDS. This is done using a modification to the buckling analysis method described in [6]. The modification accounts for sublaminates with unsymmetric ply stacking sequences [1,2]. Third, effective reduced stiffness of the impact damage zone is calculated using results from sublaminate stability analysis. Fourth, the inplane stress concentration associated with the reduced stiffness is determined. Finite elements are used for this step in order to account for specimen width/damage size interactions. Finally, a maximum strain failure criteria is applied to predict CAI.

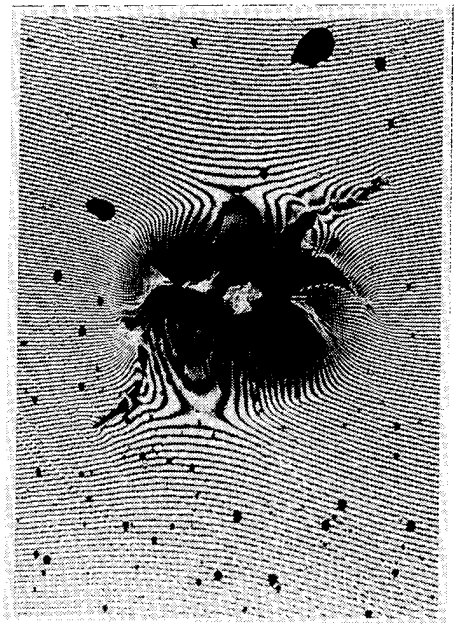
Note that steps 2 through 4 of the sublaminate stability analysis method should be modified for the most general CDS in which sublaminate parameters (e.g., diameter, thickness and stacking sequence) vary significantly through the laminate thickness. The more general model is currently being developed.

Experimental Determination of Sublaminate Buckling and Strain Distribution of Impacted Laminates

Sublaminate stability and subsequent load redistribution of compressively loaded impact damaged coupons are being examined experimentally. Moire interferometry was employed to measure both in-plane and out-of-plane displacements of impacted coupons as a function of load. A micro-Moire grid (600 lines/millimeter) used to measure inplane displacements was applied to the tool side while the other side used shadow Moire (60 lines/cm) to measure out-of-plane displacements. A typical Moire fringe pattern displaying out-of-plane displacements for a $[45,0,-45,90]_{3S}$ specimen with a damage diameter of 1.28" is shown. The in-plane *u*-displacements are shown next to it. By examination of the in-plane displacement contours, one can discern that an inplane strain concentration occurs near the damage area.



Out-of-Plane Displacement Contours

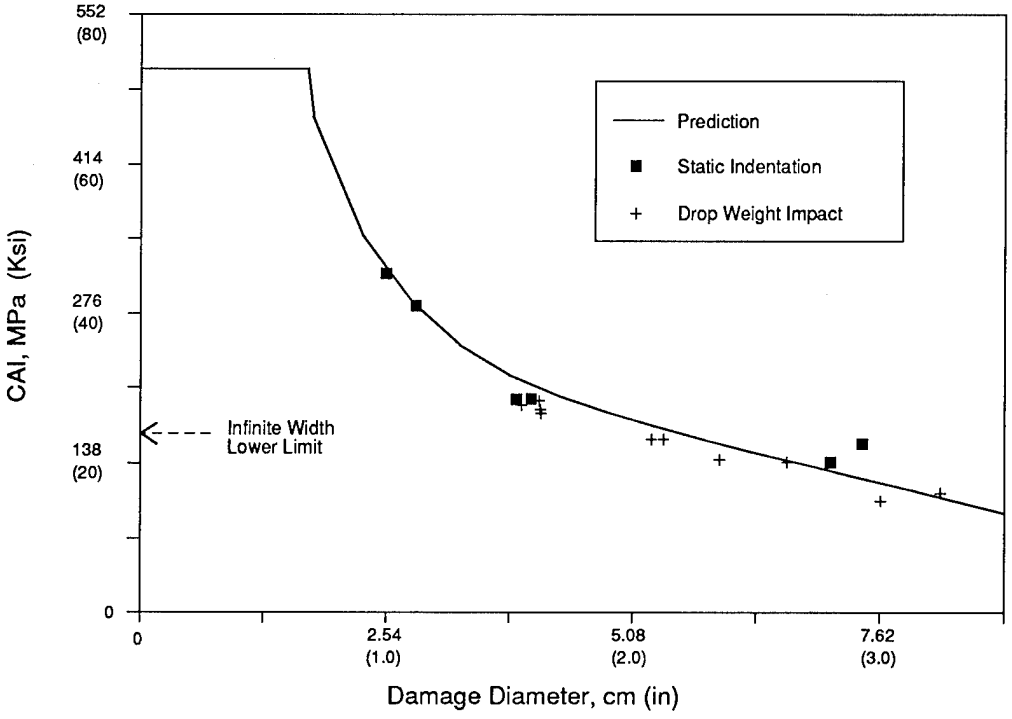


In-Plane Displacement Contours

Sublaminate Stability/Reduced Stiffness and Experimental Results for AS6/3501-6, $(45,0,-45,90)_{5S}$

This figure shows good comparisons between predictions and experimental results using a graphite/epoxy material (AS6/3501-6). The undamaged compressive strength was measured as 501 MPa (72.7 Ksi). Damage was created by both static indentation and drop weight impact. Finite specimen width becomes important as damage diameters increase. As shown, the model accurately predicted CAI throughout the range studied. The CAI lower limit for infinitely wide coupons would correspond to the maximum stress concentration of three for a quasi-isotropic laminate (i.e., 167 MPa).

Sublaminate Stability/Reduced Stiffness Predictions and Experimental Results for AS6/3501-6, (45,0,-45,90) $_{5S}$



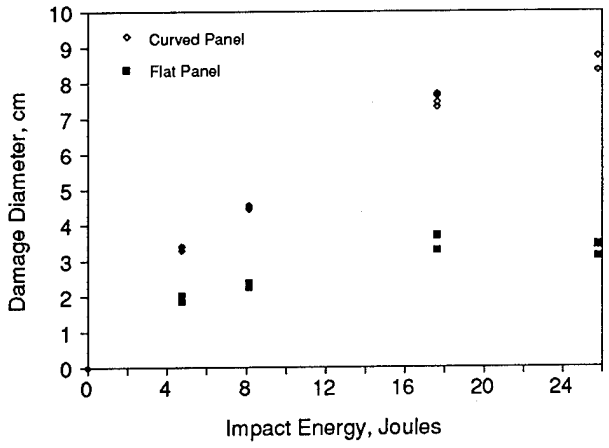
Impact Damage Behavior of Curved Laminates

The influence of laminate curvature on damage resistance and post-impact compression strength was investigated for a "brittle" material system. The stacking sequence was $(45/90/-45/0)_{3S}$ and the nominal laminate thickness was 0.38 cm. The dimensions of the flat panels were 10.2x15.2 centimeters with the 15.2 cm direction parallel to the 0 degree direction of the laminate. The curved laminates were cylindrical in shape with a radius of curvature of 22.9 cm and dimensions of 10.2x15.2 centimeters. The impact procedure was performed by placing the coupons in a support fixture that approximates simply supported boundary conditions. Coupons were held with clamps on both sides to prevent rebound during impact. A special fixture was fabricated for the curved panels such that the curvature of the fixture matched the curvature of the test coupons. Impacting was performed using an instrumented impact tower. During the post-impact compression tests, the coupons were mounted in a side-supported fixture developed by The Boeing Company for compression residual strength tests. A special modification of the fixture was fabricated to enable compression testing of the curved panels.

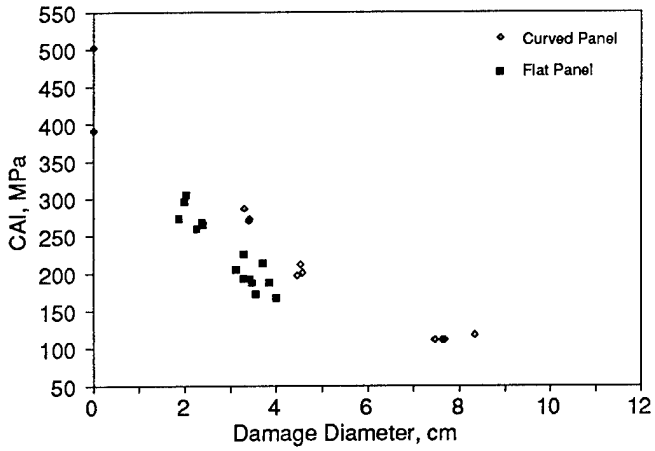
Damage area as a function of impact energy is presented in the first figure below. The flat panels exhibited a maximum damage diameter of approximately 4 cm, whereas the curved laminates exhibited damage diameters of up to 8.5 cm before significant interaction with boundaries occurred. Recalling that the total width of a coupon is 10.2 cm indicates that significant area of the coupon was damaged. The massive increase in damage area in the curved coupons is believed due to the curvature induced increase in laminate stiffness, which results in higher impact and shear loads. Further analysis of curvature effects is continuing.

Post-impact compression strength as a function of damage area is presented in the second figure. The curved panels exhibited higher CAI strength for a given damage area. This is assumed due to the increase in stability imparted by coupon curvature..

Damage Resistance: Flat versus Curved Panel $(45,90,-45,0)_{3S}$



Residual Strength: Flat versus Curved Panel $(45,90,-45,0)_{3S}$



LVDT Measured and STAGSC-1 Predicted Specimen Post-Buckling for $(45_3,90_3,-45_3,0_3)_S$

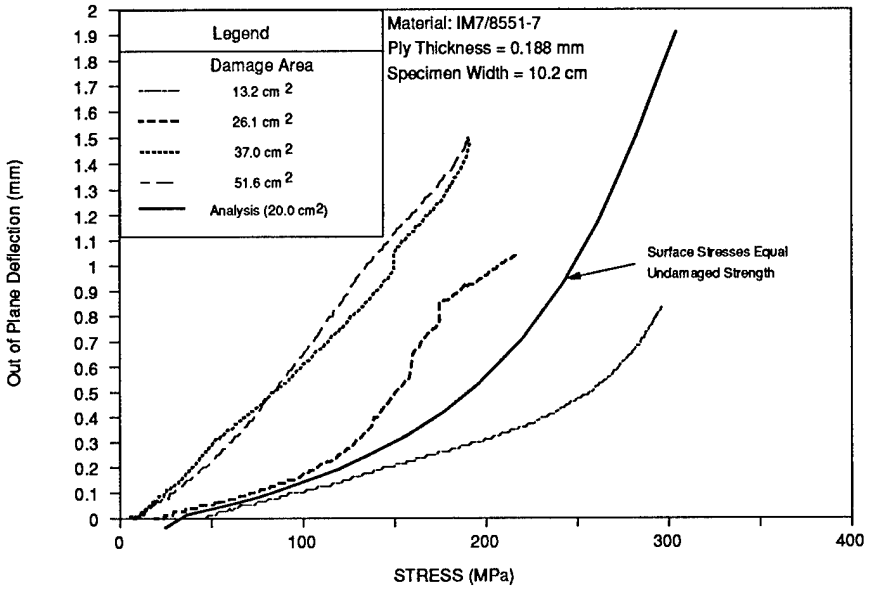
The large delaminations visible in the ultrasonic c-scan occur in the back half of the $[45_3,90_3,-45_3,0_3]_S$ laminate, effectively breaking it into two sublaminates. The sublaminate located toward the back side has octants containing 0, 3, 6 and 9 plies while the thicker, base sublaminate has octants containing 24, 21, 19, and 15 plies, respectively.

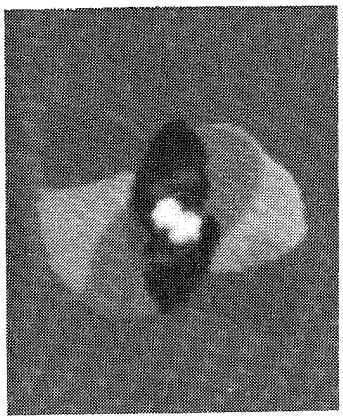
Despite a limited number of test results, post impact failure data trends were found to vary significantly from sublaminate stability/reduced stiffness prediction for this laminate. The most striking difference occurred for large damage areas where a finite width effect was not evident in the data [3].

A STAGSC-1 [7] geometrically nonlinear finite element (FE) analysis was performed on a discrete sublaminate model using damage details described above to better understand the observed behavior. The FE results are plotted together with experimental measurements of out-of-plane displacement versus load. The analysis demonstrated that specimen stability was affected by sublaminate stability. Outward buckling in the +Z direction of the sublaminate forced overall coupon instability in this direction. The change in specimen stability resulting from sublaminate buckling exhibits trends similar to those observed in postbuckling analysis with increasing applied imperfections.

Out-of-plane specimen displacements were measured with a linear variable displacement transducer (LVDT). It can be seen that the amount of "imperfection" imparted to the specimen increases with damage size. The predicted displacements for 20.0 cm^2 damage area fall between experimental data curves for 13.2 and 26.1 cm^2 damage areas in the figure below. Note that the out-of-plane displacement corresponding to a surface stress of 478 MPa (undamaged compressive strength) in the model was 0.95 mm. This also compares well with the experimental data for 13.2 and 26.1 cm^2.

LVDT Measured and STAGSC-1 Predicted Specimen Post-Buckling for $[45_3,90_3,-45_3,0_3]_S$





Pulse-Echo C-Scan

Impact Energy = 40.7 Joules

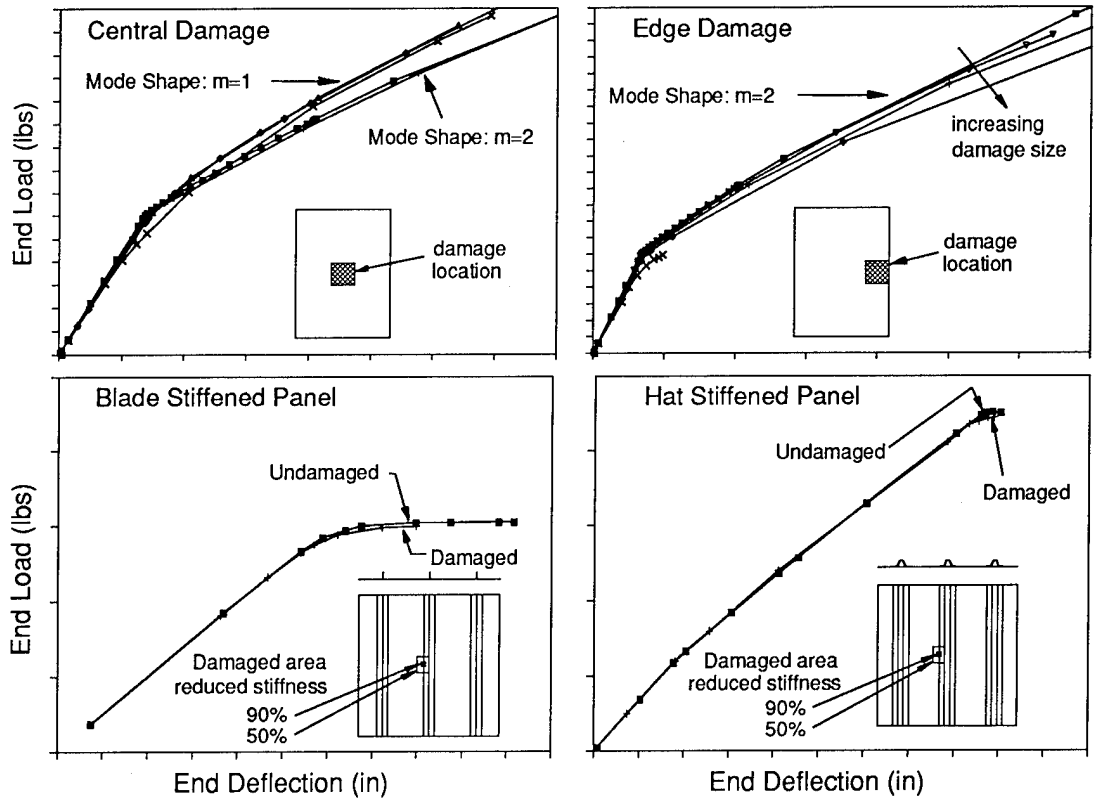
Effect of Damage on Stiffness and Stability

The previous chart demonstrated that impact damage can significantly alter panel stability. Analytical studies on the effect of hypothetical damage on coupon stability were performed to examine this. Two types of simulated damage were used in these studies, both having an axial stiffness reduction of 50%. The symmetric damage was simulated with a 50% reduction in axial moduli, while unsymmetric damage was simulated with 1/2 the laminate stacking sequence and an offset. Analyses were run with damage simulations in the middle and on the edge of 24" by 12" rectangular plates. Damage size was varied from 2" x 2" to 5" x 5".

Center damage was found to lower initial buckling load for small damage sizes. As damage size increased the postbuckling mode shape changed from two halfwaves to a single halfwave. A stiffer postbuckling response was associated with this switch in mode shape. Plates with unsymmetric damage had a lower postbuckling stiffness than those with symmetric damage. Both symmetric and unsymmetric simulated damage on the edge of a plate were found not to change postbuckling mode shape. Postbuckling stiffness was found to decrease with increasing damage size. The difference in postbuckling stiffness between symmetric and unsymmetric damage tended to increase with increasing damage size, with unsymmetric damage having a lower stiffness.

The effect of hypothetical damage on stiffened panel stability was examined using analytical studies similar to those described previously. The simulated damage used in these studies was symmetric and had an axial stiffness reduction of 90% in a 1"x1" core region surrounded by 4"x2" 50% reduced stiffness zone. Analyses were run with the damage simulation at the edge of the stiffener attaching flange for both hat and blade stiffened panels. There was negligible change in postbuckling response of these panels for the described damage. Note: This was not nessessarily the worst case scenario, but a demonstration of the concept. Other damage states and locations may have more effect on panel response.

Effect of Damage on Stiffness and Stability



Impact Designed Experiment Involving Multiple Variables

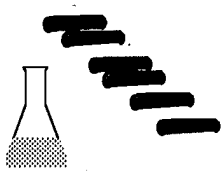
A statistically based designed experiment is being used to study impact damage resistance of fuselage structure. A total of 16 variables are being investigated to determine their relative importance to different potential failure modes. Interactions between variables are believed to be important; therefore, the approach of changing one variable at a time is inadequate. A fully crossed experiment would yield information on all main effects and all interactions, but would require 65536 tests (not including replication) when studying 16 variables. A fractional factorial design provides an understanding of all main effects and significant insight to interactions with only 32 tests [8].

A significant number of variables listed below relate to the impactor. Past impact studies have been performed using aircraft assembly/maintainance tools and other inservice threats for evaluation impact damage. The 1.0" diameter hemispherical impactor was found to produce the same results as the majority of possible threats. "Brittle" materials of the day tended to absorb impact energy through the creation of delaminations and transverse cracks which would dominate compression after impact strength (CAI). The large delaminations effectively decreased the local flexural stiffness, reducing contact pressures, and hence local fiber failures. Composite materials development concentrated on increasing CAI by reducing damage size. Smaller damage sizes lead to higher contact pressures and more fiber failure; thus impactor variables such as shape, size, and stiffness may be accentuated.

Results from this experimental study will guide material and structural configuration decisions for aircraft fuselage structures. It will also provide guidance in the development of analysis tools for predicting post-impact performance of composite structures.

Impact Designed Experiment Involving Multiple Variables

Material Variables



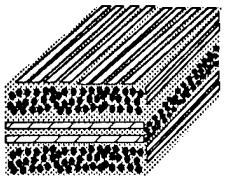
Fiber
- AS4
- IM7

Resin
- 938 (3501-6)
- 977-2

Fiber Volume
- 0.480
- 0.565

Material Form
- Tape
- Tow

Laminate Variables

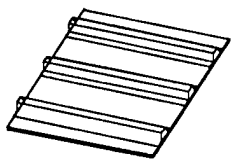


Stiffener Layup
- Hard
- Soft

Skin Layup
- Hard
- Soft

Thickness
- Thick (Approx. 0.2 in.)
- Thin (Approx. 0.1 in.)

Structural Variables

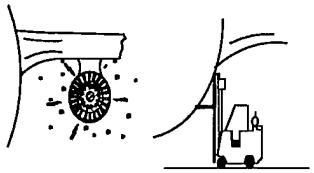


Stiffener Type
- Blade
- Hat

Stiffener Spacing
- 7 in.
- 12 in.

Stiffener Adhesive Layer
- With
- Without

Extrinsic Variables



Impact Mass
- 0.5 lbm.
- 12.0 lbm.

Impact Energy (Skin/Stiffener)
- 80 in lb / 200 in lb
- 1200 in lb / 2000 in lb

Impact Temperature
- 70° F
- 180° F

Impactor Diameter
- 0.25 in.
- 1.0 in.

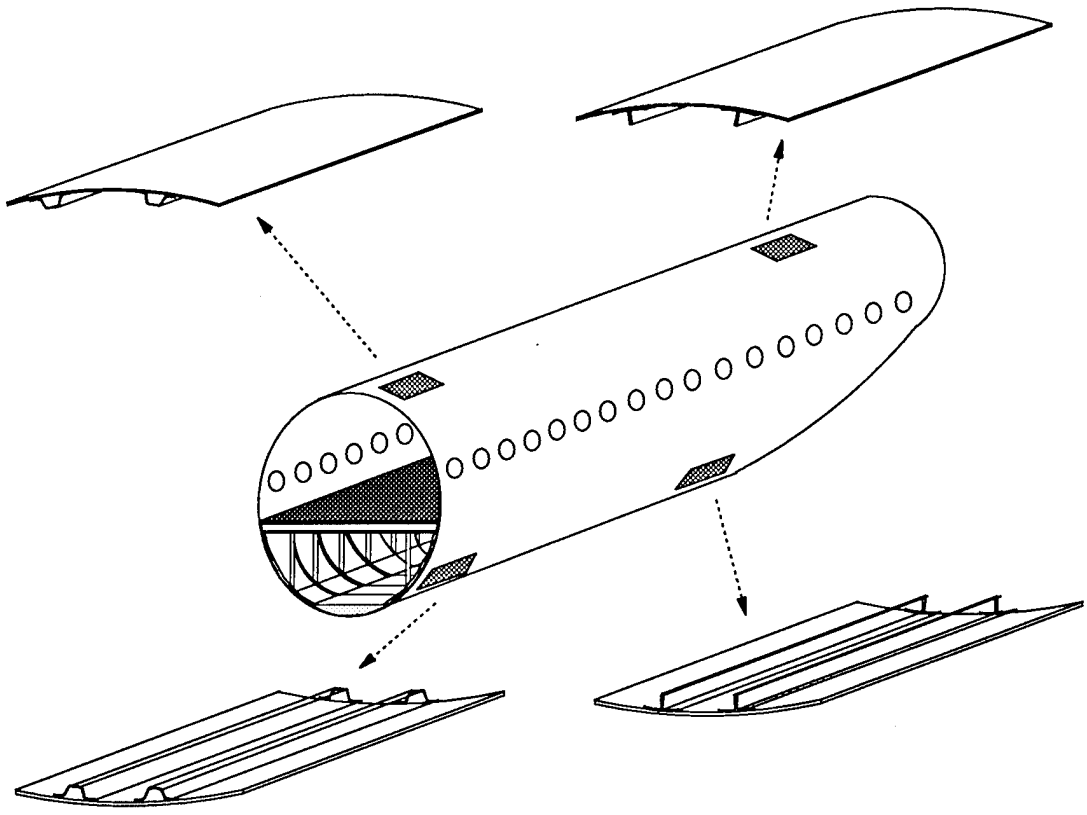
Impactor Tup Shape
- Flat
- Spherical

Impactor Stiffness
- 0.5 Msi
- 30 Msi

Fuselage Locations Represented by Test Panels

The panel configurations and materials chosen for the impact damage resistance designed experiment are representative of a variety of locations around the fuselage. The fuselage crown is tension dominated structure and hence a stiffener spacing of 12.0 inches and thin skin gages can be used. The fuselage keel on the other hand is compression dominated and requires a closer stiffener spacing and thicker gages. Matrix material toughness may be required for the keel when considering high levels of impact energy resulting impact from runway debris. The crown, however has hail impact as a design criteria and may not require costly toughened materials to resist damage. The panels built for this experiment have combinations of the variables listed above covering a range of locations on the fuselage.

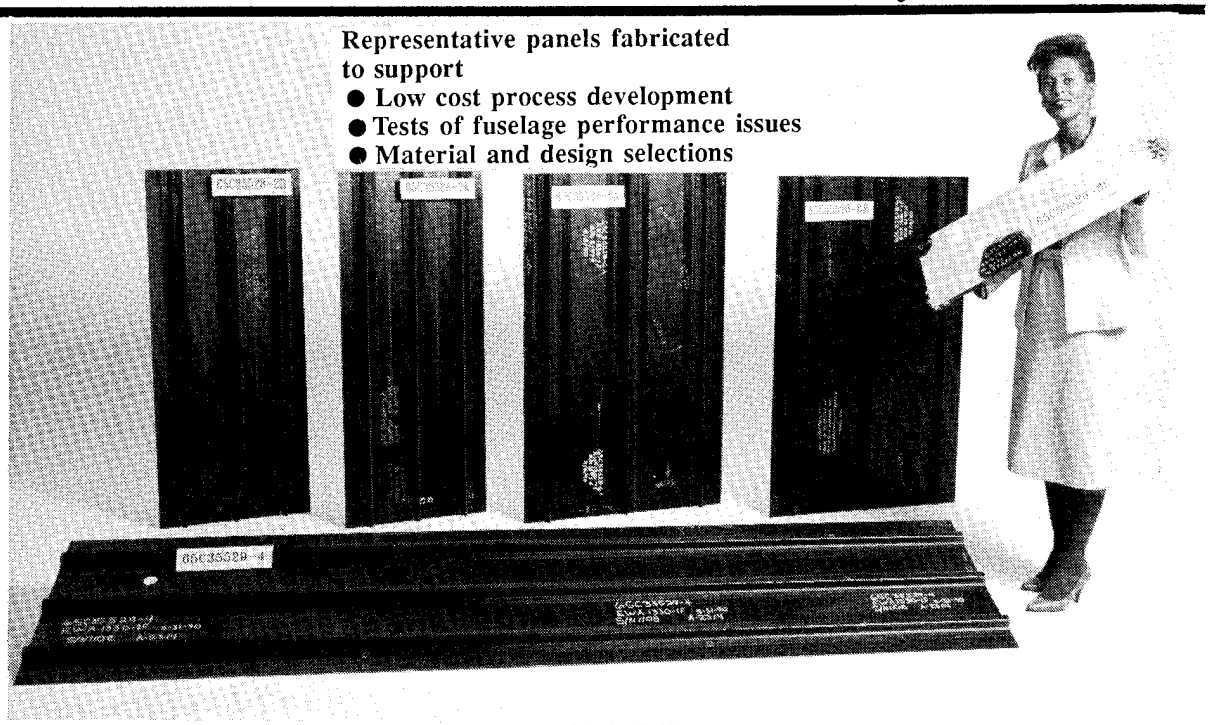
Fuselage Locations Represented by Test Panels



Integrated Approach to Manufacturing Demonstration and Structural Performance

Design, manufacturing , and material selection for low-cost composite fuselage are made by the Boeing ATCAS Design Build Team. The selection criteria is based on a potential for low cost and weight in the fully assembled structure. The panels fabricated for ATCAS serve multi-functions devised to develop and validate composite manufacturing and structures technologies. Manufacturing trials and test articles for performance evaluation are coupled. This results in an efficient use of contract funds and allows test evaluation of process anomalies characteristic of panels fabricated with design details. To date, panel fabrication in ATCAS has evaluated (1) drape forming and tooling concepts for a low cost stiffener fabrication process, (2) advanced fiber placement for skin panels that include ply drop-offs characteristic of fuselage design, (3) process modifications for eight material types identified as candidates for fuselage structures. The 110 in. stiffened panels fabricated will be machined into specimens and test elements for assembly trials, impact damage resistance evaluation, damage tolerance tests, and stiffness/stability measurements.

Integrated Approach to Manufacturing Demonstration and Structural Performance



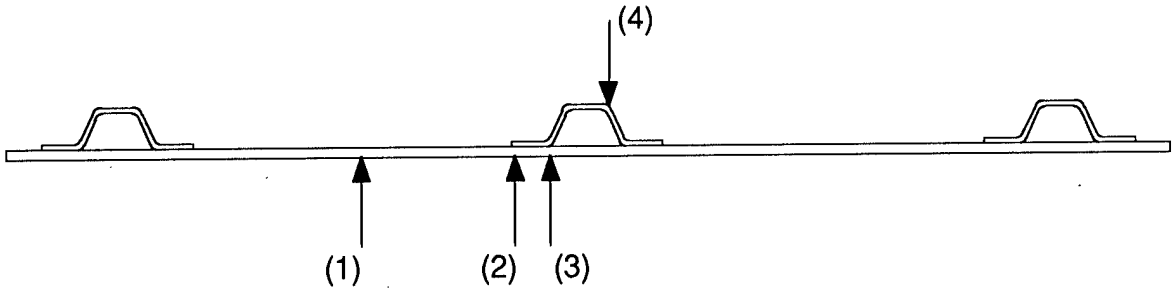
NASA/BOEING
ATCAS

Critical Impact Locations

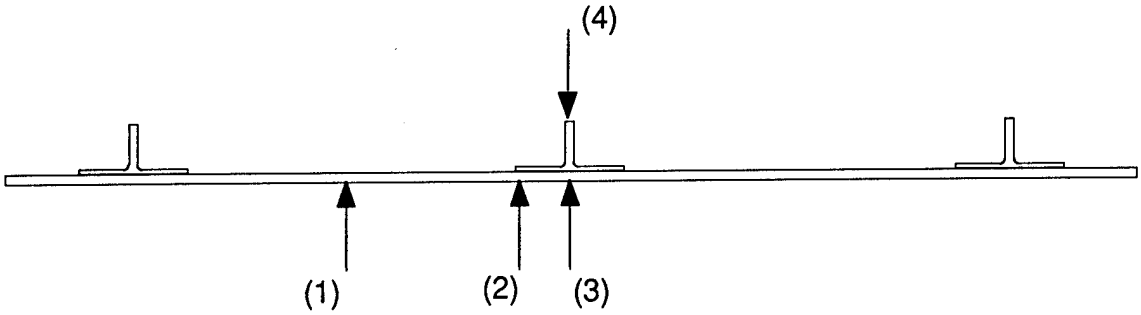
All 32 impact damage resistance panels will be impacted at the structural locations shown below. These are thought to represent those most critical for stiffened panels of this sort. All impacts will be instrumented to determine force/time relations. Each impact site will be nondestructively inspected to determine the maximum extent of damage created. Final impact locations will be based on extent and location of previous impact damage sites.

The impact damage states will be characterized both in terms of lateral extent and through-the-thickness distribution of matrix and fiber damage. The impact sites will be inspected using time-of-flight pulse-echo ultrasonics to map out delamination depth and extent. Resin burnoff will be used to map out fiber failures which exist. Coupons will be machined and compressively tested to failure. The variables will then be ranked versus the different failure modes and residual strength to determine which variables and variable interactions are most significant to each failure mode.

CRITICAL IMPACT LOCATIONS



(1) Skin Midbay
(2) Edge of Stiffener Attachment Flange
(3) Base of Stiffener Web
(4) Top of Stiffener



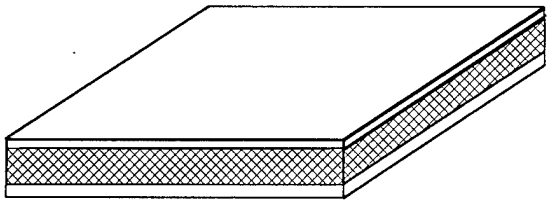
Impact Damage Resistance/Residual Strength of Sandwich Structure for Aircraft Fuselage

Impact damage resistance/residual strength of sandwich panels will be investigated experimentally to define impact damage related structural requirements for aircraft fuselage. Past investigations of low velocity impact on sandwich structure have been performed on panels with thin gauge face sheets and low density cores to support secondary structure applications. These typically have studied skin gauges less than 0.05 inch and core densities between 3 and 6 lb/ft^3 [9,10]. Impact damage resistance/residual strength studies will be performed on laminates with facesheets ranging from 0.15 to 0.3 inches and core densities from 6 to 18 lb/ft^3.

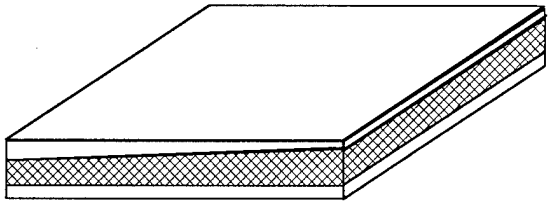
The response of tapered structure to impact damage will be studied. The 10.0 inch long tapered region of the stiffened panel designed experiment will be fabricated into sandwich panels with a 3/4 inch core, representative of the aircraft keel. Facesheet delamination/transverse cracking, fiber damage, and core shear/crushing failures will be the measured responses.

Impact Damage Resistance/Residual Strength of Sandwich Structure for Aircraft Fuselage

Constant Gauge



Tapered



Variables

Core Type: Foam vs. Honeycomb

Core Density: 6 - 18 lbs/ft^3

Core Thickness: 0.25 - 0.75 inches

Face Sheet Thickness: 0.1 - 0.3 in.

Fiber Type: AS4 vs. IM7

Matrix Type: 3501-6 vs. 8551-7

Impactor Shape: Flat vs. Spherical

Impactor Diameter: 0.25 - 1.0 in.

Laminate Layup: Hard vs. Soft

Fiber Type: AS4 vs. IM7

Matrix Type: 938 vs. 977-2

Fiber Volume: 0.480 vs. 0.565

Material Form: Tow vs. Tape

Summary

Models to predict residual strength of impacted laminates must include stacking sequence dependent details of the damage state.

CAI for laminates with symmetric size distributions of matrix damage through the thickness was predicted with a sublaminate stability/stress redistribution analysis method.

Post-impact performance for laminates with unsymmetric size distributions of matrix damage through the thickness was best termed a change in specimen stability.

Variables most crucial to fuselage impact damage resistance will be identified.

References

1.) Dost, E.F., Ilcewicz, L.B., and Gosse, J.H., "Sublaminate Stability Based Modeling of Impact Damaged Composite Laminates," in Proc. of 3rd Tech. Conf. of American Soc. for Composites, Technomic Publ. Co., 1988, pp. 354-363.

2.) Ilcewicz, L.B., Dost, E.F., and Coggeshall, R.L., "A Model for Compression After Impact Strength Evaluation," in Proc. of 21st Inter. SAMPE Tech. Conf., Soc. for Advanc. of Material and Process Eng., 1989, pp. 130-140.

3.) Dost, E.F., Ilcewicz, L.B., and Avery, W.B., "The Effects of Stacking Sequence On Impact Damage Resistance and Residual Strength for Quasi-Isotropic Laminate," in Composite Materials: Fatigue and Fracture, ASTM STP 1110, 1991.

4.) Cairns, D.S. and Lagace P.A., "Residual Tensile Strength of Graphite/Epoxy and Kevlar/Epoxy Laminates with Impact Damage," Massachusetts Institute of Technology, TELAC Report 88-3, 1988.

5.) Gosse, J.H., and Mori, P.B.Y., "Impact Damage Characterization of Graphite/Epoxy Laminates," in Proc. of 3rd Tech. Conf. of American Soc. for Composites, Technomic Publ. Co., 1988, pp. 344-353.

6.) Shivakumar, K.N., and Whitcomb, J.D., "Buckling of a Sublaminate in a Quasi-Isotropic Composite Laminate," J. Composite Materials, Vol. 19, 1985, pp 2-18.

7.) Almroth, B.O., Brogan, F.A., and Stanley, G.M., Structural Analysis of General Shells, Vol. 2 User Instructions for STAGS-C1, Lockheed Palo Alto Research Laboratory, Palo Alto, CA, Jan. 1983.

8.) Wheeler, D.J., Understanding Industrial Experimentation, Statistical Process Controls, Inc., Knoxville, Tenn. 37919.

9.) Rhodes, M.D., "Low Velocity Impact on Composite Sandwich Structures," Presented at the Second Air Force conference on Fibrous Composites in Flight Vehicle Design, Dayton, Ohio, May 22-24, 1974.

10.) Bernard, M.L., "Impact Resistance and Damage Tolerance of Composite Sandwich Plates," Massachusetts Institute of Technology, TELAC Report 87-11, 1987.

*References in bold were published while under Contract NAS1-18889.

MULTI-PARAMETER OPTIMIZATION TOOL FOR LOW-COST COMMERCIAL FUSELAGE CROWN DESIGNS

University of Washington Faculty

Zelda Zabinsky
Mark Tuttle

University of Washington Research Assistants

Douglas Graesser, Ph.D Candidate
Gun-In Kim, Ph.D Candidate
Darrin Hatcher, Master's Candidate

Boeing Commercial Airplanes

Gary Swanson
Larry Ilcewicz

INTRODUCTION

This paper describes the work-in-progress on developing a methodology and software tool to aid in the optimal design of composite structures. The methodology is being developed to take advantage of the ability to tailor the composite material, in conjunction with the design of the structure.

- A fundamental objective during aircraft design is to identify "optimal" structural components
- Advanced composites allow the engineer to "design" the *material*, as well as the overall geometry of the structure
- A software tool is being developed using a state-of-the-art random search global optimization algorithm to find and explore the "best design"

OPTIMAL DESIGN OF A REINFORCED COMPOSITE PANEL

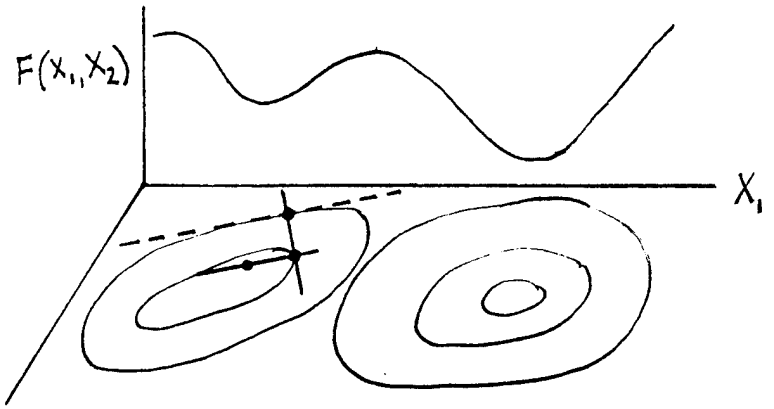
When designing a reinforced composite panel, two questions must be addressed: what are the design variables, and what makes a design the best? A list of possible variables that must be specified by the design engineer are included below. Stiffener geometry variables may include blade-, hat-, J-, and C- stiffeners, as well as height, width and stiffener spacing. The laminate description may include number of plies, ply angles, and stacking sequence. Possible criteria for an optimal design may include objectives such as minimum weight, maximum stiffness, maximum strength, maximum buckling stability, or minimum costs. Typically, a combination of these objectives must be included in optimization methodology that identify *trends in the designs* and aids the engineer in selecting an optimal design.

- What are the design variables? They include (at least)
  - type of material system(s) used
  - stiffener geometry
  - laminate description for both skin and stiffener
- All of these variables can be adjusted by the engineer. What is the "optimal" design?
  - low weight
  - high performance
  - low cost
- Typically, the user wants to optimize a *combination* of these objectives and identify TRENDS IN THE DESIGNS

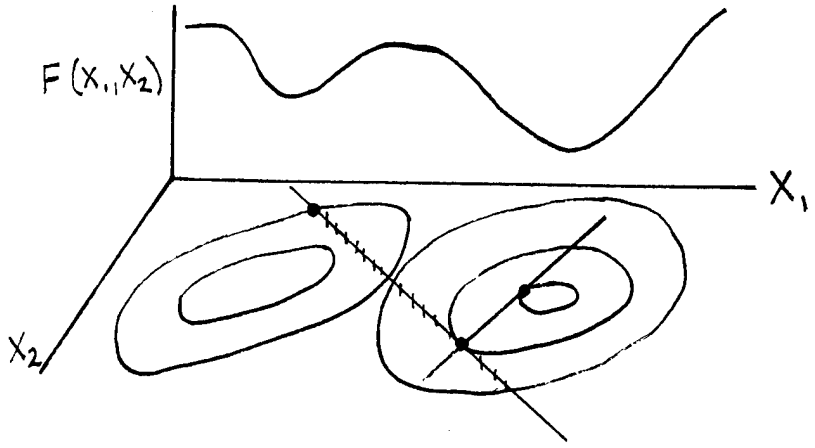
NEED AN OPTIMIZATION ALGORITHM TO FIND AN "OPTIMAL" DESIGN

Once the design variables and the criteria for an "optimal" design are identified, an optimization problem is specified. An optimization problem involves an "objective function" F(X), where F(X) is a user-defined function of the design variables X, and a set of constraint equations. The optimal solution is defined as the set of design variables which minimize the objective function F(X), while satisfying user-defined constraints. Now, an optimization algorithm must be chosen to automatically search the design space for the optimal solution. Two types of algorithms are available: "local" optimization algorithms and "global" optimization algorithms. The local optimization algorithms include quasi-Newton methods and gradient search, and converge quickly to a local minimum. If the objective function is not convex, but has several local minima, then the solution from a local optimizer depends on the starting point. The global optimization algorithms including random search methods converge slower, but have a high probability of finding the global minimum. These algorithms are less sensitive to the starting point. We are using a state-of-the-art global optimization algorithm called Adaptive-Mixing.

- A "local" optimization algorithm, e.g. gradient search



- A "global" optimization algorithm, e.g. adaptive mixing



OPTIMAL DESIGN OF COMPOSITE STRUCTURES

Optimal design of composite materials has recently become a well-known topic in the literature. One way our approach differs is in that we are using a "global" optimization algorithm, rather than a "local" optimization algorithm.

- Most existing composites optimization algorithms are based upon "local" optimizers. When using these codes, the user either
    - Reduces the number of design variables, such that the composite design process becomes a "local" problem, or
    - The global nature of the problem is ignored; results obtained depend on starting point.
- The objective of the UW study
    - To develop a composites design philosophy based on Adaptive Mixing, a state-of-the-art "global" optimization algorithm
    - To identify and implement objective function(s) (which may be global, nondifferentiable, discontinuous) and constraints which can be used to represent the many design variables involved in composite structures

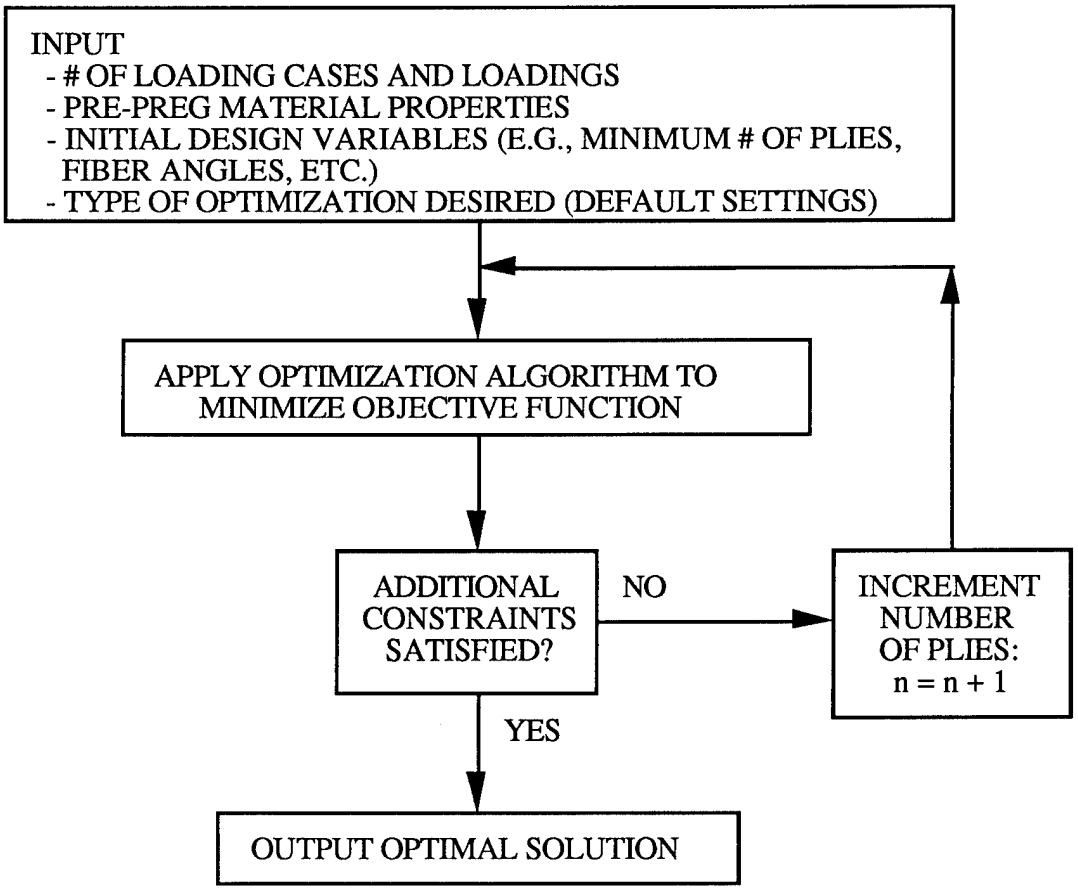
APPROACH

An optimization code called UWCODA (**U**niversity of **W**ashington **C**omposite **O**ptimal **D**esign **A**lgorithm) is being developed. The approach taken is to base UWCODA on classical lamination theory, and an Adaptive-Mixing "global" optimization algorithm.

- The current objective functions and constraints being developed are based on
    - Minimum weight of skin and stiffener
    - Maximum strain failure criteria
    - Multiple load cases
    - Various "design" tools (provided by Boeing engineers), representing
        - Hoop tension damage tolerance criteria
        - Axial load damage tolerance criteria
        - Buckling resistance criteria
        - Impact resistance criteria
- Future objective functions and constraints will be developed based on minimum cost:
    - Material cost
    - Labor cost, as a function of stringer type, stringer spacing, ...

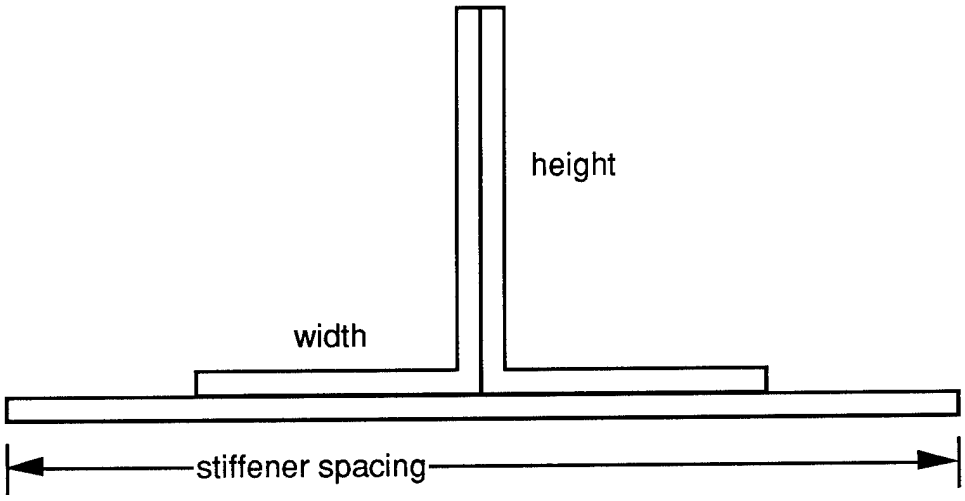
OVERALL FLOW DIAGRAM OF UWCODA

Below is a flow diagram of UWCODA. Notice that the additional constraints are checked after the optimization routine is applied. This allows the optimizer to select an "infeasible" design, that is, one that does not meet all of the constraints, while providing feedback to the engineer of the best possible design with n plies. If the design is infeasible with n plies, the outer loop increments the number of plies and reoptimizes. This outer loop encourages finding a minimum number of plies, and consequently minimum weight, that satisfy all of the constraints.



POSSIBLE DESIGN VARIABLES FOR A STIFFENED COMPOSITE PANEL

A list of possible design variables are listed below. These variables include parameters that a design engineer can control. The ply angles and stiffener geometry variables are currently included in UWCODA. The type of material is a potential design variable for future development.



- Ply fiber angles and number of plies for both the skin and the stiffener
    - n plies in the skin
    - n' plies in the stiffener
- Stiffener geometry
    - type of stiffener (blade-, hat- stiffeners)
    - width and height of stiffener
    - stiffener spacing
- Type of materials used
    - type of material for skin
    - type of material for stiffener
    - type of material for each individual ply

TYPICAL OBJECTIVE FUNCTION

The objective function used in UWCODA is a combination of weight and several performance criterion. This type of combined function is sometimes referred to as a multi-objective function. The equations used to calculate ply strains come from classical lamination theory, and the other equations are provided by Boeing in the form of "design tools". The approach of taking a normalized difference in the exponent, as shown below, is similar for all of the terms. This also makes a straightforward approach for extending the objective function to include additional criterion.

- Minimize (weight)(sum of performance criterion)

  where (sum of performance criterion) = (sum of ply strains) + (hoop tension damage tolerance) + (axial load damage tolerance) + ...

  and (sum of ply strains) =

$$\sum_{j=1}^{m}\left[\sum_{k=1}^{n}\left[\left(\delta*\exp\frac{\left|\varepsilon_1^k\right|_j-\varepsilon_1^{cr}}{\varepsilon_1^{cr}}\right)+\left(\delta*\exp\frac{\left|\varepsilon_2^k\right|_j-\varepsilon_2^{cr}}{\varepsilon_2^{cr}}\right)+\left(\delta*\exp\frac{\left|\gamma_{12}^k\right|_j-\gamma_{12}^{cr}}{\gamma_{12}^{cr}}\right)\right]\right]$$

  and (hoop tension damage tolerance) =

$$\sum_{j=1}^{m} n*\left(\delta*\exp\frac{\left|P_h^j\right|-P_h^a}{P_h^a}\right)$$

  where n = number of plies
  m= number of loading cases

$$\delta = \text{magnification factor} = \begin{cases} 1 \text{ if numerator is positive} \\ 10 \text{ if numerator is negative} \end{cases}$$

TYPICAL ADDITIONAL CONSTRAINTS

Note that when using a multi-objective function and minimizing a summation, there is a possibility that the total summation is at a minimum even though an individual term may violate a constraint. For example, if two terms should be less than 1, a sum of 0.2 and 1.01 is less than the sum of 0.8 and 0.8. The possibility is lessened by using exponentiation and a magnification factor; however, we also check all individual terms in additional constraints. If any constraint is violated the design is considered infeasible.

- the maximum strain failure criterion must satisfy the additional constraints:

$$\left|\varepsilon_1^k\right|_j < \varepsilon_1^{cr}$$

$$\left|\varepsilon_2^k\right|_j < \varepsilon_2^{cr}$$

$$\left|\gamma_{12}^k\right|_j < \gamma_{12}^{cr} \quad \text{for k=1,n (\# of plies) and j=1,m (\# of load cases)}$$

- the hoop tension damage tolerance must satisfy the additional constraint:

$$\left|P_h^j\right| < P_h^a \quad \text{for j=1,m (\# of load cases)}$$

- other constraints, such as axial load damage tolerance and cost constraints will be included

SAMPLE RESULTS WITH UWCODA: MATERIAL INPUTS

Sample results using UWCODA are shown for a laminated plate subjected to different combinations of variables. IM6, AS4, and S-Glass fibers were chosen for comparison since they represent a range of structural properties and cost. To show the importance of failure criteria on the optimization results, two different sets of strain failure allowables were applied to the optimization. The first failure criteria is applied such that matrix cracking is prevented (ε_2^{cr} is based on the in-situ strength for a -75°/Dry condition). The second failure criteria is a tension damage tolerance allowable such that crack growth is suppressed in a pressurized cylinder with an 8" notch. This is typical of a failsafe load criteria. The ε_1^{cr} (fiber failure) is limited to a lower value than used previously to resist this failure mode. The shear strain allowable (γ_{12}^{cr}) is also reduced to constrain the optimized laminate layup against nonlinear shear distortion. The material properties used as inputs to the program are listed below:

MATERIAL PROPERTIES

	IM6/3501-6	AS4/3501-6	S-Glass
E_1 (msi)	22.30	19.20	7.40
E_2 (msi)	1.32	1.36	2.20
G_{12} (msi)	0.78	0.72	0.77
ν_{12}	0.32	0.32	0.264
MATRIX CRACKING ALLOWABLE STRAINS			
ε_1^{cr}	0.0145	0.0140	0.0420
ε_2^{cr}	0.0060	0.0060	0.00825
γ_{12}^{cr}	0.0200	0.0200	0.0200
TENSION DAMAGE TOLERANCE ALLOWABLE STRAINS			
ε_1^{cr}	0.0026	0.0028	0.0079
ε_2^{cr}	0.0060	0.0060	0.00825
γ_{12}^{cr}	0.0100	0.0100	0.0100

SAMPLE RESULTS WITH UWCODA: MECHANICAL BEHAVIOR

Sample results describing the mechanical behavior of the laminated plates constrained by the two different failure criteria are presented. A significant number of additional plies are required for damage tolerance, indicating that it is more critical than matrix cracking criteria for the load conditions studied. Note that several of the optimum layups were unbalanced. Additional constraints could be imposed during optimization to force balanced layups.

LOADING CONDITIONS

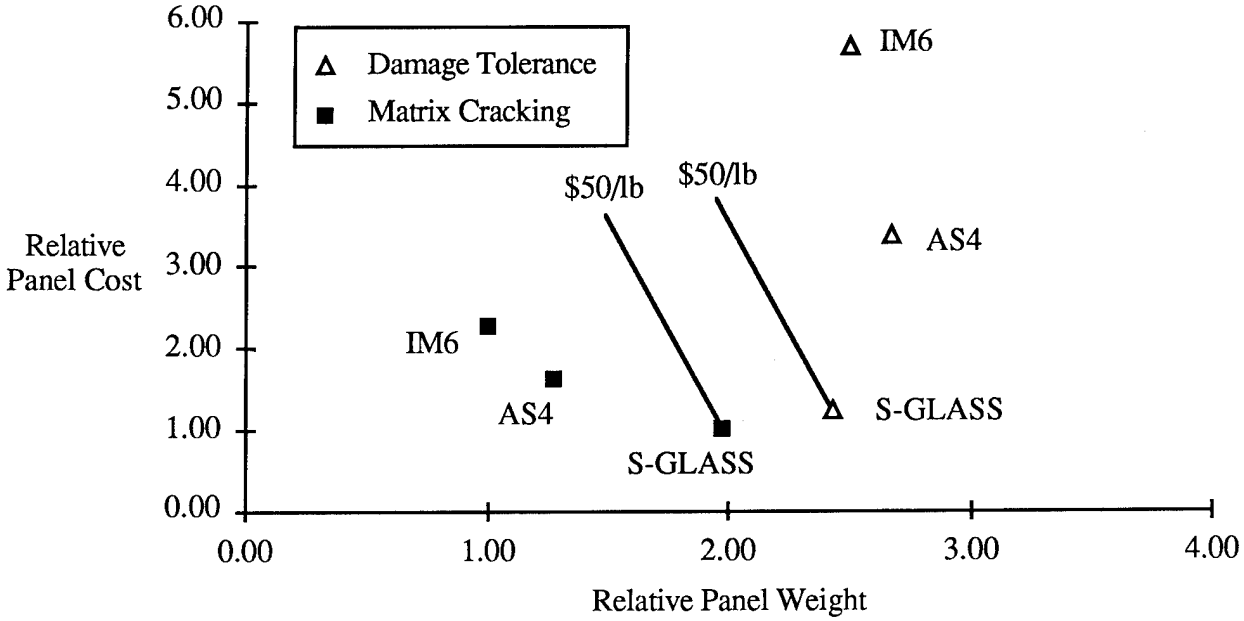
Load Case	N_x	N_y	N_{xy}
1	4000 lbs/in	0	0
2	0	4000 lbs/in	0
3	0	0	2000 lbs/in
4	0	0	-2000 lbs/in

	MATRIX CRACKING		DAMAGE TOLERANCE	
MATERIAL	LAYUP	# PLIES	LAYUP	# PLIES
IM6/3501-6	$[12/-12/78/-78]_S$	8	$[15_3/80_3/-20_2/-68/-84]_S$	20
AS4/3501-6	$[90_2/-17_2/17]_S$	10	$[0_5/70_3/-67_2/\overline{-67}]_S$	21
S-GLASS	$[-51.5/-30_3/65/38/\overline{65}]_S$	13	$[22_2/-22_2/-66_2/66_2]_S$	16

SAMPLE RESULTS WITH UWCODA: COST VS WEIGHT

The results from the sample cases comparing relative cost and weight are presented. A significant difference in the cost/weight relationship can be seen depending on the failure criteria imposed. For the damage tolerance criteria, the weight of the optimized laminate is nearly the same for the three different material systems considered, but the cost varies widely. For the matrix cracking criteria, the weight and cost relationship is much different. To evaluate which material is most desirable for a given criteria, a dollar value must be established for every pound of weight added to a design. This dollars/pound ($/lb) value can be evaluated by plotting lines centered at the lowest cost design. "Good" designs (i.e. cost effective) will fall below the line of interest and "bad" designs (i.e. not cost effective) will fall above the line. Using this approach and a value of $50/lb, it can be seen that S-Glass is the best material for tension damage tolerance and that the more expensive IM6 is the most cost effective material to resist matrix cracking. This type of range in the results indicate the importance of choosing the right criteria. In an aircraft application involving both criteria, the damage tolerance was found to be dominant. Therefore, the cost savings associated with using fiberglass are apparent and can be significant. Other criteria such as overall limit of fuselage flexibility will likely force the material used in this application to be stiffer than fiberglass. This leads one to consider a graphite/fiberglass hybrid material to attain a compromise in stiffness and damage tolerance characteristics.

	MATRIX CRACKING			DAMAGE TOLERANCE		
MATERIAL	# PLIES	WT	COST	# PLIES	WT	COST
IM6/3501-6	8	1.00	2.27	20	2.50	5.68
AS4/3501-6	10	1.27	1.61	21	2.68	3.38
S-GLASS	13	1.98	1.00	16	2.44	1.23



POTENTIAL FUTURE OBJECTIVE FUNCTIONS

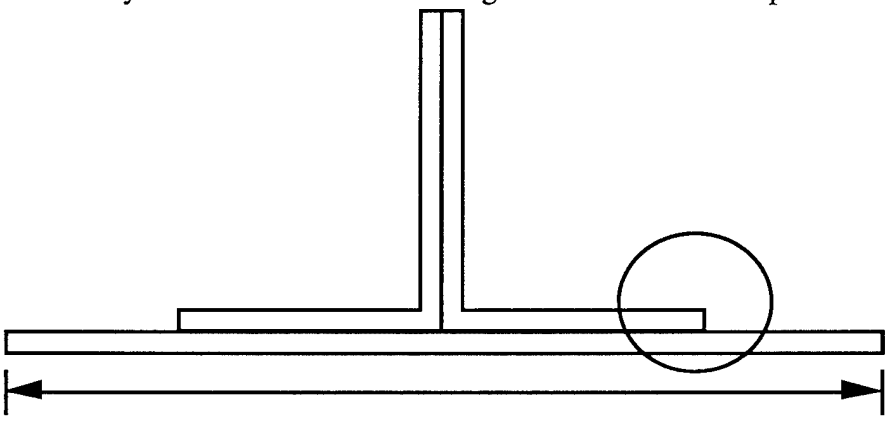
It is possible to develop future objective functions to optimize the cost-weight relationship, as well as satisfying the performance criterion. Several potential objective functions are listed below, as well as future constraints. Cost considerations will include material costs as well as operating costs, production costs, and assembly costs. Manufacturing considerations may include ease of layup, and sensitivity to manufacturing tolerances.

- Need to develop an objective function to reflect cost/weight/performance trades, such as
  - Minimize (weight)(sum of performance criterion)
  - Minimize (cost)(sum of performance criterion)
  - Minimize (cost)(weight)(sum of performance criterion)
  - Minimize (cost)(weight)

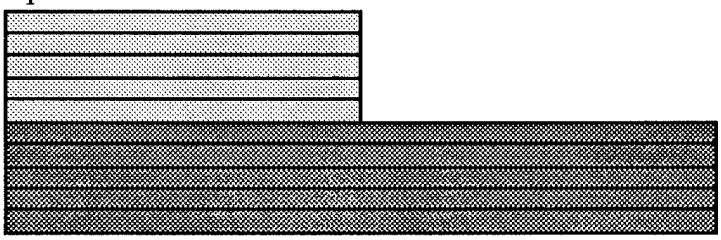
- Need to develop additional constraints or goals, such as
  - satisfy performance criterion
  - cost considerations
  - manufacturing considerations

POTENTIAL FUTURE DESIGN OPTIONS

The type of material may be included as a future design variable in several options.



- Design option 1: user specifies materials for the skin and stiffener
- Design option 2: optimizer selects materials for the skin and stiffener





- Design option 3: optimizer selects materials for individual plies

SUMMARY AND CONCLUSIONS

The composites optimization design software UWCODA has been found to be very successful in preliminary testing and early experience. There is a lot of potential to make the program very useful to design engineers working with composite structures.

- UWCODA is a composites optimization design algorithm
  - uses number of plies and fiber angles as design variables
  - uses Adaptive-Mixing "global" optimization algorithm
  - uses maximum strain failure criteria for objective function and additional constraints
  - includes Boeing "design tools" for stiffened panels
  - includes stiffener geometry in the design variables

- Future work
  - develop "cost tools" to include in UWCODA
  - expand design variables to include material types
  - refine optimizer
  - apply UWCODA to the design of a composite fuselage crown panel

COMPARISON OF HAND LAID-UP TAPE AND FILAMENT WOUND COMPOSITE CYLINDERS AND PANELS WITH AND WITHOUT IMPACT DAMAGE

Dawn C. Jegley and Osvaldo F. Lopez
NASA Langley Research Center
Hampton, VA

INTRODUCTION

Composite materials can be used to construct lightweight, structurally efficient components for aircraft applications. Graphite-epoxy parts can be used to replace many aluminum parts on today's aircraft. However, the low density and high stiffness and strength of laminated composites does not necessarily make them practical alternatives to metals for all applications. Fabrication techniques used to construct composite parts differ from those used to construct metal parts. Until recently most graphite-epoxy parts were fabricated from unidirectional tape involving an expensive and labor intensive procedure. Other methods of construction, such as filament winding, could significantly reduce the cost of fabrication and may improve the quality of some structures. However, few studies of the effects on structural response of fabrication-induced defects, such as fiber cross-overs (caused during filament winding of off-axis layers), are available. These defects could cause the structural response of hand laid-up tape and filament wound specimens of the same stacking sequence to differ significantly.

The structural response of hand laid-up tape and filament wound cylinders and flat panels subjected to axial compressive loading and impact damage is presented in the present paper. A series of tests were conducted on graphite-epoxy cylinders of the same nominal dimensions and stacking sequence constructed using filament winding and using unidirectional hand laid-up tape. These cylinders were loaded to failure in axial compression. Some filament wound cylinders had fiber cross-overs while others did not. Flat graphite-epoxy panels were filament wound with fiber cross-overs and without fiber cross-overs and loaded to failure in axial compression. Additionally, some specimens were subjected to low speed impact damage prior to compressive loading. A comparison between the structural response of control (unimpacted) and impact damaged cylinders and flat panels is also presented.

SPECIMENS TESTED

Descriptions of the thirty-six graphite-epoxy specimens tested are presented in figure 1. Eight cylinders and eight flat panels were constructed by filament winding. Eleven cylinders and nine flat panels were constructed by hand laying unidirectional tape. Half the filament wound specimens were constructed with fiber cross-overs and half had no fiber cross-overs. (None of the tape specimens had fiber cross-overs). Cylinders had a nominal radius-to-thickness ratio of 9 and a length-to-radius ratio of 4.8. Two dimensions of flat panels were used, some with a length-to-width ratio of 2.5 and a length-to-thickness ratio of 70 and some with a length-to-width ratio of 2.0 and a length-to-thickness ratio of 40. Two families of stacking sequences, $[\pm 45/90]_{ns}$ and $[\pm 30/90]_{n}$, were considered. Two material systems were considered. All cylinders and all hand-laid tape panels were constructed from Hercules Incorporated AS4 graphite fiber and 3502 epoxy resin. The filament wound panels were constructed from Celion 6k graphite fiber and Shell Epon 9400 epoxy resin.

Stacking Sequence	Material	Fiber Cross-overs	Number of Specimens
Filament Wound Cylinders			
$[\pm 45/90]_{3s}$	AS4-3502	Yes	4
$[\pm 45/90]_{3s}$	AS4-3502	No	4
Hand Laid-up Tape Cylinders			
$[\pm 45/90]_{3s}$	AS4-3502	No	11
Hand Laid-up Tape Panels			
$[\pm 45/90]_{4s}$	AS4-3502	No	8
$[\pm 30/90]_{16}$	AS4-3502	No	1
Filament Wound Panels			
$[\pm 30/90]_{10}$	K6-9400	Yes	4
$[\pm 30/90]_{10}$	K6-9400	No	4

Figure 1

CYLINDRICAL SPECIMENS

A filament wound cylindrical specimen with a band of fiber cross-overs around the circumference in the axial center of the specimen is shown in figure 2. Four specimens were filament wound and cut to length in this configuration. Four specimens were filament wound and cut to length in a configuration with no fiber cross-overs in the test section. Each cylinder is six inches long and has an inner diameter of 2.5 inches. The ends of each cylindrical specimen were potted in one inch of an epoxy material prior to testing, simulating clamped loaded edges. A hand laid-up tape specimen which has been potted and gaged with interior and exterior back-to-back strain gage rosettes is also shown in figure 2. This specimen has the same nominal dimensions as the filament wound specimen. All cylinders were constructed from AS4-3502 graphite-epoxy material. Loaded edges were ground flat and parallel prior to loading to ensure uniform edge displacement during loading. One side of each specimen was painted white so a moire fringe technique could be used to monitor out-of-plane displacements during the test.

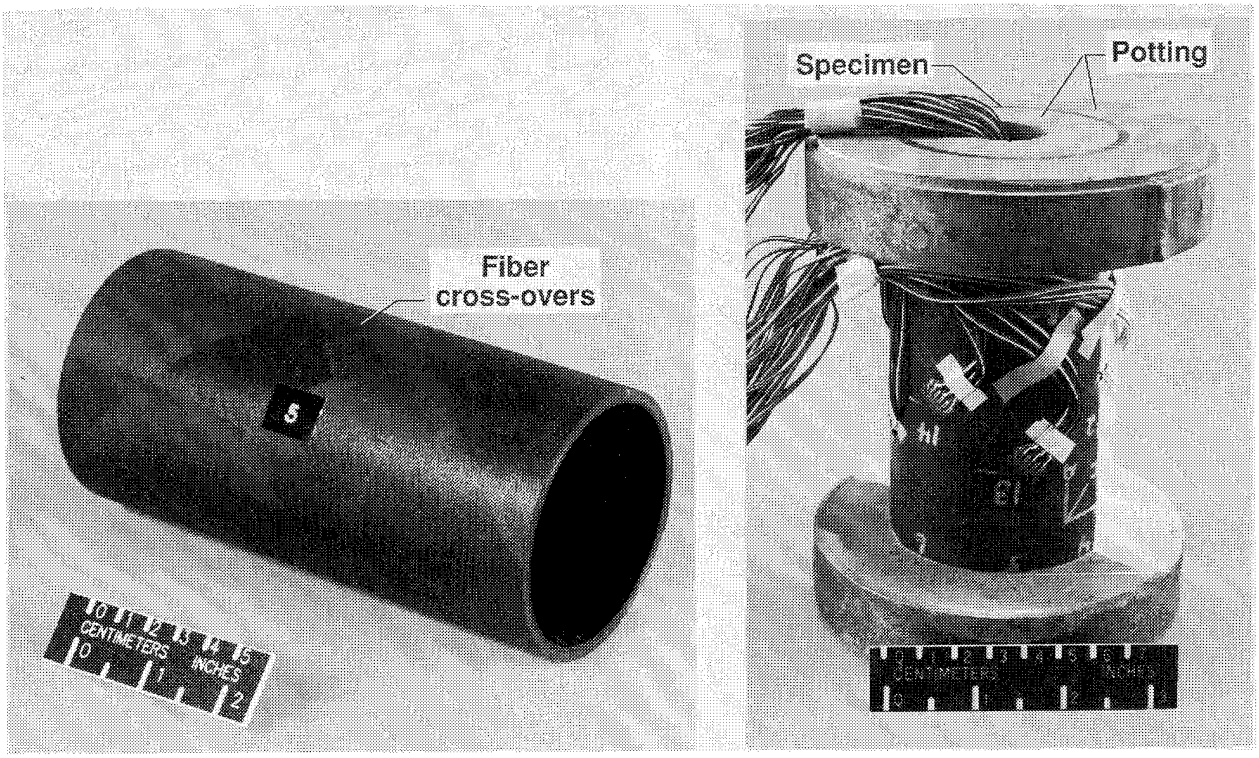


Figure 2

FILAMENT WOUND AND TAPE FLAT PANELS

Eight filament wound flat plate specimens with stacking sequence $[\pm 30/90]_{10}$, one hand laid-up tape flat plate specimen with stacking sequence $[\pm 30/90]_{16}$ and eight flat plate specimens with stacking sequence $[\pm 45/90]_{4s}$ were loaded to failure in axial compression. All flat plates had clamped loaded edges and simple support knife edge constraints on the unloaded edges during testing. A photograph of two specimens after loading in axial compression is shown in figure 3. A filament wound plate specimen is shown on the left side of the photograph and a hand laid-up tape plate specimen is shown on the right. Fiber cross-overs can be seen in the filament wound plate. Four filament wound plates had fiber cross-overs and four did not. Each plate with stacking sequence $[\pm 30/90]_n$ is five inches wide, ten inches long and approximately .25 inches thick.

A delamination failure occurred near the top of the tape specimen along the loaded edge. The filament wound specimen delaminated and failed along a fiber cross-over band located at the center of the plate. Each flat control (unimpacted) specimen buckled immediately prior to failure. One control specimen of each type was tested and the rest were subjected to impact damage prior to compressive loading.

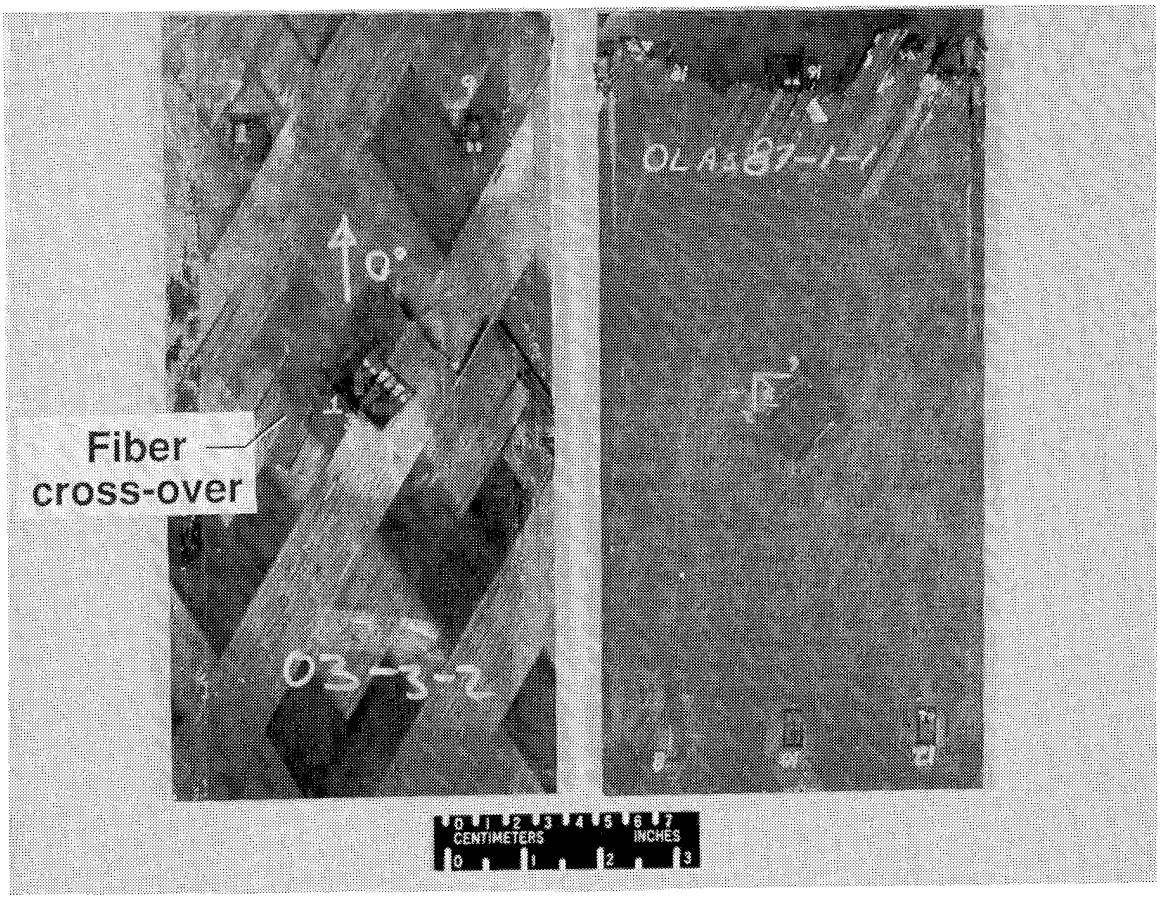


Figure 3

FAILURE STRAIN OF CONTROL CYLINDERS

Five control (unimpacted) filament wound and six control hand laid-up tape cylinders with stacking sequence $[\pm 45/90]_{3s}$ were loaded in axial compression to failure. Three filament wound specimens had fiber cross-overs mid-length. Two cylinders had no fiber cross-overs in the test section. Failure strains based on measured end shortening δ and initial specimen length L of each control cylinder are shown in figure 4. The symbols in the figure represent the failure strain δ/L of each specimen and horizontal bars represent average failure strains of specimens of each type. Individual data points are shown to demonstrate the scatter in failure strains within each group. A small difference in average failure strains between the filament wound specimens with and without cross-overs can be seen from the data; however, scatter in the data indicates that this difference may be an artifact of the limited number of specimens tested. The scatter range for the tape specimens also suggests that there is no real evidence of a difference in failure strain among the three type of specimens.

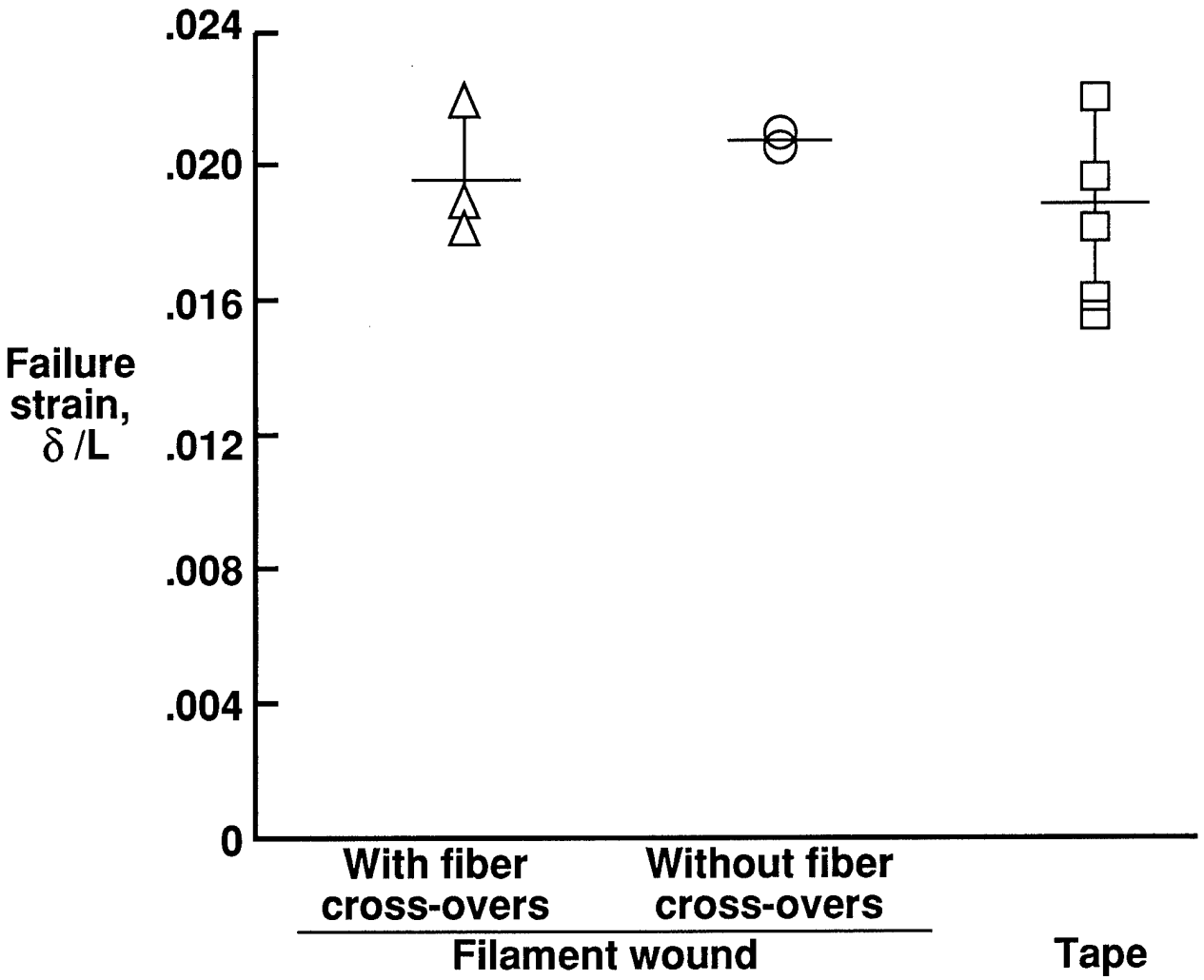


Figure 4

STIFFNESS OF TAPE AND FILAMENT WOUND GRAPHITE-EPOXY CYLINDERS

The relationship between normalized load P/EA (where P is applied load, E is specimen axial stiffness and A is specimen cross-sectional area) and normalized displacement δ/L (where δ is end shortening and L is initial specimen length) for two typical control cylinders is shown in figure 5. The axial stiffness calculated from experimental data in the linear-elastic range indicate that the filament wound cylinder's average stiffness is about 5 percent below that of the tape specimens. When cross-sectional area is considered, this difference reverses. The average EA for the filament wound cylinders is 420,000 lb while the average EA for the tape cylinders is 380,000 lb. In both types of cylinders, the scatter of values for EA among the cylinders tested is about 8 percent while the scatter for E is about 20 percent. However, the load-displacement relationship is nonlinear in both types of cylinders and the stiffness decreases when the average strain is above about .01 in both types of specimens.

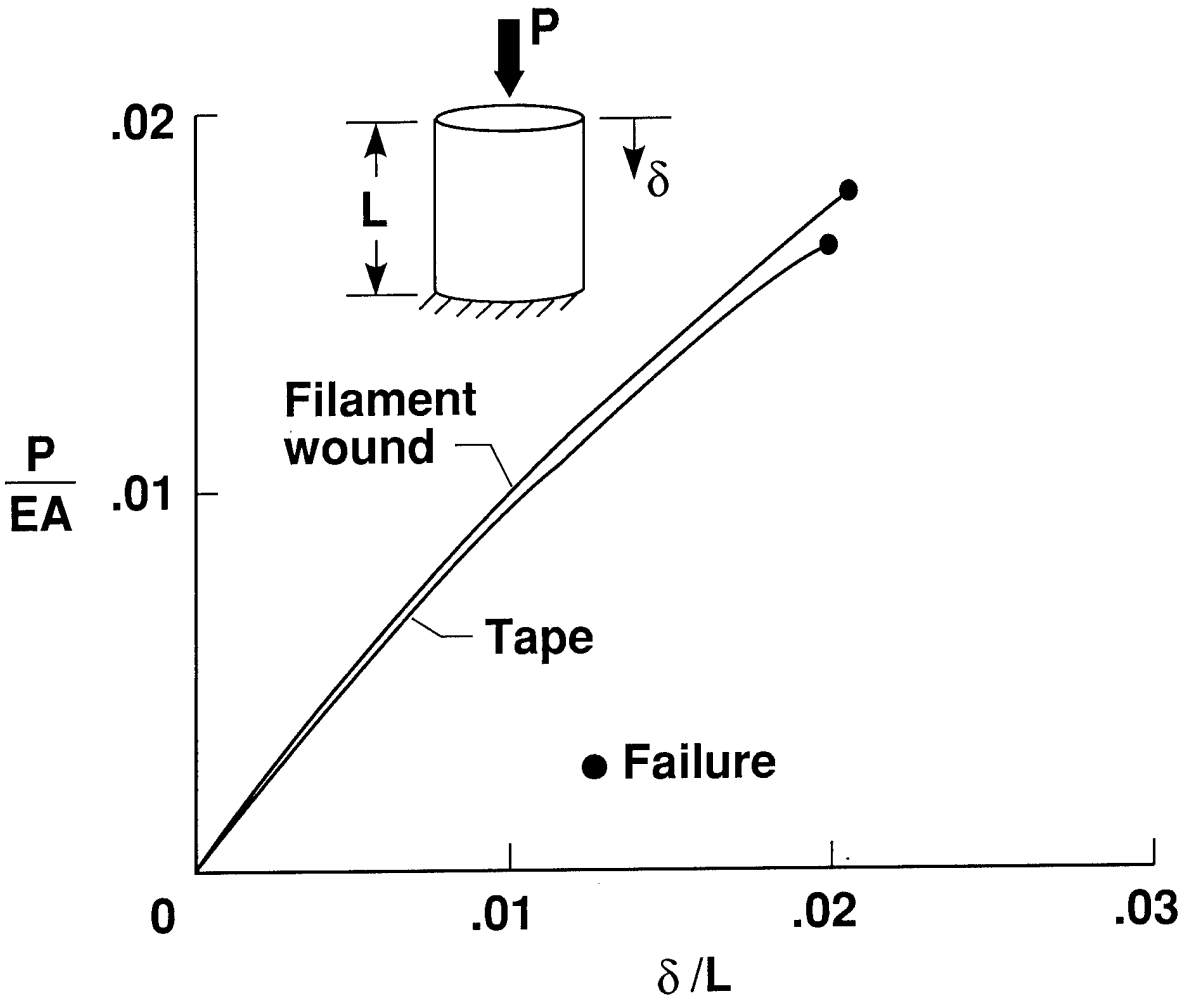


Figure 5

FAILED GRAPHITE-EPOXY TAPE CYLINDER

Photographs of a graphite-epoxy tape cylinder after failure are shown in figure 6. The entire specimen is shown to demonstrate the extent of damage induced at failure. The damage region extends around the entire circumference and over one third or more of the length of the test section and is concentrated around the axial centerline. The failure mode involved delamination of the innermost and outermost plies. Delaminated fibers broke, leading to specimen failure. Little visible or audible warning occurred prior to failure. Failure quickly progressed around the circumference of the tube. Measured axial surface strains were just over .02 at failure for each specimen. Strain gages in the direction of the outermost fibers (45 degrees) recorded a failure strain in the range of .007 to .008. A close-up view of one section of the cylinder is also shown on the right of the figure to show that the exterior layers of fibers pulled away from the cylinder during failure. The outer two plies are of stacking sequence +45 and -45 degrees. Both of these plies separated from the interior plies of the cylinder. The same failure mode was seen in the filament wound cylinders as in the tape cylinders.

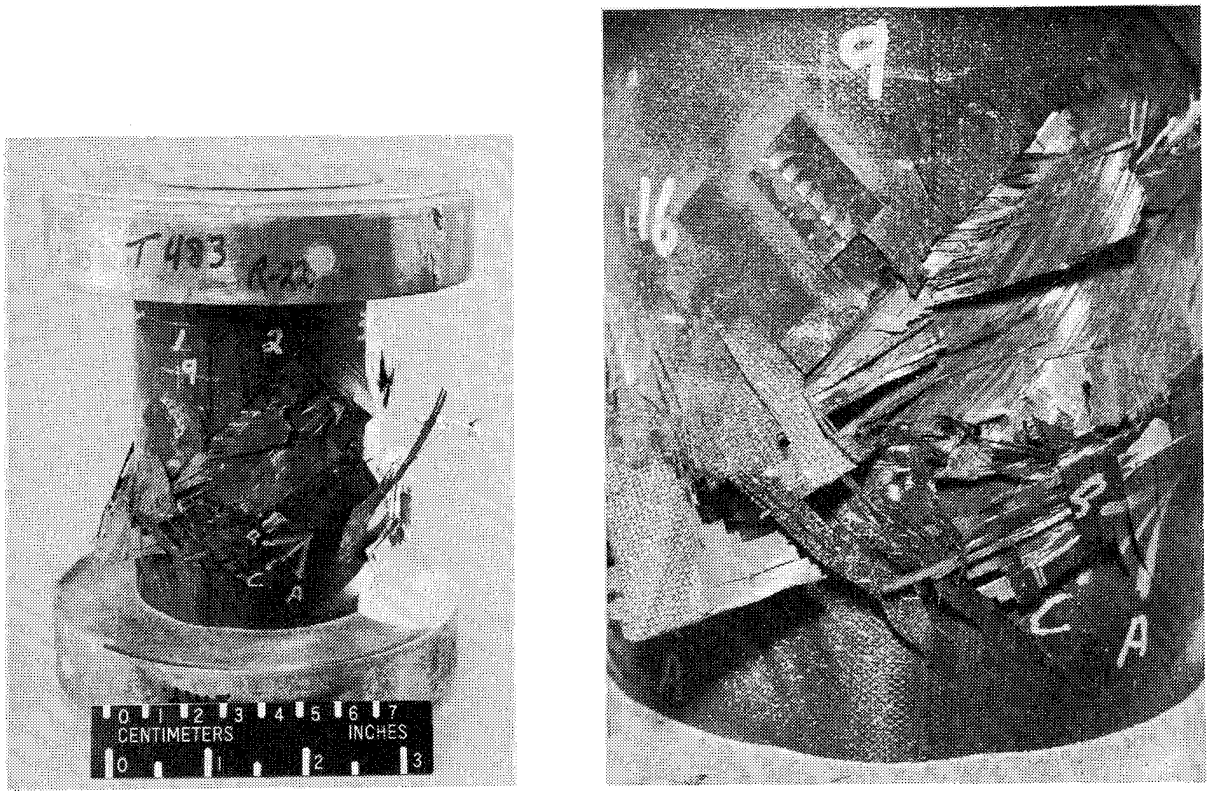


Figure 6

EFFECT OF IMPACT DAMAGE ON $[\pm 45/90]_{ns}$ SPECIMENS

Impact damage was induced into many specimens by propelling a .5-inch-diameter aluminum sphere at the center of the specimen at a specified speed (as described in reference 1). Three filament wound and four hand laid-up tape cylinders with stacking sequence $[\pm 45/90]_{3s}$ were impacted prior to loading with impact speeds up to 400 ft/sec (impact energies up to 16 ft-lb). All cylinders were impacted at mid-length. Seven hand laid-up tape flat panels with stacking sequence $[\pm 45/90]_{4s}$ were impacted at the center of the panel prior to loading. All specimens had a nominal thickness of .14 inches. The failure strain of each impacted specimen and the average failure strain of all control specimens of each type are shown in figure 7. These results indicate that impact damage reduces the failure strain to approximately 60 percent of the average failure strain of unimpacted specimens for impact speeds over 200 ft/sec (impact energy 4 ft-lb) for filament wound and tape cylinders. Failure modes for impacted cylinders were the same as for unimpacted cylinders. All cylinders failed at the mid-length of the specimen (through the impact site). Flat panels impacted at speeds above 200 ft/sec did not buckle prior to failure and failed through the impact site. Flat panels failed at lower axial strains than the cylinders for each impact speed. However, this difference is most pronounced in the control specimens where the flat panel buckled and the cylinders did not. The percentage reduction in failure strain in flat panels is smaller because the flat control specimen failed at a lower strain than the cylindrical control specimens. The minimum failure strain of each type of specimen is achieved for impact speeds above 200 ft/sec. This minimum threshhold is lower for the flat panels than for the cylinders because of curvature effects.

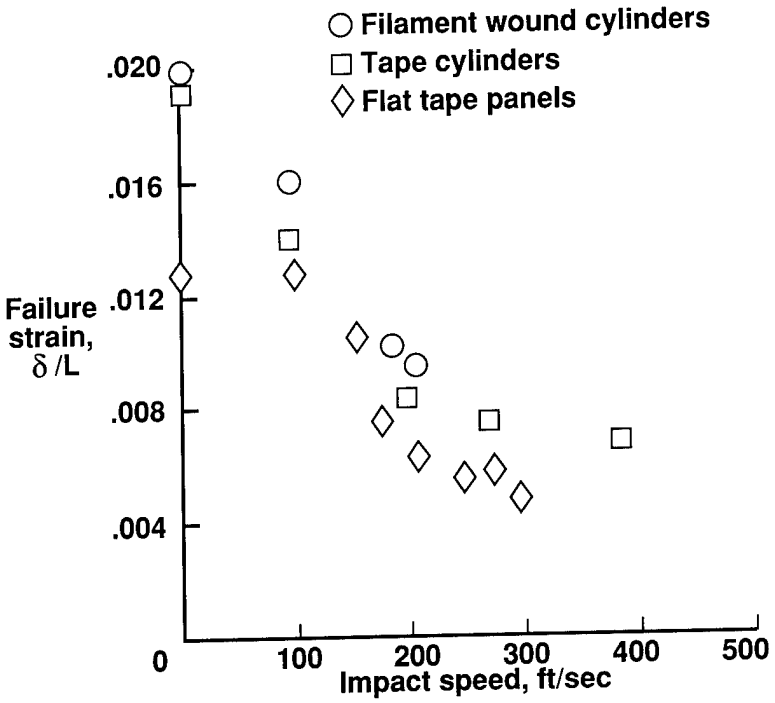


Figure 7

STIFFNESS OF FILAMENT WOUND PLATES

The relationship between normalized load P/EA and normalized end shortening δ/L for three control plate specimens with stacking sequence $[\pm 30/90]_n$ is shown in figure 8. Two of the control specimens are filament wound plates. One filament wound plate contains fiber cross-overs and the second plate does not. The third control specimen is a hand-laid tape plate (with no fiber cross-overs). The filament-wound plates were fabricated from Celion 6k fiber and Shell Epon 9400 resin and the tape-laid plate was fabricated from AS4/3502 prepreg tape.

The test results indicate a similar load-displacement behavior between the filament-wound plate with fiber cross-overs and the tape-laid plate; however, since these plates were fabricated from different materials, the similarity may not be caused by factors relating to plate construction. A stiffness comparison of nominally identical plates constructed of the two material systems indicate that the AS4-3502 plate has a noticably higher bending stiffness than the Celion 6k-9400 plate. However, the load-displacement response differs in the two filament-wound plates. For example, at an end shortening of .0095 in/in, a 20 percent difference is obtained in normalized load between both filament-wound plates. This comparison suggests that fiber cross-overs may affect the load-displacement response in filament-wound plates.

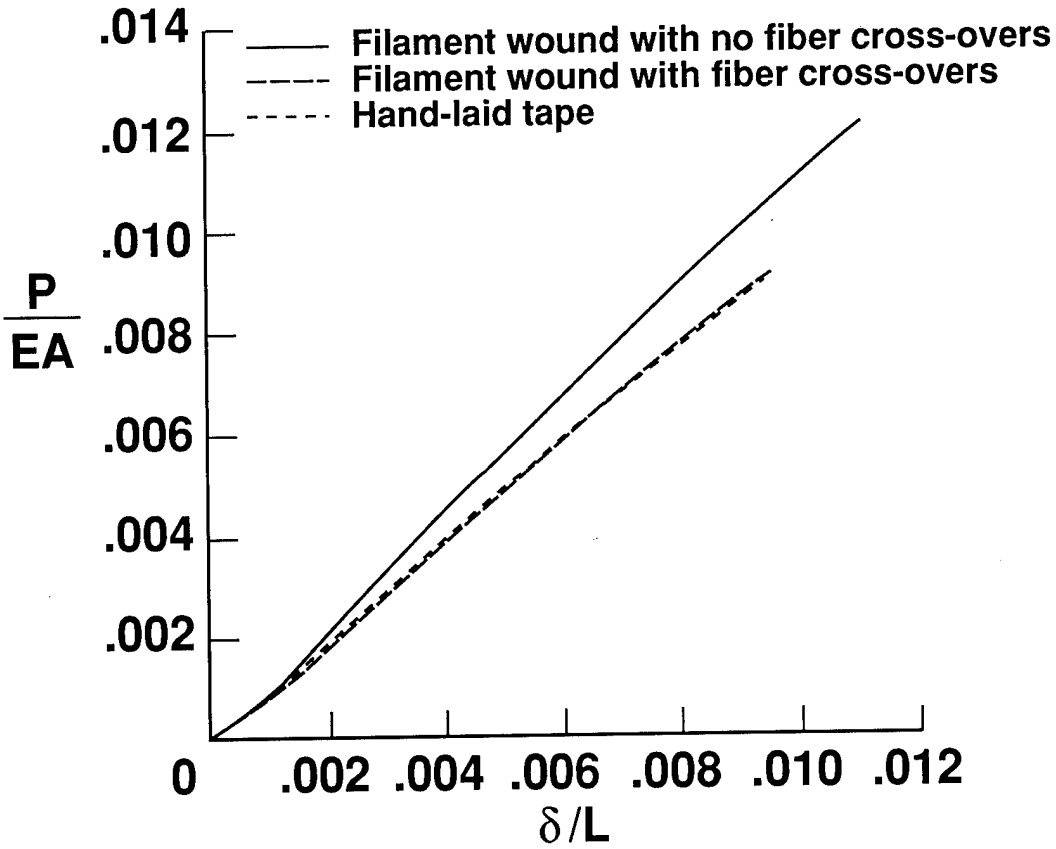


Figure 8

EFFECT OF IMPACT DAMAGE ON FAILURE STRAIN OF FLAT PLATES

The relationship between failure strain and impact speed for eight filament-wound plate specimens with stacking sequence $[\pm 30/90]_{10}$ and one hand laid-up tape plate specimen with stacking sequence $[\pm 30/90]_{16}$ is shown in figure 9. Six plate specimens were impacted at the center of each specimen with a .5-inch-diameter aluminum sphere at speeds ranging from 300 to 500 ft/sec. Three of the impacted specimens contained fiber cross-overs and three did not. The failure strain for three control (unimpacted) specimens is also shown.

The results of these compression-after-impact tests indicate that for all impact speeds examined, the plate specimens without fiber cross-overs failed at higher strains than specimens with fiber cross-overs. This comparison suggests that fiber cross-overs can affect the performance of filament-wound plates. The percentage difference in failure strain for the two types of specimens diminishes as the impact speed increases. At an impact speed of 300 ft/sec, a 30 percent reduction in failure strain is obtained for specimens with fiber cross-overs compared to specimens which have no fiber cross-overs. However, at an impact speed of 500 ft/sec, the difference in failure strain between specimens with and without fiber cross-overs is only 12 percent.

The results also show that failure strain decreases as impact speed increases for specimens with fiber cross-overs and for specimens without fiber cross-overs. Specimens impacted with an impact of speed 500 ft/sec failed at a strain level less than half that of the control specimen for each type of specimen.

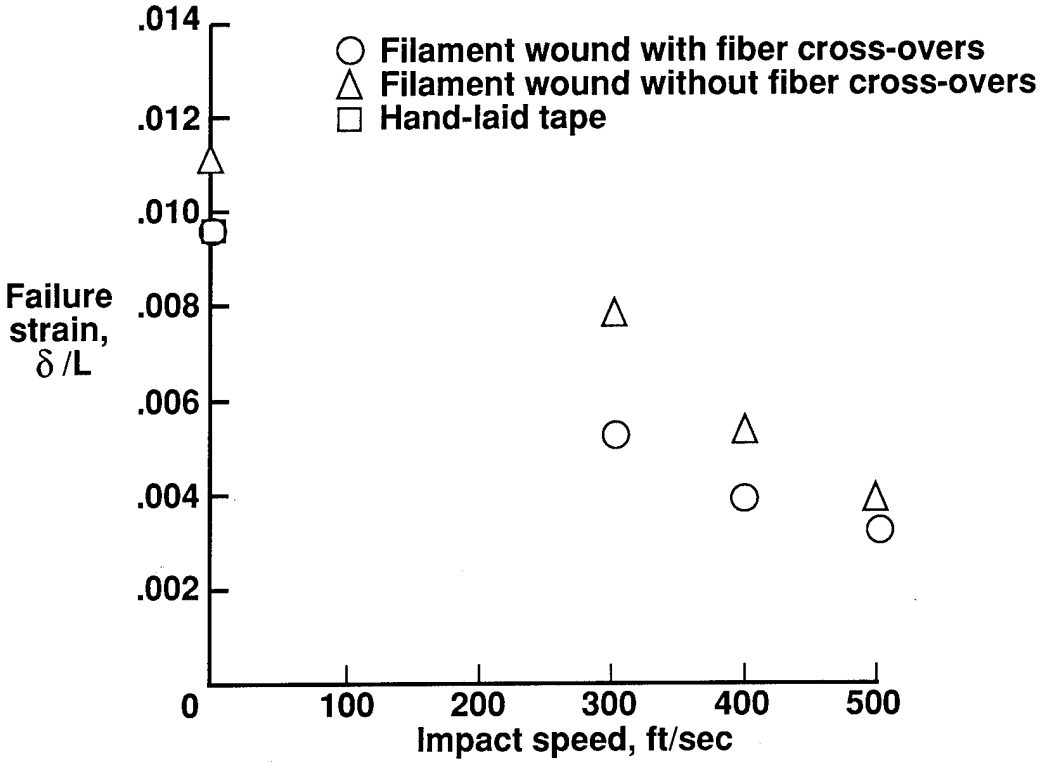


Figure 9

CONCLUDING REMARKS

The results of this experimental comparison of filament wound control (unimpacted) cylinders loaded to failure in axial compression indicates that one fiber cross-over location has no effect on the failure mode or strain in thick-walled filament wound graphite-epoxy specimens with stacking sequence $[\pm 45/90]_{3s}$. A comparison between filament wound and hand laid-up tape control cylinders indicates that there is little or no difference in the response of cylinders constructed by using the two different fabrication methods. However, unimpacted panels with many fiber cross-overs fail at up to 15 percent lower strains than panels with no fiber cross-overs.

A comparison of specimens subjected to low speed impact damage prior to compressive loading indicates that impact damage reduces the strain at failure by over 60 percent in tape and filament wound graphite-epoxy cylinders and in tape flat panels. The presence of fiber cross-overs were observed to reduce the strength of filament wound impact-damaged panels, but to have no significant effect on the strength of filament wound impact-damaged cylinders.

REFERENCES

1. Starnes, J. H., Jr.; Rhodes, M. D.; and Williams, J. G.: Effect of Impact Damage and Holes on the Compression Strength of a Graphite/Epoxy Laminate. Nondestructive Evaluation and Flaw Criticality for Composite Materials, edited by R. B. Pipes, ASTM STP 696, 1979, pp. 145-171.

EFFECTS OF SCALE IN PREDICTING GLOBAL STRUCTURAL RESPONSE[1]

R. B. Deo
H. P. Kan

Northrop Corporation
Aircraft Division
Department 3853/82
One Northrop Avenue
Hawthorne, California

ABSTRACT

In the course of previous composite structures test programs, the need for and the feasibility of developing analyses for scale-up effects has been demonstrated. The analysis techniques for scale-up effects fall into two categories. The first category pertains to developing analysis methods independently for single, unique failure modes in composites, and using this compendium of analysis methods together with a global structural model to identify and predict the response and failure mode of full-scale built-up structures. The second category of scale-up effects pertains to similitude in structural validation testing. In this latter category, dimensional analysis is used to develop scale-up laws that enable extrapolation of sub-scale component test data to full-scale structures. This Work-In-Progress paper describes the approach taken and some accomplishments in the first category of analysis for scale-up effects. A building block approach is proposed where each structural detail is analyzed independently; then, the probable failure sequence of a selected component is predicted, taking into account load redistribution subsequent to first element failure. Layup dependence of composite material properties severely limits the use of the dimensional analysis approach and these limitations are illustrated by examples.

INTRODUCTION

The high cost of design and testing of full-scale composite structures has necessitated the use of scale model testing and analytical scaling techniques for structural response prediction. Recent experience (References 1 and 2) in structural testing indicates that scale-up effects in composite structures are strongly influenced by the structural configuration and substructural arrangement. This is because of the multitude of failure modes that may occur in built-up composite structure. Even in the case of structural elements with a single unique failure mode, scaling effects are influenced by factors unique to composite materials, such as layup, (References 3 through 7) and, therefore, a complete set of scaling rules can not always be established.

[1] This work was performed under NASA/Northrop Contract NAS1-18842, entitled "Innovative Composite Fuselage Structures."

The analysis techniques for scale-up effects fall into two categories. The first category pertains to developing analysis methods independently for single, unique failure modes in composites and using this compendium of analysis methods together with a global structural model to identify and predict the response and failure mode of full-scale, built-up structures. Examples of this technique are the building-block approach of Reference 1, the semi-empirical approach of Reference 2, and the global/local analysis procedure of Reference 8. The second category of scale-up effects pertains to similitude in structural validation testing. In this category, dimensional analysis is used to develop scale-up laws that enable extrapolation of sub-scale component test data to full-scale structures. The applicability of this technique is limited to self-similar scale models. Examples in this category are the static and dynamic beam and plate models of References 3 through 7.

In this Work-In-Progress paper, both approaches to scale up law development are reviewed. The applicability and limitations of the existing methods are summarized. Layup dependence of composite material properties severely limits the use of the dimensional analysis approach and these limitations are illustrated by examples. A simplified similitude relationship for shells and curved panels is presented. Finally, the building-block approach, where each structural detail is analyzed independently, and the probable failure sequence on a selected component is predicted, taking into account load redistribution subsequent to first element failure is described.

BACKGROUND

Several scale-up law development approaches have been investigated in the literature. Application of the principles of similitude to transversely impacted composite beams was studied in Reference 3. In this reference, a set of scaling rules was established for the dynamic response of composite beams subjected to low velocity impact. Potential scaling conflicts were also discussed. A test program was then conducted to verify the rules established from dimensional analysis. The results of the tests indicated that within elastic range of beam response, the duration of impact and the impact force closely followed the theoretical scaling rules. The impact duration scaled as the geometric scale factor and the impact force as the scale factor squared. The scatter in the test data was approximately ±10 percent, which was attributed to the deviation of the specimen thickness from the nominal thickness of the laminate.

Two important observations were made in Reference 3. First, the rate effects were found to be insignificant for the material and layup considered. Since the rate effect may cause a scaling conflict in the dimensional analysis, this observation justifies the use of the principle of similitude for certain type of composites. Secondly, where the impact resistance strength is concerned, significant size effects were noted. Smaller specimens were stronger than the larger specimens. The latter observation, if verified in general, will limit the scale-up of model tests.

Experimental investigations of scaling rules for composite plate response to impact were conducted in References 4 and 5. In these references, a set of scaling rules was established based on dimensional analysis. By considering the equations of motion of the plate, and assuming that material properties were unchanged, References 4 and 5 showed that geometric dimensions must be scaled uniformly. That is, the scale factors for length, width, and thickness of the plate should be identical. The

time parameter must also be scaled in accordance with the geometric scale factor. The experimental results in these references showed that, when the impact velocity is sufficiently low so that no significant material damage is produced, the strain response closely followed the scaling rules. The strain response was the same for different size specimens with time scaled by the geometric factor and the impactor mass scaled by the cube of the geometric factor.

It should be noted that in the preceding studies (References 3, 4, and 5) damage due to impact was not considered in scaling. No attempts were made to relate the extent of damage with specimen size. This is because the extent of impact damage is known to be a strong function of size and boundary conditions and is usually analyzed by applying fracture mechanics. This requires more complex scaling analysis.

Scaling effects in the large deflection response of composite beams were studied in References 6 and 7. Reference 6 investigated the static response and Reference 7 investigated the dynamic response. The beams were loaded under an eccentric axial compressive load to promote large deflections and global failure. The static test results (Reference 6) showed that the beam response followed the scaling rules in the small deflection, elastic region; however, deviations from the scaling rules appeared as the beams underwent large deflections and rotations. That resulted in a significant size effect in the failure behavior. The smaller beams failed at a higher normalized load and higher normalized end displacement than the larger beams. This observation of size effects agrees with the results of Reference 3.

Impact tests were conducted in Reference 7 on the large deflection beam used in Reference 6. Scaling rules, based on dimensional analysis, were also established in Reference 7. These rules are similar to those proposed in References 3 through 5. The experimental results in Reference 7 indicated that load and strain responses of the unidirectional beam followed the scaling rules quite well. However, the results were inconsistent for specimens with other laminate layups (cross-ply, angle-ply, and quasi-isotropic). The significant size effects on failure behavior observed in static tests (Reference 6) were not found in the impact test results of Reference 7.

From the results of References 3 through 8, the following general observations can be made on scaling of composites.

1. Scaling rules based on dimensional analysis are not unique. Different sets of scaling rules may be established for one type of structure.

2. Simple scaling rules can only be established for the same family of laminate layups. This significantly limits the general application of the principle of similitude on actual structures.

3. Size effects exist in composite structures, which may be caused by material inhomogeneity. Direct application of the scaling rules may result in unconservative estimates of full-scale structural response.

4. Structural response beyond the elastic limit does not follow simple scaling rules. Therefore, the principle of similitude may not be useful for failure prediction.

5. Extensive tests are required to verify the applicable scaling rules and establish guidelines for test data interpretation.

PRACTICAL APPLICATION EXAMPLES

The applicability of classical dimensional analysis principles in composite structural mechanics was assessed by examining two fundamental problems: (1) axial tension loading of a narrow laminate and (2) buckling of a narrow laminated plate. These problems were selected to highlight two important parameters in the scaling of composites - layup and stacking sequence. These parameters are not relevant to the scaling of metallic structures but have significant effects in scaling of composites. The applicability of classical dimensional analysis is illustrated by the following examples.

Consider a 24-ply baseline laminate of 1-inch width and subjected to tensile loading along the 0 degree direction. The laminate stacking sequence is $[\pm 45/0_2/\pm 45/0_2/\pm 45/90/0]_s$, which gives a (42/50/8) distribution of plies. The lamina mechanical properties are

$E_L = 18.7 \times 10^6$ psi $\qquad \nu_{LT} = 0.3$

$E_T = 1.9 \times 10^6$ psi $\qquad t = 0.0052$ in.

$G_{LT} = 0.85 \times 10^6$ psi $\qquad \epsilon_f = 0.011$ in/in.

The calculated Young's modulus in the loading direction is $E_x = 9.977 \times 10^6$ psi. The strain response of the laminate can be approximated by

$$\epsilon = \frac{P}{AE_x} = \frac{P}{nbtE_x}, \tag{1}$$

where, P is the applied load, n is the number of plies, and b is the laminate width. To scale down the laminate and simulate the strain response, two assumptions were made. First, it was assumed that symmetry of the laminate is maintained and second, that the orthotropy of the laminate is maintained throughout the scaling process. These assumptions ensure that Equation 1 holds true for all of the scaled-down laminates.

Now consider the failure load P_f based upon the maximum strain criterion. Equation 1 becomes

$$P_f = nbtE_x\epsilon_f \tag{2}$$

The failure load calculated for the baseline laminate is 13,681 lb. For cases of constant modulus E_x, such as metals, the failure load would vary linearly with the cross-sectional area of the specimen. This is shown by the solid line in **Figure 1**. For composite laminates, however, the modulus E_x is a function of the thickness (number of plies) and the layup. Scaling in thickness by adding or reducing the number of plies gives rise to a nonlinear relationship between the failure load and cross-sectional area. To illustrate this point, suppose that the laminate width is given a constant value of b = 1.0 inch while the number of plies is reduced. The failure loads will depend upon the type of plies (0°, ±45°, 90°) removed from the laminate. For example, if the baseline 24-ply laminate is reduced to 22 plies by removing two 0 degree plies, two ±45 degree plies, or two 90 degree plies, the corresponding failure loads are 11,500 lb, 13,300 lb, and 12,900 lb, respectively. As the

number of plies is reduced still further, the possible failure loads are found to lie in an envelope centered about the linear failure load versus cross-sectional area relationship as shown in **Figure 1**.

To further illustrate the issues pertinent to the scaling of composite structures, consider a second problem involving a narrow laminated composite plate subjected to axial compressive load. The buckling load for a plate of this kind with clamped ends and free edges is

$$N_{cr} = k \left(\frac{2\pi}{L}\right)^2 D_{11} \qquad (3)$$

where

L = total length of the plate

D_{11} = bending rigidity in the loading direction

k = a constant equal to 1.0306 for the first buckling mode

From Equation 3, the scaling parameters to be considered in this problem are L and D_{11}. Because D_{11} depends upon the thickness, modulus, and stacking sequence, this problem represents one higher level of complexity than the problem discussed previously.

Consider the same 24-ply baseline laminate as in the first problem, with an unsupported length L = 3.0 inches. The axial bending rigidity of the plate is 1,777 lb-in. If the modulus is constant, as for metals, D_{11} varies with h^3 (h is the total thickness). As the thickness reduces to 22 plies, the possible combinations of layup and stacking sequence along with the associated bending rigidity and buckling load are given in **Figure 2**. **Figure 3** shows the buckling load as a function of laminate thickness. The buckling loads for the composite laminate fall in an envelope centered about the solid curve, which is the buckling load versus thickness relationship for a constant modulus material.

The results shown in **Figures 1 and 3** show that scaling in composites, even for the simplest structural mechanics problems, involves more than dimensional parameters. Because of the multiplicity of possible laminate constructions, structural mechanics methods of analysis must be used to develop similitude rules.

Similar results can be obtained for two-dimensional problems. The thickness, ply-orientations and stacking sequence effects on bending of a rectangular composite plate subjected to uniform lateral pressure is shown in **Figure 4**. The buckling load of a simply supported rectangular plate is shown in **Figure 5**. Both **Figures 4 and 5** show that structural response deviates from the classical dimensional analysis results. The deviation is caused by the layup and stacking sequence effects on the plate rigidity parameters, D_{ij}. In comparing the results of the two-dimensional problems with that of one-dimensional, **Figures 4 and 5** show a narrower band in the structural response. This occurs because the results of the one-dimensional problems are affected only by the axial properties E_x and D_{11}, whereas, the results of the two-dimensional problems are affected by all components of the in-plane mechanical properties. The overall effect of all four rigidity components (D_{11}, D_{12}, D_{22}, D_{26}) is less significant than that of a single component.

SPECIALIZED SCALING TECHNIQUES IN COMPOSITES

The previous section discussed the difficulties in direct application of the principle of similitude in composites. It was also pointed out that scale model can be designed with the aid of structural mechanics. In this section, an analytical procedure to design scale models is presented. The procedure is similar to the one proposed in Reference 8 and is illustrated by the following example.

Consider an unstiffened composite cylinder of radius R_s, thickness t_s, and length L_s. The scaling parameters significant to buckling can be divided into three categories:

1. Load Parameter

$$P_r = (N_{cr})_m/(N_{cr})_s \tag{4}$$

where N_{cr} is the buckling load per unit length around the cylinder circumference.

Subscripts m and s denote the scaled model and the full-scale structure, respectively.

2. Geometric Parameters

Length Ratio	$L_r = L_m/L_s$	(5)
Radius Ratio	$R_r = R_m/R_s$	(6)
Thickness Ratio	$t_r = t_m/t_s$	(7)

3. Property Parameters

Modulus Ratio	$E_r = E_m/E_s$	(8)
Stiffness Ratio	$D_r = D_m/D_s$	(9)

where E and D are Young's modulus and bending rigidity, respectively.

The load parameter P_r is a predetermined design factor for the model. The load requirement for the test model is usually higher than the actual structure. In the case where the exact buckling load of the structure is to be simulated, P_r = 1.0.

The geometric and property parameters interact when buckling is considered. For composite structures, the property parameters are usually not unique because of the anisotropy of the materials. These parameters are also affected by the thickness parameter because of the ply orientations. Therefore, it is not possible to establish a simple scaling law for composite structures as discussed in the preceding section.

In the present analysis, the scaled model is designed using an iterative procedure. The analysis method for symmetric buckling of isotropic cylinders is first used to estimate the key scaling parameters. The buckling load of an isotropic cylinder with R >> t is given in Reference 9 as

$$N_{cr} = \frac{2}{R}(EDt)^{1/2} \tag{10}$$

Based on this expression, the key scaling parameters can be written as

$$R_r = \frac{1}{P_r}(E_r D_r t_r)^{1/2} \tag{11}$$

$$t_r = \frac{(R_r P_r)^2}{E_r D_r} \tag{12}$$

$$E_r = \frac{(R_r P_r)^2}{t_r D_r} \tag{13}$$

$$D_r = \frac{(R_r P_r)^2}{E_r t_r} \tag{14}$$

For isotropic material

$$D = \frac{Et^3}{12(1-\nu^2)} \tag{15}$$

Assuming that the test model is fabricated from the same material as the full-scale structure, then the Poisson ratios $\nu_m = \nu_s$ and the stiffness ratio becomes

$$D_r = E_r t_r^3 \tag{16}$$

Equation 10 indicates that the length parameter is an arbitrary number if only buckling load is to be simulated. The length of the cylinder controls the buckling mode, but not the buckling load.

For composite cylinders, the scale parameters are first estimated using Equations 11 through 16. Then the following procedure is used:

1. Define the load requirement (P_r).

2. Select the radius and length ratio (R_r, L_r). Because length has no significant effect on buckling load, assume $L_r = R_r$.

3. Maintain approximately the same axial Young's modulus ($E_r \approx 1.0$).

4. Estimate t_r from Equations 12 and 16:

$$t_r^2 = P_r R_r \tag{17}$$

5. Based on the estimated t_r, determine the practical thickness of the model, t_m. The practical thickness is determined based on the number of plies.

6. Determine the ply orientations. The ply orientations should be similar to the full-scale structure in the initial estimate, because $E_r \approx 1.0$.

7. Determine the laminate stacking sequence based on D_r given in Equation 14. The practical rules for laminate stacking should be taken into consideration.

8. Conduct orthotropic (anisotropic) buckling analysis to confirm P_r.

9. Perform iterations until the required P_r is obtained.

The following example problem illustrates this procedure:

Consider a full-scale cylinder 45 inches in radius and 25 inches in length. The cylinder is made of AS4/3501-6, 16-ply $(\pm 45/0_2/\pm 45/90/0)_s$ laminate with a thickness of 0.0832 inch. A 1/5 subscale model with a load requirement of $P_r = 1.5$ will be designed.

For the full-scale cylinder buckling,

$$(N_{cr})_s = 669.66 \text{ lb/in}$$

The required buckling load for the subscale model is

$$(N_{cr})_m = 1005 \text{ lb/in}$$

The dimension requirement gives

$$R_m = 9.0 \text{ in}$$

$$L_m = 5.0 \text{ in}$$

From Equation 17 the initial estimate of the model thickness is

$$t_r = (P_r R_r)^{1/2} = 0.548$$

or

$$t_m = (0.548)(0.0832) = 0.0456 \text{ in}$$

For the material considered, a 9-ply laminate is required, which has the nominal thickness of 0.0468 inch.

For $E_r \approx 1.0$, the percentage distribution of 0°, 45°, and 90° plies for the 9-ply laminate is either (33.3/55.6.11.1) or (44.4/44.5/11.1). A $(\pm 45/0_2/90/0_2/\mp 45)_T$ was chosen in this example. A 9-inch radius cylinder with this laminate resulted in

a buckling load of 939.6 lb/in or $P_r = 1.4$ which is below the load requirement of 1.5. Hence, further iteration on the scale parameters is required. Two approaches to vary the subscale model were considered in order to meet the load requirement. First, if the dimensional requirement ($R_r = 0.2$) can be changed, then the load requirement can be met by reducing the radius to 8.4 inches. With this radius, the buckling load increases to 1011 lb/in or $P_r = 1.510 > 1.50$. Second, by changing the laminate stacking sequence to $(45/0/-45/0/90/0\text{-}45/0/45)_T$ with all other parameters fixed, the buckling load increases to 1051 lb/in or $P_r = 1.569$.

The final values for the subscale model (for illustration purposes only) are

$R_m = 8.4$ in

$L_m = 4.7$ in

$t_m = 0.0468$ in 9-ply $(\pm 45/0_2/90/0_2/\mp 45)_T$

The scaling parameters are

$D_r = 0.15$		(0.164)
$E_r = 1.11$		(1.0)
$t_r = 0.5625$		(0.548)
$P_r = 1.505$		(1.50)
$R_r = 0.187$		(0.2)
$L_r = 0.188$		(0.2)

Numbers in parentheses denote initial estimates.

To further scale down the structure, a cylindrical panel instead of a subscale cylinder can be considered. This requires determining the panel width (or central angle θ), with all other parameters unchanged. Parametric study indicates that for simply supported cylindrical panels, the panel buckling load (N^P_{cr}) is higher than that of a complete cylinder (N^C_{cr}). However, the panel buckling load approaches the buckling load of a complete cylinder as the panel width increases. Beyond a minimum panel width, N^P_{cr} is within 5 percent of N^C_{cr} as shown in **Figure 6**. The minimum width depends on the radius of the cylinder and can be determined analytically. For the example cylinder discussed earlier, the minimum panel width is 4.75 inches (or central angle $\theta = 32.4°$).

Figure 6 shows the effect of panel width on buckling load. From this figure, it can be seen that the buckling load of the full-scale cylinder can be experimentally determined by testing a curved panel with a minimum width of 4.75 inches. It may be noted, that although the buckling load of a complete cylinder can be simulated by a portion of a subscale cylinder (panel), the buckling mode is difficult to simulate.

THE BUILDING BLOCK APPROACH

As discussed earlier, another category of scale-up laws pertains to using structural analysis methods with a structural model to identify and predict the response and failure mode of full-scale built-up structures. These scale-up effects are investigated through a building block approach. In the following paragraphs, this approach is first illustrated by an example. The analytical development procedure is then discussed.

An example illustrating this category of scale-up laws is that of post-impact compression strength of coupons and built-up 3-spar panels representative of an upper wing skin. Scale-up effects test data and the accompanying analysis for this case were developed in Reference 2. The scale-up effects observed from test data in this example are shown in **Figure 7**. This figure compares the post-impact compression strength of the 5-inch wide coupon to that of built-up panels of similar layup and thickness subjected to the same level of impact energy. The shift in strength data from coupons to 3-spar panels is indicative of the scale-up effect.

The accompanying structural mechanics scale-up analysis in Reference 2 was based on an extensive set of data for static strength of impact-damaged built-up composites. It was observed, in the reference, that failure of damaged coupons was single-stage, with damage propagating from the impact site to the edges at the failure load. For a built-up structure, the overall post-impact strength was significantly influenced by the structural configuration. It was observed that failure in most of the 3-spar panels was in two stages. At initial failure, the damage propagated to the spar fastener lines. The initial failure load (strain) corresponded to the final failure load of coupon specimens. The damage propagation was arrested by the spars, with final failure taking place at a higher applied load.

A semi-empirical analysis method was developed in Reference 2 to predict the scale-up effects on post-impact damage strength. The model for the coupon failure is based on an elastic stiffness reduction technique. The structural configuration scale-up effects on residual strength are incorporated in the stiffness reduction to predict the two-stage failure.

A comparison of observed and predicted post-impact failure strains is shown in **Figure 8**. The figure shows that the predicted initial and final failure strains agree well with test data. This structural mechanics scale-up law to predict residual compression strength after impact was exercised on a large test data base for built-up structures, including a full-scale wing box. **Figure 9** shows the test analysis correlation for a wide range of structural geometries and materials.

The above example illustrates the feasibility of and the methodology for the development of structural mechanics scale-up laws for composite structures.

The building block approach used here is similar to the experimental approach proposed in Reference 1 and summarized in **Figure 10**. This figure shows that design development testing is characterized by five levels of complexity, with the fifth level assigned to the full-scale component.

The wing skin coupon specimens represent the first complexity level in the building-block approach and simulate simple tension and compression failure modes. Six specimen types were tested in Reference 1. These were either open or filled hole

specimens tested under tension (lower wing skin) or compression (upper wing skin) with laminates representing different locations on an actual fighter wing structure. At this level of complexity, the analysis task is to correctly predict the failure stress/strain and failure load from the available lamina properties. The required analytical tools are open and filled hole analyses and an appropriate failure criterion. Scaling law development at this level of complexity involves correlating observed and predicted failure stress, strain, and loads. Analysis and correlation for the wing skin coupon specimens will be carried out during the next reporting period.

The second complexity level in the test program of Reference 1 contains three specimen types. Each of these specimens has two potential failure modes. An upper skin/rear spar mechanical joint (WE-2) was designed to check the influence of load transfer on compression strength. Potential failure modes for this specimen are laminate failure and bearing failure at a fastener hole. Loaded hole analysis will be conducted on this specimen. Both bearing and net-section failure criteria will be required for failure prediction. The scaling law development here will involve the use of open and filled hole test data to predict (or correlate) the specimen failure load and failure mode.

Another specimen type at the second level of complexity is an intermediate spar/lower skin cocured joint (WEC-1). This specimen is designed to check spar web strength in the presence of a fuel drain hole and the cocured bonded joint strength under combined shear, fuel pressure and chordwise loading. Potential failure modes are web failure at the fuel drain hole and bondline failure in the cocured joint. The applicability of the open hole analysis will be re-examined for this problem. In addition, stress analysis of the bondline will be conducted.

A third specimen, the front spar/skin joint (WE-1) shown in **Figure 10**, is representative of the graphite/epoxy front spar-to-skin joint. The specimen was subjected to corner bending and shear induced by fuel pressure. The potential failure modes for this specimen are joint failure (fastener pull-through and adhesive failure) and interlaminar tension failure at the corner. Joint analysis and corner radius analysis will be conducted and failure criteria will be established for this specimen type. Coupon test data are not applicable for this specimen type because the potential failure modes are both out-of-plane in nature.

The third complexity level in the test program of Reference 1 is represented by an intermediate spar/pylon rib load transfer joint (WEC3), and is designed to check load transfer from the discontinuous spar into the rib and back to the spar. This specimen combines the potential failure modes of the wing coupons and WEC-1, i.e., upper and lower skin failures at a rib attachment fastener hole, spar web failure and intermediate spar/lower skin failure in the cocured joint. The fourth and final level of complexity in the torsion box design development testing is represented by the wing subcomponent (WS-1) which is a three bay box beam, and root rib/aft trunnion subcomponent which represents the highly loaded root rib/aft trunnion area. All of the failure modes of the wing coupons, WE-2, WE-1, and WEC-3 are represented in the WS-1 specimen. In addition, an upper skin access hole provides a further potential failure mode. The fifth level of complexity is the wing component, which is fully representative of the actual wing structure.

Comprehensive structural analysis will be conducted at the subcomponent level and the component level for both the wing and fuselage structures. The analysis results will then be correlated with test data to establish scaling laws.

SUMMARY

Analytical techniques for scale-up effects have been reviewed. The advantages and limitations of applying the principles of similitude to composite structures have been summarized and illustrated by simple examples. An analytical procedure was formulated to design scale models of an axially compressed composite cylinder. A building-block approach was outlined where each structural detail is analyzed independently and the probable failure sequence of a selected component is predicted, taking into account load redistribution subsequent to first element failure. Details of this building-block approach are under development.

REFERENCES

1. Whitehead, R. S., et al., "Composite Wing/Fuselage Program," AFWAL-TR-88-3098, Volumes I-IV, February 1989.

2. Horton, R. E., Whitehead, R. S., et al., "Damage Tolerance of Composites," AFWAL-TR-87-3030, Volumes I, II, and III, July 1988.

3. Morton, J., "Scaling of Impact-Loaded Carbon-Fiber Composites," AIAA Journal, Volume 26, No. 8, August 1988, pp 989-994.

4. Dian, Y. and Swanson, S. R., "Experimental Measurement of Impact Response in Carbon/Epoxy Plates," proceedings of the 30th AIAA/ASME/ASCE/AHS/ASC Structures, Structural Dynamics, and Materials Conference, April 1989, pp 1023-1029.

5. Dian, Y, Swanson, S. R., Nuismer, R. J., and Bucinell, R. B., "An Experimental Study of Scaling Rules for Impact Damage in Fiber Composites," Journal of Composite Materials, Volume 24, May 1980, pp 559-570.

6. Jackson, K. E. and Fasanella, E. L., "Scaling Effects in the Statis Large Deflection Response of Graphite-Epoxy Composite Beams," proceedings of the American Helicopter Society National Technical Specialist's Meeting on Advanced Rotorcraft Structure, October 25-27, 1988.

7. Jackson, K. E. and Fasanella, E. L., "Scaling Effects in the Impact Response of Graphite-Epoxy Composite Beams," SAE General Aviation Aircraft Meeting and Exposition, Wichita, Kansas, April 11-13, 1989, Paper No. 891014.

8. McCullers, L. A. and Neberhans, J. D., "Automated Structural Design and Analysis of Advanced Composite Wing Models," Composite and Structures, Volume 13, 1973, pp 925-935.

9. Timoshenko, S. P. and Gere, J. M., Theory of Elastic Stability, McGraw Hill Book Company, New York, 1961.

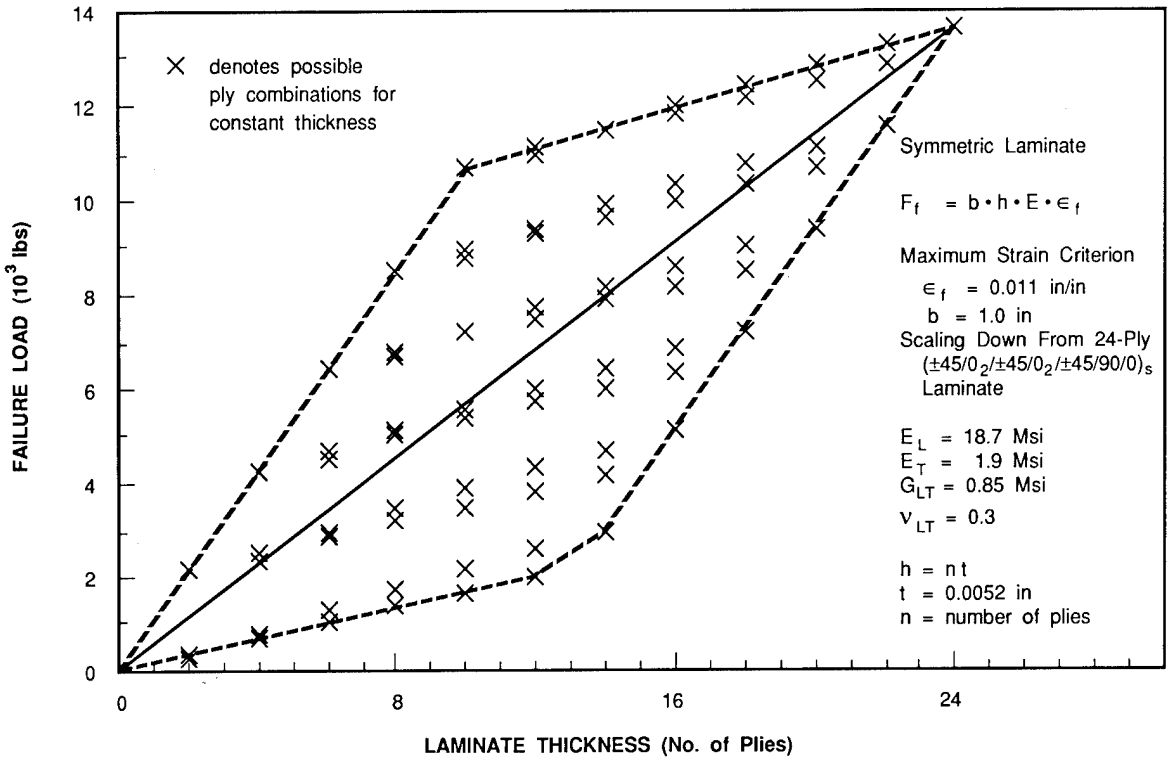


Figure 1. Tensile Failure Load of a Narrow Composite Plate as a Function of Laminate Thickness.

LAYUP	STACKING SEQUENCE	D_{11} (lb-in)	N_{cr} (lb-in)
(45.5/45.5/9)	$[45/0_2/\pm 45/0_2/\pm 45/90/0]_s$	1541	6966
	$[\pm 45/0_2/45/0_2/\pm 45/90/0]_s$	1421	6424
	$[\pm 45/0_2/\pm 45/0_2/45/90/0]_s$	1358	6137
(36/55/9)	$[\pm 45/0/\pm 45/0_2/\pm 45/90/0]_s$	1222	5526
	$[\pm 45/0_2/\pm 45/0/\pm 45/90/0]_s$	1314	5940
	$[\pm 45/0_2/\pm 45/0_2/\pm 45/90]_s$	1358	6143
(45/55/0)	$[\pm 45/0_2/\pm 45/0_2/\pm 45/0]_s$	1360	6150

Figure 2. Possible 22-Ply Laminates in Example Buckling Problem.

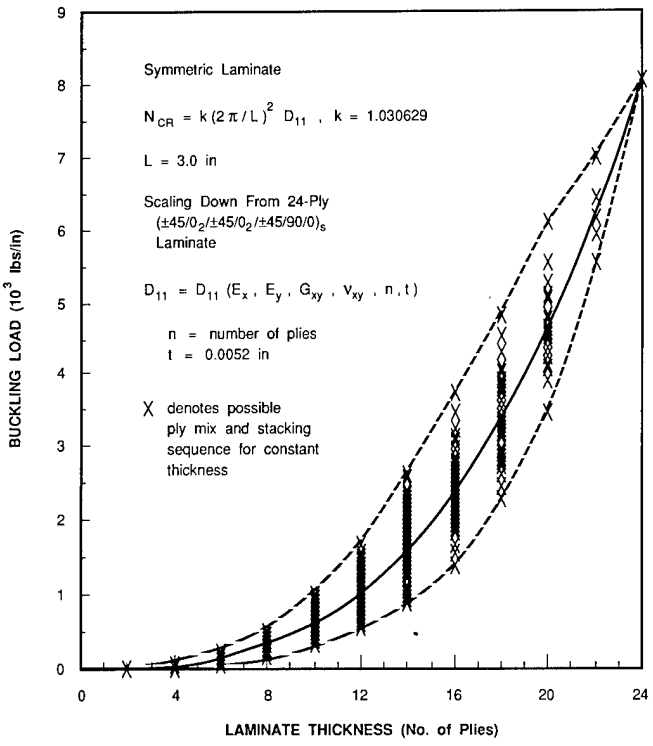


Figure 3. Buckling Load as a Function of Laminate Thickness.

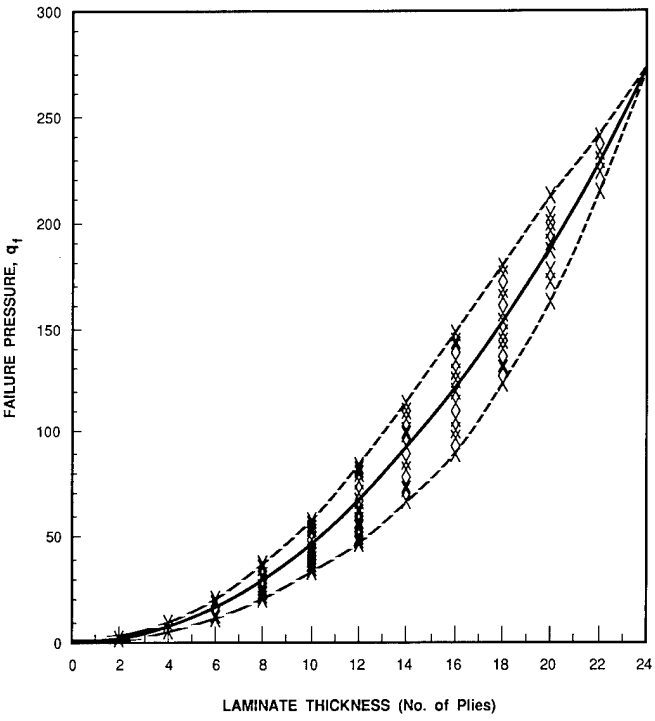


Figure 4. Failure Pressure of a Rectangular Plate as a Function of Plate Thickness.

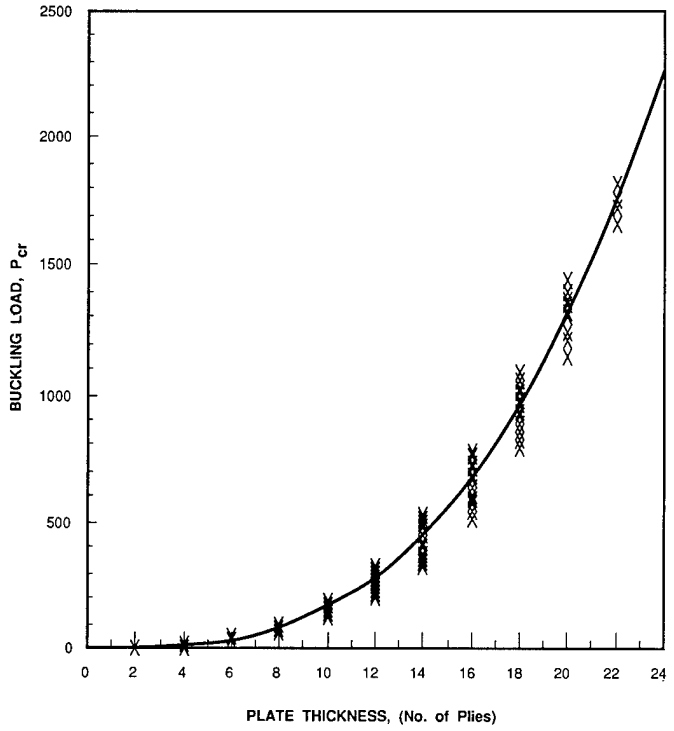


Figure 5. Buckling Load of a Simply Supported Rectangular Plate as a Function of Plate Thickness.

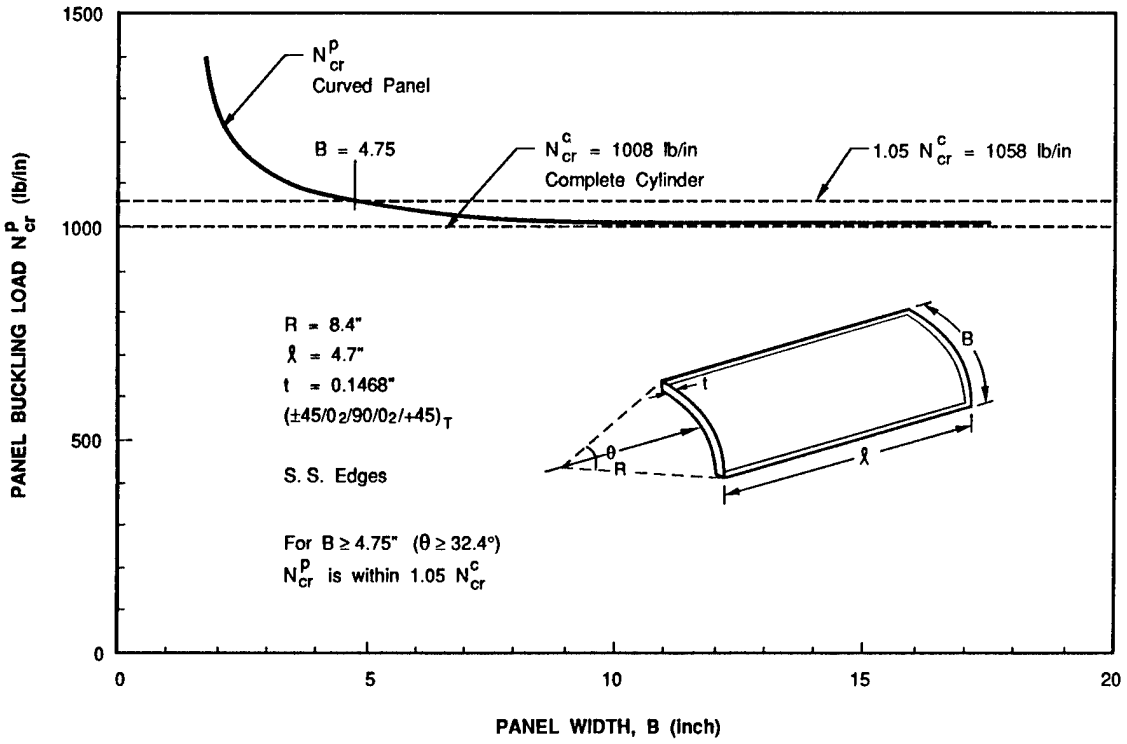


Figure 6. Effect of Panel Width on Buckling Load.

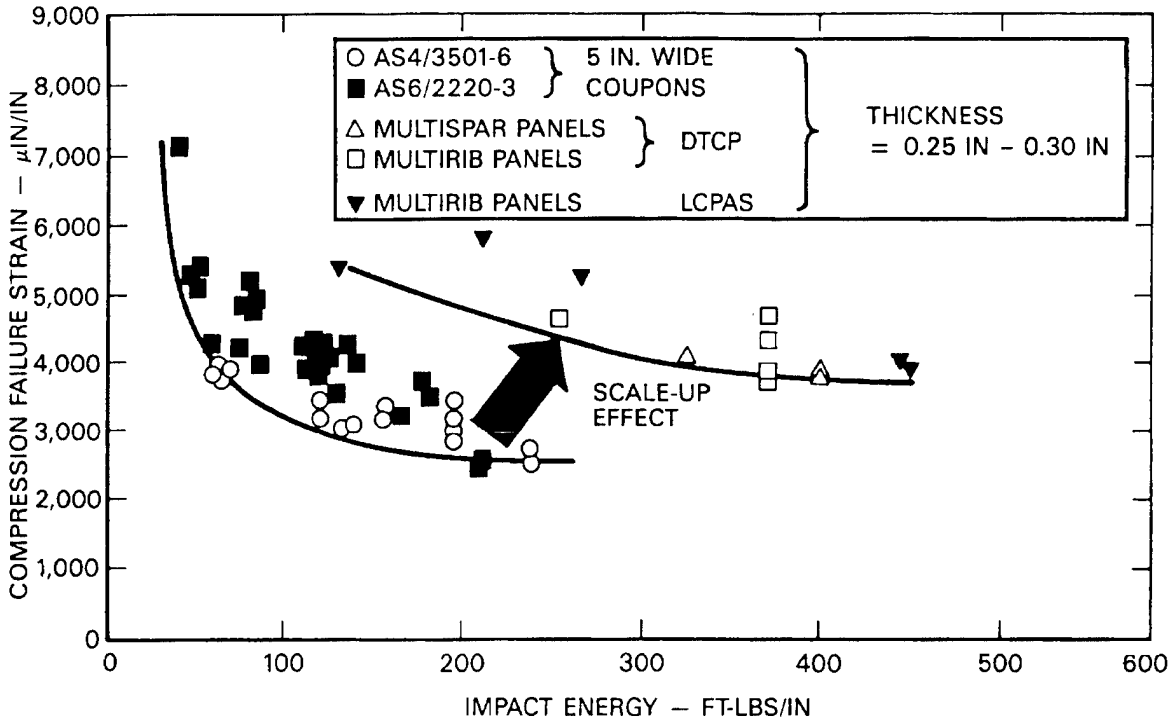


Figure 7. Scale-Up Effects on Post-Impact Compression Strength.

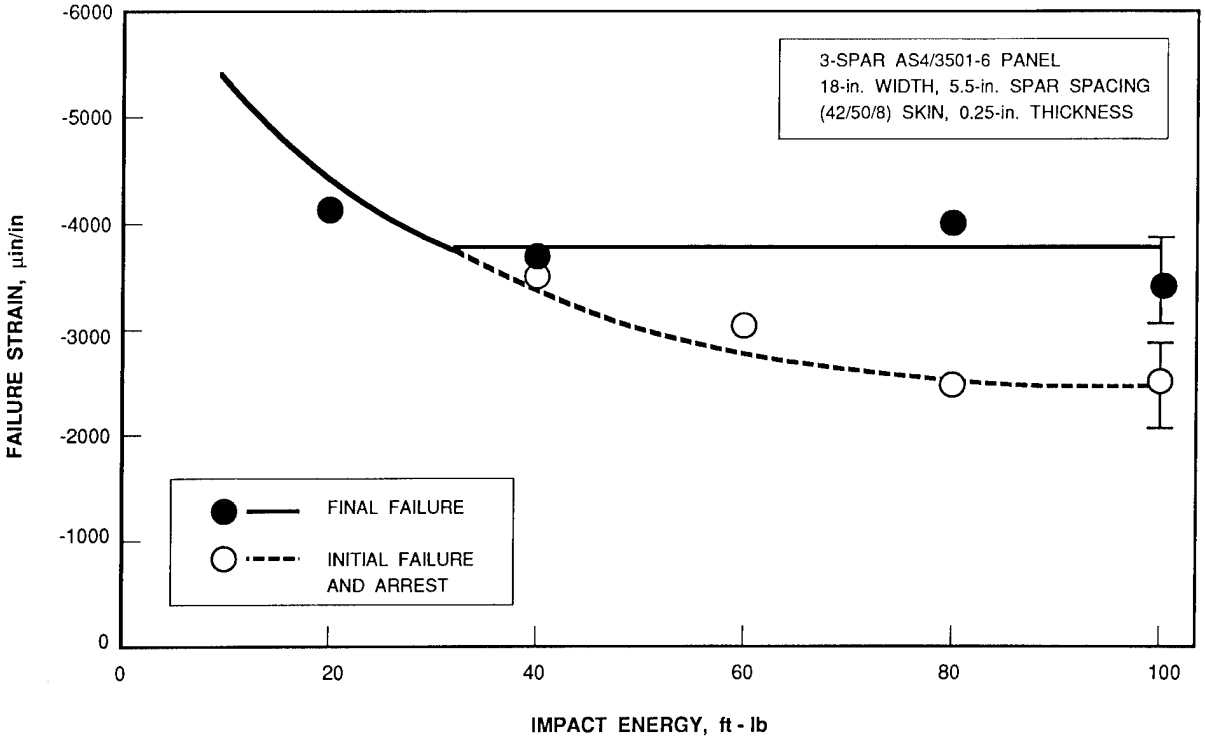


Figure 8. Comparison of Observed and Predicted Strain.

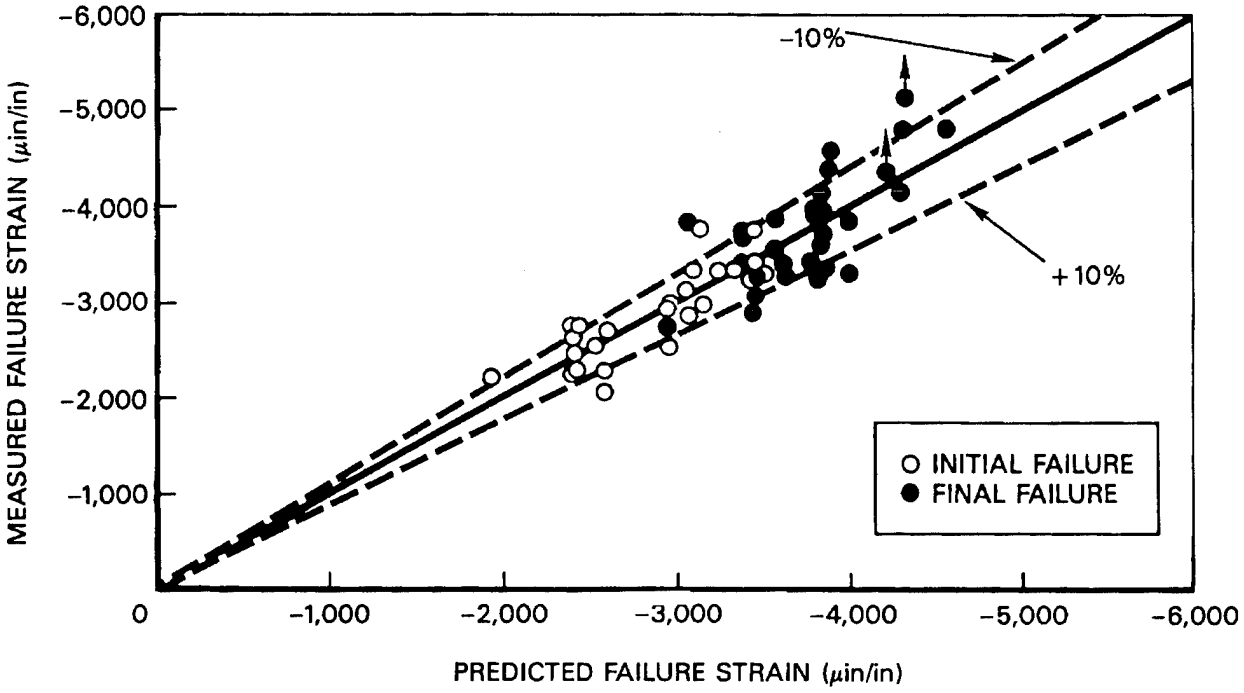


Figure 9. Comparison of Measured and Predicted Post-Impact Compression Strength for Built-Up Structures.

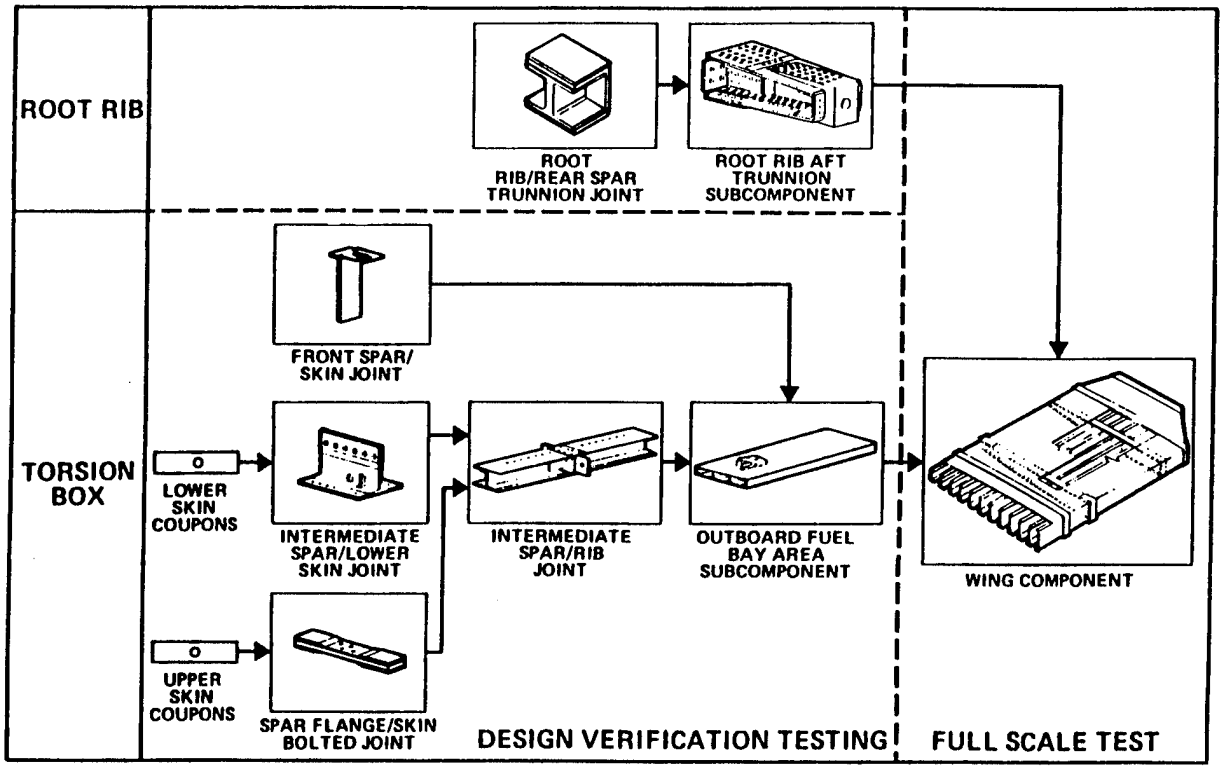


Figure 10. Building Block Approach for the Wing Structure in the Composite Wing/Fuselage Program (Reference 1).

DESIGN AND ANALYSIS OF GRID STIFFENED CONCEPTS FOR AIRCRAFT COMPOSITE PRIMARY STRUCTURAL APPLICATIONS

Damodar R. Ambur
NASA Langley Research Center
Hampton, Virginia

INTRODUCTION

Structural efficiency is of paramount importance in aircraft structures in order to produce affordable aircraft. This requirement has dictated use of stiffened composite structures where a flat or curved skin is reinforced with stiffeners by cocured, bonded, or bolted attachment. Of the above, stiffened structures produced by cocuring have reduced part count and, hence, are cost effective. Although many manufacturing processes are available to produce cocured structures, automated tow or tape placement and filament or tape winding methods have emerged as some of the most viable ones due to their amenability to automation.

Although there have been many studies and applications involving continuous filament grid stiffened structures, most of these designs were based on prior experience and finite element analysis. Such an approach is cumbersome and does not always result in an optimum design. An analytical tool is thus necessary to understand the sensitivity of the buckling behavior of grid stiffened structures to different geometric and material parameters and to make rational choices of stiffening configurations based on detailed and well understood parametric studies. This paper presents an approach to buckling resistant design of general grid stiffened flat panels based on smeared stiffener theory for combined in-plane loading. Some results from parametric studies performed to assess the validity of smeared stiffener theory for practical stiffener configurations and to illustrate the benefits of different stiffening concepts are presented. Details of a design study are discussed where the present analysis method is used to design a grid stiffened panel for a fuselage application and verified using finite element analysis results.

a	Length of grid unit cell
a_1	Base dimension of triangular plate
A	Panel In-plane stiffness matrix
b	Width of grid unit cell
B	Panel bending-extension coupling stiffness matrix
C_{44}, C_{45}, C_{55}	Shear stiffnesses
d	Width of stiffener element
D	Panel bending stiffness matrix
E_{11}, E_{22}	Young's moduli of stiffener element in the longitudinal and transverse directions
G_{12}, G_{13}	Shear modulus of stiffener element
h	Height of triangular plate element
l	Length of the stiffener element
m,n	Number of half-waves in the plate length and width directions
M	Moment resultant
M_x, M_y, M_{xy}	Moment resultants about x and y axes and torsional moment
N	Force resultant
N_x, N_y, N_{xy}	Force resultants in the x and y directions and in-plane shear force
$[N_x]_{cl}$	Classical buckling load
$[N_x]_{cr}$	Critical load
Q_x, Q_y	Shear force resultants
$\overline{S}_z$	Transverse shear stiffness
t, t_1, t_2, t_3	Thickness of stiffeners
u,v,w	Displacements in the x, y, and z directions
x,y,z	Cartesian coordinates
$\varepsilon_x, \varepsilon_y$	Extensional strains in the x and y directions
ϕ_x, ϕ_y	Section rotations about x and y axes
$\gamma_{xy}, \gamma_{yz}, \gamma_{xz}$	Shear strains
$\kappa_x, \kappa_y, \kappa_{xy}$	Bending and twisting curvatures
μ_{12}	Major Poisson's ratio
θ	Grid angle, triangular plate base angle

ANALYSIS PROCEDURE

General Instability

Constitutive Relations

A general grid stiffened panel is shown in figure 1 where a flat skin is stiffened with solid rectangular blades in the x, y, and $\pm\theta$ directions. This generality in choosing the grid pattern is sufficient to address several stiffened panel configurations that are likely in aircraft fuselage and wing structures. The constitutive properties used in panel general instability analysis are based on smeared stiffener theory. The unit cell configuration used for this purpose is shown on the right side of figure 1. In the general constitutive relations of equation 1, the stiffness matrices A, B, and D and the shear stiffness coefficients C_{44}, C_{45}, and C_{55} assume values corresponding to the smeared plate problem that is being solved. The details at stiffener intersections are not included in this model.

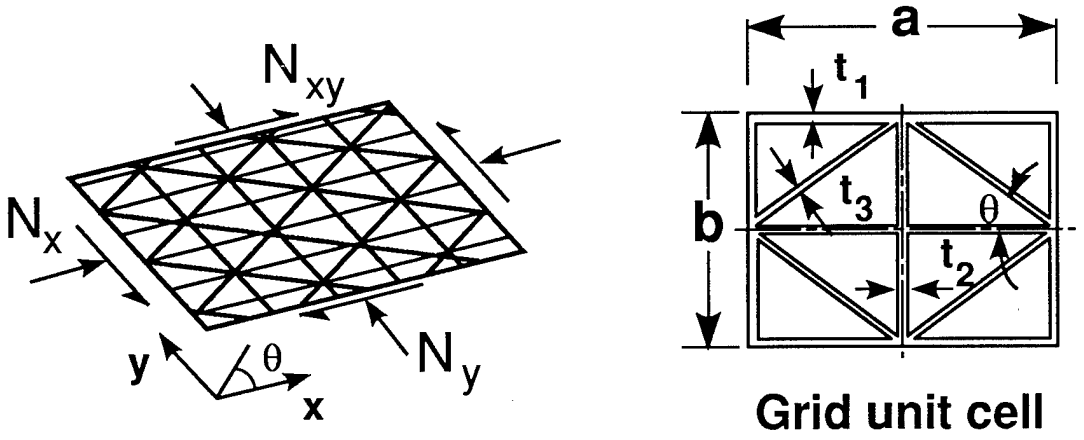


Figure 1

$$\begin{Bmatrix} N \\ M \end{Bmatrix} = \left[\begin{array}{c|c} A & B \\ \hline B & D \end{array}\right] \begin{Bmatrix} \varepsilon \\ \kappa \end{Bmatrix} \tag{1}$$

$$\begin{Bmatrix} Q_y \\ Q_x \end{Bmatrix} = \begin{bmatrix} C_{44} & C_{45} \\ C_{54} & C_{55} \end{bmatrix} \begin{Bmatrix} \gamma_{yz} \\ \gamma_{xz} \end{Bmatrix}$$

Kinematic Relations and Stability Equations

The analytical model is for stiffened panels where the stiffeners are made of unidirectional material oriented along the stiffener length. While this material orientation is efficient structurally, the transverse shear stiffness that results is low and is largely determined by the matrix properties. The effects due to transverse shear deformation are shown to be important in reference 1 and are included in the global analysis through a first order shear deformation theory. This theory is an adequate representation of shear deformation for global buckling analysis. The linear kinematic relations used are given in equation 2 and governing equations for general stability are given in equation 3. For the case of a simply supported panel considered here, solution to this eigenvalue problem is obtained in a closed form for the case of compression loading while the Galerkin method is used to estimate the eigenvalues for combined in-plane loading.

$$
\begin{aligned}
\varepsilon_x &= u,x \\
\varepsilon_y &= v,y \\
\gamma_{xy} &= v,x + u,y \\
\gamma_{xz} &= \phi x + w,x \\
\gamma_{yz} &= \phi y + w,y \\
\kappa_x &= \phi x,x \\
\kappa_y &= \phi y,y \\
\kappa_{xy} &= \phi y,x + \phi x,y
\end{aligned}
\qquad (2)
$$

$$
\begin{aligned}
N_{x,x} + N_{xy,y} &= 0 \\
N_{xy,x} + N_{y,y} &= 0 \\
M_{x,x} + M_{xy,y} &= Q_x \\
M_{xy,x} + M_{y,y} &= Q_y \\
Q_{x,x} + Q_{y,y} + N_x\, W,xx + 2\, N_{xy}\, W,xy + N_y\, W,yy &= 0
\end{aligned}
\qquad (3)
$$

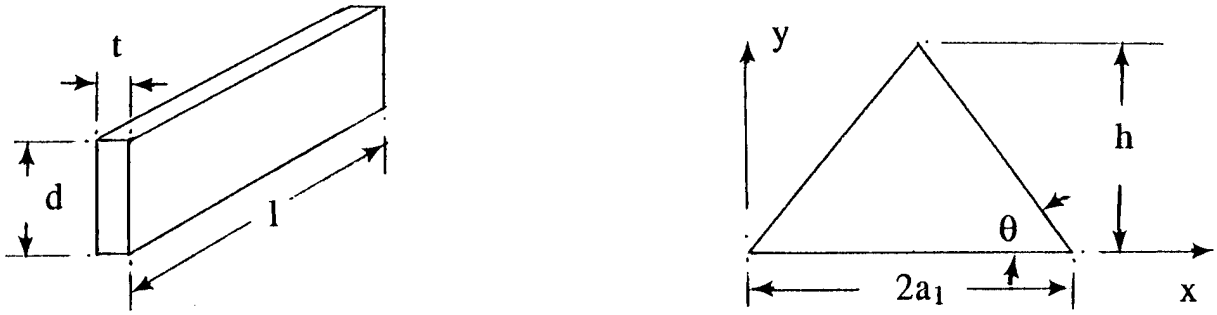
Buckling analyses of stiffener and skin elements are included in the local analysis and are used as constraints on the panel design. The analytical modeling details for these buckling constraints are presented in this section.

Stiffener Buckling

The stiffener is modeled as an orthotropic plate with clamped boundary conditions at the ends and simply supported and free boundary conditions along the other two edges. A schematic of a stiffener element is shown in figure 2. The expression for the stiffener buckling load is given in equation 4. When transverse shear effects are included, this expression takes the form of equation 5. The approximate shear correction factor of 5/6 in equation 6 is taken from reference 2.

Skin Buckling

Skin geometries of rectangular and triangular shapes are included in the analysis. The skin element is treated as a laminated plate with specially orthotropic properties and simply supported edges. The buckling loads of rectangular plates are obtained using expressions from reference 3. For triangular plate buckling analysis a deflection function shown in equation 7 is used. This function satisfies all simply supported boundary conditions on the triangular plate shown on the right of figure 2 except the zero moment condition along the inclined edges. Hence, the modified Galerkin method is used here to obtain the buckling load. Transverse shear deformation effects in the skins are neglected due to its thinness.



Stiffener Element Skin Element

Figure 2

$$[N_x]_{cl} = t^3 \left[\frac{4\pi^2 E_{11}}{12 l^2 \left[1-\mu_{12}^2 \frac{E_{22}}{E_{11}}\right]} + \frac{G_{12}}{d^2} \right] \quad (4)$$

$$[N_x]_{cr} = \frac{\bar{S}_z}{2}\left[\sqrt{1+\frac{4[N_x]_{cl}}{\bar{S}_z}} - 1\right] \quad (5)$$

$$\bar{S}_z = \frac{5}{6} G_{13}\, b \quad (6)$$

$$w = \sum_m \sum_n w_{mn} \left[\sin\frac{m\pi x}{a_1} \sin\frac{n\pi y}{h} - \sin\frac{n\pi x}{a_1} \sin\frac{m\pi y}{h}\right] \quad (7)$$

PARAMETRIC STUDIES

A computer program has been written to facilitate a systematic parametric design search. For a given set of loading conditions, stiffening concept, and skin laminate choice, minimum weight designs are sought by varying the stiffener spacings a and b, diagonal stiffener orientation angle θ and stiffener dimensions.

Several parametric studies are conducted to ensure applicability of the present analysis approach that uses smeared stiffener theory for its constitutive relations and also to assess the efficiency of different stiffening concepts. Some of the results obtained on a flat panel of 30 in. length and 24 in. width with a symmetric skin layup of +45,-45, and 0 degree plies made of AS4/3501-6 graphite-epoxy material are presented in this section.

Assessment of Smeared Stiffener Theory

Buckling load results obtained from the present analysis on prismatic stiffened panels are compared with those from the Panel Analysis and Sizing COde (PASCO), which uses a discrete stiffener analysis for a prismatic stiffened panel subjected to axial compression (reference 4). This study is primarily to establish the range of stiffener spacing for which the present analysis method is applicable. The minimum weight results of prismatic stiffened panels obtained from each of these analysis methods for two compression loading cases are presented in figure 3 for increasing numbers of unit cells. The unit cell definitions used in this paper for different stiffening configurations are shown on the left side of figure 3. In both load cases, the present analysis gives an upper bound for panel weight. At an applied axial loading of 3,000 lb/in., the PASCO analysis results and the present results agree well when the number of unit cells is larger than four. The maximum difference between the two sets of results is seven percent and corresponds to the case with two unit cells. A similar trend is obtained for an applied loading of 10,000 lb/in., and the maximum difference in results for two unit cells is 13 percent. This study suggests that the present approach is adequate for studying the buckling response of panels with practical stiffener spacings which are normally less than 8 in.

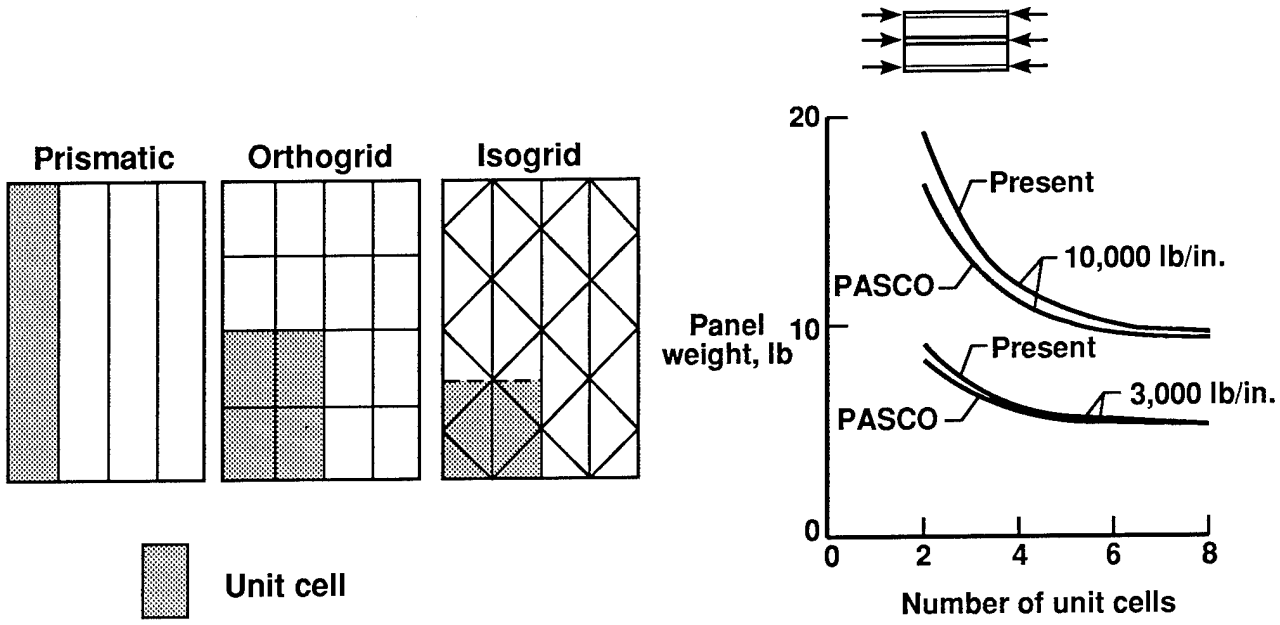


Figure 3

Evaluation of Stiffening Concepts

Results from preliminary studies on prismatic stiffener, orthogrid, and isogrid structural configurations are presented in figure 4. The figure to the left illustrates the weight efficiencies of the above structural configurations for an axial compression loading of 3,000 lb/in. as a function of the number of unit cells along the panel width. The number of unit cells shown on the abscissa of figure 4 for the orthogrid configuration represents the number of unit cells in both the panel width and length directions. Such choice was made for this study in spite of the flexibility to choose any number of unit cells along the panel length. In the case of an isogrid structural concept, the number of unit cells along the panel length are dependent on the number of unit cells along the panel width. For the panel length of 30 in., the numbers of unit cells along the length of the isogrid panel are rounded off to be 4, 8, 13, and 17 and correspond to 2, 4, 6, and 8 unit cells across the panel width. This resulted in a variation of the diagonal stiffener angle θ from 58 to 60 degrees. The results for this compression loading case suggest that the orthogrid and isogrid stiffener concepts are more efficient than the prismatic stiffener concept by at least 11 percent.

A loading case with a combination of 3000 lb/in. axial compression loading and 1500 lb/in. shear loading is also investigated and the results of this study are presented on the right side of figure 4. Weight efficiency trends similar to the compression loading case are plotted. The orthogrid and isogrid concepts demonstrate 13 and 16 percent weight advantage, respectively, compared to the prismatic stiffener concept.

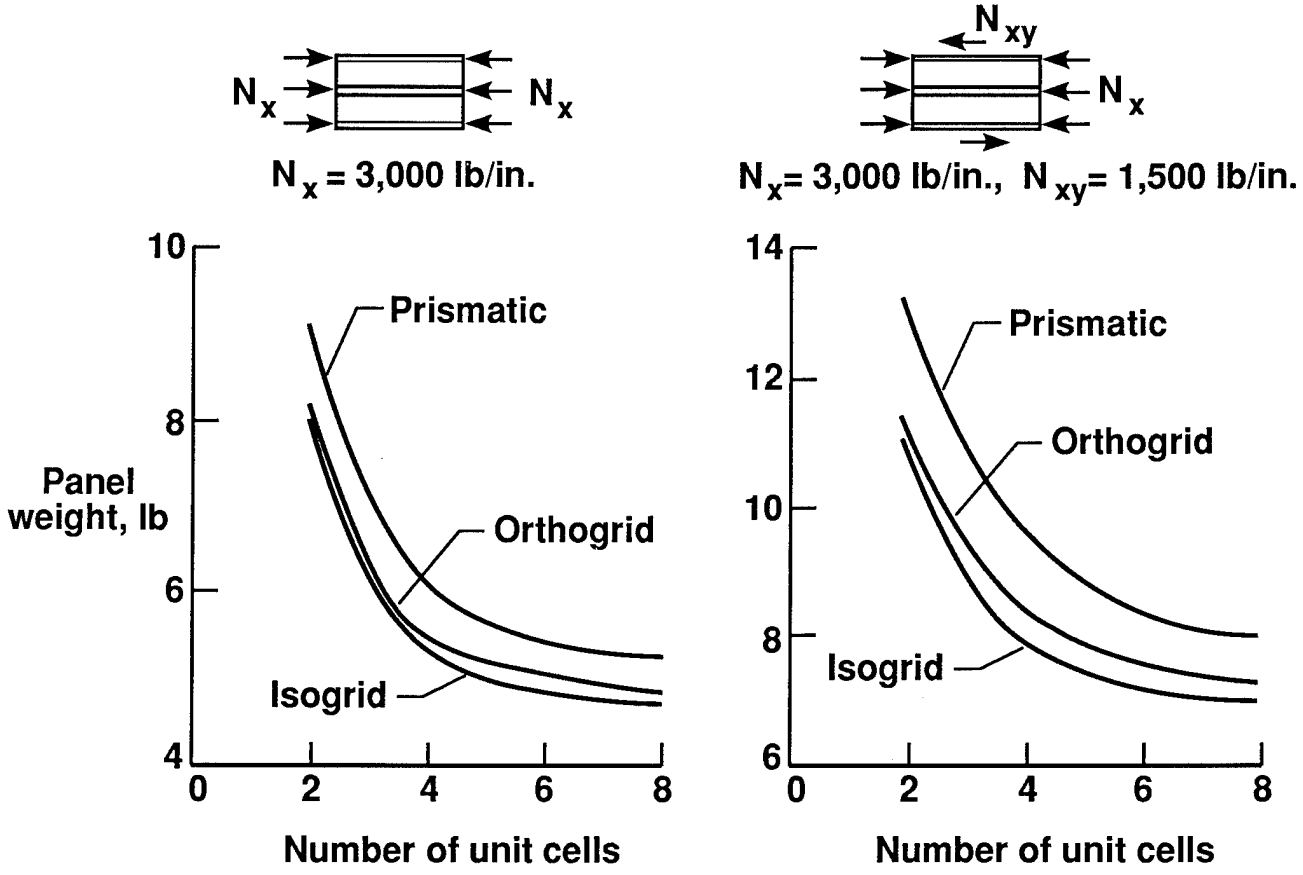


Figure 4

DESIGN STUDY

The purpose of this study is to design a panel to carry a combined loading condition that is typical of a fuselage structure using the present sizing procedure and to verify the accuracy of this design with finite element analysis. The dimensions of the panel, applied loading, skin ply details, and material type considered are listed in table 1. The final stiffener dimensions of the panel presented in this table were obtained with a preselected orientation of the diagonal stiffeners equal to 24 degrees.

A finite element model of the above panel has been generated using the DIAL Finite Element Analysis System (reference 5) and is shown in figure 4. Modified shear deformable shell elements are used for modeling both skin and stiffeners. The total number of degrees of freedom for this problem is about 19000. A bifurcation buckling analysis has been performed on this structure with simply supported boundary conditions to obtain buckling loads and corresponding mode shapes.

Panel dimensions:	60 in. length, 36 in. width
Design Loading:	N_x = -3000 lb/in., N_y = 1500 lb/in., N_{xy} = 600 lb/in.
Diagonal stiffener angle:	24 degrees
Skin layup:	$(45/0_2/-45/0_2/-45/90/45)_s$
Material:	IM7/8551-7A graphite-epoxy
Final stiffener dimensions:	1.65 in. height, 0.32 in. width

Table 1

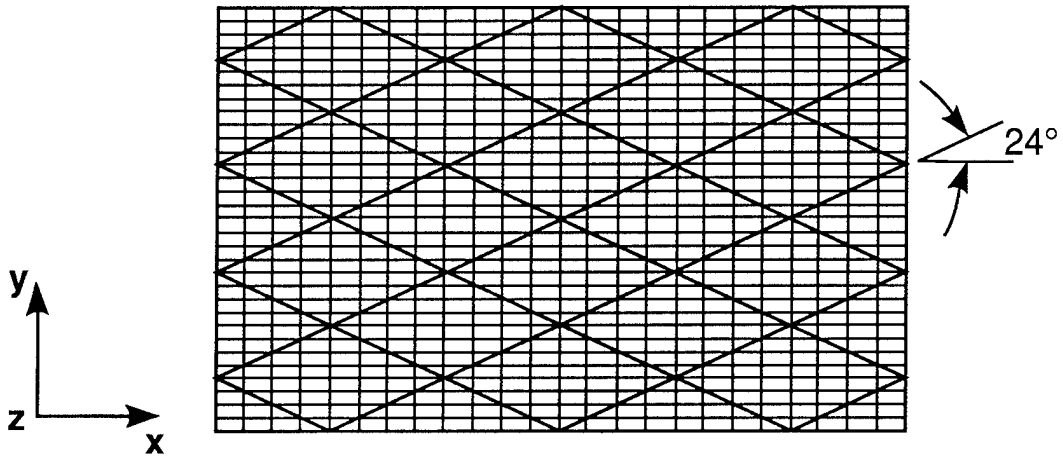


Figure 5

Finite Element Analysis Results

The buckling analysis results obtained using this finite element model are presented in figure 6 which shows the out-of-plane deflection contours. The first buckling event occurs at 92 percent of the design loading and involves local buckling of the triangular skin elements as shown on the left side of figure 6. There are three additional skin buckling modes prior to the global buckling of the panel illustrated on the right side of this figure. The finite element analysis result corresponding to this global buckling mode is 113 percent of the design load for essentially the same mode shape of two half waves in the length direction obtained from the present analysis. This design study demonstrates that the present analysis approach provides a good tool for preliminary sizing of general grid stiffened flat panels subjected to combined in-plane loading.

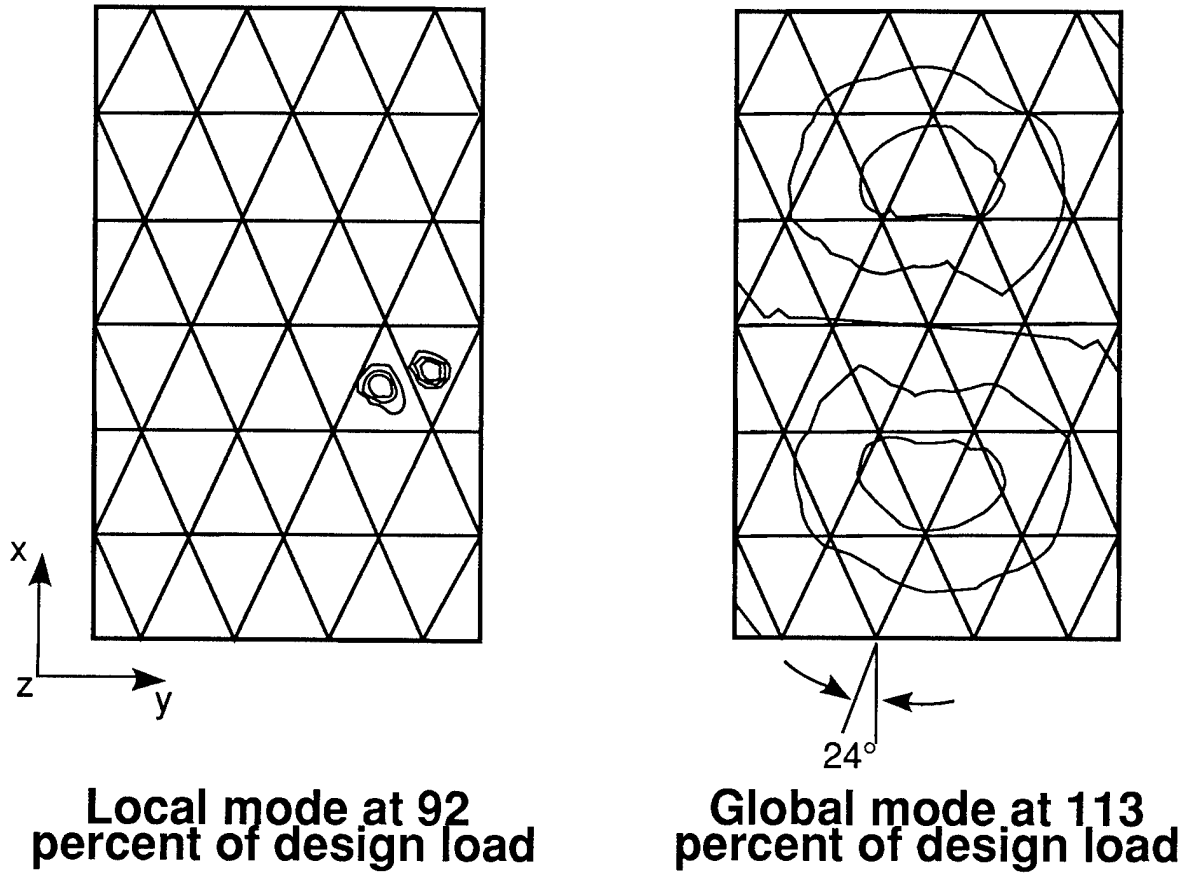


Figure 6

CONCLUDING REMARKS

The parametric studies conducted to date suggest that the present approach for analyzing general grid stiffened panels for combined loading with buckling constraints is adequate for design purposes. Comparison of present results with PASCO analysis results established the applicability of this approach for practical stiffener spacings. Results from weight efficiency studies on prismatic, isogrid, and orthogrid structural configurations for different loading conditions suggest sensitivity of the design to geometric and loading parameters. The design study demonstrates the usefulness of the present analysis method in the preliminary design phase of general grid stiffened structures subjected to combined loading.

REFERENCES

1. Reddy, A. D.: Behavior of Continuous Filament Advanced Composite Isogrid Structure. Ph.D. Thesis, Georgia Institute of Technology, November 1980.

2. Reissner, E.: The Effect of Transverse Shear Deformation on the Bending of Elastic Plates. Journal of Applied Mechanics, vol. 12, 1945, pp. 469-477.

3. Jones, R. M.: Mechanics of Composite Materials. McGraw-Hill Book Company. 1975.

4. Anderson, M. S.; Stroud, W. J.; Durling, B. J.; and Hennessy, K. W.: PASCO : Structural Panel Analysis and Sizing Code. NASA TM-80182, November 1981.

5. DIAL Finite Element Analysis System - Version L3D2. Lockheed Missiles and Space Company, July 1987.

Optimization of Composite Sandwich Cover Panels Subjected to Compressive Loadings

Juan R. Cruz
NASA Langley Research Center
Hampton, VA

ABSTRACT

An analysis and design method is presented for the design of composite sandwich cover panels that includes transverse shear effects and damage tolerance considerations. This method is incorporated into an optimization program entitled SANDOP (SANDwich OPtimization). SANDOP is used in the present study to design optimized composite sandwich cover panels for transport aircraft wing applications as a demonstration of its capabilities. The results of this design study indicate that optimized composite sandwich cover panels have approximately the same structural efficiency as stiffened composite cover panels designed to identical constraints. The results also indicate that inplane stiffness requirements have a large effect on the weight of these composite sandwich cover panels at higher load levels. Increasing the maximum allowable strain and the upper percentage limit of the 0° and ±45° plies can yield significant weight savings. The results show that the structural efficiency of these optimized composite sandwich cover panels is relatively insensitive to changes in core density. Thus, core density should be chosen by criteria other than minimum weight (e.g., damage tolerance, ease of manufacture, etc.).

INTRODUCTION

Composite materials are being widely considered for application to heavily loaded primary aircraft structures such as wing cover panels. To date, much of the research conducted on aircraft wing cover panels has focused on stiffened plate designs. The analysis of stiffened cover panels is well understood, and tools exist to perform analysis and design optimization of these panels [1, 2]. Relatively less emphasis, however, has been placed on cover panels of sandwich construction.

The present paper describes a design analysis method that has been developed for composite sandwich cover panels loaded in compression, including damage tolerance considerations. The analysis and appropriate design variables have been incorporated into a constrained optimization procedure named SANDOP (SANDwich OPtimization). SANDOP utilizes weight per unit area as the objective function to be minimized subject to several constraints. SANDOP is written in SOL (Sizing and Optimization Language, [3, 4]), a high-level computer language developed

specifically for the application of numerical optimization methods to design procedures.

As a practical demonstration of SANDOP, composite sandwich cover panels for transport aircraft wing applications have been designed subject to constraints appropriate for this kind of structure. These composite sandwich cover panels are compared with stiffened composite cover panels that were designed to identical constraints using PASCO [1, 2]. Furthermore, the effect of changing the constraint values on the structural efficiency of these composite sandwich cover panels is investigated.

ANALYSIS, DESIGN, AND OPTIMIZATION METHODOLOGY

This section describes the analysis and design methods used in this study of sandwich cover panels with composite material facesheets. Dominant response mechanisms for composite sandwich cover panels are presented and analyzed. The analysis is combined with an optimization procedure to obtain structurally efficient designs. The objective function, design variables, and constraints for the structural optimization problem are explained in this section.

The sandwich cover panel considered in the present study is shown in figure 1. This sandwich panel is rectangular, flat, and simply supported on all four edges. A single, constant longitudinal stress resultant N_x is applied at opposite ends of the panel as shown in figure 1. The facesheets are symmetric composite laminates with specially orthotropic material symmetry. The sandwich core also exhibits specially orthotropic material symmetry in its transverse shearing stiffnesses. The corresponding transverse shearing stiffnesses of the core are denoted by G_{xz} and G_{yz}. The principal directions of the core material are assumed to coincide with the x and y coordinate directions (see figure 1).

Response Mechanisms

Three response mechanisms are included in SANDOP for designing composite sandwich cover panels loaded in compression. These mechanisms are global buckling (including transverse shear deformation), symmetric facesheet wrinkling, and material failure. A brief description of each of these mechanisms is presented as follows.

Global Buckling.- The equations governing global buckling of sandwich panels, including transverse shear effects, is derived in reference 5 and is given by

$$\left[D_{11}\,D_{66}\left(\frac{1}{D_{Qy}} + \frac{N_x}{D_{Qx}\,D_{Qy}}\right)\right]\frac{\partial^6 w}{\partial x^6}$$

$$+\left[\frac{D_{11}\,D_{66}}{D_{Qx}} + \left(D_{11}\,D_{22} - D_{12}^2 - 2\,D_{12}\,D_{66}\right)\left(\frac{1}{D_{Qy}} + \frac{N_x}{D_{Qx}\,D_{Qy}}\right)\right]\frac{\partial^6 w}{\partial x^4\,\partial y^2}$$

$$+\left[D_{22}\,D_{66}\left(\frac{1}{D_{Qy}} + \frac{N_x}{D_{Qx}\,D_{Qy}}\right) + \left(\frac{D_{11}\,D_{22} - D_{12}^2 - 2\,D_{12}\,D_{66}}{D_{Qx}}\right)\right]\frac{\partial^6 w}{\partial x^2\,\partial y^4} \qquad (1)$$

$$+\left[\frac{D_{22}\,D_{66}}{D_{Qx}}\right]\frac{\partial^6 w}{\partial y^6} - \left[D_{11} + N_x\left(\frac{D_{11}}{D_{Qx}} + \frac{D_{66}}{D_{Qy}}\right)\right]\frac{\partial^4 w}{\partial x^4}$$

$$-\left[2\left(D_{12} + 2\,D_{66}\right) + N_x\left(\frac{D_{22}}{D_{Qy}} + \frac{D_{66}}{D_{Qx}}\right)\right]\frac{\partial^4 w}{\partial x^2\,\partial y^2} - D_{22}\frac{\partial^4 w}{\partial y^4} + N_x\frac{\partial^2 w}{\partial x^2} = 0$$

where the transverse shear stiffnesses for an orthotropic core material, D_{Qx} and D_{Qy}, are given in reference 6 by

$$D_{Qx} = G_{xz}\frac{(t_c + t_f)^2}{t_c} \qquad (2)$$

and

$$D_{Qy} = G_{yz}\frac{(t_c + t_f)^2}{t_c} \qquad (3)$$

Solutions to the buckling equations for sandwich panels are determined directly by assuming a buckling mode shape that satisfies both the differential equation (eqn. (1)), and the boundary conditions (simply supported on all four edges). A buckling mode shape that meets this criterion is expressed as

$$w = A_{mn}\sin\left(\frac{m\,\pi\,x}{a}\right)\sin\left(\frac{n\,\pi\,y}{b}\right) \qquad (4)$$

where

$m = 1, 2, \ldots \qquad 0 \le x \le a$

$n = 1, 2, \ldots \qquad 0 \le y \le b$

Substituting this mode shape into equation (1) yields a homogeneous linear algebraic equation that depends on the wave numbers m and n, and thus constitutes an eigenvalue problem. For nontrivial solutions, the resulting equation can be solved for N_x as a function of m and n. The global buckling stress resultant N_x^b is obtained by minimizing N_x with respect to m and n.

This formulation for global buckling includes shear crimping as a response mechanism for sandwich plates. Shear crimping is given by the degenerate case of global buckling for which the wave parameter m is very large.

Facesheet Wrinkling.- Another stability-related response mechanism for sandwich structures is facesheet wrinkling. For this mechanism, the facesheets buckle locally with a wavelength of the same order as the thickness of the sandwich core. Facesheet wrinkling can be symmetric or antisymmetric in form as shown in figure 2. In the present study, only symmetric facesheet wrinkling is included.

Since wrinkling in sandwich panels with honeycomb cores is usually of the symmetric type (Ref. 7), the current wrinkling analysis is valid for honeycomb cores. The current wrinkling analysis may not be valid for sandwich panels with foam cores since they may buckle in an antisymmetric wrinkling mode.

The equation used in the present study to determine the onset of symmetric facesheet wrinkling [7] is given by

$$N_x^w = 0.33\, b\, E_f \left(\frac{E_{c_z}\, t_f}{E_f\, t_c}\right)^{\frac{1}{2}} \tag{5}$$

Material Failure.- For a given panel design, the facesheet material may fail before the onset of either of the stability mechanisms previously discussed. Material failure is determined by specifying a maximum allowable longitudinal strain criterion. Specifically, the onset of material failure is assumed to occur when the axial strain ε_x exceeds a $\varepsilon_{x_{max}}$. This maximum strain value is based on an experimentally determined lower-limit compression-after-impact failure strain of the composite facesheet. The use of this allowable strain criterion implicitly incorporates a damage tolerance constraint into the design process.

Objective Function and Design Variables

Structural efficiency is defined by a minimum cover panel weight for the given design loads. The objective function used in this study is the weight per unit area, W, of the cover panel.

The design variables used in this study are classified as either facesheet design variables or core design variables. The composite facesheets are considered to be homogeneous through the thickness and to consist of 0°, ±45°, and 90° plies only. These two assumptions allow the facesheets to be completely defined by using only three design variables: t_0, t_{45}, and t_{90}. The variables t_0, t_{45}, and t_{90} are the thicknesses of the 0°, ±45°, and 90° plies, respectively, in the facesheet laminates. Both facesheets are symmetric, specially orthotropic, and identical. The sandwich core is defined by two design variables: t_c and ρ_{core}, the core thickness and core density, respectively. The three core material properties used in the analysis, G_{xz}, G_{yz}, and E_{c_z}, are determined by the core type, core material, and core density.

Constraints

The constraints used to perform the optimization are based on the response mechanisms for sandwich panels previously described and on current design practices for composite facesheets and sandwich cores. A brief description of the constraints is presented as follows.

Response Mechanism Constraints.- The cover panel designs for the present study are constrained to have buckling and wrinkling stress resultants N_x^b and N_x^w greater than the applied stress resultant N_x. In addition, the longitudinal strain, ε_x, due to the applied N_x is constrained to be less than the maximum allowable longitudinal strain, $\varepsilon_{x_{max.}}$ This maximum allowable strain corresponds to the presence of residual compressive strength for an impact-damaged composite laminate and is an empirical value.

Facesheet and Core Constraints.- Constraints are placed on the laminate and the inplane stiffnesses of the composite facesheets. The laminate is constrained by placing upper and lower limits on the relative thicknesses of each ply group (plies with the same orientation) with respect to the total facesheet thickness. These constraints are written as

$$L_0 < \frac{t_0}{t_0 + t_{45} + t_{90}} < U_0 \tag{6}$$

$$L_{45} < \frac{t_{45}}{t_0 + t_{45} + t_{90}} < U_{45} \tag{7}$$

$$L_{90} < \frac{t_{90}}{t_0 + t_{45} + t_{90}} < U_{90} \tag{8}$$

where L and U denote the lower and upper percentage limits, respectively, for a given ply group. These constraints are used to exclude laminate designs that are dominated by one ply orientation. Practical laminate designs are often required to have fibers oriented in several directions to satisfy requirements not specifically considered herein, e.g., repair requirements [8].

The composite facesheet designs are also required to satisfy minimum inplane stiffness constraints. The facesheet stiffnesses A_{11} and A_{66} are required to be greater than some specified minimum stiffnesses $A_{11_{min}}$ and $A_{66_{min}}$, respectively. The minimum stiffnesses used in this study are discussed in the Results and Discussion section.

The sandwich core density is constrained to a range of densities that is practical for aircraft cover panels. Upper and lower limits for core density are specified for the present study.

SANDOP

The design and optimization method described above has been incorporated into a computer program entitled SANDOP (SANDwich OPtimization). SANDOP is written in SOL (Sizing and Optimization Language, references 3 and 4), a high-level computer language developed specifically for the application of numerical optimization methods to design problems. SANDOP allows the user to optimize composite sandwich cover panels. The input parameters available to the user are the facesheet and core material properties, the panel dimensions, the design stress resultant N_x, and the parameter values for the various constraints. SANDOP can be modified to expand the present analysis and constraints.

RESULTS AND DISCUSSION

As a demonstration of the capabilities of SANDOP, the program was used to design optimized composite sandwich cover panels for transport aircraft wing applications. These optimized sandwich panels are compared with stiffened composite cover panels designed to satisfy identical constraints. The effect of the constraints on the optimal design is also investigated.

Baseline Design

A baseline set of design parameters and constraints were selected to establish a reference design for subsequent comparison. These design parameters and constraints are typical of those used to design sandwich cover panels for transport wing applications. All the cover panels considered in the study are assumed to be square, with 30-in. side dimensions. Cover panels were optimized for load levels ranging from 3,000 to 24,000 lb/in.

The unidirectional composite material properties used for the facesheets are those of Hercules Inc. IM6 carbon fibers and American Cyanamid 1808I epoxy interleaved material given in ref. 9 as shown in Table 1. The core material used in this study is Hexcel 5052 Aluminum Alloy Hexagonal Honeycomb, whose properties were obtained from reference 10. Since core material properties are only available for specific values of the core density, SANDOP interpolates these data to obtain core properties at densities other than those given in reference 10.

The constraints used for the baseline design are shown in Table 2. The minimum required inplane stiffnesses, $A_{11_{min}}$ and $A_{66_{min}}$, are functions of the load level as indicated by figure 3. This correlation between the minimum required inplane stiffness and N_x is based on historical data for transport aircraft wings that were presented in reference 11. The limits on the relative thickness of each ply group, with respect to the total facesheet thickness, is based on the recommendations of reference 8. These recommendations are designed to yield laminates suitable for bolted and riveted joints. A maximum allowable strain of 0.0045 in./in. was selected to provide acceptable damage tolerance capability consistent with current composite material systems.

Comparison with Stiffened Cover Panels

The structural efficiency of composite sandwich cover panels optimized with SANDOP is shown in figure 4. In this figure, the weight per unit area of the cover panel, W, is shown as a function of N_x. In addition, the structural efficiency of hat- and blade-stiffened composite panels optimized with PASCO (refs. 1 and 2), are shown in figure 4 for comparison. Optimum designs for both the sandwich and the stiffened cover panels were determined using the baseline material properties and constraints. The composite sandwich cover panels have approximately the same structural efficiency as the composite stiffened cover panels when designed to identical constraints. This behavior is to be expected, since the maximum allowable strain and the inplane stiffness requirements are the active constraints for the optimum designs. These two constraints determine the amount of composite material required by both the sandwich and stiffened cover panels. Since the weight of composite material constitutes the major component of the cover panel weight, the structural efficiency of both the sandwich and stiffened cover panels are approximately equal.

Effect of Varying the Constraints on the Optimum Design

To assess the sensitivity of the structural efficiency of composite sandwich cover panels to changes in the constraints, new sets of optimum composite sandwich cover panels were designed while varying the constraints one at a time. By comparing these new cover panel designs with the baseline designs, the effect of varying the constraints is identified.

Effect of varying the maximum allowable strain.- The effect of varying the maximum allowable strain constraint on the structural efficiency is shown in figure 5. This figure shows the structural efficiency W of optimized sandwich cover panels as a function of N_x for three values of the maximum allowable strain $\varepsilon_{x_{max}}$. For the baseline design, $\varepsilon_{x_{max}}$ = 0.0045 in./in. and this maximum allowable strain is an active constraint for N_x greater than 15,000 lb/in. Increasing the maximum allowable strain to 0.006 in./in. yields significant improvements in the structural efficiency at load levels above 15,000 lb/in. Increasing the maximum allowable strain beyond 0.006 in./in. yields little or no further improvements since $\varepsilon_{x_{max}}$ is replaced by the minimum inplane stiffness requirements as one of the active constraints. If $\varepsilon_{x_{max}}$ is decreased to 0.003 in./in., the maximum allowable strain becomes the active constraint for load levels of 7,500 lb/in. and above. The weight of sandwich cover panels designed with a maximum allowable strain of 0.003 in./in. increases for load levels above 7,500 lb/in. as compared to the baseline design.

Effect of varying the minimum inplane stiffness requirements.- The effect of varying the minimum inplane stiffness requirements on structural efficiency is shown in figure 6. This figure shows the structural efficiency W of optimized sandwich cover panels as a function of N_x for three values of the inplane stiffness requirements. In this figure k_A is a scaling factor for the baseline values of $A_{11_{min}}$ and $A_{66_{min}}$. When

$k_A = 1.0$, $A_{11_{min}}$ and $A_{66_{min}}$ are the baseline values. When k_A has a value other than one, the baseline values of $A_{11_{min}}$ and $A_{66_{min}}$ are multiplied by k_A at all load levels. Since the minimum inplane stiffness constraint is active for the baseline design at load levels below 15,000 lb/in., letting $k_A = 0.5$ reduces the weight of the cover panels at load levels below 15,000 lb/in. Further reductions in the minimum inplane stiffness requirements yield little or no further improvements since $\varepsilon_{x_{max}}$ replaces $A_{11_{min}}$ and $A_{66_{min}}$ as one of the active constraints. Letting $k_A = 2.0$ increases the weight of the cover panels at all load levels considered. The minimum inplane stiffness requirements become an active constraint at all load levels, replacing $\varepsilon_{x_{max}}$ as the active constraint at load levels above 15,000 lb/in. This is an important trend, since the inplane stiffness requirements are likely to increase for newer technology transport aircraft with higher aspect ratio wings. For such a wing, stiffness may become a more important consideration than a higher $\varepsilon_{x_{max}}$ for improved damage tolerance in the selection of appropriate materials for future transport aircraft.

Effect of varying the upper percentage limit of all ply group thicknesses.- The results of this study indicate that the upper limit on the percentage of 0° and ±45° plies (U_0 and U_{45}, respectively) is an active constraint at all load levels. The fact that this constraint is active indicates that the structural efficiency of these cover panels can be increased by allowing laminates with higher values of U_0 and U_{45}.

The structural efficiency W of optimized sandwich cover panels is shown in figure 7 as a function of N_x for two values of the upper percentage limits of all ply groups (U_0, U_{45}, and U_{90}). The upper curve in figure 7 is for the baseline value of this constraint ($U_0 = U_{45} = U_{90} = 0.375$), while the lower curve shows the effect of setting $U_0 = U_{45} = U_{90} = 1.0$. In both cases the lower percentage limits for all ply angles (L_0, L_{45}, and L_{90}) are equal to 0.125.

This figure shows that the weight of all cover panels is reduced by allowing higher values of U_0, U_{45}, and U_{90}. For the loading case investigated ($N_{xy} = N_y = 0$, $N_x \neq 0$), the optimum percentage of 0° layers lies between 48 and 54 percent, while the optimum percentage of ±45° layers lies between 33 and 40 percent. The optimization procedure always drives the percentage of 90° layers to its minimum allowable value; 12.5 percent in this case. The weight savings achieved by using higher values of U_0, U_{45}, and U_{90} indicate the importance of developing ways to understand and utilize laminates in which a high percentage of the plies are oriented in one direction.

Effect of varying the core density.- The optimum core density at all load levels is quite low; typically about 1.0 lb/ft^3. For reasons other than minimum weight, it may be preferable to use cores with a higher density. Thus, the effect of increasing the core density on the structural efficiency was investigated.

The results in figure 8 indicate the weight efficiency W of sandwich cover panels using cores of two different densities; ρ_{core} = 1.0 and 9.5 lb/ft^3. As can be seen from

this figure, the weight of these sandwich cover panels is not very sensitive to changes in the core density; a ninefold increase in core density increases the weight by approximately 11 percent. There are two reasons for this behavior. First, the core is only a small percentage of the total weight of the sandwich cover panel; large differences in the core density have a small effect on the total weight. Second, as the core density is increased, so is its transverse shear stiffnesses G_{xz} and G_{yz}. Thus, the core thickness required to prevent global buckling from occurring is reduced. As can be seen from the data in Table 3, the core thickness is reduced by up to 33% when the core density is increased from 1.0 to 9.5 lb/ft^3. Also note that the facesheet thickness does not vary as the core density is increased. Since the facesheet thickness t_f is mainly determined by the maximum strain and inplane stiffness constraints, changing the core density has no effect on t_f.

Since weight is relatively insensitive to changes in the core density, the selection of core density is probably best made based on criteria other than minimum weight, e.g., damage tolerance and ease of manufacture.

CONCLUDING REMARKS

An analysis and design methodology has been developed for the design of composite sandwich cover panels, including transverse shear effects and damage tolerance considerations. This methodology has been incorporated into an optimization program entitled SANDOP (SANDwich OPtimization).

A set of optimized sandwich cover panels were designed with SANDOP with input values typical of those used for transport aircraft wing applications. Based on the designs generated by SANDOP, several observations can be made about the use of composite sandwich cover panels for transport aircraft wing applications. The composite sandwich cover panels considered in this study have approximately the same structural efficiency as composite stiffened plate cover panels designed to identical constraints when the dominant design load is axial compression. Increasing the maximum allowable strain from 0.0045 to 0.006 in./in. decreases the weight of composite sandwich cover panels at the higher load levels considered, while having no effect on weight at the lower load levels. Increasing the maximum allowable strain beyond 0.006 in./in. has little or no effect on the weight of the composite sandwich cover panels considered in this study. Decreasing the inplane stiffness requirements reduces the weight of composite sandwich cover panels at the lower load levels, while having no effect on weight at the higher load levels. Increasing the inplane stiffness requirements induces a weight increase at all load levels. Increasing the upper limit on the percentage of $0°$ and $\pm 45°$ plies of the facesheet laminate reduces the weight of composite sandwich cover panels. The weight of the sandwich cover panel designs in this study are not very sensitive to changes in the core density. Core density selection is probably best made on the basis of criteria other than that included in the present analysis (e.g., damage tolerance and ease of manufacture).

SYMBOLS

a	cover panel length (see figure 1)
A_{mn}	modal amplitudes (see equation (4))
A_{11}, A_{12}, A_{16}, A_{22}, A_{26}, A_{66}	inplane stiffnesses of cover panel
$A_{11_{min}}$, $A_{66_{min}}$	minimum required inplane stiffness of the facesheets
$A_{11_{min_{bl}}}$, $A_{66_{min_{bl}}}$	baseline values of the minimum required inplane stiffness of the facesheets
b	cover panel width (see figure 1)
D_{11}, D_{12}, D_{16}, D_{22}, D_{26}, D_{66}	bending stiffnesses of cover panel
D_{Qx}, D_{Qy}	transverse shear stiffnesses of cover panel (see equations (2) and (3))
E_{c_z}	sandwich core modulus in z-direction (see figure 1)
E_f	effective facesheet modulus in longitudinal direction
E_L, E_T	lamina modulus in longitudinal and transverse direction, respectively
G_{LT}	lamina shear modulus
G_{xz}, G_{yz}	sandwich core transverse shear modulus in x- and y-directions, respectively
k_A	scaling factor for minimum required inplane stiffness
L_0, L_{45}, L_{90}	lower percentage limit of the 0°, ±45°, and 90° plies, respectively
m	number of longitudinal half waves for cover panel buckling mode
n	number of transverse half waves for cover panel buckling mode
N_x	applied longitudinal stress resultant (see figure 1)

N_x^b	longitudinal stress resultant at buckling
N_x^w	longitudinal stress resultant for facesheet symmetric wrinkling
N_{xy}	applied shear stress resultant
N_y	applied transverse stress resultant
t_c	core thickness (see figure 1)
t_f	facesheet thickness (see figure 1)
t_0, t_{45}, t_{90}	thickness of the facesheet 0°, ±45°, and 90° plies, respectively
U_0, U_{45}, U_{90}	upper percentage limit of the 0°, ±45°, and 90° plies, respectively
w	out-of-plane displacement of the cover panel
W	weight per unit area of cover panel
x, y, z	Cartesian coordinate system (see figure 1)
ε_x	longitudinal strain of the cover panel
$\varepsilon_{x_{max}}$	maximum allowable longitudinal strain
ν_{LT}	lamina major Poisson's ratio
ρ_{core}	core density
$\rho_{C/E}$	carbon-epoxy material density

REFERENCES

1. Stroud, W. Jefferson; and Anderson, Melvin S.: PASCO: Structural Panel Analysis and Sizing Code, Capability and Analytical Foundations. NASA TM 80181, 1981.

2. Anderson, Melvin S.; Stroud, W. Jefferson; Durling, Barbara J.; and Hennessy, Katherine W.: PASCO: Structural Panel Analysis and Sizing Code, Users Manual. NASA TM 80182, 1981.

3. Lucas, Stephen H.; and Scotti, Stephen J.: The Sizing and Optimization Language, SOL - A Computer Language for Design Problems. NASA TM 100565, April 1988.

4. Lucas, Stephen H.; and Scotti, Stephen J.: The Preliminary SOL Reference Manual. NASA TM 100566, January 1989.

5. Libove, Charles; and Batdorf, S. B.: A General Small-Deflection Theory for Flat Sandwich Plates. NACA Report No. 899, 1948.

6. Bert, Charles W.; Crisman, W. C.; and Nordby, Gene M.: Buckling of Cylindrical and Conical Sandwich Shells with Orthotropic Facings. AIAA Journal, Vol. 7, No. 2, February 1969.

7. Camarda, Charles J.: Tests of Graphite/Polyimide Sandwich Panels in Uniaxial Edgewise Compression. NASA TP 1785, 1980.

8. Hart-Smith, L. J.: Design and Analysis of Bolted and Riveted Joints in Fibrous Composite Structures. International Symposium on Joining and Repair of Fibre-Reinforced Plastics, Imperial College, London. September 1986.

9. Madan, Ram C.: Composite Transport Wing Technology Development. NASA CR 178409, February 1988.

10. Anon.: Mechanical Properties of Hexcel Honeycomb Materials. TSB 120, Hexcel Corporation, 1988.

11. Mikulas, Martin M., Jr.; Bush, Harold G.; and Rhodes, Marvin D.: Current Langley Research Center Studies on Buckling and Low-Velocity Impact of Composite Panels. Third Conference on Fibrous Composites in Flight Vehicle Design, Part II, NASA TM X-3377, 1976, pp. 633 - 663.

Table 1. Properties of IM6/1808I Carbon-Epoxy Tape [a]

Longitudinal Young's Modulus	E_L, Msi	18.5
Transverse Young's Modulus	E_T, Msi	1.09
Shear Modulus	G_{LT}, Msi	0.70
Major Poisson's Ratio	ν_{LT}	0.33
Density	$\rho_{C/E}$, lb/in^3	0.058

[a] Values obtained from reference 9, except for the density, which is estimated.

Table 2. Baseline Design Constraint Values

$\varepsilon_{x_{max}} = 0.0045$ in./in.

$A_{11_{min}} = f(N_x)$

$A_{66_{min}} = g(N_x)$

See figure 3

$L_0 = 0.125$	$U_0 = 0.375$
$L_{45} = 0.125$	$U_{45} = 0.375$
$L_{90} = 0.125$	$U_{90} = 0.375$

$1.0 \text{ lb/ft}^3 < \rho_{core} < 9.5 \text{ lb/ft}^3$

Table 3. Core and Facesheet Thicknesses

N_x, lb/in.	3,000	7,500	15,000	24,000
Core thickness, in. $\rho_{core} = 1.0$ lb/ft^3	0.30	0.44	0.61	0.63
Core thickness, in. $\rho_{core} = 9.5$ lb/ft^3	0.28	0.40	0.52	0.42
Facesheet thickness, in. $\rho_{core} = 1.0$ and 9.5 lb/ft^3	0.117	0.154	0.186	0.298

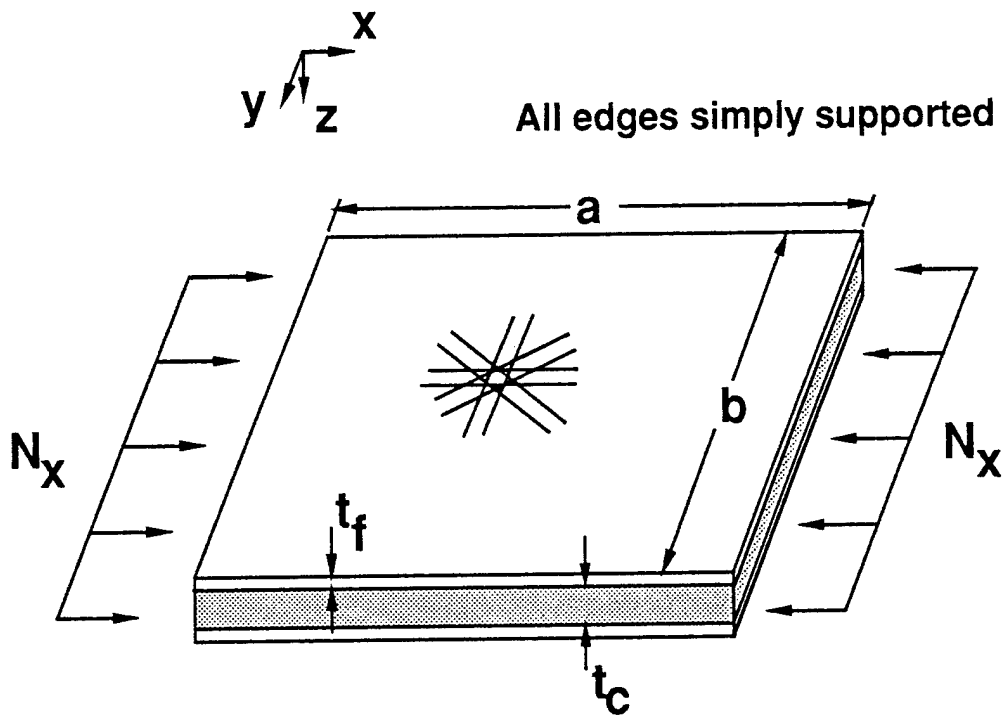


Figure 1. Plate geometry and loading

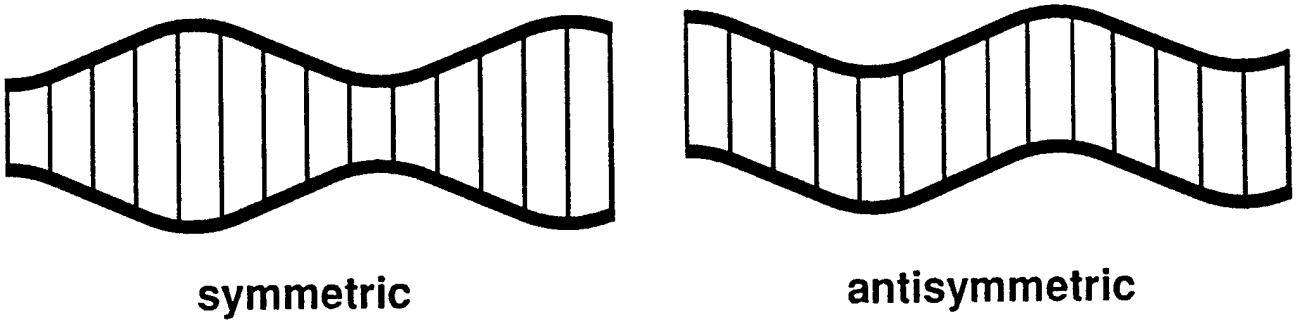


Figure 2. Symmetric and antisymmetric facesheet wrinkling

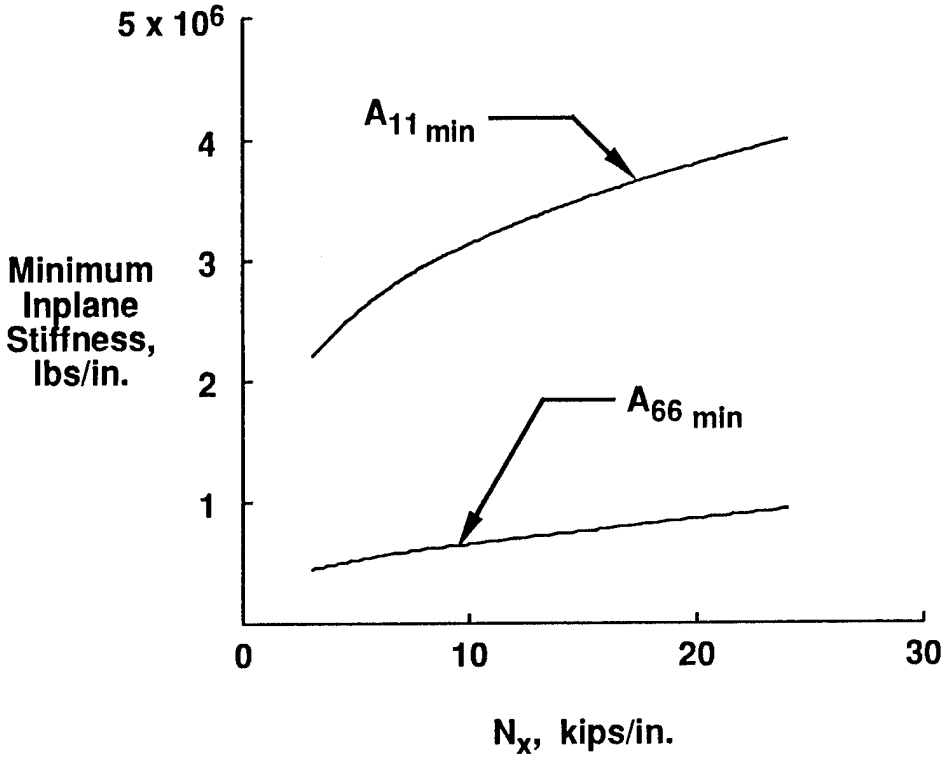


Figure 3. Minimum required inplane stiffnesses for cover panels [11]

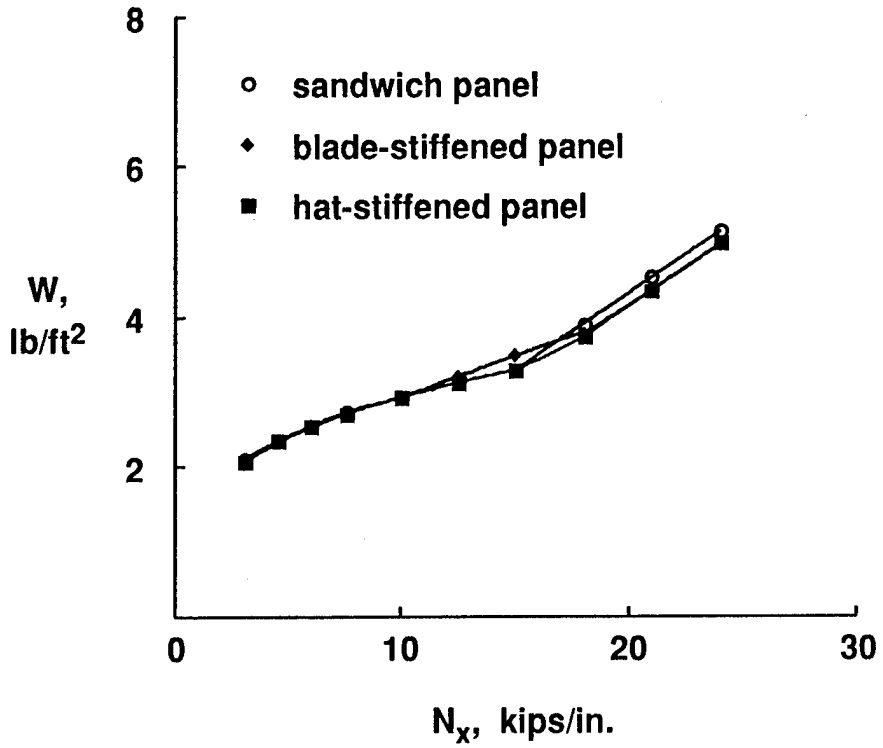


Figure 4. Weight comparison between sandwich and stiffened plate composite cover panels

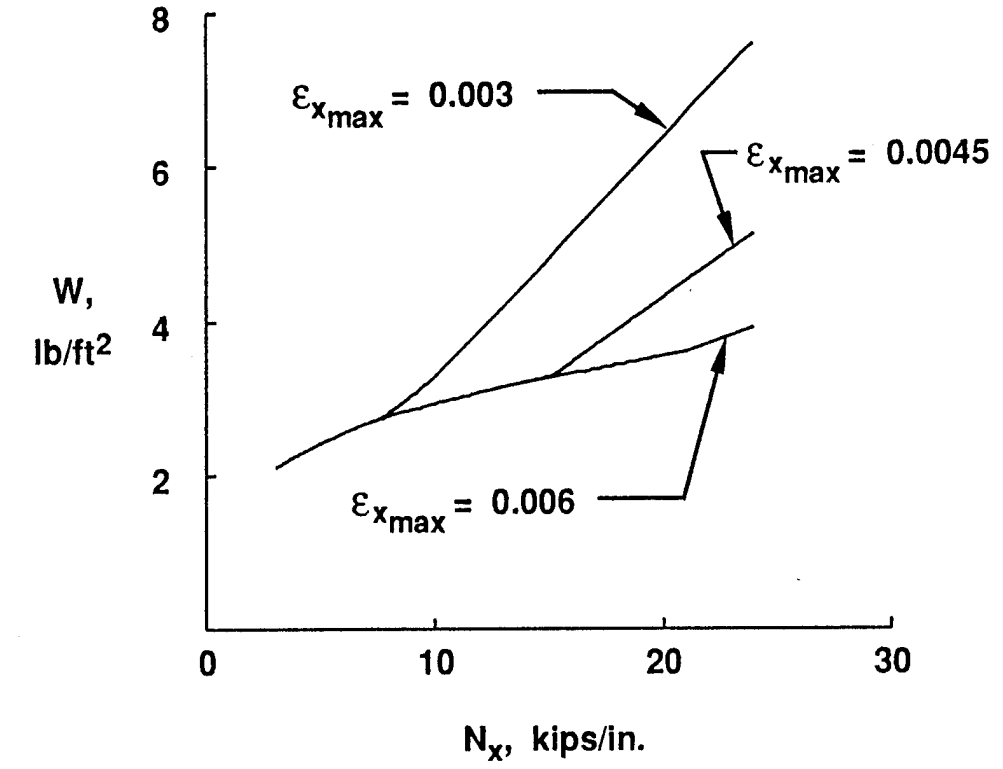


Figure 5. Effect of the maximum longitudinal allowable strain on the structural efficiency of composite sandwich cover panels

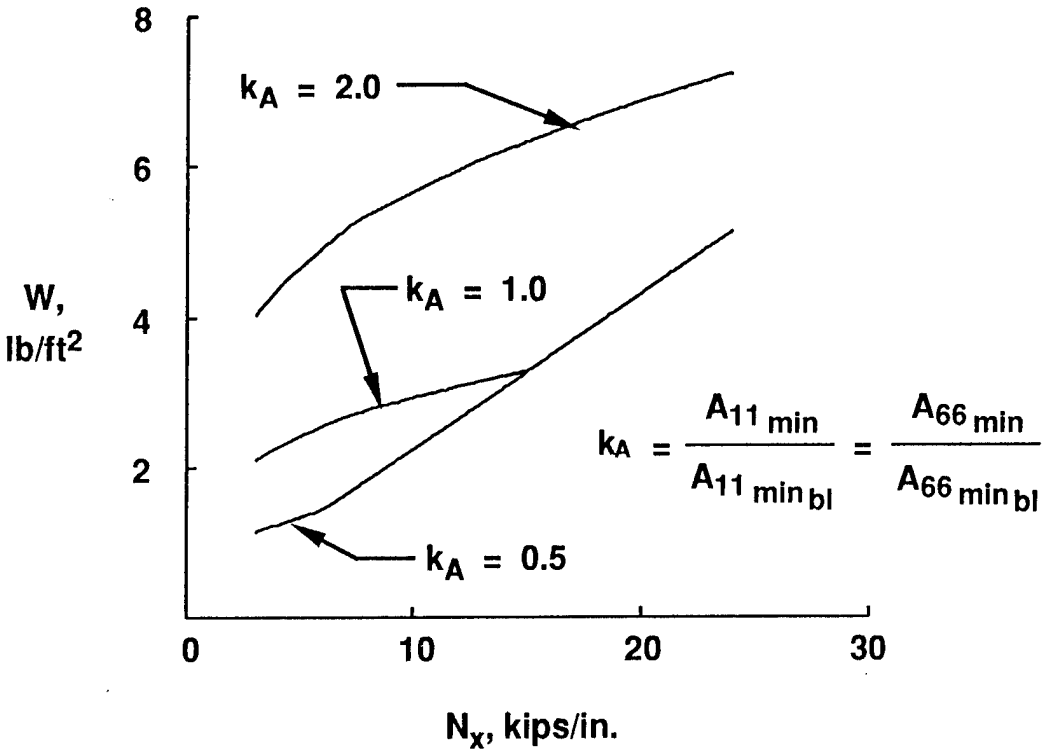


Figure 6. Effect of the minimum required inplane stiffness on the structural efficiency of composite sandwich cover panels

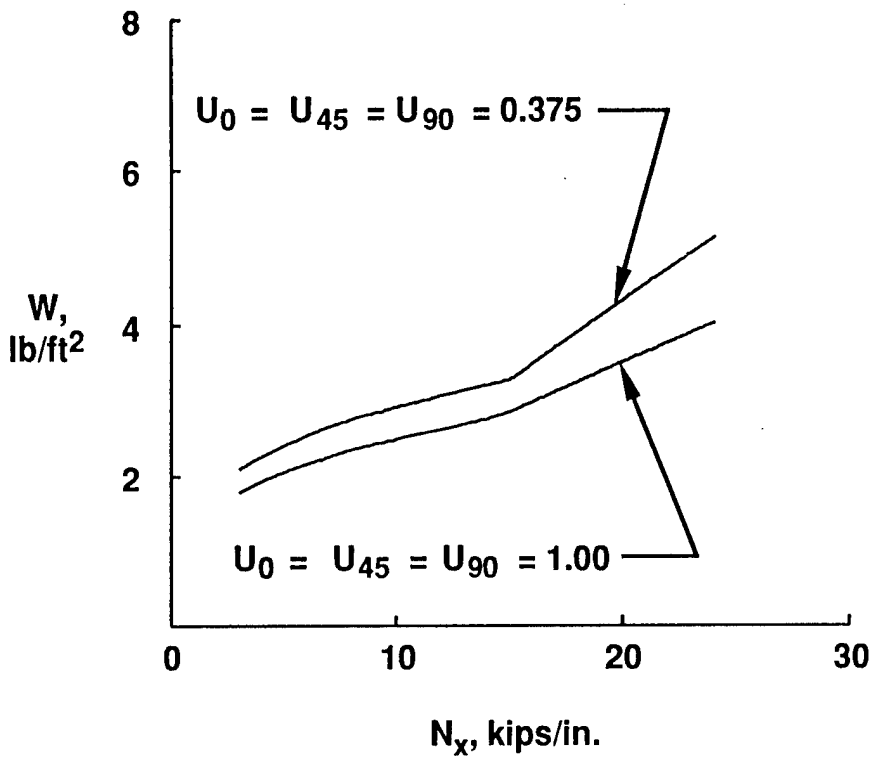


Figure 7. Effect of the upper percentage limit of all ply orientations on the structural efficiency of composite sandwich cover panels

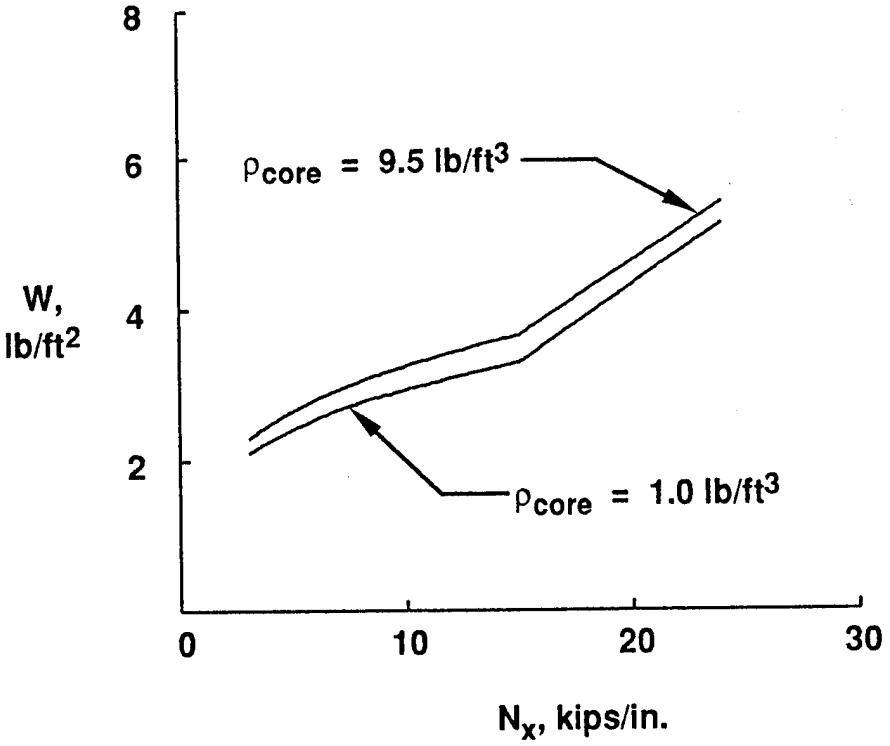


Figure 8. Effect of core density, ρ_{core}, on the strucutral efficiency of composite sandwich cover panels

A COMPARISON OF CLASSICAL MECHANICS MODELS AND FINITE ELEMENT SIMULATION OF ELASTICALLY TAILORED WING BOXES

Lawrence W. Rehfield, Richard D. Pickings, Stephen Chang and Michael Holl

University of California, Davis

SUMMARY

Structural tailoring concepts have been developed by Rehfield to create wings with elastically produced camber for the purpose of increasing lift during take-off conditions.

Simple models based upon enhancements to the thin-walled composite beam theory of Rehfield have been developed to investigate prospects for elastic tailoring of the chordwise deformation of wing structures. Previous correlation studies have shown that the thin-wall beam theory is very accurate for predicting bending and twisting deformation of thin-wall composite box beams, structural tubes, and rotor blades with both single and multiple cells. However, earlier work has not emphasized chordwise deformations.

Application of the modified theory to real-world problems must be executed with confidence and minimum risk. Consequently, it is imperative that the theory is of high enough fidelity to accurately predict not only the intentionally produced tailoring mechanisms, but also the actual overall behavior of wing box structures. Therefore, extensive correlation studies must be performed to establish that the theory is valid for predicting chordwise deformations.

Validation will be carried out in two steps: finite element correlation and experimental correlation. Extensive testing using scale models of wing box structures is planned. However, the purpose of present work is to provide a comparison of the theoretical results with a finite element model for the bending method of producing camber.

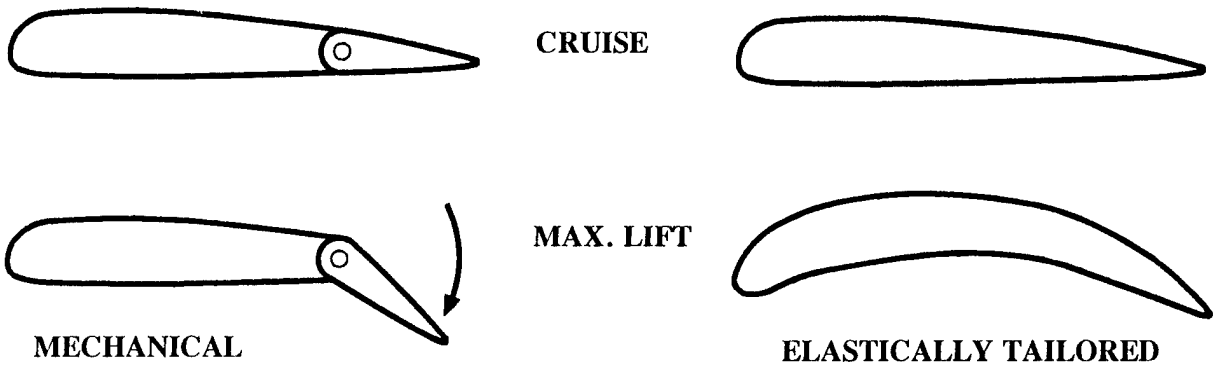
At present, finite element correlation studies have been completed for two cases: a bonded unstiffened structural box, and a bolted unstiffened structural box. Results from these studies show an error of less than one percent for the bonded case and less that six percent for the bolted case in predicting camber curvature for the structural box. Examination of the results shows that the theory is very accurate for the cases studied and therefore, will provide an excellent basis for conducting further tailoring studies.

ELASTIC TAILORING

THE USE OF

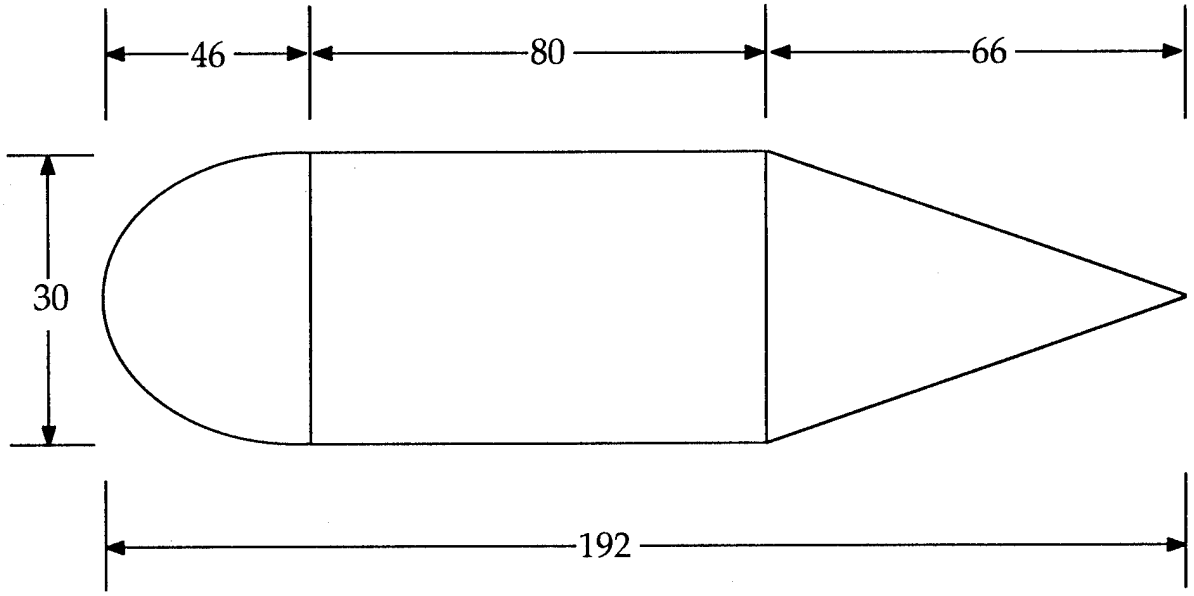
- STRUCTURAL CONCEPT
- FIBER ORIENTATION
- STACKING SEQUENCE
- BLEND OF MATERIALS

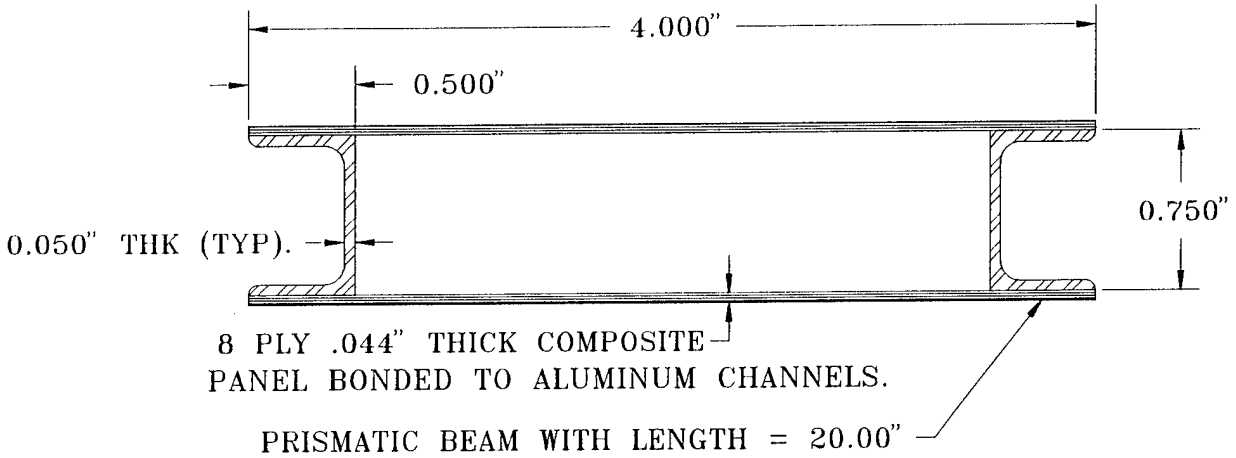
TO ACHIEVE SPECIFIC PERFORMANCE GOALS



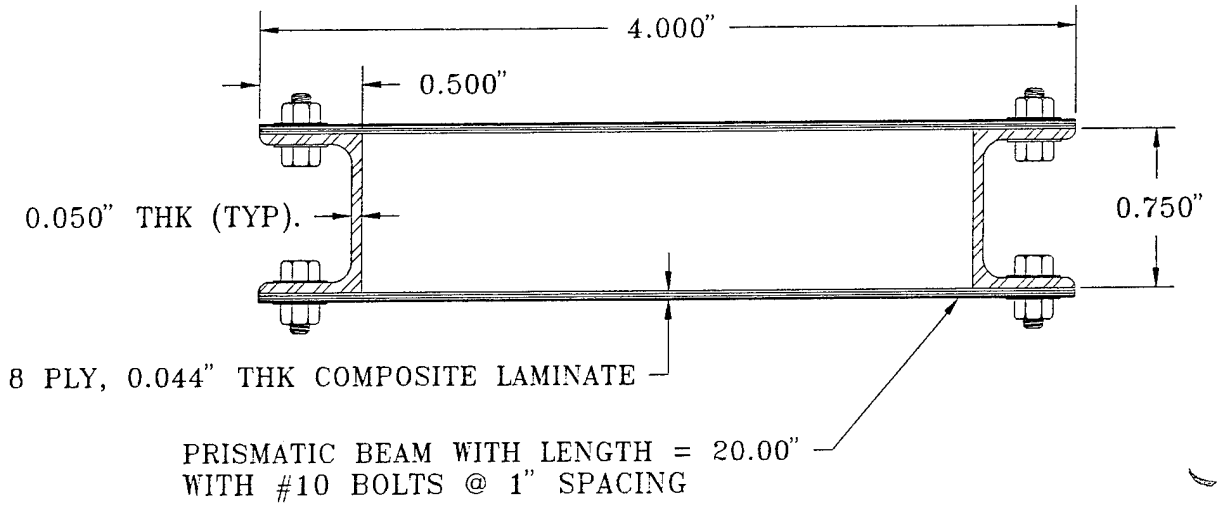
METHODS OF INCREASING AIRFOIL LIFT

C – 130 CENTER WING BOX MODEL





STRUCTURAL BOX CROSS SECTION



CROSS SECTION OF BOLTED STRUCTURAL BOX

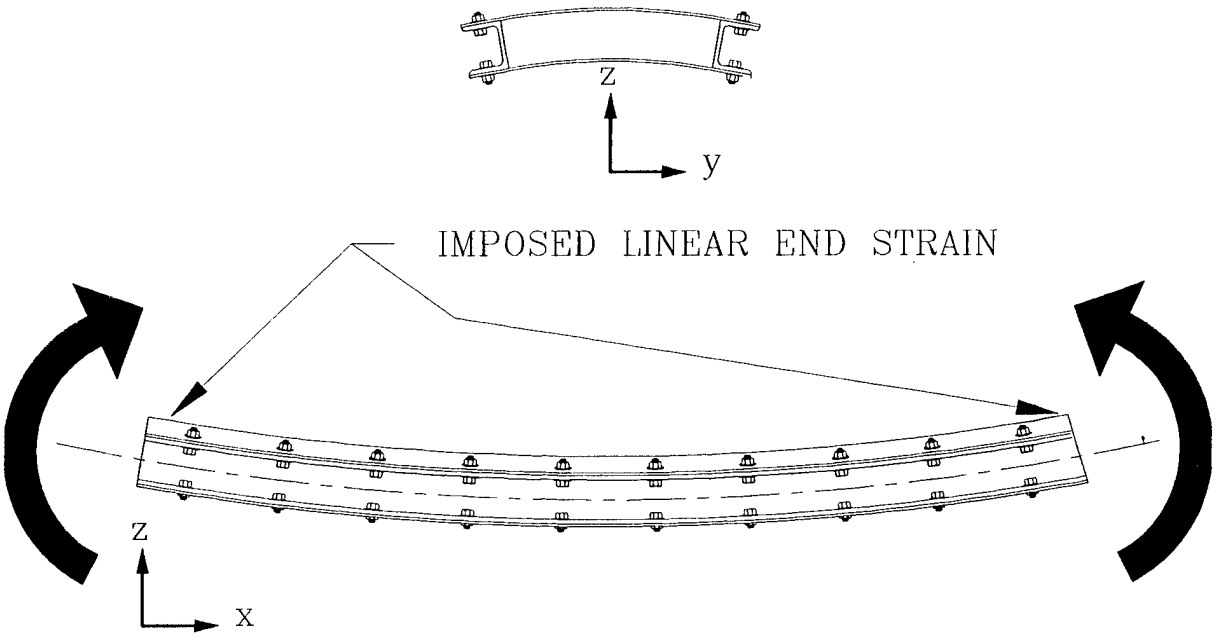
MATERIAL PROPERTIES

AS4/3501–6 GRAPHITE EPOXY

- E_{11} = 20.0 MSI
- E_{22} = 1.7 MSI
- G_{12} = 0.85 MSI
- ν_{12} = 0.3

ALUMINUM CHANNEL

- E = 10.0 MSI
- ν = 0.33

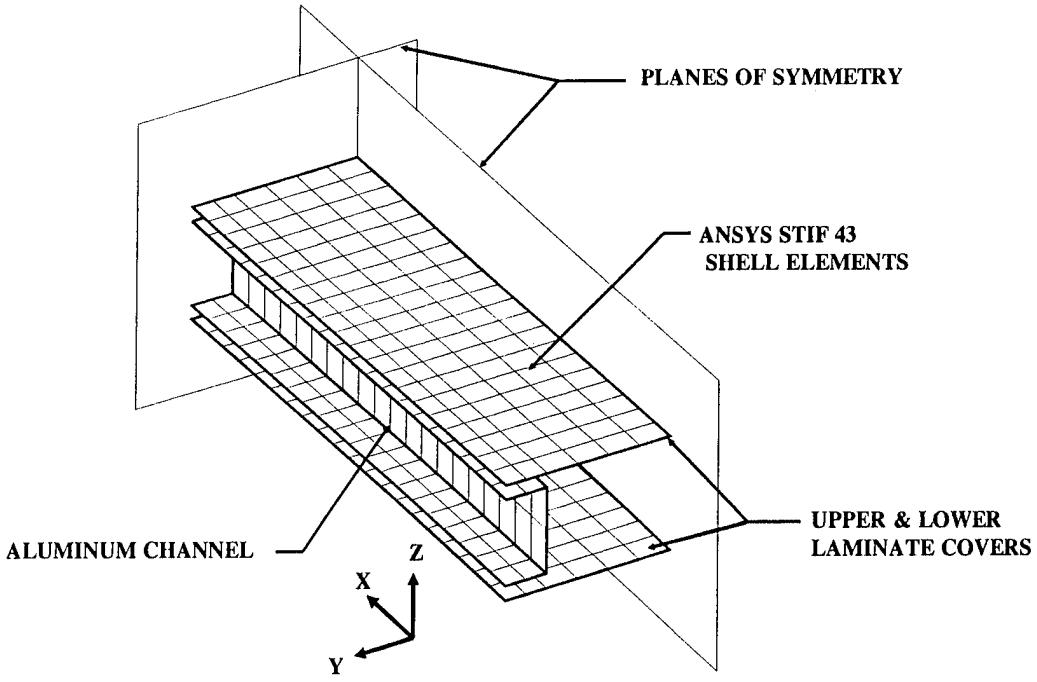


DEFORMED SHAPE OF STRUCTURAL BOX

ESTABLISHING A TECHNOLOGY BASE

GOAL: UTILIZATION OF TECHNOLOGY WITH CONFIDENCE AND LIMITED RISK

- PROOF OF CONCEPT
- DESIGN ANALYSIS METHODOLOGY
- FIDELITY OF MODELING
  - FINITE ELEMENT CORRELATION
  - EXPERIMENTAL CORRELATION
- CAUSE & EFFECT RELATIONSHIPS



FINITE ELEMENT MODEL

RESULTS OF CORRELATION STUDY

CHORDWISE CAMBER CURVATURE (IN^{-1})

MODEL TYPE	BOLTED	BONDED
CLASSICAL	0.01040	0.00954
FINITE ELEMENT	0.00982	0.00947
PERCENT DIFFERENCE	-5.6	-0.7

CONCLUSIONS

- CORRELATION EXCELLENT
- CLASSICAL MODEL MAY BE USED FOR DESIGN

ADVANCED FIBER PLACEMENT OF COMPOSITE FUSELAGE STRUCTURES

Robert L. Anderson, Hercules Aerospace
Manager, Composite Structures Programs
Hercules Composite Structures Group

Carroll G. Grant, Hercules Aerospace
Program Manager, NASA ACT Contracts
Hercules Composite Structures Group

ABSTRACT

The Hercules/NASA ACT program will demonstrate the low cost potential of the automated fiber placement process. Hercules fiber placement machine has been developed for cost effective production of composite aircraft structures. The Hercules fiber placement process uses a low cost prepreg tow material form and achieves equivalent laminate properties to structures fabricated with prepreg tape lay up. Fiber placement demonstrations planned for the Hercules ACT program include fabrication of stiffened test panels which represent crown, keel, and window belt segments of a typical transport aircraft fuselage.

Hercules fiber placement has been selected for evaluation by other participants in the NASA ACT program. Douglas Aircraft has selected Hercules fiber placement for their ICAPS program. Several stiffened test articles varying in size from 21-in. × 36-in. flat panels to 4-ft to 5-ft curved panels will be fabricated and tested for comparison with similar RTM panels.

Boeing Commercial Airplanes will also evaluate fiber placement for their ATCAS program. The ATCAS test panels are 110 in. × 26 in. and have three co-cured stringers. Each panel has ply drops in the skin laminate that reduce thickness from 24 plies to 12 plies.

HERCULES ADVANCED FIBER PLACEMENT

Hercules began the development of fiber placement technology for the automated placement and in-process consolidation of ribbonized prepreg tow in 1980. In 1983, our first machine (FPM1) was operational and was used to manufacture flat panels, curved panels, and 360° cross sections, including stiffened and unstiffened skins.

Hercules fiber placement process makes use of robotic machine technology to provide an automated fabrication process for complex-shaped, high performance composite structures (Figure 1). The process involves the precise automated

placement and in-process compaction of ribbonized prepreg tow. Multiple tows are laid down as a band with band location and angle precisely controlled. Material cut and add features, incorporated into the process, provide high production rate potential, enhance design tailorability, and minimize material scrap.

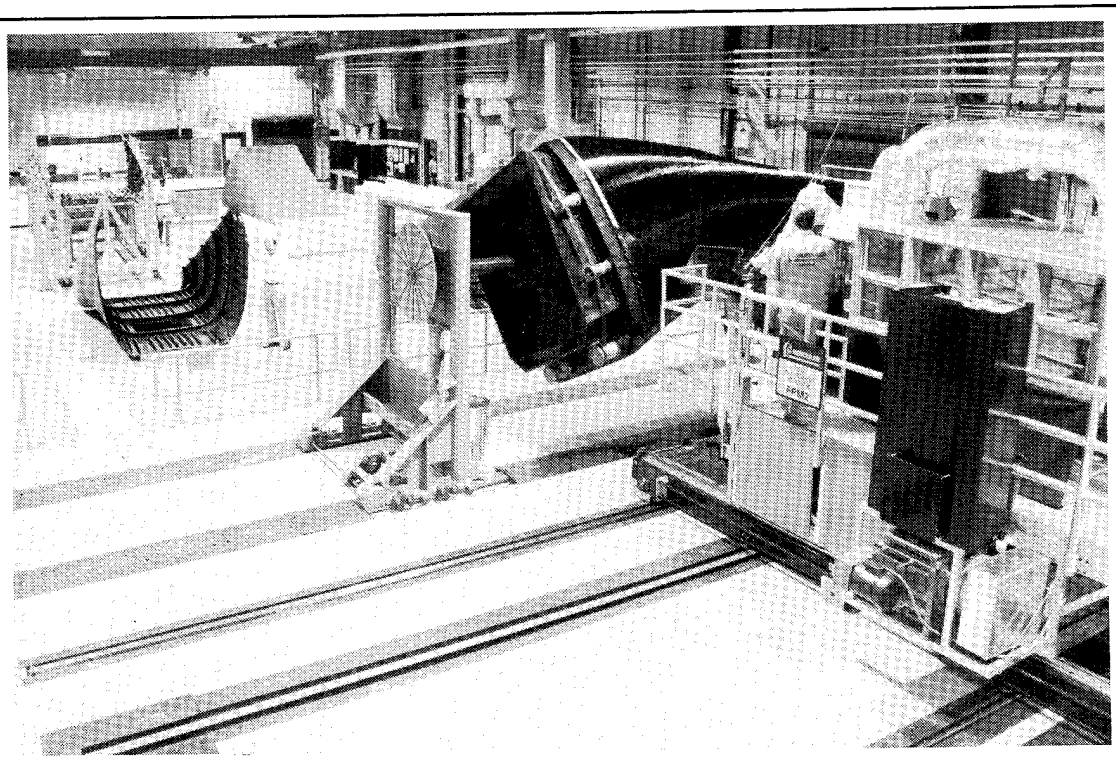


Figure 1

Hercules has successfully demonstrated the capability to fabricate a wide variety of complex structures using this technology. Aircraft wing components including ribs and spars, air inlet ducts, and fuselage structures have been successfully fiber placed.

Hercules currently has two operational fiber placement machines. FPM1 is a six-axis machine that has the capability to manufacture structures with a 20-ft maximum length and 11-ft maximum swing diameter. Our new production rated machine (FPM2 shown in Figure 1), which became operational in early 1990, is a seven-axis machine that has the capability to manufacture structures with a 33-ft long and 15-ft swing diameter. The first two MANTECH V-22 Aft Fuselage structures were manufactured on FPM1 and the third fuselage structure was manufactured on FPM2. Figure 2 shows a typical FPM2 setup with an explanation of the various axes of motion.

These fiber placement machines use a computerized mathematical model (Figure 3) of the part to generate a fiber path of a specified width, thickness, and orientation and to control tow cut and add functions. The software and hardware provide synchronization control and movement. The material delivery system processes, delivers, and compacts the prepreg tow material on the mandrel as demanded by part geometry.

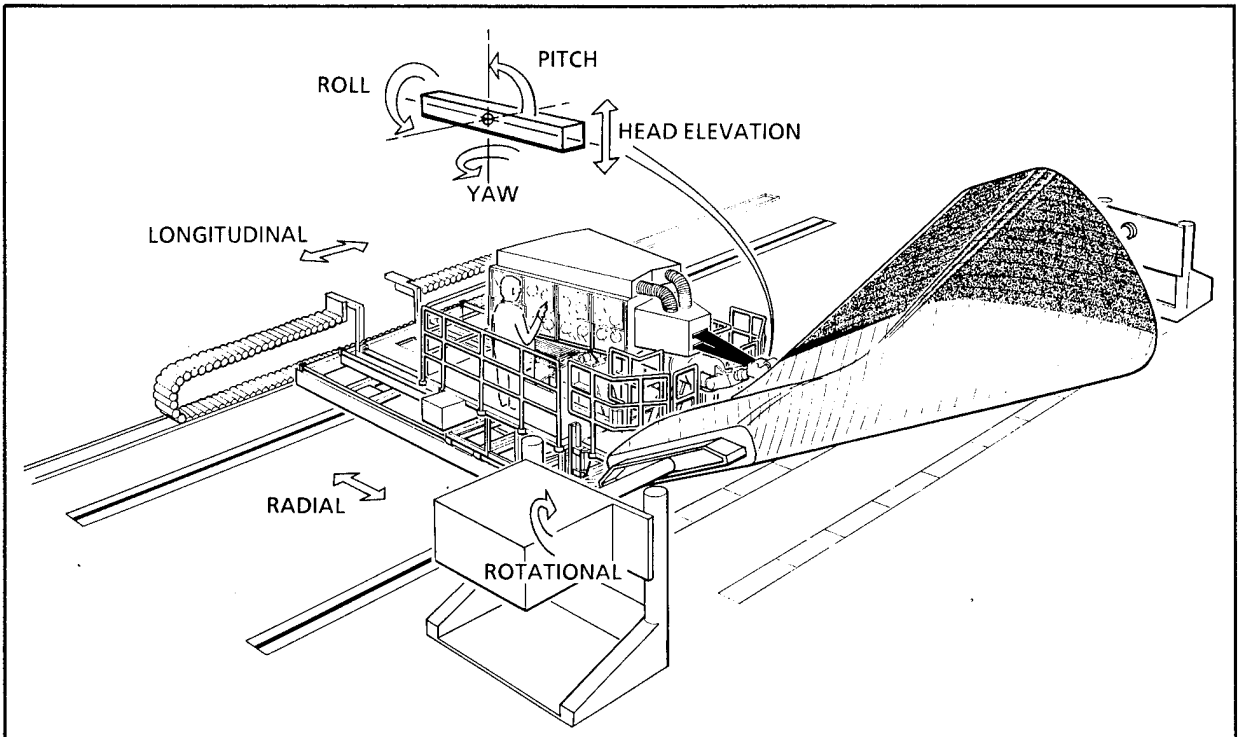
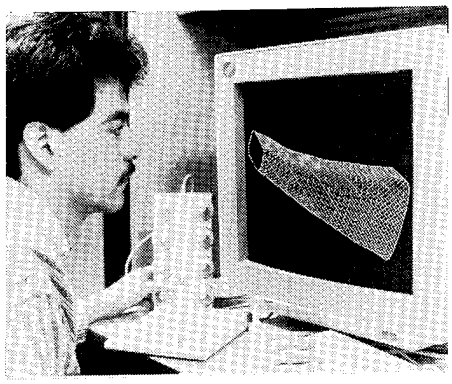


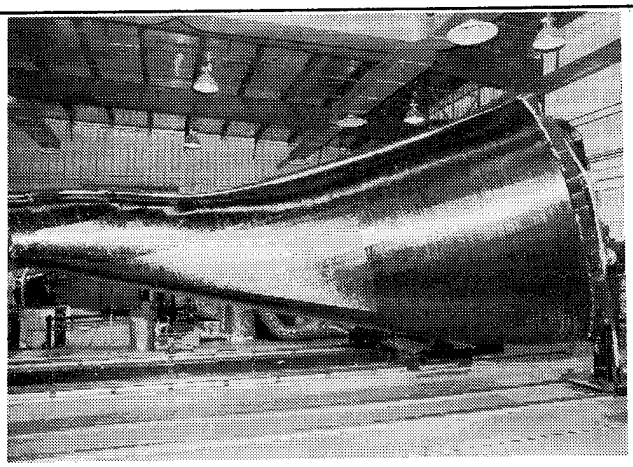
Figure 2. Multi-axis fiber placement machine

We currently have two delivery head designs that are operational on our fiber placement machines. The tow cut and add head allows for individual tow cutting and adding for ply tailoring on complex, nongeodesic structures. The band cut and add head is used for all structural shapes that do not require individual tow cut and add capabilities. Both of these delivery heads are designed for 12 tows. We also have a tow cut and add head that is designed for 32 tows. The 32-tow head was used on the MANTECH V-22 Aft Fuselage shown in Figure 1.

Fiber tow placement offers many improvements over hand lay up that contribute directly or indirectly to cost savings. Tow width control allows for non-standard ply thicknesses which optimize part design while maintaining constant band width. Gaps and overlaps are kept within a tolerance of 0.75 mm (0.030 in.). Constant ply thickness can be maintained by adding or dropping tows as the part changes cross section (Figure 4). Tow and band cut/add features reduce material scrap to as low as 5% by placing the material only where required. Fiber placement also uses prepreg tow that is projected to be the lowest cost material form available. The tow-placed product is also comparable in performance to hand lay up prepreg tape parts (Figure 5).

During the fiber tow placement process, a conformable roller rides directly on the part or tool, providing in-process compaction while delivering the tow material. This minimizes the need for intermediate compaction steps. The placement head flexibility allows fiber placement on convex and concave surfaces. The delivery head delivers individual tows as a flexible band to minimize material distortion. This flexibility provides fiber angle control that allows for fiber placement of non-geodesic shapes which cannot be fabricated with filament winding (Figure 6).





- Models 3-D surface
- Calculates 3-D fiber paths
- Calculates machine positions to deliver the fiber
- Translates machine positions into a control table
- Can generate program from customer tooling

The fiber placement control program provides instructions for a multi-axis machine to deliver material on a precise path over a complex 3-D surface.

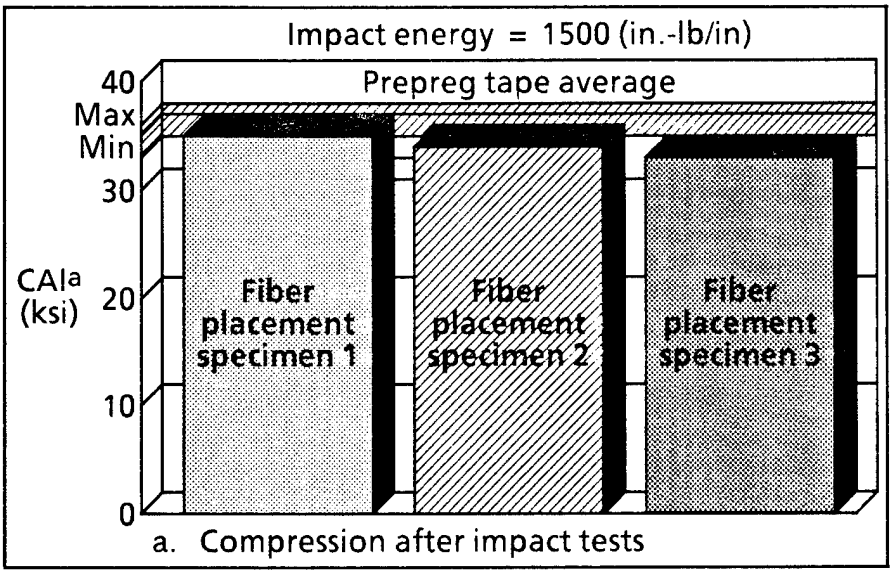
Figure 3. An off-line programming system generates fiber placement paths based on mathematical model

The winding angle is not limited. Axial (0°) plies can be readily placed with this process.

FIBER PLACEMENT OFFERS STRUCTURAL PERFORMANCE ADVANTAGES

- Ply Thickness Control
  - Thin Plies (to 5 mils), Prepreg Tape Equivalent
  - Control Independent of Geometry
- In-Process Compaction
- Void Volume 1% or Less
- No Limitation on Fiber Angles
  - Tailored for Design Requirements
  - Nongeodesic Paths
  - Convex or Concave
  - Capable of Helical, Hoop, and Longitudinal Orientations

Figure 4.



a. Compression after impact tests

- Damage tolerant IM7/8551-7A towpreg demonstrated
- Fiber placement process CAI results demonstrate equal quality to prepreg layup process
- Concave surface, variable skin thickness, tapered cross section and thin ply laminates now possible with automated process

Figure 5. Compression after impact test data

Item	Filament Winding (Wet)	Fiber Placement (Prepreg Tow)
Void content	4-8%	<1%
Thickness	• 0.010-0.025 in/ply • Not constant for tapered parts	• 0.005 - 0.015 in/ply • Constant for tapered parts
Tow cut and add	No	Yes
Winding angle	>15° 15 - 90°	No limit 0 - 90°
Laps and gaps	0.125 in.	0.030 in.
Geometry	Best for bodies of revolution	• Complex • Concave
Scrap rate	20 - 40%	5 - 20%

Figure 6. Filament winding/fiber placement comparison

HERCULES NASA ACT PROGRAM

In early 1989, Hercules received a contract award from NASA LaRC to participate in the advanced composites technology program. The objective of the contract was to exploit the utility of Hercules fiber placement process to achieve low cost manufacturing of transport aircraft fuselage structure. The basic design selected by Hercules for this program was an isogrid-stiffened skin panel that would be fabricated in one fiber placement operation. The unidirectional tow stiffeners would be tow placed into cavities on a mandrel and the skin would be placed over the stiffeners (Figure 7). The skin and isogrid-pattern blade stiffeners would be co-cured in an autoclave using the mandrel as the cure tool.

The design for the isogrid-stiffened structure was to be provided by NASA LaRC. Hercules would conduct an in-depth study to resolve the critical issues of blade stiffener intersections (crossovers) and skin to stiffener interface.

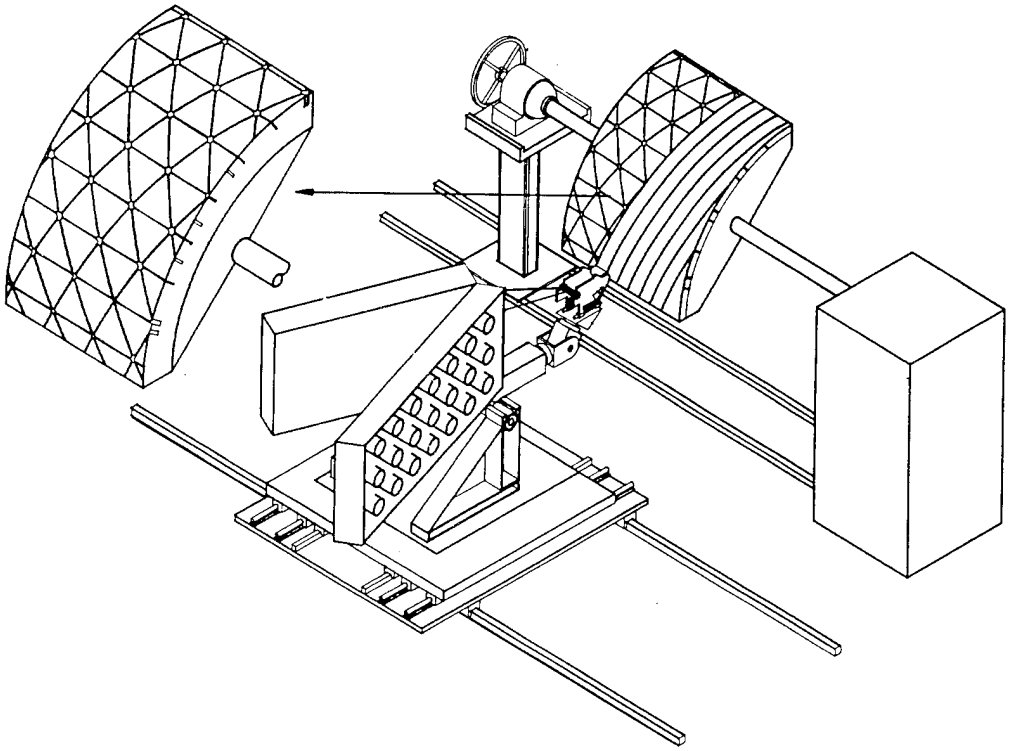


Figure 7. Isogrid panel in 7-axis (FPM2) machine

The Hercules isogrid-stiffened fuselage program was slow in getting started as NASA LaRC was unable to provide an acceptable stiffener design and there was some concern about producibility of the isogrid design with unidirectional tow.

In early 1990, NASA LaRC notified Hercules that the ACT program would be redirected toward a more conventionally stiffened fuselage structure. Several options were considered for the Hercules program and in April we were asked by NASA LaRC to work with Boeing to complement the ATCAS program.

The new Hercules program will be a cooperative endeavor between Boeing Commercial Airplanes and Hercules Incorporated. Hercules will fabricate test

elements and panels representative in design of crown, keel and window belt quadrant of a typical Boeing Commercial transport aircraft. The fabrication process for all elements will be Hercules advanced fiber placement. Boeing will provide design and testing of all elements and panels on the Hercules ACT program (Figure 8).

Fuselage Quadrant	Test Article	Undamaged Elements	Tension With Damage	Shear With Damage	Comp. With Damage	Bi. Tension With Damage	Comp/ Shear With Damage
Crown	Flat, unstiffened skin panels (12 ft × 5 ft)		2				
Crown	Flat, stiffened panels (12 ft × 5 ft)		1				
Crown	Curved, stiffened panels (3.5 ft × 3.5 ft)					2	
Keel	Flat, coupons (5 in. × 7 in.)				24		
Keel	Flat, stiffened panels (3 ft × 2 ft)				6		
Keel	Curved, stiffened panels (3.5 ft × 3.5 ft)						1
Window belt	Tension coupons with thick taper (12 in. × 12 in.)	3	3				
Window belt	Curved panel with taper and cutout		1				
Window belt	Panel w/double window frame (3.5 ft × 3.5 ft)			1			

Figure 8. Test matrix for Boeing/Hercules ACT Program integration

HERCULES NASA ACT SUBCONTRACTS

Hercules advanced fiber placement process was identified for evaluation on several NASA ACT contracts (Figure 9). We currently have several subcontracts in process for fiber placement of various aircraft related structures. We are also discussing future subcontracts with other NASA ACT program participants. Our current subcontracts are with Boeing and Douglas. We have had discussions with Lockheed regarding fiber placement of stiffened wing skins and stiffened fuselage skins. However, at this time, sufficient detail about these subcontracts was not available to be included in this paper. We have also had preliminary discussions with Northrop about subcontracts on their ACT program, but due to redirection in the Northrop program, this has been delayed.

Boeing	DOE Panels Hybrid panels Crown panels
Douglas	Stiffened skin panels
Lockheed	Wing skin panels Fuselage skin panels
Northrop	TBD

Figure 9. Hercules ACT subcontracts

Boeing ATCAS Program

Hercules currently has three subcontracts in process from the Boeing ATCAS program. We are working on the DOE panels, graphite glass hybrid panels, and stiffened crown panels. The DOE panel and hybrid panel contracts are mostly complete; the crown panel contract is just getting started. Preliminary discussions have started regarding future subcontracts for window belt and keel panel fabrication. These contracts are for Boeing evaluation of the structural performance and cost effectiveness of the fiber placement process.

ATCAS DOE Panels

Hercules recently completed fabrication of eight flat stiffened DOE panels, four of these panels were 31 in. × 110 in. and four were 21 in. × 110 in. Three hat section stiffeners were used on four panels and three blade stiffeners were used on the other four. The panel skins (Figure 10) and stiffeners were fiber-placed materials. The stiffeners were kitted from fiber-placed panels and formed into hat and blade stiffeners. The skins taper in thickness from 24 plies to 12 plies down the length of the panel and the stiffeners taper from 16 plies to 8 plies.

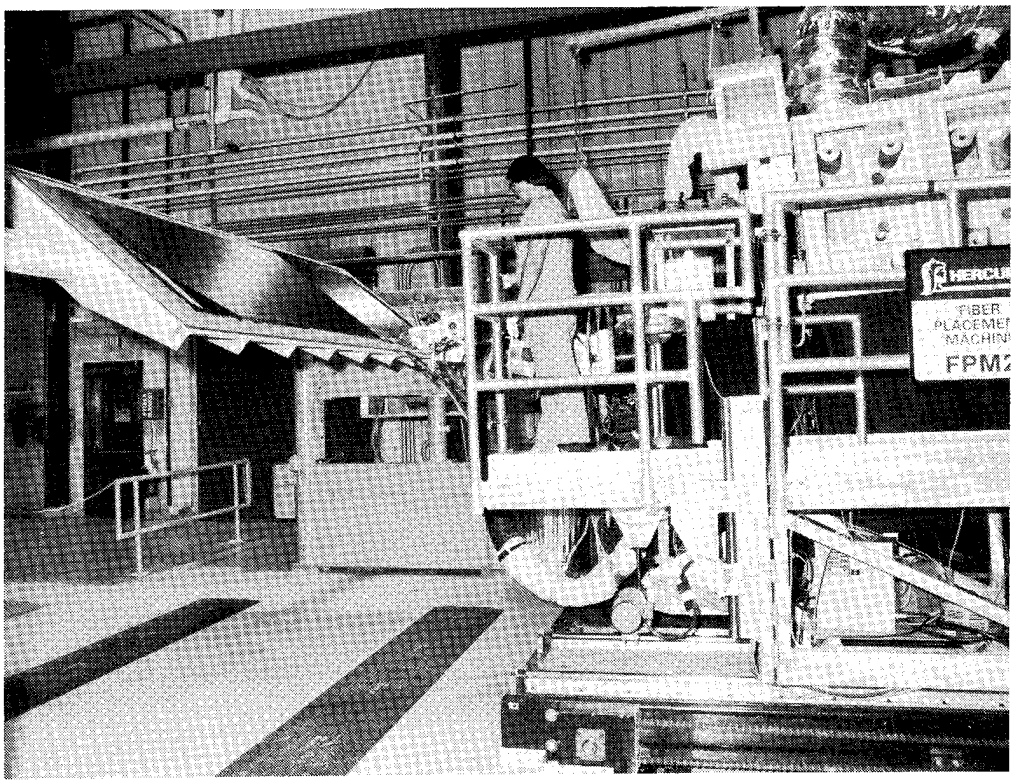


Figure 10.

The skin and stiffeners were assembled and co-cured in an autoclave. Four resin/fiber material combinations were used for fabrication of these panels: IM7/938, IM7/977-2, AS4/938, and AS4/977-C.

Fabrication of these DOE panels is complete and they have been delivered to Boeing for testing . (Figures 11 and 12.)

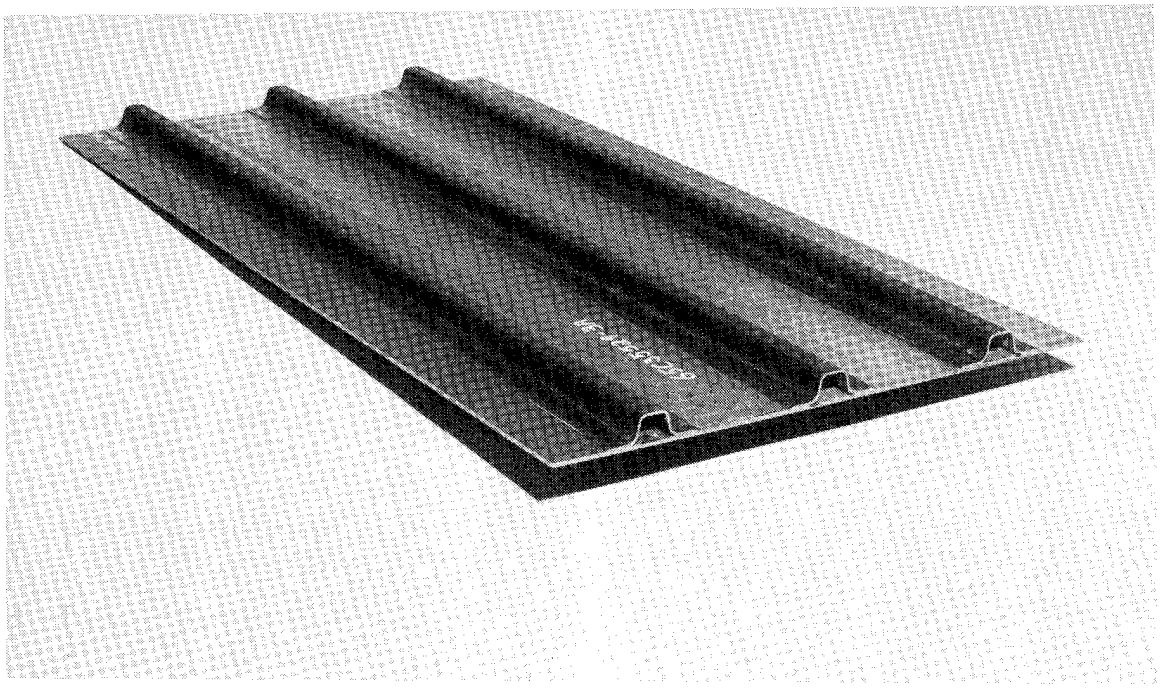


Figure 11. ATCAS DOE panels

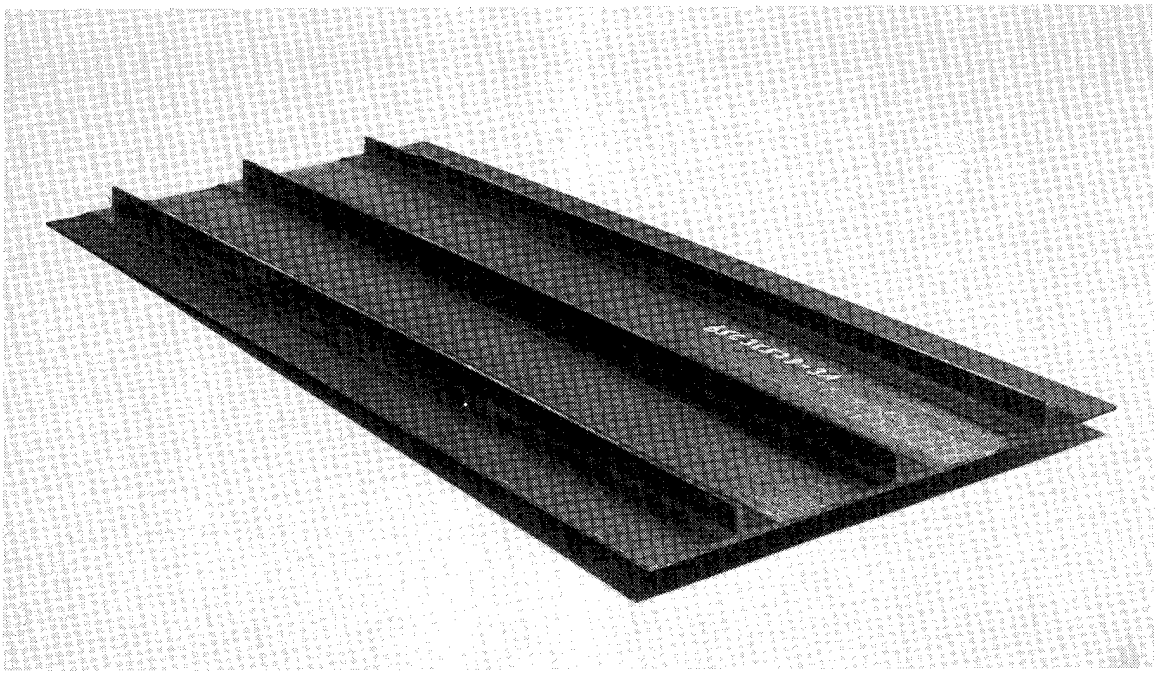


Figure 12. ATCAS DOE panels

ATCAS Hybrid Panels

The Hercules fiber placement process was selected for fabrication of graphite/S-2 glass hybrid panels. Because the fiber placement machine uses individual tows to form a band, the graphite to glass ratio can be varied. Seven panel configurations were fabricated for testing (Figure 13). Five of the panels were fabricated with different graphite to glass tow ratios and the sixth and seventh panels were each of a single material type. The panels were 10-plies thick and 22 in. × 68 in. dimension (Figure 14). Fiber types were AS4 (6K), T1000 G (12K), and S-2 glass (750 yield). The resin used was Fiberite 938 epoxy. As each hybrid configuration was set up in the machine, 5 lb of tow-placed tape was dispensed and sent to Stanford University as part of this contract.

Material	Fiber 1	Fiber 2	Adjacent Tows of Fiber 1	Adjacent Tows of Fiber 2
1	AS4	S-Glass	3	1
2	AS4	S-Glass	2	2
3	AS4	S-Glass	6	6
4	AS4	S-Glass	9	3
5	AS4	T1000G	9	3
6	S-Glass	None	NA	NA
7	AS4	None	NA	NA

Figure 13. Material definitions

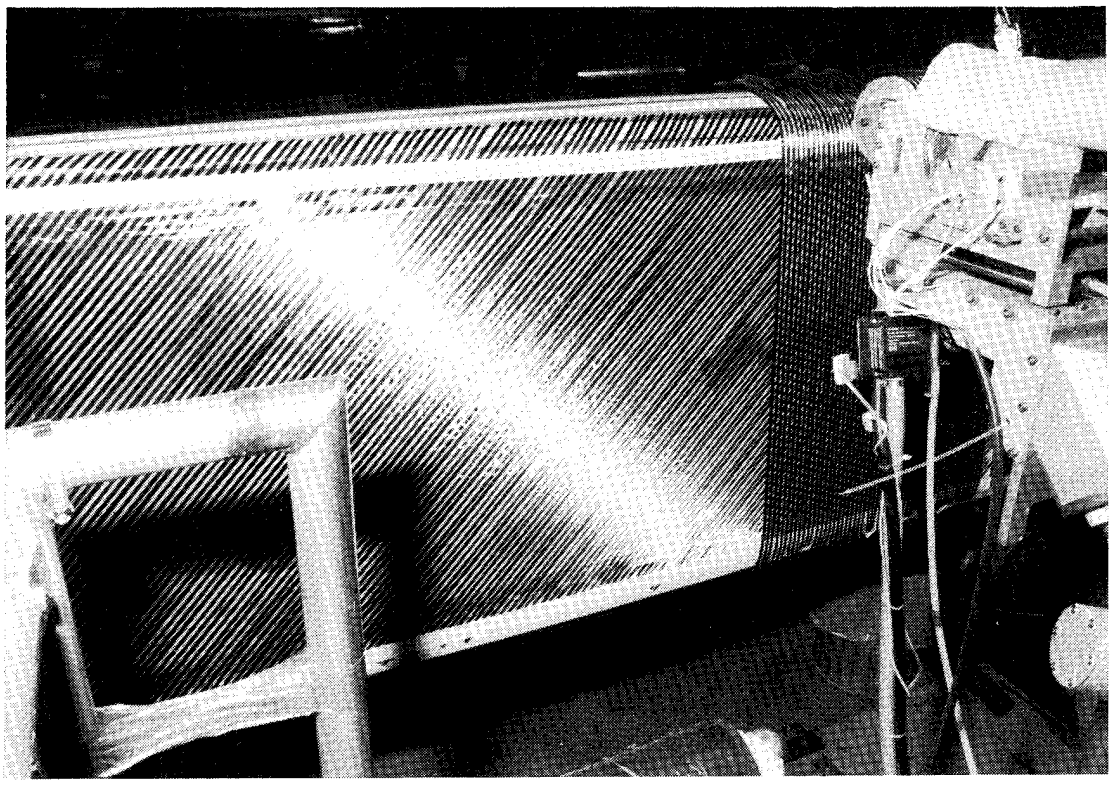


Figure 14.

ATCAS Crown Panels

Hercules recently received an ATCAS subcontract for fiber placement of three large crown panels. These panels will be representative in design of body Section 46 crown quadrant on the proposed Boeing 767-X aircraft and will be made in two basic configurations--skin/stringer/frame and core-stiffened skin. Materials will be a graphite/S-2 glass hybrid form.

To expedite this program, Hercules will use an existing large rocket motor mandrel for fiber placement of skins for two of the panels. A large fiber placement mandrel (Figure 15) is being designed for producing two crown panels approximately 8 ft × 9 ft in one operation.

The fabrication process for these panels has been demonstrated at Hercules recently and is a simple, low risk approach. Skins are fiber placed on a mandrel and transferred to an OML mold for cure. The pre-formed stringers are located to the IML surface of the skin and the assembly is vacuum bagged for autoclave cure. On the 8-ft x 9-ft panel, a thin graphite molded caul sheet will be used on the IML surface.

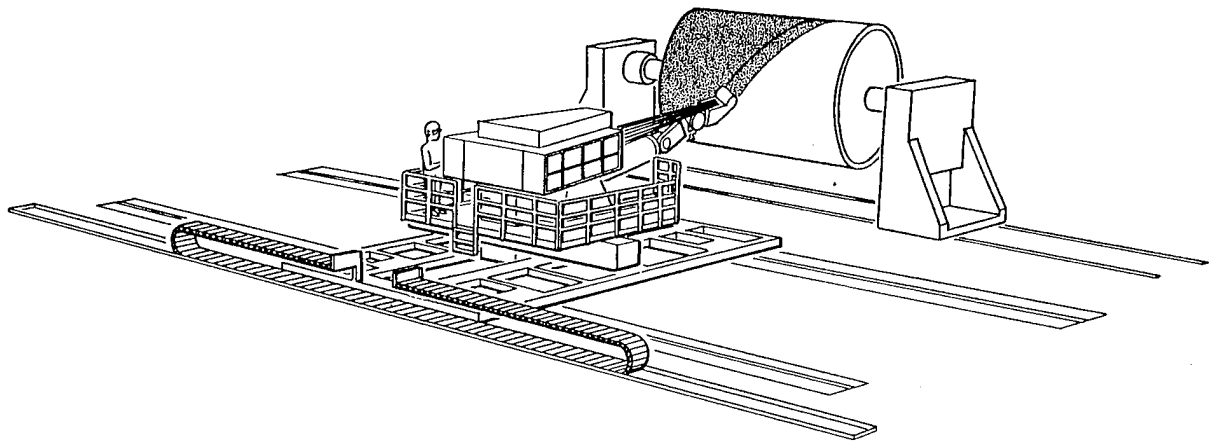


Figure 15.

Douglas ICAPS Program

Hercules currently has a large subcontract with the Innovative Composite Aircraft Primary Structures (ICAPS) program at Douglas Aircraft Company. The contract is for Douglas evaluation of the fiber placement process and specifically, to compare fiber placement with resin transfer molding (RTM) for structural performance and cost effectiveness. This program is approximately half completed; we are currently building tooling for the last deliverable parts.

Hercules ICAPS Panels

The Hercules ICAPS subcontract is for fiber placement of CAI specimens, 21-in. × 36-in. stiffened, flat element panels and 4-ft × 5-ft stiffened, curved subcomponent panels. A toughened resin system (8551-7A and 8551-7) was selected for this program to achieve maximum damage tolerance performance. Stiffeners for the element and subcomponent panels are hand formed J-stiffeners. The CAI specimens and element panels have been completed and delivered to Douglas. Fabrication of the large subcomponent panels will begin in late October.

A fabrication process was developed for the ICAPS element panels that proved to be low risk, cost effective, and produces consistent, high quality parts. The process uses the fiber placement machine, low-cost tooling, and stringer to skin co-curing. Skins are fiber placed on a mandrel that can be made with inexpensive, low temperature materials because it will not be subjected to a high temperature and pressurized autoclave environment. When the skins are complete, they are transferred to an OML cure mold that can be made of composite, steel, or aluminum. Stringers are fitted with aluminum cure mandrels and located on the IML surface of the skin with the aid of a picture frame location template. A thin, flexible caul sheet with molded cavities for the stringers is positioned to the IML surface of the panel assembly (Figure 16). The "flex caul" is 3- to 4-plies thick and is fabricated from a master model. The assembly is vacuum bagged and autoclave cured. The result is a panel with a smooth, aerodynamic OML surface and a "finished" IML surface as well. Seven stiffened element panels were fabricated with this process and quality consistency was remarkable (Figures 17 and 18).

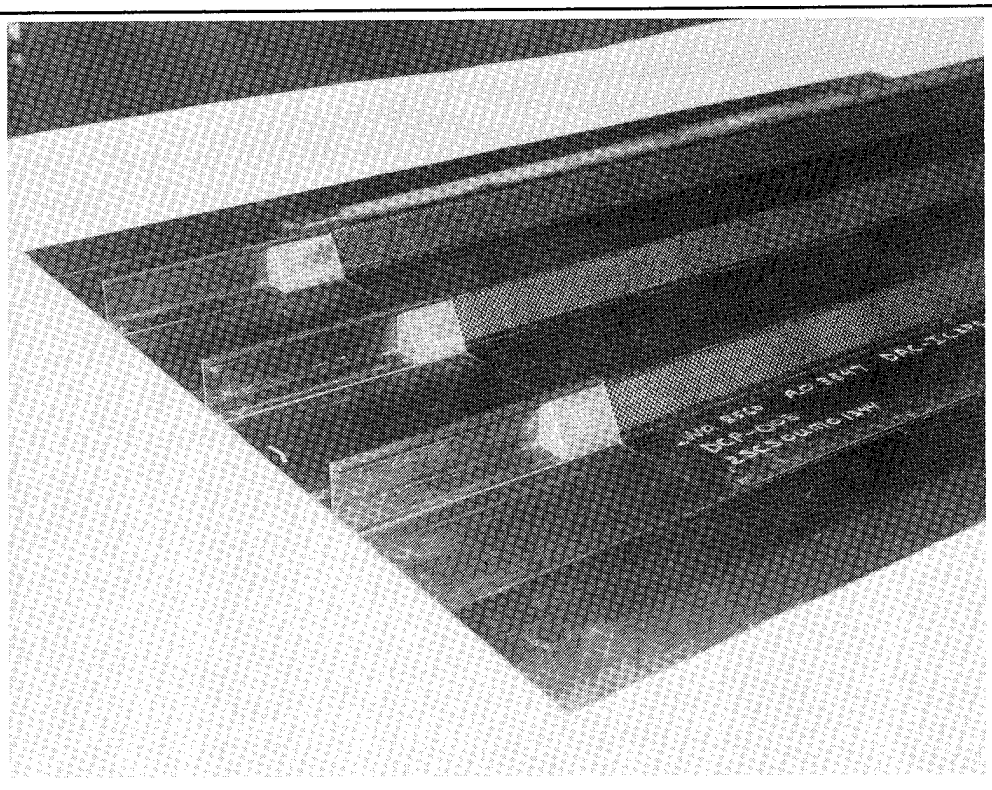


Figure 16. ICAPS element panel photo flex caul

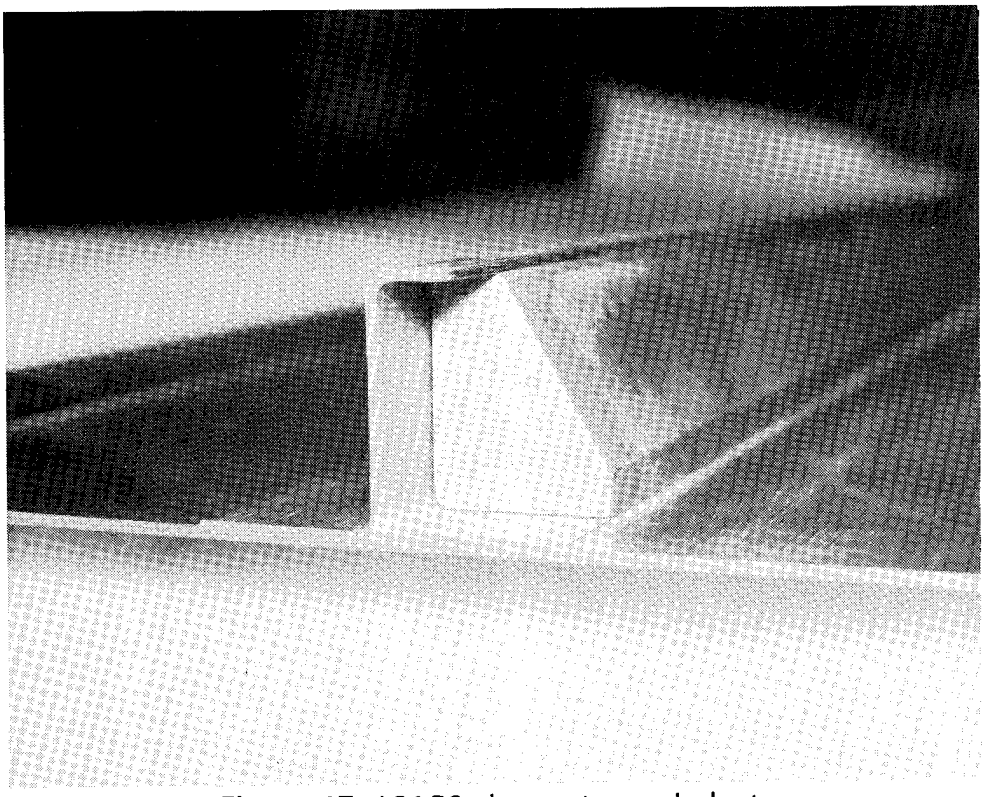


Figure 17. ICAPS element panel photo

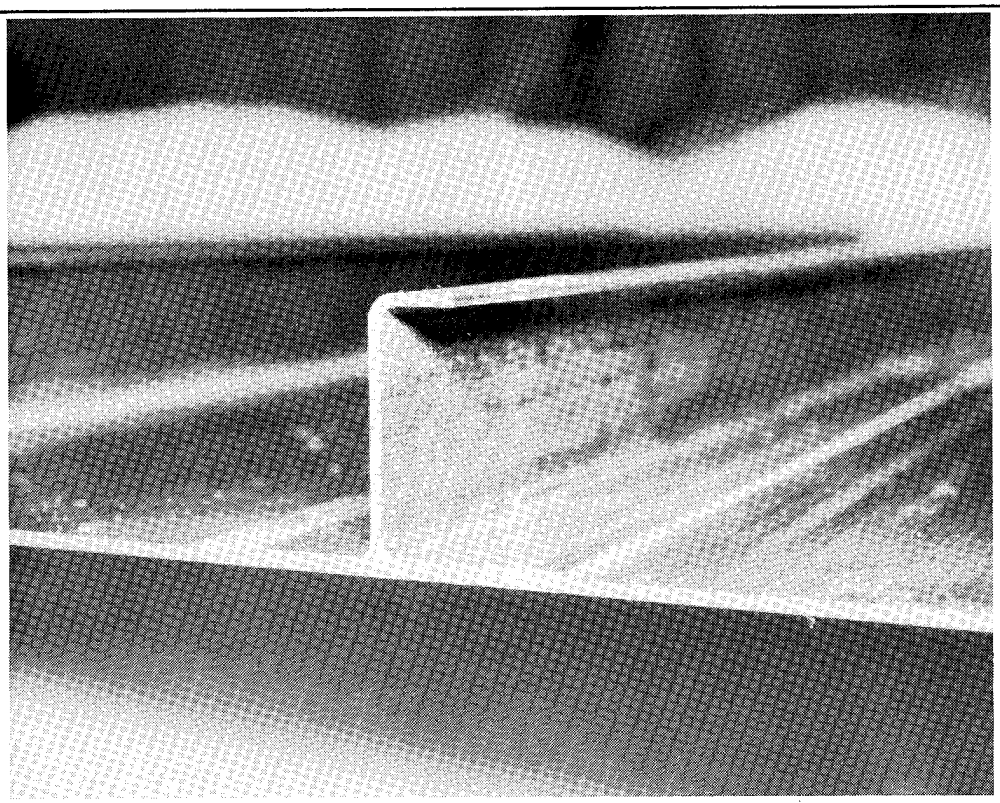


Figure 18.

The "flex caul" process will be used on the 4-ft × 5-ft curved subcomponent panels that will be fabricated later this year and in early 1991. These parts will close out our current ICAPS subcontract. We have had discussions with Douglas about future NASA related projects that we may be involved in.

Summary

At the time of this paper, Hercules has had discussions with Lockheed and Northrop about fiber placement subcontracts, but programs were not sufficiently defined to include in this paper. We look forward to demonstrating Hercules fiber placement to both Lockheed and Northrop and continuing to provide fiber placement evaluation requirements of the Boeing ATCAS and Douglas ICAPS programs as well.

Hercules is excited to be a part of the NASA Advanced Composites Technology program and we appreciate the opportunity NASA has given us to demonstrate fiber placement to the aerospace community.

Process and Assembly Plans for Low Cost Commercial Fuselage Structure

Kurtis Willden, Stephen Metschan, Val Starkey

Boeing Commercial Airplanes

Design / Manufacturing Selection Process

Cost and weight reduction for a composite structure is a result of selecting design concepts that can be built using efficient low cost manufacturing and assembly processes. Since design and manufacturing are inherently cost dependent, concurrent engineering in the form of a "Design-Build Team" is essential for low cost designs. Detailed cost analysis from DBT designs and hardware verification must be performed to identify the cost drivers and relationships between design and manufacturing processes. Results from the global evaluation are used to quantitatively rank design, identify cost centers for higher ranking design concepts, define and prioritize a list of technical/economic issues and barriers, and identify parameters that control concept response. These results are then used for final design optimization (figure 1).

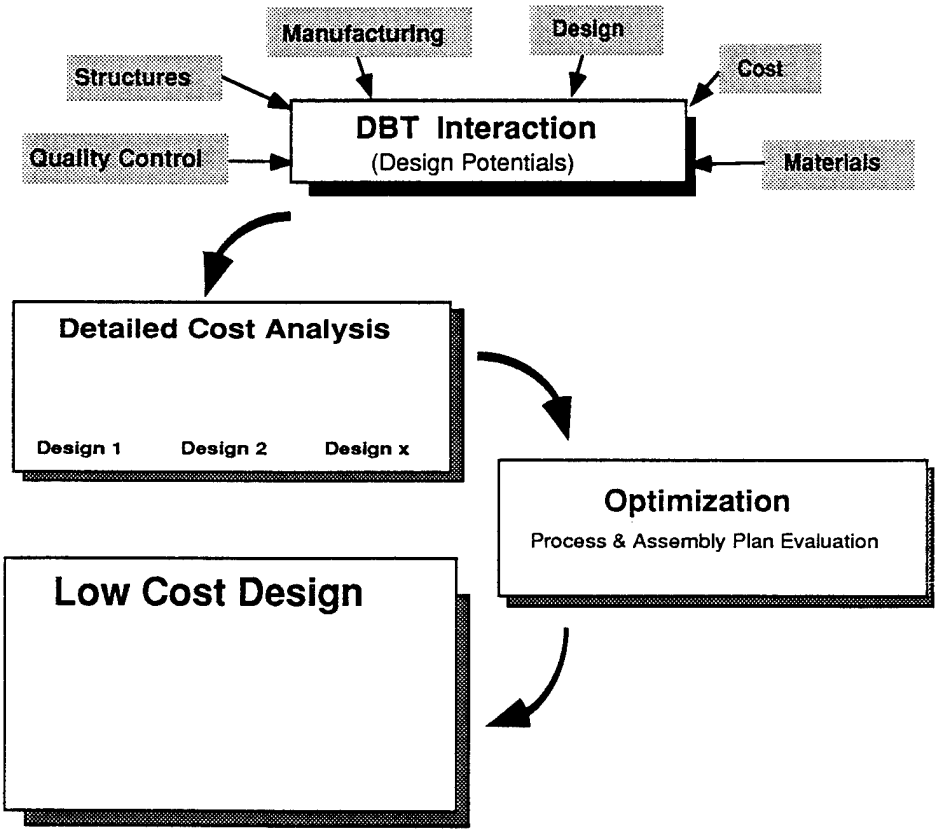


Figure 1.

Parameter Evaluation

A range of design concepts and several manufacturing processes were evaluated in order to isolate cost centers and identify cost efficient processes for a crown panel design (figure 2). A list of the major manufacturing parameters that effect cost are listed in Table 1. The cost driver for a design is not governed by one particular parameter but by the relationships of several parameters that are interdependent. Therefore, the optimal low cost design is realized when the optimal relationship is selected. These qualitative and quantitative relationships can be identified when trading design and manufacturing processes.

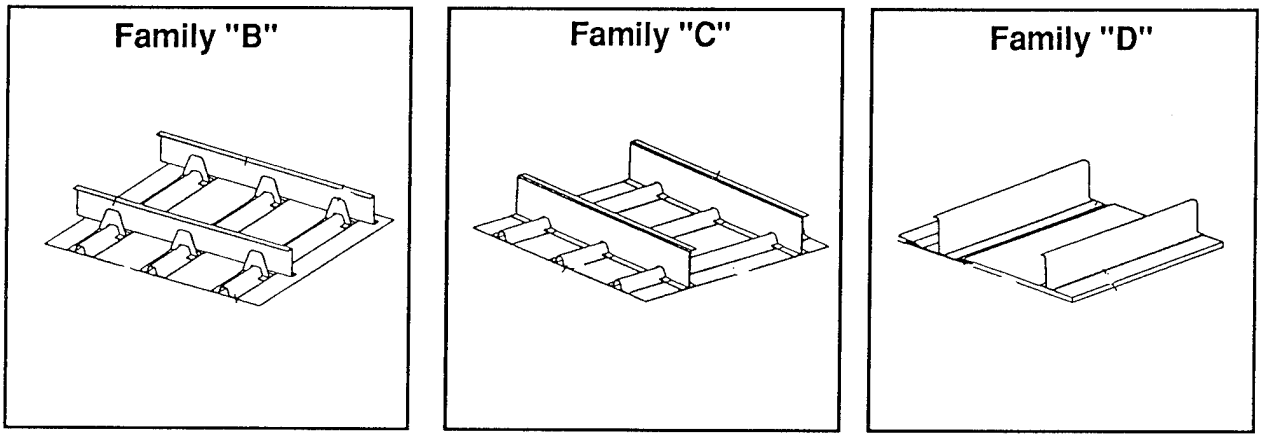


Figure 2.

Process & Assembly Parameters

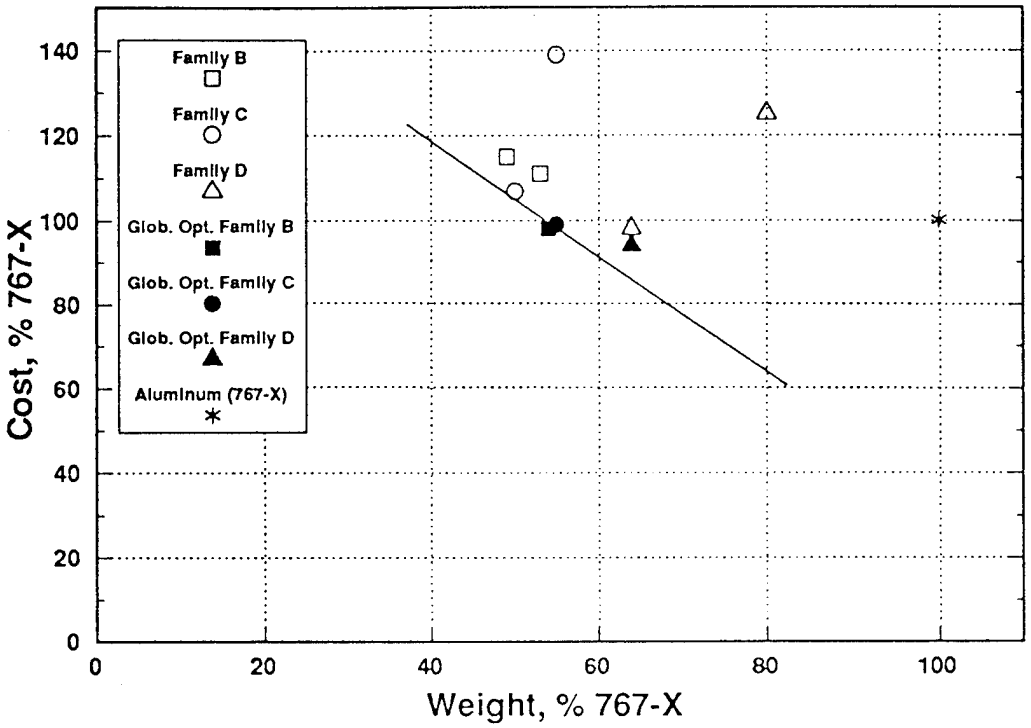
Minimize	Maximize
Material Cost / Scrap	Tolerance control
Part Complexity	Part commonality
Part Count	Automation
Tooling	Tooling Simplicity
Shimming	Material Performance
Touch Labor	Quality-Process Control
Inspection	Lay-up / Forming Efficiency
Repair	Assembly Accessibility
Maintenance	

Table 1.

Crown Panel Global Optimization

Process & Assembly Selection

The most cost effective materials, fabrication processes, and component designs were combined to provide the most cost and weight efficient design. Figure 3 shows that all designs benefited from the global optimization process with significant cost savings and little weight penalty. Although all three globally optimized designs were comparable in cost and weight, the intricate bond design is more damage tolerant (figure 3.). The globally optimized intricate bond design uses precured RTM braided frames, drape formed constant gage stringers and tow placed tailored skin cured together.



Frames

Compression Molding
Pultrusion
RTM / Textile
(Batch mode)
Stretch Forming

Stringers

Drape Formed
Pultrusion

Constant/ non Constant Gage
Precured, Cocured

Skins

Tow Placement
CTLM

Element Attachments

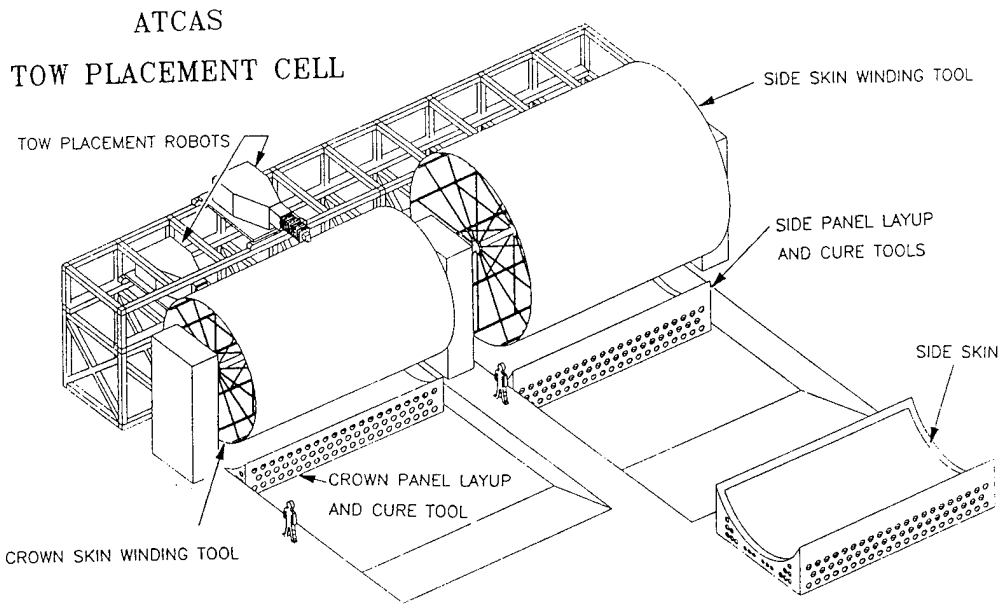
Cocure
Co-bond
Fastened

Figure 3.

Crown Panel Skin Fabrication

The ability to accurately and efficiently fabricate tailored skins on contoured surfaces with various forms of materials, makes the tow placement process ideal for crown panel fabrication (figure 4). Additional advantages are realized when considering batch mode fabrication of several crown panels on one mandrel. The same work station can also produce side and keel panels or a full barrel fuselage section. The pay-out rate for a single head ranges between 10-50 lbs./hr. depending on design requirements. Although the tow placement head has been demonstrated for a single head dispenser, additional heads that are single or multiple task oriented may be implemented. The use of multiple robot end defectors within the same work station can perform additional operations such as trimming and in-line inspection. These types of improvements could increase skin fabrication by 100% if the cost of increased efficiency is justified.

Tow Placement Work Station



- o Full Barrel Capabilities
- o Efficient Ply add/drop
- o Cut and Trim Capabilities
- o Ply Thickness Control
- o Hybrid Material Handling
- o Scrape rate 5-20%
- o Single Head rate -50 lbs./hr.
- o Temperature Conditioning

Figure 4

Crown Panel Frame Fabrication

Some of the significant cost drivers for frame fabrication that were identified from the global evaluation were dimensional tolerance control for skin-stringer bond integrity, batch mode processing, and use of raw material forms. Textile/RTM frames offer these advantages for low cost structure that can not be fully realized by other frame processes for the given design requirements. (See figure 5.) Batch mode RTM processing shows at least a 30% cost reduction over other methods for Design C1.

The RTM/ frame work station uses four key processes; 1) controlled triaxial braiding, 2) automated flange cut and fold techniques, 3) batch mode resin transfer molding of long constant gage frames, and 4) controlled edge trimming. The 17' long triaxial braided mandrels are separately braided and trimmed and then located into the mold cavity for subsequent resin transfer molding. After cure, the frames are demolded and edges and mouse holes are trimmed. The parts are then inspected for panel bond assembly. It is critical that feedback control is required for these processes to ensure part quality and cobond integrity.

RTM / Frame Work Station

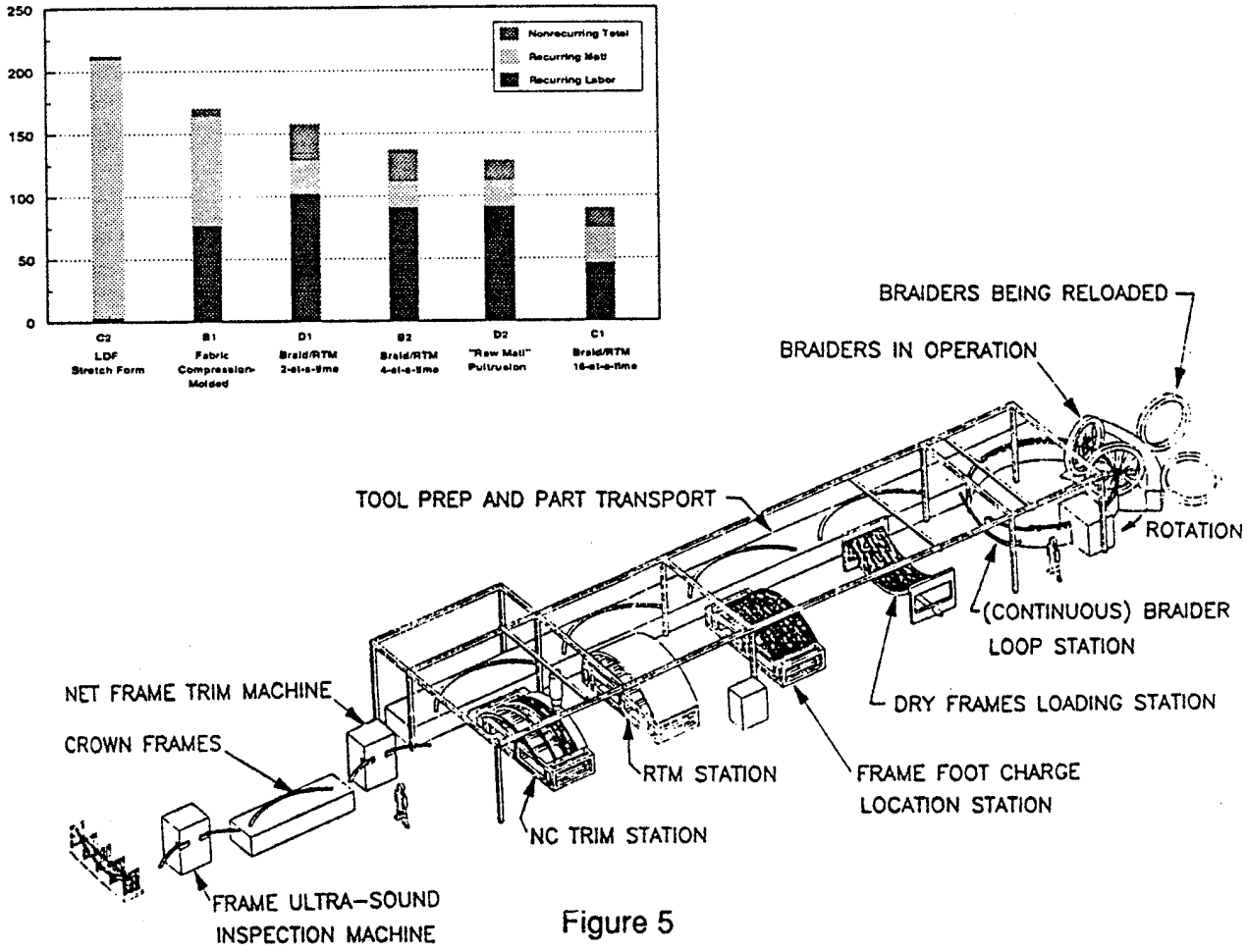
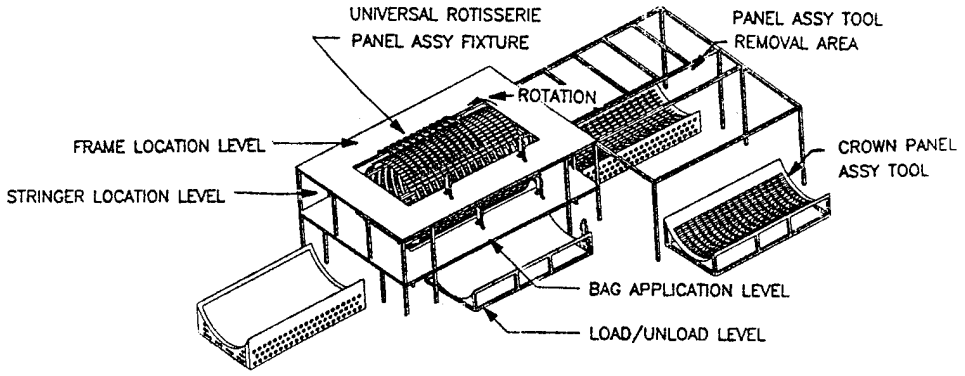
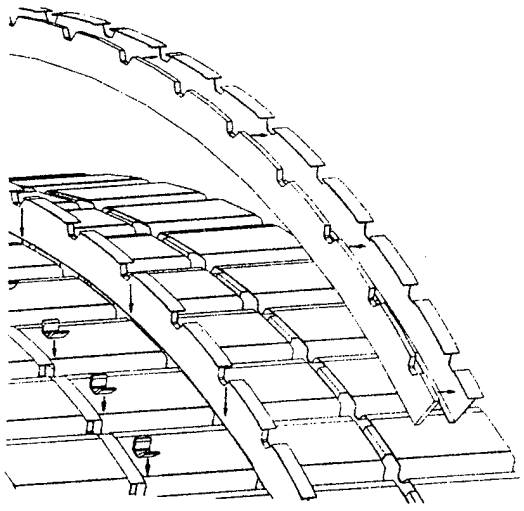


Figure 5

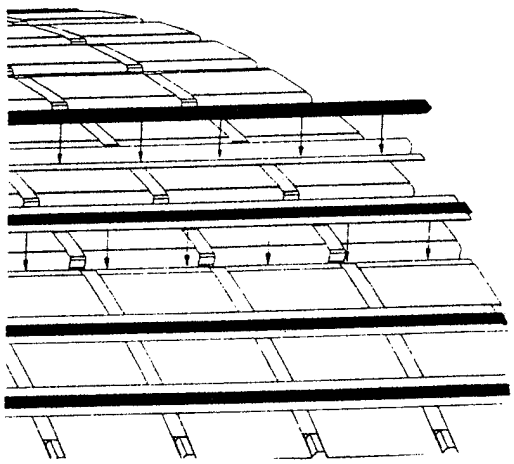
Quadrant Panel Assembly

The intricate bond design (Family "C") dictates that unique tooling concepts be employed to control component location and bond quality. One of the major concerns is the ability to locate each component and account for tolerance build-up at the stringer / frame intersections. Some tolerance pay-off can be realized with a combination of sacrificial adhesive and resin flow during cure of the skin and stringers. Due to the panel curvature, a reverse assembly of the skin, frame, and stringers is required to eliminate interference during part subassembly (figure 6). One possible tooling approach uses a reusable net shape bag/overpress located onto the rotisserie tool. The precured frames with the associated cure tooling are located into the net-shaped pockets of the overpress. Depending on the mouse hole configuration, designed pressure pads are then located into the mouse hole cavities of each frame. The uncured hat stringers are then located. After the stringers and frames have been assembled, the exposed surface can be inspected for out-of-tolerance conditions. The skin and stringer / frame subassembly are then collocated with the prefabricated skin into a OML cure tool.





Frame and Pressure Pad Insertion

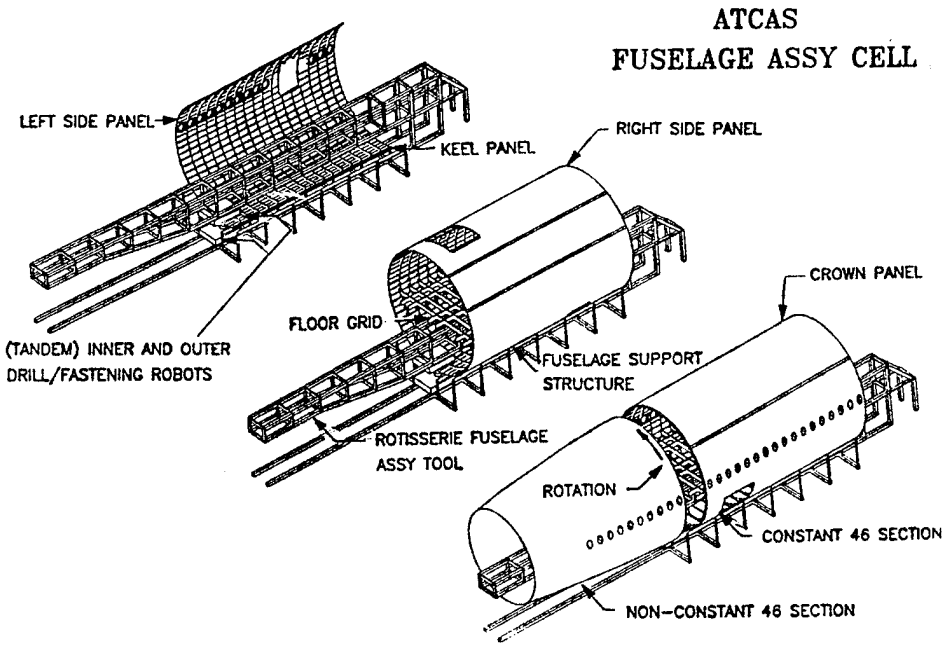


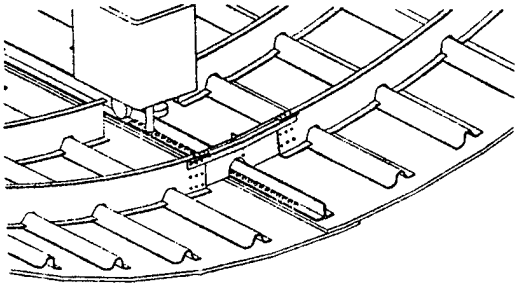
Stringer Insertion

Figure 6

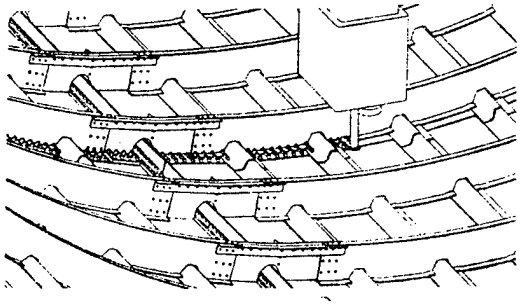
Fuselage Assembly

Low cost assembly of large stiff composite panels assumes that panel warpage as well as stringer and frame alignment are controlled to minimize expensive detail splicing. This requirement can only be maintained by controlling all previous subassembly fabrication processes. The four panel assembly process starts by overlapping the side panels with the keel panel as shown in figure 7. Tandem multi-head robots drill, clean, insert, and fastens the bolts along the lap joints. The precured composite frame splices are then installed along the lap joint. The crown panel is installed in the same fashion so that it overlaps the two side panels. After all the frame splices have been installed, the adjoining body section is mated and the circumferential joint is fastened. An internal splice plate is located and fastened to the two fuselage sections and stringer splices are installed. The remaining sections are assembled and mated with the same process.





Lap Splice and Frame Splice



Circumferential and Stringer Splices

Figure 7

Fuselage Factory Concept

The cost for building a composite fuselage section depends on the factory logistics. Since the quadrant panels are 21' x 32', material, part handling, and work cell capacity must be coordinated to avoid a factory flow bottle-neck syndrome. Fig. 8 shows one possible scenario of a composite fuselage factory based on some of the results of the crown panel evaluations. Each work station is automated except where cost is prohibitive or manual intervention does not effect part quality. An automatic guided delivery and retrieval vehicle is used to transfer parts or material to the requesting work station. Quality control is maintained at each work station with techniques such as Statistical Process Control instead of the traditional step by step inspection.

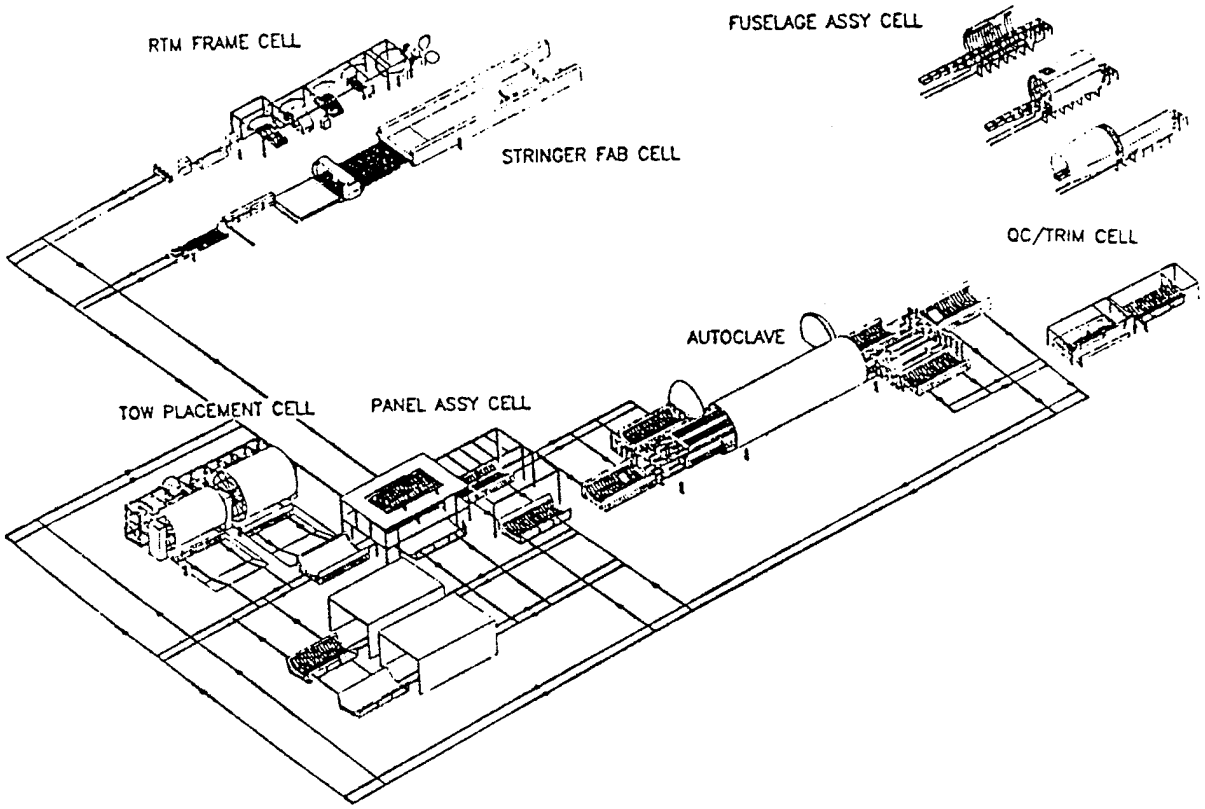


Figure 8.

Program Status

Several tests and hardware coupons are or have been completed to understand the cost impact of material /structural performance and manufacturing processes for low cost structure. (See figure 9.) Low cost damage tolerant materials and processibility of these materials are under investigation and will be demonstrated in support of the near term local optimization for the crown panel and future activities with the keel and side panels. Panel warpage and part tolerance control will be demonstrated with innovative tooling, fastening, and splice details.

To Date

- **Tow placed flat hybrid panels**
  (AS4 / S-2, AS4 / T-1000)
- **Tow placed tailored hat and blade panels**
  (combinations of 977-2, 938, AS4, IM6, RC 35%,44%)
- **Thermoplastic fastener trials**
- **Tooling trials for blades, hats, and intricate bond**

Near Term

- **Large Intricate bond demonstration panels**
  (Tooling Development 8'x9')
- **RTM-braided frames (3'-10')**
- **Panel warpage / assembly evaluations**
- **Innovative design splices**

Figure 9.

Fiber Placement of Tappered Stiffened Panel

Figure 10 shows one of the eight fiber placed panels (24" x 110") produced by Hercules on the seven axis fiber placement machine. Eight panels with various combinations of resins (Fiberite 938, 977-2), resin contents (35 %, 44%), fibers (AS4, IM6), and stringer geometries (blade, hat) were fabricated for impact damage evaluations. The blade and hat stringers were also tow placed into charges and then individually trimmed and formed. The panel thickness varied from 12 plies to 24 plies. Each tow was conditioned to a .0074" tow thickness for uniform panel thickness control. The flexible hat cocure tooling permitted the stringer to conform to the tapered skin without sacrificing bond quality.

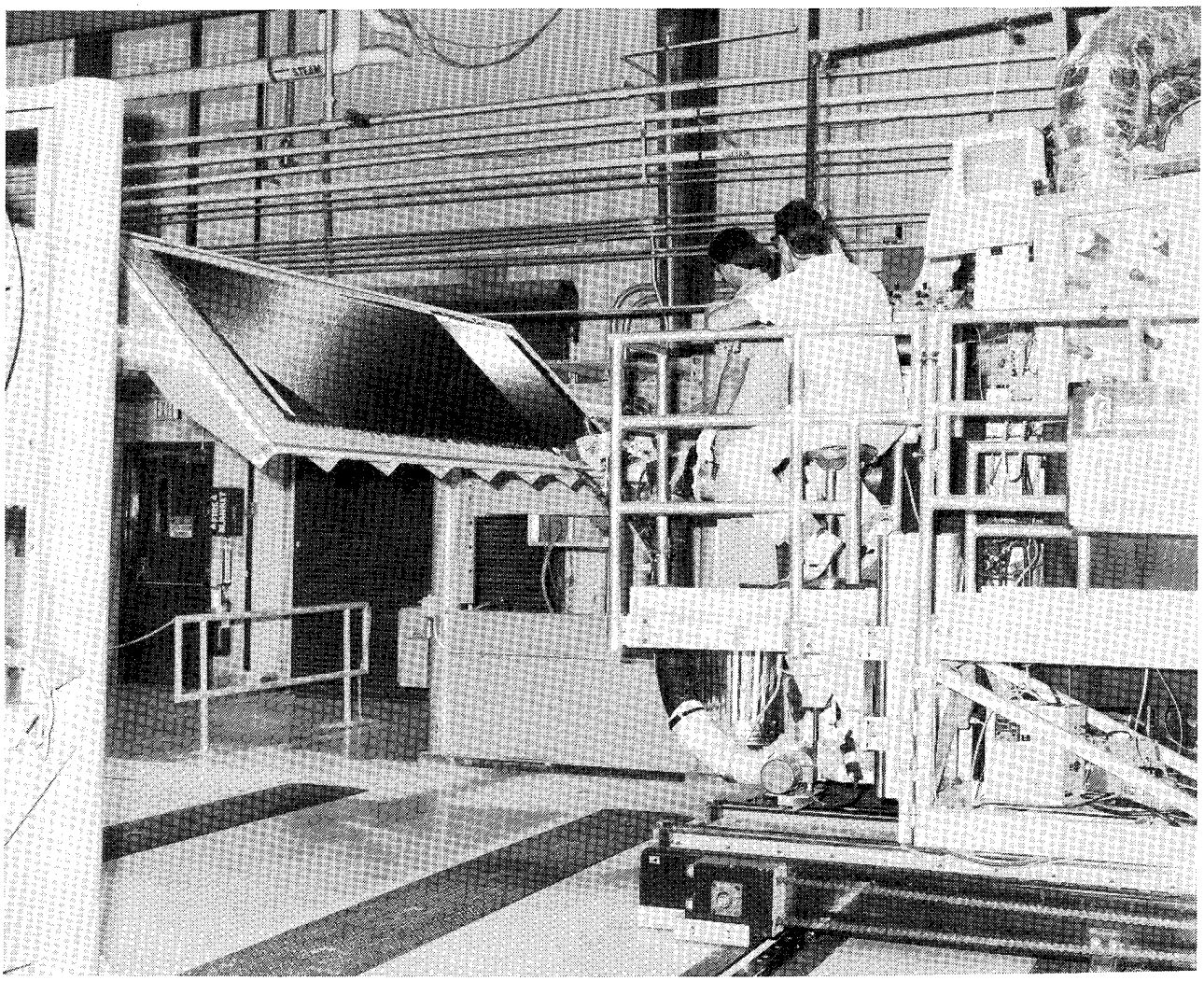


Figure 10.

Fiber Placement of Hybrid Panel

Figure 11. shows one of the seven intraply hybrid panels that were fabricated by Hercules with the fiber placement process. To determine relationship between tension/ fracture performance and material cost, S-2 glass and T-1000 fibers were used to hybridize a AS4/938 system (57% fiber volume). Hybridizing - fiber ratios of 25% and 50% of S-2/AS4 fiber were used to determine the cost/weight impact of a less expensive, lower stiffeness fiber. A second combination of T-1000 (25%) / AS4 fibers was also used to determine weight reduction with a more expensive, higer performance fiber. A twelve or four tow repeat pattern was used for the various fiber combinations to evaluate the performance impact of tow pattern sequence.

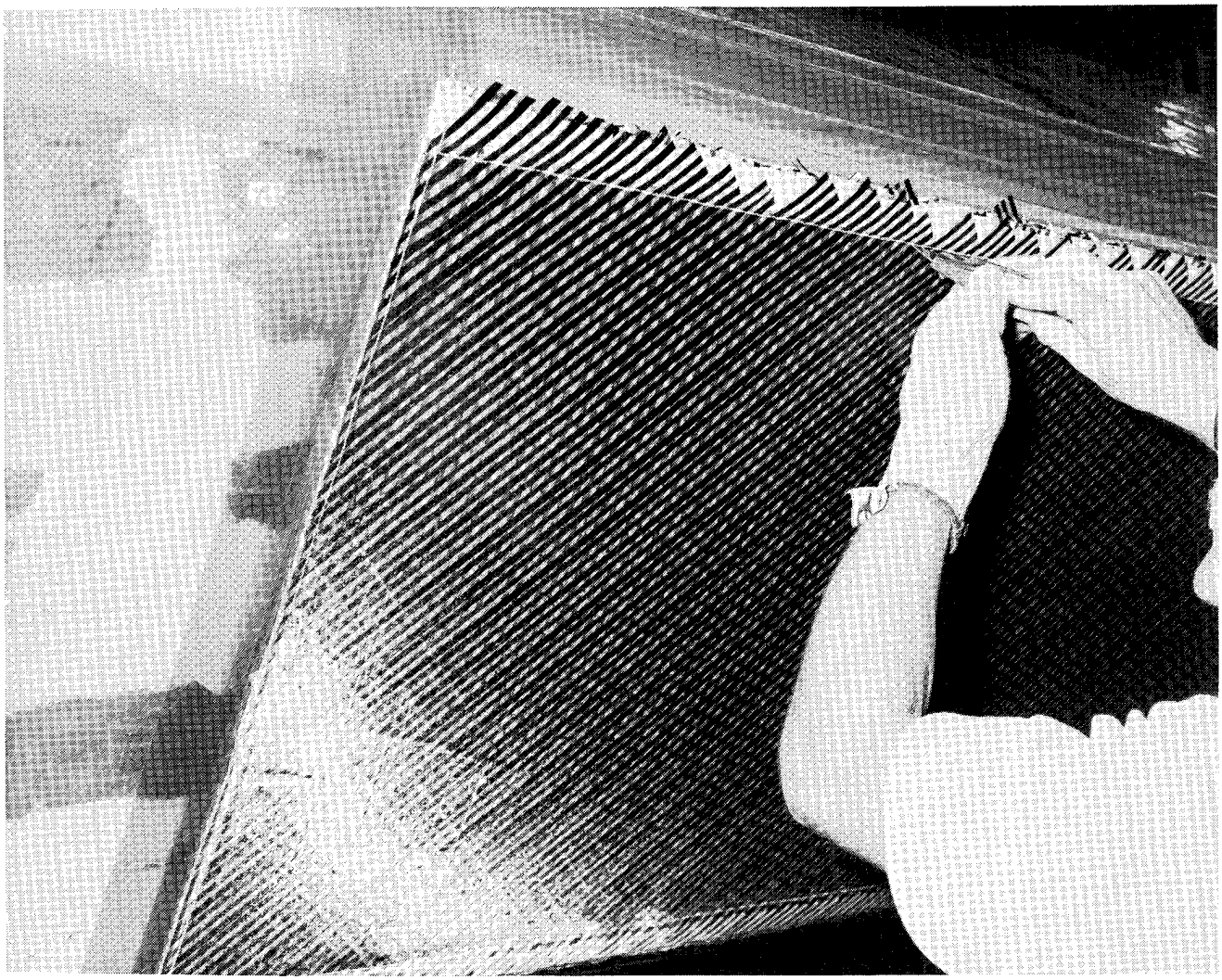


Figure 11.

BIOGRAPHY

Kurtis S. Willden, ATCAS Manufacturing Lead Engineer
Boeing Commercial Airplanes

Graduated from Brigham Young University with a Bachelor and Masters degree in Mechanical Engineering. Experience includes advanced research and development of manufactured composite structures with General Dynamics and Boeing.

PROGRESSIVE FAILURE METHODOLOGIES FOR PREDICTING RESIDUAL STRENGTH AND LIFE OF LAMINATED COMPOSITES

Charles E. Harris[1]
David H. Allen[2]
T. Kevin O'Brien[3]

ABSTRACT

This paper describes two progressive failure methodologies currently under development by the Mechanics of Materials Branch at NASA Langley Research Center. The "damage tolerance/fail safety methodology" developed by O'Brien is an engineering approach to ensuring adequate durability and damage tolerance by treating only delamination onset and the subsequent delamination accumulation through the laminate thickness. The "continuum damage model" developed by Allen and Harris employs continuum damage mechanics concepts and uses loading history dependent damage growth laws to predict laminate strength and life. The philosophy, mechanics framework, and current implementation status of each methodology are presented in the paper.

INTRODUCTION

The next generation commercial transport aircraft are likely to have a significant amount of primary airframe structure fabricated of advanced composite materials with graphite fiber reinforcement in an organic matrix. The damage tolerance characteristics of composite materials are fundamentally different from monolithic metallic materials and, therefore, cannot be predicted by current metals-based methods. For example, composite structures are not susceptible to the development of dominant macro-cracks through the fatigue growth of micro-cracks as are metallic structures. Therefore, there is no single parameter such as the stress intensity factor that can be used to predict crack growth and the subsequent residual strength of a composite structure. However, microcracking frequently develops in a progressive fashion leading to laminate failure. Zones of damage (sublaminate cracking) may develop in high strain gradient fields produced by geometric discontinuities and may also be produced by foreign object impacts. These zones of damage may consist of intraply matrix cracks, local fiber fracture, and interply delaminations. The individual damage mechanisms are often interactive with one mode of damage being the initiator of a second mode of damage. At the local level, these zones of damage will result in the failure of the principal load-carrying plies which will eventually

[1]Head, Mechanics of Materials Branch, NASA Langley Research Center
[2]Professor, Aerospace Engineering Department, Texas A&M University
[3]Senior Scientist, U.S. Army Aerostructures Directorate, NASA Langley Research Center

precipitate global structural failure. Additionally, the local damage development will also effect the global structural response through changes in the local stiffness properties which will alter the structural load paths. Therefore, an iterative analysis procedure between the global and local levels is required to rigorously predict progressive damage development leading to structural failure.

Two progressive failure methodologies are being independently developed in the Mechanics of Materials Branch at NASA Langley Research Center. While considerable synergism exits between the two efforts, the two models are being developed from quite different mechanics philosophies. The damage tolerance/fail safety methodology developed by O'Brien is an engineering approach to ensuring adequate durability and damage tolerance by treating only delamination onset and the subsequent delamination accumulation through the laminate thickness. On the other hand, the continuum damage model developed by Allen and Harris employs continuum damage mechanics concepts and uses loading history dependent damage growth laws to predict laminate strength and life. This paper will review the mechanics formulation of each methodology and will discuss recent advances in using the methods to analyze relevant structural geometries.

The purposes of this paper are to establish the philosophy guiding the development of each methodology, to review the model formulations, and to establish the current progress toward structural analysis implementation. It is well beyond the scope of this paper to present all of the mathematical details associated with the two subject methodologies. The details of the mathematical formulations have been previously published by the authors and references to these publications are cited throughout this paper. The interested reader is strongly encouraged to review the references and contact the authors for further details or to discuss issues for clarification.

PART I: DAMAGE THRESHOLD/FAIL SAFETY APPROACH

Many papers have been published recently where the rate of delamination growth with fatigue cycles, *da/dN*, has been expressed as a power law relationship in terms of the strain energy release rate, *G*, associated with delamination growth [*1-4*]. This fracture mechanics characterization of delamination growth in composites is analagous to that of fatigue crack growth in metallic structures, where the rate of crack growth with cycles is correlated with the stress intensity factor at the crack tip. However, delamination growth in composites occurs too rapidly over a fairly small range of load to be incorporated into a classical damage tolerance analysis for fail safety [*2,5,6.*]. While in metals the range of fatigue crack growth may be described over as much as two orders of magnitude in *G*, the growth rate for a delamination in a composite is often characterized over barely one order of magnitude in *G*. Hence, small uncertainties in the applied load may yield large (order of magnitude) uncertainties in delamination growth.

Different damage mechanisms may also interact with the delamination and increase the resistance to delamination growth. Delamination growth resistance curves may be generated to characterize the retardation in delamination growth from other mechanisms [*7-9*]. These delamination resistance curves are analogous to the R-curves generated for ductile metals that account for stable crack growth resulting from extensive

plasticity at the crack tip. However, unlike crack-tip plasticity, other composite damage mechanisms, such as fiber bridging and matrix cracking, do not always retard delamination growth to the same degree. Hence, the generic value of such a characterization is questionable.

One alternative to using the classical damage tolerance approach for composites as it is used for metals would be to use a strain energy release rate threshold for no delamination growth and design to levels below this threshold for infinite life. Composites materials are macroscopically heterogeneous, with stiffness discontinuities that give rise to stress singularities at known locations, such as straight edges, internal ply drops, and matrix cracks. Although these singularities are not the classical $r^{-1/2}$ variety observed at crack tips, and hence cannot be characterized with a single common stress intensity factor, they can be characterized in terms of the strain energy release rate, G, associated with the eventual delamination growth.

The most common technique for characterizing delamination onset in composite materials is to run cyclic tests on composite specimens, where G for delamination growth is known, at maximum load or strain levels below that required to create a delamination under quasi-static loading. A strain energy release rate threshold curve for delamination onset may be developed by running tests at several maximum cyclic load levels and plotting the cycles to delamination onset versus the maximum cyclic G, corresponding to the maximum cyclic load or strain applied [*10-14*]. This G threshold curve may then be used to predict delamination onset in other laminates of the same material, or from other sources in the same laminate [*10-15*].

One concern with a no-growth threshold design criteria for infinite life has been the uncertainty inherent in predicting service loads. If service loads are greater than anticipated, then corresponding G values may exceed no-growth thresholds and result in catastrophic propagation. This concern is paramount for military aircraft and rotorcraft, where original mission profiles used to establish design loads are often exceeded once the aircraft is placed in service. However, unlike crack growth in metals, catastrophic de'amination growth does not necessarily equate to structural failure. In situations where the structure experiences predominantly tensile loads, such as composite rotor hubs and blades, delaminated composites may have inherent redundant load paths that prevent failure and provide a degree of fail safety [*5*]. This degree of fail safety has led some designers to think of composite delamination as a benign failure mode. Unfortunately, delaminations may occur at several locations in a given component or structure. Delaminations will typically initiate at edges, holes, ply drops, and ultimately, matrix cracks. Hence, a composite mechanics analysis that considers each of these potential sites must be performed to ensure that the structure is fail safe. Previously, a damage-threshold/fail-safety approach for composite fatigue analysis was proposed [*5*] that involved the following steps:

1. Predict delamination onset thresholds using fracture mechanics.

2. Assume delamination threshold exceedence corresponds to complete propagation.

3. Determine the remaining load-carrying capability of the composite with delamination present using composite mechanics (i.e., check for fail safety).

4. Iterate on Steps 1 to 3 to account for multiple sources of delamination.

This type of analysis need only be applied to primary structures. However, Step 1 may be used to demonstrate the delamination durability of any composite structure, thereby providing an assessment of component repair or replacement costs over anticipated structural service lives. Step 2 reflects a conservative way to deal with the rapid delamination growth rates observed relative to metals as discussed earlier. An alternative to Step 2 would be to predict delamination growth rates using growth laws that incorporate *R*-curve characterizations, thereby taking into account the resistance provided by other damage mechanisms. Such a characterization has been attempted previously [9], but should be used with caution because it is not truly generic. A third approach for Step 2 is to monitor stiffness loss in real time, and hence reflect the consequence of delamination growth, and other damage mechanisms, as they occur. However, in most structural applications, real-time monitoring of stiffness loss may not be practical, so the conservative approach outlined in Step 2 would be applied. Finally, Step 3 acknowledges that the residual strength of the composite is a function of laminate structural variables (such as layup, stacking sequence, and ply thickness), and it is not uniquely a question of material characterization. Hence, the damage-threshold/fail-safety concept offers both the benefits of generic material characterization using fracture mechanics, while reflecting the unique structural character of laminated composite materials.

Tension Fatigue Life Prediction: A Case Study

The damage-threshold/fail-safety approach was used to predict the tension fatigue life of graphite/epoxy, glass/epoxy, and glass/graphite/epoxy hybrid laminates [*16*]. First, delamination onset behavior for the glass/epoxy and graphite/epoxy materials in fatigue was characterized in terms of the strain energy release rate using edge delamination onset fatigue data. Then, stiffness loss associated with damage onset and growth was measured. Next, the influence of local delaminations from matrix cracks on the strain in the load-bearing zero degree plies was quantified. The onset of local delaminations through the laminate thickness was predicted using a strain energy release rate solution for local delamination. Finally, fatigue life was determined by predicting the accumulation of these local delaminations through the thickness, calculating their effect on the strain in the zero degree plies, and comparing this local strain to the increase in global strain due to stiffness loss associated with damage.

Delamination Onset Characterization

Delamination onset behavior for the glass/epoxy and graphite/epoxy materials in fatigue was characterized in terms of the strain energy release rate using edge delamination onset fatigue data. Fig. 1 compares fatigue delamination onset criteria for E-glass/epoxy and graphite/epoxy laminates with the same epoxy matrix. The lines shown in Fig.1 are fit through the lowest data point for quasi-static and cyclic loading, and hence, represent a lower bound characterization of delamination onset. Linear plots of the

maximum cyclic G versus log N, the number of cycles to delamination onset, were generated yielding a linear delamination onset criteria in the form

$$G = m \log N + G_c \qquad (1)$$

where G_c and m are material parameters. The slope, m, was the same for both materials; however, the static G_c values were lower for the glass/epoxy because the glass/epoxy laminates failed in the fiber matrix interface.

Stiffness Loss

In order to predict stiffness loss as a function of fatigue cycles, the onset and growth of damage must be characterized in terms of a generic parameter that is representative of the composite material being tested, but is independent of laminate structural variables such as lay-up, stacking sequence, and ply thickness. For delamination, this characterization is typically achieved using the strain energy release rate. For example, Fig. 2 shows the steps that would be required to predict stiffness loss associated with delamination as a function of fatigue cycles using a G characterization of delamination onset and growth. First, plots of the maximum cyclic G versus log N must be generated to characterize the onset of delamination [*5,6,12,15*] and power law relationships between G_{max} and the rate of growth of delamination with fatigue cycles are needed to characterize damage growth [*1-4,6*] (Fig. 2*a*). Using these material characterizations, the increase in delamination size, a, with fatigue cycles may be predicted (Fig. 2*b*). This information, in turn, may be used to predict the decrease in modulus with cycles associated with delamination, which, when combined with the stiffness loss due to other mechanisms that may be present (such as matrix plasticity and matrix cracking) yields the increase in global strain with cycles for a constant cyclic stress amplitude test (Fig. 2*c*).

Although the steps outlined above are straightforward, application of this procedure is complicated by the interaction between matrix crack formation and delamination growth, making it difficult to achieve a generic characterization of either one alone [17]. Therefore, instead of trying to predict stiffness loss as outlined in Fig. 2, stiffness loss was monitored experimentally. However, regardless of whether stiffness loss is measured or predicted, knowledge of the increase in global strain with cycles resulting from a loss in stiffness as damage accumulates is necessary, but not sufficient, to predict fatigue life. The final failure of the laminate is governed not only by loss in stiffness but also by the local strain concentrations that develop in the primary load-bearing plies (which in most laminates are zero-degree plies) as local delaminations originating at matrix ply cracks accumulate through the laminate thickness.

Strain Concentrations in Zero Degree Plies

Figure 3*a* shows that fatigue failures typically occur after the global strain has increased because of the fatigue damage growth, but before this global strain reaches the global strain at failure ε_F, measured during a static strength test [*11,15,18,19*]. Therefore, local strain concentrations must be present in the zero-degree plies that control the laminate strength. Once delaminations initiate at matrix ply cracks anywhere through the

laminate thickness, the local strain will increase significantly throughout the remaining through-thickness cross section [*5,11,16,18-21*]. These local strain concentrations may be calculated simply as

$$K_\varepsilon = E_{LAM}t_{LAM} / E_{LD}t_{LD} \qquad (2)$$

where E and t are the moduli and thickness, respectively, of the original laminate (LAM) and the locally delaminated region (LD) which consists of the original laminate minus the cracked off-axis plies. These local strain increases may not have an immediate influence on the global strain measurement because delaminations starting from matrix cracks grow very little once they form. However, enough of them will eventually form to have some contribution to the global stiffness loss. The local strain concentration in the zero degree plies, however, is present as soon as the local delamination forms. If several delaminations form at matrix cracks throughout the laminate thickness at one location, then the local strain on the zero-degree plies at that location may reach the static failure strain, resulting in fatigue failure (Fig. 3*b*).

Each time a delamination initiates from a matrix crack, the local strain in the remaining through-thickness cross section, and hence in the zero-degree plies, increases to an amount equal to K_ε times the global cyclic strain, ε_{max}, until it reaches the static failure strain, ε_F, (Fig. *4a*). A simpler way to visualize this process, however, is to reduce the static failure strain to some effective global ε_F value each time a new local delamination forms through the thickness. Hence, the effective ε_F would be equal to $\varepsilon_F/K_\varepsilon$. As local delaminations accumulate through the thickness, the effective ε_F would decrease incrementally. Meanwhile, the global strain would be rising due to stiffness loss associated with damage. Fatigue failure would correspond to the number of cycles where the damage growth increased the global maximum cyclic strain, ε_{max}, to the current value of the effective ε_F (Fig. *4b*). This approach does not require a prediction of damage growth with fatigue cycles if the laminate stiffness loss, and hence the increase in global strain, can be monitored in real time. When this is possible, only the incremental decreases in the effective ε_F associated with local delamination accumulation through the thickness need to be predicted to determine fatigue life.

Local Delamination Onset Prediction

The number of fatigue cycles to onset of each local delamination through the thickness was predicted by using the linear delamination onset criteria with the strain energy release rate for the locally delaminated region (Fig.5) [*16*]. As shown in Fig.5, the thickness and modulus terms in the G equation for local delamination change for each successive local delamination that forms through the thickness. Therefore, as local delaminations accumulate through the thickness under a constant σ_{max}, the driving force (i.e., G) for each new delamination changes. Hence, fatigue life prediction for composite laminates requires a "cumulative damage" calculation, even for constant amplitude loading.

For the hybrid laminates [17], the number of cycles required for onset of local delaminations between two graphite/epoxy plies was predicted using G_C and m values for graphite/epoxy. The number of cycles required for onset of local delaminations that occurred between two glass/epoxy plies, or between adjacent glass/epoxy and graphite/epoxy plies, was predicted using the G_C and m values for glass/epoxy. As each local delamination formed through the laminate thickness, the reduction in the effective failure strain of the zero degree plies was calculated as outlined in the previous section.

Fatigue Life Determination

As previously mentioned, fatigue failure was assumed to occur when the increased global strain in the laminate, determined from measured stiffness loss, reached the reduced effective failure strain in the zero degree plies, resulting from the accumulation of local delaminations through the laminate thickness (Fig.4b). However, because of the scatter in the experimental data due to the variation in laminate modulus (i.e., the variation in ε_{max}) and the variation in static failure strain from specimen to specimen, a range of fatigue lives was determined for each stress level rather than a single value of life (Fig. 6). Figure 7 shows the fatigue life determination for $[45/-45/0]_s$ hybrid laminates. The agreement between measured and calculated fatigue lives was very good, although calculated values were somewhat conservative at the higher cyclic loads.

In this tension fatigue case study, as each local delamination formed, ε_F was reduced by the appropriate K_ε to obtain an effective ε_F that was compared with the current value of ε_{max}, based on measured stiffness loss, to determine if fatigue failure had occurred. Hence, the ability to predict local delamination onset, and its effect on ε_F, facilitates the use of measured stiffness loss to determine fatigue life. However, for many composite structures, real-time stiffness measurement may not be practical. In these cases, the conservative approach for Step 2 in the damage-threshold/fail-safety approach outlined earlier could be applied. If the conservative approach was used to predict the tension fatigue life of $[45/-45/0/90]_s$ laminates, for example, stiffness would decrease incrementally, i.e., ε_{max} would increase incrementally, with the onset of each damage mechanism. Figure 8 shows a sketch for conservative fatigue life prediction in $[45/-45/0/90]_s$ graphite/epoxy and glass/epoxy laminates. Because matrix cracks can develop under static loading, ε_{max} is increased in the first load cycle, corresponding to the stiffness loss associated with saturation crack spacing in the off-axis plies. This stiffness loss would be greater for glass/epoxy laminates than for graphite/epoxy laminates [*15*]. When edge delamination occurs in the 0/90 interfaces, ε_{max} will increase again, corresponding to complete delamination across the laminate width. This stiffness loss would be greater for graphite/epoxy laminates than for glass/epoxy laminates [*15*]. However, ε_F would not change because edge delaminations do not create local strain concentrations in the zero-plies [*16*]. As each local delamination forms, the effective ε_F will decrease incrementally

based on the appropriate K_ε, and ε_{max} will increase incrementally, corresponding to delamination growth throughout the particular interface. When enough local delaminations form through the thickness such that $(\varepsilon_{max})_i \geq (\varepsilon_F)_i$, fatigue failure will occur.

Damage-Threshold/Fail-Safety Approach for Compression and Low-Velocity Impact

In the previous case study, and in the examples cited in Ref *5*, the damage-threshold/fail-safety approach was illustrated for problems that involved only tension loading. However, this same approach may be applied to laminates subjected to compression loading. Delamination onset characterization would be conducted in the same way, with only the assessment of fail safety (Step 3) changing significantly.

The significance of accumulated delaminations on compression strength has been documented previously by comparing the strength of graphite epoxy $[45/-45/90/0/45/-45/0_2/45/-45/0_2]_s$ wing skin laminates with one, two, or three implanted delaminations through the thickness to identical laminates with either barely visible or visible impact damage (Fig. 9) [*22*]. These results show that the compression strength for laminates with 5.08 cm (2.0 in.) diameter implanted delaminations, normalized by the compression strength for the same laminates with a 6.33-mm (l/4-in.) open hole, decreases as the number of delaminations increases through the thickness. Still lower compression strengths were observed for the impacted laminates, which typically contain delaminations in nearly every interface [*23*]. Similar studies have compared the residual compression strength of virgin laminates, or laminates that had implanted delaminations in a single interface, to identical laminates without implants that had undergone low-velocity impact with subsequent cycling [*24,25*]. For example, Fig. 10 shows a plot of cycles to failure as a function of stress amplitude for $[0/90/0/45/-45/0]_s$ graphite/epoxy laminates subjected to fully reversed cyclic loading, either in the initially undamaged state, or following an impact with a energy per unit thickness of 1790 J/m [*25*]. The data in Fig. 10 indicate that the compression strength after impact is very low compared with the fatigue behavior of the virgin laminate. Furthermore, most of the strength reduction occurs after the impact, with very little degradation due to subsequent cyclic loading.

For composites loaded in compression, final failure is not necessarily determined by the local strain concentration in the zero-degree plies, but often results from a global instability that occurs after delaminations accumulate through the thickness and become locally unstable. The sublaminates that are formed by the delaminations may buckle locally which in turn may lead to more delaminations forming in adjacent interfaces and subsequently buckling. Because of this progressive buckling mode of failure, compression fatigue lives are typically much lower than tension fatigue lives for identical laminates subjected to identical load amplitudes [*25*]. Combined tension/compression fatigue lives may be reduced even further as a result of delaminations forming from matrix cracks under tension loads and then growing as a result of local instabilities under the compression loads [*26*]. In each case, however, the final failure results from an accumulation of delaminations through the thickness. The damage-threshold/fail-safety approach could be used to estimate fatigue lives in each case. First, delamination onset would be predicted using an appropriate analysis for G depending upon the source of the original

delamination. Next, delaminations would be assumed to grow throughout the interface immediately, or solutions for instability driven delamination growth in compression would have to be incorporated if stiffness loss could not be monitored directly in real time. Several fracture mechanics models have been developed for the growth of through-width and elliptical patch delaminations in a single interface [*27,28*] These analyses would have to be extended to model laminates with multiple edge delaminations to simulate compression fatigue damage and laminates with multiple delaminations that were formed by matrix cracks to simulate tension/compression fatigue damage. Finally, fail safety may be assessed in compression, as delaminations form near the surface and then accumulate through the thickness, using appropriate analyses for local and global buckling of the damaged laminate.

These same models could be used to evaluate the consequence of low-velocity impact damage. Previous studies have shown that low-velocity impact damage develops as extensive matrix cracking and associated delaminations through the thickness [*23,29*]. Delamination onset in these cases has been modeled as delaminations initiating from matrix cracks under bending loads [*30*]. In brittle matrix composites, impacts that are barely visible on the impacted surface may be extensive throughout the laminate thickness. This extensive delamination results in greatly reduced compression strength. Subsequent cyclic loading may create only slightly greater damage growth, which would explain the relatively flat *S-N* curves observed for impacted brittle matrix laminates (Fig. 10). Tougher matrix composites, however, suppress some of the delaminations that would otherwise form through the thickness during the impact [*29*]. Therefore, the compression strength following impact is greater than the compression strength for similar laminates with brittle matrices, but cyclic loading subsequent to an impact may cause further damage and corresponding reductions in residual compression strength. In either case, the damage-threshold/fail-safety approach may be used to characterize the delamination onset and assess the fail safety of the damaged laminate.

PART II: CONTINUUM DAMAGE MODEL

The foundation of the progressive failure methodology developed by Allen and Harris is a constitutive relationship which analytically predicts damage-dependent laminate stiffness properties and damage-dependent ply level stresses. The kinematic effects of microstructural damage are introduced into the constitutive relationship by an internal state variable (ISV). The ISV's are strain-like quantities which are mathematically expressed as second-order tensors. Progressive damage development is accounted for by specifying the loading history dependent present value of the ISV's. The present value of any specific ISV is calculated from a damage growth law which depends on both the loading history and the present value of any other operative damage mechanism. The constitutive relationship and the ISV growth laws form the mechanics framework for a "damage model" which has the potential to predict sublaminate damage accumulation and laminate failure.

The primary objective of a progressive failure methodology is to predict the residual strength and life of structural components. Since these components may have many dif-

ferent geometries and laminate stacking sequences, it is essential that the required inputs to the damage model be independent of geometry and stacking sequence. In other words, the damage model must be capable of explicitly predicting the effects of geometry and stacking sequence on damage development and failure. Therefore, the approach taken to achieve this objective is to construct a nonlinear damage-dependent lamination theory (damage model) which can be implemented to any computational structural algorithm such as a finite element code. This then allows for modification of linear elastic codes via a time stepping scheme to account for load history dependent damage and an iterative algorithm to account for nonlinearity on each time step. The necessary parts of the damage model are as follows: 1) a kinematic description of the damage state (ISV's); 2) a damage dependent lamination theory which models the effects of interply delaminations; 3) a set of damage growth laws for predicting the load history dependence of the damage state at each material point; 4) a structural algorithm for modelling the response of components with spatially variable and load history dependent stresses and damage; and 5) residual strength and life prediction based on a failure function for unstable crack growth. Each of the above steps will be reviewed briefly in the following sections.

Kinematic Description of the Damage State

It is hypothesized that a local volume element may be selected which is small compared to the structural component of interest and, at least for the case of matrix cracking, the damage can be assumed to be homogeneous in this element. It is further hypothesized that the effects of the microcracks within this volume element may be locally averaged on a scale which is small compared to the structural component. A straightforward and direct approach to averaging the kinematic effects of cracks within the local volume element was taken by Vakulenko and M. L. Kachanov in 1971 [31]. This average is given by the following second order tensor:

$$\alpha_{ij}^{M} = \frac{1}{V_L}\int_{S_c} u_i^c n_j^c \, dS \qquad (3)$$

where α_{ij}^{M} is the internal state variable (ISV) for the microcracking contained in the local volume (V_L), u_i^c are crack opening displacements in V_L, n_j^c are the components of a unit normal to the crack faces, and S_C is the surface area of matrix cracks in V_L, as shown in Fig. 11. It is significant to note that the deformed geometry shown in Fig. 11 gives rise to a physical interpretation of the ISV. Consider the perceived macroscale strain to be defined by the relative positions of points A"0'B" which consist of the material deformation state A"0"B" plus the relative crack face displacement 0'0". Then the ISV defined by equation (3) is the value of the crack face displacements integrated over the crack surface area and divided by an appropriately defined local volume. The ISV is, therefore, a strain-like quantity representing the average kinematic effects of the microcrack within a local volume of material.

Since matrix cracks are contained within an individual ply, or a grouping of adjacent plies with the same fiber orientation, the local volume for matrix cracks may be defined at the ply level. Ply level stress-strain equations may then be defined by integrat-

ing the governing field equations over a homogeneous local volume within which the effects of matrix cracks are introduced as a strain-like quantity by the ISV given in equation (3). The complete mathematical formulation is given in Reference 32.

The definition of the ISV given by equation 3 has a physical interpretation. Therefore, micromechanics and fracture mechanics approaches may be used to develop ISV mathematical models for specific cracks. However, this approach is quite cumbersome. A phenomenological approach is more straightforward provided a testing procedure can be defined which isolates the individual modes of cracking. In this approach, stiffness loss is experimentally determined as a function of the damage state and the ISV's are specified from the resulting empirical relationship. The authors have extensively employed this latter technique to specify the ISV's for matrix crack damage [33]. The appropriateness of this approach was verified for the case of matrix cracks in the 90° plies of cross-ply laminates by comparing the empirical results to those determined rigorously by using equation (3) and a micromechanics analysis to determine the crack-opening displacements [34].

Damage Dependent Lamination Theory

Unlike the ply level model for matrix cracking, spatial homogeneity cannot be assumed for delaminations. Even if the delaminations may appear to be evenly distributed in the plane of the laminate, the same cannot be said for the through-thickness direction. The damage is, therefore, accounted for by area averaging in the laminate plane, accompanied by a kinematic assumption through the thickness. Accordingly, the laminate equations are constructed by assuming that the Kirchhoff-Love hypothesis may be modified to include the effects of jump displacements u_i^D, v_i^D, and w_i^D as well as jump rotations β_i^D and ψ_i^D for the ith delaminated ply interface, as shown in Fig. 12. The displacement fields in the x, y, and z directions are mathematically defined as

$$u(x,y,z) = u^o(x,y) - z\left[\beta^o + H(z - z_i)\beta_i^D\right] + H(z - z_i)u_i^D \qquad (4)$$

$$v(x,y,z) = v^o(x,y) - z\left[\psi^o + H(z - z_i)\psi_i^D\right] + H(z - z_i)v_i^D \qquad (5)$$

and

$$w(x,y,z) = w^o(x,y) + H(z - z_i)w_i^D \qquad (6)$$

where the superscripts "o" imply undamaged midsurface quantities, and $H(z-z_i)$ is the Heavyside step function. Also, a repeated index i in a product is intended to imply summation, and the supercripts D imply displacement components across the delamination. Locally averaging the above equations and applying standard lamination theory will result in the following laminate equations [32]:

$$\{N\} = \sum_{k=1}^{n} [Q]_k (z_k - z_{k-1}) \{\varepsilon_L^0\} - \tfrac{1}{2} \sum_{k=1}^{n} [Q]_k \, (z_k^2 - z_{k-1}^2) \{\kappa_L\} + \tag{7}$$

$$\sum_{l=1}^{d} [\overline{Q}_1]_l \, t_l \begin{Bmatrix} 0 \\ \alpha_{1l}^D \\ \alpha_{2l}^D \\ \alpha_{3l}^D \\ 0 \end{Bmatrix} + \sum_{l=1}^{d} (z_l - z_{l-1}) [\overline{Q}_2]_l \begin{Bmatrix} 0 \\ 0 \\ \alpha_{4l}^D \\ \alpha_{5l}^D \\ 0 \end{Bmatrix} - \sum_{k=1}^{n} (z_k - z_{k-1}) [Q]_k \{\alpha^M\}_k$$

$$\{M\} = \tfrac{1}{2} \sum_{k=1}^{n} [Q]_k (z_k^2 - z_{k-1}^2) \{\varepsilon_L^0\} - \tfrac{1}{3} \sum_{k=1}^{n} [Q]_k \, (z_k^3 - z_{k-1}^3) \{\kappa_L\} + \tag{8}$$

$$\sum_{l=1}^{d} [\overline{Q}_3]_l \, t_l^2 \begin{Bmatrix} 0 \\ \alpha_{1l}^D \\ \alpha_{2l}^D \\ \alpha_{3l}^D \\ 0 \end{Bmatrix} + \sum_{l=1}^{d+1} (z_l^2 - z_{l-1}^2) [\overline{Q}_4]_l \begin{Bmatrix} 0 \\ 0 \\ \alpha_{4l}^D \\ \alpha_{5l}^D \\ 0 \end{Bmatrix} - \tfrac{1}{2} \sum_{k=1}^{n} [\overline{Q}]_k (z_k^2 - z_{k-1}^2) \{\alpha^M\}_k$$

where {N} and {M} are the resultant forces and moments per unit length, respectively, and $\{\alpha^M\}_k$ and α_i^D represent the damage due to matrix cracking and interply delamination, respectively. Furthermore, n is the number of plies, and d is the number of delaminated ply interfaces. The ISV for delamination, α_i^D, has the same mathematical form as does equation (3) for general microcracking. All other terms in equations 7 and 8 have the standard lamination theory definitions.

An initial inspection of equations 7 and 8 raises the question of how many additional material constants and ISV's are required to include damage in the laminate equations. No additional material constants are required because the constants in $\overline{Q}_1$, $\overline{Q}_2$, $\overline{Q}_3$, and $\overline{Q}_4$ are related to the individual ply moduli as is Q. Unique ISV's are required for each ply developing matrix cracks and for each delamination. There are 3 unique ISV's for matrix cracks and 5 unique ISV's for delaminations. However, only 2 matrix crack ISV's and 1 delamination ISV are operative for symmetric laminates subjected to in-plane loading conditions. For the predictions reported in this paper, the matrix crack ISV's

are determined phenomenologically from test data obtained from $[0/90/0]_T$ and $[\pm 45]_{2S}$ laminates. The delamination ISV is determined analytically from strain energy release rate considerations. The mathematical expressions for the ISV's contain explicit laminate stacking sequence terms so that they may be used to model damage in any general laminate. The detailed development of these mathematical descriptions are given in reference 33.

A measure of the accuracy of laminate equations (7) and (8) can be obtained by comparing predictions of damage-dependent stiffness to experimental results. Predictions have been made for a typical graphite/epoxy system, AS4/3501-6. The bar chart shown in Fig. 13 compares the model predictions to the experimental values for the engineering modulus, E_x, for combined matrix cracking and delamination. The delamination interface location and percent of delamination area are listed in the figure underneath the laminate stacking sequence. As can be seen, the comparison between model results and the experimental results is quite good. Some limited results for Poisson's ratio are given in Fig. 14 using the same bar chart format.

A computer code has been constructed to determine the effect of damage on the average ply stresses in laminates [33]. Several laminates have been analyzed for an applied strain of $\varepsilon_{xo} = 0.01$ with all other components of strain being zero. Damage variables were calculated for the damage state determined experimentally using edge replication and x-ray radiography. The 90° plies use the matrix crack ISV α_{22}^{M} for normal extension while the off-axis plies use ISV α_{12}^{M} for shear deformation as well as α_{22}^{M}. No damage is assumed in the 0° plies. Since the laminate is subjected only to ε_{xo}, ISV α_{13}^{D} for shear deformation is assumed to be the only delamination damage component. The stress analysis results are shown in Table 1. Matrix cracks caused substantial stress reductions in ply stresses in the 90° plies in cross-ply laminates. For example, in the 90° plies of the $(0_2/90_2)_s$ laminate the matrix cracks resulted in a thirty-four percent average ply stress reduction. The two quasi-isotropic laminates developed different damage resulting in dissimilar far-field ply stresses.The$(90/\pm 45/0)_s$ laminate exhibited little matrix cracking, thus producing only a small reduction in ply stress in both the 90° and ±45° plies. The $(0/\pm 45/90)_s$ laminate exhibited a similar stress reduction in the ± 45° plies, but showed a substantial stress reduction (fifteen percent verses one percent) in the 90° plies when compared to the $(90/\pm 45/0)_s$ laminate. This alteration in ply stresses should significantly affect the growth of new damage in the composite.

Damage Growth Laws

It is hypothesized that the growth of damage in each ply is driven by the current stress state at the crack tips within that ply [35]. The form of the damage growth law for matrix cracks currently implemented in the damage model is based on the observation made by Wang, et al. [36] that for some materials the damage growth rate per load step follows a power law with the strain energy release rate, G, and a material parameter, n, serving as the basis and exponent, respectively. To develop ISV growth law equations,

α_{ij}^{M} must be related to the surface area of damage and the far-field applied loads. To date, phenomenological growth laws have been developed only for matrix crack growth.

The growth law has been used to predict the matrix crack growth histories for two crossply laminates [37]. The model predictions for the damage state in $[0_2/90_2]_s$ laminates loaded in fatigue at R = 0.1 and maximum applied laminate stress of 38 ksi and 43 ksi are shown in Figs. 15 and 16, respectively. The lower stress is equivalent to eighty percent of the monotonic matrix crack initiation stress, while the higher stress is equal to ninety percent of the initiation stress. The experimentally measured damage states were originally specified in terms of the crack density. The corresponding ISV for each damage level can be approximated by the relationship proposed by Lee, et al. [34]. The damage growth for the thicker $[0_2/90_3]_s$ laminate is shown in Fig. 17. This laminate was loaded at a maximum laminate stress of 26 ksi. This stress corresponds to eighty percent of the monotonic matrix crack initiation stress. The results for this load case indicated good agreement with the experimental data. The effect of the load redistribution on the damage evolution is apparent in this load case. A decrease in the rate of damage growth after fifty thousand load cycles was predicted by the model. On the other hand, the experimental data showed this decrease to occur after only ten thousand load cycles. This decrease in the predicted rate of damage growth is attributed only to the matrix crack induced transfer of load from the 90° plies to the adjacent 0° plies and the resulting decrease in the available crack driving force. However, the experimental values of the damage growth rate may have been influenced by the formation of delaminations observed to occur along the free edges and in the interior.

To examine the amount of stress redistribution that occurs during the damage accumulation, the model was used to determine the axial stress in the 90° plies of the $[0_2/90_3]_s$ laminate loaded in fatigue at R = 0.1 and at three different maximum stresses. Fig. 18 shows that for the laminate stress of 38 ksi, the axial stress in the 90° plies after forty thousand cycles was less than fifty percent of the original stress level in the undamaged laminate. Therefore, the rate of damage growth is expected to be relatively low during the latter stages of the loading history because of the reduction in the ply-level stress. This is observed in Fig. 19, which shows the corresponding values of the ISV, α_{22}^{M}, for the three load cases. The 26 ksi stress amplitude load case, on the other hand, produced only gradual changes in the axial stress and damage state as compared to the other two stress amplitudes. The percentage decrease from the original undamage stress level increased with the fatigue stress amplitude. These results demonstrate that the stress redistribution characteristics among the plies in the laminate are dependent on the loading conditions. These redistribution characteristics will affect the manner in which damage develops in the surrounding plies as well as the eventual failure of the laminate.

An Algorithm for Structural Analysis

In order to predict the response of a structural component with spatially variable stresses, it is necessary to incorporate the damage dependent lamination theory into a structural analysis algorithm. This was accomplished via the finite element method. A plate element formulation was achieved by integrating the governing plate equilibrium

equations against variations in the displacement components and employing Green's Theorem. The resulting formulation of the laminated plate equilibrium equations is described in detail in reference 38. These equations are then discretized spatially by the finite element method, which utilizes five degrees of freedom at each node. These consist of two in-plane displacements, one out-of-plane displacement, and two rotational terms.

A finite element code has been developed based on the above formulation and implemented for matrix crack growth. The implementation of the damage growth law requires that the solution algorithm be repeated for every load cycle. During each cycle, the ply stresses are calculated and used to determine the increment in the matrix crack ISV for each ply. The updated damage state is then used in the calculation of the laminate and ply response at the next load cycle.

The response of a laminated tapered plate subjected to an in-plane uniaxial fatigue loading condition has been examined. This beam has a $[0/90_2]_s$ stacking sequence and possesses the material properties of AS4/3501 graphite/epoxy. The plate length is 17.78 cm and the width is 4.50 cm at the clamped end and tapered to 2.87 cm at the end where the load is applied. The plate is loaded at a distributed load amplitude of 17.5×10^3 N/m and $R = 0.1$. Since the plate is symmetric about its length, it is sufficient to model half of the plate with a mesh containing 28 elements, 24 nodes, and 120 degrees of freedom. The spatial variation and growth of the matrix crack ISV's during the loading history in the 90° and 0° plies, is shown in Figs. 20 and 21, respectively. For clarity, the plotted values of the ISV's in each ply are normalized by the largest value of the ISV within that ply at the end of the loading history, 22500 cycles. The predicted results indicate that the matrix cracks first occur in the 90° plies at the narrow end and progress toward the wider end as loading continues. Axial splits in the 0° plies do not develop until after the appearance of the matrix cracks in the 90° plies. Thus, the matrix cracks accumulate in the 90° plies and load is transferred to the 0° plies. Depending on the amplitude of the fatigue load, more than half of the load initially carried by the undamaged 90° plies will be transferred to the 0° plies. The additional load carried by the 0° plies coupled with the stress concentrations caused by the matrix cracks in the 90° plies create suitable conditions for the growth of matrix cracks in the 0° plies. The results also show that the progression of matrix cracks along the length of the tapered beam decelerates near the midway point. The stresses in the region beyond the midway point are insufficient to promote additional damage growth. The matrix crack growth will increase at the narrow end until the matrix cracks have either reached the saturation level or the laminate fails.

Residual Strength and Life Prediction

Typically fiber fracture is the final damage event to occur in a laminate. Fiber fracture in the principal load-carrying plies may lead directly to catastrophic laminate failure. In this case, an ISV representing fiber fracture is not required and the fracture can be predicted by a ply level failure function such as the Tsai-Wu criterion [39]. However, stable fiber fracture may accumulate throughout a loading history. For example, fiber fracture may occur in the damage zone produced by a high strain gradient field at a geometric discontinuity such as an open hole or a bolt hole. In this case, significant load redistribution around the damage zone will occur prior to a catastrophic failure. An ISV

representing the kinematic effects of the fiber fracture will be necessary to accurately predict the local laminate stiffness and associated load redistribution. A global-local iterative analysis methodology will be necessary to distinguish between these two conditions. The logic flow of the global-local iterative analysis methodology required to predict laminate residual strength and life is shown in Fig. 22. Obviously a finite element based structural analysis would be required to facilitate this methodology.

Damage growth laws for delamination and fiber fracture are currently being developed and, once available, the damage model will be fully developed for tensile failure dominated structures. Following completion of these activities, the mechanics framework will be developed for compression failure. Once the compression failure mechanics are incorporated into the damage model, the methodology will be extended to treat impact damage. This formulation seems particularly well suited to predicting damage development during the impact event and subsequent damage growth. This is because the damage model will be incorporated into a finite element formulation which can be used to predict the structural dynamics characteristics of the impact event.

SUMMARY

The damage threshold/fail safety methodology developed by O'Brien assumes the existence of matrix cracks throughout the off-axis plies of the laminate and predicts delamination onset using a strain energy release rate characterization. Delamination growth is accounted for in one of three ways: either analytically, using delamination growth laws in conjunction with strain energy release rate analyses; experimentally, using measured stiffness loss; or conservatively, assuming delamination onset corresponds to catastrophic growth. Fail safety is assessed by accounting for the accumulation of delaminations through the laminate thickness. The utility of this approach has been demonstrated for predicting the tension fatigue life of graphite/epoxy, glass/ epoxy and hybrid laminates. In addition, this methodology can probably be employed to predict compression fatigue life and post impact residual strength.

The progressive failure methodology developed by Allen and Harris employs damage-dependent constitutive relationships to calculate damage-dependent ply level stresses which are then input into appropriate criteria to predict laminate failure. Using the concept of continuum damage mechanics, internal state variables (ISV's), defined for each mode of damage, are used to introduce the kinematic effects of damage into the laminate constitutive relationships. A global/local analysis strategy is used to calculate the global structural response to the applied loads and the local analysis is used to calculate the ply level stresses in high strain gradient fields produced by structural discontinuities such as circular cutouts. Damage growth laws for the ISV's are loading history dependent and, through an iterative process between the global/local analyses, are continuously updated until laminate failure is predicted. This methodology is in the process of being implemented into a finite element code for predicting the residual strength and life of structures under tensile loading but has not been developed, to date, for compressively loaded structure. Once compression failure is implemented, the methodology can be used in conjunction with a structural dynamics analysis to predict the formation of damage during an impact event.

Finally, the question of which methodology is preferred must be addressed. This, of course, is problematic because one method may be preferred for some applications and the second method for other applications. The damage tolerance/fail safety method is well suited for initial design analyses while the "automated" features of the continuum damage model are well suited for detailed finite element stress analyses. If it is not practical to model sublaminate damage as free surfaces, the continuum damage model also offers the versatility of describing the effects of damage on load redistribution at the global structural level. However, the continuum damage mechanics approach must be coupled with a local analysis such as fracture mechanics or the damage tolerance/fail safety method to predict material level sublaminate damage growth and subsequent failure.

REFERENCES

[1] Wilkins, D. J.; Eisenmann, J. R.; Camin, R. A.; Margolis, W. S.; and Benson, R. A.: Characterizing Delamination Growth in Graphite-Epoxy, Damage in Composite Materials, ASTM STP 775, American Society for Testing and Materials, June 1982, p. 168.

[2] Mall, S.; Yun, K. T.; and Kochnar, N. K.: Characterization of Matrix Toughness Effects on Cyclic Delamination Growth in Graphite Fiber Composites. ASTM STP 1012, April 1989, pp. 296-312.

[3] Russell, A. J. and Street, K. N.: Predicting Interlaminar Fatigue Crack Growth Rates in Compressively Loaded Laminates, ASTM STP 1012, April 1989 pp. 162-180.

[4] Gustafson, C. G. and Hojo, M.: Delamination Fatigue Crack Growth in Unidirectional Graphite/Epoxy Laminates, Journal of Reinforced Plastics, Vol. 6, No. 1, January 1987, pp. 36-52.

[5] O'Brien, T. K.: Generic Aspects of Delamination in Fatigue of Composite Materials, Journal of the American Helicopter Society, Vol. 32, No. 1, January 1987, pp. 13-18.

[6] Martin, R. H. and Murri, G. B.: Characterization of Mode I and Mode II Delamination Growth and Thresholds in Graphite/PEEK Composites, ASTM STP 1059, pp. 251-270.

[7] O'Brien, T. K.: Characterization of Delamination Onset and Growth in a Composite Laminate, Damage in Composite Materials, ASTM STP 755, American Society for Testing and Materials, 1982, pp. 140-167.

[8] Russell, A. J. and Street, K. N.: Moisture and Temperature Effects on the Mixed-Mode Delamination Fracture of Unidirectional Graphite/Epoxy, Delamination and Debonding of Materials, ASTM STP 876, American Society for Testing and Materials, October 1985, pp. 349-370.

9] Poursartip, A.: The Characterization of Edge Delamination Growth in Composite Laminates Under Fatigue Loading, Toughened Composites, ASTM STP 937, American Society for Testing and Materials, 1987, pp. 222-241.

[10] O'Brien, T. K.: Mixed-Mode Strain Energy Release Rate Effects on Edge Delamination of Composites, Effects of Defects in Composite Materials, ASTM STP 836, American Society for Testing and Materials, 1984, pp. 125-142.

[11] O'Brien, T. K.: Tension Fatigue Behavior of Quasi-Isotropic Graphite/Epoxy Laminates, Fatigue and Creep of Composite Materials, Proceedings, 3rd Riso International Symposium on Metallurgy and Materials Science, Riso National Laboratory, Roskilde, Denmark, 1982, pp. 259-264.

[12] O'Brien, T. K.: Fatigue Delamination Behavior of PEEK Thermoplastic Composite Lamines, Journal of Reinforced Plastics, Vol. 7, No. 4, July 1988, pp. 341-359.
[13] O'Brien, T. K.; Murri, G. B.; and Salpekar, S. A.: Interlaminar Shear Fracture Toughness and Fatigue Thresholds for Composite Materials, Composite Materials: Fatigue and Fracture--Second Volume, ASTM STP 1012, American Society for Testing and Materials, 1989, pp. 222-250.
[14] Adams, D. F.; Zimmerman, R. S.; and Odem, E. M.: Frequency and Load Ratio Effects on Critical Strain Energy Release Rate G_c Thresholds of Graphite Epoxy Composites, Toughened Composites, ASTM STP 937, American Society for Testing and Materials, Philadelphia, 1987, p. 242.
[15] O'Brien, T. K.; Rigamonti, M.; and Zanotti, C.: Tension Fatigue Analysis and Life Prediction for Composite Laminates, International Journal of Fatigue, Vol. 11, No. 6, Nov. 1989, pp. 379-394.
[16] O'Brien, T. K.: Analysis of Local Delaminations and Their Influence on Composite Laminate Behavior, Delamination and Debonding of Materials, ASTM STP 876, American Society for Testing and Materials, 1985, pp. 282-297.
[17] Caslini, M.; Zanotti, C.; and O'Brien, T. K.: Study of Matrix Cracking and Delamination in Glass/Epoxy Laminates, Journal of Composites Technology and Research, Vol. 9, No. 4, Winter 1987, pp. 121-130.
[18] O'Brien, T. K.; Crossman, F. W.; and Ryder, J. R.: Stiffness, Strength, and Fatigue Life Relationships for Composite Laminates, Proceedings, Seventh Annual Mechanics of Composites Review, AFWAL-TR-82-4007, Air Force Wright Aeronautical Laboratories, Dayton, OH, April 1982, pp. 79-90.
[19] O'Brien, T. K.: The Effect of Delamination on the Tensile Strength of Unnotched, Quasi-Isotropic, Graphite Epoxy Laminates, Proceedings, SESA/JSME Joint Conference on Experimental Mechanics, Honolulu, HI, May 1982, Part I, SESA, Brookfield Center, CT, pp. 236-243.
[20] Ryder, J. T. and Crossman, F. W.: A Study of Stiffness, Residual Strength, and Fatigue Life Relationships for Composite Laminates, NASA CR-172211, National Aeronautics and Space Administration, Washington, DC, October 1983.
[21] Jamison, R. D.; Schulte, K.; Reifsnider, K. L.; and Stinchcomb, W. W.: Characterization and Analysis of Damage Mechanisms in Tension-Tension Fatigue of Graphite/Epoxy Lamines, Effects of Defects in Composite Materials, ASTM STP 836, American Society for Testing and Materials, 1984, pp. 21-55.
[22] McCarty, J. E. and Ratwani, M. M.: Damage Tolerance of Composites, Interim Report No. 3, AFWAL Contract F33615-82-C-3213, Boeing Military Airplane Co., Dayton, OH, March 1984.
[23] Guynn, E. G. and O'Brien, T. K.: The Influence of Lay-up and Thickness on Composite Impact Damage and Compression Strength, AIAA-85-0646, Proceedings, 26th AIAA/ASME/ASCE/AHS Structures, Structural Dynamics, and Materials Conference, Orlando, FL, April 1985, pp. 187-196.
[24] Byers, D. A.: Behavior of Damaged Graphite/Epoxy Laminates Under Compression Loading, NASA CR 159293, National Aeronautics and Space Administration, Washington, DC, August 1980.
[25] Bishop, S. M. and Dorey, G.: The Effect of Damage on the Tensile and Compressive Performance of Carbon Fiber Laminates, Characterization, Analysis, and Significance of Defects in Composite Materials, AGARD CP-355, Advisory Group for Aerospace Research and Development, Paris, April 1983.

[26] Bakis, C. E. and Stinchcomb, W. W.: Response of Thick, Notched Laminates Subjected to Tension-Compression Cyclic Loads, Composite Materials: Fatigue and Fracture, ASTM STP 907, American Society for Testing and Materials, Philadelphia, June 1986, pp. 314-334.
[27] Chai, H.; Babcock, D. D.; and Knauss, W. G.: One-Dimensional Modeling of Failure in Laminated Plates by Delamination Buckling, International Journal of Solids and Structures, Vol. 17, No. 11, pp. 1069-1083.
[28] Whitcomb, J. D.: Finite Element Analysis of Instability-related Delamination Growth, Journal of Composite Materials, Vol. 15, 1981, pp. 403-426.
[29] Carlile, D. R. and Leach, D. C.: Damage and Notch Sensitivity of Graphite/PEEK Composite, Proceedings, 15th National SAMPE Technical Conference, October 1983, pp. 82-93.
[30] Murri, G. B. and Guynn, E. G.: Analysis of Delamination Growth from Matrix Cracks in Laminates Subjected to Bending Loads, Composite Materials: Testing and Design, (Eighth Conference), ASTM STP 972, American Society for Testing and Materials, 1988, pp. 322-339.
[31] Vakulenko, A. A.and Kachanov, M. L.: Continuum Theory of Cracked Media, Izv. AN SSR, Mekhanika Tverdogo Tela, Vol. 6, p. 159, 1971.
[32] Allen, D. H.: Groves, S. G.;and Harris, D. C.: A Cumulative Damage Model for Continuous Fiber Composite Laminates with Matrix Cracking and Interply Delamination, Composite Materials: Testing and Design (8th Conference), ASTM STP, American Society for Testing and Materials, 1987.
[33] Allen, D. H.; Nottorf, E. W.; and Harris, C. E.: Effect of Microstructural Damage on Ply Stresses in Laminated Composites, Recent Advances in the Macro- and Micro-Mechanics of Composite Materials Structures, AD-Vol. 13, ASME, pp. 135-146, 1988.
[34] Lee, J. W.; Allen, D. H.; and Harris, C. E.: Internal State Variable Approach for Predicting Stiffness Reductions in Fibrous Laminated Composites With Matrix Cracks, Journal of Composite Materials, Vol. 23, pp. 1273-1291, 1989.
[35] Allen, D. H.; Harris, C. E.; and Groves, S. E.: A Thermomechanical Constitutive Theory for Elastic Composites with Distributed Damage - Part I: Theoretical Development, Int. Journal Solids & Structures, Vol. 23, No. 9, pp. 1301-1318, 1987.
[36] Wang, A. S. D.; Chou, P. C.; and Lei, S. C.: A Stochastic Model for the Growth of Matrix Cracks in Composite Laminates, Journal of Composite Materials, Vol. 18, pp. 239-254, 1984.
[37] Lo, D. C.; Allen, D. H.;and Harris, C. E.: A Continuum Model for Damage Evolution in Laminated Composites, Proceedings IUTAM Symposium, Troy, N.Y., 1990 (to appear).
[38] Buie, K. D.: A Finite Element Model for Laminated Composite Plates with Matrix Cracks and Delaminations, Texas A&M University Thesis, December, 1988.
[39] Tsai, S. W. and Wu, E. M.: A General Theory of Strength for Anisotropic Materials, Journal Composite Materials, pp. 58-80, 1971.

Table 1 PLY STRESSES RESULTING FROM MATRIX CRACKING AND DELAMINATION

LAMINATE	PLY	INITIAL PLY STRESS σ (ksi)	STRESS W/MATRIX CRACKS σ (ksi)	STRESS W/MATRIX CRACKS & DELAM. σ (ksi)	DELAMINATION LOCATION MAGNITUDE (%) ISV α_{13}^{D}	MATRIX DAMAGE ISV's α_{22}^{M}	α_{12}^{M}
$[0/90]_s$	0	211.4	211.4	211.4	0/90	0	0
	90	14.0	9.6	8.5	16.6%	.00318	0
					.00076		
$[0/90_2]_s$	0	211.4	211.4	211.4	0/90	0	0
	90	14.0	9.5	7.9	24.2%	.00326	0
	90	14.0	9.5	7.9	.001109	.00326	0
$[0_2/90_2]_s$	0	211.4	211.4	211.4		0	0
	0	211.4	211.4	211.4	0/90	0	0
	90	14.0	9.2	6.0	49.5%	.00344	0
	90	14.0	9.2	6.0	.002267	.00344	0
$[0/90_3]_s$	0	211.4	211.4	211.4		0	0
	90	14.0	10.6	8.3	0/90	.00247	0
	90	14.0	10.6	8.3	35.3%	.00247	0
	90	14.0	10.6	8.3	.001617	.00247	0
$[0/\pm45/90]_s$	0	211.4	211.4	211.4		0	0
	45	64.4	64.0	64.0	-45/90	0	.00067
	-45	64.4	64.0	64.0	57%	0	-.00067
	90	14.0	11.8	8.2	.002611	.00157	0
$[90/\pm45/0]_s$	90	14.0	13.9	13.9		.00060	0
	+45	64.4	64.0	64.0	+45/-45	0	.00067
	-45	64.4	64.0	48.7	52%	0	-.00067
	0	211.4	211.4	161.0	.002382	0	0

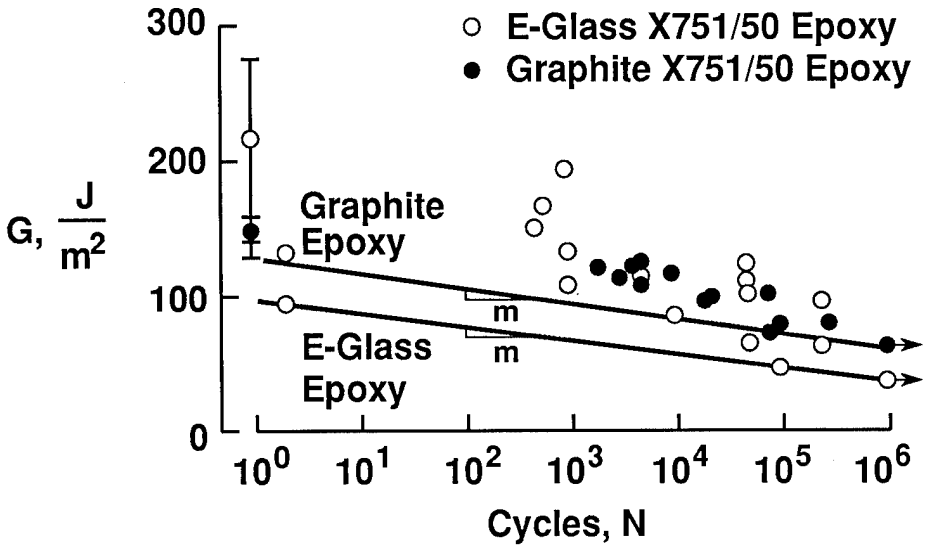
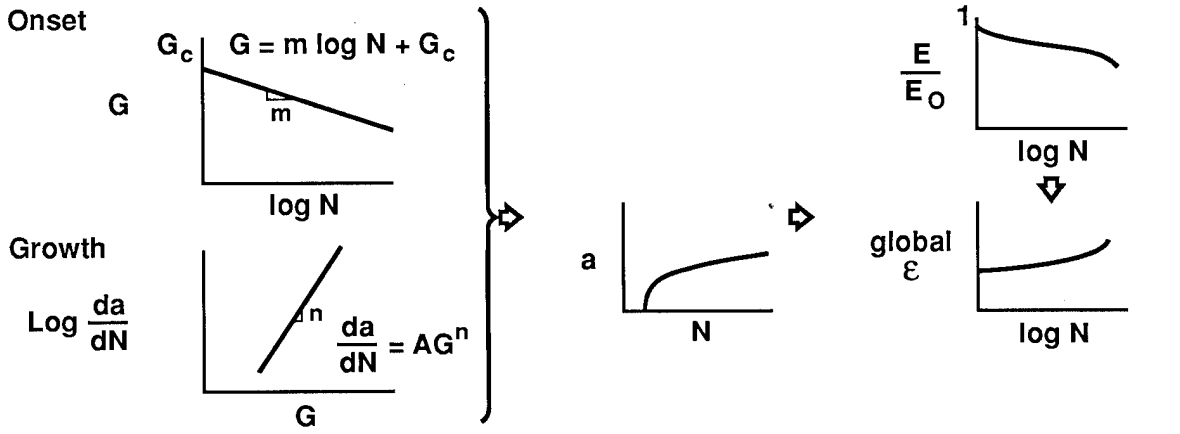


Figure 1. Comparison of Lower Bound Delamination Onset Criteria for E-Glass Epoxy and Graphite Epoxy.



(a) Characterization of delamination onset and growth

(b) Prediction of delamination growth with fatigue cycles

(c) Prediction of stiffness loss with fatigue cycles

Figure 2. Prediction of stiffness loss due to delamination in composite laminates.

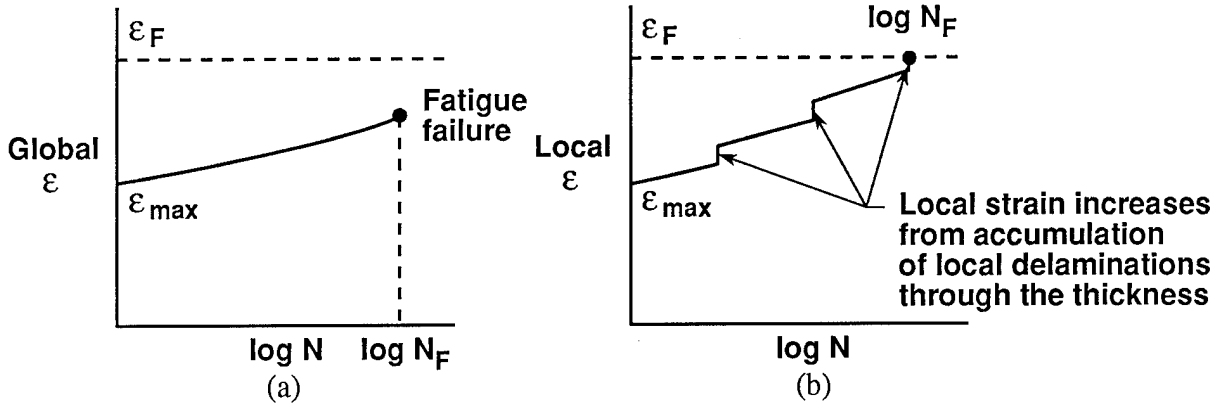


Figure 3. Increase in global versus local strain in 0° plies.

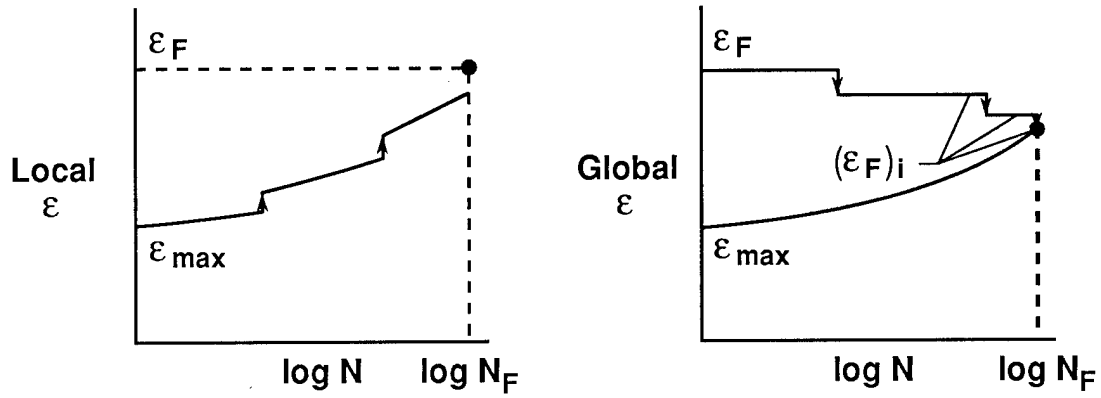


Figure 4. Effective reduction in ε_F due to local delamination accumulation through the laminate thickness.

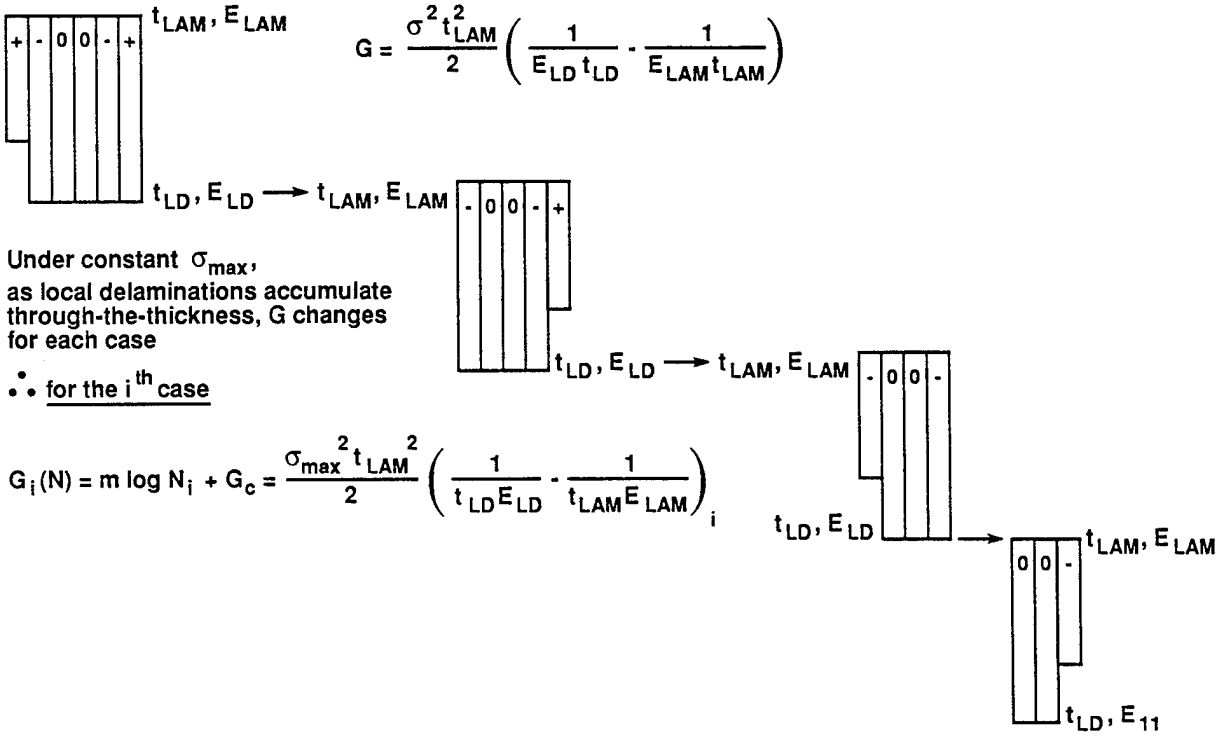


Figure 5. Strain energy release rate for local delamination onset.

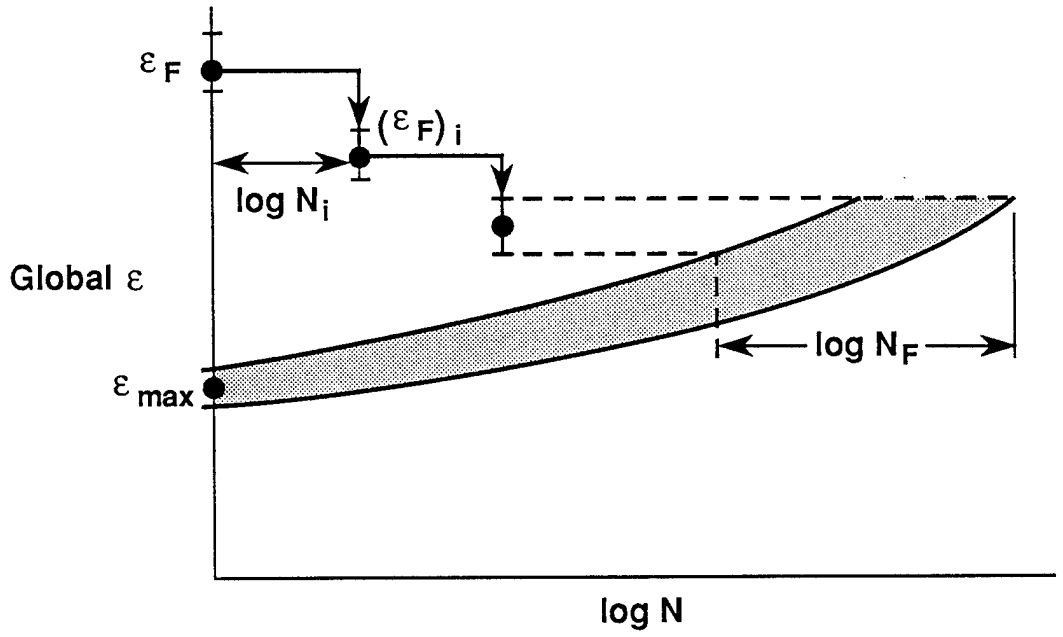


Figure 6. Tension fatigue life prediction for composite laminates. (σ_{max} = constant)

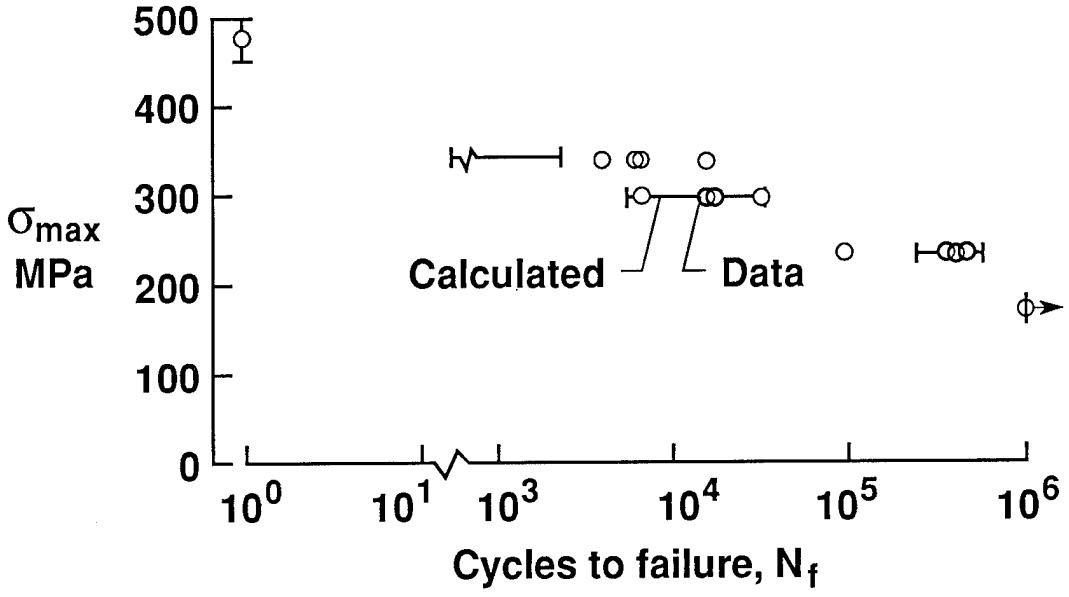
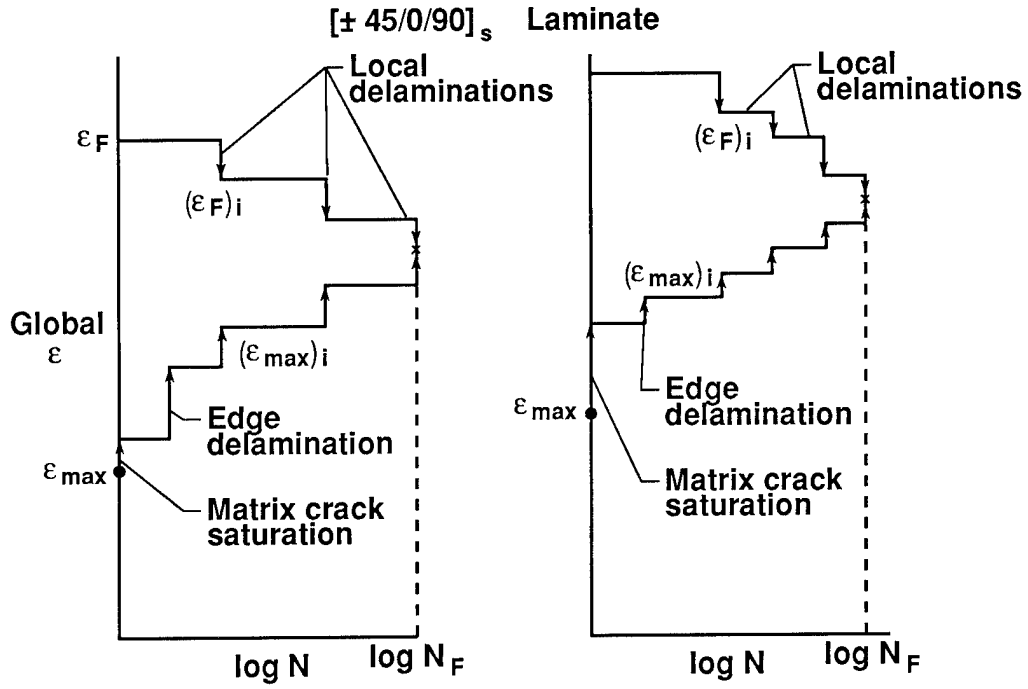


Figure 7. Fatigue Life Determination for $(45/-45/0)_S$ Graphite/E-Glass Epoxy Hybrid Laminates.



(a) Graphite epoxy (b) Glass epoxy

Figure 8. Damage-threshold/fail-safety analysis.

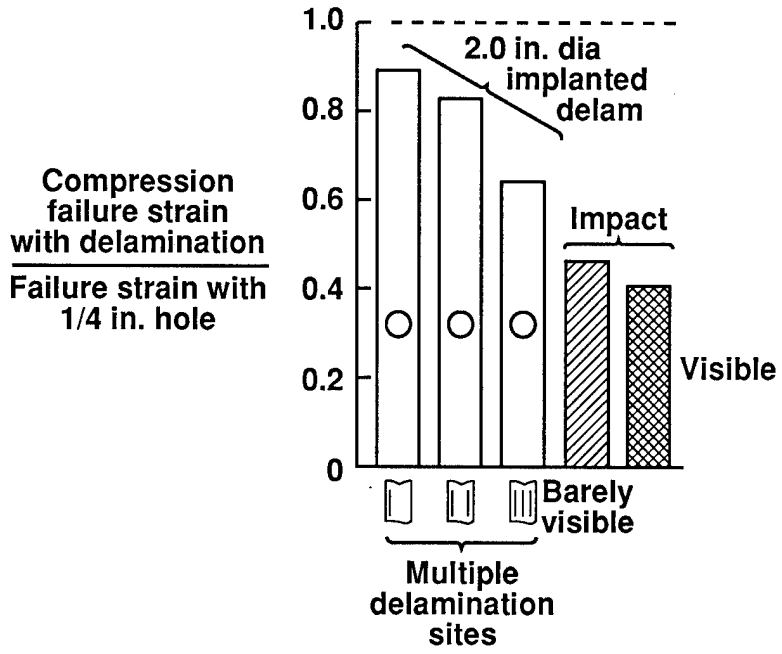


Figure 9. Normalized compression failure strain reduction for laminates with implanted delaminations or impact damage.

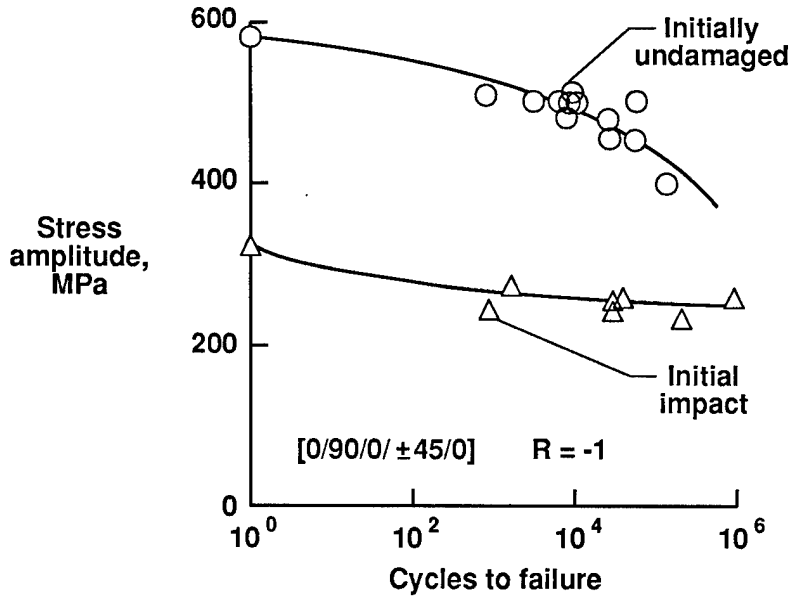


Figure 10. Fatigue behavior of initially undamaged and impacted graphite/epoxy laminates under fully reversed cyclic loading.

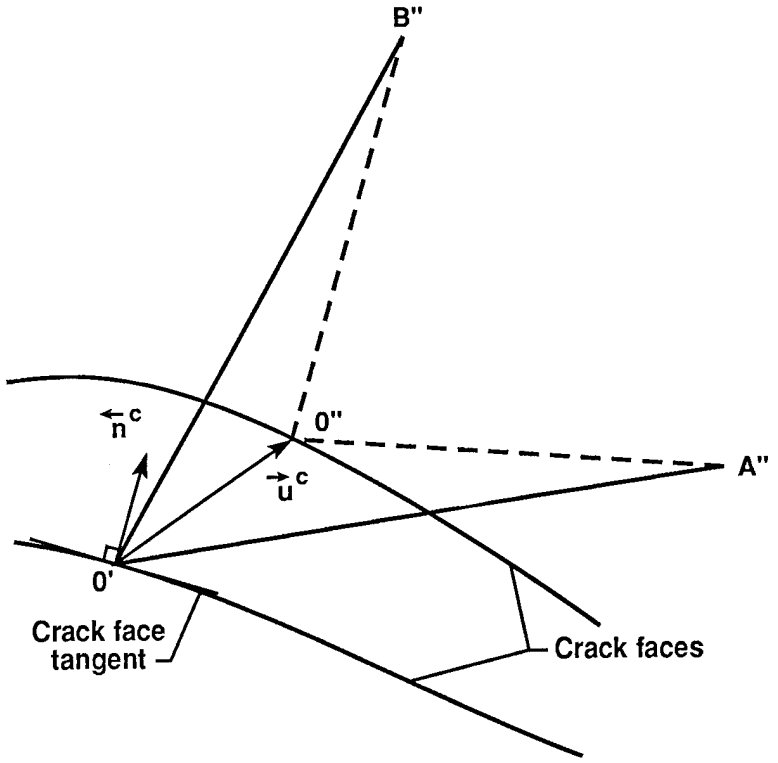


Figure 11. Local delamination and internal state variable defined for material point 0'.

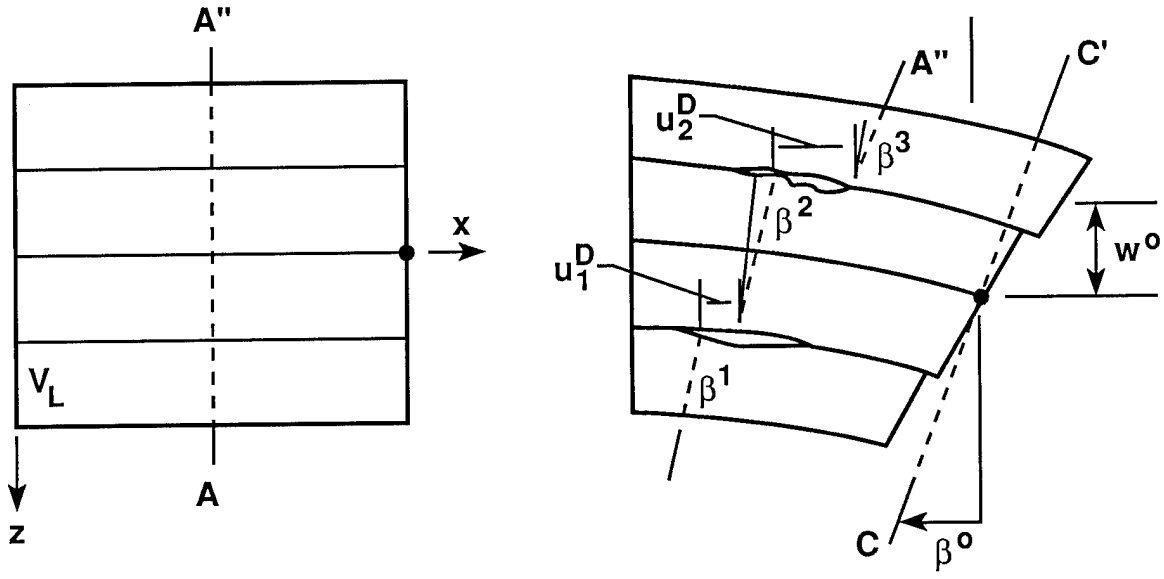


Figure 12. Discontinuities in the through-the-thickness deformation due to delaminations.

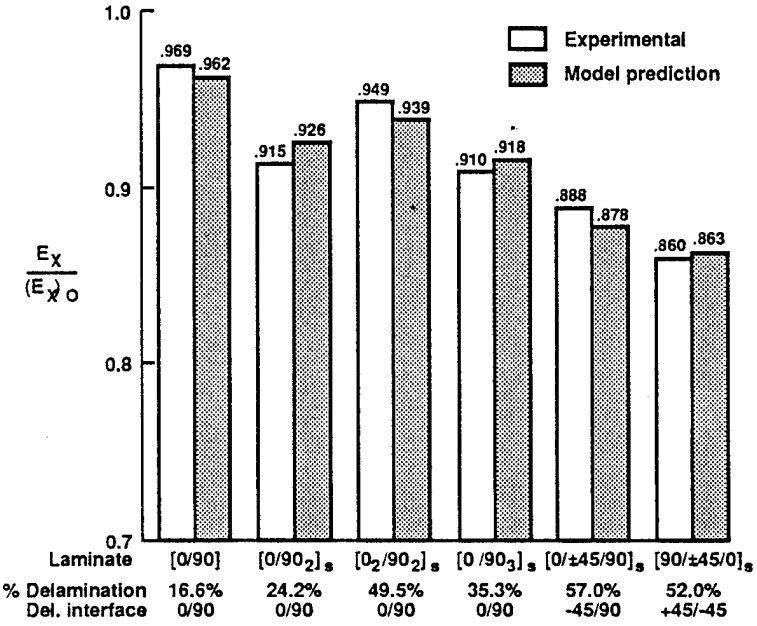


Figure 13. Comparison of experimental results and model predictions of the laminate engineering modulus, E_x, degraded by both matrix cracking and delamination damage.

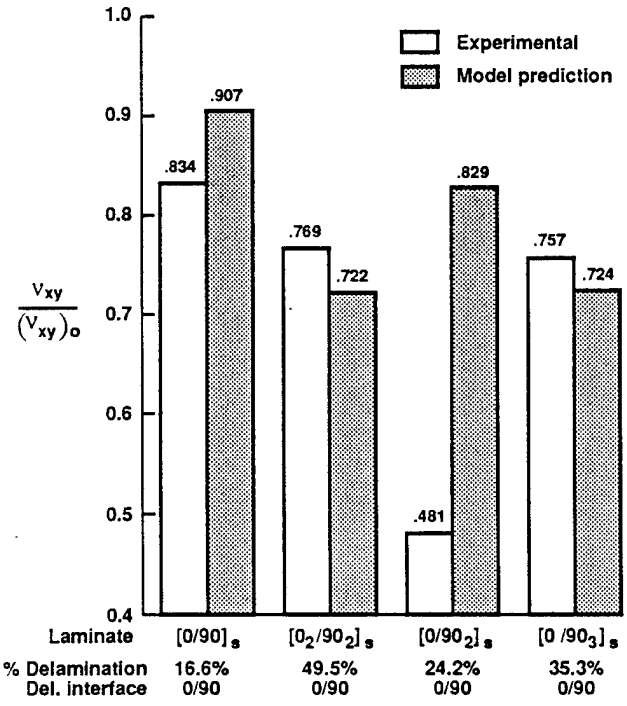


Figure 14. Comparison of experimental results and model predictions of the laminate engineering Poisson's ratio, ν_{xy}, degraded by both matrix cracking and delamination damage.

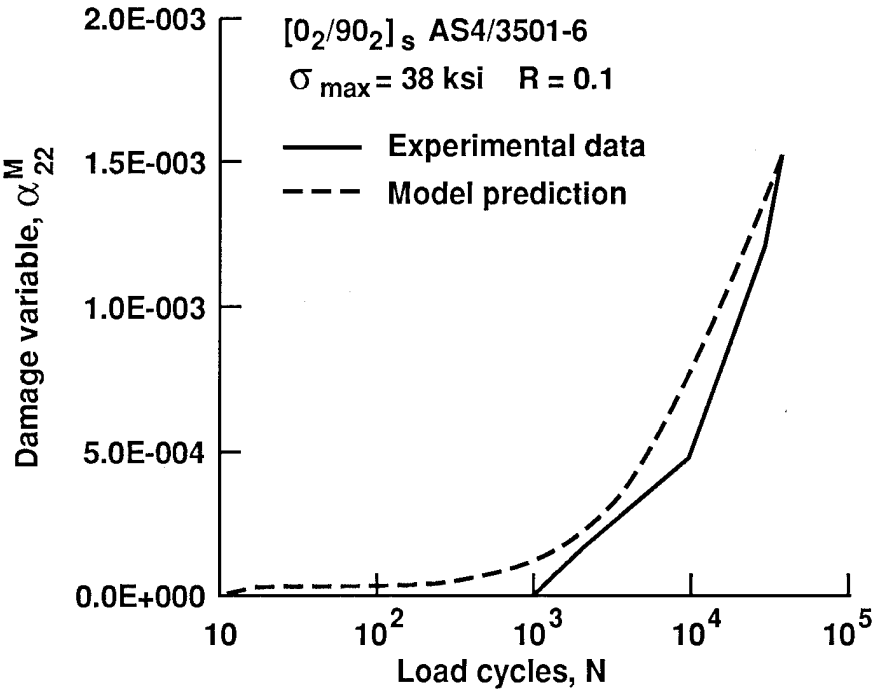


Figure 15. Matrix crack damage in the 90 plies of a $[0_2/90_2]_s$ laminate for a maximum applied laminate stress of 38 ksi and R = 0.1.

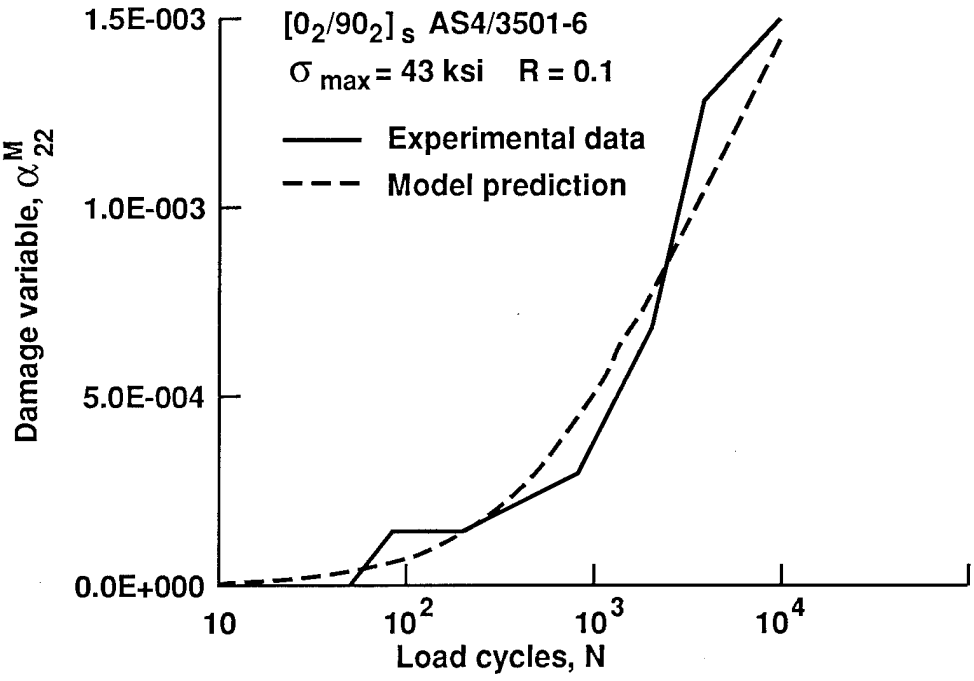


Figure 16. Matrix crack damage in the 90° plies of a $[0_2/90_2]_s$ laminate for a maximum applied laminate stress of 43 ksi and R = 0.1.

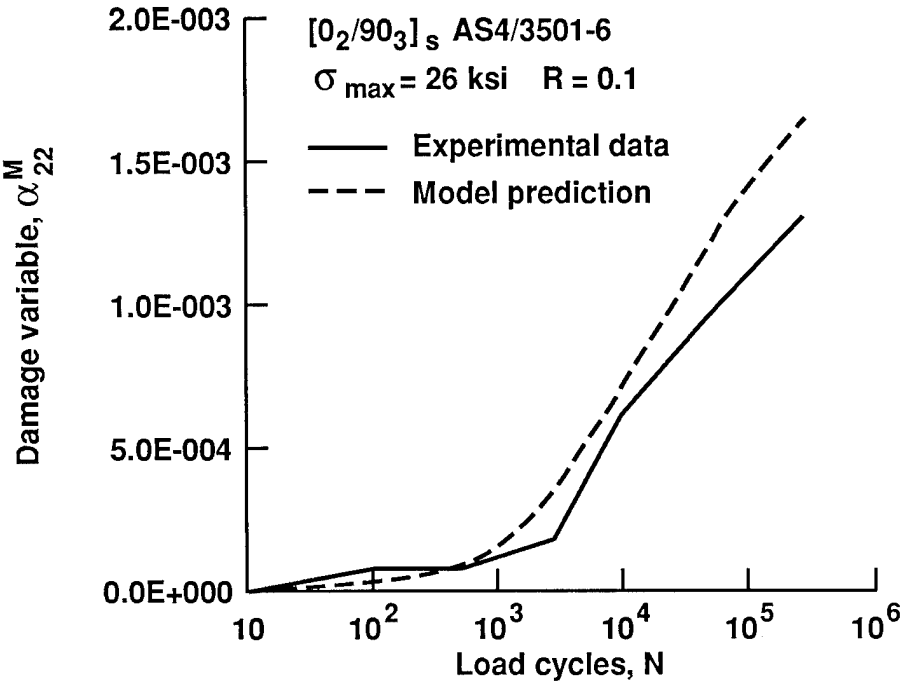


Figure 17. Matrix crack damage in the 90° plies of a $[0_2/90_3]_s$ laminate for a maximum applied laminate stress of 26 ksi and R = 0.1.

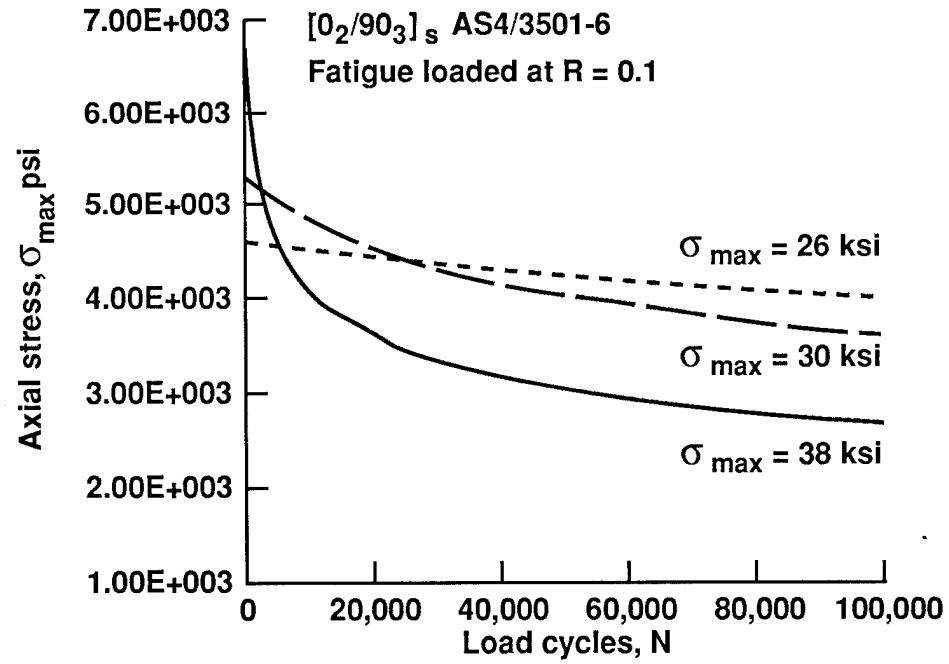


Figure 18. Damage-induced stress redistribution in the 90° plies of a $[0_2/90_3]_s$ laminate subjected to constant amplitude fatigue at R = 0.1.

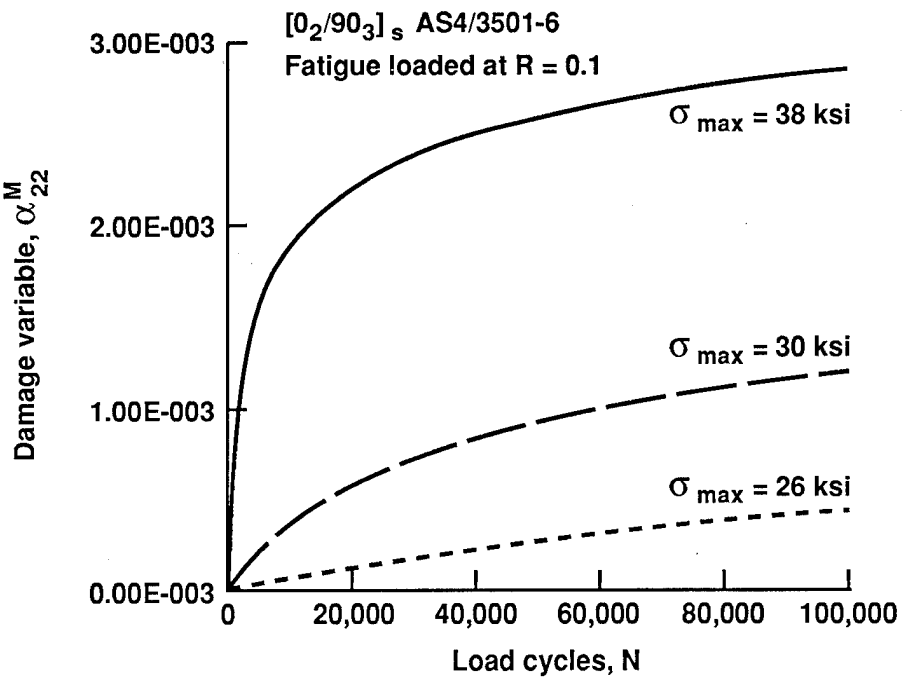


Figure 19. Evolution of damage ISV in the 90° plies of a $[0_2/90_3]_s$ laminate subjected to constant amplitude fatigue at R = 0.1.

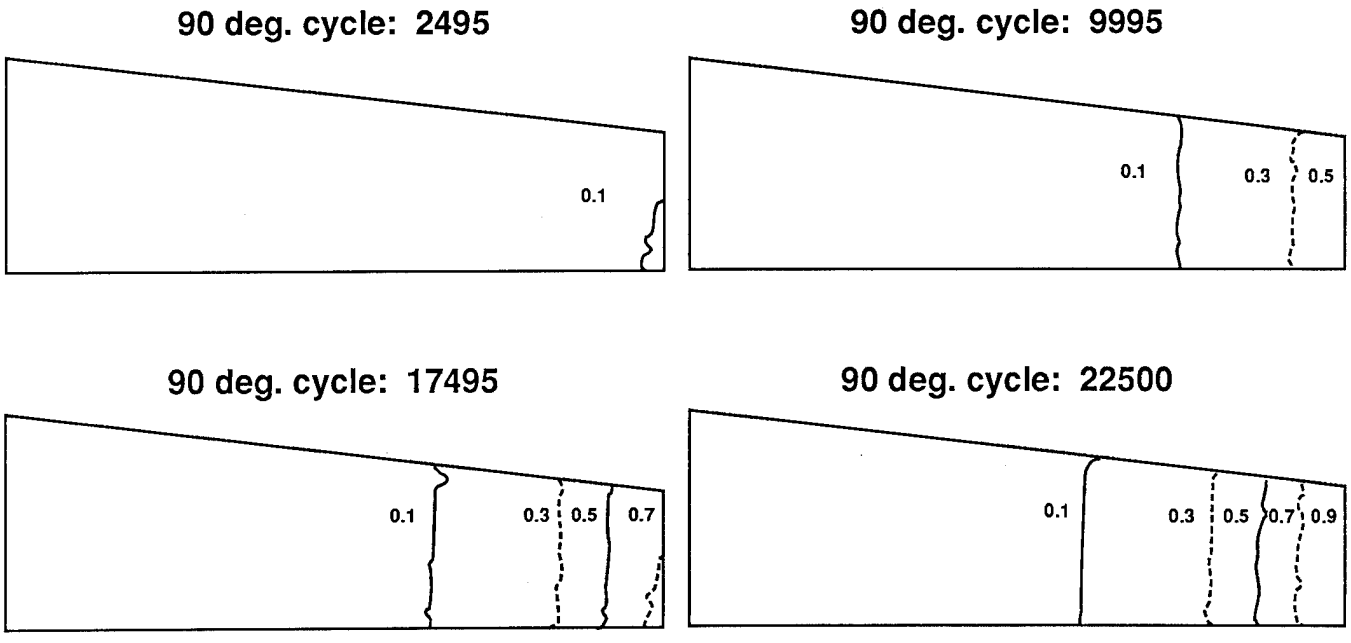


Figure 20. The accumulation of matrix cracks in the 90° plies during various points in the loading history.

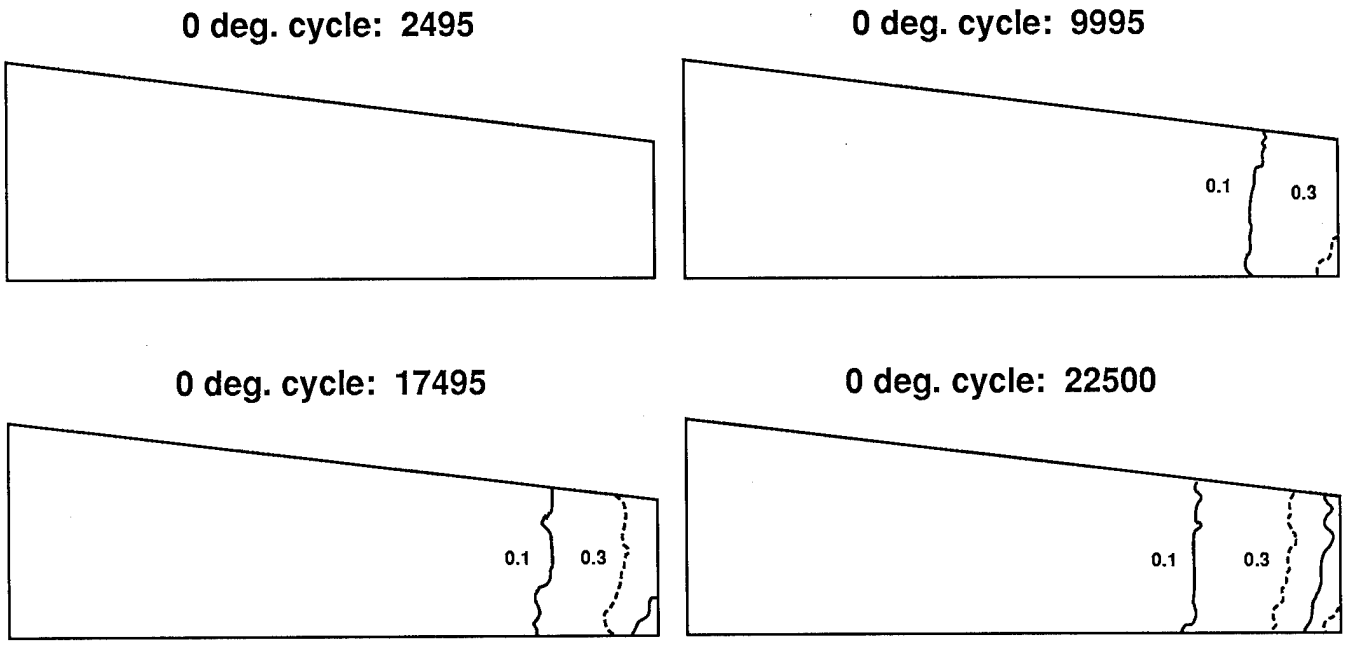


Figure 21. The accumulation of matrix cracks in the 0° plies during various points in the loading history.

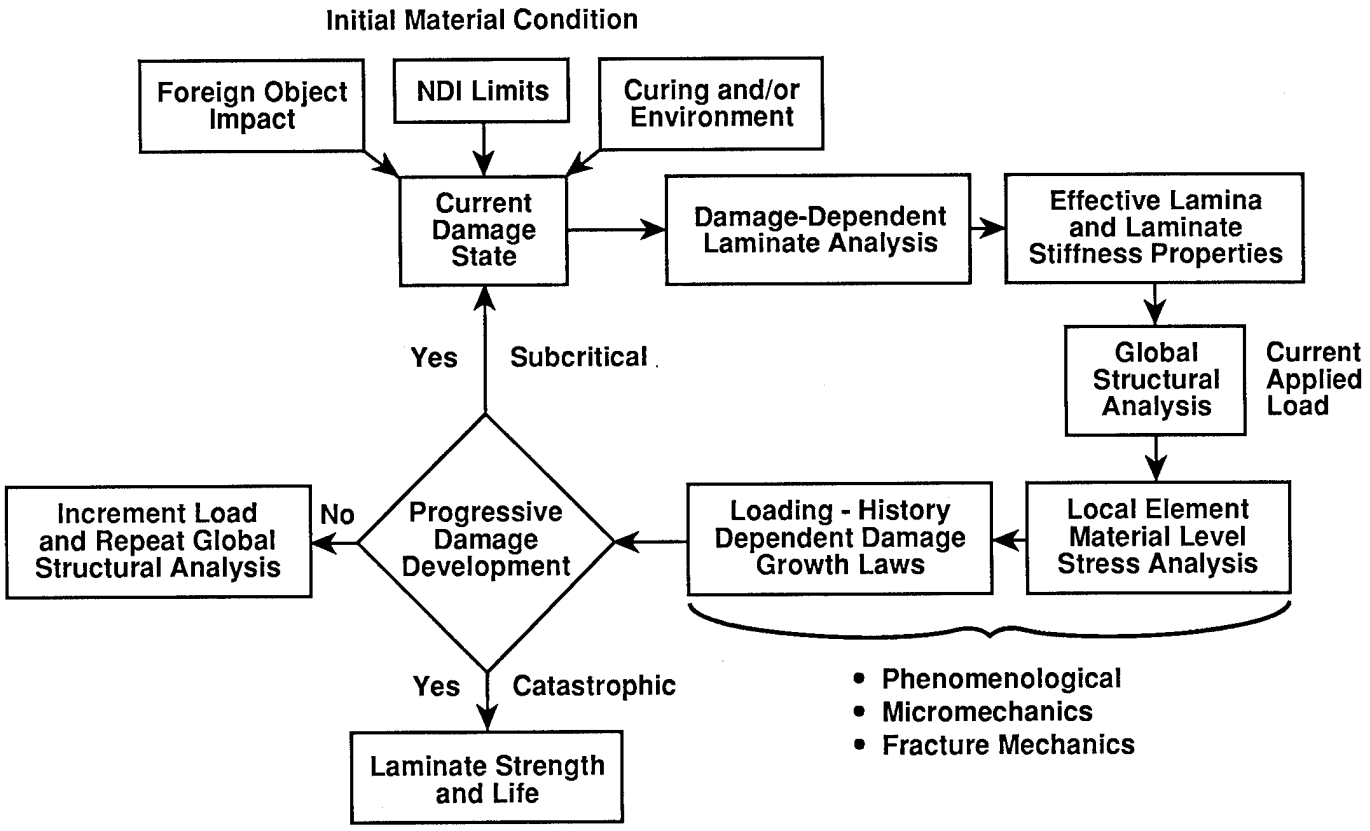


Figure 22. Logic for laminate strength and life prediction methodology.

MULTIPLE METHODS INTEGRATION FOR STRUCTURAL MECHANICS ANALYSIS AND DESIGN

J. M. Housner
NASA Langley Research Center
Hampton, VA

and

M A. Aminpour
Analytical Services and Materials
Hampton, VA

Abstract

A new research area of multiple methods integration is proposed for joining diverse methods of structural mechanics analysis which interact with one another. Three categories of multiple methods are defined: those in which a physical interface is well-defined; those in which a physical interface is not well-defined, but selected; and those in which the interface is a mathematical transformation. The integration procedures required in each of these categories is of necessity generally different. It is discussed how multiple methods integration is needed in order to effectively use analysis and design methods in the most appropriate structural region and to enable hierarchial analysis and design so that the effect of component design changes on full vehicle performance can be readily addressed. Two fundamental integration procedures are presented which can be expanded to integrate various methods (*e.g.*, finite elements, Rayleigh Ritz, Galerkin and integral methods) with one another. Since the finite element method will likely be the major candidate method to be integrated, its enhanced robustness under element distortion is also examined and a new robust shell element is demonstrated.

Introduction

Over the past three decades, finite elements have become the workhorse of structural analysis. This is due in part to the ability of finite elements to allow modeling of arbitrary and complex geometric shapes. With the increased utilization of composite aerospace structures, there is an even greater desire for modeling flexibility. Manufacturing of composite aerospace components, leading to new geometric configurations, and the need for detailed modeling as required for composite failure prediction are both producing a desire for added modeling flexibility.

Though finite elements dominate the structural analysis discipline, this does not imply that other modeling methods are not valuable. To the contrary, special purpose modeling techniques and their associated software abound throughout the industry because of their proven utility. However, little has been done to combine these modeling methods with one another and with finite element modeling. Consequently, the special purpose analyses are rarely used in a hierarchial sense where analyses at different levels of detail or on different structural component levels inherit data from the other levels and interact with one another. One purpose of this paper is to present a relatively new endeavor referred to as multiple methods integration which will enable hierarchial analysis and to present some illustrative examples with fundamental equations for the integration process. Giles and Norwood[1] initiated this area of research thus, the intent here is not to claim a new concept, but to build on their work and to continue to motivate research which will lead to practical application.

Since the finite element method will likely be one of the multiple methods which is integrated with other methods, it is desirable to examine the finite element capability in the light of its readiness for integration since an integrated method will be no better than its constituents. Thus, a second purpose of this paper is to examine the robustness of the finite elements themselves which provides the modeling flexibility of the finite element method. In spite of the plethora of finite elements types presently available, (see references [2] and [3] for a broad review), the need still exists for robust elements which provide adequate performance even when the finite elements have distorted shapes. This paper reviews the distortion resistant capability of several types of shell finite elements as well as a newly developed shell element which is very distortion insensitive.

Multiple Methods Integration

Over the years, many special purpose structural analysis methods have been developed for various classes of structural components under a variety of loading conditions. Also, the finite element method has emerged as the leading method for general purpose analysis. Just as the various components comprising an aerospace vehicle must be integrated together, so must the methods developed for their analysis. Herein this process is referred to as multiple methods integration. For several reasons it is advantageous to be able to readily and efficiently merge or integrate the various special purpose analysis methods with each other and with the general purpose finite element method. Among the reasons for multiple methods integration are the following: utilization of the preferred analysis method in the most appropriate structural region; utilization of high performance computers which operate in parallel on different regions and on different methods; retention of modularity in software architecture; refinement of structural regions independently of one another; and hierarchial analysis. It is expected that multiple methods integration should lead to more accurate and efficient analysis and design, since the total analysis becomes more tailored to the article being analyzed. Even more important than reduced computer time, however, is the promise that multiple methods integration can reduce the time spent by the analyst or designer.

If done properly, the integration procedure will allow the designer to modify the design and/or refine the model of one structural article independently of models of other articles. This is not now generally available. The effect of a redesigned component may propagate to other components as well as to the full vehicle. Predicting this propagation and the trade-offs it causes is critical to efficient design. However, not only does the redesign propagate to the rest of the vehicle, but in general, so does the remodeling which is done to account for the redesign. It is difficult to separate these two effects. Multiple methods integration should be such so as to allow the remodeling effects to be filtered out of the redesign.

On the other hand, certain affects may be very localized, and in accordance with St. Venant's principle do not propagate far. These can be handled by specialized methods and then interfaced to methods treating the global response.

Once the integration procedures are established, the COMET (COmputational MEchanics Testbed) at LaRC (reference [4]) can be used as the vehicle for implementing the integration and validating the integration procedure. The special purpose computer software associated with each method can then be readily integrated with one another and with the finite element software capability residing in COMET.

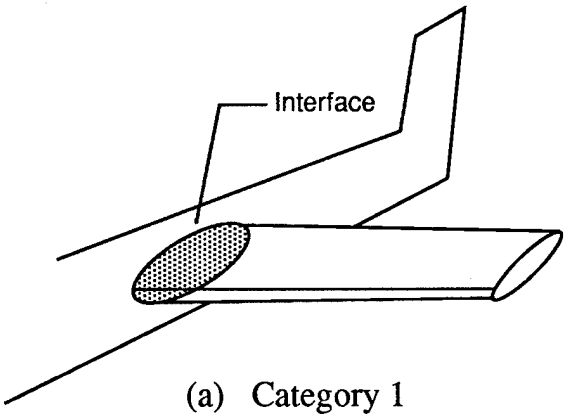
In this section three categories of multiple methods are outlined and some concepts for integrating the methods are presented. These categories are identified by the type of interface existing between the multiple methods. They are as follows: (1) the case where two or more methods are employed in different structural regions and the physical interface between the regions is known or well-defined; (2) simlar to the first case in that the interface is physical, but it cannot be defined, is not known or is selected by the analyst to produce an efficient model; and (3) the interface is not physical, but mathematical. Examples of the three categories are given in Figure 1.

Category 1. Physical Interface Well-Defined - In this category there are several well-known procedures for integration, such as, component substructuring, modal synthesis and interdisciplinary analysis such as fluid-structure analysis. Except in the case of interdisciplinary analysis, the general practice is to use the same methods in each structural region. Little has been done to interface different types of methods such as finite elements with Galerkin methods. Moreover, modal synthesis methods still have serious shortcomings and little has been done in the non-linear area for this entire category of methods.

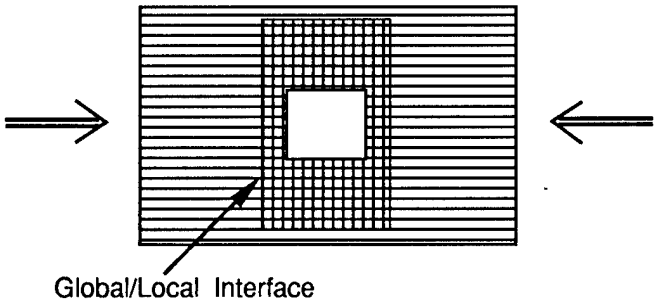
Category 2. Physical Interface Not Well-Defined - In this category as in the first, the interface is physical; however, it is not the intersection between two structural components. Rather, the

interface is chosen by the analyst in order to produce a more efficient model of a single structural component. For example, this category includes such techniques as, global-local modeling where there are near and far field models, multiple transient analysis modeling where different time steps or different temporal integrators may be used in different regions, and 2D-to-3D modeling where plate finite elements may be tied to brick finite elements. Often, the accuracy of the model is highly dependent on the placement of the interface.

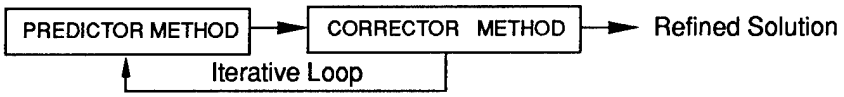
Category 3. Mathematical Interface - In this category two or more methods are used to model the same structural article and hence there is no physical interface. Rather, the interface is mathematical and often represents the transformation(s) between two or more modeling phases of the analysis. Examples in this category are methods such as predictor/corrector, hybrid, re-analysis multi-grid methods and reduced basis methods. An example of a category 3 multiple method is depicted in Figure 2. References [5-8] develop this procedure wherein finite element generated results are enhanced by a process called re-continualization. This process derives a functional fit to the discrete finite element results. Once the functional fit is derived, detail stresses may be calculated by differentiating the function. The critical aspect of the process in deriving the function is that no differencing of the discrete finite element results is required.



(a) Category 1



(b) Category 2



(c) Category 3

Figure 1. Three Categories of Multiple Methods.

Multiple methods integration enables hierarchial analysis by tying together the results of various levels of structural detail. This can be accomplished in category (1) multiple methods where results from one component level become input to the next level and in category (3) multiple methods wherein levels of interacting methods treat levels of progressively complex structural detail. This is especially needed in composites since detail stresses are required for failure prediction.

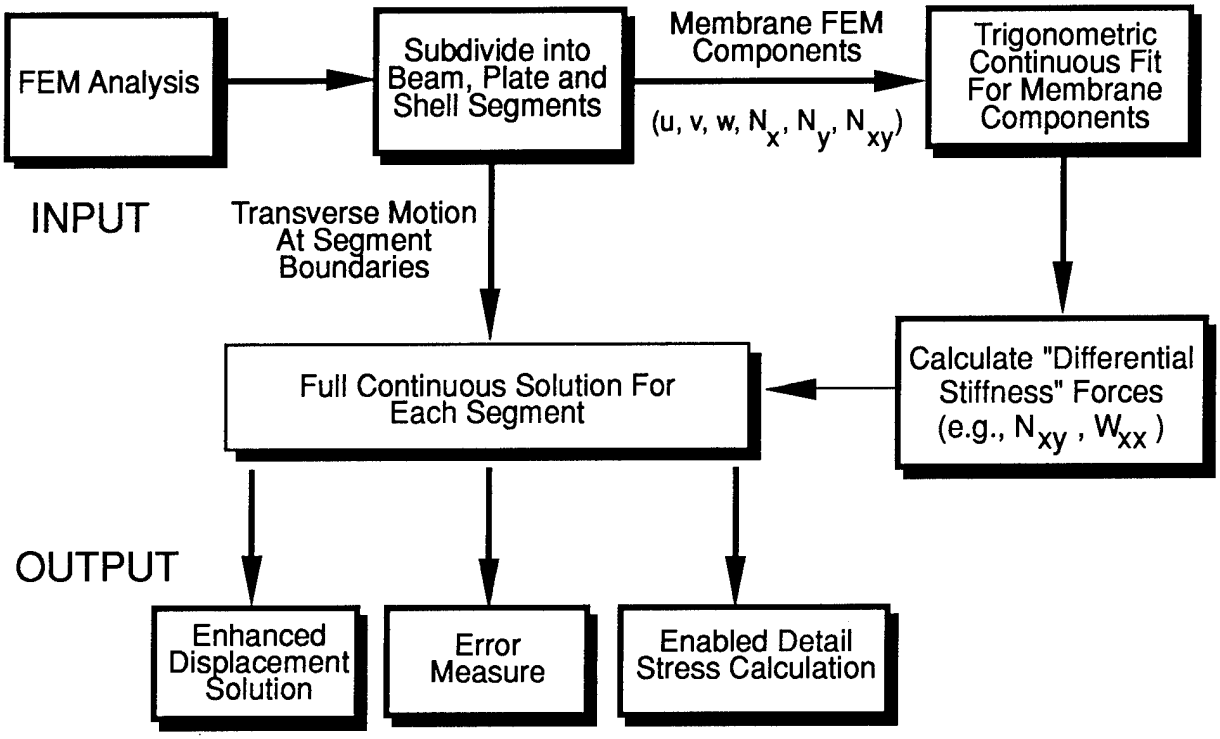


Figure 2. New Method Developed for Enchancing Finite Element Derived Results.

The remainder of this section concentrates on two integration methods for categories (1) and (2). Whereas, the two concepts laid down here are applicable to both categories, one tends to be more applicable to category (1) and the other to category (2). In category (1) multiple methods it is often critical to model the interface with sufficient refinement to predict accurate stresses, since the interface between two components is a stress critical region where failures usually initiate. The model of the interface for category (1) tends to refine as the design matures. On the other hand, category (2) multiple methods do not necessarily seek accurate stresses at the interface since they are used where the stress field does not contain steep stress gradients. The category (2) integration should be such that the results are insensitive to the precise placement of the interface.

The concept of each method is described by considering two structural regions having a common interface (see Figure 3). In these concepts, the displacements and/or normal gradients along the interface are assumed to be described by some functional forms. The two concepts are distinguished by the way the models for the two regions are tied to the functional forms. In the first concept, the models are rigidly tied to the functional form whereas in the second they are loosely tied to the functional form by a least squares procedure. As stated in the introduction, the intent here is not to claim some new concepts, but rather to stimulate research into the large variety of integration procedures possible so as to develop methods for practical application.

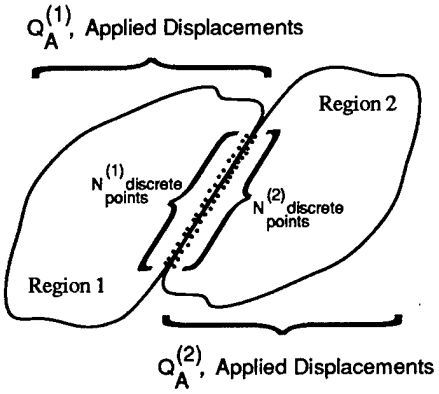


Figure 3. Two Connected Regions.

Method 1: Rigid Connection via Functional Form

Consider an interface between two structural regions. A displacement or normal gradient component along this interface is assumed to have a functional form given by

$$\bar{q} = \bar{q}(s) \tag{1}$$

where s is the interfacial path coordinate which is defined in terms of the analysis coordinate system. The functional form for $\bar{q}(s)$ uses unknown coefficients and when the function is evaluated at a discrete coordinate, one has,

$$\bar{q}(s_i) = \bar{t}_i \bar{a} \tag{2}$$

where, for a polynomial of order $M-1$,

$$t_i = (1, s_i, s_i^2, s_i^3, \ldots, s_i^{M-1}) \tag{3}$$

and $\bar{a}$ is a column vector of coefficients for the polynomial $\bar{q}(s)$.

It is assumed that the values of $\bar{q}$ associated with the model of region (1) and those of region (2) can be expressed as two sets of discrete points lying along the common interface between the regions. These discrete values are then slaved to the assumed functional form as,

$$\bar{q}(s_i) - \bar{q}_i^{(1)} = 0 \text{ and } \bar{q}(s_j) - \bar{q}_j^{(2)} = 0; \quad i = 1, 2, \ldots, \overline{N}^{(1)}; \quad j = 1, 2, \ldots, \overline{N}^{(2)} \tag{4}$$

where, $\bar{q}_i^{(1)}$ and $\bar{q}_j^{(2)}$ are discrete values of q associated with region (1) or (2) respectively, at values of s_i and s_j. (The values of s_i and s_j need not be coincident.) Then,

$$\overline{Q}_I^{(k)} = \overline{T}^{(k)} \bar{a}; \quad k = 1, 2 \tag{5}$$

where, $\overline{Q}_I^{(k)}$ is a column vector associated with the interface of region (k), all of whose entries are of one type of degree-of-freedom (either a displacement component or its gradient). The matrix $\overline{Q}_I^{(k)}$ is $\overline{N}^{(k)} \times 1$ and is to be made continuous across the interface. The matrix $\overline{T}^{(k)}$ is $\overline{N}^{(k)} \times M$ and its rows are $\bar{t}_i$. Equations (5) represents $N^{(k)}$ constraints and the functional form introduces M new unknown variables, thus there are $N^{(1)} + N^{(2)} - M$ interface constraints using this interfacing technique.

The order of the polynomials used to represent different types of degrees-of-freedom need not be the same, but for simplicity, they are assumed to be of the same order in this paper. Hence, for all degrees-of-freedom which are to be made continuous across the interface,

$$Q_I^{(k)} = T^{(k)} a; \quad k = 1, 2 \tag{6}$$

where $Q_I^{(k)}$ is an extended column vector of all degrees-of-freedom which are to be continuous across the interface and $T^{(k)}$ is a block diagonal matrix whose blocks are $\overline{T}^{(k)}$. Thus, $Q_I^{(k)}$ is $N^{(k)} \times 1$, $T^{(k)}$ is $N^{(k)} \times M$ and a is $M \times 1$ where $N^{(k)}$ is $n\overline{N}^{(k)}$ with n the number of different types of degrees-of-freedom which are to be made continuous across the interface.

Variational Equations - The models associated with each of the regions yields the virtual work of each as,

$$\delta U^{(k)} = \delta D^{(k)^T} K^{(k)} D^{(k)} \tag{7}$$

where $D^{(k)}$ is the column vector of all degrees-of-freedom on the boundary of region (k) and $K^{(k)}$ is the associated stiffness matrix for region (k) which is typically derived from the full stiffness matrix by reducing out the interior degrees-of-freedom. It could be generated by a finite element model or some other model. The vector $D^{(k)}$ is now partitioned into three parts; those $N^{(k)}$ free degrees-of-freedom lying on the interface of region (k); those $L^{(k)}$ free degrees-of-freedom lying elsewhere on the boundary of region (k), and those $P^{(k)}$ degrees-of-freedom on the boundary of region (k) which correspond to fixed or applied boundary displacements. After partitioning, equation (7) becomes,

$$\delta U^{(k)} = \left(\delta Q_I^{(k)^T},\ \delta Q_F^{(k)^T},\ 0\right) \begin{bmatrix} K_{II}^{(k)} & K_{IF}^{(k)} & K_{IA}^{(k)} \\ K_{FI}^{(k)} & K_{FF}^{(k)} & K_{FA}^{(k)} \\ K_{AI}^{(k)} & K_{AF}^{(k)} & K_{AA}^{(k)} \end{bmatrix} \begin{Bmatrix} Q_I^{(k)} \\ Q_F^{(k)} \\ Q_A^{(k)} \end{Bmatrix} \tag{8}$$

For the case of no applied external forces,

$$\delta U^{(1)} + \delta U^{(2)} = 0 \tag{9}$$

Since equation (9) must be valid for all variations, the governing equation for the case of a rigid interface connection via a functional form is,

$$\begin{bmatrix} S_{II} & S_{I1} & S_{I2} \\ S_{1I} & S_{11} & 0 \\ S_{2I} & 0 & S_{22} \end{bmatrix} \begin{Bmatrix} a \\ Q_F^{(1)} \\ Q_F^{(2)} \end{Bmatrix} = - \begin{bmatrix} T^{(1)^T} & K_{IA}^{(1)} & Q_A^{(1)} + T^{(2)^T} & K_{IA}^{(2)} & Q_A^{(2)} \\ & & K_{FA}^{(1)}\ Q_A^{(1)} & & \\ & & K_{FA}^{(2)}\ Q_A^{(2)} & & \end{bmatrix} \tag{10}$$

where,

$$\begin{aligned} S_{II} &= T^{(1)^T} K_{II}^{(1)} T^{(1)} + T^{(2)^T} K_{II}^{(2)} T^{(2)} \\ S_{I1} &= T^{(1)^T} K_{IF}^{(1)} \\ S_{I2} &= T^{(2)^T} K_{IF}^{(2)} \\ S_{11} &= K_{FF}^{(1)} \\ S_{22} &= K_{FF}^{(2)} \end{aligned}$$

Solution of equation (10) for a, $Q_F^{(1)}$ and $Q_F^{(2)}$ gives,

$$\begin{aligned} a &= \hat{S}^{-1}\left[\left(S_{I1} S_{11}^{-1} K_{FA}^{(1)} - T^{(1)^T} K_{IA}^{(1)}\right) Q_A^{(1)} + \left(S_{I2} S_{22}^{-1} K_{FA}^{(2)} - T^{(2)^T} K_{IA}^{(2)}\right) Q_A^{(2)}\right] \\ Q_F^{(1)} &= -S_{11}^{-1}\left[K_{FA}^{(1)} Q_A^{(1)} + S_{I1}^T a\right] \\ Q_F^{(2)} &= -S_{22}^{-1}\left[K_{FA}^{(2)} Q_A^{(2)} + S_{I2}^T a\right] \end{aligned} \tag{11}$$

where,

$$\hat{S} = S_{II} - S_{I1} S_{11}^{-1} S_{I1}^T - S_{I2} S_{22}^{-1} S_{I2}^T$$

Thus, the procedure for a rigid interface connection via a functional form is

1. Model regions 1 and 2 independently
2. Create stiffness matrix with all degrees-of-freedom lying interior to the boundaries reduced out
3. Calculate a, $Q_F^{(1)}$ and $Q_F^{(2)}$ from equations (11)
4. Recover interface values from equations (6)

Method 2: Least Squares Interface Connection via a Functional Form

In this method, equation (4) is replaced by the squared equations,

$$\sum_{i=1}^{N^{(1)}} \left[q(s_i) - q_i^{(1)}\right]^2 = 0 \text{ and } \sum_{j=1}^{N^{(2)}} \left[q(s_j) - q_j^{(2)}\right]^2 = 0 \tag{12}$$

Using the process of least squares and equation (6) produces $2M$ equations, namely,

$$T^{(1)^T}(T^{(1)}a - Q_I^{(1)}) = 0 \text{ and } T^{(2)^T}(T^{(2)}a - Q_I^{(2)}) = 0$$

which yields M constraint equations between $Q_I^{(1)}$ and $Q_I^{(2)}$, namely,

$$\left(T^{(1)^T}T^{(1)}\right)^{-1}T^{(1)^T}Q_I^{(1)} - \left(T^{(2)^T}T^{(2)}\right)^{-1}T^{(2)^T}Q_I^{(2)} = 0$$

or,

$$CD = 0 \tag{13}$$

where, C is a constraint matrix of order $M \times (N^{(1)} + N^{(2)} + L^{(1)} + L^{(2)})$ expressed as,

$$C = \left[\Gamma^{(1)}, 0, -\Gamma^{(2)}, 0\right];\ D = \left[Q_I^{(1)}, Q_F^{(1)}, Q_I^{(2)}, Q_F^{(2)}\right]^T$$

and

$$\Gamma^{(k)}_{M\times N^{(k)}} = \left(T^{(k)^T}T^{(k)}\right)^{-1}_{M\times M} T^{(k)^T}_{M\times N^{(k)}}$$

Returning to equation (7) and applying the constraints via Lagrangian multiplier technique yields,

$$\begin{bmatrix} K_{II}^{(1)} & K_{IF}^{(1)} & 0 & 0 \\ K_{FI}^{(1)} & K_{FF}^{(1)} & 0 & 0 \\ 0 & 0 & K_{II}^{(2)} & K_{IF}^{(2)} \\ 0 & 0 & K_{FI}^{(2)} & K_{FF}^{(2)} \end{bmatrix} \{D\} = \begin{bmatrix} -K_{IA}^{(1)}Q_A^{(1)} \\ -K_{FA}^{(1)}Q_A^{(1)} \\ -K_{IA}^{(2)}Q_A^{(2)} \\ -K_{FA}^{(2)}Q_A^{(2)} \end{bmatrix} - C^T\lambda \tag{14}$$

subject to the constraints,

$$CD = 0$$

With λ a Lagrangian multiplier vector, the term $C^T\lambda$ in equation (14) represents the interfacial forces between regions (1) and (2). From equation (13), these forces are orthogonal to the displacement vector D which does not violate the constraints.

Method (2) produces one interface constraint for each polynomial coefficient. That is, the number of constraints is M. This is in contrast with method (1) which produces $N^{(1)} + N^{(2)} - M$ constraints.

Equation (14) may be solved by transforming to a reduced set of response variables as,

$$D = \hat{B}\hat{D} \tag{15}$$

with $\hat{B}$ of the order $\hat{N} \times (\hat{N} - R)$ where $\hat{N}$ is $N^{(1)} + N^{(2)} + L^{(1)} + L^{(2)}$ and R is the rank of the matrix $E = C^T C$. If all the constraints are linearly independent, than the rank R will be equal to the number of constraints, namely, M. Under certain circumstances, the constraints may not be all independent. For example, if some gridpoints along the interface are coincident and are also rigidly constrained to one another. This difficulty is handled by establishing $\hat{B}$ through a singular value decomposition (SVD) which produces $\hat{B}$ such that its columns are the eigenvectors of E associated with zero eigenvalues. Substituting equation (15) into equation (14), pre-multiplying by B^T and solving for $\hat{D}$ yields

$$\hat{D} = (\hat{B}^T \hat{K} \hat{B})^{-1} \hat{B}^T \hat{Q} \tag{16}$$

where $\hat{K}$ and $\hat{Q}$ are the matrix and column vectors of equation (14) and the Lagrangian multiplier term has vanished since $\hat{B}^T C^T$ vanishes. Equation (15) is then used to recover the full displacement vector D.

It is not difficult to extend the integration methods (1) and (2) to the case where the analysis methods of the regions are of the global Ritz or Galerkin type. It is quite likely though, that one region will be modeled using finite elements especially if this region is characterized by complex geometry, for the finite element method is typically thought of as having the positive attribute of treating arbitrary geometry. However, arbitrary geometry often leads to distorted finite elements. Unfortunately most finite elements are not robust to element distortion, (*i.e.*, they are distortion sensitive). Thus attention is next focused on the robustness issue since it will be a critical aspect of making multiple methods integration a practical reality.

Robustness of Finite Elements

The finite element modeling of general aerospace shell structures usually requires the use of distorted meshes. Additional complexities arise if the original finite element discretization is further refined through an adaptive refinement procedure. Most of the 4-node shell elements developed in the past do not produce reliable results for distorted meshes. Whereas, the element developers are usually aware of the limitations and pitfalls of the elements, the users may not be aware of all these limitations and may make invalid use of them. Therefore, it is desirable to formulate simple 3-node and 4-node shell elements that are free from the usual limitations and pitfalls, such as locking, sensitivity to mesh distortion, non-invariance, and spurious modes, and more importantly produce accurate and reliable results.

One way of attacking the shortcomings of *membrane* elements is to include the nodal normal rotational or "drilling" degrees of freedom in the element formulation. In early attempts, these rotational degrees of freedom were used in cubic displacement functions. However, Irons and Ahmad demonstrated that this approach had serious deficiencies[9]. The elements formed in this manner force the shearing strain to be zero at the nodes, and because these elements do not pass the patch test, they could produce erroneous results in some structural analysis problems. Recently researchers have used these rotational degrees of freedom in quadratic displacement functions with more success[10-15]. In previous papers, this latter method has been employed in the following way. First, the element is internally assumed to be an 8-node isoparametric element with 4 corner nodes and 4 midside nodes each having two displacement degrees of freedom, and the stiffness matrix associated with this "internal" element is calculated. Then, this stiffness matrix is condensed to that corresponding to a 4-node element with 12 degrees of freedom by associating the displacement degrees of freedom at the midside nodes with the displacement and rotational degrees of freedom at the corner nodes. MacNeal[12] has used this approach to develop a 4-node displacement-based *membrane* element with selective reduced-order integration. Yunus et al., in reference [13], have also used this method to develop an

assumed-stress hybrid/mixed *membrane* element. Aminpour[14] has also used this method to develop an assumed-stress hybrid/mixed *shell* element.

In this paper, a 4-node assumed-stress hybrid quadrilateral *shell* element with "drilling" degrees of freedom is presented. The formulation is based directly on a 4-node element from the outset in contrast to elements whose formulations began with an "internal" 8-node element. Formulating the element in this manner bypasses the formation of the stiffness matrix for an 8-node isoparametric element and the subsequent transformation of this stiffness matrix to that corresponding to the stiffness matrix of a 4-node element.

Hybrid Variational Principle

The classical assumed-stress hybrid formulation of Pian[16] is based on the principle of minimum complementary energy. The displacements are described on the element boundary and an equilibrating stress field is described over the the domain of the element. It was later recognized that the same method may be derived from the Hellinger-Reissner principle (*e.g.*, see reference [17]). However, in the Hellinger-Reissner principle, the stress field does not have to satisfy the equilibrium equations a priori, and the displacement field has to be described over the domain of the element and not just on the boundaries. The membrane element in reference [13] and the shell element in reference [14] were both developed using the Hellinger-Reissner principle. However, an assumed-stress hybrid 4-node shell element similar to that of reference [14] may also be easily formulated using the minimum complementary energy principle with the advantage being that only the displacements on the boundary of the element enter into the formulation. As such, the formulation is then based directly on a 4-node element rather than internally formulated as an 8-node element and then condensed to a 4-node element.

The invariant properties of the element are preserved by the proper choice of a local element Cartesian-coordinate system. The local element Cartesian-coordinate system is shown in Figure 4 and is obtained by bisecting the diagonals of the element. The axes of this coordinate system are approximately parallel to the edges of the element for non-rectangular geometries (*e.g.*, tapered and skewed elements) which would make the element less sensitive to mesh distortion.

The assumed-stress hybrid formulation is based on assuming an equilibrating stress field σ in the interior of the element as $\sigma = P\beta$, and assuming the displacement field u only on the boundary of the element as $u = Nq$. The matrices P and N consist of the interpolating functions for stresses and displacements, respectively, and coefficients β and q are the unknown stress parameters and nodal displacements and rotations, respectively.

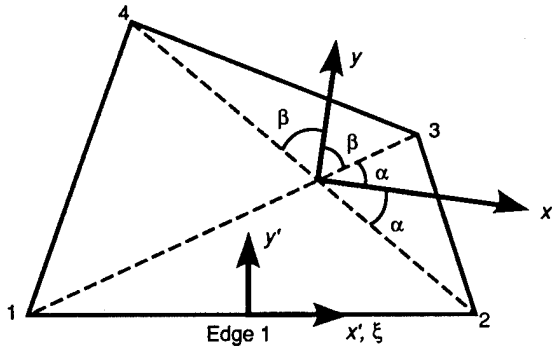


Figure 4. Element coordinate system definition.

Displacement Field Description

All three displacement components on the element boundary are assumed to vary quadratically and all three rotational components to vary linearly. The expressions for these boundary displacements and rotations were derived in detail in reference [14] and only the final results are

given herein. The in-plane boundary displacements on edge 1 of Figure 4 are given by

$$u = \frac{1}{2}(1-\xi)u_1 + \frac{1}{2}(1+\xi)u_2 + \frac{\Delta y_1}{8}(1-\xi^2)(\theta_{z2} - \theta_{z1})$$
$$v = \frac{1}{2}(1-\xi)v_1 + \frac{1}{2}(1+\xi)v_2 - \frac{\Delta x_1}{8}(1-\xi^2)(\theta_{z2} - \theta_{z1}) \tag{17}$$

and the out-of-plane boundary displacement and rotations on edge 1 of Figure 4 are given by

$$w = \frac{1}{2}(1-\xi)w_1 + \frac{1}{2}(1+\xi)w_2 - \frac{\Delta y}{8}(1-\xi^2)(\theta_{x2} - \theta_{x1}) + \frac{\Delta x}{8}(1-\xi^2)(\theta_{y2} - \theta_{y1})$$
$$\theta_x = \frac{1}{2}(1-\xi)\theta_{x1} + \frac{1}{2}(1+\xi)\theta_{x2} \tag{18}$$
$$\theta_y = \frac{1}{2}(1-\xi)\theta_{y1} + \frac{1}{2}(1+\xi)\theta_{y2}$$

where, Δx_1 and Δy_1 are the Δx and Δy of edge 1 with respect to the reference local element x-y coordinate system (*e.g.*, $\Delta x_1 = x_2 - x_1$) and ξ is a non-dimensional coordinate on edge 1 such that $\xi = -1$ at node 1 and $\xi = +1$ at node 2. The description for the displacements and rotations on the other edges of the element are readily obtained.

The displacement and rotation descriptions in equations (17) and (18) allow for in-plane shearing strain and transverse shearing strains, respectively. This feature is in contrast to cubic interpolations of in-plane or out-of-plane displacements which force the in-plane shearing strain or the transverse shearing strains to be zero at the element nodes. The elements using cubic interpolation do not pass the patch test and perform poorly for some structural analysis problems[9]. The elements constructed using quadratic interpolation, on the other hand, pass the patch test which is a necessary condition for convergence to the correct solution.

Stress Field Description

The stress field should be selected in such a manner that no spurious zero-energy mode is produced. In order to avoid spurious zero-energy modes, each independent stress term must suppress one independent deformation mode. Therefore, the minimum number of stress terms required is equal to the number of degrees of freedom of the element less the number of rigid body modes. The equilibrating stress field is expressed in the local element Cartesian-coordinate system shown in Figure 4 and is similar to that proposed by reference [14]. However, in reference [14] the Hellinger-Reissner principle was used, and the stresses were expressed in the natural-coordinate system.

The following equilibrating stress (resultant) field is considered for the membrane part

$$N_x = \beta_1 + \beta_4 y + \beta_6 x + \beta_8 y^2$$
$$N_y = \beta_2 + \beta_5 x + \beta_7 y + \beta_9 x^2 \tag{19}$$
$$N_{xy} = \beta_3 - \beta_6 y - \beta_7 x$$

The first five terms of the stress field in equation (19) represent the stress field that was used in the original 4-node (see reference [16]) assumed-stress hybrid membrane element with 8 degrees of freedom which did not include any normal rotational degrees of freedom. The remaining four terms are present to suppress the four rotational degrees of freedom present in this formulation.

The following equilibrating stress (resultant) field is selected here for the bending part

$$M_x = \bar{\beta}_1 + \bar{\beta}_4 y + \bar{\beta}_6 x + \bar{\beta}_8 xy$$
$$M_y = \bar{\beta}_2 + \bar{\beta}_5 x + \bar{\beta}_7 y + \bar{\beta}_9 xy$$
$$M_{xy} = \bar{\beta}_3 + \bar{\beta}_{10} x + \bar{\beta}_{11} y + \frac{1}{2}\bar{\beta}_{12} x^2 + \frac{1}{2}\bar{\beta}_{13} y^2 \tag{20}$$
$$Q_x = (\bar{\beta}_6 + \bar{\beta}_{11}) + (\bar{\beta}_8 + \bar{\beta}_{13})y$$
$$Q_y = (\bar{\beta}_7 + \bar{\beta}_{10}) + (\bar{\beta}_9 + \bar{\beta}_{12})x$$

The stress fields in equations (19) and (20) produce no spurious zero-energy modes[14] and [15]. It is observed that both the membrane and bending stress (resultant) fields remain invariant upon node renumbering.

NUMERICAL RESULTS

The performance of the 4-node quadrilateral shell element developed in this paper (herein referred to as AQD4) is evaluated in this section. The element has been implemented in the NASA Langley COMET software system[4]. Selected test problems in this article are the straight cantilever beam and the Scordelis-Lo roof. More extensive test problems for this element are reported in reference [15]. The results for the present element are compared with the results using the QUAD4 element of the MSC/NASTRAN from reference [20], the Q4S element from reference [12], the ES1/EX47[18], and ES5/E410[19] elements of the NASA Langley CSM Testbed. A brief description of these elements is given in reference [15]. The dimensions and properties for the test problems are chosen in consistent units.

Straight Cantilever Beam

The straight cantilever beam problem suggested in reference [20] is solved for the three discretizations shown in Figure 5. Normalized results for the present element along with the results for other elements are shown in Table 1. These results indicate that all elements perform well for the rectangular mesh. However, for the trapezoidal and parallelogram meshes which contain considerable amount of distortion, only the Q4S and the present element (AQD4) perform well. The present element produces an error of less than 3.5% for all meshes and loads which indicates the insensitivity of the present element to mesh distortion.

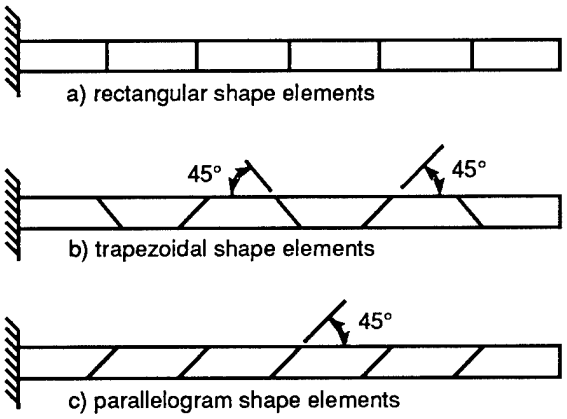


Figure 5. Straight cantilever beam problem. Length=6., height=0.2, depth=0.1, $E=10^7$, $\nu=0.3$, mesh=6x1. Loading: unit forces at the free end.

Table 1. Normalized tip displacements in direction of loads for straight cantilever beam.

Tip Loading / Direction	QUAD4 MSC/ NASTRAN	ES1/ EX47 (ANS)†	ES5/ E410 (STAGS)†	AQD4 (present)
(a) rectangular shape elements				
Extension	.995	.995	.994	.998
In-plane Shear	.904*	.904	.915	.993
Out-of-Plane Shear	.986	.980	.986	.981
Twist	.941**	.856	.680	1.011
(b) trapezoidal shape elements				
Extension	.996	.761	.991	.998
In-plane Shear	.071*	.305	.813	.986
Out-of-Plane Shear	.968	.763	#	.965
Twist	.951**	.843	#	1.009
(c) parallelogram shape elements				
Extension	.996	.966	.989	.998
In-plane Shear	.080*	.324	.794	.972
Out-of-Plane Shear	.977	.939	.991	.980
Twist	.945**	.798	.677	1.010

† These elements are not invariant and do not pass the patch test.

* The results from MacNeal's new Q4S element (not shown in table) for in-plane shear load are reported in reference [12] to be .993, .988, and .986 for the meshes (a), (b), and (c) in Figure 5 respectively.

** These results for twist were normalized with .03028 in reference [20]. Herein, all the other results for twist are normalized using .03046 according to Timoshenko and Goodier's Theory of Elasticity.

\# The element produces a singular stiffness matrix for this mesh.

Scordelis-Lo Roof

The Scordelis-Lo roof is shown in Figure 6. This structure is a singly-curved shell problem, loaded under gravity, in which both the membrane and bending contributions to the deformation are significant. Because of symmetry, only one quadrant of the problem is modeled. The mesh on one quadrant is chosen to be N×N for N=2,4,6,8,10 (N=number of elements along each edge) to show the convergence of the solutions for the present element. Normalized results are shown in Table 2. For this problem, the mesh is made of uniform rectangular-shaped elements and all the elements in the table perform well. It is observed that the convergence rate to the reference solution for the present element is roughly the same as the other elements and thus, the addition of the rotational degrees of freedom does not affect the convergence rate of the present element for this problem.

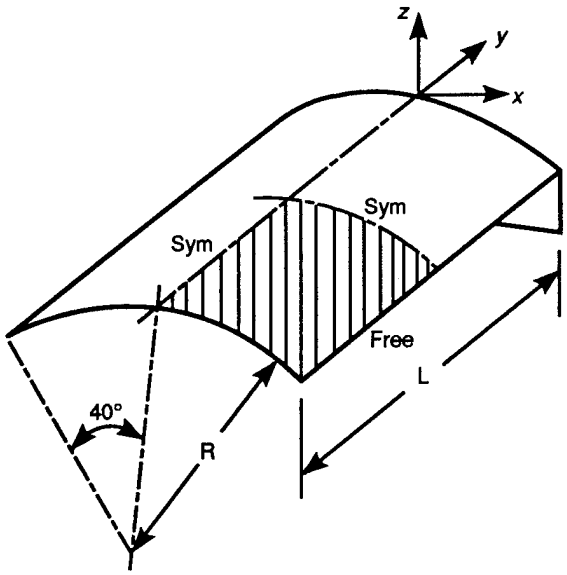


Figure 6. Scordelis-Lo roof problem. Length=50., radius=25., thickness=0.25, E=4.32×10^8, ν=0.3, mesh=N×N. Loading: 90. per unit area in vertical direction, *i.e.*, gravity load; $u_x=u_z=0$ on curved edges. Reference solution: vertical displacement at midpoint of free-edge=0.3024 from reference [20].

Table 2. Normalized displacements at the midpoint of the free-edge for Scordelis-Lo roof.

Mesh	QUAD4 MSC/ NASTRAN	ES1 EX47/ (ANS)	ES5 E410/ (STAGS)	AQD4 (present)
2×2	1.376	1.387	1.384	1.218
4×4	1.050	1.039	1.049	1.021
6×6	1.018	1.011	1.015	1.006
8×8	1.008	1.005	1.005	1.003
10×10	1.004	1.003	1.001	1.001

Concluding Remarks

A new research area of multiple methods integration is proposed for joining diverse methods of structural mechanics analysis which interact with one another. Three categories of multiple methods are defined: those in which a physical interface is well-defined; those in which a physical interface is not well-defined, but selected; and those in which the interface is a mathematical transformation. The integration procedures required in each of these categories is of necessity generally different.

Two fundamental integration procedures have been formulated. One which establishes a tight interface connection and finds application in the first category, and one which establishes a more forgiving connection and finds application in the second category.

Moreover, since the most likely candidate for integration with other methods is the general purpose finite element method, the robustness issue of finite elements to element distortion has been examined and a new robust 4-node quadrilateral shell element demonstrated.

The membrane part of the element formulation includes the drilling degrees of freedom and the bending part is of class C^0 and takes into account the effects of transverse shear deformations.

The element formulation is simple and straightforward, and is derived directly for a 4-node element rather than being reduced from "internal" 8-node isoparametric elements. Thus the formation of the element kernel does not require the time consuming transformation from an 8-node to a 4-node element.

REFERENCES

1. Giles, Gary L. and Norwood, R. Keith: *Coupled Finite Element and Equivalent Plate Analysis of Aircraft Structures.* Presented at the Third Air Force/NASA Symposium on Recent Advances in Multidisciplinary Analysis and Optimization. San Francisco, CA. September, 1990.
2. Hughes, T. J. R.; and Hinton, E.: *Finite Element Methods for Plate and Shell Structures, Volume 1: Element Technology.* Pineridge Press Limited, 1986.
3. Crisfield, M. A.: *Finite Elements and Solution Procedures for Structural Analysis, Volume 1: Linear Analysis.* Pineridge Press Limited, 1986.
4. Knight, N. F., Jr.; Gillian, R. E.; McCleary, S. L.; Lotts, C. G.; Poole, E. L.; Overman, A. L.; and Macy, S. C.: *CSM Testbed Development and Large-Scale Structural Applications.* NASA TM-4072, April 1989.
5. Sistla, Rajaram; and Thurston, Gaylen A.: *Error Analysis of Finite Element Solutions for Post-buckled Cylinders*, AIAA Paper No. 89-1417. April, 1989.
6. Sistla, Rajaram; and Thurston, Gaylen A.: *Error Analysis of Finite-Element Solutions for Post-buckled Plates*, AIAA Paper No. 88-2216. April, 1988.
7. Sistla, Rajaram; and Thurston, Gaylen A.: *Elimination of Gibbs' Phenomena From Error Analysis of Finite Element Results*, AIAA Paper No. 90-0932. April, 1990.
8. Sistla, Rajaram; Thurston, Gaylen A.; and Bains, Jane C.: *EAC: A Program for the Error Analysis of Stags Results for Plates.* NASA TM 100640, 1989.
9. Irons, B. M.; and Ahmad, S.: *Techniques of Finite Elements.* John Wiley and Sons, New York, 1980.
10. Allman, D. J.: A Compatible Triangular Element Including Vertex Rotations for Plane Elasticity Analysis. *Computers and Structures*, Vol. 19, No. 1-2, 1984, pp. 1-8.
11. Cook, R. D.: On the Allman Triangle and a Related Quadrilateral Element. *Computers and Structures*, Vol. 22, No. 6, 1986, pp. 1065-1067.
12. MacNeal, R. H.; and Harder R. L.: A Refined Four-Noded Membrane Element with Rotational Degrees of Freedom. *Computers and Structures*, Vol. 28, No. 1, 1988, pp. 75-84.
13. Yunus, S. H.; Saigal S.; and Cook, R. D.: On Improved Hybrid Finite Elements with Rotational Degrees of Freedom. *International Journal for Numerical Methods in Engineering*, Vol. 28, 1989, pp. 785-800.
14. Aminpour, M. A.: *A 4-Node Assumed-Stress Hybrid Shell Element with Rotational Degrees of Freedom.* NASA CR-4279, 1990.
15. Aminpour, M. A.: *Direct Formulation of a 4-Node Hybrid Shell Element with Rotational Degrees of Freedom.* NASA CR-4282, 1990.
16. Pian, T. H. H.: Derivation of Element Stiffness Matrices by Assumed Stress Distributions. *AIAA Journal*, Vol. 2, 1964, pp. 1333-1336.
17. Pian, T. H. H.: *Finite Elements Based on Consistently Assumed Stresses and Displacement.* Finite Elements in Analysis and Design, Vol. 1, 1985, pp. 131-140.
18. Park, K. C.; and Stanley, G. M.: A Curved C^0 shell Element Based on Assumed Natural-Coordinate Strains. *Journal of Applied Mechanics*, Vol. 108, 1986, pp. 278-290.

19. Rankin, C. C.; Stehlin, P.; and Brogan, F. A.: *Enhancements to the STAGS Computer Code.* NASA CR-4000, 1986.

20. MacNeal, R. H.; and Harder, R. L.: A Proposed Standard Set of Problems to Test Finite Element Accuracy. *Finite Elements in Analysis and Design*, Vol. 1, No. 1, 1985, pp. 3-20.

PROBABILISTIC COMPOSITE ANALYSIS

C. C. Chamis and P. L. N. Murthy
NASA Lewis Research Center
Cleveland, OH

SUMMARY

Formal procedures are described which are used to computationally simulate the probabilistic behavior of composite structures. The computational simulation starts with the uncertainties associated with all aspects of a composite structure (constituents, fabrication, assembling, etc.) and encompasses all aspects of composite behavior (micromechanics, macromechanics, combined stress failure, laminate theory (and including structural response and tailoring (optimization). Typical sample cases are included to illustrate the formal procedure for the computational simulation. The collective results of the sample cases demonstrate that uncertainties in composite behavior and structural response can be probabilistically quantified.

INTRODUCTION

Probabilistic composite mechanics and probabilistic composite structural analysis are formal methods which are used to quantify the scatter that is observed in composite material properties and structural response. The observed scatter in composite material properties is the range of measured values in modulus, strength, thermal expansion coefficient, etc., while that in structural response is the range of measured values for displacement, frequency, buckling load, etc. The formal methods relate the scatter in the observed values to the corresponding scatter in the physical parameters which make up the composite and/or the composite structure. For example, these parameters include constituent material properties, fabrication process variables, structural component geometry, and any other variables which contribute to the composite behavior and/or structural response.

The development of these types of formal methods has been the subject of considerable research at NASA Lewis Research Center. This research has led to computational simulation methods for relating the scatter (uncertainties) in the composite properties or composite structural response to the corresponding uncertainties in the respective parameters (primitive variables) which are used to describe the composite in all its inherent scales: micro, macro, laminate and structural. The objective of this paper is to summarize salient features of these computational simulation methods and to present typical results to illustrate their applications.

Specifically, the paper covers (1) a brief description of the fundamental concepts, (2) probabilistic composite micromechanics, (3) probabilistic laminate theory, (4) probabilistic laminate tailoring, and (5) elementary probabilistic structural analysis.

FUNDAMENTAL CONCEPTS

The fundamental concepts/assumptions in the probabilistic composite mechanics described herein are (1) the scatter in all the primitive variables, which describe the composite, can be represented by well known probabilistic distributions, (2) the values for the primitive variables can be randomly selected from the known distributions for a specific composite, (3) these values can be used in composite mechanics to predict composite behavior, (4) the whole process can be repeated many times to obtain sufficient information to develop the distribution of the ply property, composite property, or structural response. These concepts are analogous to making and testing a composite. The probabilistic distributions represent available materials that the composite can be made from. The composite mechanics represent the physical experiment and the processes repetition represents several experiments. Subsequent statistical analysis of the data is the same for both approaches.

The primitive variables which describe the composite are identified by examining the fabrication process. A schematic depicting the fabrication process for an aircraft wing top cover using top cover is shown in figure 1. The respective primitive variables with their corresponding probabilistic distributions and parameters are listed in Table 1. The use of these in composite mechanics and structural analysis are described in subsequent sections.

PROBABILISTIC COMPOSITE MICROMECHANICS

The probabilistic simulation is performed by considering the ply as an assembly (equivalent laminate) of 15 subplies, where each subply is made from randomly selected properties from Table 1. The composite mechanics used in the simulation is that available in the Integrated Composite Analyzer (ICAN) (ref. 1). The structure of ICAN is schematically shown in figure 2.

Typical probabilistic results obtained for ply shear modulus and shear strength are shown in figure 3 and for ply longitudinal compressive strength in figure 4. Additional details are found in references 2 and 3.

PROBABILISTIC LAMINATE THEORY

Probabilistic laminate theory consists of using probabilistic ply properties in the laminate theory equations. In the present simulation the probabilistic ply properties are available from the probabilistic micromechanics previously described. The simulation for laminate properties is performed using ICAN (fig. 2).

Typical probabilistic laminate properties for a quasi-isotropic (Θ = 45° in fig. 5) laminate from graphite-fiber/epoxy composite are shown in figure 6 for laminate modulus (E_{xx}). The mean value of the modulus is about 6.2 mspi, which is at 50 percent probability, while the range is from about 2 to 14 mspi. Corresponding results for the compressive strength are shown in figure 7 with a mean of about 80 ksi and a range from 45 to 140 ksi. Those for the thermal expansion coefficient are shown in figure 8 with a mean value of 1.6 μ-in/°F and a range from 0.0 to about 7.5 μ-in/°F. The ranges for the laminate

modulus and compressive strength include those measured (table 5, and fig. 16 in ref. 4,), although the scatter in the measured properties is considerably smaller than the simulation results. One reason may be that the scatter assumed for the primitive variables should be tightened. The important conclusion is that the computational simulation for probabilistic composite mechanics has sufficient flexibility to capture the observed scatter in composite properties. The probabilistic evaluation of laminate properties also provides sensitivities of the primitive variables. For the laminate modulus, these sensitivities are summarized in Table 2. The fiber modulus is the most sensitive. The details are described in a forthcoming report.

PROBABILISTIC LAMINATE TAILORING

Computational simulation methods have been developed for tailoring laminates with probabilistic properties and subjected to probabilsitic loads. The probabilistic properties are obtained as described in the previous two sections while the probabilistic loads are described by assuming appropriate probabilistic distributions. A flowchart of the tailoring procedure is shown in figure 9. Typical results obtained are shown in figure 10. As can be seen, laminate tailoring with probabilsitic loads and strength yields heavier laminates for the same probability of failure. On the other hand, laminate tailoring for probabilsitic loads with fixed strength probability is independent of laminate weight, lending credence to safety factor designs. The important conclusion is that computational simulation methods can be developed for probabilistic laminate tailoring. Additional details are given in reference 5.

ELEMENTARY PROBABILISTIC COMPOSITE STRUCTURAL ANALYSIS

Computational simulation methods for elementary probabilistic composite structural analysis have been developed. These are based on the same fundamental concepts described previously, where the scatter in all of the primitive variables which describe the structure is expressed in terms of probabilistic distributions. Values from these distributions are then substituted in classical structural mechanics equations to evaluate the corresponding probabilistic distribution in the structural response.

The entire computational simulation is illustrated in figure 11, where the probabilistic buckling load of an eccentrically loaded composite cantilever is evaluated. The schematic with the eccentric load is shown. The equation for the buckling load is given under the schematic. The primitive variables (all the variables in the equation are listed under the equation). Respective probabilistic distributions for each of the primitive variables are shown. The probability density function (PDF) (frequency of occurrence) is shown at the top right of the figure; the corresponding cumulative distribution function (CDF) (probability of occurrence) is shown below the PDF. The sensitivity of the buckling load to primitive variables is given at the bottom right for two probability levels.

The important points to observe in figure 11 are (1) the mean load is approximately equal to the deterministic load which is calculated by using mean values for the primitive variables; (2) the thickness dominates the sensitivity at high probabilities (0.999) with all others being relatively small, while at low probabilities (0.02813) even though the thickness sensitivity still dominates those for modulus and length have doubled; and (4) the shear modulus has relatively negligible effect on the buckling load.

shear modulus has relatively negligible effect on the buckling load.

As was already mentioned, figure 11 summarizes schematically the entire probabilistic structural analysis. For structures of practical interest such as aircraft wings and fuselages, the single equation for the structural analysis model is replaced by a finite element model, the primitive variables increase many fold, and several global responses are usually needed, as well as local stresses and strains. The important conclusion is that the uncertainties in composite structural behavior can be quantified by the probabilistic methods described herein. Several other examples of this cantilever are described in a forthcoming report. Parallel research activities at Lewis led to the development of probabilistic structural analysis methods for select components for the Space Shuttle Main Engine (ref. 6).

CONCLUSIONS

Probabilistic composite mechanics and probabilistic structural analysis methods can be developed to quantify the uncertainties at all levels of composite behavior. These methods use probabilistic concepts in conjunction with composite mechanics and structural mechanics. Application of these methods to quantify scatter in ply properties, laminate properties, laminate tailoring, and elementary structural analysis demonstrate that uncertainties in composite behavior and composite structural response can be probabilistically quantified.

REFERENCES

1. Murthy, P. L. N. and Chamis, C. C.: Integrated Composite Analyzer (ICAN) - User's and Programmers's Manual. NASA TP 2515, 1986.

2. Stock, T. A., Bellini, P. X., Murthy, P. L. N., and Chamis, C. C.: A Probabilsitic Approach to Composite Micromechanics. NASA TM 101366, 1988.

3. Chamis, C. C. and Stock, T. A.: Probabilistic Simulation of Uncertainties in Composite Uniaxial Strengths. NASA TM 102483, 1990.

4. Chamis, C. C.: Mechanics of Composite Materials: Past, Present and Future. NASA TM 100793, 1988.

5. Thanedar, P. B. and Chamis, C. C.: Composite Laminate Tailoring with Probabilistic Constraints and Loads. NASA TM 102515, 1990.

6. Chamis, C. C.: Probabilistic Structural Analysis Methods for Space Propulsion System Components. NASA TM 88965, 1986.

Table 1. Constituent Input Distribution Parameters for ICAN.

	Units	Distribution Type	Parameter 1	Parameter 2
E_{f11}	Msi	Normal	μ = 31.0	σ = 1.5
E_{f22}	Msi	Normal	μ = 2.0	σ = .10
G_{f12}	Msi	Normal	μ = 2.0	σ = .10
G_{f23}	Msi	Normal	μ = 1.0	σ = .05
ν_{f12}	---	Normal	μ = .20	σ = .01
ν_{f23}	---	Normal	μ = .25	σ = .01
α_{f11}	ppm/°F	Normal	μ = .2	σ = .01
α_{f22}	ppm/°F	Normal	μ = .2	σ = .01
ρ_f	lb/in^3	Normal	μ = .063	σ = .003
N_f	---	Fixed	μ = 10,000	σ = 0
d_f	inches	Normal	μ = .003	σ = .00015
C_f	BTU/lb/°F	Normal	μ = .20	σ = 0.01
K_{f11}	*	Normal	μ = 580	σ = 2.9
K_{f22}	*	Normal	μ = 58	σ = 2.9
K_{f33}	*	Normal	μ = 58	σ = 2.9
S_{ft}	ksi	Weibull	β = 400	α = 40
S_{fc}	ksi	Weibull	β = 400	α = 40
E_m	Msi	Normal	μ = .500	σ = .025
G_m	Msi	Normal	μ = .185	σ = .009
ν_m	---	Normal	μ = .35	σ = .035
α_m	ppm/°F	Normal	μ = 36	σ = 4
ρ_m	lb/in^3	Normal	μ = .0443	σ = .0022
C_m	BTU/lb/°F	Normal	μ = .25	σ = .0125
K_m	*	Normal	μ = 1.25	σ = .06
S_{mT}	ksi	Weibull	β = 15	α = 5
S_{mc}	ksi	Weibull	β = 35	α = 20
S_{mS}	ksi	Weibull	β = 13	α = 7
β_m	in/in/1% mois	Normal	μ = .004	σ = .0002
D_m	in^2/sec	Normal	μ = .002	σ = .0001

* = BTU·in/hr/in^2/°F

Table 2. Nonzero Sensitivity Parameters for E_{xx} from FPI at $\pm 0.3\sigma$ Away From Mean of μ=5.744 Msi.

Primitive Variable	Sensitivity Parameter
E_{f11}	0.624
E_{f22}	0.260
G_{f12}	0.130
G_{f23}	0.0
ν_{f12}	0.360E-4
ν_{f23}	0.360E-4
E_{mP}	0.036
G_{mP}	0.060
ν_{mP}	0.386E-3
k_f	0.778
k_v	0.0

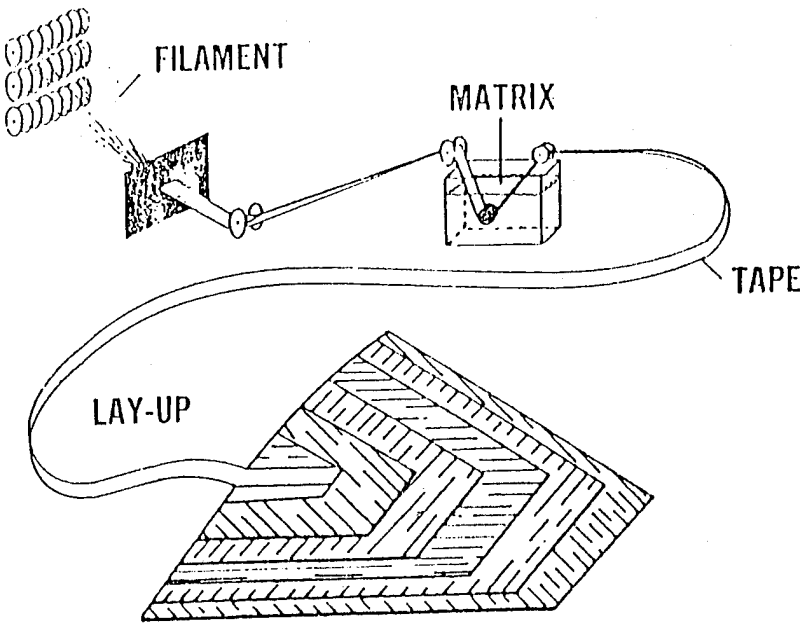


Figure 1. Schematic of Composite Fabrication Process

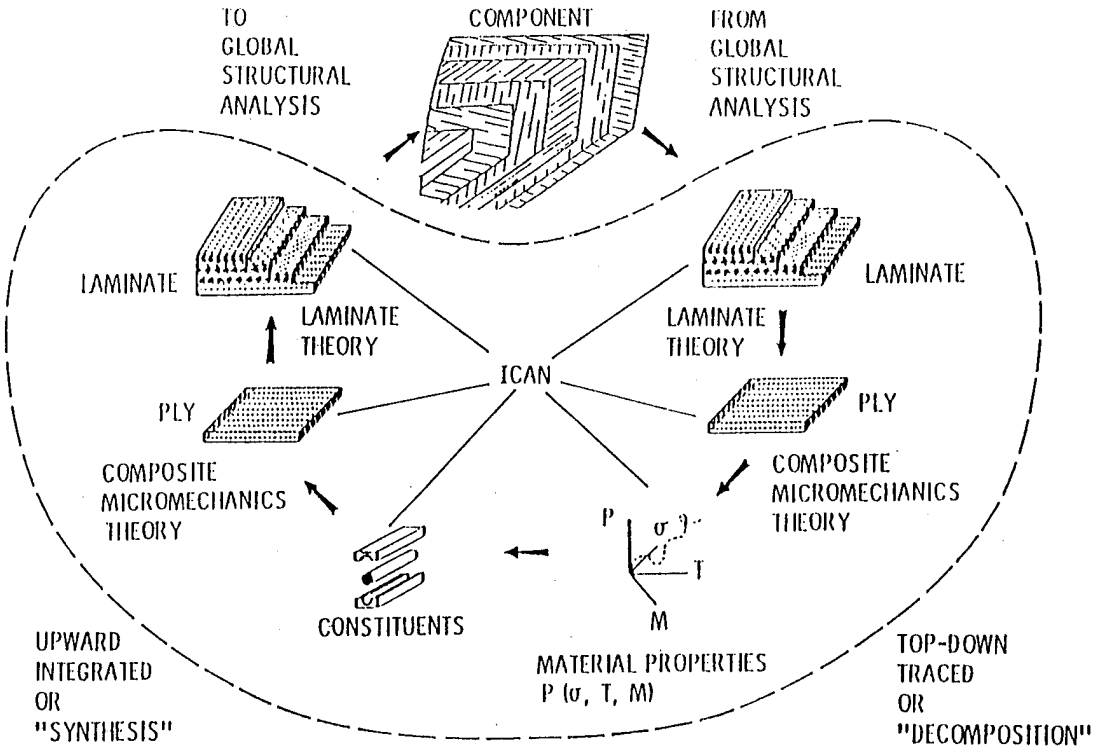


Figure 2. ICAN Intergrated Analyzer

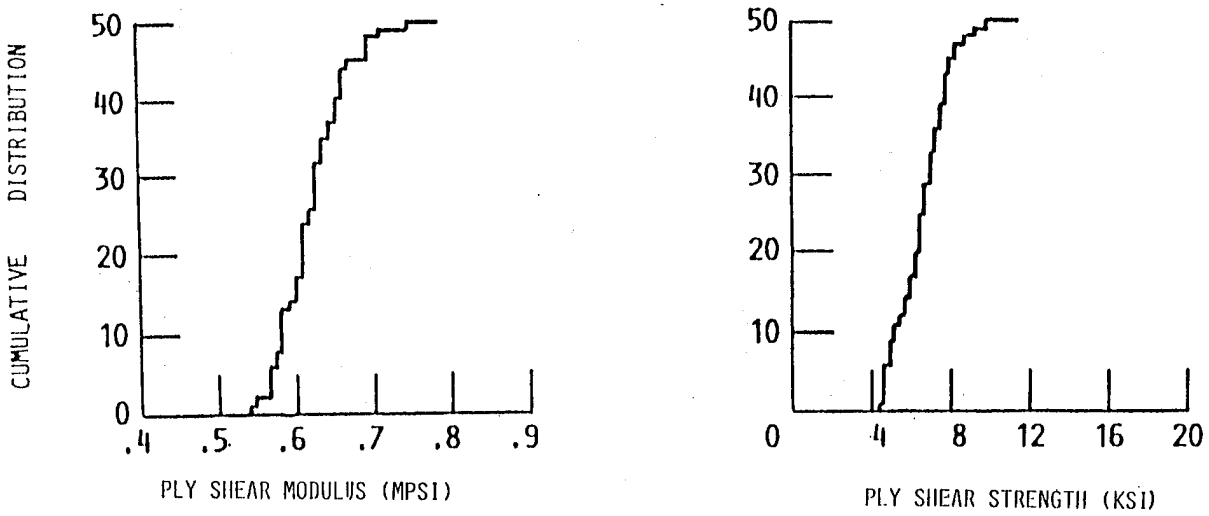


Figure 3. Probabilistic Ply Properties

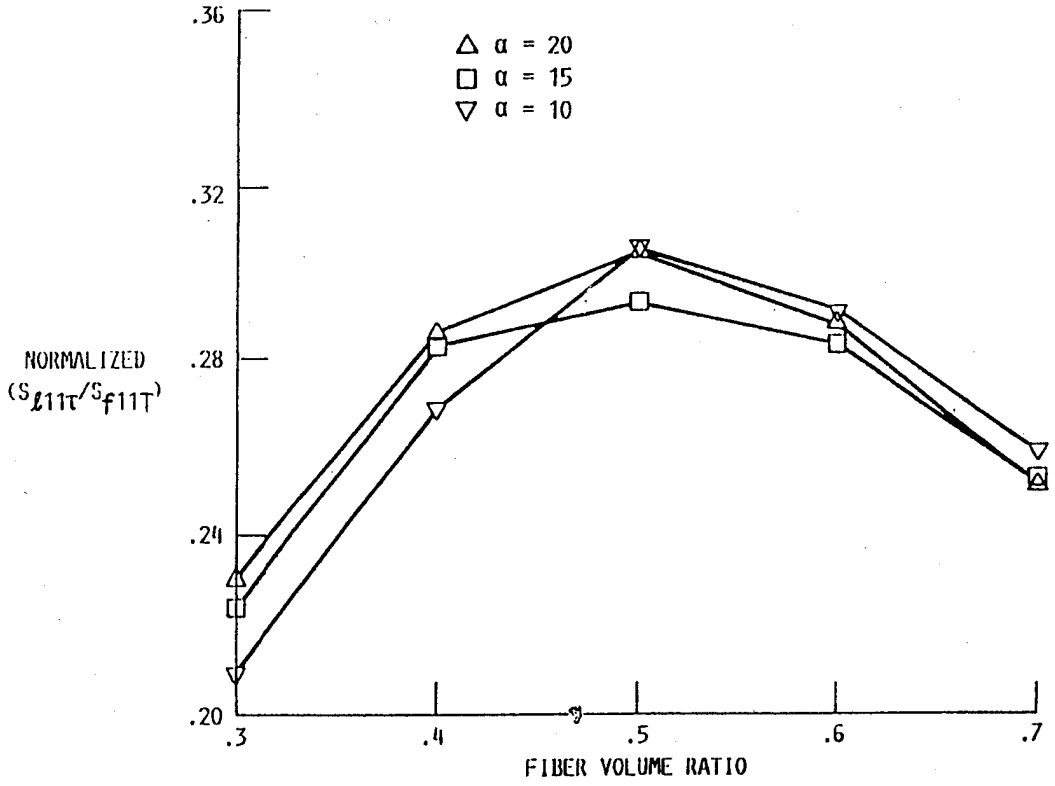


Figure 4. Probabilistic Ply Longitudinal Compression Strength

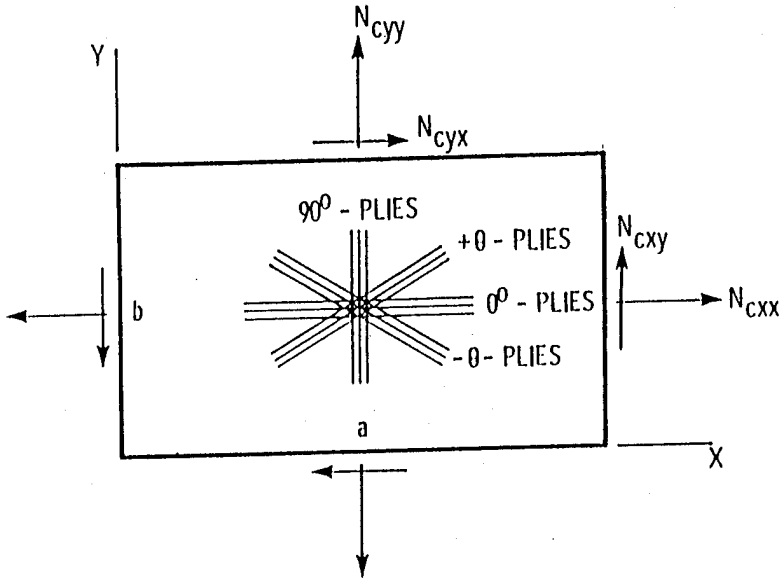


Figure 5. Schematic of Angleplied Fiber Composite Panel Subjected To Combined In-Plane Loads

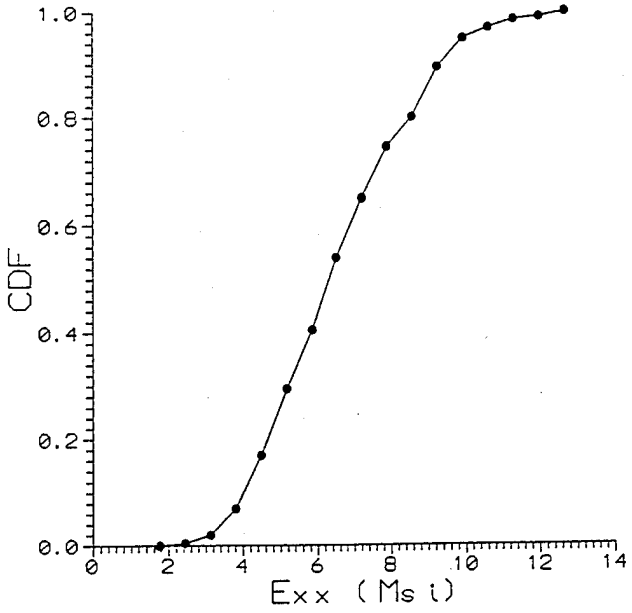


Figure 6. Laminate Modulus E_{cxx} -Quasi-isotropic Laminate (Graphite Fiber/Epoxy)

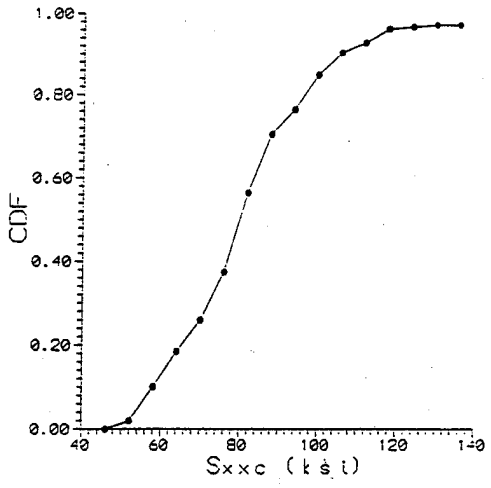


Figure 7. Longitudinal Compressive Strength of a Quasi-Isotropic Laminate (Graphite Fiber-Epoxy)

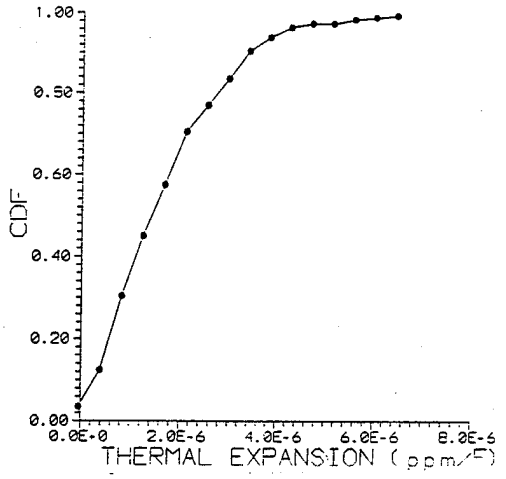


Figure 8. Thermal Expansion Coefficient of Quasi-Isotropic Laminate (Graphite Fiber-Epoxy)

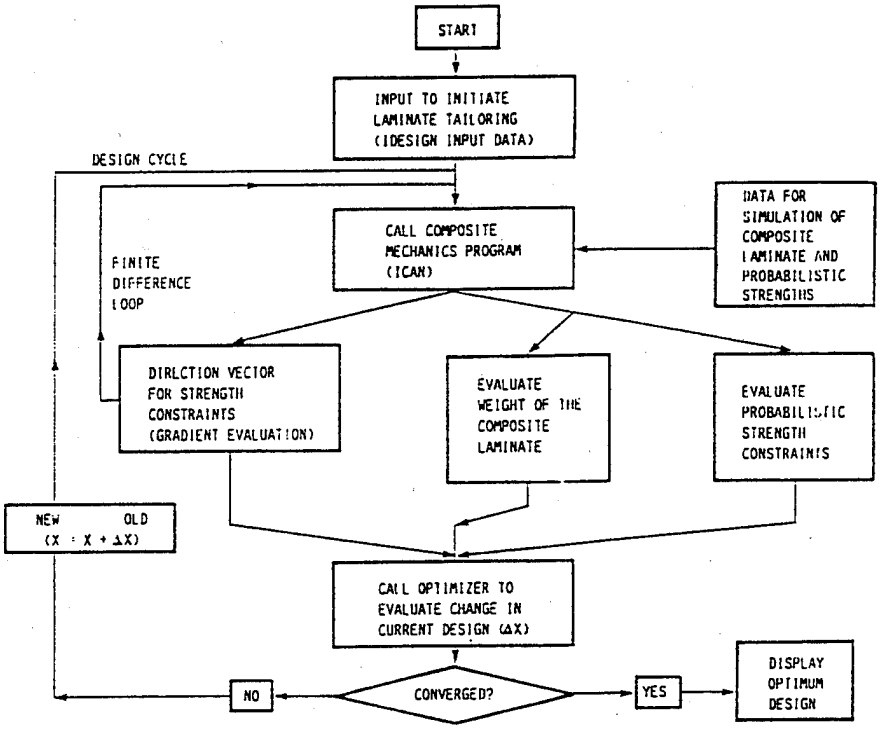


Figure 9. Flowchart For Composite Laminate Tailoring With Probabilistic Loads and/or Constraints.

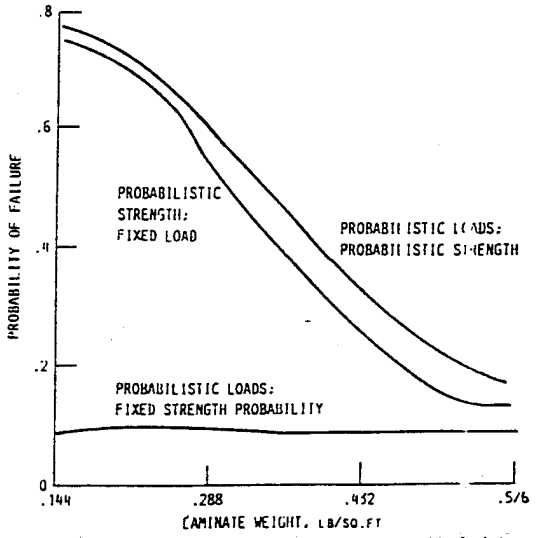


Figure 10. Laminate Optimum Weight For Specified Reliability.

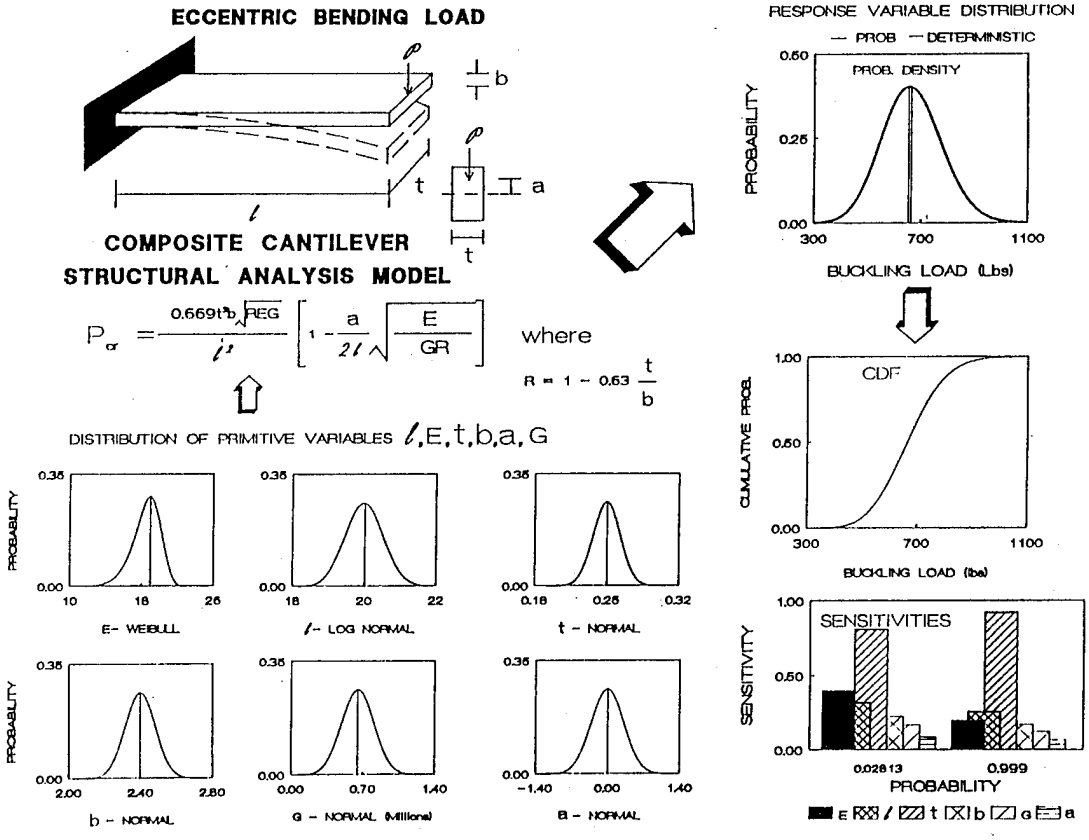


Figure 11. Probabilistic Structural Analysis.

A RAYLEIGH-RITZ ANALYSIS METHODOLOGY FOR CUTOUTS IN COMPOSITE STRUCTURES[1]

Steven G. Russell
Northrop Corporation
Aircraft Division
Department 3853/82
One Northrop Avenue
Hawthorne, California

ABSTRACT

This paper describes a new Rayleigh-Ritz stress analysis methodology that has been developed for composite panels containing cutouts. The procedure, which makes use of a general assumed displacement field, accommodates circular and elliptical cutouts in biaxially loaded rectangular composite panels. Symmetric integral padups around the cutout can be included in the analysis. Benchmark results are presented to demonstrate the accuracy of the technique, and strength predictions based on the average stress criterion are generated and compared with experimental data. Finally, the stress analysis methodology is integrated into a design procedure for sizing integral padups around circular cutouts, and a sample problem is solved to illustrate its use.

INTRODUCTION

Cutouts of various shapes and sizes occur at numerous locations in typical aircraft structures. These cutouts range in complexity from simple holes designed to accommodate fasteners in bolted wing splices to large, reinforced openings that provide systems routing and access in major fuselage bulkheads. The design of these details in composite structures requires an accurate stress analysis technique and a realistic criterion to predict structural failure.

The analysis of cutouts in orthotropic and anisotropic materials has been the focus of numerous research efforts over the years. Both analytical and numerical methods have been developed for a variety of cutouts under different loading conditions. Many of the analytical methods are based upon the use of complex stress functions from the theory of elasticity. Lekhnitskii (Reference 1) developed analyses for elliptical, triangular, oval, and square cutouts in infinite anisotropic plates under in-plane loading. DeJong (Reference 2) extended this body of work in an analysis of rectangular cutouts with rounded corners in infinite orthotropic plates.

[1] This work was performed under NASA/Northrop Contract NAS1-18842, entitled "Innovative Composite Fuselage Structures."

Recently, Prasad and Shuart (Reference 3) developed a general, closed form solution for the moment distribution in infinite anisotropic plates containing circular or elliptical holes and subjected to applied bending moments.

Numerical procedures such as finite element, boundary element, and boundary collocation analysis have been widely used to provide stress analysis of finite plates with cutouts. Hong and Crews (Reference 4) used the finite element method to calculate stress concentration factors around circular holes in uniaxially loaded finite orthotropic plates. The SY5 computer program (Reference 5) uses the finite element method to provide stress analysis for finite isotropic or orthotropic plates with circular, elliptical, square, oval, or rectangular cutouts. Generalized in-plane loading conditions can be accommodated, and padups around cutouts can be modeled using the first three rows of elements around the cutout. The CREPAIR computer program (Reference 6) can be used to analyze elliptical, slotted, and rectangular cutouts in finite orthotropic plates by the boundary element method. CREPAIR is restricted to problems involving biaxial tension/compression or in-plane shear loading conditions. The SASCJ computer code (Reference 7) uses the boundary collocation method to provide stress analysis for loaded fastener holes in finite orthotropic plates. Recently, Klang and Owen (Reference 8) have used the boundary collocation method to develop a stress analysis for finite anisotropic panels containing circular or elliptical cutouts and subjected to in-plane shear loading conditions.

Despite the substantial body of work devoted to stress analysis of orthotropic and anisotropic plates with cutouts, several deficiencies remain in the overall analysis capability. The analytical methods, which are often well-suited for repeated design calculations, are usually valid only for infinite plates. The finite element method requires elaborate preprocessing and postprocessing routines to provide specialized results for cutout problems. The boundary element and boundary collocation approaches, which are especially useful for cutouts with irregular shapes, are difficult to extend to problems involving reinforced cutouts. This paper describes a new approach to cutout stress analysis that is being developed to overcome some of these limitations.

The cutout analysis methodology documented in this paper is based on the Rayleigh-Ritz structural analysis technique, and it makes use of a general assumed displacement field that can be used to treat a wide variety of cutout problems in finite orthotropic plates. This approach eliminates elaborate preprocessing and postprocessing requirements, allows for direct calculation of stress concentration factors at the edge of the cutout, and easily accommodates padups and reinforcements around the hole. As presented here, the methodology is applicable to circular and elliptical cutouts in biaxially loaded orthotropic plates, but it can be extended to include other configurations and loading conditions.

The following sections of the paper provide a description of the Rayleigh-Ritz analysis methodology and a presentation of benchmark results to demonstrate the accuracy of the approach. Next, the analysis methodology is correlated with experimental results and used to generate strength predictions for composite tension specimens with open circular holes. Finally, a design procedure and sample problem are presented to show how the analysis methodology can be used in the design of integral padups around circular cutouts. A complete listing of the equations that are required to implement the cutout analysis methodology is provided in the Appendix.

ANALYSIS METHODOLOGY

Consider an elliptical cutout in a biaxially loaded composite panel as shown in **Figure 1**. The panel is modeled as a thin, elastic orthotropic plate under in-plane loading. Due to the symmetry of the cutout geometry and loading, the analysis is confined to the first quadrant $x,y > 0$ of a rectangular coordinate system with origin at the center of the cutout. Polar coordinates r,θ are defined with respect to the rectangular coordinates x,y by the usual transformation relations $r = (x^2+y^2)^{\frac{1}{2}}$, $\theta = \tan^{-1}(y/x)$.

The principle of virtual work for the loaded panel can be expressed as

$$\int_A \delta\{\epsilon\}^T\{N\}dA - \int_S \delta\{u\}^T\{t\}dS = 0 \qquad (1)$$

where,

$\{u\}$ = vector of panel displacements

$\{N\}$ = vector of panel stress resultants

$\{\epsilon\}$ = vector of strains at the panel middle surface

$\{t\}$ = vector of surface tractions applied along the panel boundary

In Equation 1, A is the panel area and S is the curve that defines the panel boundary. The symbol, δ, represents an arbitrary variation of a quantity consistent with the displacement boundary conditions, which require vanishing normal displacements along the axes of symmetry.

Stress analysis of the panel can be carried out using the Rayleigh-Ritz method. In this procedure, an assumed displacement field containing unknown parameters is developed for the panel and substituted into the principle of virtual work, Equation 1, to yield equations for determination of the unknown parameters. The stress analysis of circular or elliptical cutouts in biaxially loaded panels is based upon the assumed displacement field

$$u_r = \sum_{j=0}^{N} \sum_{k=1}^{M} q_j^k f_k(r)\cos 2j\theta$$

$$u_\theta = \sum_{j=0}^{N} \sum_{k=1}^{M} q_j^{M+k} f_k(r)\sin 2j\theta \qquad (2)$$

where u_r, u_θ are polar coordinate displacement components and q_j^k are unknown parameters. (NOTE that k is used here as a superscript.) The functions $f_k(r)$ are given by

$$f_k(r) = r^{2(k-M)+1} \quad \text{for } k = 1,\ldots,M \qquad (3)$$

where the superscripted quantity is an exponent. The displacement field of Equation 2 satisfies the symmetry conditions, which require vanishing normal displacement and

shear stress along the x and y axes in **Figure 1**. The parameters M and N in Equation 2 can be adjusted to give the required number of series terms necessary for accurate solution of the problem. Substitution of Equations 2 and 3 into the principle of virtual work leads to a system of linear algebraic equations of the form

$$[K]\{q\} = \{T\} \tag{4}$$

where

$[K]$ = stiffness matrix

$\{q\}$ = vector of unknown coefficients

$\{T\}$ = load vector

Details of the derivation of Equation 4 and the subsequent calculation of panel stresses and strains are given in the Appendix.

The foregoing analysis procedure can be extended to account for the presence of symmetric integral padups around the cutout. Consider an integral padup around a circular cutout as shown in **Figure 2**. The reinforced region, A_1, has thickness t_p and the unreinforced region, A_3, has thickness t. These two constant thickness regions are joined by a tapered region, A_2, where the thickness varies linearly with the radial coordinate. The stiffness matrix [K] for the reinforced panel is calculated by carrying out the integration over the panel area, A, in three parts for regions A_1, A_2, and A_3, respectively. In Region A_2, a linear variation of the extensional stiffness is assumed. Hence,

$$A_{jk}^{(2)} = \frac{(r-R_2)}{(R_1-R_2)} A_{jk}^{(1)} + \frac{(r-R_1)}{(R_2-R_1)} A_{jk}^{(3)} \tag{5}$$

where, R_1, R_2 are defined in **Figure 2**, $A_{jk}^{(i)}$ are the extensional stiffness for region i, and j,k = 1,2, or 6. The general procedure given in the Appendix for calculation of the unreinforced panel stiffness matrix can be used for the reinforced panel as well.

BENCHMARK RESULTS

The analysis methodology discussed in the previous section was implemented in a FORTRAN computer program, and benchmark results were generated to test its accuracy relative to well-established cutout stress analysis techniques. **Figure 3** shows a comparison of results for the stress concentration factor at a circular hole in a uniaxially loaded rectangular plate. Rayleigh-Ritz analysis results were checked against results generated using the anisotropic finite width correction factors developed by Tan (Reference 9). Both (25/50/25) quasi-isotropic (i.e., 25% 0°, 50% ±45°, and 25% 90° plies) and (50/39/11) orthotropic laminates were considered. For both types of laminates, very good agreement was obtained for a wide range of hole diameter/plate width ratios. The Rayleigh-Ritz results shown in **Figure 3** were generated by taking N=5, M=6 in the assumed displacement field given in Equation 2.

Figure 4 shows benchmark results for the stress concentration factor at an elliptical hole in a uniaxially loaded rectangular plate. In this comparison, Rayleigh-Ritz analysis results were again compared with the anisotropic finite width correction factors developed by Tan (Reference 9). The aspect ratio of the ellipse was b/a=2.0, and a (50/39/11) orthotropic laminate was considered. Two different versions of Tan's solution were used. The first version, designated as the basic solution, was developed from an approximate stress analysis for an anisotropic plate containing an elliptical cutout. The second version, designated as the modified solution, was developed to obtain improved agreement between analysis and test data. **Figure 4** shows good agreement between the Rayleigh-Ritz solution and Tan's basic solution for cases where $2b/w < 0.5$. For cases where $2b/w \geq 0.5$, the Rayleigh-Ritz solution lies between the two Tan solutions. The Rayleigh-Ritz results shown in **Figure 4** were obtained by taking N=15,M=6 in the assumed displacement field given in Equation 2.

Figure 5 shows benchmark results for the stress concentration factor at circular cutouts with symmetric padups in uniaxially loaded rectangular plates. Rayleigh-Ritz analysis results were compared with results for isotropic plates given by Peterson (Reference 10). The Rayleigh-Ritz results were found to agree fairly closely with Peterson's results for padup thicknesses of up to twice the unreinforced panel thickness.

EXPERIMENTAL CORRELATION AND STRENGTH PREDICTION

The strength prediction of composite laminates with cutouts requires that an appropriate stress analysis procedure be combined with a suitable criterion for prediction of material failure. For practical applications, one of the simplest of these material failure criteria is the semi-empirical average stress criterion originally suggested by Whitney and Nuismer (Reference 11). In the average stress criterion for uniaxial tension loading, laminate failure is predicted when the average stress over a characteristic material distance, a_o, ahead of the cutout equals the unnotched strength of the laminate. The stress is averaged along the line perpendicular to the applied loading that coincides with the symmetry axis of the cutout. The characteristic material distance, a_o, must be determined by correlation with experimental data.

To demonstrate the use of the Rayleigh-Ritz cutout stress analysis procedure in an overall strength prediction methodology, the stress analysis was correlated with experimental data to obtain an appropriate value of a_o for use in the average stress criterion. For this purpose, the strength data published by Tan (Reference 12) for 8-ply AS4/3502 $(0/90/\pm45)_s$ open-hole tension specimens was used. For different hole sizes, the Rayleigh-Ritz stress analysis procedure was used to calculate laminate stresses in the tension specimens, and the value of a_o required to bring the average stress criterion prediction into agreement with the experimental failure stress was determined. The a_o values were generated for circular holes with diameters of 0.1, 0.25, 0.3, 0.41, and 0.61 inch. The specimen dimensions given by Tan (Reference 12) for each of these cases were used in the calculations. The average a_o value for the entire range of hole sizes and specimen dimensions was found to be a_o = 0.09 inch.

To verify the predictive capability of the strength prediction procedure, the ratio of notched to unnotched laminate strength, σ_N/σ_o, was calculated and com-

pared with experimental data published by Nuismer and Whitney (Reference 13). The value a_o=0.09 inch was used in the calculations, which were carried out for 16-ply T300/5208 laminates with $(0/\pm45/90)_{2s}$ and $(0/90)_{4s}$ layups and nominal hole diameters of 0.1, 0.3, 0.6, and 1.0 inch. The specimen dimensions given by Nuismer and Whitney (Reference 13) were used in each of the eight analytical predictions. **Figure 6** shows a comparison between the analytical predictions and experimental data as a function of hole diameter. For the quasi-isotropic $(0/\pm45/90)_{2s}$ laminate, the predictions were 10 to 20 percent conservative for the range of hole sizes considered. The predictions for the orthotropic $(0/90)_{4s}$ laminate were approximately 20 to 30 percent conservative. A plot of predicted versus measured values of σ_N/σ_o for the eight test cases is shown in **Figure 7**.

Based upon the limited number of data considered, the analytical strength prediction procedure for open hole tension specimens seems to provide a conservative estimate of the specimen notched strength. Improved agreement between analysis and experiment can be obtained by adopting a more sophisticated form of the average stress criterion in which the parameter, a_o, is adjusted for different layups and hole sizes. At the time of this writing, experimental correlation and verification of this semi-empirical strength prediction procedure was continuing.

DESIGN PROCEDURE AND SAMPLE PROBLEM

The strength prediction methodology discussed in the previous section can be incorporated into a design procedure for symmetric integral padups around cutouts in composite plates. To illustrate this procedure, consider **Figure 2**, which shows a circular cutout of radius R surrounded by a circular padup in a biaxially loaded composite panel. The padup has a central region of radius R_1 and thickness t_p which tapers to the unreinforced panel thickness t at radius R_2. The object of the design procedure is to determine the padup layup corresponding to a specific uniaxial panel design strength σ_N^*. It is assumed that the padup has the same ply percentages as the parent laminate.

The design task can be carried out by (1) determining the padup region thickness t_p corresponding to σ_N^* and (2) finding a practical padup layup that closely approximates the calculated t_p value. The solution to the first problem can be obtained by iterative application of a strength prediction procedure based on the average stress criterion. For this purpose, consider an unreinforced panel with unit applied load, $N_{x,app}$ (lb/in). The average value of N_x along the x-axis over the line segment $\frac{1}{2}D \leq x \leq \frac{1}{2}D + a_o$ is denoted as $N_{x,av}$. Due to the linear elastic behavior of the panel, the ratio of notched strength, σ_N, to unnotched strength, σ_o, is

$$\frac{\sigma_N}{\sigma_o} = \frac{N_{x,app}}{N_{x,av}} \quad . \tag{6}$$

Next, consider a panel with a padup of the type shown in **Figure 2**. By similar reasoning, the ratio of the notched panel strength, σ_{NP}, for the reinforced panel to the unnotched panel strength is

$$\frac{\sigma_{NP}}{\sigma_o} = \frac{N_{x,app}}{N^*_{x,av}} \frac{t_p}{t} \quad , \tag{7}$$

where, $N^*_{x,av}$ is the average stress along the x-axis over the line segment $\frac{1}{2}D \leq x \leq \frac{1}{2}D+a_o$. The * superscript indicates that the average stress resultant $N^*_{x,av}$ is computed in the reinforced region that has thickness t_p. Since the value of t_p influences the overall load transfer into the padup region from the unreinforced portion of the panel, $N^*_{x,av}$ is a complicated function of t_p.

In the design problem, the desired value of t_p corresponds to the case where $\sigma_{NP} = \sigma^*_N$. For this case, combination of Equations 6 and 7 gives

$$\frac{N^*_{x,av}(t_p)}{N_{x,av}} \frac{\sigma^*_N}{\sigma_N} - \frac{t_p}{t} = 0 \qquad (8)$$

Equation 8 must be solved iteratively to determine the padup region thickness, t_p. For this purpose, a design function, $g(t_p)$, equal to the left-hand side of Equation 8 is introduced. Using two initial estimates for t_p, the secant method can be used to find t_p such that $g(t_p) < \delta$, where δ is a sufficiently small number.

After the padup thickness, t_p, corresponding to σ^*_N has been determined, it remains to find a practical padup layup with the same percentage of plies as the parent laminate. For the case of symmetric integral padups, material of thickness, $(t_p-t)/2$, must be added to each side of the panel. Therefore, the practical padup layup for each side of the panel is the least number of plies that (1) maintains ply percentages of the parent laminate and (2) has total thickness of at least $(t_p-t)/2$.

A flowchart for the padup design procedure is shown in **Figure 8**. To illustrate the use of this procedure, consider a sample problem involving the panel geometry shown in **Figure 2**. The parent laminate is a 36-ply (25/50/25) AS4/3502 panel. The geometrical parameters are L=10 inches, W=4 inches, R=0.5 inch, R_1=0.75 inch, R_2=1 inch, and t=0.1872 inch. The unnotched panel strength is σ_o=71.7 ksi and the panel design strength is σ^*_N=40 ksi. A value a_o=0.09 inch is assumed for the average stress criterion.

For the unreinforced panel with cutout radius R=0.5 inch, the notched panel strength σ_N= 27.1 ksi. Therefore, a padup is necessary if the panel is to withstand the design strength σ^*_N=40 ksi. Using the iterative procedure illustrated in **Figure 8** with initial thickness estimates of t_p=t and t_p=1.1t, the necessary value of t_p was found to be t_p=0.2996 inch. The practical padup corresponding to this value of t_p has 12 plies (three 0°, six ±45°, three 90°) of material on each side of the panel.

For the practical padup, t_p=0.312 inch. A strength analysis for this value of t_p gives a reinforced notched panel strength of σ_{NP}=41.4 ksi. Since this value of σ_{NP} gives a positive margin of safety with respect to the design strength σ^*_N=40 ksi, the padup design procedure has achieved its purpose.

SUMMARY AND FUTURE PLANS

In the previous sections, a Rayleigh-Ritz stress analysis methodology for composite panels with cutouts has been described, and its applications to panel strength prediction and design of symmetric integral padups around cutouts have been illustrated. In its current state of development, this methodology can be applied to

circular or elliptical cutouts in rectangular panels under biaxial tension/ compression loading. The advantages of the procedure are its ability to provide accurate numerical stress analysis solutions with a minimum of input data, and its capability to accommodate cutout reinforcements, such as padups. Its disadvantage is its restricted applicability, which currently includes only a limited number of cutout geometries and panel loading conditions.

Future development efforts for the Rayleigh-Ritz cutout stress analysis methodology will be focused on the incorporation of substructural effects into the analysis, and the extension of the procedure to more complex cutout geometries and loading conditions. The effect of integral stiffeners can be included in the analysis by assuming strain compatibility between the stiffeners and the panel. The strain in the stiffeners can then be calculated using the assumed displacement field given in Equations 2 and 3, and virtual strain energy terms for the stiffener elements can be added to the left-hand side of Equation 1. By this approach, the effect of any number of stiffener elements can be included in the analysis without increasing the number of degrees of freedom in the solution process. An effort to implement the substructural effects analysis for the common case of a "picture-frame" stiffening arrangement around a cutout is currently underway.

Future analysis efforts will also include attempts to extend the existing methodology to include more complex cutout shapes and loading conditions. The analysis of complex cutout shapes, such as slotted holes and rectangles with rounded corners, will require some modification of the basic analysis procedure presented here. One promising approach that will be investigated is use of the penalty function method (Reference 14) in conjunction with the assumed displacement field of Equations 2 and 3. This approach, which involves constructing penalty functions from specified constraint conditions, will make it possible to closely satisfy stress-free boundary conditions along the cutout perimeter without introducing additional degrees of freedom. Further modifications will be required to enable the stress analysis procedure to accommodate more complex loading conditions. For in-plane shear loading, a different assumed displacement field will be constructed to exploit symmetries in the deformation of the panel under this type of loading. This displacement field will be implemented into the analysis using the procedures illustrated in the Appendix. Stress analysis results for problems involving generalized in-plane loading can then be obtained by superposing results obtained from the separate analyses for biaxial and shear loading.

In future work, a concurrent approach to the development of design procedures and enhanced stress analysis methodologies will be pursued. The initial portion of this work, which consists of a design procedure for symmetric integral padups around circular holes in uniaxially loaded panels, was illustrated in this paper. A generalization of this design procedure to permit sizing of cutout reinforcements and stiffening elements will be developed as the extensions to the stress analysis methodology are completed.

REFERENCES

1. Lekhnitskii, S.G., Anisotropic Plates, Second Edition, translated from Russian by S.W. Tsai and T. Cheron, Gordon and Breach Science Publishers, 1968.

2. DeJong, Theo, "Stresses Around Rectangular Holes in Orthotropic Plates," Journal of Composite Materials, Volume 15, 1981, pp 311-328.

3. Prasad, C.B. and Shuart, M.J., "Moment Distributions Around Holes in Symmetric Composite Laminates Subjected to Bending Moments," AIAA Journal, Volume 28, 1990, pp 877-882.

4. Hong, C.S. and Crews, J.H., Jr., "Stress Concentration Factors for Finite Orthotropic Laminates With a Circular Hole and Uniaxial Loading," NASA TP-1469, May 1979.

5. Eisenmann, J.R., "Stress Distribution Around Cutouts," General Dynamics, Convair Aerospace Division, Report FZM-5555, August 1970.

6. Hinkle, T. and Hoehn, G., "Verification of Analytical Methodology for Designing Repairs to Composite Skin, Volume I - Theoretical Development and Test Correlations," McDonnell Aircraft Company, AFWAL-TR-87-3049, Volume I, October 1987.

7. Ramkumar, R.L., Saether, E.S., and Cheng, D., "Design Guide for Bolted Joints in Composite Structures," Northrop Corporation, AFWAL-TR-85-3064, August 1985.

8. Klang, E.C. and Owen, V.L., "Shear Buckling of Specially Orthotropic Plate With Centrally Located Cutouts," Proceedings of the Eighth DoD/NASA/FAA Conference on Fibrous Composites in Structural Design, November 1989.

9. Tan, S.C., "Finite-Width Correction Factors for Anisotropic Plate Containing a Central Opening," Journal of Composite Materials, Volume 22, 1988, pp 1080-1097.

10. Peterson, R.E., Stress Concentration Factors, John Wiley and Sons, New York, 1974.

11. Whitney, J.M. and Nuismer, R.J., "Stress Fracture Criteria for Laminated Composites Containing Stress Concentrations," Journal of Composite Materials, Volume 8, 1974, pp 253-265.

12. Tan, S.C., "Laminated Composites Containing an Elliptical Opening II. Experiment and Model Modification," Journal of Composite Materials, Volume 21, 1987, pp 949-968.

13. Nuismer, R.J. and Whitney, J.M., "Uniaxial Failure of Composite Laminates Containing Stress Concentrations," Fracture Mechanics of Composites, ASTM STP 593, American Society for Testing and Materials, 1975, pp 117-142.

14. Cook, R.D., Concepts and Applications of Finite Element Analysis, Second Edition, John Wiley and Sons, New York, 1981.

APPENDIX

For problem solution, it is convenient to represent the assumed panel displacements given in Equation 2 in the matrix form

$$\{u\} = \begin{Bmatrix} u_r \\ u_\theta \end{Bmatrix} = \sum_{j=0}^{N} [U_j]\{q_j\} \tag{A-1}$$

where $\{q_j\}$ is a vector of dimension 2M containing unknown parameters and $[U_j]$ is a 2 x 2M matrix of the form

$$[U_j] = \begin{bmatrix} f_1\cos 2j\theta \; . \; . \; . \; f_M\cos 2j\theta & 0 \; . \; . \; . \; . \; . \; 0 \\ 0 \; . \; . \; . \; . \; 0 & f_1\sin 2j\theta \; . \; . \; . \; f_M\sin 2j\theta \end{bmatrix} \tag{A-2}$$

The strain vector $\{\epsilon\}$ is obtained by applying the strain-displacement relations for polar coordinates:

$$\{\epsilon\} = \begin{Bmatrix} \epsilon_r \\ \epsilon_\theta \\ \gamma_{r\theta} \end{Bmatrix} = \begin{bmatrix} \frac{\partial}{\partial r} & 0 \\ \frac{1}{r} & \frac{1}{r}\frac{\partial}{\partial \theta} \\ \frac{1}{r}\frac{\partial}{\partial \theta} & \frac{\partial}{\partial r} - \frac{1}{r} \end{bmatrix} \{u\} \tag{A-3}$$

Substitution of Equations A-1 and A-2 into Equation A-3 leads to a relation of the form

$$\{\epsilon\} = \sum_{j=0}^{N} [H_j]\{q_j\} \tag{A-4}$$

where $[H_j]$ is a 3 x 2M matrix whose entries are given by

$$H_{j,1m} = \begin{cases} f'_m \cos 2j\theta & \text{for} \quad m = 1,\ldots,M \\ 0 & \text{for} \quad m = M+1,\ldots 2M \end{cases} \tag{A-5}$$

$$H_{j,2m} = \begin{cases} \frac{1}{r} f_m \cos 2j\theta & \text{for} \quad m = 1,\ldots,M \\ 2j\frac{1}{r} f_{m-M}\cos 2j\theta & \text{for} \quad m = M+1,\ldots 2M \end{cases} \tag{A-6}$$

$$H_{j,3m} = \begin{cases} -2j\,\frac{1}{r} f_m \sin 2j\theta & \text{for} \quad m = 1,\ldots,M \\ (f'_m - \frac{1}{r} f_m)\sin 2j\theta & \text{for} \quad m = M+1,\ldots 2M \end{cases} \tag{A-7}$$

The superposed prime denotes differentiation with respect to r. The stress resultant vector {N} is obtained by application of the stress-strain relations. Let E_x, E_y, G_{xy}, ν_{xy} be the orthotropic elastic constants for the panel. Let

$$\bar{A}_{11} = \frac{E_x t}{1-\nu_{xy}\nu_{yx}} \qquad \bar{A}_{12} = \frac{\nu_{xy} E_y t}{1-\nu_{xy}\nu_{yx}}$$

$$\bar{A}_{22} = \frac{E_y t}{1-\nu_{xy}\nu_{yx}} \qquad \bar{A}_{66} = G_{xy} t \tag{A-8}$$

where $\nu_{yx} = \nu_{xy}(E_y/E_x)$ and t is the panel thickness. The stress resultant vector is given by

$$\{N\} = \begin{Bmatrix} N_r \\ N_\theta \\ N_{r\theta} \end{Bmatrix} = \begin{bmatrix} A_{11} & A_{12} & A_{16} \\ A_{12} & A_{22} & A_{26} \\ A_{16} & A_{26} & A_{66} \end{bmatrix} \begin{Bmatrix} \epsilon_r \\ \epsilon_\theta \\ \gamma_{r\theta} \end{Bmatrix} \tag{A-9}$$

where

$$\begin{aligned}
A_{11} &= \bar{A}_{11}\cos^4\theta + 2(\bar{A}_{12} + 2\bar{A}_{66})\sin^2\theta\cos^2\theta + \bar{A}_{22}\sin^4\theta \\
A_{12} &= (\bar{A}_{11} + \bar{A}_{22} - 4\bar{A}_{66})\sin^2\theta\cos^2\theta + \bar{A}_{12}(\cos^4\theta + \sin^4\theta) \\
A_{16} &= -(\bar{A}_{11} - \bar{A}_{12} - 2\bar{A}_{66})\sin\theta\cos^3\theta - (\bar{A}_{12} - \bar{A}_{22} + 2\bar{A}_{66})\sin^3\theta\cos\theta \\
A_{22} &= \bar{A}_{11}\sin^4\theta + 2(\bar{A}_{12} + 2\bar{A}_{66})\sin^2\theta\cos^2\theta + \bar{A}_{22}\cos^4\theta \\
A_{26} &= -(\bar{A}_{11} - \bar{A}_{12} - 2\bar{A}_{66})\sin^3\theta\cos\theta - (\bar{A}_{12} - \bar{A}_{22} + 2\bar{A}_{66})\sin\theta\cos^3\theta \\
A_{66} &= (\bar{A}_{11} + \bar{A}_{22} - 2\bar{A}_{12} - 2\bar{A}_{66})\sin^2\theta\cos^2\theta + \bar{A}_{66}(\sin^4\theta + \cos^4\theta)
\end{aligned} \tag{A-10}$$

Equation A-9 can be written in the compact matrix form

$$\{N\} = [A]\{\epsilon\} \tag{A-11}$$

where [A] is the 3 x 3 matrix in Equation A-9.

For the rectangular panel of length L and width W shown in **Figure 1**, the r coordinate defining the boundary is a function of θ given by

$$R_b(\theta) = \begin{cases} \dfrac{L}{2\cos\theta} & \text{for } 0 \le \theta \le \phi \\ \dfrac{W}{2\sin\theta} & \text{for } \phi \le \theta \le \dfrac{\pi}{2} \end{cases} \tag{A-12}$$

where $\phi = \tan^{-1}(W/L)$. The r coordinate defining the edge of the elliptical cutout is also a function of θ given by

$$R_c(\theta) = \frac{ab}{(a^2\sin^2\theta + b^2\cos^2\theta)^{1/2}} \tag{A-13}$$

where a,b are the dimensions of the ellipse semiaxes. The surface traction vector along the panel boundary is

$$\{t\} = \begin{Bmatrix} t_r \\ t_\theta \end{Bmatrix} \tag{A-14}$$

$$t_r = \begin{cases} \frac{1}{2} N_x(1+\cos 2\theta) & \text{for } 0 \le \theta \le \phi \\ \frac{1}{2} N_y(1-\cos 2\theta) & \text{for } \phi \le \theta \le \frac{\pi}{2} \end{cases} \tag{A-15}$$

$$t_\theta = \begin{cases} \frac{-1}{2} N_x \sin 2\theta & \text{for } 0 \le \theta \le \phi \\ \frac{1}{2} N_y \sin 2\theta & \text{for } \phi \le \theta \le \frac{\pi}{2} \end{cases} \tag{A-16}$$

Introducing Equations A-1, A-4, A-11, and A-14 into Equation 1 leads to a matrix equation of the form

$$[K]\{q\} = \{T\} , \tag{A-17}$$

where [K] is an M(2N+1) x M(2N+1) stiffness matrix, {q} is an M(2N+1) x 1 vector of unknown displacement field parameters and {T} is an M(2N+1) x 1 load vector.

The stiffness matrix [K] can be represented in the partitioned form

$$[K] = \begin{bmatrix} [K_{00}] & [K_{01}] & \cdots & [K_{0N}] \\ [K_{10}] & [K_{11}] & \cdots & [K_{1N}] \\ \vdots & \vdots & & \vdots \\ [K_{N0}] & [K_{N1}] & \cdots & [K_{NN}] \end{bmatrix} \tag{A-18}$$

where the partition $[K_{00}]$ is an M x M matrix, the partitions $[K_{01}],\ldots,[K_{0N}]$ are M x 2M matrices, the partitions $[K_{10}],\ldots,[K_{N0}]$ are 2M x M matrices, and the remaining partitions are 2M x 2M matrices. The elements of a general partition $[K_{jk}]$ are given by the relations

$$\begin{aligned} K_{jk,mn} = \int_0^{\frac{\pi}{2}} \{ & [A_{11}\beta_{mn} + A_{12}(\delta_{mn} + \delta_{nm}) + A_{22}\phi_{mn}]\cos 2j\theta \cos 2k\theta \\ & - 2k(A_{16}\delta_{nm} + A_{26}\phi_{mn})\cos 2j\theta \sin 2k\theta \\ & - 2j(A_{16}\delta_{mn} + A_{26}\phi_{mn})\sin 2j\theta \cos 2k\theta \\ & + 4jkA_{66}\phi_{mn}\sin 2j\theta \sin 2k\theta \} d\theta \end{aligned} \tag{A-19}$$

$$\text{for } 1 \le m \le M,\ 1 \le n \le M$$

$$K_{jk,mn} = \int_0^{\frac{\pi}{2}} [2k(A_{12}\delta_{n-M,m} + A_{22}\phi_{m,n-M})\cos 2j\theta\cos 2k\theta$$

$$+ (A_{16}\lambda_{m,n-M} + A_{26}\eta_{m,n-M})\cos 2j\theta\sin 2k\theta$$

$$- 4jkA_{26}\phi_{m,n-M}\sin 2j\theta\cos 2k\theta$$

$$- 2jA_{66}\eta_{m,n-M}\sin 2j\theta\sin 2k\theta]d\theta \qquad \text{(A-20)}$$

$$\text{for } 1 \le m \le M,\ M+1 \le n \le 2M$$

$$K_{jk,mn} = \int_0^{\frac{\pi}{2}} [2j(A_{12}\delta_{m-M,n} + A_{22}\phi_{m-M,n})\cos 2j\theta\cos 2k\theta$$

$$- 4jkA_{26}\phi_{m-M,n}\cos 2j\theta\sin 2k\theta$$

$$+ (A_{16}\lambda_{n,m-M} + A_{26}\eta_{n,m-M})\sin 2j\theta\cos 2k\theta$$

$$- 2kA_{66}\eta_{n,m-M}\sin 2j\theta\sin 2k\theta]d\theta \qquad \text{(A-21)}$$

$$\text{for } M+1 \le m \le 2M\ ,\ 1 \le n \le M$$

$$K_{jk,mn} = \int_0^{\frac{\pi}{2}} [4jkA_{22}\phi_{m-M,n-M}\cos 2j\theta\cos 2k\theta$$

$$+ 2jA_{26}\eta_{m-M,n-M}\cos 2j\theta\sin 2k\theta$$

$$+ 2kA_{26}\eta_{n-M,m-M}\sin 2j\theta\cos 2k\theta$$

$$+ A_{66}\omega_{m-M,n-M}\sin 2j\theta\sin 2k\theta]d\theta \qquad \text{(A-22)}$$

$$\text{for } M+1 \le m \le 2M\ ,\ M+1 \le n \le 2M$$

where,

$$\beta_{mn} = \int_{R_c}^{R_b} f_m' f_n' r dr \qquad \text{(A-23)}$$

$$\delta_{mn} = \int_{R_c}^{R_b} f_m' f_n dr \qquad \text{(A-24)}$$

$$\phi_{mn} = \int_{R_c}^{R_b} \frac{1}{r} f_m f_n dr \qquad \text{(A-25)}$$

$$\lambda_{mn} = \int_{R_c}^{R_b} f_m'(f_n' - \frac{1}{r}f_n) r dr = \beta_{mn} - \delta_{nm} \qquad \text{(A-26)}$$

$$\eta_{mn} = \int_{R_c}^{R_b} f_m(f_n' - \frac{1}{r}f_n)dr = \delta_{mn} - \phi_{mn} \qquad \text{(A-27)}$$

$$\omega_{mn} = \int_{R_c}^{R_b} (f_m' - \frac{1}{r}f_m)dr = \beta_{mn} - \delta_{mn} - \delta_{nm} + \phi_{mn} \qquad \text{(A-28)}$$

for $1 \leq m,n \leq M$. In Equations A-23 through A-31, the prime denotes differentiation with respect to r. Using the functions defined in Equation 3, the integrals in Equations A-23 through A-25 can be evaluated to obtain

$$\beta_{mn} = \begin{cases} \dfrac{[2(m-M)+1][2(n-M)+1]}{[2(m+n) - 4M+2]} \left\{ R_b^{[2(m+n)-4M+2]} - R_c^{[2(m+n)-4M+2]} \right\} \\ \qquad\qquad \text{for } m+n \neq 2M-1 , \\ [2(m-M)+1][2(n-M)+1]\ \ln(R_b/R_c) \\ \qquad\qquad \text{for } m+n = 2M-1 \end{cases} \qquad \text{(A-29)}$$

$$\delta_{mn} = \begin{cases} \dfrac{[2(n-M)+1]}{[2(m+n) - 4M+2]} \left\{ R_b^{[2(m+n)-4M+2]} - R_c^{[2(m+n)-4M+2]} \right\} \\ \qquad\qquad \text{for } m+n \neq 2M-1 , \\ [2(n-M)+1]\ln(R_b/R_c) \\ \qquad\qquad \text{for } m+n = 2M-1 \end{cases} \qquad \text{(A-30)}$$

$$\phi_{mn} = \begin{cases} \dfrac{1}{[2(m+n) - 4M+2]} \left\{ R_b^{[2(m+n)-4M+2]} - R_c^{[2(m+n)-4M+2]} \right\} \\ \qquad\qquad \text{for } m+n \neq 2M-1 , \\ \ln(R_b/R_c) \\ \qquad\qquad \text{for } m+n = 2M-1 \end{cases} \qquad \text{(A-31)}$$

The quantities R_b and R_c are functions of θ as defined in Equations A-12 and A-13. The integrals in Equations A-19 through A-22 can be evaluated numerically using Simpson's rule.

The load vector {T} in Equation A-17 can be represented in the partitioned form

$$\{T\} = \begin{Bmatrix} \{T_0\} \\ \{T_1\} \\ \vdots \\ \{T_j\} \\ \vdots \\ \{T_N\} \end{Bmatrix} \tag{A-32}$$

where $\{T_0\}$ is an M x 1 vector and the remaining partitions are 2M x 1 vectors. The elements of a general partition $\{T_j\}$ are given by the relations

$$T_{j,m} = \frac{1}{2} N_x L \int_0^{\phi} f_m(R_b)\cos 2j\theta \, d\theta$$

$$+ \frac{1}{2} N_y W \int_{\phi}^{\frac{\pi}{2}} f_m(R_b)\cos 2j\theta \, d\theta \qquad \text{for } m = 1,\ldots,M \tag{A-33}$$

$$T_{j,m} = -\frac{1}{2} N_x L \int_0^{\phi} f_{m-M}(R_b)\sin 2j\theta \tan\theta \, d\theta$$

$$+ \frac{1}{2} N_y W \int_{\phi}^{\frac{\pi}{2}} f_{m-M}(R_b)\sin 2j\theta \cot\theta \, d\theta \qquad \text{for } m = M+1,\ldots,2M \tag{A-34}$$

These integrals can be evaluated numerically using Simpson's rule. Finally, the vector of unknown displacement field parameters $\{q\}$ in Equation A-17 can be written in the partitioned form

$$\{q\} = \begin{Bmatrix} \{q_0\} \\ \{q_1\} \\ \vdots \\ \{q_j\} \\ \vdots \\ \{q_N\} \end{Bmatrix} \tag{A-35}$$

where $\{q_0\}$ is an M x 1 vector and the remaining partitions are 2M x1 vectors.

Solution of the system of linear algebraic equations represented by Equation A-17 yields the vector of displacement field parameters $\{q\}$. Displacements, strains, and stress resultants at any point in the cutout panel can be calculated by evaluating Equations A-1, A-4, and A-9, respectively.

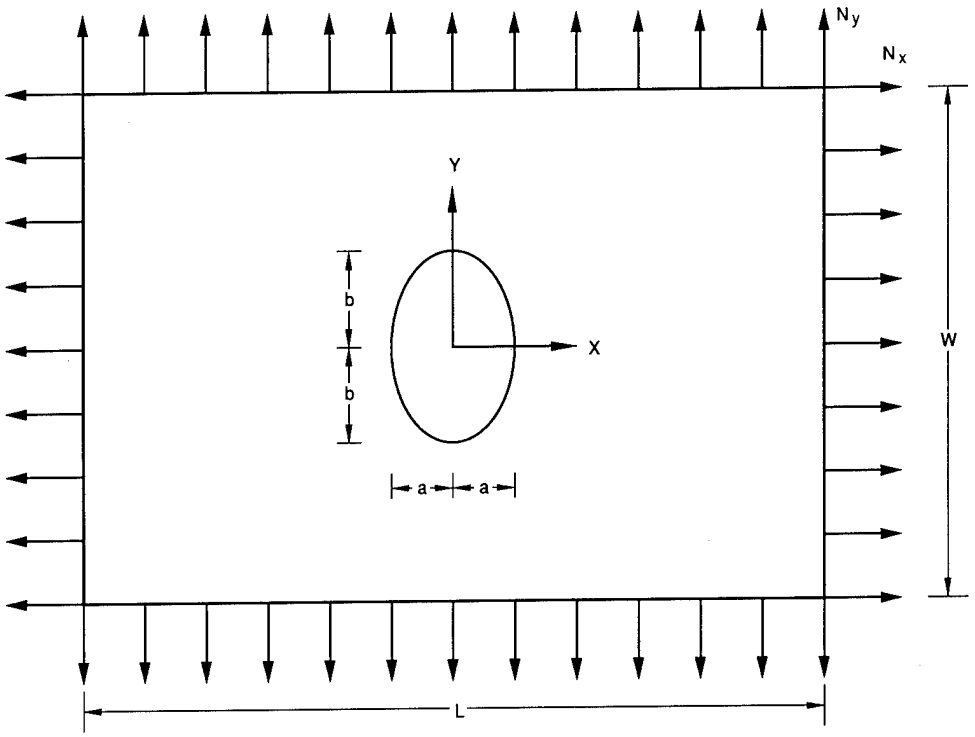


Figure 1. Geometry for cutout analysis methodology.

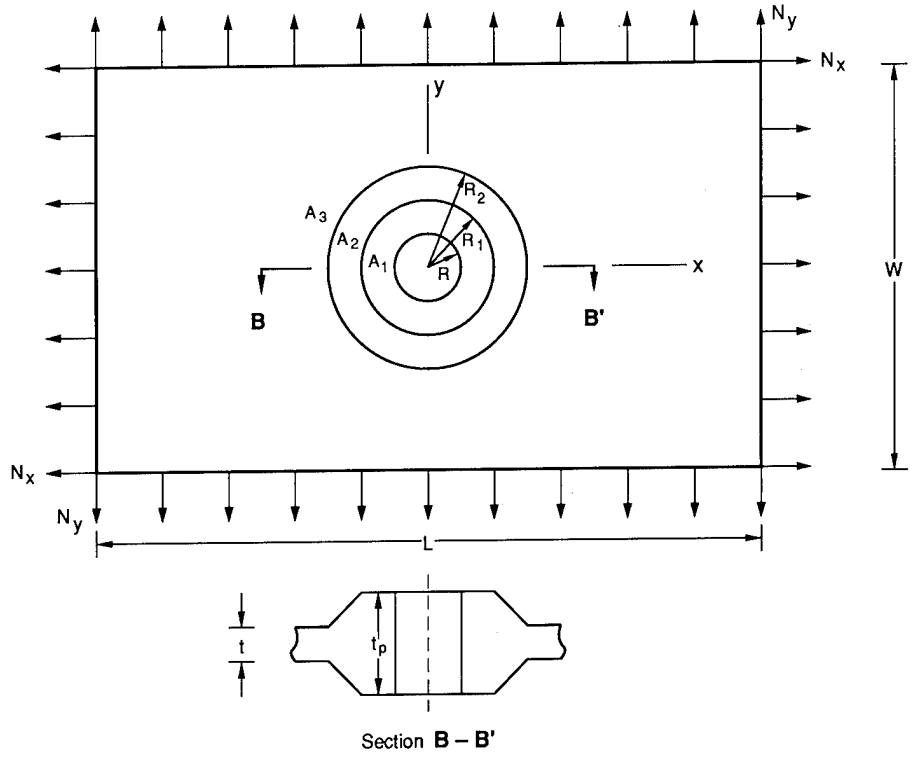


Figure 2. Symmetric integral padup around a circular hole.

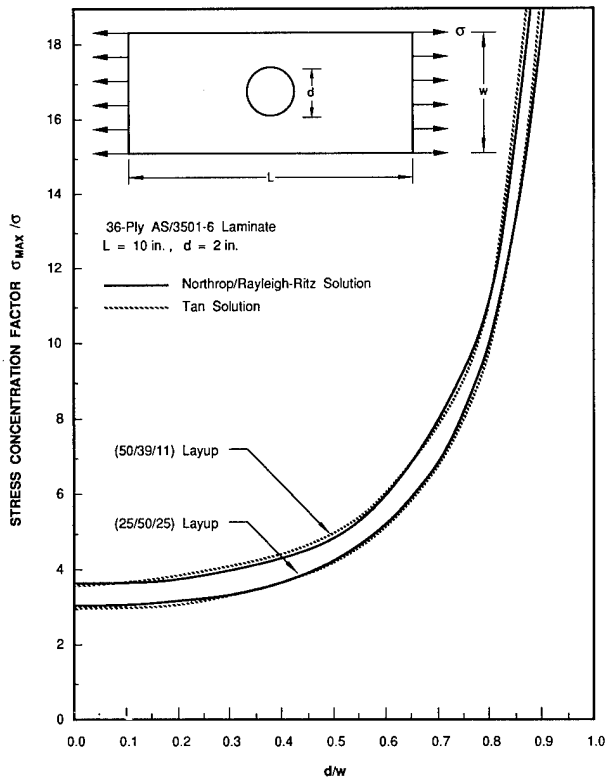


Figure 3. Benchmark results for finite structure circular cutout analysis.

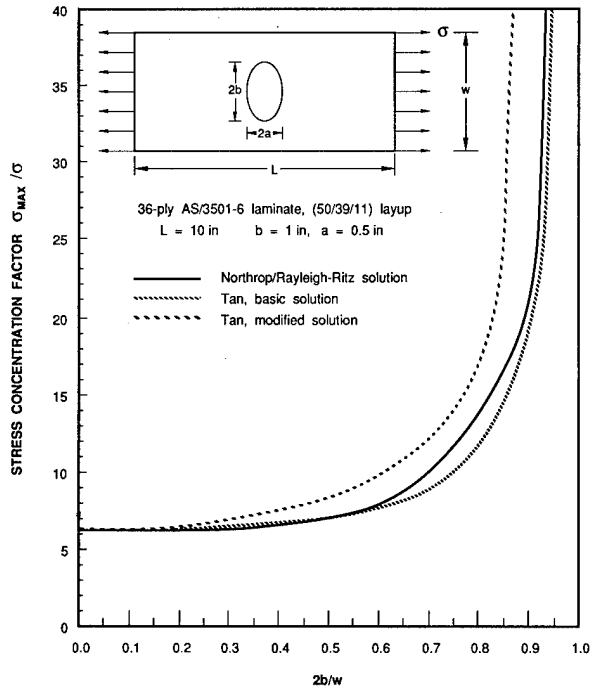


Figure 4. Benchmark results for finite structure elliptical cutout analysis.

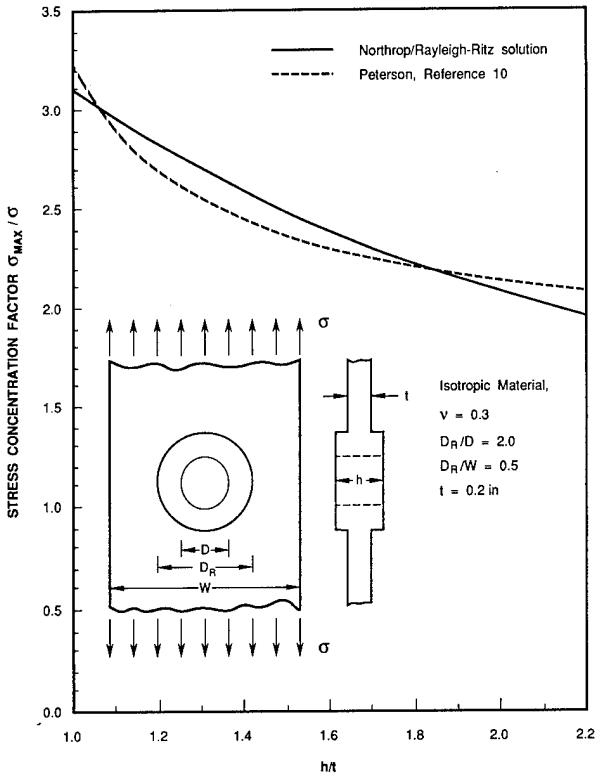


Figure 5. Benchmark results for uniform thickness circular padups.

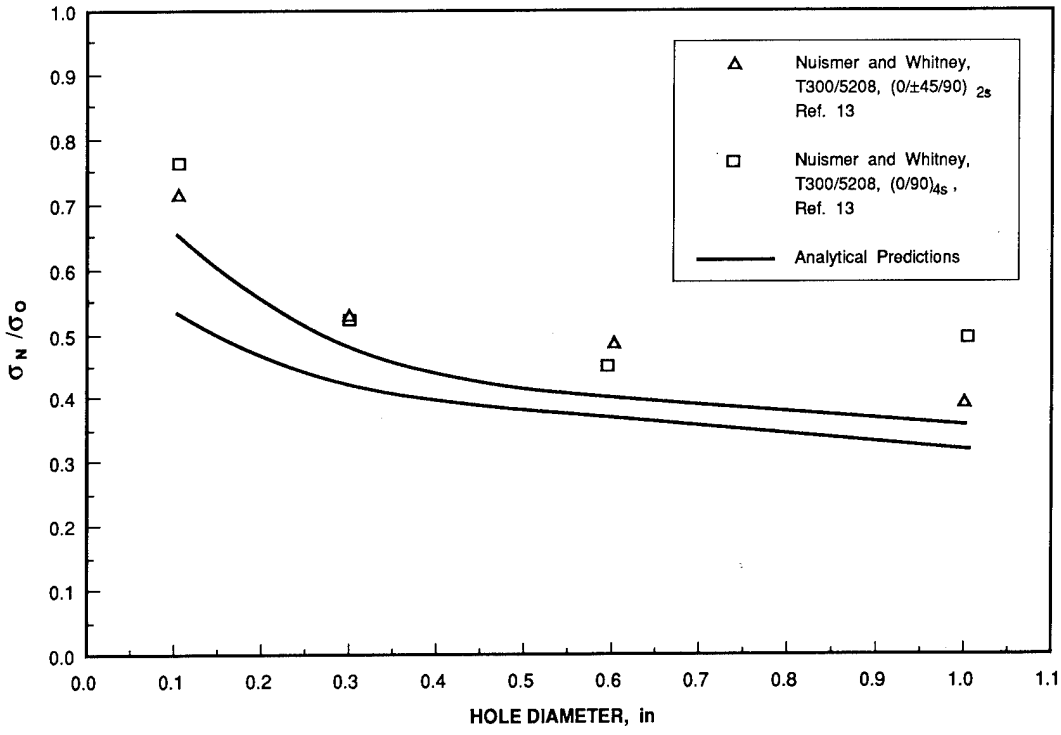


Figure 6. Analytical strength predictions and experimental data for different hole sizes.

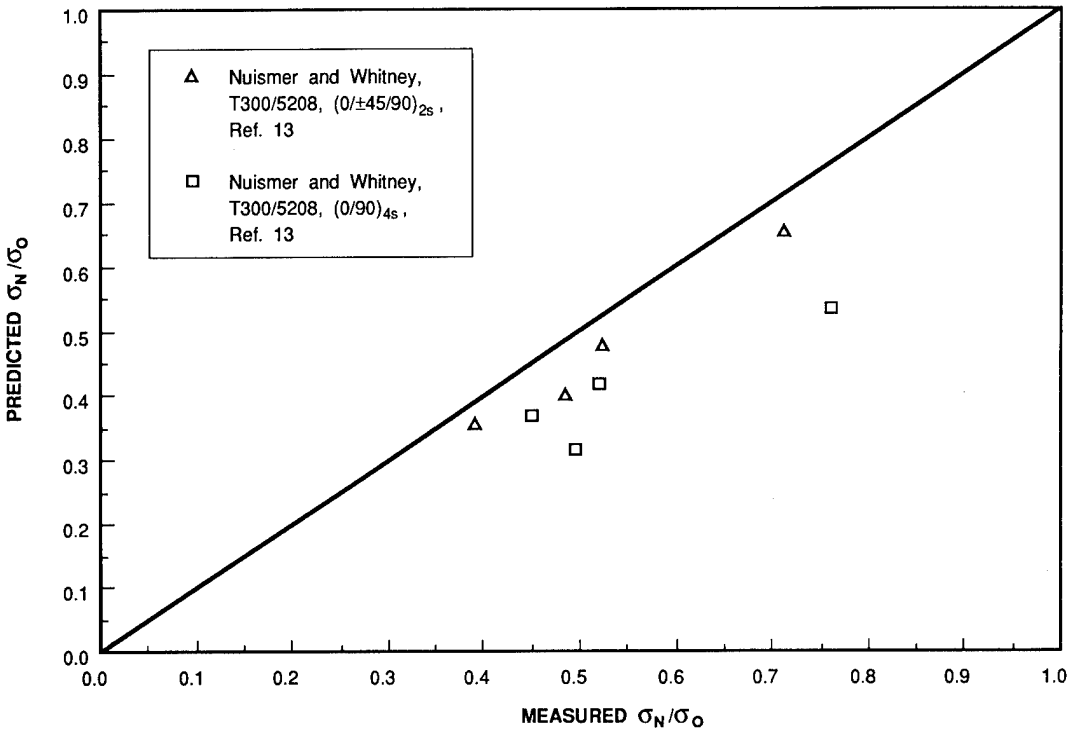


Figure 7. Analytical strength predictions versus experimental data.

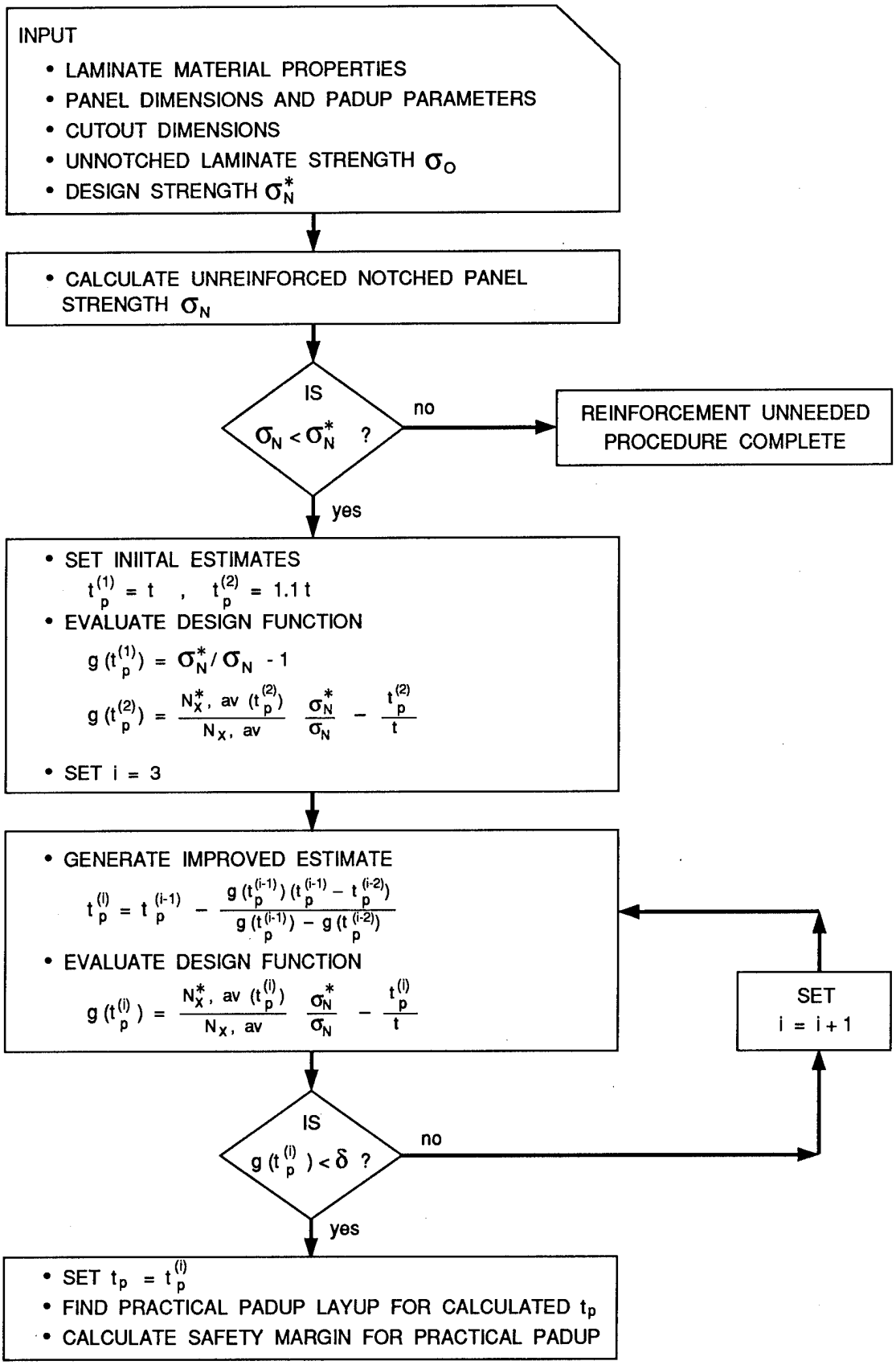


Figure 8. Flowchart for Padup Design Procedure.

EFFECTS OF BOLT-HOLE CONTACT ON BEARING-BYPASS DAMAGE-ONSET STRENGTH

John H. Crews, Jr. and Rajiv A. Naik[1]

NASA Langley Research Center
Hampton, Virginia

ABSTRACT

A combined experimental and analytical study was conducted to investigate the effects of bolt-hole contact on the bearing-bypass strength of a graphite/epoxy laminate. Tests were conducted on specimens consisting of 16-ply quasi-isotropic T300/5208 laminates with a centrally located hole. Bearing loads were applied through a clearance-fit steel bolt. Damage-onset strength and damage mode were determined for each test case. A finite element procedure was used to calculate the bolt-hole stresses and bolt contact for each measured damage-onset strength.

For the tension bearing-bypass cases tested, the bolt contact half-angle was approximately 60° at damage onset. For compression, the contact angle decreased by 20° as the bypass load increased. A corresponding decrease in the bearing-damage onset strength was attributed to the decrease in contact angle which made the bearing loads more severe.

Hole boundary stresses were also computed by superimposing stresses for separate bearing and bypass loading. Stresses at the specimen net section were accurately approximated by the superposition procedure. However, the peak bearing stresses had large errors because the bolt contact angles were not represented correctly. For compression, peak bearing stress errors of nearly 50 percent were calculated.

INTRODUCTION

A fastener hole in a structural joint is typically subjected to a combination of bearing loading that is reacted at the hole and bypass loading that is reacted elsewhere. To predict the strength of composite joints, both types of loading must be accounted for. Unfortunately, the effects of the bearing and bypass loads are often coupled, causing load-interaction effects that can complicate the prediction of bearing-bypass strength. For tension bearing-bypass loading, the load-interaction effects are essentially a linear combination of the bearing and bypass effects and are rather easily predicted [1]. However, for compression, these load-interaction effects are not as well understood. Stress analyses and strength predictions for compression bearing-bypass loading are especially complicated when bolt-hole clearance is accounted for. For such cases the bolt-hole contact varies nonlinearly with loading and is difficult to calculate [2].

The present paper has two objectives. First, it will analyze the influence of bolt-hole contact on the bearing-bypass damage-onset strength of a composite laminate. Second, this paper will examine the need to account for varying bolt-hole contact when using stress analysis procedures based on the superposition of separate bearing and bypass analyses. This paper focuses on recent NASA Langley research on single-fastener specimens loaded with a range of bearing-bypass ratios [2-4]. Specimens were made with T300/5208 graphite/epoxy laminates having a 16-ply quasi-isotropic layup. Bearing loads were applied through a steel bolt at the center of the specimen. A NASA Langley developed test apparatus [2] was used to apply

---

1 Analytical Services and Materials, Inc., Hampton, Virginia

different ratios of bearing to bypass loading in tension as well as compression. Specimens were loaded until damage was detected and this was used as the damage-onset strength. A finite element analysis was then used to calculate the bolt-hole contact arc and the hole boundary stresses corresponding to each measured damage-onset strength. An inverse technique [5] was used to study the nonlinear bolt-hole contact using linear analysis methods.

First, the damage-onset strengths are presented and discussed. Then, the computed hole-boundary stresses and contact angles are presented and used to interpret the observed strength trends and load interactions. Finally, stress analysis results for simultaneous bearing and bypass loading are compared with those calculated by superposing bearing results and bypass results. Also, areas of future bearing-bypass research are briefly discussed.

LIST OF SYMBOLS

c	bolt-hole clearance, m
d	hole diameter, m
P_a	applied load, N
P_b	bearing load, N
P_p	bypass load, N
r_b	bolt radius, m
S_b	nominal bearing stress, MPa
S_{np}	nominal net-section bypass stress, MPa
t	specimen thickness,m
w	specimen width, m
x,y	Cartesian coordinates, m
θ_1	contact half-angle for single contact, deg
θ_2	contact half-angle for dual contact, deg
β	bearing-bypass stress ratio
$\sigma_{\theta\theta}$	tangential stress component, MPa
σ_{rr}	radial stress component, MPa

BEARING-BYPASS TESTING

Test Procedure

The test specimen configuration is shown in figure 1(a). The T300/5208 specimens were machined from a single $(0/45/90/-45)_{2s}$ panel. The bolt holes, machined using an ultrasonic diamond core drill, had a diameter d of 6.396 mm, which produced a clearance of 0.076 mm with the 6.320 mm steel bolts. This clearance was 1.2 percent of the hole diameter. The width-to-hole-diameter ratio (w/d) was 7.8.

The bearing-bypass loading notations for tension and compression are shown in figure 1(b). Test results are reported in terms of nominal gross-section stress S_g, nominal bearing stress S_b, and nominal net-section bypass stress S_{np}, calculated using the following equations:

$$S_g = P_a / tw$$

$$S_b = P_b / td$$

and

$$S_{np} = P_p / t (w - d)$$

The bearing-bypass ratio β was defined as

$$\beta = S_b / S_{np}$$

The test system used in this study is shown schematically in figure 2. This system uses two servo-controls. The center of the specimen is bolted between two bearing-reaction plates that are attached to the load frame using two load cells. The ends of the specimen are then gripped and loaded independently by the two servo-control systems (called Upper and Lower in figure 2). Any difference between these two end loads produces a bearing load at the central bolt hole. This bearing load is measured by the load cells under the bearing reaction plates. The end loads are synchronized by a common input signal; as a result, a constant bearing bypass ratio is maintained throughout each test.

The bearing reaction plates were bolted to the load cells allowing either tension or compression bearing loads. During compression, the bearing-reaction plates prevent specimen buckling. Hardened steel bushings were used between the bolt and the bearing-reaction plates. These 12.7 mm bushings were machined for a sliding fit, allowing the bolt clamp-up force to be transmitted to the local region around the bolt hole. This arrangement was equivalent to having a clamp-up washer directly against the surface of the specimen. For the present tests, the bolt was finger tightened (about 0.2 Nm torque) to produce a very small clamp-up force against the specimen.

Throughout each test, specimen deformation was measured by displacement transducers mounted symmetrically on the front and back of the bearing reaction plates. The transducer rods rested on small bars that were cemented to the specimen slightly above the grip line. This arrangement provided a measurement of the relative displacement between the bearing-reaction plates and the specimen. As explained in the following, these measurements were used to determine the damage onset.

For each test, the nominal bearing and bypass loads were plotted against the specimen displacement. As the specimens were slowly loaded, these load-displacement curves gradually became nonlinear. This nonlinearity was used to indicate damage initiation at the bolt hole. The intersection of each curve with a straight line offset by 0.001d was arbitrarily selected to define the damage-onset level. Specimens were unloaded after damage onset was indicated and were treated with an X-ray opaque dye-penetrant before being radiographed to determine the damage-onset mode.

Test Results

The damage-onset modes are shown by the radiographs in figure 3. For tension dominated loading, the damage developed in the net-section tension (NT) mode, figure 3(a). The gray shadows show delaminations and the dark bands indicate ply splits. The tension-reacted bearing (TRB) and compression-reacted bearing (CRB) damage modes are similar and appear to be delamination dominated. The net-section compression (NC) mode involves rather discrete damage zones extending from the hole. This damage was caused by microbuckling in the 0^0 plies [6].

The measured S_b and S_{np} values corresponding to damage onset are plotted against one another in figure 4, as a so-called bearing-bypass diagram. Each symbol represents the average of three tests (also see Table 1). The tick marks indicate

the range of measured strengths, plotted along lines of constant β. The curves were fit through the data and provide a failure envelope for bearing-bypass damage onset.

The right side of figure 4 shows tension results for four β values (0, 1, 3, ∞). The symbol on the S_{np} axis represents all-bypass loading ($\beta = 0$) in tension. The NT next to symbols indicates the net-section tension damage mode. As expected, all test cases that resulted in NT damage can be represented by a straight line and, thus, show the linear interaction discussed in [1] and [2]. This linearity suggests that the local stress that governs NT damage onset is the sum of the local stresses due to bearing loading and bypass loading. A horizontal "bearing cutoff" line was drawn through the $\beta = \infty$ data point which is labeled TRB to indicate tension reacted bearing damage. The compression reacted bearing (CRB) damage-onset strength is slightly smaller than the TRB damage-onset strength. The CRB damage-onset strength varies with bypass stress and therefore cannot be represented by a simple horizontal cutoff line. The compressive bypass stress decreases the CRB onset strength by five percent for $\beta = -3$ and about 40 percent for $\beta = -1$. This interaction between bearing and bypass loads was caused by a decrease in the bolt-hole contact arc and will be discussed in the next section. For the all-bypass compressive loading ($\beta = -0$), net-section compression (NC) damage initiated at -422 MPa. This NC damage-onset strength was much larger than expected and suggested that dual bolt-hole contact developed, allowing load transfer across the hole. Such contact reduces the compressive stress concentration at the net section and thereby increases the specimen strength. This will also be discussed later in an analysis of bolt-hole contact.

STRESS ANALYSIS

In this section, first, the stress analysis procedures are briefly described. Next, stress distributions along the hole boundary are shown for each measured damage-onset strength. These stress distributions are then used in a discussion of the critical local stresses associated with each damage mode. Finally, the bolt contact angles are presented and used in a discussion of the measured strengths for each damage-onset mode.

Inverse Stress Analysis Procedure

The finite element model and procedures used in this study were evaluated in [3]. The finite element calculations were performed using the NASTRAN finite element code. The contact arc was represented using displacement constraints along a portion of the hole boundary. Within an assumed contact arc, nodes on the hole boundary were constrained to lie on a circular arc corresponding to the bolt radius (r_b). This procedure represented a rigid bolt having a frictionless interface with the hole. Two-dimensional elements were used to model the test specimen. Along the hole boundary, the elements subtended less than 1^0. As a result, the contact arc could be modeled very accurately.

Because a bolt clearance was used, the contact angle at the bolt-hole interface varied with bearing stress, as shown in figure 5. This nonlinear problem was reduced to a linear problem by using an inverse procedure [7] as follows. For simple bearing loading, a contact angle was assumed and the corresponding bearing load was calculated. The contact stress σ_{rr} at the last finite element node of the contact arc must be equal to zero, point B in figures 5 and 6(a). This requirement is satisfied only when the "correct" bearing stress is used with the assumed contact angle, thereby, providing a criterion for calculating the correct bearing stress. For each assumed contact angle, two finite element analyses were performed each with an arbitrarily selected bearing stress. The two corresponding nonzero values of σ_{rr}

at the end of the arc were then used to calculate the correct bearing stress for the assumed contact angle [8]. This inverse procedure was repeated for a range of contact angles to establish a relationship between contact angle and bearing stress, as shown, for example, in figure 5.

The inverse procedure was extended in [5] to include bypass as well as bearing loading. For each bearing-bypass ratio β, the combined bearing and bypass loading was expressed in terms of the bearing stress S_b and β. For a given β, the procedure was identical to that used for pure bearing [8]. The calculations were repeated to establish a relationship between contact angle and bearing-bypass loading for each β value in the test program.

The inverse procedure was further extended in [5] to analyze cases of compression bearing-bypass loading that produced dual contact between the bolt and hole, as shown in figure 6(b). Such dual contact can develop when compressive bypass stresses produce hole deformations that are comparable to the bolt-hole clearance. In contrast to the single contact case, the bearing-bypass ratio could not be assumed. However, as in the single contact case, the contact stress was required to be zero at the last node of both contact arcs, points B and E in figure 6(b). For dual contact cases, values for both contact angles were assumed and the required combination of bearing and bypass loading was calculated as follows. Three finite element runs were made each with an arbitrarily selected combination of bearing and bypass stress. The three sets of corresponding non-zero values of computed contact stresses for the ends of the two contact arcs were then used to calculate the correct bearing-bypass combination for the assumed contact angles. This inverse procedure was repeated to obtain the desired relationships between compressive bearing-bypass loading and dual contact for the clearance used in this study. Results will be shown in the next section.

Stress Results

Figure 7 shows the computed $\sigma_{\theta\theta}$ and σ_{rr} stresses plotted along the hole boundary. Because of symmetry, these stresses are shown only along one-half of the hole boundary, from $\theta = 0°$ to 180°. The four sets of curves in figure 7 correspond to the measured stress levels for damage onset in the tension bearing-bypass tests. For $\beta = 0$, 1 and 3, the $\sigma_{\theta\theta}$ curves have peak values near the specimen net section ($\theta = 90^0$), and are within about 7 percent of the average peak value of 870 MPa. All three of these cases developed damage in the NT mode; therefore, 870 MPa seems to be the critical $\sigma_{\theta\theta}$ value for NT damage onset. For the bearing critical $\beta = \infty$ case, the $\sigma_{\theta\theta}$ peak of about 690 MPa is well below the critical 870 MPa level for NT damage. The σ_{rr} peak for the $\beta = \infty$ case is about -760 MPa; this is the peak contact stress corresponding to TRB damage onset. As expected, the peak σ_{rr} values for the other two tension bearing-bypass cases (β = 1 and 3) are well below 760 MPa. Notice that the σ_{rr} curves indicate bolt-hole contact over only about 60°. Because of symmetry, this corresponds to a contact angle of 120° but the half-angle shown in the figure will be subsequently referred to simply as the contact angle.

Figure 8 plots the $\sigma_{\theta\theta}$ and σ_{rr} stresses along the hole boundary for the measured strengths corresponding to damage onset in the four compression test cases (β = -0, -1, -3, and $-\infty$). The $\sigma_{\theta\theta}$ and σ_{rr} curves for the CRB $\beta = -\infty$ case are generally similar to those for the TRB $\beta = \infty$ case shown previously in figure 7, but the $\sigma_{\theta\theta}$ peak of about 550 MPa is considerably lower than the 690 MPa peak for TRB and much lower than the critical 870 MPa level for NT damage. The σ_{rr} peak of -800

MPa for the $\beta = -\infty$ case is about five percent larger than the 760 MPa value for the $\beta = \infty$ case. The peak σ_{rr} stresses for the three CRB cases ($\beta = -\infty$, -3, and -1) in figure 8 have an average value of 807 MPa. The β = -0 (all-bypass) case in figure 8 has a $\sigma_{\theta\theta}$ peak of 940 MPa at $\theta = 90°$ which corresponds to NC damage onset. The corresponding σ_{rr} stress distributions for β = -0 indicate dual contact over about 20° at both $\theta = 0°$ and 180°.

Bolt-Hole Contact Results

The variation of contact angle θ_1 with bearing stress S_b is shown in figure 9 for the various β values used in this study. The two all-bearing cases labelled $\beta = \infty$ and $-\infty$ are noticeably different from each other, differing by about five degrees for the range of measured bearing damage-onset strengths. The β = 1 and 3 curves show larger contact angles while the β = -1 and -3 curves indicate smaller angles, compared to the all-bearing cases. For S_b = 500 MPa, contact angles could differ by as much as 40° depending on which β is used.

To further discuss bolt-hole contact, the computed contact angles in figure 9 are replotted in a different way in figure 10. The contact angles are plotted against bypass stress S_{np} for three S_b levels (300, 400, and 500 MPa) which are typical of the measured strengths. This figure can be used to discuss the separate effects of clearance and bypass stress on the contact angle. In the absence of clearance or bypass stress, contact would occur over about 82° [9]. Figure 10 shows that a 0.076-mm clearance reduces the θ_1 contact angles to about 50°-60° for S_{np} = 0. Increasing the tensile bypass stress increases the θ_1 contact angle while increasing the compressive bypass stress decreases it. For large compressive bypass stresses, the θ_1 curves are influenced by dual contact.

To put this θ_1 behavior in perspective for the present study, the combinations of measured bypass strength and computed contact angles are shown as solid symbols in figure 10. These symbols show that the contact angles were nearly constant at about 60° for all three tension bearing-bypass test cases. However, this nearly constant behavior is probably coincidental and, therefore, is not believed to be typical of other laminates and specimen configurations. For the compression test cases, the contact angle varied by more than 20° for the range of tests and had a minimum value of about 35°. Figure 10 shows that clearance and bypass stresses can combine to reduce the contact angle to values that are significantly smaller than the 90° (semi-circular) value often assumed in analyses. For example, contact was modeled by imposing zero radial displacements over a semicirclar hole boundary in [10] and [11] and by a cosine distribution of radial stress over a semicircle in [12]. The importance of correctly modelling contact will be discussed in the next section.

Recall that figure 4 showed that CRB damage-onset strength decreased with increasing levels of compressive bypass stress. When this interaction was first observed, it was unexpected because CRB damage is caused by the σ_{rr} contact stress and the compressive bypass loads were not expected to have much influence on σ_{rr}. This interaction for compression bypass loading can be explained using figure 10. As mentioned above, θ_1 decreased by about 20° as the bypass loads became more compressive. These smaller contact angles allowed smaller bearing loads to produce the same critical σ_{rr} peak. If this decrease in contact angle is ignored in the stress analyses, the corresponding predictions for CRB damage onset strength would be unconservative and equivalent to a horizontal bearing strength cutoff line in the bearing-bypass diagram.

Local Stress Superposition

Bearing-bypass stress analyses could be simplified if separate solutions for bearing and bypass loading could be superposed to obtain an approximate solution. This approach was used in [12] and is studied here by comparing results for simultaneous bearing and bypass loading from the present analysis with results based on superposition. To further simplify the approach, the bearing analysis was conducted for the linear c = 0 case as well as with the nonlinear c = 0.076mm case.

The stress distributions used in the superposition procedure are shown in figure 11. The dashed curve represents an all-bypass case with S_{np} = 250 MPa. The other three curves show different all-bearing cases with S_b = 250 MPa. The solid curve corresponds to TRB with a 0.076 mm clearance. The dash-dot curve represents the TRB case with c = 0. This special TRB case has a contact angle of about 82° which does not change with loading. This dash-dot curve represent a linear solution that can be scaled to represent other S_b loading levels. The dash-double-dot curve corresponds to the CRB case with c = 0, which is also linear and has a contact angle of about 78°.

The bearing (solid) curve with clearance and the bypass (dashed) curve in figure 11 were summed to get the dashed curve in figure 12. This dashed curve provides a reasonably good approximation to the $\sigma_{\theta\theta}$ solid curve, corresponding to simultaneous bearing-bypass (β = 1) loading. The dashed curve for σ_{rr} underestimates the contact angle by about 15°. Therefore, the σ_{rr} peak is overestimated by about 20 percent and occurs at θ = 0° rather than near 45°, as indicated by the solid curve. The dash-dot curve represents the superposition of the c = 0 bearing and the bypass case. This dash-dot curve also provides a good approximation for the $\sigma_{\theta\theta}$ distribution, but overestimates the contact angle by about 20°, resulting in a 10 percent error in the σ_{rr} peak value. In a NT critical case such as this [2], the σ_{rr} stresses are not important and either of these superposition approaches would provide accurate $\sigma_{\theta\theta}$ net-section (θ = 90°) stresses needed to predict NT damage onset.

A similar comparison for β = -1 is shown in figure 13. Again, the stresses for bypass loading can be superimposed on either the c = 0.076 mm bearing case or the c = 0 bearing case to estimate the net-section (θ = 90°) $\sigma_{\theta\theta}$ stresses needed to predict NC damage onset. However, in the present study, β = -1 loading was found to produce CRB damage as well as NC damage, so the σ_{rr} stresses are also important for this case. Neither of the superposition curves in figure 13 approximates σ_{rr} very well. The bearing case with c = 0.076 mm (dashed curve) overestimates the contact angle by about 15° and underestimates the σ_{rr} peak by almost 30 percent. The bearing case with c = 0 (dash-double-dot curve) overestimates contact by more than 40° and underestimates the σ_{rr} peak by almost 50 percent.

Although bearing-bypass superposition has been examined only for two specific cases in figures 12 and 13, these results suggest that superposition may provide useful estimates of the $\sigma_{\theta\theta}$ stresses associated with net-section damage in tension as well as compression. However, contact angle errors produce significant errors in the peak σ_{rr} values. As a result, superposition may lead to unacceptably large errors in bearing damage-onset predictions.

The superposition of stress results can also provide some insight into a load interaction for the NC damage mode that was not investigated in the present study.

Figure 11 shows that CRB loading produces tensile $\sigma_{\theta\theta}$ stress on the hole boundary at the net section (θ = 90°). Of course, compressive bypass loading produces compressive $\sigma_{\theta\theta}$ on the net section. As a result, in compressive bearing-bypass loading, the bearing loads tend to reduce the compressive $\sigma_{\theta\theta}$ stress that governs NC damage onset. Therefore, CRB loads should increase the NC damage-onset strength compared to the all-bearing bypass (β = -0) case. This is an area of bearing-bypass behavior that needs further research.

CONCLUDING REMARKS

A combined experimental and analytical study was conducted to investigate the effects of bolt-hole contact on bearing-bypass strength of a graphite/epoxy laminate. The T300/5208 specimens consisted of 16-plies with a quasi-isotropic layup and had a centrally located hole. Bearing loads were applied through a steel bolt having a clearance fit. Damage-onset strength and damage mode were determined for each test case. A 2-D finite element procedure was used to calculate hole-boundary stresses and bolt contact for each measured damage-onset strength.

For loading levels corresponding to damage onset, the cases of pure bearing in either tension or compression had bolt contact over a half-angle of only about 60°, compared to the 90° value often assumed in bearing stress analyses. For the tension bearing-bypass, the bolt contact angle at damage onset was approximately 60° for the whole range of bearing-bypass combinations investigated. In contrast, for compression, the contact angle decreased to about 35°.

In compression, the bearing damage-onset strengths showed an interaction of the bearing and bypass loads. Compressive bypass loads reduced the bearing damage-onset strength. This interaction was explained by the decrease in the bolt-hole contact angle that increased the severity of the bearing loads.

In addition to the simultaneous bearing and bypass loading, hole boundary stresses were also computed by superimposing stresses for separate bearing and bypass loading. A comparison of results showed that stresses at the specimen net section were accurately approximated by the superposition procedure. However, this procedure did not accurately calculate the peak bearing stresses because the bolt contact angles were not accurately represented. For compression bearing-bypass loading, the peak bearing stress errors of nearly 50 percent were calculated.

This study showed that bolt-hole contact had an influence on bearing damage-onset strength and must, therefore, be represented properly to obtain accurate stress analyses, especially for compression bearing-bypass loading.

REFERENCES

1. Hart-Smith, L. J.: "Bolted Joints in Graphite/Epoxy Composites". NASA CR-144899, National Aeronautics and Space Administration, January 1977.

2. Crews, J. H., Jr. and Naik, R. A.: "Combined Bearing and Bypass Loading on a Graphite/Epoxy Laminate". Composite Structures, Vol. 6, 1986, pp. 21-40.

3. Naik, R. A.: "An Analytical and Experimental Study of Clearance and Bearing-Bypass Load Effects in Composite Bolted Joints". Ph.D. dissertation, Old Dominion University, Norfolk, Virginia, August 1986.

4. Crews, J. H. ,Jr. and Naik, R. A.: "Bearing-Bypass Loading on Bolted Composite Joints". Presented at AGARD Symposium on Behavior and Analysis of Mechanically Fastened Joints in Composite Structures, AGARD-CP-427, Madrid, Spain, April 27-29, 1987. Also published as NASA TM-89153, May 1987.

5. Naik, R. A. and Crews, J. H., Jr.: "Stress Analysis Method for Clearance-Fit Joints with Bearing-Bypass Loads". Presented at AIAA/ASME/ASCE/AHS 30th Structures, Dynamics, and Materials Conference, April 3-5,1989, Mobile, Alabama, 1989 (AIAA Paper 89-1230), Also published as NASA TM-100551, Jan. 1989.

6. Naik, R. A. and Crews, J. H., Jr.: "Ply-Level Failure Analysis of a Graphite/Epoxy Laminate under Bearing-Bypass Loading". NASA TM-100578, March 1988.

7. Mangalgiri, P. D., Dattaguru, B., and Rao, A. K.: "Finite Element Analysis of Moving Contact in Mechanically Fastened Joints". Nuclear Engineering Design, Vol. 78, 1984, pp. 303-311.

8. Naik, R. A. and Crews, J. H. Jr.: "Stress Analysis Method for a Clearance-Fit Bolt under Bearing Loads". AIAA Journal Vol. 24, No. 8, August 1986, pp. 1348-1353.

9. Crews, J. H., Jr., Hong, C. S., and Raju, I. S.: "Stress-Concentration Factors for Finite Orthotropic Laminates with a Pin-Loaded Hole". NASA TP 1862, May 1981.

10. Soni, S. R.: "Failure Analysis of Composite Laminates with a Fastener Hole". AFWAL-TR-80-4010, March 1980.

11. Ramkumar, R. L.: "Bolted Joint Design". Test Methods and Design Allowables for Fiberous Composites. ASTM STP 734, C. C. Chamis, Ed., American Society for Testing and Materials, 1981, pp.376-395.

12. Garbo, S. P. and Ogonowski, J. M.: "Effect of Variances and Manufacturing Tolerances on the Design Strength and Life of Mechanically Fastened Composite Joints". Methodology Development and Data Evaluation, AFWAL-TR-81-3041, I-III, April 1981.

Table 1. Damage-onset test data.

	β	S_g (MPa)	S_b (MPa)	S_{np} (MPa)	θ_1 (deg)	Failure mode
Tension	0	265	0	304	--	NT
	1	237	237	237	60.9	NT
	3	196	468	156	62.8	NT
	∞	69.5	542	0	60.0	TRB
Compression	0	-368	0	442	--	NC
	-1	-324	324	-324	34.7	CRB/NC
	-3	-209	498	-166	47.8	CRB
	$-\infty$	-67.7	528	0	56.2	CRB

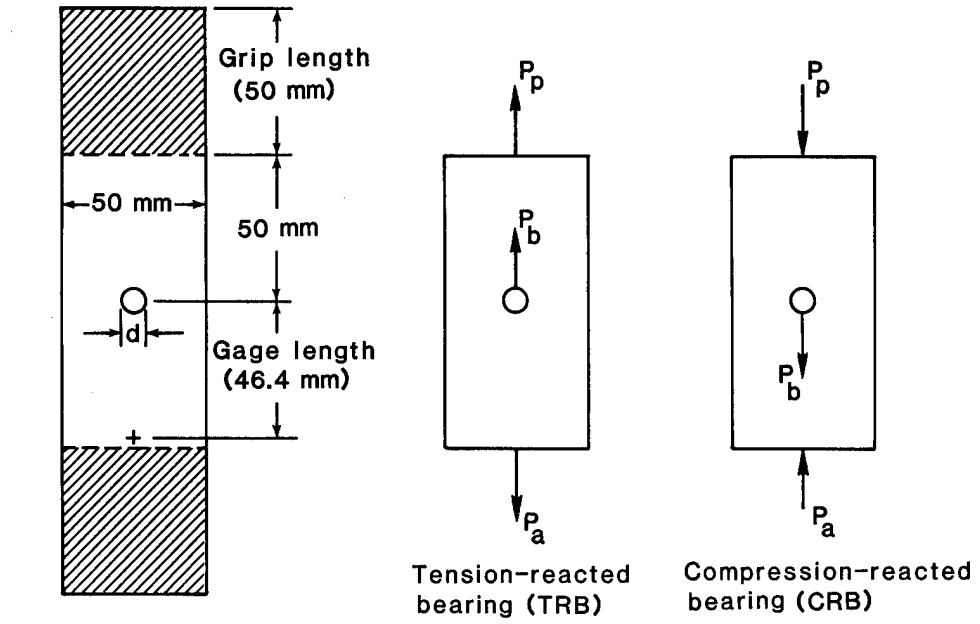


Figure 1. Specimen configuration and bearing-bypass loading.

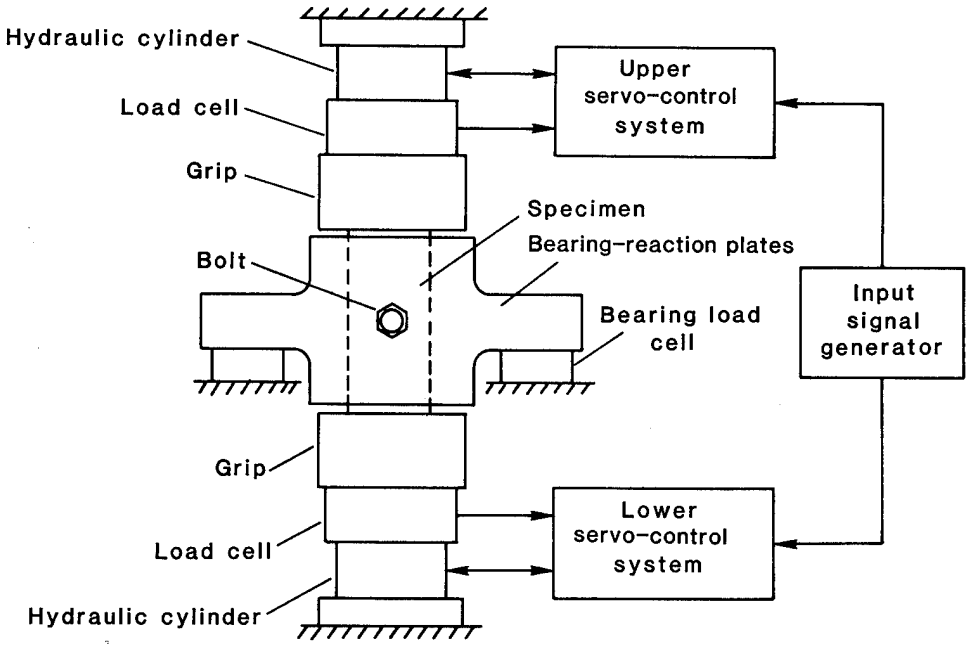


Figure 2. Schematic of the bearing-bypass test system.

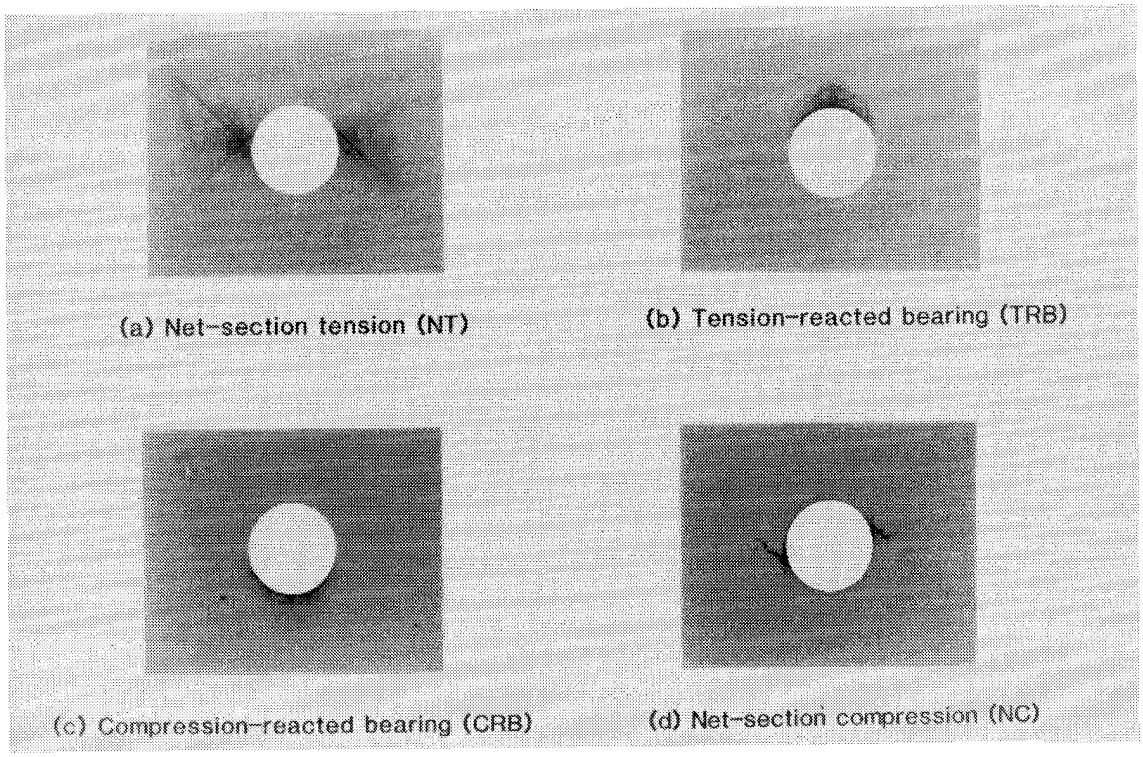


Figure 3. Radiographs of damage at fastener hole.

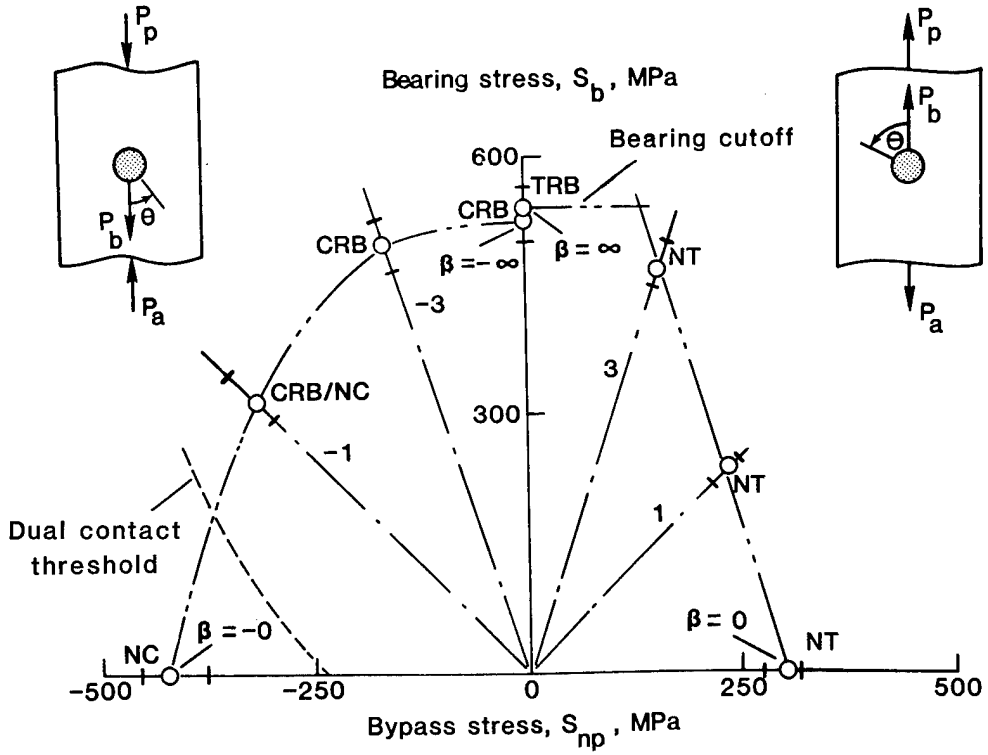


Figure 4. Bearing-bypass diagram for damage-onset strength.

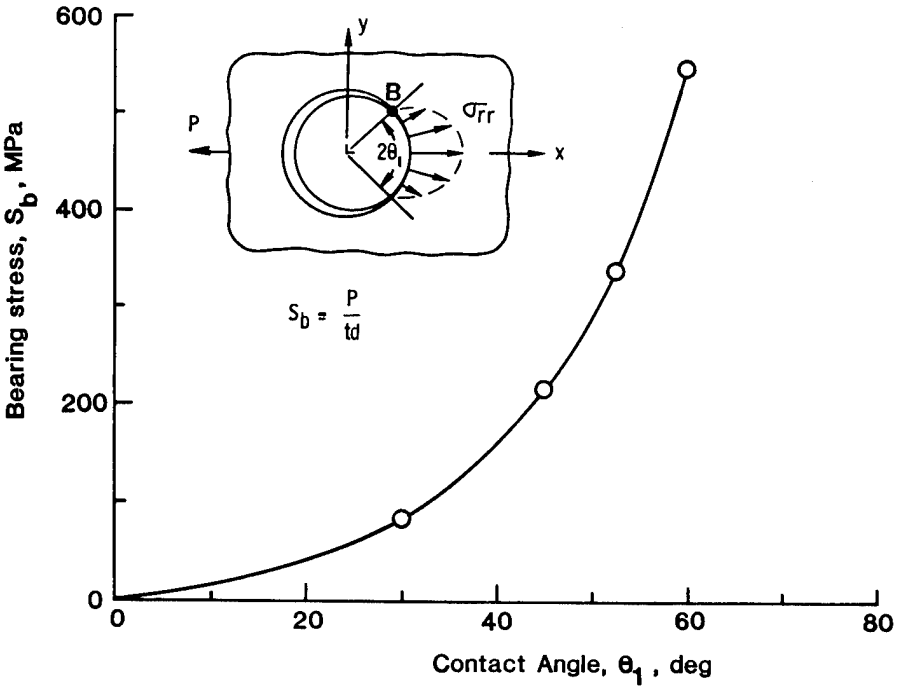
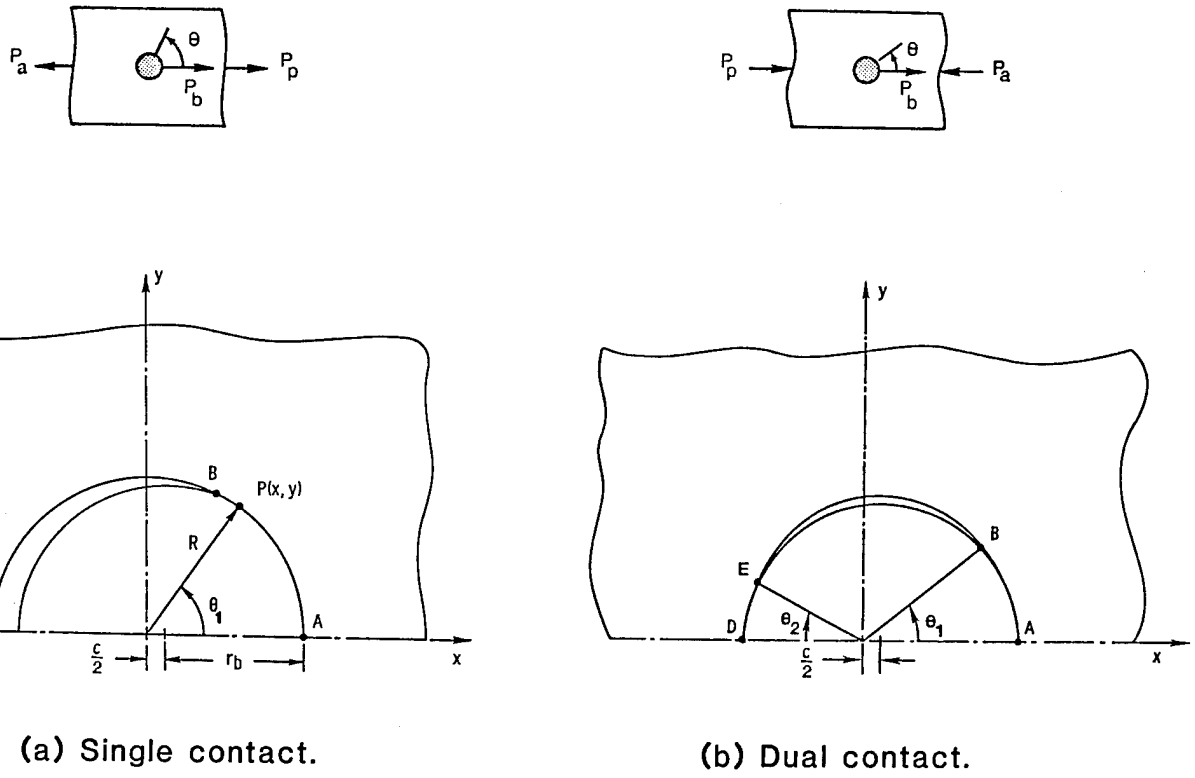


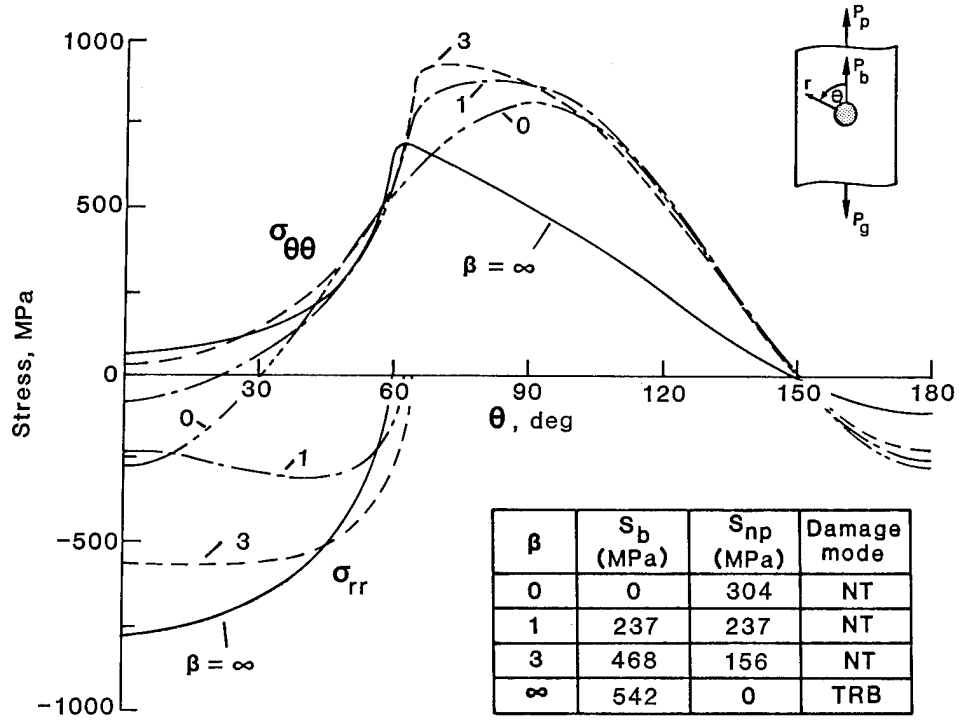
Figure 5. Nonlinear relationship between bearing stress and contact angle.



(a) Single contact.

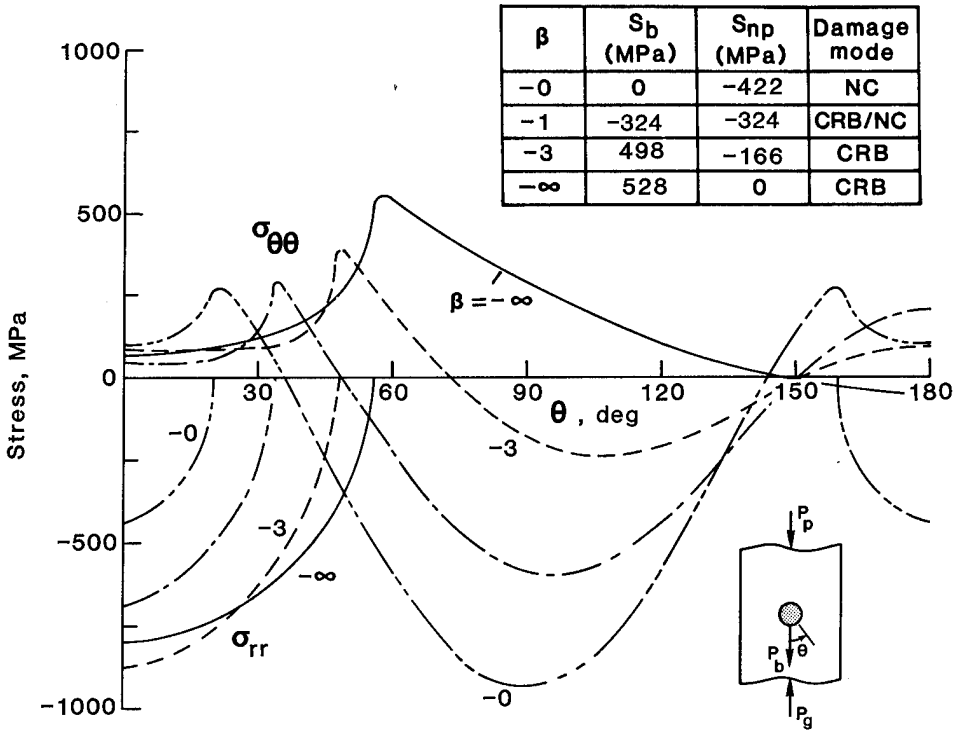
(b) Dual contact.

Figure 6. Bolt-hole contact under bearing-bypass loading.



β	S_b (MPa)	S_{np} (MPa)	Damage mode
0	0	304	NT
1	237	237	NT
3	468	156	NT
∞	542	0	TRB

Figure 7. Stress distributions for tension bearing-bypass loading.



β	S_b (MPa)	S_{np} (MPa)	Damage mode
−0	0	−422	NC
−1	−324	−324	CRB/NC
−3	498	−166	CRB
−∞	528	0	CRB

Figure 8. Stress distributions for compression bearing-bypass loading.

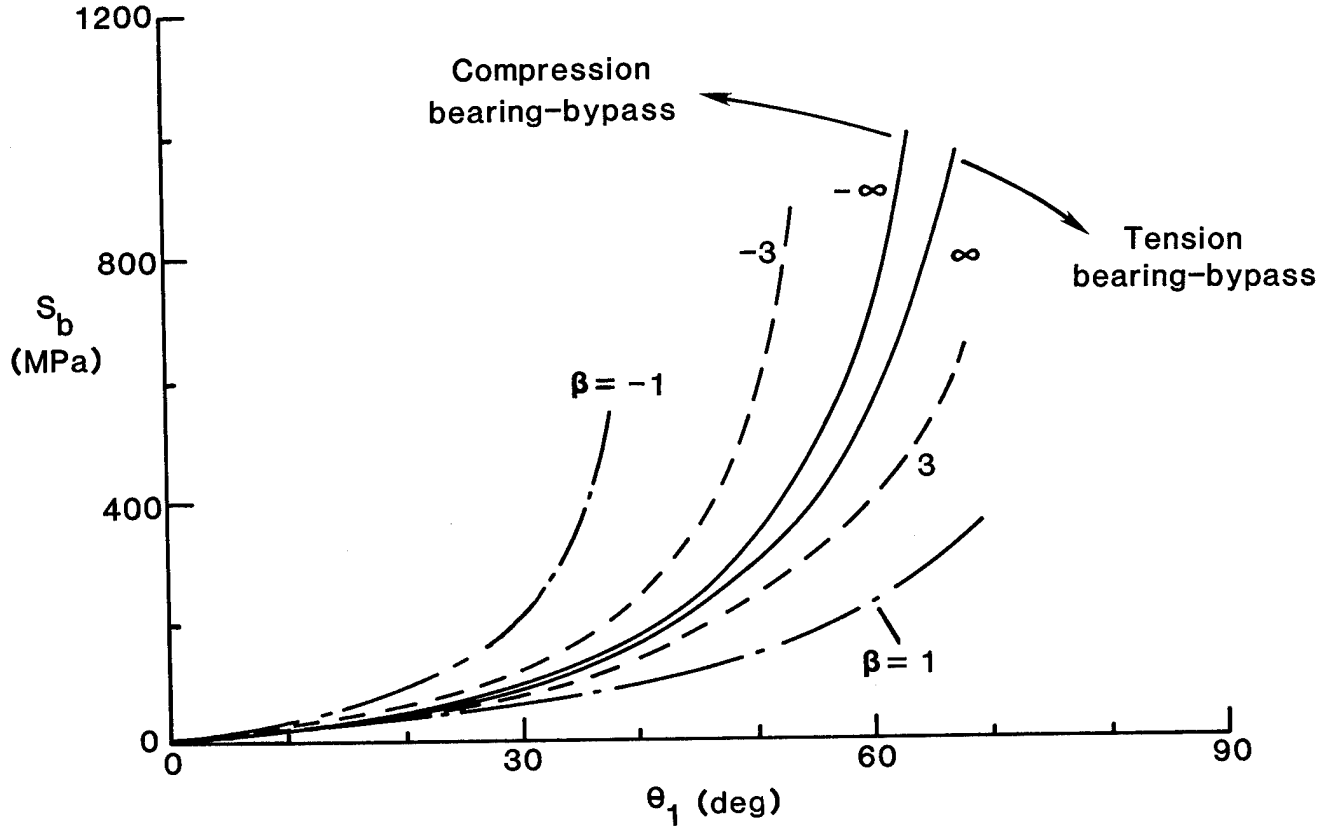


Figure 9. Variation of bolt-hole contact angle with bearing loading.

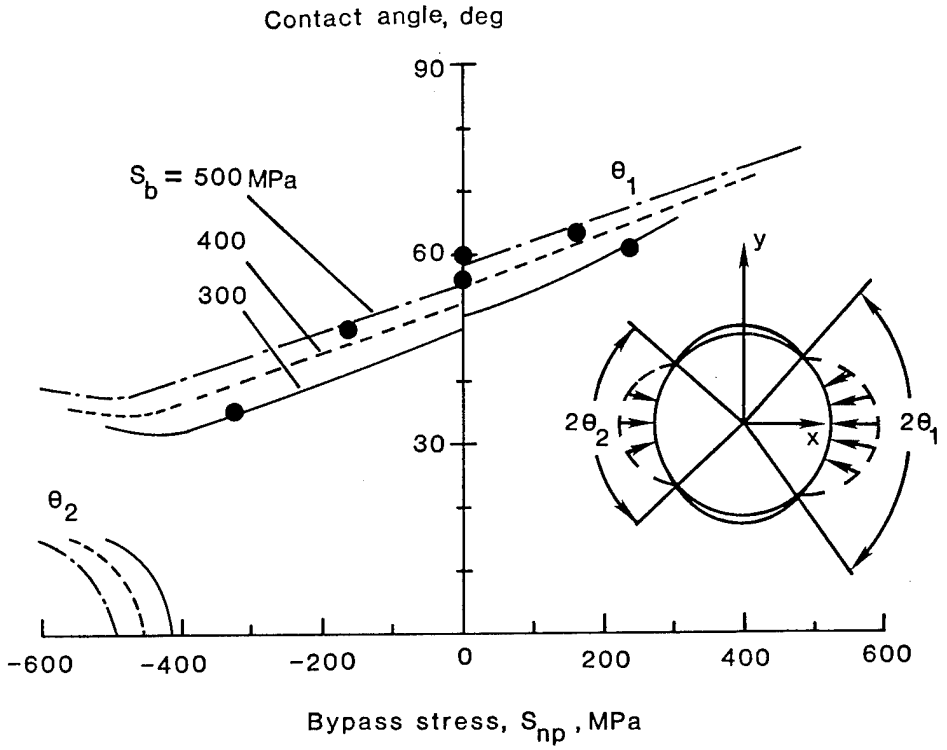


Figure 10. Variation of bolt-hole contact angle with bypass loading.

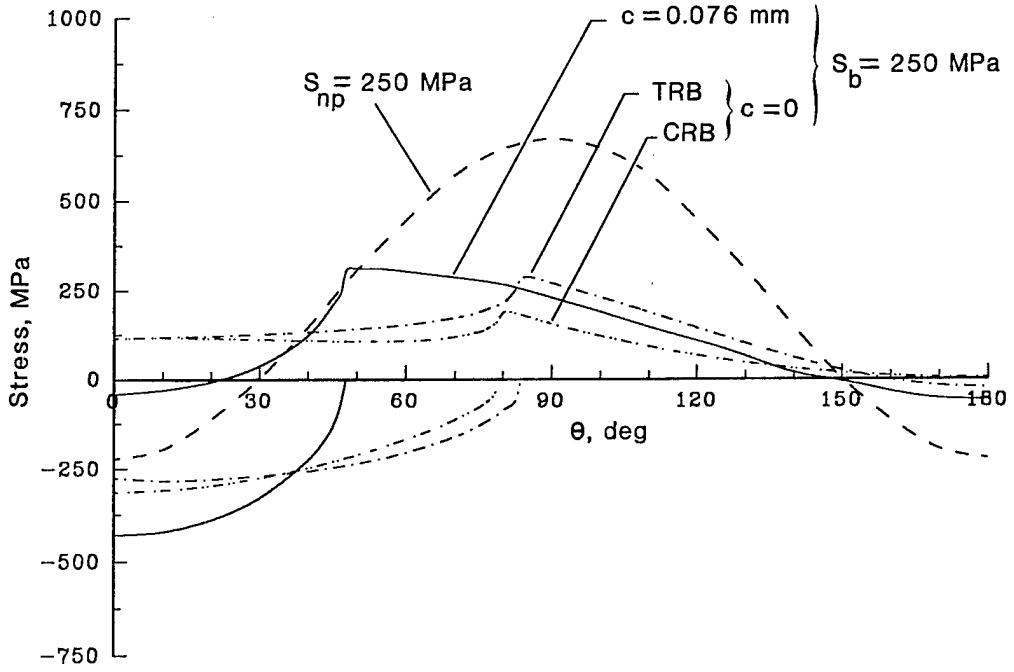


Figure 11. Stress distributions for bypass loading and bearing loading.

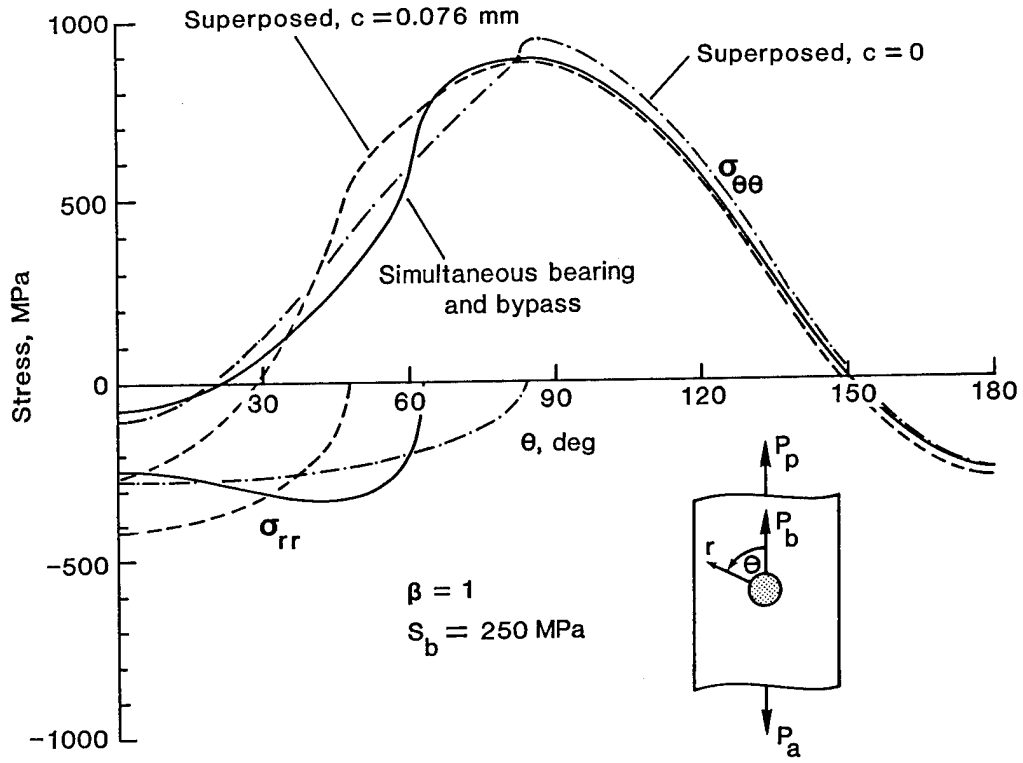


Figure 12. Superposition of tension-reacted bearing and tension bypass stresses.

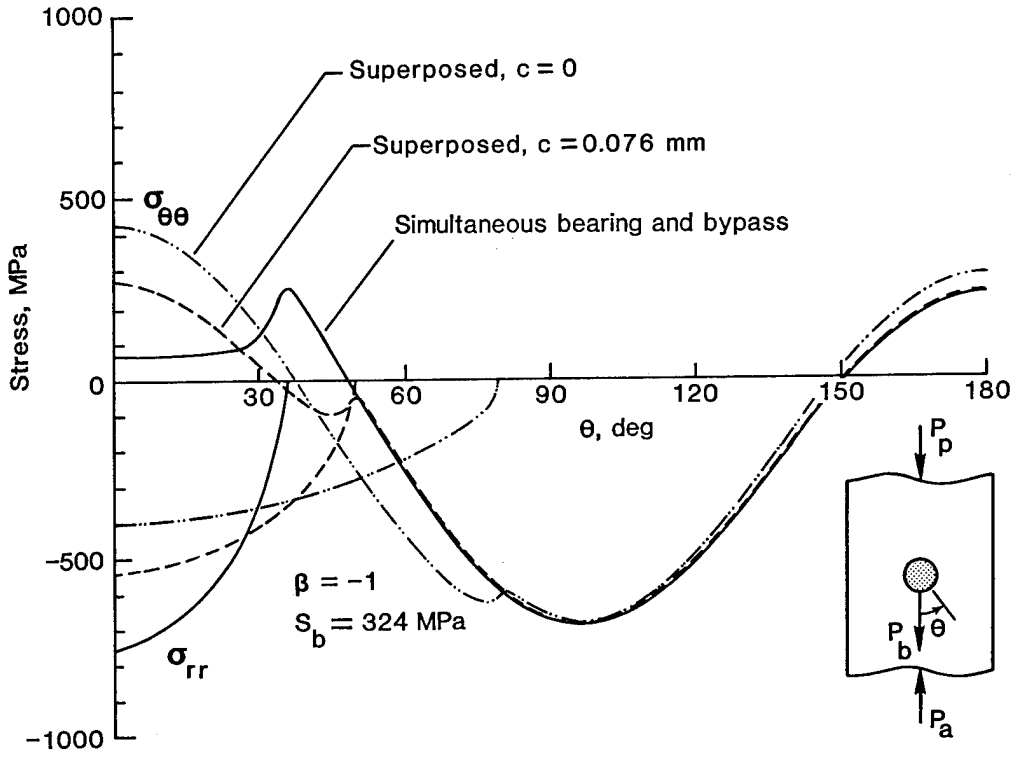


Figure 13. Superposition of compression-reacted bearing and compression bypass stresses.

PREDICTION OF STIFFENER-SKIN SEPARATION IN COMPOSITE PANELS[1]

Han-Pin Kan
Mary A. Mahler
Ravi B. Deo

Northrop Corporation
Aircraft Division
Department 3853/82
One Northrop Avenue
Hawthorne, California

ABSTRACT

A methodology has been developed to predict the failure of stiffened composite panels by stiffener-skin separation. The methodology is applicable to curved or flat panels under combined uniaxial compression and in-plane shear loads. The analytical crux of the methodology are two analysis packages: (1) PACL1 which predicts the stress and displacement fields in a stiffened postbuckled panel and (2) WEBSTER, which predicts the local interfacial (shear and normal) stresses at the skin and stiffener flange junction. PACL1 is a Rayleigh-Ritz analysis of curved composite panels loaded into the postbuckling range. WEBSTER is a two-dimensional elasticity analysis for the skin-stiffener interface. This paper presents results of the predictive methodology. The entire analysis can be performed on a personal computer.

INTRODUCTION

Recent studies have indicated that the most common mode of failure for stiffened composite panels loaded into the postbuckling range is stiffener/skin separation. An assessment of the current postbuckled stiffened panel design, analysis, and application technology (References 1 and 2) shows that, for both static and fatigue loading, stiffener/skin separation consistently occurs at loads below other competing failure modes, such as skin compression failure and delamination. Because stiffener/skin separation is not accounted for in the existing design methodology, the application of existing postbuckling methodology to the design of advanced composite panels has resulted in unconservative designs. In order to fully realize the weight saving potential of postbuckled designs, this failure mode must be accounted for.

[1] This work was performed under NASA/Northrop Contract NAS1-18842, entitled "Innovative Composite Fuselage Structures."

Several attempts have been made in the last decade to predict the stiffener/skin separation of postbuckled, stiffened composite panels. These include semi-empirical models of References 1 and 3, strength of material models in References 4, 5, and 6, and elasticity models of References 7 and 8. In Reference 1, an empirical equation is derived by analogy with the crippling data for plates with one edge simply supported and one edge free. It is hypothesized that when the panel web strain reaches the crippling strain, the interfacial stresses become high enough to cause failure. The model proposed in Reference 3 is based on the hypothesis that skin/stiffener separation is caused by the interface normal stress induced by torsional stress in the stiffener. The average torsional stress in the stiffener, obtained from postbuckling analysis method of Reference 9 is empirically related to the bondline normal stress.

In Reference 4, a stiffener/skin delamination model was developed to determine the out-of-plane stresses in postbuckled stiffened shear panels. The physical behavior is simulated by a beam aligned parallel to the diagonal buckles through the point of maximum deflection. The Rayleigh-Ritz method was used to obtain the interfacial stresses. A similar model based on the large deflection beam theory was developed in References 5 and 6.

A three-dimensional analysis, based on the principle of virtual work was developed in Reference 7. The problem was formulated based on plate theory; continuity was enforced through the adhesive interface deformation. The problem was solved by the Galerkin method. Three out-of-plane stress components were obtained. A two-dimensional local elasticity model was used in Reference 8 to investigate the state of stress at the interface between a composite skin and the flanges of a cocured or secondarily bonded stiffened panel.

The preceding investigations examined the local response at the skin/stiffener interface. No attempts were made to relate the remote loading to the local response. In this paper, a methodology is developed that integrates the postbuckling analysis method of Reference 10 and the out-of-plane stress analysis model of References 8 and 11 into a single analysis package. The analytical approach and numerical results are presented in the following sections. The entire analysis can be performed on a personal computer.

ANALYSIS METHODOLOGY

The crux of the present methodology are two analysis packages: (1) PACL1, which predicts the stress and displacement fields in a stiffened postbuckled panel and (2) WEBSTER, which predicts the local interfacial (shear and normal) stresses at the skin and stiffener flange junction. PACL1 (Reference 10) is a Rayleigh-Ritz analysis of curved composite panels loaded into the postbuckling range under axial compression and shear loads. WEBSTER (Reference 11) is a two-dimensional elasticity analysis for the skin/stiffener interface. These analysis methods and the integrated methodology are briefly discussed in the following paragraphs.

PACL1. The energy approach was used to formulate the postbuckling problem in the PACL1 analysis package. The problem was formulated for a stiffened, curved anisotropic laminated plate. The laminate was assumed to be balanced and symmetric. A small imperfection in the lateral displacement was also included in the formulation. The panel geometry and the coordinate system are shown in **Figure 1**. This

figure also shows the relationship between the overall postbuckling structural configuration and the panel geometry used in the analysis. Since the adjacent bays are assumed to deform in an identical fashion, a single bay was analyzed. **Figure 1** shows that the material properties for the skin are A^*_{ij} and D^*_{ij}, where A^*_{ij} (A^*_{11}, A^*_{12}, A^*_{22}, and A^*_{66}) is the skin stiffness matrix and D^*_{ij} (D^*_{11}, D^*_{12}, D^*_{16}, D^*_{22}, D^*_{26}, and D^*_{66}) is the skin rigidity matrix. The material axes 1 and 2 are assumed to coincide with the panel geometry coordinate axes x and y, respectively. The panel, with length a and width b, is bounded by stringers along the straight edges and frames or rings along the curved edges. The cross-sectional area, Young's modulus and moment of inertia of the stringers are A_s, E_s, and I_s, respectively. Those of the frames are A_f, E_f, and I_f. The radius of the curved panel is R.

The energy expressions are written in terms of the displacement components u, v, and w in the x, y, and z directions, respectively. The panel is assumed fixed along x = o and subjected to a system of combined compression (N_x) and shear (N_{xy}) load along the edge x = a. The out-of-plane displacement (w) is assumed to be zero along all four edges.

The total potential energy, Π, is the sum of the strain energy stored in the skin, U_w, in the stringers, U_s, in the frames, U_f, and the potential of the external loads, Ω, and is written as

$$\Pi = U_w + U_s + U_f + \Omega \tag{1}$$

The strain energy in the skin for an anisotropic plate with $A^*_{16} = A^*_{26} = 0$ is given by

$$\begin{aligned} U_w = -\frac{1}{2}\int_v \{ & A^*_{11}\epsilon_x^2 + 2A^*_{12}\epsilon_x\epsilon_y + A^*_{22}\epsilon_y^2 + A^*_{66}\gamma_{xy}^2 \\ & + D^*_{11}w_{,xx}^2 + 2D^*_{12}w_{,xx}w_{,yy} + 4D^*_{16}w_{,xx}w_{,xy} \\ & + D^*_{22}w_{,yy}^2 + 4D^*_{26}w_{,yy}w_{,xy} + 4D^*_{66}w_{,xy}^2 \} \, dv \end{aligned} \tag{2}$$

where ϵ_x, ϵ_y, and γ_{xy} are the strain components. Commas denote differentiation with respect to the subscripted variables.

The strains are expressed in terms of the displacements u, v, and w using the nonlinear strain-displacement relations.

In the derivations that follow, the coordinate variables x and y are normalized with respect to their respective panel dimensions. The normalized coordinates (ξ, η) are given by

$$\xi = \frac{x}{a}, \quad \eta = \frac{y}{b} \tag{3}$$

The strain energy in the stringer is

$$U_s = \frac{A_s E_s}{2a}\int_o^1 u_\xi^2(\xi,0)\, d\xi + \frac{I_s E_s}{2a^3}\int_o^1 v_{\xi\xi}^2(\xi,0)\, d\xi \tag{4}$$

The strain energy in the frame is

$$U_F = \frac{A_f E_f}{2b} \int_o^1 v_\eta^2 (1,\eta)\, d\eta + \frac{I_f E_f}{2b^3} \int_o^1 u_{\eta\eta}^2 (1,\eta)\, d\eta \tag{5}$$

The potential of the external loads is

$$\Omega = -bN_{xx} \int_o^1 u(1,\eta)\, d\eta - bN_{xy} \int_o^1 v(1,\eta)\, d\eta \tag{6}$$

The solution method employs the principle of minimum potential energy. In applying the principle of minimum potential energy, the displacement components are assumed to be functions of the independent variables ξ and η. The selected functions must satisfy the displacement boundary conditions and minimize the total potential energy. A generalized series expression for the displacement functions with unknown coefficients was selected for the present analysis and they are as follows:

$$\begin{aligned} u &= A_{nm} f_1 + a_1 a\xi \\ v &= B_{nm} f_2 + b_1 a\xi \\ w &= C_{nm} f_3 + D_{nm} f_4 + w_o f_5, \end{aligned} \tag{7}$$

The coefficients A_{nm}, B_{nm}, C_{nm}, D_{nm}, a_1, and b_1 are unknown coefficients to be determined by minimizing the total potential energy. The term w_o in Equation 7 is the initial imperfection at the panel center. The function $f_5 = f_5(\xi,\eta)$ is the initial imperfection function in terms of the lateral displacement and satisfies the displacement boundary conditions.

The total potential energy is minimized with respect to the unknown coefficients. The minimization process yields a system of nonlinear algebraic equations. Details of these algebraic equations are given in Reference 10. These equations can be expressed in the following form:

$$\left[\frac{\partial \pi}{\partial A} \bigg|_L \right] = \left[\frac{\partial \pi}{\partial A} \bigg|_N - C \right] \tag{8}$$

where the subscript L denotes the linear terms of the partial derivative of the total potential energy with respect to a particular unknown coefficient (A), subscript N denotes the nonlinear terms and C represents the terms that are independent of the unknown coefficients.

The number of nonlinear algebraic equations in the system given by Equation 8 depend on the number of buckling modes used in the analysis. The number of equations can be calculated from the relation 4NM+2, where N is the number of buckling modes in the x-direction and M is the number of buckling modes in the y-direction. As N and M increase, the number of nonlinear terms on the right-hand side of Equation 8 also significantly increases. A large number of nonlinear terms present numerical difficulty in solving Equation 8. On the other hand, although the postbuckling behavior of a stiffened panel is mixed-mode behavior in general, the displacement response is dominated by a single buckling mode. Therefore, if the dominant buckling

mode is known, the postbuckling behavior can be accurately described using a single-mode analysis.

In addition, for the case of no initial imperfection, i.e., $w_o = o$, the total number of integrals involved in Equation 8 is reduced to 108. The reduced system of nonlinear equations can be solved with very high accuracy by an iterative technique using the method of successive linearization. In this method, each of the unknown coefficient, A_{nm}, B_{nm}, C_{nm}, D_{nm}, a_1, and b_1 is assigned an initial value and substituted into the right-hand-side of Equation 8. Equation now becomes a system of linear algebraic equations and can be easily solved for the new values of the unknown coefficients. Using the new set of coefficients as initial values, another set of improved coefficients can be obtained by solving the linearized system. This procedure is continued until the solution converges within a desired limit. In the actual solution, only the initial values of the coefficients at the first load level need to be assigned. At higher load levels, the initial values are obtained by extrapolating the converged solutions of the preceding load levels to reduce the number of iterations. This numerical procedure for single mode analysis was coded in the PACL1 computer program.

WEBSTER. This analysis is a generalization of the elasticity method used in References 8 and 12. The method models the stiffener flange and the adjacent structure (skin) as separate orthotropic plates that are bonded together with a bondline of zero thickness. Each plate may have different mechanical properties.

The local model considers a flange terminating at the skin, as shown in **Figure 2**. The problem is formulated as a generalized plane deformation problem (i.e., the stress and strain components are independent of the z-coordinates).

The stress-strain relations are given by

$$\epsilon_i = a_{ik}\sigma_k \qquad i,k = 1,2,3,4,5,6 \tag{9}$$

and

$$a_{ik} = 0 \qquad \text{if } i \neq k \text{ for } i,k = 4,5,6$$

where a_{ik} are the components of the effective compliance matrix. The equilibrium equations are satisfied automatically by defining the stress functions

$$\sigma_x = \frac{\partial^2 F}{\partial y^2}, \quad \sigma_y = \frac{\partial^2 F}{\partial x^2}, \quad \tau_{xy} = -\frac{\partial^2 F}{\partial x \partial y} \tag{10}$$

The equations governing the stress function (F) are derived from the stress-strain relations (Equation 9) and the linear strain displacement relations. The governing equation becomes

$$\beta_{22}\frac{\partial^4 F}{\partial x^4} + (2\beta_{12} + \beta_{66})\frac{\partial^4 F}{\partial x^2 \partial y^2} + \beta_{11}\frac{\partial^4 F}{\partial y^4} = 0 \tag{11}$$

where

$$\beta_{ij} = a_{ij} - \frac{a_{i3}a_{j3}}{a_{33}}, \quad i=1,2,4,5,6 \tag{12}$$

The homogeneous solution of Equation 11 can be approximated by a series expansion in terms of complex variables, defined as $Z = x + \mu y$. The stress functions are assumed to be functions of the complex variables, specifically $F = F(Z)$. The governing equation becomes

$$[\beta_{22} + \mu^2(2\beta_{12} + \beta_{66}) + \mu^4\beta_{11}]\ F^{iv}(Z) = 0 \tag{13}$$

Thus, μ, depending on material properties, are the roots of the characteristic equation

$$\beta_{22} + \mu^2(2\beta_{12} + \beta_{66}) + \mu^4\beta_{11} = 0 \tag{14}$$

The displacements can then be expressed in terms of the stress functions as

$$\begin{aligned} u &= (\mu_k^2\,\beta_{11} + \beta_{12})\ F'(Z_k) \\ v &= \frac{1}{\mu_k}(\mu_k^2\,\beta_{12} + \beta_{22})\ F'(Z_k) \end{aligned} \tag{15}$$

where, μ_k (k = 1,2,3,4) is the kth root of Equation 14.

The series expressions for the stress functions are then stated as

$$F(Z) = \sum_{i}^{N} C_i \sum_{k=1}^{4} \alpha_{ik} \frac{Z_k^{\lambda+2}}{(\lambda+1)(\lambda+2)} \tag{16}$$

where, C_i are constants to be determined. The stresses and displacements can then be expressed in terms of the constants C_i and the complex variables Z_k.

The constants $\alpha_k^{(i)}$ are determined by satisfying prescribed boundary conditions. The boundary conditions include zero stress along the free edges, and stress and displacement continuity conditions along the interface. These conditions are satisfied by expressing the stress and displacement components in polar coordinates (r,θ). It should be noted that Equations 9 through 16 are derived for the skin and the flange, such that each one actually represents two equations.

The following relations use the subscript (or superscript) 1 and 2 to denote the flange and the skin, respectively. Surfaces AB and FA are assumed to be stress free. These boundary conditions are stated respectively as

$$\sigma_\theta^{(1)}(r,\beta) = \tau_{r\theta}^{(1)}(r,\beta) = 0 \tag{17}$$

$$\sigma_\theta^{(2)}(r,-\pi) = \tau_{r\theta}^{(1)}(r,-\pi) = 0 \tag{18}$$

The bond between the flange and the skin is assumed to be ideal along the interface (i.e., the stresses and displacements along this line are continuous). The stress continuity conditions at the interface are stated as

$$\sigma_\theta^{(1)}(r,0) = \sigma_\theta^{(2)}(r,0) \tag{19}$$

$$\tau_{r\theta}^{(1)}(r,0) = \tau_{r\theta}^{(2)}(r,0) \tag{20}$$

The displacement continuity conditions at the interface are

$$u^{(1)}(r,0) = u^{(2)}(r,0) \tag{21}$$

$$v^{(1)}(r,0) = v^{(2)}(r,0) \tag{22}$$

A system of eight homogeneous equations in terms of the eight unknown constants α^i_k (i=1,2 and k=1,2,3,4) result when the stress and displacement expressions are substituted into the boundary condition relations, Equations 17 through 22.

Global analysis of the structure provides the forces that are applied to surfaces CD and EF of the local region shown in **Figure 2**. Surfaces FA, AB, and BC are stress free. The overall applied force system must satisfy the equilibrium condition of the local region ABCDEF. WEBSTER solves this problem using boundary collocation with collocation points distributed along edges CD and EF.

PACSTER. PACSTER is an integrated analysis package that utilizes the displacement field obtained from the PACL1 analysis to determine the interfacial stresses at the skin/stiffener junctions by performing WEBSTER analysis. Therefore, the stress formulation in WEBSTER must be modified. The displacements in the local (WEBSTER) coordinates system can be expressed in terms of the stress function (F(Z)) as given by Equation 15. This modification essentially changed the original prescribed boundary force problem of WEBSTER into a prescribed boundary displacement problem. The displacement field obtained from PACL1 analysis is then used as boundary displacements in the WEBSTER analysis. This procedure has been automated and resulted in the present computer code PACSTER, which is operational on a 286/386 computer.

A flowchart detailing the logic of the analysis methodology is shown in **Figure 3**. The program requires material properties, panel geometry, sectional properties of the stringers and the frames and the load parameters as input. Following input execution of PACL1 begins and the program calculates the displacement field of the entire panel. The displacements are then screened to identify critical locations. Because the objective of this analysis is to determine the applied load at which skin/stiffener separation occurs, the critical locations are selected based on the maximum displacements in the vicinity of the stringer or the frame. A total of four critical locations are selected for WEBSTER analysis. They are selected based on critical v and w displacements near the stringers and critical u and w displacements near the frames. After the critical locations are identified, the program proceeds to transfer all the required data into the local coordinate system for the WEBSTER analysis. The displacements associated with the critical locations are used as boundary conditions for the interfacial stress calculations. WEBSTER is executed four times for the four critical locations identified.

The interlaminar normal and shear stresses obtained from the local analysis are then used in the failure analysis. The failure criterion currently used in PACSTER is an average stress criterion in a quadratic form. The average stress criterion suggested in Reference 13 is applied here. The average shear (τ_{ave}) and normal (σ_{ave}) stresses over a characteristic length (a_o) are computed, and failure is defined as

$$F_I = \left[\left(\frac{\tau_{ave}}{\tau_o} \right)^2 + \left(\frac{\sigma_{ave}}{\sigma_o} \right)^2 \right]^{1/2} \geq 1 \qquad (23)$$

where, τ_o and σ_o are shear and normal strength of the interface material, respectively.

The procedure described above is repeated for each load increment until the prescribed maximum load is reached.

Figure 4 illustrates the typical critical location selection procedure. A curved panel enclosed with stiffeners and frames is considered. The stiffener flange is of length a_s and the frame flange is of length b_f. In-plane compression and shear forces are applied to the curved panel. The resulting displacement pattern obtained from PACL1 analysis is shown in **Figure 4**. For the skin/stiffener separation analyses, the region of significance is highlighted in the figure. From the displacement field, the program has identified S_{cz} and F_{cz} as critical locations. The out-of-plane stress distributions along the skin/stiffener interface at location S_{cz} are shown in **Figure 5**. This figure indicates high stress concentrations, both normal and shear, occur at the junction of the skin and the stiffener. These stress concentrations contribute to the skin/stiffener separation failure of the panel.

NUMERICAL EXAMPLE

A curved panel tested in Reference 10 is selected as an example to illustrate the analysis procedure. The composite panel is 24 inches long, 12.2 inches wide with a radius of 45 inches. The panel skin is made of A370-5H/3501-6 woven graphite/epoxy and AS/3501-6 unidirectional graphite/epoxy. The material properties, skin layup, and stiffener configurations are shown in **Figure 6**. The flange of the frame has a layup of $[\underline{45_2}/90_2/0/90_2/\underline{45_2}]$. The panel is under axial compression with total load P_x. The interfacial strengths are assumed to be σ_o=3000 psi and τ_o=11000 psi. These allowables are typical of the values obtained from flatwise tension and short beam shear tests, respectively.

The results of the PACSTER analysis are shown in **Figure 7**. The critical locations identified by the program are shown in the upper-left corner of the figure. They are denoted by (1) v-s/s: critical skin/stiffener interface due to v-displacement; (2) w-s/s: critical skin/stiffener interface due to w-displacement; (3) u-s/f: critical skin/frame interface due to u-displacement; and (4) w-s/f critical skin/frame interface due to w-displacement. As shown in the figure, these locations depend on the applied load level.

The interfacial stresses are expressed in terms of the failure index (F_I) defined in Equation 23. **Figure 7** shows that the most critical location is w-s/s. At this location, F_I = 1.0 when the total compression reaches 9100 lb. That is

skin/stiffener separation failure will be initiated at the location w-s/s at 9100 lb of axial compression. Test results in Reference 10 showed the initial buckling occurred at 325 lb/in or approximately 4000 lb, and final failure of the panel, by skin/stiffener separation, at 825 lb/in or 10,050 lb. The results in **Figure 7** show that PACSTER under-predicts the final failure by approximately 10 percent. This may be due to the conservative estimate of the interfacial strengths (σ_o and τ_o) or the uncertainty in the out-of-plane properties of the materials.

SUMMARY

A methodology has been developed to predict the failure of postbuckled, stiffened composite panels by skin/stiffener separation. The methodology is applicable to curved as well as flat panels under combined uniaxial compression and in-plane shear loads. The entire analysis can be performed on a personal computer.

Limited correlation of analytical predictions with experimental data indicated that the analysis provided reasonable prediction of failure load. Further data correlation is necessary to validate the methodology.

REFERENCES

1. Deo, R. B., Agarwal, B. L., and Madenci, E., "Design Methodology and Life Analysis of Metal and Composite Panels," AFWAL-TR-85-3096, Final Report, Volume I, Contract F33615-81-C-3208, December 1985.

2. Deo, R. B. and Madenci, E., "Design Development and Durability Validation of Postbuckled Composite and Metal Panels," AFWAL-TR-85-3077, Final Report, Technology Assessment, Contract F33615-84-C-3220, May 1985.

3. Arnold, R. R., "Disbond Criterion for Postbuckled Composite Panels," AIAA-CP-87-0732, presented at the 28th AIAA/ASME/ASCE/AHS SDM Conference, Monterey, CA, April 6-8, 1987.

4. Agarwal, B. L., "A Model to Simulate Failure Due to Stiffener/Web Separations of Composite Tension Field Panels," AIAA-CP-82-0746, presented at the 23rd AIAA/ASME/ASCE/AHS SDM Conference, New Orleans, LA, May 10-12, 1982.

5. Tsai, H. C., "Solution Method for Stiffener-Skin Separation in Composite Tension Field Panel," Report No. NADC-82171-60, October 1982.

6. Tsai, H. C., "Approximate Solution for Skin/Stiffener Separation Including Effect of Interfacial Shear Stiffness in Composite Tension Field Panel," Report No. NADC-83131-60, November 1983.

7. Wang, J. T. S. and Biggers, S. B., "Skin/Stiffener Interface Stresses in Composite Stiffened Panels," NASA Contract Report No. 172261, January 1984.

8. Hyer, M. W. and Cohen, D., "Calculation of Stresses and Forces Between the Skin and Stiffener in Composite Panels," AIAA-CP-87-0731, presented at the 28th AIAA/ASME/ASCE/AHS SDM Conference, Monterey, CA, April 6-8, 1987.

9. Arnold, R. R. and Meyers, J., "Buckling, Postbuckling, and Crippling of Materially Nonlinear Laminated Composite Plates," International Journal of Solids and Structures, Volume 20, No. 9 and 10, pp 863-880, 1984.

10. Deo, R. B., Kan, H. P., and Bhatia, N. M., "Design Development and Durability Validation of Postbuckled Composite and Metal Panels, Volume III - Analysis and Test Results," WRDC-TR-89-3030, Final Report, Contract F33615-84-C-3220, November 1989.

11. Paul, P. C., Saff, C. R., Sanger, K. B., Mahler, M. A., Kan, H. P., and Deo, R. B., "Out-of-Plane Analysis for Composite Structures," Volumes I and II, Final Report, NADC Contract N62269-87-C-0226, August 1989.

12. Wang, S. A. and Choi, I., "Boundary Layer Effects in Composite Laminates," Part I and II, Journal of Applied Mechanics, Volume 49, No. 3, pp 541-560, 1982.

13. Whitney, J. M. and Nuismer, R. J., "Stress Fracture Criteria for Laminated Composites Containing Stress Concentrations," Journal of Composite Materials, Volume 8, 1974, pp 253-265.

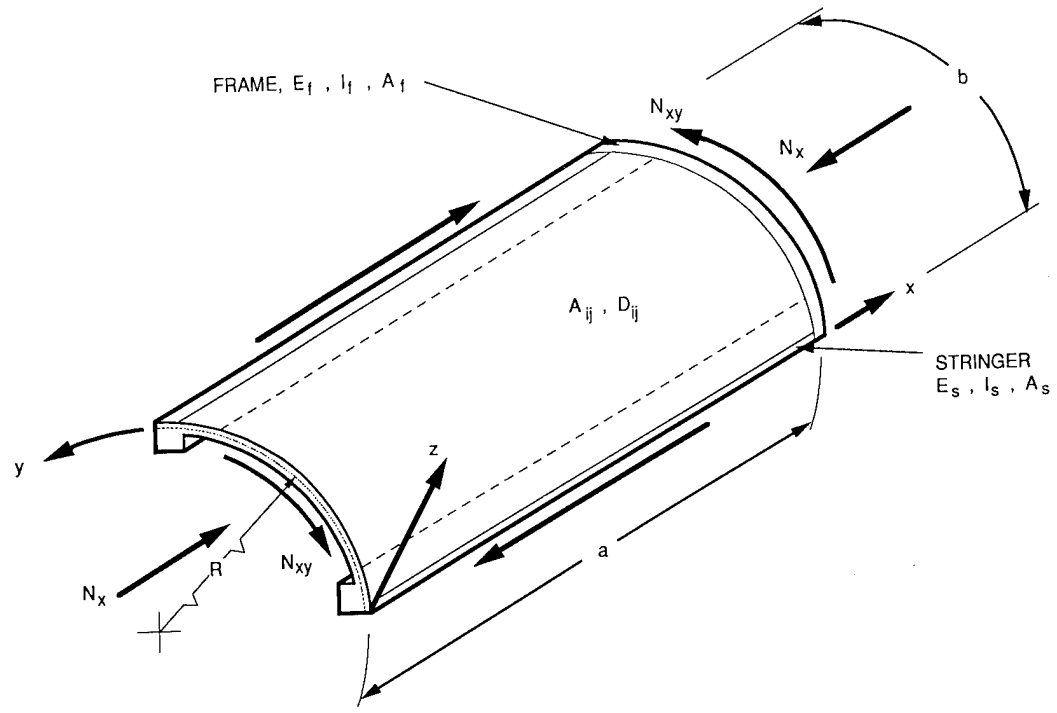


Figure 1. Curved Panel Geometry and Coordinate System Used in PACLI Analysis.

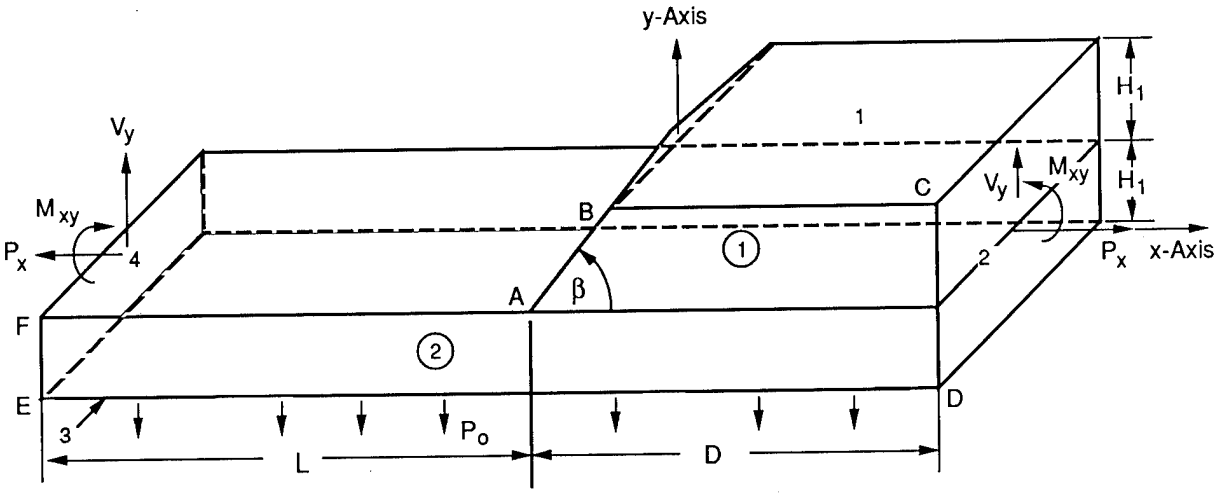


Figure 2. Local Elasticity Model for WEBSTER Analysis.

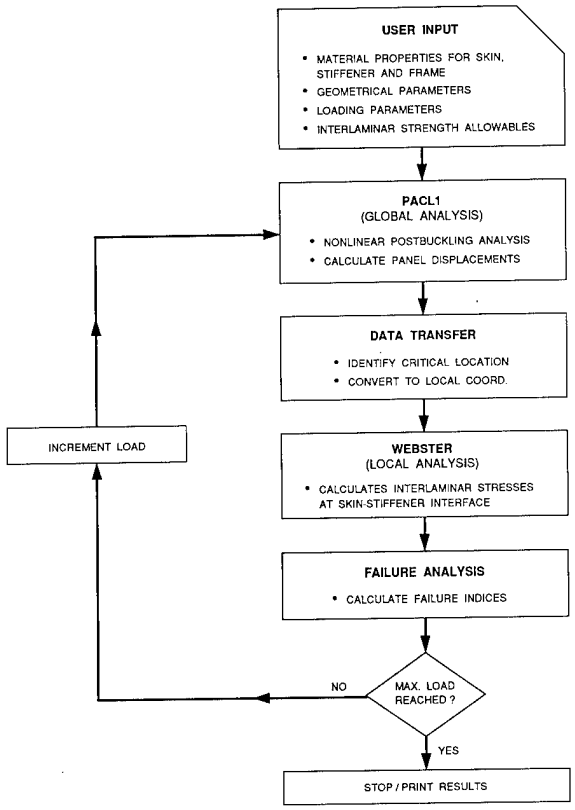


Figure 3. Flowchart for Analysis of Skin-Stiffener Separation in Postbuckled Panels.

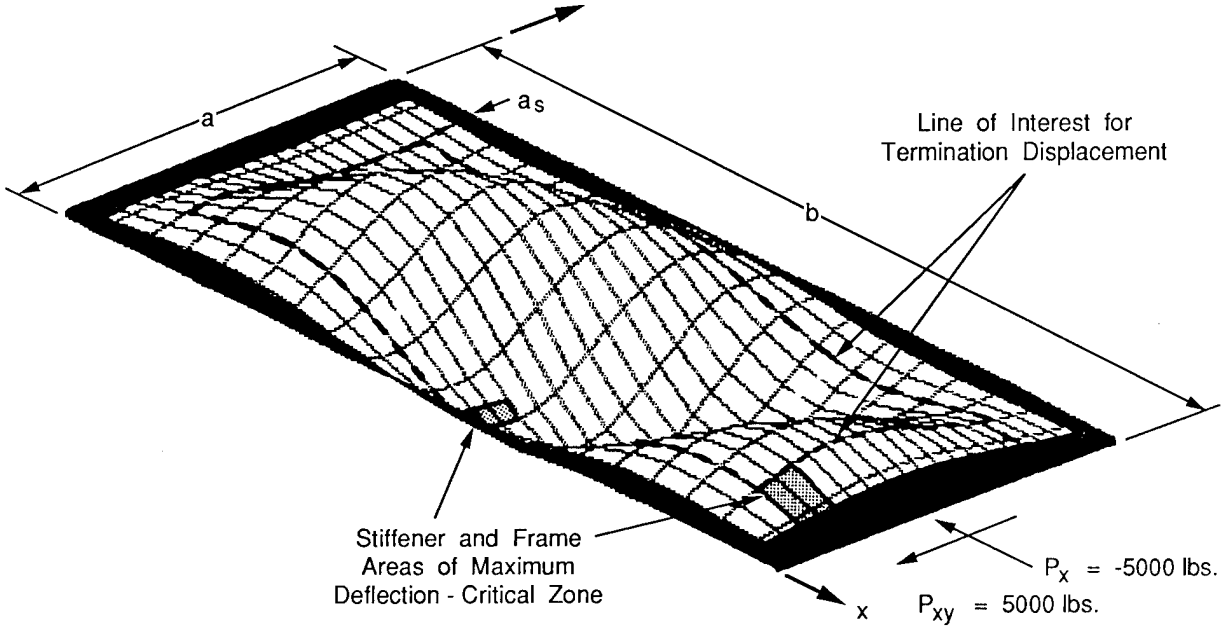


Figure 4. Postbuckled Panel With Stiffener Termination Details.

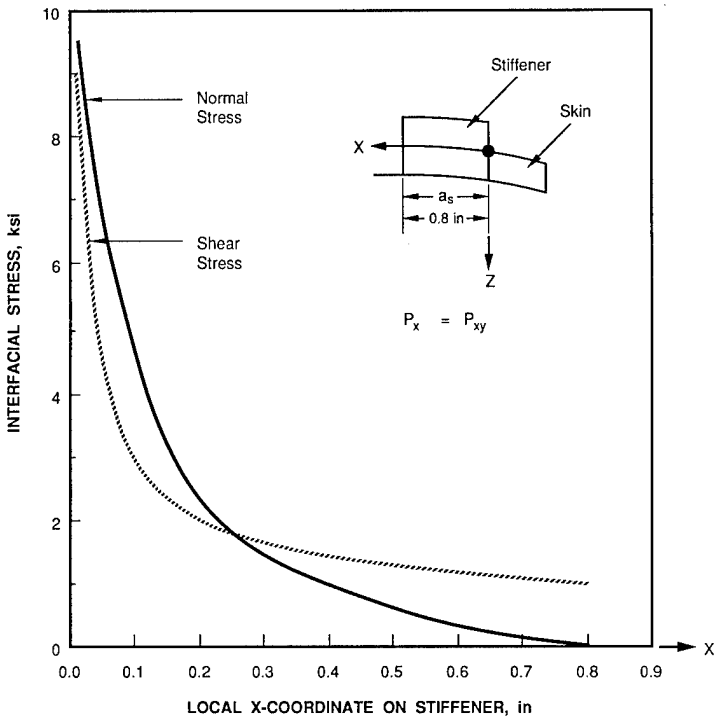


Figure 5. Interlaminar Stress Distribution at Stiffener Termination in Stiffener Critical Zone.

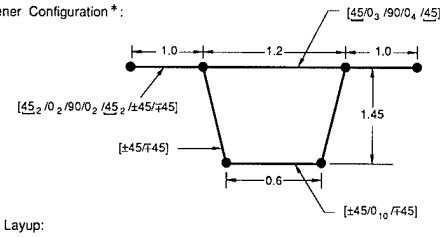
Panel Configuration: Hat stiffened, 45-in radius, 24-in length, 12.2-in stiffener spacing

Material: A370-5H/3501-6 woven graphite/epoxy
AS/3501-6 unidirectional graphite/epoxy

Lamina Properties:

	A370-5H/3501-6	AS/3501-6
Per ply thickness, in	0.013	0.0052
EL, psi	10.0×10^6	18.7×10^6
ET, psi	9.2×10^6	1.87×10^6
GLT, psi	0.9×10^6	0.85×10^6
NULT	0.055	0.3

Stiffener Configuration*:



Skin Layup:

[45$_2$ /90/45$_2$]

Compression Ultimate Strains: $\varepsilon_c^{ult} = 0.012$ for layups with at least 40% 0-degree plies

$\varepsilon_c^{ult} = 0.015$

* An underscore _ denotes woven ply

Figure 6. Example Problem Data for Program PACSTER.

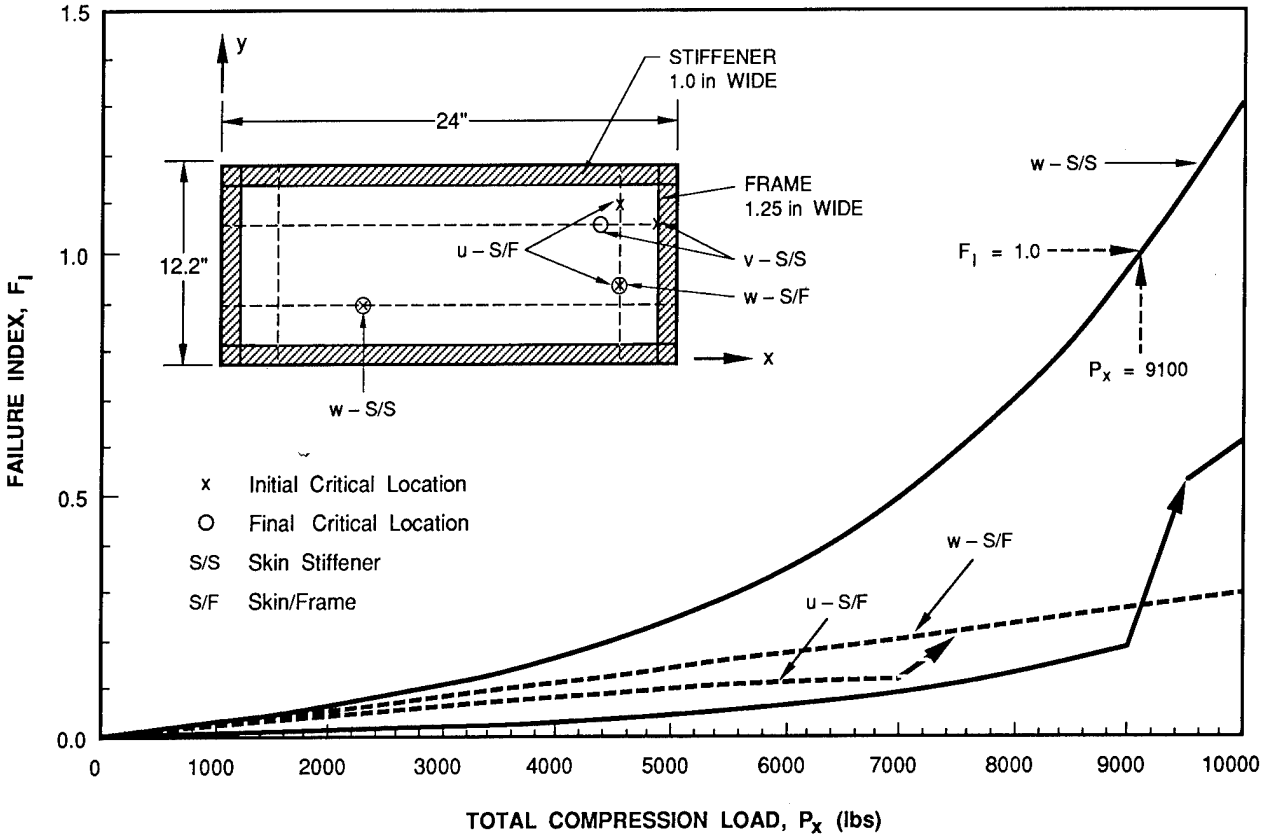


Figure 7. Analytical Results of the Example Problem.

EXPERIMENTAL BEHAVIOR OF GRAPHITE-EPOXY Y-STIFFENED SPECIMENS LOADED IN COMPRESSION

P. D. Sydow and M. J. Shuart
NASA Langley Research Center
Hampton, Virginia

ABSTRACT

An experimental investigation of the behavior of graphite-epoxy Y-stiffened specimens loaded in compression is presented. Experimental results are presented for element specimens with a single stiffener and for panel specimens with three stiffeners. Response and failure characteristics of the specimens are described. Effects of impact damage on structural response for both specimen configurations are also presented. Experimental results indicate that impact location may significantly affect the residual strength of the Y-stiffened specimens. The failure results indicate that the critical failure mode is buckling of the stiffener webs for Y-stiffened element specimens and buckling of both stiffener web and stiffener blade for the Y-stiffened panel specimens.

INTRODUCTION

Composite materials provide the aerospace engineer with greater freedom in designing aircraft and spacecraft components and appear to have advantages not exhibited by metals. Realizing the potential long-term advantages of composite structures, such as weight savings and high performance, NASA initiated the Advanced Composites Technology (ACT) Program. An objective of the ACT Program is to investigate advanced design concepts for composite aircraft structures. Such advanced concepts include designs that exploit unique characteristics of composite structures and utilize cost-effective manufacturing procedures using advanced material systems or material forms. Stiffness-tailoring is a well-known example of a unique characteristic for composite structures that can be exploited to obtain structurally efficient composite components. Pultrusion is an example of a potentially cost-effective manufacturing procedure for composite structures. Long prismatic structural elements may be pultruded to decrease costly hand lay-up and assembly efforts. An example of an advanced material system is a low-cost damage-tolerant composite material with high compression strength. Such a material would overcome many of the shortcomings of state-of-the-art material systems, and hence become attractive for many aircraft structures applications. Once the attributes of composite materials and the benefits of advanced concepts are fully understood and demonstrated, composite structures technology will mature to the point of being a key factor in the design of state-of-the-art high performance aircraft.

Advanced concepts for composite structures that take advantage of both structural geometry and stiffness tailoring to enhance structural efficiency are being studied for application to primary aircraft structures such as wing cover panels. Previous design studies for metal structures have shown that a Y-stiffened panel is a highly structurally efficient configuration [1,2]. The Y-stiffener configuration combines the desired torsional rigidity of a closed-section stiffener with the bending stiffness of a simple blade stiffener. A stiffness-tailored composite Y-stiffened panel is more structurally efficient than a similar metal panel, and the composite panel may also be fabricated cost effectively.

The objectives of the present paper are to describe the development of a structurally optimized graphite-epoxy Y-stiffened cover panel concept and to present the results of an experimental study of the behavior of several compression-loaded graphite-epoxy Y-stiffened specimens. Experimental results are presented for specimens with a single stiffener, referred to as Y-stiffened element specimens, and for panels with three stiffeners, referred to as Y-stiffened panel specimens. Response and failure characteristics of the specimens are described. Effects of impact damage on structural response for Y-stiffened element specimens and Y-stiffened panel specimens are also presented.

CONCEPT DEFINITION

The concept of a Y stiffener configuration was first conceived in the late 1940's [1,2] and was referred to as the NACA Y-stiffener. This stiffener is shown in Figure 1a. Design requirements for metal stiffeners included both a high resistance to an overall column-like buckling mode and a high resistance to local buckling modes. The metal NACA Y-stiffener design uses the stiffener cap primarily to satisfy the high column-like buckling load design requirement and uses the web thicknesses as a design parameter to suppress local buckling. Optimized configurations were determined using a graphical technique that plotted a weight index as a function of the average stress resultant for the panel [1].

A composite Y-stiffener is shown in Figure 1b. The optimized design for this stiffener was obtained using the Panel Analysis and Sizing COde, PASCO [3]. The structurally optimized panel was designed to carry a combined loading of N_x =14660 lbs/in., N_y =733 lbs/in., and N_{xy} =1367 lbs/in. where N_x, N_y, and N_{xy} are inplane stress resultants of classical plate theory. This loading condition was assumed to be representative of a high compression-dominated loading for the cover panel of a high-aspect-ratio subsonic commercial transport wing. The design variables used in the structural optimization of this panel were stiffener planform dimensions and thicknesses. Lamina properties used for the structural optimization are given in Table 1. The optimized stiffener of the combined-load panel previously described is the stiffener investigated in the present study. The stacking sequences for this composite stiffener are shown in Figure 2. An important simplification indicated in Figures 1 and 2 is the absence of the stiffener cap on the composite stiffener. The optimization results indicate that the stiffness and load-carrying capacity design requirements can be fulfilled without the stiffener cap by tailoring the stiffnesses of the blade, webs, and skin. This design simplification also illustrates how stiffness tailoring can be used to simplify fabrication requirements on a composite structure.

SPECIMENS, APPARATUS, AND TESTS

Composite Y-stiffened specimens were fabricated from a commercially available advanced damage-tolerant material system, Hercules IM7/8551-7 graphite-epoxy preimpregnated tape. The tapes were laid to form 24-ply-thick flat laminates for the specimen skins with laminate stacking sequence $[\pm 45/0/\mp 45/0/\pm 45/0/\mp 45/90]_S$. Tapes were also laid on the manufacturing tool as shown in Figure 2 to form halves for the specimen Y-stiffeners. The flanges and webs of the stiffeners are 16-ply-thick laminates with a $[\pm 45/90/\mp 45/90/\pm 45]_S$ stacking sequence. The blade region for the stiffener halves of the

stiffeners are 23-ply-thick laminates having a $[+45/0_4/-45/0_3/+45/0/\bar{0}]_s$ stacking sequence. Some of the ±45° plies from the flanges and webs are continuous through the blade. All laminates were cured in an autoclave using the manufacturer's recommended procedures. Following cure, the laminates were ultrasonically C-scanned to establish specimen quality. The stiffener halves were bonded together after curing to form the Y-stiffener, and the Y-stiffeners were subsequently bonded to the specimen skins. Hysol EA 934 adhesive was used for all bonding. Bond lines were controlled using 0.005-in.-diameter glass beads.

Typical specimens used in this study are shown in Figure 3. The Y-stiffened element specimen consists of a 20-in.-long by 5.78-in.-wide skin and a single stiffener as shown in Figure 3a. The Y-stiffened panel specimen consists of a 20-in.-long by 17.34-in.-wide skin and three evenly spaced stiffeners as shown in Figure 3b. The specimen ends were secured in a potting material used to introduce load into the structure. The specimen ends were inserted approximately one inch into the potting material, making the effective test section of the specimen approximately 18 inches long. The loaded ends of the specimens were machined flat and parallel to permit uniform compressive end-shortening. The unstiffened side of the skin of each specimen was painted white so that a moire-fringe technique could be used to detect and monitor any out-of-plane deformations during testing. Three element specimens and two panel specimens were fabricated and tested. Stiffened element specimens were designated NY1 through NY3, and stiffened panel specimens were designated NYP1 and NYP2. The specimens were loaded quasi-statically in uniform axial compression to failure using a 300-kip-capacity hydraulic testing machine. The unloaded edges of the skins were simply supported to prevent the specimens from buckling as a column.

A procedure for impacting graphite-epoxy components described in reference 4 was used in the current investigation. Aluminum spheres 0.50 in. in diameter were used as projectiles. These spheres were propelled by a compressed-air gun equipped with an electronic detector to measure projectile speed. All projectile speeds in this study were approximately 550 ft/sec. which corresponds to an impact energy of approximately 27.5 ft-lbs. A schematic of the air gun and a description of its operation are given in reference 4.

Impact sites for specimens in this study are shown in Figure 4. Y-stiffened element specimens NY2 and NY3 were subjected to impact damage prior to testing. Specimen NY2 was impacted at two locations on the unstiffened side of the skin opposite the attachment flanges. The first impact site was located at one-quarter of the test section length, and the second impact site was located at the midpoint of the test section length as shown in Figure 4a (indicated by locations 1a and 1b in Figure 4a). Specimen NY3 was impacted once at the midpoint of the test section length on the blade in the vicinity of the transition region of the web and the blade as shown in Figure 4a (indicated by location 2 in Figure 4a).

Y-stiffened panel NYP2 was subjected to impact damage. Specimen NYP2 was impacted at two locations on the unstiffened side of the skin opposite of the center stiffener attachment flanges prior to testing. The first impact site was located at one-quarter of the test section length, and the second impact site was located at the midpoint of the test section length as shown in Figure 4b (indicated by locations 1a and 1b in Figure 4b). This panel was loaded to a 0.006 in./in. strain level and then unloaded with no visible signs of damage apart from the local delaminations at the sites of impact. Specimen NYP2 was then

impacted at the midpoint of the central blade in the vicinity of the transition region of the web and the blade and loaded to failure (direction of impact was at the minimum angle that would accommodate the compressed-air gun).

The specimens were instrumented with electrical resistance strain gages applied to the flanges, webs, and blades of the Y-stiffened elements and to the skin, webs, and blades of the Y-stiffened panels. Direct-current differential transformers were used to measure specimen end-shortening and out-of-plane displacements. Electrical signals from the instrumentation and the corresponding applied loads were electronically recorded at regular time intervals during the test.

RESULTS AND DISCUSSION

Y-Stiffened Element Specimens

Curves of normalized load versus end-shortening are presented in Figure 5 for the three Y-stiffened element specimens. The applied load P is normalized by the membrane stiffness EA and the end-shortening d is normalized by the specimen length L. This normalized end-shortening d/L is a measure of the specimen's average axial strain. The filled circles appearing in the figure indicate specimen failure.

These normalized load-shortening results appear nearly linear up to a d/L of approximately 0.004 in./in. The slight deviation from a linear response may be attributed to initial geometric imperfections. Specimen NY1 failed at 93.0 kips and an average strain of 0.0096 in./in. Specimen NY2, which was impacted on the unstiffened side of the skin opposite the attachment flanges, failed at 74.3 kips and an average strain of 0.0075 in./in. Specimen NY3, which was impacted near the web-blade interface, failed at 50.1 kips and an average strain of 0.0051 in./in. The failure loads for damaged specimens NY2 and NY3 are 20 percent lower and 46 percent lower, respectively, than the failure load for the undamaged specimen NY1. The effects of impact damage on element specimen failure are discussed below.

The results obtained from strain gages placed on the Y-stiffened element specimens are shown in Figures 6-8. These results were obtained from strain gages located on each specimen as shown in Figures 6a, 7a, and 8a. The circle and square symbols are used in Figures 6-8 to distinguish between individual gages and represent specimen failure. Strain gage results for the undamaged specimen NY1 are presented in Figure 6. The axial strain obtained from back-to-back gages located on the skin-flange region is shown in Figure 6b as a function of the applied load. The strain results presented in this figure exhibit slightly nonlinear behavior similar to the corresponding load-shortening behavior. No strain reversal is observed. Thus these results indicate that no bending or buckling occurred in the skin-flange region during the test. The axial (parallel to the load direction) and the transverse (perpendicular to the load direction) strain in the webs are shown in Figure 6c as a function of the applied load. Axial strains in each specimen web are shown for gage location B1 indicated in Figure 6a, and these strains are always compressive. Transverse strains in each web are shown for gage location B2, and these strains are always tensile. The axial strain results for the webs are similar to the axial strain results for the skin-flange region (Figure 6b). The transverse strain results for the webs show the onset of strain reversal indicating that the webs slightly bend or begin to buckle prior to failure. Axial strain results for the blade are presented in Figure 6d. These results are similar to the axial strain results for the skin-flange region and the web.

Strain gage results for the impact damaged element specimen NY2 are presented in Figure 7. The axial strain from back-to-back strain gages located on the skin-flange region is shown in Figure 7b as a function of applied load. The slight differences in the back-to-back strains for a given load level indicate that local bending or buckling may be initiating. The axial and transverse strains in the webs are shown in Figure 7c as a function of the applied load. The compressive axial strain behavior is linear to failure for one gage and nonlinear for the other gage. The nonlinear strain behavior indicates bending of the web. The slight strain reversal observed for the tensile transverse strain results suggests that the webs buckle just prior to failure. The web transverse strain behavior for the damaged specimen is similar to the web transverse strain behavior for the undamaged specimen NY1, but the failure strain for the damaged specimen is less than the failure strain for the undamaged specimen. Axial strain results for the blade of specimen NY2 are presented in Figure 7d. These results are similar to the axial strain results for the skin-flange region of this specimen. All failure strains on Figure 7 for damaged specimen NY2 are less than the corresponding failure strains on Figure 6 for undamaged specimen NY1. However, the average failure strain for damaged specimen NY2 is greater than 0.0075 in./in. indicating good residual strength in spite of impact damage at the skin-flange region. Good residual strength is defined in this study as average failure strains greater than or equal to 0.006 in./in., in spite of the presence of impact damage.

Strain gage results for the impact damaged element specimen NY3 are presented in Figure 8. The gage locations and orientations are shown in Figure 8a. The axial strain from back-to-back strain gages located on the skin-flange region is shown in Figure 8b as a function of applied load. These strain results are approximately linear to failure, and no strain reversal is observed. The axial and transverse strains in the webs are shown in Figure 8c as a function of the applied load. The compressive axial strain behavior is linear to failure for one web and nonlinear for the other web. The nonlinear behavior indicates bending of this web that is located adjacent to the impact damaged region. The strain reversal observed for the tensile transverse strain results indicates that these webs buckled prior to failure. The axial and transverse strain behavior of the webs of the damaged specimen NY3 is similar to the strain behavior for the damaged specimen NY2. Axial strain results for the blade of specimen NY3 are presented in Figure 8d. The strain reversal observed for these axial strains indicates that the blade buckles prior to failure. All failure strains on Figure 8 for specimen NY3 are less than the corresponding failure strains on Figure 7 for specimen NY2. These failure strain data, failure load data, and global failure strain results for specimens NY2 and NY3 indicate that, for the same impact energy, impact damage at the blade-web interface degrades the structural response of this Y-stiffener configuration more than impact damage at the skin-flange region. The average failure strain for damaged specimen NY3 is approximately 0.005 in./in. indicating marginal residual strength for this specimen with impact damage at the blade-web interface.

The dominant response that initiates failure of these Y-stiffened element specimens is web buckling. Web buckling is a significant design consideration for Y stiffeners since the webs support the blade, and the blade is the primary load-carrying member for this configuration. All three specimens have web strain data that indicate web buckling prior to failure. No buckling was observed from the moire fringe pattern during the element specimen tests indicating that the specimen skin does not buckle. Blade buckling, as indicated by strain gage reversal, only occurs for the specimen impacted at the blade-web intersection. Web buckling may also contribute to the debonding of the adhesively bonded halves of these Y-stiffener blades. A typical failed element specimen and a close-up of the failure region are shown in Figure 9.

Y-Stiffened Panel Specimens

Curves of normalized-load versus end-shortening results are presented in Figure 10 for the two Y-stiffened panel specimens. For the panels, the applied load P is also normalized by the membrane stiffness EA and the end-shortening d is also normalized by the specimen length L. The solid circles indicate failure of the specimen and the open circle indicates termination of the test prior to failure. All results appear nearly linear up to an average strain of approximately 0.005 in./in. The slight deviation from a linear response may be attributed to initial imperfections. Photographs of moire-fringe patterns just prior to specimen failure are shown in Figure 11. The photograph of the first specimen, NYP1, shown in Figure 11a indicates that the buckle pattern of the skin has five half-waves along the length and two half-waves across the width of the region between the stiffeners of the specimen. Specimen NYP1 failed at 285.2 kips, and an average strain level of 0.0078 in./in. The test of the second test specimen, NYP2, was conducted in two phases. First, NYP2 was impacted at two locations on the unstiffened side of the skin opposite the attachment flanges of the center stiffener, in a similar manner as Y-stiffened element NY2 (see Figure 4b). The panel was then loaded to a 0.006 in./in. average strain level to simulate the ultimate compressive strain level a wing cover panel is expected to experience in flight. The panel did not buckle or fail when loaded to an average strain level of 0.006 in./in. In the next phase of the test, NYP2 was impacted once more. The second impact site was located at the midpoint of the test section length and on the central blade in the vicinity of the transition region of the web and the blade (see Figure 4b). This location was determined to be the critical impact site from the previous tests of Y-stiffened element specimens. The panel was then loaded until the center stiffener failed. The failure load was 137.1 kips and corresponds to an average axial strain of 0.0045 in./in. The photograph of specimen NYP2 in Figure 11b shows that the buckling pattern of the skin has a single half-wave along the length and width of the central region between the outermost stiffeners. This mode shape occurred after the center stiffener separated from the skin but prior to separation of the skin from the remaining stiffeners. Specimen NYP2 failed when the skin debonded from the outer stiffeners at a load of 137.2 kips and an average strain of 0.0057 in./in. The maximum loading for the impact-damaged panel was 48 percent less than the maximum loading for the undamaged panel. The effects of damage on panel specimen failure are discussed below.

The strain gage results for the Y-stiffened panel specimens are shown in Figures 12 and 13. These results were obtained from strain gages located on each specimen as shown in Figures 12a and 13a. The circle and square symbols are used in Figures 12 and 13 to distinguish between individual gages and represent specimen failure. Strain results for the undamaged specimen NYP1 are presented in Figure 12. The axial strain obtained from back-to-back strain gages located on the skin between stiffeners is shown in Figure 12b as a function of the applied load. The results presented in this figure indicate slight nonlinear strain behavior similar to the nonlinear load-shortening behavior shown in Figure 10. No strain gage reversal is observed. These results indicate that a slight amount of bending occurs in this region just prior to failure. The axial and the transverse strain in the webs are shown in Figure 12c as a function of the applied load. Axial strains in each specimen web are shown for location B1, and these strains are always compressive like the axial strains obtained in the webs of the stiffened element specimens. Transverse strains in each web are shown for location B2, and, similarly, these strains are always tensile like the transverse strains found in the webs of the stiffened element specimens. Results of Figures 12b and 12c indicate that the axial strain in the webs is similar to the axial strain in the skin (Figure 12b). The transverse strain results for the webs clearly show strain gage reversal which indicates that the webs buckle prior to failure. Axial strain results for the blade are presented in Figure 12d. These results also show strain gage reversal which indicates buckling of the blade.

Strain gage results for the impact damaged panel specimen NYP2 are presented in Figure 13. These results correspond to the second phase of the test in which the panel was loaded to failure. All results obtained in the first phase of the test are linear and have the same slope as the initial slope of the corresponding load versus strain curves obtained in the second phase of the test. The axial strain obtained in the second phase of the test, from back-to-back strain gages located on the skin between stiffeners, is shown in Figure 13b as a function of applied load. These strain results show only a slight indication of local bending in the skin. The axial and transverse strains in the webs are shown in Figure 13c as a function of the applied load. These compressive axial strain results indicate that buckling of both webs has occurred. The strain gage reversal observed for the tensile transverse strain results occur at a strain level of 0.0005 in./in. and indicates that these webs buckled prior to failure. Axial strain results for the blade of specimen NYP2 are presented in Figure 13d. The strain gage reversal observed for these axial strains indicates that the blade of the impact damaged specimen buckles at a much lower load level than the blade of the undamaged specimen. The significant difference in the strains of the back-to-back strain gages suggests that buckling of the blade may have caused a midplane interlaminar shear failure of the blade. All failure strains on Figure 13 for specimen NYP2 are less than the corresponding failure strains on Figure 12 for specimen NYP1. The average axial failure strain for the damaged specimen NYP2 is approximately 0.0057 in./in., indicating marginal residual strength of this panel subjected to a combined impact at the skin-flange region and at the blade-web interface.

Photographs of the failed panel specimens NYP1 and NYP2 are shown in Figures 14 and 15, respectively. Both specimens failed in the test section of the panel. The damage, as a result of failure, appears to be more severe in specimen NYP1 than in specimen NYP2. This difference is due to the much higher failure load of specimen NYP1. The strain results for these panel specimens indicate that buckling of both the web and blade occurs. These results, however, do not conclusively indicate which element buckles first. The results do reinforce the idea that web buckling and blade buckling are important design considerations for Y-stiffened panels.

CONCLUDING REMARKS

This paper describes an experimental investigation of the behavior of graphite-epoxy Y-stiffened specimens loaded in compression. Response and failure characteristics are presented for specimens with a single stiffener, referred to as Y-stiffened element specimens, and for specimens with three stiffeners, referred to as Y-stiffened panel specimens. Effects of impact damage on structural response for both specimen configurations are discussed.

The results presented in this paper indicate that impact location may significantly affect the residual strength of the Y-stiffened specimens. The element specimen impacted on the unstiffened side of the skin opposite the stiffener flanges had an average failure strain greater than 0.0075 in./in. indicating good residual strength. The element specimen impacted near the blade-web interface had an average failure strain of approximately 0.005 in./in. indicating marginal residual strength. The failure results for the damaged element specimens show that, for the same impact energy, an impact at the blade-web interface degrades the maximum load carrying capacity more than an impact at the skin-flange region. The dominant mechanism that initiates failure for all of the Y-stiffened element specimens is bending or buckling of the webs.

Results are also presented for a damaged panel specimen that was first impacted on the unstiffened side of the skin opposite the stiffener flanges of the center stiffener, and

loaded to a global strain level of 0.006 in./in. After unloading the specimen it was then impacted near the blade-web interface of the center stiffener which resulted in an average failure strain of 0.0057 in./in. indicating marginal residual strength. The dominant mechanism that initiated failure in both of the Y-stiffened panel specimens was a combination of web and blade buckling.

ACKNOWLEDGMENTS

The authors gratefully acknowledge the computer support given by Janice S. Myint for the reduction of the experimental data.

REFERENCES

1. Dow, N. F.; and Hickman, W. A.: Design Charts for Flat Compression Panels Having Longitudinal Extruded Y-Section Stiffeners and Comparison with Panels Having Formed Z-Section Stiffeners. NACA TN 1389, 1947.

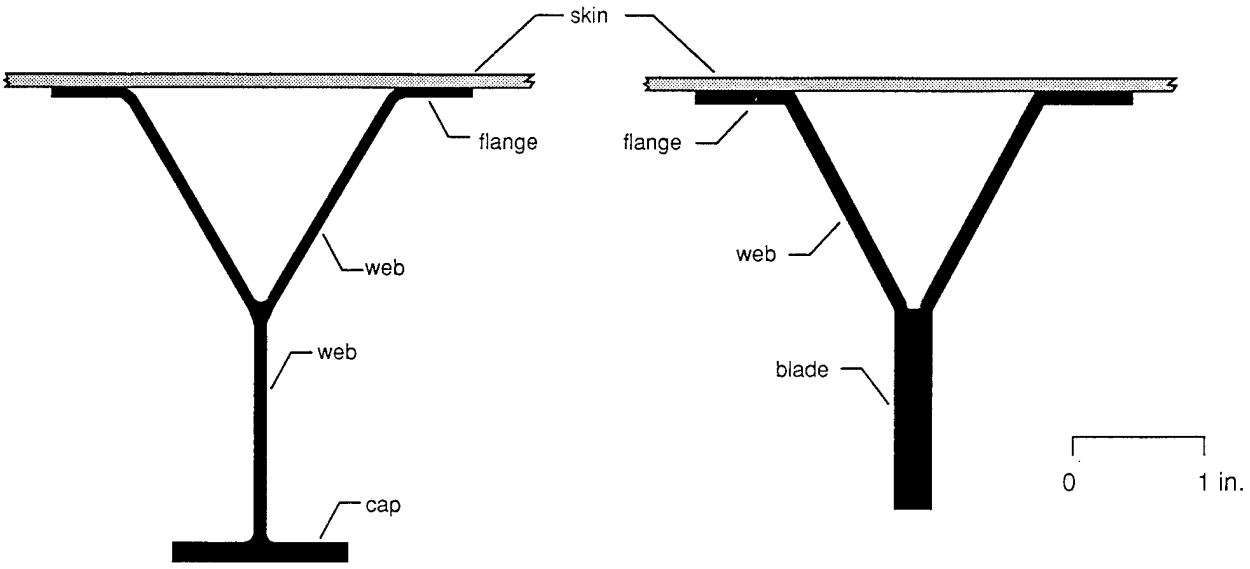
2. Dow, N. F.; and Hickman, W. A.: Comparison of the Structural Efficiency of Panels Having Straight-Web and Curved-Web Y-Section Stiffeners. NACA TN 1787, 1949.

3. Anderson, M. S. ; and Stroud, W. J.: General Panel Sizing Computer Code and Its Application to Composite Structural Panels. AIAA Journal, Vol. 17, Aug. 1979, pp. 892-897.

4. Starnes, J. H., Jr.; Rhodes, M. D.; and Williams, J. G.: Effect of Impact Damage and Holes on the Compressive Strength of a Graphite/Epoxy Laminate. Nondestructive Evaluation and Flaw Criticality for Composite Materials, STP 696, R. B. Pipes, ed., American Society for Testing and Materials, 1979, pp. 145-171.

Table 1. Properties for IM7/8551-7A used for structural optimization.

Longitudinal Young's modulus, E_{11}, Msi	20.9
Transverse Young's modulus, E_{22}, Msi	1.5
Shear modulus, G_{12}, Msi	0.72
Poisson's ratio, ν_{12}	0.33
Nominal ply thickness, in.	0.0055



a. Metal NACA Y-stiffener

b. Composite Y-stiffener

Figure 1. Y-Stiffener Configurations.

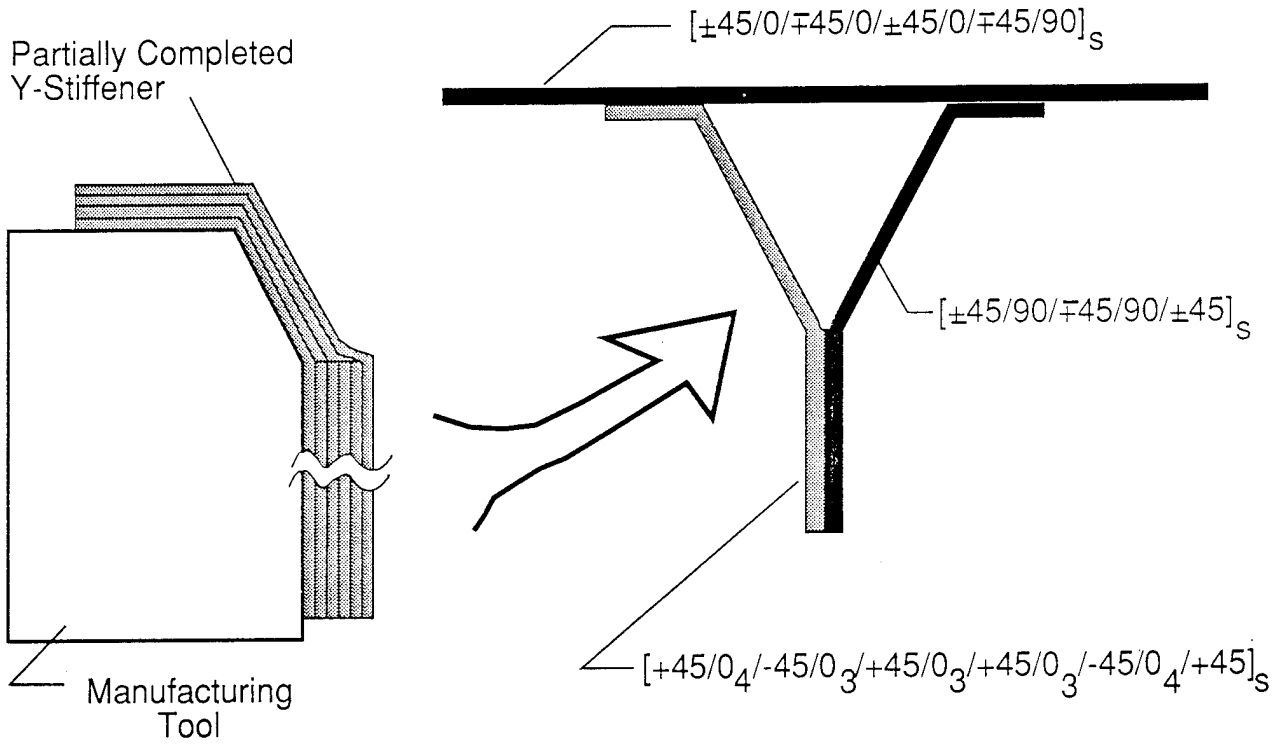


Figure 2. Fabrication of Composite Y-Stiffened Element.

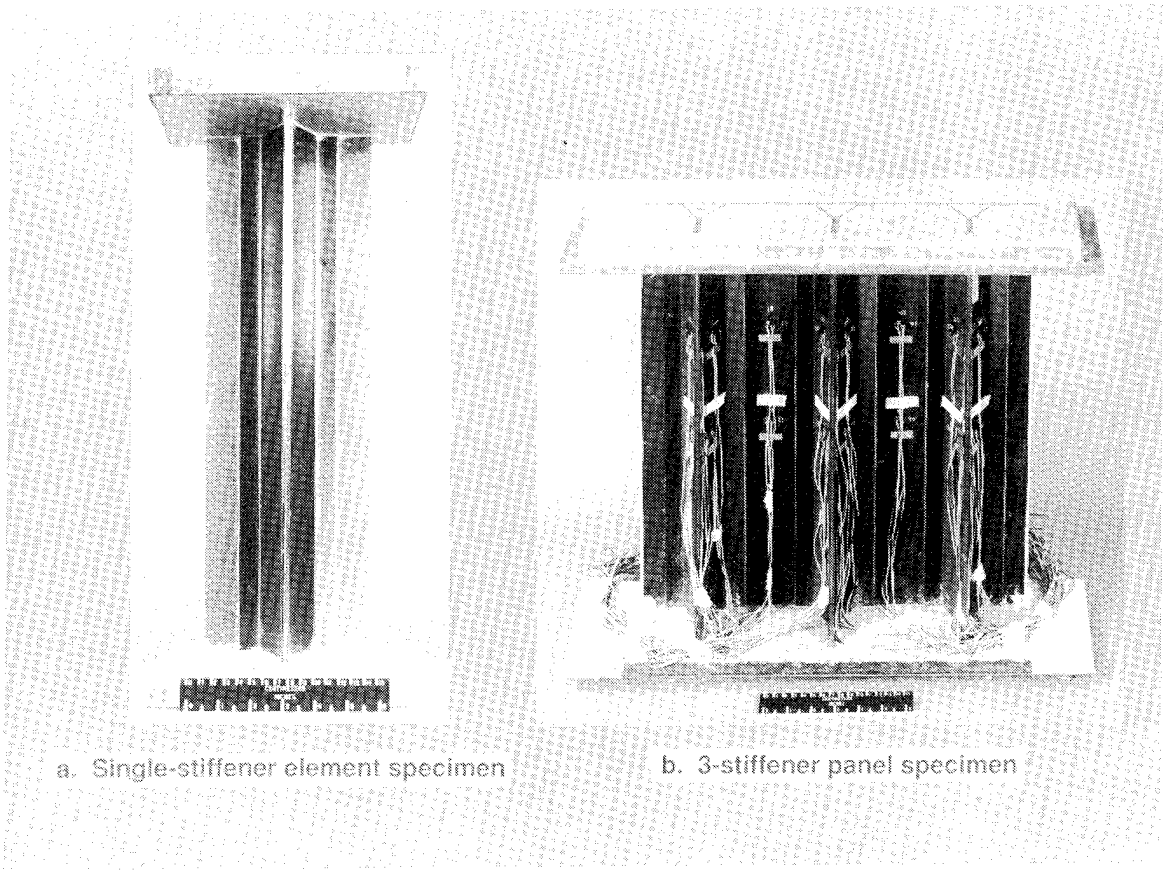


Figure 3. Y-stiffened specimens.

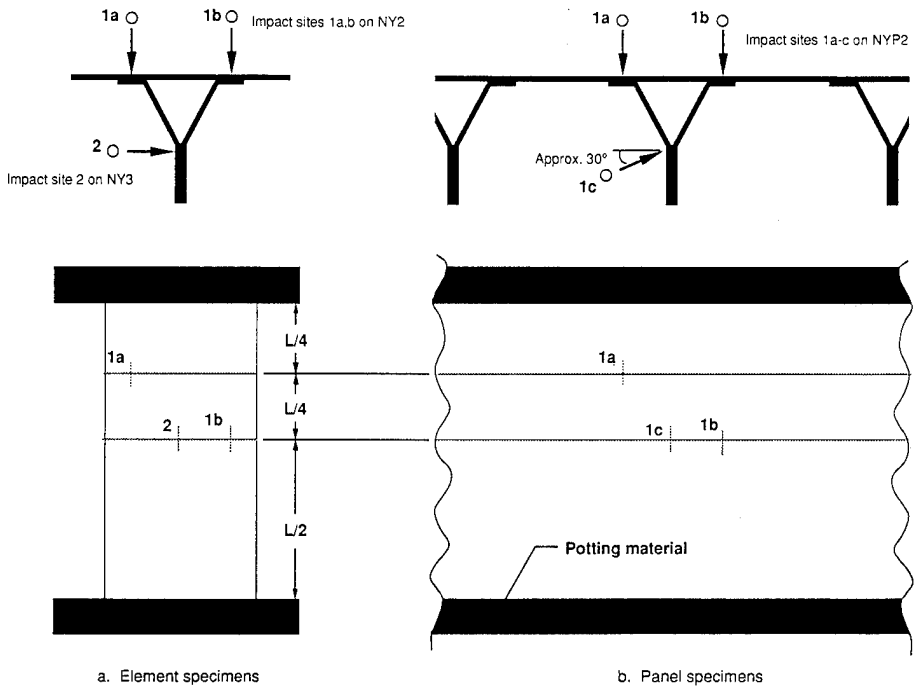


Figure 4. Impact sites for Y-stiffened specimens.

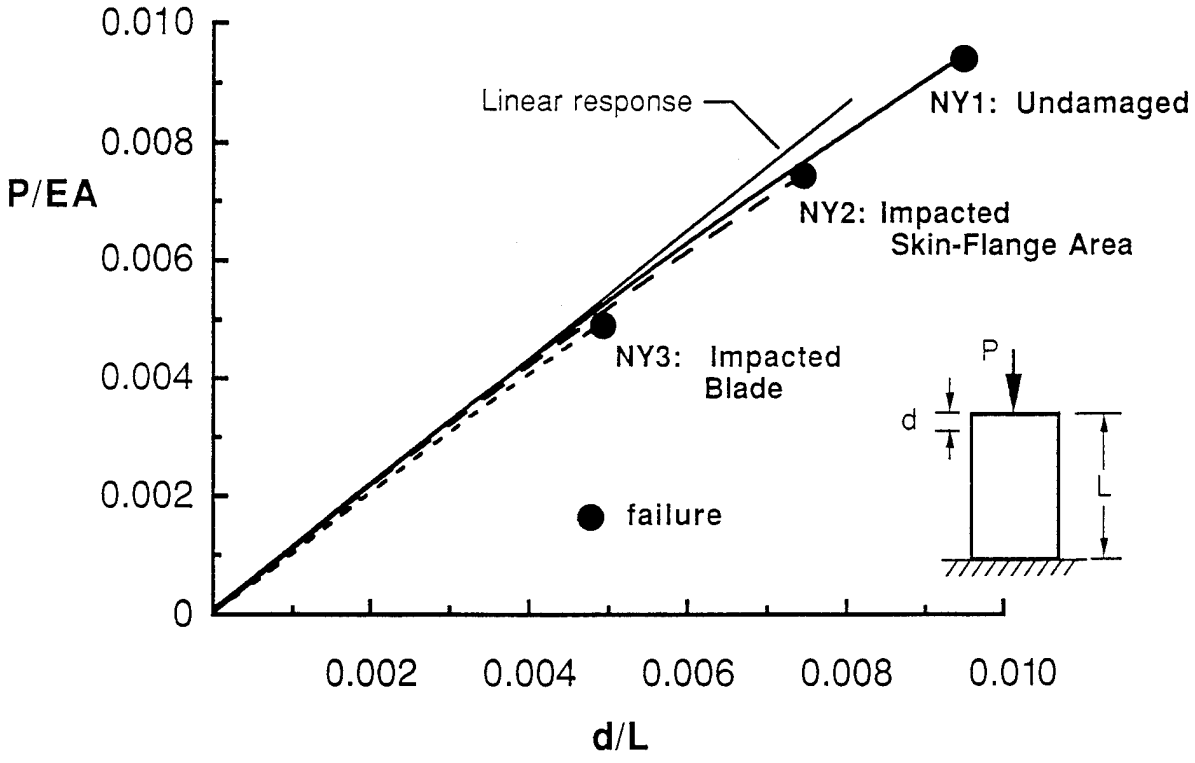


Figure 5. Normalized load versus end-shortening for Y-stiffened element specimens.

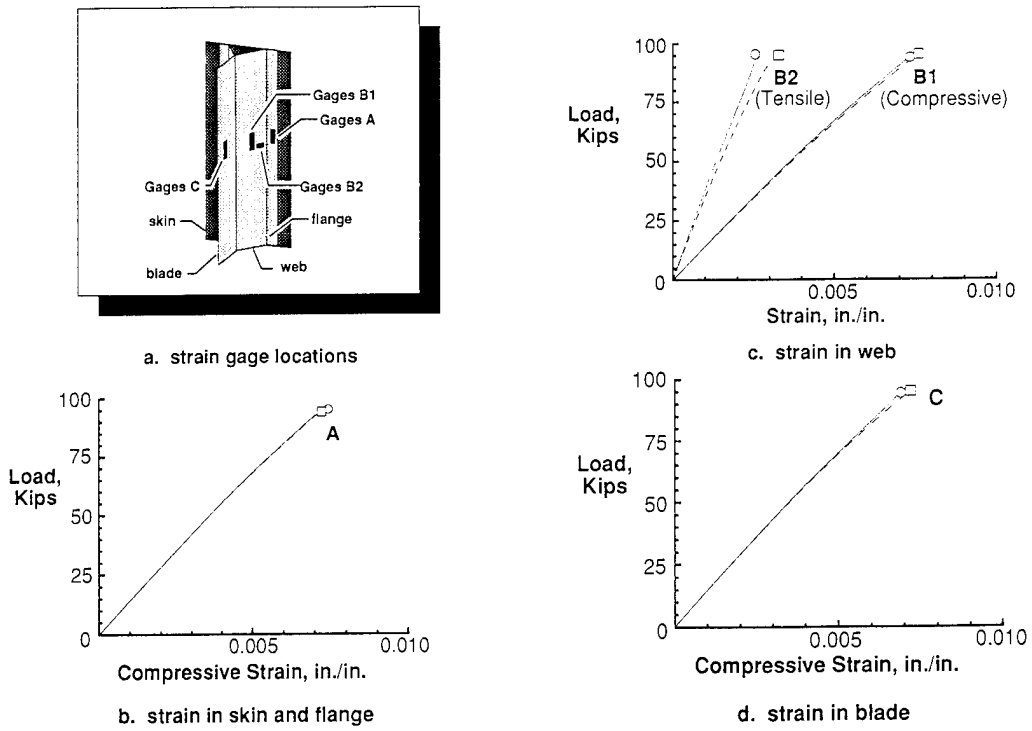


Figure 6. Strain gage results for undamaged element specimen NY1 (square and circular symbols used to distinguish between individual gages).

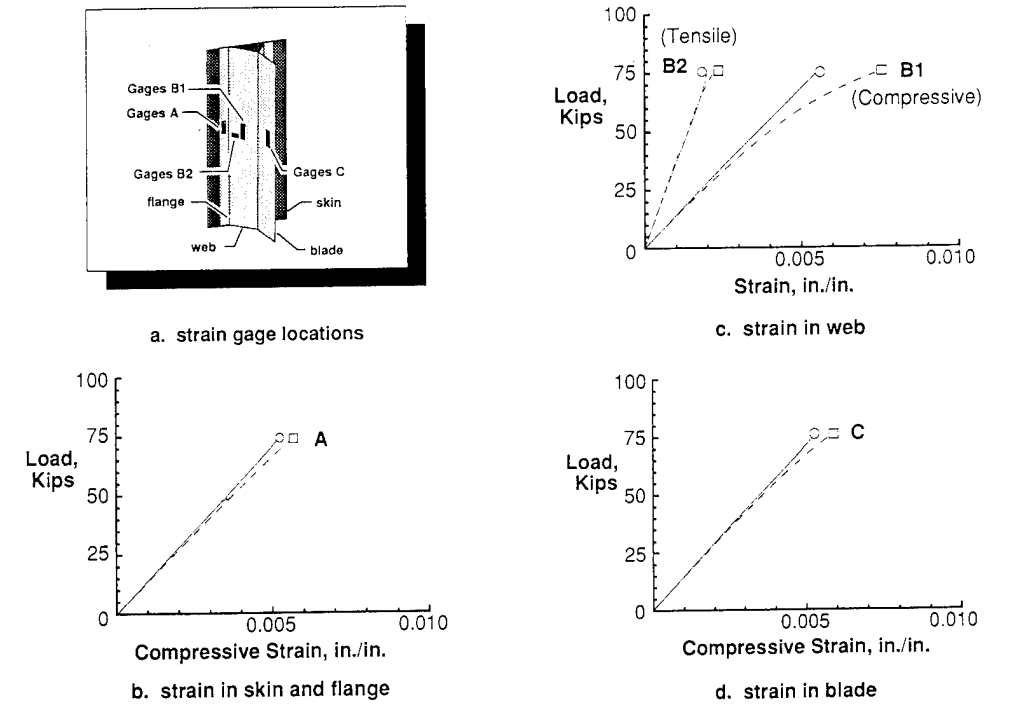


Figure 7. Strain gage results for impact damaged element specimen NY2 (square and circular symbols used to distinguish between individual gages).

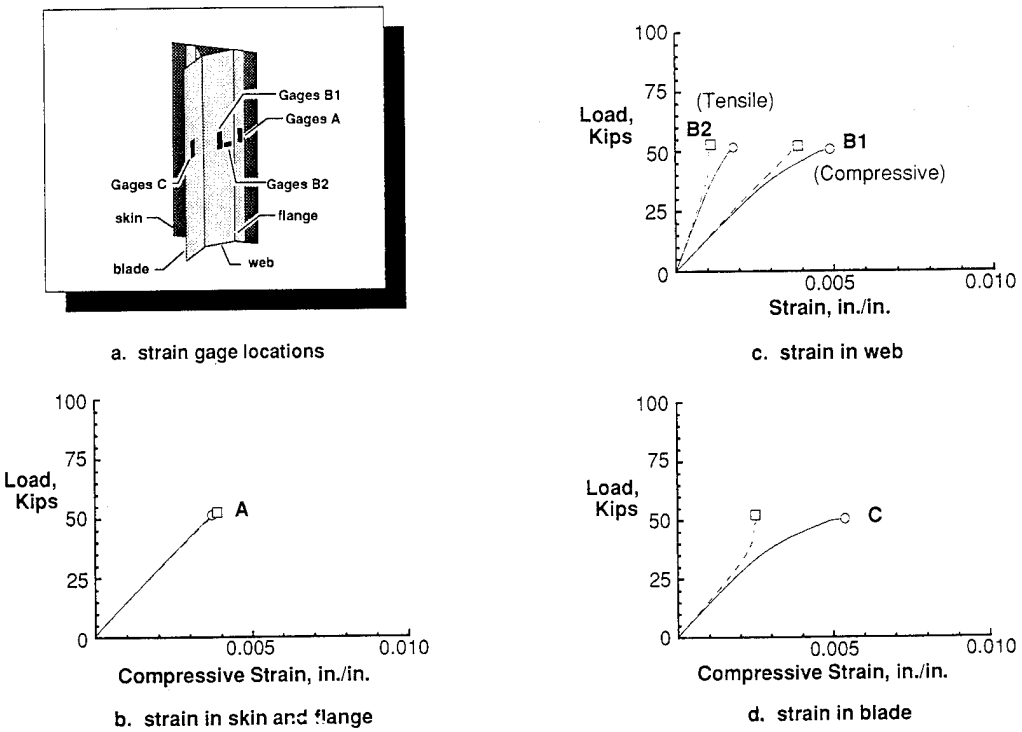


Figure 8. Strain gage results for impact damaged element specimen NY3 (square and circular symbols used to distinguish between individual gages).

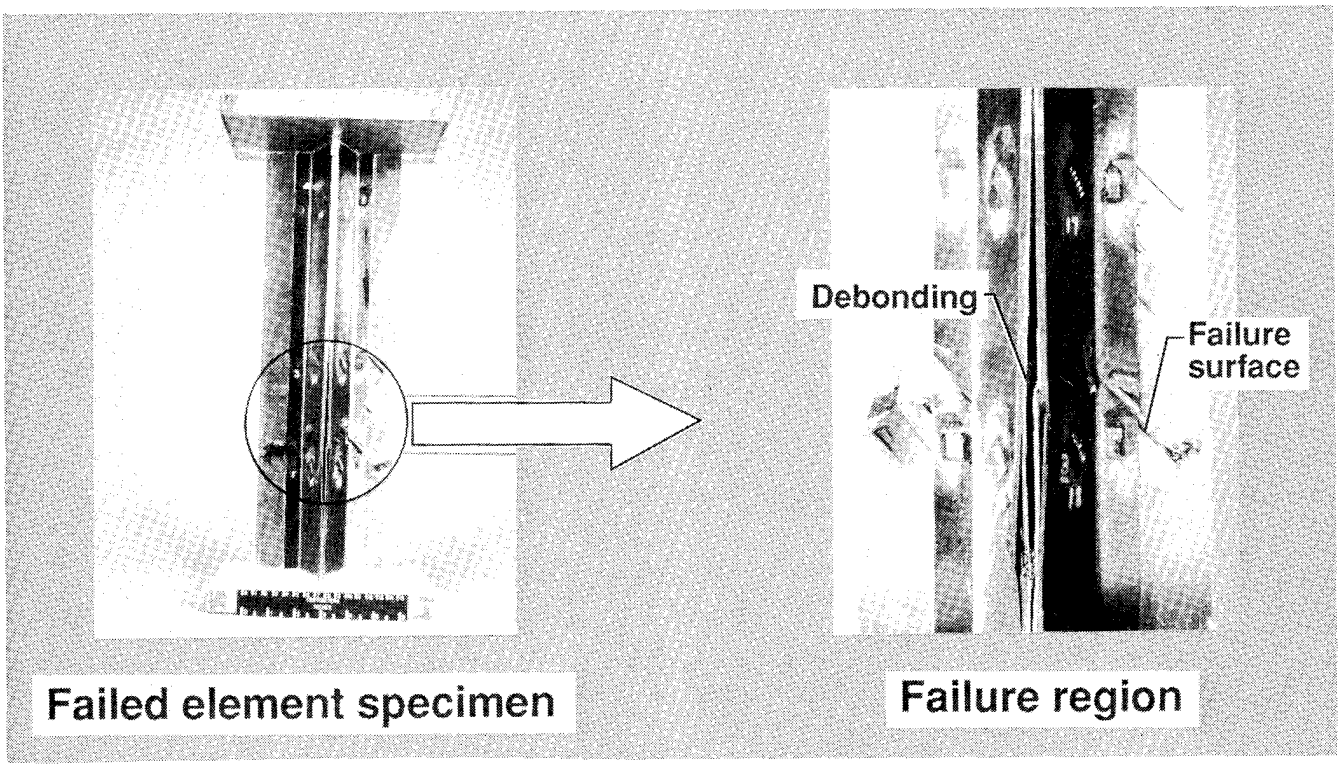


Figure 9. Typical failure of Y-stiffened element specimen.

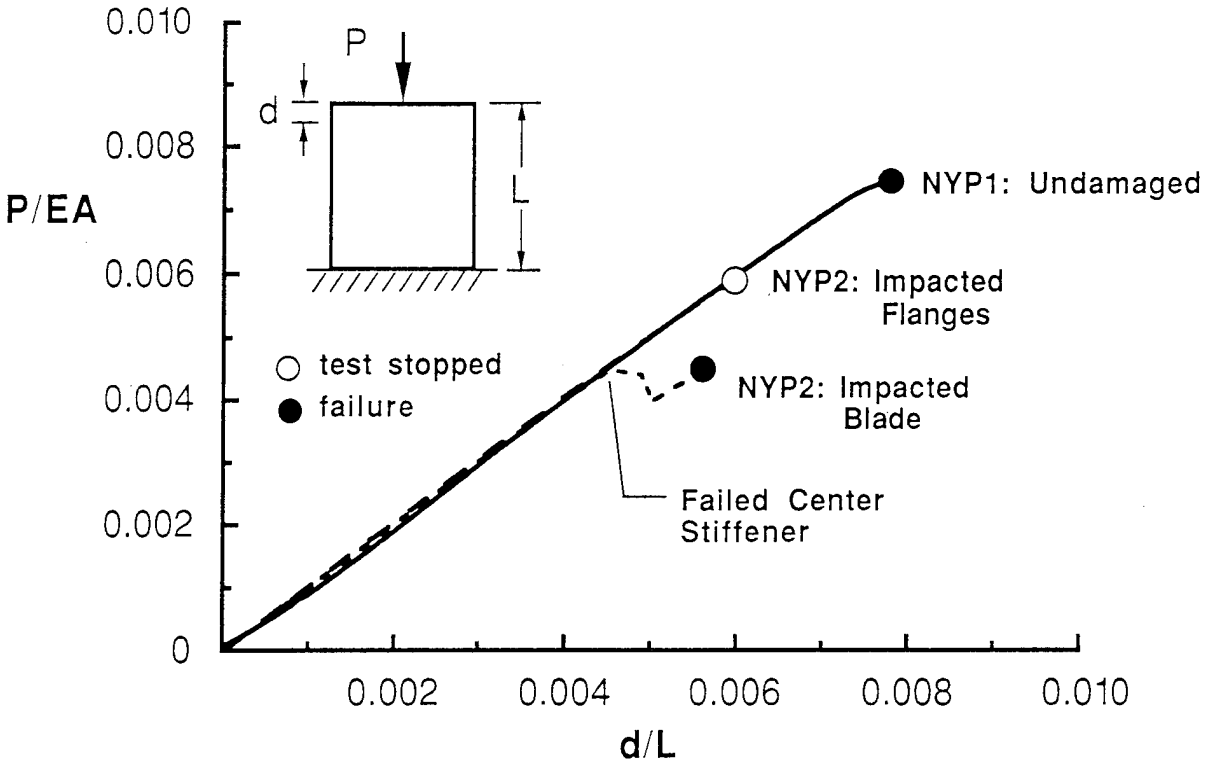


Figure 10. Normalized load versus end-shortening for Y-stiffened panel specimens.

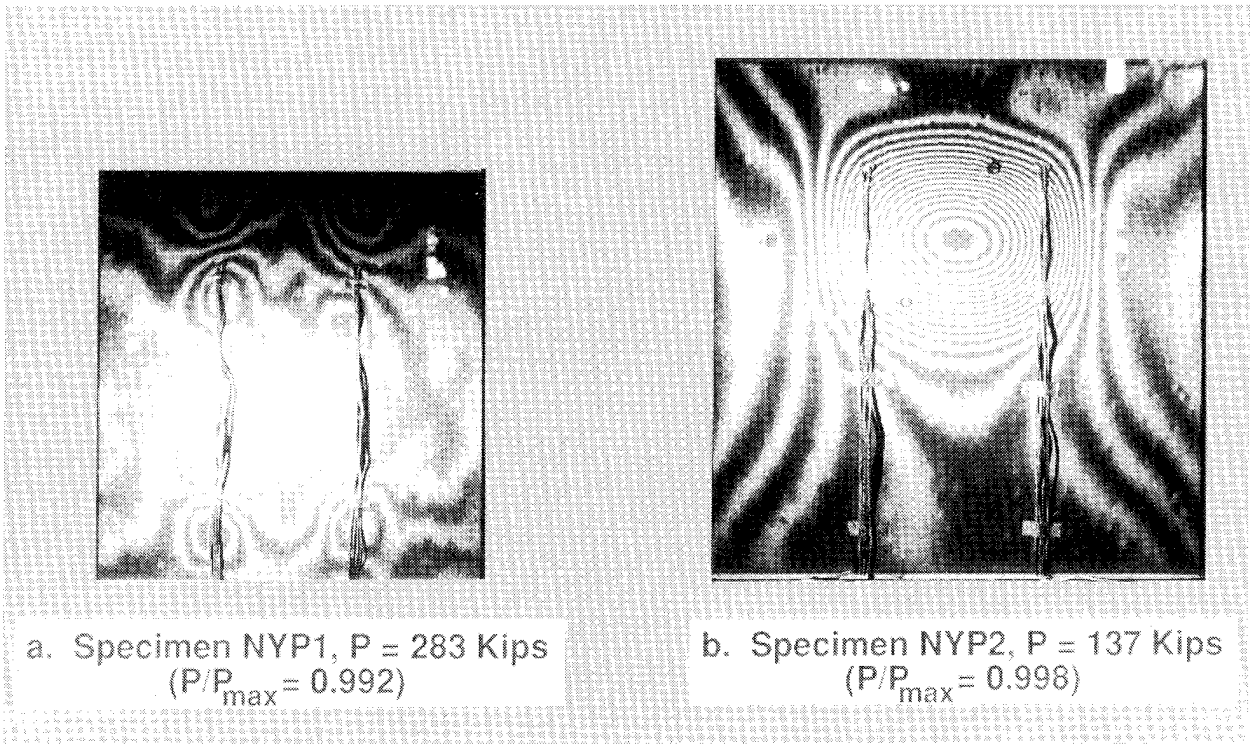


Figure 11. Photographs of moire fringe patterns for Y-stiffened panel specimens.

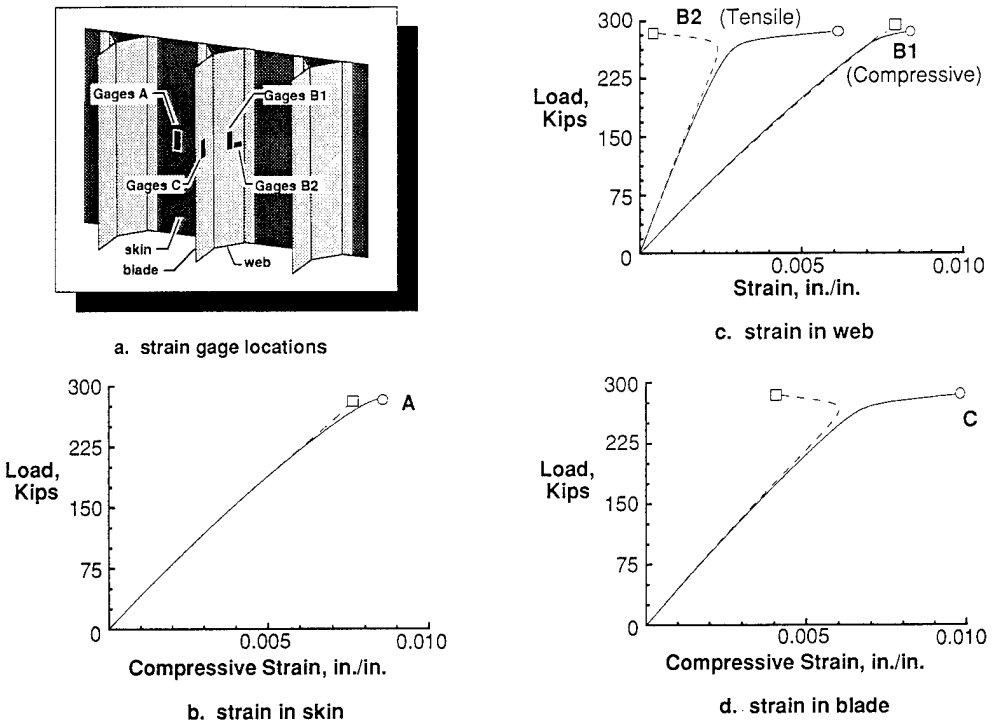


Figure 12. Strain gage results for undamaged panel specimen NYP1 (square and circular symbols used to distinguish between individual gages).

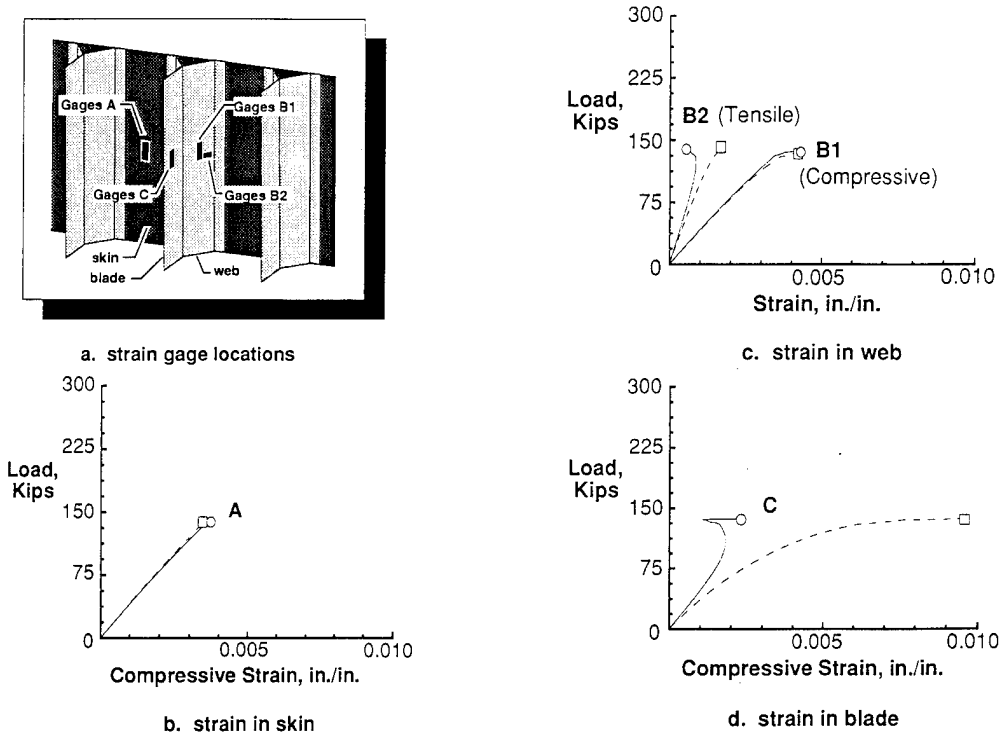


Figure 13. Strain gage results for impact damaged panel specimen NYP2 (square and circular symbols used to distinguish between individual gages).

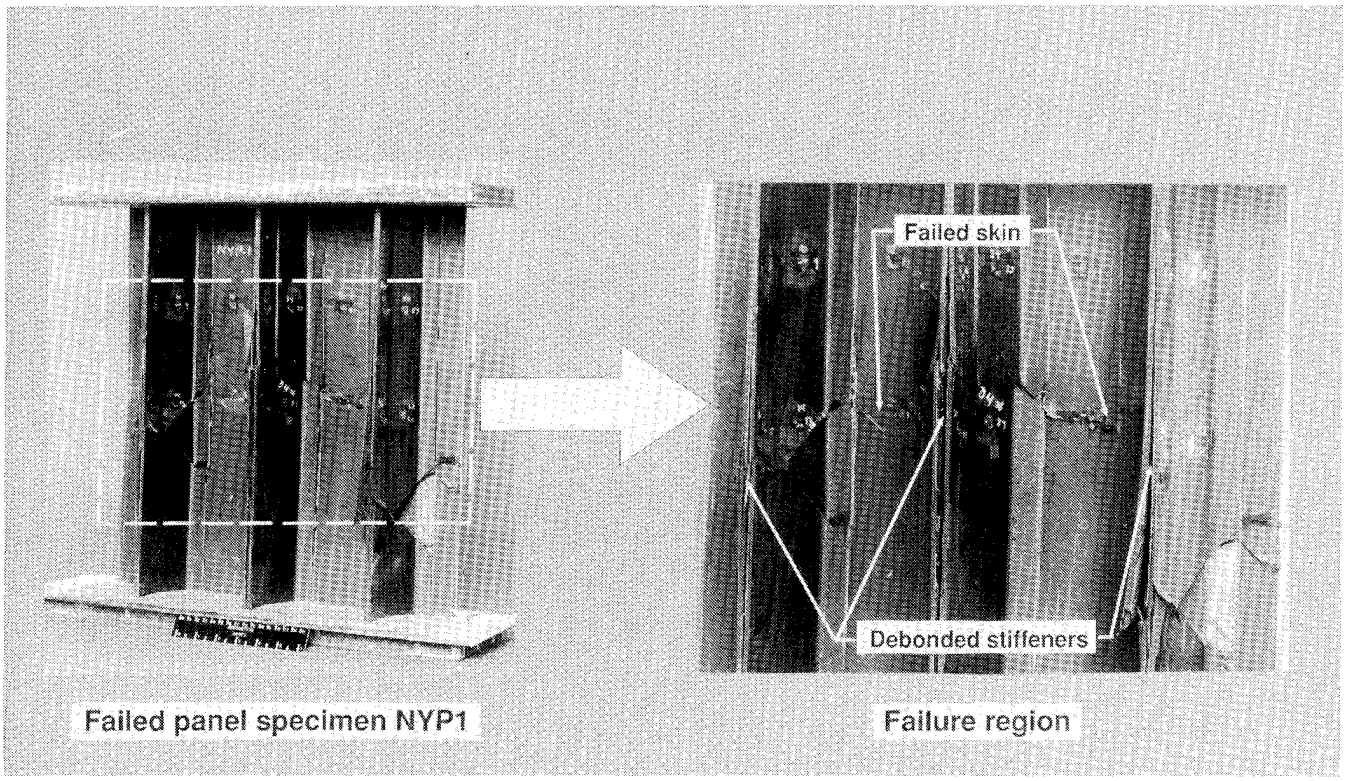


Figure 14. Failure mode of Y-stiffened panel specimen NYP1.

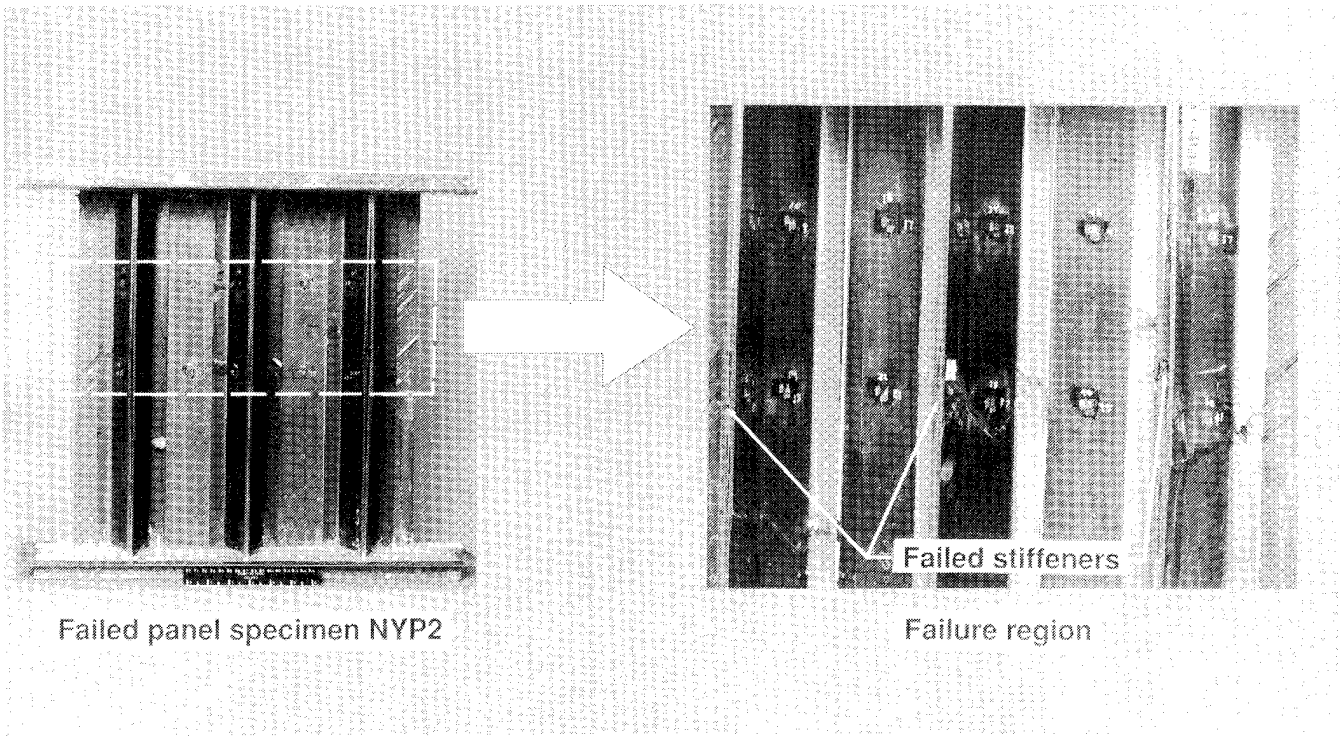


Figure 15. Failure mode of Y-stiffened panel specimen NYP2.

STRUCTURAL RESPONSE OF BEAD-STIFFENED THERMOPLASTIC SHEAR WEBS

Marshall Rouse
NASA Langley Research Center
Hampton, VA

INTRODUCTION

Advanced composite materials offer an attractive potential for reducing the mass of modern aircraft structural components. To achieve this potential, the ability to provide reliable structural designs that can safely carry the desired loads must be developed. Current design practices allow some metallic structural components (e.g., fuselage and stabilizer panels) to buckle under various loading conditions and, as a result, are said to have postbuckling strength. The corresponding structural response characteristics of graphite-thermoplastic composites must be evaluated before such composites can be considered for application to civil transport aircraft structures. One aspect of the design of aircraft structural components is the structural behavior of panels loaded in shear. Experimental results have been presented that describe buckling and postbuckling behavior of graphite-epoxy and graphite-thermoplastic specimens under various loading conditions (References 1 and 2). An advanced concept for stiffened graphite-thermoplastic panels is a thermoformed bead-stiffener. The thermoforming process is a potentially cost-effective manufacturing technique for these bead stiffeners. The postbuckling response of bead-stiffened graphite-thermoplastic shear webs has not been fully described. The influences of local effects, such as bead-stiffener geometry and orientation, on the postbuckling response of graphite-thermoplastic shear webs has also not been adequately described.

The present paper describes the results of an experimental and analytical study of the structural response and failure characteristics of selected bead-stiffened thermoplastic shear webs. Experimental results are presented for specimens with one stiffener, two stiffeners, and different stiffener geometries. Selected analytical results that were obtained with the Computational Structural Mechanics (CSM) Testbed (Ref. 3) computer code are presented. Analytical results that describe normal and transverse shear stress resultants are also presented.

TEST SPECIMEN DESCRIPTION

The graphite-thermoplastic specimens tested in this investigation were fabricated from commercially available unidirectional tapes of Hercules Incorporated AS4 graphite fiber and ICI ACP PEEK resin. All of the specimens tested in this investigation were made from 16-ply laminates with a $[\pm 45_2/0/\pm 45/90]_S$ stacking sequence. The specimens had a 12-inch by 12-inch test section and the edges were reinforced with fiberglass reinforcements bonded to the specimens with a room-temperature-cure adhesive. A total of three specimens were tested in this investigation. All of the specimens were tested had bead stiffeners oriented parallel to one side of the specimen. The bead stiffeners had an 11-inch length, 0.5-inch height, and a stiffener width b_s of either 2 or 3 inches. One specimen was tested with one 3-inch-wide bead stiffener located at the center of the test section. Two specimens were tested with two bead stiffeners located 3.5 inches from the edges of the test section. One of the two-stiffener specimens had 2-inch-wide bead stiffeners and the other specimen had 3-inch-wide bead stiffeners. Photographs of specimens with one and two bead stiffeners are shown in Figure 1.

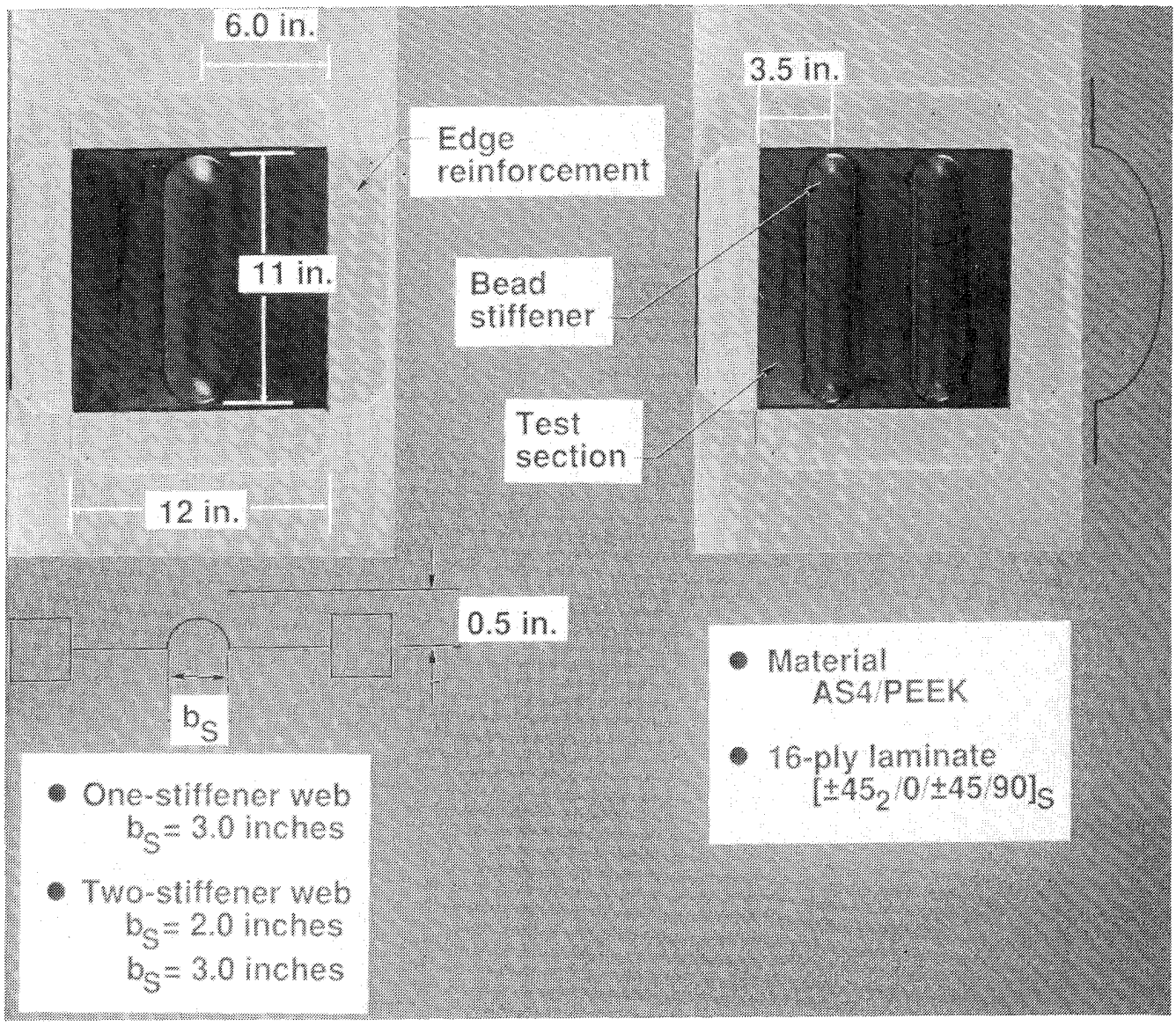


Figure 1

SUMMARY OF TEST RESULTS FOR BEAD-STIFFENED WEBS

A summary of results for all of the bead-stiffened shear webs that were tested is shown in Figure 2. All of the specimens were tested using a picture-frame fixture which is composed of two back-to-back steel rails bolted to the edge reinforcements on each specimen edge. The rails are connected with high strength pins, and the pins are positioned with their center lines coincident with the corners of the test section of the specimen. A uniaxial loading condition was used to test each specimen. The uniaxial loading condition consisted of applying a tension load P along one diagonal of the specimen. The sketch on the left of Figure 2 illustrates the applied load P. The applied shear flow q was calculated from the applied load by imposing equilibrium conditions on the test section of the specimen and by assuming that the picture-frame fixture and edge reinforcements are rigid and pinned at the corners.

Applied shear flow q as a function of extension along the diagonal δ in the direction of the applied load is shown on the right of the figure. The theoretical shear flow at buckling for the specimen with one bead stiffener (one-stiffener web) is indicated in the figure by the open circle. Only the specimen with one centrally located stiffener failed at an applied load greater than the theoretical buckling load. Failure of the specimen with one bead stiffener is indicated by the filled circle. Failure of the specimens with two bead stiffeners (two-stiffener web) is indicated by the filled squares. The specimen with one 3-inch-wide bead buckled at an applied shear flow of approximately 1,000 lb/in. and failed at an applied shear flow of approximately 1,500 lb/in. The specimens that were tested with two bead stiffeners failed prior to buckling. The two-stiffener specimens with 2-inch-wide bead stiffeners and 3-inch-wide stiffeners failed at a value of applied shear flow of approximately 1,400 lb/in. and 1,900 lb/in., respectively.

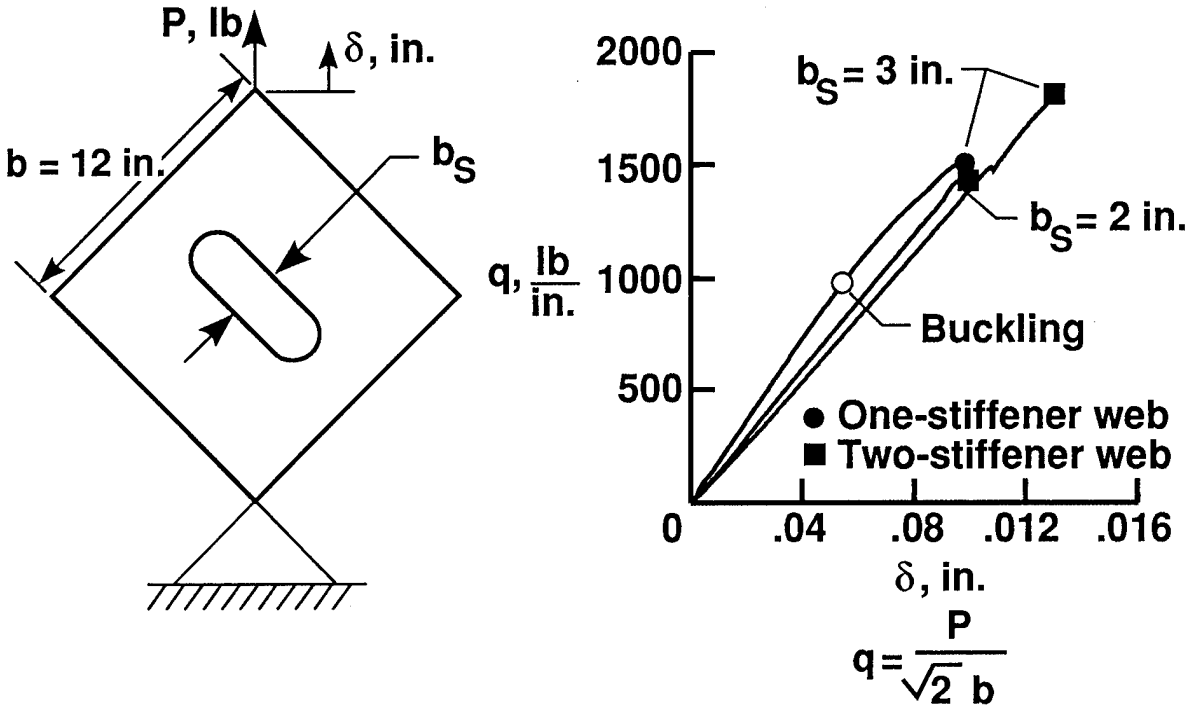


Figure 2

OUT-OF-PLANE DEFLECTION OF BEAD-STIFFENED WEBS

Out-of-plane deflection w was measured at the center of a bead normalized by the laminate thickness t is shown in Figure 3 as a function of applied shear flow q for all of the specimens that were tested. Failure of the one-stiffener specimen is indicated by the filled circle. Failure of the two-stiffener specimens is indicated by the filled squares. All of the specimens deformed out-of-plane when loaded. Photographs of typical moire-fringe patterns for a one-stiffener and a two-stiffener specimen are shown on the right of the figure. The one-stiffener specimen with a 3-inch-wide bead stiffener exhibited the most out-of-plane deflection during loading with a maximum value of almost 10 times the laminate thickness. The two-stiffener specimens with 2- and 3-inch-wide bead stiffeners had a maximum out-of-plane deflection of approximately two and one times the laminates thickness, respectively. The change in slope of the curves shown in Figure 3 suggests that the bead-stiffened webs have a nonlinear response when loaded to failure.

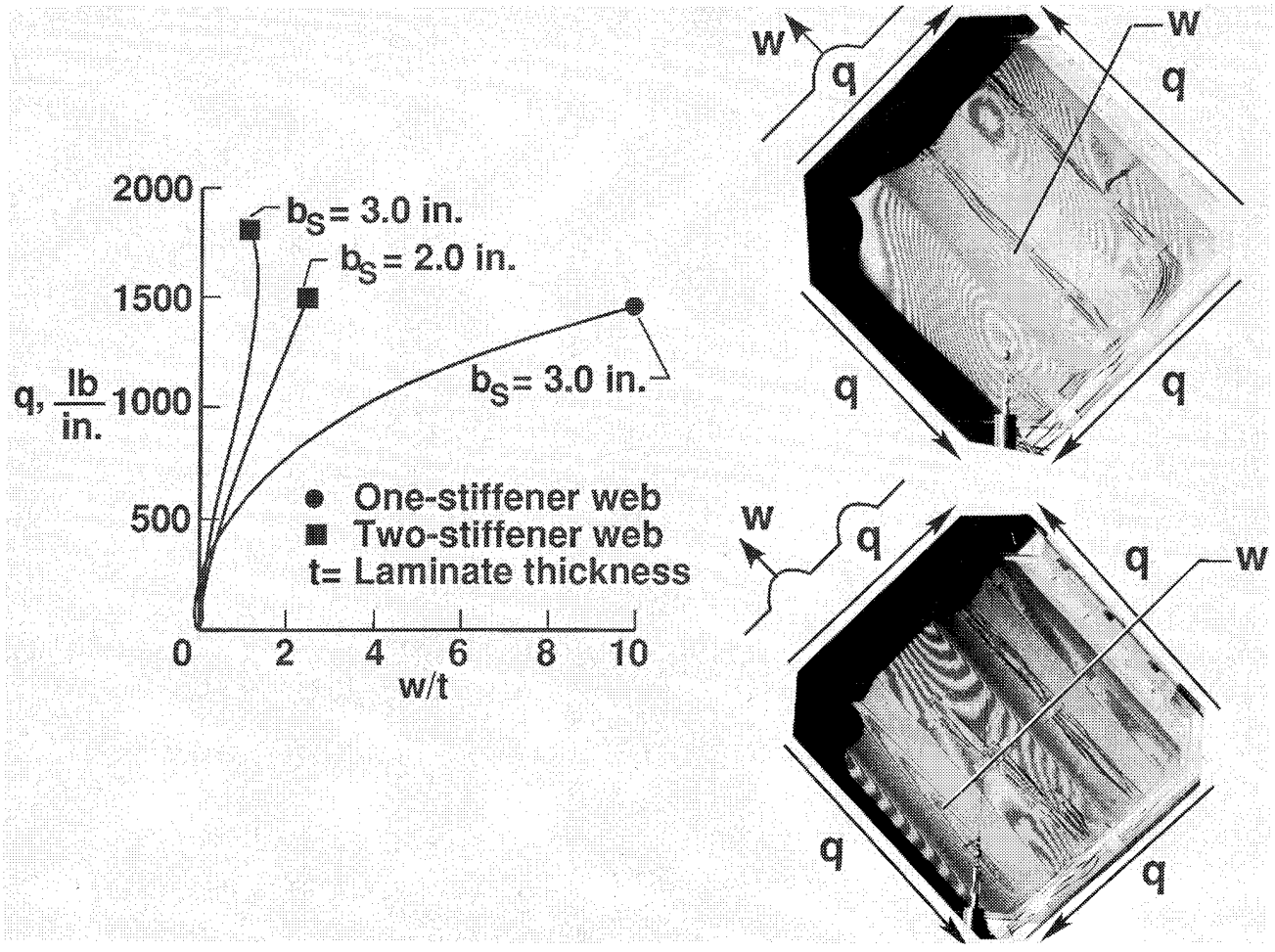


Figure 3

BACK-TO-BACK SURFACE STRAIN RESULTS FOR WEBS WITH 3-INCH-WIDE STIFFENERS

A comparison of surface strain results for one- and two-stiffener specimens with 3-inch-wide stiffeners is presented in Figure 4 as a function of applied shear flow q. The surface strains ϵ were recorded from back-to-back strain gage rosettes located at the center of a bead stiffener. Results for the one-stiffener specimen are indicated by the filled circles. Results for the two-stiffener specimens are indicated by the filled square. Surface strain measurements ϵ_t from strain gages oriented parallel to the direction of applied load are shown in the upper left of the figure. The one-stiffener specimen had a maximum tensile strain approximately of 0.006 in./in. at failure. The two-stiffener specimen had a maximum tensile strain value of approximately 0.004 in./in. at failure. Surface strain measurements ϵ_c from strain gages oriented normal to the direction of applied load are shown in the upper right of the figure. The one- and two-stiffener specimens had a maximum compressive strain of approximately -0.001 in./in. and -0.004 in./in., respectively. The change in slope of the curve for the one-stiffener specimen suggests a nonlinear load-strain response. The divergence of the back-to-back strain gage results also suggests that bending strains occur at the center of the bead stiffener in the direction of applied load and increase as the specimen is loaded to failure. Surface strain measurements ϵ_x from back-to-back strain gages oriented parallel to the longitudinal direction of the stiffener are shown in the lower left of the figure. The one-stiffener specimen had a maximum strain value in the x-direction of approximately 0.004 in./in. at failure. The two-stiffener specimen had a maximum strain value of approximately 0.001 in./in. at failure. Also, the change in slope of the curves suggests that the load in the stiffeners was redistributed as the specimen was loaded to failure.

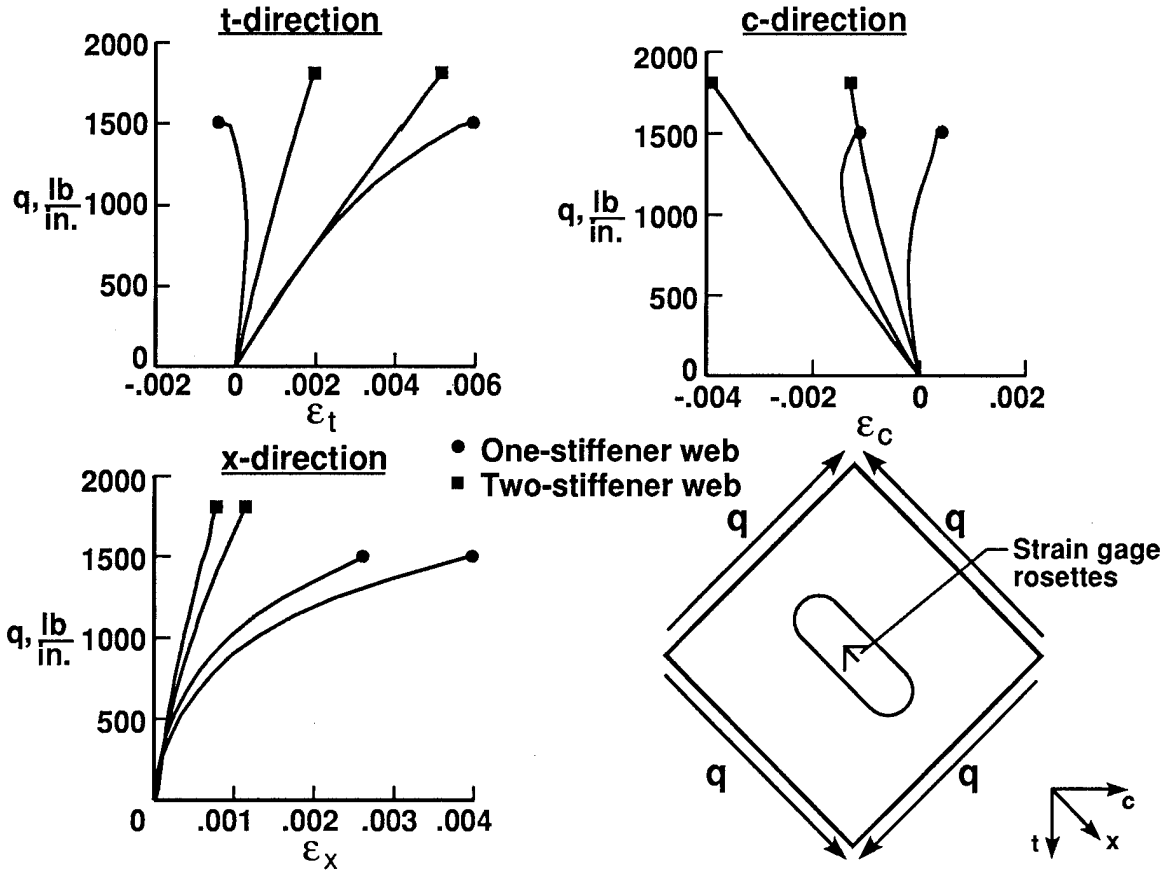


Figure 4

BACK-TO-BACK SURFACE STRAIN RESULTS FOR WEBS WITH TWO STIFFENERS

A comparison of surface strain results for two-stiffener specimens with 2- and 3-inch-wide (b_s) stiffeners are presented in Figure 5 as a function of applied shear flow q. The surface strains ϵ were recorded from back-to-back strain gage rosettes located at the center of a bead stiffener. Results for a two-stiffener specimen with 2.0-inch-wide stiffeners are indicated by the filled circle. Results for the two-stiffener specimens with 3-inch-wide stiffeners are indicated by the filled square. Surface strain measurements ϵ_t from strain gages oriented parallel to the direction of applied load are shown in the upper left of the figure. Back-to-back surface strain results in the t-direction indicate that two-stiffeners specimens with 2- and 3-inch-wide stiffeners had the same load-strain response up to failure. However, the two-stiffener specimen with 3-inch-wide stiffeners failed at higher values of applied shear flow and tension strain. Surface strain measurements ϵ_c from strain gages oriented normal to the direction of applied load are shown in the upper right of Figure 5. Back-to-back surface strain results in the c-direction indicate that the two-stiffener specimen with 2-inch-wide stiffeners had higher values of compressive strain at corresponding values of applied shear flow than the two-stiffener specimen with 3-inch-wide stiffeners. Surface strain results ϵ_x from back-to-back strain gages oriented parallel to the longitudinal direction of the stiffener are shown in the lower left of the figure. Back-to-back surface strain results in the x-direction indicate that the two-stiffener specimen with 3-inch-wide stiffeners had higher bending strains than the specimen with 2-inch-wide stiffener. The change in slope of the curves for back-to-back surface strain in the x-direction suggests that a redistribution of load occurred in the bead stiffener as the specimens were loaded to failure. Also, the difference in back-to-back surface strain results shown in the figure indicates that significant bending strains occurred as the specimens were loaded to failure.

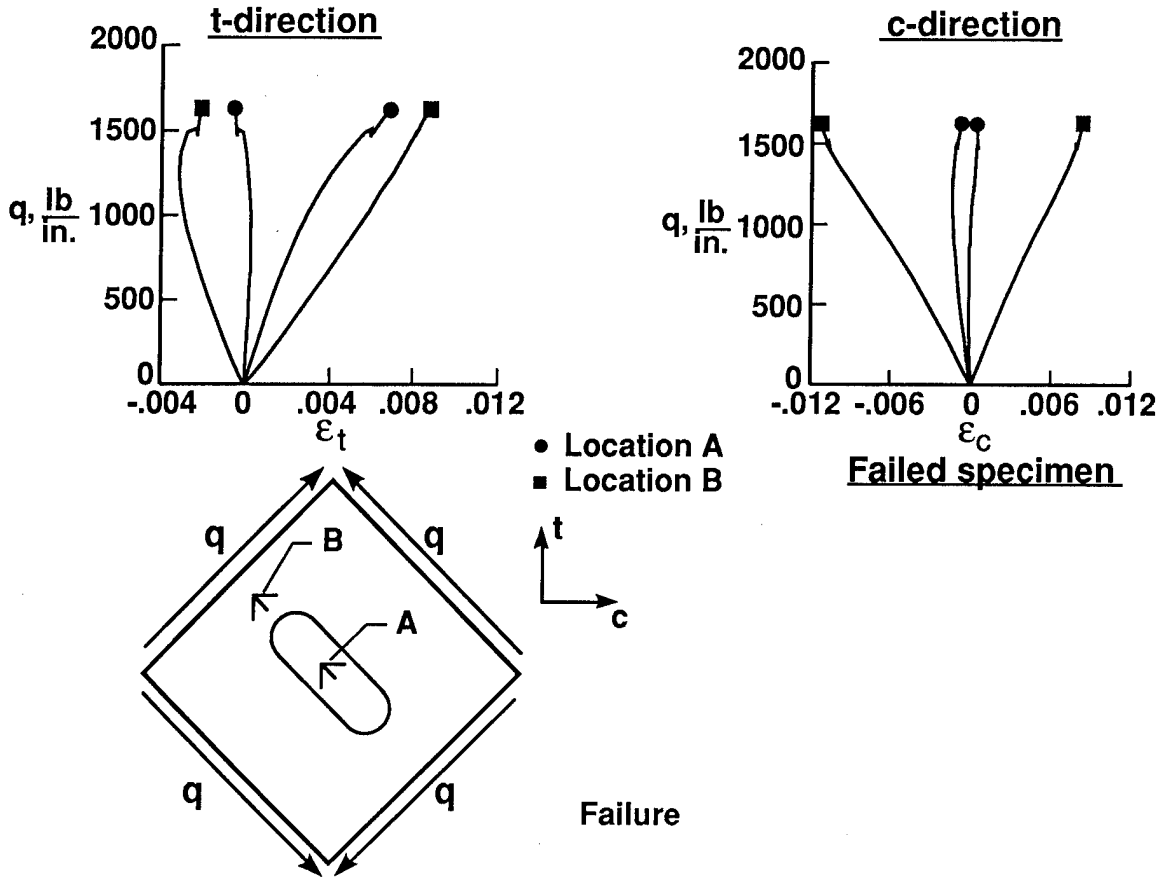


Figure 5

TYPICAL FAILURE CHARACTERISTICS OF BEAD-STIFFENED WEBS

Typical failure characteristics of the bead-stiffened shear webs that were tested are shown in Figure 6. The surface strain results for a one-stiffener specimen are presented in Figure 6 as a function of applied shear flow. The surface strain results were recorded from back-to-back strain gage rosettes at two locations. Surface strain results from strain gage rosettes at Location A, which is near the center of the stiffener, are indicated by the filled circles. Surface strain results from strain gage rosettes at Location B, which is near the end of the stiffener, are indicated by the filled squares. Surface strain measurements ϵ_t from strain gages oriented parallel to the t-direction ϵ_t are shown in the upper left of the figure. Surface strain measurements ϵ_c from strain gages in the c-direction are show in the upper right of the figure. The surface strain results indicate that much higher tensile and compressive strains occur near the end of the bead stiffener. Also, divergence of the back-to-back strain gage results indicate that higher bending strains occur near the ends of the stiffener than at the center as the specimen was loaded to failure. The bending strains near the end of a stiffener is caused by the eccentricity of the stiffener with respect to the midplane of the test section. A photograph of the failed specimen with one stiffener is shown in the lower right of Figure 6. The failure of the specimen initiated at the end of bead stiffener. The failure was probably caused by the high strains that occur near the end of the stiffener.

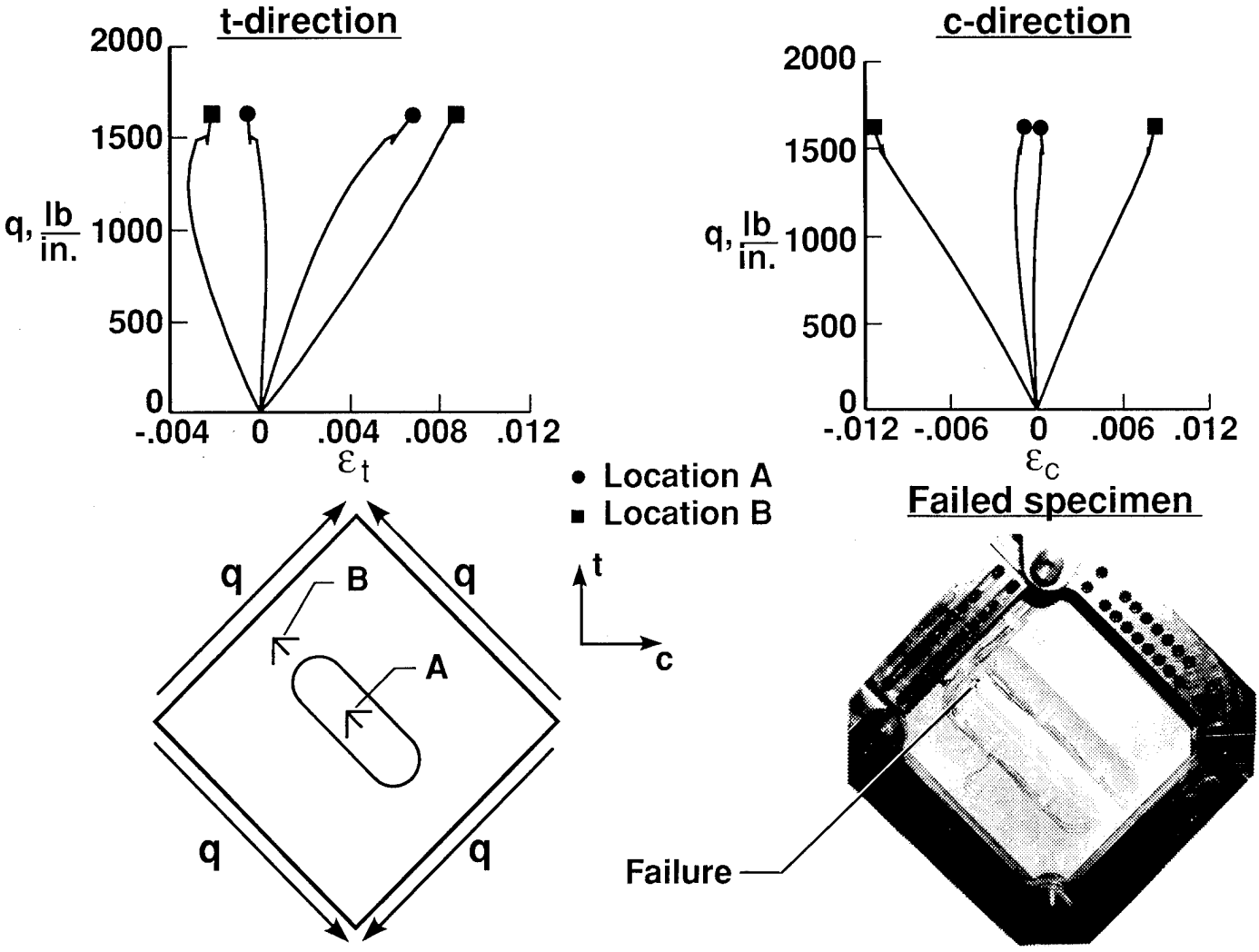


Figure 6

STRESS RESULTANTS DISTRIBUTION IN A BEAD-STIFFENED WEB

Stress resultant contours for a one-stiffener specimen calculated from a geometrically nonlinear finite element analysis at an applied shear flow value of 1553 lb/in. which included transverse shear deformation effects are presented in Figure 7. Contour plots of the inplane normal stress resultants N_x in a direction parallel to the longitudinal direction of the stiffener are shown in the upper left of the figure. The inplane normal stress resultant contour results show that regions of high normal stress resultants exist near the ends of the bead stiffener where failure initiated during the tests. Contour plots of the inplane shear stress resultants N_{xy} are shown in the upper right of the figure. The shear stress resultant contour results show that regions of high shear stress resultants exist near the ends of the bead stiffener and away from the stiffener in the test section area. Contour plots of the transverse shear stress resultants Q_x and Q_y are shown in the lower left and right of the figure, respectively. The transverse shear stress resultant Q_x contours show regions of high transverse shear stress resultants occur near the ends of the bead stiffener. The transverse shear stress resultant Q_y contours show regions of high transverse shear stress resultants occur near to and along the edges where the bead stiffener intersects with the skin. The stress resultant contour results suggest that the stiffener eccentricity causes significant local transverse shear stress resultants in a bead-stiffened shear web.

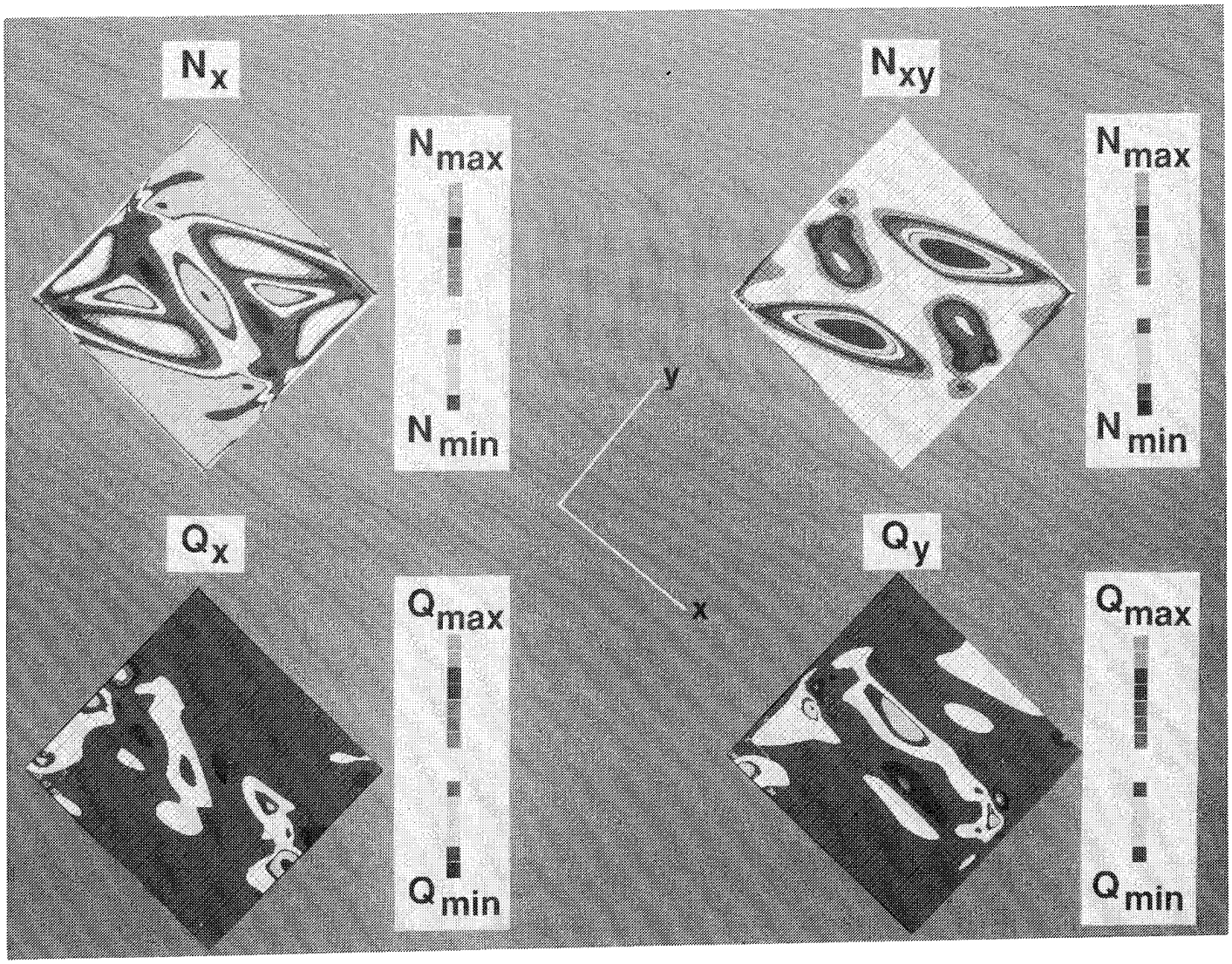


Figure 7

CONCLUDING REMARKS

An experimental and analytical investigation has been conducted to study the structural response and failure characteristics of bead-stiffened graphite-thermoplastic shear webs. Results are presented for specimens with one and two stiffeners. Results are presented for specimens with different bead stiffener widths. Results from a nonlinear finite element analysis are also presented that describe inplane and transverse stress resultant distribution of a bead-stiffened composite plate loaded in shear. Experimental results suggest that bead-stiffened shear webs have a nonlinear response when loaded to failure. Surface strain results suggest that bending strains occur near the bead stiffener when loaded to failure. Analytical results suggest that stiffener eccentricity causes significant local transverse shear stress resultants to occur in bead-stiffened webs. The bead-stiffened webs failed near the end of the stiffener where analysis indicates that significant inplane stress resultants exist.

REFERENCES

1. Jegley, Dawn C.: Compression Behavior of Graphite-Thermoplastic Panels with Circular Holes or Impact Damage. 8th DOD/NASA/FAA Conference on Fibrous Composites in Structural Design, November 28-30, 1989. NASA CP-3087, September 1990.

2. Rouse, Marshall: Effect of Cutouts or Low-speed Impact Damage on the Postbuckling Behavior of Composite Plates Loaded in Shear. AIAA Paper NO. 90-0966; Proceedings of AIAA/ASME/ASCE/ASH/ASC 31st Structures, Structural Dynamics and Materials Conference, Long Beach, CA, April 1990.

3. Stewart, C. B.: The Computational Structural Mechanics Testbed User's Manual. NASA TM-100644, October 1989.

Evaluation of Some Scale Effects in the Response and Failure of Composite Beams

Karen E. Jackson
U.S. Army Aerostructures Directorate, AVSCOM
NASA Langley Research Center

John Morton
Virginia Polytechnic Institute and State University
Blacksburg, VA

SUMMARY

The feasibility of using scale model testing for predicting full-scale behavior of composite beams loaded in tension and flexure was investigated. Classical laws of similitude were applied to fabricate and test replica model beams to identify scaling effects in the load response, strength, and mode of failure. Experiments were conducted using graphite-epoxy composite beams having different laminate stacking sequences and a range of scaled sizes. Results indicated that the elastic response of scaled composite beams was independent of specimen size. However, a significant scale effect in strength was observed. In addition, a transition in failure mode was observed among scaled beams of certain laminate stacking sequences. Weibull statistical and fracture mechanics based models were applied to predict the strength scale effect since standard failure criteria cannot account for the influence of absolute specimen size on failure.

INTRODUCTION

The high specific strength and stiffness characteristics of composite materials have led to their application in the development of advanced, weight-efficient military and commercial aircraft. Government, industry, and universities are currently working in cooperation on a research program designed to encourage the increased use of composite materials. The objective of this program, the Advanced Composites Technology (ACT) Program sponsored by the National Aeronautics and Space Administration (NASA), is to develop and demonstrate the technology base needed to ensure the cost effective use of advanced composite materials in primary structures of future aircraft [1]. In the absence of the broad design base available for metal structures, composite prototypes must be fabricated and tested as part of design evaluation. Such testing, especially if it involves destruction of the composite test article, is expensive and time consuming. Consequently, there is a growing interest in the use of structural scale model testing and the application of the principles of dimensional analysis to the testing and evaluation of fiber composite components. These principles have long played an important role in aerodynamic design and are being applied increasingly to complex structural problems. Currently, research efforts are in progress to study scaling effects in the fundamental behavior of composite coupons. Later this research will be applied to construct scale models of innovative fuselage concepts using composite materials through the ACT program. It is essential, however, to understand the limitations involved in testing scale model structures to ensure that the results obtained from sub-scale specimens provide valid predictions of prototype behavior.

In this paper, the results obtained from two investigations which were conducted to examine scaling effects in the response and failure of graphite-epoxy composite beams will be discussed. In the first study, Kellas and Morton [2] performed tensile tests on replica model beams having four different laminate stacking sequences and four different scaled sizes (1/4, 1/2, 3/4, and full-scale). The laminates were scaled on a ply level and were chosen

to highlight individual and interacting failure modes. In the second study, a series of tests were conducted by Jackson [3] to investigate the large deflection, flexural response of composite beams. Scale model beams ranging in size from 1/6 to full-scale were tested statically under an eccentric axial compressive load until failure. The loading configuration for the flexural tests is shown schematically in Figure 1. Four laminate stacking sequences including unidirectional, angle ply, cross ply, and quasi-isotropic were tested to examine a diversity of composite response and failure modes. For both the tensile and flexural tests, comparisons of elastic response, stiffness, ultimate strength and mode of failure between the prototype and scale model beams are made for each laminate type. Correlation of the test results will determine whether full-scale behavior can be predicted from scale model testing and indicate the limitations of applicability of scale model testing for composite structures.

BACKGROUND INFORMATION

The problem of designing and building a scale model structure constructed of advanced, fiber-reinforced composite materials is challenging due to the complexity of the material. In general, the construction of a scaled composite component may be examined on two levels. The most fundamental approach is to scale the constituent materials, the fiber and matrix. This approach is similar to the technique used to fabricate reinforced concrete model structures in which the reinforcing bars and aggregate size are scaled [4-7]. For a typical graphite-epoxy composite material system, scaling of the microstructure on this level would involve scaling of the fiber geometry and spacing within the matrix. Fiber volume fractions should be the same for both model and prototype systems. However, for most structural problems, this degree of scaling becomes impractical and infeasible.

The second approach is to scale the composite laminate on a macroscopic level by assuming that the individual lamina properties are smeared, i.e., the heterogeneous nature of the material is ignored on the microscopic level and the laminate is treated as a homogeneous, orthotropic sheet. Thus, in-plane and bending stiffnesses of the composite component are scaled by adjusting the number and location of plies within the laminate stacking sequence. This approach is practical when macroscopic structural aspects of the problem are more significant than material considerations for achieving scaled response. For example, to build a scale model of a stiffened panel, construction details such as stiffener geometry and spacing may influence the response to a higher degree than perhaps a minor irregularity in the microstructure of a single ply in the laminated panel. Thus, each level of structural complexity has its own unique set of scaling difficulties and special concerns.

In addition, it is necessary to understand how changes in the microstructure, including the initiation and growth of damage, accumulate in the material and affect the overall structural response at various dimensional scales. Haritos, et. al. [8] have introduced the term "mesomechanics" to describe the area of research which bridges the microstructure studies of fiber reinforced composites with structural mechanics theories. Unfortunately, little research has been published on this topic. Test data obtained in the laboratory on small coupon-type specimens are routinely assumed to be valid for full-scale structures with no regard for possible distortions due to size or scale. This assumption is made even though a size effect in failure behavior of metallic structures has been well documented [9-12].

Previous research on testing of scale model composite structures is limited. However, the available data generally fall into two categories. First is the application of scale model testing to large, complex structures. A few examples of research of this type include (1) construction and testing of a one-half scale helicopter fuselage sub-floor made from graphite-epoxy to investigate the nonlinear load-deflection behavior by Gustafson, et. al. [13], (2) development of a flexible wing model using a hybrid of E-glass and graphite-epoxy for wind tunnel testing by McCullers and Naberhaus [14], and (3) fabrication of a scale model of the Filament Wound Case (FWC) of the solid rocket motor of the space shuttle by Verderaime [15]. Each of these studies identified specific problems associated with fabricating and testing scale model structures using composite materials.

The second category of research which has been reported on scaling effects in composites concerns the influence of specimen size on failure. Often the term "scale effect" does not refer to replica model testing, but is used to describe the influence of varying certain geometrical parameters on the structural response. For example, Fairfull [16] studied scaling effects in the energy absorption behavior of axially crushed composite tubes. He varied the thickness-to-diameter (t/d) ratio of the tube while leaving the length unchanged. Even though the length had little effect on the mean crush load, it is often difficult to quantify the scale effect in failure response from geometrically distorted models. Recently, tests have been conducted to examine scaling effects in the impact response and failure of composite beams by Morton [17], and composite plates by Qian, et al, [18]. Results from these tests indicate that classical scaling laws apply for elastic dynamic response, but a size effect was observed as the beams became damaged under greater impact loads. In general, standard failure criteria used for composite strength analysis such as maximum stress, maximum strain, and tensor polynomial, cannot predict the strength scale effect. Statistical methods based on Weibull distributions [19-22], and fracture mechanics based theories [12,23] have been used to analyze the strength scale effect since they incorporate some measure of the absolute specimen size. The scaling studies performed on composite beams loaded in tension and flexure are significant because they bridge the gap between detailed microstructural studies on a material level and the testing of large, complicated structures on a macroscopic level.

CONCEPTS OF SIMILITUDE

The non-dimensional parameters which form the scaling law *for a given phenomenon* may be derived either from the governing equations and boundary conditions, or from the Pi Theorem. Both techniques are described and the advantages and disadvantages of each are discussed by Baker, et al. [24]. The Pi Theorem is the more general method of the two and consists of identifying the important physical variables relevant to the problem under consideration. Each variable is represented dimensionally in terms of a fundamental set of units, typically either the Force-Length-Time (F-L-T) system or the Mass-Length-Time (M-L-T) system. The law of dimensional homogeneity and the Pi Theorem are used in conjunction to derive the independent dimensionless products, or Pi terms. The Pi terms are not unique and may be multiplied together to form new combinations which are equally acceptable.

In the development of a scale model experiment, attempts are made to ensure that the Pi terms are identical for both the model and the prototype. In general, this may or may not be possible given the constraints of the problem. Scaling conflicts arise when Pi terms are not satisfied or when two Pi terms cannot be satisfied simultaneously. Typically, the geometric scale factor, λ (defined as the ratio of the model to the full-scale dimension), is chosen for the experiment. The scale factors for all other variables are then derived in terms of the geometric scale factor from the Pi terms and other conditions set by the experiment. When the constants of proportionality between variables used to describe the problem are known, then results from model tests can be "scaled up" to predict prototype response.

Various types of similarity may be defined between a model and prototype system including geometric, kinematic, dynamic (kinetic), and constitutive similarity. A model is said to be geometrically similar to its prototype if the dimensions have been scaled by the same factor. Thus, geometric similarity is ensured by fabricating beams with scaled lengths, widths, and thicknesses. In addition, for the flexural tests, the boundary conditions are scaled by applying a constant geometric scale factor to the hinge supports which provide the offset for the axial load. Kinematic similarity has been defined by Langhaar [25] as follows: "The motions of two systems are similar if homologous particles lie at homologous points at homologous times." Thus, kinematic similarity implies a relationship between the motions of two systems and is defined by the scale factors for position, time, velocity,

frequency, and acceleration between the model and prototype. Dynamic similarity between two systems exists if homologous parts of the systems experience homologous forces. If kinematic similarity exists for systems which have similar mass distributions, then dynamic similarity is easily inferred from Newton's Second Law. Since, in the present investigations, both the tensile and flexural tests were conducted under quasi-static conditions, kinematic and dynamic similarity were enforced by scaling the applied loads and boundary conditions.

Constitutive similarity is defined as homologous stress-strain behavior between the model and prototype systems in the loading range of interest. For laminated composite materials, constitutive similarity requires that the in-plane stiffnesses (A_{ij}) and bending stiffnesses (D_{ij}) of the model and prototype scale as λ and λ^3, respectively. If the same pre-preg material system is used to fabricate the laminated composite specimens, then density scales as unity. Geometrically scaled specimens are constructed by machining the length and width dimensions by the geometric scale factor, λ. The thickness dimension can be scaled by increasing the number of layers at each angular ply orientation within the laminate stacking sequence by the appropriate amount. This technique is often referred to as ply level scaling. Alternatively, the thickness dimension may be scaled on a sub-laminate level by increasing the number of ply groups within the laminate stacking sequence. For example, using ply level scaling, an eight ply, symmetric quasi-isotropic laminate $[0/90/\pm45]_S$ may be scaled up by a factor of two to yield $[0_2/90_2/+45_2/-45_2]_S$. The same laminate would scale as $[(0/90/\pm45)_2]_S$ using the sub-laminate approach. For this example, the in-plane stiffness of the one-half scale model and full-scale prototype is properly scaled using both techniques; however, the bending stiffness of the sub-laminate scaled specimen is distorted. The beam specimens which were fabricated for the tensile and flexural experiments were scaled on a ply level and were machined to the appropriate length and width dimensions for geometric similarity. Thus, modulus, cross-sectional area, and moment of inertia were properly scaled to achieve laminate scaling on a macroscopic level and to ensure constitutive similarity.

Scaling conflicts arise when time-dependent material properties are introduced into a dimensional analysis. Morton [17] has discussed the effect of rate-sensitive material behavior on constitutive similarity. If the same material is used to fabricate both the model and the prototype, then the strain rate parameter will be improperly scaled. This scaling distortion causes the model to experience greater strain rates than the prototype. For high strain rates, this result could cause brittle behavior in the model while the prototype exhibits ductile behavior at corresponding times during the loading. However, based on the findings from his investigation, Morton [17] concluded that rate effects were insignificant for the composite material system and laminates that he tested, but noted that these effects may become important for matrix-dominated laminates.

Elementary approaches to scaling indicate that under scaled loading conditions the stress state in the model is identical to that in the prototype, i.e., stress scales as unity. Ideally, then, failure should occur at the same stress and strain levels for both the model and full-scale specimens. However, deviations from this elementary approach to strength scaling are commonly observed. Typically, scale models predict higher failure loads than full-scale prototypes when the data are "scaled up" for comparison. One explanation for this size effect in strength is based on the principles of linear elastic fracture mechanics. A scaling conflict for stress is introduced when the critical stress intensity factor, K_Q, is included in a dimensional analysis [2,3]. Rather than a maximum stress or strain at failure, a critical stress intensity factor is defined as the parameter which governs the onset of unstable crack growth. Since composite materials often exhibit brittle fracture, it is reasonable to include a variable such as the critical stress intensity factor to model the failure behavior. The critical stress intensity factor, K_Q, is generally assumed to be a material property which is independent of loading conditions, initial crack geometry and size, or any other parameter. As such, K_Q should have the same value for both the model and the prototype. However, a dimensional analysis including K_Q as a variable requires that K_Q

be scaled in proportion to $\lambda^{1/2}$. Since this condition is violated when the geometric scale factor is λ, the stress at initiation of unstable crack propagation scales as $\lambda^{-1/2}$. Thus, the stress required to propagate a crack in a linear elastic model will be greater by a factor of $\lambda^{-1/2}$ than the stress needed to propagate a crack in a geometrically and constitutively similar prototype. As an example, the stress for crack propagation in a 1/4 scale structural model will be twice the value required for the full-scale structure. Consequently, the model will appear twice as strong.

EXPERIMENTAL PROGRAM

Two experimental investigations were conducted to examine scaling effects in the response and failure of composite beams loaded in tension and flexure. In both studies, scale model beams were constructed of Magnamite AS4/3502 graphite-epoxy composite material by adjusting the number of plies for each angular orientation in the laminate stacking sequence. Ply level scaling in this manner should produce composite beams in which the in-plane and bending stiffnesses are properly scaled. For both the tensile and flexural tests, care was taken to ensure that boundary and loading conditions were scaled for each beam specimen.

Tensile Tests.- Four laminates and four scaled sizes were selected for tensile testing; full-scale, 3/4, 1/2, and 1/4. The four laminates were

Laminate A: $(\pm 30_n/90_{2n})_S$
Laminate B: $(\pm 45_n/0_n/90_n)_S$
Laminate C: $(90_n/0_n/90_n/0_n)_S$
Laminate D: $(\pm 45_n/\pm 45_n)_S$

with n equal to 4, 3, 2, and 1, respectively. These laminate stacking sequences were chosen to highlight individual and interacting failure modes. Beam specimen geometric details are given in Table 1. The grip length of each beam was scaled to provide similar end conditions during loading, as indicated in Table 1. Beam specimens were tested in a mechanical load test machine equipped with wedge type grips. The cross-head displacement of the testing machine was adjusted such that each specimen was tested at approximately the same strain rate. Load and cross-head displacement were recorded from output of the testing machine. Strain was measured from both a foil strain gage located at the center of the beam and an extensometer for each scaled beam specimen. More details of the experimental procedure are provided in Reference [2].

Flexural Tests.- Beams having unidirectional, angle ply, cross ply, and quasi-isotropic laminate stacking sequences were tested under an eccentric compressive load to examine unique composite response and failure behaviors in flexure. Eight different sizes of beams were tested including full-scale, 5/6, 3/4, 2/3, 1/2, 1/3, 1/4, and 1/6 scale. The dimensions and lay-ups of each of the scale model beams are listed in Table 2. Note that use of ply level scaling rendered it impossible to construct a 1/4 or 3/4 scale quasi-isotropic beam.

The basic loading configuration for the scaled beams is shown in the schematic drawing of Figure 1. Each beam specimen was gripped in a set of hinges which offset the axial load with a moderate eccentricity. A detailed drawing of the hinge and beam attachment is shown in Figure 2. Eight sets of hinges were constructed (one for each of the eight scale factors) to ensure that the boundary and loading conditions were properly scaled. For each hinge, the eccentricity, grip length, and total distance from the center of the pin to the unsupported or free portion of the beam were scaled.

The hinges were pinned to the platens of a standard load test machine which applied the compressive vertical load. The hinged-pinned connection allowed the beam to undergo large rotations during deformation. Beam specimens were loaded in this manner until

catastrophic failure, defined as loss of load-carrying capability. The beam-column loading configuration was chosen, in part, because failures occur in a global fashion at the center of the beam where the maximum bending moment occurs. Thus, failures are not introduced by local effects at the grip supports. Although the beam was loaded as a beam-column, the bending strains were several orders of magnitude greater than those due to the axial compressive load. Therefore, the beam was nearly in a state of pure bending.

The vertical applied load was measured from a load platform located at the base of the bottom hinge support which was attached to the lower platen of the test machine. The distance traveled by the platens of the load test machine during a test is defined as the end displacement for that test. End displacement was measured from a string potentiometer displacement transducer. Strain measurements were recorded from back-to-back gages applied at the midpoint of the beams. Additional information on the experimental procedure used for the flexural tests is reported in Reference [3].

RESULTS

Scaling Effects in Initial Stiffness and Response

Tensile Tests.- A summary of the longitudinal initial stiffness (modulus) values as determined from extensometer and central strain gage data are listed in Table 3 for each of the scaled beams tested under tensile loading conditions. The stiffness values are valid for small strains only (0.2%, 0.5%, 0.5%, and 0.35% strain for Laminates A, B, C, and D, respectively). In addition, the initial stiffnesses of the beams, as determined from lamination theory, are included in Table 3 for comparison with the experimental data. The material properties of the AS4/3502 composite material used in the lamination theory predictions are

E_1 = 19.85 Msi
E_2 = 1.43 Msi
G_{12} = 0.70 Msi
ν_{12} = 0.293

These data were determined by Sensmeier [26] from material characterization tests on the AS4/3502 material system. A correction factor of 0.87 was applied to the shear modulus, G_{12}, which was originally reported as 0.82 Msi to account for the non-uniformity of the shear stress field in the test method used [27]. The data presented in Table 3 show that the stiffness measurements derived from the central strain gage and from the extensometer are fairly consistent, and that the stiffness values calculated from lamination theory are slightly higher than the experimentally determined values for each of the four laminates. The data listed in Table 3 indicate that all specimen sizes of a particular laminate stacking sequence have approximately the same initial stiffness or modulus. Thus, no scale effect is seen in the initial stiffness of the composite beams loaded in tension.

Flexural Tests.- The effective bending stiffness of each of the scale model beams tested under flexural loading was determined empirically using a technique described in Reference [3]. The bending stiffnesses were calculated from the load versus end displacement plots in the linear elastic, small deflection response region and were used to investigate scaling effects in the elastic response. In Figure 3, the bending stiffness values for the scale model beams were multiplied by the appropriate factor, normalized by the full-scale value, and plotted versus scale factor for the unidirectional, angle ply, cross ply, and quasi-isotropic laminates. Any significant deviation from the straight line drawn at 1.0 in Figure 3 may be interpreted as a scale effect. Results for the unidirectional, cross ply, and quasi-isotropic beams show deviations of less than 10% from scaled response. This variation can be explained by minor differences in thicknesses of the cured beams and experimental

error. However, the angle ply laminates exhibit a large scale effect in the bending stiffness response. The smaller beams are significantly stiffer than the full-scale beam to the extent that the 1/6 scale beam response is 1.5 times stiffer than the prototype response. This effect may be attributed to the presence of matrix cracks in the larger scale model beams which are not found in the smaller beams. The cracks may be induced from curing and fabrication stresses caused by blocking large numbers of plies of the same orientation together, as required to fabricate the scaled beams.

Based on the normalized load versus end displacement data reported in Reference 3, no deviations from scaled response were observed for the unidirectional and cross ply laminates, even under severe rotations and deformations. However, the angle ply and quasi-isotropic laminates deviated from scaled response as the deflections became large due to damage events which altered the beam stiffness. The effect was especially dramatic for the angle ply laminates which contain no 0° plies. In general, the degree of success in achieving scaled response is highly dependent on the laminate stacking sequence and, particularly, is a function of the number of 0° plies in the laminate.

Scaling Effects in Strength

Tensile Tests.- A summary of the tensile strength results is given in Table 4 including the failure stress and strain values and the normalized failure stress and strain values. Tensile failure stress, or strength, is defined as the maximum load divided by the measured cross sectional area of the beam specimen. Likewise, failure strain is the maximum recorded displacement divided by the extensometer gage length. The data from Table 4 indicate that tensile strength depends on specimen size. For all four lay-ups, the tensile strength decreases with increasing specimen size. However, the amount of strength degradation depends on the percentage of 0° plies in the given stacking sequence. In general, laminates with a high percentage of 0° plies exhibit a lower strength scale effect. For example, an 83% increase in strength was observed in 1/4 scale specimens of the matrix dominated Laminate A as compared to the full-scale specimens. In contrast, the average strength of the 1/4 scale specimens of the fiber dominated Laminate C was only 7% higher than the average strength of the full-scale specimens. This trend is depicted in Figure 4 which is a plot of the normalized strength versus scaled size.

The failure strains were also affected by specimen size, as indicated by the data listed in Table 4. The sensitivity of the size effect was determined by the laminate stacking sequence. For Laminates A, C, and D, the failure strains tended to increase with decreasing specimen size. However, an opposite effect was observed for Laminate B. Generally, the failure strains were found to depend on the method of measurement with noticeable differences between the gage readings and the extensometer data. Strain gages were often detached from the specimens prior to final failure and did not provide a true measure of the failure strain. Due to these difficulties, a failure analysis based on stress was considered more suitable for predicting the strength scale effect.

Flexural Tests.- A significant scale effect in strength was also observed for the four laminate types tested under flexural loading to failure. The loads, end displacements, and strains at failure increased as the size of the beams decreased from full-scale to 1/6 scale. To illustrate the magnitude of the strength scale effect, the failure loads for each of the scale model beams were multiplied by the appropriate scale factor ($1/\lambda^2$), normalized by the full-scale value, and plotted as a function of scale factor in Figure 5. If no scaling effects in strength were present, then all of the data would fall on the line drawn at 1.0. The plot indicates that a scale effect is evident even between the full and 5/6 scale beams. The effect increases as the size of the beams decreases. The cross ply laminate family exhibits the largest scale effect in strength among the laminates tested. The unidirectional laminates appear to be the least sensitive to the size effect in strength; although the effect is still observed.

Scaling Effects in Failure Mechanisms

Tensile Tests.- Final failure modes are shown in Figures 6-9 for Laminates A-D, respectively. The modes of failure for the fiber dominated laminates (B and C) were dependent on specimen size. In contrast to the strength behavior, the laminates containing the largest number of 0° plies were more sensitive to failure mode related scale effects than laminates having little or no 0° plies. For example, specimens of Laminate C which contained 50% 0° plies showed little variation in tensile strength with size. However, the mode of failure, as shown in Figure 8, changed from a clean fracture in the 1/4 scale beam to a brush-like fracture in the full-scale beam. Conversely, specimens of Laminate A and D which contained no 0° plies and exhibited a large strength-related size dependency, showed no apparent differences in failure mode related to specimen size.

For Laminate A, the smaller scale beams showed more delamination between the -30° and 90° plies at failure than the larger scale beams. However, in general, the overall mode of final failure was similar for all four sizes, as indicated in Figure 6. In the case of Laminate B, a transition in mode of failure was observed with increasing specimen size. Figure 7 shows that a localized type of fracture occurred in the small size beams whereas the larger beams showed an extensive fracture. Furthermore, small specimens exhibited a delamination in the 0°/90° interface as opposed to delamination between all interfaces in the larger sizes. Modes of final failure for Laminate C are shown in Figure 8. This family of specimens displayed the most pronounced transition in mode of final failure which changed from a clean, localized fracture in the small specimens to an extensive fracture occupying the whole gage length in the larger specimens. For matrix-dominated Laminate D, all four specimen sizes shared a very similar final failure mode, as shown in Figure 9, which was a localized ±45° shear fracture with minor delamination between the ±45° interfaces.

Flexural Tests.- Photographs of a complete set of failed beams are shown in Figures 10-13 for the unidirectional, angle ply, cross ply, and quasi-isotropic laminate families, respectively. No size-related differences in failure mechanism were observed for the unidirectional beams, shown in Figure 10, which failed by fiber fracture and longitudinal splitting. Since the maximum bending moment occurs in the center of the beam, final fracture of the fibers in the central region resulted in catastrophic beam failure. Likewise, the angle ply laminates showed no size dependency in mode of final failure. Figure 11 indicates that all specimen sizes failed by transverse matrix cracking along the 45° fiber direction. No fiber fractures were observed. Only the cross ply beams exhibited a size dependency in mode of failure, as shown in Figure 12. A transition in failure mechanism occurred between the 1/2 and 1/3 scale model beams in which the small size beams contained fiber fractures in the outer 0° plies and numerous transverse matrix cracks in the 90° core layer. However, no fiber fractures were observed for the larger size beams and a delamination between the 0° and 90° layers developed along the entire gage length. The quasi-isotropic beams failed through a combination of matrix cracking, delamination, and some fiber fractures, as shown in Figure 13. Although the smaller size beams appear to have sustained more damage than the larger beams, the mode of failure is similar for each size of beam.

DISCUSSION OF RESULTS

It was observed that initial stiffness and linear elastic, small-deflection response scale for the composite beams loaded in tension and flexure. This result implies that the fabrication technique used to construct the scale model composite beams provided constitutive similarity, and that the loading and boundary conditions were properly scaled to ensure scaled elastic response. A noted exception was the increase in bending stiffness with decreasing beam size exhibited by the angle ply laminates loaded in flexure. This behavior may be explained by the presence of damage in the larger size virgin specimens. Although evaluation techniques were not used to determine the damage state of the pre-tested beam

specimens for the flexural tests, evidence of matrix cracking in virgin specimens was detected in the tensile coupons of Laminate D. Figure 14 contains x-ray radiographs of virgin specimens of Laminate D which illustrate that the full-scale beam contained numerous transverse matrix cracks. The mechanism of crack formation and propagation is unknown at this time; however, crack density is higher in specimens containing large blocks of plies having the same orientation. Kellas and Morton [2] hypothesize that the observed cracks are driven by thermal residual stresses and may be triggered by specimen cutting, or by the generation of free edge stresses. For laminates containing some 0° plies, the effect of matrix damage in off-axis plies should not reduce the initial stiffness by a significant amount. However, transverse matrix cracks in angle ply laminates with no 0° plies could significantly reduce the stiffness and, thus, the elastic response of these laminates.

The presence of pre-existing damage in untested beam specimens may also contribute to the differences observed in the mode of failure among scaled sizes for certain laminates. As noted from the tensile test results, the fiber-dominated laminates B and C exhibited a transition in mode of final failure, whereas the matrix-dominated laminates A and D appeared to fail in a similar manner for each scaled size. For example, in Laminate A final failure is largely controlled by the load-bearing ±30° plies. The mode of failure was uniform for all four sizes because transverse matrix cracking along the ±30° fiber directions was a more likely failure mode than fiber breakage. The effect of transverse matrix cracking in the larger size beams was merely reflected in the reduced tensile strength. Similar behavior was seen for the matrix-dominated angle ply laminates tested under flexural loading. The progression of transverse matrix cracks along the ±45° fiber direction was the only failure mechanism available in these laminates. The effect of pre-existing cracks, if present, in the larger size specimens would be to reduce the ultimate strength. Thus, no transition in mode of failure was observed.

For fiber-dominated laminates loaded in tension, matrix cracks in the pretested beams served to decouple the plies which led to differences in failure mechanism between the smaller and larger scaled beams. Transverse matrix cracks in the small sizes of Laminate B, for example, developed as the beam was loaded and imposed a stress concentration in the neighboring 0° plies. As a result, a clean fracture in the 0° plies was observed. In the larger sizes of Laminate B, numerous transverse matrix cracks were already present in the virgin specimens. Consequently, under load, the larger size beams delaminated between the 0°/90° interface at a much lower applied stress than the smaller size beams. A similar transition in failure mechanism was seen in the response of the cross ply laminates under flexural loading. Fiber fractures were observed in the 0° plies of the 1/3 scale beams and smaller, while large delaminations were seen in the 0°/90° interface of the 1/2 scale beams and larger.

In general, it is believed that the size effect in strength which is observed on the macroscopic level is the result of microscopic damage which initiates within the laminate and develops in a certain manner under the applied load. The accumulation of damage and interaction of failure mechanisms eventually produce ultimate failure of the structure. Detailed investigations on the effect of test specimen size on failure need to be performed on a material level before the phenomenon can be thoroughly understood on the macroscopic level.

Analytical Predictions of the Strength Scale Effect

The increase in failure stress with decreasing specimen size in the tensile coupons, listed in Table 4, and the increase in failure load with decreasing specimen size in the flexure specimens, shown in Figure 5, demonstrate the magnitude of the strength scale effect. The observed differences in strength for replica model beams loaded under scaled conditions cannot be predicted based on standard failure criteria such as maximum stress, maximum strain, or tensor polynomial. Previous researchers have attempted to model the scale effect in strength of fiber-reinforced composite materials using either a statistical

approach [19-22] or a fracture mechanics model [12,23].

The application of statistical techniques for modeling the size effect in strength of brittle materials is based on the observation that these materials are flaw-sensitive. Since the presence of imperfections can be statistical in nature, it is reasonable to assume that larger specimens will exhibit lower strength simply because there is a higher probability that a strength-critical flaw is present in the greater volume of material. Weibull statistical theory has been applied in conjunction with a weakest link theory to develop a mathematical model for predicting the scale effect in strength. Bullock [20] found that the ratio of ultimate strengths between a geometrically similar model and prototype is given by

$$\frac{S_m^{ult}}{S_p^{ult}} = \left[\frac{V_p}{V_m}\right]^{1/\beta}$$

where the subscripts m and p refer to the model and prototype, respectively, and S^{ult} is the ultimate stress, V is the volume, and β is the Weibull shape parameter, sometimes called the flaw density parameter since it provides a measure of the scatter in the strength data. The flaw density parameter, β, is assumed to be a material constant. If β is determined empirically from two specimens of differing size, then the strength of geometrically similar scale models can be predicted.

Atkins and Caddell [12] used a fracture mechanics approach to derive a simple size-strength relationship for notched brittle materials. As discussed earlier in this paper, if the critical stress intensity factor is included in a dimensional analysis, the laws of similitude require that stress scale as $\lambda^{-1/2}$. Thus, the stress needed to propagate a crack in a full-scale prototype structure, σ_p, and the corresponding stress, σ_m, in a model structure are related by

$$\sigma_p = \sigma_m \sqrt{\lambda}$$

where λ is the geometric scale factor.

The Weibull statistical model and the fracture mechanics model were used to predict the strength of the full-scale laminates (A-D) for the tensile beam specimens and the results are listed in Table 5 along with the experimental data. For both models, the strength predictions were made by "scaling up" the 1/4 size strength data. The value of the flaw density parameter, β, was determined empirically based on strength data from the 1/4 and 1/2 scale sizes for each laminate type. Numerical values of β are listed in Table 5 and they ranged from 7.22 for Laminate A to 156.0 for Laminate C. The results presented in Table 5 indicate that the Weibull model provides the best strength prediction. However, this is expected since the flaw density parameter allows a curve to be fitted to the data.

The two strength prediction models were also applied to the flexure beam specimens. Figure 15 contains plots of the unidirectional, angle ply, cross ply, and quasi-isotropic normalized strength data with the Weibull statistical and the fracture mechanics based model predictions. In this case, the flaw density parameter was determined based on strength data from the 1/6 and full-scale size beams. As was observed for the tensile data, the Weibull model gives better strength predictions than the fracture mechanics model for the flexure data. The flaw density parameter varies depending on the laminate stacking sequence and must be determined empirically. The success of the Weibull model in predicting strength degradation depends heavily on the flaw density parameter which may be influenced by the initial state and size of the laminates used to derive it. For example, the flaw density parameter may be derived based on data from a 1/6 and a 1/4 scale model beam, neither of which contained pre-existing matrix cracks. If the full-scale laminate contained transverse matrix cracks due to fabrication stresses, then the Weibull model would overpredict the strength of the full-scale beam. Likewise, a transition in mode of final

failure between scaled sizes could reduce the effectiveness of a Weibull model if the transition is not somehow accounted for in the flaw density parameter.

Results of applying statistical and fracture mechanics based models for predicting the strength scale effect show that neither approach can explain the phenomenon in a satisfactory manner. Research by Crossman [28], Wang [29], and Laws [30] on the effects of transverse matrix cracking on the final fracture of cross ply laminates suggests that a model which incorporates both theories is needed. A statistical approach is used to determine which microflaws within the 90° core will coalesce to form a transverse matrix crack given a random distribution of flaws and flaw sizes. Once a crack has formed, fracture mechanics theories are applied to determine the stability of the crack under the given loading conditions. The progression of crack formation and stability are continually monitored until ultimate laminate failure. A model of this type has been used to predict the tensile failure of cross ply laminates in which the number of 90° plies was varied from 2 to 16 [30]. Although these laminates were not replica models since the number of 0° plies was not adjusted in the same proportion as the number of 90° plies, the success of the model indicates that it may be able to predict the stress required to initiate cracks in the transverse plies of scaled laminates of various stacking sequences.

CONCLUDING REMARKS

Two experimental investigations were conducted to examine scaling effects in the response and failure of graphite-epoxy composite beams loaded in tension and flexure. In both studies, the composite beams were fabricated using ply level scaling to ensure constitutive similarity. Both the tensile and flexural tests were performed under scaled loading and boundary conditions to determine the influence of specimen size on stiffness, elastic response, strength and failure mechanism. A variety of laminate stacking sequences were included in the experimental program to highlight individual and interacting failure modes. Major findings from these investigations are summarized in the following list.

1. In both the tensile and flexural tests, beam stiffnesses appeared to be independent of specimen size, especially in the loading range where small deflections, and small strains are valid and the material is linear elastic. Deviations from scaled response are observed when damage develops in the composite beams.
2. All specimens exhibited a scale effect in strength. Several factors influence the degree of sensitivity including the initial state of the laminate, and the laminate stacking sequence. For the tensile specimens, x-ray radiographs of the specimens prior to testing indicated that the larger size beams contained matrix cracks not seen in the smaller scale beams. These cracks may have initiated from fabrication or curing stresses. Once present, they serve as stress concentrations and contribute to the ultimate failure of the larger size beams. Also, the size effect in strength is influenced by the lay-up of the beam. Laminates with a higher percentage of 0° plies showed a smaller strength scale effect for tensile loaded specimens.
3. Transitions in the mode of final failure were evident for both tensile and flexural beams as the beam size increased. Again, this effect is dependent on lay-up. Scale model and prototype unidirectional, angle ply, and quasi-isotropic beams showed consistent failure mechanisms when tested to failure in flexure. However, cross ply beams showed a transition from matrix cracking and fiber breakage in the small scale beams, to delamination in the larger scaled beams. Some of the differences in failure mechanisms which occur as the size of the beam increases may be attributed to pre-existing matrix cracks.
4. The scale effect in strength was analyzed using a Weibull statistical approach and a fracture mechanics based model. These techniques have the capability of predicting a size effect in failure which standard composite failure criteria such as maximum stress, maximum strain, and tensor polynomial, cannot predict. The Weibull statistical model provided better correlation with the experimental results for both the tensile and flexural data than the fracture mechanics based model. However, the Weibull model requires additional empirical data and neither model is sensitive to the unique failure modes exhibited by composite laminates.

REFERENCES

1. Freeman, W. T.: "Innovation, Damage Tolerance, and Affordability NASA's New Thrust for Composites Research." presentation at the 1989 General Aviation Aircraft Meeting and Exposition, sponsored by the SAE, Wichita, Kansas, April 13, 1989.

2. Kellas, S.; and Morton, J.: "Strength Scaling in Fiber Composites." NASA CR 4335, October, 1990.

3. Jackson, K. E.: "Scaling Effects in the Static and Dynamic Response of Graphite-Epoxy Beam-Columns." NASA TM 102697, July, 1990.

4. Davies, I. L.: "Studies of the Response of Reinforced Concrete Structures to Short Duration Dynamic Loads." *Design For Dynamic Loading, The Use of Model Analysis*, G. S. T. Armer and F. K. Garas (eds.) London: Construction Press, 1982.

5. Murayama, Y.; and Noda, S.: "Study on Small Scale Model Tests for Reinforced Concrete Structures- Small Scale Model Tests by Using 3MM Diameter Deformed Re-bars." Kajima Institute of Construction Technology, Tokyo, Feb. 1983.

6. Pletta, D. H.; and Frederick, D.: "Model Analysis of a Skewed Rigid Frame Bridge and Slab." *Journal of the American Concrete Institute*, Vol. 26, No. 3, Nov. 1954, pp. 217-230.

7. Pletta, D. H.; and Frederick, D. : "Experimental Analysis." *Proceedings ASCE*, Vol. 79, No. 224, 1953.

8. Haritos, G. K.; Hager, J. W.; Amos, A. K.; Salkind, M. J.; and Wang, A. S. D.: "Mesomechanics: The Microstructure-Mechanics Connection." AIAA Paper 87-0726, *A Collection of Technical Papers Part 1*, 28th Structures, Structural Dynamics and Materials Conference, April 1987, pp. 812-818.

9. Booth, E.; Collier, D.; and Miles, J.: "Impact Scalability of Plated Steel Structures." *Structural Crashworthiness.* Jones and Wierzbicki, eds., London: Butterworths, 1983, pp. 136-174

10. Duffey, T. A.: "Scaling Laws For Fuel Capsules Subjected to Blast, Impact, and Thermal Loading." *Proceedings of the 1971 Intersociety Energy Conversion Engineering Conference*, Boston, Mass., August 1971, pp. 775-786.

11. Jones, N.: "Scaling of Inelastic Structures Loaded Dynamically." *Structural Impact and Crashworthiness*, Davies, ed., Vol. 1 Keynote Lectures, London: Elsevier Applied Science Publishers, 1984, pp. 46-71.

12. Atkins, A. G.; and Caddell, R. M.: "The Laws of Similitude and Crack Propagation." *International Journal of Mechanical Sciences*, Vol. 16, 1974, pp. 541-548.

13. Gustafson, A. J.; Ng, G. S.; and Singley, G. T.: "Impact Behavior of Fibrous Composites and Metal Substructures." USAAVRADCOM TR-82-D-31, 1982.

14. McCullers, L. A.; and Naberhaus, J. D.: "Automated Structural Design and Analysis of Advanced Composite Wing Models." *Computers and Structures*, Vol. 3, 1973, pp. 925-937.

15. Verderaime, V. S.: "Scaling Phenomena of Graphite-Epoxy Wound Cases." *Proceedings of the Seventh Conference on Fibrous Composites in Structural Design*, AFWAL-TR-85-

3094, June 1985.

16. Fairfull, A. H.: "Scaling Effects in the Energy Absorption of Axially Crushed Composite Tubes." Ph.D. dissertation, University of Liverpool, 1986.

17. Morton, J.: "Scaling of Impact-Loaded Carbon-Fiber Composites." *AIAA Journal* , Vol. 26, No. 8, August 1988, pp. 989-994.

18. Qian, Y.; Swanson, S. R.; Nuismer, R. J.; and Bucinell, R. B.: "An Experimental Study of Scaling Rules for Impact Damage in Fiber Composites." *Journal of Composite Materials*, Vol. 24, No. 5, May 1990, pp. 559-570.

19. Zweben, C.: "The Effect of Stress Nonuniformity and Size on the Strength of Composite Materials." *Composites Technology Review*, Vol. 3, No. 1, 1981, pp. 23-26.

20. Bullock, R. E.: "Strength Ratios of Composite Materials in Flexure and Tension." *Journal of Composite Materials,* Vol. 8, April 1974, pp. 200-206.

21. Wang, A. S. D.; Tung, R. W.; and Sanders, B. A.: "Size Effect on Strength and Fatigue of a Short Fiber Composite Material." *Emerging Technologies in Aerospace Structures, Design, Structural Dynamics and Materials*, ASME, August 1980, pp. 37-52.

22. Chou, P. C.; and Croman, R.: "Scale Effect in Fatigue of Composite Materials." *Journal of Composite Materials*, Vol. 13, July 1979, pp. 178-194.

23. Carpinteri, A.; and Bocca, P.: "Transferability of Small Specimen Data to Full-Size Structural Components." *Composite Material Response: Constitutive Relations and Damage Mechanisms*, G. C. Sih, G. F. Smith, I. H. Marshall, and J.J. Wu (eds.) London: Elsevier Applied Science, 1987.

24. Baker, W. E.; Westine, P. S.; and Dodge, F. T.: *Similarity Methods in Engineering Dynamics*. Rochelle Park, N.J.: Hayden Book Company, 1973.

25. Langhaar, H. L.: *Dimensional Analysis and Theory of Models*. New York: John Wiley and Sons, Inc., 1951.

26. Sensmeier, M. D.; Griffin, O. H.; and Johnson, E. R.: "Static and Dynamic Large Deflection Flexural Response of Graphite-Epoxy Beams." NASA CR 4118, March 1988.

27. Morton, J.; Ho, H.; Tsai, M. Y.; and Farley, G. L.: "An Evaluation of the Iosipescu Specimen for Composite Materials Shear Properties Measurement." to be published in *Journal of Composite Materials.*

28. Crossman, F. W.; Warren, W. J.; and Wang, A. S. D.: "Influence of Ply Thickness on Damage Accumulation and Final Fracture." *Advances in Aerospace Structures, Materials, and Dynamics: A Symposium on Composites*, ASME Publication AD-06, 1983, pp. 215-226.

29. Wang, A.S.D.; Chou, P.C.; and Lei, S.C.: "A Stochastic Model for the Growth of Matrix Cracks in Composite Laminates." *Advances in Aerospace Structures, Materials, and Dynamics: A Symposium on Composites*, ASME Publication AD-06, 1983, pp. 7-16.

30. Laws, N.; and Dvorak, G.J.: "Progressive Transverse Cracking in Composite Laminates." *Journal of Composite Materials*, Vol. 22, October 1988, pp. 900-916.

TABLE 1.- Tensile specimen geometric details.

	1/4 SIZE	2/4 SIZE	3/4 SIZE	FULL SCALE
No. of plies	8	16	24	32
Average thickness in.x10^{-3}	44	88	133	176
Nominal width in.	0.5	1.0	1.5	2.0
Nominal gage length / in.	3.5	7.0	10.5	14.0
Nominal gripped length / in.	0.75	1.50	2.25	3.00
No. of specimens	22	10	12	10

TABLE 2.- Flexural beam specimen dimensions and lay-ups.

Scale	Beam dimension	Uni-directional	Angle ply	Cross ply	Quasi-isotropic
1/6	0.5" x 5.0"	$[0]_{8T}$	$[45_2/-45_2]_s$	$[0_2/90_2]_s$	$[-45/0/45/90]_s$
1/4	0.75" x 7.5"	$[0]_{12T}$	$[45_3/-45_3]_s$	$[0_3/90_3]_s$	---------
1/3	1.0" x 10.0"	$[0]_{16T}$	$[45_4/-45_4]_s$	$[0_4/90_4]_s$	$[-45_2/0_2/45_2/90_2]_s$
1/2	1.5" x 15.0"	$[0]_{24T}$	$[45_6/-45_6]_s$	$[0_6/90_6]_s$	$[-45_3/0_3/45_3/90_3]_s$
2/3	2.0" x 20.0"	$[0]_{32T}$	$[45_8/-45_8]_s$	$[0_8/90_8]_s$	$[-45_4/0_4/45_4/90_4]_s$
3/4	2.25" x 22.5"	$[0]_{36T}$	$[45_9/-45_9]_s$	$[0_9/90_9]_s$	----------
5/6	2.5" x 25.0"	$[0]_{40T}$	$[45_{10}/-45_{10}]_s$	$[0_{10}/90_{10}]_s$	$[-45_5/0_5/45_5/90_5]_s$
6/6	3.0" x 30.0"	$[0]_{48T}$	$[45_{12}/-45_{12}]_s$	$[0_{12}/90_{12}]_s$	$[-45_6/0_6/45_6/90_6]_s$

TABLE 3.- Initial longitudinal stiffness (modulus) values from tensile tests. Values shown represent the average of six or more extensometer tests. Stiffness values are valid for small strains only: 0.2%, 0.5%, 0.5%, and 0.35% strain for Laminates A, B, C, and D, respectively.

INITIAL STIFFNESS (MODULUS), MSI

SIZE n=1,2,3,4	CENTRAL GAGES	EXTENSOMETER	LAMINATION THEORY
	LAMINATE A: $(\pm 30_n/90_{2n})_S$		
1/4	5.4	5.1	6.3
1/2	5.3	5.2	6.3
3/4	5.1	5.2	6.3
Full	5.0	6.1	6.3
	LAMINATE B: $(\pm 45_n/0_n/90_n)_S$		
1/4	7.0	6.8	7.7
1/2	6.8	6.8	7.7
3/4	*	*	7.7
Full	6.4	6.5	7.7
	LAMINATE C: $(90_n/0_n/90_n/0_n)_S$		
1/4	9.8	9.4	10.7
1/2	10.0	10.2	10.7
3/4	*	*	10.7
Full	*	*	10.7
	LAMINATE D: $(45_n/-45_n/45_n/-45_n)_S$		
1/4	2.4	2.2	2.5
1/2	2.5	2.4	2.5
3/4	2.4	2.4	2.5
Full	2.4	2.8	2.5

* - indicates insufficient data

TABLE 4.- Summary of the experimental strength and failure strain results from tensile tests: average values from six or more valid tests per condition.

SIZE	TENSILE STRENGTH ksi	FAILURE STRAIN %	NORMALIZED STRENGTH	NORMALIZED STRAIN
		Lay-Up **A** $(+30°_n/-30°_n/90°_{2n})_s$		
1/4	30.28	0.60	1.83	1.88
2/4	22.70	0.55	1.37	1.74
3/4	19.01	0.33	1.15	1.04
full scale	16.58	0.32	1.00	1.00
		Lay-Up **B** $(+45°_n/-45°_n/0°_n/90°_n)_s$		
1/4	80.78	1.20	1.39	0.82
2/4	72.35	1.18	1.24	0.81
3/4	61.97	1.42	1.06	0.97
full scale	58.34	1.47	1.00	1.00
		Lay-Up **C** $(90°_n/0°_n/90°_n/0°_n)_s$		
1/4	128.26	1.38	1.07	1.48
2/4	126.56	1.17	1.05	1.26
3/4	125.58	1.25	1.04	1.34
full scale	120.42	0.93	1.00	1.00
		Lay-Up **D** $(+45°_n/-45°_n/+45°_n/-45°_n)_s$		
1/4	19.63	1.05	1.56	2.49
2/4	17.08	0.96	1.36	2.29
3/4	14.96	0.74	1.19	1.77
full scale	12.56	0.42	1.00	1.00

TABLE 5.- Tensile strength predictions for full-scale Laminates A-D, based on Weibull statistical model and a fracture mechanics based model.

LAMINATE TYPE	STRENGTH ksi		
	EXPERIMENT FULL-SCALE	WEIBULL STATISTICAL MODEL	FRACTURE MECHANICS MODEL
A	16.6	17.0 (β=7.22)	15.1
B	58.3	64.7 (β=18.8)	40.4
C	120.4	124.9 (β=156.0)	64.1
D	12.6	14.8 (β=14.87)	9.8

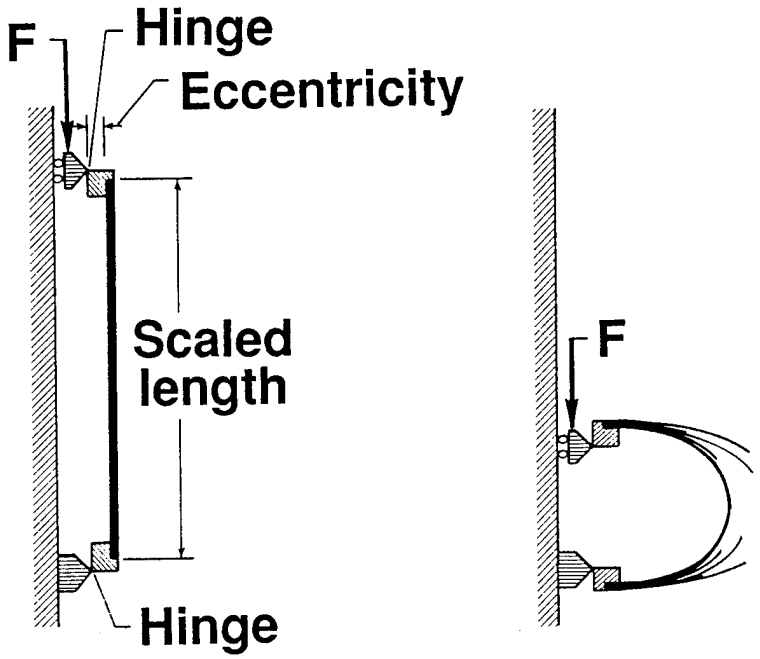


FIGURE 1. Schematic drawing of the flexural test configuration.

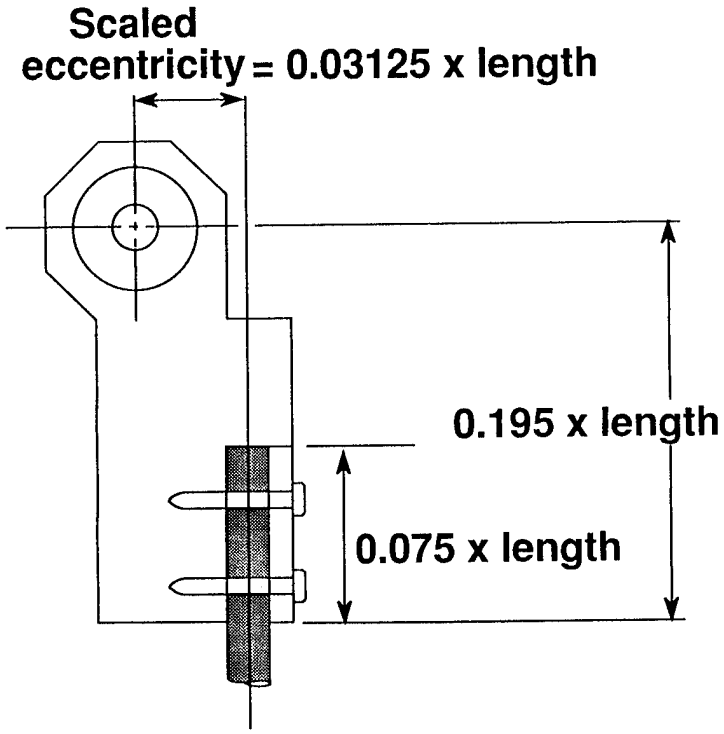


FIGURE 2. Detailed drawing of the hinge-beam attachment.

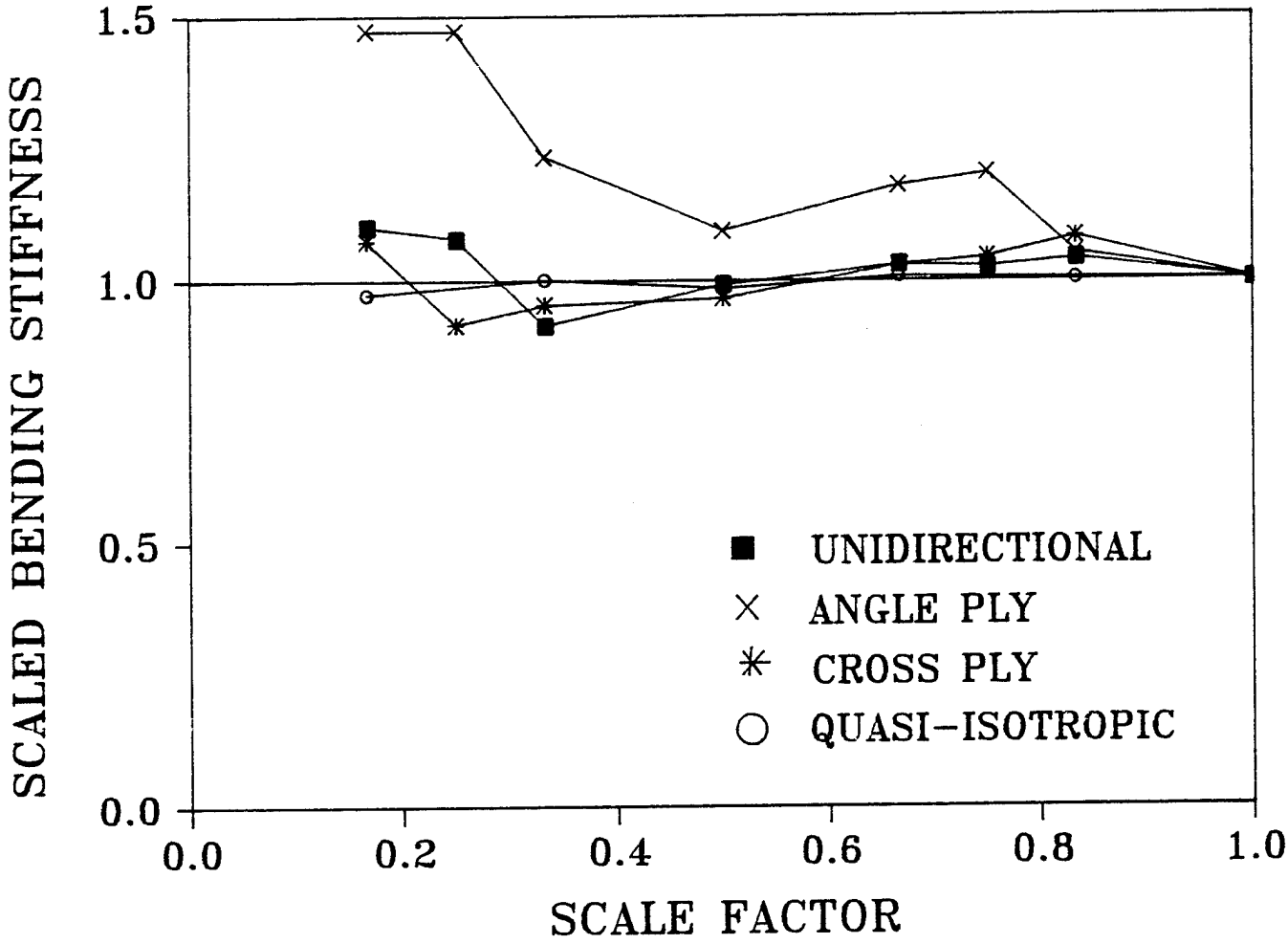


FIGURE 3. Normalized scaled bending stiffness versus scale factor for unidirectional, angle ply, cross ply, and quasi-isotropic beams loaded in flexure.

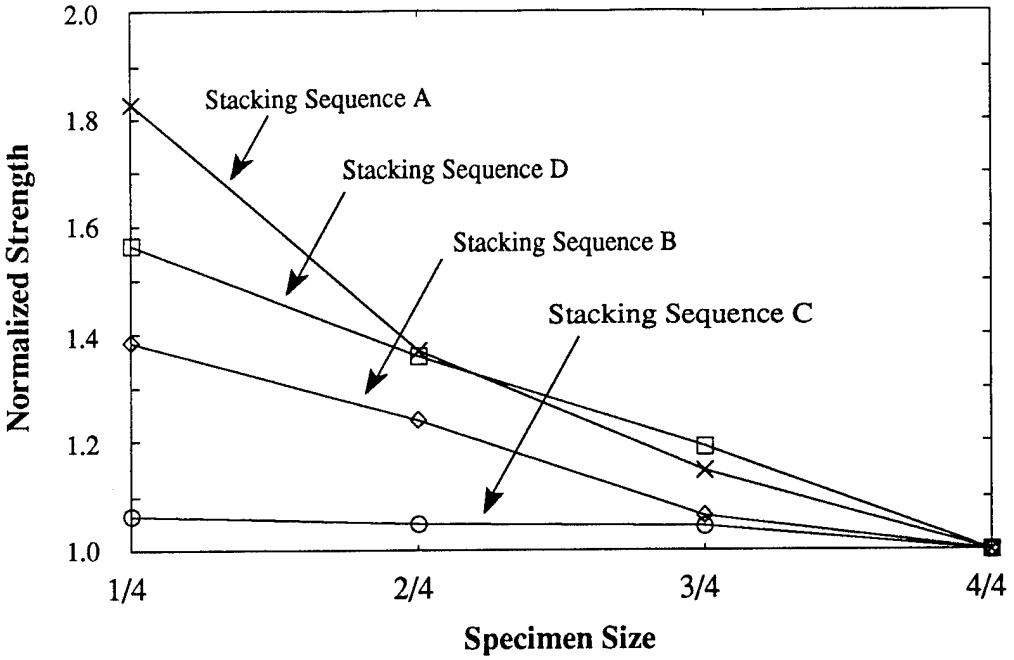


FIGURE 4. Normalized strength versus specimen size for Laminates A-D loaded in tension.

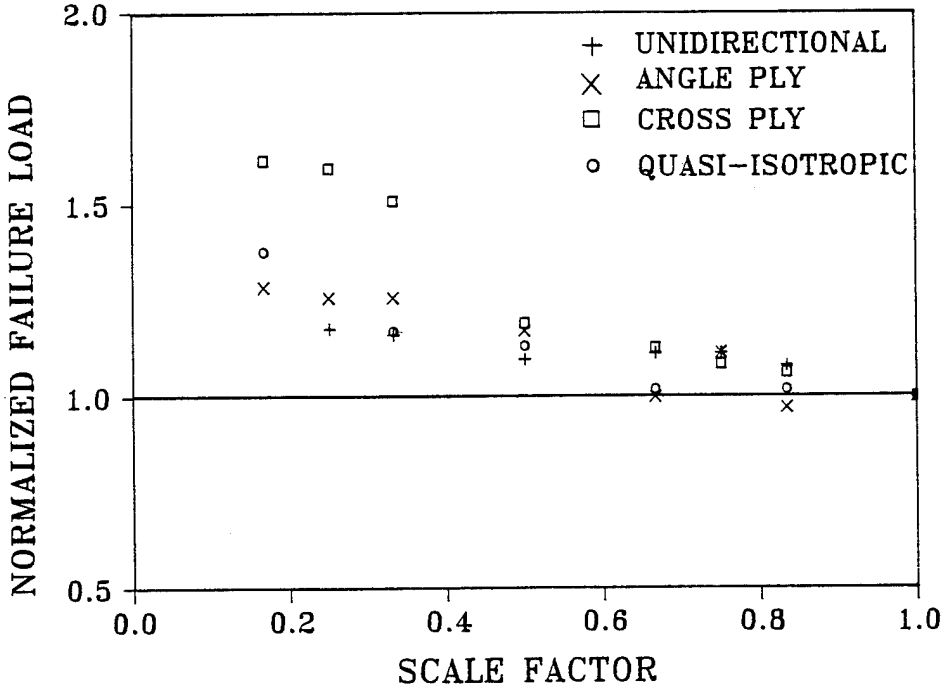


FIGURE 5. Normalized failure load versus scale factor for unidirectional, angle ply, cross ply, and quasi-isotropic beams tested under flexural loading.

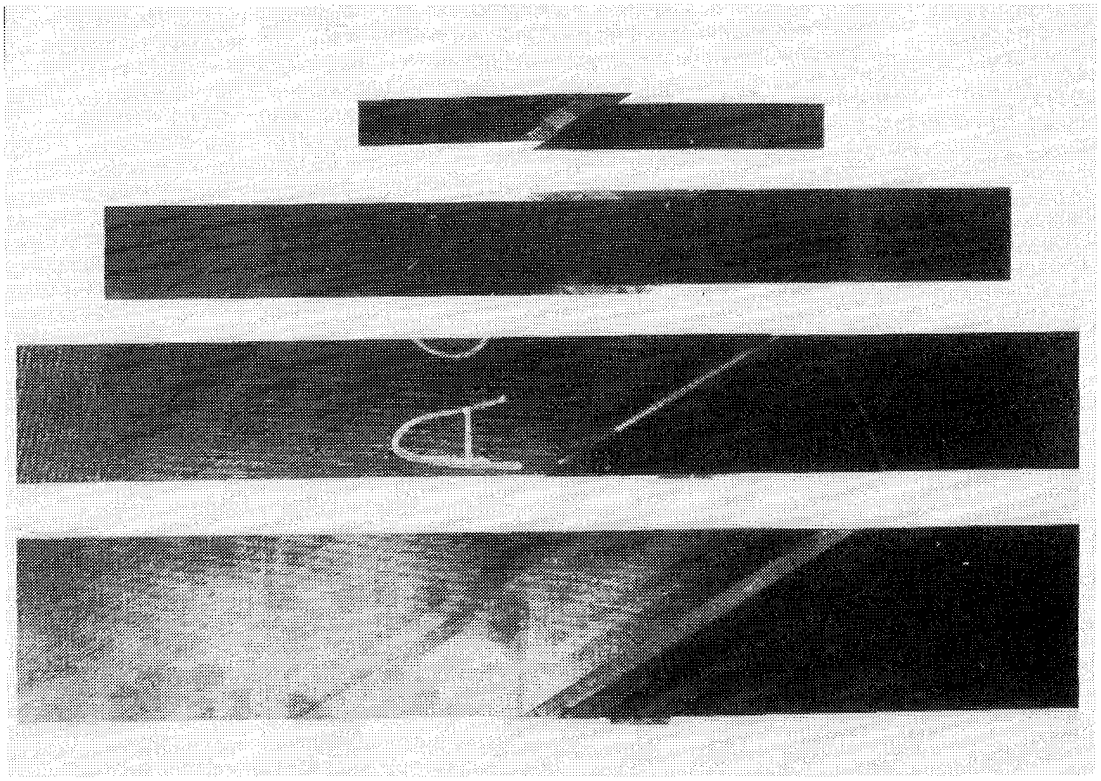


FIGURE 6. Typical failures in four scaled size specimens of Laminate A loaded in tension.

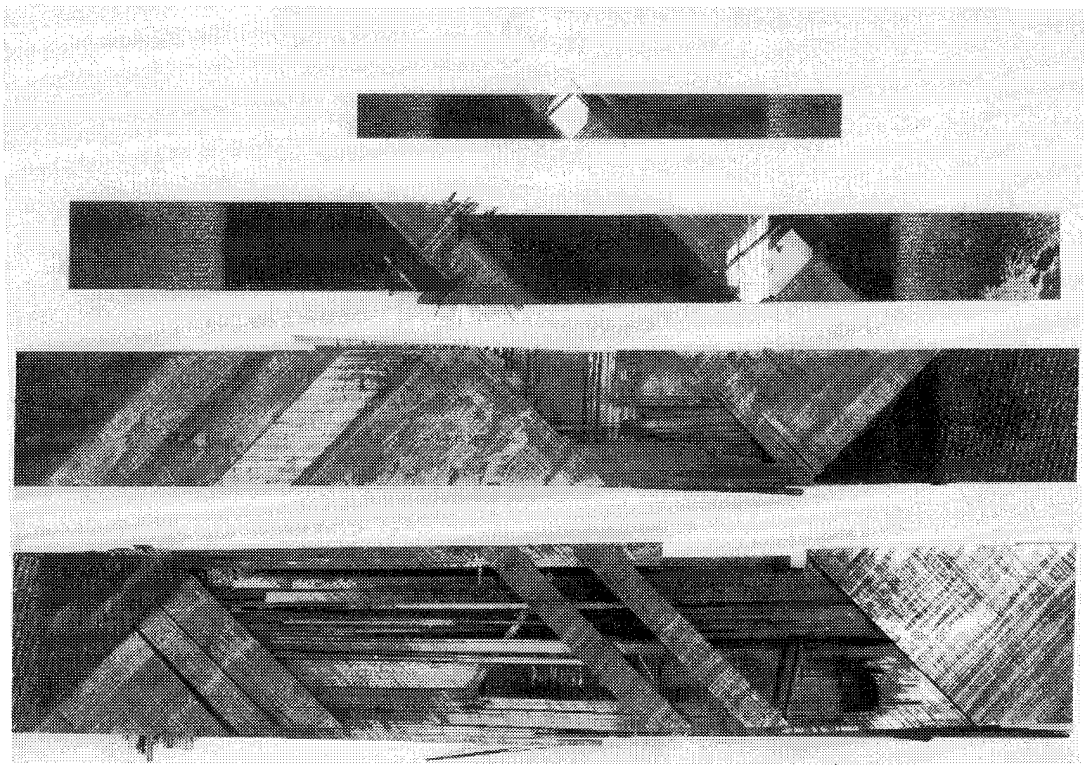


FIGURE 7. Typical failures in four scaled size specimens of Laminate B loaded in tension.

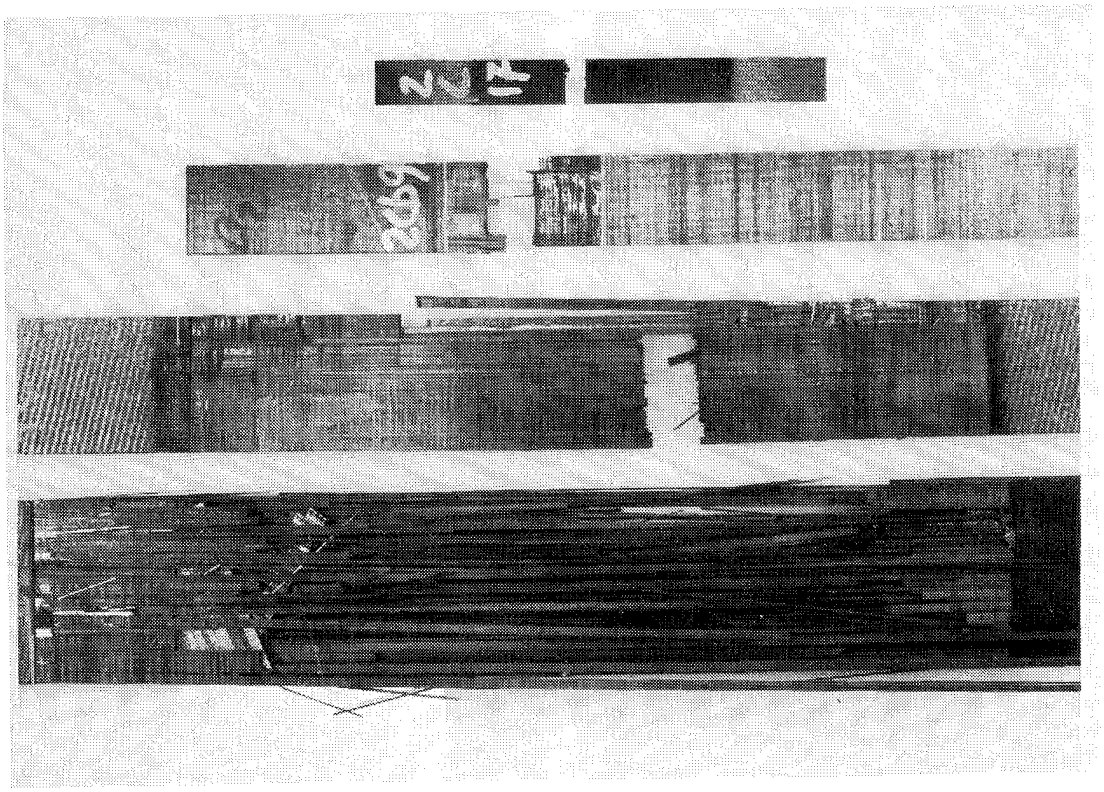


FIGURE 8. Typical failures in four scaled size specimens of Laminate C loaded in tension.

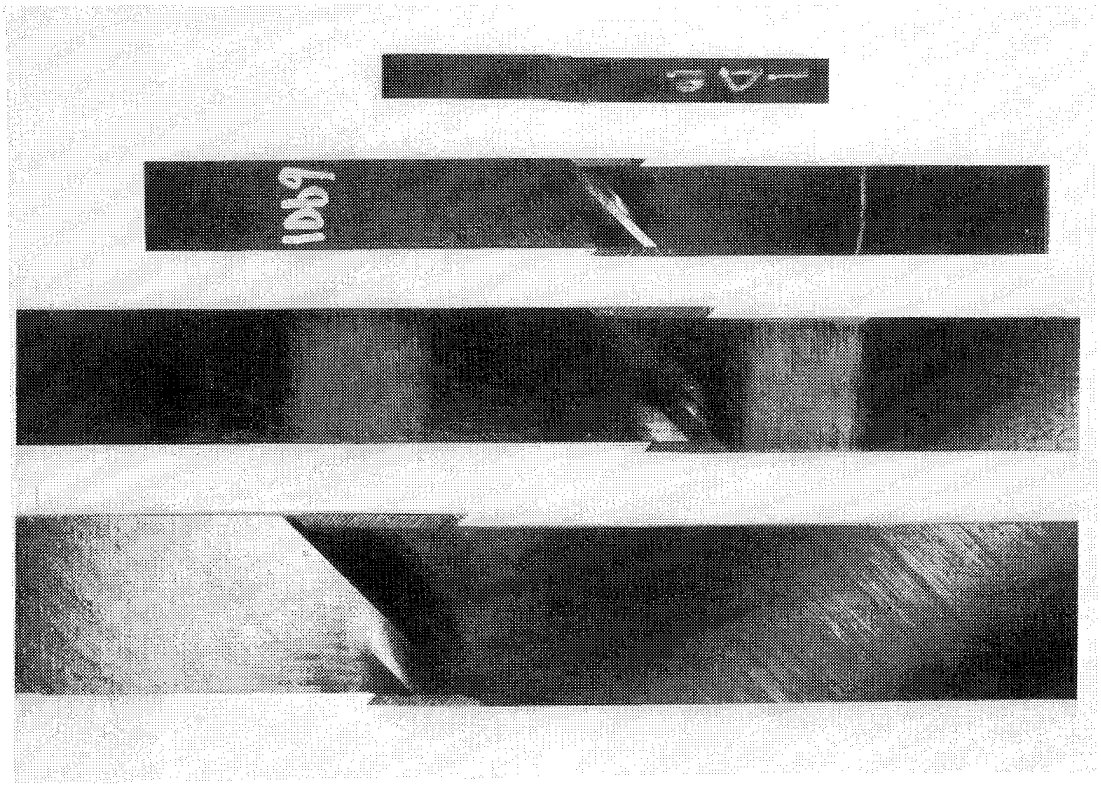


FIGURE 9. Typical failures in four scaled size specimens of Laminate D loaded in tension.

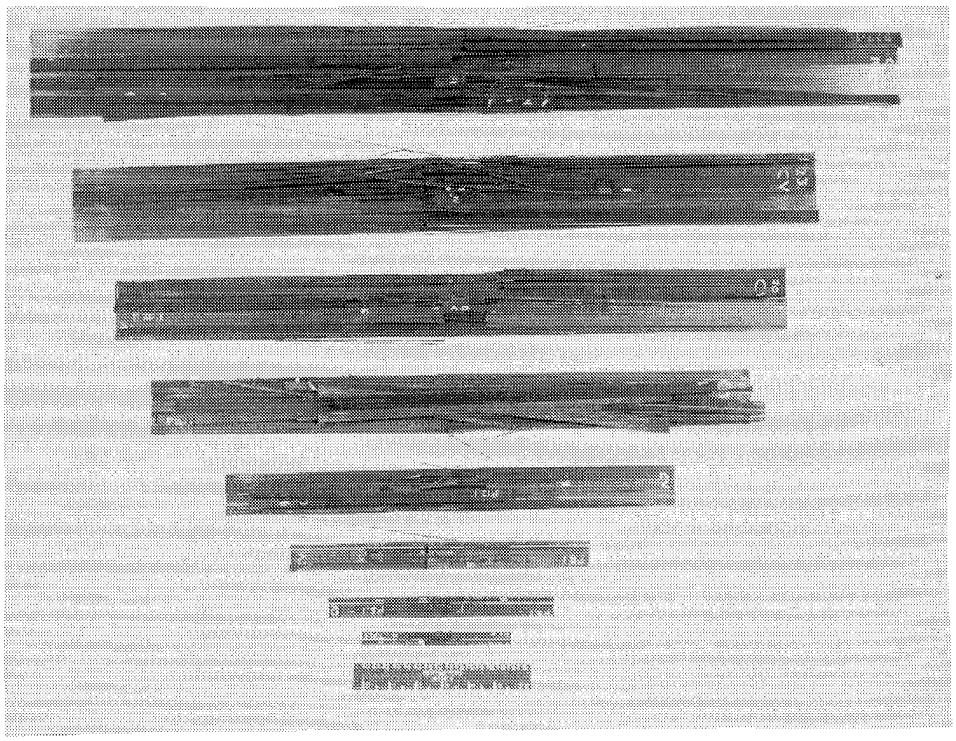


FIGURE 10. Failed unidirectional beams (1/6 through full-scale) tested under flexure.

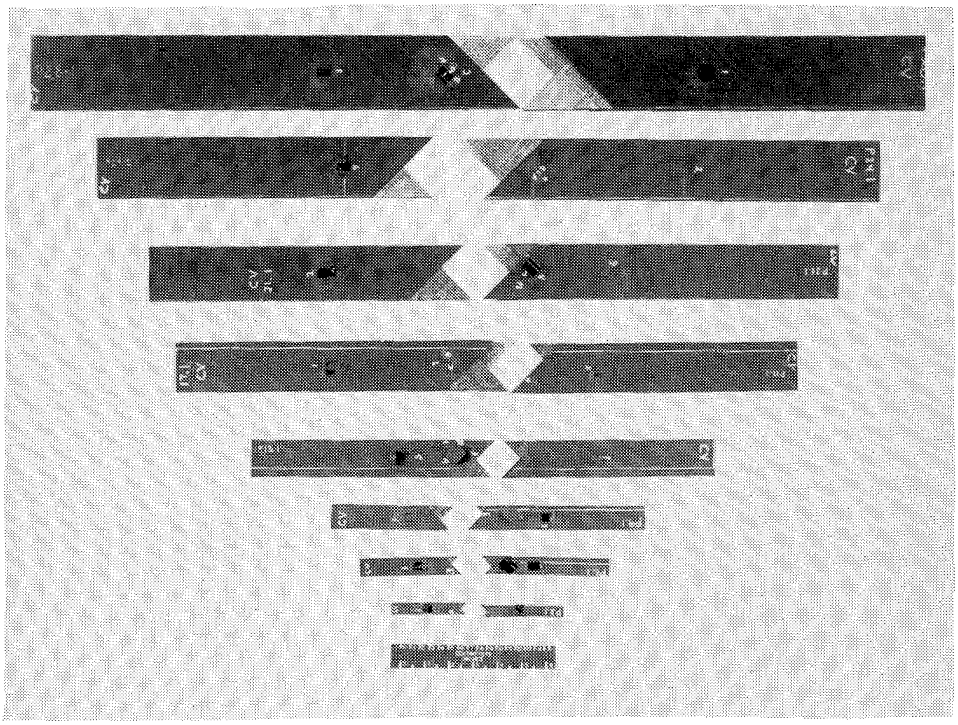


FIGURE 11. Failed angle ply beams (1/6 through full-scale) tested under flexure.

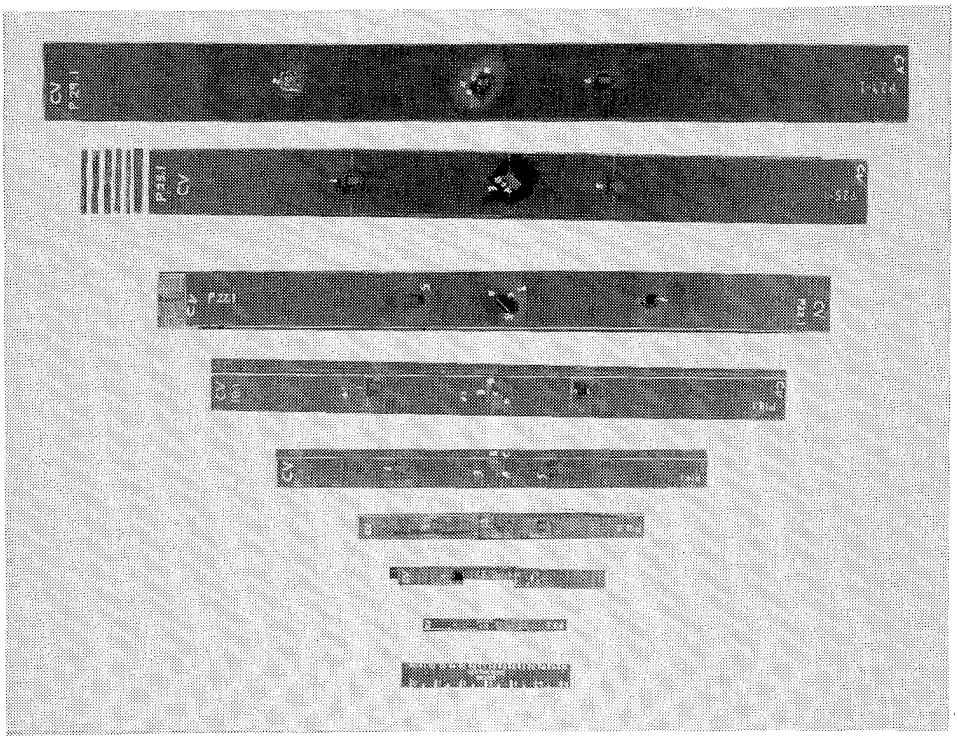


FIGURE 12. Failed cross ply beams (1/6 through full-scale) tested under flexure.

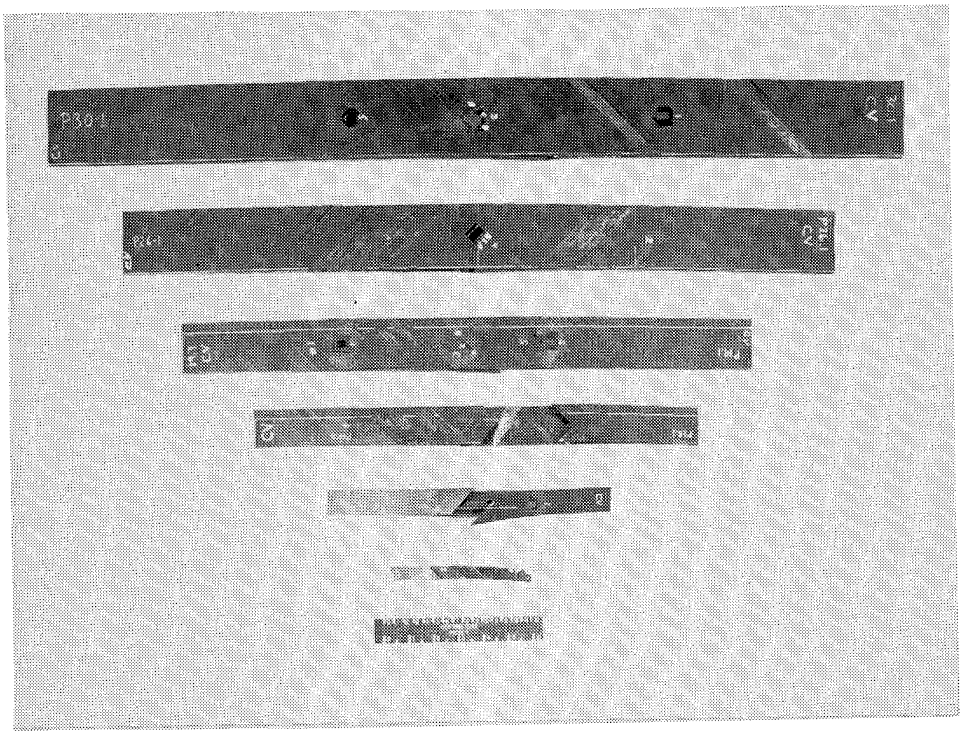


FIGURE 13. Failed quasi-isotropic ply beams (1/6 through full-scale) tested under flexure.

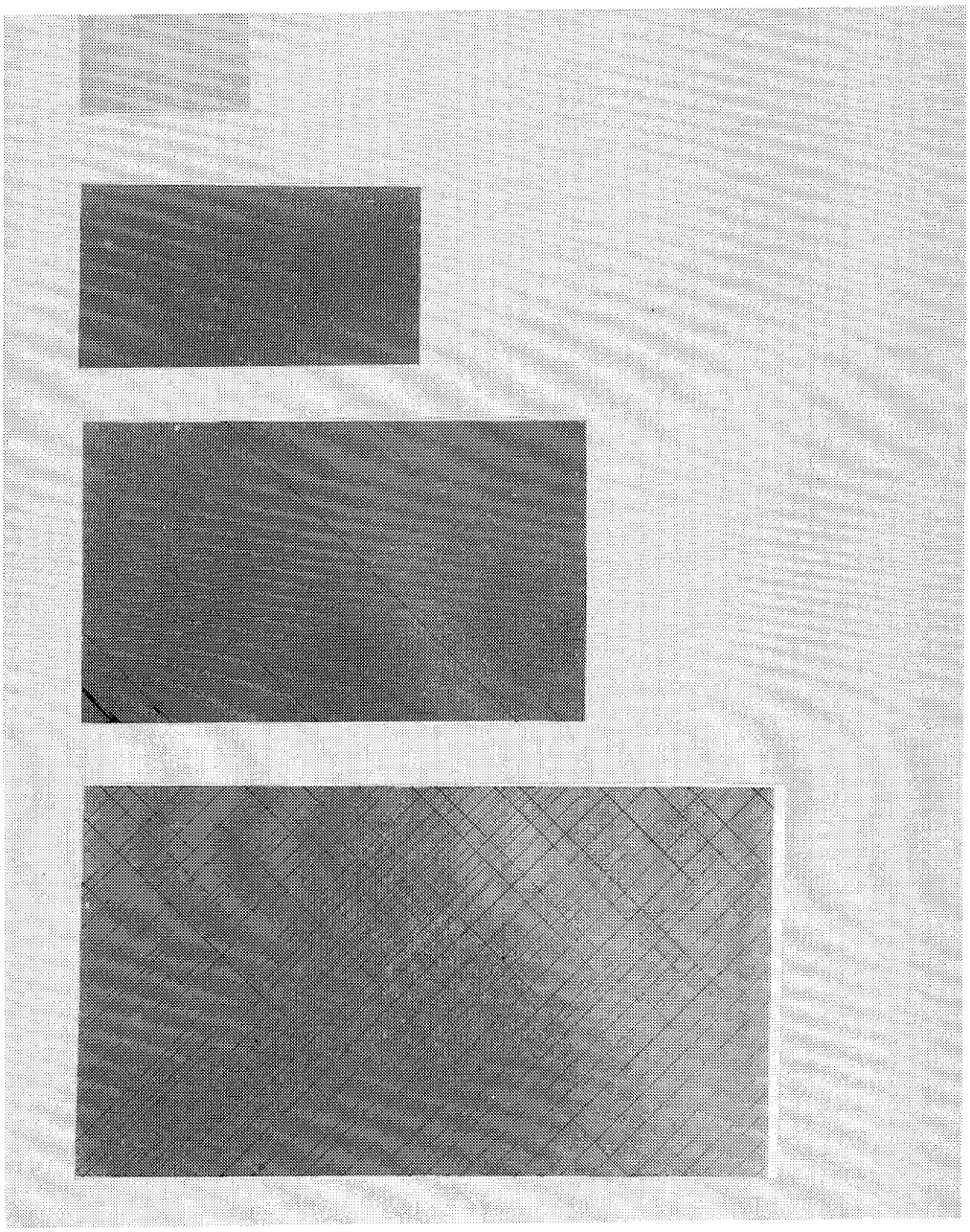


FIGURE 14. X-ray radiographs of virgin specimens of Laminate D.

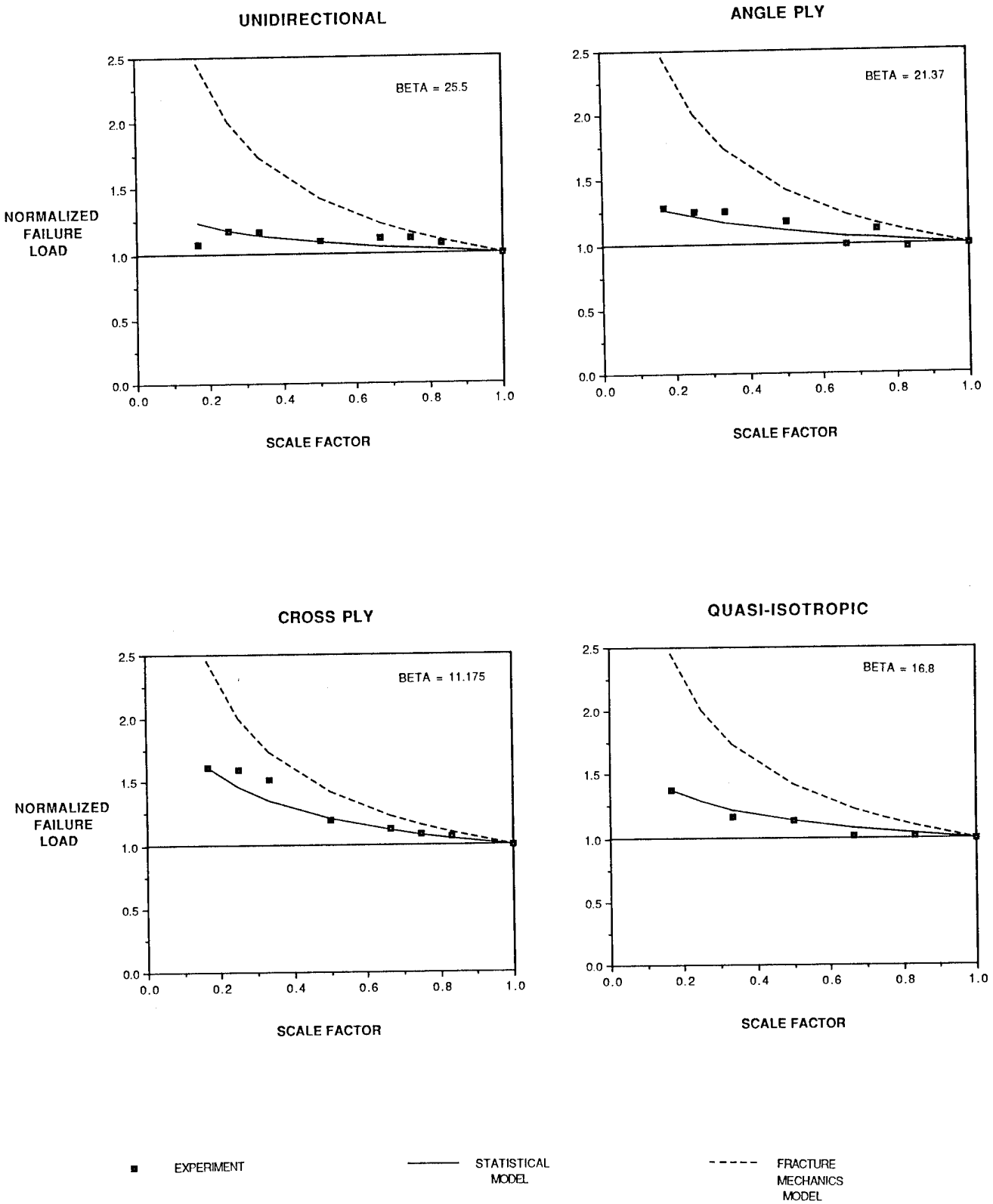


FIGURE 15. A comparison of normalized failure load versus scale factor with statistical and fracture mechanics based analytical models for unidirectional, angle ply, cross ply, and quasi-isotropic scale model beams tested under flexural loading.

AN OVERVIEW OF THE CRASH DYNAMICS FAILURE BEHAVIOR OF METAL AND COMPOSITE AIRCRAFT STRUCTURES

Huey D. Carden
NASA Langley Research Center
Hampton, VA

Richard L. Boitnott
U.S. Army Aerostructures Directorate
NASA Langley Research Center
Hampton, VA

Edwin L. Fasanella, and Lisa E. Jones
Lockheed Engineering and Sciences Company
Hampton, VA

SUMMARY

An overview of the failure behavior results is presented from some of the crash dynamics research conducted with concepts of aircraft elements and substructure not necessarily designed or optimized for energy absorption or crash loading considerations. To achieve desired new designs which incorporate improved energy absorption capabilities often requires an understanding of how more conventional designs behave under crash type loadings. Experimental and analytical data are presented which indicate some general trends in the failure behavior of a class of composite structures which include fuselage panels, fuselage sections, individual fuselage frames, skeleton subfloors with stringers and floor beams without skin covering, and subfloors with skin added to the frame-stringer structure. Although the behavior is complex, a strong similarity in the static/dynamic failure behavior among these structures is illustrated through photographs of the experimental results and through analytical data of generic composite structural models. It is believed that the thread of similarity in behavior is telling the designer and dynamist a great deal about what to expect in the crash behavior of these structures and can guide designs for improving the energy absorption and crash behavior of such structures.

INTRODUCTION

The NASA Langley Research Center has been involved in crash dynamics research for several years, dating to the early 1970's. For about 10 years the emphasis of the research was on metal aircraft structures during the General Aviation Crash Dynamics Program (References 1 to 13) and the Controlled Impact Demonstration (CID) Program, a transport aircraft program which culminated in the controlled crash test of a Boeing 720 aircraft in 1984 (References 14 to 16). Subsequent to the transport work, the emphasis has been on composite structures with efforts directed at developing a data base for understanding the behavior, responses, failure mechanisms, and general loads associated with the composite material systems under crash type loadings (See figure 1). Considerable research has been conducted into determining the energy absorption characteristics (References 17 to 20) which indicated that composites can absorb as much if not considerably more energy than comparable aluminum structures. Because of the brittle nature of the composites, attention must be given to proper geometry and designs which will take advantage of their good energy absorbing properties while at the same time providing desired structural integrity when the composites are fabricated into aircraft structural elements and substructures. To achieve the desired new designs often requires an understanding of how more conventional designs behave under crash loadings.

The purpose of this paper is to present an overview of data on the failure behavior from research conducted with concepts of aircraft elements and substructure not necessarily designed or optimized for energy absorption or crash loading considerations. Experimental and analytical data are presented which indicate some general trends in the failure behavior of a class of composite structures which include fuselage panels, fuselage sections, individual fuselage frames, skeleton subfloors with stringers and floor beams but without skin covering, and subfloors with skin added to the frame-stringer arrangement. Although the behavior is complex, a strong similarity in the static and dynamic failure behavior among these structures is illustrated through photographs of the experimental results and through analytical data of generic composite structural models. It is believed that the thread of similarity in behavior is telling the designer and dynamist a great deal about what to expect in the crash behavior of these structures and can guide designs for improving the energy absorption and crash behavior of such structures.

IMPACT DYNAMICS RESEARCH FACILITY

The information presented in this report was generated and published during the transport and composite aircraft components phases of the impact dynamics research programs at NASA Langley Research Center. The research reported herein (with one exception) was conducted by personnel at the Langley Impact Dynamics Research Facility (shown in figure 2) and with other testing equipment associated with the installation. The facility is the former Lunar Landing Facility used to train astronauts for moon landings. The facility is 230 feet high and 400 feet long. Three sets of legs on the sides and two on the east end support the upper levels of the gantry. Access to the top levels is provided through an elevator. In the early 1970's, the structure was converted for crash testing of full-scale general aviation aircraft. Reference 21 provides complete details of the facility and test techniques for full-scale aircraft testing. Figure 3 is a photograph of a 70 foot high Vertical Drop Test Apparatus used for full-scale aircraft section, components, and/or seat testing. Static testing machines, and other apparatus are also added capabilities at the facility for metal and composite aircraft structural testing.

ANALYSIS TOOLS

To gain understanding of fundamental phenomena and the physics of behavior, the experimental research with structures under crash loadings is generally accompanied by analytical prediction or correlation studies whenever feasible. Thus, various finite element codes which have capabilities for handling dynamic, large displacement, nonlinear response problems of metal and composite structures are used as tools in the research efforts.

DYCAST Computer Code

The analytical results presented in this overview were generated with a nonlinear finite element computer code called DYCAST (DYnamic Crash Analysis of STructures (Reference 22) developed by Grumman Aerospace Corporation with principal support from NASA and FAA. The basic element library consists of (1) stringers or rod elements with axial stiffness only; (2) three-dimensional beam elements with 12 fixed cross-sectional shapes typical of aircraft structures with axial, two shear, torsional, and two bending stiffnesses; (3) isotropic and orthotropic membrane skin triangles with membrane stiffnesses; (4) isotropic plate bending triangles with membrane and out-of-plane bending stiffnesses; and (5) nonlinear translational or rotational spring elements that provide stiffness with user-specified force-displacement or moment-rotation tables (piece-wise linear). The spring element can be either elastic or dissipative. The springs are useful to model crush behavior of components for which data are available and/or whose behavior may be too complex or time consuming to model otherwise. A contractual effort is underway to add curved composite beams, composite plate, and curved shell elements to the DYCAST element library.

TEST SPECIMENS AND DESCRIPTION

Full-Scale Metal Aircraft Structures

NASA Langley Research Center has conducted several tests of metal aircraft sections to support transport research efforts. Selected data on the crash behavior of full-scale metal transport category aircraft sections (References 23 and 24) are included in the present paper to demonstrate what appears to be important similarities in behavior noted not only with the metal fuselage structures but also in the composite structures discussed herein.

Two 12-foot long fuselage sections cut from an out-of-service Boeing 707 transport aircraft were drop tested to measure structural, seat and occupant responses to vertical crash loads and to provide data for nonlinear finite element modeling. One section was from a location forward of the aircraft wings and one was from aft of the wing location. Figure 4 presents a photograph of one of the sections suspended in the Vertical Drop Test Apparatus at the Impact Dynamics Research Facility. The sections were loaded with seats, anthropomorphic dummies, data acquisition system pallet, power pallet, cameras, and batteries to test not only structure, seat, and occupant responses but also to test the pallet equipment to be used in the full-scale transport crash conducted later. The reader should refer to the particular reports for more complete descriptions of the test articles since such information is not repeated in this report.

Composite Structures

Composite Fuselage Panel.-As part of the Aircraft Energy Efficiency (ACEE) Program, static and dynamic behavior of a lower fuselage composite structure was evaluated (reference 25). Development tests were performed on the composite structures to verify that the composite structure, designed to the same operating load as the metal design, could have at least the same energy absorption capability as aluminum structure. A photograph of the composite fuselage panel in the static testing machine (at Lockheed-California Company) is shown in figure 5 . Load-displacement and failure behavior determined for the corrugated frame/skin test panel are included herein for comparison with other composite structures. The frame/skin specimen had a 117.5 inch radius (to outside skin), was 60 inches long by 30 inches wide and had two corrugated frames on 20 inch spacing. Fabrication techniques and more complete details of the frame/skin panel are given in reference 25.

Single Composite Frames.- Various cross-sectional shapes for fuselage frames are used in metal aircraft and are often proposed for composite aircraft structures. Figure 6 presents sketches and photographs illustrating four of the more common geometries, I-, J-, C- and Z-cross sectional shapes of which several circular frames were fabricated for testing to add to the composite structures data base. To add out-of-plane stability to the frame concepts (with the exception of the Z-section frames), 3 1/2 inch wide skin material was added which enhanced the ease of testing of both symmetric and other antisymmetric sections. The skin, a $[\pm 45/0/90]_{2S}$ lay-up sixteen ply (.08 inches) thick, was cocured with the 6 foot diameter frames. The frames were constructed in two different heights, 1 1/4 inches high and 3/4 inches high, to investigate the effect of frame height on behavior and responses.

One of the first geometries to be studied under static and dynamic loadings was the Z-cross section. Figure 6(b) is a photograph of Z-cross section fuselage frames used in the initial studies of the behavior of composite structural elements under impact loads. Figure 7 shows a Z-frame suspended in the drop apparatus prior to testing. The apparatus was constructed with guide rails, a rear metal backstop, and a front Plexiglas sheet. During free-fall the specimen was guided, and the front and rear backstops prevented appreciable (but not all) out-of-plane bending or twisting during impact and allowed photographs/motion picture coverage through the front Plexiglas plate . The six-foot diameter frames were constructed of 280-5HA/3502, a five harness satin weave graphite fabric composite material. The height of the frame was 3 inches with a total width of 2.25 inches and was about 0.08 inches thick. Lay-up of the frames was quasi-isotropic. Initial tests were with 360° frames made from four 90°segments joined with splice plates as shown

in figure 6(b). Additional tests were conducted with half frames since the top half of the complete frames were undamaged in the tests.

The approach of studying simple structural elements and then moving to combinations of these elements into more complex substructures has been taken in the development of a data base on the dynamic response and behavior of composite aircraft structures. The approach parallels the one used during the general aviation and transport aircraft programs. Consequently, three composite subfloor structures were fabricated following the initial investigation of the Z-frames discussed above.

Subfloor Structures.- Figure 8 is a photograph of the skeleton and skinned subfloor specimens constructed with three of the single Z-section frames similar to those that were studied earlier. Pultruded J-stringers attached the three frames through metal clips and secondary bonding methods. Aluminum floor beams tied the top diameter of the frames together to form the lower half of the subfloor. Notches in the frames allowed the stringers to pass through the frames. Two subfloors without skin (called skeleton subfloors) were fabricated. A third specimen (called skinned subfloor) had a ±45 lay-up skin bonded and riveted to the frames to form the lower fuselage type structure.

RESULTS AND DISCUSSION

Figures 9 to 20 present results from the studies of full-scale aircraft structures, composite fuselage frames, and subfloors under static and/or dynamic loadings. Analytical results are also included which illustrate crash related behavior of some of the structures. Photographs are included which emphasize the failure behavior of the composite and metal aircraft components and show a strong similarity in their behavior. The behavior is thought to be an important aspect which must be considered in the design of new structures for improving the energy absorption and crash behavior of this type components and structural elements.

Full-Scale Metal Aircraft Structures

Experimental and analytical results from studies with full-scale transport category aircraft sections (References 23 and 24) are presented in figure 9.

Dynamic tests.- Structural damage and behavior of the transport aircraft structures resulting from the 20 ft/s drop tests is shown in figure 9(a) and (b). The damage to the transport sections was confined to the lower fuselage below the floor level. Under the vertical impact of 20 ft/s, all seven of the frames ruptured near the bottom impact point. Plastic hinges formed in each frame along both sides of the fuselage at about 50° up the circumference from the bottom contact point (See figure 9(c)). The upward movement of the lower fuselage was approximately 22-23 inches at the forward end and 18-19 inches at the rear for the section taken from forward of the wing location (figure 9(a)) whereas in the section from aft of the wing location (figure 9(b)), the crushing was about 14 inches forward and 18 inches in the rear. Although the aircraft structures are metal and the failures discussed above involve plastic deformations with some tearing of the metal rather than brittle fractures, the general observed failure pattern and locations for the transport fuselage sections will be shown to be quite similar to the results of the composite frames and subfloors discussed later.

Analytical studies.- A DYCAST model of the section (from forward of the wing location) was constructed with sufficient detail to model the floor, two seats with lumped mass occupants, and the fuselage structure to determine if such a model could predict the response of the complete section with fidelity. The geometry of the finite element model is shown in figure 10. Stiff ground springs simulated the concrete impact surface. Each frame of the fuselage below the floor was modeled with eight beam elements and floor and seat rails were also appropriate beam elements. Fuselage structure above the floor (not expected to fail) was modeled in less detail.

The predicted deformation pattern of the two frame model is shown in figure 11. As may be noted, the overall impression from the analytical model deformation pattern is quite similar to the visual behavior seen in the experiment shown in figure 9. The full section behavior was basically contained in the two frame model.

In the following sections the composite impact dynamics studies have taken the building block approach of utilizing a sequence of testing and analysis which begins with 'simpler' elements and moves to more 'complicated' components or substructures. As mentioned earlier, this approach was used in the General Aviation and Transport programs although the GA data base was being concurrently developed through full-scale testing. Eventually it is desired to add to the program the full-scale tests using currently available composite aircraft specimens and/or other full-scale structures that are designed and constructed for that purpose.

Composite Fuselage Panel Study

Static load-displacement data for the corrugated frame/skin specimen from the ACEE program and the failure behavior are shown in figure 12. Figure 12(a) indicates that the load increased linearly to failure whereupon the load dropped substantially as a result of fracturing of the corrugated frames at locations (0° and 6.2°) near the center (loading region) of the panel. Additionally, some delamination of the frame caps occurred during the loading. Once the panel was removed from the test apparatus, the snap-through condition of the skin was reversed as may be noted in the figure 12(b). The fractures of the corrugated frame and some delamination of the frame caps, mentioned above, are the only visible damage to the structure.

Composite Single Frame Studies

Static tests.- Figure 13 presents static results from tests of single composite Z-frames discussed in reference 26. A photograph of the static test apparatus in figure 13(a) shows that the splice plate was at the load point. The frame failed just outside the doubler splice plate area by a complete fracture across the Z-section. Load-deflection data and the location of failures of the frame are shown in figure 13(b). The load-deflection data show a saw-toothed behavior beginning with the essentially linear behavior of the frame up to initial failure with subsequent loading of the frame after failure being at a new, reduced stiffness for the damaged frame. Photographic data in figure 13(c) show that the initial failure was induced by a local buckling of the frame which occurred at about 18° from the bottom loading point outside the splice plate area. Second and third fractures occurred up the side at about 54° and 58° under continued loading as may be noted in the sketch at the right of figure 13(b). The sequence of events was local buckling near the splice plate induced out of plane deformations which led to a fracture of the section; the ends then remained in contact (jammed together under the compressive loads in the frame), the initial point of fracture moved vertically, essentially in a guided manner until two additional fractures occurred farther up the frame.

Static analytical studies.- To demonstrate analytically the apparent behavior of the frames under load (exclusive of the local buckling which actually initiated the failure in the static case), a DYCAST finite element model was constructed. For ease of analysis, an I-section was modeled from the specimens described in the "Single Composite Frame" section. The frame was loaded at the top and a simulated ground plane (ground contact springs) resisted the vertical movement of the frame during load application. Boundary conditions were imposed at the bottom node of the model to account for the symmetrical situation thus only half the frame had to be modeled. The top node was constrained to allow only vertical displacement thus simulating the effect of a very stiff floor across the frame diameter. The static load was slowly increased until an input failure strain for the material (0.0086) was exceeded at the point of loading and failure was indicated. The curve labeled case I, *unbroken frame,* in figure 14(a) is the load-deflection plot for this case.

An examination of the normalized distribution of the bending moment on the frame shown in figure 14(b) provides insight and a better understanding of the failure/behavior. Maximum moments are indicated (just prior to failure) to be at the 0° location and between 50°-60° from the bottom contact area. The locations correlate well with the failure locations in the experiment with the Z-frame.

A second DYCAST model, case II, was also run wherein the bottom point of the frame was modeled with two short skin segments to represent the different structural condition following the initial failure of the frame. This condition will be discussed further, relative to the composite subfloor test with the skinned subfloor specimen. The curve in figure 14(a) labeled case II, *broken frame,* is the load-deflection response for this frame-loading case. Initially, the frame load increases to the point of failure at the bottom of the frame. After the frame fractures, the structure (boundary) changes to one considerably weakened--down to the bending stiffness of the skin alone at that location. The load therefore drops to the lower curve which represents the stiffness of the section with the weakened boundary on the bottom end of the frame, as indicated by the dashed vertical line between the case I curve and the case II curve. The load continues to increase again along the *broken frame* case until a failure at some other locations on the frame circumference occurs, thus repeating the cycle.

Figure 14(c) presents the normalized bending moment distribution on the broken frame. As may be noted, the distribution is quite similar to the initial model results in figure 14(b). The failure location is at the maximum bending moment location predicted to be about 45° which is somewhat lower than the same location shown in the initial model of the unbroken frame. The agreement between the two models, however, is still considered good. The effect of diameter on the moment distribution of the frame was assessed with a model having a 75 inch diameter (twice the initial diameter). The distribution was identical to the smaller diameter results; however, the loads producing the moments differed between the two models (as expected).

A comparison of the analytical cases (figure 14(a)) with the actual static load-deflection of the Z-section (figure 13(b)) indicates very similar load-deflection behavior patterns as discussed above. Although the Z-frame had no skin, if the ends jam together (as they did in several cases), the boundary is effectively between the skin stiffened case and a guided boundary. Thus, the predicted failure location in the simple beam-frame model at about 50° (See figure 14(b)) agrees well with the 54° and 58° failure locations in the experiment with the Z-section frame.

Without a priori knowledge of the manner of the failure noted and discussed above, the initial formulation of a finite element model would unlikely incorporate the necessary failure mechanism/behavior for the frames. However, knowing the pattern of behavior can enable the analysts to formulate adequate finite element models to predict dynamic responses including the failure/loads. Additionally, such information is important to designers of new structures to be able to design for impact loads on such structural elements of an aircraft fuselage.

Dynamic tests.- Figure 15 presents results from the dynamic studies of the response of composite frames (Reference 27). As noted in figure 15(a) or (b), the splice plates joining the segments of the frame are ±45° up the circumference from the point of impact. As shown in figure 15(b) complete failures (fractures) of the Z-section frames occurred at the bottom and approximately ±60° from the bottom. Potentially, it appears that the presence of the splice plates may have influenced the locations by moving the top failure points up a few degrees to about the ±60° locations.

Composite Subfloor Studies

For the three composite subfloor specimens used for impact studies, two static and two dynamic tests were conducted on the subfloors. With the skeleton subfloor, both a static and a dynamic test to destruction was conducted. With the skinned subfloor, a nondestructive static test followed by a dynamic test to failure was conducted.

Static tests.- Figure 16 presents experimental results (Reference 28) of the skeleton subfloor specimen following a static test. As noted in figure 16(a) and (b), failures on the three Z-section frames occurred at 13 discrete locations. Unlike the unnotched single Z-frame, the failures in this specimen occurred at notches (which served as stress risers) in the frame through which the stringer passed. However, as shown in figure 16(b) the failures were still near the point of load application (approximately 11°) and at other circumferential

locations of approximately 45-68°. In the absence of skin material, twisting and bending out-of-plane occurred with the frames. The stringers had minimal effect on the subfloor response with the exception of maintaining the lateral spacing of the three Z-frames.

Dynamic tests.- Figure 17 shows the skeleton subfloor after an impact test onto a concrete surface at 20 feet per second. In the dynamic test of the skeleton subfloor, fractures were produced at notches in the frames (Figure 17(a)). The locations, shown in figure 17(b), were also near the point of impact (about 11° because of the splice plate) and at two other locations up the circumference of the frames (±45° and ±78°) and involve all three frames for a total of 15 fractures. The impact energy exceeded the energy absorbed by the local fractures and the floor bottomed out in the impact. Figure 17(c) is a normalized strain distribution measured on the first (end) frame during the dynamic test just before first failure. A comparison of the distribution to the moment distribution of Figure 14(b) and (c) shows essentially identical shape between the single frame and skeleton frame distributions. Maximums at 0° and at approximately ±50° to 55° agree well with the analytically predicted locations on the frame.

Figure 18 presents impact results for the subfloor with skin after an impact of 20 feet per second. Figure 18(a) is the subfloor specimen after the test. Points of failure of the frames in this specimen are indicated in figure 18(b). Again the points of failure are at/near the impact point (within 12°) and on the circumference at about ±56° up both sides of the frame on the middle and back frame and 11°, 22.5° and 45° on the front frame. It was observed that the subfloor impacted first on the front area which possibly explains the 11° and 22.5° fractures being different from the other locations. Again all three frames were involved in the failures. Some delamination of the frames from the skin was evident but the skin remained intact. Figure 18(c) is a normalized strain distribution (just prior to first failure) measured on the first (end) frame during the dynamic test. A comparison of the distribution to the moment distribution of Figure 14(b) and (c) and the strain distribution in Figure 18(c) shows essentially identical shape as the single frame and skeleton frame distributions. As was the case for the skeleton subfloor maximums at 0° and at approximately ±50° to 55° agree well with the analytically predicted locations on the frame.

As mentioned previously in the frame studies, once the frames fail at or near the point of impact the broken ends of the frame often jammed together and moved upward in a guided manner. In the subfloor structure, the frames may still fail completely across the section, but the skin remains intact and serves as a much less stiff boundary condition for the broken frames as the deflection increases. Little energy is involved in snapping the skin through as the load increases on the structure (See reference 29 on snap-through of composite arches). In this manner, the structural stiffness of the frame/skin before fracture changes to the skin only at the location of frame fracture. The analytical models discussed under the static frame response/behavior simulated this type of behavior.

Analytical studies.-The contribution of the skin to the stiffness of the section with the antisymmetric frames is illustrated in figure 19. Static load-deflection data for the unskinned subfloor and the skinned subfloor along with the DYCAST predictions are shown in the figure. It can be noted that the subfloor stiffness (with skin) is approximately three times the stiffness of the skeleton subfloor, thus the skin's contribution to the structure is to maintain in-plane deflections of the non-symmetrical Z-section and prevent any substantial twisting of the frames. Out-of-plane bending and twist were allowed in the skeleton subfloor predictions. As a further note of interest, if for the skeleton subfloor, load in the load-deflection results (with three frames) is reduced by a factor of three, good correlation with single frame data is evident.

General Observations

The response behavior determined during the studies of full-scale aircraft sections, fuselage panels, fuselage frames, and subfloors are summarized in figure 20. Figure 20(a) shows normalized moment distribution on a representative frame of the various specimens and Figure 20(b) shows the failure locations which were noted from static or dynamic tests. The visual impression is quite striking among the various specimens. It is suggested that from the results of simpler frames to the more complex subfloors and full-scale sections, a strong similarity is evident in the failure behavior of the structures. The structures share in

common the generally circular or cylindrical shape, the normal loading situations, and what appears to be a similar pattern of failure behavior. Analytical models of frame structures under vertical loads have moment distributions which have maximums at the point of loading and at approximately ±45° to 50° (depending on boundary conditions) around the circumference from the ground contact point. Failures of the structures were noted at these same locations. Such observations can help dynamists gain a better understanding of what to expect from such structures in crash-loading situations, can guide designers of new structures to better account for the vertical crash loads, and allow better energy absorption to be included in the new designs. Additionally, the observations can help analysts better model the aircraft structures for predicting the failure responses and behavior under crash situations. The latter task is a difficult and challenging one, not only for composite structures but for metal structures as well. Studies are currently underway to improve the analysis capabilities of code and to add composite elements to finite element libraries such as the DYCAST program. In addition, new analysis approaches are being explored through grants to universities as an extension of NASA Langley Research Center's efforts.

CONCLUDING REMARKS AND OBSERVATIONS

Some unique failure behavior results from the research with composite full-scale aircraft sections, composite structural elements, and subfloors have been presented. Some observations on the failure behavior of these structures have been made and discussed and analytical results have been included to help explain some of the behavior noted.

From the observations made in the overview the following conclusions are made:

(1) Starting with simple representative structural elements and moving to more complex components can often provide better understanding of the complex local and global structural responses and behavior.

(2) Unique failure behavior patterns were found to be common among full-scale fuselage panels, aircraft sections, composite frames, and subfloors with and without skin.

(3) General locations of failures appear to occur at the same structural regions among the specimens as a result of similar geometry (cylindrical shape), similar loading (vertical), and similar moment distribution on the structures under vertical loads.

(4) Noted failures were located in the same regions as the maximums in the moment (strain) distribution on the structures.

(5) The shape of the distribution of the moment was independent of the size (diameter) of the frame/component. Loads, however, which produced the failures varied with the structural size.

Based upon the conclusions drawn from the various research efforts discussed in this paper, the following observations are also summarized:

(1) The general similarity of the failure behavior among the aircraft structures can

(a) assist the designer and dynamist to better anticipate how the structures probably will fail.

(b) provide guidance on how and where to incorporate and/or optimize better energy absorption into new aircraft structural designs.

(c) aid analysts to better model the structures for predicting failure/loads behavior under crash situations.

(2) To analytically predict, in a dynamic loading situation, such complex failure events and the loads which initiate the failures as noted in the composite structural elements and sub-components is a challenge.

(3) Composite curved beam, composite plate, and shell elements that are being developed and included in finite element code should improve the capability to analyze composite type structures.

REFERENCES

1. Alfaro-Bou, Emilio; and Vaughan, Victor L., Jr.: Light Airplane Crash Tests at Impact Velocities of 13 and 27 m/sec. NASA TP 1042, November 1977.

2. Castle, Claude B.; and Alfaro-Bou, Emilio: Light Airplane Crash Tests at Three Flight-Path Angles. NASA TP 1210, June 1978.

3. Hayduk, Robert J.: Comparative Analysis of PA-31-350 Chieftain (N44LV) Accident and NASA Crash Test Data. NASA TM 80102, October 1979.

4. Castle, Claude B.; and Alfaro-Bou, Emilio: Light Airplane Crash Tests at Three Roll Angles. NASA TP 1477, October 1979.

5. Vaughan, Victor L., Jr.; and Alfaro-Bou, Emilio: Light Airplane Crash Tests at Three Pitch Angles. NASA TP 1481, November 1979.

6. Vaughan, Victor L., Jr.; and Hayduk, Robert J.: Crash Tests of Four Identical High-Wing Single-Engine Airplanes. NASA TP 1699, August 1980.

7. Carden, Huey D.; and Hayduk, Robert J.: Aircraft Subfloor Response to Crash Loadings. SAE Paper 810614, April 1981.

8. Williams, M. Susan; and Fasanella, Edwin L.: Crash Tests of Four Low-Wing Twin-Engine Airplanes with Truss-Reinforced Fuselage Structure. NASA TP 2070, September 1982.

9. Carden, Huey D.: Correlation and Assessment of Structural Airplane Crash Data with Flight Parameters at Impact. NASA TP 2083, November 1982.

10. Carden, Huey D.: Impulse Analysis of Airplane Crash Data with Consideration Given to Human Tolerance. SAE Paper 830748, April 1983.

11. Castle, Claude B.; and Alfaro-Bou, Emilio: Crash Tests of Three Identical Low-Wing Single-Engine Airplanes. NASA TP 2190, September 1983.

12. Thomson, Robert G.; Carden, Huey D.; and Hayduk, Robert J.: Survey of NASA Research on Crash Dynamics. NASA TP 2298, April 1984.

13. Carden, Huey D.: Full-Scale Crash Test Evaluation of Two Load-Limiting Subfloors for General Aviation Airframes. NASA TP 2380, December 1984.

14. Hayduk, Robert J.(Editor): Full-Scale Transport Controlled Impact Demonstration. NASA CP 2395, April 1985.

15. Fasanella, Edwin L.; Widmayer, E.; and Robinson, M. P.: Structural Analysis of the Controlled Impact Demonstration of a Jet Transport Airplane. AIAA Paper 86-0939-CP, May 1986.

16. Fasanella, Edwin L.; Alfaro-Bou, Emilio; and Hayduk, Robert J.: Impact Data from a Transport Aircraft During a Controlled Impact Demonstration. NASA TP 2589, September 1986.

17. Farley, Gary L.: Energy Absorption of Composite Materials. NASA TM 84638, AVRADCOM TR-83-B-2, 1983.

18. Bannerman, D.C.; and Kindervater, C.M.: Crashworthiness Investigation of Composite Aircraft Subfloor Beam Sections. IB 435-84/3(1984), Deutsche Forschungs-und Versuchasanstalt fur Luft- und Raumfarht, February 1984.

19. Cronkhite, J.D.; Chung, Y.T.; and Bark, L.W.: Crashworthy Composite Structures. ASAAVSCOM TR-87-D10, U.S. Army, December 1987. (Available from DTIC as AD B121 522.)

20. Jones, Lisa E.; and Carden, Huey D.: Evaluation of Energy Absorption of New Concepts of Aircraft Composite Subfloor Intersections. NASA TP 2951, November 1989.

21. Vaughan, Victor L.; and Alfaro-Bou, Emilio: Impact Dynamics Research Facility for Full-Scale Aircraft Crash Testing. NASA TN D-8179, April 1976.

22. Pifko, A.B.; Winter, R.; and Ogilvie, P.L.: DYCAST - A Finite Element Program for the Crash Analysis of Structures. NASA CR 4040, January 1987.

23. Williams, M. Susan; and Hayduk, Robert J.: Vertical Drop Test of a Transport Fuselage Section Located Forward of the Wing. NASA TM 85679, August 1983.

24. Fasanella, Edwin, L.; and Alfaro-Bou, Emilio: Vertical Drop Test of a Transport Fuselage Section Located Aft of the Wing. NASA TM 89025, September 1986.

25. Jackson, A.C.; Balena, F.J.; LaBarge, W.L.; Pei, G.; Pitman, W.A.; and Wittlin, G.: Transport Composite Fuselage Technology--Impact Dynamics and Acoustic Transmission. NASA CR 4035, Contract NAS1-17698, December 1986.

26. Boitnott, Richard L.; and Kindervater, Cristof: Crashworthy Design of Helicopter Composite Airframe Structure. Fifteenth European Rotorcraft Forum, Amsterdam, Holland, Paper Nr; 93, September 1989.

27. Boitnott, Richard L.; Fasanella, Edwin L.; Calton, Lisa E.; and Carden, Huey D.: Impact Response of Composite Fuselage Frames. SAE Paper 871009, April 1987.

28. Boitnott, Richard L.; and Fasanella, Edwin L.: Impact Evaluation of Composite Floor Sections. SAE Paper 891018, General Aviation Aircraft Meeting and Exposition, Wichita, Kansas, April 1989.

29. Carper, Douglas M.; Hyer, Michael W.; and Johnson, Eric R.: Large Deformation Behavior of Long Shallow Cylindrical Composite Panels. Virginia Polytechnic Institute and State University, VPI-E-83-37, September 1983.

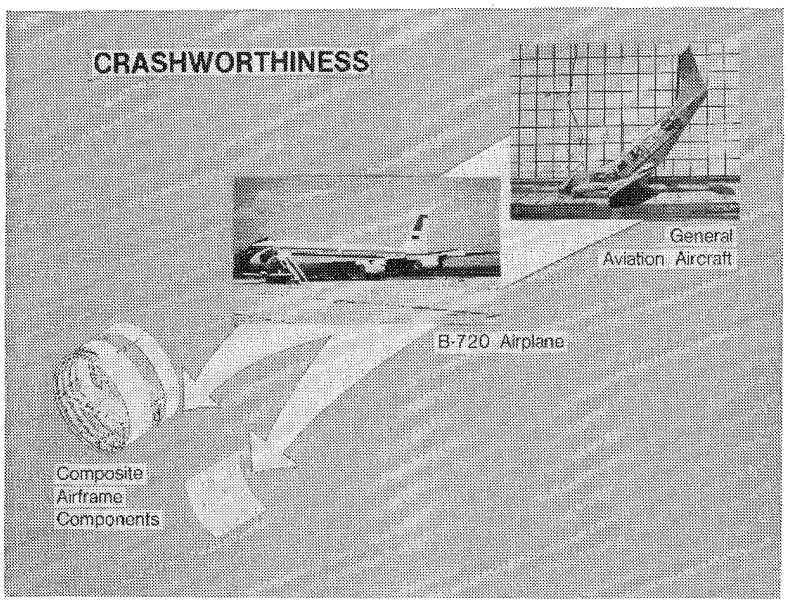


Figure 1.- Progression of research areas in crash dynamics at NASA Langley Research Center.

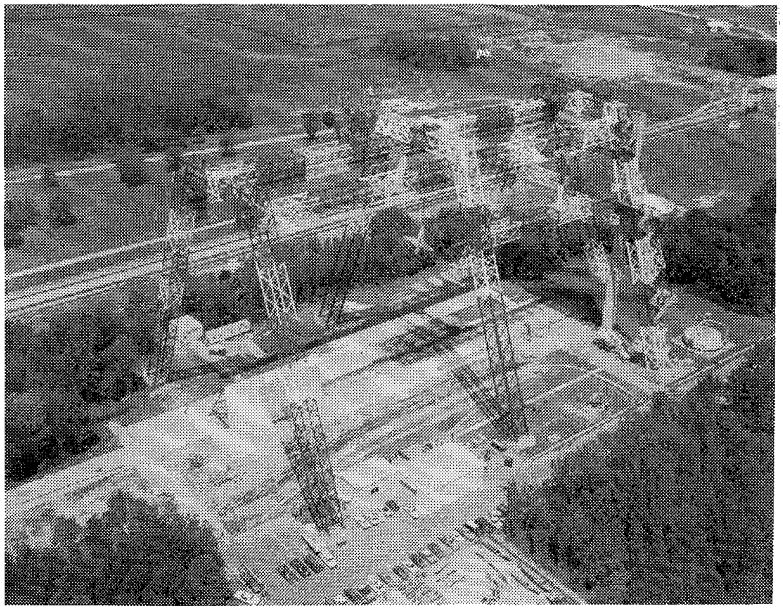


Figure 2. - Impact Dynamics Research Facility (IDRF) a NASA Langley Research Center.

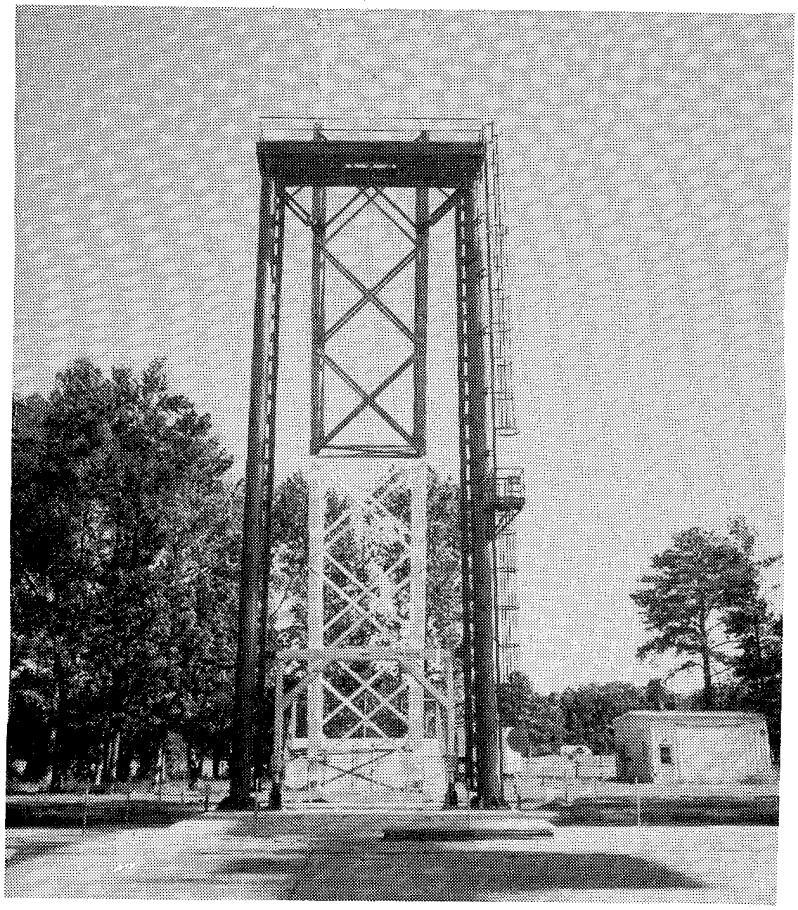


Figure 3. - 70 Foot Vertical Drop Test Apparatus.

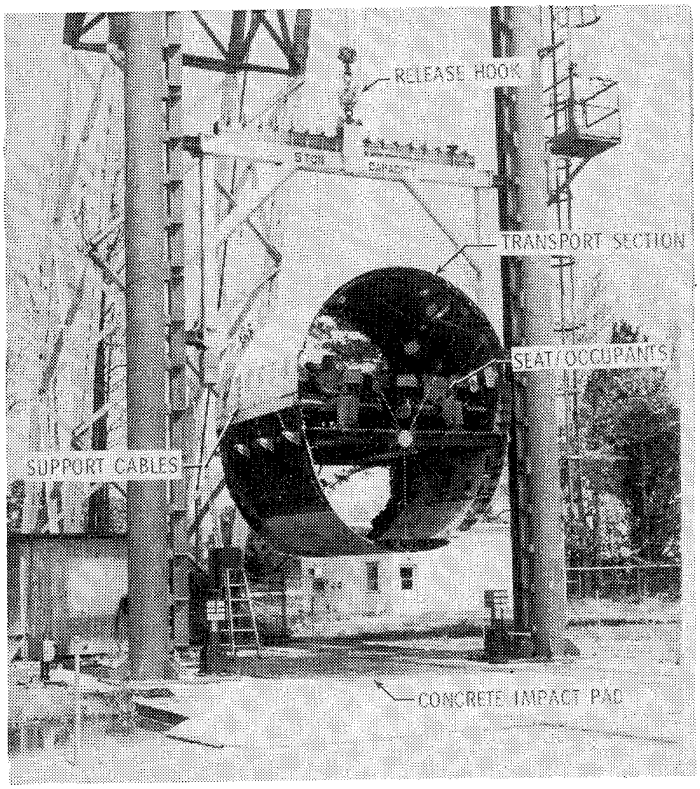


Figure 4. - Metal transport section suspended in Vertical Test Apparatus.

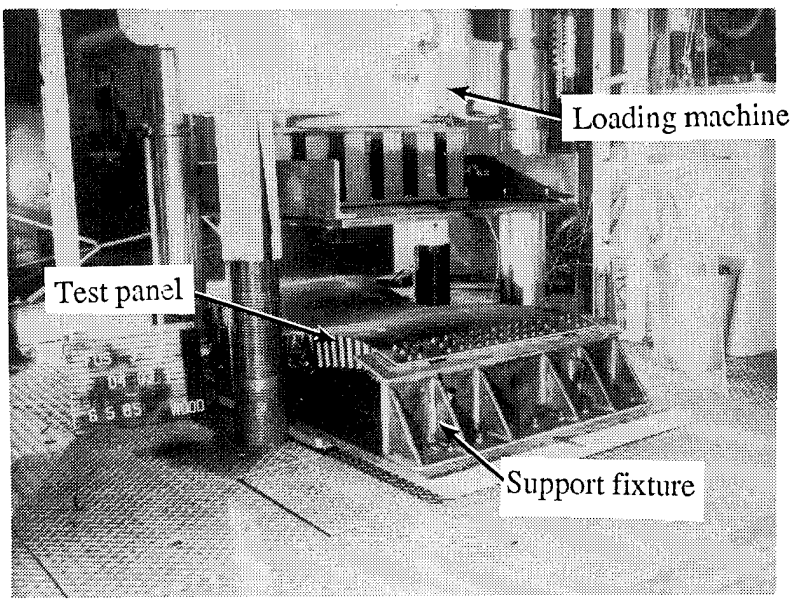
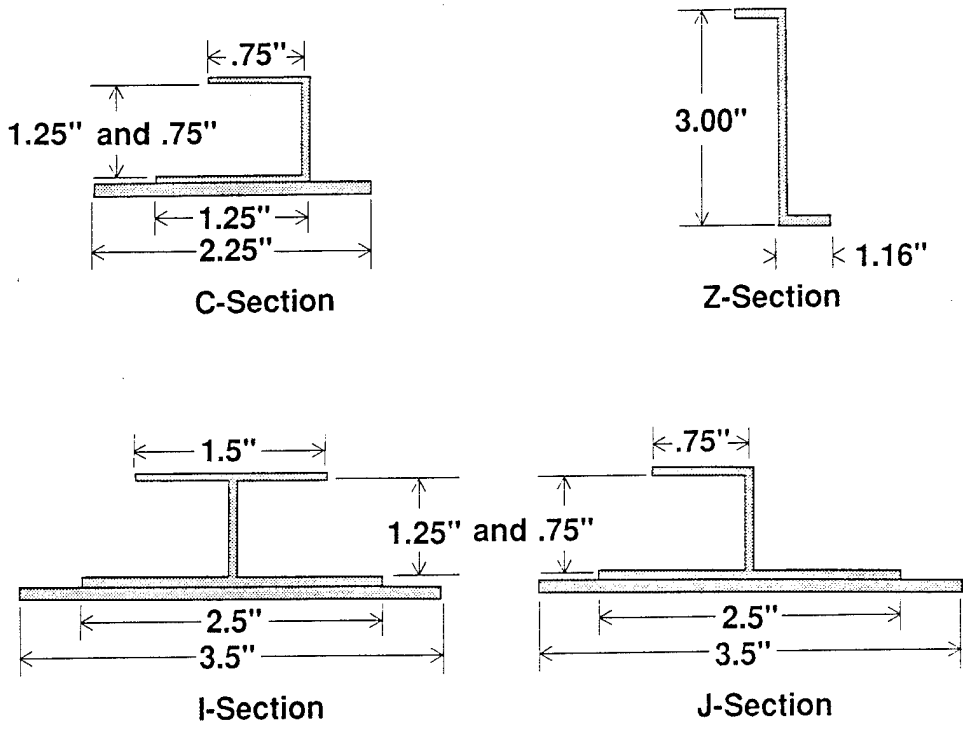
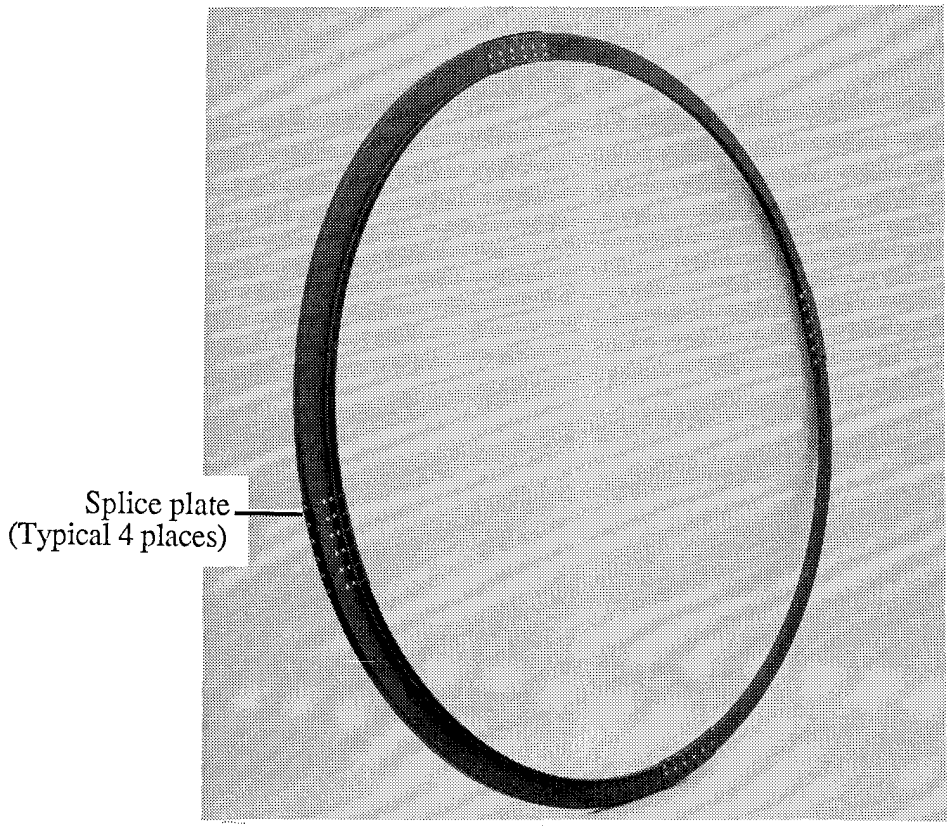


Figure 5.- Composite fuselage panel in static test machine. Panel from Aircraft Energy Efficieny (ACEE) Program. Photo courtesy of Lockheed-California Company.



(a) Cross-sectional dimensions.

Figure 6.- Various cross-sectional shapes of composite fuselage frames.



(b) Z-cross section fuselage frame.

Figure 6.- Concluded.

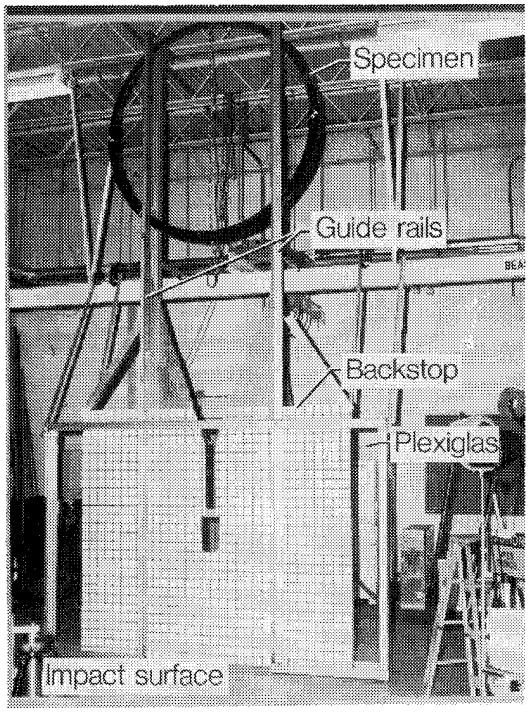


Figure 7.- Composite Z-frame in drop apparatus.

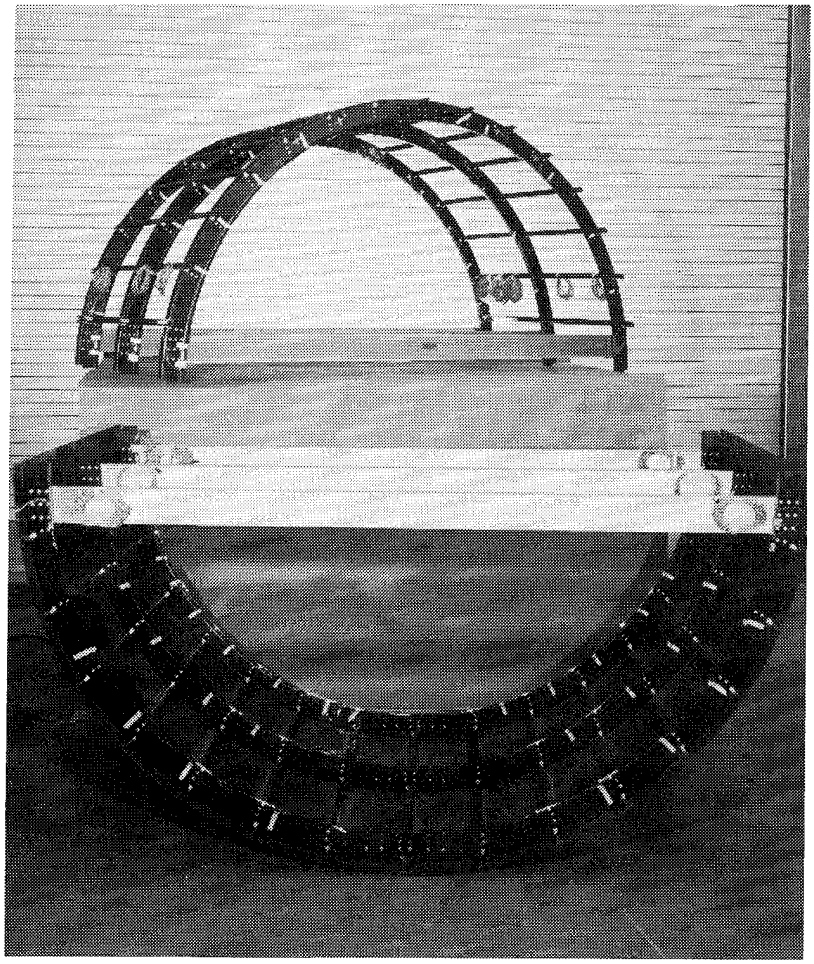
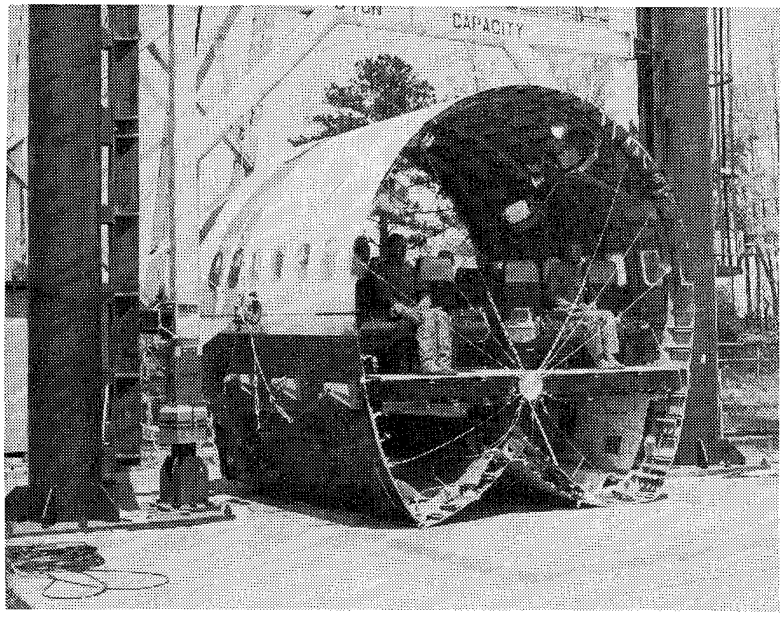
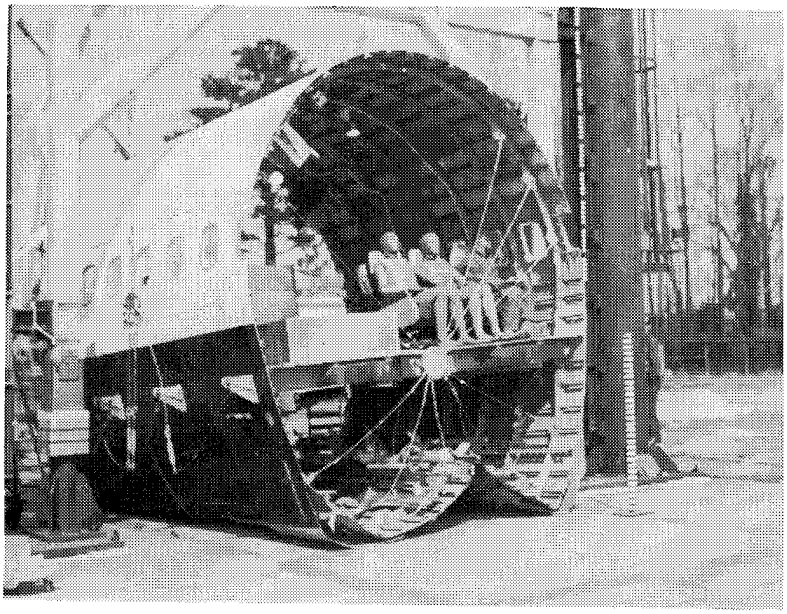


Figure 8.- Composite subfloor sections (skeleton/unskinned (top), skinned (bottom)).

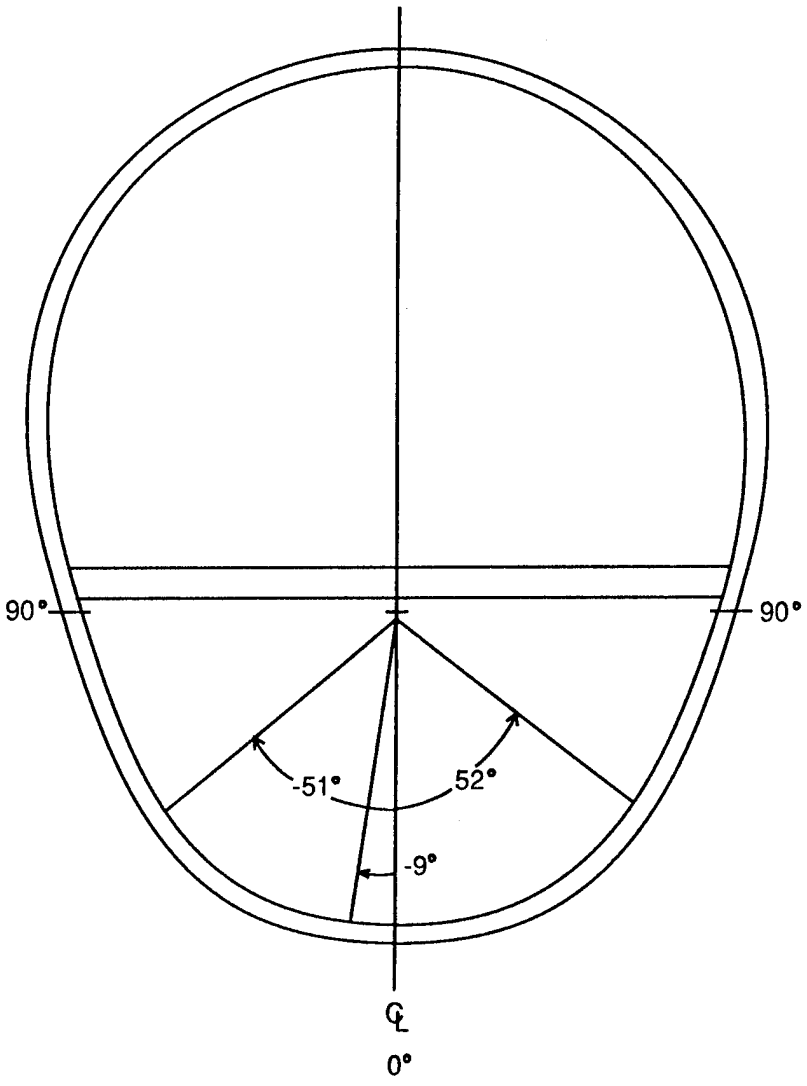


(a) Section from forward of wing.



(b) Section from aft of wing.

Figure 9.- Structural damage to metal aircraft structures.



(c) Angular location of failures.

Figure 9.- Concluded.

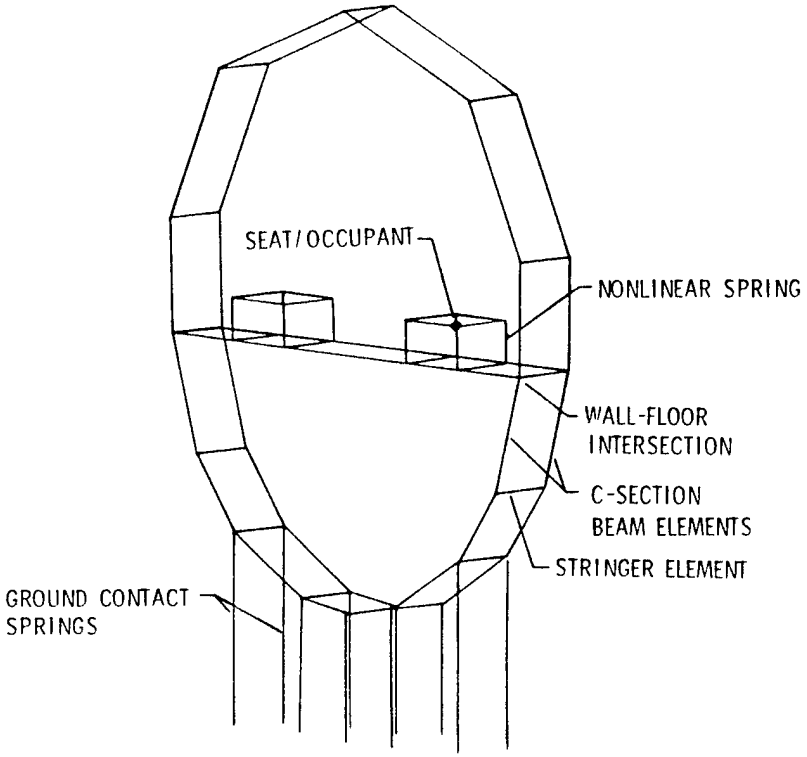


Figure 10.- Finite element two-frame model of metal transport section.

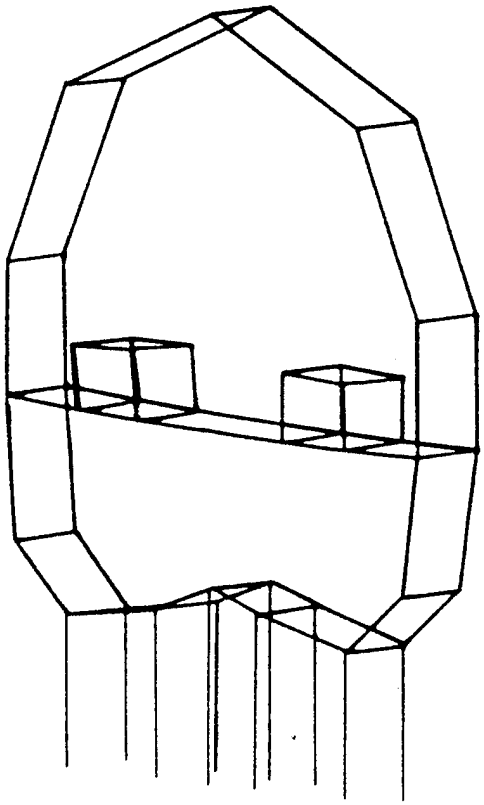
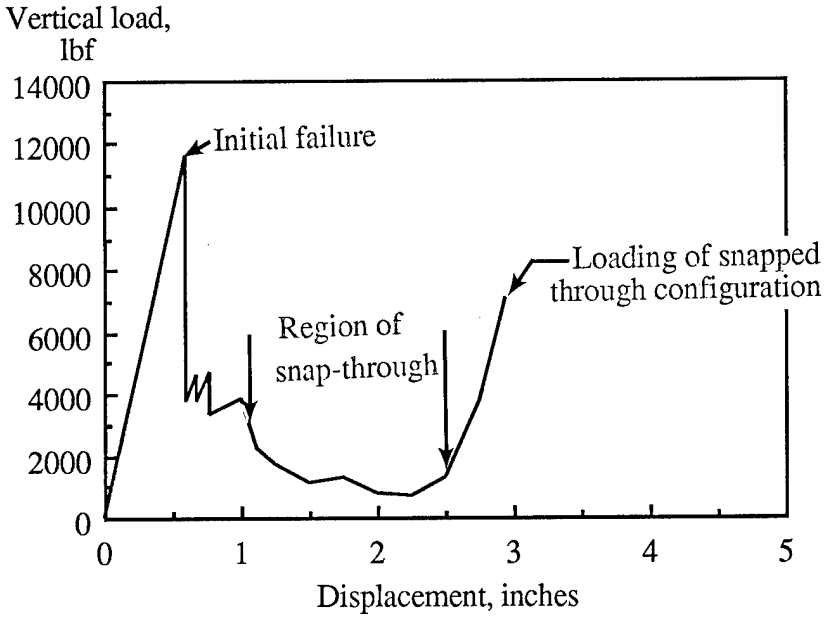
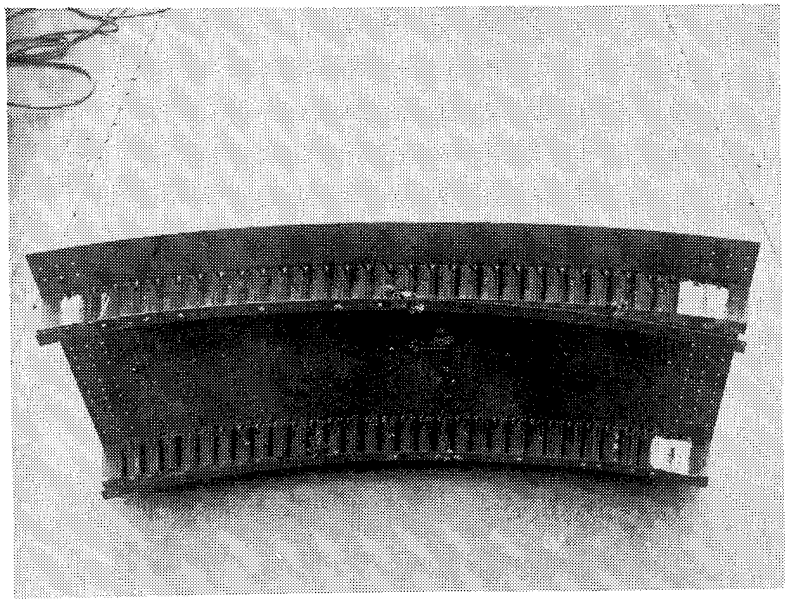


Figure 11.- Computer graphics showing analytical failure of metal transport section.

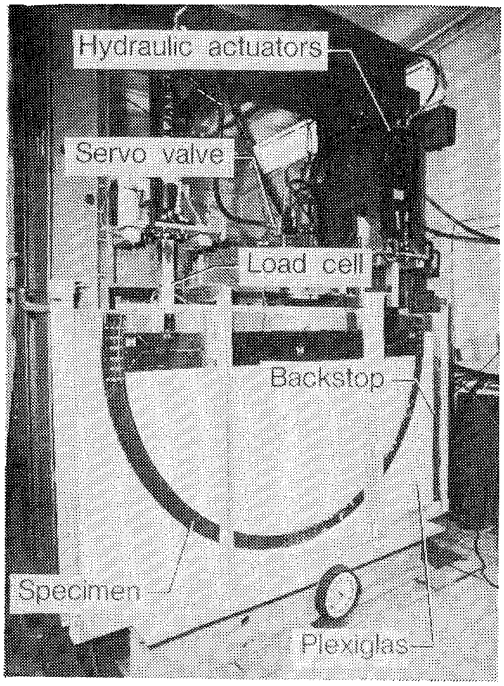


(a) Load-displacement.

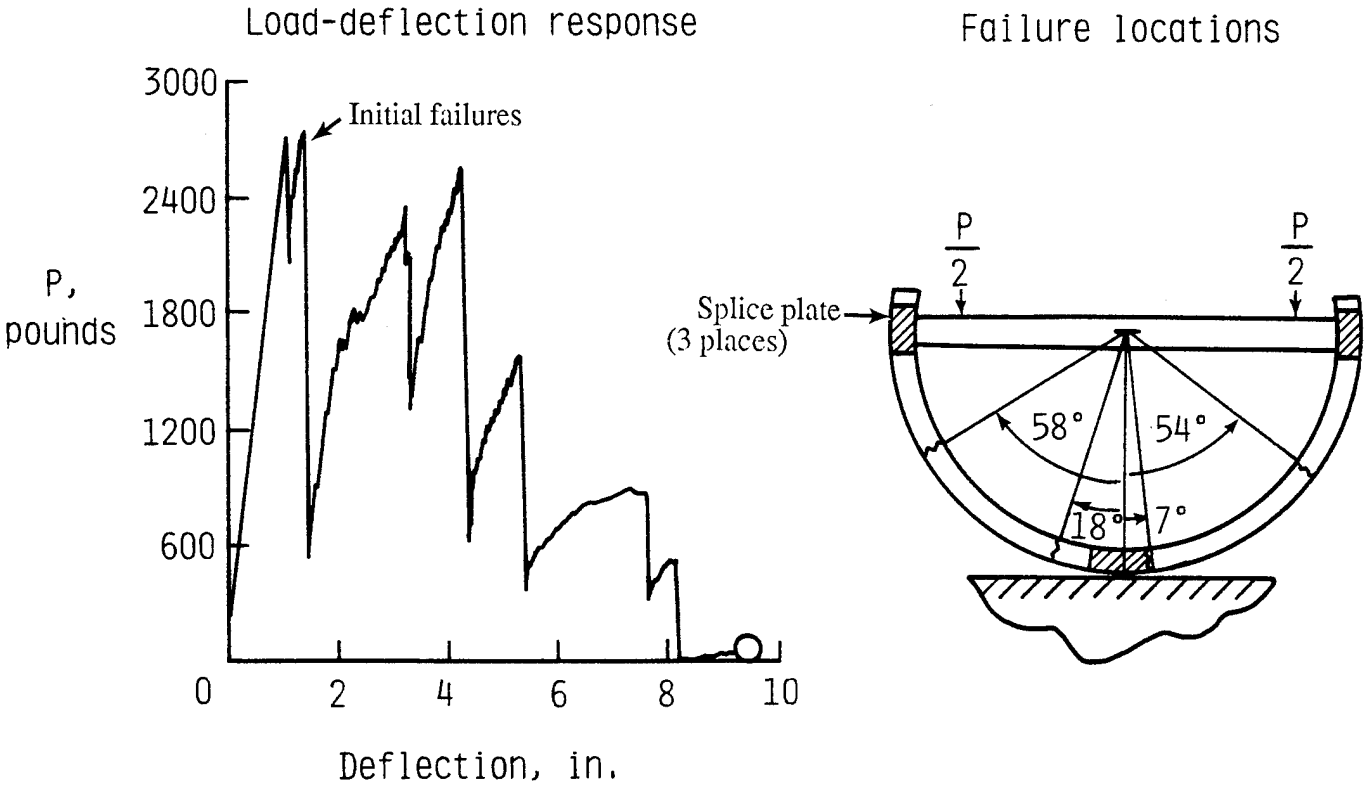


(b) Composite panel-post test.

Figure 12.- Behavior of composite fuselage panel under static loading.

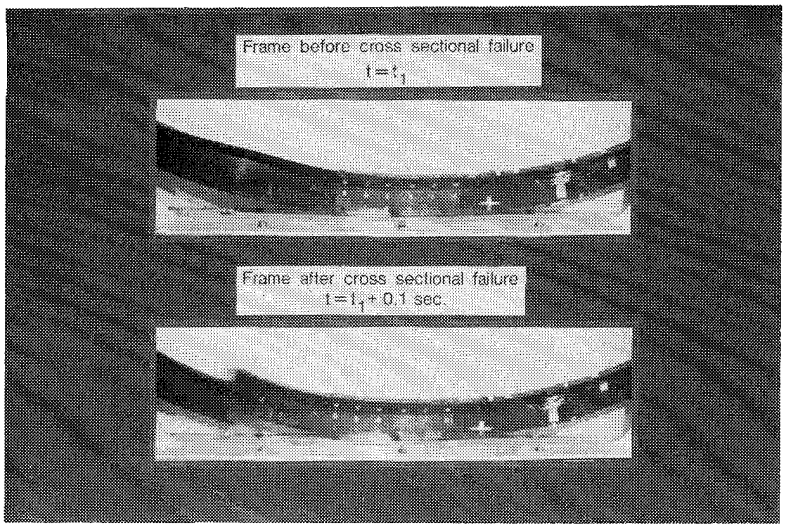


(a) Static test apparatus.



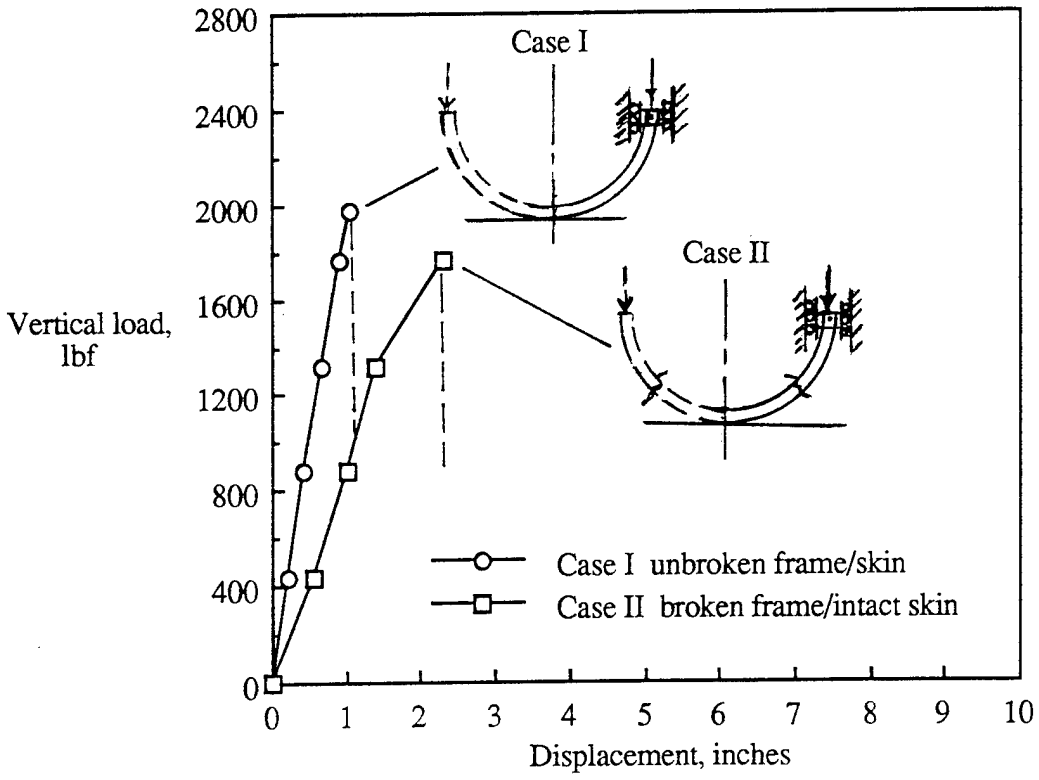
(b) Load-displacement and failure locations.

Figure 13.- Static results from tests of single composite Z-frame.



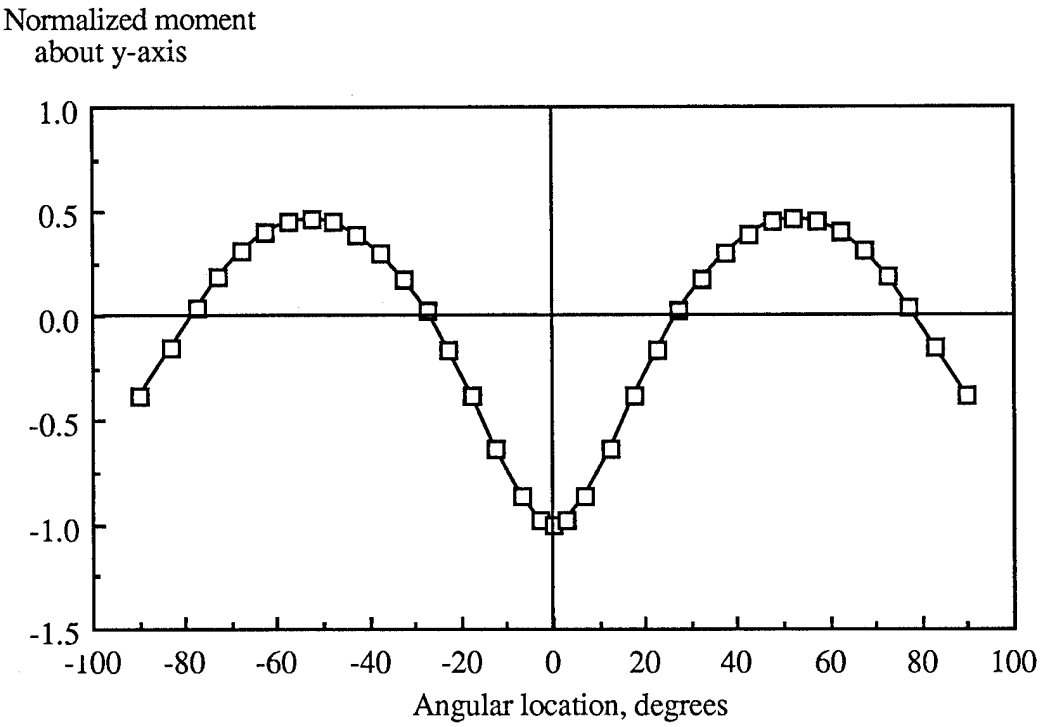
(c) Frame local instability.

Figure 13.- Concluded.

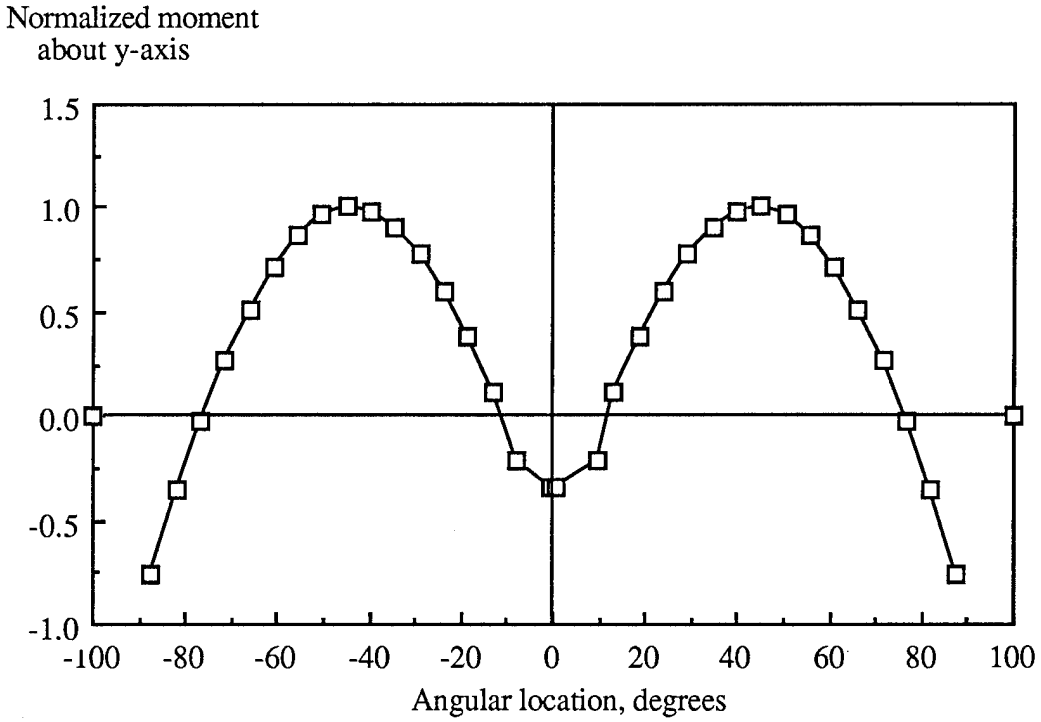


(a) Load-displacement.

Figure 14.- Typical analytical results for composite frame skin using I-section for ease of analysis.

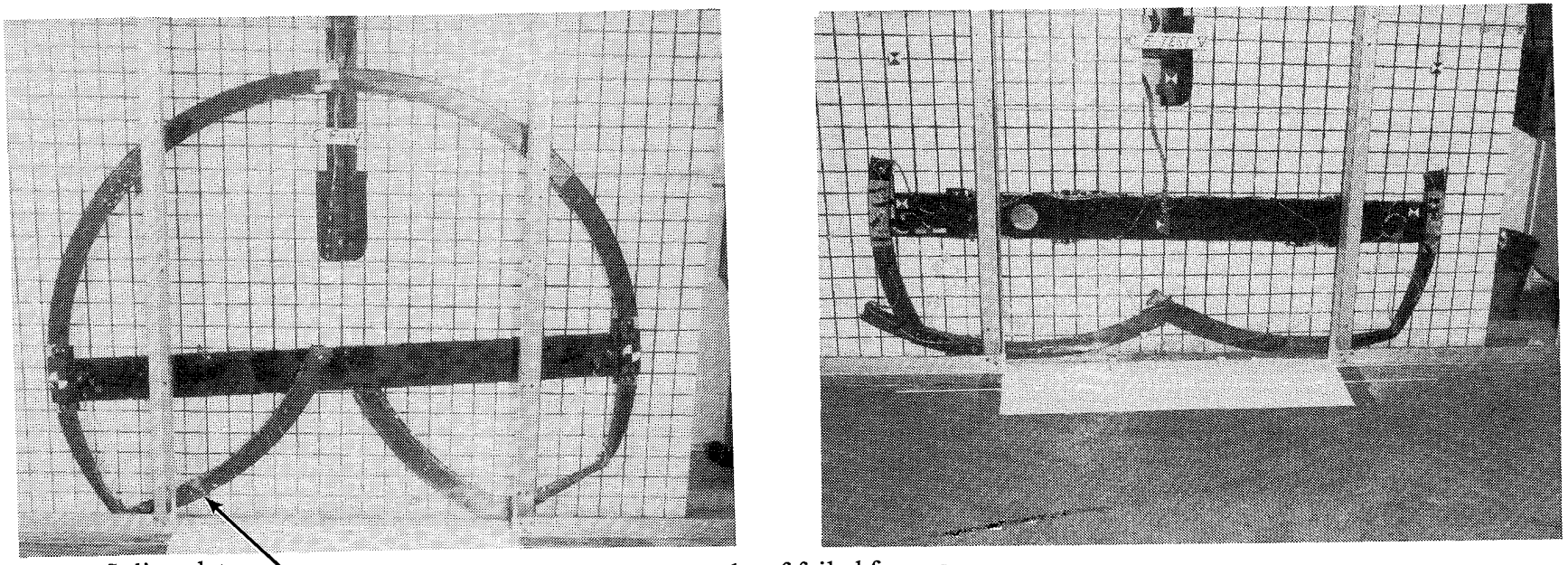


(b) Case I----Normalized moment (Prior to failure).

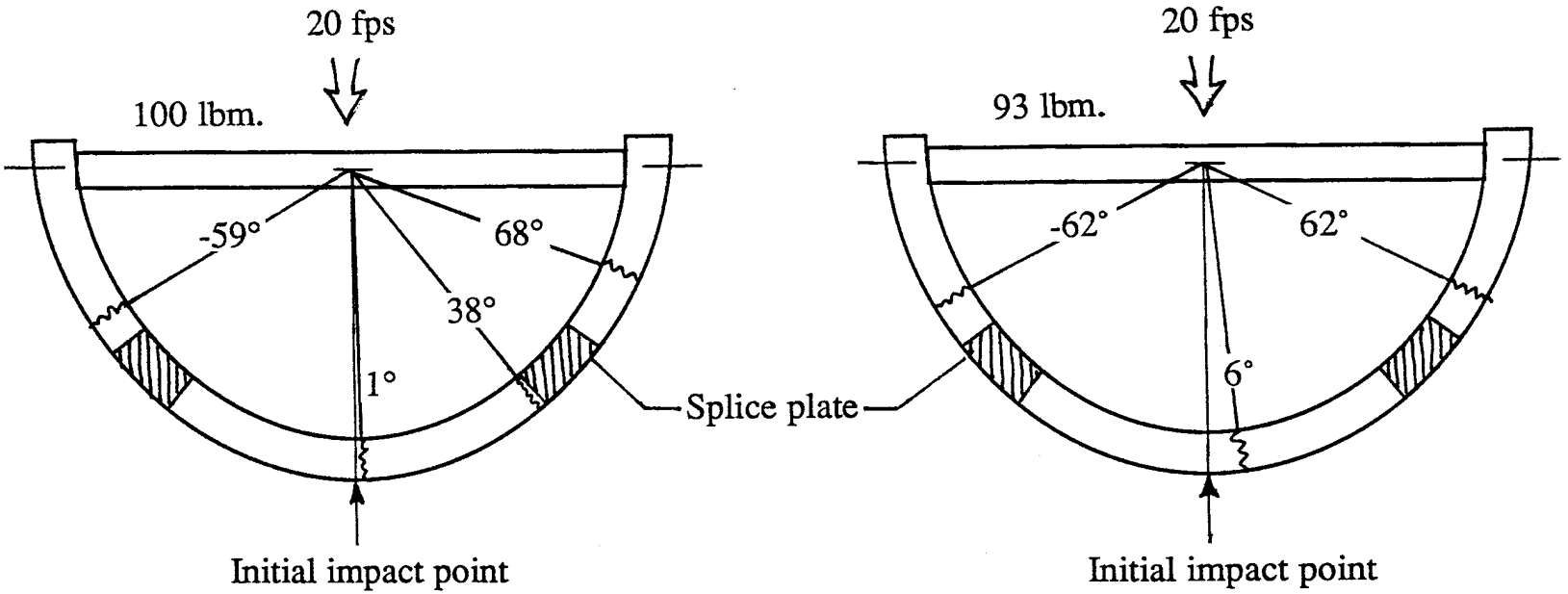


(c) Case II---Normalized moment (Broken frame-intact skin).

Figure 14.- Concluded.

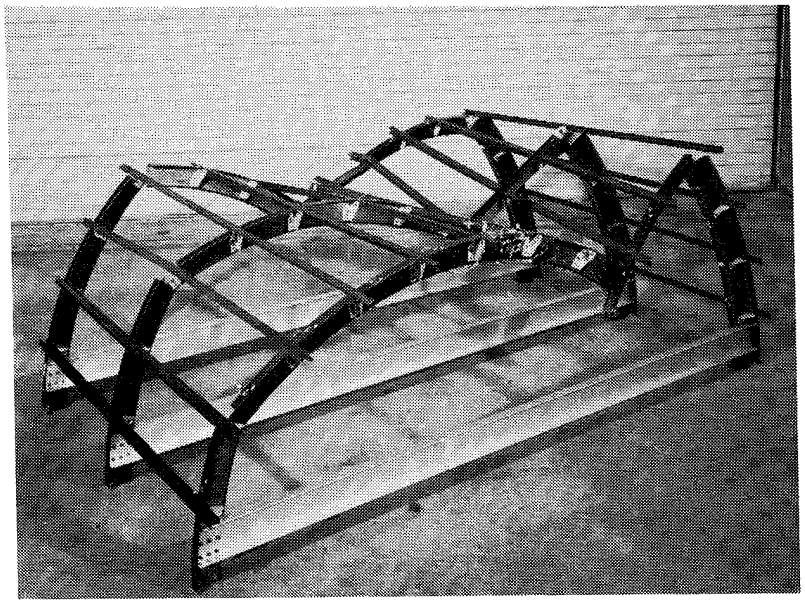


(a) Photographs of failed frames.

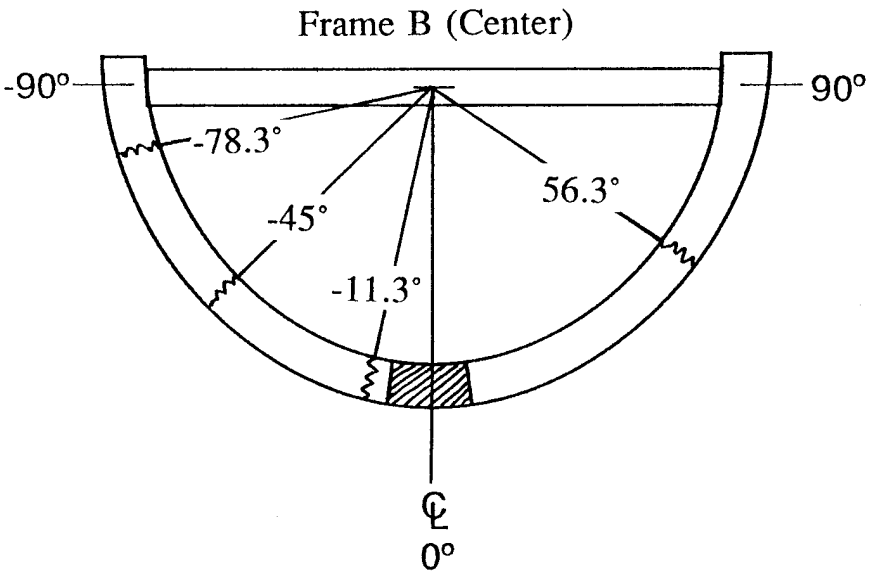


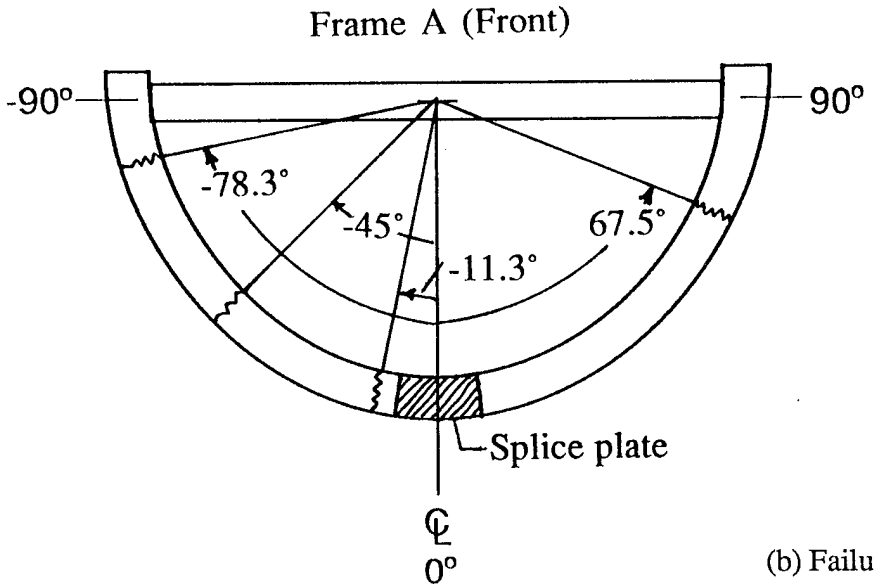
(b) Location of failures in frames.

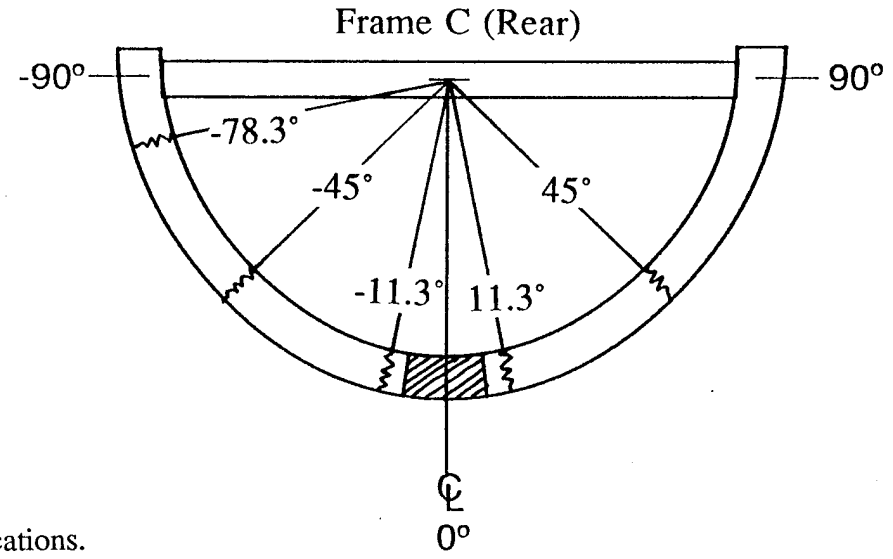
Figure 15.- Behavior of composite Z-frame under dynamic loads.



(a) Failed skeleton subfloor.

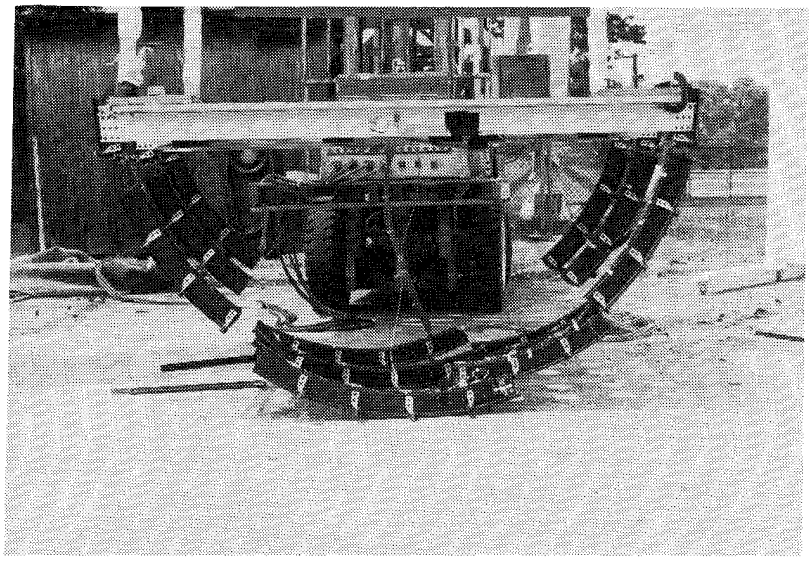




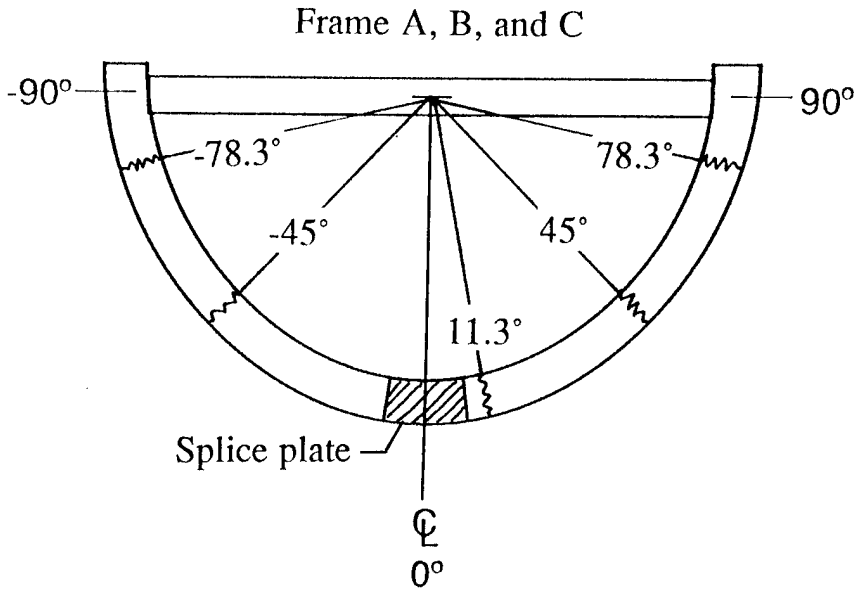


(b) Failure locations.

Figure 16.- Behavior of composite skeleton subfloor under static loading tests.

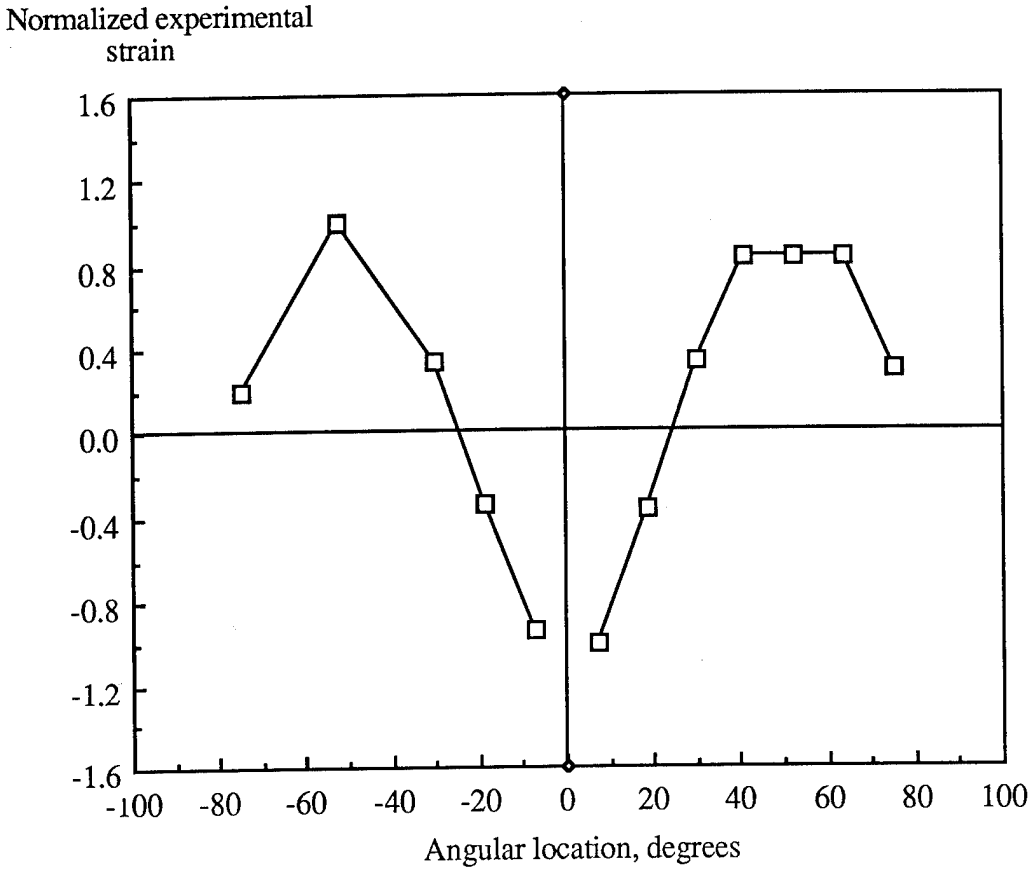


(a) Failed skeleton subfloor.



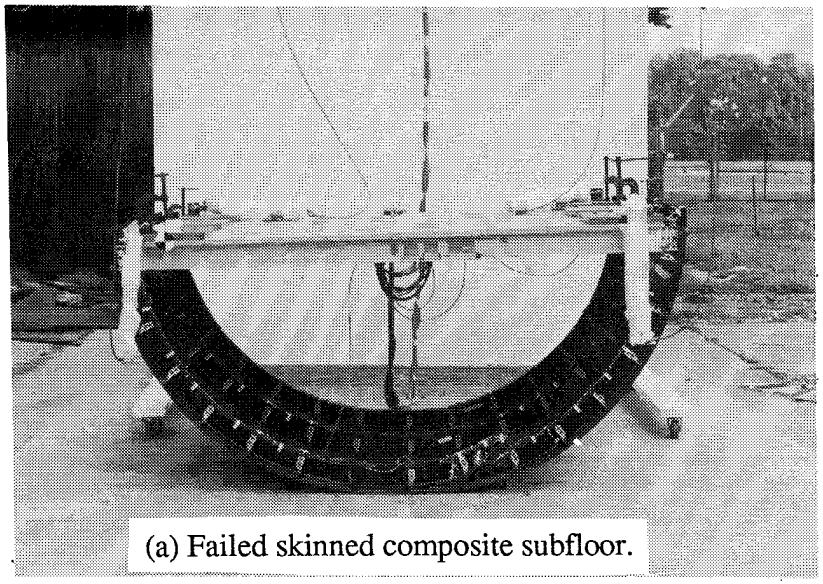
(b) Failure locations.

Figure 17.- Behavior of skeleton composite subfloor under dynamic loading tests.

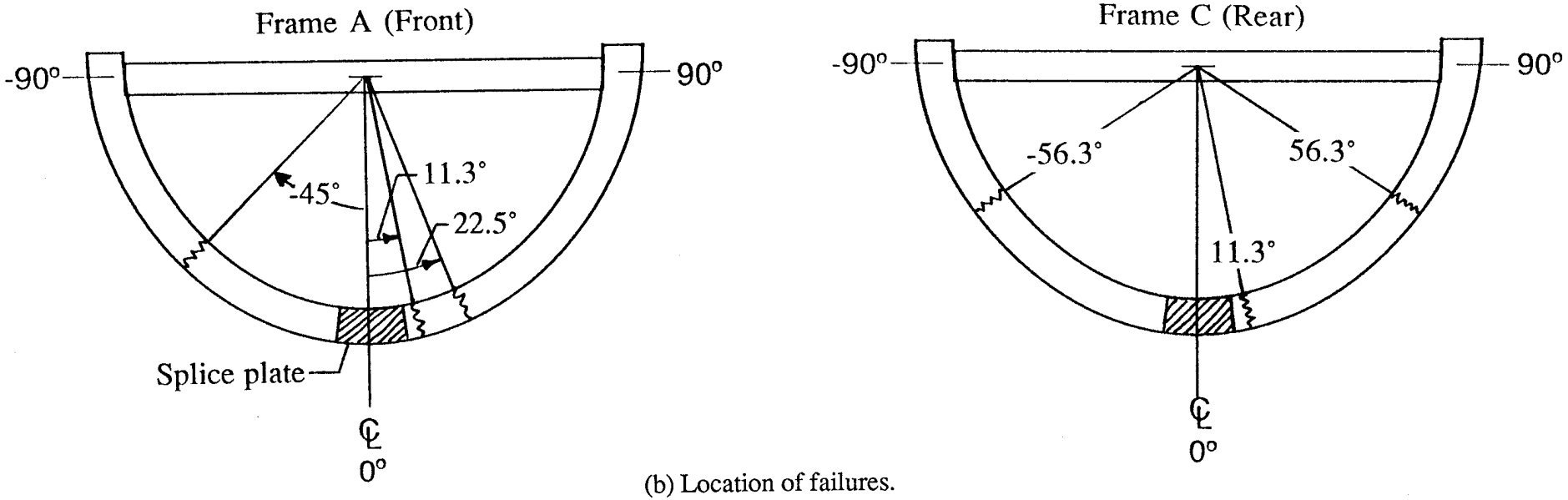


(c) Normalized strain distribution.

Figure 17.- Concluded.

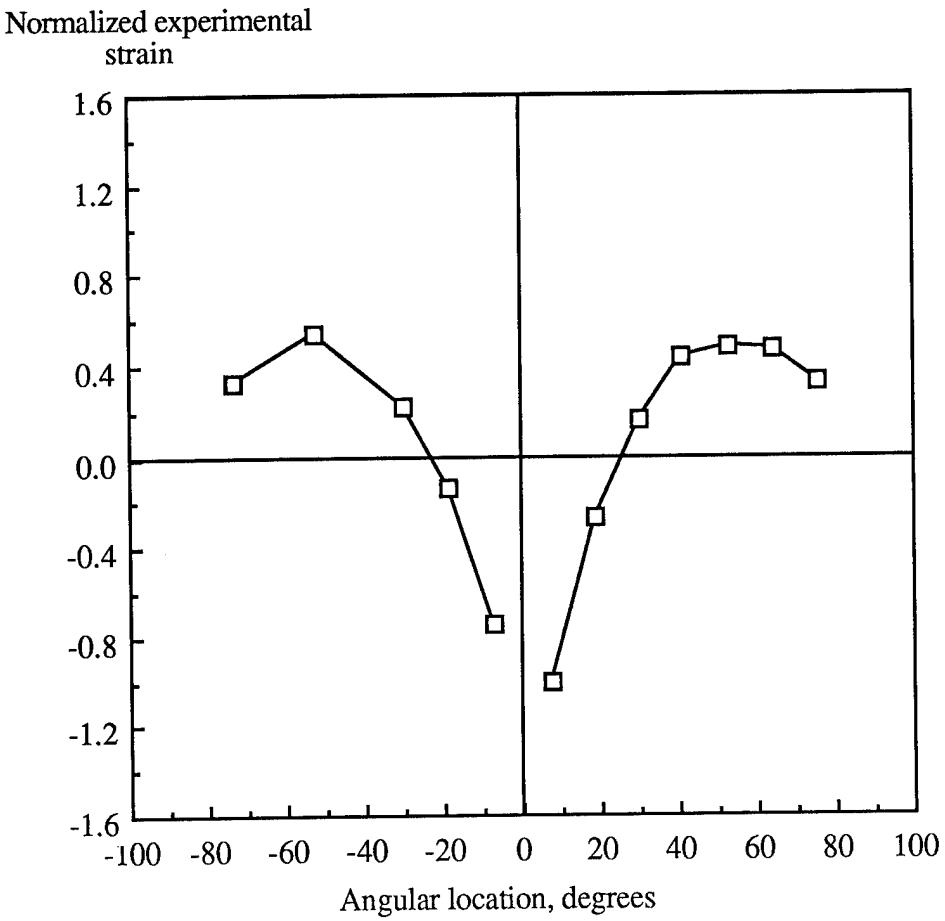


(a) Failed skinned composite subfloor.



(b) Location of failures.

Figure 18.- Behavior of skinned composite subfloor under dynamic loading tests.



(c) Normalized strain distribution.

Figure 18.- Concluded.

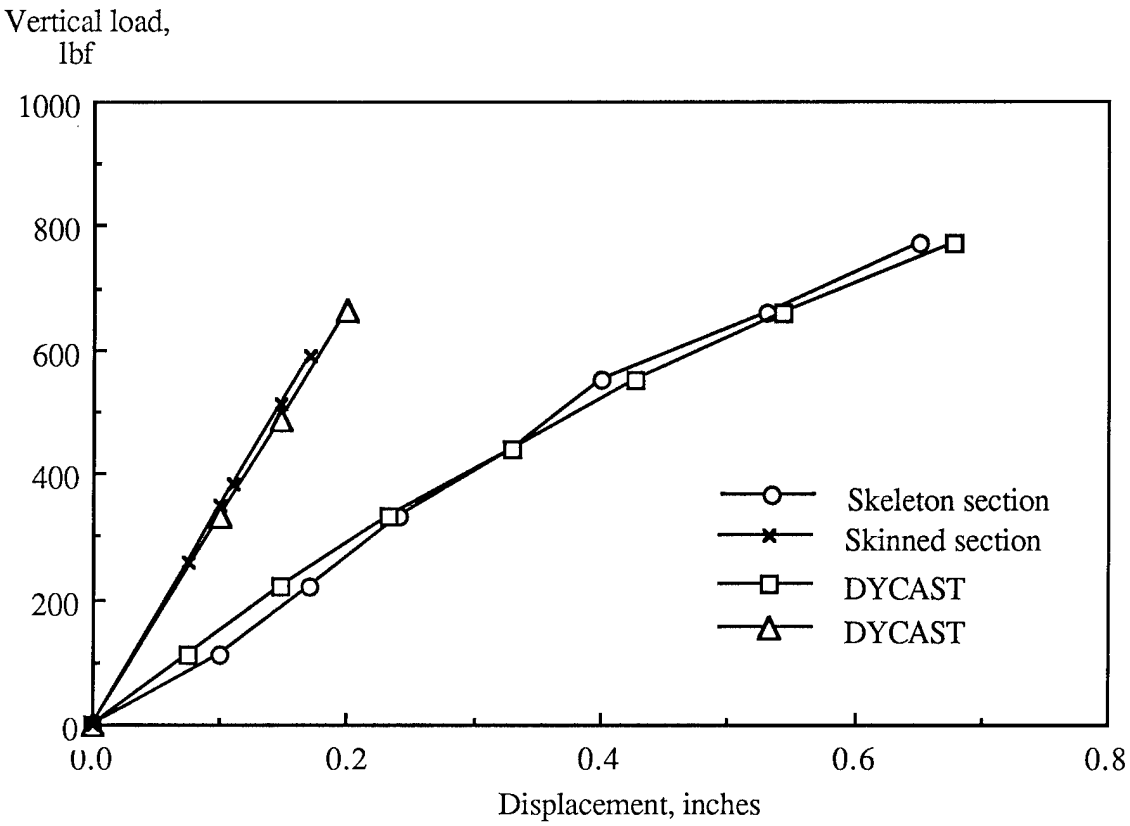
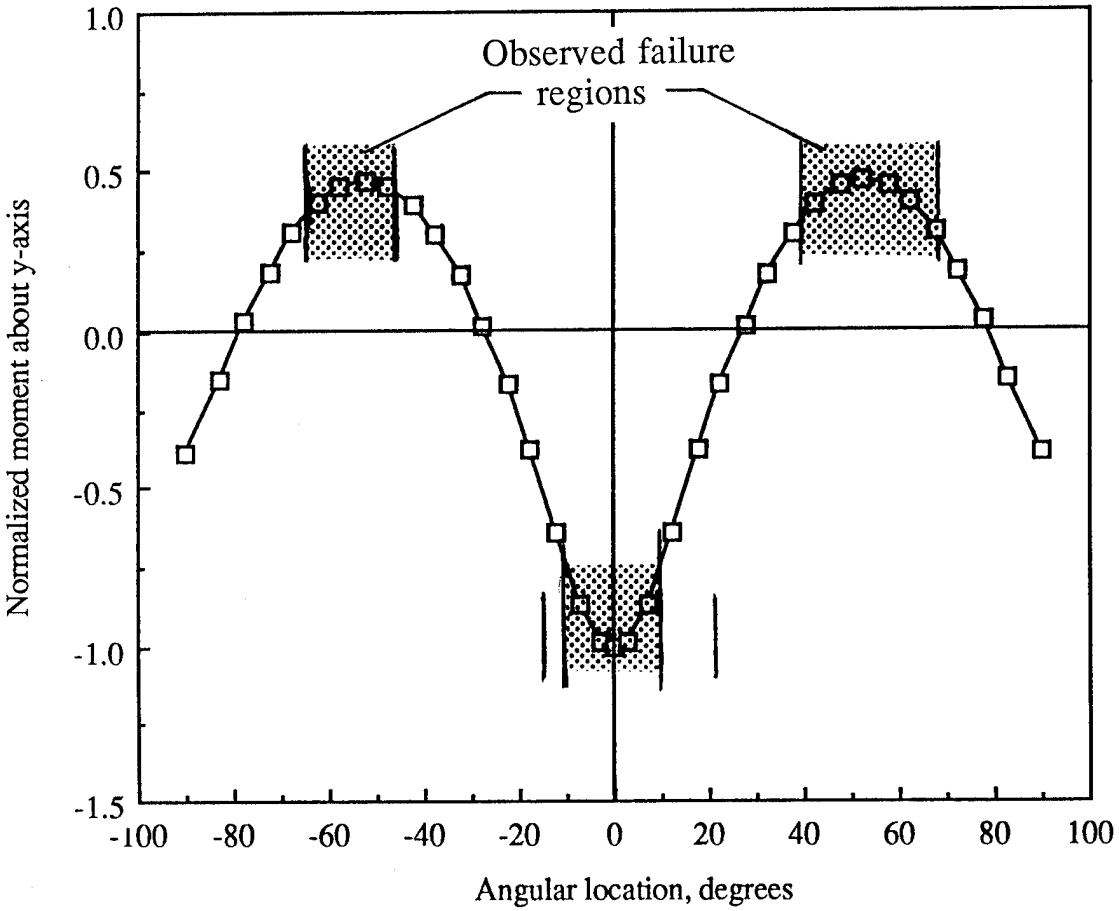
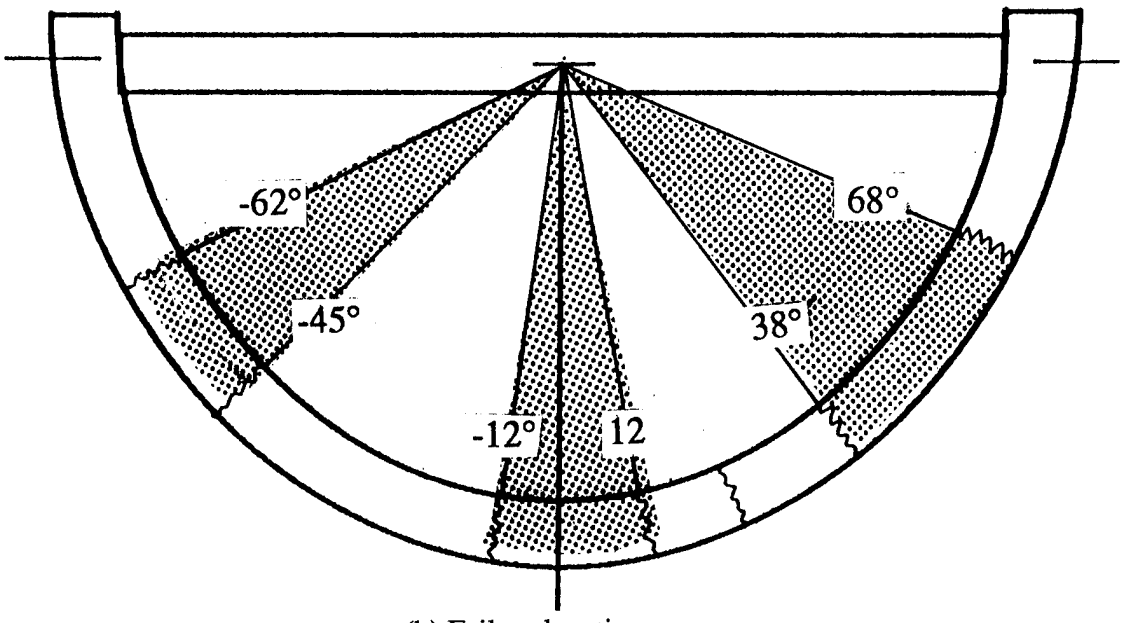


Figure 19.- Comparison of experimental and analytical stiffness of skeleton and skinned composite subfloors.



(a) Normalized moment distribution.



(b) Failure locations.

Figure 20.- Comparison of nondimensional analytical moment distribution predicted by finite element frame model and observed failure locations on metal and composite fuselage components and structures.

TAILORED COMPOSITE WINGS WITH ELASTICALLY PRODUCED CHORDWISE CAMBER*

Lawrence W. Rehfield, Stephen Chang, Peter J. Zischka, Richard D. Pickings and Michael W. Holl

University of California, Davis

SUMMARY

Four structural concepts have been created which produce chordwise camber deformation that results in enhanced lift. A wing box can be tailored to utilize each of these with composites. In attempting to optimize the aerodynamic benefits, we have found that there are two optimum designs that are of interest. There is a "weight" optimum which corresponds to the maximum lift per unit structural weight. There is also a "lift" optimum that corresponds to maximum absolute lift. Experience indicates that a large weight penalty accompanies the transition from weight to lift optimum designs.

New structural models, the basic deformation mechanisms that are utilized, and typical analytical results are presented. It appears that lift enhancements of sufficient magnitude can be produced to render this type of wing tailoring of practical interest.

INTRODUCTION

A combination of reasons are responsible for the popularity of resin matrix laminated composites. They resist chemical action, exhibit outstanding mechanical properties and high fatigue resistance, are light in weight and possess an established technology base. If mechanical performance can be compromised, a host of low cost manufacturing approaches can be utilized such as winding, weaving, braiding and pultrusion.

A significant attribute of laminated composites is their design flexibility. The layers or plies of a laminate are, in fact, modular units which can be selected to provide distinct material properties and fiber orientations. It is possible, therefore, to "tailor" the properties of composites to meet specific design requirements. Engineers are learning to exploit this flexibility to produce unique structures tailored to the application. An outstanding example is the swept forward wing of the Grumann/AF/DARPA X-29 Fighter.

A working definition of elastic tailoring is the use of structural concept, fiber orientation, ply stacking sequence and a blend of materials to achieve specific performance goals. In the design process, materials and dimensions are selected to yield specific elastic response characteristics which cause the goals to be achieved. Common choices for goals of elastic tailoring are the creation of favorable deformations, often for the purpose of preventing or controlling aeroelastic phenomena or vibration, improved aerodynamic performance and damage tolerance. Tailoring can be utilized effectively if

1) The behavior in question is thoroughly understood physically.
2) The mechanism(s) is (are) clearly identified.
3) Favorable changes of sufficient magnitude can be produced.

*Sponsored by the NASA Langley Research Center under Contract NAS1- 18754.

It has become accepted practice to consider tailoring of wing bending and twisting deformations. In the present work, a new step is taken - - - tailoring of chordwise deformations.

Structural tailoring concepts have been developed to create wings with elastically produced camber for the purpose of increasing the lift generated by the wing. Currently, the usual means of accomplishing this is with controls, the most common of which are flaps. If natural, intrinsic means are used to enhance lift, flap requirements and their associated systems may be reduced or, possibly, even eliminated. The fundamental mechanisms that are utilized produce camber deformations in response to the usual loading of the wing such as bending moments and torque. The camber enhances the production of lift and further modifies the loads. Significant lift increases may be produced by using modern composite material systems.

A Record of Invention has been filed with the University of California Patent, Trademark and Copyright Office pertaining to our camber-producing structural concepts. It is designated UC Case No. 90-116-1 and is entitled "Wings With Elastically Produced Camber." Valentin Fikovsky ((415) 748-6600) is the attorney assigned to the case. Mr. Fikovsky's office would be glad to supply more details on the concept and authorize discussions of the invention under the cover of a Non-Disclosure Agreement. The desired effects are depicted in figure 1.

TAILORING CONCEPTS

In view of the proprietary nature of the camber producing structural concepts, detailed information may be obtained through Mr. Fikovsky's office as mentioned above. There are, however, several general concepts that have been used that are illustrated in figures 2 and 3. A central feature of our wing designs is the use of continuous filament grid stiffened configurations (figure 3) for the wing box covers. This type of stiffening concept is particularly useful for tailoring because unidirectional stiffeners can be oriented and placed to create a wide variation of elastic properties.

We have developed four methods of producing camber from elastic deformations. They have been designated the bending, twisting, pressure and thermal methods, respectively. Only results from the use of the first two methods will be presented.

MODELING AND ANALYSIS METHODOLOGY

The modeling and analysis methodology had its origin in the development and application of new structural models for composite rotor blades with both single and multiple cells. The theory for single cell construction is presented in ref. 1. An extensive numerical comparative study appears in ref. 2, which compares the new elementary theory's predictions with a finite element analysis. Both predictions are in excellent agreement for three benchmark loading cases for a Langley Research Center model blade.

In ref. 3 a comparison is made between theoretical predictions and experimental measurements on a thin-walled box beam. This study shows that strains at points can be predicted with the elementary beam-like theory. In addition, circular tube experiments conducted by Nixon (ref. 4) exhibit good agreement with the theory.

The body of knowledge consisting of the above references establishes a sound technology base for applications and design-related studies. Composite rotor blade modeling is reviewed in ref. 5. Additional studies (refs. 6-11) have been based upon the model of ref. 1. This beam-like model is generic and applies equally well to high aspect wings. The model has been modified appropriately for chordwise camber deformation and serves as the basis for the present work.

The wing box model appears in figure 4. Only the structural box is assumed to be load bearing. The structural model is based upon the center wing structural box of the Lockheed C-130 transport. This avoids the complexity of wing sweep. All dimensions other than skin thicknesses are those of the C-130.

For study of the bending method, a symmetric configuration with identical upper and lower wing covers for the single cell structural box has been selected. The primary structural elements are the stiffened covers. The material properties correspond to AS4/3501-6 graphite-epoxy; they appear in table 1.

DESIGN ANALYSIS: BENDING CASE

A design analysis algorithm has been created for evaluating the benefits of tailored camber. An allowable strain level for bending related response and a distributed axial loading in the covers are assigned initially. The running axial cover stiffness can be directly estimated.

$$K_{11} = \overline{N}_{xx}/\varepsilon \tag{1}$$

The distributed running load in the cover is $\overline{N}_{xx}$. The extensional membrane stiffness is K_{11}. The strain level ε is the allowable spanwise bending strain.

The stiffness K_{11} is composed of two contributions, one due to the skin and the other due to the stiffeners. The influence of stiffeners is accounted for in an averaged manner. The stiffeners are "smeared" or "averaged" over the area of the skin. Also, the stiffeners are taken to be unidirectional configurations with rectangular cross sections of the type that may be created by winding or weaving technology. Since membrane behavior is considered for the upper and lower wing box covers, local bending effects due to cover buckling or postbuckling are excluded at this level of modeling. The influence of the box webs are neglected for convenience. The stiffness may be written as

$$K_{11} = K_{11}^{o} + E_{11}^{1} h\, n\, F \tag{2}$$

We adopt the convention that supercripts "o" and "1" refer to the skin and stiffeners, respectively. The extensional modulus of the stiffeners is E_{11}^{1}, h is the skin thickness, n is the stiffening parameter and F is a parameter that reflects the stiffener spatial distribution and pattern.

The stiffening parameter n is defined as

$$n = A_1/p_1 h \tag{3}$$

The cross-sectional area of an individual stiffener is A_1 and p_1 is the pitch or distance between parallel rows of stiffeners.

It is convenient to define the membrane stiffness per unit skin thickness k_{11} as

$$k_{11} = K_{11}/h \tag{4}$$

This stiffness parameter may be calculated directly from lamination theory and a knowledge of the stiffener pattern. It permits the skin thickness to be evaluated as

$$h = \bar{N}_{xx}/k_{11}\varepsilon \tag{5}$$

An appropriate measure of structural weight for configurations fabricated from one material is the equivalent smeared thickness of skin and stiffeners denoted h'. It is

$$h' = h\,(1+nf) \tag{6}$$

The parameter f reflects the stiffener spatial distribution and pattern.

The incremental contribution to the section lift coefficient due to elastic camber may be expressed as

$$\Delta C_\ell = GS\,\varepsilon \tag{7}$$

This equation is based upon linear two-dimensional thin airfoil theory (ref. 12). The factor G is a geometric factor that depends on the cross-sectional shape, structural box dimensions and overall section dimensions. The factor S is a dimensionless stiffness factor which depends on stiffness-related material properties, stiffener configuration and skin layup configuration.

The design analysis proceeds as follows:

1. A configuration is selected and k_{11} is determined;
2. The skin thickness is found using Equation (5);
3. The lift coefficient contribution is calculated using Equation (7);
4. The weight related measure of the lift created is evaluated from the parameter.

$$\Delta C_\ell/h'$$

5. Parametric and optimization studies can be conducted based upon the lift created (eq. (7)) or lift per unit of structural weight (step 4).

In attempting to optimize the aerodynamic benefits, we have found that there are two optimum designs that are of interest. There is a "weight" optimum which corresponds to the maximum lift per unit structural weight. There is also a "lift" optimum that corresponds to maximum absolute lift. Experience indicates a large weight penalty accompanies the transition from weight to lift optimum designs.

DESIGN ANALYSIS: TWISTING CASE

If the twisting method of producing camber deformations is employed, a design analysis algorithm can be created which parallels that associated with the bending method. In addition to specifying a design level for bending strain, a design level of shear strain or shear flow must be prescribed. In place of eq. (7), the following equation must be used:

$$\Delta C_\ell = G(S_1\varepsilon + S_2\,\gamma) \tag{8}$$

The factors S_1 and S_2 are stiffness-related. They depend upon material properties, stiffener configuration and skin layup configuration. The shear strain in the covers is denoted by γ.

While configuration details will not be given, it is well to mention that optimal configurations for the bending and twisting methods are distinct and bear little resemblance to each other.

RESULTS AND DISCUSSION

Benchmark Wing Cover Design

A benchmark configuration was created and analyzed for which no effort was made to create elastically produced camber. This configuration carries the design level bending strain and utilizes AS4/3501-6 graphite-epoxy as a material system. The stiffeners are unidirectional and oriented at [0] degrees to the wing beam axis. The skin is composed of only [±45] plies.

The overall level of stiffening, as indicated by the factors "nF" in eq. (2), remains comparable (but not necessarily equal) in all designs. Also the design extensional strain level ϵ is taken as 4500 microinches per inch. The applied running load $\overline{N}_{xx}$ is set at 25,000 pounds per inch, a value consistent with the center wing of a large transport. Rather than prescribe shear strain, we have elected to use a design value of shear flow of 5000 pounds per inch.

Bending Method Design

Optimal values for bending method designs are presented in table 2. The results correspond to n = 1.5, which is considered to be heavy stiffening. It is to be noted that the section lift coefficient increments for both the weight optimum design (WOD) and lift optimum design (LOD) are large enough to be of practical interest. As a reference, the basic lift contribution due to angle of attack from linear thin airfoil theory is

$$\Delta C_\ell \cong 0.110\ \alpha \qquad (9)$$

where α, the angle of attack, is given in degrees.

The transition from the WOD to the LOD corresponds to an approximate increase in section lift coefficient of 18 percent. The weight increase, however, is 56 percent. Thus, as mentioned earlier, a substantial weight penalty is required for the additional lift. Also, the two designs correspond to totally different configurations.

Even though no effort was made to produce elastic camber with the benchmark design, there is a small contribution due to anticlastic curvature. The transition from the benchmark design to the WOD corresponds to an increase of 234 percent in section lift coefficient for a weight increase of only 11 percent. This suggests that elastic camber tailoring is weight efficient.

Twisting Method Design

Optimal values for twisting method designs are presented in table 3. The absolute section lift coefficient increments achieved by this method are somewhat less than for the bending method. They are large enough to be of practical interest and the corresponding weights (thicknesses) are less. On the basis of the parameter $\Delta C_\ell/h'$ (inches^{-1}), the twisting method gives 0.295 in.$^{-1}$ and the bending method yields 0.299 in.$^{-1}$ for WOD's. Therefore on a relative basis, the two methods are competitive.

If absolute lift is important, the twisting method is more efficient. Twisting method designs and bending method designs correspond to entirely different configurations, however. There are, therefore, manufacturing factors which would enter into the decision of which method to adopt.

CONCLUDING REMARKS

A new type of elastic tailoring for wings which produces chordwise camber has been created and demonstrated. Typical results for lift enhancement of a transport wing are of sufficient magnitude to warrant practical consideration. Detailed configuration and design information have not been provided due to the fact that a patent is being pursued. Complete information may be obtained under the cover of a Non-Disclosure Agreement through the University of California Patent, Trademark and Copyright Office.

All of the design analysis results presented herein are based upon the premise that the wing sections are completely free to deform in chordwise camber. If restraints to this form of deformation are present, such as may be near a wing-fuselage juncture, section lift benefits will be diminished locally.

REFERENCES

1. Rehfield, L.W., "Design Analysis Methodology for Composite Rotor Blades," Proceedings of the Seventh DoD/NASA Conference on Fibrous Composites in Structural Design, AFWAL-TR-85-3094, June 1985, pp. (V(a)-1)-(V(a)-15).

2. Hodges, R.V., Nixon, M.W. and Rehfield, L.W., "Comparison of Composite Rotor Blade Models: Beam Analysis and an MSC Nastran Shell Element Model," NASA Technical Memorandum 89024, January 1987.

3. Bauchau, O., Coffenberry, B.S. and Rehfield, L.W., "Composite Box Beam Analysis: Theory and Experiments," Journal of Reinforced Plastics and Composites, Vol. 6, January 1987, pp. 25-35.

4. Nixon, M.W., "Extension-Twist Coupling of Composite Circular Tubes with Application to Tilt Rotor Blade Design," Proceedings of the 28th Structures, Structural Dynamics and Materials Conference, April 6-8, 1987, Monterey, CA, AIAA Paper No. 87-0772, pp. 295-303.

5. Hodges, D.H., "Review of Composite Rotor Blade Modeling, AIAA Journal, Vol. 28, No. 3, March 1990, pp 561-565.

6. Rehfield, L.W., Hodges, D.H., and Atilgan, A.R., "Nonclassical Behavior of Thin-Walled Beams with Closed Cross Sections, Journal of the American Helicopter Society, Volume 35, No. 2, April 1990, pp. 42-50.

7. Rehfield, L.W., Atilgan, A.R. and Hodges, D.H., "Structural Modeling for Multicell Composites Rotor Blades," AIAA Paper 88-2250, 29th Structures, Structural Dynamics and Materials Conference, 18-22 April 1988, Williamsburg, VA.

8. Rehfield, L.W. and Atilgan, A.R., "Toward Understanding the Tailoring Mechanisms for Thin-Walled Composites Tubular Beams," Proceedings of the First USSR-US Symposium on Mechanics of Composite Materials, 23-25 May 1989, Riga, Latvia, USSR, USSR Academy of Sciences.

9. Hodges, D.H., Atilgan, A.R., Fulton, M.V. and Rehfield, L.W., "Dynamic Characteristics of Composite Beam Structures," presented at the AHS National Specialists' Meeting on Rotorcraft Dynamics, Ft. Worth, TX, 13-14 November 1989. To appear in the Journal of the American Helicopter Society.

10. Rehfield, L.W. and Atilgan, A.R., "Shear Center and Elastic Axis and Their Usefulness for Composite Thin-Walled Beams," Proceedings of the American Society for Composites Third Technical Conference, October 3-6, 1989, Blacksburg, VA, Technomic Publishing Co., Ltd., Lancaster, PA, pp. 179-188.

11. Atilgan, A.R. and Rehfield, L.W., "Vibrations of Composite Thin-Walled Beams with Designed-in Elastic Couplings," Proceedings of the Fifth Japan-US Conference on Composite Materials," Tama-City, Japan, 24-27 June 1990, Japan Society of Composite Materials.

12. Bertin, J.J. and Smith, M. L., Aerodynamics for Engineers, Prentice-Hall, Inc., 1979, pp. 109-125.

TABLE 1. – NOMINAL MATERIAL PROPERTIES FOR AS4/3501– 6
UNIDERECTIONAL GRAPHITE – EPOXY
(ROOM TEMPERATURE, DRY)

YOUNGS MODULUS (TENSION), FIBER DIRECTION (E_{11})	20.0×10^6 PSI
YOUNGS MODULUS (TENSION), TRANSVERSE DIRECTION (E_{22})	1.7×10^6 PSI
SHEAR MODULUS, IN - PLANE (G_{12})	0.85×10^6 PSI
POISSON RATIO (ν_{12})	0.30

TABLE 2. – OPTIMUM VALUES – BENDING METHOD

(n = 1.5)

	ΔC_1	h' (IN.)
LIFT OPTIMUM	0.138	0.610
WEIGHT OPTIMUM	0.117	0.391
BENCHMARK	0.035	0.353

TABLE 3. – OPTIMUM VALUES – TWISTING METHOD

(n = 1.5)

	ΔC_1	h' (IN.)
LIFT OPTIMUM	**0.125**	**0.429**
WEIGHT OPTIMUM	**0.109**	**0.369**
BENCHMARK	**0.035**	**0.353**

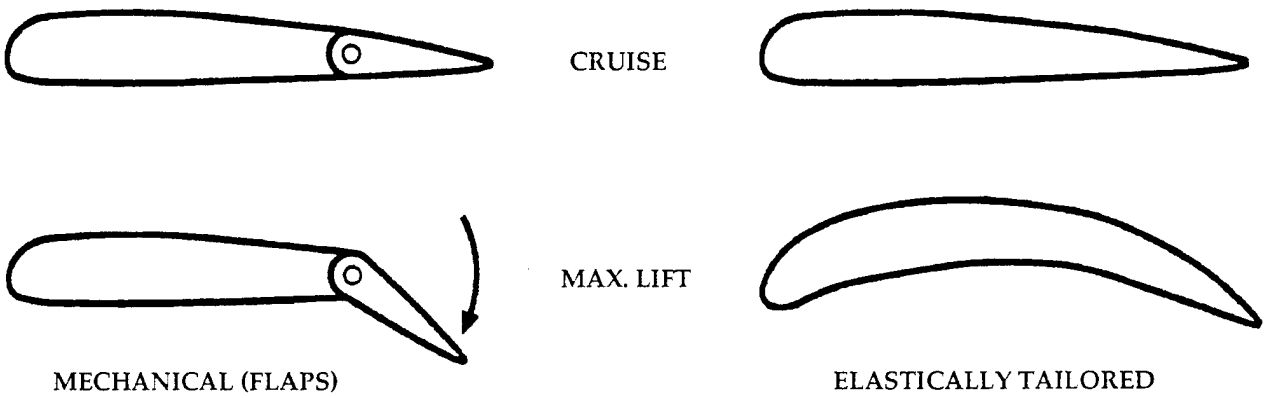


FIGURE 1. – METHODS OF INCREASING AIRFOIL LIFT

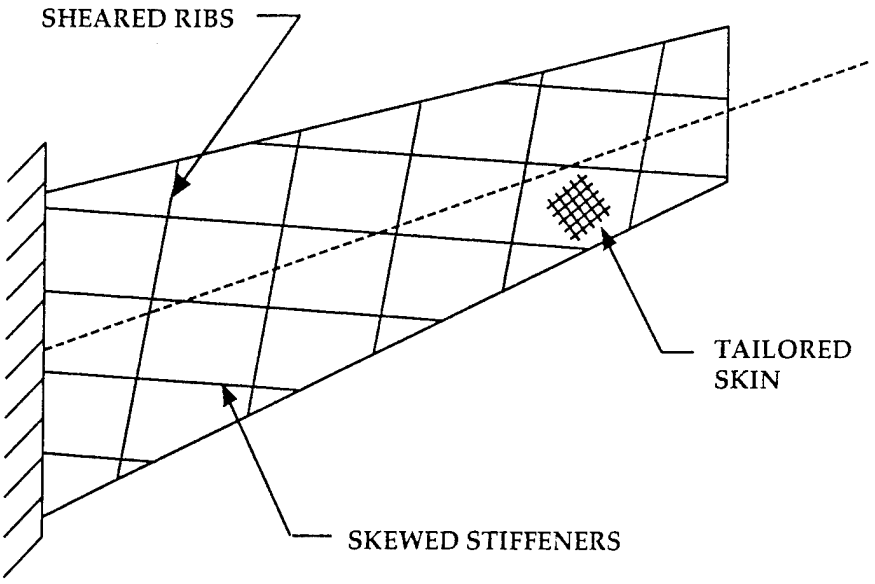


FIGURE 2. – METHODS FOR PRODUCING ELASTIC COUPLING IN HIGH ASPECT RATIO WINGS

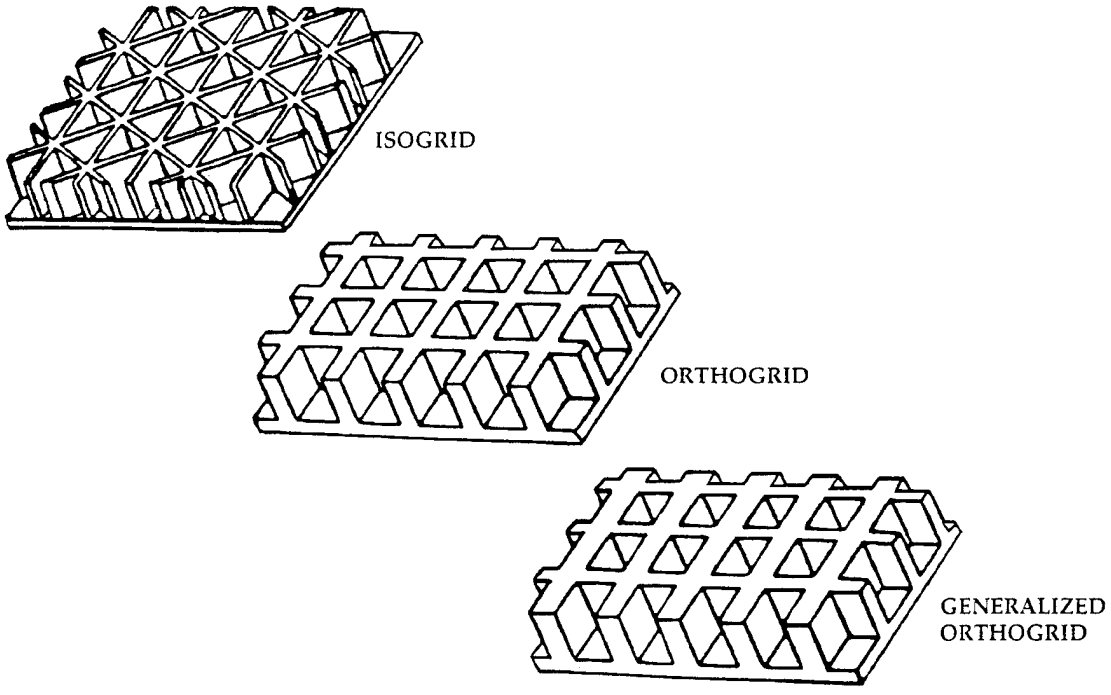


FIGURE 3. – GRID CONFIGURATIONS

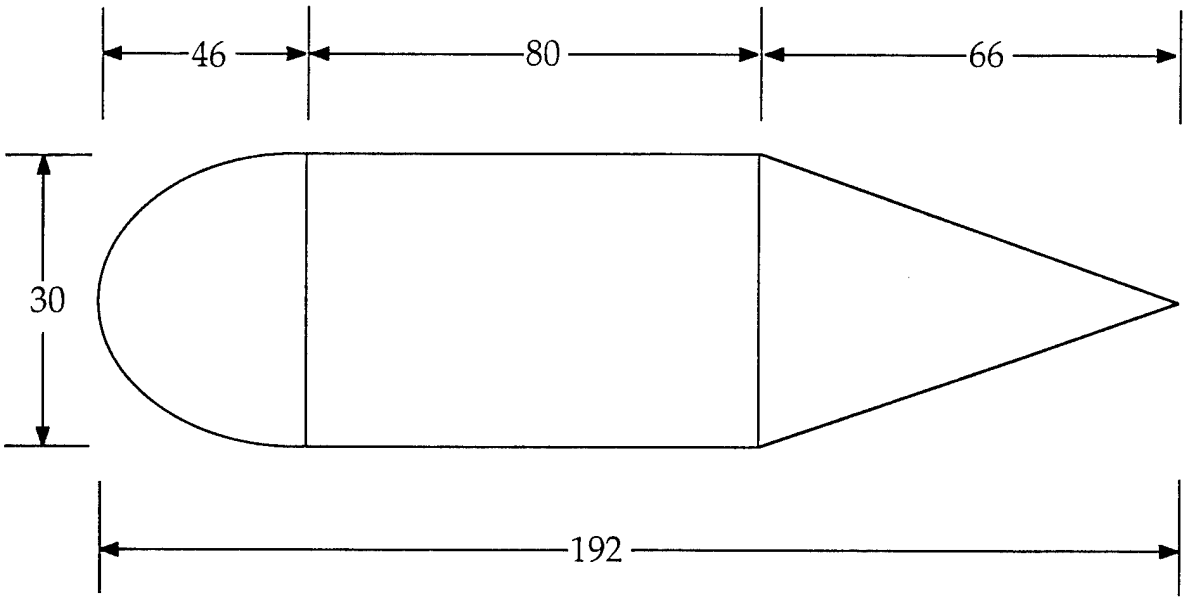


FIGURE 4. – C-130 CENTER WING BOX MODEL

NASA
National Aeronautics and Space Administration

Report Documentation Page

1. Report No.	2. Government Accession No.	3. Recipient's Catalog No.
NASA CP-3104, Part 2		

4. Title and Subtitle	5. Report Date
First NASA Advanced Composites Technology Conference	January 1991
	6. Performing Organization Code
7. Author(s)	8. Performing Organization Report No.
John G. Davis, Jr., and Herman L. Bohon, Compilers	L-16889
9. Performing Organization Name and Address	10. Work Unit No.
NASA Langley Research Center Hampton, Virginia 23665-5225	510-02-11
	11. Contract or Grant No.
12. Sponsoring Agency Name and Address	13. Type of Report and Period Covered
National Aeronautics and Space Administration Washington, DC 20546-0001	Conference Publication
	14. Sponsoring Agency Code

15. Supplementary Notes

John G. Davis, Jr.: NASA Langley Research Center, Hampton, Virginia.
Herman L. Bohon: Lockheed Engineering & Sciences Company, Hampton, Virginia.

16. Abstract

This document is a compilation of papers presented at the first NASA Advanced Composites Technology (ACT) Conference held in Seattle, Washington, from October 29–November 1, 1990. The ACT program is a major new multiyear research initiative to achieve a national goal of technology readiness before the end of the decade. Conference papers recorded results of research in the ACT Program on new materials development and processing, innovative design concepts, analysis development and validation, cost effective manufacturing methodology, and cost tracking and prediction procedures. Papers presented on major applications programs approved by the Department of Defense are also included in this document.

17. Key Words (Suggested by Authors(s))		18. Distribution Statement
Thermoplastics	Aircraft	FEDD
Thermosets	Composite design	
Stitching	Manufacturing	Review for General Release January 1993
Graphite fibers	Analysis	
Processing		Subject Category 24

19. Security Classif. (of this report)	20. Security Classif. (of this page)	21. No. of Pages	22. Price
Unclassified	Unclassified	639	

NASA-Langley, 1991